Lecture Notes in Earth System Sciences
LNESS

Olga V. Frank-Kamenetskaya
Dmitry Yu. Vlasov
Elena G. Panova
Sofia N. Lessovaia *Editors*

Processes and Phenomena on the Boundary Between Biogenic and Abiogenic Nature

Springer

Lecture Notes in Earth System Sciences

Series Editors

Philippe Blondel, Department of Physics, University of Bath, Bath, Avon, UK
Joachim Reitner, Göttingen, Germany
Kurt Stüwe, Graz, Austria
Martin H. Trauth, Potsdam, Brandenburg, Germany
David A. Yuen, Department of Geology and Geophysics, University of Minnesota, Minneapolis, MN, USA

Founding Editors

G. M. Friedman, Brooklyn, USA
A. Seilacher, Tübingen, USA

The Lecture Notes in Earth System Science (LNESS) series reports on new developments in research and teaching in the entire field of earth system science: from the focused study of phenomena on the nano and micro-scales to the entire earth system including its early formation, evolution and future status. The series is thoroughly interdisciplinary presenting studies of the litho-, atmo-, hydro- and biospheres and humanities interactions with them. The series publishes: monographs on advanced topics, technical reports of high quality and broad interest and reports of workshops, expeditions and surveys, provided they are of exceptional interest and focused on a single topic. As the name implies, the submission of manuscripts based on advanced courses such as collections of lectures and tutorials, course materials for laboratory and field courses and summer schools is highly encouraged. The Lecture Notes in Earth System Science (LNESS) is now also the home of Springer Earth Sciences Open Access proceedings. Conference proceedings published in the series are free to read online under the Creative Commons License Agreement whereby the copyright of the contributions remains with the authors.

More information about this series at http://www.springer.com/series/10529

Olga V. Frank-Kamenetskaya ·
Dmitry Yu. Vlasov · Elena G. Panova ·
Sofia N. Lessovaia
Editors

Processes and Phenomena on the Boundary Between Biogenic and Abiogenic Nature

Springer

Editors
Olga V. Frank-Kamenetskaya
Department of Crystallography
Saint Petersburg State University
Saint Petersburg, Russia

Elena G. Panova
Department of Geochemistry
Saint Petersburg State University
Saint Petersburg, Russia

Dmitry Yu. Vlasov
Department of Botany
Saint Petersburg State University
Saint Petersburg, Russia

Sofia N. Lessovaia
Department of Physical Geography and Landscape Planning
Saint Petersburg State University
Saint Petersburg, Russia

ISSN 2193-8571 ISSN 2193-858X (electronic)
Lecture Notes in Earth System Sciences
ISBN 978-3-030-21613-9 ISBN 978-3-030-21614-6 (eBook)
https://doi.org/10.1007/978-3-030-21614-6

© Springer Nature Switzerland AG 2020
This work is subject to copyright. All rights are reserved by the Publisher, whether the whole or part of the material is concerned, specifically the rights of translation, reprinting, reuse of illustrations, recitation, broadcasting, reproduction on microfilms or in any other physical way, and transmission or information storage and retrieval, electronic adaptation, computer software, or by similar or dissimilar methodology now known or hereafter developed.
The use of general descriptive names, registered names, trademarks, service marks, etc. in this publication does not imply, even in the absence of a specific statement, that such names are exempt from the relevant protective laws and regulations and therefore free for general use.
The publisher, the authors and the editors are safe to assume that the advice and information in this book are believed to be true and accurate at the date of publication. Neither the publisher nor the authors or the editors give a warranty, expressed or implied, with respect to the material contained herein or for any errors or omissions that may have been made. The publisher remains neutral with regard to jurisdictional claims in published maps and institutional affiliations.

This Springer imprint is published by the registered company Springer Nature Switzerland AG
The registered company address is: Gewerbestrasse 11, 6330 Cham, Switzerland

Preface

The book represents a collection of papers presented at VI International Symposium "Biogenic-abiogenic interactions in natural and anthropogenic systems" which was devoted to the 150th anniversary of the St. Petersburg Society of Naturalists. Symposium was held on September 24–27, 2018, in Saint Petersburg, Russia. The previous symposiums on this topic took place in St. Petersburg in 2002, 2004, 2007, 2011, and 2014.

St. Petersburg Society of Naturalists is one of the oldest natural science societies of Russia. It was founded in 1868. The first president of Society Karl Kessler was the rector of St. Petersburg State University. Presidents of the St. Petersburg Society of Naturalists were such famous scientists as Prof. Beketov, Academician Vernadsky, Academician Ukhtomsky, and others. The priorities of the society in our days are complex interdisciplinary study in the different fields of earth science and life science.

According to the results of the previous symposium, a monograph was published in 2016 by Springer. The present book continues to discuss wide range of issues connecting with biogenic and abiogenic interactions in lithosphere, biosphere, and technosphere. It devoted to the processes and phenomena on the boundary between biogenic and abiogenic nature. The book has an interdisciplinary character and contains eight parts:

1. Biomineralization and Nature-like Materials and Technologies
2. Methods for Studying the Interactions in Biogenic–Abiogenic Systems
3. Geochemistry of Biogenic–Abiogenic Systems
4. Biomineral Interactions in Soil
5. Effect of Microorganisms on Natural and Artificial Materials
6. Organic Mineralogy
7. Medical Geology
8. Philosophical and Historical Aspects

In part "Biomineralization and Nature-like Materials and Technologies," two reviews are devoted to collagen-based biomaterials for tissue engineering applications (Radhakrishnan et al.) and chitosan and chitosan-based nanocomposites for

applications as a drug delivery carrier (Nivethaa et al.). The results of the following experimental studies are presented: on the formation of calcium and magnesium phosphates of the renal stones depending on the composition of the crystallization medium (Kuz'mina et al.), on the solubility of hydroxyapatite as a function of solution composition (Kuranov et al.), on the pathogenic phase formation in human blood plasma (Golovanova), on the features of molecular water in bone apatite (Kalinichenko et al.), and on the effect of heat treatment and bioresorbability of silicate containing biological apatites (Panova, Golovanova).

The part "Methods for Studying the Interactions in Biogenic–Abiogenic Systems" focuses on a variety of methods and approaches used in studying such systems. The following topics are regarded: tool supply and application examples of singlet oxygen monitoring in the lower atmosphere (Chelibanov et al.), determination of water-soluble fraction in soils (Panova et al.), using of X-RAY computed microtomography in the study of hard tooth tissue (Pixur et al.), and experimental–theoretical evaluation of the biogenic peat system affecting moisture transfer (Kremcheev et al.). Special attention is paid to methods of research of the role of microorganisms in different processes: oil biodegradation (Svarovskaya et al.), stromatolites formation (Litvinova), and change in wettability of clays (Sofinskaya et al.).

Geochemical aspects of biogenic–abiogenic interactions have been discussed in the part "Geochemistry of Biogenic–Abiogenic Systems." The result of the experiment with using biochar for neutralizing wastewater olive plant was considered by Obiageli et al. M. Charykova and V. Krivovichev show data on thermodynamic stability of arsenic minerals in the environment. L. Inisheva and co-authors consider biogenic and abiogenic forms of migration compounds in swamps of different genesis. The work of S. Lebedev et al. is connected with assessment of long-lived radionuclides (^{3}H, ^{14}C) and heavy metals in snow cover of urban areas. The work of D. Rybakov is devoted to biogeochemistry of soils in the industrial pollution zone in Petrozavodsk. The special attention is given to biogeochemical processes in plain forest ecosystem (Torbatov et al.).

In part "Biomineral Interactions in Soil," different aspects of biogenic–abiogenic interactions have shown based on soil studies. The result of the experiment with pine-derived biochar, which has attracted as a possible way to sequester carbon from the atmosphere in the soil, illustrated that the biochar layers formed preferred zones for root development and microbial proliferation compared to the sandy layers (Olivier et al.). The specificity of soil organic matter was revealed based on study of phylogenetic structure of prokaryotic community in the forest and urban soils (Aparin et al.) and humic substances formation and stabilization in suspended soils of tropical forest (Rodina et al.). The micromorphology study of biotic–abiotic interactions was focused on soils affected by waste mining and processing production of sulfide-tungsten deposits, which lead to soil contamination by toxic elements (Doroshkevich et al.), and soils in the Antarctic region to reveal the specific of their structural organization (Lupachev et al.). The special attention was given to biotic–abiotic interactions in the cold environments, including biogenic-induced rock weathering (Lessovaia et al.) and pedogenesis in the different regions of

Antarctica (Lupachev et al., Shamilishvili et al.). These findings are corrected the most acceptable scenario of abiotic physical processes development in the cold environments.

In part "Effect of Microorganisms on Natural and Artificial Materials," the different aspects of microbial influence on different substrates are discussed. Special attention is paid to the problem of biological damage of cultural heritage objects in various ecological conditions (Lobzova et al., Vlasov et al.). In these works, the role of microorganisms in the transformation of natural stone is shown. The role of microorganisms is also considered in the corrosion processes of other materials (Simakova and Leonova). Particular attention is given to study of microbial communities on the different museum objects (Zaitsev et al., Abramova). The authors note the ability of biodestructors to influence on people's health. Soil microorganisms are considered in the context of biogenic–abiogenic interactions. They can develop under various conditions, including technogenic pollution (Redkina et al.) and exposure to VUV radiation (Zvereva and Kirtsideli). Among the experimental works of this part, it is necessary to note the study of the processes of crystallization of calcium oxalate hydrates by interaction of apatites and fossilizes tooth tissue with fungus of *Aspergillus niger* (Zelenskaya et al.).

In part "Organic Mineralogy," the structure, symmetry, formation, and transformation of organic matter in nature are discussed. The following topics are regarded: the generality of organic and inorganic (Oleynikova et al.); limits of solid solutions and polymorph diversity of acids with chiral molecules (Kotelnikova et al.); geometry, classification, and nomenclature of capsids of viruses (Voytekhovsky); calcium ion complexes with amino acids in human body (Tomashevskiy et al.); paleobiological significance of carbon isotope ratios in the hard tissues of conodont elements (Zhuravlev et al.).

Different aspects of biogenic–abiogenic interactions in human body have been discussed in the part "Medical Geology." The common properties of some geophagic clay based on their mineral composition and landscapes specificity were studied (Ekosse et al.). The accumulation of heavy metals in hair, depending on the state of the environment of different territories of Kola North (Belisheva) and Bashkortostan (Semenova et al.) are considered. The possibility of physicochemical modeling in the study of affecting of chemical composition of water on the health of the population is analyzed (Mazukhina et al.; Masloboev et al.).

In part "Philosophical and Historical Aspects," the time and space of biological morphogenesis are regarded as phenomena arising from the flow of energy in the Universe and their own structure set by this process (Sumin and Sumina). The environmental problems are regarded in a historical retrospect. The impact of geodynamic processes on the emergence and evolution on the man is discussed (Nesterov et al.).

Saint Petersburg, Russia

Olga V. Frank-Kamenetskaya
Dmitry Yu. Vlasov
Elena G. Panova
Sofia N. Lessovaia

Contents

Part I Biomineralization and Nature-Like Materials and Technologies

1 Collagen Based Biomaterials for Tissue Engineering Applications: A Review 3
Socrates Radhakrishnan, Sakthivel Nagarajan, Mikhael Bechelany and S. Narayana Kalkura

2 Chitosan and Chitosan Based Nanocomposites for Applications as a Drug Delivery Carrier: A Review 23
E. A. K. Nivethaa, Catherine Ann Martin, Olga V. Frank-Kamenetskaya and S. Narayana Kalkura

3 Solubility of Hydroxyapatite as a Function of Solution Composition (Experiment and Modeling) 39
George Kuranov, Konstantin Mikhelson and Alexandra Puzyk

4 Thermodynamics and Kinetics of Crystallization of Mineral Phases of Vascular Calcificates 59
Olga A. Golovanova

5 Water in Termally Treated Bioapatites and Their Synthetic Analogues: ^{1}H NMR Data 79
Olena A. Kalinichenko, Aleksandr B. Brik, Olga V. Frank-Kamenetskaya, Anatoliy M. Kalinichenko, Natalya O. Dudchenko and Anton M. Nikolaev

6 The Formation of Calcium and Magnesium Phosphates of the Renal Stones Depending on the Composition of the Crystallization Medium 107
Mariya A. Kuz'mina, Anton M. Nikolaev and Olga V. Frank-Kamenetskaya

7 The Effect of Heat-Treatment and Bioresorbability of Silicate-Containing Hydroxyapatite 119
Tatyana Panova and Olga A. Golovanova

Part II Methods for Studying the Interactions in Biogenic–Abiogenic Systems

8 Singlet Oxygen in the Lower Atmosphere: Origin, Measurement and Participation in Processes and Phenomena at the Boundary Between Biogenic and Abiogenic Nature 137
Vladimir P. Chelibanov, Ivan V. Chelibanov, Olga V. Frank-Kamenetskaya, Egor A. Iasenko, Alexandr M. Marugin and Olga A. Pinchuk

9 Determination of Water-Soluble Fraction in Soils 155
Elena G. Panova, Kseniia A. Bakhmatova, Natalia N. Matinian and Galina A. Oleynikova

10 Contact Angle Hysteresis in the Clay-Water-Air System of Soils 179
Oxana A. Sofinskaya, Akhmet A. Galeev and Eduard A. Korolev

11 Bio-inert Interactions in an Oil—Microorganisms System 195
Lidia I. Svarovskaya, Andrey Y. Manakov, Lyubov K. Altunina, Larisa A. Strelets and Andrey S. Stoporev

12 Biogenic–Abiogenic Interactions in Stromatolites: Study Possibilities and Outlooks 207
Tatiana V. Litvinova

13 Using X-ray Computed Microtomography for Investigation of the Morphology and Composition of the Hard Tooth Tissue . . . 221
Oksana L. Pikhur, Yulia V. Plotkina and Alexander M. Kulkov

14 Changing Hydraulic Conductivity After Rupturing Native Structure of Peat Under Limited Evaporation Conditions 233
Eldar A. Kremcheev, Dmitriy O. Nagornov and Dinara A. Kremcheeva

Part III Geochemistry of Biogenic-Abiogenic Systems

15 Mineral Systems and Thermodynamic Stability of Arsenic Minerals in the Environment 259
Marina V. Charykova and Vladimir G. Krivovichev

16 Abiogenic and Biogenic Forms of Migration Compounds in Swamps of Different Genesis 277
Lidia I. Inisheva, Ekaterina V. Porokhina, Alla V. Golovchenko and Lech W. Szajdak

17 Assessment of Long-Lived Radionuclides (^{3}H, ^{14}C) and Heavy Metals in Snow Cover of Urban Areas as Indicators of Environmental Pollution (St. Petersburg, Russia) 297
Sergey V. Lebedev, Marianna A. Kulkova, Larisa M. Zarina and Evgeny M. Nesterov

18 Experience of Large-Scale Analysis of the Spatial Patterns of Plain Forest Ecosystem Productivity and Biogeochemical Processes 315
Sergei A. Tobratov and Olga S. Zheleznova

19 Heavy Metals and Metalloids in Soils and Macromycetes from the Accumulated Environmental Damage Zone in Petrozavodsk, Republic of Karelia 345
Dmitrii S. Rybakov

20 Assessment of Biochar Potential to Neutralize the Effect of Olive Mill Wastewater on Plant Growth in Alkaline Sand 363
Obiageli P. Umeugochukwu, Andrei B. Rozanov and Ailsa G. Hardie

Part IV Biomineral Interactions in Soil

21 Macroscopic Observation of Biotic-Abiotic Interactions in Biochar Layers Within a Sandy Soil in a Pot Trial with Wheat *Triticum aestivum* 383
Charl F. Olivier, Ian L. Belford, Leandra Moller, Andrei B. Rozanov, Alf Botha and Ailsa G. Hardie

22 Structure of Microbial Community in Forest and Anthropogenic Changed Soils of Megalopolis (St. Petersburg, Russia) 395
Boris F. Aparin, Elena Yu. Sukhacheva, Arina A. Kichko, Evgeny E. Andronov and Yaroslavna V. Valchenko

23 Humic Substances Formation as a Result of Biogenic-Abiogenic Interactions in Epiphytic Structures of the South Vietnam Tropical Forest 417
Oksana A. Rodina, Evgeny V. Abakumov, Alen K. Eskov and Nikolay G. Prilepskiy

24 Soils of Technogenic Landscapes from Tungsten Mine: Micromorphological Structure, Mineral and Chemical Compositions 435
Svetlana G. Doroshkevich, Olga K. Smirnova and Anastasiya A. Sheshukova

25 Biogenic-Abiogenic Interactions and Soil Formation in Extreme Conditions of Untersee Oasis, Surroundings of Lake Untersee, Central Queen Maud Land, East Antarctica 457
George Shamilishvili, Evgeny V. Abakumov and Dale Andersen

26 Levels of Biogenic-Abiogenic Interaction and Structural Organization of Soils and Soil-Like Bodies in Antarctica 481
Aleksei V. Lupachev, Stanislav V. Gubin and Evgeny V. Abakumov

27 Modeling Biogenic Weathering of Rocks from Soils of Cold Environments 501
Sofia N. Lessovaia, Ruben Gerrits, Anna A. Gorbushina, Yury S. Polekhovsky, Stefan Dultz and Gennady G. Kopitsa

Part V Effect of Microorganisms on Natural and Artificial Materials

28 Crusts and Incrustations on Natural and Architectural Objects 519
Raisa V. Lobzova, Oxana V. Karimova and Elena I. Antonova

29 Biofilms on Granite Rapakivi in Natural Outcrops and Urban Environment: Biodiversity, Metabolism and Interaction with Substrate 535
Dmitry Yu. Vlasov, Elena G. Panova, Marina S. Zelenskaya, Alexey D. Vlasov, Katerina V. Sazanova, Oksana A. Rodina and Olga A. Pavlova

30 Microorganisms of the Technogenic Landscapes: The Case of Nepheline-Containing Sands, the Murmansk Region 561
Vera V. Redkina, Maria V. Korneykova and Regina R. Shalygina

31 Crystallization of Calcium Oxalate Hydrates by Interaction of Apatites and Fossilized Tooth Tissue with Fungus *Aspergillus niger* 581
Marina S. Zelenskaya, Aleksei V. Rusakov, Olga V. Frank-Kamenetskaya, Dmitry Yu. Vlasov, Alina R. Izatulina and Mariya A. Kuz'mina

32 Features of the Effect of VUV Radiation on Microfungi from Polar Regions 605
Galina N. Zvereva and Irina Yu. Kirtsideli

33 Sol-Gel Derived TiO_2 and Epoxy-Titanate Protective Coatings: Structure, Property, Fungicidal Activity and Biomineralization Effects 619
Olga A. Shilova, Dmitry Yu. Vlasov, Marina S. Zelenskaya, Yuliya V. Ryabusheva, Tamara V. Khamova, Irina B. Glebova, Alexandr A. Sinelnikov, Alexandr M. Marugin and Olga V. Frank-Kamenetskaya

34 The Impact of Microorganisms on Monuments in the Underground Archaeological Museum of Moscow 639
Tamara T. Abramova

35 Biocorrosion in the Central Heating System 657
Yulia S. Simakova and Liubov V. Leonova

36 Microbiology of the Laetolil Tuff 7 with 3.66 Ma *Australopithecus Afarensis* Footprints, Ngorongoro Conservation Area, Tanzania 669
Anatoly N. Zaitsev, Dmitry Yu. Vlasov, Marina S. Zelenskaya, Olga A. Zaitseva, Olga A. Pavlova, Anton R. Chakhmouradian, Anton I. Savchenok, Larissa Leach, Michael Leach and Joshua Mwankunda

Part VI Organic Mineralogy

37 Acids with Chiral Molecules as Essential Organic Compounds of Biogenic–Abiogenic Systems 695
Elena N. Kotelnikova, Anton I. Isakov, Lyudmila Yu. Kryuchkova, Andrey A. Zolotarev, Jr., Sergey N. Bocharov and Heike Lorenz

38 Geometry, Classification and Nomenclature of Capsids of Icosahedral Viruses 721
Yury L. Voytekhovsky

39 On the Generality of Organic and Inorganic 729
Galina A. Oleynikova, Elena G. Panova and Yaroslav Yu. Fadin

40 Carbon Isotope Ratios in the Apatite-Protein Composites of Conodont Elements—Palaeobiological Proxy 749
Andrey V. Zhuravlev, Artem N. Plotitsyn and Denis A. Gruzdev

41 Coordination Compounds of Calcium Ions (II) with the Biogenic Amino Acids: Their Stability, Kinetic and Thermodynamic Characteristics of the Formation 765
Ivan A. Tomashevskiy, Olga A. Golovanova and Svetlana V. Anisina

Part VII Medical Geology

42 Landscape Settings and Mineralogy of Some Geophagic Clay Occurrences in South Africa 785
Georges-I. Ekosse, Kirill V. Chistyakov, Andrei B. Rozanov, Nadezhda N. Bashkirova, Stefan Dultz, Yury S. Polekhovsky and Sofia N. Lessovaia

43 Comparative Analysis of Morbidity and Elemental Composition of Hair Among Children Living on Different Territories of the Kola North 803
Natalia K. Belisheva

44 Formation of the Chemical Composition of Underground Waters of the Khibiny Mountain Range (On the Example of One Water Intake) 829
Vladimir A. Masloboev, Vladimir I. Pozhilenko, Sergey S. Sandimirov, Svetlana V. Drogobuzhskaya, Stanislav V. Ivanov, Anton V. Gudkov, Pavel S. Tereshchenko and Svetlana I. Mazukhina

45 Heavy Metal Content in Soils and Hair of the Inhabitants Near Copper Zinc Mine (Bashkortostan, Russia) 847
Irina N. Semenova, Yuliya S. Rafikova, Rezeda F. Khasanova and Yalil T. Suyundukov

46 Modeling: The New Prospects of Studying Biological Systems as Illustrated by the Human Stomach 863
Svetlana I. Mazukhina, Konstantin V. Chudnenko, Pavel S. Tereshchenko, Svetlana V. Drogobuzhskaya and Stanislav V. Ivanov

Part VIII Philosophical and Historical Aspects

47 Time and Space of Biological Morphogenesis 881
Dmitry L. Sumin and Evgeniya L. Sumina

48 The Impact of Geodynamic Processes on the Emergence and Evolution of the Man 891
Evgeny M. Nesterov, Peter Mavopulos and Pavel I. Egorov

Index 903

Contributors

Evgeny V. Abakumov Department of Applied Ecology, Saint Petersburg State University, Saint Petersburg, Russian Federation

Tamara T. Abramova Geological Faculty, Lomonosov Moscow State University, Moscow, Russia

Lyubov K. Altunina Institute of Petroleum Chemistry SB RAS, Tomsk, Russia

Dale Andersen Carl Sagan Center for the Study of Life in the Universe, SETI Institute, Mountain View, CA, USA

Evgeny E. Andronov All-Russia Research Institute for Agricultural Microbiology, Saint Petersburg, Russia

Svetlana V. Anisina F. M. Dostoevsky Omsk State University, Omsk, Russia

Elena I. Antonova State Research Institute for Restoration, Moscow, Russia

Boris F. Aparin Saint Petersburg State University, Saint Petersburg, Russia; The Dokuchaev Central Soil Museum, Saint Petersburg, Russia

Kseniia A. Bakhmatova Saint Petersburg State University, Saint Petersburg, Russia

Nadezhda N. Bashkirova Higher School of State Audit, Moscow State University, Moscow, Russia

Mikhael Bechelany Institut Européen des Membranes, IEM-UMR 5635, ENSCM, CNRS, Université de Montpellier, Montpellier, France

Ian L. Belford Department of Microbiology, Stellenbosch University, Matieland, South Africa

Natalia K. Belisheva Research Centre for Human Adaptation in the Arctic, KSC RAS, Apatity, Russia

Sergey N. Bocharov Saint Petersburg State University, Saint Petersburg, Russia

Alf Botha Department of Microbiology, Stellenbosch University, Matieland, South Africa

Aleksandr B. Brik M.P. Semenenko Institute of Geochemistry, Mineralogy and Ore Formation of the National Academy of Sciences of Ukraine, Kyiv, Ukraine

Anton R. Chakhmouradian Department of Geological Sciences, University of Manitoba, Winnipeg, Canada

Marina V. Charykova Saint Petersburg University, Saint Petersburg, Russia

Ivan V. Chelibanov Herzen State Pedagogical University of Russia, Saint Petersburg, Russia

Vladimir P. Chelibanov OPTEC JSC, Saint Petersburg, Russia

Kirill V. Chistyakov Institute of Earth Sciences, Saint Petersburg State University, Saint Petersburg, Russia

Konstantin V. Chudnenko Russia Federal State Budgetary Institution of Science A.P. Vinogradov Institute of Geochemistry SB RAS, Irkutsk, Russia

Svetlana G. Doroshkevich Geological Institute of SB RAS, Ulan-Ude, Russia

Svetlana V. Drogobuzhskaya Tananaev Institute of Chemistry—Subdivision of the Federal Research Centre, "Kola Science Centre of the Russian Academy of Sciences", Akademgorodok, Apatity, Russia

Natalya O. Dudchenko M.P. Semenenko Institute of Geochemistry, Mineralogy and Ore Formation of the National Academy of Sciences of Ukraine, Kyiv, Ukraine

Stefan Dultz Institute of Soil Science, Leibniz Universität Hannover, Hannover, Germany

Pavel I. Egorov Herzen State Pedagogical University of Russia, Saint Petersburg, Russia

Georges-I. Ekosse University of Venda, Thohoyandou, Limpopo, South Africa

Alen K. Eskov Russian Academy of Sciences, Moscow, Russia

Yaroslav Yu. Fadin All Russian Geological Institute, Saint Petersburg, Russia

Olga V. Frank-Kamenetskaya Department of Crystallography, Institute of Earth Sciences, Saint Petersburg State University, Saint Petersburg, Russia;
Institute of Silicate Chemistry, Russian Academy of Sciences, Saint Petersburg, Russia;
Saint Petersburg State Electrotechnical University "LETI", Saint Petersburg, Russia

Akhmet A. Galeev Federal University, Kazan (Volga Region), Russia

Ruben Gerrits Department of Earth Sciences and Department of Biology Chemistry Pharmacy, Freie Universität Berlin, Berlin, Germany;
Federal Institute of Materials Research and Testing (BAM), Berlin, Germany

Irina B. Glebova Institute of Silicate Chemistry, Russian Academy of Sciences, Saint Petersburg, Russia

Olga A. Golovanova F. M. Dostoevsky Omsk State University, Omsk, Russia

Alla V. Golovchenko Tomsk State Pedagogical University, Tomsk, Russia

Anna A. Gorbushina Federal Institute of Materials Research and Testing (BAM), Berlin, Germany;
Department of Earth Sciences and Department of Biology Chemistry Pharmacy, Freie Universität Berlin, Berlin, Germany

Denis A. Gruzdev Institute of Geology, Komi SC UrB RAS, Syktyvkar, Russia

Stanislav V. Gubin Institute of Physico-Chemical and Biological Problems in Soil Science RAS, Moscow, Russian Federation

Anton V. Gudkov Geological Institute—Subdivision of the Federal Research Centre "Kola Science Centre of the Russian Academy of Sciences", Apatity, Murmansk Region, Russia

Ailsa G. Hardie Department of Soil Science, Stellenbosch University, Matieland, South Africa

Egor A. Iasenko OPTEC JSC, Saint Petersburg, Russia

Lidia I. Inisheva Tomsk State Pedagogical University, Tomsk, Russia

Anton I. Isakov Saint Petersburg State University, Saint Petersburg, Russia

Stanislav V. Ivanov Luzin Institute for Economic Studies—Subdivision of the Federal Research Centre, "Kola Science Centre of the Russian Academy of Sciences", Apatity, Russia

Alina R. Izatulina Saint Petersburg State University, Saint Petersburg, Russia

Anatoliy M. Kalinichenko M.P. Semenenko Institute of Geochemistry, Mineralogy and Ore Formation of the National Academy of Sciences of Ukraine, Kyiv, Ukraine

Olena A. Kalinichenko M.P. Semenenko Institute of Geochemistry, Mineralogy and Ore Formation of the National Academy of Sciences of Ukraine, Kyiv, Ukraine

S. Narayana Kalkura Crystal Growth Centre, Anna University, Chennai, India

Oxana V. Karimova Institute of Geology of Ore Deposits RAS (IGEM RAS), Moscow, Russia

Tamara V. Khamova Institute of Silicate Chemistry, Russian Academy of Sciences, Saint Petersburg, Russia

Rezeda F. Khasanova Institute for Strategic Studies of the Republic of Bashkortostan, Sibay, Russia;
Sibay branch of Bashkir state University, Sibay, Russia

Arina A. Kichko All-Russia Research Institute for Agricultural Microbiology, Saint Petersburg, Russia

Irina Yu. Kirtsideli Komarov Botanical Institute RAS, Saint Petersburg, Russia

Gennady G. Kopitsa B.P. Konstantinov Petersburg Nuclear Physics Institute NRC KI, Gatchina, Russia;
I.V. Grebenshchikov Institute of Silicate Chemistry RAS, Saint Petersburg, Russia

Maria V. Korneykova Institute of North Industrial Ecology Problems—Subdivision of the Federal Research Centre "Kola Science Centre of Russian Academy of Science", Apatity, Russia

Eduard A. Korolev Federal University, Kazan (Volga Region), Russia

Elena N. Kotelnikova Saint Petersburg State University, Saint Petersburg, Russia

Eldar A. Kremcheev Saint Petersburg Mining University, Saint Petersburg, Russia

Dinara A. Kremcheeva Saint Petersburg Mining University, Saint Petersburg, Russia

Vladimir G. Krivovichev Saint Petersburg University, Saint Petersburg, Russia

Lyudmila Yu. Kryuchkova Saint Petersburg State University, Saint Petersburg, Russia

Alexander M. Kulkov Saint Petersburg State University, Saint Petersburg, Russia

Marianna A. Kulkova Herzen State Pedagogical University of Russia, Saint Petersburg, Russia

George Kuranov Institute of Chemistry, Saint Petersburg State University, Saint Petersburg, Russian Federation

Mariya A. Kuz'mina Saint Petersburg State University, Saint Petersburg, Russia

Larissa Leach GMP Consulting Engineers Ltd., Arusha, Tanzania

Michael Leach GMP Consulting Engineers Ltd., Arusha, Tanzania

Sergey V. Lebedev Saint Petersburg State University, Saint Petersburg, Russia

Liubov V. Leonova Institute of Geology and Geochemistry, Urals Branch of RAS, Yekaterinburg, Russia

Sofia N. Lessovaia Institute of Earth Sciences, Saint Petersburg State University, Saint Petersburg, Russia

Tatiana V. Litvinova Geological Institute, Russian Academy of Sciences, Moscow, Russia

Raisa V. Lobzova State Research Institute for Restoration, Moscow, Russia

Heike Lorenz Max Planck Institute for Dynamics of Complex Technical Systems, Magdeburg, Germany

Aleksei V. Lupachev Institute of Physico-Chemical and Biological Problems in Soil Science RAS, Moscow, Russian Federation

Andrey Y. Manakov Institute of Inorganic Chemistry SB RAS, Novosibirsk, Russia

Catherine Ann Martin Crystal Growth Centre, Anna University, Chennai, India

Alexandr M. Marugin OPTEC JSC, Saint Petersburg, Russia

Vladimir A. Masloboev Institute of North Industrial Ecology Problems—Subdivision of the Federal Research Centre "Kola Science Centre of the Russian Academy of Sciences", Apatity, Russia

Natalia N. Matinian Saint Petersburg State University, Saint Petersburg, Russia

Peter Mavopulos Aristotle University of Thessaloniki, Thessaloniki, Greece

Svetlana I. Mazukhina Institute of North Industrial Ecology Problems—Subdivision of the Federal Research Centre "Kola Science Centre of the Russian Academy of Sciences", Akademgorodok, Apatity, Russia

Konstantin Mikhelson Institute of Chemistry, Saint Petersburg State University, Saint Petersburg, Russian Federation

Leandra Moller Department of Microbiology, Stellenbosch University, Matieland, South Africa

Joshua Mwankunda Ngorongoro Conservation Area Authority, Arusha, Tanzania

Sakthivel Nagarajan Institut Européen des Membranes, IEM-UMR 5635, ENSCM, CNRS, Université de Montpellier, Montpellier, France

Dmitriy O. Nagornov Saint Petersburg Mining University, Saint Petersburg, Russia

Evgeny M. Nesterov Herzen State Pedagogical University of Russia, Saint Petersburg, Russia

Anton M. Nikolaev Saint Petersburg State University, Saint Petersburg, Russia; Institute of Silicate Chemistry RAS, Saint Petersburg, Russia

E. A. K. Nivethaa Crystal Growth Centre, Anna University, Chennai, India

Galina A. Oleynikova All Russian Geological Institute, Saint Petersburg, Russia; Russian Geological Research Institute, Saint Petersburg, Russia

Charl F. Olivier Department of Soil Science, Stellenbosch University, Matieland, South Africa

Elena G. Panova Institute of Earth Science, Saint Petersburg State University, Saint Petersburg, Russia

Tatyana Panova F.M. Dostoevsky State University, Omsk, Russia

Olga A. Pavlova Beagle Ltd., Saint Petersburg, Russia;
Resource Center "Development of Cellular and Molecular Technologies", Saint Petersburg State University, Saint Petersburg, Russia

Oksana L. Pikhur Institute of Bioregulation and Gerontology, Saint Petersburg, Russia

Olga A. Pinchuk ITMO University, Saint Petersburg, Russia

Artem N. Plotitsyn Institute of Geology, Komi SC UrB RAS, Syktyvkar, Russia

Yulia V. Plotkina Institute of Precambrian Geology and Geochronology RAS, Saint Petersburg, Russia

Yury S. Polekhovsky Institute of Earth Sciences, Saint Petersburg State University, Saint Petersburg, Russia

Ekaterina V. Porokhina Tomsk State Pedagogical University, Tomsk, Russia

Vladimir I. Pozhilenko Geological Institute—Subdivision of the Federal Research Centre "Kola Science Centre of the Russian Academy of Sciences", Apatity, Murmansk Region, Russia

Nikolay G. Prilepskiy Lomonosov Moscow State University, Moscow, Russia

Alexandra Puzyk Institute of Chemistry, Saint Petersburg State University, Saint Petersburg, Russian Federation

Socrates Radhakrishnan Crystal Growth Centre, Anna University, Chennai, India

Yuliya S. Rafikova Institute for Strategic Studies of the Republic of Bashkortostan, Sibay, Russia

Vera V. Redkina Institute of North Industrial Ecology Problems—Subdivision of the Federal Research Centre "Kola Science Centre of Russian Academy of Science", Apatity, Russia

Oksana A. Rodina Department of Applied Ecology, Saint Petersburg State University, Saint Petersburg, Russian Federation

Andrei B. Rozanov Department of Soil Science, Stellenbosch University, Stellenbosch, South Africa

Aleksei V. Rusakov Saint Petersburg State University, Saint Petersburg, Russia

Yuliya V. Ryabusheva Saint Petersburg State University, Saint Petersburg, Russia

Dmitrii S. Rybakov Karelian Research Centre, RAS, Institute of Geology, Petrozavodsk, Russia

Sergey S. Sandimirov Research Centre for Human Adaptation in the Arctic—Branch of the Federal Research Centre "Kola Science Centre of the Russian Academy of Science", Apatity, Russia

Anton I. Savchenok Department of Mineralogy, Saint Petersburg State University, Saint Petersburg, Russia

Katerina V. Sazanova Botanical Institute of the Russian Academy of Sciences, Saint Petersburg, Russia

Irina N. Semenova Institute for Strategic Studies of the Republic of Bashkortostan, Sibay, Russia;
Sibay branch of Bashkir state University, Sibay, Russia

Regina R. Shalygina Institute of North Industrial Ecology Problems—Subdivision of the Federal Research Centre "Kola Science Centre of Russian Academy of Science", Apatity, Russia

George Shamilishvili Saint Petersburg State University, Saint Petersburg, Russian Federation

Anastasiya A. Sheshukova Saint Petersburg State University, Saint Petersburg, Russia

Olga A. Shilova Institute of Silicate Chemistry, Russian Academy of Sciences, Saint Petersburg, Russia;
Saint Petersburg State Electrotechnical University "LETI", Saint Petersburg, Russia

Yulia S. Simakova Institute of Geology, Komi Science Center, Urals Branch of RAS, Syktyvkar, Russia

Alexandr A. Sinelnikov Voronezh State University, Voronezh, Russia

Olga K. Smirnova Geological Institute of SB RAS, Ulan-Ude, Russia

Oxana A. Sofinskaya Federal University, Kazan (Volga Region), Russia

Andrey S. Stoporev Institute of Inorganic Chemistry SB RAS, Novosibirsk, Russia

Larisa A. Strelets Institute of Petroleum Chemistry SB RAS, Tomsk, Russia

Elena Yu. Sukhacheva Saint Petersburg State University, Saint Petersburg, Russia;
The Dokuchaev Central Soil Museum, Saint Petersburg, Russia

Dmitry L. Sumin Network of Independent Scientists (NISEEB), Moscow, Russia

Evgeniya L. Sumina Department of Paleontology, Geological Faculty, M.V. Lomonosov MSU, Moscow, Russia

Yalil T. Suyundukov Institute for Strategic Studies of the Republic of Bashkortostan, Sibay, Russia;
Sibay branch of Bashkir state University, Sibay, Russia

Lidia I. Svarovskaya Institute of Petroleum Chemistry SB RAS, Tomsk, Russia

Lech W. Szajdak Tomsk State Pedagogical University, Tomsk, Russia

Pavel S. Tereshchenko Research Centre for Human Adaptation, Arctic—Branch of the Federal Research Centre, "Kola Science Centre of the Russian Academy of Science", Akademgorodok, Apatity, Russia

Sergei A. Tobratov Ryazan State University Named for S.A. Yesenin, Ryazan, Russia

Ivan A. Tomashevskiy F. M. Dostoevsky Omsk State University, Omsk, Russia

Obiageli P. Umeugochukwu Department of Soil Science, Stellenbosch University, Matieland, South Africa;
Department of Soil Science, Federal University of Technology, Minna, Niger State, Nigeria

Yaroslavna V. Valchenko The Dokuchaev Central Soil Museum, Saint Petersburg, Russia

Alexey D. Vlasov The Archive of the Russian Academy of Sciences, Saint Petersburg, Russia

Dmitry Yu. Vlasov Saint Petersburg State University, Saint Petersburg, Russia

Yury L. Voytekhovsky Saint Petersburg Mining University, Saint Petersburg, Russia

Anatoly N. Zaitsev Department of Mineralogy, Saint Petersburg State University, Saint Petersburg, Russia;
Image and Analysis Centre, The Natural History Museum, London, UK

Olga A. Zaitseva The Manege, Central Exhibition Hall, Saint Petersburg, Russia

Larisa M. Zarina Herzen State Pedagogical University of Russia, Saint Petersburg, Russia

Marina S. Zelenskaya Saint Petersburg State University, Saint Petersburg, Russia

Olga S. Zheleznova Ryazan State University Named for S.A. Yesenin, Ryazan, Russia

Andrey V. Zhuravlev Institute of Geology, Komi SC UrB RAS, Syktyvkar, Russia

Andrey A. Zolotarev Jr. Saint Petersburg State University, Saint Petersburg, Russia

Galina N. Zvereva State University of Civil Aviation, Saint Petersburg, Russia; S. I. Vavilov State Optical Institute, Saint Petersburg, Russia

Part I
Biomineralization and Nature-Like Materials and Technologies

Chapter 1
Collagen Based Biomaterials for Tissue Engineering Applications: A Review



Socrates Radhakrishnan, Sakthivel Nagarajan, Mikhael Bechelany and S. Narayana Kalkura

Abstract In the search for biomaterials that exhibit both versatility and compatibility with human-tissues, considerable interest has been shown in collagen-based biomaterial for the repair and replacement of the body tissues such as tendons, skin, vascular grafts, heart valves, dental and bones. Some of the general properties of collagen which makes it an interesting biomaterial are the high mechanical strength of the fibers, low antigenicity, its suitability as a substrate for cell growth, and its tunable stability by chemical or physical cross-linking. Collagen based composites are used in various biomedical applications as collagen shields in ophthalmology, sponges for burns and wounds, mini-pellets and tablets for protein delivery, gel formulation in combination with liposome for sustained drug delivery, as controlling material for transdermal delivery, basic matrices for cell culture systems, coating material of metal implant for bone replacement and 3-D printed matrix for various tissue engineering applications. For an adequate biomedical application of collagen, basic knowledge about collagen structure, hierarchical structural organisation and the processing technology in combination with understanding of the physico-chemical properties is of vital importance.

Keywords Biomaterials · Antigenicity · Biomedical · Collagen

1.1 Introduction

Collagen is the most abundant protein responsible for maintaining the structural integrity of vertebrates and many other multicellular organisms. Collagen represents the major structural protein accounting for approximately 30% of proteins found in the vertebrate organism. There are 28 types

S. Radhakrishnan · S. N. Kalkura (✉)
Crystal Growth Centre, Anna University, Chennai 600025, India
e-mail: kalkurasn@annauniv.edu; kalkura@yahoo.com

S. Nagarajan · M. Bechelany
Institut Européen des Membranes, IEM-UMR 5635, ENSCM, CNRS, Université de Montpellier, Montpellier, France

© Springer Nature Switzerland AG 2020

O. V. Frank-Kamenetskaya et al. (eds.), *Processes and Phenomena on the Boundary Between Biogenic and Abiogenic Nature*, Lecture Notes in Earth System Sciences,
https://doi.org/10.1007/978-3-030-21614-6_1

of collagen which have been identified (Gelse et al. 2003). Among these collagen types, type I collagen is the most abundant type found in the extracellular matrix (ECM) of most connective tissues such as tendon and bone (Gelse et al. 2003). Collagen type I is widely used in the fabrication of biomaterials for tissue engineering applications. In this review, we will discuss the structure of collagen, hierarchical structure of collagen, source of collagen, cross-linking of collagen, advantages of collagen over other biomaterials and the biomedical application of collagen based biomaterials. In addition, the challenges faced and solutions regarding collagen based biomedical research is also discussed in conclusion.

1.2 Structure of Collagen Type I

The mature collagen molecule contains three polypeptide helical α chains, two of which are identical, termed α1(I), and one α2(I) chain with a different amino acid composition (Fig. 1.1). Collagen molecules are synthesized as pro-collagen molecules which later converted into mature collagen molecules upon the removal of their pro-peptide domain present on either side, by pro-collagen peptidase. The pro-peptide released from the pro-collagen molecules serves as biomarkers of collagen synthesis. Further, Assembly and cross-linking of mature collagen molecules lead to the development of collagen fibrils and fibers. During physiological and pathological ECM remodelling, the telopeptides present on both amino and carboxyl terminal of mature collagen are cleaved resulting in the degradation of the collagen fibers. The cleaved telopeptides act as the biomarkers for collagen degradation.

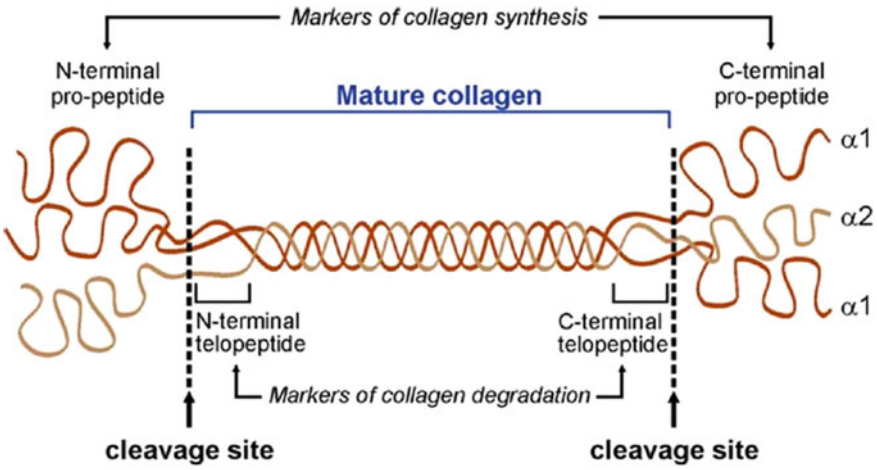


Fig. 1.1 Structure of collagen molecule (Fan et al. 2012)

In mature collagen, the three polypeptide chains are intertwined to form a right-handed super-helix (Fig. 1.2b) with a pitch of approximately 8.6 nm. The rod-shaped triple helical molecule has an average molecular weight of approximately 300 kDa, a length of 300 nm with a diameter of 1.5 nm. Each α-chain consists of more than 1000 amino acids. The amino acids are arranged in a unique triple-helix forming a sequence i.e. Gly-X-Y. Glycine with its smallest side group repeats at every third position on the sequence allowing the close packing of the chains into a helix leaving little space for residues in the core. About 35% of the non-glycine positions in the repeating units of Gly-X-Y sequence are occupied by proline in X-position and 4-hydroxyproline in the Y-position (Fig. 1.2a). Due to the steric repulsion between proline and hydroxyproline residues in the X- and Y-positions, the central domain of the collagen α-chains is folded into a tight left-handed helix (Ramachandran and Kartha 1954). The occurrence of glycine in every third position in the triplet is essential for the formation of three left-handed helices which subsequently form a right-handed super helix. In the collagen molecule, all glycine residues are placed inside the coil while other amino acids project outside (Ramachandran and Kartha 1954).

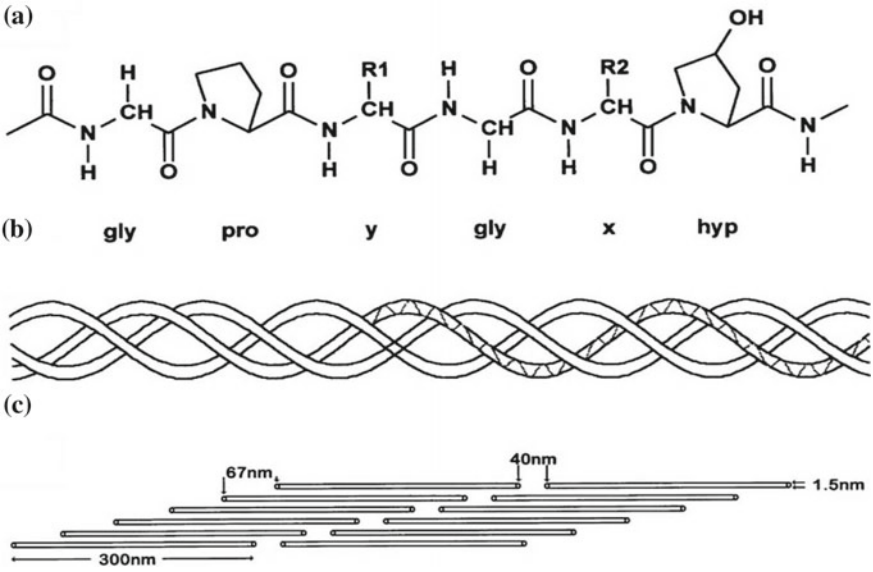


Fig. 1.2 Hierarchical structural organisation of collagen type I. **a** Primary amino acid sequence, **b** secondary left handed helix and tertiary right handed triple-helix structure and **c** staggered quaternary structure (Friess 1998)

1.2.1 Hierarchical Structural Organization of Collagen

Collagen fibrillogenesis is a sequence of self-assembling of the triple-helical collagen molecules which stagger longitudinally and laterally to form fibrils in the extracellular space with distinct periodicity (Fig. 1.2c). The collagen molecules aggregate into microfibrils consisting of four to eight collagen molecules and further into fibrils. These fibrils grow laterally from 10 to 500 nm in diameter depending on tissue type and stage of development (Nimni and Harkness 1988). In the collagen fibril, the triple-helices overlap by 0.4D and stagger by 0.6D where D equals 67 nm. The collagen fibrils organize into fibers, which on their part can form even larger fiber bundles.

1.3 Collagen Origin and Variability

Collagen is produced by fibroblast cells derived from the lineage of pluripotential advential cells. Some of the most common sources of collagen for biomedical applications include bovine skin and tendons, porcine skin and rat tail among others. Marine life forms also serve as a considerable source of collagen, which can be extracted from sponges, fish and jellyfish. Recently, collagen has been discovered in marine coral reefs and further research is going on to explore its biomedical application. These collagens find wide industrial applications, but comparatively used less in biomedical research and clinical usage. Further, the recombinant human collagen has been prepared by Fibrogen® with less immunogenic and identical in composition (Parenteau-Bareil et al. 2010). Collagen obtained from decellularized ECM serve as a scaffolding material for tissue engineering. Acellular ECM obtained from human/porcine dermis, swine intestine and bladder submucosa are also employed in biomedical applications (Badylak 2004).

1.4 Cross-Linking of Collagen

Cross-linking is crucial to stabilize the collagen matrix. Various biocompatible cross-linkers are widely utilized to fabricate self-standing, stable collagen scaffolds. Cross-linking controls immunogenic properties, rapid degradation and calcification (Jorge-Herrero et al. 1999). Various cross-linkers widely employed for cross-linking the collagen based scaffolds are shown in the Fig. 1.3. The amine and carboxylic groups of collagen are mainly responsible for cross-linking. Glutaraldehyde is one of the cheap and highly reactive water soluble cross-linker and widely employed for stabilizing the collagen scaffolds. Amine groups of collagen favors the cross-linking through Schiff base formation. EDC and N-hydroxy succinimide forms a stable ester known as o-acylisourea, on reacting with carboxylic acid group of collagen

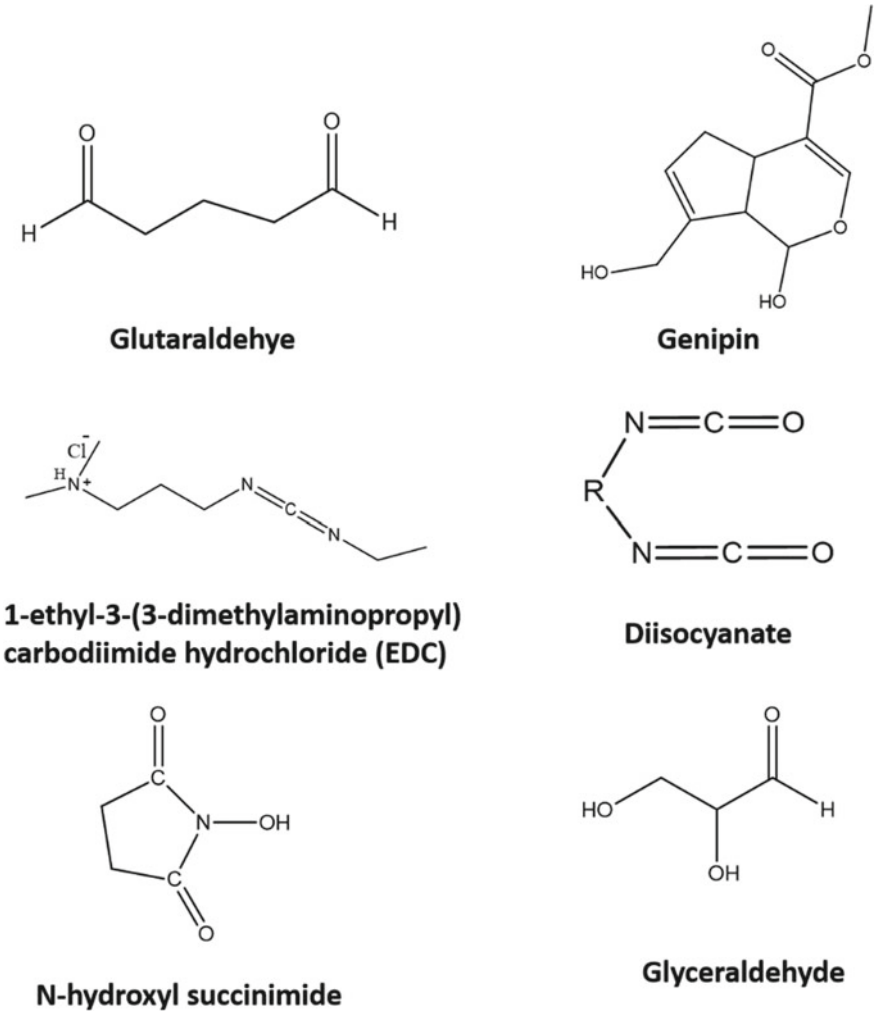


Fig. 1.3 Various cross-linkers widely employed for cross-linking collagen

and contributes to the cross-linking (Usha et al. 2012). Powell et al. fabricated collagen scaffolds which display prolonged degradation with collagenase enzyme and improved mechanical property without affecting the biocompatibility (Powell and Boyce 2006). It is also widely reported that amine groups of collagen can effectively crosslink with EDC in the absence of NHS. Genipin is extracted from plant extract and utilized for cross-linking collagen (Sundararaghavan et al. 2008). Transglutaminase enzyme was also successfully used for cross-linking collagen (Orban et al. 2004). Charulatha et al. provided a detailed review about various cross-linker and their influence on mechanical properties of collagen scaffolds. Briefly, GTA display enhanced degree of cross-linking and amino acid side chains are crucial for cross-

linking, increasing degree of cross-linking significantly improves the mechanical properties (Charulatha and Rajaram 2003).

1.5 Collagen Over Other Biomaterials

Collagen is extracted from the wide range of various animal tissues by well studied isolation and purification process. The structural, physical, chemical and biological properties of the collagen are well studied (Stamov and Pompe 2012). Further collagen is biocompatible, biodegradable with less immunological property compared to other biomaterials. Collagen posses the cell binding RGD sequence is responsible for adhesion, growth and proliferation of cells which is almost absent in other biomaterials. Collagen can be casted into films, beads, hydrogels, sponges and 3-D matrices (Sinha and Trehan 2003). In addition, it can be easily functionalized with wide range of materials for its utilization in desired biomedical application. Hence, several clinical medicines are based on collagen for the wound dressing, hemostasis, hernia repair, nerve regeneration, drug delivery, heart valves, ocular device and as vascular grafts (Lee et al. 2001).

1.6 Collagen Based Scaffold in Tissue Engineering Applications

In recent years, the demand for the development of biomaterials aimed at the replacement of injured or damaged tissues in humans or animals has increased. Collagen can be easily made into different material forms such as particles, fibers, hydrogel, films/membranes, sponges, blends and composites. Collagen has then been employed in a wide diversity of applications in the field of medicine including: sutures, hemostatic agents, tissue replacement and regeneration materials (bone, cartilage, skin, blood vessels, trachea, oesophagus, etc.), cosmetic surgery (lips, skin), dental composites, skin regeneration templates, membrane oxygenators, contraceptives (barrier method), biodegradable matrices, protective wrapping of nerves, implants, corneal bandage, contact lens, drug delivery, etc. (Meena et al. 1999; Pannone 2007; Ratner et al. 2004). Here, we will discuss the tissue engineering applications of biomaterial fabricated from collagen, collagen blended with inorganic material, synthetic polymer and biopolymers, collagen composites with native structure and denatured collagen i.e. gelatin.

1.6.1 Collagen

Collagen is widely employed as biomaterial for the preparation of scaffold in tissue engineering. Collagen films with porous structure were developed by Liu et al. using NaCl ion leaching technique. Here the author had prepared cross-linked collagen films with different amount of NaCl. Further, the porosity of the film was created by leaching out of NaCl from the membrane. The developed porous membrane exhibit biocompatibility with corneal epithelial cells leading to the growth of 2–3 layers of corneal epithelial cells within a week. The author suggest that the developed porous collagen film can be used to solve the problems in corneal regeneration (Liu et al. 2012).

Collagen type II is widely used as a scaffold material for cartilage tissue engineering. Here the author has prepared lyophilized sponge of collagen type I and type II and studied its influence on chondrocytes. The in vitro studies revealed that the cells are viable and evenly distributed over both sponges. Further, Collagen type I and type II sponge exhibit similar gene expression of type I, type II and aggrecan. These results conclude that collagen type I sponge can be used for developing hyaline cartilage-like tissue at initial stage of tissue regeneration (Ohno et al. 2004).

Chen et al. prepared 20–30 nm diameter collagen I particles using high-voltage electrostatic field system. In vitro analysis done using rat Bone marrow stromal cells (BMSCs) revealed the promotion of cell proliferation, osteogenic differentiation and formation of bone nodules. From the observations the author suggested that collagen I nanospheres might have a greater potential for its application in bone tissue engineering (Chen et al. 2009).

Collagen hydrogel formed by cross-linking using four-armed polyethylene glycol succinimidyl glutarate (PEG-SG) (Fig. 1.4) resist fibroblast mediated contraction and thus act as a supporting dermal layer matrix for full thickness skin model. Cross-linked matrix are mechanically stable and resist the collagenase degradation can be

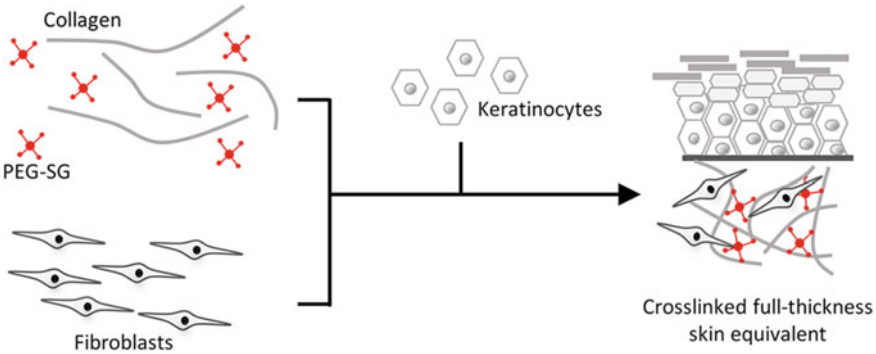


Fig. 1.4 Schematic representation of development of skin graft equivalent using collagen and PEG-SG (Lotz et al. 2017)

used as skin graft equivalent after culturing with human epidermal keratinocytes (Lotz et al. 2017).

1.6.2 Collagen/Inorganic Composite

Inorganic materials such as calcium phosphate (Cap), bioglass, clay, silica, zeolite are widely utilized to reinforce collagen. Inorganic materials are incorporated into collagen matrix in order to improve the bioactivity, mechanical stability and durability. Various methods are widely practiced to fabricate collagen/Cap scaffolds such as (I) In situ mineralization of inorganic particles in fibrous collagen scaffolds or interconnected non fibrous porous scaffolds, (II) Direct blending of inorganic particles along with the fibrous or non-fibrous collagen matrix.

Calcium phosphate has been utilized to fabricate the scaffolds for tissue engineering application owing to their osteoconductivity, osteoinductivity, biocompatibility, biointegration with the host and surrounding tissue and bioresorbability (Samavedi et al. 2013; Vallet-Regí and González-Calbet 2004). Calcium phosphate display various phases such as monocalcium phosphate monohydrate (MCPM), anhydrous monocalcium phosphate (MCPA), dicalcium phosphate dihydrate (DCPD), and anhydrous dicalcium phosphate (DCPA) which are known as acidic calcium phosphate. Other phases such as octacalcium phosphate (OCP), α- and β-tricalcium phosphate (α-TCP, β-TCP), amorphous calcium phosphate (ACP) and hydroxyapatite (HAp) are also observed (Dorozhkin 2012). The [Ca]/[P] ratio of various phase of calcium phosphates are specific which ranges from 0.5 to 2. Bone contains hydroxyapatite as one of the major inorganic constituent and collagen as an organic constituent. Hence mimicking the architecture of bone and fabricating scaffolds using collagen and calcium phosphate based materials can facilitate the healing of damaged bone tissues and considered as a suitable alternate for xenograft. Apart from chemical similarity of calcium phosphate with the chemical constituent of bone and teeth, it also displays enhanced osteoblast attachment, proliferation and differentiation which are indispensable properties of bioactive scaffolds (Villa et al. 2015).

Porous collagen scaffolds display poor mechanical properties which can be significantly improved using nano HAp reinforcement (Sionkowska and Kozłowska 2013). HAp can be incorporated through mineralization or insitu precipitation methods. Kozlovska et al. fabricated interconnected porous scaffolds and successfully demonstrated the insitu precipitation of Cap in collagen matrix (Kozłowska and Sionkowska 2015). Simulated body fluid was also employed for mineralization of HAp on collagen scaffolds (Al-Munajjed et al. 2009). Incorporation of HAp into collagen maintains structural stability such as size, shape and pore architecture of the scaffolds compare to pristine collagen scaffolds as shown in the Fig. 1.5 (Kane et al. 2015). Collagen films incorporated with HAp also demonstrated as a composite material for tissue engineering. Yamauchi et al. synthesized multilayer sheets of collagen and HAP which are deposited alternatively through enzymatic mineralization. These scaffolds are transparent and display excellent mechanical stability (Tensile strength

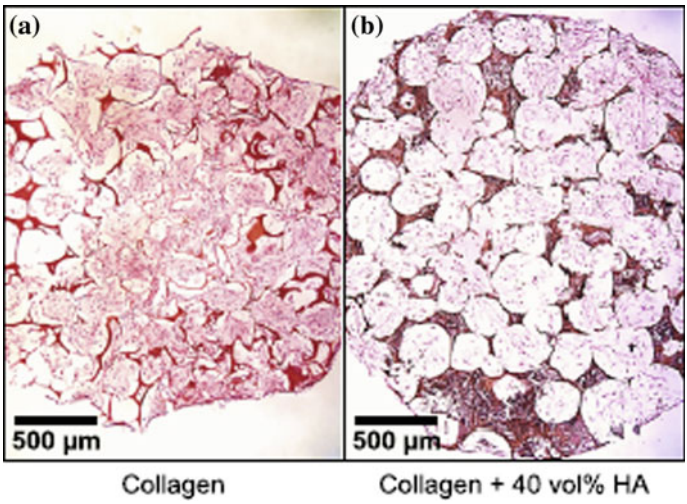


Fig. 1.5 Histological sections (H&E stained) showing the infiltration of hASCs. **a** 0 vol.% and **b** 40 vol.% HA whiskers after 14 days in culture (Kane et al. 2015)

and modulus) (Yamauchi et al. 2004). 3D printing technique was also employed to fabricate collagen/HAp scaffolds. Ardelean et al. produced collagen-calcium ink and fabricated the 3D printed structures. 3D printed structures were cross-linked using GTA in phosphate buffer saline which allows the precipitation of HAp crystals in 3D printed matrix producing biocompatible scaffolds (Ardelean et al. 2018; Ogata et al. 2005). HAp displays poor osteoinductivity which can be improved through ionic substitution (carbonates, magnesium) (Samavedi et al. 2013). Collagen scaffolds are also fabricated using β-TCP and amorphous calcium phosphate. Baheiraei et al. fabricated β-TCP incorporated collagen scaffolds and cultured bone marrow derived mesenchymal stem cells (BMMSCs) which displayed improved differentiation of BMMSC into osteoblast (Baheiraei et al. 2018).

Bioglass (SiO_2–CaO–P_2O_5) contains silica, calcium and phosphorous as a major chemical constituent. It is biocompatible, bioactive and facilitates the osteogenic differentiation (Jones et al. 2016; Li et al. 2016). Bioglass incorporated interconnected porous scaffolds are fabricated and utilized for bone tissue engineering application. Sharifi et al. fabricated bioglass incorporated collagen fibers and porous scaffolds which are highly biocompatible (Sharifi et al. 2016). Long et al. produced porous collagen/BG scaffolds which facilitate bone stromal cells attachment and proliferation (Long et al. 2015). Bioglass incorporated collagen scaffolds improve in vitro mineralization and accelerate the osteogenic differentiation of MC-3T3 cells (Marelli et al. 2011). Miri et al. synthesized injectable collagen/BG scaffolds and analysed their in vivo performance using adult rats which evidenced that the injectable hydrogels are highly osteoconductive (Miri et al. 2016). Collagen also used as a coating material to enhance cell attachment and proliferation. Hum et al. produced bioglass scaffolds and coated with collagen scaffolds which display improved cell attachment

and proliferation (Hum and Boccaccini 2018). Incorporation of antimicrobial metal ion in bioglass imparts antimicrobial property which were utilized for the fabrication of collagen scaffolds for treating osteomyelitis (Ryan et al. 2019).

Clay is a layered silicate material, montmorillonite (MMT), saponite, smectite and hectorite are some of the clay materials which are widely employed for biomedical application. Clay has been employed for the fabrication of hydrogel, porous polymer scaffolds for tissue engineering applications (Dawson and Oreffo 2013). Reyna-Valencia et al. introduced laponite clay into collagen hydrogel which significantly improved its mechanical property (Reyna-Valencia et al. 2012). Zeolites which are aluminosilicate minerals were also tested for use in tissue engineering applications. Faraji et al. synthesized collagen/zeolite composite and evaluated their biological activity using rabbit in vivo model which evidenced that the composites are suitable for the reconstruction of bone defects (Faraji et al. 2017).

1.6.3 Collagen/Synthetic Polymer Composite

Various synthetic polymers have been employed to improve the mechanical property of collagen based matrix, such as synthetic polymers such as poly ethylene glycol (PEG), Poly caprolactone (PCL), polyacrylamide, poly(lactic-co-glycolic acid) (PLGA), polyvinyl alcohol (PVA), poly(glycolic acid) (PGA), poly(lactic acid) (PLA) etc. Collagen based synthetic polymeric based biomaterial has been prepared by coating, immobilization, coupling the collagen over the synthetic polymers.

PEG has been used in the preparation of scaffold because of its bio-inert property and its capability to be molded into variety of structures to form scaffold with different architectures. Sargeant et al. developed a collagen-PEG in situ hydrogel forming material for filling the defects with complex geometry and for adherence to adjacent tissue for supporting cell proliferation. The hydrogel exhibits tunable mechanical property, biodegradation and assisting cell adhesion and proliferation. These results suggest that the developed collagen-PEG hydrogel exhibit mechanical, physical and biological properties suitable for its application as an injectable tissue scaffold for the treatment of a variety of simple and complex tissue defects (Sargeant et al. 2012).

PCL having biocompatible, mechanical and biodegradable properties, has been widely used as a biomaterial in tissue engineering. PCL coated collagen matrix was developed by immobilizing collagen over acrylic acid modified 3-D printed PCL matrix. Sousa et al. developed square porous interconnected PCL filamentous network with filament diameter 350 μm using bioextruder. Collagen coated PCL matrix shows better biological properties such as adhesion, growth and proliferation of cells and could be used as a biomaterial for tissue engineering (Sousa et al. 2013).

Yamamoto et al. fabricated collagen-polyacrylamide hydrogel by immobilizing the gradient of collagen type I into the polyacrylamide hydrogel. The authors prepared the biomaterial by coupling the amine groups of collagen with carboxyl group generated in the polyacrylamide hydrogel by sodium hydroxide treatment. The in vitro studies reveal that the number of L929 fibroblasts cells adhered to the hydrogel

depend on the amount of collagen immobilized. These results suggest that the cell adhesion can be tuned by varying the concentration gradient of collagen. This diffusion controlled fabrication could be used to modify the functional group of the scaffold with chemicals for coupling with biomolecules for its desired biomedical applications (Yamamoto et al. 2010).

PLGA formed by copolymerization of PLA and PGA is used for the preparation of scaffold with designed shapes having high mechanical property. PLGA scaffold exhibit hydrophobic nature making it unsuitable for cell adhesion and cell growth. Hence, a hybrid 3D scaffolds combining the advantages of natural type I collagen and synthetic poly(lactic-co-glycolic acid) (PLGA) knitted mesh was developed by Dai et al. 2010. 3-D matrix was prepared by incorporating collagen in interstice, one side and both side of the skeletal PLGA mesh to give THIN, SEMI and SANDWICH composite respectively. SEM analysis clearly reveals the development of porous collagen sponge within the PLGA mesh (Fig. 1.6). When cultured with bovine chondrocytes all composites exhibit uniform distribution of cells with chondrocyte morphology and abundant cartilaginous ECM deposition. While SEMI and SANDWICH composites exhibit higher production of glycosaminoglycans (GAG) and expression of type II collagen and aggrecan mRNA. Hence, these scaffolds with the designed structure

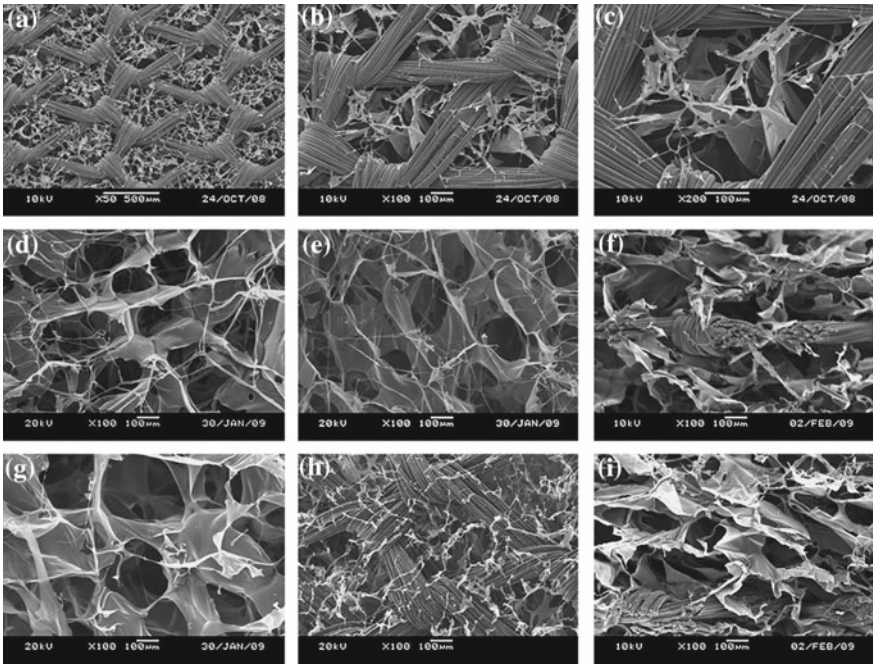


Fig. 1.6 SEM micrograph of composites. **a**, **b**, **c** top view of the THIN scaffolds; **d**, **g** top view of the SEMI and SANDWICH scaffolds, respectively; **e**, **h** bottom view of the SEMI and SANDWICH scaffolds, respectively; **f**, **i** cross-sectional view of the SEMI and SANDWICH scaffolds, respectively (Dai et al. 2010)

could be used with tunable thickness for tissue regeneration of articular cartilage. Also this method also provides a new route for the design and fabrication of 3D biodegradable porous scaffolds in tissue engineering (Dai et al. 2010).

PVA is water soluble, biocompatible and biodegradable that is used for the preparation of biomaterials. Biomimetic 3-D matrix with collagen and PVA was prepared by coating collagen over the photo cross-linked electrospun fibers of methacrylated polyvinyl alcohol system. Morphological analysis showed uniform nanofibrous structure with fiber diameter of 220–250 μm. In vitro analysis of the 3-D matrix with 3T3 mouse fibroblasts and human umbilical vein endothelial cells (ECV304) cells revealed attachment and growth of cells throughout the matrix (Fig. 1.7). Oktay et al. concluded that the biocompatibility of the PVA fibres was enhanced by coating with the collagen molecules and thus fulfilling the requirements of the scaffold for tissue engineering application (Oktay et al. 2015).

PGA is a synthetic polymer with biodegradability and mechanical resistance which could be combined with collagen to provide better mechanical and biological properties to the scaffolds. Hiraoka et al. found that incorporation of PGA fiber increased the compression modulus of collagen sponge by six fold with the weight ratio of collagen to PGA fiber at 0.2. Moreover, PGA incorporation lowers the shrinkage of collagen sponge thereby facilitating increased attachment of fibroblast L929 cells. It also favours deeper infiltration of cells when implanted subcutaneously on the back of the mice. The incorporation of PGA fiber reinforces collagen sponge without compromising the biocompatibility (Hiraoka et al. 2003).

PLA is the one such resorbable synthetic polymer with better mechanical strength than the most of the natural polymers which is used for the fabrication of tissue

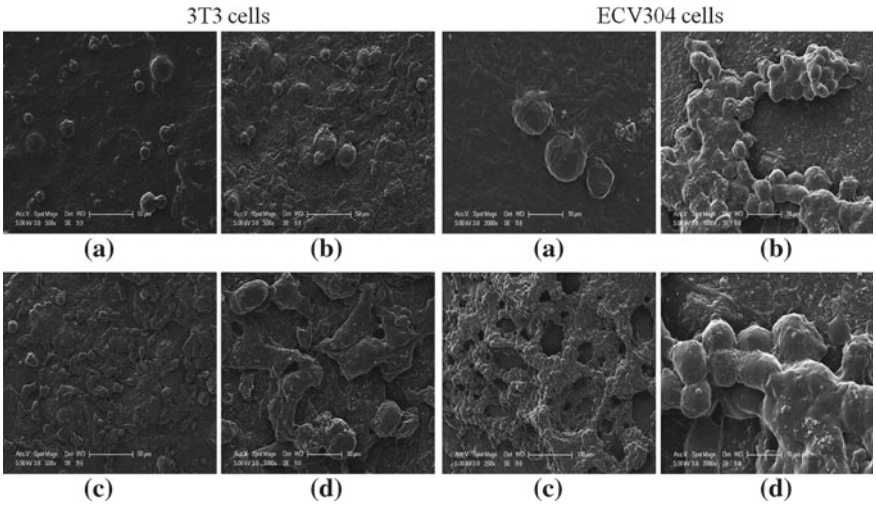


Fig. 1.7 Scanning electron microscopy images of attached cells on collagen-modified scaffold **a** after 2 h of cell culture, **b** 24 h, **c** 72 h (low-magnification), and **d** high-magnification (Oktay et al. 2015)

regeneration scaffolds. Collagen-PLA composite was developed by blending the PLA with the collagen fibres formed by extrusion and cross-linking techniques. The mechanical property of the developed collagen-PLA composites were found to be superior that the collagen-collagen composite, which is formed by grafting collagen with collagen fibers. The collagen-PLA composites support the formation of fibrous tissue in growth and exhibit delayed resorption when implanted into New Zealand white rabbit. Hence, Dunn et al. suggest that the developed composite can be used in the reconstruction of anterior cruciate ligament of knee (Dunn et al. 1997).

1.6.4 Collagen/Biopolymer Composites

Several biopolymers which are produced by the biological systems are utilized for the fabrication of the biomaterials. Biopolymers exhibit biocompatible and biodegradable property which is one of the major criteria of the scaffold. Here the collagen based scaffold with several biopolymers such as alginate, chitosan, silk fibroin, elastin, fibroin, hyaluronic acid and cellulose has been discussed below.

Alginate is a naturally occurring anionic and hydrophilic polysaccharide composed of (1→4) linked β-D mannouronate (M) and α-L guluronate (G) in different composition and sequence. Because of its properties in terms of biocompatibility, bioresorbability, non-antigenicity, and elasticity, alginate has been used as a biomaterial in tissue engineering. Here, Guillaume et al. had fabricated **c**ollagen-alginate composite by lyophilisation to obtain porous and shape memory property to fill the defects in degenerated intervertebral discs. In vitro and ex vivo organ defect model studies also reveal the compatibility of the composite towards bone marrow derived mesenchymal stem cells. Hence, it could be used as an effective biomaterial for intervertebral disc repair (Guillaume et al. 2015).

Chitosan is an amino cationic polysaccharide obtained by deacetylation of chitin. Chitosan is comprised of glucosamine and N-acetyl glucosamine connected through β (1–4) linkage. Chitosan mimics glycosaminoglycan (GAG) which is one of the components of extracellular matrix (ECM) involved in cell-cell and cell matrix interaction. Mighri et al. developed a material by coating chitosan over the collagen membrane and further it was stabilized by cross-linking with glutaraldehyde. This composite membrane support chondrocyte adhesion, proliferation, and IL-6 secretion which were confirmed by the in vitro studies using human chondrosarcoma cell line. This hybrid membrane could be employed as a potential biomaterial for cartilage regeneration (Mighri et al. 2015).

Silk fibroin is a protein extracted from silkworm cocoons mostly from Bombyx mori. Silk fibroin fibers possess excellent mechanical strength, toughness, biocompatibility, biodegradability and thermal stability. Hence, it represents one of the best biopolymers with superior properties to many synthetic and natural polymers. Tissue-engineered nerve conduit (TENC) was developed by blending silk fibroin-collagen nerve scaffold and co-cultured Schwann cells and adipose-derived stem cells. Morphology of the schwann cells exhibited elongated spindle shape and immunocyto-

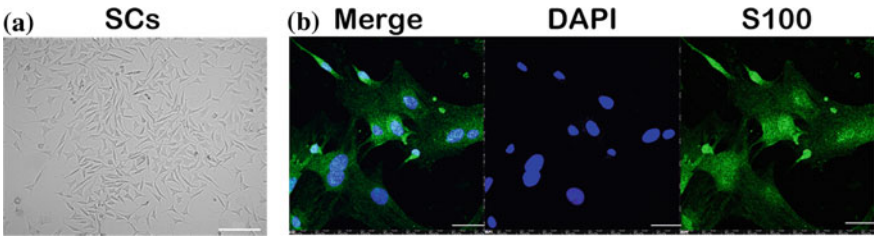


Fig. 1.8 Morphology of Schwann cells. **a** Phase contrast microscopy. **b** An immunocytochemical assessment of Schwann cells. Scale bar, 100 (**a**) and 50 μm (**b**) (Xu et al. 2016)

chemical analysis reveals the presence of S-100 protein which is the characteristic of positive Schwann cells (Fig. 1.8). It was developed with an intension to bridge a 1-cm gap in the rat sciatic nerve transection model. Electrophysiological examinations and morphological analyses of the developed TENC resulted in the nerve regenerative outcome similar to that of the autologous nerve grafts and superior to that of individual collagen and silk fibroin scaffold. Based on the results it is concluded that the developed TENC could be a promising material for peripheral nerve repair (Xu et al. 2016).

Elastin is the major component of the elastic fibres present in the connective tissue of extra cellular matrix. It provides the mechanical strength and elasticity to the connective tissues. Minardi et al. developed a biomimetic mesh from the blend of collagen type 1 and elastin for the application in ventral hernia repair. They developed flat sheet and porous scaffolds from the blended composite to compare the morphological effect on the performance of the implant. Both the sheet and porous scaffolds were analysed for in vitro studies using human bone marrow-derived mesenchymal stem cells (h-BM-MSC) and then implanted in a rat ventral hernia model. Porous scaffold displayed mechanical property similar to that of native tissue and stimulated the gene expression of genes associated with de novo matrix deposition, angiogenesis, adipogenesis and skeletal muscles, when compared to that of sheet. Thus, the results conclude the capability of the collagen-elastin composite material for ventral hernia repair application (Minardi et al. 2017).

Fibrin is the insoluble network of fibrous protein derived from soluble fibrinogen after tissue injury to cease the bleeding of blood. Kim et al. developed a fibrin network on the collagen sponge by immersing the collagen sponge in the fibrin polymerisation solution having different concentration of fibrinogen and thrombin. The porosity and water uptake capacity of the collagen-fibrin matrix was reduced due to the cross-linking and fibrin network formation over the collagen sponge. The developed collagen-fibrin matrix seeded with MG-63 cells had shown enhanced cell attachment, proliferation and osteoblast differentiation. Suggesting the incorporation of fibrin network to the collagen scaffold support and improves the differentiation of osteoblast cells for stimulating bone repair (Kim et al. 2013).

Hyaluronic acid is an unsulfated glycosaminoglycan found in the extra cellular matrix of soft tissues. 3-D collagen–hyaluronic acid scaffolds with uniform, intercon-

nected pore structure (total porosity of about 85%) were fabricated by freeze-drying technique and cross-linking with 1-ethyl-3-(3-dimethylaminopropyl)-carbodiimide hydrochloride. The addition of hyaluronic acid improved the thermal stability, compressive modulus and elastic collapse stress of the composite. In vitro studies of the composites with murine pre-adipocyte (3T3-L1) cell line has shown the increased expression of genes, adipsin and PPARγ (adipogenesis transcription factor). Thus collagen–hyaluronic acid scaffolds may exhibit porous and permeable 3-D matrices that support the growth and differentiation of mammary stromal tissue for its application in adipose tissue engineering (Davidenko et al. 2010).

Li et al. developed a porous collagen-cellulose matrix loaded gelatin microspheres having basic fibroblast growth factor (bFGF) for skin tissue regeneration. The material was fabricated for the long term release of the bFGF growth factor for enhancing angiogenesis, which is as revealed from ELIZA analysis. The composites also support the proliferation of human umbilical vein endothelial cells when cultured in vitro. Further, subcutaneous implantation of the composite into Sprague-Dawley rats also resulted in formation of new blood vessels as observed from hematoxylin and eosin and immunohistochemical staining. Thus the fabricated composite posses the capability to repair the damaged skin tissue and can be effectively used in skin tissue engineering (Li et al. 2015).

1.6.5 Collagen Composite with Native Structure

Biomaterial mimicking the native structures has been developed to improve the biomaterial interaction with surrounding tissues through biomolecular recognition (Sakiyama-Elbert and Hubbell 2001). Biomaterial mimicking the characteristics of extracellular matrix (ECM) will serve as an excellent biomaterial for tissue engineering application. To mimic the ECM, several researchers utilize collagen type I which is one of the component of the ECM and fabricate the biomaterial using self-assembling process to mimic the molecular structure of collagen fibril formation in natural tissue. Here, few of such collagen composites having native structures have been discussed below.

Biomimetic collagen–apatite scaffold with a multi-level lamellar structure was developed by combining a time-dependent self-compression process with controllable freeze casting of a mineralized collagen hydrogel. A mineralized collagen hydrogel composed of bone-like mineralized fiber bundles was prepared by a simple biomineralization technique using collagen containing m-SBF. The multilevel lamellar porous structure resulted in a 12-fold increase in Young's modulus and a two-fold increase in the compression modulus along the aligned direction compared to the conventional scaffold with an equiaxed pore structure. Further, In vitro studies reveal that the lamellar scaffold supported adhesion and spreading of osteoblast over the scaffold. Therefore, Xia et al. concluded that the developed scaffold with hierarchical biomimetic structure showed improved anisotropic mechanical strength and has great potential for its application in bone tissue engineering (Xia et al. 2014).

Li et al. fabricated densified collagen films (up to 100 μm thick) by a plastic compression technique and cross-link them using carbodiimide chemistry. Initially the author developed mineralized collagen by using a polymer-induced liquid-precursor (PILP) mineralization process to mimic the in vivo mineralization process and used it for preparing densified film. The hardness and elastic modulus of the film in dry state was observed to be as comparable to that of woven bone. Hence the author suggest that the biomimetic mineralized collagen film with tunable mineral and mechanical stability can be used for the development of bone substitutes (Li et al. 2012).

Socrates et al. describes the preparation of a novel tAgNPs incorporated native fibrillar collagen-HAp composite having antibacterial property. The author prepared spherical silver nanoparticles of mean diameter 25 nm and incorporated on to collagen and initiated collagen fibril formation to yield composites exhibiting native collagen fibril with D-periodicity. Later the composites were biomimetically mineralized by using m-SBF for mimicking the bone mineral. The formed composites are biocompatible and antibacterial which was shown form in vitro studies with MG-63 cells and antibacterial activity with *E. coli* and *Staphylococcus aureus* respectively. Hence, the author concluded that their developed material can be used as a bone repair material for preventing infection and for faster calcified tissue repair (Socrates et al. 2015).

Biomimetic fabrication of mineralized native fibrillar collagen-chitosan composites with incorporated silver nanoparticles exhibiting an antibacterial property was developed by Socrates et al. The surface and cross-sectional micrographs of the composite reveal the presence of fibrillar collagen similar to the native tissue. The composites exhibit mineralization of spherulitic calcium phosphate mineral onto the surface. The composites displayed collagen in the native fibrillar state, improved mechanical property, hemocompatibility, biocompatibility towards MG-63 cells and antibacterial property. These fabricated composites could be employed as a promising bone scaffold for preventing infection and assisting faster healing of the bone (Socrates et al. 2019).

1.7 Conclusion

Collagen based biomaterials are widely employed in several biomedical applications owing to their better biocompatibility, biodegradability and low immunogenicity. It was extracted and purified from various sources of animal tissues and functionalized with different inorganic and organic polymeric materials for improving its mechanical, biodegradable and other biological properties for specific biomedical application. Collagen scaffold faces several challenges such as stability and immunogenicity caused from utilization of collagen from xenogenic source. In order to reduce the immunogenicity caused from the xenogenic source non helical portion was cleaved during the extraction of collagen. In that course we are eliminating non helical portion, we are losing several cell binding sites and cross-linking sequences which may play a vital role in tissue engineering. To overcome this, recombinant collagen has

been utilized for the preparation of composites for tissue engineering. At present several researches are being carried out on the fabrication of collagen based biomaterial cultured with cells to mimic the in vivo structures by biomimetic process to cut down the gap between the in vitro and in vivo studies.

Acknowledgements We would like to thank and acknowledge the financial support from Indo-French Centre for the Promotion of Advanced Research, IFCPAR/CEFIPRA (Project No. 5608-1).

References

Al-Munajjed AA, Plunkett NA, Gleeson JP, Weber T, Jungreuthmayer C, Levingstone T, Hammer J, O'Brien FJ (2009) Development of a biomimetic collagen-hydroxyapatite scaffold for bone tissue engineering using a SBF immersion technique. J Biomed Mater Res B Appl Biomater 90B(2):584–591. https://doi.org/10.1002/jbm.b.31320

Ardelean IL, Gudovan D, Ficai D, Ficai A, Andronescu E, Albu-Kaya MG, Neacsu P, Ion RN, Cimpean A, Mitran V (2018) Collagen/hydroxyapatite bone grafts manufactured by homogeneous/heterogeneous 3D printing. Mater Lett 231:179–182. https://doi.org/10.1016/j.matlet.2018.08.042

Badylak Stephen F (2004) Xenogeneic extracellular matrix as a scaffold for tissue reconstruction. Transpl Immunol 12(3):367–377. https://doi.org/10.1016/j.trim.2003.12.016

Baheiraei N, Nourani MR, Mortazavi SM, Movahedin M, Eyni H, Bagheri F, Norahan MH (2018) Development of a bioactive porous collagen/β-tricalcium phosphate bone graft assisting rapid vascularization for bone tissue engineering applications. J Biomed Mater Res, Part A 106(1):73–85. https://doi.org/10.1002/jbm.a.36207

Charulatha V, Rajaram A (2003) Influence of different crosslinking treatments on the physical properties of collagen membranes. Biomaterials 24(5):759–767. https://doi.org/10.1016/S0142-9612(02)00412-X

Chen K-Y, Chung C-M, Kuo S-M, Chen Y-S, Yao C-H (2009) Influence of collagen I nanospheres on the growth and osteogenic difference of rat bone marrow stromal cells. J Med Biol Eng 29(6):284–289

Dai W, Kawazoe N, Lin X, Dong J, Chen G (2010) The influence of structural design of PLGA/collagen hybrid scaffolds in cartilage tissue engineering. Biomaterials 31(8):2141–2152. https://doi.org/10.1016/j.biomaterials.2009.11.070

Davidenko N, Campbell JJ, Thian ES, Watson CJ, Cameron RE (2010) Collagen–hyaluronic acid scaffolds for adipose tissue engineering. Acta Biomater 6(10):3957–3968. https://doi.org/10.1016/j.actbio.2010.05.005

Dawson JI, Oreffo ROC (2013) Clay: new opportunities for tissue regeneration and biomaterial design. Adv Mater 25(30):4069–4086. https://doi.org/10.1002/adma.201301034

Dorozhkin SV (2012) Biphasic, triphasic and multiphasic calcium orthophosphates. Acta Biomater 8(3):963–977. https://doi.org/10.1016/j.actbio.2011.09.003

Dunn MG, Bellincampi LD, Jr Tria, Alfred J, Zawadsky JP (1997) Preliminary development of a collagen-PLA composite for ACL reconstruction. J Appl Polym Sci 63(11):1423–1428. https://doi.org/10.1002/(SICI)1097-4628(19970314)63:11%3c1423:AID-APP4%3e3.0.CO;2-O

Fan D, Takawale A, Lee J, Kassiri Z (2012) Cardiac fibroblasts, fibrosis and extracellular matrix remodeling in heart disease. Fibrogenesis & Tissue Repair 5(1):15. https://doi.org/10.1186/1755-1536-5-15

Faraji D, Jahandideh A, Asghari A, Akbarzadeh A, Hesaraki S (2017) Effect of zeolite and zeolite/collagen nanocomposite scaffolds on healing of segmental femur bone defect in rabbits. Iran J Vet Surg 12(2):63–70. https://doi.org/10.22034/ivsa.2018.112807.1133

Friess W (1998) Collagen—biomaterial for drug delivery. Eur J Pharm Biopharm 45(2):113–136. https://doi.org/10.1016/S0939-6411(98)00017-4

Gelse K, Pöschl E, Aigner T (2003) Collagens—structure, function, and biosynthesis. Adv Drug Deliv Rev 55(12):1531–1546. https://doi.org/10.1016/j.addr.2003.08.002

Guillaume O, Naqvi SM, Lennon K, Buckley CT (2015) Enhancing cell migration in shape-memory alginate–collagen composite scaffolds: in vitro and ex vivo assessment for intervertebral disc repair. J Biomater Appl 29(9):1230–1246. https://doi.org/10.1177/0885328214557905

Hiraoka Y, Kimura Y, Ueda H, Tabata Y (2003) Fabrication and biocompatibility of collagen sponge reinforced with poly(glycolic acid) fiber. Tissue Eng 9(6):1101–1112. https://doi.org/10.1089/10763270360728017

Hum J, Boccaccini AR (2018) Collagen as coating material for 45S5 bioactive glass-based scaffolds for bone tissue engineering. Int J Mol Sci 19(6):1807

Jones JR, Brauer DS, Hupa L, Greenspan DC (2016) Bioglass and bioactive glasses and their impact on healthcare. Int J Appl Glass Sci 7(4):423–434. https://doi.org/10.1111/ijag.12252

Jorge-Herrero E, Fernandez P, Turnay J, Olmo N, Calero P, García R, Freile I, Castillo-Olivares JL (1999) Influence of different chemical cross-linking treatments on the properties of bovine pericardium and collagen. Biomaterials 20(6):539–545. https://doi.org/10.1016/S0142-9612(98)90205-8

Kane RJ, Weiss-Bilka HE, Meagher MJ, Liu Y, Gargac JA, Niebur GL, Wagner DR, Roeder RK (2015) Hydroxyapatite reinforced collagen scaffolds with improved architecture and mechanical properties. Acta Biomater 17:16–25. https://doi.org/10.1016/j.actbio.2015.01.031

Kim B-S, Kim JS, Lee J (2013) Improvements of osteoblast adhesion, proliferation, and differentiation in vitro via fibrin network formation in collagen sponge scaffold. J Biomed Mater Res, Part A 101A(9):2661–2666. https://doi.org/10.1002/jbm.a.34567

Kozłowska J, Sionkowska A (2015) Effects of different crosslinking methods on the properties of collagen–calcium phosphate composite materials. Int J Biol Macromol 74:397–403. https://doi.org/10.1016/j.ijbiomac.2014.12.023

Lee CH, Singla A, Lee Y (2001) Biomedical applications of collagen. Int J Pharm 221(1):1–22. https://doi.org/10.1016/S0378-5173(01)00691-3

Li H, He J, Yu H, Green CR, Chang J (2016) Bioglass promotes wound healing by affecting gap junction connexin 43 mediated endothelial cell behavior. Biomaterials 84:64–75. https://doi.org/10.1016/j.biomaterials.2016.01.033

Li W, Lan Y, Guo R, Zhang Y, Xue W, Zhang Y (2015) In vitro and in vivo evaluation of a novel collagen/cellulose nanocrystals scaffold for achieving the sustained release of basic fibroblast growth factor. J Biomater Appl 29(6):882–893. https://doi.org/10.1177/0885328214547091

Li Y, Thula TT, Jee S, Perkins SL, Aparicio C, Douglas EP, Gower LB (2012) Biomimetic mineralization of woven bone-like nanocomposites: role of collagen cross-links. Biomacromol 13(1):49–59. https://doi.org/10.1021/bm201070g

Liu Y, Ren L, Yao H, Wang Y (2012) Collagen films with suitable physical properties and biocompatibility for corneal tissue engineering prepared by ion leaching technique. Mater Lett 87:1–4. https://doi.org/10.1016/j.matlet.2012.07.091

Long T, Yang J, Shi S-S, Guo Y-P, Ke Q-F, Zhu Z-A (2015) Fabrication of three-dimensional porous scaffold based on collagen fiber and bioglass for bone tissue engineering. J Biomed Mater Res B Appl Biomater 103(7):1455–1464. https://doi.org/10.1002/jbm.b.33328

Lotz C, Schmid FF, Oechsle E, Monaghan MG, Walles H, Groeber-Becker F (2017) Cross-linked collagen hydrogel matrix resisting contraction to facilitate full-thickness skin equivalents. ACS Appl Mater Interfaces 9(24):20417–20425. https://doi.org/10.1021/acsami.7b04017

Marelli B, Ghezzi CE, Mohn D, Stark WJ, Barralet JE, Boccaccini AR, Nazhat SN (2011) Accelerated mineralization of dense collagen-nano bioactive glass hybrid gels increases scaffold stiffness and regulates osteoblastic function. Biomaterials 32(34):8915–8926. https://doi.org/10.1016/j.biomaterials.2011.08.016

Meena C, Mengi SA, Deshpande SG (1999) Biomedical and industrial applications of collagen. Proc Indian Acad Sci—Chem Sci 111(2):319–329. https://doi.org/10.1007/BF02871912

Mighri N, Mao J, Mighri F, Ajji A, Rouabhia M (2015) Chitosan-coated collagen membranes promote chondrocyte adhesion, growth, and interleukin-6 secretion. Materials 8(11):5413

Minardi S, Taraballi F, Wang X, Cabrera FJ, Van Eps JL, Robbins AB, Sandri M, Moreno MR, Weiner BK, Tasciotti E (2017) Biomimetic collagen/elastin meshes for ventral hernia repair in a rat model. Acta Biomater 50:165–177. https://doi.org/10.1016/j.actbio.2016.11.032

Miri AK, Muja N, Kamranpour NO, Lepry WC, Boccaccini AR, Clarke SA, Nazhat SN (2016) Ectopic bone formation in rapidly fabricated acellular injectable dense collagen-bioglass hybrid scaffolds via gel aspiration-ejection. Biomaterials 85:128–141. https://doi.org/10.1016/j.biomaterials.2016.01.047

Nimni ME, Harkness RD (1988) Molecular structures and functions of collagen. In: Nimni ME (ed) Collagen–biochemistry (pp 1–79). CRC Press, Boca Raton. https://doi.org/10.1201/9781351070799

Ogata K, Imazato S, Ehara A, Ebisu S, Kinomoto Y, Nakano T, Umakoshi Y (2005) Comparison of osteoblast responses to hydroxyapatite and hydroxyapatite/soluble calcium phosphate composites. J Biomed Mater Res, Part A 72A(2):127–135. https://doi.org/10.1002/jbm.a.30146

Ohno T, Tanisaka K, Hiraoka Y, Ushida T, Tamaki T, Tateishi T (2004) Effect of type I and type II collagen sponges as 3D scaffolds for hyaline cartilage-like tissue regeneration on phenotypic control of seeded chondrocytes in vitro. Mater Sci Eng, C 24(3):407–411. https://doi.org/10.1016/j.msec.2003.11.011

Oktay B, Kayaman-Apohan N, Erdem-Kuruca S, Süleymanoğlu M (2015) Fabrication of collagen immobilized electrospun poly(vinyl alcohol) scaffolds. Polym Adv Technol 26(8):978–987. https://doi.org/10.1002/pat.3512

Orban JM, Wilson LB, Kofroth JA, El-Kurdi MS, Maul TM, Vorp DA (2004) Crosslinking of collagen gels by transglutaminase. J Biomed Mater Res, Part A 68A(4):756–762. https://doi.org/10.1002/jbm.a.20110

Pannone PJ (2007) Trends in biomaterials research. Nova Publishers

Parenteau-Bareil R, Gauvin R, Berthod F (2010) Collagen-based biomaterials for tissue engineering applications. Materials 3(3):1863–1887. https://doi.org/10.3390/ma3031863

Powell HM, Boyce ST (2006) EDC cross-linking improves skin substitute strength and stability. Biomaterials 27(34):5821–5827. https://doi.org/10.1016/j.biomaterials.2006.07.030

Ramachandran GN, Kartha G (1954) Structure of collagen. Nature 174(4423):269–270. https://doi.org/10.1038/174269c0

Ratner BD, Hoffman AS, Schoen FJ, Lemons JE (2004) Biomaterials science: an introduction to materials in medicine. Elsevier

Reyna-Valencia A, Chevallier P, Mantovani D (2012) Development of a collagen/clay nanocomposite biomaterial. Mater Sci Forum 706–709:461–466

Ryan EJ, Ryan AJ, González-Vázquez A, Philippart A, Ciraldo FE, Hobbs C, Nicolosi V, Boccaccini AR, Kearney CJ, O'Brien FJ (2019) Collagen scaffolds functionalised with copper-eluting bioactive glass reduce infection and enhance osteogenesis and angiogenesis both in vitro and in vivo. Biomaterials 197:405–416. https://doi.org/10.1016/j.biomaterials.2019.01.031

Sakiyama-Elbert SE, Hubbell JA (2001) Functional biomaterials: design of novel biomaterials. Annu Rev Mater Res 31(1):183–201. https://doi.org/10.1146/annurev.matsci.31.1.183

Samavedi S, Whittington AR, Goldstein AS (2013) Calcium phosphate ceramics in bone tissue engineering: a review of properties and their influence on cell behavior. Acta Biomater 9(9):8037–8045. https://doi.org/10.1016/j.actbio.2013.06.014

Sargeant TD, Desai AP, Banerjee S, Agawu A, Stopek JB (2012) An in situ forming collagen–PEG hydrogel for tissue regeneration. Acta Biomater 8(1):124–132. https://doi.org/10.1016/j.actbio.2011.07.028

Sharifi E, Ebrahimi-Barough S, Panahi M, Azami M, Ai A, Barabadi Z, Kajbafzadeh AM, Ai J (2016) In vitro evaluation of human endometrial stem cell-derived osteoblast-like cells' behavior on gelatin/collagen/bioglass nanofibers' scaffolds. J Biomed Mater Res, Part A 104(9):2210–2219. https://doi.org/10.1002/jbm.a.35748

Sinha VR, Trehan Aman (2003) Biodegradable microspheres for protein delivery. J Controlled Release 90(3):261–280. https://doi.org/10.1016/S0168-3659(03)00194-9

Sionkowska A, Kozłowska J (2013) Properties and modification of porous 3-D collagen/hydroxyapatite composites. Int J Biol Macromol 52:250–259. https://doi.org/10.1016/j.ijbiomac.2012.10.002

Socrates R, Prymak O, Loza K, Sakthivel N, Rajaram A, Epple M, Narayana Kalkura S (2019) Biomimetic fabrication of mineralized composite films of nanosilver loaded native fibrillar collagen and chitosan. Mater Sci Eng, C 99:357–366. https://doi.org/10.1016/j.msec.2019.01.101

Socrates R, Sakthivel N, Rajaram A, Ramamoorthy Usha, Narayana Kalkura S (2015) Novel fibrillar collagen–hydroxyapatite matrices loaded with silver nanoparticles for orthopedic application. Mater Lett 161:759–762. https://doi.org/10.1016/j.matlet.2015.09.089

Sousa I, Mendes A, Bártolo PJ (2013) PCL scaffolds with collagen bioactivator for applications in tissue engineering. Procedia Eng 59:279–284. https://doi.org/10.1016/j.proeng.2013.05.122

Stamov DR, Pompe T (2012) Structure and function of ECM-inspired composite collagen type I scaffolds. Soft Matter 8(40):10200–10212. https://doi.org/10.1039/C2SM26134K

Sundararaghavan HG, Monteiro GA, Lapin NA, Chabal YJ, Miksan JR, Shreiber DI (2008) Genipin-induced changes in collagen gels: correlation of mechanical properties to fluorescence. J Biomed Mater Res, Part A 87A(2):308–320. https://doi.org/10.1002/jbm.a.31715

Usha R, Sreeram KJ, Rajaram A (2012) Stabilization of collagen with EDC/NHS in the presence of l-lysine: a comprehensive study. Colloids Surf, B 90:83–90. https://doi.org/10.1016/j.colsurfb.2011.10.002

Vallet-Regí M, González-Calbet JM (2004) Calcium phosphates as substitution of bone tissues. Prog Solid State Chem 32(1):1–31. https://doi.org/10.1016/j.progsolidstchem.2004.07.001

Villa MM, Wang L, Huang J, Rowe DW, Wei M (2015) Bone tissue engineering with a collagen–hydroxyapatite scaffold and culture expanded bone marrow stromal cells. J Biomed Mater Res B Appl Biomater 103(2):243–253. https://doi.org/10.1002/jbm.b.33225

Xia Z, Villa MM, Wei M (2014) A biomimetic collagen–apatite scaffold with a multi-level lamellar structure for bone tissue engineering. J Mater Chem B 2(14):1998–2007. https://doi.org/10.1039/C3TB21595D

Xu Y, Zhang Z, Chen X, Li R, Li D, Feng S (2016) A silk fibroin/collagen nerve scaffold seeded with a co-culture of Schwann cells and adipose-derived stem cells for sciatic nerve regeneration. PLoS ONE 11(1):e0147184. https://doi.org/10.1371/journal.pone.0147184

Yamamoto M, Yanase K, Tabata Y (2010) Generation of type I collagen gradient in polyacrylamide hydrogels by a simple diffusion-controlled hydrolysis of amide groups. Materials 3(4). https://doi.org/10.3390/ma3042393

Yamauchi K, Goda T, Takeuchi N, Einaga H, Tanabe T (2004) Preparation of collagen/calcium phosphate multilayer sheet using enzymatic mineralization. Biomaterials 25(24):5481–5489. https://doi.org/10.1016/j.biomaterials.2003.12.057

Chapter 2
Chitosan and Chitosan Based Nanocomposites for Applications as a Drug Delivery Carrier: A Review



E. A. K. Nivethaa, Catherine Ann Martin, Olga V. Frank-Kamenetskaya and S. Narayana Kalkura

Abstract Chitosan is a biopolymer possessing extensive properties like biodegradability and biocompatibility due to which it has been extensively used for multifunctional applications. Among the various uses the biomedical applications of chitosan have produced results which has taken us a step closer towards the inhibition of various lethal diseases. In order to improve the activity of chitosan or to improve the drug loading efficiency, composites of chitosan with other polymers, noble metals, nanotubes, bioglass and various other moieties have been prepared. The current review, focusses on the application of chitosan and chitosan based nanocomposites for the delivery of drugs thereby throwing light on how chitosan based systems enable the sustained and prolonged release of drugs thus leading to the effective treatment of infections and diseases.

Keywords Chitosan · Nanocomposites · Polymers · Noble metals · Nanotubes · Bioglass · Drug delivery

2.1 Introduction

Chitosan (CS), is the second most abundant natural polymer which was first delineated from mushrooms by Professor Henri Braconnot in 1811. It is obtained by the deacetylation of chitin, which is the major component of shells from crustaceans and insects and a copolymer of N-acetyl-d-glucosamine and d-glucosamine units linked with β-(1-4) glycosidic bond. Chitin is generally prepared from the shells of crab or shrimp or fungal mycelia. Treatment of the extracted chitin with 40–50% NaOH yields chitosan. Complete deacetylation of chitin is not possible, only about 85% has been achieved.

E. A. K. Nivethaa · C. A. Martin · S. N. Kalkura (✉)
Crystal Growth Centre, Anna University, Chennai 600025, India
e-mail: kalkurasn@annauniv.edu; kalkura@yahoo.com

O. V. Frank-Kamenetskaya
Department of Crystallography, Institute of Earth Sciences,
Saint Petersburg State University, Saint Petersburg 199034, Russia

© Springer Nature Switzerland AG 2020

O. V. Frank-Kamenetskaya et al. (eds.), *Processes and Phenomena on the Boundary Between Biogenic and Abiogenic Nature*, Lecture Notes in Earth System Sciences,
https://doi.org/10.1007/978-3-030-21614-6_2

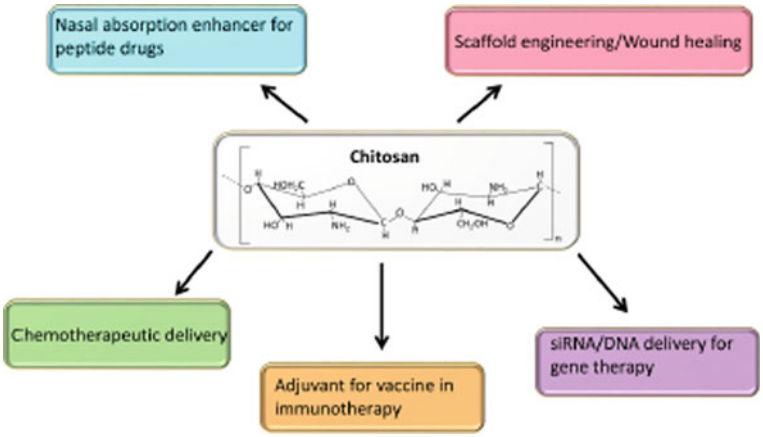


Fig. 2.1 Applications of chitosan in medicine. *Source* Mar. drugs, 2017, 15, 96

Chitosan has been actively used in various genres like food processing, waste management, water treatment, biotechnology and medicine. This is due to the eco-friendly, biocompatible, biodegradable, antimicrobial and non-toxic nature of chitosan. Apart from this chitosan possesses active sites for the chelation of drugs and other molecules, which makes it a suitable choice for various biomedical applications. Chitosan can be made to react with other moieties to form a composite, in the form of a solution by dissolving chitosan in mild organic acids. Solubility occurs due to the protonation of amino groups, making it positively charged and thereby opening up avenues for its use in flocculation and binding studies.

The current review, focusses on the application of chitosan and chitosan based nanocomposites for the delivery of drugs thereby throwing light on how chitosan based systems enable the sustained and prolonged release of drugs thus leading to the effective treatment of infections and diseases (Fig. 2.1).

2.2 Chitosan as a Drug Delivery Carrier

Chitosan by itself can act on tumor cells and inhibit cell growth by interfering with the cell metabolism, thus leading to cell death by improving the immunity of the body. The inefficiency of water-insoluble chitosan having a high molecular weight (650 kDa) against tumor has been reported by Maeda et al. So, the authors have studied the effect of low molecular weight chitosan on sarcoma-180 bearing mice. They have concluded that the low molecular weight chitosan is capable of inhibiting the cancer cells (Maeda and Kimura 2004) (Fig. 2.2).

The use of chitosan modified with biotin and avidin for the inhibition of HepG2 cells has been studied by Yao et al. Biotin-CS-NPs and avidin-B-CS-NPs significantly inhibited the growth of tumor cells. The author has concluded that the anticancer

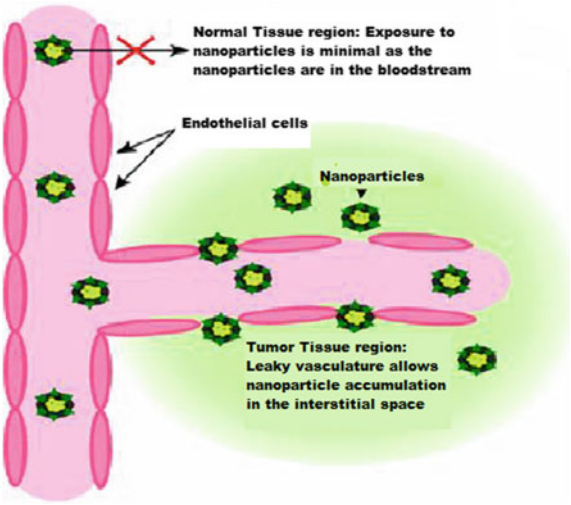


Fig. 2.2 Antitumor activity of chitosan nanoparticles. *Source* International journal of innovative pharmaceutical research, 4(3), 318–324, 2013

activity of avidin-biotin-CS-NPs were seen to be more efficient in suppressing the tumor cells when compared to B-CS-NPs. This study also demonstrates that avidin-biotin-CS-NPs may be used as a potent vehicle for the treatment of hepatic carcinoma (Yao et al. 2013).

The use of 5-Fluorouracil encapsulated chitosan nanoparticles for pH-stimulated drug delivery has also been reported by Ayd et al. TPP-initiated ionic gelation mechanism has been used for the synthesis of CS nanoparticles and a simple chemical method was used to synthesize 5-FU encapsulated chitosan nanoparticles and 70% 5-FU encapsulation has been achieved in this case. The author has demonstrated the pH dependent release of the drug from CS and the release profile shows a sustained and controlled release after the initial burst release thus, substantiating that the CS nanoparticles will serve as carriers for the effective delivery of the anticancer drug 5-FU (Seda Tığlı Aydın and Pulat 2012) (Fig. 2.3).

The successful delivery of cyclosporine A (CyA) to the ocular mucosa has been reported. CS loaded with FITC-BSA has been synthesized and has been used to deliver drugs to the ocular surface. It is observed that uptake of CSNPs was temperature dependent and continuous for the first 2 h. The in-vivo studies clearly indicate the absence of inflammation or alteration in rabbit ocular surface after exposure to CS nanoparticles when compared to the control. Thus, it is evident that these nanoparticles are well tolerated by the ocular surface tissues and are suitable for drug delivery to the ocular surface (de Salamanca et al. 2006).

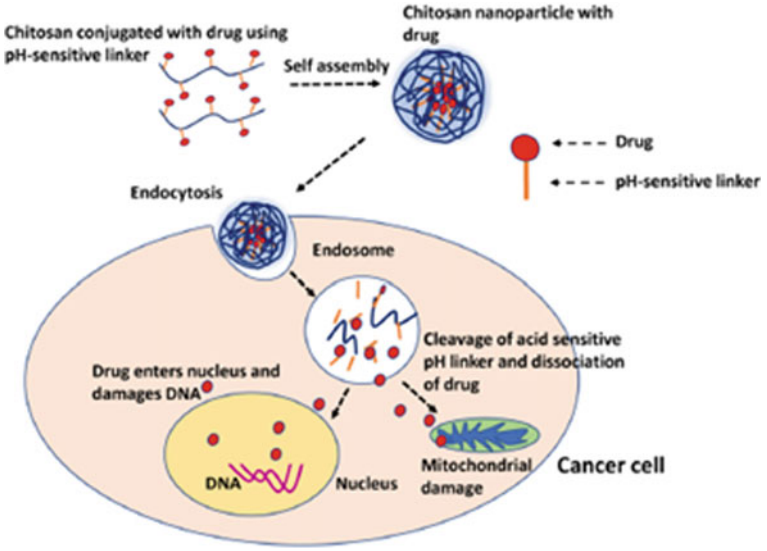


Fig. 2.3 Mechanism of pH sensitive drug delivery using chitosan. *Source* Mar. drugs, 2017, 15, 1996

2.3 Chitosan Based Nanocomposites for Drug Delivery Applications

Nanocomposites of chitosan with other polymers, nanotubes, magnetic oxides and noble metal nanoparticles have been used for the efficient delivery of drugs. A few such chitosan based nanocomposite systems will be discussed in the forthcoming sections.

2.3.1 Systems Containing Chitosan in Combination with Other Polymers

Rui Yang et. al. has reported the synthesis of chitosan modified PLGA nanoparticles for the specific delivery of the anticancer drug paclitaxel and has used it for the treatment of lung cancer. Herein, PLGA nanoparticles containing paclitaxel were first prepared by the solvent evaporation method and chitosan modified PLGA nanoparticles were obtained by dispersing the synthesized paclitaxel containing PLGA nanoparticles in chitosan solution overnight. A preferential accumulation of paclitaxel in the lungs with a distribution index of 99.9 has been reported on administering the drug containing nanoparticles such that the drug concentration would be 10 mg/kg through the tail vein in metastatized mice. It has been concluded that the formation of large sized nanoparticles due to aggregation in the plasma, slow release of pacli-

taxel by the nanoparticles, and electrical interaction between the positively charged nanoparticle surfaces and negatively charged endothelium of lung tumor vasculature are the reasons for the lung specific accumulation of paclitaxel (Yang et al. 2009).

CS-PLGA nanoparticles have also been used for the delivery of the anticancer drug 5-Fluorouracil (5-FU). 5-FU encapsulated PLGA modified chitosan nanoparticles have been prepared using two methods viz. physical adsorption and chemical binding. After the initial burst release in the first 4 h, a sustained and prolonged release of approximately 75% of the encapsulated drug occurs in the next 120 h (Wang et al. 2013). Similarly, Boting Lu et al. has reported the loading of paclitaxel into chitosan modified PLGA nanoparticles wherein, only 41.9 and 60.9% of paclitaxel were released from CS-PLGA after 2 h at pH 7.4 ad 5.5, respectively. It is also clearly reported that paclitaxel loaded CS-PLGA showed better cellular uptake and cytotoxicity towards MBA-MD 231 cells when compared to paclitaxel and paclitaxel loaded PLGA nanoparticles (Lu et al. 2019).

Paclitaxel loaded chitosan and polyethylene glycol coated PLGA (PLGA–C-S–PEG) nanoparticles have been prepared and characterized to efficiently encapsulate hydrophobic drugs, and to avoid the phagocytic uptake thus, increasing the bioavailability of the drug. A combinatorial coating of PEG and CS leading to a prolonged circulation of drug in the blood, reduced macrophage uptake with only a small quantity of the nanoparticles cloistered in the liver have been deduced from the in-vitro and in-vivo results. It is further established that PEG and CS coating significantly enhanced their cellular uptake and cytotoxicity towards various cancer cell lines (Parveen and Sahoo 2011).

Curcumin loaded chitosan/poly(butyl cyanoacrylate) [PBCA] nanoparticles have been synthesized and their efficacy towards the inhibition of HepG2, Huh7 and Bel7402 cells have been evaluated. Here, PBCA was prepared by emulsion polymerization and chitosan and curcumin were dissolved in the polymerization medium containing HCl to obtain drug loaded nanoparticles. The obtained nanoparticles were able to suppress VEGF and COX-2 expression and inhibit the proliferation of hepatocarcinoma cells (Duan et al. 2010).

Chitosan/poly(vinyl alcohol) blend has been used as carrier for dexamethasone. In this article, the preparation of nanocomposite containing different concentrations of PVA and the response of the nanocomposite system at different pH have been studied. The studies at different pH shows that the maximum swelling of the composite system occured at neutral pH while only low swelling was observed in acidic and basic pH thus, making these samples more suitable for use as a drug delivery system. The in-vitro analysis of hydrogels loaded with dexamethasone in Simulated Gastro Instestinal Fluid (SGF) (pH 1.2) showed a release of 9.4% of dexamethasone in 2 h, after which a sustained release of remaining dexamethasone was observed in simulated intestinal fluid (pH 6.8) at 7 h (Islam and Yasin 2012).

Similarly, the preparation of CS-PVA blends by using solution casting method has been reported. This has been used for the delivery of curcumin. It is reported that the release rate of the drug is more in case of PVA rich blends and that CS-PVA blend (80–20) showed a minimum release of approximately 10.48% of curcumin in

180 min. The tensile strength values of these blends show that they can be used as band-aid and in related applications (Vidyalakshmi et al. 2004).

A hydrogel based on crosslinked chitosan/gelatin has been prepared and used for the pH-dependent release of levamisole, cimetidine and chloramphenicol. This is in order to study the effect that the properties of the drug will have on its solubility in the host HPN hydrogel. All the drugs are soluble in water except for chloramphenicol which is only slightly soluble. It is observed that levamisole, which is most soluble in water is quickly released when compared to the other drugs from the hydrogel. This fast release has been attributed to its high solubility in the matrix. It has been established from this study that drug solubility in water plays a major role in the release and also that the release of the drugs occurs due to diffusion and relaxation processes. Moreover, the diffusion coefficient and the relaxation time are highly dependent on the pH of the medium (Yao et al. 1995).

There are also reports on using a combination of chitosan and pectin for the delivery of drugs. For instance, Sonia Pandey et al. has reported the use of chitosan-pectin polyelectrolyte complex prepared using the simple interaction between positively charged chitosan and negatively charged pectin for colon targeted drug delivery of theophylline. The concentration of polyelectrolyte complex (PEC) with respect to coating has been optimized and the optimized concentration consisting of PEC (1.1%) and coating (3%) shows a release of 92.16% drug within 12 h whereas, the ex-vivo drug release was found to be approximately 98.58% in the presence of rat caecal content. Anomalous transport has been reported as the cause for the release of the drug from PEC (Pandey et al. 2013).

Seung Won Hwang et al. has achieved the slow release of curcumin in the digestive system by synthesizing curcumin-loaded pectin coated chitosan microparticles and curcumin-loaded chitosan-pectin composite microparticles. The release of the drug from the systems has been analyzed at pH 1.2 and 6.8. Glutaraldehyde is employed as a hardening agent for chitosan and Mg^{2+} is utilized as a pectin-crosslinking agent in this study. Prolonged release of curcumin was obtained for the case of pectin-coated micro particles when compared to chitosan-pectin composite particles. The release of drug from micro particles crosslinked with Mg^{2+} was slower in the absence of pectinase, whereas it was faster in the presence of pectinase compared with Ca^{2+} crosslinked systems. Thus the evident role of pectin layer and the pectin-crosslinking agent in delaying the release of curcumin has been well established (Hwang and Shin 2018).

Alginate has also been used along with chitosan for the delivery of various drugs. Rajendran et al. has studied the release of nimodipine from CS-alginate system. In this report, nimodipine-loaded alginate-chitosan beads were prepared by ionic gelation method and the release of the drug was studied at pH 1.2 and 6.8. The concentration of chitosan in the gelation medium was seen to affect the surface morphology, particle size and drug loading efficiency. About 73% of drug release is reported for the case of alginate beads treated with chitosan. Anomalous transport or case II transport has been reported to be the phenomenon responsible for release from the system. It is thus inferred that modulated release of the drug can be achieved on treating the alginate beads with chitosan (Rajendran and Basu 2009).

Chitosan-alginate system has also been used for the delivery of antineoplastic drugs. Yu et al. reports the synthesis of drug encapsulated microparticles by directly shredding the drug loaded beads into micro particles in a commercial food processor. The release of two drugs namely 5-FU and tegafur are studied and it was concluded that chitosan reinforcement was able to effectively sustain the release of drugs with low molecular weights. The release of drug at pH 5.0 and 7.4 from the CS-alginate system does not show much difference, implying that the combination will efficiently decrease the diffusion of the encapsulated drugs thus, retarding the release of drug (Yu et al. 2008).

Another promising bipolymer based system is the one containing chitosan and cellulose. Remuñán-López et al. has reported the synthesis of CS-containing microparticles by the solvent evaporation technique and also microencapsulated CS cores. This work analyzes, the capability of these microparticles for the entrapment and controlled release of drugs and proteins, using sodium diclofenac (SD) and fluorescein isothiocyanate-labeled bovine serum albumin (FITC-BSA) as model compounds. The obtained results, clearly illustrate that the entrapment efficiency of SD was very high irrespective of the processing conditions. Furthermore, it is also evident from this report that the in-vitro drug release can also be engineered for both model compounds by changing the core properties or the polymer used for coating. Moreover, the stability of the microparticles at low pH has thus, been established which renders the system suitable for oral delivery without requiring any harmful cross-linkage treatment (Remuñán-López et al. 1998) (Fig. 2.4).

There are also reports on the use of chitosan-cellulose nanocrystal polyelectrolyte-macroion complexes (PMC) for drug delivery. PMC was prepared by the drop wise addition of a cellulose nanocrystal (CNC) suspension and was added dropwise to a solution of chitosan having the same pH and ionic strength. The reaction mixture immediately became opaque. This attributed to the formation of an insoluble complex. So, after checking the formation of PMC by taking different concentrations of the two moieties, the authors have concluded that the formation and properties of

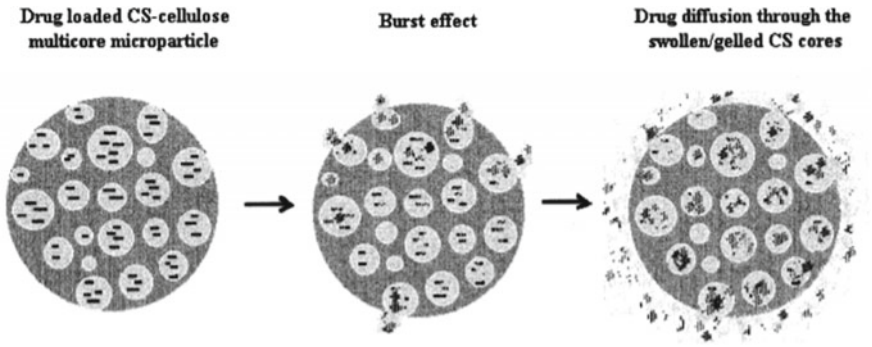


Fig. 2.4 Theoretical cross section structure and release mechanisms of drug containing core/coat microparticles. *Source* European Journal of Pharmaceutics and Biopharmaceutics 45, 49–56, 1998

the PMC particles is governed by the strong mismatch in the densities of ionizable groups of the two components. Moreover, PMC formation is strongly dependent on the CNC concentration in the reaction medium (i.e.) higher the CNC concentration higher is the PMC particle aggregation. Hence forth, this study established that a net positive charge and a size <10 μm, are obtained at N/S ratios 1.33 g of the PMCs make them suitable candidates for use as a multiparticulate oral drug delivery system (Wang and Roman 2011).

2.3.2 Chitosan and Noble Metal and/or Carbon Nanotube Containing Nanocomposites

Chitosan and noble metal containing nanocomposites have been used in a wide range of applications like biosensors, colorimetric sensors, as antimicrobial agents, wound healing as well as in drug delivery. A few reports on the use of these systems as carriers of drugs and in photo thermal treatment of cancer will be discussed below.

Boca et al. have synthesized CS coated triangular silver nanoparticles via cell seed growth method and used it for the photo thermal destruction of the lung cancer cells. Moreover, the authors have demonstrated the biocompatibility of CS-Ag towards the normal HEK cells while simultaneously exhibiting a dose dependent cytotoxicity against NCI-H460 cancer cells. Hence, this report clearly evidences the efficacy of the nanocomposite to ablate the cancer cells by producing heat when light is supplied (Boca et al. 2011).

Vimala et al. has reported the fabrication of curcumin encapsulated chitosan-PVA silver nanocomposite films by the chemical route. The results obtained clearly indicate that CS-PVA-Ag nanoparticles exhibit a better curcumin encapsulation efficiency when compared to CS-PVA (Kanikireddy et al. 2011). Banerjee et al. has shown that modified chitosan encapsulated core-shell Ag NPs exhibit cytotoxicity towards human cervical HeLa cancer cell, and they exhibit an IC_{50} value of 8 μg/ml which illustrates the suitability of the sample for use as an anticancer agent (Banerjee et al. 2016).

Nivethaa et al. has synthesized CS/Ag nanocomposite by the chemical method and encapsulated the anticancer drug 5-FU into the nanocomposite and studied the cytotoxicity of the drug loaded system towards the inhibition of MCF-7 (breast cancer cells). The study reports the formation of a polymer matrix nanocomposite with CS as the matrix and silver as the filler phase. An increase in the particle size of Ag on addition of 5-FU has also been reported. The reason for such an increase has been given as the binding of the drug to more than one Ag nanoparticle, which has been established using elemental mapping. About 88.1% of the drug was released from the system in 72 h and the cytotoxicity results showed that about 100 μg/ml of drug loaded sample was able to inhibit 50% of the cancer cells. This shows the efficacy of the system as a drug delivery vehicle (Nivethaa et al. 2016a, b) (Fig. 2.5).

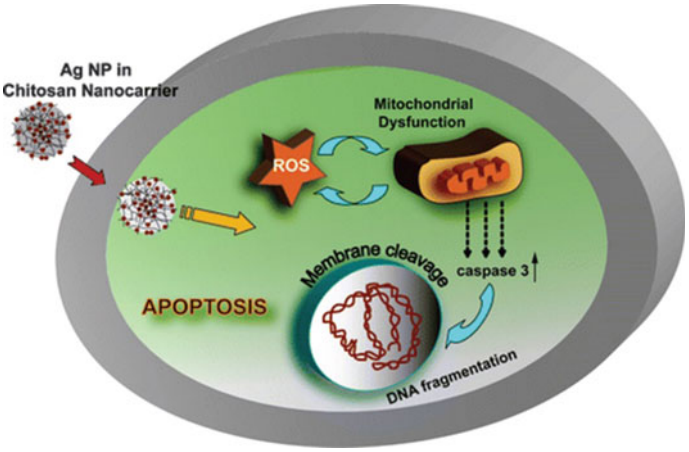


Fig. 2.5 Mechanism of cell apoptosis while using chitosan/Ag nanoparticles. *Source* J. Biomed. Nanotechnol. 12, 1585–1603, 2016

Doxorubicin encapsulated chitosan–gold hybrid hydrogel has been synthesized by Rui Chen et al. using the insitu reduction method and have exclusively explained the mechanism for the formation of the hydrogel. It has been reported that the encapsulated doxorubicin was released from the system in a sustained manner over a period of 10 days. It is observed that release of the drug was in accordance to the external pH stimuli, showing the efficacy of the sample for use in smart drug delivery. From the in-vitro cytotoxicity experiments the non toxicity of the hydrogel towards C6 cells has been confirmed and it has also been concluded that doxorubicin maintains its biological effect to kill the tumor cells when released from the hydrogel (Chen et al. 2012) (Fig. 2.6).

Chandran et al. has reported an electric field responsive drug delivery system based on chitosan–gold nanocomposites (CGNC) for site specific and controlled delivery of 5-fluorouracil. The encapsulation of drug into 3D network CGNC at higher pH and release of the drug from CGNC at low pH due to the reversible gel–sol transition of CGNC has been established. The authors have controlled the release of the drug from CGNC using a weak external DC electric field. About 63% of the encapsulated drug was released on application of electric field. The biocompatibility of CGNC has also been demonstrated by growing SiHa cells on a CGNC film which was electrodeposited on an indium tin oxide (ITO) coated glass plate. These cells exhibited less viability initially and complete cell death was observed on application of an electric field of 1.5 V (Chandran and Sandhyarani 2014).

Another report elucidating the complete preparation of 5-FU encapsulated CS/Au nanocomposite has been published by Nivethaa et al. The scheme for the synthesis is given below. About 97% of the loaded drug was released from the system in 72 h in a two step manner. 50% MCF-7 cell apoptosis was obtained while using a sample concentration of 31.2 μg/ml. The non-toxicity of the system towards VERO cells

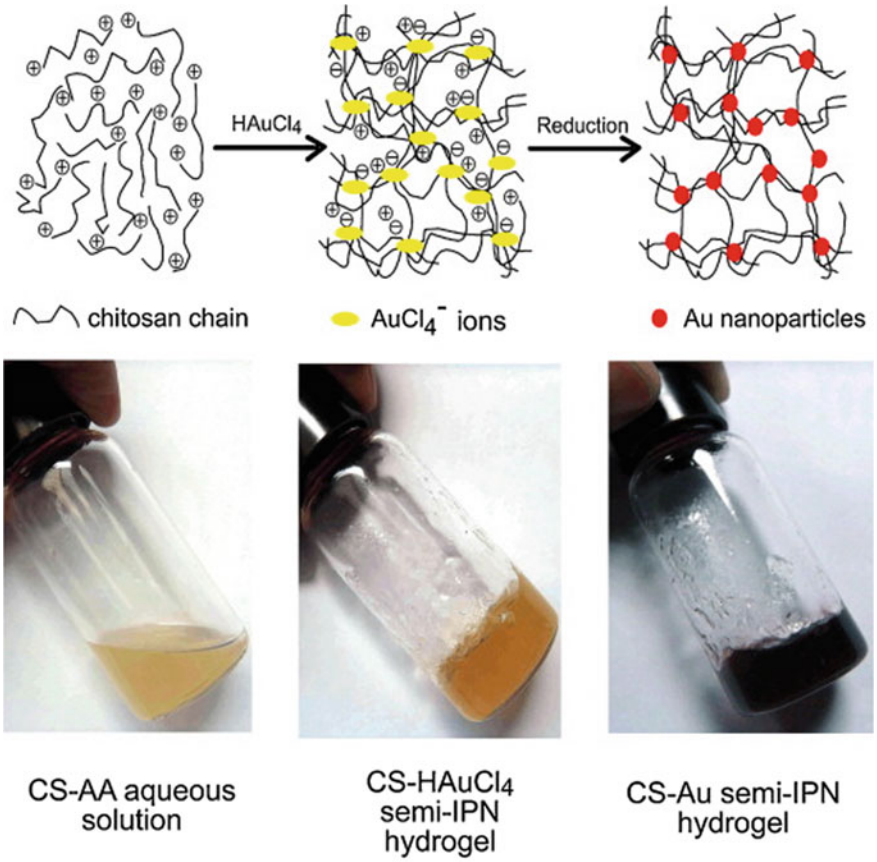


Fig. 2.6 CS–Au hydrogel formation mechanism. *Source* Colloids and Surfaces B: Biointerfaces 97, 132–137, 2012

at the concentration wherein IC_{50} is obtained has also been analyzed and reported. Moreover, the release kinetics has been studied by the authors and the obtained results clearly indicate the adherence of the maximum portion of the release profile to zero order kinetics, which pertains to the constant release of the drug from the delivery vehicle. All these features clearly substantiate the potency of the system to deliver 5-FU effectively (Nivethaa et al. 2015) (Figs. 2.7 and 2.8).

Dhanavel et al. has studied the cytotoxicity of dual drug loaded chitosan/palladium nanocomposite towards HT-29 cancer cells. In this study, curcumin (CUR) and 5-FU loaded CS/Pd nanocomposite has been prepared using the chemical reduction method. On the basis of the regression coefficient values obtained on fitting the drug release to the various kinetic models, the authors have concluded that the major portion of the release profile of co-delivery system fits well to the zero order kinetics which clearly indicates the capability of the CS/Pd for the sustained and prolonged

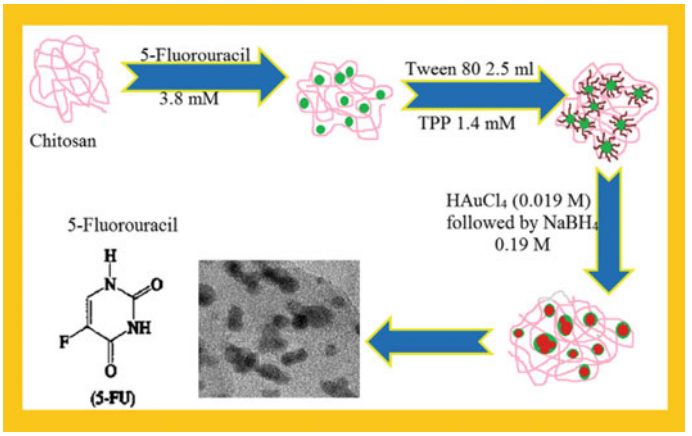


Fig. 2.7 Schematic representing the preparation of 5-Fluorouracil loaded CS/Au nanocomposite. *Source* RSC Adv., 5, 1024, 2015

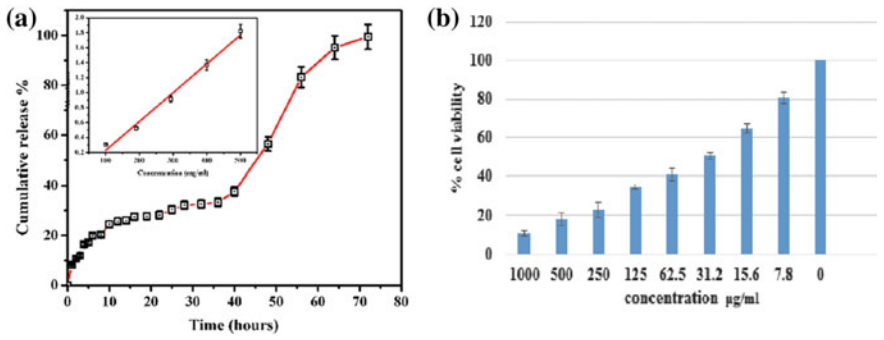


Fig. 2.8 **a** Drug release profile of 5-FU encapsulated CS/Au nanocomposite. **b** Cytotoxity analysis of 5-FU encapsulated CS/Au nanocomposite towards MCF7 and VERO cells. *Source* RSC Adv., 5, 1024, 2015

release of 5-FU and CUR. The cytotoxicity analysis has been used to study the cytotoxicity of drug encapsulated nanocomposite towards human colorectal HT-29 cells and it has been concluded that the co-encapsulated nanocomposite shows superior inhibitory effect on growth of HT-29 cells over 5-FU, CUR monotherapy. So from the report it is clearly evident that the CS/Pd system will be useful as a multidrug delivery platform (Dhanavel et al. 2017).

Naficy et al. has reported the use of chitosan–carbon nanotube films for the release of dexamethasone. In this paper, the modulated release of dexamethasone (DEX) by electrical stimulation has been studied using chitosan and single walled carbon nanotubes (SWCNT). Dexamethasone has been loaded into chitosan hydrogels with and without single walled carbon nanotubes. The role of SWCNTs as a diffusion barrier for DEX thus, slowing down its release in the absence of electrical potential

is observed (passive release). It is further reported that the release of DEX could be accelerated comparitively by inducing electrostatic repulsion which in turn can be achieved by negatively charging the SWCNTs. In this way, the release of DEX has been effectively turned on and off by controlling the applied electrochemical potential thus, making the system an attractive drug delivery carrier (Naficy et al. 2009).

Chitosan functionalized carbon nanotubes have been used for delivery of SNX-2112 in cancer cells. The exceptional drug-loading capability of SWCNTs–CS system has been established in this study. LDH release assay and western-blotting studies show the significant inhibiting effect of SWCNT-CHI/SNX-2112 on K562 cells. Therefore, it can be concluded that SWCNT-CHI/SNX2112 shows great potential as a drug delivery system for anti-tumor therapy (Zheng et al. 2016).

5-FU encapsulated CS/MWCNT preparation has also been reported by Nivethaa et al. The authors have reported about 72% of release of 5-FU from the system in 72 h. IC_{50} for MCF-7 is observed on taking 60 μg/ml of drug loaded sample, showing the suitability of the system for the eradication of cancerous cells (Nivethaa et al. 2016a, b).

The same group has also worked on the delivery of 5-FU using ternary compounds of CS. They have investigated the used of systems containing CS along with MWCNT and Au or Ag and also a system containing Ag and Au in the form of alloy. A release of about 63.1% of drug from CS/Ag/MWCNT has been reported and a release of 67.6% of drug from CS/Ag-Au was observed in 72 h. Similarly 50% apoptosis of MCF-7 cells was observed on taking 55 μg/ml of CS/Ag-Au and 50 μg/ml of CS/Ag MWCNT. Based on their extensive studies on the use of binary and ternary nanocomposites of chitosan for the delivery of 5-FU they have concluded that CS/Au/MWCNT is the most suitable system for the sustained and prolonged release of 5-FU and also that the CS/Au/MWCNT system exhibits higher cytotoxicity towards MCF-7 cells even when taken in small quantities when compared to the other systems (Nivethaa et al. 2016a, b, 2017).

2.3.3 Chitosan-Bioglass (CS–BGn) for Drug Delivery

Nanocomposites with bone-bioactivity and drug eluting capacity are considered as potential candidates for coating materials for metallic bone implants. Patel et al. has reported the use of chitosan–bioactive glass nanoparticles for the delivery of ampicillin. The sustained release of the therapeutic drug effectively incorporated during the coating process has been shown for a period of 10–11 weeks. The effect of drug release has also been confirmed by an antibacterial test against Streptococcus mutants. So it has been concluded that CS–BGn allows a range of potential applications for coatings of metallic implants and scaffolds for bone repair and regeneration (Patel et al. 2012).

Similarly, Jayalekshmi et al. has reported the use of gold nanoparticle incorporated polymer/bioactive glass composite for controlled drug delivery application. In

this report, the system has been used for the delivery of doxorubicin, wherein 18% of the drug has been reportedly released from the system on the 8th day at pH 7.4. Thus, it has been concluded that the drug delivery efficiency was high due to the nanosize of the composite and also that the non-toxicity of the composite, biocompatibility and controlled release of doxorubicin from the system were conclusive of the effectiveness of the system for chemotherapeutic applications (Jayalekshmi and Sharma 2015).

2.4 Conclusion

Chitosan is the second most abundant natural biopolymer which has been extensively studied since many decades. It has been used for multifunctional applications due to the attractive properties it possesses. Among the various fields, the use of chitosan in the biomedical field has yielded remarkable results, mainly in the genre of drug delivery. This polymer alone or in the form of composites with other moieties has helped in the successful delivery of drugs to specific sites and has also helped in reducing the number of dosages administered by prolonging the bioavailability of the drugs. Moreover, it has aided in the sustained and prolonged release of many antibiotics and anticancer drugs, thus taking us a step closer in treating lethal infections and diseases. So on the whole chitosan and its composites are a boon to us. Eventhough, chitosan and chitosan based systems have been studied for long in an extensive manner, there is still scope for the preparation of more composites based on chitosan and using them for the delivery of highly effective drugs, whose usage has been abandoned due to their harmful side effects. Hence, from this review we conclude that chitosan nanoparticles conjugated to noble metals are better suited for drug delivery and treatment of cancer as they enable the sustained and prolonged release of drugs while simultaneously acting as a platform for the photothermal treatment of cancer cells and also that chitosan will remain in the limelight for decades to come.

References

Banerjee SL, Khamrai M, Sarkar K, Singha NK, Kundu PP (2016) Modified chitosan encapsulated core-shell Ag Nps for superior antimicrobial and anticancer activity. Int J Biol Macromol 85:157–167

Boca SC, Potara M, Gabudean A-M, Juhem A, Baldeck PL, Astilean S (2011) Chitosan-coated triangular silver nanoparticles as a novel class of biocompatible, highly effective photothermal transducers for in vitro cancer cell therapy. Cancer Lett 311(2):131–140

Chandran PR, Sandhyarani N (2014) An electric field responsive drug delivery system based on chitosan–gold nanocomposites for site specific and controlled delivery of 5-fluorouracil. RSC Advances 4(85):44922–44929

Chen R, Chen Q, Huo D, Ding Y, Hu Y, Jiang X (2012) In situ formation of chitosan–gold hybrid hydrogel and its application for drug delivery. Colloids Surf, B 97:132–137

de Salamanca AE, Diebold Y, Calonge M, García-Vazquez C, Callejo S, Vila A, Alonso MJ (2006) Chitosan nanoparticles as a potential drug delivery system for the ocular surface: toxicity, uptake mechanism and in vivo tolerance. Invest Ophthalmol Visual Sci 47(4):1416–1425

Dhanavel S, Nivethaa EAK, Narayanan V, Stephen A (2017) In vitro cytotoxicity study of dual drug loaded chitosan/palladium nanocomposite towards HT-29 cancer cells. Mater Sci Eng, C 75:1399–1410

Duan J, Zhang Y, Han S, Chen Y, Li B, Liao M, Chen W, Deng X, Zhao J, Huang B (2010) Synthesis and in vitro/in vivo anti-cancer evaluation of curcumin-loaded chitosan/poly(butyl cyanoacrylate) nanoparticles. Int J Pharm 400(1–2):211–220

Hwang SW, Shin JS (2018) Pectin-coated curcumin-chitosan microparticles crosslinked with Mg^{2+} for delayed drug release in the digestive system. Int J Polym Sci 2018:7

Islam A, Yasin T (2012) Controlled delivery of drug from pH sensitive chitosan/poly(vinyl alcohol) blend. Carbohyd Polym 88(3):1055–1060

Jayalekshmi AC, Sharma CP (2015) Gold nanoparticle incorporated polymer/bioactive glass composite for controlled drug delivery application. Colloids Surf, B 126:280–287

Kanikireddy V, Yallapu M, Varaprasad K, Nagireddy N, Ravindra S, Neppalli S, Raju K (2011) Fabrication of curcumin encapsulated chitosan-PVA silver nanocomposite films for improved antimicrobial activity, vol 2

Lu B, Lv X, Le Y (2019) Chitosan-modified PLGA nanoparticles for control-released drug delivery. Polymers 11(2)

Maeda Y, Kimura Y (2004) Antitumor effects of various low-molecular-weight chitosans are due to increased natural killer activity of intestinal intraepithelial lymphocytes in sarcoma 180–bearing mice. J Nutr 134(4):945–950

Naficy S, Razal JM, Spinks GM, Wallace GG (2009) Modulated release of dexamethasone from chitosan–carbon nanotube films. Sens Actuators, A 155(1):120–124

Nivethaa EAK, Dhanavel S, Narayanan V, Vasu CA, Stephen A (2015) An in vitro cytotoxicity study of 5-fluorouracil encapsulated chitosan/gold nanocomposites towards MCF-7 cells. RSC Adv 5(2):1024–1032

Nivethaa EA, Dhanavel S, Rebekah A, Narayanan V, Stephen A (2016a) A comparative study of 5-Fluorouracil release from chitosan/silver and chitosan/silver/MWCNT nanocomposites and their cytotoxicity towards MCF-7. Mater Sci Eng, C 66:244–250

Nivethaa EAK, Dhanavel S, Narayanan V, Stephen A (2016b) Fabrication of chitosan/MWCNT nanocomposite as a carrier for 5-fluorouracil and a study of the cytotoxicity of 5-fluorouracil encapsulated nanocomposite towards MCF-7. Polym Bull 73(11):3221–3236

Nivethaa EAK, Dhanavel S, Narayanan V, Stephen A (2017) Chitosan stabilized Ag-Au nanoalloy for colorimetric sensing and 5-Fluorouracil delivery. Int J Biol Macromol 95:862–872

Pandey S, Mishra A, Raval P, Patel H, Gupta A, Shah D (2013) Chitosan–pectin polyelectrolyte complex as a carrier for colon targeted drug delivery. J Young Pharm 5(4):160–166

Parveen S, Sahoo SK (2011) Long circulating chitosan/PEG blended PLGA nanoparticle for tumor drug delivery. Eur J Pharmacol 670(2):372–383

Patel KD, El-Fiqi A, Lee H-Y, Singh RK, Kim D-A, Lee H-H, Kim H-W (2012) Chitosan—nanobioactive glass electrophoretic coatings with bone regenerative and drug delivering potential. J Mater Chem 22(47):24945–24956

Rajendran A, Basu S (2009) Alginate-chitosan particulate system for sustained release of nimodipine, vol 8

Remuñán-López C, Lorenzo-Lamosa ML, Vila-Jato JL, Alonso MJ (1998) Development of new chitosan–cellulose multicore microparticles for controlled drug delivery. Eur J Pharm Biopharm 45(1):49–56

Seda Tığlı Aydın R, Pulat M (2012) 5-fluorouracil encapsulated chitosan nanoparticles for pH-stimulated drug delivery: evaluation of controlled release kinetics. J Nanomater 2012:10

Vidyalakshmi K, Rashmi KN, Pramod Kumar TM, Siddaramaiah (2004) Studies on formulation and in vitro evaluation of PVA/chitosan blend films for drug delivery. J Macromol Sci, Part A 41(10):1115–1122

Wang H, Roman M (2011) Formation and properties of chitosan–cellulose nanocrystal polyelectrolyte–macroion complexes for drug delivery applications. Biomacromol 12(5):1585–1593

Wang Y, Li P, Kong L (2013) Chitosan-modified PLGA nanoparticles with versatile surface for improved drug delivery. AAPS Pharm Sci Tech 14(2):585–592

Yang R, Yang S-G, Shim WS-, Cui F, Cheng G, Kim I-W, Kim D-D, Chung S-J, Shim C-K (2009) Lung-specific delivery of paclitaxel by chitosan-modified PLGA nanoparticles via transient formation of microaggregates. J Pharm Sci 98(3):970–984

Yao KD, Yin YJ, Xu MX, Wang YF (1995) Investigation of pH-sensitive drug delivery system of chitosan/gelatin hybrid polymer network. Polym Int 38(1):77–82

Yao Q, Liu W, Gou X-J, Guo X-Q, Yan J, Song Q, Chen F-Z, Zhao Q, Chen C, Chen T (2013) Preparation, characterization, and cytotoxicity of various chitosan nanoparticles. J Nanomater 2013:6

Yu C-Y, Zhang X-C, Zhou F-Z, Zhang X-Z, Cheng S-X, Zhuo R-X (2008) Sustained release of antineoplastic drugs from chitosan-reinforced alginate microparticle drug delivery systems. Int J Pharm 357(1):15–21

Zheng L, Wu S, Tan L, Tan H, Yu B (2016) Chitosan-functionalised single-walled carbon nanotube-mediated drug delivery of SNX-2112 in cancer cells. J Biomater Appl 31(3):379–386

Chapter 3
Solubility of Hydroxyapatite as a Function of Solution Composition (Experiment and Modeling)



George Kuranov, Konstantin Mikhelson and Alexandra Puzyk

Abstract Solubility of hydroxyapatite in aqueous solutions and artificial blood serum was studied at 37 °C. The obtained results demonstrate non-monotonous changes of the concentration of calcium ions in solution over time: the respective curves contain a maximum. This may be evidence in favor that dissolution of hydroxyapatite is an incongruent process. It was shown that equilibrium can be achieved in three weeks. The logarithm of activity of calcium ions exhibits a direct relation on the pH. Results of the determination of the chemical composition of solid phase obtained by XPS, EDX and ICP-OES methods confirm the incongruent nature of hydroxyapatite dissolution. In this study, we have performed a modeling of the chemical and phase equilibria in solution that served as a prototype of the blood serum with application to calcification of tissues. The concentrations of molecular–ionic forms containing calcium and hydrogen cations and phosphate anions were calculated, and the nonideality of the solutions was accounted for by the Debye–Hückel theory. The calculated degrees of salt supersaturation of different phosphates, which tend to crystallize in blood serum, demonstrate that hydroxyapatite is the most supersaturated phosphate at any values of calcium and phosphorus overall concentrations.

Keywords Hydroxyapatite solubility · Aqueous solutions · Artificial blood serum

3.1 Introduction

Hydroxyapatite (HAP) is the main mineral component of teeth, bones and one of the most common minerals in pathologic masses in human body. The solubility of hydroxyapatite has been the subject of extensive studies for several decades (Dorozhkin 2017a). Initially, the interest in this topic was caused by the need for study of the impact of external factors on dental enamel, and for the development of dental materials and means for the enamel protection. For this reason the solubility

G. Kuranov (✉) · K. Mikhelson · A. Puzyk
Institute of Chemistry, Saint Petersburg State University, Universitetsky Av., 26, Saint Petersburg 198504, Russian Federation
e-mail: g_kuranov@mail.ru

© Springer Nature Switzerland AG 2020

O. V. Frank-Kamenetskaya et al. (eds.), *Processes and Phenomena on the Boundary Between Biogenic and Abiogenic Nature*, Lecture Notes in Earth System Sciences,
https://doi.org/10.1007/978-3-030-21614-6_3

of hydroxyapatite was studied under acidic conditions. Biocompatibility of hydroxyapatite allows using this mineral as a material for various artificial implants, and a huge number of works devoted to this issue has been published in recent years (Dorozhkin 2017b). The phenomena of calcification of soft tissues also attract a lot of attention. To date, many works on the solubility of hydroxyapatite in water were published, but the reported data poorly fit together. Some literature experimental data on hydroxyapatite solubility in aqueous solutions at different pH are presented in Fig. 3.1.

It was even concluded (Levinskas and Neuman 1955) that it is impossible to determine the HAP solubility product constant. Based on the analysis of existing data on the solubility of hydroxyapatite in water, the authors of the review (Pan and Darvell 2009) concluded that it is necessary to obtain new reliable data.

One of the reasons for the discrepancy between experimental data is called incongruence of the dissolution process. It is assumed that chemical reactions take place on the surface of hydroxyapatite during the dissolution process. However, there is no reliable information about chemical transformations occurring in the system. Incongruent solubility can be attributed to differences in the rate of formation and dissolution of an intermediate solid phase (Kaufman and Kleinberg 1979). In this way, it cannot be said with confidence what solid substance (i.e., in contact with the solution) is relevant to the equilibrium. In fact, the second phase formed on hydroxyapatite may have a different composition. For example, octacalcium phosphate has been found to form on the surface of a hydroxyapatite seed in a supersaturated calcium phosphate solution (Pan and Darvell 2009). Eight dissolution models for

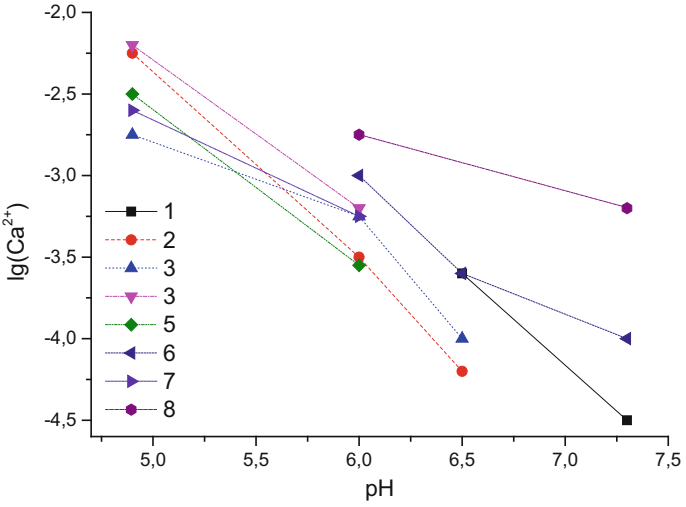


Fig. 3.1 Experimental data on hydroxyapatite solubility in aqueous solutions at different pH from literature sources: (1) Rootare et al. (1962), (2) Wier et al. (1971), (3) Avnimele et al. (1973), (4) Chuong (1973), (5) McDowell et al. (1977), (6) Bell et al. (1978), (7) Verbeeck et al. (1980), (8) Mahapatra et al. (1982)

hydroxyapatite are considered in the review (Dorozhkin 2002), but none of these is free of drawbacks.

Difficulties of the study of hydroxyapatite solubility are caused by long duration of the setting of chemical and phase equilibria and extremely low solubility. Until now, no studies of influence of electrolyte and protein composition of body fluids on the solubility of hydroxyapatite have been carried out.

Low solubility of hydroxyapatite complicates the experimental study, because even a small sampling can shift the equilibrium in the system. In this regard, it is important to provide non-destructive analysis of the composition of a solution that is in contact with hydroxyapatite. This can be done by a direct potentiometric measurement with electrode selective to calcium ions. The use of calcium ion-selective electrode (Ca-ISE) allows for a continuous measuring the composition of the solution in time, directly in the cell, without sampling. This method has an important additional advantage: the signal of the sensor depends on the activity rather than the concentration of calcium ions in solution. Thus, the data obtained by Ca-ISE are more relevant thermodynamically than those obtained by classical "wet chemistry" or by ICP-MS or other modern methods which deliver data on total (free + complexed) calcium concentration.

The lack of reliable experimental data hampered the development of thermodynamic modeling of chemical and phase equilibria in solutions that served as a prototype of the blood serum. The problems of calculating phase equilibria in calcium phosphate systems—blood serum were discussed elsewhere (Golovanova 2018; Glinkina et al. 2004).

The main goal of the present work was to get reliable data on the solubility of hydroxyapatite as a function of the solution composition, to advance in the understanding of incongruent features of HAP dissolution, and to develop a modeling approach capable of describing chemical and phase equilibria in the systems under consideration.

3.2 Experimental

3.2.1 Ca-ISE Fabrication

Calcium ionophore I diethyl N,N′-[(4R,5R)-4,5-dimethyl-1,8-dioxo-3,6-dioxaoctamethylene]bis(12-methylaminododecanoate)] (ETH 1001), potassium tetrakis-*p*-Cl-phenylborate (KClTPB), lipophilic salt tetradodecylammonium tetrakis-*p*-Cl-phenylborate (ETH 500), solvent plasticizers 2-nitrophenyloctyl ether (oNPOE) and bis(2-ethylhexyl)sebacate (DOS), high molecular weight poly(vinyl chloride) (PVC) were Selectophore grade reagents from Fluka (Switzerland). Volatile solvents were extra pure cyclohexanone (CH) and HPLC grade tetrahydrofuran (THF) from Vekton (Russia). Inorganic salts were from Reaktiv (Russia).

Table 3.1 Membrane compositions (weight percent and molality of the components)

Component	Membrane 1	Membrane 2
ETH 1001	1.03%, 0.023 m	1.02%, 0.023 m
KClTPB	0.52%, 0.016 m	0.52%, 0.016 m
ETH 500	0	1.19%, 0.016 m
Plasticizer	oNPOE, 65.63%	DOS, 64.85%
PVC	32.82%	32.42%

All aqueous solutions were prepared with deionized (DI) water with resistivity 18.2 MΩ cm (Milli-Q Reference, Millipore, France).

The membrane cocktails were prepared by dissolving appropriate amounts of PVC and oNPOE or DOS in THF. After that, ETH 1001, KClTPB and ETH 500 were added as appropriate aliquots of stock solutions in cyclohexanone. In this way, weighing of small amounts was avoided, ensuring high accuracy of the membrane composition. To obtain the membranes, the cocktails were stirred for 30 min using roller-mixer Selecta Movil Rod (Spain) and then cast on glass Petri dishes with diameter of 70 mm. The dishes were closed with filter paper to slow down the evaporation of THF. The complete evaporation of THF and CH took 2 days, and after that master membranes with a thickness of about 0.7 mm were obtained. Two membranes, respectively with oNPOE or DOS were prepared, for the membrane compositions see Table 3.1.

The electrodes were prepared by cutting disks with a diameter of 12 mm from the master membrane and gluing them to PVC bodies with outer diameter of 12 mm and inner diameter of 8 mm. A solution of PVC in CH was used as the glue. The internal reference electrode was chlorinated silver wire in a polypropylene body. Six replicate electrodes with each membrane composition were used in this work.

Initially, the ISEs were filled with 0.01 M $CaCl_2$ and conditioned in this solution for 3 days prior to measurements. After that, zero-current EMF measurements have been performed in $CaCl_2$ solutions with Lawson EMF-16 (Lawson Labs, Inc, USA). The reference electrode was a single junction Ag/AgCl electrode in 3.5 M KCl, with a salt bridge with a limited leak of KCl. Control measurements (to check the suitability of the ISEs) were carried out at room temperature (22 ± 1 °C) from 0.1 M down to 10^{-8} M $CaCl_2$ using automatic diluter Metrohm 700 Dosino controlled by Metrohm 711 Liquino Controller.

Ca^{2+}-selective membranes based on ETH 1001 are typically plasticized with polar plasticizer oNPOE because high polarity favors selectivity to divalent ions over monovalent (Bakker et al. 1997; Mikhelson 2013). However, high polarity also makes membranes prone to sorption of proteins which deteriorates the ISE response. This is why we also used DOS as plasticizer. It is known that the selectivity can be improved by adding background electrolyte: a lipophilic salt like ETH 500 (Nägele et al. 1998). Furthermore, it was shown that Ca-ISEs with low-polar membranes containing ETH 1001 and also ETH 500 show the same selectivity as those plasticized with oNPOE (Mikhelson et al. 2001; Vázquez et al. 2001).

In contact with pure $CaCl_2$ solutions, both kinds of ISEs: containing oNPOE or DOS as plasticizers, showed linear response with the slope of 29.8 mV/log(a_{Ca}) from

Table 3.2 Composition of MABS (mmol/l)

Na^+	K^+	Mg^{2+}	Cl^-	HCO_3^-	HPO_4^{2-}	$H_2PO_4^-$	$C_6H_{12}O_6$	$(NH_2)_2CO$	HEPES
135.5	5	0.5	109	27	2	0.5	5.5	5.5	80 g/l

0.1 to 10^{-5} M $CaCl_2$ with the detection limit of 10^{-6} M $CaCl_2$. However, in contact with model solutions containing glucose and urea ISEs with oNPOE as plasticizer did not show stable results, so we did not use these ISEs in further studies. The behavior of ISEs plasticized with DOS appeared more promising. The calibrations were stable over time and did not deteriorate after contact with model solutions containing organic substances.

3.2.2 HAP Solubility Measurement Procedure

In this work we studied the solubility of HAP in aqueous solutions at pH from 5.5 to 8.0 and in a model artificial blood serum (MABS) (but without Ca^{2+} ions and proteins) at pH = 7.4.

Sigma-Aldrich NaCl (99.5%), $NaHCO_3$ (99.5%), KCl (99.0%), $Na_2HPO_4 \cdot H_2O$ (99.5%), NaH_2PO_4 (99.5%), $MgCl_2 \cdot 6H_2O$ (98%), $C_6H_{12}O_6$ (99.6%), $(NH_2)_2CO$ (99.2%), $CaCl_2 \cdot 2H_2O$ (99%), HEPES (99.5%) and DI water were used in the preparation of stock solutions. MABS solutions were prepared by dissolving of aliquots of stock solutions of the respective components in DI water. The composition of MABS solutions is presented in Table 3.2. The final pH value was adjusted with small aliquots of HCl or NaOH solutions at 37 °C.

Different amounts of HAP from Sigma-Aldrich (0.2 and 0.1 g) were added to glass beakers (80 ml) filled with solutions (40 ml) of the compositions studied. Closed beakers were placed in a thermostated shaker at 37.0 ± 0.5 °C. EMF measurements by Ca-ISEs were performed every two or three days until the values stabilized. It took long time (some weeks), and the MABS solutions deteriorated due to bacterial activity. To prevent that, we tried different antibacterial agents such as sodium azide, sodium benzoate, myristamidopropyldimethylbenzyl ammonium chloride, but the best results were achieved by daily irradiation with UV lamp for 15 min.

3.2.3 EMF Measurements

Before measurements in samples, ISEs were always calibrated either in aqueous $CaCl_2$: to study solubility of HAP in water, or in MABS solutions containing known amounts of $CaCl_2$: to study HAP solubility in MABS. Calibrations were performed within the range of Ca^{2+} concentration from 10^{-5} to 10^{-3} M. Model solutions containing glucose and urea did not last. Therefore, fresh calibration solutions were

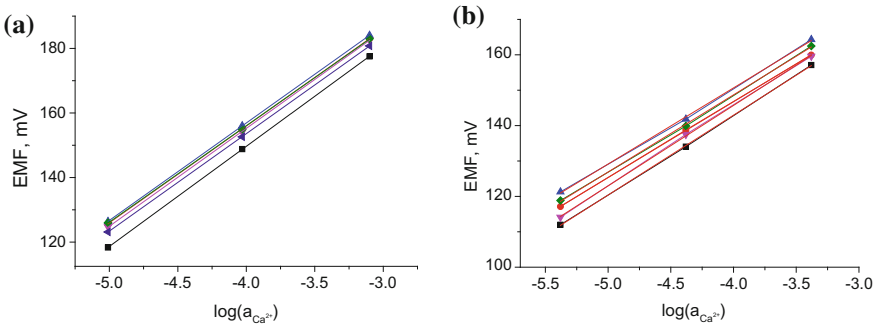


Fig. 3.2 Calibration plots of the ISEs in aqueous (**a**) and model solutions (**b**)

prepared on daily basis by dissolving of aliquots of stock solutions of the respective components in DI water.

Activities of Ca^{2+} ion in solutions were calculated according to the Davis' equation (3rd approximation of the Debye-Hückel theory):

$$\log \gamma_I = -\frac{0.512 z_I^2 \sqrt{J}}{1 + a_{Kiel} \cdot 0.328\sqrt{J}} + 0.1 z_I J$$

Here γ_I is the ion activity coefficient, z_I is the ion charge number, J is the solution ionic strength, and a_{Kiel} is the Kielland parameter (6 for Ca^{2+}) (Dvorak et al. 1975).

Examples of the calibration results of the ISEs in aqueous and model solutions are presented in Fig. 3.2.

Preliminary measurements revealed rather low concentrations of ionized calcium in model solutions.

Therefore, to reduce the transmembrane fluxes of $CaCl_2$ co-extracted from the internal solution, the ISEs were re-filled with 10^{-3} M $CaCl_2$ and stored in the same solution in between the experiments.

3.3 Results of the Measurements

The results of the measurements reproduced several times demonstrate that the concentration of calcium ions in solution non-monotonously changes over time: the respective curves contain a maximum. The height of the maximum depends on the initial amounts of HAP (Fig. 3.3).

It took about 30 days for the equilibrium to establish, and only after that calcium ion activity becomes equal in all solutions with the same pH regardless of initial amounts of HAP.

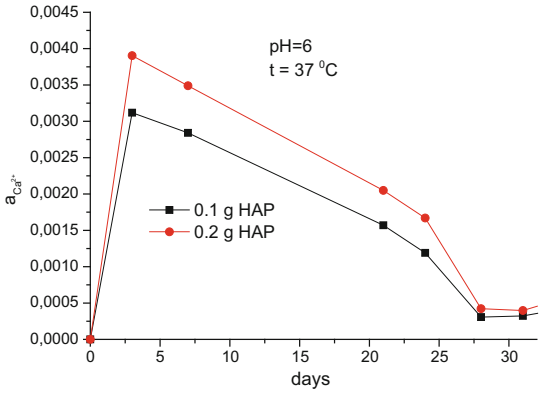


Fig. 3.3 Dependence of Ca^{2+} ion activity on time and on initial amounts of HAP in aqueous solutions (average data for 6 ISEs)

Averaged data for 6 ISEs in three parallel experiments (18 independent measurements for solution of one composition) demonstrate a linear correlation between $\log(a_{Ca})$ and the pH (Fig. 3.4).

The HAP solubility in MABS solutions has the same dynamics, but the value of solubility is lower (Fig. 3.5).

We interpret the non-monotonous change of the activity of calcium ions over time as evidence in favor of incongruent dissolution of HAP. This is in line with data reported elsewhere. Apparently, some chemical reactions occur on the surface of HAP during its dissolution. Therefore, we made some studies of the solid phase.

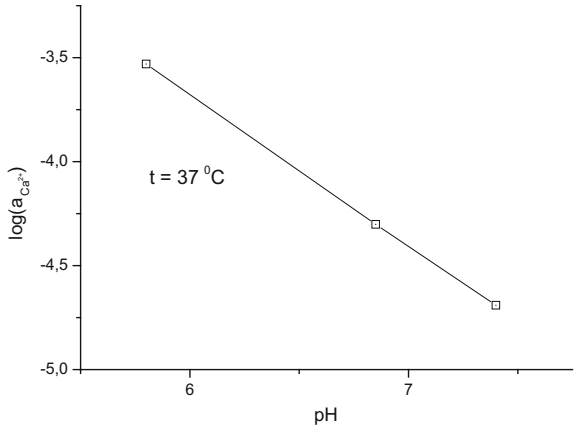


Fig. 3.4 The correlation between calcium ion activity and the pH in aqueous solutions

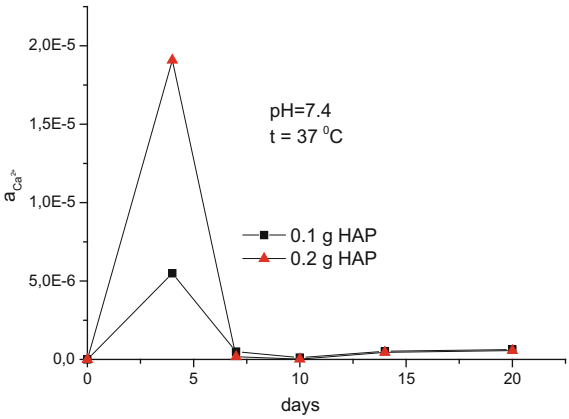


Fig. 3.5 Dependence of activity of Ca^{2+} in MABS solutions on time and on initial amounts of HAP (average data for 6 ISEs)

3.4 Study of Solid Phase

X-Ray photoelectron spectroscopy (XPS), energy-dispersive X-ray microanalysis (EDX) and inductive coupled plasma optical emission spectroscopy (ICP-OES) were used for the determination of the chemical composition of solid phase. XPS is the surface method; depth of the electron emission is about several nanometers from the surface. ICP-OES is used for the estimation of the total composition. EDX can be considered as intermediate analysis with the depth of the electron emission about several micrometers. Using all three methods simultaneously allows obtaining data of the element distribution over the volume of a solid sample.

3.4.1 Sample Preparation

Equilibrium solid phase was decanted and washed twice with ice DI water. After centrifugation the sediment was dried at 40 °C during 24 h. We studied solid phases which were in equilibrium with aqueous solutions at pH 5.6, 6.6 and 7.9, and the respective samples are denoted as S5.6, S6.6 and S7.9.

3.4.2 X-Ray Photoelectron Spectroscopy

XPS study was performed at Thermo Fisher Scientific Escalab 250Xi using AlKα (1486.6 eV) radiation. The measured binding energies were corrected referring the energy position of C_{1s} 284.8 eV. All the data was obtained and processed using program complex Avantage v5.9.

3.4.3 Scanning Electron Microscopy (SEM) and Energy Dispersive X-Ray (EDX) Microanalysis

Morphology of the samples was studied with scanning electron microscope Hitachi S-3400N, accelerating voltage was 20 kV. EDX analysis was carried out with Oxford X-Max 20 add-on, probe diameter 2 μm, probe current was 1 nA.

3.4.4 Inductively Coupled Plasma–Optical Emission Spectroscopy

ICP-OES study was carried out using Shimadzu ICPE-9000. Standard samples for the calibration solutions were made of multi- and mono standards MERC in 0.1 N HNO_3.

3.4.5 Results of Solid Phase Study

SEM images of samples of HAP before and after 30 days stay in water demonstrate erosion of particles; their sizes decrease over time (Fig. 3.6).

The results of the study of elemental composition of solid phase and of the initial sample of HAP are presented in Table 3.3.

As mentioned above, XPS delivers data on the composition of the sample layers in the immediate vicinity to the interface, EDX—at depths of a few micrometers, and ICP-OES—on the whole volume of the sample. This is why the difference between

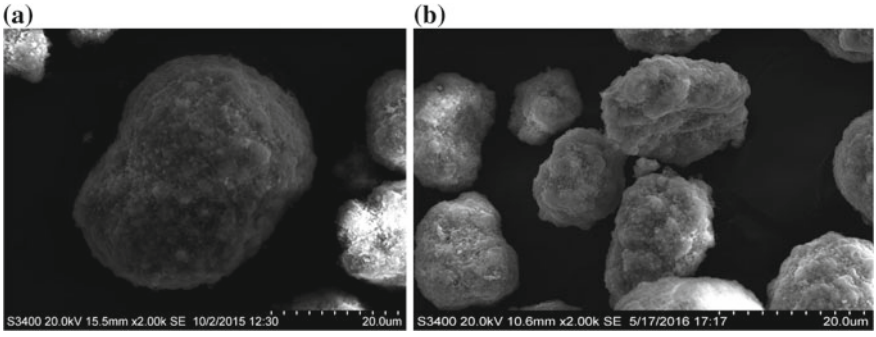


Fig. 3.6 SEM images of HAP particles before (**a**) and after (**b**) 30 days of contact with water at 37 °C

Table 3.3 Elemental composition of untreated HAP and samples by XPS, EDX, ICP-OES methods

Sample	XPS (at.%)				EDX (at.%)				ICP-OES (mol/kg)		
	O	P	Ca	Ca/P	O	P	Ca	Ca/P	P	Ca	Ca/P
S5.6	59.7	14.6	25.6	1.75	65.0	13.7	21.5	1.58	5.3	7.5	1.43
S6.6	60.5	14.9	24.6	1.65	64.5	13.7	21.8	1.57	7.0	10.2	1.45
S7.9	61.8	14.8	23.3	1.57	69.5	12.2	18.3	1.53	5.5	7.8	1.42
HAP	63.3	15.2	21.6	1.42	67.3	13.1	19.6	1.53	6.0	10.0	1.67

the numbers obtained by these three methods shows how the composition varies with the distance from the surface. The data confirm our guess about heterogeneous chemical processes occurring during dissolution of HAP. The greatest changes can be observed in the surface layer at lower pH. The relative contents of phosphorus and oxygen decrease; it may be explained by the replacement of phosphate by carbonate groups. A molar ratio of calcium to phosphorus in the samples decreases over distance from surface to bulk of the particles (Fig. 3.7). However, the results obtained by ICP-OES which refer to the total composition of a sample may be biased because the impact from the surface to the overall result increases with the decrease of the particle size.

The acidity of solutions affects primarily the composition of the surface layer (Fig. 3.8).

Figure 3.9 shows the XPS spectra of the O 1s region of S5.6 and HAP samples. Height and area of the peak of untreated HAP are bigger, besides this, one can observe an asymmetry of the pick of S5.6. The asymmetry suggests that the observed peak represents a superposition of two non-resolved peaks which refer to different binding energies. In turn, this implies that oxygen in S5.6 is involved in different chemical bonds which were not in untreated HAP.

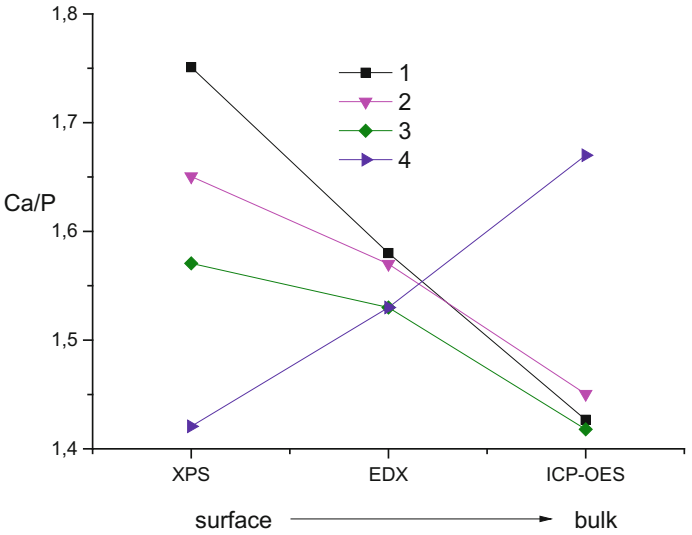


Fig. 3.7 Qualitative change profile of Ca/P in the samples: (1) S5.6, (2) S6.6, (3) S7.9, (4) HAP

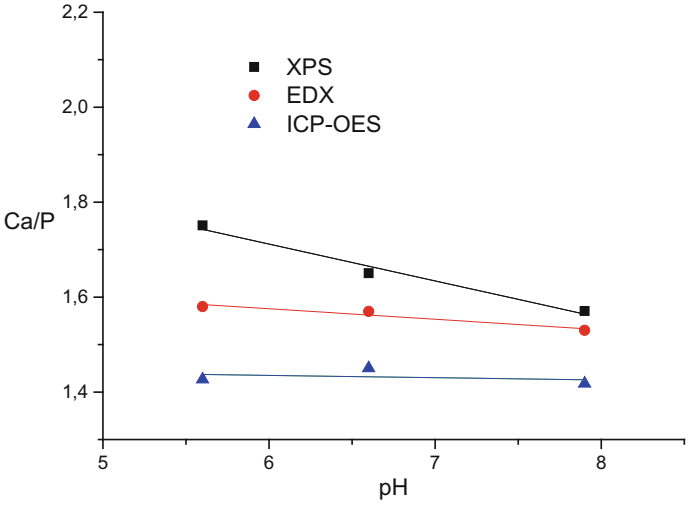


Fig. 3.8 Dependence of Ca/P on the pH of equilibrium solutions

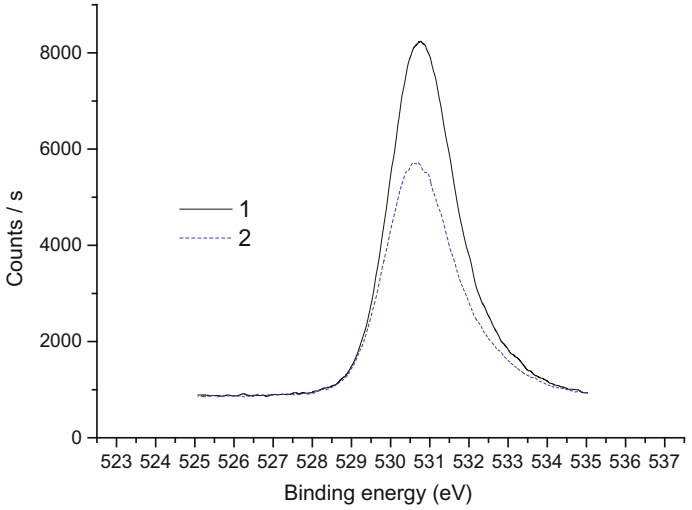


Fig. 3.9 XPS spectra of the O 1s region of HAP (1) and S5.6 (2)

3.5 Modeling

In earlier models, organic components and ions, which do not participate in calcification of the tissues, were not taken into account, with the exception of sodium and chloride ions. Their role was assumed to be confined to their influence on the degree

of nonideality of the solutions due to electrostatic ionic interactions described by the ionic strength of the solution.

We have considered the full set of the chemical equilibria taking into account the dissociation of water and of phosphoric acid, as well as formation of both neutral and charged calcium phosphates. The equilibrium constants were written in the thermodynamic form:

$H^+ + OH^- \leftrightarrow H_2O$	$K_W = \gamma_{H^+} * C_{H^+} * \gamma_{OH^-} * C_{OH^-}$	(3.1)
$H^+ + PO_4^{3-} \leftrightarrow HPO_4^{2-}$	$K_2 = \frac{\gamma_{HPO_4^{2-}} * C_{HPO_4^{2-}}}{\gamma_{H^+} * C_{H^+} * \gamma_{PO_4^{3-}} * C_{PO_4^{3-}}}$	(3.2)
$H^+ + HPO_4^{2-} \leftrightarrow H_2PO_4^-$	$K_3 = \frac{\gamma_{H_2PO_4^-} * C_{H_2PO_4^-}}{\gamma_{H^+} * C_{H^+} * \gamma_{H_2PO_4^-} * C_{H_2PO_4^-}}$	(3.3)
$H^+ + H_2PO_4^- \leftrightarrow H_3PO_4$	$K_4 = \frac{\gamma_{H_3PO_4} * C_{H_3PO_4}}{\gamma_{H^+} * C_{H^+} * \gamma_{H_2PO_4^-} * C_{H_2PO_4^-}}$	(3.4)
$Ca^{2+} + H_2PO_4^- \leftrightarrow CaH_2PO_4^+$	$K_6 = \frac{\gamma_{CaH_2PO_4^+} * C_{CaH_2PO_4^+}}{\gamma_{Ca^{2+}} * C_{Ca^{2+}} * \gamma_{H_2PO_4^-} * C_{H_2PO_4^-}}$	(3.5)
$Ca^{2+} + H_2PO_4^- \leftrightarrow CaH_2PO_4^+$	$K_6 = \frac{\gamma_{CaH_2PO_4^+} * C_{CaH_2PO_4^+}}{\gamma_{Ca^{2+}} * C_{Ca^{2+}} * \gamma_{H_2PO_4^-} * C_{H_2PO_4^-}}$	(3.6)
$Ca^{2+} + OH^- \leftrightarrow CaOH^+$	$K_7 = \frac{\gamma_{CaOH^+} * C_{CaOH^+}}{\gamma_{Ca^{2+}} * C_{Ca^{2+}} * \gamma_{OH^-} * C_{OH^-}}$	(3.7)

C_i and γ_i are the molarity and activity coefficient of species i. For the neutral (molecular) species the activity coefficients were assumed to be unity and for the charged particles they were calculated by the Debye–Hückel equation.

Material balances of calcium and phosphorus are defined by Eqs. (3.8) and (3.9):

$$\left[Ca^{2+}\right] + [CaHPO_4] + \left[CaH_2PO_4^+\right] + \left[CaOH^+\right] = Ca^0 \tag{3.8}$$

$$\left[PO_4^{3-}\right] + \left[HPO_4^{2-}\right] + \left[H_2PO_4^-\right] + [CaHPO_4] + \left[CaH_2PO_4^+\right] + [H_3PO_4] = P^0 \tag{3.9}$$

where Ca^0 and P^0 are the overall concentrations of calcium and phosphorus in all forms that contain them.

The acidity of solution is defined by Eq. (3.10):

$$pH = -\lg(\gamma_{H^+} * C_{H^+}) \tag{3.10}$$

So we have a set of ten nonlinear equations for calculation of the concentrations of 10 ionic and molecular species at given values of overall concentrations Ca^0 and P^0, pH and concentrations of sodium and chloride ions (140 mM). Thermodynamic equilibrium constants (Eqs. (3.1)–(3.7)) are known for T = 298 K (Sillen and Martell 1964).

The concentrations of molecular and ionic forms in the range of overall concentrations Ca^0 and from 0.5 to 1.5 mM and at the solution pH of 3.5–7.5 were calculated. An example of the calculated mole fractions of species at $Ca^0 = P^0 = 1$ mM is presented in Fig. 3.10.

The particular kinds of calcium phosphates which are the most important for the description of calcification of soft tissues (and therefore are of special interest) are presented in Table 3.4, together with their solubility products (Hay et al. 1982; Eidelman et al. 1987).

The calculated equilibrium concentrations of species and their activity coefficients were used to calculate the thermodynamic analogues of solubility products K'_{sp}, for example, for $Ca_3(PO_4)_2$:

$$K'_S = C^3_{Ca^{2+}} * \gamma^3_{Ca^{2+}} * C^2_{PO_4^{3-}} * \gamma^2_{PO_4^{3-}}$$

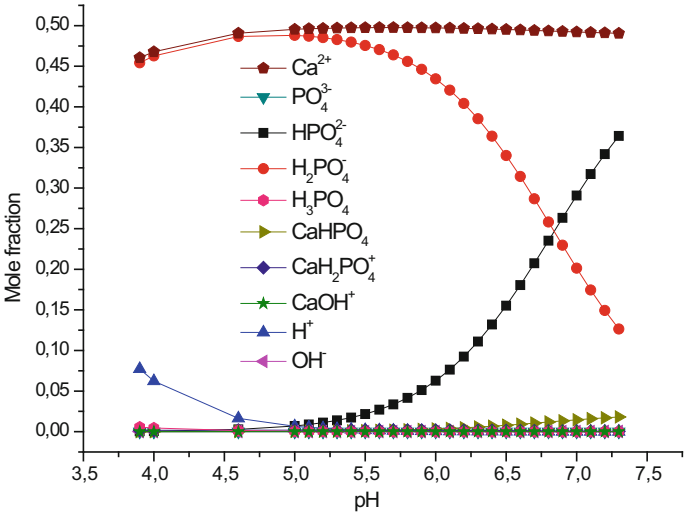


Fig. 3.10 Dependence of mole fraction of species on the pH

Table 3.4 Calcium phosphates under consideration and their solubility products (K_{sp}) (Sillen and Martell 1964)

Calcium phosphate	Formula	K_{sp}
Calcium hydrophosphate dihydrate (CHPD)	$CaHPO_4 * 2H_2O$	2.56×10^{-7}
Calcium orthophosphate (CP)	$Ca_3(PO_4)_2$	1.15×10^{-29}
Octacalcium phosphate (OCP)	$Ca_4H(PO_4)_3 * 2H_2O$[a]	1.03×10^{-47}
Hydroxyapatite (HAP)	$Ca_5(PO_4)_3OH$[a]	3.37×10^{-58}

[a]To simplify the calculations we used here reduced formulas of substances

The calculated values of K'_{sp} were compared with solubility products K_{sp} of the phosphates under consideration (Table 3.4). The comparison of the calculated values of K'_{sp} with the solubility products K_{sp} in solutions with different overall concentrations Ca^0 and P^0 (in all 9 compositions) at pH = 7.4 is presented in Table 3.5.

If a condition $K'_{sp} > K_{sp}$ is met for some phosphate it means that the solution is supersaturated with respect to its thermodynamically equilibrium state, and, therefore, this salt is prone to precipitation. For any values of Ca^0 and P^0 the calculated solubility product analogs for *CHPD* do not exceed the value K_{sp} and so this phosphate does not participate in the calcification of soft tissues. In the case of hydroxyapatite, all calculated values K'_{sp} are in orders of magnitude higher than the tabular data of the solubility product. Therefore from the thermodynamic point of view precipitation of hydroxyapatite plays the main role in the calcification of soft tissues.

The solution composition and the possibility of its supersaturation may conveniently be displayed graphically. The values of $\log([Ca^{2+}][OH^-]^2)$ are plotted as abscissas and the values of $\log([H^+]^3[PO_3{}^-])$ as ordinates. The domain of states that are supersaturated with respect to certain phosphate is above the straight line corresponding to the equation (Glinkina et al. 2004):

$$\log\left(a^3_{H^+} * a_{PO_4^{3-}}\right) = A * \log\left(a_{Ca^{2+}} * a^2_{OH^-}\right) + B \tag{3.11}$$

where A is the molar ratio Ca/P in the corresponding calcium phosphate and B is the constant defined by the equation for corresponding calcium phosphate (Table 3.6).

The thermodynamic state of solution with different overall concentrations Ca^0 and P^0, regarding crystallization boundaries of phosphates under study is shown in Fig. 3.11.

The distance between the point which refers to the thermodynamic state of the solution and the crystallization boundary of phosphate under study is the quantitative degree of supersaturation (χ) in respect to certain phosphates. It can be calculated according the equation:

$$\chi = \frac{A * x_0 - y_0 + B}{\sqrt{A^2 + 1}} \tag{3.12}$$

where x_0 and y_0 are coordinates of points describing the thermodynamic state of the solution in Fig. 3.10, A and B are coefficients of Eq. (3.11) (Table 3.6). Results of calculations of degrees of supersaturation are presented in Table 3.5.

Influence of overall concentrations Ca^0 and P^0 on the degree of supersaturation with respect to phosphates under study is shown in Fig. 3.12.

Positive values of χ indicate that at given overall concentrations of Ca^0 and P^0 the solution is in a state of supersaturation. At all concentrations under consideration, HAP exhibits the highest degree of supersaturation. The degrees of supersaturation of the two other supersaturated phosphates are close to each other and much lower than for HAP. It's interesting to notice that the degree of supersaturation with respect

Table 3.5 The calculated values of K'_{sp} and supersaturation degrees χ in solutions with different overall concentrations Ca^0 and P^0 at pH = 7.4

Ca^0 (mM)	P^0 (mM)	CHPD $K_{sp} = 2.56 * 10^{-7}$		CP $K_{sp} = 1.15 * 10^{-29}$		OCP $K_{sp} = 1.03 * 10^{-47}$		HAP $K_{sp} = 3.37 * 10^{-58}$	
		K'_{sp}	χ	K'_{sp}	χ	K'_{sp}	χ	K'_{sp}	χ
0.5	0.5	1.27×10^{-8}	−0.92	2.26×10^{-30}	0.19	1.19×10^{-50}	−0.55	9.61×10^{-54}	0.73
0.5	1	1.88×10^{-8}	−0.36	2.34×10^{-31}	0.14	4.89×10^{-51}	−0.25	2.84×10^{-53}	0.93
0.5	1.5	4.53×10^{-8}	−0.53	2.77×10^{-29}	0.11	5.25×10^{-49}	−0.23	4.03×10^{-51}	1.01
1	0.5	3.07×10^{-8}	−0.65	3.30×10^{-29}	0.13	4.24×10^{-49}	−0.24	8.48×10^{-51}	1.07
1	1	7.48×10^{-8}	−0.38	1.92×10^{-28}	0.34	6.02×10^{-48}	−0.014	1.17×10^{-50}	1.26
1	1.5	1.10×10^{-7}	−0.26	4.07×10^{-28}	0.43	1.88×10^{-47}	0.085	3.59×10^{-50}	1.34
1.5	0.5	4.49×10^{-8}	−0.53	1.06×10^{-28}	0.27	1.98×10^{-47}	−0.11	5.92×10^{-50}	1.21
1.5	1	1.10×10^{-7}	−0.26	6.15×10^{-27}	0.48	2.83×10^{-47}	0.12	8.24×10^{-50}	1.41
1.5	1.5	1.61×10^{-7}	−0.14	1.31×10^{-26}	0.57	8.84×10^{-47}	0.22	2.53×10^{-49}	1.49

Table 3.6 The coefficients of Eq. (3.11) for phosphates under consideration

Calcium phosphate	A	B
CHPD	1	$-\log\left(K_w^2 * K_{sp} * K_2^{-1}\right)$
CP	1.33	$-\log\left(K_w^8 * K_{sp}\right)^{\frac{1}{3}}$
OCP	1.5	$-\log\left(K_w^3 * K_{sp}^{\frac{1}{2}}\right)$
HAP	1.67	$-\log\left(K_w^3 * K_{sp}^{\frac{1}{3}}\right)$

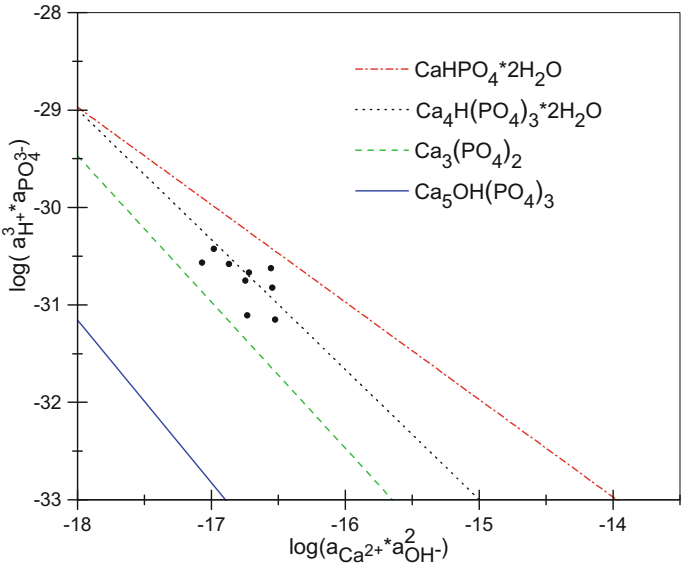


Fig. 3.11 States of the system regarding crystallization boundaries of phosphates at different overall concentrations of calcium and phosphorus at pH = 7.4

to CP is higher than that for OCP although according the values of solubility products (Table 3.4) OSP is less soluble form of calcium phosphate than CP.

It is known that the phenomena of spontaneous homogeneous and heterogeneous crystallization can be caused by various thermodynamic and kinetic factors. But the approach developed in this work allows us to give a quantitative characterization of one of the most important factors—the degree of supersaturation.

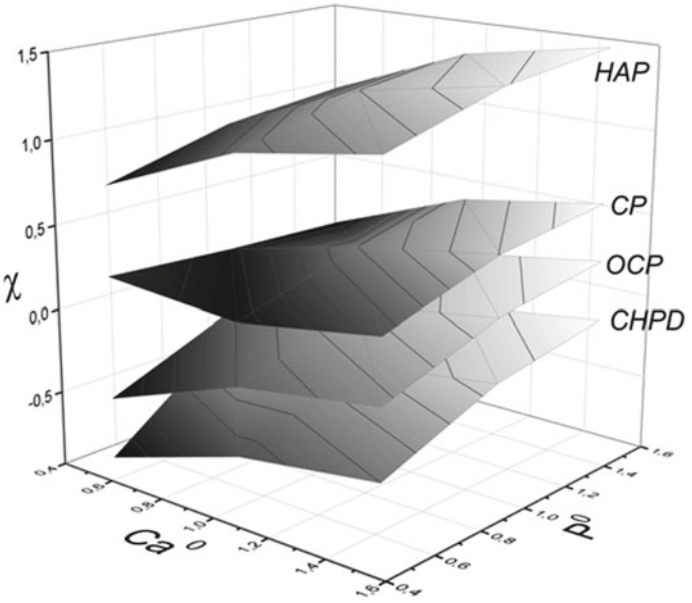


Fig. 3.12 Dependence of a degree of supersaturation on overall concentrations Ca^0 and P^0 at pH = 7.4

3.6 Conclusions

The obtained experimental data demonstrate that the concentration of calcium ions in HAP solutions non-monotonously changes over time. This may suggest that dissolution of hydroxyapatite is an incongruent process. The logarithm of calcium ion activity linearly correlates with the pH: activity of Ca^{2+} decreases with the pH. In principle, this is an expected result: solubility of calcium salts decreases in alkaline media. Results of determination of the chemical composition of solid phase obtained by XPS, EDX and ICP-OES reveal the changes which occurred during dissolution of HAP. All in all, the obtained results confirm that dissolution of hydroxyapatite is an incongruent process.

Calculations have been performed of molecular and ionic forms containing calcium and hydrogen cations, and phosphate anions in the total calcium and phosphorus concentrations range from 0.5 to 1.5 mM, and at the solution pH of 4.0–8.0. The calculated degrees of salt supersaturation of different phosphates, which tend to crystallize in blood's serum, demonstrate that HAP is the most supersaturated phosphate at any values of calcium and phosphorus concentrations.

Acknowledgements The instrumental investigations have been performed at the Research Resource Centers of St. Petersburg State University: Center for Geo-Environmental Research and Modelling (GEOMODEL), Chemical Analysis and Materials Research Center, Center for Physical Methods of Surface Investigation.

References

Avnimele Y, Moreno EC, Brown WE (1973) Solubility and surface properties of finely divided hydroxyapatite. J Res Natl Bur Stand Sect A-Phys Chem A 77(1):149–155. https://doi.org/10.6028/jres.077A.008

Bakker E, Bühlmann P, Pretsch E (1997) Carrier-based ion-selective electrodes and bulk optodes. 1. General characteristics. Chem Rev 97(8):3083–3132. https://doi.org/10.1021/cr940394a

Bell LC, Mika H, Kruger BJ (1978) Synthetic hydroxyapatite solubility product and stoichiometry of dissolution. Arch Oral Biol 23(5):329–336. https://doi.org/10.1016/0003-9969(78)90089-4

Chuong R (2016) Experimental Study of Surface and Lattice Effects on the Solubility of Hydroxyapatite. J Dent Res 52(5):911–914

Dorozhkin SV (2002) A review on the dissolution models of calcium apatites. Prog Cryst Growth Charact Mater 44(1):45–61. https://doi.org/10.1016/s0960-8974(02)00004-9

Dorozhkin SV (2017a) Hydroxyapatite and other calcium orthophosphates: general information and history. Hydroxyapatite and other calcium orthophosphates: general information and history. Nova Science Publishers Inc., New York

Dorozhkin SV (2017b) A history of calcium orthophosphates ($CaPO_4$) and their biomedical applications. Morphologie 101(334):143–153. https://doi.org/10.1016/j.morpho.2017.05.001

Dvorak J, Koryta J, Bohackova V (1975) Elektrochemie. Academia, Praha

Eidelman N, Chow LC, Brown WE (1987) Calcium-phosphate phase-transformations in serum. Calcif Tissue Int 41(1):18–26. https://doi.org/10.1007/bf02555126

Glinkina IV, Durov VA, Mel'nitchenko GA (2004) Modelling of electrolyte mixtures with application to chemical equilibria in mixtures—prototypes of blood's plasma and calcification of soft tissues. J Mol Liq 110(1–3):63–67. https://doi.org/10.1016/s0167-7322(03)00233-2

Golovanova OA (2018) Thermodynamic modeling of poorly soluble compounds formation in biological fluid. J Therm Anal Calorim 133(2):1219–1224. https://doi.org/10.1007/s10973-018-7369-6

Hay DI, Schluckebier SK, Moreno EC (1982) Equilibrium dialysis and ultrafiltration studies of calcium and phosphate binding by human salivary proteins—implications for salivary supersaturation with respect to calcium-phosphate salts. Calcif Tissue Int 34(6):531–538. https://doi.org/10.1007/bf02411299

Kaufman HW, Kleinberg I (1979) Studies on the incongruent solubility of hydroxyapatite. Calcif Tissue Int 27(2):143–151. https://doi.org/10.1007/bf02441177

Levinskas GJ, Neuman WF (1955) The solubility of bone mineral. 1. Solubility studies of synthetic hydroxylapatite. J Phys Chem 59(2):164–168. https://doi.org/10.1021/j150524a017

Mahapatra PP, Mishra H, Chickerur NS (1982) Solubility and thermodynamic data of cadmium hydroxyapatite in aqueous media. Thermochim Acta 54(1–2):1–8. https://doi.org/10.1016/0040-6031(82)85059-4

McDowell H, Gregory TM, Brown WE (1977) Solubility of $Ca_5(PO_4)_3OH$ in system $Ca(OH)_2$–H_3PO_4–H_2O at 5, 15, 25 and 37 °C. J Res Natl Bur Stand Sect A-Phys Chem A 81(2–3):273–281. https://doi.org/10.6028/jres.081A.017

Mikhelson KN (2013) Ion-selective electrodes, vol 81. Lecture notes in chemistry. Springer, Heidelberg-New York-Dordrecht-London

Mikhelson KN, Bobacka J, Lewenstam A, Ivaska A (2001) Potentiometric performance and interfacial kinetics of neutral lonophore based ISE membranes in interfering ion solutions before and after contact with primary ions. Electroanalysis 13(10):876–881. https://doi.org/10.1002/1521-4109(200106)13:10%3c876:aid-elan876%3e3.0.co;2-%23

Nägele M, Mi Y, Bakker E, Pretsch E (1998) Influence of lipophilic inert electrolytes on the selectivity of polymer membrane electrodes. Anal Chem 70(9):1686–1691. https://doi.org/10.1021/ac970903j

Pan HB, Darvell BW (2009) Calcium phosphate solubility: the need for re-evaluation. Cryst Growth Des 9(2):639–645

Rootare HM, Deitz VR, Carpenter FG (1962) Solubility product phenomena in hydroxyapatite-water systems. J Colloid Sci 17(3):179–206. https://doi.org/10.1016/0095-8522(62)90035-1

Sillen LG, Martell AE (eds) (1964) Stability constants of metal-ion complexes, 2nd edn. Pergamon Press, Oxford

Vázquez M, Mikhelson K, Piepponen S, Räinö J, Sillanpää M, Ivaska A, Lewenstam A, Bobacka J (2001) Determination of Na^+, K^+, Ca^{2+}, and Cl^- ions in wood pulp suspension using ion-selective electrodes. Electroanalysis 13(13):1119–1124. https://doi.org/10.1002/1521-4109(200109)13:13%3c1119:aid-elan1119%3e3.0.co;2-m

Verbeeck RMH, Thun HP, Driessens FCM (1980) Effect of dehydration of hydroxyapatite on its solubility behaviour. Z Phys Chem 119(1):79–84. https://doi.org/10.1524/zpch.1980.119.1.079

Wier DR, Chien SH, Black CA (1971) Solubility of hydroxyapatite. Soil Sci 111(2):107. https://doi.org/10.1097/00010694-197102000-00005

Chapter 4
Thermodynamics and Kinetics of Crystallization of Mineral Phases of Vascular Calcificates



Olga A. Golovanova

Abstract Vascular calcification is the process of calcium salt precipitation in vessel walls. In-depth understanding of the mechanisms of crystallization of calcifications in blood vessels is crucial for developing effective protective therapy. The paper presents the results of the thermodynamic calculation of the formation of calcification mineral phases and experimental results of phase formation under conditions typical of the human blood plasma prototype (inorganic composition). The regularities of nucleation in a model solution of human blood plasma under the conditions similar to physiological have been investigated. The induction order and constants are determined. It is shown that an increase in supersaturation leads to a transition from heterogeneous to homogeneous nucleation of crystallites. The critical nucleus size is estimated for a pure model system blood plasma. The kinetic regularities of crystallization (growth order and constants) in a model solution of blood plasma have been investigated. It is shown that the impurities affect to a greater extent the nucleation rather than the growth stage.

Keywords Kinetic thermodynamics · Modeling · Insoluble compounds · Crystallization · Supersaturation · Calcium phosphates · Blood plasma · Synthesis · Gibbs energy · Dissolution kinetics

4.1 Introduction

Researchers have always paid much attention to the crystallization of poorly soluble compounds from biological fluids (Fridriksson et al. 2004; Pak et al. 2011; Vaitheeswari et al. 2015; Golovanova and Chikanova 2015; Solodyankina et al. 2016; Golovanova and Solodyankina 2017a, b), because these compounds enter the composition of pathogenic minerals causing human diseases. An example is arteriosclerosis—a disease related to deposition of calcium salts in vessels. Concerning the abundance among all sclerotic lesions of arterial vessels, arteriosclerosis

O. A. Golovanova (✉)
F.M. Dostoevsky State University, 55A Prospect Mira, Omsk 644077, Russia
e-mail: golovanoa2000@mail.ru

© Springer Nature Switzerland AG 2020

O. V. Frank-Kamenetskaya et al. (eds.), *Processes and Phenomena on the Boundary Between Biogenic and Abiogenic Nature*, Lecture Notes in Earth System Sciences,
https://doi.org/10.1007/978-3-030-21614-6_4

is in the second place after atherosclerosis (Sigel et al. 2008; Füredi-Milhofer 2010; Furukawa 2014; Kazuyuki et al. 2015). The percentage of pathogenic mineral formation in blood vessels and heart valves of patients has increased in the last years. The biological fluids from which these compounds are formed consist of many components, both inorganic and organic (Sajadi 2010; Habraken et al. 2016).

The crystallization dynamics and crystallographic pattern of the structural trace of biological fluid are determined by a number of external and internal factors. Under standard examination conditions, the structural organization features depend mainly on the molecular composition and character of interaction between individual components of biological fluid. The occurrence of any new material in this fluid in pathological state leads to a change in the chemical composition and intermolecular interaction, which manifests itself in specific features of crystal structure. These molecular changes most exactly characterize the state of the internal medium of organism and may be useful for detecting a pathological process in early stages (Shock et al. 1997; Shanahan 2005; Golovanova et al. 2011, 2016; Karwowski et al. 2012; Indulekha et al. 2017).

The chemical composition of blood and plasma is relatively constant in the normal state. A healthy organism levels off all random fluctuations of the blood composition. A series of studies (Golovanova and Solodyankina 2017a, b) were aimed at analyzing the change in the content of inorganic components of blood plasma in pathological states. It is well known that the main inorganic phase in the pathogenic calcification of collagen and muscular tissues, as well as bone and dental ones, is calcium phosphate. This compound is considered (with a certain degree of approximation and idealization) as a carbonate-containing hydroxylapatite, which is generally weakly crystallized and nonstoichiometric because of the presence of a large number of foreign ions (Frank-Kamenetskaya et al. 2014; Rabelo et al. 2015; He et al. 2015; Solodyankina et al. 2016). This apatite is a typical biogenic mineral, which is closely related (spatially, genetically structurally, and morphologically) to the components of organism tissues.

Two genetically determined species of apatite are distinguished: physiogenic apatite, entering the composition of bones and teeth, and apatite of pathogenic origin, which enters the composition of uric, salivary, and dental stones and plaques on walls of blood vessels. Pathogenic apatite is not so closely related to exchange processes in organism as the physiogenic one. The degree of structure imperfection of pathogenic apatite is always high and depends to a greater extent on local processes than on the state of the organism as a whole. According to the numerous data in the literature, the calcium–phosphorus (Ca/P) ratio in calcifications varies in rather wide limits (Golovanova et al. 2011, 2016; Frank-Kamenetskaya et al. 2014). Hence, one can conclude that the crystallography of natural inorganic apatite is incredibly complicated, and the bioapatite structure has a number of additional features. The mineralization of tissues has been studied poorly. In this paper, we report the results of studying the character of crystallization from solutions modeling the human blood plasma composition under the conditions similar to physiological.

Significant progress in studying the features of phase formation in biological media can be achieved through thermodynamic calculations and laboratory model

experiments (Engi 1992; Elnikov et al. 2007; Atkins and De Paula 2014; Golovanova et al. 2015a, b). The margins of the equilibrium thermodynamics to describe the pathogenic phase formation in human blood plasma have not been focused on.

The purpose of this research is a comprehensive study of the above issue. This study includes:

1. Detailed calculation (taking into account ion hydrolysis) of solubility diagrams of basic poorly soluble compounds (PSC) formed in the prototype human plasma (inorganic composition).
2. The results of studying the character of crystallization from solutions modeling the human blood plasma composition under the conditions similar to physiological.

4.2 Experimental

In thermodynamic modeling, a bio-liquid analog was the solution with inorganic composition, temperature, ionic strength and pH (6–8.0) corresponding to the blood plasma (inorganic composition) of an adult average person (Table 4.1) with an increase in the initial physiologic supersaturation (PS) by the factor of 10 (PS*10) and 50 (FS*50).

Theoretical determination of the conditions for precipitation of poorly soluble calcium and magnesium compounds in model media was carried based on the calculations of thermodynamic criteria, which characterize the degree of deviation of the studied system from an equilibrium state.

The supersaturation indexes (SI) for each of the compounds (Korolkov et al. 2016; Golovanova 2018) were calculated from Eq. (4.1) to determine the conditions for their crystallization and stability regions (4.1):

Table 4.1 Mineral composition of human plasma (Sigel et al. 2008)

Component ion	Average value concentration (mmol/l)
Ca^{2+}	2.35
Na^{+}	143
K^{+}	4.35
Mg^{2+}	0.95
NH_4^{+}	0.04
Cl^{-}	103
SO_4^{2-}	0.45
CO_3^{2-}	26
PO_4^{3-}	1.3

$$\Omega = \left(\frac{IAP}{K_S^{\hat{l}}}\right)^{\frac{1}{\nu}} \Rightarrow SI = \lg(\Omega) \tag{4.1}$$

where Ω is supersaturation that occurs in the solution for a given salt; IAP is the ion activity product in the degrees of stoichiometric coefficients; $K_S^{\hat{l}}$ is the thermodynamic product of the PSC solubility; ν is the number of PSC ions.

The driving force of the crystallization process was determined through the change in Gibbs free energy (ΔG) upon the system transition from the supersaturated state to equilibrium (Korolkov et al. 2016; Golovanova 2018) (4.2):

$$\Delta G = -RT \ln \Omega = \frac{RT}{\nu} \ln \frac{IAP}{K_S^o} \tag{4.2}$$

ΔG is the Gibbs energy of PSC crystallization from solution, J/mol; R is the universal gas constant, J/mol K; T is temperature, K.

If the proposed functions of the system state take the values SI > 0 and ΔG < 0, the thermodynamic probability of precipitation of poorly soluble compound from the solution can be assumed.

Thermodynamic modeling was used to determine the conditions for the precipitation of poorly soluble calcium and magnesium compounds from the model solution of human blood plasma (inorganic composition). The effect of ions (Table 4.2) on the test system with respect to its nonideality caused by their electrostatic interactions was described with allowance for the ionic strength of the solution. The ion activity coefficients were determined by the Davis equation (Korolkov et al. 2016; Golovanova 2018) which allows calculation of the activity coefficients for ionic forces of 0.2–0.5 M (characteristic of blood plasma) with an error not exceeding 10%. The acidity of the medium was varied from 6 to 8 with an increment of 0.1. To determine the stepwise hydrolysis of carbonate and phosphate ions in the solution, the molar fraction of the types of the ion found in the PSC composition at the given pH was introduced into the formulas for equilibrium constants since it is known that the molar fractions of the cation $\alpha_{M^{m+}}$ and anion $\alpha_{A^{n-}}$ are a function of pH:

Table 4.2 Solubility products of compounds calcium at 298 K

№	A slightly soluble compound	$K^0_{s,298}$	$pK^0_{s,298}$
1	$MgHPO_4 \cdot 3H_2O$	1.51×10^{-6}	5.82
2	$CaHPO_4 \cdot 2H_2O$	2.34×10^{-7}	6.59
3	$Ca_8H_2(PO_4)_6 \cdot 5\ H_2O$	2.51×10^{-97}	96.6
4	β-$Ca_3(PO_4)_2$	1.26×10^{-29}	28.9
5	$Ca_{10}(PO_4)_6(OH)_2$	1.58×10^{-117}	116.8
6	$Ca_{10}(PO_4)_6(CO_3)_{0.5}OH$	7.94×10^{-86}	85.1

$$\alpha_{M^{m+}} = \frac{[M^{m+}]}{C_{M^{m+}}} = \frac{[M^{m+}]}{[M(OH)_m] + [M(OH)^{+}_{m-1}] + \cdots + [M^{m+}]}$$
$$= \frac{1}{\frac{10^{m(pH-14)}}{K_{b1}K_{b2}\ldots K_{bm}} + \frac{10^{(m-1)(pH-14)}}{K_{b2}K_{b3}\ldots K_{bm}} + \cdots + \frac{10^{(pH-14)}}{K_{bm}} + 1}$$
$$\alpha_{A^{n-}} = \frac{[A^{n-}]}{C_{A^{n-}}} = \frac{[A^{n-}]}{[H_nA] + [H_{n-1}A^{-}] + \cdots + [A^{n-}]}$$
$$= \frac{1}{\frac{10^{-npH}}{K_{a1}K_{a2}\ldots K_{an}} + \frac{10^{-(n-1)pH}}{K_{a2}K_{a3}\ldots K_{an}} + \cdots + \frac{10^{-pH}}{K_{an}} + 1}$$

where $C_{M^{m+}}$ and $C_{A^{n-}}$ are the total concentrations of all types of the cation and anion, and $K_{b1}\ldots K_{bn}$, $K_{a1}\ldots K_{an}$ are the stepwise constants of the interaction of cation and anion with water (Plyasunova et al. 2004).

According to (Plyasunova et al. 2004) the following poorly soluble compounds can be formed in aqueous solutions containing carbonate, phosphate ions and calcium and magnesium ions (Table 4.2): $CaHPO_4 \cdot 2H_2O$ (brushite, DCPDH), $Ca_8H_2(PO_4)_6 \cdot 5H_2O$ (octacalcium phosphate), $Ca_{10}(PO_4)_6(OH)_2$ (hydroxyapatite, HA), β-$Ca_3(PO_4)_2$ (tricalcium phosphate), $Ca_{10}(PO_4)_6(CO_3)_{0.5}OH$, (carbonate hydroxyapatite, CHA), $MgHPO_4 \cdot 3H_2O$ (newberyite).

The composition of model systems was calculated using average concentrations of the inorganic materials entering the human blood plasma (Table 4.1). The initial reagents and their ratios in solution were chosen so as to make the ion concentrations and ionic strength of solution maximally close to the corresponding parameters of modeled system. The initial reagents were salts of analytical and chemically pure grades and distilled water. Solutions containing cations and anions, in the joint presence of which poorly soluble compounds are not formed under the given conditions, were prepared for each series of experiments. In each experiment pH was corrected to the physiological value (7.4 ± 0.01) by adding a 30% solution sodium hydroxide solution or hydrochloric acid id (conc.). Mixing equivalent volumes of solutions, we obtained a solution with a specified supersaturation and calculated component concentration. Compositions of blood plasma model solutions with supersaturations $S = 3, 5, 7, 10, 12, 15, 20, 25, 30, 40, 50, 70$, or 90 were used. All experiments were performed under thermostatic conditions at a temperature of 25 °C in the absence of mixing.

4.3 Technique for Determining Crystallization Induction Periods

The nucleation parameters were found using the method based on measuring induction periods τ_{ind} (induction period is the time interval between the instant at which critical supersaturation is reached and the instant when a new phase is formed). This method is based on the dependence of the induction period on the initial concen-

tration of supersaturated solutions. The induction time was determined visually by estimating the solution turbidity.

Double-distilled water was used as a solvent. Salts of analytical grade were used to prepare initial solutions. The nucleation process was standardized by providing the same conditions in all experiments. The solution opacification time was measured using a stop watch. Five or six simultaneous experiments were performed for each concentration; the relative standard deviation Sr of induction periods τ_{ind} was found to be 0.01–0.02. All experiments were carried out under thermostated conditions at a temperature t = 37.0 ± 0.2 °C in the absence of mixing.

The data obtained were processed using the Eq. (4.3) where t is the induction time, S is the supersaturation, and n is the reaction order (graphically using kinetic curves).

The nucleation parameters were determined by the method based on measuring the induction periods (τ_{ind} is the time from the instant of merging two solutions to the precipitation onset (hidden period of the crystallization onset)). The induction time is known to be inversely proportional to the nucleation rate J: $\tau \sim 1/J$. In turn, the dependence of the nucleation rate on the solution supersaturation is expressed in terms of an exponential function containing the specific surface energy σ (4.3):

$$J \sim \exp\left[-\frac{16\pi\sigma^3 v^2}{3k_B^3 T^3 (m \ln \mathrm{S})^2}\right] = \exp\left[-\frac{\mathrm{B}}{(\ln \mathrm{S})^2}\right], \tag{4.3}$$

where v is the molecule volume, kB is the Boltzmann constant, S is the supersaturation, T is temperature, m = 2 is the number of ions into which the molecule (calcium phosphate—$CaHPO_4$) dissociates in the solution, and B is a constant (Golovanova et al. 2006). The induction time was determined visually by estimating the solution turbidity. The study was performed under laboratory conditions in a medium having a composition close to that of physiological solution of human blood plasma (inorganic composition). The crystal growth was studied by the conductometric method, which implies measurement of the concentration of solutions during their crystallization. It is based on the principle of determining the electrical conductivity of solution in a Kohlrausch cell. Based on the thermodynamic model of nucleation, one can use the calculated value of surface energy to estimate the critical-nucleus size from the Eq. (4.4) (Pigozzi 2011; Golovanova and Chikanova 2015; Golovanova and Solodyankina 2017a, b).

$$\mathrm{r}_{crit} = \frac{2\sigma\upsilon}{kT \ln S}, \tag{4.4}$$

Turbidimetric method, which is used to analyze turbid media, is based on measuring the intensity of light absorbed by them. Measurements were performed with a KFK-2 instrument at different supersaturations: $S = 5$, 10, 20, 30, or 40; distilled water was used as the idle solution. The optical density of solutions was measured at a wavelength λ = 670 nm in glass cells with a thickness of light-absorbing layer $l = 2.007$ cm, at a crystallization temperature of 25 °C. Colorimeter readings were

recorded with a stop watch after certain (empirically chosen) time intervals. Readings were taken until the optical density ceased to change with time. Three parallel measurements were performed in each experiment. The measurement error did not exceed 5%.

The dependences of the crystallization kinetics with respect to the precipitate-forming (calcium) ions were analyzed by the potentiometric method using an I-150-MI. The concentration of calcium ions during crystallization was determined by direct potentiometric applying an ion-sensitive electrode. Crystallization was performed in a thermostatic cell at a temperature of 25 ± 0.5 °C. The potential in the solution was measured after certain time intervals, and the concentration of Ca^{2+} ions was determined using a calibration plot. Each experiment was repeated thrice. The measurement error was 5–10%. All experiments were performed under thermostatic conditions at a temperature of 25 °C, in the absence of mixing.

A drop of the solution under study was deposited on the surface of object glass at different time intervals and then dried under atmospheric conditions. The thus prepared specimens were analyzed in an optical microscope MBR-1 with a total magnification of 120 (eyepiece magnification of ×15 and objective magnification of ×8). Photographing could be performed using any digital camera.

4.4 Results and Discussion

4.4.1 Results of Thermodynamic Calculation

According to (Plyasunova et al. 2004) the following poorly soluble compounds can be formed in aqueous solutions containing carbonate, phosphate ions and calcium and magnesium ions (Table 4.2): $CaHPO_4 \cdot 2H_2O$ (brushite, DCPDH), $Ca_8H_2(PO_4)_6 \cdot 5H_2O$ (octacalcium phosphate), $Ca_{10}(PO_4)_6(OH)_2$ (hydroxyapatite, HA), β-$Ca_3(PO_4)_2$ (tricalcium phosphate), $Ca_{10}(PO_4)_6(CO_3)_{0.5}OH$, (carbonate hydroxyapatite, CHA), $MgHPO_4 \cdot 3H_2O$ (newberyite).

When comparing the supersaturation indexes (SI) of PSC calculated using conditional solubility products, it was found that the thermodynamically driven crystallization in the model solution of human blood plasma can be as follows: $Ca_8H_2(PO_4)_6 \cdot 5H_2O$, β-$Ca_3(PO_4)_2$, $Ca_{10}(PO_4)_6(OH)_2$, $Ca_{10}(PO_4)_6(CO_3)_{0.5}OH$. When supersaturation in calcium ions and phosphate ions increases (10 and 50 fold as compared to physiological solution), $CaHPO_4 \cdot 2H_2O$ is found to precipitate, and no magnesium-containing phases are formed (Table 4.3).

Thus, it was found that the crystallization of poorly soluble calcium phosphates, which can precipitate from blood plasma solutions, does not virtually depend on supersaturation. Consequently, the supersaturation value (varying from PS to PS*50) does not affect the conditions and sequence of calcium phosphate precipitation, but it affects the mass of the solid phase produced.

Table 4.3 *SI* values in the pH range of 6– 8 poorly soluble compounds from supersaturation of the solution

S (supersaturation)	PS	PS*10	PS*50
$CaHPO_4 \cdot 2H_2O$	−0.72–(−0.15)	−0.12–0.42	0.19–0.72
$Ca_8H_2(PO_4)_6 \cdot 5\,H_2O$	1.80–1.97	2.27–2.42	2.54–2.68
β-$Ca_3\,(PO_4)_2$	2.03–2.47	2.55–2.97	2.86–3.27
$Ca_{10}(PO_4)_6\,(OH)_2$	2.20–2.79	2.64–3.22	2.92–3.48
$MgHPO_4 \cdot 3H_2O$	−1.24–(−0.67)	−0.75–(−0.20)	−0.60–(−0.08)
$Ca_{10}(PO_4)_6(CO_3)_{0,5}OH$	0.84–1.35	1.29–1.79	1.58−2.06

Note PS (physiological supersaturation) for a solution of blood plasma

Earlier, we found that the pH of the solution affects the composition of the solid phase formed (Golovanova et al. 2015a, b; Golovanova and Chikanova 2015; Golovanova and Korol'kov 2017). In the case of the model solution of human blood plasma, it was proved that the pH of the solution in the range of 6–8 units virtually affects the parameters and the sequence of PSC calcium and magnesium crystallization (Table 4.4), except for the pH change at the beginning of brushite precipitation.

To illustrate and determine the thermodynamic probability of the formation of poorly soluble compounds in the solution modeling the blood plasma ionic composition, the dependences of the supersaturation index and Gibbs energy on the pH of the solution were built. Within a single coordinate space, these dependences indicate the possibility of solid phase formation at fixed values of anion and cation concentrations in the studied pH range of the solution (Fig. 4.1a, b).

It is known that brushite is a metastable phase, and a precursor for hydroxyapatite crystallization (Elnikov et al. 2007). The thermodynamic calculation indicated that when supersaturation is increased 10 fold or more, the probability of brushite formation increases, which is evidenced by the positive value of the supersaturation index (SI) and the negative Gibbs energy value (ΔG) (Tables 4.3 and 4.5).

Based on the results obtained, a series has been proposed to reduce the thermodynamic probability of calcium and magnesium formation from the analogue blood plasma solution: $Ca_{10}(PO_4)_6(OH)_2$, β-$Ca_3(PO_4)_2$, $Ca_8H_2(PO_4)_6 \cdot 5H_2O$, $Ca_{10}(PO_4)_6(CO_3)_{0.5}OH$, $CaHPO_4 \cdot 2H_2O$, and $MgHPO_4 \cdot 3H_2O$. It can be seen that the highest probability of formation is characteristic of hydroxyapatite (HA) fol-

Table 4.4 pH values of the beginning of precipitation of poorly soluble compounds from supersaturation

S (supersaturation)	PS	PS*10	PS*50
$CaHPO_4 \cdot 2H_2O$	–	6.3	6.0
$Ca_8H_2(PO_4)_6 \cdot 5\,H_2O$	6.0		
β-$Ca_3\,(PO_4)_2$	6.0		
$Ca_{10}(PO_4)_6\,(OH)_2$	6.0		
$MgHPO_4 \cdot 3H_2O$	–		
$Ca_{10}(PO_4)_6(CO_3)_{0,5}OH$	6.0		

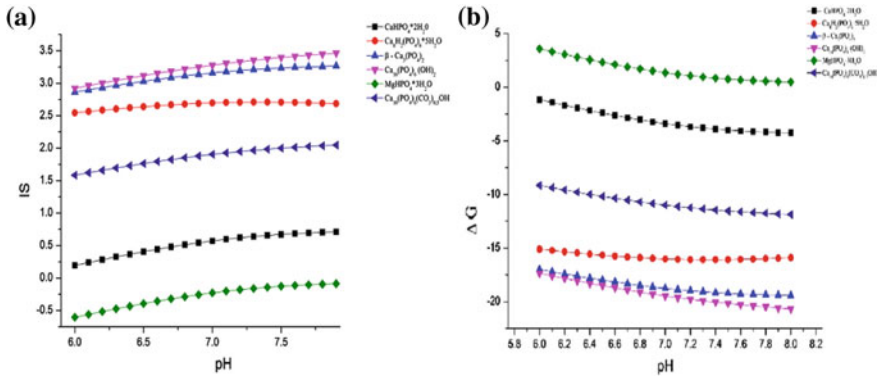


Fig. 4.1 Dependence of IS (**a**) and ΔG kJ/mole (**b**) on pH for a model solution of human blood plasma at supersaturation S = 50

Table 4.5 The values of ΔG, kJ/mol of poorly soluble compounds from supersaturation in the pH range of 6–8

S (supersaturation)	PS	PS*10	PS*50
$CaHPO_4 \cdot 2H_2O$	4.27–0.92	0.73–(−2.51)	−1.16–(−4.26)
$Ca_8H_2(PO_4)_6 \cdot 5\ H_2O$	−10.66–(−11.67)	−13.46–(−14.37)	−15.10–(−15.89)
β-$Ca_3\ (PO_4)_2$	−12.04–(−14.70)	−15.11–(−17.65)	– 16.99–(−19.40)
$Ca_{10}(PO_4)_6\ (OH)_2$	−13.06–(−16.58)	−15.68–(−19.10)	−17.35–(−20.64)
$MgHPO_4 \cdot 3H_2O$	7.33–3.98	4.93–1.19	3.58–0.48
$Ca_{10}(PO_4)_6(CO_3)_{0,5}OH$	−4.84–(−7.79)	−7.47–(−10.32)	−9.14–(−11.87)

lowed by precursor phases, which lead to the formation of biomineral, an inorganic constituent bone, and hydroxyapatite, dental tissue of human, through crystallization and secondary precipitation.

The analysis of the studies performed by a number of scientists has shown that the mineral composition of calcifications is CHA (Pigozzi 2011; Frank-Kamenetskaya et al. 2014). Therefore, to assess the effect of the carbonate ion concentration (2 and 3 fold decrease in the carbonate ion concentration as compared to the physiological one) on formation of CHA from the model solution of human blood plasma, supersaturation indexes (SI), the Gibbs energy of crystallization (ΔG) were determined and a three-dimensional diagram, "stability field", was built (Tables 4.6, 4.7 and Fig. 4.2).

It was found that the change in the carbonate ion concentration in the model solution of human blood plasma does not affect the sequence of PSC precipitation (Tables 4.6, 4.7 and Fig. 4.2), since the supersaturation index and Gibbs energy of the mineral phase formation vary insignificantly, and the diagram does not show abrupt changes.

Table 4.6 The values of IS poorly soluble compounds from the concentration of carbonates in the pH range of 6–8

C (CO_3^{-2}) (mmol/l)	PC	PC/2	PC/3
$CaHPO_4 \cdot 2H_2O$	−0.72–(−0.15)	−0.72– (−0.14)	−0.71–(−0.14)
$Ca_8H_2(PO_4)_6 \cdot 5\,H_2O$	1.80–1.97	1.80–1.98	1.80–1.98
β-$Ca_3\ (PO_4)_2$	2.03–2.47	2.03–2.49	2.03–2.49
$Ca_{10}(PO_4)_6\ (OH)_2$	2.20–2.79	2.20–2.81	2.21–2.81
$MgHPO_4 \cdot 3H_2O$	−1.24–(−0.67)	−1.23–(-0.66)	−1.23–(−0.65)
$Ca_{10}(PO_4)_6(CO_3)_{0,5}OH$	0.84–1.35	0.83–1.35	0.83–1.35

Note PC (physiological concentration CO_3^{-2}) for a solution of blood plasma

Table 4.7 The values of ΔG, kJ/mol of poorly soluble compounds from the concentration of carbonates in the pH range of 6–8

C (CO_3^{-2}) (mmol/l)	PC	PC/2	PC/3
$CaHPO_4 \cdot 2H_2O$	4.27–0.92	4.25–0.84	4.24–0.81
$Ca_8H_2(PO_4)_6 \cdot 5\,H_2O$	−10.66–(−11.67)	−10.68–(−1.74)	−10.69–(−11.76)
β-$Ca_3\ (PO_4)_2$	−12.04–(−14.70)	−12.06–(−14.77)	−12.07–(−14.80
$Ca_{10}(PO_4)_6\ (OH)_2$	−13.06–(−16.58)	−13.06–(−16.65)	−13.09–(−16.67)
$MgHPO_4 \cdot 3H_2O$	7.33–3.98	7.31–3.90	7.30–3.88
$Ca_{10}(PO_4)_6(CO_3)_{0,5}OH$	−4.84–(−7.79)	−4.82–(−7.81)	−4.79–(−7.81)

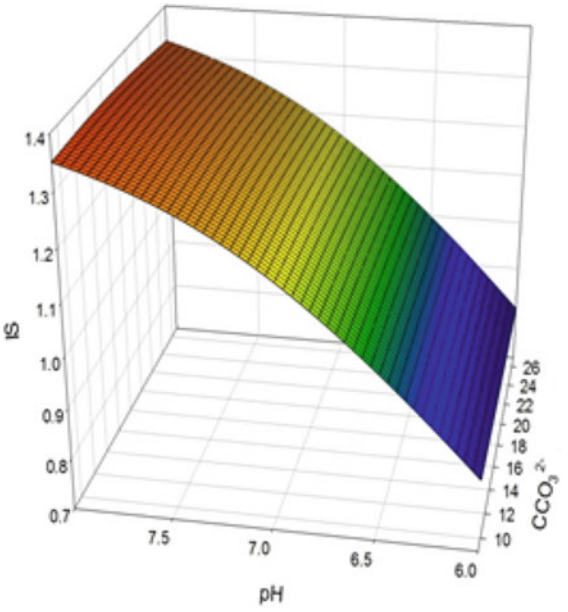


Fig. 4.2 Dependence of IS-pH-C (CO_3^{-2}), mmol/l with physiological supersaturation of the solution

Thus, the results of thermodynamic calculations indicate that hydroxyapatite is the most stable phase in the range of pH and concentrations typical of physiological human blood plasma.

It is important to note that the proposed thermodynamic model shows the probability of solid phase formation based on data on their thermodynamic stability in a standard state. It does not take into account the kinetic factors and hydrodynamic conditions that affect sample formation under real conditions. Therefore, a model experiment under laboratory conditions is crucial for determining the kinetics of the formation of PSC in the solution with inorganic macrocomponents, temperature and pH close to the parameters of human blood plasma.

4.4.2 Results of Experimental Simulation

A study of the dependence of induction time on the supersaturation (Fig. 4.3, Table 4.8) revealed that the curves are nonlinear and can be divided into three portions: the induction times are very short at large supersaturations (S = 30–90), amount to few seconds at intermediate S values (12–30) and rapidly increase (tending to infinity) at small S (3–12). This behavior is quite consistent with the theoretical concepts, according to which the induction time exponentially depends on supersaturation. The nucleation order and constant (kinetic parameters of the formation of a poorly soluble compound in the system under study) were determined graphically based on the equation from (Schukin et al. 2016) (Fig. 4.4). The nucleation order and constant were found to be 1.62 ± 0.11 and 87.09 ± 0.68 $mol^n\ L^{-n}\ s^{-n}$, respectively. The order indicates the number of particles entering the nucleus composition, while the constant characterizes the total number of particles formed (Golovanova et al. 2015a, b). Note that these parameters are useful for comparing the nucleation kinetics in the systems under consideration; however, they are not directly related with the physical

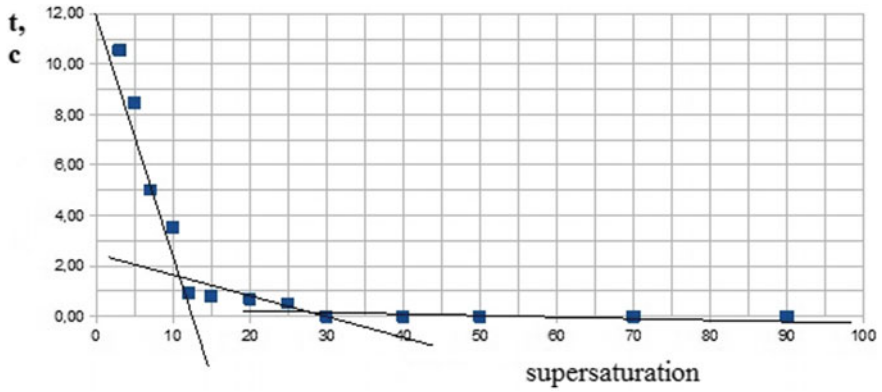


Fig. 4.3 Dependence of the induction time on supersaturation in model solutions of blood plasma

Table 4.8 Dependence of the nucleation parameters on supersaturation

S	Induction time (s)	σ (mJ/m^2)	r_{crit} (Å)
3	Stable system	22.0	1.2
4	10.56		1.0
5	8.48		0.87
7	5.02		0.73
10	3.54		0.61
12	0.92	24.0	0.60
15	0.80		0.55
20	0.70		0.50
25	0.52		0.47
30	0.10	25.0	0.46
40–90	0.06		0.42–0.35

σ is the specific surface energy and r_{crit} is the critical nucleus size

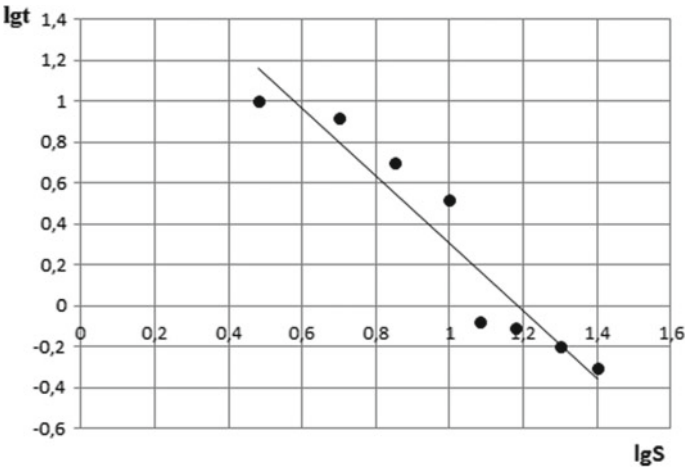


Fig. 4.4 Logarithmic dependence of the induction time on supersaturation

values determining the nucleation process. The dependence of the nucleation rate on supersaturation was used to calculate the specific surface energy according to the Gibbs–Volmer theory. The induction time is inversely proportional to the crystallization rate: $\tau = 1/J$ (Schukin et al. 2016). Therefore, specific surface energy σ was calculated based on the dependence of the induction time on supersaturation.

The following dependence was revealed: an increase in supersaturation leads to an increase in the surface energy (Table 4.8), which characterizes the change in the crystallite nucleation mechanism from heterogeneous to homogeneous (Schukin et al. 2016). Within the thermodynamic model of nucleus formation, the calculated surface energy can be used to estimate the critical nucleus size (r_{crit}) (Golovanova

et al. 2015a, b). Is known (Schukin et al. 2016) that nuclei with sizes above critical are capable of further growth. An analysis of the data obtained (Table 4.4) showed that the critical nucleus size decreases with an increase in the initial supersaturation in solution, which is in agreement with theoretical concepts.

The crystal growth kinetics was analyzed at different supersaturations: $S = 5$, 10, 20, 30, and 40. Kinetic curves were recorded at each supersaturation (Fig. 4.5). There are two pronounced portions in all experimental dependences of the optical density on the crystallization time (Fig. 4.5). The first portion (1) corresponds to the growth of newly formed particles, and the second portion (2) describes their aggregation. The order was determined by the graphical method to be zero (Table 4.9) for both the first and second portions; this situation is characteristic of heterogeneous ion-exchange reactions occurring in solution (Schukin et al. 2016). The corresponding growth rate constants were also calculated. This parameter was found to be larger for the first portion than for the second portion at all supersaturations under study.

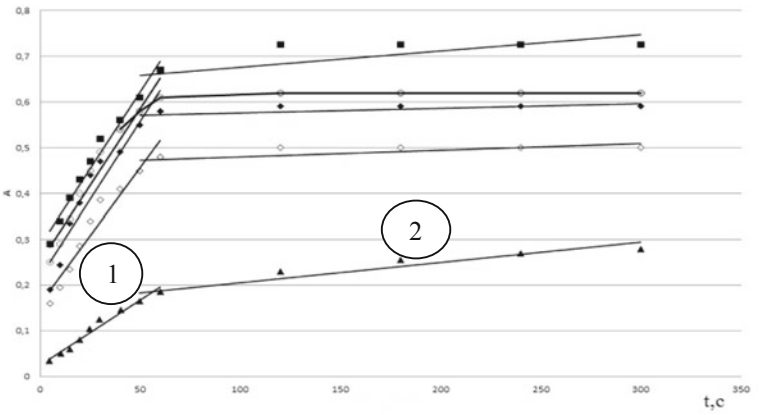


Fig. 4.5 Dependences of the optical density on the crystallization time at supersaturations

Table 4.9 Kinetic crystallization parameters

Region	Supersaturation	$k \times .10^3$ (mol/L s)
1	5	18.36
	10	6.50
	20	6.60
	30	6.90
	40	6.85
2	5	4.45
	10	0.20
	20	0.25
	30	0.15
	40	0.15

This behavior indicates that the first stage occurs in the domain of mixed kinetics, whereas the second stage is limited by the velocity of ion diffusion to the surface of solid phase material, as confirmed by the data of (Elnikov et al. 2007; Golovanova and Korol'kov 2017).

The experimental dependences and results of statistical data processing indicate that supersaturations above $S = 10$ affect only slightly the growth rate constant. Apparently, this is related to the high content of precipitate-forming components: their concentration is so high that the loss on the formation and growth of crystals looks negligible.

This fact is confirmed by optical microscopy data (Fig. 4.6), which show that an increase in the solution supersaturation leads to the formation of a fine-grained precipitate, whose particles begin to resemble aggregates consisting of very small crystallites, a pattern characteristic of apatite.

To study the characteristics of crystallization kinetics, we obtained time dependences of the calcium ion concentration at the supersaturations under study (Fig. 4.7). One can see that the dependences in Fig. 4.7 are nonlinear. To compare the crystallization processes occurring at different supersaturations, we used the degree of crystallization completeness (or degree of transformation α) (Schukin et al. 2016).

It is known (Golovanova and Korol'kov 2017) that the crystallization rate as a function of the ion concentration by instant t can be calculated from the formula (4.5):

$$\frac{d\alpha}{d\tau} = kA \cdot (C_\tau - C_s)^n, \tag{4.5}$$

where A is the total surface area of precipitate, k is the crystallization constant, and n is the crystallization order. The total surface area for particles of constant shape can be estimated from the expression (4.6):

$$A = \beta \cdot N_\tau^{1/3} \cdot V_\tau^{2/3}, \tag{4.6}$$

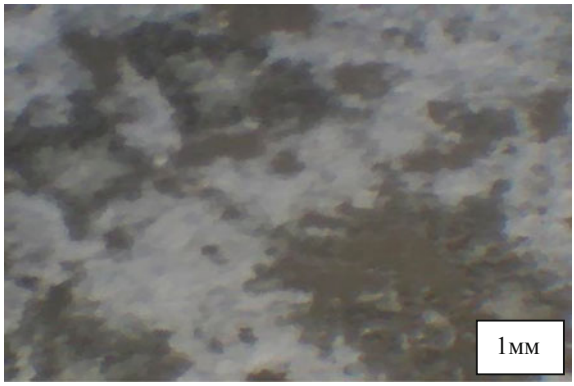


Fig. 4.6 Optical microscopy data on the crystallization from blood plasma model solution at supersaturations $S = 50$

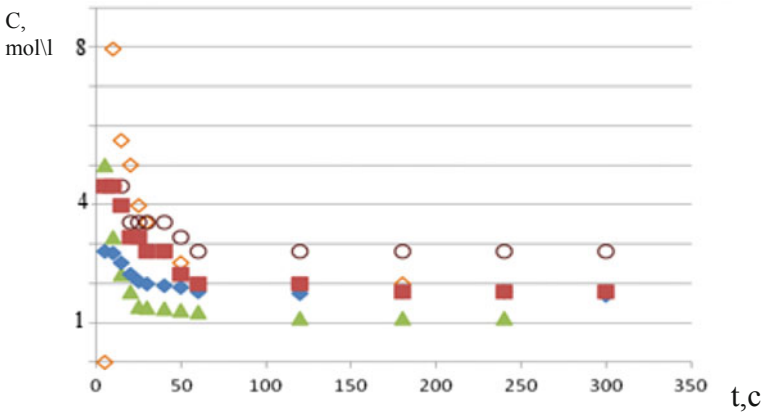


Fig. 4.7 Change in the calcium ion concentration during crystallization at supersaturations $S =$ (▲) 5, (◊) 10, (⬥) 20, (○) 30, and (x) 40

where β is the shape factor, N_τ is the total number of particles, and V_τ is the precipitate volume by the instant τ.

Taking into account that and V_{max} is the maximum precipitate volume at complete supersaturation removal and carrying out necessary transformations, we obtain the following formula for calculating the kinetic characteristics of crystallization (on the assumption that the number of particles is constant: $N_\tau = N = \text{const}$) (4.7):

$$\left(\frac{d\alpha}{d\tau}\right) \cdot \alpha^{-2/3} = k'(C_\tau - C_s)^n, \tag{4.7}$$

where k′ contains all constants (V_{max}, β, N, and k) and is time-independent under given initial conditions. Logarithmation yields the following relation (4.8):

$$\lg\left(\frac{d\alpha}{d\tau}\right) - \frac{2}{3}\lg\alpha = \lg k' + n\lg(C_\tau - C_s) \tag{4.8}$$

Plotting in the coordinates $\lg(d\alpha/d\tau) - 2/3\lg\alpha = f(\lg(C_\tau - C_s))$ should yield a straight line. The segment cut by this line on the ordinate axis gives the value of lgk′, and the slope of this line corresponds to the crystallization order n.

Processing of experimental data revealed the following regularities: the curves have two portions (Fig. 4.8), the first of which (1) corresponds to the increase in the total number of particles due to the formation of crystallization nuclei, and the second portion (2) describes the decrease in the total number of newly formed particles due to the dissolution of small aggregates and growth of large ones (Schukin et al. 2016). When studying the crystal growth, the second portion (corresponding to the growth stage) is most interesting; therefore, specifically this portion was used to calculate the main kinetic characteristics.

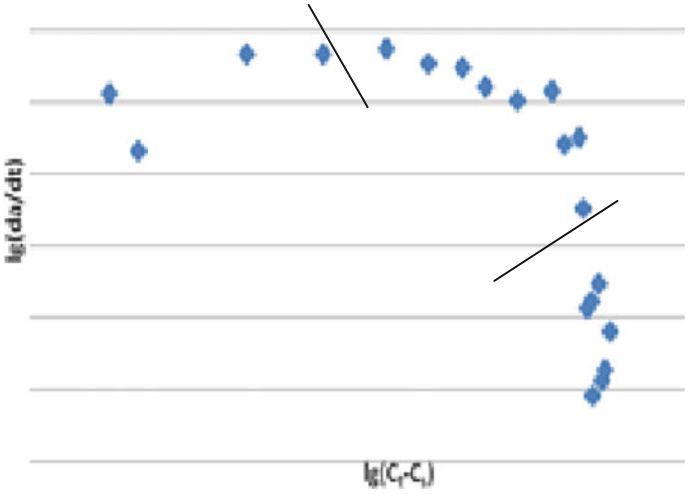


Fig. 4.8 Logarithmic dependences of the crystallization rate on the driving force at $S = 10$

The constants obtained by processing experimental data (for stage *2*) are listed in Table 4.10. One can see that the particular order with respect to calcium ions for the system under study is below unity and decreases with an increase in supersaturation.

Note that the crystallization rate constant also decreases with an increase in supersaturation. This can be explained by the fact that the number of crystallization nuclei rises with an increase in the calcium content in the initial solution; therefore, the crystal growth rate slows down. The difference in the growth rate constants becomes statistically insignificant at $S > 20$. A possible reason is that the mechanism of crystal growth changes at a certain concentration of mineral-forming ions (Schukin et al. 2016). At small supersaturations, heterogeneous nucleation and further growth dominate in the system, whereas a system with a higher content of crystal-forming components is characterized by a homogeneous mechanism of nucleation, with a larger number of critical nuclei; in this case, coagulation processes are dominant (Golovanova et al. 2015a, b; Golovanova and Korol'kov 2017).

The solution pH plays an important role in the formation of a mineral component from prototypes of biological fluid. The particular importance of this parameter is that it determines the existence of different forms of phosphate and carbonate ions in

Table 4.10 Particular kinetic characteristics found from the change in calcium ion concentration

S	Order	k (mol^n L^{-n} min^{-n})
5	0.59	371.54
10	0.58	102.33
20	0.46	10.72
30	0.41	11.22
40	0.32	10.47

solution, depending on pH. To study the influence of pH on the kinetic characteristics of crystallization from model systems (based on the data in the literature), we chose it to vary in the range of 7.0–8.0; the analysis was performed at $S = 5$, 10, 20, 30, and 40. Then, we recorded kinetic curves for the aforementioned supersaturations and selected two portions, as for the previously investigated systems (Fig. 4.5). Based on these results, the order and growth rate constants were determined for each portion by the graphical method. The order turned out to be zero ($R > 0.90$) for the both portions. The constants in the first portion are larger than in the second one and change in dependence of supersaturation, which is in agreement with the previous data (Table 4.9). The constants were found to be independent of pH in both the first and second portions. This behavior may be related to the presence of efficient buffers controlling the composition of the system.

Thus, the change in pH within 7.0–8.0 does not affect the crystallization parameters of the system modeling the human blood plasma composition.

4.5 Conclusion

The results of thermodynamic calculations revealed the compounds that can be crystallized in the model solution of human blood plasma, which are as follows: $Ca_{10}(PO_4)_6(OH)_2$, β-$Ca_3(PO_4)_2$, $Ca_8H_2(PO_4)_6 \cdot 5H_2O$, $Ca_{10}(PO_4)_6(CO_3)_{0.5}OH$ and $CaHPO_4 \cdot 2H_2O$. The supersaturation value, the pH of the solution, and variation in the carbonate ion concentration do not have a significant effect on the parameters and sequence of formation of poorly soluble calcium and magnesium compounds.

The character of crystallization from solutions modeling the human blood plasma composition was investigated under the conditions similar to physiological. When studying the nucleation stage, the nucleation order and constant were found to be $n = 1.62 \pm 0.11$ and $k = 87.62 \pm 0.68$ mol^l L^{-n} s^{-n}, respectively. It was established that an increase in supersaturation causes a transition from the heterogeneous mechanism of crystallite nucleation to homogeneous. The order and growth rate constants were determined. It was shown that the order is zero in both the growth and aggregation stages. The crystallization constant in the growth stage was found to be larger than in the aggregation stage. The order and growth constant found from the change in the calcium ion concentration in the solution are, respectively, $n < 1$ and $k = 12.30$–26.91 mol^l L^{-n} s^{-n}.

The order and growth rate constants were determined. It was shown that the order is zero in both the growth and aggregation stages. The crystallization constant in the growth stage was found to be larger than in the aggregation stage. The order and growth constant found from the change in the calcium ion concentration in the solution are, respectively, $n < 1$ and $k = 12.30$–26.91 mol^n L^{-n} s^{-n}. A change in pH within 7.0–8.0 was found to have no effect on the crystallization parameters in the system under study.

Acknowledgements The author thanks prof. Olga V. Frank-Kamenetskaya for helpful comments.

References

Atkins P, De Paula Julio (2014) Physical chemistry: thermodynamics, structure, and change, 10th edn. W.H. Freeman and Company, New York

Elnikov VY, Rosseeva EV, Golovanova OA, Frank-Kamenetskaya OV (2007) Thermodynamic and experimental modeling of the formation of major mineral phases of uroliths. Russ J Inorg Chem 52:150–157

Engi M (1992) Thermodynamic data for minerals: a critical assessment. In: Price GD, Ross NL (eds) The stability of minerals. Kluwer Academic Publishers, Dordrecht

Frank-Kamenetskaya OV, Rozhdestvenskaya IV, Rosseeva EV, Zhuravlev AV (2014) Refinement of apatite atomic structure of albid tissue of late devon conodont. J Crystallogr Rep 59:41–47

Fridriksson T, Neuhoff PS, Viani BE, Bird DK (2004) Experimental determination of thermodynamic properties of ion-exchange in heulandite: binary ion exchange experiments at 55 and 85 °C involving Ca^{2+}, Sr^{2+}, Na^{+} and K^{+}. Am J Sci 304:287–332

Füredi-Milhofer H (2010) Physiological and pathological mineralization: some problems and possible solutions. J Medicinski vjesnik 42:33–44

Furukawa K (2014) Recent advances in research on human aortic valve calcification. J Pharmacol Sci 124:129–137

Golovanova OA (2018) Thermodynamic modeling of poorly soluble compounds formation in biological fluid. J Therm Anal Calorim, 1219–1224

Golovanova OA, Chikanova ES (2015) Kinetic characteristics of crystallization from model solutions of the oral cavity. J Crystallogr Rep 60:970–978

Golovanova OA, Korol'kov VV (2017) Thermodynamics and kinetics of calcium oxalate crystallization in the presence of amino acids. J Crystallogr Rep 62:787–796

Golovanova OA, Solodyankina AA (2017a) Main features of nucleation in model solutions of blood plasma. J Crystallogr Rep 62:342–348

Golovanova OA, Solodyankina AA (2017b) Kinetic characteristics of the crystallization from model solutions of blood plasma. J Crystallogr Rep 62:497–503

Golovanova OA, Achkasova EY, Punin YO, Zhelyaev EV (2006) Main regularities of crystallization of calcium oxalate in the presence of amino acids. J Crystallogr Rep 51:348–354

Golovanova OA, Frank-Kamenetskaya OV, Punin YO (2011) Specific features of pathogenic mineral formation in the human body. Russ J Gen Chem 81:1392–1406

Golovanova OA, Chikanova ES, Malyshev AV, Mylnikova TS (2015) Data on granulometric composition of calcium phosphate obtained by dispersion method. In: IOP conference series: materials science and engineering, "International scientific conference on radiation-thermal effects and processes in inorganic materials"

Golovanova OA, Chikanova ES, Punin YO (2015b) Main features of nucleation in model solutions of oral cavity. J Crystallogr Rep 60:438–445

Golovanova O, Gerk S, Mylnikova T (2016) Biogenic, Abiogenic interactions in natural and anthropogenic systems, pp 443–460

Habraken W, Habibovic P, Epple M, Bohner M (2016) Calcium phosphates in biomedical applications: materials for the future? Mater Today, 69–87

He J, Lin R, Long H, Liang Y (2015) Adsorption characteristics of amino acids on to calcium oxalate. J Colloid Interface Sci 454:144–151

Indulekha P, Li S, Romay M et al (2017) Cardiac fibroblasts adopt osteogenic fates and can be targeted to attenuate pathological heart calcification. J Cell Stem Cell 20:218–232

Karwowski W, Naumnik B, Szczepański M, Myśliwiec M (2012) The mechanism of vascular calcification—a systematic review. J Med Sci Monit 18:1–11

Kazuyuki Y, Frank D, Kolodgie Fumiyuki O (2015) Pathophysiology of native coronary, vein graft, and in-stent atherosclerosis. J Nat Rev Cardiol 10:1038

Korolkov V, Golovanova O, Kuimova M (2016) Biogenic–abiogenic interactions in natural and anthropogenic systems, pp 485–500

Pak CY, Sakhaee K, Moe OW, Poindexter J (2011) Defining hypercalciuria in nephrolitiasis. Kidney Int 80:777–782

Pigozzi F (2011) Endothelial (dys)function: the target of physical exercise for prevention and treatment of cardiovascular disease. J Sports Med Phys Fitness 51:260–267

Plyasunova N, Plyasunov A, Shock E (2004) Database of thermodynamic properties for aqueous organic compounds. Int J Thermophys 25:351–360

Rabelo N, Knopf J, Fredel T et al (2015) Synthesis and characterization of calcium phosphate compounds with strontium and magnesium ionic substitutions. Int J Morphol 33:1189

Sajadi S (2010) Metal ion-binding properties of L-glutamic acid and L-aspartic acid, a comparative investigation. J Nat Sci 2:85–90

Schukin ED, Pertsov AV, Amelina EA (2016) Colloid chemistry: a textbook for bachelors, 7th ed, Rev and add. M. Yurait Publishing House. (In Russian)

Shanahan CM (2005) Mechanisms of vascular calcification in renal disease. J Clin Nephrol 63:146–157

Shock E, Sassini D, Willis M, Sverjensky D (1997) Inorganic species in geologic fluids: correlations among standard molal thermodynamic properties of aqueous ions and hydroxide complexes. J Geochim Cosmochim Acta 61:907–950

Sigel A, Sigel H, Sigel KO (2008) Biomineralization: from nature to application. Metal ions in life sciences. John Wiley

Solodyankina A, Nikolaev A, Frank-Kamenetskaya O, Golovanova O (2016) Synthesis and characterization of nanocrystalline apatites from solution modeling human blood. J Molec Struct 1119:484–489

Vaitheeswari S, Sriram R, Brindha P (2015) Studying inhibition of calcium oxalate stone formation: an in vitro approach for screening hydrogen sulfide and its metabolites. Int Braz J Urol 41:503–510

Chapter 5
Water in Termally Treated Bioapatites and Their Synthetic Analogues: ^{1}H NMR Data

Olena A. Kalinichenko, Aleksandr B. Brik, Olga V. Frank-Kamenetskaya, Anatoliy M. Kalinichenko, Natalya O. Dudchenko and Anton M. Nikolaev

Abstract The molecular water incorporation in bioapatites obtained by bone pyrolysis at temperatures of 600–1100 °C has been investigated using in situ solid ^{1}H nuclear magnetic resonance (solid ^{1}H NMR) method in the temperature range of T = 25–300 °C and, in addition, ^{1}H magic-angle spinning NMR, X-ray diffraction and infrared spectroscopy at room temperature. For comparison, synthetic analogues of bioapatite, precipitated hydroxyapatite (HA), HA with La impurity and carbonate fluorapatite were investigated as well. It was established that there are water molecules adsorbed on crystallites surfaces and bound in structure (H_2O_s) in studied apatites. More rigid H_2O_{s1} molecules cause the doublet under normal conditions and the wide singlet at $T \geq 150$ °C in situ ^{1}H solid NMR spectra. In addition, H_2O_{s3} molecules with reorientation mobility at T = 150–300 °C are presented in bioapatite and HA annealed at lower temperatures and La-HA. Water incorporation into structure of bioapatite annealed at 600–1100 °C and its synthetic analogues HA is established to be zeolite-like. Presumably, the configuration of cavities is formed in the apatite crystal scaffold during annealing of studied apatites. These cavities are related with vacancy clusters in original structures and connected between themselves and with surface by the channels with a diameter of not more than 0.3 nm. Water molecules trapped in smaller (H_2O_{s2}) and larger cavities (H_2O_{s1}) cause the doublet and singlet, respectively; water molecules in OH vacancies in channels (H_2O_{s3}) are due to narrow lines.

O. A. Kalinichenko · A. B. Brik (✉) · A. M. Kalinichenko · N. O. Dudchenko
M.P. Semenenko Institute of Geochemistry, Mineralogy and Ore Formation of the National Academy of Sciences of Ukraine, Kyiv-142, Acad. Palladin Avenue, 34, 03680 Kyiv, Ukraine
e-mail: abrik.igmr@gmail.com

O. A. Kalinichenko
e-mail: elenakalinichenko97@gmail.com

O. V. Frank-Kamenetskaya · A. M. Nikolaev
Saint Petersburg State University, Universitetskaya Embankment, 7/9, 199034 Saint Petersburg, Russia

Institute of Silicate Chemistry, Makarova Embankment, 2, 199034 Saint Petersburg, Russia

© Springer Nature Switzerland AG 2020

O. V. Frank-Kamenetskaya et al. (eds.), *Processes and Phenomena on the Boundary Between Biogenic and Abiogenic Nature*, Lecture Notes in Earth System Sciences,
https://doi.org/10.1007/978-3-030-21614-6_5

Keywords Bioapatite · Thermal treatment · Solid-state ^{1}H NMR · Structural water · Biomimetic apatites

5.1 Introduction

The mineral component of solid tissues (bones, teeth) of vertebrates is mainly nanocrystalline non-stoichiometric hydroxyapatite (HA) with a noticeable number of substitutions and vacancies (V) (Elliott 1994; Combes et al. 2016; Frank-Kamenetskaya et al. 2016). Bone bioapatite is structurally similar to carbonate hydroxyapatite (CHA), predominantly B-type (the substitution of CO_3^{2-} ions with PO_4^{3-} ions) synthesized at low temperatures in water environment. Bone bioapatite differs from its synthetic analogues in a variety of substitutions (Ca → Na, Mg, Zn, Al, Sr), variations in a content of OH-groups (from 0 to 50% sites in the channels) and inhomogeneous distribution of structural defects (Elliott 1994; Wilson et al. 2006; Figueiredo et al. 2010; Liu et al. 2015; Combes et al. 2016; Frank-Kamenetskaya et al. 2016).

The study of structure transformations of bioapatite and its synthetic analogues during heating are of great interest for a number of areas, first of all, such as medicine and material science, in order to create biocompatible materials and adsorbents for various purposes (Figueiredo et al. 2010; Tonsuaadu et al. 2011; Liu et al. 2015; Combes et al. 2016). Composite materials based on HA matrices, obtained by thermally treatment of bioapatites, are more accurately chemically and structurally close to natural biominerals and are characterized by higher biocompatibility and bioactivity than materials based on synthetic HA.

Bone tissue is a complex composite structure formed by assembly of non-stoichiometric, poorly ordered CHA nanocrystallites separated by hydrated nanolayers, and in addition to water, it contains a significant amount of organic matrix (Figueiredo et al. 2010; Liu et al. 2015; Pavlychev et al. 2016). Synthetic co-precipitated HA and CHA, synthetic analogues of bioapatite, are nanodimensional, with poorly ordering apatite structure and significant amounts of adsorbed and structural water (Frank-Kamenetskaya et al. 2011; Combes et al. 2016).

Incorporation of various water forms (OH groups and H_2O molecules) into bioapatite and its synthetic analogues has been studied to a certain extent (Elliott 1994; Wilson et al. 2006; Kaflak and Kolodziejski 2011; Yoder et al. 2012; Combes et al. 2016; Pavlychev et al. 2016, etc.). Variations in structural environment and orientation of OH groups in bioapatite cause increase of ion diffusion, primarily of H ions in channels, in contrast to synthetic CHA with more highly ordered structure (Combes et al. 2016). It leads to the easier reorganization of bioapatite structure under change of external conditions.

The water adsorption on surface of nanocrystallites of bioapatite and its synthetic analogues is due to the presence of adsorption centers on surface—P–OH and Ca–OH groups (Kaflak and Kolodziejski 2011; Pavlychev et al. 2016). The H_2O molecule is adsorbed so that the oxygen ion forms an hydrogen (H-) bond with a proton of

a surface group (Yoder et al. 2012). F ions are present also on the basal surface of carbonatefluorapatite (CFA) crystallites, besides P–OH and Ca–OH groups (Elliot 1994; Sandstrom et al. 2006; Yoder et al. 2012). The mechanism of water molecule adsorption on CFA surface and the adsorbed layer structure differs significantly from HA and CHA, since the protons of H_2O molecules form H-bonds with F ions.

H_2O molecules in nanocrystalline HA structure can occupy OH vacancies (V_{OH}) in channels and sites outside channels, possibly, Ca vacancies (V_{Ca}) (Wilson et al. 2006; Kaflak and Kolodziejski 2011; Yoder et al. 2012, etc.). This partially compensates for steric distortions arising from formation of such vacancies under synthesis conditions (Frank-Kamenetskaya et al. 2011; Combes et al. 2016). The incorporation of H_2O molecules into structure of bone bioapatite and nanocrystalline CHA is largely the same and is related with the same structural defects due to B type carbonate substitutions (Wilson et al. 2006; Frank-Kamenetskaya et al. 2011; Combes et al. 2016). In addition, H_2O molecules in CHA can occupy oxygen vacancies (V_{Op}) appeared near $(CO_3)_B$ groups during B-type carbonate substitutions (Ivanova et al. 2001).

The following changes of bone bioapatite structure occur during heating (Figueiredo et al. 2010; Tonsuaadu et al. 2011; Liu et al. 2015). Adsorbed water is reversibly removed in the range of $T = 25$–200 °C. Decomposition of $(CO_3)_B$ groups begins at $T \sim 100$ °C. Heating of these structures at $T \geq 400$ °C leads to destruction of such groups (Tonsuaadu et al. 2011). Organic matrix burns at $T = 500$–650 °C, recrystallization of disordered near-surface layers of nanocrystallites, and partial decarbonization lead to increase in apatite structure ordering and nanocrystallites aggregation; impurity phases may appear. The OH group content in bioapatite can increase with dehydration and decarbonization of structure under certain conditions of heating (Combes et al. 2016). Removal of impurity groups and aggregation of nanocrystallites lead to formation of porous microstructure (with nanopore sizes less than 6 nm) in apatite crystal structure. Decarbonization is completed and dehydroxylation (destruction of structural OH-groups) begins in the range of $T = 800$–900 °C. Dehydroxylation continues as annealing temperature rises to 1300 °C. Transformations of bioapatite structure at such temperatures lead to increase in ordering and nanocrystallite sizes (Figueiredo et al. 2010; Tonsuaadu et al. 2011).

Structure changes of such apatites during heating, in general, are similar to those for bioapatite (Tonsuaadu et al. 2011). The removal of adsorbed (25–200 °C) and structurally bound water (200–500 °C) depend on surface structure of nanocrystallites. Dehydroxilation of HA and CHA occurs in the range of 800–1100 °C and tricalciumphosphate and tetracalciumphosphate phases form with further increase of the anneal temperature.

The methods of nuclear magnetic resonance (NMR) on ^1H, ^{13}C, ^{31}P etc. significantly expand possibilities of investigation of molecular water uptake in apatite structures with isomorphic substitutions, including bioapatites. The parameters of ^1H NMR signals of OH groups and H_2O molecules depend on their closest environment and participation in H–bonds (Abragam 1961; Wilson et al. 2006; Kaflak and Kolodziejski 2011; Brik et al. 2013; Combes et al. 2016 etc.). Substitutions of $OH^- \rightarrow CO_3^{2-}$, Cl^-, F^- and formation of H-bonds result in a high-frequency shift of ^1H

NMR signals from OH groups and H_2O molecules in apatite structure (Wilson et al. 2006; Kaflak and Kolodziejski 2011; Brik et al. 2013; Kalinichenko et al. 2015 etc.).

Uptake of molecular water in structure of bioapatites and their synthetic analogues, thermally treated previously, are poorly studied. Such investigations are of great interest for obtaining porous bioapatite-based matrices. The molecular water incorporation in bioapatites and thermally treated HA can be assumed to be determined by parameters of porous microstructure formed in crystalline matrix of apatite during heating.

Therefore, the objective of this work was to establish features of molecular water accommodation (structural environment of H_2O molecules and their content) in bone bioapatite and its synthetic analogues, depending on temperature of preliminary annealing of these materials, using ^{1}H solid state NMR (^{1}H solid NMR) method.

5.2 Materials and Methods

Samples. The native cortical cow bone and synthesized hydroxyapatite (HA) and annealed bone and HA samples were investigated. Bioapatite was obtained by annealing bone at 600 °C for 1.5 h for complete removal of the organic component followed by grinding. Synthetic HA was obtained by precipitation (Frank-Kamenetskaya et al. 2011) with calcining the obtained precipitate at 600 °C for 1 h. Obtained samples were annealed in the temperature range of $T_{ht} = 600$–1100 °C with a step of $\Delta T_{ht} = 100$ °C. Further, samples are designated as B–T_{ht} (bioapatite) and HA–T_{ht}, respectively, where T_{ht} is the annealing temperature.

In addition, synthetic HA with La impurity (La-HA) (Kalinichenko et al. 2015) and carbonated fluorapatite (CFA) with (in wt%): 3.5—F, 4—CO_2 and 0.04—H_2O in the OH group form (Brik et al. 2013) were studied.

Methods. The samples were studied by ^{1}H NMR methods: ^{1}H solid NMR and ^{1}H magic-angle spinning ($\nu_0 = 5$ kHz) NMR (^{1}H MAS NMR) according to the methodology Kalinichenko et al. (2015). The ^{1}H NMR spectra were recorded on polycrystalline 0.1 mm fraction of a sample (≈1 g) on an AVANCE 400 Fourier transform NMR spectrometer (Bruker) using the single-pulse SP program. In situ ^{1}H solid NMR spectra were recorded in the temperature range of $T = 25$–300 °C, increasing the temperature gradually, and ^{1}H MAS NMR spectra were recorded at room temperature. Chemical shifts were measured relatively to tetramethylsilane. Obtained spectra fitting with components were performed using TopSpin 4.0.2. The NMR signal line width $\Delta\nu_{1/2}$ was determined as the full width at half maximum (FWHM).

In addition, the samples were studied by X-ray powder diffraction (XRD) and infrared spectroscopy (IR).

X-ray powder diffraction was employed to identify phases and to determine unit cell parameters and nanocrystallite sizes. The measurements were performed using a Stoe ICSD and a Bruker Phaser D2 (Cu Kα radiation) diffractometers. The obtained data were processed using the PDWin4.0 software package and the UnitCell program.

Phase identification was performed with reference to the JCPDS PDF-2 database. Unit cell parameters were calculated by the least squares technique using 10–14 reflections using germanium ($a_{Ge} = 0.56571$ nm) as an internal standard. The crystallite sizes of bioapatite along the [001] direction was determined by the Debye-Scherrer equation using the (002) reflection. Natural apatite crystal was used as a standard for determining the instrumental contribution to peak broadening.

Infrared (IR) spectroscopy was applied to detect OH^- and CO_3^{2-} ions and H_2O molecules in samples. The spectra were collected at room temperature using a Bruker spectrometer (IFS 66v/S; Globar (MIR), DTGS Detector) in the 400–4000 cm^{-1} region. The samples were prepared as standard pressed pellets containing 1.0 mg of a studied sample in 200 mg of KBr.

5.3 Experimental Results

XRD data. *Bioapatite*. The bone diffractogram demonstrates the characteristic apatite reflexes, no other mineral phase was detected (Fig. 5.1a). The broad signal due to amorphous phase is characteristic of unannealed bone (Figueiredo et al. 2010). Anneal at 600 °C results to narrow diffraction peaks substantially and to increase apatite crystallite sizes from 38 to 110 nm along the [001] direction. There is no signal due to amorphous phase. The narrowing of diffraction peaks continues to $T_{ht} = 800$ °C, but does not change significantly with a further increase in annealing temperature.

The unit cell parameters of bone bioapatite (Table 5.1) are in the range of those of bioapatites, and slightly higher than anhydrous stoichiometric HA (st-HA) (Liu et al. 2015; Combes et al. 2016; Frank-Kamenetskaya et al. 2016). Annealing at $T_{ht} = 600$ °C leads to noticeable decrease in the unit cell parameters of bioapatite. Further increase in preliminary annealing temperature practically doesn't affect these parameters.

The *synthetic HA* diffractograms are similar to those of bioapatite. The synthesized HA diffractogram show the characteristic apatite reflexes, no other mineral phase was detected.

Annealing of HA at $T_{ht} = 600$ °C leads to narrowing of diffraction peaks, but to a lesser extent than for B-600 (Fig. 5.1). The widths of apatite structure peaks decreases approximately to those of B-800 and the β-whitlockite $Ca_3(PO_4)_2$ reflexes appear on the diffractogram of synthetic HA after annealing at $T_{ht} = 800$ °C (Fig. 5.1b). HA annealing at higher temperatures leads to increase in numbers and intensity of the β-whitlockite reflexes that indicates its content increase.

The unit cell parameters of synthesized HA (Table 5.1) differ significantly from those of st-HA (Table 5.1): $a_{HA} > a_{st\text{-}HA}$, but $c_{HA} < c_{st\text{-}HA}$. These parameters of synthesized HA change more significantly than those of bioapatite after annealing at 600 °C: a_{HA} decreases, but c_{HA} increases by 0.002 and 0.001 nm, respectively. Deviations of these values from those of st-HA decrease, but the above relations

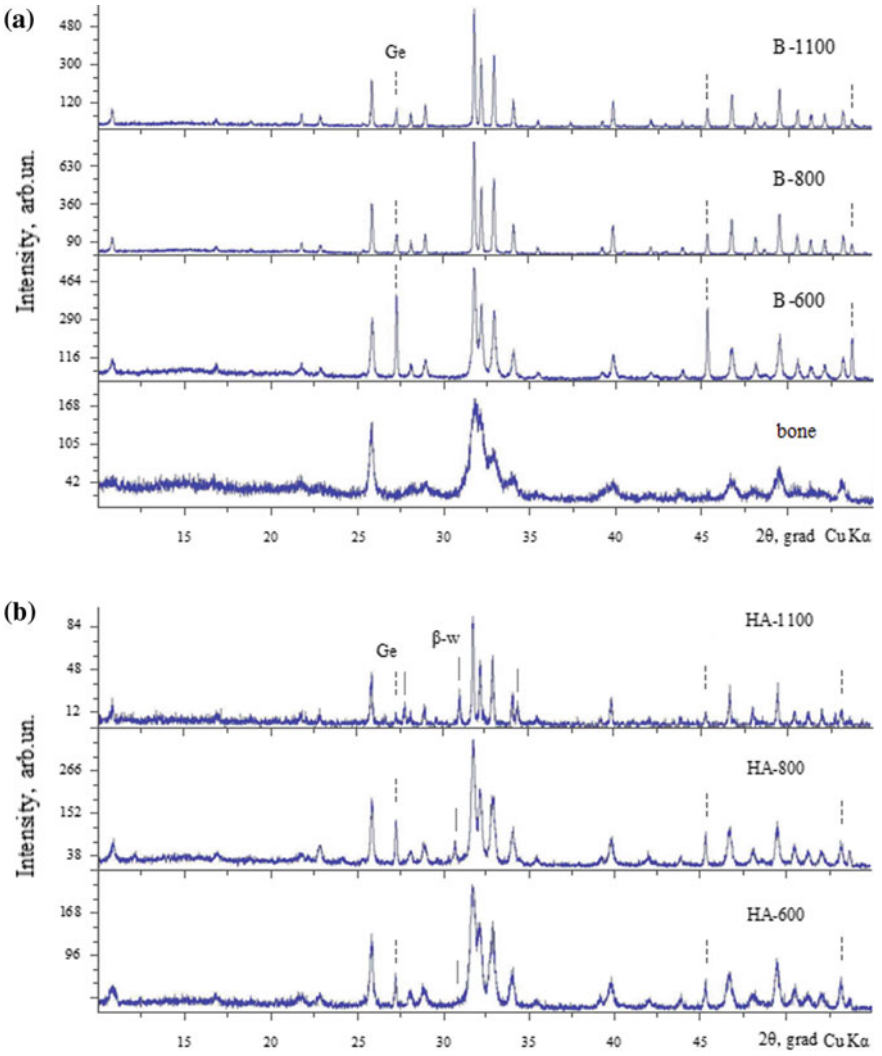


Fig. 5.1 Diffractograms of bioapatite (**a**) and HA (**b**), annealed at $T_{ht} = 600$, 800 and 1100 °C, respectively, the original bone is marked "bone". Reflexes of β-whitlockite are indicated by solid lines, Ge—by dashed lines

Table 5.1 Parameters (a, c) of the unit cell and crystallite sizes of studied apatites by the XRD data and evaluation of their specific surface areas (S)

Sample	a (nm)	c (nm)	Crystallite size (nm)	S (m^2/g)[1]
	XRD			Evaluation
Bioapatite				
Unburned bone	0.9425(4)	0.6890(3)	38	54.9
B-600	0.9411(1)	0.6883(1)	110	19.0
B-800	0.9415(1)	0.6882(2)	*160*	*13.1*
B-1100	0.9412(1)	0.6884(1)	*160*	*13.1*
Synthetic apatites				
HA[2]	0.9440(1)	0.6872(1)	n/d[3]	n/d
HA-600	0.9420(2)	0.6883(2)	n/d	n/d
HA-800	0.9422(1)	0.6881(2)	110	17.3
HA-1100	0.9420(1)	0.6879(1)	n/d	n/d
La-HA[3]	0.9424(1)	0.6878(1)	35	51.9
CFA[4]	0.9322(1)	0.6899(1)	35	54.8
Stoichiometric apatite: database: Powder Diffraction File. PDF-2. 2011				
HA 09-432	0.9418	0.6884	–	–
FA 15-0876	0.9368	0.6884	–	–

Notes
1—the specific surface area was estimated assuming that the crystallite form is cubic by the formula: S (m^2/g) $= 10^{-4} \cdot s/(v \cdot \rho)$, where $s = 6h^2$, $v = h^3$, ρ (g/cm^3) $= m_0/(N_A v_c)$—apatite density, h (cm)—the crystallite size, m_0 (g/mol)—the sample molecular mass, v_c (cm^3) - the unit cell volume, N_A—the Avogadro number. The m_0 values were calculated based on approximate crystallochemical formulas of bioapatite and nanocrystalline HA and data for La-HA and CFA: m_0 = 913.6; 1005.7; 1051.4 and 973.5 g/mol, respectively
2—data from Frank-Kamenetskaya et al. (2011)
3—not determined
4—data from Kalinichenko et al. (2015)
5—data from Brik et al. (2013)

do not change. Further increase in annealing temperature on unit cell parameters of synthesized HA has practically no effect.

IR data. The IR-spectra of original and annealed samples of bone and HA demonstrate characteristic bands of apatite structure, due to vibrations of P–O bonds in PO_4^{3-} ions (570, 610, 640, 1040, 1070, 1105 cm^{-1}) (Elliott 1994; Figueiredo et al. 2010).

In addition, the IR spectrum of bone (Fig. 5.2) shows bands due to B-type CO_3^{2-} ions (870 cm^{-1} and the doublet at 1420 and 1460 cm^{-1}), structurally bonding H_2O molecules (3400–3500 cm^{-1}), OH groups (about 3620 cm^{-1}) and organic matrix ions (1500–1800, 2850 and 2920 cm^{-1}) (Elliott 1994; Figueiredo et al. 2010). The bands of protein component are absent and of structural H_2O molecules are very weak after annealing of bioapatite at 600 °C. The intensity of type B carbonate bands noticeably

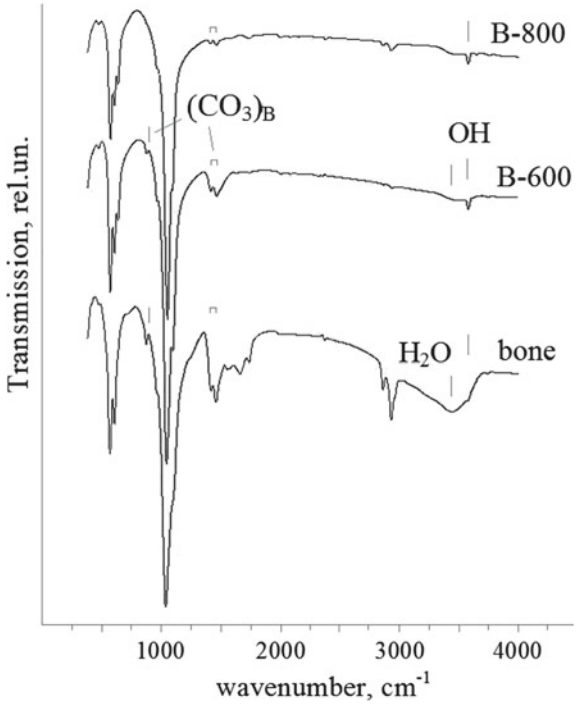


Fig. 5.2 IR spectra of bone tissue: initial ("bone") and annealed at 600 and 800 °C

decreases and drops almost to zero after annealing at 600 and 800 °C, respectively. The OH band intensity decreases at $T_{ht} = 600$ °C, but practically does not change with further increase in T_{ht} to 1100 °C (Fig. 5.2).

The HA-600 IR spectrum demonstrates the broad band (3400–3500 cm^{-1}) due to structurally bonding H_2O molecules and the weak band at about 3600 cm^{-1} due to OH groups. In addition, very weak bands are observed in the range of 1420–1460 cm^{-1}, which characteristic of B-type carbonate ions. The bands of H_2O molecules and B-type carbonate ions are absent in IR spectra of HA after annealing at 800 and 1200 °C.

^{1}H MAS NMR. The spectra of bioapatite annealed at different temperatures (Fig. 5.3) show two sufficiently well distinguished signals at about 1 and 6 ppm due to OH groups and H_2O molecules, respectively. There may be two components in apatite spectra at about 6 ppm caused by H_2O molecules: adsorbed on crystallites surfaces and captured in structure (Wilson et al. 2006; Yoder et al. 2012; Brik et al. 2013, etc.).

The OH group band intensity increases to approximately 95% from ^{1}H MAS NMR signal as a result of bioapatites anneal at 1000 °C and reduces by ≈10%—at 1100 °C, possibly due to partial water resorption (Ivanova et al. 2001; Tonsuaadu et al. 2011). These data show that annealing at $T_{ht} = 1000$ °C leads to almost complete dehydration of bioapatite, but a significant amount of OH groups remains in the structure.

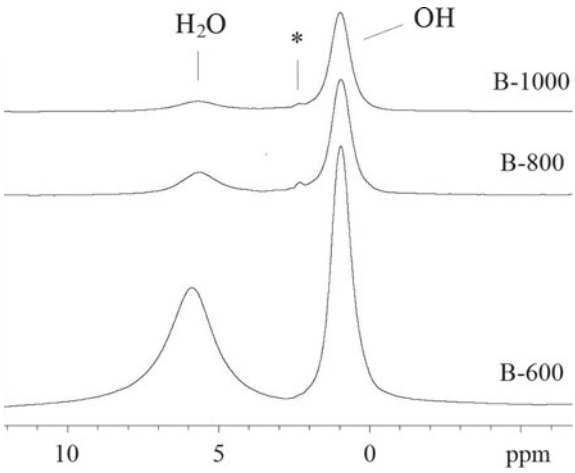


Fig. 5.3 ^{1}H MAS NMR (T = 25 °C) spectra of some bioapatites. The asterisk denotes the false rotor signal

The synthetic HA spectra are similar to bioapatite those, but the OH group band intensity reduced by ≈20% for HA-1100. This shows that water resorption in HA structure is more intense.

^{1}H solid NMR. Synthetic nanodimensional HA is the effective water adsorbent (Wilson et al. 2006; Kaflak and Kolodziejski 2011; Tonsuaadu et al. 2011 etc.). Therefore, further studies were conducted by in situ ^{1}H solid NMR method after rehydration of annealed samples in order to distinct signals from different types of molecular water.

It should be noted that chemical shifts and bandwidths of ^{1}H solid NMR and ^{1}H MAS NMR signals due to protons in the same structural environment differ. A ^{1}H solid NMR signal demonstrates isotropic and anisotropic components, while a ^{1}H MAS NMR signal shows an isotropic component. ^{1}H MAS NMR signal bandwidths are mainly caused by deviations of chemical shifts (due to differences of structural environments), but those of ^{1}H solid NMR, besides,—by dipole–dipole interactions between protons and their mobility. This makes it possible to identify different structural environments of OH groups and H_2O molecules and evaluate their mobility using the shape and width of ^{1}H solid NMR signal (Abragam 1961; Gabuda and Rzhavin 1978; Yoder et al. 2012 etc.). The moving of ions or molecules (reorientational, rotational, etc.) leads to line narrowing.

^{1}H solid NMR at T = 25 °C. Spectra of all studied samples are similar. There are five components in these spectra, except for B-1000 and B-1100 (Fig. 5.4a; Table 5.2). The components δ_2 and δ_3 are poorly distinct. The component δ_2 in B-1000 and B-1100 spectra is absent. The chemical shifts of the most high-frequency (δ'') and low-frequency ($\delta' < 0$) components are abnormally high, with practically identical widths (Figs. 5.4a and 5.5).

The respective parameters of components are approximately the same in all the spectra (Table 5.2). The widths and intensity ratios of components are noticeable different.

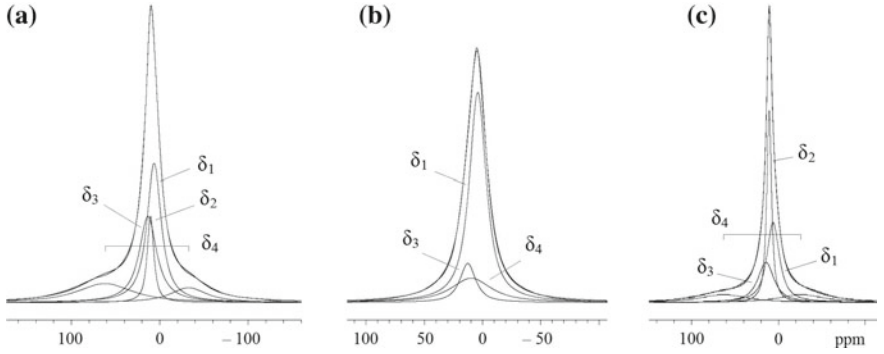


Fig. 5.4 ^{1}H solid NMR B-800 spectra of initial sample (**a**) and sample kept at normal conditions during 1 h (**b**) and 7 days (**c**) after warming at 150 °C. The spectra were recorded at $T = 25$ °C. The spectra fitting with the doublet splitting are showed

The component δ_1 was assigned to OH groups, similar to that in ^{1}H MAS NMR spectra. The chemical shift of the OH group component is lower than H_2O molecule components because of the greater electron shielding of protons in OH groups.

The parameters of ^{1}H solid NMR signal due to H_2O molecules represent strength bonding of water molecules in structure: singlet signals are caused by relatively mobile molecules, but a doublet signal is due to interacting protons of the same H_2O molecule that indicates strong H-bonding with surrounding ions (Abragam 1961; Yoder et al. 2012 etc.). Therefore, one can conclude that the narrow singlet δ_2 in obtained spectra is caused by relatively mobile H_2O molecules adsorbed on crystallite surfaces (H_2O_{ads}), and the wide singlet δ_3—by lower mobile H_2O molecules (H_2O_{s2}) (Fig. 5.4a; Table 5.2). The components δ' and δ'' can be assigned with the Pake doublet at $\delta_4 \approx 16$ ppm and the splitting of $\Delta_4 \approx 80$ ppm. Such doublet is caused by H_2O molecules rigid bound in structure (Abragam 1961) in another structural environment (H_2O_{s1}).

All water types removed from bioapatites warmed at $T = 150$ °C rehydrate almost completely during 7 days of sample keeping under normal conditions (Fig. 5.4—sample B-800).

The component parameters of synthetic apatite spectra are approximately the same as those of annealed bioapatites (Fig. 5.5; Table 5.2). The original synthetic HA contains plenty of water adsorbed on crystallite surfaces. Therefore, signals in spectra of HA heated at $T_{ht} = 600$ and 700 °C, were practically not fitted with separate components. All components can be resolved in these spectra, but the H_2O_{s1} molecule component intensity is very low (<5% of the spectrum intensity). The spectra of HA heated at 800 °C (HA-800) and initial La-HA were fitting with components well. The doublet intensity in these spectra is about 10% (Table 5.2).

The synthetic CFA spectrum is similar to those of HA, with some differences. The OH group component is overlapped with the H_2O_{ads} component. The OH group content in CFA is insignificant—about 0.04 wt% H_2O (Brik et al. 2013). Therefore, the doublet is resolved well (Fig. 5.5). The doublet intensity is relatively high—about

Table 5.2 Parameters (chemical shift δ, bandwidth $\Delta\nu$ and intensity I) components in ^{1}H solid NMR spectra ($T = 25$ °C) of samples and B-800 after heating at $T = 150$ °C

Sample	Components											
	OH			H_2O_{ads}/H_2O_{s3}			H_2O_{s2}			H_2O_{s1}		
	δ_1(ppm)	$\Delta\nu_1$ (ppm)	I_1 (%)	δ_2(ppm)	$\Delta\nu_2$ (ppm)	I_2 (%)	δ_3(ppm)	$\Delta\nu_3$ (ppm)	I_3 (%)	Doublet [2]		
										δ_4(ppm)	$\Delta\nu_4$ (ppm)	I_4 (%)
Bioapatite												
B-600	5.6	15.0	27	10.2	5.2	40	13.4	12.3	23	18.9	62	10
B-700	6.0	17.4	42	9.5	9.3	28	12.4	23.3	19	16.1	78	11
B1-800[3]	5.6	10.9	35	10.6	8.0	11	17.3	26.1	18	15.5	85	36
B2-800	5.0	20.4	48	8.1	5.0	2	15.0	30.7	26	15.8	67	24
B3-800	5.1	18.0	25	10.4	7.3	27	16.2	23.8	20	15.5	77	28
B-900	5.7	18.5	34	10.4	8.0	14	14.6	16.5	22	15.7	81	32
B-1000	6.2	10.9	70	–	–	–	9.1	15.1	13	17.7	70	17
B-1100	6.7	17.8	77	–	–	–	13.0	16.9	9	9.5	81	14
Synthetic apatites												
HA-800	4.6	17.4	34	10.7	6.1	36	12.5	22.9	23	15.3	95	7
La-HA	5.2	15.3	28	10.4	5.3	39	12.9	17.5	23	20.4	80	10
C-61	2.9	13.4	12	8.8	8.5	47	17.6	25.2	14	18.8	77	27

Notes

1—in % to the total intensity of the spectrum

2—the chemical shift of the center and splitting of the doublet, transforming into the singlet when in situ ^{1}H solid NMR spectra temperature raises (explanation in text)

3—B-800 (Fig. 5.4): initial (B1-800) and after 1 h (B2-800) and 7 days (B3-800) kept under normal conditions after warming at 150 °C

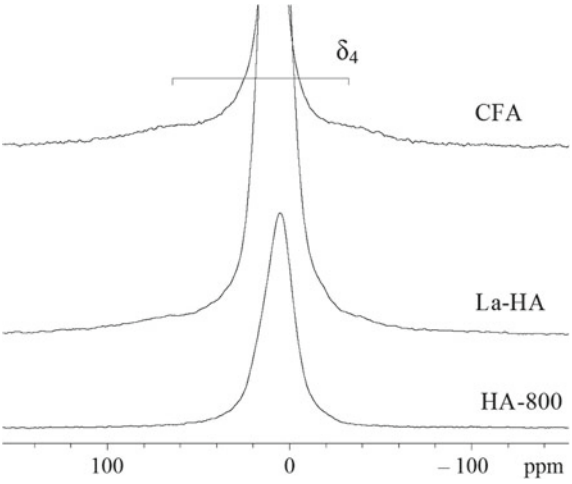


Fig. 5.5 ^{1}H solid NMR (T = 25 °C) spectra of synthetic apatites

of 30% of the signal intensity. The lower value of δ_1 in the CFA spectrum (Table 5.2) reflects increase in electron shielding of hydroxyl protons surrounded by F ions.

In situ ^{1}H *solid NMR* spectra of B-600—B-900 bioapatites and synthetic apatites were recorded at T = 25–300 °C to find structural environments of different types of molecular water in studied samples. The components δ_3 should be noted to be well distinguished after disappear of H_2O_{ads} intense bands (Fig. 5.4).

The doublet is practically not observed in B-600 spectra at T > 25 °C. The H_2O_{s1} doublet isn't observed or is poorly resolved in other bioapatite spectra at T = 150–300 °C. These spectra show the broad singlet at approximately the same chemical shift as the doublet (Fig. 5.5).

Figure 5.6 demonstrates the B-600 spectra at T = 150, 300 and 25 °C (after sample cooling). The doublet component isn't shown because of the low intensity of the spectrum at room temperature—by the intense H_2O_{ads} component. The additional component appears in the B-600 spectra at T = 150–250 °C at approximately the chemical shift δ_2, besides bands listed in Table 5.2. This component disappears at T = 25 °C after sample cooling (Fig. 5.6). This component can be assigned conventionally to water molecules in other structural environment (H_2O_{s3}). This component may not to be observed in spectra at T = 20–100 °C due to the intense H_2O_{ads} band at the same chemical shift.

Figure 5.7 demonstrates the bandwidths of different types of H_2O molecules dependent on temperature. The wide singlet, instead of the doublet, was noted above to be observed at about the same chemical shift at temperature raise (Fig. 5.4). Therefore, Fig. 5.7c shows the $\Delta\nu_4$ value that is the doublet splitting at T = 25 °C and the width of the band δ_4 at higher temperatures.

Components δ_2 and δ_3 are associated with more and less mobile H_2O molecules, respectively, at normal temperatures. The mobility of these molecules almost does not change at T = 100–300 °C, as is shown slight change in corresponding bandwidths (Fig. 5.7a, b). H_2O_{s1} molecules are rigidly bound in structure. Their transition into

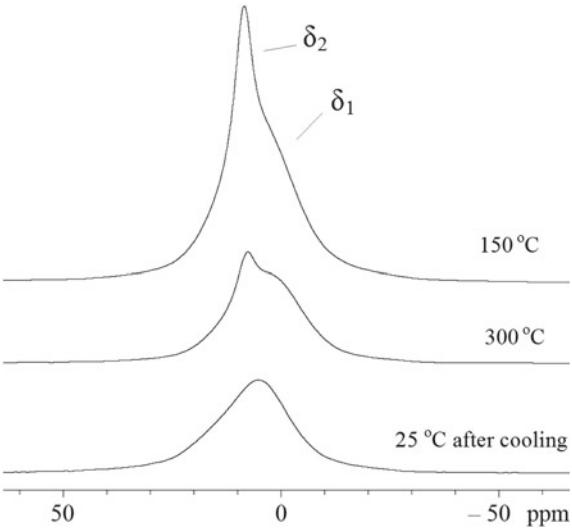


Fig. 5.6 The central part of in situ ^{1}H solid NMR B-600 spectra at some temperatures. The original sample spectrum is not shown due to the intense signal from H_2O_{ads} molecules

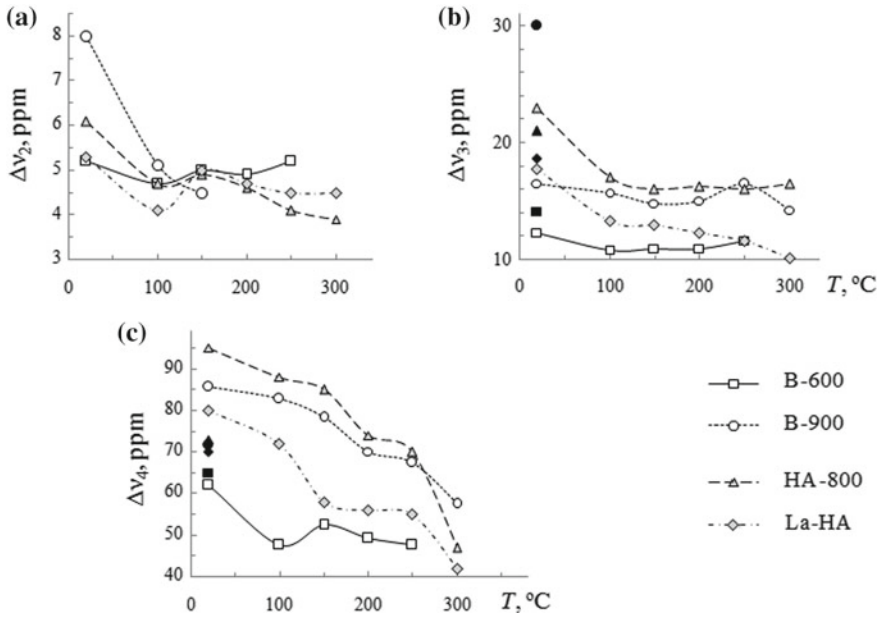


Fig. 5.7 In situ ^{1}H solid NMR: the bandwidths of components δ_2 (**a**), δ_3 (**b**) and δ_4 (**c**) versus temperature for some samples. Dark symbols indicate values in spectra recorded after sample cooling

the mobile state is reflected in decrease of the doublet splitting or the width of the band δ_4 (Fig. 5.7c) in B-600 spectra at $T = 100$ °C (that does not change with further T increase). The $\Delta\nu_4$ values in other bioapatites spectra decrease gradually with T raise.

Figure 5.8 shows the temperature dependences of H_2O band intensities relative to the OH band intensity. Dehydroxylation of bioapatites and HA begins at temperature about 850 °C (Figueiredo et al. 2010; Tonsuaadu et al. 2011). Therefore, one can assume that OH group contents in studied samples do not change when heated at $T \leq 300$ °C. Accordingly, Fig. 5.8 demonstrates the contents of H_2O molecules in different structural environments in studied apatites when the temperature raise.

There are absent bands of adsorbed water in spectra of bioapatites annealed at $T_{ht} \geq 700$ °C when temperature elevates to $T = 150$ °C (Fig. 5.8c). The imtensity of the band δ_2 in B-600 spectra drops at $T = 150$ °C and almost does not change at $T =$ 150–300 °C. This component disappears or is not presented when the more intense H_2O_{ads} band is observed after sample cooling (Figs. 5.6 and 5.8).

The band intensities of structural bound H_2O_{s1} molecules (except for B-600) and H_2O_{s2} decreases noticeably at $T = 150$ °C, and they almost do not change at $T =$ 150–300 °C (Fig. 5.8b, c). The intensity of the wide singlet δ4 in the B-600 spectrum at $T = 100$–250 °C is approximately equal to the doublet one at $T = 25$ °C unlike other samples.

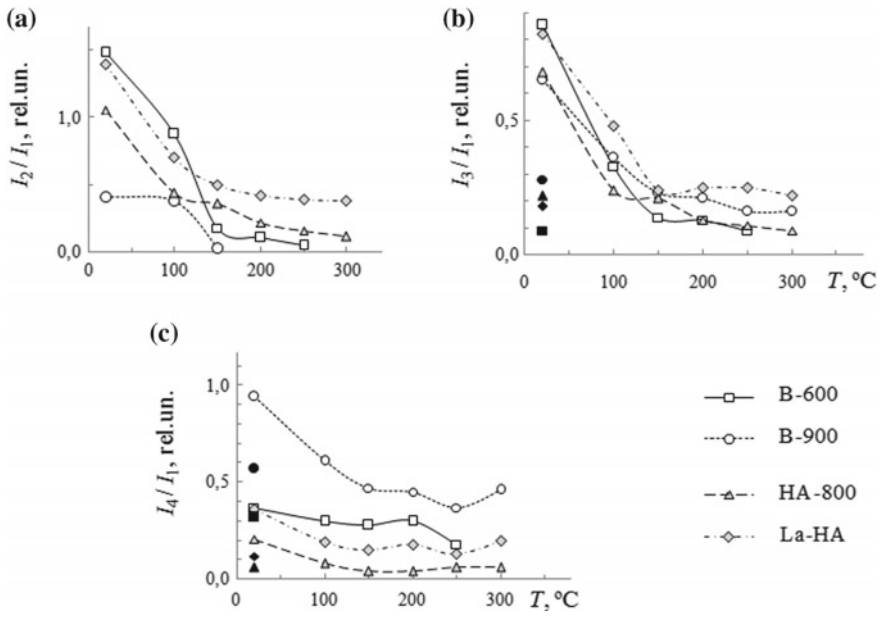


Fig. 5.8 In situ ^{1}H solid NMR: the integrated intensities (I) of components δ_2 (**a**), δ_3 (**b**) and δ_4 (**c**) relative to the integrated intensity of the component δ_1 versus temperature for some samples. Dark symbols indicate values in spectra recorded after sample cooling

The parameters of in situ ^{1}H solid NMR spectra of synthetic HA and CFA change approximately like parameters of bioapatite spectra (Figs. 5.7 and 5.8). Water adsorbed on surface disappears when heating to 150 °C, but the narrow component δ_2 is presented in these spectra. The doublet is absent at 100 °C, and the narrow component at δ_2 is observed to 300 °C and disappears when the temperature drops to 100 °C in HA-800 spectra. The doublet and narrow component change similarly in La-HA spectra, but their intensities are higher than those in HA-800 spectra (Figs. 5.7 and 5.8; Table 5.2). The doublets of different intensities are observed in CFA spectra at $T \leq 300$ °C.

^{1}H solid NMR spectra at $T = 25$ °C after sample cooling under normal conditions. The spectra of all samples recorded after heating up to $T = 150$–300 °C show the doublet of different intensity dependent on the duration of sample kept after heating. Cooling samples under normal conditions leads to rapid recovery of the components presented in the original sample spectra.

The low intensity doublet or the broad singlet can be distinguished in the spectrum of B-800 cooled for 1 h after heating to $T = 150$ °C, but the doublet intensity has almost recovered to its original level after sample keeping during 7 days (Fig. 5.4; Table 5.2). This shows that water is almost simultaneously recorded by surface and structure of annealed bioapatites.

5.4 Discussions

The performed investigation established that incorporation of molecular water in bioapatites and their synthetic analogues annealed at $T_{ht} = 600$–1100 °C are similar but depend on sample peculiarities. However, comparison of obtained data of NMR, IR and X-ray diffraction shows that molecular water uptake in bioapatites and their synthetic analogues largely depends on origin and thermal treatment of a sample.

Thermal treatment effect on structure of bioapatite and HA. Bone apatite differs from st-HA in poorly structure ordering and presence of impurity groups detected by X-ray diffraction and IR data (Figs. 5.1 and 5.2).

Bone pyrolysis at 600 °C leads to the loss of the organic component, a significant part of molecular water (Fig. 5.2) and formation of nanodimension CHA like synthetic HA by X-ray diffraction (Fig. 5.1). A further increase of annealing temperature does not affect bioapatite structure ordering, although decarbonization occurs at 800 °C (Fig. 5.2). In contrast to bioapatite, the apatite ordering of the synthetic HA increases and β-whitlockite impurity phase is formed when HA is annealed to 1100 °C (Fig. 5.1b). The apatite structure ordering of B-600 and HA-800 is approximately the same.

The apatite unit cell parameters of samples (Table 5.1) reflect changes in their structures. In general, presence of H_2O molecules, Ca vacancies, cations of K^+, NH_4^+, Sr^{2+} (larger than Ca) and HPO_4^{2-} ions in apatite structure leads to *a* parameter increase (Elliott 1994; Frank-Kamenetskaya et al. 2011). The V_{Ca} presence, in

addition, leads to c parameter decrease. Carbonate substitutions, especially type B, lead to opposite effects: a parameter reduction and c parameter increase.

The obtained XRF data (Table 5.1) show the following based on the above relations. The unit cell parameters of carbon-free HA are typical for Ca-deficit HA contained H_2O molecules and HPO_4^{2-} ions (Frank-Kamenetskaya et al. 2011): $a_{HA} > a_{st\text{-}HA}$, $c_{HA} < c_{st\text{-}HA}$. The high a_{HA} value and low c_{HA} one indicate, in addition, noticeable amounts of NH_4^+ ions and V_{Ca}, respectively. The unit cell parameters of bone bioapatite are in the ranges of characteristic values (Liu et al. 2015; Frank-Kamenetskaya et al. 2016). Bioapatite (bAp) , despite the presence of H_2O molecules and HPO_4^{2-} ions, differs from HA by a noticeable content of B-type CO_3^{2-} ions and, possibly, by lower V_{Ca} content: $a_{bAp} < a_{st\text{-}HA} < a_{HA}$, $c_{HA} < c_{st\text{-}HA} < c_{bAp}$. The c_{bAp} increase can be associated with a high content of H_2O molecules in the channels (Wilson et al. 2006) and presence of Sr^{2+} ions (Combes et al. 2016).

The unit cell parameters of La-HA reflect presence of V_{Ca}, H_2O molecules, HPO_4^{2-} and NH_4^+ ions in La-HA, like HA: $a_{La\text{-}HA} > a_{st\text{-}HA}$, $c_{La\text{-}HA} < c_{st\text{-}HA}$ (Table 5.1). One can assume that La-HA is structurally similar to bone bioapatite to a greater extent than HA: $a_{La\text{-}HA} \approx a_{bAp}$, $c_{HA} < c_{La\text{-}HA} < c_{bAp}$.

There are H_2O molecules, ions of CO_3^{2-} (type B predominantly) and NH_4^+ and a low amount of OH groups in channels but no V_{Ca} in CFA. This structure differs markedly from bioapatite and HA (Table 5.1): $a_{CFA} < a_{st\text{-}FA} < a_{st\text{-}HA}$, $c_{st\text{-}HA} = c_{st\text{-}FA} < c_{bAp} < c_{CFA}$, where st-FA designates the stoichiometric fluoroapatite.

The transformations of bioapatite and HA structures at the same annealing temperature are partially similar, so the changes of their unit cell parameters are similar as well. Annealing of bioapatite and HA at 600 °C leads to destruction of HPO_4^{2-} ions and removal of H_2O molecules from structure, and, moreover, NH_4^+ ions from HA: the parameter a decreases and a_{HA}—to a greater extent (Table 5.1). The parameter c_{bAp} of B-600 declines as a result of dehydration and partial decarbonization of bioapatite (Elliott 1994; Ivanova et al. 2001). The parameter c_{HA} increase may be caused by decrease in V_{Ca} content as a result of partial recrystallization during annealing.

The structures of bioapatite and HA differ significantly when annealing temperatures are lower (600–700 °C). There are $(CO_3)_B$ groups in B-600 (Fig. 5.2), but the apatite structure ordering of this sample is higher than HA-600 (Fig. 5.1). The apatite structure ordering of HA-800 rises to B-600 one as a result of HA annealing at 800 °C. Annealing of bioapatite and HA at 600–800 °C leads to the formation of structures which are similar substantially along the hexagonal axis (Table 5.1): $c_{bAp} \approx c_{HA}$.

Small changes in unit cell parameters of bioapatite and HA with a further increase in T_{ht} (Table 5.1) indicate moderate structure transformations upon such annealing. The parameter c of bioapatite does not practically change, that indicates no dehydroxilation. Thermal stability of hydroxyls in bioapatite containing impurity ions is higher than in HA (Liu et al. 2015; Combes et al. 2016). Increase of HA apatite structure ordering (Fig. 5.1b) and the parameter c_{HA} decrease at $T_{ht} = 1100$ °C can be caused by HA dehydroxilation at such temperatures (Tonsuaadu et al. 2011). These

results are consistent with data Figueiredo et al. (2010), Tonsuaadu et al. (2011) and Liu et al. (2015).

Thus, bioapatite annealing at $T_{ht} = 600$ °C leads to formation of higher ordered apatite structure with a noticeable content of $(CO_3)_B$ groups and without organic matrix, according to X-ray diffraction and IR data. This shows that $T_{ht} = 600$ °C is the lower limit of the temperature range of bioapatite annealing in order to obtain biogenic HA matrices with no organic component.

The ^{1}H NMR data complements obtained results. The OH group content in structure increases as a result of bioapatite annealing at $T_{ht} = 700$ °C (Table 5.2). This may be caused by formation of OH groups during decarbonization and dehydration of bioapatite under such heating (Combes et al. 2016).

The comparison of ^{1}H NMR data shows that the OH group content in bioapatite does not change during annealing at temperatures of at least up to 1000 °C. The ratios of the component intensities of molecular water and OH groups (in H_2O terms) in ^{1}H solid NMR spectra of B-800 and B-1000 are ≈1.9 and 0.4, respectively (Table 5.2). The H_2O molecules content in B-800 is ≈4.3 times higher than in B-1000 if the OH group content in these samples is the same. ^{1}H MAS NMR spectra of these samples demonstrate approximately this ratio of H_2O component intensities, with the same signal from OH groups (Fig. 5.3). The same hydroxyl content in these samples may be also indicated by bioapatite structure at such T_{ht} similar to st-HA one (Fig. 5.1a—no impurity phases), and practically no change in unit cell parameters (Table 5.1). This correlates with the data that thermal stability of bioapatite is higher than nanocrystalline HA under normal conditions, and bioapatite dehydroxylation occurs at T ~ 1300 °C (Tonsuaadu et al. 2011).

The δ_1 values increase in B-1000 and B-1100 spectra and a decrease one—in CFA spectrum (Table 5.2) shows that structural environment of OH groups in these apatites differs from other samples significantly. The decrease in electron density on hydroxyl protons in B-1000 *и* B-1100 may be caused by changes in their structural environment due to diffusion of cations and vacancies at such temperatures. The OH groups in CFA are surrounded by F ions that explain an increase in electron density on hydroxyl protons, relative to HA.

Content of different types of molecular water. Obtained ^{1}H NMR data showed that molecular water incorporation in annealed bioapatites and HA is similar after samples rehydrated under normal conditions (Table 5.2). There are several types of molecular water in bioapatites annealed at $T_{ht} \leq 900$ °C: water adsorbed on crystallite surfaces and structural water trapped in two different environments: H_2O_{s2} and H_2O_{s1} molecules. The slower moving H_2O_{s2} molecules are bound weakly but H_2O_{s1} molecules are rigid at 25 °C. The same water types are presented in synthetic apatites: HA after annealing at 600–800 °C and initial La-HA and CFA. There are H_2O_{s2} and H_2O_{s1} molecules in bioapatites after annealing at $T_{ht} = 1000$–1100 °C also, but no adsorbed water.

The molecules of H_2O_{ads}, H_2O_{s2} and H_2O_{s1} are located in similar structural environments in all samples, respectively, as demonstrated by the similar parameters of components in studied apatites spectra (Table 5.2).

At the same time, there are certain differences in molecular water incorporation in studied apatites that depend on structural features. All samples can be divided into several groups, according to ratios of H_2O component intensities, approximately the similar in each group (Table 5.3): bioapatites with $T_{ht} = 600–700$ °C and synthetic HA (HA-800 and La-HA), bioapatites with $T_{ht} = 800–900$ and 1000–1100 °C, and CFA. The lowest crystallite sizes and more poorly ordered apatite structure are characteristic of bioapatites with $T_{ht} = 600–700$ °C, HA-800, La-HA and CFA, and with some differences in their structures due to presence of CO_3^{2-} ions (bioapatites, CFA) and monovalent cation impurities (bioapatites, La-HA, CFA). Apatite structure ordering and crystallite sizes of bioapatite increase with annealing temperature rises. The CFA structure differs from other samples: F ions occupy the channel sites, with a small degree of OH group substitutions (Table 5.3), and no V_{Ca} (Brik et al. 2013).

The OH group content in La-HA is $[OH]_{La\text{-}HA} \approx 1.8$ apfu (atom per formula unit) (Kalinichenko et al. 2015). This corresponds to water content in $\{H_2O_{OH}\}_{La\text{-}HA} = ([OH]_{La\text{-}HA}/[OH]_{st\text{-}HA})\{H_2O_{OH}\}_{st\text{-}HA} \approx 1{,}6$ wt% H_2O, where $[OH]_{st\text{-}HA} = 2$ apfu and $\{H_2O_{OH}\}_{st\text{-}HA} = 1.8$ wt%—the OH group content in the st-HA unit cell and the corresponding content of molecular water based on the st-HA crystallochemical formula, respectively. The OH group content in HA-800 can be assumed to be approximately the same (≈1.8 apfu), taking into account that there is V_{OH} in precipitated nanocrystalline HA (Frank-Kamenetskaya et al. 2011), and HA dehydroxylation begins at $T \sim 900$ °C (Tonsuaadu et al. 2011).

The upper limit of the OH group content in studied bioapatites can be estimated similarly to La-HA: $\{H_2O_{OH}\}_{bAp} = 0.45$ wt% with $[OH]_{bAp} = 0.5$ apfu (on the average), since OH groups in bone bioapatite occupy from 0 to 50% positions (Combes et al. 2016). The OH group content in studied bioapatites annealed $T_{ht} = 800–1000$ °C is practically the same as noted above.

Based on ^1H solid NMR data, the contents of molecular water different types in studied apatites were estimated by the formula: $\{H_2O_w\}$ (wt%) $= (I_n/I_1)\{H_2O_{OH}\}$, where all values are for the same sample, $w =$ ads, s2 and s1 for $n = 2, 3$, and 4, respectively, I—the component intensities (Table 5.2); the estimated values of $\{H_2O_{OH}\} =$ 0.45 and 1.6 wt% were used for bioapatites and HA, respectively, $\{H_2O_{OH}\}_{La\text{-}HA} =$ 1.6 wt% (calculated above), $\{H_2O_{OH}\}_{CFA} = 0.04$ wt%.

The obtained data (Table 5.3) show that H_2O contents in different structural environment in studied apatites is noticeably differed, depending on annealing temperature T_{ht} and chemical composition of a sample. The values calculated in this way for bioapatites and HA-800 should be noted to be the upper limits of the possible value ranges.

H_2O_{ads} molecules. Increase in T_{ht} of bioapatite leads to decrease in the adsorbed water content (Table 5.3). H_2O_{ads} molecules make a contribution of about 50 and 20% of molecular water in bioapatites annealed at $T_{ht} = 600–700$ and 800–900 °C, respectively. There is no adsorbed water in bioapatites annealed at $T_{ht} = 1000–1100$ °C. The adsorbed water content in synthetic HA-800 and La-HA is higher than in B-600, but one in CFA is an order of magnitude lower than in La-HA (Table 5.3). Adsorbed water in synthetic apatites is about of 55% of molecular water.

Table 5.3 The intensity ratios of molecular water components in ^{1}H solid NMR spectra at $T = 25$ °C[1] and the evaluation of contents of different types of water in studied apatites

	Samples								
	B-600	B-700	B-800	B-900	B-1000	B-1100	HA-800	La-HA	CFA
Intensity ratios (rel.un.)									
I_3/I_2	0.6	0.7	1.6	1.6	–	–	0.6	0.6	0.3
I_3/I_4	2.3	1.8	0.5	0.7	0.8	0.6	3.3	2.3	0.5
Water content (wt%)									
$\{H_2O_{OH}\}$	≤0.45[2]						≤1.6[2]	1.6[3]	0.04[4]
$\{H_2O_{ads}\}$	0.67	0.30	0.14	0.19	0.00	0.00	1.72	2.26	0.16
$\{H_2O_{s2}\}$	0.38	0.29	0.23	0.29	0.08	0.05	1.10	1.33	0.05
$\{H_2O_{s1}\}$	017	0.12	0.45	0.42	0.11	0.08	0.33	0.58	0.09

Notes

1—from Table 5.2 data

2—$\{H_2O_w\}$ (wt%) $= (I_n/I_1)\{H_2O_{OH}\}$, where all values are for one sample, w = ads, s2 and s1 for $n = 2$, 3 and 4, respectively, I—the component intensity in ^{1}H solid NMR spectra (Table 5.2), $\{H_2O_{OH}\}$ values for bioapatites and HA are estimated (not higher than those given)

3—data by Kalinichenko et al. (2015)

4—data by Brik et al. (2013)

H_2O_{s2} molecules. La-HA and HA-800 have the highest H_2O_{s2} contents (Table 5.3). This content for annealed bioapatites decreases with increase of T_{ht} to 1100 °C by almost an order of magnitude. CFA has the lowest H_2O_{s2} contents. These molecules make up about 30 and 40% of molecular water in bioapatites at $T_{ht} \leq 900$ °C and 1000–1100 °C, respectively. This ratio is approximately the same for synthetic HA (≈35%), but much lower for CFA (≈16%).

H_2O_{s1} molecules. Their content depends on structural features of samples (Tables 5.2 and 5.3). The H_2O_{s1} molecules content is 2–3 times less than OH groups and molecules of H_2O_{ads} and H_2O_{s2} in bioapatites with $T_{ht} = 600$–700 °C, HA-800 and La-HA. The H_2O_{s1} content increases with bioapatite annealing temperature rises to $T_{ht} = 800$–900 °C, but decreases with further increase in T_{ht} (Table 5.3). The H_2O_{s1} content in CFA is low, but higher than that of OH groups and H_2O_{s2} molecules.

H_2O_{s1} molecules are about of 15% of molecular water in bioapatites with $T_{ht} =$ 600–700 °C, HA-800 and La-HA, ≈30% in CFA and ≈50% in bioapatites with $T_{ht} \geq 800$ °C.

Structure peculiarities effect on water adsorption. The δ_2 values are almost identical in sample spectra, except for CFA (Table 5.2). This demonstrates that adsorption center structure on surface of these samples is approximately the same. The adsorption centers formed on the surface of annealed bioapatites and HA cooled under normal conditions can be assumed to be similar to those on the surface of HA cooled after heating at about 500 °C (Tonsuaadu et al. 2011).

The H_2O_{ads} content decrease in HA-800 and bioapatites with $T_{ht} = 600$–700 °C, relative to La-HA, is caused by decrease in the specific surface area of nanocrystallites with increase in their sizes (Table 5.1) and differences in structures. The evaluation of the specific surface area of samples was calculated using crystallite sizes and assuming the cubic form of crystallites (Table 5.1). The specific surface area of La-HA is three times higher than HA-800 and B-600 (Table 5.1). The value of $\{H_2O_{ads}\}/S$ is about of 0.04 for B-600 and La-HA and is higher (~0.1) for HA-800. This shows that La incorporation in HA and the low content of OH groups in annealed bioapatite structure reduces significantly the adsorption capacity of HA.

Decrease in $\{H_2O_{ads}\}$ with increase in bioapatite annealing temperature to $T_{ht} =$ 800–900 °C (Table 5.3) is partly due to the specific surface area decrease with crystallite size increase (Table 5.1). In addition, adsorption properties of surface (the surface concentration of adsorption centers and/or the H_2O molecule adsorption energy) change as a result of structure changes during decarbonization with this annealing. Decrease of the value of $\{H_2O_{ads}\}/S$ to ~0.02 shows this.

The CFA surface structure differs significantly from other samples, both P–OH and Ca–OH groups and F ions are present on the surface (Elliot 1994; Sandstrom et al. 2006; Yoder et al. 2012). The mechanism of water molecule adsorption on such surface differs markedly from HA. This fact and the low hydroxyl content can explain the low H_2O_{ads} content in CFA, relative to La-HA (Table 5.3).

Space nanostructure of studied apatites. The adsorbed water and the most of H_2O molecules trapped in structure were removed when studied apatites were heated to 300 °C under normal conditions. The H_2O_{ads} and H_2O_{s2} molecules resorbed rapidly, but H_2O_{s1} molecules—slower when samples were cooled after such warm-

ing under normal conditions. Therefore, the space structure of studied apatites can be assumed to be zeolite-like: there are cavities interconnected by transition channels in the apatite crystalline scaffold. This assumption is in the agreement with Figueiredo et al. (2010), who showed that bone tissue annealing at 600–1200 °C leads to formation of porous microstructure in the apatite crystalline scaffold.

The Pake doublets in ^{1}H solid NMR spectra of samples (Figs. 5.4 and 5.5; Table 5.2) show that H_2O_{s1} molecules are rigid in structure. The doublet disappears when all samples, except CFA, are warmed to 300 °C. The wide component with the bandwidth close to the doublet splitting is observed in the spectrum at approximately the same chemical shift. This bandwidth decreases with increasing temperature (Fig. 5.7c). This shows that the doublet signal may be observed due to several H_2O molecules nearby.

The ^{1}H solid NMR spectra of annealed bioapatite and its synthetic analogues obtained in the present work are partially similar to those of molecular water in zeolites. There are up to 30 H_2O molecules in zeolite structural cavities with a diameter of about 1.2 nm. These molecules cause narrow lines in ^{1}H solid NMR spectra under normal conditions and the doublet signal at low temperatures (Gabuda and Rzhavin 1978).

The following can be assumed by comparing ^{1}H solid NMR spectra obtained in this work and data of Gabuda and Rzhavin (1978). The space structure of studied samples is similar to zeolite one, but smaller sizes, since the bandwidths of components δ_3 and δ_4 in obtained spectra (Fig. 5.7b, c) are much higher than in zeolite spectra at higher temperatures (Gabuda and Rzhavin 1978). There are two types of cavities in the crystal structure of studied apatites, where H_2O_{s1} and H_2O_{s2} molecules are captured. Such cavities are interconnected by transition channels. There are 3–5 H_2O molecules in each cavity. So, there are no significant differences in the component intensities of H_2O_{s1} and H_2O_{s2} molecules (Fig. 5.8b, c) and the values of δ_3 and δ_4, are approximately the same for all samples except for B-600, B-1000, B-1100 and La-HA (Table 5.2).

The sizes of cavities were estimated, similarly to Gabuda and Rzhavin (1978), using the parameters of the doublet and singlet signals. Calculations showed that the sizes of such cavities are about 0.5 and 0.8 nm, where H_2O_{s1} and H_2O_{s2} molecules are captured, respectively. Studied apatites dehydrate almost completely when heated to 300 °C. The samples rehydrate under normal conditions: H_2O_{s2} molecules enter the structure within 1 h, H_2O_{s1} molecules—up to 7 days. The rapid removal of H_2O_{s1} molecules from structure heated to 300 °C and noticeably slower rehydration show that the diameter of transition channels should be approximately equal to the H_2O molecule size (about 0.3 nm).

The formation of such cavities may be caused by heterovalent isomorphism in cationic and anionic positions. For example, there are possibility to form the clusters of closely spaced V_{Ca} and V_{OH} vacancies due to substitutions in bioapatite or co-precipitated HA (Frank-Kamenetskaya et al. 2011; Combes et al. 2016).

Dehydration and decarbonization of bioapatite at $T_{ht} = 800$–900 °C leads to an increase in contents of H_2O_{s2} (relative to B-700) and H_2O_{s1}. This fact points to the relationship of cavities with defects appeared during such processes. Annealing

bioapatite at temperatures of 700–800 °C can lead to formation of cavities in structure, for example, by removing the adjacent $(CO_3)_B$ group and H_2O molecule occupied V_{OH} and/or V_{Op} in the original structure (Ivanova et al. 2001).

Perhaps, La-HA, to a greater extent than HA-800, is structurally similar to B-600, which is shown by comparing their unit cell parameters (Table 5.1) and ratios of component intensities in ^{1}H solid NMR spectra (Tables 5.2 and 5.3). The differences between these structures are caused by the wide range of impurity ions presented in bioapatite, including carbonate ions to $T_{ht} = 800$ °C, but the significantly lower hydroxyl content (Combes et al. 2016).

Similar cavities due to by isomorphic substitutions can be assumed to be formed in La-HA and CFA structures. There may be the clusters of closely spaced vacancies, $V_{Ca} + V_{OH}$ and $V_{OH} + V_{Op}$—$(CO_3)_B$, respectively, in these apatites. Such clusters can be linked with impurity ions of La^{3+} and Na^+ in La-HA and CFA, respectively, and NH_4^+ ions—in both samples. The presence of impurity cations can ensure stronger bonding of H_2O_{s1} molecules.

Structural environment of water molecules. Incorporation of H_2O_{s1} and H_2O_{s2} molecules into structure of studied apatites is interrelated, but depends on structural features of samples and for bioapatites also on annealing temperature. H_2O_{s2} molecules are first removed from sample structures, and then, except of B-600, about half of H_2O_{s1} molecules are removed when heated to 300 °C (Fig. 5.8b, c).

Similar parameters of components δ_3 and δ_4 (Table 5.2) show that the structural environments of H_2O_{s2} and H_2O_{s1} molecules in studied apatites are approximately the same, respectively. The relation $\delta_3 \approx \delta_4$ (Table 5.2) shows that the structural environments of H_2O_{s1} and H_2O_{s2} molecules in HA-800 and bioapatites with $T_{ht} =$ 800–900 °C are approximately the same.

Low mobile H_2O_{s2} molecules are located in the near-surface layer. This may explain the rapid rehydration of these molecules for 1 h (Elliott 1994) during sample cooling. The doublet waveform in ^{1}H solid NMR spectra shows H_2O_{s1} molecules rigid fixed in structure (Figs. 5.4 and 5.5; Table 5.2).

Obtained data is consistent with results of study of synthetic CHA and CFA by ^{2}H solid NMR (Yoder et al. 2012). The rigid and mobile D_2O molecules caused by the characteristic Pake triplets and singlet lines due to the quadrupole deuterium nuclei, respectively, in spectra of these apatites. Structural water was removed when warming at 500 °C. Yoder et al. (2012) suggested that water molecules in CHA and CFA structure are bound likewise in zeolites A: H_2O molecules are located in channels elongated along the hexagonal axis, some of them may be located near monovalent cations.

It should be noted that H_2O_{s2} and H_2O_{s1} molecules in La-HA and CFA have been captured in structure during sample synthesis. Therefore, these molecules are located, most likely, near structural defects due to substitutions. This is partially compensated by appearing steric stresses (Elliott 1994; Frank-Kamenetskaya et al. 2011).

The H_2O molecule leaves the hydroxyl channel during HA dehydration by the proton diffusion through the channel to surface where the H_2O molecule is formed ($H^+ + OH^- \rightarrow H_2O$) (Tonsuaadu et al. 2011; Yoder et al. 2012). This molecule

diffuses then into adsorbed layer and atmosphere. Partial dehydration of La-HA and CFA occurs upon heating to 300 °C. Based on this, it can be concluded that H_2O_{s2} molecules and at least some of H_2O_{s1} molecules in La-HA are located in hydroxyl channels—in the surface layer (as noted above) and more distant from surface, respectively.

It was noted above that the structural environments of H_2O_{s2} and H_2O_{s1} molecules in all studied apatites are approximately the same, respectively. Therefore, it can be assumed that H_2O_{s2} and H_2O_{s1} molecules are placed in the hydroxyl channels in all samples. Part of these molecules is possible to be located near monovalent cations (except for HA-800, where such cations are absent), taking into account data of Yoder et al. (2012).

La-HA. The significantly different values of δ_3 and δ_4 (Table 5.2) demonstrate that H_2O_{s2} and H_2O_{s1} molecules are located near different structural defects. It can be concluded that H_2O_{s2} molecules in La-HA occupy several V_{OH} in the channel fragments reached surface, taking into account the high H_2O_{s2} content (Table 5.3). There are present V_{Ca} near these structural sites that explains increase in H_2O_{s2} molecule mobility with temperature increasing (Fig. 5.7b). The H_2O_{s1} content can be estimated as about of 0.3 apfu, taking into account that 1 apfu H_2O corresponds to 1.8 wt% H_2O and based on Table 5.3 data. This value is approximately equal to the V_{Ca} amount, and two times lower than La^{3+} ion content in La-HA (Kalinichenko et al. 2015). Therefore, H_2O_{s1} molecules can be assumed to be located near La^{3+} ions and V_{Ca}. This may explain the decrease in electron density on H_2O_{s1} molecule protons that the high δ_4 value demonstrates (Table 5.2).

CFA. The structural environments of H_2O_{s2} and H_2O_{s1} molecules are approximately the same, since $\delta_3 \approx \delta_4$ (Table 5.2). The low contents of these molecules (Table 5.3) is caused by F ions that occupy most of the channel sites. H_2O_{s1} molecules in CFA are rigid because the doublet in the spectrum is observed when heated to 300 °C, although its intensity decreases. CFA has the significant content of $(CO_3)_B$ groups (≈0.83 apfu). Therefore, H_2O_{s2} and H_2O_{s1} molecules in CFA can be assumed to locate in the channels near the $(CO_3)_B$ groups—in the near-surface layer and more distant from surface, respectively.

Annealed bioapatites. H_2O_{s1} molecules in B-600 are more strongly bound than in other samples, and do not leave the structure when heated to 300 °C (Fig. 5.8 c), although their mobility increases (Fig. 5.7c). The δ_4 values in B-600 and CFA spectra are approximately the same, one in the B-700 spectrum—slightly lower (Table 5.2). Carbonate groups are present in bioapatite, at least, at annealing up to $T_{ht} < 800$ °C (Fig. 5.2). Therefore, H_2O_{s1} molecules in B-600 and B-700 can be assumed to place in the channels near $(CO_3)_B$ groups. This explains the H_2O_{s2} content decrease with the higher decarbonization degree in B-700. The H_2O_{s2} contents in these bioapatites are higher than that of H_2O_{s1}, and their structural environments are different, since $\delta_3 < \delta_4$ (Table 5.2). The H_2O_{s2} molecules are possible to occupy several positions in the channel fragments reached surface, taking into account their high content (Table 5.3).

Rise in T_{ht} leads to increase in sizes, that is, a volume of bioapatite crystallite. The increase in contents of H_2O_{s2} (relative to B-700) and H_2O_{s1} in bioapatite at T_{ht} = 800–900 °C is related with increase in crystallite volumes and transformations of

channel structures with removal of CO_2 molecules. The ratio $\delta_3 \approx \delta_4$ (Table 5.2) shows that H_2O_{s2} and H_2O_{s1} molecules in B-800 and B-900 are approximately in the same structural environment, possibly near V_{Ca} and/or structural defects formed during $(CO_3)_B$ groups removal from structure. The binding strength of H_2O_{s1} molecules in the hydroxyl channels of these structures is lower—most of these molecules are removed when heated to 300 °C, in contrast to B-600 (Fig. 5.8c).

The structure ordering of bioapatite at $T_{ht} \geq 800$ °C does not change practically (Fig. 5.1a). However, annealing at $T_{ht} \geq 1000$ °C leads to decrease in H_2O_{s1} and H_2O_{s2} contents (Table 5.3), that indicates significant changes in structure of channels. It was noted above that the hydroxyl content in bioapatite during such annealing practically does not change, at least at $T_{ht} = 1000$ °C, but, the most likely, cations diffusion occurs at these temperatures. This leads to V_{Ca} disappearing and partial recrystallization of structure, including the disordered near-surface layer. The low values of δ_3 in B-1000 spectra and δ_4—in B-1100 one (Table 5.2) indicate in the electron density increase on protons of H_2O_{s2} and H_2O_{s1} molecules, respectively. This may be due to appearance in their environment of monovalent cations which have occupied V_{Ca} as a result of diffusion. The δ_3 and δ_4 values in B-1100 and B-1000 spectra, respectively, are approximately the same as for bioapatites with $T_{ht} = 800$–900 °C. The structural environment of H_2O_{s2} and H_2O_{s1} molecules can be assumed to be similar—such ions locate near V_{Ca} and/or structural defects formed during removal of $(CO_3)_B$ groups from structure, respectively.

HA-800. The parameters of components δ_3 and δ_4 in HA-800 spectrum are approximately the same as in La-HA and bioapatite spectra with $T_{ht} = 800$–900 °C, respectively, since $\delta_3 \approx \delta_4$ (Table 5.2). Therefore, H_2O_{s2} and H_2O_{s1} molecules can be assumed to be approximately in the same structural environments, in the channels near V_{Ca}, in HA-800 with a lower structure ordering. Such vacancies in HA-800 have been formed during synthesis of co-precipitated HA and during annealing due to removal of NH_4^+ ions. The H_2O_{s2} molecules occupy several sites in the channel fragments reached the surface, taking into account their high content (Table 5.3). The H_2O_{s1} molecules are located farther from surface, possibly near V_{Ca}, but after several sites occupied by OH groups. This can explain the markedly lower content of H_2O_{s1} molecules (Table 5.3) and their low mobility at $T \leq 250$ °C (Fig. 5.7c). It is possible that H_2O_{s1} molecules, which are more strongly bound (Fig. 5.8c), are located near other structural defects, for example, impurity ions.

H_2O_{s3} molecules appear at 150–300 °C in ^{1}H solid NMR spectra of samples with poorly ordered apatite structure (B-600, HA-800 and La-HA). The low bandwidth at $T = 150$–300 °C can be due to the reorientational motion of H_2O_{s3} molecule protons at such temperatures (Yoder et al. 2012). This points that H_2O_{s3} molecules are captured in vacancies in the crystal structure, but form weak H-bonds with surrounding ions. These molecules can appear in the doublet form in the spectra at 25 °C, but tend not be observed because of the more intense H_2O_{s1} component.

H_2O_{s3} molecules are absent in bioapatite spectra after annealing at $T_{ht} \geq 700$ °C. Therefore, H_2O_{s3} molecules can be assumed to occupy structural sites in B-600 and HA-800, because of these molecules have been retained in structures during annealing. H_2O_{s3} molecules are possible to occupy V_{Op} near $(CO_3)_B$ groups in bone

bioapatite and B-600, but they are removed from structure during bioapatite decarbonization when T_{ht} rises to 700 °C. The H_2O_{s3} molecules can occupy V_{Ca} located near other vacancies, for example, V_{OH}, in HA-800 and La-HA. Ascertainment of the structural environment of H_2O_{s3} molecules in studied apatites requires additional research.

Molecular water binding in sample structures. Experimental results obtained in this work suggest that the configuration of nanodimensional cavities forms during annealing as a result of dehydration, decarbonization and partial recrystallization of bioapatites and their synthetic analogues HA contained impurity ions and vacancies. This nanoporous structure is to a certain extent similar to zeolite structure: the structure cavities are located in the crystalline apatite scaffold. The molecules of H_2O_{s2} and H_2O_{s1} are captured in hydroxyl channels in larger and smaller cavities, respectively. Such cavities can be related with clusters of vacancies in the original structure and are connected to each other and to surface by hydroxyl channels with a diameter of about 0.3 nm. H_2O molecules are trapped in cavities by H-bonds with surrounding ions with such sizes of channels. H_2O molecules will diffuse into a cavity located nearby, and, along the channel, to nanocrystallite surface when temperature rise (Yoder et al. 2012).

The configuration of cavities in the crystalline scaffold of bioapatites annealed in different temperature ranges (600–700, 800–900, and 1000–1100 °C) differs significantly. The binding of molecular water in bioapatites annealed at lower temperatures is largely caused by interaction of H_2O molecules with the outer surface of nanocrystallites but in those annealed at higher temperatures—by trap of H_2O molecules in cavities formed during annealing in the crystalline apatite scaffold. The content of H_2O_{ads} and H_2O_{s2} molecules is higher in samples with lower structure ordering (B-600, HA-800, La-HA), but H_2O_{s1} molecules—in bioapatites annealed at 800–900 °C with higher structure ordering. The crystallite surface hydrophobization and decrease in the molecular water content in bioapatites annealed at 1000–1100 °C is most likely observed due to increase in apatite structure ordering during such annealing.

Dehydration of studied apatites can be represented by obtained data as follows. HA dehydration occurs in the way of proton transfer along hydroxyl channels (Yoder et al. 2012). Water molecules adsorbed on crystallite surfaces are almost completely removed at heating at $T = 25$–150 °C. At such temperatures, part of H_2O_{s2} molecules leaves structure, part of H_2O_{s1} molecules occupies their place. The other part of H_2O_{s1} molecules with reorientational mobility remains in structure up to $T = 300$ °C.

These results are consistent with Wilson et al. (2006) showed that H_2O molecules in synthetic CHA structure are trapped in V_{OH} and, presumably, in V_{Ca} in two, slightly different types of structural environment. The latter become distinguishable in situ ^1H MAS NMR spectrum at 225 °C. Wilson et al. (2006) suggested that H_2O molecules trapped in V_{Ca} are approximately in the same structural environment, but in the subsurface layer and bulk structure, with lower and higher binding energies in structure, respectively.

The assumed nanoporous structure of bioapatites thermally activated at temperatures $T_{ht} \leq 900$ °C can provide relatively rapid adsorption and desorption of H_2O molecules, and possibly ions, from aqueous solutions.

5.5 Conclusions

It is established using in situ ^{1}H solid NMR that molecular water incorporation in bioapatites annealed at 600–1100 °C and synthetic HA (annealed at 800 °C), La-HA and CFA is similar when annealed samples are cooled under normal conditions. The structural features of studied apatites were determined using powder X-ray diffraction and IR spectroscopy.

There are H_2O molecules adsorbed on crystallite surfaces and captured in structure, H_2O_{s2} and H_2O_{s1} molecules, in the studied apatites. Such molecules are located in the hydroxyl channels closer and more distant from surface, respectively, based on obtained data. There are H_2O_{s3} molecules that are presented most likely in OH vacancies in the channels in samples with lower ordering of apatite structure (B-600, HA-800 and La-HA).

It is shown that the content of adsorbed water decreases but one of water trapped in mineral structure increases with temperature increasing of bone pyrolysis in the ranges of 600–1100 and 600–900 °C, respectively. The contents of H_2O_{ads} and H_2O_{s2} molecules are higher in lower structure ordering (B-600, HA-800, La-HA), but H_2O_{s1} molecules—in samples thermally activated at 800–900 °C.

The water incorporation in structure of annealed bioapatite and its synthetic analogues HA is assumed to be zeolite-like, based by the obtained results. There is possible formation of the configuration of nanoporous cavities related with vacancy clusters, including near substitutions in PO_4 sites, in studied apatites. The doublet and broad singlet in NMR spectra can be caused by H_2O_{s1} and H_2O_{s2} molecules in cavities of smaller (about 0.5 nm) and large (about 0.8 nm) sizes, respectively. Such cavities are connected to each other and the surface by hydroxyl channels with a diameter of about 0.3 nm.

References

Abragam A (1961) The principles of nuclear magnetism. Clarendon, Oxford

Brik AB, Frank-Kamenetskaya OV, Dubok VA, Kalinichenko EA, Kuz'mina MA, Zorina ML, Dudchenko NO, Kalinichenko AM, Bagmut NN (2013) The features of isomorphic substitutions in synthetic carbonatefluorapatites. Mineralogie J (Ukraine) 35(3):3–10 (in Russian)

Combes C, Cazalbou S, Rey C (2016) Apatite biominerals. Minerals 6:34–59

Elliott JC (1994) Structure and chemistry of the apatites and other calcium orthophosphate. Elsevier, Amsterdam London, New York, Tokyo

Figueiredo M, Fernando A, Martins G, Freitas J, Judas F, Figueiredo H (2010) Effect of the calcination temperature on the composition and microstructure of hydroxyapatite derived from human and animal bone. Ceram Int 36:2383–2393

Frank-Kamenetskaya O, Kol'tsov A, Kuz'mina M, Zorina M, Poritskay L (2011) Ion substitutions and non-stoichiometry of carbonated apatite-(CaOH) synthesised by precipitation and hydrothermal methods. J Mol Struct 992:9–18

Frank-Kamenetskaya OV, Izatulina AR, Kuz'mina MA (2016) Ion substitutions, non-stoichiometry, and formation conditions of oxalate and phosphate minerals of the human body. Lecture Notes in Earth System Sciences, pp 425–442

Gabuda SP, Rzhavin AF (1978) Nuclear magnetic resonance in crystal hydrates and hydrated proteins. Nauka, Novosibirsk (In Russian)

Ivanova TI, Frank-Kamenetskaya OV, Kol'tsov AB, Ugolkov VL (2001) Crystal structure of calcium-deficient carbonated hydroxyapatite Thermal decomposition. J Solid State Chem 160:340–349

Kaflak A, Kolodziejski W (2011) Complementary information on water and hydroxyl groups in nanocrystalline carbonated hydroxyapatites from TGA, NMR and IR measurements. J Mol Struct 990:262–270

Kalinichenko EA, Brik AB, Nikolaev AM, Kalinichenko AM, Frank-Kamenetskaya OV, Dubok OV, Bagmut NN, Kuz'mina MA, Kolesnikov IE (2015) The structure features of synthetic apatites with REE impurities by data of spectroscopy and X-ray analysis methods: I Hydroxyapatites. Mineralogie J (Ukraine) 37(4):21–35 (In Russian)

Liu Q, Pan H, Chen Z, Matinlinna JP (2015) Insight into bone-derived biological apatite: ultrastructure and effect of thermal treatment. BioMed Res Int, ID 601025:1–11

Pavlychev AA, Avrunin AS, Vinogradov AS, Filatova EO, Doctorov AA, Krivosenko YS, Samoilenko DO, Svirskiy GI, Konashuk AS, Rostov DA (2016) Local electronic structure and nanolevel hierarchical organization of bone tissue: theory and NEXAFS study. Nanotechnology 27(50):1–8

Sandstrom DE, Jarlbring M, Antzutkin ON, Forsling W (2006) A spectroscopic study of calcium surface sites and adsorbed iron species at aqueous fluorapatite by means of ^{1}H and ^{31}P MAS NMR. Langmuir 22(26):11060–11064

Tonsuaadu K, Gross KA, Pluduma L, Veiderma MA (2011) Review on the thermal stability of calcium apatites. J Therm Anal Calorim 110(2):647–659

Wilson EE, Awonusi A, Morris MD, Kohn DH, Tecklenburg MMJ, Beck LW (2006) Three structural roles for water in bone observed by solid-state NMR. Biophys J 90:3722–3731

Yoder CH, Pasteris JD, Worcester KN, Schermerhorn DV (2012) Structural water in carbonated hydroxylapatite and fluorapatite: confirmation by solid state H^{-2} NMR. Calcif Tissue Int 90:60–67

Chapter 6
The Formation of Calcium and Magnesium Phosphates of the Renal Stones Depending on the Composition of the Crystallization Medium



Mariya A. Kuz'mina, Anton M. Nikolaev and Olga V. Frank-Kamenetskaya

Abstract The study of the phase formation of phosphates in the solutions simulating the normal inorganic composition of human urine was carried out by the precipitation method. All calcium and magnesium phosphates typical for the kidney stones were synthesized: brushite, octacalcium phosphate, hydroxyapatite, struvite and Mg-whitlockite. The regularities of the calcium and magnesium phosphates formation in the crystallization medium of variable composition were found out. The borders of the crystallization areas of the synthesized phases were determined in the axes «initial pH value—main components' concentration». In general, phosphates crystallization areas are defined by the starting concentrations of the main components, pH value of the crystallization medium and by the presence of the additional ions in the solution. It was shown that crystallization of any calcium phosphate leads to the significant decreasing of the pH value of the crystallization medium. Adding of the inorganic components typical for the human urine into the $Ca–PO_4$ system leads to the moving of the crystallization area borders of the calcium phosphates (brushite, octacalcium phosphate, apatite). Crystallization doesn't occur in the areas that are characterized by the composition and pH typical for the normal human urine. Increasing amount of the precursors or pH values leads to the start of the phosphate crystallization.

Keywords Biominerals · Pathogenic crystallization · Phase equilibrium · Precipitation method · Renal stones · Apatite · Brushite · Struvite · Octacalcium phosphate · Whitlockite

M. A. Kuz'mina (✉) · A. M. Nikolaev · O. V. Frank-Kamenetskaya
Saint Petersburg State University, Universitetskaya nab. 7/9, Saint Petersburg 199034, Russia
e-mail: mak_5262@mail.ru

A. M. Nikolaev · O. V. Frank-Kamenetskaya
Institute of Silicate Chemistry RAS, Makarova nab. 2, Saint Petersburg 199034, Russia

© Springer Nature Switzerland AG 2020

O. V. Frank-Kamenetskaya et al. (eds.), *Processes and Phenomena on the Boundary Between Biogenic and Abiogenic Nature*, Lecture Notes in Earth System Sciences,
https://doi.org/10.1007/978-3-030-21614-6_6

6.1 Introduction

The ecological state of the environment in the modern cities leads to the increasing level of the diseases associated with stone formation in humans and animals. Therefore interest in studying the causes and mechanisms of crystallization of pathogenic phases in living organisms is constantly growing (Fisang et al. 2015; Nyame et al. 2015). The lifetime risk of kidney stone formation is about 10–15% in the developed countries, but can be as high as 25% (Chatterjee et al. 2018). Despite the fact that the most common phases of kidney stones are calcium oxalates (Chou et al. 2011; Chatterjee et al. 2018), phosphates of calcium and magnesium are also quite common phases and play an important role in the formation of kidney stones, so the present work is focused on them. It is reported earlier, that extracellular phosphate is toxic to the cell at high concentrations (Kuro-o 2013), but at the same time calcium and magnesium phosphates influence on the formation of oxalate stones (Xie et al. 2015). Since hydroxyapatite ($Ca_{10}(PO_4)_6(OH)_2$) is the main mineral of human bone and dental tissues, the study of phase formation in phosphate systems is important for progress in studying the mechanisms of biomineralization and for the development of biocompatible biomaterials (Driessens 1981; Muller et al. 2007; Zhang 2013). So, in the present work we focused our attention on phosphate phases occurring in the composition of kidney stones (Lagier and Baud 2003; Abbona and Boistelle 1979; Ronteltap et al. 2010; Englert et al. 2013): brushite ($Ca(HPO_4)x2H_2O$, dicalcium phosphate dihydrate, DCPD), octacalcium phosphate (OCP, mineral name is absent) ($Ca_8(HPO_4)_2(PO_4)_4x5H_2O$) and hydroxyapatite (HAP) ($Ca_{10}(PO_4)_6(OH)_2$), Mg-whitlockite (WT) ($Ca_9Mg(HPO_4)(PO_4)_6$) and struvite (STR) ($MgNH_4(PO_4)x6H_2O$).

The crystallization of calcium phosphate phases in different conditions was investigated by various authors (Iijima et al. 1998; Oliveira et al. 2007 and others). There are a lot of data regarding the crystallization conditions of DCPD, OCP and HAP. Usually the researchers paid most attention to the joint precipitation of various phosphate phases or mutual recrystallization of one phosphate phase into another. Unfortunately, as a result of these experiments, obtained data sometimes demonstrated opposite regularities.

For example, Koutsoukos and Nancollas (1981) showed that apatite crystals epitaxially grow on brushite crystals, and this was confirmed by later research (Chhiber et al. 2014). It was shown in several papers that DCPD can be the precursor for the apatite growth (Ferreira et al. 2003; Stulaiterova and Medvedsky 2008; Komlev et al. 2012). At the same time Oliveira et al. (2007) showed, that apatite can transform into DCPD (when the pH of the crystallization medium decreases). In the Perez et al. (1989) research it was shown that DCPD transforms into OCP (at the pH value of 6.4–7.0). At the same time OCP can be the substrate for the DCPD crystallization (Heughebaert et al. 1986). Other researches state that OCP is the precursor for the apatite crystallization (De Rooij et al. 1984; Iijima et al. 1998; Xin et al. 2006; Arellano-Jimenez et al. 2009). The relationship between amorphous calcium phosphate (ACP), OCP and HAP is more straightforward. ACP is stated as a precursor

for both DCPD and HAP (Xie et al. 2015). Still, apatite can grow even without precursors at the low supersaturation values not forming additional phases (Amjad et al. 1981, 1984).

Since various researchers have shown that oxalate kidney stones can form on brushite crystals and subsequently grow on them (Tang et al. 2006; O'Kell et al. 2018), a significant number of experimental studies were devoted to the mutual influence of phosphate ions and oxalate ions on the crystallization of calcium phosphates and oxalates. For example, Furedi-Milhofer et al. (1987) showed that in the system of $Ca(OH)_2$–H_3PO_4–$H_2C_2O_4$–NaCl–H_2O presence of phosphate-ions in the solution inhibits the precipitation of oxalate phases. It was confirmed by the further research in vivo (Bushinsky et al. 2000). From the other hand Xie et al. (2015) stated in their work that что crystal growth of DCPD will decrease the calcium concentration in urine and as a result decrease the supersaturation with respect to Calcium oxalate monohydrate (at the same time COM crystallize at the ACP aggregates, which transforms into DCPD later). Thus, the direct formation of DCPD in vivo will suppress the nucleation and growth of COM, which is in conflict with early thinking of DCPD promoting the formation of calcium oxalate stones by heterogeneous nucleation.

Some researchers carried out experimental modeling on the formation of mineral phases from a medium similar in composition to human urine. Grases et al. (1996) executed an experiment where precipitation from synthetic urine containing, in addition to inorganic ions (sodium, potassium, ammonium, magnesium, calcium, phosphate ions, chloride ions and sulfate ions) also organic anions (oxalate ions and citrate ions) was carried out. Precipitation was carried out at the pH value from 6.0 to 8.0 during 8 h. DCPD, HAP and STR were detected in the precipitate. DCPD prevailed at the pH values lower than 7.0. STR and HAP prevailed at the pH values 7.5 and 8.0. In their next work Grases and Llobera (1998) showed that DCPD and HAP form masses similar to the kidney stones in the conditions of the moving solution from the artificial urine with organic components. Unfortunately, only three phases were detected during the experiment (DCPD, HAP and STR). Furedi-Milhofer (2010) stated that spontaneous precipitation is practically absent during renal stone formations, because compounds presented in the urine inhibit this process. Therefore, precipitation of the minerals in the urine occurs from high ionic strength solutions upon/within a preformed organic matrix and the presence or deficiency of crystallization promoters or inhibitors plays a decisive role.

Also, the influence of the bacteria should be taken into consideration during the modeling of the kidney stones formation, including phosphate ones. It was shown that during STR precipitation bacteria change pH value and form biofilms that become the base for the consequent stone growth (Clapham 1990). Englert et al. (2013) state that struvite and carbonated hydroxyapatite can be the markers of the bacterial infection.

Along with experiments in vitro and in vivo of the formation of minerals of kidney stones, thermodynamic calculations and computer simulations were also carried out. El'nikov et al. (2007) calculated supersaturation indices and stability diagrams of the main pathogenic minerals of renal, dental and salivary stones. It was shown that in human urine, the formation of pathogenic aggregates can occur in a wide range of pH: uric acid (pH = 4.5–5.5), calcium oxalates (pH = 4.5–6.4), apatite

(pH = 6.4–8.0), brushite (pH = 6.0–7.5), struvite (pH = 7.5–8.0). A comparison of the results of theoretical and experimental modeling showed that apatite is the most stable of pathogenic aggregates, and its formation is possible in a wide range of pH and concentrations of its precursors. The formation of the remaining phases is under the stronger influence of the kinetic factors. This result explains the wide distribution of apatite in the composition of pathogenic aggregates in the human body. Rodgers et al. (2013) during their calculations of supersaturation values established the optimal combination of 13 core parameters that determine the stone formation in the human urine, namely: Ca, Na, K, Mg, Oxalate ($C_2O_4^{2-}$), Citrate, Phosphate (PO_4^{3-}), Sulfate (SO_4^{2-}), Chloride (Cl^-), uric acid, ammonium (NH_4^+), pH and volume. However, it is still difficult to test experimentally in vitro the simultaneous influence of numerous factors affecting the formation of kidney stones. In the simpler systems like precipitation of struvite in the presence of Ca ions it was shown that theoretical calculated model can correlate with experiment with 95% R-factor (Lee et al. 2013). Still, similar verification wasn't carried out for the more complex systems with greater amount of components.

Generally, we can conclude that the experimental studies carried out earlier were mainly selective and non-systematic. Studying of the complex and multicomponent system, i.e. human urine (Borodin 1991; Furedi-Milhofer 2010), should be carried out from the simple systems towards more complex ones. Of course, the phase crystallization in the urine is also under the influence of the several factors that weren't taken into consideration in this work: organic components, diet or concomitant diseases like osteopenia/osteoporosis (Arrabal-Polo et al. 2013). But we excluded them from the model and tried to focus our attention on the inorganic components. So, the main aim of our experimental research was to study the phase formation of phosphates in the solutions that simulate the normal composition of human urine, and to identify the regularities of the calcium and magnesium phosphates formation in the crystallization medium of variable composition.

6.2 Materials and Methods

6.2.1 Synthesis

Calcium and magnesium phosphates were synthesized by precipitation in 1 l water solutions mixing the certain amounts of the 1 mol/l solutions of calcium chloride and sodium dihydrophosphate at 37 °C during 5–20 days. Starting concentrations of the phosphate ions were set either at 13 or at 33 mmol/l, starting concentration of Ca^{2+} ions varied from 1 to 20 mmol/l. Starting values of pH varied from 5.0 to 8.5. About 150 syntheses were conducted in total. pH value was checked with the pH-meter «410-base» with standard error (0.02).

Table 6.1 The initial concentrations of inorganic components used in the experiments on the synthesis of calcium and magnesium phosphates

Components	Systems without additional components (mmol/l)		Systems simulating the normal composition of human urine (mmol/l)	
	$CaPO_4$-13	$CaPO_4$-33	Urine-13	Urine-33
Ca^{2+}	1–20	1–20	1–20	1–20
Mg^{2+}	–	–	5.3	11
Na^{+}	>300	>300	60	73
K^{+}	–	–	22	102
NH_4^{+}	–	–	13	25
PO_4^{3-}	13	33	13	33
Cl^{-}	>300	>300	67	80
CO_3^{2-}	–	–	–	33
SO_4^{2-}	–	–	22	69

Studying of the calcium phosphates crystallization was initially performed in the systems without additives (systems $CaPO_4$-13 and $CaPO_4$-33), with sodium chloride as the ionic strength controller (Table 6.1). The inorganic components added to the crystallizing solutions corresponded to the minimum (Urine-13 system) and maximum (Urine-33 system) concentrations of components typical for the normal composition of human urine (El'nikov et al. 2007) (Table 6.1).

Obtained precipitates were filtered, washed with distilled water and dried at the room temperature.

6.2.2 Characterization

Morphology of the synthesized crystals was studied by light microscopy using microscopes MBS-9 and Polam-113.

Phase identification was carried out by X-Ray powder diffraction method using Rigaku MiniFlexII diffractometer (CuKa radiation, graphite monochromator; 2θ range 10°–60° with a 0.05° step and speed equal to 5°/min).

Electron probe microanalysis was performed using the scanning electron microscopes Camscan-4 and ATB-55 equipped with X-ray energy microanalysers at a 25 kV acceleration voltage and 2 lm electron beam diameter (the analysts were Yu. L. Kretser and M. P. Pavlov). SEM Calibration Specimens (registered standard number 1413) from MICROANALYSIS CONSULTANTS Ltd were used as standards.

6.3 Results

X-ray analysis of the precipitates in the systems ($CaPO_4$-13) and ($CaPO_4$-33) showed presence of brushite, octacalcium phosphate and hydroxyapatite. The phase composition of the precipitates from the Urine-13 and Urine-33 (Table 6.1) systems includes mainly brushite, octacalcium phosphate, whitlockite and struvite.

Figure 6.1 shows the typical morphology of the synthesized calcium and magnesium phosphates. Brushite usually crystallize as colorless transparent plates either without side edges (Fig. 6.1a), as in the systems ($CaPO_4$-13) and ($CaPO_4$-33), or with clear side edges (Fig. 6.1b) as in the systems Urine-13 and Urine-33, that is typical for the presence of sulfate ions (Kuz'mina et al. 2013). Octacalcium phosphate crystallize as spherulites consisting of colorless elongated lamellar crystals with a silky sheen (Fig. 6.1c). Struvite crystallizes as the solid (sometimes skeletal) transparent prismatic crystals (Fig. 6.1d). Whitlockite and apatite crystallize as fine white powder.

The crystallization area of each type of synthesized phosphate is determined, first of all, by the initial concentrations of the main components (calcium cations and phosphate ions) and the initial value of the pH of the crystallization medium.

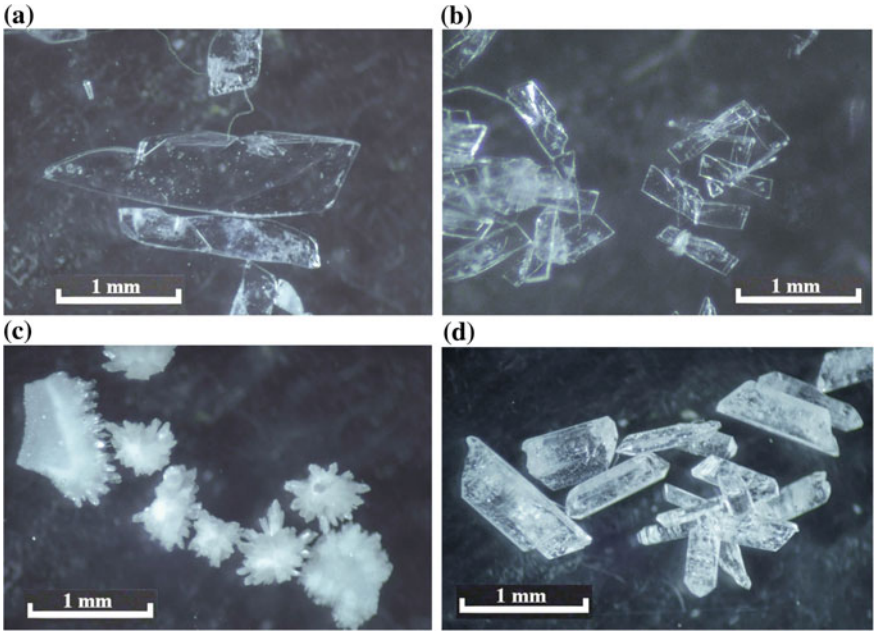


Fig. 6.1 The morphology of the synthesized phosphates of calcium and magnesium: **a** brushite crystals synthesized in the systems ($CaPO_4$-13) and ($CaPO_4$-33), **b** brushite crystals synthesized in the system (Urine-33), **c** spherulites of octacalcium phosphate synthesized in the systems ($CaPO_4$-13) and ($CaPO_4$-33), **d** struvite crystals synthesized in the system (Urine-33)

Three calcium phosphates crystallize in the systems ($CaPO_4$-13) and ($CaPO_4$-33) in the pH range from 5.0 to 8.5, namely brushite, octacalcium phosphate and apatite. Brushite crystallizes in the pH range from 5.5 to 6.75, octacalcium phosphate crystallizes in the pH range from 6.25 to 7.25, apatite crystallizes at the pH values above 7.0. Figures 6.2a and 6.3a show the crystallization areas of these calcium phosphates in dependence on the initial pH values of the solutions and starting concentrations of calcium ions with the fixed concentrations of the phosphate ions—either 13 mmol/l (Fig. 6.2a) or 33 mmol/l (Fig. 6.3a).

New phosphates appear in the Urine-13 and Urine-33 systems due to the addition of the Mg cations into the crystallization medium. Thus, Urine-13 system (with Mg concentration 5.3 mmol/l) is characterized by the presence of brushite, small amount

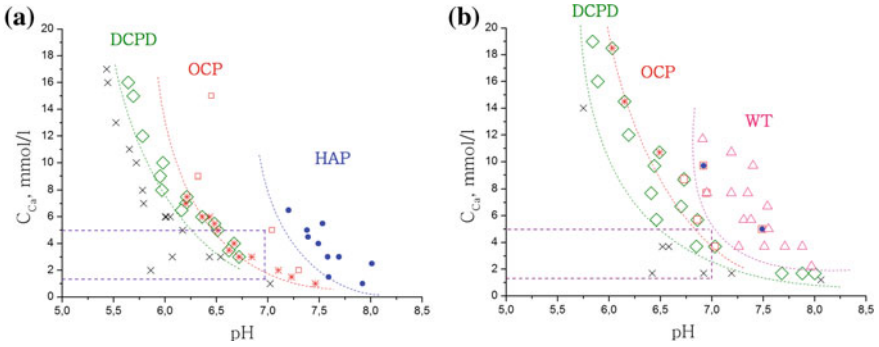


Fig. 6.2 Crystallization areas of the calcium and magnesium phosphates formed in the systems ($CaPO_4$-13) (**a**) and (Urine-13) (**b**) at the varying calcium concentrations and different starting pH values. Symbols: ◇ brushite, □ octacalcium phosphate, * spherulites of octacalcium phosphates, △ whitlockite, • hydroxyapatite, × area without crystallization. The area typical for the human urine is marked with the rectangle

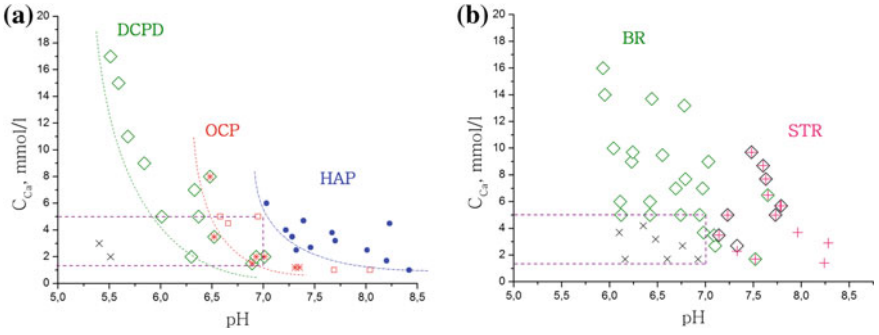


Fig. 6.3 Crystallization areas of the calcium and magnesium phosphates formed in the systems ($CaPO_4$-33) (**a**) and (Urine-33) (**b**) at the varying calcium concentrations and different starting pH values. Symbols: + struvite, the rest are the same as in the Fig. 6.2. The area typical for the human urine is marked with the rectangle

of octacalcium phosphate and significant amount of whitlockite (Fig. 6.2b). Urine-33 system (with Mg concentration 11.0 mmol/l) is characterized by the presence of brushite and at the pH values higher than 7.2 struvite (Fig. 6.3b).

During the crystallization process of all the calcium phosphates decreasing of the residual concentration of the calcium ions in the solution occurs, and the higher pH value is, the lower concentration of calcium ions is (Figs. 6.4a,b and 6.5a,b). Residual concentration of calcium ions for brushite is equal to its solubility. Residual concentration of magnesium ions for struvite is equal to its solubility and decreases to the 5.3–5.5 mmol/l during struvite crystallization (Fig. 6.5b).

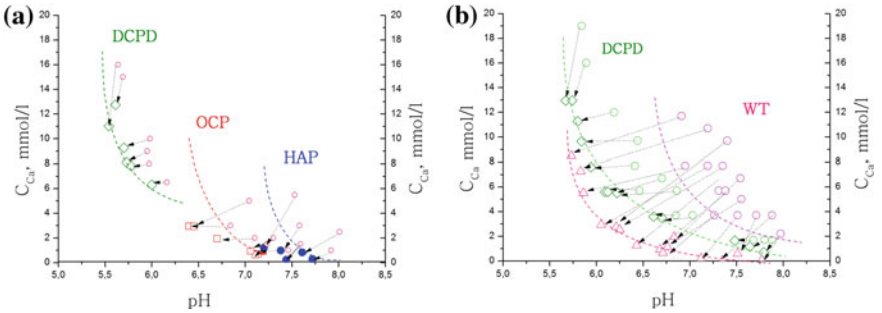


Fig. 6.4 Residual concentration of the calcium ions (C_{Ca}) for the different calcium and magnesium phosphates in the systems ($CaPO_4$-13) (**a**) and (Urine-13) (**b**), depending on the final pH values of the solutions. The starting concentrations of the calcium cations (C_{Ca}) are marked as (○) at the initial pH values. The symbols are the same as in the Fig. 6.2

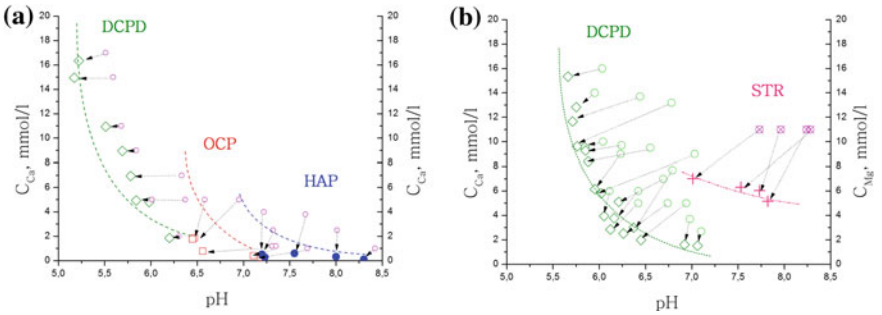


Fig. 6.5 Residual concentration of the calcium ions (C_{Ca}) for the different calcium and magnesium phosphates in the systems ($CaPO_4$-33) (**a**) and (Urine-33) (**b**), depending on the final pH values of the solutions. The starting concentrations of the calcium cations (○) and magnesium (⊗) ions are marked at the initial pH values. The symbols are the same as in the Figs. 6.2 and 6.3

6.4 Discussion

Several main phases crystallize in the systems ($CaPO_4$-13, $CaPO_4$-33, Urine-13 and Urine-33) under the varying conditions: brushite, octacalcium phosphate, apatite, whitlockite and struvite. During spontaneous crystallization hydroxyapatite, octacalcium phosphate and whitlockite form fine crystalline powder precipitates similar to the renal stones minerals. Brushite crystallizes as lamellar transparent colorless crystals, although during the renal stone formation brushite grows in the form of parallel-columnar aggregates, each crystal in which does not have a pronounced cut.

Phosphates crystallization areas are defined by the starting concentrations of the main components, pH value of the crystallization medium and by the presence of the additional components in the solution. Calcium phosphates crystallization areas in the systems $CaPO_4$-13 and $CaPO_4$-33 are defined by the starting concentrations of the components and by the pH value of the solutions. As the initial pH value of the solution increases from 5.0 to 8.5, the crystallization area of brushite switches to the octacalcium phosphate area, and then—to the apatite area. Other Mg-containing phosphate phases form in the systems Urine-13 and Urine-33 along with the already mentioned phases. Whitlockite forms at the low and struvite forms at the high concentrations of Mg ions in the solution.

In the systems modeling urine composition in respect to inorganic components (Urine-13 and Urine-33) new phosphates start to appear. Also, the borders of the crystallization areas of brushite, octacalcium phosphate and apatite change their position. Specifically, borders of the crystallization areas of brushite and octacalcium phosphate in the Urine-13 system move to the alkaline area from pH value 6.4 to 6.8 (for brushite) and from 6.6 to 7.0 (for octacalcium phosphate) (Fig. 6.2b). Crystallization border of the brushite area in the Urine-33 system also moves from pH value 6.0 to 7.0 (Fig. 6.3b).

Changes of the crystallization areas borders position of the main calcium phosphate phases can explain the fact that normal human urine doesn't form precipitates. As it was shown earlier (Figs. 6.2a and 6.3a), intensive precipitation of brushite and octacalcium phosphate occurs in the systems $CaPO_4$-13 and $CaPO_4$-33 at the components' concentrations typical for the normal urine within the pH value from 6.0 to 7.0. In the Urine-13 and Urine-33 systems phosphate precipitation is either less intensive (Urine-13) or absent (Urine-33) at the same conditions (Figs. 6.2b and 6.3b). So, changing of the crystallization medium composition can prevent the crystallization of the phosphates in the specific areas of pH values and main components' concentrations.

During the crystallization process of all the calcium phosphates decreasing of the residual concentration of the calcium ions in the solution occurs, and the higher pH value is, the lower concentration of calcium ions is. Thus, after the phosphates crystallization from solutions with the same initial calcium concentration but different pH values the final solution contains less calcium in the alkaline medium than in acidic one. It is worth mentioning that at the close (still different) starting conditions residual concentration of the calcium ions in the solution after whitlockite

crystallization is lower than after brushite crystallization (Fig. 6.4b). Also, experimental data show that during the struvite crystallization the residual concentration of magnesium ions is at least 5.3–5.5 mmol/l (Fig. 6.5b). So, at the magnesium concentration 5.3 mmol/l the phosphate crystallization in the Urine-13 system occurred without struvite (Fig. 6.2b).

Also, decreasing of the pH value that was noted in the experiments during the crystallization of calcium phosphates is the most possible cause of the presence of the several different phases in the precipitate. It was shown that crystallization of any calcium phosphate leads to the significant decreasing of the pH value of the crystallization medium, from 0.5 to 1.5 (Figs. 6.4 and 6.5). As a result the final pH of the solution can correspond to the crystallization area of the other calcium phosphate phase. As far as each calcium phosphate phase possesses its unique crystallization area in respect to pH values and precursors concentrations, several phases can precipitate consequently, and in the resulting precipitate two or even three phases can be found (Figs. 6.2 and 6.3).

6.5 Conclusion

All calcium and magnesium phosphates typical for the kidney stones were synthesized during the experiment: brushite, octacalcium phosphate, hydroxyapatite, struvite (Iijima et al. 1998; Oliveira et al. 2007; Grases et al. 1996), as well as Mg-whitlockite, which is rarely observed as the kidney stones component but is found in the calcificates of the blood vessels, cartilage and muscles (Lagier and Baud 2003).

The borders of the crystallization areas of the synthesized phases were determined in the axes «initial pH value—main components' concentration». It was shown that the change of the pH caused by the calcium and magnesium phosphates precipitation determines the change of the actual crystallization area. In the new crystallization area both the growth of the new phase and recrystallization of the existing phase is possible. For example, decreasing of the pH value will cause the hydroxyapatite-octacalcium phosphate-brushite transition, and increasing of the pH value causes the opposite transition. So, transitions from the one phosphate phase to another are determined by the change of the pH values of crystallization medium. Struvite crystallization is determined mainly by the magnesium ions concentration that should be higher than 5.3 mmol/l, excluding the cases of the high-alkaline solutions (pH value more than 7.2), and whitlockite crystallizes at the lower magnesium concentrations.

As the brand-new result it was shown that the addition of the inorganic components typical for the human urine into the $Ca\text{-}PO_4$ system leads to the moving of the crystallization area borders of the calcium phosphates (brushite, octacalcium phosphate, apatite). Thus, crystallization doesn't occur in the areas that are characterized by the composition and pH typical for the human urine. Still, increasing amount of the precursors or pH values leads to the phosphate crystallization.

Acknowledgements This work was supported by President of Russian Federation grant for leading scientific schools (No. NSh-3079.2018.5) and Russian Foundation for Basic Research (№19-55-45019 IND_a). The instrumental investigations have been performed at the Research Resource Centers of St. Petersburg State University: Centre for X-ray Diffraction Studies, Centre of Microscopy and Microanalysis, Nanotechnologies Centre. The authors are deeply grateful to Yu. O. Punin, Professor at the Department of Crystallography at St. Petersburg State University, who proposed and organized this experimental study of crystallization in phosphate systems that simulate the normal composition of human urine with respect to the inorganic components.

References

Abbona F, Boistelle R (1979) Growth morphology and crystal habit of struvite crystals (MgNH4PO4x6H2O). J Cryst Growth 46:339–354

Amjad Z, Koutsoukos PG, Nancollas GH (1981) The crystallization of fluorapatite. A constant composition study. J Colloid Interface Sci 82(2):394–400

Amjad Z, Koutsoukos PG, Nancollas GH (1984) The crystallization of hydroxyapatite and fluorapatite in the presence of magnesium ions. J Colloid Interface Sci 101(1):250–256

Arellano-Jimenez MJ, Garcia-Garcia R, Reyes-Gasga J (2009) Synthesis and hydrolysis of octacalcium phosphate and its characterization by electron microscopy and X-ray diffraction. J Phys Chem Solids 70:390–395

Arrabal-Polo MA, Giron-Prieto MS, Orgaz-Molina J, Zuluaga-Gomez A, Arias-Santiago S, Arrabal-Martin M (2013) Calcium renal lithiasis and bone mineral density. Importance of bone metabolism in urinary lithiasis. Actas Urol Esp 37(6):362–367

Borodin EA (1991) Biochemical diagnoisis. Part II. Blagovesthensk: 77 (in Russian)

Bushinsky DA, Parker WR, Asplin JR (2000) Calcium phosphate supersaturation regulates stone formation in genetic hypercalciuric stone-forming rats. Kidney Int 57:550–560

Chatterjee P, Chakraborty A, Mukherjee AK (2018) Phase composition and morphological characterization of human kidney stones using IR spectroscopy, scanning electron microscopy and X-ray Rietveld analysis. Spectrochim Acta Part A Mol Biomol Spectrosc 200:33–42

Chhiber N, Sharma M, Kaur T, Singla SK (2014) Mineralization in health and mechanism of kidney stone formation. Int J Pharm Sci Invention 3(10):25–31

Chou Y-H, Li C-C, Hsu H, Chang W-C, Liu C-C, Li W-M, Ke H-L, Lee M-H, Liu M-E, Pan S-C, Wang H-S (2011) Renal function in patients with urinary stones of varying compositions. Kaohsiung J Med Sci 27:264–267

Clapham L (1990) The influence of bacteria on struvite crystal habit and its importance in urinary stone formation. J Cryst Growth 104:475–484

De Rooij JF, Heughebaert JC, Nancollas GH (1984) A pH study of calcium phosphate seeded precipitation. J Colloid Interface Sci 100(2):350–358

Driessens FCM (1981) Metastable states in calcium phosphate—aqueous phase equilibrations. J Cryst Growth 53:55–62

El'nikov VY, Rosseeva EV, Golovanova OA, Frank-Kamenetskaya OV (2007) Thermodynamic and experimental modeling of the formation of major mineral phases of uroliths. Russ J Inorg Chem 52(2):150–157

Englert KM, McAteer JA, Lingeman JE, Williams JC (2013) High carbonate level of apatite in kidney stones implies infection, but is it predictive? Urolithiasis 41(5):389–394

Ferreira A, Oliveira C, Rocha F (2003) The different phases in the precipitation of dicalcium phosphate dihydrate. J Cryst Growth 252:599–611

Fisang C, Anding R, Muller SC, Latz S, Laube N (2015) Urolithiasis—an interdisciplinary diagnostic, therapeutic and secondary preventive challenge. Dtsch Arztebl Int 112:83–91

Furedi-Milhofer H (2010) Physiological and pathological mineralization: some problems and possible solutions. Med Vjesn 42(3–4):33–44

Furedi-Milhofer H, Marcovic M, Uzelac M (1987) Precipitation and solubility of calcium phosphates and oxalates in the system Ca(OH)2-H3PO4-H2C2O4-NaCl-H2O. J Cryst Growth 80:60–68

Grases F, Llobera A (1998) Experimental model to study sedimentary kidney stones. Micron 29(2/3):105–111

Grases F, Sohnel O, Vilacampa AI, March JG (1996) Phosphates precipitation from artificial urine and fine structure of phosphate renal calculi. Clin Chim Acta 224:45–67

Heughebaert JC, De Rooij JF, Nancollas GH (1986) The growth of dicalcium phosphate dihydrate on octacalcium phosphate at 25 C. J Cryst Growth 77:192–198

Iijima M, Kamemizu H, Wakamatsu N, Goto T, Doi Y, Moriwaki Y (1998) Effects of Ca addition on the formation of octacalcium phosphate and apatite in solution at pH 7.4 and at 37 °C. J Cryst Growth 193:182–188

Komlev VS, Rau JV, Fosca V, Fomin AS, Gurin AN, Barinov SM, Caminiti R (2012) Single-phase bone cement based on dicalcium phosphate dihydrate powder and sodium silicate solution. Mater Lett 73:115–118

Koutsoukos PG, Nancollas GH (1981) Crystal growth of calcium phosphates—epitaxial considerations. J Cryst Growth 53:10–19

Kuro-o M (2013) A phosphate-centric paradigm for pathophysiology and therapy of chronic kidney disease. Kidney Int Suppl 3:420–426

Kuz'mina MA, Zhuravlev SV, Frank-Kamenetskaya OV (2013) The effect of medium chemistry on the solubility and morphology of brushite crystals. Geol Ore Deposits 55(8):1–6

Lagier R, Baud C-A (2003) Magnesium whitlockite, a calcium phosphate crystal of special interest in pathology. Pathol Res Pract 199:329–335

Lee SH, Yoo BH, Lim SJ, Kim TH, Kim SK, Kim JY (2013) Development and validation of an equilibrium model for struvite formation with calcium co-precipitation. J Cryst Growth 372:129–137

Muller FA, Muller L, Caillard D, Conforto E (2007) Preferred growth orientation of biomimetic apatite crystals. J Cryst Growth 304:464–471

Nyame YA, De S, Sarkissian C, Brown R, Kartha G, Babbar P, Monga M (2015) Kidney stone models for in vitro lithotripsy research: a comprehensive review. J Endourol 29(10):1106–1109

O'Kell AL, Lovett AC, Canales BK, Gower LB, Khan SR (2018) Development of a two-stage model system to investigate the mineralization mechanisms involved in idiopathic stone formation: stage 2 in vivo studies of stone growth on biomimetic Randall's plaque. Urolithiasis. https://doi.org/10.1007/s00240-018-1079-1

Oliveira C, Ferreira A, Rocha F (2007) Dicalcium phosphate dihydrate precipitation. Characterization and crystal growth. Chem Eng Des 85(A12):1655–1661

Perez L, Shyu LJ, Nancollas GH (1989) The phase transformation of calcium phosphate dihydrate into octacalcium phosphate in aqueous suspensions. Colloids Surf 38:295–304

Rodgers AL, Allie-Hamdulay S, Jackson GE, Durbach I (2013) Theoretical modeling of the urinary supersaturation of calcium salts in healthy individuals and kidney stone patients: precursors, speciation and therapeutic protocols for decreasing its value. J Cryst Growth 382:67–74

Ronteltap M, Maurer M, Hausherr R, Gujer W (2010) Struvite precipitation from urine—influencing factors on particle size. Water Res 44:2038–2046

Stulaiterova R, Medvedsky L (2008) Effect of calcium ions on transformation brushite to hydroxyapatite in aqueous solutions. Colloids Surf A Physicochem Eng Aspects 316:104–109

Tang R, Nancollas GH, Giocondi LJ, Hoyer JR, Orme CA (2006) Dual roles of brushite crystals in calcium oxalate crystallization provide physicochemical mechanisms underlying renal stone formation. Kidney Int 70:71–78

Xie B, Halter TJ, Borah BM, Nancollas GH (2015) Aggregation of calcium phosphate and oxalate phases in the formation of renal stones. Cryst Growth Des 15(1):204–211

Xin R, Leng Y, Wang N (2006) In situ TEM examinations of octacalcium phosphate to hydroxyapatite transformation. J Cryst Growth 289:339–344

Zhang S (2013) Hydroxyapatite coatings for biomedical applications. CRC Press, Boca Raton, London, New York, p 463

Chapter 7
The Effect of Heat-Treatment and Bioresorbability of Silicate-Containing Hydroxyapatite



Tatyana Panova and Olga A. Golovanova

Abstract The possibility of modification of hydroxyapatite of a prototype extracellular liquid synthesized from solution under close physiological conditions by silicate ions was studied. The formation of chemically structured hydroxyapatite with various degrees of substitution of phosphate groups in silicate groups was established by chemical and X-ray diffraction analysis, IR spectroscopy and optical microscopy. It is shown that apatite modified by silicon has an imperfect structure and crystallizes in the nanocrystalline state. It was found that during the experiment an increase in the calcination temperature to 200–1000 °C leads to weight loss. The greatest loss of mass occurs at temperatures in the range of 25–400 °C, which is due to the removal of crystallization and adsorption water and volatile impurities. Three main stages of thermal decomposition of Si-HA are isolated, the final product is a mixture consisting of two phases: Si-HA and β-TKF. The results of the research can be used to study the kinetics of dissolution and the biocompatibility of ceramic materials for medicine, namely for reconstructive surgery, dentistry, and development of drug delivery systems.

Keywords Hydroxyapatite · XRD · IR spectroscopy · Extracellular fluid · Structure · Phase composition · Degradation · Thermal effects · Bioresorbability

7.1 Introduction

The global bioceramics demand on the market currently reaches ~40 billion euros per year, the estimated annual growth rate is of 7–12% and the required amount of the material to meet the demand is estimated at tens of tons (Bandyopadhyay et al. 2006; Saki 2009; Hench and Jones 2007). The number of patients in need of surgery to restore the integrity of the bone is increasing every year: in the US, the annual number of patients exceeds more than one million people (of which over 300 thousand people need hip and knee prosthetics, the same holds true for dental implants).

T. Panova · O. A. Golovanova (✉)
F.M. Dostoevsky State University, 55A Prospect Mira, Omsk 644077, Russia
e-mail: golovanoa2000@mail.ru

© Springer Nature Switzerland AG 2020

O. V. Frank-Kamenetskaya et al. (eds.), *Processes and Phenomena on the Boundary Between Biogenic and Abiogenic Nature*, Lecture Notes in Earth System Sciences,
https://doi.org/10.1007/978-3-030-21614-6_7

Materials based on hydroxyapatite $Ca_{10}(PO_4)_6(OH)_2$ are analogs of the mineral component of bone, and they are considered the most promising biocomposites to be used as substitutes for bone defect repair due to their high bioactivity (Murugan and Ramakrishna 2005; Soin et al. 2007; Gomes et al. 2011; Wang et al. 2007; Grubova et al. 2014; Solonenko and Golovanova 2013; Khlusov et al. 2012; Morgan et al. 2000; Chang et al. 2003; Golovan et al. 2007). It is known that silicon plays a bridging role in physiological processes of growth and re-construction of bone and cartilaginous tissues; therefore, the development of the techniques for silicon-substituted hydroxyapatite (Si-HA) synthesis is a relevant physical-chemical problem (Saki 2009). For complete physiological response of the organism when restoring a damaged bone, hydroxyapatite chemical modification should be carried out in the near-physiological solutions.

An important characteristic of synthesized Si-HA is its thermal stability (Murugan and Ramakrishna 2005). In Soin et al. (2007) it was found that heat treatment of the biological bone at 1000 °C provides formation of silicon-magnesium-substituted oxyapatite which transforms into hydroxyapatite upon cooling, retains a balanced composition of natural nanoimpurities that support the stability of the structure, phase and chemical composition to ensure the best features of the coatings on titanium implants under all application techniques (electrochemical, plasma, slip processing). The data obtained through scanning microscopy indicated bimodal (inter-aggregate and intergranular) porosity of the sample, and the grain size was 20–60 nm, which theoretically facilitates osteoinduction (Gomes et al. 2011; Khlusov et al. 2012).

An important factor is that, regardless of the degree of the texture and stoichiometry of the Si-HA sample, the obtained nanohardness varies in the range from 11 to 12 GPa, and thermal stability and uniformity of the chemical composition are provided. However, the most important characteristic is preservation of bioactivity, which allows full use of these samples (Wang et al. 2007).

Silicon-substituted hydroxyapatite is known to be thermally more stable than unmodified hydroxyapatite (Grubova et al. 2014). Thus, we can conclude that silicon ions are beneficial and improve the characteristics of unmodified hydroxyapatite, and after calcination, the Si-HA samples possess properties similar to those of the normal human bone.

Modern materials used in orthopedics and traumatology must mimic the body's natural tissues. A necessary process is the inclusion in the structure of calcium phosphates of ions that are part of biological fluids. The biomimetic method consists in the precipitation of phosphate from prototypes of biological fluids and in this work SBF (Simulated Body Fluid) is used as such biofluid (Berdinskaya et al. 2014).

The presented data allow us to state that samples of silicon-substituted hydroxyapatite (Si-HA) synthesized from the SBF (Simulated Body Fluid) solution are promising materials for their use in medicine.

7.2 Materials and Methods

Synthesis was carried out by precipitation from aqueous solutions; The initial components of the system were solutions of $CaCl_2$, $MgCl_2$, K_2HPO_4, $NaHCO_3$, Na_2SO_4, NaCl containing ions Table 7.1.

Synthesis of the substituted calcium phosphate crystals is carried out by deposition from aqueous solution through spontaneous crystallization by the chemical reaction:

$$10CaX_2 + 6M_2HPO_4 + MOH \rightarrow Ca_{10}(PO_4)6(OH)_2 \downarrow +20MX + 6H_2O \quad (7.1)$$

The ratio of Ca/P = 1.67 in the solid phase corresponded to the development of stoichiometric hydroxyapatite (Morgan et al. 2000). The pH value of the solution was kept equal 7.40, the temperature of the synthesis was 22°–25°, characteristic of SBF, and remained constant.

The main compounds for silicate groups were Na_2SiO_3 and tetraethoxysilane (TEX) as the frequently used compounds. The weight content of silicate ions in the initial solution was 0.5, 2.5 and 5.0 wt%.

The resulting education process can be schematically represented in accordance with reaction 7.2:

$$10Ca(NO_3)_2 + (6 - x)(NH_4)_2HPO_4 + xSiO_2(aq) + (14 + x)NH_4OH \rightarrow Ca_{10}(PO_4)_{6-x}(SiO_4)_x(OH)_{2-x} \downarrow +20NH_4NO_3 + (21 - 2x)H_2O \quad (7.2)$$

where x is the coefficient or degree of substitution of silicon.

After 48 h, the precipitates were filtered under vacuum, dried at 80 °C, weighed and examined by a group of physicochemical methods.

The solid phase was filtered, dried and analyzed with FT-IR spectroscopy and X-ray diffraction analysis (XRD). IR spectra were recorded with FT-801 spectrometer (samples made in the form of pellets with KBr).

X-ray powder diffraction patterns of synthetic samples were recorded on a D8 Advance (Bruker) diffractometer equipped with the EVA program package (Bruker)

Table 7.1 Composition of the extracellular fluid model solution "Simulated Body Fluid" (Meshkova and Severina 1979)

Component-ion	C (mmol/L)
Ca^{2+}	2.5
Na^+	142
K^+	5
Mg^{2+}	1.5
Cl^-	105
HPO_4^{2-}	1
HCO_3^{2-}	27
SO_4^{2-}	0.5

for interpretation. The quantitative phase analysis of calcium phosphate mixtures was performed and crystallite sizes (coherent scattering lengths) were calculated using the TOPAS 3.0 program (Bruker). The identification of phases was performed using the ICDD PDF database.

The study of morphology, determination of the shape of particles of solid phases was carried out by optical microscopy using the XSP-104 series microscope.

Determination of the specific surface of the samples was carried out on the analyzer by the method of Brunauer, Emmett and Teller-BET (SBET-N2). During the study, nitrogen gas of special purity (99.999 vol.%). Was used as a standard adsorbent. Adsorption of nitrogen was carried out under cryogenic conditions at 77.4 K. before adsorption measurements, the samples were conditioned for 1.5 h at 353 K in a nitrogen flow. This method of BET allows you to determine the surface in the range from 0.1 to 2000 m^2/g with a relative error of 2–5%.

The liquid separated from the precipitate was analyzed for residual calcium [subject to RD 52.24.40394] and residual phosphates [subject to the Russian State Standard (GOST) 1830972], and the reduction in their concentrations during the syn thesis was used to ascertain the ratio Ca^{2+}/PO_4^{3-} in the sample.

After that, the thermogravimetric analysis was performed. The samples Si-HA $m = 0.2000 \pm 0.0005$ g were placed in crucibles and then in a muffle furnace for 2 h. The calcination temperature varied from 200 to 1000 °C with 200 °C space. After 2 h, they were weighed with an analytical balance, and analyzed examined by a group of physicochemical methods.

Dissolution of the produced samples was performed in Tris-HCl buffer at physiological pH equal to 7.4 under continuous stirring. Several experiments we performed with different initial sample mass of calcium phosphate ($m = 0.100$ and 0.200 g) and under different temperatures.

At regular intervals, the values of acidity and calcium ion concentration were recorded via direct potentiometry. The experimental data obtained were used to plot the graphic dependences in $pCa = f(\tau)$ coordinates to evaluate the solubility of the synthesized samples. To determine the dissolution rate for each of the samples, the kinetic curves were analyzed using the regression analysis (Wang et al. 2007). After that, these curves were mathematically processed according to the algorithm suggested in Grubova et al. (2014).

Statistical data processing was carried with StatSoft Statistica 6.0.

7.3 Results and Discussion

The results of X-ray diffraction analysis of solid phases synthesized in the presence of silicic agents (Fig. 7.1) indicate the formation of hydroxyapatite. No other calcium phosphates were detected.

When the concentration of silicate ions in the system increases, the peaks observed in the region of $2\theta = 25°–35°$ broaden due to low degree of sample crystallinity. It should be noted that the diffraction patterns corresponding to the solid phases

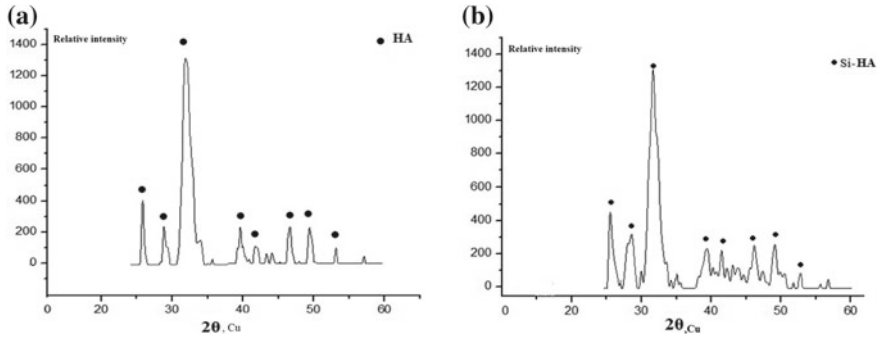


Fig. 7.1 The diffraction patterns for hydroxyapatite samples modified by Na_2SiO_3: **a** HA, **b** HA + C(SiO_3^{2-}) 0.5 wt%

with different sources materials for Na_2SiO_3/TEL silicate groups are found to be similar. Thus, the nature of the reagent containing SiO_4^{4-} ions does not affect the hydroxyapatite structure.

The size of the prepared unmodified HA crystallite was 6.3 nm, and the size of Si-HA was 6.0–7.1 nm, it is shown that the modified apatites are an imperfect structure and crystallize in the nanocrystalline state. The parameters of the crystal lattice of the formed solid phase grew larger as compared to the unmodified hydroxyapatite. This confirms the possible substitution of the orthophosphate-ion by the silicate-ion of different size (distance Si–O = 1.66 Å, P–O = 1.55 Å; Tkhuan et al. 2011). The parameters of the crystal lattice of the formed solid phases are increased in comparison with those of unmodified hydroxyapatite, which is corroborated by substitution of the orthophosphate ion by the silicate ion: they are different in size (bond lengths Si–O = 1.66 Å, P–O = 1.55 Å; Khlusov et al. 2012) (Table 7.2).

A substantial increase of parameter c indicates the fact that the silicate ion predominantly occupies the position of the phosphate ion rather than the hydroxyl ion in the HA structure (Khlusov et al. 2012) which is responsible for natural changes in the crystal shape: a needle stretched along the c axis is 'flattened' until a plate that coincides with the biogenic apatite morphology (Khlusov et al. 2012). As follows from the data of Table 7.3, a larger substitution degree is attributed to the samples

Table 7.2 Crystal lattice parameter

Sample	Concentrations silicate agent (%)	Lattice constants (Å)	
		a	c
HA	–	9.414	6.865
Na_2SiO_3	0.5	9.466 ± 0.007	6.885 ± 0.007
Na_2SiO_3	2.5	9.413 ± 0.005	6.877 ± 0.005
TEX	0.5	9.490 ± 0.001	7.320 ± 0.001
TEX	2.5	9.546 ± 0.007	6.975 ± 0.008

Table 7.3 Solid phase ratios Ca/P and Ca/P+Si

C SiO_3^{2-}, in solution (%)	Ca/P+Si		Ca/P		Solid phase composition
	Na_2SiO_3	TEX	Na_2SiO_3	TEX	
0.5	2.44	2.32	2.48	2.34	Excess calcium HA
2.5	1.92	1.88	2.31	2.23	

obtained in the presence of TES: their crystal lattice parameters change to a higher degree. To sum up, the process of silicon substituted hydroxyapatite formation is accompanied by changes in the crystal lattice of hydroxyapatite and the increase of its defect level, which, in turn, result in better resorbability and, therefore, bioactivity of hydroxyapatite modified into the SiHA form. Also, one should mention that the HA samples synthesized in the presence of TES are characterized by a higher degree of lattice distortion, which indicates the formation of biomaterials with better bioactivity (Tkhuan et al. 2011).

In the IR spectra of the samples formed in the presence of the silicate ions, the absorption bands characteristic of hydroxyapatite can be observed (Fig. 7.2), (Berdinskaya et al. 2014; Solonenko and Golovanova 2014). The HA structure is defined by the following bands: the bands at 1040–1080 (ν_3), 960, 840 (ν_2), 602, 574 (ν_4) and 473 (ν_2) cm^{-1} corresponding to the vibrations of the phosphate groups, the broad band at 3440–3570 cm^{-1} which corresponds to deformation vibrations of OH^--groups and valence vibrations of the adsorbed water. High intensity of this peak in the modified HA is related to the fact that SiO_4^{4-} ions have high affinity for water molecules which results in hydration. Since HA is synthesized in air, during its formation carbon dioxide is adsorbed from atmospheric air, and carbonate ions are localized in the lattice in the position of the phosphate ion, and in the IR spectra, the bands absorbing deformation vibrations of C–O bonds of the CO_3^{2-} ion at 875 cm^{-1} and valence vibrations at 1422–1457 cm^{-1} correspond to these ions.

According to Marchat et al. (2013), the inclusion of impurity anions into the composition of a solid phase results in the appearance of a set of absorption bands due to the vibrations of Si–OH, Si–O–Si, and Si–O bonds in the IR spectra of the samples. However, because of the structural similarity of the tetrahedral anions and, a number of absorption maximums manifested themselves at close frequencies. The spectra of nonstoichiometric carbonated hydroxyapatites (nCHAs) obtained in the presence of silicates contain overlapped characteristic bands: 477–483 $cm^{-1} \Rightarrow \nu_2$(P–O) + ν(Si–O–Si), 958–962 $cm^{-1} \Rightarrow \nu 1$(P–O) + ν(Si–O), 1020 $cm^{-1} \Rightarrow \nu_3$(P–O) + ν(Si–OH), 1089–1095 $cm^{-1} \Rightarrow \nu_3$(P–O) + ν(Si–O), 2500–3700 $cm^{-1} \Rightarrow \delta$(H–O–H) + ν(Si–OH). The superposition of these strong bands does not allow us to estimate the presence of silicates in the samples based on these absorption bands. It can be concluded that solid phases are included in the composition based on weak peaks at 504 and 800 cm^{-1}. A slight increase in their intensity was observed with an increase in the silicon content in the initial reaction media. Simultaneous extinction of the oscillation modes of P-6 ions (630 and 3570 cm^{-1}) indicates the replacement of phosphates by silicates with the participation of hydroxyl groups. The schemes of

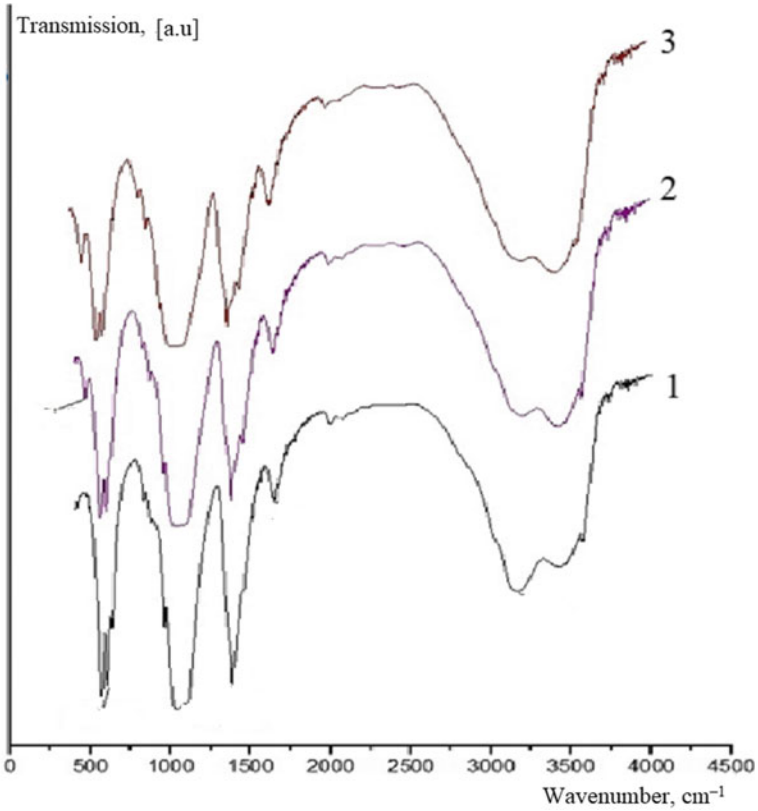


Fig. 7.2 IR spectra for hydroxyapatite samples modified by Na_2SiO_3: (1) HA, (2) HA + $C(SiO_3^{2-})$ 0.5 wt%, (3) HA + $C(SiO_3^{2-})$ 2.5 wt%

reactions ($PO_4^{3-} + OH^- \leftarrow SiO_4^{4-} + \square_{OH}$) of the above types of substitution are given; the change in the parameters of the HA unit cell correlates with the change in the parameters *a* and *c* (Table 7.2). It has been observed that IR spectra contain a low intensity band of absorption of the silicate group bond vibrations at 511 cm^{-1} due to the deformation vibrations of Si–O bonds. The absorption band of the Si–O bond vibration at 945 cm^{-1} is overlapped with the absorption band which corresponds to P–O bond vibrations at 960 cm^{-1}. Occurrence of these signals in the spectrum indicates the substitution of PO_4^{3-} by SiO_4^{4-} in the HA structure. This leads to distortion of the PO_4^{3-} tetrahedra, and as a result, the parameters of the cell change. Thus, the data obtained by IR spectroscopy are in agreement with that obtained by XRD.

Due to the similarity of the structural tetrahedral groups and a number of absorption maxima of the bonds in both ions are manifested at close frequency values. The overlapping of strong bands around 1020, 1080, 2500–3700 cm^{-1}, and others does not allow estimation of the presence of silicates in the fabricated samples. A con-

clusion on the presence of groups in the precipitate compositions can be made from the low intensity peaks at 504 and 800 cm^{-1} corresponding to modes of deformation vibrations of the Si–O bonds and the symmetric valence vibrations of the bridge Si–O–Si bonds in SiO_4 tetrahedra (Wang et al. 2007; Khlusov et al. 2012). One can trace the weak growth of their intensities on the increase of the silicon content in the initial reaction media. The simultaneously occurring extinction of modes of HA OH^- ions (3570 cm^{-1}) indicates phosphate substitution by silicates with the additional participation of hydroxyl groups ($PO_4^{3-} + OH^- \leftarrow SiO_4^{4-} + \square_{OH}$), which is in good agreement with the data in the literature (Bandyopadhyay et al. 2006; Wang et al. 2007). The samples of hydroxyapatite modified by silicate ions from the TEOS structure are characterized by the band broadening around 3570 cm^{-1}, which is, in our opinion, related to the overlapping with the absorption band at 2800–2900 cm^{-1} corresponding to vibrations of the C–H groups. The emergence of these bands in the spectra can be explained by the fact that synthesis was carried out in a TES alcohol solution. The IR absorption spectrum of the annealing product of the silicon substituted HA at 800 °C contains an intensive narrow band at 3570 cm^{-1} characteristic for the crystalline calcium hydroxyapatite. The IR spectrum contains valence and deformation vibration bands at 1020–1080, 960, 840, 600, 570, and 473 cm^{-1}, but the carbonate groups bands are absent; i.e., the temperature effect results in the removal of carbonate ions from the HA structure. The experimental results of determining the liquid phase composition upon the completion of the synthesis reaction and precipitate separation are shown in Table 7.3. The Ca/P ratios in the obtained compounds calculated from liquid phases data analysis exceed the preset value of 1.67 (Chang et al. 2003) characteristic for the stoichiometric hydroxyapatite. The latter indicates the decrease of the quantity of phosphate ions in the obtained solid phases, which, in our opinion, is related to the substitution of phosphate groups by silicate ones and does not contradict the data in the literature (Golovan et al. 2007). Here, it has been demonstrated that the maximal substitution degree corresponds to samples with the silicon content in the system of 0.5 and 1.0%.

A further increase in the concentration of Si init leads to the formation of HA containing an excess of Ca/P, since phosphate ions are replaced by silicate ions. It is obtained that an increase in the content of silicate ions in the initial solution leads to an increase in its content in the sediment (Table 7.2). The calcium ions concentration in the obtained precipitates in the presence of Na_2SiO_3 and TES remains constant. In the course of studies of the obtained precipitates' morphology, no difference was revealed between the samples obtained in the presence of Na_2SiO_3 and TES. The particles of hydroxyapatite modified by silicate ions can be characterized as loose aggregates formed by randomly located spherical fragments (Fig. 7.4). One observes particles' aggregation at the increase of the content in the precipitate.

Based on the determination of the BET specific surface area, it has been found that an increase in the concentration of silicate ions leads to an increase in the specific surface area from 86 to 151 m^2/g. Thus, samples of silicon hydroxylapatite possess a more developed specific surface area with respect to unmodified HA due to the formation of smaller particles. This indicates an increase in bioresorbability of

materials obtained on the basis of silicon-containing hydroxylapatite, which makes it possible to use them as a medical implant.

The presence of silicon ions in the resulting powders was determined by chemical analysis of the supernatant after separation of the solid phase (Table 7.3). It was found that when the concentration of silicate ions increases in the initial system, the number of silicon ions in the solid phase increases, which leads to a decrease in the Ca/P+Si ratio. The ratio of Ca/P in synthesized compounds exceeds the set value of 1.67, typical for stoichiometric hydroxyapatite, and corresponds to the phase of excess calcium of HA. This indicates a decrease in the amount of phosphate ions in the solid phases formed, which, in our opinion, is due to the possible replacement of phosphate groups by silicate ones.

The study of samples of modified hydroxyapatite by thermogravimetric analysis showed a constant weight loss (Tables 7.4 and 7.5) during heating. Comparison of the data from Tables 7.4 and 7.5 showed that a great mass loss was observed for Si-HA samples produced in the presence of TEX due to the removal of the organic component from the structure under temperature increase. It should be noted that the greatest mass loss is observed at low concentrations of TEX as the HA structure

Table 7.4 The change in the mass of the synthesized samples during heat treatment

Samples HA-Na_2SiO_3					
t (°C) pavements	The concentration of silicate ions in the model solution (%)				
	0.50	1.00	1.50	2.50	5.00
	Weight (g)				
200	0.0110	0.0299	0.0105	0.0062	0.0113
400	0.0137	0.0223	0.0116	0.0143	0.0155
600	0.0252	0.0332	0.0296	0.0325	0.0383
800	0.0356	0.0385	0.0339	0.0244	0.0355
1000	0.0289	0.0355	0.0507	0.0357	0.0384

Table 7.5 The change in the mass of the synthesized samples during heat treatment

Samples HA-TEX					
t (°C) прокаливания	The concentration of silicate ions in the model solution (%)				
	0.50	1.00	1.50	2.50	5.00
	Weight (g)				
200	0.0608	0.0259	0.0105	0.0104	0.0102
400	0.0159	0.0263	0.0148	0.0174	0.0130
600	0.0782	0.0442	0.0383	0.0311	0.0268
800	0.0804	0.0348	0.0358	0.0354	0.0389
1000	0.0840	0.0514	0.0400	0.0389	0.0447

Table 7.6 Phase transformations in crystallization products during heat treatment

ΔT (°C)	The process causing the mass loss of the sample
25–373	Removal of chemically unbound water $[\text{Si-HA} \cdot \text{H}_2\text{O}]\text{H}_2\text{O}_{(\text{solid})} \rightarrow \text{Si-CHA}_{(\text{solid})} + \text{H}_2\text{O}_{(\text{gas})} + \text{Q}$
353–503	Removal of loosely bound (adsorbed) water from the sediment composition $\text{Si-CHA} \cdot \text{H}_2\text{O}_{(\text{solid})} \rightarrow \text{Si-CHA}_{(\text{solid})} + \text{H}_2\text{O}_{(\text{gas})} + \text{Q}$
>600	Removal of carbonate ions from the HA structure, decomposition of nHA with formation of a phase β-TCF и $\text{Si-HA} \cdot \text{Si-nHA} \rightarrow \beta\text{-TCF} + \text{Si-HA}$

is not stabilized by silicate ions, probably, due to the predominant influence of the organic component decomposition.

The changes occurring as a result of heat treatment can be represented by the following reaction equations presented in Table 7.6. In the temperature ranges 25–503 °C, unbound and adsorption water is removed from the sample composition. At t = 600 °C, carbonate ions emerge from the structure of the HA. For the precipitates obtained, the thermal degradation begins at temperatures of the order of 800 °C (7.3).

$$\begin{aligned} &\text{Ca}_9(\text{PO}_4)_{6-\text{x}-\text{y}}(\text{HPO}_4)\text{x}(\text{CO}_3)\text{x}(\text{OH})_{2-\text{x(s)}} \\ &\quad \rightarrow 3\beta\text{Ca}_3(\text{PO}_4)_{2(\text{s})} + \text{xCO}_{2(\text{g})} + 2\text{H}_2\text{O}_{(\text{g})} - \text{Q} \end{aligned} \tag{7.3}$$

Silicon-containing hydroxyapatites formed in the sodium silicate medium are of the highest thermal stability. It is found that increase in the silicon content in the solid phase results in the reduction of the total mass loss during heating up to 1000 °C. The analysis of the obtained data revealed that hydroxyapatite is the prevailing phase within the entire temperature range. The greatest reduction in the sample mass corresponds to the temperature range of 25–400 °C which is caused by the removal of the crystallization and adsorption water and volatile impurities in samples with the organic additive of silicon ions.

Further removal of carbonate ions from the apatite structure and partial decomposition of the excess calcium HA followed by formation of the stoichiometric compound and phase of β-tricalcium phosphate occurs in the temperature range of 600–1000 °C (Solonenko and Golovanova 2013).

As can be seen from the diffraction patterns, the beginning of phase transition and Si-HA peak splitting are observed at 600 °C, and splitting of the peak from singlet into doublet can be clearly seen at 800 °C. However, the temperature increase up to 1000 °C does not cause further changes in the phase composition of samples. As can be seen from the comparison of the XRD spectra presented above, the form of doublets in the angular range (30–32) 2θ is different that indicates their different thermal stability at the given temperature. Thus, the presence of SiO_4^{4-} groups in the HA structure enhances thermal stability of HA-based materials. For samples after exposure to temperature, the unit cell parameters for the synthesized samples were calculated (Table 7.7). Compared with unmodified carbonate hydroxylapatite

Table 7.7 Parameters of a unit cell for HA samples with different contents of silicate ions

T (°C)	Sample	Unit cell parameters	
		a (Å)	c (Å)
800	HA	9.434	6.881
	HA + C(SiO_3^{2-}) 0.5 wt%	9.435	6.889
	HA + C(SiO_3^{2-}) 2.5 wt%	9.635	6.913
900	HA	9.436	6.889
	HA + C(SiO_3^{2-}) 0.5 wt%	9.735	6.886
	HA + C(SiO_3^{2-}) 2.5 wt%	9.641	6.915
1000	HA	9.441	6.890
	HA + C(SiO_3^{2-}) 0.5 wt%	9.439	6.887
	HA + C(SiO_3^{2-}) 2.5 wt%	9.645	6.936

for silicon-containing samples, the unit cell increases. This confirms the replacement by large silicate ions of phosphate (distance Si–O = 1.66 Å, P–O = 1.55 Å). In favor of the fact that silicate-ions preferentially replace phosphate ions, and not hydroxyl ions in the structure of hydroxylapatite, the parameter increases with.

After calcinations, the morphology of the synthesized silicon-containing samples was studied, it was revealed that sintering occurs after the heat treatment, resulting in the formation of agglomerates of a larger size (Fig. 7.3).

The results of XRD agree with the data of IR spectroscopy (Fig. 7.4); this is proved by IR absorption spectra for samples obtained by changing the concentration of silicate ions and the product of their calcination (at 800 °C) synthesized at C SiO_3^{2-}0.5 − 5.0 wt%. The absorption bands corresponding to those for hydroxyapatite are observed in IR spectra of the obtained products (Khlusov et al. 2012). The bands at 1020–1080 (ν_3), 960, 840 (ν_2), 600, 570 (ν_4) and 473 (ν_2) cm^{-1} correspond to the vibrations of the phosphate groups, the bands at 3570 and 630 cm^{-1} correspond to the vibrations of the hydroxyl groups, the bands at 1650, 1410–1570 (ν_3), 880 and 873 (ν_2) cm^{-1} correspond to the vibrations of the carbonate groups.

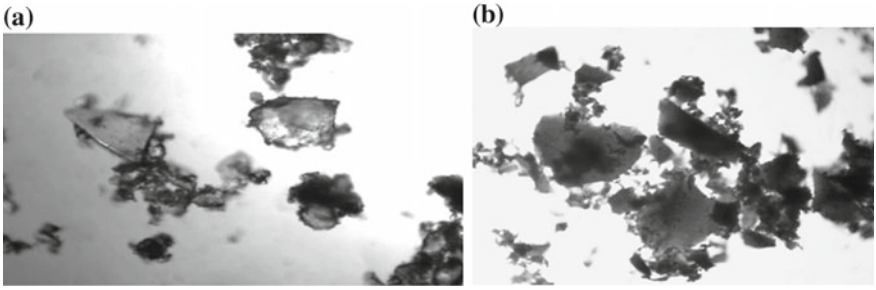


Fig. 7.3 Micrographs of samples Si-HA: **a** before calcination, **b** after calcination (800 °C), with an increase of x 10

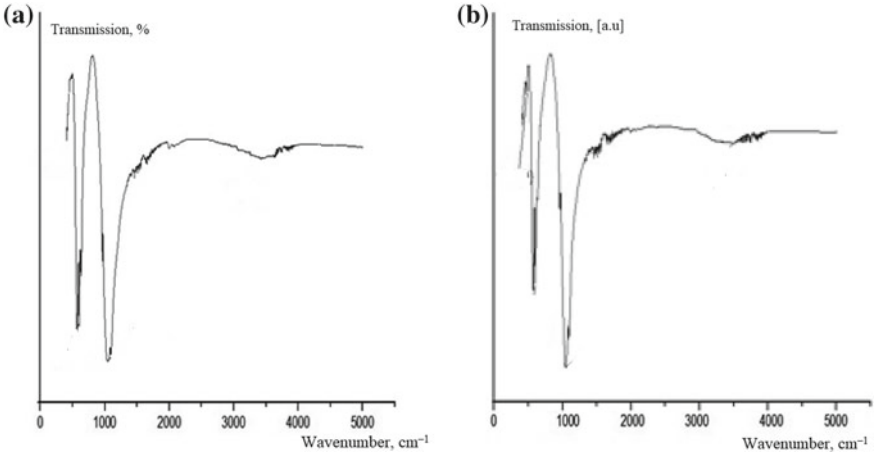


Fig. 7.4 IR spectra for hydroxyapatite samples modified by Na_2SiO_3 at 800 °C: **a** HA, **b** HA + $C(SiO_3^{2-})$ 0.5 wt%

The presence of the carbonate groups indicates the presence of all silicon substituted apatites in the structure, which is caused by the presence of HCO_3 ions in the initial synthesized solution. The peak of deformation vibrations of the OH^- groups at 3570 cm^{-1} is observed in the background of the high intensity band in the region of 3200–3700 cm^{-1}, which may be due to the presence of the adsorbed water in the produced apatite form (Solonenko and Golovanova 2013). As the silicate concentration in the reaction medium grows, the mode intensities of OH^- ions HA vibrations (3570 cm^{-1}) decrease. The resolution of the phosphate absorption bands (1040 and 1090 cm^{-1}) decreases similarly to the reflexes in the range of 30°–33°/2θ in the sample diffraction patterns (Fig. 7.1). Due to the structural similarity of the tetrahedral groups PO_4^{3-} and SiO_4^{4-}, a set of the bond absorption maxima in both ions is observed at similar frequencies. The superposition of strong bands in the region of 1020, 1080, 2500–3700 cm^{-1} and others does not allow identification of silicates in the produced samples.

The presence of SiO_4^{4-} group in precipitates can be determined by the low intensity peaks with maxima at 504 and 800 cm^{-1}, which correspond to the modes of deformation vibrations of Si-O bonds and symmetric valent vibrations of Si–O–Si bridges in SiO_4 tetrahedra (Berdinskaya et al. 2014; Tkhuan et al. 2011). Insignificant increase in their intensity can be observed with the increase of silicon content in the initial reaction medium. Simultaneous decay of the vibrational modes of OH^- ions HA (3570 cm^{-1}) indicates the substitution of phosphates for silicates with the hydroxyl groups involved: $PO_4^{3-} + OH^- \Leftarrow SiO_4^{4-} + \square_{OH}$ that agrees with the literature data (Bandyopadhyay et al. 2006; Tkhuan et al. 2011).

Broadening of the band in the region of 3570 cm^{-1} is typical of the hydroxyapatite samples modified by silicate ions from the tetraethoxysilane structure, which we believe is due to the superposition on the absorption band at 2800–2900 cm^{-1} that

corresponds to the vibrations of C–H groups. The occurrence of these bands in the spectra can be attributed to the fact that the synthesis was carried out in the TEX alcohol solution.

The processes that take place during heat treatment of synthesized samples depend on the ratio of Ca/P, Ca/(P+Si) and the concentration of silicate ions in the solid phase. As a result of the thermal destruction process, $Ca_{10}(PO_4)_{6-x}(SiO_4)_x(OH)_{2-x}$, as well as its mixture with β-$Ca_3(PO_4)_2$, can be obtained. Composite materials based on two-phase ceramics consisting of a mixture of Si-HA and β-TCΦ are widely used in medicine. This is due to the different solubility of the constituent components, which allows controlling the rate of resorption of the material in the body.

As is known, the human body contains buffer solutions, and the study of the processes of resorption of samples is one of the objectives of their promotion for practical use. One of the most common buffers emitting the physiological environment of the human body is Tris-HCl buffer, the pH of which is 7.4 and corresponds to the physiological values of the organism, therefore this buffer was chosen as a solvent to simulate a living environment.

From the results of the dissolution of Si-HA (Fig. 7.5a–d), it can be seen that the saturation with calcium ions is observed in two stages. This effect is especially

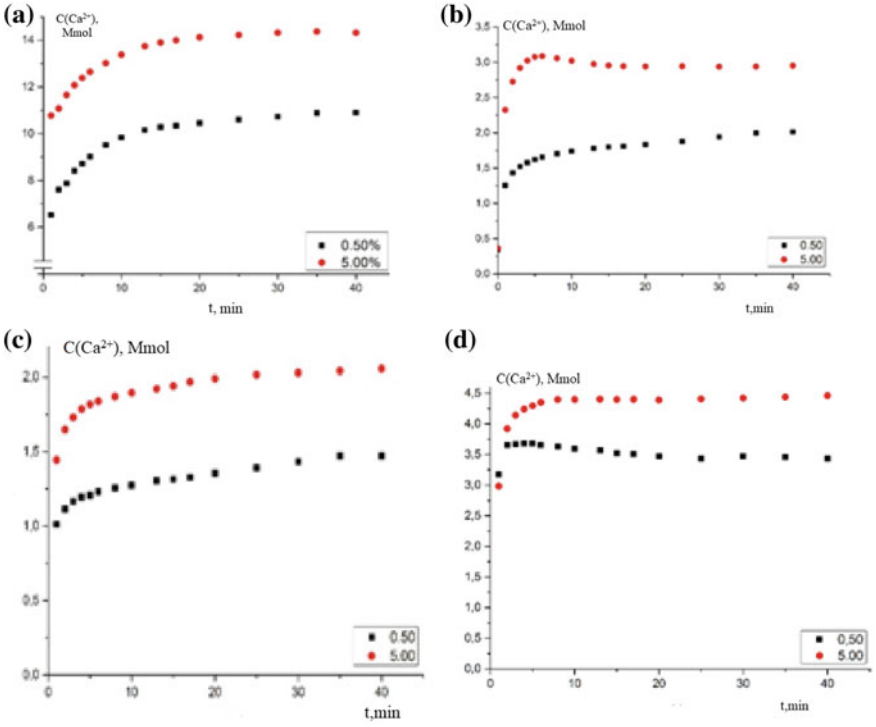


Fig. 7.5 Kinetic curves for the dissolution of Si-HA in a solution of Tris-HCl buffer (silicon carrier reagent Na_2SiO_3) with varying temperature: **a** 20 °C, **b** 37 °C, **c** 50 °C, **d** 80 °C

pronounced at 37 °C for a sample containing 5.00 wt% silicon. For this sample, a characteristic peak of saturation with calcium ions is observed, after which the kinetic curve gradually reaches a plateau.

As a result of an increase in temperature to 50 °C we observe a deviation of pH from physiological values to the slightly acidic region, and at 80 °C they reach pH = 6.03. Most likely, this is due to the occurrence of a side reaction with the formation of acid sites. The result of dissolution in Tris-HCl buffer indicates a rather complex system of dissolution of samples of silicon-containing hydroxyapatite.

As a result of the process of dissolving samples (Fig. 7.6) containing silicate ions of TEX as an agent, a clear maximum was observed in Tris-HCl buffer at a temperature of 20 °C (Fig. 7.6a), after which the resorption process slowed down and gradually began to decrease the concentration of calcium ions, indicating the beginning of the remodeling process. When the temperature rises to 37 °C (Fig. 7.6b), no saturation with calcium ions is observed, and an increase in the concentration of Ca^{2+} is observed during the entire exposure time. As the temperature increases to 50 °C (Fig. 7.6c), intense resorption is observed, and already in the second minute a small dip in the concentration of calcium ions is observed, after which their content levels out and increases throughout the whole experiment. But when the temperature of the solvent

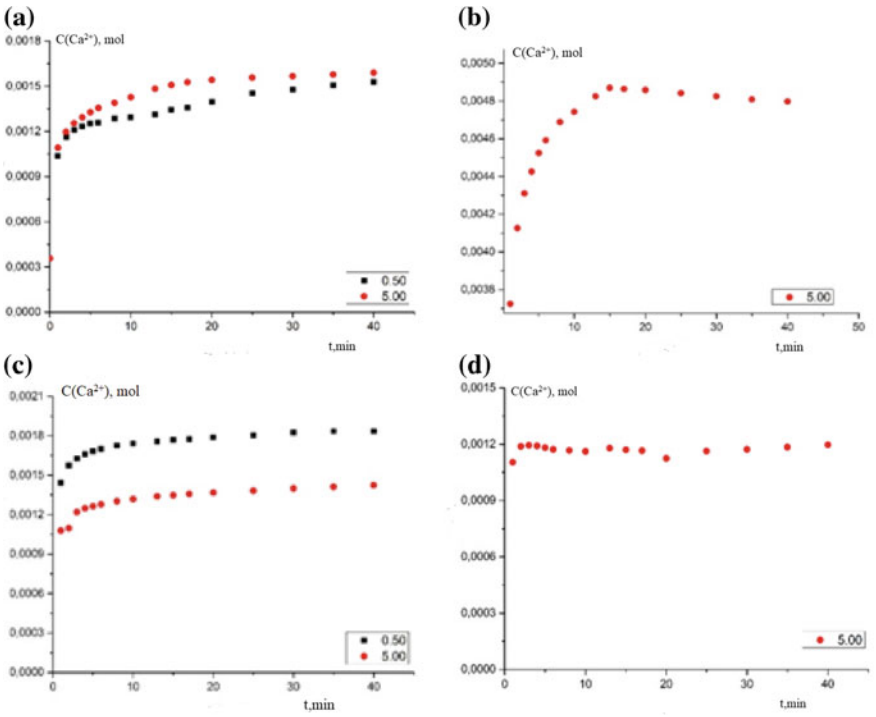


Fig. 7.6 Kinetic curves for the dissolution of Si-HA in a solution of Tris-HCl buffer (silicon carrier reagent TEX) with varying temperature: **a** 20 °C, **b** 37 °C, **c** 50 °C, **d** 80 °C

increased to 80 °C (Fig. 7.6d), such dips on the kinetic curve began to appear more often, which indicates a high competition of the resorption/remodeling reaction, as a result of which we can speak of the high bioactivity of the Si-HA sample.

As temperature increases to physiological, weak dissolution and segregation are observed. With a further increase in temperature to 50 °C, there is no change in the dissolution process. Only one kinetic curve of a Si-HA sample synthesized with an organic silicon additive dissolved at 80 °C has the appearance similar to the curve of sample dissolution with an inorganic additive.

The results of the research can be used to study the kinetics of dissolution and the biocompatibility of ceramic materials for medicine, namely for reconstructive surgery, dentistry, and development of drug delivery systems.

7.4 Conclusion

The formation of the silicon-substituted hydroxyapatite of the extracellular fluid obtained from the model solution by a chemical method and the analysis of XRD and FTIR was established. The structure of the modified apatite is imperfect and crystallizes in the nanocrystalline state. The ratio Ca/(P+Si) ratio decreases with increasing concentration of silicate ions in the initial solution, which indicates isomorphous replacement of phosphate ions by silicate ions in the structure of hydroxylapatite. As the amount of silicon in Si-HA increases, the thermal stability of the samples increases. The greatest loss of mass is observed at temperatures of 25–400 °C, which is associated with the removal of crystallization and adsorption water and volatile impurities. Three main stages of thermal degradation of Si-KHA are isolated, the final product is a mixture consisting of two phases: Si-HA and β-TKF. The kinetic parameters of the dissolution of the synthesized samples were determined experimentally and showed that the Si-HA samples have a higher bioactivity.

References

Bandyopadhyay A, Bernard S, Xue W, Bose S (2006) Calcium phosphate-based resorbable ceramics: influence of MgO, ZnO and SiO_2 dopants. J Am Ceram Soc 89:2675–2678

Berdinskaya MV, Golovanova OA, Zaits AV, Drozdov VI, Leont'eva NN Anthonicheva NV (2014) A physicochemical study of the structure, composition, and properties of hydroxylapatite modified by silicate ions. J Struct Chem 5:954–961

Chang MC, Ko CC, Douglas WH (2003) Preparation of hydroxyapatite-gelatin nanocomposite. Biomaterials 24:2853–2862

Golovan AP, Turov VV, Barvinchenko VM, Mishchenko VM, Gorbik PP, Shevchenko YB (2007) Nanostructured composites based on proteins of bone tissue, highly disperse silica and hydroxyapatite. J Khimiya, fizika ta tekhnologiya poverhni 13:309–316

Gomes S, Nedelec J, Jallot E, Sheptyakov D, Renaudin G (2011) Silicon location in silicate-substituted calcium phosphate ceramics determined by neutron diffraction. J Cryst Growth Des 11:4017–4026

Grubova IY, Ivanova AA, Primak O, Epple M (2014) Osteoinductive coatings based on silicon-substituted hydroxylapatite: physical and chemical properties and in vitro studies. New technologies for creating and using bioceramics in regenerative medicine, pp 154–159

Hench L, Jones D (2007) Biomaterials, artificial organs and tissue engineering. J Technosphere 301

Khlusov IA, Surmeneva MA, Surmenev RA, Ryazantseva NV, Saveleva OE, Ivanova AA, Prokhorenko TS, Tashireva LA, Dvornichenko MV, Pichugin VF (2012) Cell-molecular aspects of immunological compatibility of implants with nanostructured calcium-phosphate coating. J Bull Siberian Med 4:78–85

Marchat D, Zymelka M, Coelho C et al (2013) Accurate characterization of pure silicon-substituted hydroxyapatite powders synthesized in a new deposition pathway. Acta Biomater 9:6992–7004

Meshkova NP, Severina SE (1979) Workshop on biochemistry. Moscow State University, Moscow

Morgan H, Wilson RM, Elliott JC, Dowker SE et al (2000) Preparation and characterisation of monoclinic hydroxyapatite and its precipitated carbonate apatite intermediate. J Biomater 21:617–627

Murugan R, Ramakrishna S (2005) Crystallografic study of hydroxyapatite bioceramics derived from various sources. J Cryst Growth Des 5:111–116

Saki M (2009) Biocompatibility study of a hydroxyapatite-alumina and silicon carbide composite scaffold for bone tissue engineering. J Yakhteh 11:55–60

Soin AV, Evdokimov PV, Veresov AG, Putlyaev VI (2007) Synthesis and study of silicon-substituted hydroxyapatites Ca10(PO4), 6–x(SiO4)x(OH). J Altern Energy Ecol 45:130

Solonenko AP, Golovanova OA (2013) Thermal effects in composite materials based on calcium phosphates. Russ J Inorg Chem 1–2:33–38

Solonenko AP, Golovanova OA (2014) Silicate-substituted carbonated hydroxyapatite powders prepared by precipitation from aqueous solutions. Russ J Inorg Chem 59:1228–1236

Tkhuan LV, Dat DV, Temirkhanova GE (2011) Synthesis and investigation of the morphology of silicon substituted hydroxyapatite, in Sbornik material. IV Vserossiiskoi konferentsii "Nauchnaya initsiativa inostrannykh studentov and aspirantov rossiiskikh vuzov". pp 346–349 (in Russian)

Wang Y, Zhang S, Zeng X, Cheng K, Qian M, Weng W (2007) In vitro behavior of fluoridated hydroxyapatite coatings inorganic-containing simulated body fluid. J Mater Sci Eng 27:244–250

Part II
Methods for Studying the Interactions in Biogenic–Abiogenic Systems

Chapter 8
Singlet Oxygen in the Lower Atmosphere: Origin, Measurement and Participation in Processes and Phenomena at the Boundary Between Biogenic and Abiogenic Nature



Vladimir P. Chelibanov, Ivan V. Chelibanov, Olga V. Frank-Kamenetskaya, Egor A. Iasenko, Alexandr M. Marugin and Olga A. Pinchuk

Abstract The present paper contains a review of literature data on sources of singlet oxygen in lower atmosphere and methods of its registration. Singlet oxygen gas analyzer developed in OPTEC JSC (St Petersburg, Russia), which operation principle is based on the 9,10-definilantracene chemiluminescent reaction is described in the present paper. The new gas analyzer used for solving a wide range of fundamental and applied problems connected with the processes and phenomena at the boundary between biogenic and abiogenic nature. Its capabilities demonstrated on the examples for monitoring pollutant concentrations in atmospheric air, on the experiments in vivo and in vitro on recording singlet oxygen on the surface of snow and near plants infected by pathogenic fungus, as well as on tests of photocatalytic materials developed for use in medicine and in protection of architectural and sculptural monuments from biodeterioration.

Keyword Singlet oxygen · Singlet oxygen sources · Singlet oxygen monitoring · Ozone monitoring · Singlet oxygen gas analyzer · Photocatalytic materials testing

V. P. Chelibanov (✉) · E. A. Iasenko · A. M. Marugin
OPTEC JSC, Saint Petersburg, Russia
e-mail: chelibanov@gmail.com

I. V. Chelibanov
Herzen State Pedagogical University of Russia, Saint Petersburg, Russia

O. V. Frank-Kamenetskaya
Saint Petersburg University, Saint Petersburg, Russia
e-mail: ofrank-kam@mail.ru

O. A. Pinchuk
ITMO University, Saint Petersburg, Russia

© Springer Nature Switzerland AG 2020

O. V. Frank-Kamenetskaya et al. (eds.), *Processes and Phenomena on the Boundary Between Biogenic and Abiogenic Nature*, Lecture Notes in Earth System Sciences,
https://doi.org/10.1007/978-3-030-21614-6_8

8.1 Introduction

Under the conditions of the Earth's oxidative atmosphere living organisms have developed in them prooxidant and antioxidant systems that are balanced with each other (Jacob and Winyard 2009; Poljsak et al. 2013). The prooxidant system serves to protect against pathogenic microorganisms and takes part in cell renewal and reproduction processes (Khan 1991). At the same time, it plays a major role in the oxidative stress which leads to pathology of various organs (Farkhutdinova 2015). For example, it accelerates the growth of apatite aggregates of urinary stones (Golovanova et al. 2010; Khan 2013).

Prooxidant system is an open type system. In addition to the corresponding endogenous enzymes and intracellular reactive oxygen forms, it includes the exogenous part—solar radiation, as well as active oxygen forms and free radicals which are present on the underlying surface, in air, in water and in food. As a result of anthropogenic environmental impact, an increase in the activity of the exogenous part of the prooxidant system occurs. The antioxidant system, which protects the body from the unbalanced action of the prooxidant system, does not have enough time to adapt to this increase.

Singlet oxygen ($^1O_2$) is one of the active forms of oxygen. In recent decades, this form of oxygen has been increasingly mentioned in context with scientific and practical human activities. Its connection with biological systems is being studied (Krinsky 1977). Its use is being considered in laser technology (Boreysho 2005), its healing properties are being studied and applied (Khan 1991; Hulten et al. 1999; Martusevich et al. 2015; Razumovsky et al. 2016; Zakharov et al. 2014). Its negative impact in the formation of photochemical smog (Pitts et al. 1969; Pitts 1970) and in the oxidation of food (Min and Boff 2002) is being explored as well. Its bactericidal action is used for air purification, for developing methods for disinfecting water (Bartusik et al. 2012) and protecting sculptural monuments from biodegradation (Marugin et al. 2005; Vlasov et al. 2019). At the same time, the space-time characteristics of singlet oxygen in the lower atmosphere are practically not studied, primarily due to the lack of specialized analytical techniques. In the present work, the sources of singlet oxygen in the lower atmosphere are reviewed, the description of the newly developed $^1O_2$ gas analyzer capable of operating in field conditions is presented, and the examples of its use in studying the variability of singlet oxygen concentration in atmospheric air are given.

8.2 Sources of Singlet Oxygen in the Surface Atmosphere and Methods for Its Determination (Literature Data)

The predominant number of oxygen molecules (O_2) in the lower atmosphere of Earth is in a stable state, which is determined by the strong double covalent bond between oxygen atoms. The peculiarity of the O_2 molecule is the presence of two

degenerate (equal in energy) external orthogonal to each other molecular orbitals, usually denoted as $\pi_g^{\pm}$ orbitals (Minaev 2007). Each of these orbitals is not filled, each one contains one electron in it, and thus stable oxygen is a biradical. The spin vectors of electrons on $\pi_g^{\pm}$ orbitals are parallel, and the quantum numbers of the spins are 1/2. The total spin of the molecule is 1, its projection on the z axis (axis perpendicular to the plane of symmetry of the molecule) can have three values: 1, 0, −1. For this reason, stable oxygen is called triplet. This state of the O_2 molecule is designated as $O_2\left({}^3\sum_g^-\right)$ or ${}^3O_2$.

Usually, free radicals have increased reactivity compared to organic matter in the biosphere. However, the biradical molecules of triplet oxygen, due to quantum-mechanical prohibitions, under normal conditions, rather slowly react with organic matter, which in the majority of cases consists of singlet molecules. The quantum mechanical prohibition on triplet-singlet interactions saves organic matter from rapid oxidation, in fact—from combustion, in an atmosphere containing approximately 21% of triplet oxygen (Minaev 2007). A whole another matter is a more active oxidizing agent—singlet oxygen, which is formed as a result of reorganization of the electronic structure of $\pi_g^{\pm}$ orbitals in such a way that the total spin of the molecule becomes equal to 0. This reorganization may occur:

- as a result of resonant transfer of excitation from sensitizers to which ${}^3O_2$ molecules are adsorbed (Schweitzer and Schmidt 2003);
- during the exchange processes with electron-hole structures of crystalline photocatalysts to which ${}^3O_2$ is adsorbed (Daimon end Nosaka 2007);
- as a result of photochemical or chemical reactions of the decomposition of molecules containing oxygen atoms, and the formation of ${}^1O_2$ molecules from them (Wayne 1994);
- as a result of lifting the degeneracy of $\pi_g^{\pm}$ orbitals of the triplet oxygen molecule in a strong static electric field (Mikheikin et al. 2002).

Reorganization options are shown in Fig. 8.1. The excess energy of singlet oxygen in the first ${}^1\Delta_g$ and second ${}^1\sum_g^+$ excited states equals to 95 and 158 kJ/mol, respectively. Due to the fact that singlet-singlet transitions are allowed, the second

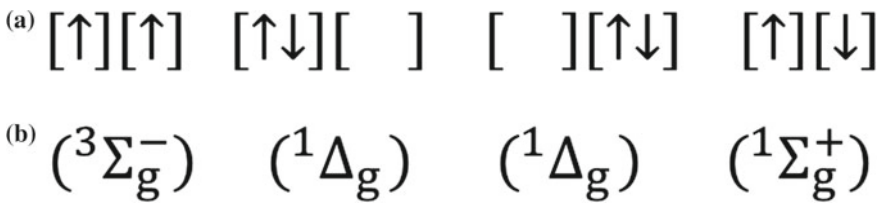


Fig. 8.1 **a** Variants for filling $\pi_g^{\pm}$ orbitals of the O_2 molecule (the direction of the spin vectors is shown conventionally), **b** the designation of stable and three excited states of the O_2 molecule. The ${}^1\Delta_g$ state is doubly degenerate

electronically excited state quickly translates into the first. When the excited states of singlet oxygen molecules relax, radiation is observed at wavelengths of 1269 nm and 761 nm. In addition to monomolecular, synchronous transitions of two O_2 molecules bound by van der Waals forces are possible when they are excited (Naus and Ubachs 1999). Relaxation of $^1O_2$ dimers, the excess energy of which is a combination of the first and second $^1O_2$ states, produces radiation wavelengths of 634, 476 and 381 nm.

One of the main sources of $^1O_2$ in the troposphere is the reaction of photochemical decomposition of ozone by solar radiation in the spectral range of 200–310 nm with a maximum at 256 nm (Jones and Wayne 1969): $O_3 + h\upsilon \rightarrow O_2(a^1\Delta g) + O(^1D)$. The quantum yield of $^1O_2$ is approximately equal to 0.9. The singlet oxygen atoms $O(^1D)$ are also able to contribute to the formation of $^1O_2$ as a result of the reaction $O(^1D) + O2(^3\sum_g^-) \rightarrow O(^3P) + O2(^1\sum_g^+)$ (Young and B1ack 1967). The source of $O_2(^1\Delta_g)$ can also be an exothermic reaction of ozone with nitric oxide, which is present in the exhaust gases of urban vehicles (Pitts 1970). Possible sources of $O_2(^1\Delta_g)$ are "dark" ozone reactions with other numerous pollutants that may be present as aerosols in the surface layer of the atmosphere (Muñoz et al. 2001). The formation of $^1O_2$ was observed when a mixture of NO_2 and O_2 was irradiated with light in the region of wavelengths 330–590 nm (Jones and Bayes 1973). Significant sources of $^1O_2$ are $^3O_2$ molecules that interact with numerous natural or anthropogenic photosensitizers and photocatalysts, which can be in different aggregative states and in varying degrees of dispersion (Krasnovsky 2018; Larson and Marley 1999; DeRosa and Crutchley 2002; Pitts 1970; Wayne 1994; Schweitzer and Schmidt 2003; Daimon end Nosaka 2007). In the case of photosensitizers (Phr), the reaction of the formation of $^1O_2$ has the form $^3O_2 + (^1Phr + h\upsilon) \rightarrow {}^3O_2 + {}^3Phr \rightarrow {}^1O_2 + {}^1Phr$. An important source of reactive oxygen forms, including $^1O_2$, is the activated surface of many solid-phase substances, in particular, transition metal oxides (Boreskov 1982). Extracellular production of singlet oxygen (Steinbeck et al. 1993; Morita et al. 1997) may be the source of the latter in the air as a result of the action of the enzyme complex NADPH-oxidase in the epidermis of plants and animals. Due to the prohibition of singlet-triplet transitions, the lifetime of the first state of free $O_2(^1\Delta_g)$ molecules is rather long ~72 min (Schweitzer and Schmidt 2003). Spontaneous transitions of free molecules occur with time variation, therefore, the intensity of spontaneous luminescence of singlet oxygen is not large and its registration by methods of emission spectroscopy is difficult. With induced transitions associated with the interaction of excited oxygen molecules with gas or condensed molecules, as well as with electromagnetic radiation at certain wavelengths, the lifetime of singlet oxygen is significantly reduced. For example, in water, the $O_2(^1\Delta_g)$ lifetime does not exceed 3.1 μs (Rodgers 1983). One of the possible schemes for the formation of $^1O_2$ molecules in the lower atmosphere is shown on Fig. 8.2.

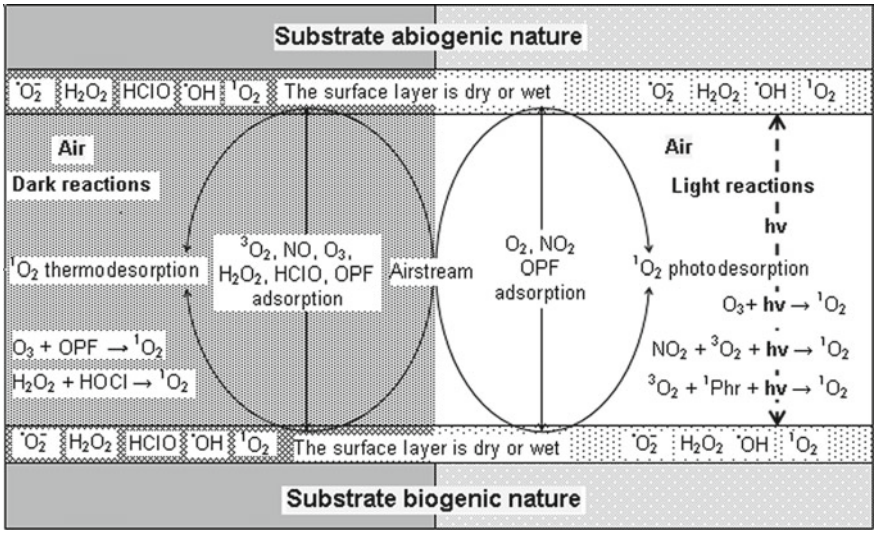


Fig. 8.2 Scheme of the appearance of $^1O_2$ molecules in the lower atmosphere. Sources $^1O_2$ are homogeneous and heterogeneous reactions that can occur in the light or in the dark. Substrate is a substance of different nature and degree of dispersion, which is in the air in the form of aerosols, snowflakes, drops or on the underlying surface. Abiogenic substrate is acid-base catalysts, photocatalysts, photosensitizers, transition metal oxides, solutions with nucleophilic anions (NO_2^-, N_3^-, I^-, Br^-, CN^-), amines, etc. Biogenic substrate is acid-base enzymes, photosensitizers, components of DNA, cysteine, methionine, albumin, HClO, uric acid, etc. In the case of heterogeneous reactions, $^3O_2$, active forms of oxygen, HClO vapor and organic pollutants fume (OPF) are adsorbed into the surface layer of the substrate. Free radicals, reactive oxygen species, including $^1O_2$, are desorbed. Desorption contribute to air flow. In the case of homogeneous reactions $^3O_2$, O_3, a vapor of singlet organic photosensitizers (^{1}Phr), OPF, a vapors of HClO and H_2O_2, interacting with each other and with photons are sources of $^1O_2$

Induced transitions can be radiative and non-radiative. In the case of non-radiative transitions, the energy of the excited singlet oxygen molecules is transferred to heat, which can be measured in a gas medium by the calorimetric method (Kearns 1971), and in the aquatic environment—by the holographic method (Belashov et al. 2014). With radiative induced transitions, the intensity of luminescence increases significantly and it can be registered by emission spectroscopy (Krasnovsky 1993). To measure singlet oxygen there are another methods, such as laser spectroscopy using a multi-pass optical cell (Naus and Ubachs 1999); chemical singlet oxygen traps (Ogawa et al. 1991); electron paramagnetic resonance (Falick et al. 1965); spin label method (Kruk et al. 2002); ionization method (Clark and Wayne 1970; Chandler and Houston 1987). There are publications on the registration of singlet oxygen using metal oxide semiconductor sensors (Zavyalov and Myasnikov 1981). Probably one of the most sensitive methods for detecting singlet oxygen is based on the use of chemiluminescence (Romanov and Rufov 1998; Adam et al. 2005; Wu et al. 2011).

8.3 Methodical Results of the Work and Their Discussion

Singlet oxygen gas analyzer

The gas analyzer $^1O_2$ is developed in St. Petersburg in accordance with the patent RU 2415401 (Chelibanov and Chelibanova 2010). Figure 8.3 shows a block diagram of $^1O_2$ gas analyzer. The principle of its operation is based on the effect of solid-state multistage chemiluminescence of 9,10-definilantracene, which selectively interacts with singlet oxygen molecules. The metrological support of the gas analyzer is implemented using an integrated photochemical $^1O_2$ source, the calibration of which is performed using an external photocatalytic $^1O_2$ generator. A PTFE membrane with a photocatalytic composition of anatase and polyphenolic compounds of plant origin is installed in the generator. UV LEDs are used to illuminate the PTFE membrane. The performance of the photocatalytic generator in singlet oxygen was determined in accordance with the methodology developed in St. Petersburg State University and in the Russian Scientific Center "Applied Chemistry" (Ovechkin et al. 2015). The gas analyzer of singlet oxygen is built according to the comparator scheme: the air from the built-in $^1O_2$ source and the air from the external environment is periodically pumped through the sensor and the signals from the photomultiplier are compared. As a result, the readings of the gas analyzer do not depend on the changes of the sensor sensitivity.

The gas analyzer consists of:

- An optical-electronic system containing a replaceable sensor and a multi-alkaline photomultiplier. A latex porous membrane in which a chemiluminescent composition is embedded works as a sensor. The sensor is installed in a flow-through air reactor, next to the photomultiplier. The flow reactor and photomultiplier are separated by an optical window and are protected from external illumination by a casing and light traps installed in it.

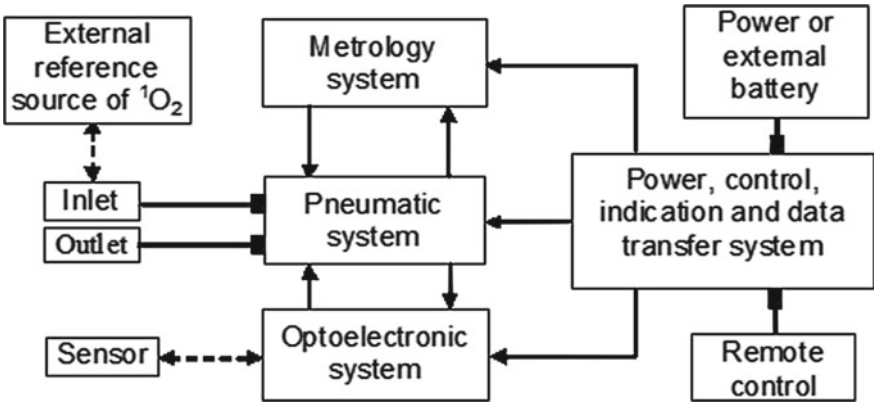


Fig. 8.3 The singlet oxygen gas analyzer structure

- The metrological support system consists of a photochemical reactor in which a lower pressure hydrogen discharge lamp is installed. Air pumped through a photochemical reactor is preliminary cleaned of interfering impurities in the pneumatic system.
- Pneumatic system. Provides pumping air through the sensor from the external environment or from a photochemical reactor. The process of switching air flows is managed by the controller in accordance with the embedded algorithm of the gas analyzer.
- Power, control, display and data transfer system. It provides power supply and generation of control signals, processing and visualization of measurement results, as well as transfer of these results for archiving and remote use.

Technical (operational) characteristics of the gas analyzer can be found in the catalog of the OPTEC JSC (Chelibanov and Zykova 2017).

Examples of the application of the developed gas analyzer

The expansion of the functionality of the air monitoring equipment

Along with analyzers of other small gas and aerosol components of atmospheric air and meteorological sensors $^1O_2$ gas analyzer is included in the software and hardware complex SKAT (Fig. 8.4a). In the case of use under the open air, the SKAT complex should be installed in a module protected from external influences, which includes the life support system for the complex (Fig. 8.4b). At present, several SKAT complexes are connected to the atmospheric air monitoring network of the North-West region of the Russian Federation through the merge and data storage server. This network is intended for educational and research work in the field of environmental ecology and the study of processes and phenomena on the border of biogenic and abiogenic nature.

Since 2007, the air environment in various districts of St. Petersburg and its suburbs has been monitored with the help of the SKAT hardware complex (Chelibanov et al. 2019). Since 2012, with help of the development of a high-speed gas analyzer for singlet oxygen, it has become possible to perform simultaneous measurements of

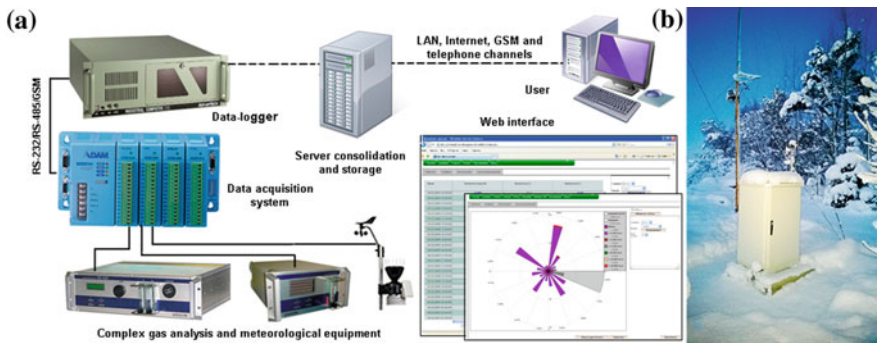


Fig. 8.4 **a** SKAT measuring system, **b** SKAT in thermostatted casing

$^1O_2$ together with other small gas and aerosol components of the atmosphere. As an illustration in Fig. 8.5 shows the graphs of mean monthly concentrations of ozone, singlet oxygen and mean monthly temperatures in the air from June 2017 to June 2018. The measurements were carried out in the Priozersky District, an ecologically clean green zone located 80 km from the center of St. Petersburg and in the center of St. Petersburg, Maly 58 Ave., on Vasilyevsky Island (an industrial site of the OPTEC JSC). The highest concentrations of $^1O_2$ at 55 and 10.8 μg/m^3 in the respective regions were observed in the spring, when the earth surface was overgrown with fresh vegetation. The annual course of ozone concentration in the lower atmosphere is similar to that observed in Mace Head, Ireland (Lelieved and Dentener 2000).

Figure 8.6 shows the results of simultaneous measurements of concentrations of NO, NO_2, O_3, $^1O_2$, temperature, relative humidity and wind speed for a limited period

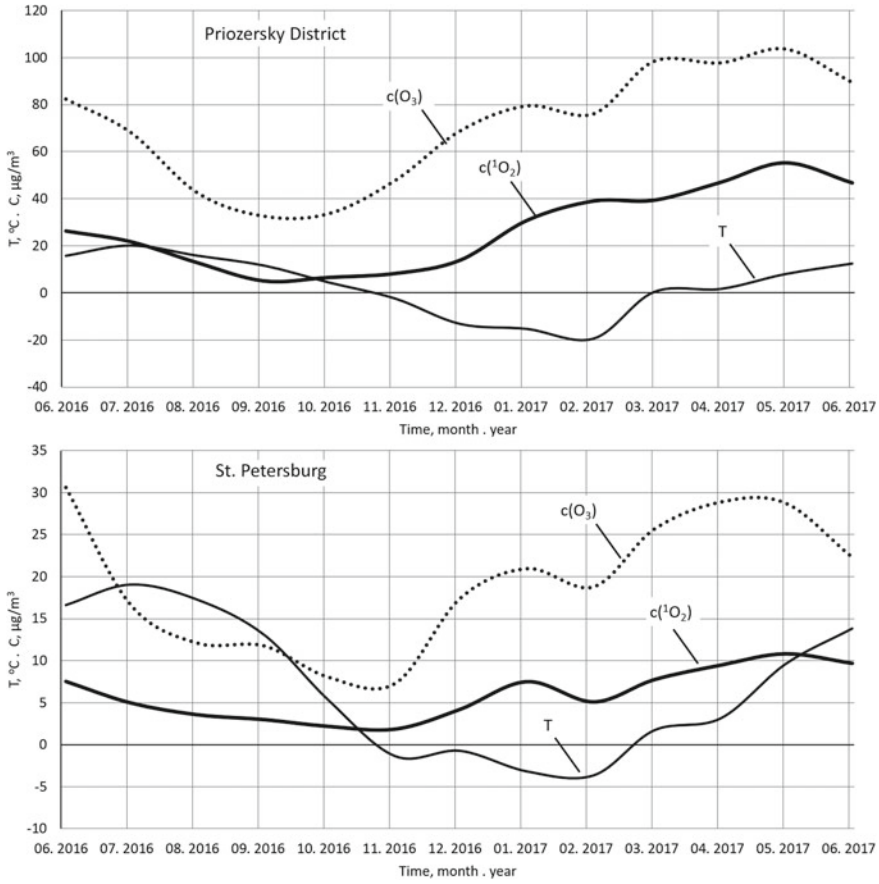


Fig. 8.5 Monthly mean values of concentrations (C) of ozone and singlet oxygen, as well as temperatures (T) in the period from June 2017 to June 2018 in the Priozersky District and in the St. Petersburg (Maly pr. 58)

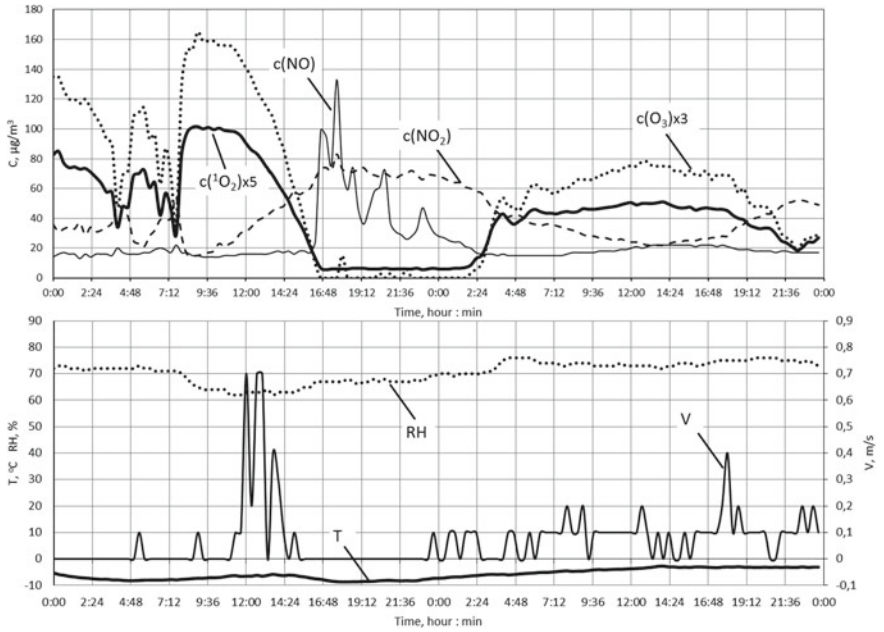


Fig. 8.6 Changes in the concentration (C) of nitric oxide, ozone, singlet oxygen, temperature (T), humidity (RH) and wind speed (V) in the period from December 17 to December 18, 2018, in the Priozersky District

of time (two days). These results were selected from the monitoring database archive in such a way that the graphics represent sunny and overcast days. The left half of the graphs corresponds to the date of December 17, 2018, when it was a sunny day. The right half of the graphs corresponds to the date of December 18, 2018, when it was an overcast day. The location around the complex SKAT was covered with snow (Fig. 8.4b). The height of the air sampling was 2 m. The observed increased content of nitrogen oxides in the atmospheric air is associated with the emissions from motor vehicles used in connection with the repair work near the SKAT complex. As can be seen from the graphs, the content of $^1O_2$ in the near surface layer of atmospheric air is associated with weather conditions and the content of ozone and nitrogen oxides. The concentration of $^1O_2$ reached maximum values of 20 $\mu g/m^3$ on a sunny day at elevated wind speeds.

Figure 8.7 shows the results of simultaneous measurement of concentrations of NO, O_3, $^1O_2$, temperature and atmospheric pressure by the complex SKAT, located in the St. Petersburg on Maly Ave 58. The measurements correspond to a period between January 10 and 11, 2016, when a temperature inversion layer formed in the near surface atmosphere, and a period of destruction of this layer on January 12, 2016. During the period of the inversion layer existence, an elevated content of the NO pollutant was observed. The content of $^1O_2$ in air exceeded the content of O_3 and reached values of 4 $\mu g/m^3$.

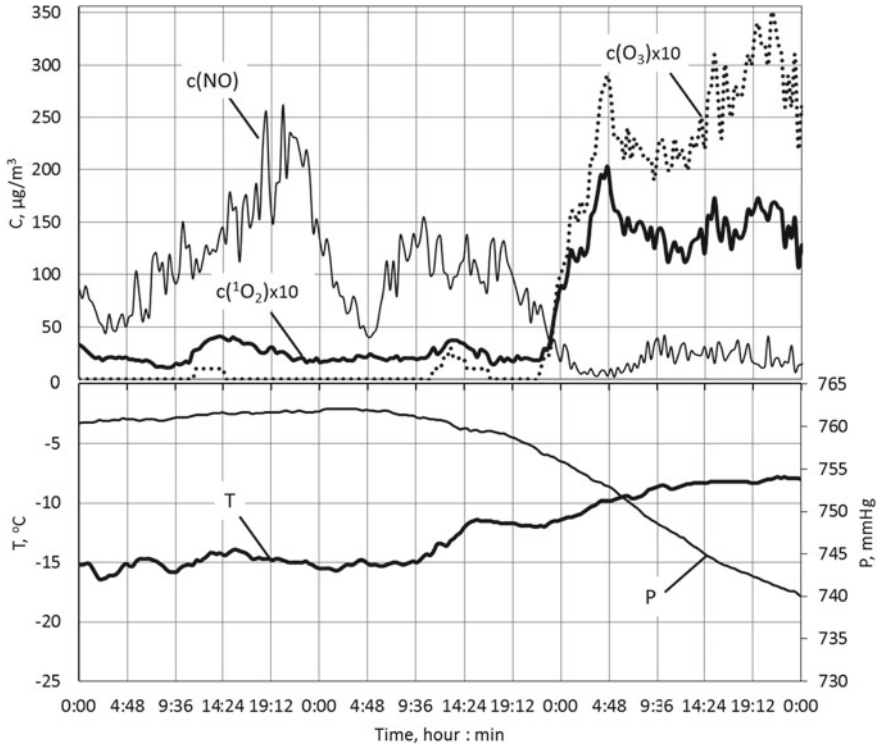


Fig. 8.7 Changes in the concentration (C) of nitric oxide, ozone, singlet oxygen, temperature (T) and atmospheric pressure (P) in the period from December 10 to December 12, 2016, in the St. Petersburg (Maly pr. 58)

Figure 8.8 shows the results of simultaneous measurements of concentrations of CO, O_3, $^1O_2$, temperature and humidity by the complex SKAT, located in the Priozersk region. Measurements correspond to a daily period of May 13, 2018. Elevated values of ozone and singlet oxygen are typical for the spring period. Carbon monoxide emissions were associated with an experiment on burning freshly picked grass 20 m from the SKAT complex.

In Vivo experiments on the formation of singlet oxygen above the snow surface

As a result of the measurements carried out using the $^1O_2$ gas analyzer, an effective source of singlet oxygen formation in the surface atmosphere was found (Sysoeva et al. 2016), which was associated with photoinduced processes on the snow surface. This source was previously predicted by (Grannas et al. 2007) and detected by (Bower and Anastasio 2013). Concentration of $^1O_2$ on a sunny day at −8 °C at 12 o'clock on January 7, 2012, at the Antarctic station Progress 2 above the snow surface at a distance of 5 cm was 35 μg/m^3, and at a distance of 2 m from the surface—27 μg/m^3.

The relationship between the evolution of the thickness of the ozone layer above the SKAT station located in the Priozersky District (Fig. 8.4b) and the ratio of ozone

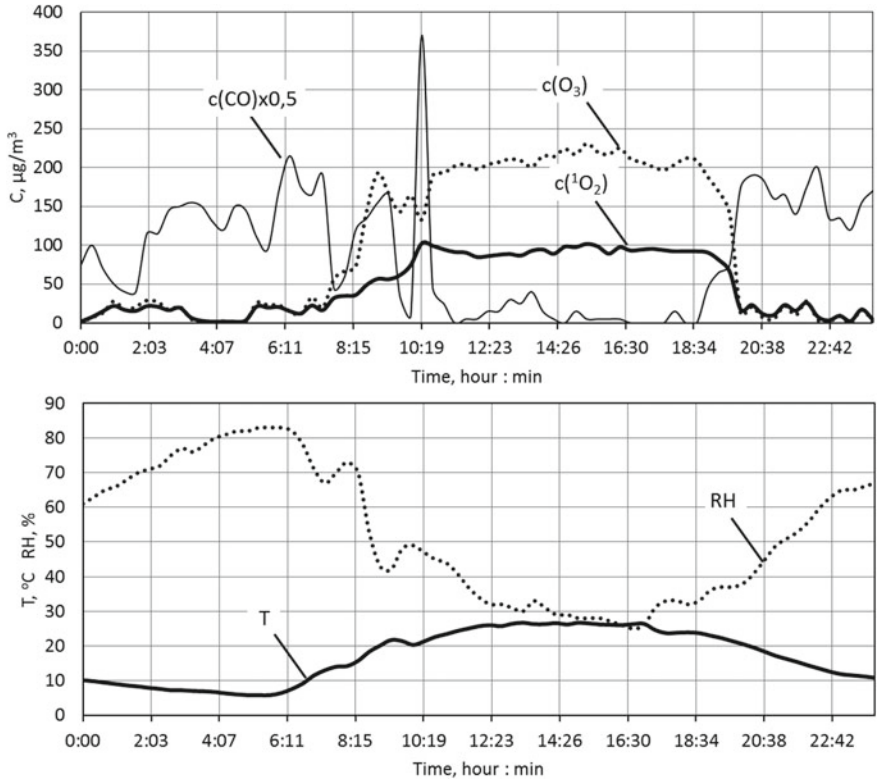


Fig. 8.8 Changes in the concentration (C) of carbon monoxide, ozone, singlet oxygen, temperature (T), humidity (RH) during the day on May 13, 2018, in the Priozersky District on a cloudy day

and singlet oxygen concentrations in the lower atmosphere was also been established (Iasenko et al. 2016a, b). An increase in the content of singlet oxygen in the air relative to the ozone content from a level of 52–67% was observed on January 28, 2016. This increase is most likely due to a change in the spectral composition of solar illumination during a period of decreasing ozone layer thickness. Information on the change in the thickness of the ozone layer over the North-Western region of Russia was taken from the website (URL: http://exp-studies.tor.ec.gc.ca/cgi-bin/selectMap).

In vitro experiments on observing singlet oxygen near plants infected with the pathogenic fungus

The $^1O_2$ gas analyzer was used to conduct experiments on recording the stress state of a plant infected with the pathogenic fungus *Cochliobolus sativus*. Figure 8.9 shows a graph of the release of singlet oxygen over wheat shoots after 4 min after spraying the spores of the fungus. Before the start of the experiment, the plants were placed in a climatic chamber. The air intake tubes of gas analyzers were placed above the

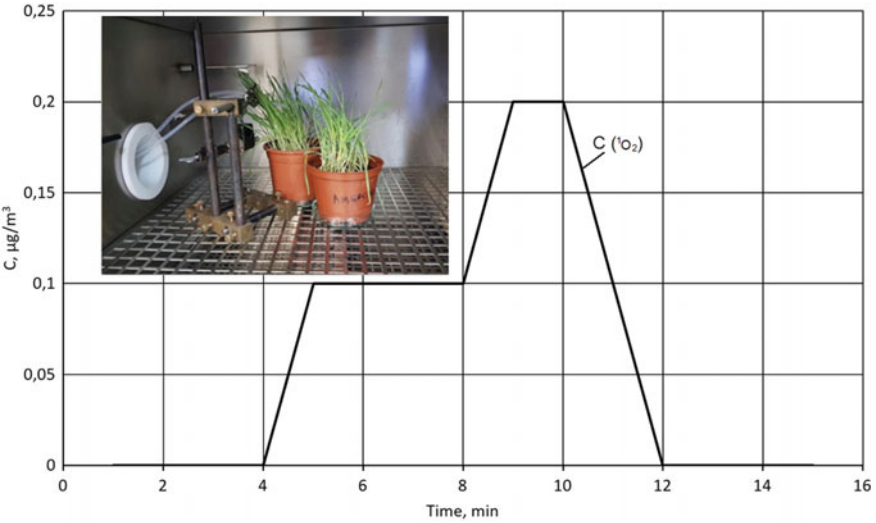


Fig. 8.9 Changes in the concentration (C) of singlet oxygen near wheat seedlings after infection with spores of the fungus *Cochliobolus sativus*. The inset in the graph shows a photograph of plants and air intake hoses in the climate chamber

surface of the plants. The experiments were conducted to study the formation of induced immunity by higher plants for agricultural purposes (Chelibanov 2018).

Testing the effectiveness of photocatalytic coatings developed to protect monuments from biodegradation

The $^1O_2$ gas analyzer was also used to test photocatalytic coatings (Marugin et al. 2005; Chelibanov et al. 2019). It should be noted that due to climatic changes, the processes of biological destruction of various constructions (Warscheid and Braams 2000), including monuments made of stone (of carbonate rocks in particular), accelerated substantially and took on new forms. Traditionally, chemical biocides are used to protect against biodegradation—quaternary ammonium compounds, organotin compounds, organosilicon compounds. In new climatic conditions, these biocides have to be used in large quantities that are dangerous to the environment. In addition, their inhibitory effect on the microbial community is short, and their regular use can lead to the emergence of new, even more aggressive biological species.

An alternative are biocides based on reactive oxygen forms. They are produced as a result of a photocatalytic effect in a coating containing a nano-dispersed photocatalyst, as follows (Fig. 8.10). In the crystalline particle of the photocatalyst, free charge carriers, electrons and holes, appear as a result of the action of photons hυ. Electrons join the adsorbed O_2 molecules. Excited superoxide anions O_2^{*-} are formed. In dry conditions, the holes neutralize the O_2^{*-} anions, forming a biocidal $^1O_2$. In the presence of water containing H^+ cations, the O_2^{*-} anions are dismuted into biocides—hydrogen peroxide and HO^* hydroxyl-radical.

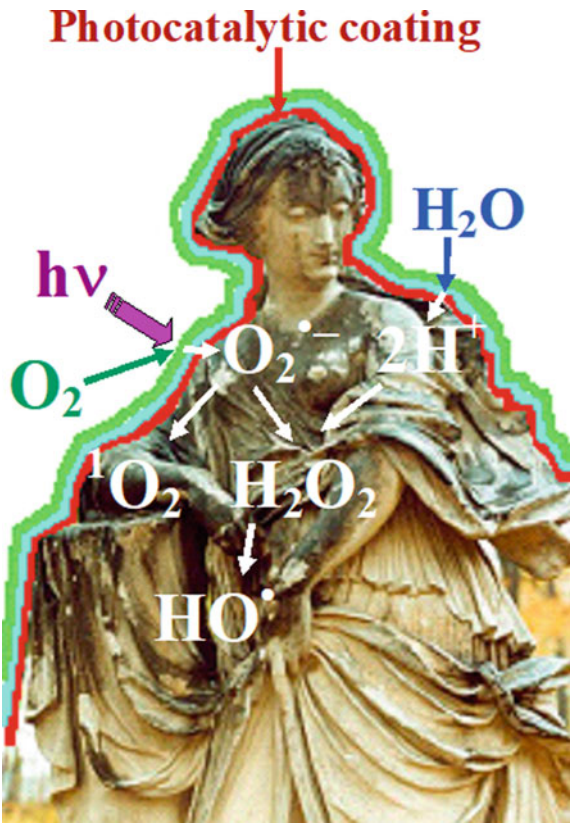


Fig. 8.10 The scheme of photocatalytic protection of monuments from biodeterioration

The advantage of photocatalytic coatings in addition to biocidity is their self-purification from the products of the metabolism of microorganisms. Due to the diversity of climatic conditions, types of biodestructors and materials of monuments, the development of suitable photocatalytic coatings is a complex task that requires testing of numerous variants. There are several methods of testing photocatalysts proposed by the standards ISO 10676, ISO 10677, ISO 10678, ISO 27447, ISO 27448. The methods are based on registration of the changes of certain parameters of the reference substances in contact with photocatalysts. The implementation of these techniques is very time consuming (Mills et al. 2012). Figure 8.11 shows a device that reduces the process of photocatalysts testing to several minutes and just measures the concentration of $^1O_2$ in the air flow pumped over the photocatalytic coating. The same device was also used to test hydroxyapatite powder photocatalytic composites (Khamova et al. 2018). In this case, the equivalent weights of the developed photocatalysts were embedded into the porous fluoroplastic membrane. The photocatalytic activity of the composites was determined as a ratio to the industrial sample of the photocatalyst Aeroxide TiO_2 P 25.

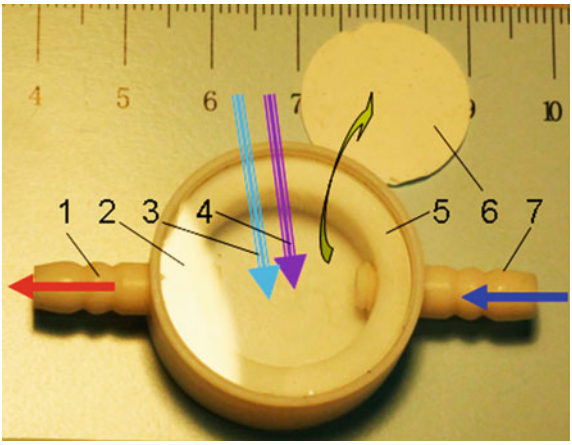


Fig. 8.11 The device for testing of photocatalysts: **1** outlet fitting for $^1O_2$ gas analyzer connection; **2** quartz window; **3**, **4** light beams of a different spectrum; **5** casing **6** photocatalyst sample; **7** inlet fitting for connection to the air conditioning system

8.4 Conclusion

These studies demonstrate wide possibilities of the $^1O_2$ gas analyzer for solving a wide range of fundamental and applied problems associated with the processes and phenomena at the boundary between biogenic and abiogenic nature. The undoubted advantages of the developed device are: high selectivity and sensitivity, high dynamic range, as well as low response time. It is also important to note that the device is easy to use and does not require highly qualified service. It is advisable to use it to monitor the air environment and test surfaces that activate redox reactions.

As shown by the results of air monitoring in St. Petersburg and Priozersk areas using the equipment complex SKAT (Chelibanov et al. 2019), the main sources of $^1O_2$ in the lower atmosphere determining its background concentrations are photochemical ozone decomposition and the interaction of ozone with some natural and anthropogenic air pollutants. Vegetation and snow cover make a significant contribution to the content of $^1O_2$ in the near-surface layer of the atmosphere. According to the results of the registration of $^1O_2$ near plants, which were under stress, it can be concluded that singlet oxygen has an important communicative value for biology. Spatio-temporal distribution of $^1O_2$ significantly depends on meteorological and environmental conditions. From the analysis of the literature data, it can be assumed that the presence of singlet oxygen in low concentrations in the near surface atmosphere plays, in general, a positive role for human health. Its dosed medical application is more physiological and natural than the use of ozone.

References

Adam W, Kazakov DV, Kazakov VP (2005) Singlet-oxygen chemiluminescence in peroxide reactions. Chem Rev 105(9):3371–3387

Bartusik D, Aebisher D, Lyons AM, Greer A (2012) Bacterial inactivation by a singlet oxygen bubbler: identifying factors controlling the toxicity of $^1O_2$ bubbles. Environ Sci Technol 46(21):12098–12104

Belashov AV, Beltyukova DM, Vasyutinsky OS, Petrov NV, Semenova IV, Chupov AS (2014) Registration of spatial distributions of singlet oxygen in water by the holographic method. Pisma v GTF 40(24):94–98 (in Russian)

Boreskov GK (1982) Catalytic activation of dioxygen. In: Andersen J, Boudait M (eds) Catalysis: science and technology. Springer, Berlin-Heidelberg-New-York, pp 39–137

Boreysho AS (2005) High-power mobile chemical lasers. Quantum Electron 35(5):393–406

Bower JP, Anastasio C (2013) Measuring a 10,000-fold enhancement of singlet molecular oxygen ($^1O_2$*) concentration on illuminated ice relative to the corresponding liquid solution. Atmos Environ 75:188–195

Chandler DW, Houston PL (1987) Two-dimensional imaging of state-selected photodissociation products detected by multiphoton ionization. J Chem Phys 87(2):1445–1447

Chelibanov IV (2018) Features of the formation of reactive oxygen species in wheat leaves under the influence of phytopathogens and immunity inducers. Final qualifying work. Herzen University, St. Petersburg, pp 1–55 (in Russian)

Chelibanov VP, Chelibanova MG (2010) Procedure and device for detecting singlet oxygen Patent RU2415401-C1

Chelibanov VP, Zykova IA (2017) Analytical devices for ecology, industry and scientific research. Catalog 2017 Saint Petersburg, p 33 (in Russian) http://www.optec.ru/images/optec_catalog_2017.pdf

Chelibanov VP, Marugin AM, Sazanova KV, Abakumov EV, Vlasov DY, Manurtdinova VV, Frank-Kamenetskaya OV (2019) Outdoor environment of the monuments in the Necropoleis. In: Frank-Kamenetskaya OV, Vlasov DY, Rytikova VV (eds) The effect of the environment on Saint Petersburg' s cultural heritage: results of monitoring the historical necropolis monuments. Springer Nature Switzerland AG, pp 45–74

Clark ID, Wayne RP (1970) The absolute cross section for photoionization of O_2 ($^1\Delta_g$). Mol Phys 18(4):523–531

Daimon T, Nosaka Y (2007) Formation and behavior of singlet molecular oxygen in TiO_2 photocatalysis studied by detection of near-infrared phosphorescence. J Phys Chem C 111(11):4420–4424

DeRosa MC, Crutchley RJ (2002) Photosensitized singlet oxygen and its applications. Coord Chem Rev 233:351–371

Falick AM, Mahan BH, Myers RJ (1965) Paramagnetic resonance spectrum of the $^1\Delta_g$ oxygen molecule. J Chem Phys 42(5):1837–1838

Farkhutdinova LM (2015) Oxidative stress. History of research. The Herald of the ASRE 20(1):42–49 (in Russian)

Golovanova OA, Frank-Kamenetskaya OV, Punin YO (2010) Features of pathogenic mineral formation in the human body. Russ Chem J 54(2):124–136 (in Russian)

Grannas AM, Jones AE, Dibb J, Ammann M, Anastasio C, Beine HJ, Bergin M, Bottenheim J, Boxe CS, Carver G, Chen G, Crawford JH, Dominé F, Frey MM, Guzmán MI, Heard DE, Helmig D, Hoffmann MR, Honrath RE, Huey LG, Hutterli M, Jacobi HW, Klán P, Lefer B, McConnell J, Plane J, Sander R, Savarino J, Shepson PB, Simpson WR, Sodeau JR, von Glasow R, Weller R, Wolff EW, Zhu T (2007) An overview of snow photochemistry: evidence, mechanisms and impacts. Atmos Chem Phys 7:4329–4373

Hulten LM, Holmstrem M, Soussi B (1999) Effect of singlet oxygen energy on reactive oxygen species generation by human monocytes. Free Radic Biol Med 27(11/12):1203–1207

Iasenko EA, Chelibanov VP, Marugin AM, Kozliner M (2016a) Monitoring of singlet oxygen in the lower troposphere and processes of ozone depletion. In EGU2016 General Assembly Conference Abstracts, vol 18, p 12947

Iasenko EA, Chelibanov VP, Frank-Kamenetskaya OV, Nesterov EM, Marugin AM (2016b) Simultaneous monitoring of ozone and singlet oxygen in the low troposphere In: Proceedings of International Seminar: GEOLOGY, GEOECOLOGY, EVOLUTIONAL GEOGRAPHY 2016 Nesterov EM, Snytko VA, Makhov SI. Eds. St Petersburg Herzen University 15:224–227

Jacob C, Winyard PG (eds) (2009) Redox signaling and regulation in biology and medicine, p 514. Wiley

Jones ITN, Bayes KD (1973) Formation of O_2 ($a\,^1\Delta_g$) by electronic energy transfer in mixtures of NO_2 and O_2. J Chem Phys 59(6):3119–3124

Jones ITN, Wayne RP (1969) Photolysis of ozone by 254-, 313-, and 334-nm radiation. J Chem Phys 51(8):3617–3618

Kearns DR (1971) Physical and chemical properties of singlet molecular oxygen. Chem Rev 71(4):395–427

Khamova TV, Frank-Kamenetskaya OV, Shilova OA, Chelibanov VP, Marugin AM, Yasenko EA, Kuz'mina MA, Baranchikov AE, Ivanov VK (2018) Hydroxyapatite/anatase photocatalytic core-shell composite prepared by sol-gel processing. Crystallogr Rep 63(2):254–260

Khan AU (1991) The discovery of the chemical evolution of singlet oxygen. some current chemical, photochemical, and biological applications. Int J Quantum Chem 39:251–267

Khan SR (2013) Reactive oxygen species as the molecular modulators of calcium oxalate kidney stone formation: evidence from clinical and experimental investigations. The Journal of urology 189(3):803–811

Krasnovsky AA (1993) Detection of photosensitized singlet oxygen luminescence in systems of biomedical importance. steady-state and time-resolved spectral measurements based on application of s − 1 photomultiplier tubes. Proc SPIE 1887:177–186

Krasnovsky AA Jr (2018) Singlet molecular oxygen: early history of spectroscopic and photochemical studies with contributions of AN Terenin and Terenin's school. J Photochem Photobiol, A 354:11–24

Krinsky NI (1977) Singlet oxygen in biological systems. Trends Biochem Sci 2(2):35–38

Kruk I, Michalska T, Kladna A, Aboul-Enein HY (2002) Spin trapping study of reactive oxygen species formation during bopindolol peroxidation. Biopolym Original Res Biomol 65(2):89–94

Larson RA, Marley KA (1999) Singlet oxygen in the environment. In: Environmental photochemistry, pp. 123–137. Springer, Berlin, Heidelberg

Lelieved J, Dentener FJ (2000) What controls tropospheric ozone. J Geophys Res Atmos 105(D3):3531–3551

Martusevich AK, Kovaleva LK, Martusevich AA, Makarov AP (2015) The effect of a long course of inhalation of singlet oxygen on the crystallogenic properties of blood serum. Vrach-aspirant 73(6.1):186–191 (in Russian)

Marugin AM, Arkhipova MA, Dolmatov VY, Shilova OA, Vlasov DY, Chelibanov VP, Fujimura T (2005) The possibilities of photocatalic biocides application in preservation of cultural heritage. In: Proceedings of International Conference SREN 2005. Comenius University, pp 130–132

Mills A, Hill C, Robertson PKJ (2012) Overview of the current ISO tests for photocatalytic materials. J Photochem Photobiol, A 237:7–23

Min DB, Boff JM (2002) Chemistry and reaction of singlet oxygen in foods. Compr Rev Food Sci Food Safet 1(2):58–72

Mikheikin ID, Vorontsova IK, Abronin IA (2002) Reactivity of molecular oxygen on the surface of ionic crystals. Int J Quantum Chem 88(4):489–495

Minaev BF (2007) Electronic mechanisms of activation of molecular oxygen. Russ Chem Rev 76(11):988–1010

Morita A, Werfel T, Stege H, Ahrens C, Karmann K, Grewe M, Grether-Beck S, Ruzicka T, Kapp A, Klotz L-O, Sies H, Krutmann J (1997) Evidence that singlet oxygen-induced human T

helper cell apoptosis is the basic mechanism of ultraviolet-a radiation phototherapy. J Exp Med 186(10):1763–1768

Muñoz F, Mvula E, Braslavsky SE, von Sonntag Clemens (2001) Singlet dioxygen formation in ozone reactions in aqueous solution. J Chem Soc Perkin Trans 2:1109–1116

Naus H, Ubachs W (1999) Visible absorption bands of the (O_2) 2 collision complex at pressures below 760 Torr. Appl Opt 38(15):3423–3428

Ogawa S, Fukui S, Hanasaki Y, Asano K, Uegaki H, Sumiko F, Ryosuke S (1991) Determination method of singlet oxygen in the atmosphere by use of α-terpinene. Chemosphere 22(12):1211–1225

Ovechkin AS, Reingeverts MD, Kartsova LA (2015) GC determination of singlet oxygen using α-terpinene. Sorpt Chromatogr Process 15(1):35–41 (in Russian)

Pitts JN Jr, Khan AU, Smith EB and Wayne RP (1969) Singlet oxygen in the environmental sciences. Singlet molecular oxygen and photochemical air pollution. Environ Sci Technol 3(3):241–247

Pitts JN (1970) Singlet molecular oxygen and the photochemistry of urban atmospheres. Ann N Y Acad Sci 171(1):239–272

Poljsak B, Šuput D, Milisav I (2013) Achieving the balance between ROS and antioxidants: when to use the synthetic antioxidants. Hindawi Publishing Corporation (Article ID 956792) Oxidative medicine and cellular longevity 2013:1–11

Razumovsky AV, Martusevich AK, Martusevich AA (2016) Experimental study of the rehabilitation possibilities of inhalations of singlet oxygen in the postburn period. Bioradikaly i antioksidanty 3(3):82–84 (in Russian)

Rodgers MA (1983) Solvent-induced deactivation of singlet oxygen: additivity relationships in nonaromatic solvents. J Am Chem Soc 105(20):6201–6205

Romanov AN, Rufov YuV (1998) Highly sensitive chemiluminescent method of recording singlet oxygen in the gas phase. Russ J Phys Chem 72(9):2094–2097 (in Russian)

Schweitzer C, Schmidt R (2003) Physical mechanisms of generation and deactivation of singlet oxygen. Chem Rev 103(5):1685–1758

Steinbeck MJ, Khan AU, Karnovsky MJ (1993) Extracellular production of singlet oxygen by stimulated macrophages quantified using 9,10-diphenylanthracene and perylene in a polystyrene film. J Biol Chem 268(21):15649–15654

Sysoeva TI, Petkun AS, Kuchin VA, Chelibanov VP (2016) The results from ten years of measuring several parameters of the antarctic atmosphere with tethered balloons. Bull Russ Acad Sci Phys 80(5):541–544 (in Russian)

Vlasov DY, Parfenov VA, Zelenskaya MS, Plotkina YV, Geludova VM, Frank-Kamenetskaya OV and Marugin AM (2019) Methods of monument protection from damage and their performance in the effect of the environment on Saint Petersburg's cultural heritage: Results of monitoring the historical necropolis monuments. In: Frank-Kamenetskaya OV, Vlasov DY, Rytikova VV (eds) Springer Nature Switzerland AG, pp 161–178

Warscheid Th, Braams J (2000) Biodeterioration of stone: a review. Int Biodeterior Biodegrad 46(4):343–368

Wayne RP (1994) Singlet oxygen in the environmental sciences. Res Chem Intermed 20(3–5):395–422

Wu H, Song Q, Ran G, Lu X, Xu B (2011) Recent developments in the detection of singlet oxygen with molecular spectroscopic methods. TrAC Trends Anal Chem 30(1):133–141

Young RA, Black G (1967) Deactivation of O (1 D). J Chem Phys 47(7):2311–2318

Zakharov SD, Korochkin IM, Yusupov AS, Bezotosny VV, Cheshev EA, Frantzen F (2014) Application of diode lasers in light-oxygen cancer therapy. Semiconductors 48(1):123–128

Zavyalov SA, Myasnikov IA (1981) Study of the emission of singlet oxygen molecules from the surface of solids by the method of semiconductor detectors. Doklady Acad Sci USSR 257(2):392–396 (in Russian)

Chapter 9
Determination of Water-Soluble Fraction in Soils



Elena G. Panova, Kseniia A. Bakhmatova, Natalia N. Matinian and Galina A. Oleynikova

Abstract Method of allocation and analysis of mobile forms of chemical elements in soil are considered. Chemical characteristics of the extracted liquid phase of the soil reflect its water-soluble part properties. Two reference soil profiles on glacio-lacustrine clays (soddy-eluvial-metamorphic soil) and sands (soddy podzol) were investigated on the Russian Plain. The comparison of the data obtained with the results of analysis for the whole soil allows assessment of a share of highly mobile and less mobile forms of chemical compounds. The behavior of macro- and microelements was studied in soils and their liquid phase. Mobile forms of chemical elements play the important role as the basis for the development of a model describing their migration on soil profile, used in prospecting geochemistry and in environmental geochemistry.

Keywords Soddy-podzol (Albic Podzol) · Soddy-eluvial-metamorphic soil (Stagnosol) · Soil chemistry–Water-soluble fraction

9.1 Introduction

Many studies demonstrated that soil liquid phase plays an important role in soil formation and function, by enabling a multitude of chemical and biological transformations of organic and mineral compounds in water soil solution (Sparks 1989; Sposito 1989; Bockheim and Gennadiev 2000; Cornu et al. 2014; Van den Bogaert et al. 2016). Water-dispersible and water-soluble soil components are capable of migration are attracting particular attention (Moreno-Jimenéz et al. 2011; Lin et al. 2016; Imoto et al. 2018). Moreover, the bioavailability and toxicity of the metals in polluted soils depends on free metal ion concentrations in the water contained within the pores of the soil (Cancès et al. 2003), with the solid phase acting as an

E. G. Panova (✉) · K. A. Bakhmatova · N. N. Matinian
Saint Petersburg State University, Saint Petersburg, Russia
e-mail: e.panova@spbu.ru

G. A. Oleynikova
Russian Geological Research Institute, Saint Petersburg, Russia

© Springer Nature Switzerland AG 2020

O. V. Frank-Kamenetskaya et al. (eds.), *Processes and Phenomena on the Boundary Between Biogenic and Abiogenic Nature*, Lecture Notes in Earth System Sciences,
https://doi.org/10.1007/978-3-030-21614-6_9

ion exchanger and frame for ion migration (Orlov 1985; Karavanova and Timofeeva 2009; Trofimov and Karavanova 2009).

The soil solution contains both dissolved elements, as well as the components bound to nanoparticles and colloids (Weihrauch and Opp 2018). The importance of colloid fraction (1 nm–1 μm in size) for mobilization of chemical elements and their transport in soils is been well documented. Behavior of soil colloids received special attention because of their capability to facilitate the transport of nutrients (e.g. P), as well, as of heavy metals, pesticides and other contaminants (El-Farhan et al. 2000; de Jonge et al. 2004; Siemens et al. 2004; Van Oort et al. 2006; Shein and Devin 2007; Klitzke et al. 2008; Bin et al. 2011; Séquaris et al. 2013). Karavanova and Timofeeva (2009) studied the distribution of chemical elements in soil solution in pores of different sizes, and demonstrated that concentrations of Al, Fe, Mn, Pb, Ni, V, Ba and a number of other elements were 1.5–3.5 times (up to 60 times for some cases) lower in the macropores than in the micropores. The ratio of elements' concentrations between those the soil water solution and those contained within the solid phase of the soil matrix in the macro- and micropores differed by several orders of magnitude.

Over the last two decades, development of analytical techniques like ICP-MS or X-ray radiometric method, spurred extensive investigations of rare earth elements' content and behavior in soils. Most In soils, rare earth elements (REE; includes lanthanide group as well as scandium and yttrium) are typically observed in the 3^+ oxidation state The exceptions are cerium that can form, compounds with the 4^+ oxidation state, europium and ytterbium that both form stable compounds with the 2^+ oxidation state.

The abundance of REE in soils and patterns of their distribution in different soil types were the subject of multiple studies (Wang et al. 2001; Kabata-Pendias and Mukherjee 2007; Vodyanitskii et al. 2011; Perelomov et al. 2012; Chen et al. 2014; Mihajlovic et al. 2014; Vermeire et al. 2016). REE distributions are presently considered as tracers of weathering and pedogenic processes (Aide and Smith-Aide 2003; Harlavan et al. 2009; Laveuth and Cornu 2009; Vermeire et al. 2016). Clarke values of REE in soil is small (a total of 1×10^{-2}%). Relatively high REE content is observed in acidic and alkaline igneous rocks and it is reduced in basic and ultrabasic rocks (Perelman 1989).

REE content in soils depends on a large number of factors, such as the composition and properties of soil-forming rocks, the degree of weathering of minerals, the genesis of soils, the content of clay minerals and organic matter, the nature and level of anthropogenic loads, etc. (Gouveia et al. 1993; Prudencio et al. 1993; Minarik et al. 1998; Land et al. 1999; Aide and Smith-Aide 2003). It was shown that it depends on the mineralogy of parent material (Brioschi et al. 2013). Absorption of REE on clay minerals and amorphous Fe–Mn oxides as well as formation of phosphate or organic complexes all impact the geochemical fractionation and mobility of REE, with the mobility tending to increase with decreasing pH (Mihajlovic et al. 2014). Previous studies have shown the depletion of REE in eluvial and their accumulation in illuvial horizon (Tyler 2004; Vodyanitskii et al. 2011). Weathering of clay minerals, iron and manganese hydroxides and dissolution of iron and manganese phosphates

causes a decline in REE content the eluvial horizon. The crucial role particle-size distribution plays in REEs' concentration distribution in soil profile had also been reported (Mihajlovic et al. 2014).

The analysis of the content of rare earth elements in different soils of the world leads to the conclusion that, despite the geographical diversity of the regions, most of the studied soils have comparable concentrations of the REE, indicating REE's relative chemical inertness in the course of pedogenesis and the absence of significant contributions from anthropogenic sources. However, most of the known data on the REE content covers their location only in the upper soil horizon, without consideration of the possible impact on the distribution of these elements by soil formation processes. In addition, the question of the precise forms of REE in soils and the determination of potentially mobile elements involved in the formation of soil profiles on different types of parent rocks remains controversial. Of particular interest is the study of REE concentrations in soils of areas remoted from possible sources of emission of trace elements, areas, where anthropogenic influence is minimized.

There is currently no universally accepted methodology to extract soil liquid phase (Adams et al. 1980; Orlov 1985; Kaplan et al. 1993; Malinina and Motuzova 1994; Giesler et al. 1996; Essington 2004; Trofimov and Karavanova 2009). The first attempts to isolate and analyze soil solution were made by Saussure in the early nineteenth century. Nowadays, there are 3 groups of procedures to sample the soil aqueous phase: (1) displacement of soil solutions with alcohol or other immiscible liquid; (2) lysimetric methods (without application of pressure); and (3) methods using positive or negative pressure (pressing, centrifugation, extraction with gas under pressure, vacuum-filtration).

Dobrovol'skii et al. (1997) have developed a methodology of extracting water-soluble forms of metals and the fraction of metals bound to humic acids. Electrodialysis was applied on the obtained dialysate to separate the soluble forms of metals into two groups: those that are positively or negatively charged and electroneutral. It was also used for determination of charged metals' proportion in ion-phoretic OE-101 Labor device. While quantitative data on metal content can be obtained using atomic absorption spectrometry, a great number of procedures allowed only for semi-quantitative results.

In another approach deionized water was used for obtaining water-dispersible soil colloids with soil to water ratio of 1:20 (Seta and Karathanasis 1996) or of 1:10 (Yan et al. 2017). Here, soil samples were shaken for 12–24 h, soil suspensions were then centrifuged at 750 rpm for 3.5 min and decanting to collect the <2 μm clay fraction (Seta and Karathanasis 1996) or sequential centrifugations were done for fractionation of dispersed colloids into three size fractions—<0.1, 0.1–0.45 and 0.45–1.0 μm (Yan et al. 2017). Seta and Karathanasis (1997) also suggested a method of isolating colloids based on the analysis of elements in the filtrate using a Microplate Reader (Bio-Tec EL 311). The sensitivity of this analysis was insufficient to detect many of the elements with low soil concentrations.

Thus, despite the well-established general concepts of mobile and fixed forms of elements in soil and of the methods of their extraction, there is a lack of experimental

quantitative data, which would allow analysis of the behavior of mobile forms of many macro- and microelements in the soil.

The aims of this study were to develop a methodology for the isolation of soil solution to determine the content of microelements at the low level of their detection, and to study the distribution of chemical elements in the liquid phase of two contrasting widespread types of soils on glaciolacustrine deposits typical for Northwest Russia.

9.2 Objects and Methods

Two widespread types of soils on glaciolacustrine deposits in Northwest Russia were selected for the study of the behavior of chemical elements in the soil profiles. Research areas were selected to be far from cities and local sources of technogenic pollution.

Soil description The gleyic soddy eluvial-metamorphic soil (Retic Albic Stagnosol (Clayic)) on varved clays (Classification and Diagnostic System of Russian Soils 2004; IUSS Working Group WRB 2014) is formed under forest, and its profile is represented by the following horizons: O–AYg–ELg–BELg–BMg1–BM2–BC–C. This soil is characterized by the accumulative type of humus profile distribution, fulvate type of humus, acid reaction in the upper horizons, and well-pronounced eluvial distribution of clay. The texture of the eluvial (AYg, ELg, and BELg) and metamorphic (BMg1 and BM2) horizons differs from that of the parent material by the lower content of clay fraction. Strong excessive moistening of the upper horizons and acidification of the soil result in the mobility of many elements with variable valence, especially iron and manganese. The determination of various iron and aluminum compounds in the soil using the Tamm method shows maximum content of mobile iron (mineral–amorphous and weakly crystallized in the ELg horizon), where the gley process is especially well pronounced. The maximum content of mobile aluminum is observed in the eluvial horizons. The predominant clay minerals are dioctahedral illites and mixed-lattice clay minerals of the illite–smectite type; the participation of kaolinite and chlorite is limited. The mixed-lattice clay minerals accumulate in the upper horizons as a result of surface gleization (Gagarina et al. 1995; Matinyan 2003).

The sandy iron-illuvial soddy-podzol (Albic Podzol) has been formed under a pine forest on lacustrine glacial sands with good surface and internal soil drainage. The soil comprises the gray-humus (AY), whitish podzolic (E), brown and ocherous illuvial (Al–Fe humus) horizons (BF1–BF2) merging into the BC–C horizons. Despite some similar features (acid reaction, fulvate humus), this podzol differs from the clayey soil in the low cation exchange capacity and low base saturation, as well as in somewhat elevated organic matter content in the iron-illuvial horizon. The distribution of iron and aluminum in the soil profile has a well-marked eluvial–illuvial character: intense leaching of silicate and non-silicate iron and aluminum from the upper horizons and

their accumulation in the illuvial ones. Amorphous compounds bound with organic matter play a significant role in the illuvial part of the soil profile.

Analysis of the water-soluble soil fraction Water-soluble soil fraction consists of colloidal particles and ions, with the typical colloidal particle size of less than 1 μm. To obtain reliable results, conditions should be chosen at which colloid particles would almost completely pass into the disperse medium (forming the disperse phase) and the solution would remain stable (without sedimentation) for a time sufficient for analysis.

General considerations: The first task is to isolate water-soluble fraction (WSF) from the soil mineral matrix. The second task is to upgrade ICP MS methods for detection of low concentrations of elements. Some relevant approaches can be taken from the geochemical methods of studying the mobile forms of chemical elements that were earlier proposed (Sokolov et al. 2005; Putikov 2008) and used in geochemical mineral exploration (methods of jet halation, partial extraction of metals, and diffuse isolation of elements, mobile metal–organic components, and analysis of superfine fraction).

Separation of particles with the size less than 1 μm can be achieved by establishing specific conditions for nanoparticles in water so they can form colloid solutions, which are stable for a long time. Then, it is possible to separate colloid particles from water using either different coagulants or by means of ultra-centrifugation. Appliance of filters with pores of 1 μm for filtration, allows for the control of the upper particle size, resulting in a solution with only sizes within the nm—to 1 μm range. The bulk of substance in the analyzed solution can be determined by weighing method through evaporation of water from an aliquot of the sample solution (Oleinikova and Panova 2007).

Water treatment of soils samples should be done under special conditions required to ensure a complete transfer into solution of all forms of chemical elements with the particle size up to 1 μm. Particles with the size more than 1 μm are removed by filtration through porous filter, then in the solution only colloid particles and the substance in ionic form (soluble salts) remain. Analysis of WSF solutions was carried out by ICP MS method at «ELAN-6100 DRC», PERKIN ELMER.

Optimized extraction method was developed to include the use of: (1) deionized water of maximal purification as a disperse medium; (2) soil to water ratio (1:10) promoting the stabilization of colloid solution and preventing the coagulation of particles; (3) the weight of samples of not less than 30 g, in order to provide the uniform distribution of chemical elements in the soil sample; (4) hot water (<90 °C) to promotes the dissolution of salts and transfer of particles to the colloidal state; (5) periodical mixing of the soil with water for 6 h (forming the gradient of the transfer of particles and salts from the solid phase to liquid one); (6) sedimentation for 24 h from the beginning of the experiment (promoting the stabilization of the colloid-salt solution and precipitation of relatively coarse particles forming the suspension); (7) filtration of the solution using a Sartorius membrane fiberglass filter (1 μm); (8) analysis of the solution by mass spectrometry with inductively coupled plasma in the certified chemical analytical laboratory of the All-Russian Geological Institute.

Experiments on separation of soil water-soluble fraction (WSF) demonstrated that its amount is in the range of 0.1 6 wt%. For the analysis of the soil as a whole, a sample was dissolved using the traditional methodology (total chemical analysis). The conditions chosen for the experiment provided high reproducibility of the analytical results and the ability to determine a wide spectrum (up to 75) of chemical elements. The low detection limits were implemented by the use of ultrapure water as a solvent, which does not dissolve the soil matrix. The analysis of the water solutions allows for optimum utilization of the inductively coupled plasma mass spectrometry method. The absence of acids and other solvents prevents the possibility of uncontrolled isobaric overlaps, which leads to a decrease in detection limits of the elements. Developed method WSF extraction allowed for marked and reproducible enrichment of the samples with elements of interest as compared to common methods, which allowed for improved reproducibility of the analysis and decreased detection errors for good. Performed experiments showed the possibility to lower the detection limits of chemical elements by 2–3 orders of magnitude when analyzing water-soluble soil phase as compared to the similar limits in the total soil analysis, especially for rare elements that are present in soils in trace quantities. The detection limits (soil/WSF of soil, mg/kg) were as follows: U—0.01/0.00002; Tl—0.03/0.00006; Mo—1.0/0.0002; Cd—0.1/0.0006; Hg—0.005/0.0005; Se—0.5/0.01, Te—10/0.002; Sb—0.1/0.0006; Bi—0.2/0.0001; As—0.6/0.001; Zn—1/0.01; Ni—1/0.05; Co—0.5/0.01; Cu—1/0.05; Pb—1/0.05; In—0.01/0.0002; Pt—0.04/0.0004, Pd—0.03/0.0006, Au—0.002/0.0002; Ag—0.05/0.0001; Re—0.03/0.0001; Sc—0.1/0.0006; Ge—0.03/0.0006; Ga—0.05/0.0002; Sc—0.15/0.0006; In—0.01/0.0002; etc.

9.3 Results and Discussion

The proportion of WSF in the soils was determined by weight method from an individual aliquot after the evaporation. In the case of studied soils it was 0.1–1.7 wt% (Table 9.1). The obtained colloid solution was colorless, transparent, and responded to the Tyndall test.

Table 9.1 Water-soluble fraction in soil samples (wt%)

Clayey soil		Sandy soil	
AYg	0.63	0.1	AY
Elg	0.98	0.5	E
BMlg	0.84	0.39	BF1
BM2	0.83	0.34	BF2
BC	1.28	0.82	BC
C	1.65	1.0	C

The analysis of the solution using a Nanosize analyzer showed that the modes for colloid particles in the sandy and clayey soils were 668.2 and 575.1 nm, respectively.

The concentrations of chemical elements in the water-soluble fraction and in the whole soil samples, from which it was isolated, are presented in Tables 9.2, 9.3, 9.4 and 9.5. Complete analysis of rock-forming oxides and micro-elements in WSF demonstrated that rock-forming components make up at least 90 wt% as anticipated, with micro-elements contributing no more than 10 wt%. That was true for both macro- and micro-soil elements.

Particularly significant differences in the proportion of fixed and mobile forms of chemical elements were observed in the sandy soil, probably due to its greater pore space. In the clayey soil, the share of fixed forms of macro- and microelements was high; in the sandy soil, mobile forms predominated.

To determine the mobility's degree of chemical elements, a coefficient of accumulation (CA), in WSF, defined as the ratio of element concentration in WSF to its concentration in the whole soil sample, was calculated (Table 9.6). Thus, coefficient of accumulations reflects the enrichment of WSF in chemical elements, with its value dependent on the soil type and the horizon. For sandy soil profile the highest coefficients were observed for Ni, Sc, Zn, Mo. In the clayey soil the observed coefficients were significantly lower than that in the sandy soil (less than 11 compared to over 700 for some elements, with the highest values for Zn, Sc, Ag, Mo). No significant enrichment for WSF was observed. A relatively high migration capacity was observed for Zr and Cr, that were weakly mobile in the zone of supergene weathering.

The chemical differences in soil profiles and WSF is shown in Figs. 9.1 and 9.2. Among the petrogenic oxides the following are prominent: Al_2O_3, Fe_2O_3, CaO, K_2O, TiO_2, P_2O_5. Among the trace elements the most contrast data are obtained for: Ag, Cu, Sc, Zn, Ni. In all the horizons of the clayey soil, the share of WSF is greater than in the sandy soil. This fact can be explained by the higher content of fine-dispersed particles, including the colloidal ones. In both soil profiles, WSF share increased from the (AY/AY_g) horizon to eluvial or podzolic horizons for respective soil types, then decreased in the BF and the BM, and again increased in BC and C. When recalculating the total amount of elements in the WSF relative to the total soil mass, a tendency of the depletion of the soils in mobile elements compared to the parent rock was revealed. However, in sandy soil, Sc and Ni were present mainly in the mobile form. In that soil, the proportion of mobile chemical elements was high, while in clayey soil, their share was much lower. In both profiles, the Sc, Zn, Mo and Ag had the highest mobility.

Ni, Co, Pb, Cd, and Sb were observed in soddy podzol soils in addition to the above-mentioned elements. While in clayey soil, the maximum content in WSF was observed in BC and C horizons, in sandy soils, the pattern of water-soluble element distribution was more complicated. There, along with the group of elements exhibiting the eluvial type of distribution, were elements that were maximally accumulated in the E (Sc, Ni, Co, Pb, and Cu) and humus horizons (Ag, Mo, and Zn). In the AY horizon of the clayey soil, higher water solubility was characteristic only for Zn, Ca, Sc, Mo, and Ag; in the sandy soil, a spectrum of mobile elements was much broader. In the EL horizon, the mobility of a number of elements was higher as compared

Table 9.2 Macro elements in the clayey soil profile (%) and its water-soluble fraction (WSF), mg/L

Soil profile	SiO_2		TiO_2		Al_2O_3		Fe_2O_3		MnO	
	Soil	WSF	Soil	WSF	Soil	WSF	Soil	WSF	Soil	WSF
AYg	72.5	0.14	0.81	0.035	12.74	0.33	5.65	0.48	0.17	0.14
Elg	73.5	0.42	0.67	0.39	11.01	4.15	4.75	4.38	0.11	0.22
BMlg	70.1	1	0.74	1.04	15.31	12.1	6.15	8.16	0.09	0.13
BM2	65.2	1.01	0.68	1.02	13.11	11.3	5.17	8.92	0.07	0.12
BC	65	1	0.79	1.04	14.68	10.8	6.08	8.2	0.09	0.12
C	64.9	0.98	0.84	0.74	16.46	9.97	7.18	6.77	0.08	0.071
Soil horizon	CaO		MgO		Na_2O		K_2O		P_2O_5	
	Soil	WSF	Soil	WSF	Soil	WSF	Soil	WSF	Soil	WSF
AYg	1.24	2.22	1.08	0.8	1.09	0.25	3.11	0.22	0.16	0.045
Elg	0.97	1.61	0.73	0.82	1.22	0.47	2.91	0.4	0.13	0.099
BMlg	0.99	1.24	1.92	2.25	1.12	0.69	3.37	1.05	0.13	0.1
BM2	1.13	1.48	1.32	2.19	1.18	0.77	3.07	0.99	0.12	0.13
BC	1.13	1.35	1.69	2.27	1.13	1.02	3.28	0.96	0.14	0.11
C	1.15	1.15	2.18	2.21	1.01	0.79	3.51	0.91	0.14	0.09

Table 9.3 Micro elements in the clayey soil profile (mg/kg) and its water-soluble fraction (mg/L)

Soil profile	Be		Sc		Ga		Ge		V		Ag	
	Soil	WSF	Soil	WSF	Soil	WSF	Soil	WSF	Soil	WSF	Soil	WSF
AYg	1.79	0.21	11.8	15.7	17.1	0.8	1.84	0.085	97.3	8.2	0.94	0.8
Elg	1.4	0.83	10.1	74	13.7	9.34	1.87	0.96	72.6	67.1	0.8	3.1
BMlg	2.83	2.6	14.7	150	20.1	25.4	1.89	2.62	97.9	133	0.85	8.86
BM2	2.39	2.7	13.2	146	16.5	25.8	1.88	2.49	95.8	137	0.82	8.46
BC	2.98	2.63	14.5	132	19.9	23.3	1.86	2.05	109	134	0.86	9.52
C	3.53	2.47	16.7	107	22.9	21.4	2.09	1.64	138	113	1.05	6.82

Soil profile	Co		Ni		Cu		Zn		Mo		Cd	
	Soil	WSF	Soil	WSF	Soil	WSF	Soil	WSF	Soil	WSF	Soil	WSF
AYg	21.6	3.05	27.6	4.01	16.6	5.91	84.9	191	1.56	2.05	0.12	0.054
Elg	12.9	15.4	22.7	14.1	11.6	12.8	60.6	538	0.96	1.23	0.15	0.08
BMlg	22	25.4	70	42.4	38.1	62.9	109	422	2.67	2	0.26	0.11
BM2	15.2	19.7	34.2	49.2	33.2	90.2	61.9	246	1.08	4.82	0.19	0.21
BC	17.7	18.5	62.3	60.6	34.5	66.6	70.3	437	1.07	2.61	0.17	0.3
C	19.2	14	48.5	42.7	34.2	46.9	83.4	313	0.88	1.91	0.13	0.13

Soil profile	Sb		Pb		Y		∑REE		Th		U	
	Soil	WSF	Soil	WSF	Soil	WSF	Soil	WSF	Soil	WSF	Soil	WSF
AYg	0.41	0.21		2.5	20.9	1.05	157.26	6.67	11.2	0.67	2.92	0.48
Elg	0.32	0.36	21.8	13.8	20.4	4.88	144.14	66.04	10.6	5.39	2.9	1.54
BMlg	0.51	0.64	23.4	22.3	28.2	25.3	213.13	272.67	14.3	17.9	3.91	4.87
BM2	0.46	1	25.4	45.8	33.9	38.6	220.08	354.68	13.9	23.2	5.7	10.1

(continued)

Table 9.3 (continued)

Soil profile	Sb		Pb		Y		∑REE		Th		U	
	Soil	WSF	Soil	WSF	Soil	WSF	Soil	WSF	Soil	WSF	Soil	WSF
BC	0.62	0.6	23.3	23.7	34.1	35	224.87	326.74	14.2	20.8	5.07	7.91
C	0.42	0.51	19.8	17.6	33.8	23	249.70	233.04	15.6	15.5	4.27	3.98

Soil profile	Ba		Rb		Sr		Cr		Zr		Nb	
	Soil	WSF	Soil	WSF	Soil	WSF	Soil	WSF	Soil	WSF	Soil	WSF
AYg	560	193	136	8.57	131	85.3	89.6	9.47	304	4.27	18.3	1.15
Elg	550	432	121	62.7	137	54.5	81.5	38.2	330	52.1	14.4	12
BMlg	565	783	146	135	132	122	170	102	263	168	16	34.5
BM2	543	459	119	118	140	130	93.8	106	316	190	13.8	34.2
BC	558	979	140	119	136	150	137	94.2	253	203	16.7	37.4
C	546	645	158	113	129	114	128	84	228	137	18.1	24.3

Table 9.4 Macro elements in the sandy soil profile (%) and its water-soluble fraction (WSF), mg/L

Soil profile	SiO_2		TiO_2		Al_2O_3		Fe_2O_3		MnO	
	Soil	WSF	Soil	WSF	Soil	WSF	Soil	WSF	Soil	WSF
AY	87.5	86.1	0.23	0.7	1.34	6.98	0.29	2.25	0.008	0.077
E	87.0	95.4	0.3	0.81	1.18	3.87	0.28	0.89	0.011	0.036
BF1	76.4	90.0	0.3	1.2	2.43	15.2	0.68	4.99	0.016	0.110
BF2	66.2	88.8	0.25	1.13	3.01	18.7	0.88	5.65	0.043	0.430
BC	75	81.3	0.24	0.77	2.56	7.91	0.64	2.73	0.014	0.056
C	65.9	95.1	0.24	0.75	2.51	7.77	0.59	2.44	0.016	0.096

Soil horizon	CaO		MgO		Na_2O		K_2O		P_2O_5	
	Soil	WSF	Soil	WSF	Soil	WSF	Soil	WSF	Soil	WSF
AY	0.12	2.43	0.029	1.28	0.15	8.05	0.52	4.21	0.027	0.98
E	0.12	0.7	0.022	0.22	0.15	2.38	0.5	2.06	0.022	0.25
BF1	0.15	0.62	0.046	0.48	0.21	2.41	0.77	3.05	0.089	1.28
BF2	0.19	0.96	0.072	0.8	0.27	3.39	0.87	3.58	0.100	1.27
BC	0.23	0.59	0.075	0.42	0.31	1.74	0.9	2.66	0.064	0.8
C	0.24	0.67	0.073	0.4	0.32	1.53	0.93	2.66	0.060	0.61

Table 9.5 Micro elements in the sandy soil profile (mg/kg) and its water-soluble fraction (mg/L)

Soil profile	Be		Sc		Ga		Ge		V		Ag	
	Soil	WSF	Soil	WSF	Soil	WSF	Soil	WSF	Soil	WSF	Soil	WSF
AY	<0.01	0.95	0.48	196	1.7	14.1	0.83	5.06	3.58	97.4	0.11	1.89
E	<0.01	0.67	0.43	130	1.51	7.24	0.83	2.97	6.51	47.4	0.13	1.3
BF1	<0.01	1.6	0.88	111	3.47	28.3	0.87	4.4	8.71	117	0.12	1.06
BF2	<0.01	2.39	1.15	106	4	32	0.87	3.64	13.5	132	0.13	0.77
BC	<0.01	1.94	1.04	76.8	2.79	10.9	0.9	1.81	9.74	78.3	0.13	0.7
C	<0.01	1.77	1.05	84.5	2.71	10.3	0.9	2.02	9.45	69.8	0.11	1.89
Soil profile	Co		Ni		Cu		Zn		Mo		Cd	
	Soil	WSF	Soil	WSF	Soil	WSF	Soil	WSF	Soil	WSF	Soil	WSF
AY	0.3	13.9	1.06	324	4.8	97.2	46.4	8290	<0.6	38.3	<0.1	4.21
E	0.3	10.3	0.9	404	5.6	44	63.2	963	<0.6	5.41	0.1	0.62
BF1	0.83	14.8	1.45	247	4.46	43.2	41.6	3020	<0.6	5.15	<0.1	2.17
BF2	2.35	22	2.81	30	4.15	34.3	41.3	841	<0.6	4.81	<0.1	0.77
BC	1.26	11.1	2.01	128	4.53	26	46.7	694	<0.6	1.33	<0.1	0.76
C	1.22	11.5	1.95	123	4.29	21.1	40.3	506	<0.6	1.3	0.11	0.56

(continued)

Table 9.5 (continued)

Soil profile	Sb		Pb		Y		∑REE		Th		U	
	Soil	WSF	Soil	WSF	Soil	WSF	Soil	WSF	Soil	WSF	Soil	WSF
AY	0.16	5.27	8.49	75.6	3.14	25.7	24.6	158.63	1.93	9.72	0.62	3.44
E	0.14	0.91	6.44	82.4	4.18	14	40.9	130.21	3.11	5.13	0.82	1.88
BF1	0.15	1.86	8.75	70.4	4.44	18.4	44.4	183.09	3.58	15.9	0.91	3.31
BF2	0.12	1.44	9.79	52.5	4.19	26.4	35.2	135.65	2.69	18.5	0.78	3.55
BC	0.12	0.44	7.72	25.6	5.12	24	40.8	147.01	3.24	17.6	0.76	3.84
C	0.13	0.42	7.89	29.1	5.54	30.2	45.7	179.32	3.32	18.4	0.79	2.81
Soil profile	Ba		Rb		Sr		Cr		Zr		Nb	
	Soil	WSF	Soil	WSF	Soil	WSF	Soil	WSF	Soil	WSF	Soil	WSF
AY	178	6140	16.2	69.6	24.4	171	6.94	172	69.7	137	3.91	12.9
E	176	2330	16.7	50.1	25.3	97.8	5.81	45.2	97.8	141	4.58	12
BF1	233	3480	24.8	83.6	34.3	107	10.5	81.5	73.5	208	4.22	18.1
BF2	235	3220	29.1	106	36.8	128	11.4	98.8	58.6	163	3.96	19.8
BC	242	2650	28.4	74.1	43.8	91	9.49	46.2	63.5	148	3.61	12.1
C	239	1340	29.4	70.8	40.9	101	13.2	44.4	66.8	154	3.82	12.5

Table 9.6 Coefficients of accumulation of mobile forms of chemical elements in soil profiles (CA = WSF/Soil)

	Clayey soil	Sandy soil	
AYg	$Zn_{2,3}$ $Ca_{1,8}$ $Sc_{1,3}$ $Mo_{1,3}$	Sc_{408} Ni_{306} Zn_{179} Mo_{128} Cd_{84} Co_{56} Na_{54} Mg_{44} P_{36} Ba_{35} Sb_{33} V_{27} Cr_{25} Ca, Cu_{20} Sn_{11} Mn_{10} $Pb_{8,9}$ $Cs_{8,7}$ $Ga_{8,3}$ $Y_{8,2}$ $K_{8,1}$ $FeTl_{7,8}$ Sr_7 $Ge_{6,1}$ $U_{5,6}$ $Al_{5,2}$ Th_5 $Rb_{4,3}$ $Nb_{3,3}$ Ti_3 Zr_2 $Be_{1,9}$	AY
Elg	$Zn_{8,9}$ $Sc_{7,3}$ $Ag_{3,9}$ Mn_2 $Ca_{1,7}$ $Mo_{1,3}$ $Co_{1,2}$	Ni_{808} Sc_{302} Co_{41} Mo_{18} Na_{16} Zn_{15} Ba_{13} $Pb_{12,8}$ $P_{11,4}$ Mg_1 $Cu_{7,9}$ $Cr_{7,8}$ $V_{7,3}$ $Sb_{6,5}$ $Cd_{6,2}$ $Ca_{5,8}$ Cs_5 $TlGa_{4,8}$ $K_{4,1}$ $Sr_{3,9}$ $Ge_{3,6}$ $Y_{3,4}$ Al, Mn, $Sn_{3,3}$ $Fe_{3,2}$ Rb_3 $Ti_{2,7}$ $Nb_{2,6}$ $U_{2,3}$ $Th_{1,6}$ $Zr_{1,4}$ $Be_{1,3}$	E
BM1g	$Ag_{10,4}$ $Sc_{10,2}$ $Zn_{3,9}$ $Nb_{2,2}$ $Cu_{1,7}$ $Mn_{1,5}$ $Sn_{1,5}$ Ti, Ge, Ba, V, $Ce_{1,4}$ Fe, REE, Ga, Ca, Sb, Th, $U_{1,3}$ Mg, $Co_{1,2}$	Ni_{170} Sc_{126} Zn_{72} Cd_{43} Co_{18} Mo_{17} Ba_{15} P_{14} V_{13} Sb_{12} Na_{11} Mg, Sn_{10} $Cu_{9,9}$ $Ga_{8,2}$ $Pb_{8,1}$ $Cr_{7,8}$ $Fe_{7,3}$ $Mn_{6,9}$ $Al_{6,3}$ $Cs_{6,2}$ Ge_5 $Th_{4,4}$ $Nb_{4,3}$ Y, Tl, $Ca_{4,1}$ Ti, K4 $U_{3,6}$ $Rb_{3,4}$ $Be_{3,2}$ $Sr_{3,1}$ $Zr_{2,8}$	BH
BM2	$Sc_{11,1}$ $Ag_{10,3}$ $Mo_{4,5}$ $Zn_{3,9}$ $Cu_{2,7}$ $Nb_{2,5}$ $Sb_{2,2}$ $Sn_{2,1}$ Pb, $U_{1,8}$ Fe, $Th_{1,7}$ Mg, Mn, REE, $Ga_{1,6}$ $Ti_{1,5}$ $Ni_{1,4}$ Ge,Ca, Co, $Cs_{1,3}$	Sn_{127} Sc_{92} Zn_{20} Mo_{16} Cd_{15} Ba_{14} PNa_{13} Sb_{12} Mg,Ni_{11} Mn_{10} $V_{9,8}$ $Co_{9,4}$ Cs, $Cr_{8,7}Cu_{8,3}$ Ga_8 $Th_{6,7}$ $Ge_{6,5}$ $Fe_{6,4}$ $Y_{6,3}$ $Al_{6,2}$ $Pb_{5,4}$ Ca, Nb_5 $Be_{4,8}$ $U_{4,6}$ $Ti_{4,5}$ $Tl_{4,4}$ $K_{4,1}$ $Rb_{3,6}$ $Sr_{3,5}$ $Zr_{2,8}$	BF
BC	$Ag_{11,1}$ $Sc_{9,1}$ $Zn_{6,2}$ $Mo_{2,4}$ $Nb_{2,2}$ $Cu_{1,9}$ $Cd_{1,8}$ $Ba_{1,7}$ $U_{1,6}$ $Th_{1,5}$ REE, $Mn_{1,4}$ Mg, Fe, $Ti_{1,3}$ V, Ca, $Ga_{1,2}$	Sc_{73} Ni_{64} Cd_{15} Zn_{15} P_{13} Ba_{11} $Sn_{9,7}$ $Co_{8,8}$ V_8 $Cu_{5,7}$ Na, $Mg_{5,6}$ $Th_{5,4}$ U_5 $Cr_{4,9}$ $Y_{4,7}$ $Cs_{4,6}$ $Mo_{4,4}$ $Fe_{4,3}$ Mn_4 $Ga_{3,9}$ $Be_{3,9}$ $Sb_{3,7}$ $Nb_{3,3}$ $Pb_{3,3}$ $Ti_{3,2}$ $Al_{3,1}$ K_3 Rb, $Ca_{2,6}$ $Tl_{2,5}$ $Zr_{2,3}$ $Sr_{2,1}$ Ge_2	BC
C	$Ag_{6,8}$ $Sc_{6,2}$ $Zn_{2,5}$ $Mo_{1,6}$ $Nb_{1,3}$ $Cu_{1,2}$	Sc_{80} Ni_{63} Zn_{13} P_{10} $Co_{9,4}$ $V_{7,4}$ $Sn_{7,3}$ Mn_6 $Ba_{5,6}$ Th, Mg, $Y_{5,5}$ $Cd_{5,1}$ Cu_5 $Na_{4,8}$ $Mo_{4,3}$ $Fe_{4,1}$ $Ga_{3,8}$ $Cs_{4,1}$ $Pb_{3,7}$ $U_{3,6}$ $Be_{3,5}$ $Cr_{3,4}$ $Nb_{3,3}$ $Sb_{3,2}$ $TiAl_{3,1}$ $K_{2,9}$ $Ca_{2,8}$ $Tl_{2,5}$ $Sr_{2,5}$ $Rb_{2,4}$ $Zr_{2,3}$ $Ge_{2,2}$	C

to that in the humus horizon. The metamorphic horizons (BMg1 and BM2) of the clayey soil were characterized by the widest spectrum of water-soluble elements.

The removal of Fe, Al, Ti, K and many other elements (based on the data of the total chemical analysis) from the soil against the background of the relative accumulation of Si and Zr showed that these horizons could not be qualified as illuvial. It was suggested, the metamorphic process promoted the weakening of crystalline lattice in minerals, which resulted in increased potential mobility of many elements (Elementary pedogenic processes 1992). In the iron-illuvial horizons, the degree of mobility of most elements decreased, which was similar to that observed in the BC horizon close to the parent rock (C) in terms of chemical composition. According to the composition of water-soluble elements, the BC horizon of the clayey soil

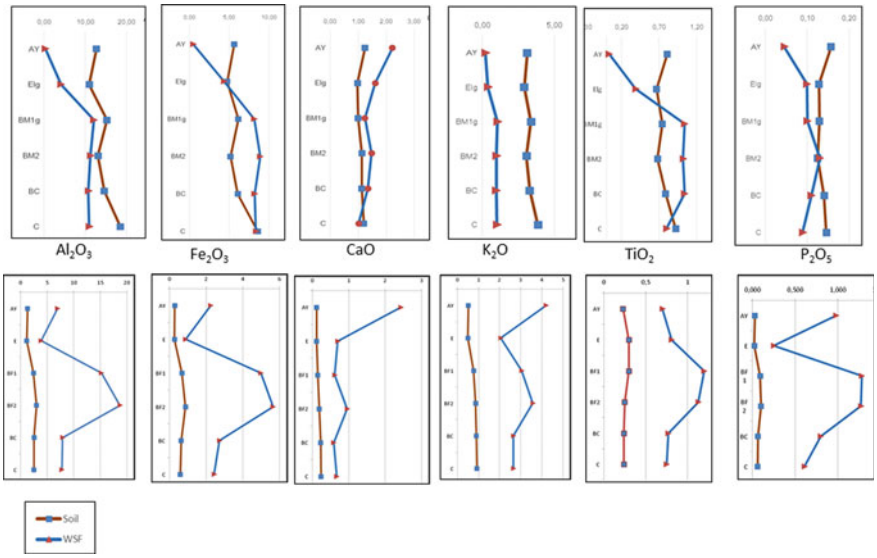


Fig. 9.1 The distribution of the total content of macro elements in the clayey (upper row) and sandy (lower row) soils and their water-soluble fraction (WSF), wt%

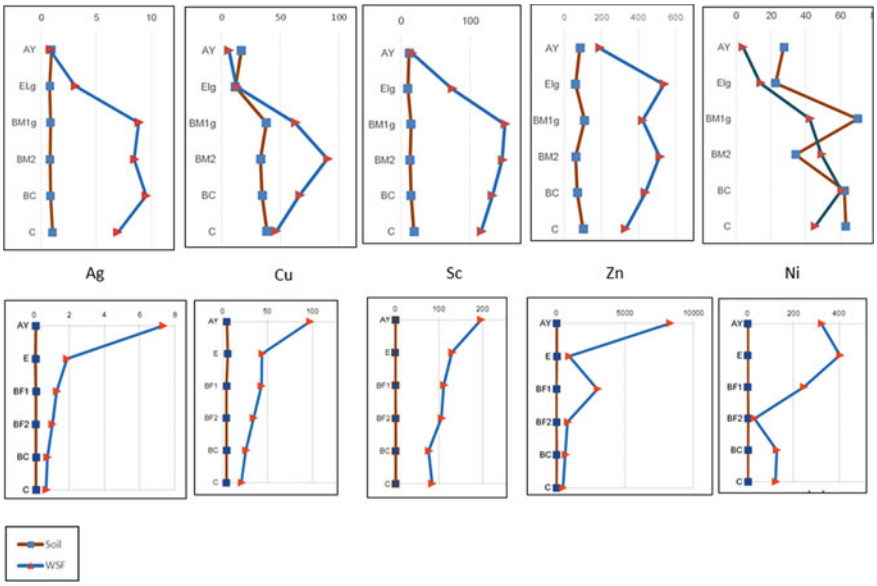


Fig. 9.2 The distribution of the total content of microelements in the clayey (upper row) and sandy (lower row) soils (mg/kg) and their water-soluble fraction (WSF), mg/L

was closer in composition to middle horizons of the soil profile than to the rock, with its decrease in mobile forms. The higher proportion of primary minerals in the soddy-podzol (as compared to that in the soddy-eluvial-metamorphic soil) affected the differences in the chemical properties of their genetic horizons.

The total REE content in the studied soils is presented in Table 9.7. The observed concentrations are comparable with the values reported previously for the average world-wide REE concentrations (Bowen 1979) as well, as for previously reported for Russian soils (Ivanov 1997). We observed, that the clayey soil had higher total content of all REE than the sandy soil, as shown on Fig. 9.3c, d. In clayey soil observed Ce concentration being twice as high as Clarke value. Enrichment of soil clay fraction by rare-earth elements has been reported previously (e.g. Aide and Smith-Aide 2003), while a low REE content in naturally occurring sandy soil had been reported for Netherlands (Stuyfzand 1991).

The common REE distribution pattern is high REE content (1–100 mg/kg) in clay soils with an about an order of magnitude lower content in the profiles on sand (0.11–19 mg/kg). Higher concentrations of REE, observed in the lower part of the profile on clay, indicate a predominantly residual, inherited nature of their location, and a decrease in the content of weathering minerals. Similar pattern had been previously described for areas with medium and low temperatures (Prudencio et al. 1993; Tyler 2004).

Light and heavy REE usually exhibit different distribution patterns in soil profile. Those are commonly compared using the ratio of the sum of light REE to the sum of heavy REE concentrations. The numerator indicates relatively alkaline conditions, while the denominator relates to more acidic conditions. The changes in light vs heavy REE ratio is shown on Fig. 9.3a. For the profile of sandy soil, a well-known distribution is observed. When the soil profile is formed, the relatively acidic conditions of the lower part of the profile are changed to more alkaline in its middle part and again to more acidic in the upper part.

The results for REE concentration in WSF and the share of mobile REE are given in Table 9.8. The highest concentration values of mobile REE forms were observed for the lower horizons of the sandy soil (BC and C). Minimal concentrations of mobile REE were found in the humus horizons of both sandy and clayey soils. The absolute values of these concentrations were an order of magnitude lower in the humus horizon of the soil on clay rock, which is depleted in many elements as a consequence of eluvial process.

The total REE content and the above mentioned ratio between light and heavy REE concentrations in WSF is shown in Fig. 9.3b–d. In both sandy and clayey soils, WSF enrichment in heavy REE can be observed in the lower horizons, along with a similar enrichment in light REE seen for the upper horizons.

REE content in soil profile samples on clay and sand and their WSFs were normalized to the average REE content in clays of the Russian Platform (Ronov and Migdisov 1996), with the results as shown in Fig. 9.4. In the clayey soil, the topsoil AYg and ELg horizons are depleted in REE compared to the lower horizons and especially to the parent material. The patterns of all horizons of the clayey soil for normalized total content are rather similar, whereas for the related WSF, the patterns

Table 9.7 The REE content in the soil (mg/kg) and in its water-soluble fraction (WSF) , mg/L

Horizon	La	Ce	Pr	Nd	Sm	Eu	Gd	Tb	Dy	Ho	Er	Tm	Yb	Lu
Soil on clay														
AYg	33.34	68.98	7.45	26.41	5.65	1.11	4.52	0.68	3.76	0.68	1.97	0.30	2.08	0.32
ELg	30.15	62.85	6.93	24.32	4.96	0.96	4.45	0.66	3.67	0.66	1.92	0.30	1.97	0.33
BM1g	41.84	94.67	10.22	36.60	7.83	1.52	6.59	0.98	5.33	0.98	2.86	0.40	2.86	0.47
BM2	42.60	94.53	10.51	38.66	8.62	1.64	7.70	1.18	6.09	1.12	3.15	0.46	3.31	0.53
BC	46.37	94.51	10.91	40.35	8.57	1.61	7.43	1.10	6.00	1.10	3.08	0.45	2.90	0.51
C	52.80	102.76	12.31	45.09	9.91	1.79	8.12	1.25	6.57	1.22	3.47	0.48	3.40	0.54
Soil on sand														
AY	5.3	10.3	1.24	4.36	0.77	0.16	0.7	0.11	0.58	0.12	0.35	0.058	0.47	0.083
E	8.57	17.7	2.14	7.51	1.32	0.18	1.07	0.16	0.81	0.17	0.48	0.081	0.61	0.097
BF1	9.8	18.9	2.21	7.88	1.49	0.26	1.23	0.2	0.91	0.18	0.47	0.084	0.63	0.110
BF2	7.47	14.7	1.75	6.4	1.23	0.26	0.93	0.16	0.84	0.18	0.51	0.083	0.6	0.096
BC	8.41	17.2	2.08	7.56	1.42	0.3	1.16	0.2	0.96	0.2	0.54	0.086	0.63	0.099
C	9.15	19	2.36	8.78	1.65	0.33	1.38	0.23	1.13	0.23	0.61	0.095	0.65	0.099
Soil on clay, WSF														
AYg	1.76	2.87	0.3	0.91	0.22	0.073	0.13	0.058	0.13	0.039	0.089	0.03	0.057	0.0083
ELg	12	30.9	3.11	12.1	1.98	0.43	1.8	0.2	1.31	0.32	0.89	0.15	0.77	0.079
BM1g	52.9	128	12.3	47.4	8.03	1.53	7.54	1.1	5.7	1.15	2.97	0.49	3.08	0.48
BM2	72	154	16.7	65.4	11.5	2.16	11.7	1.71	7.76	1.59	4.46	0.65	4.34	0.71
BC	71.5	138	16.6	58.1	10.1	2.02	11.5	1.39	7.29	1.56	3.79	0.58	3.72	0.59
C	48.4	101	11.8	41	8.01	1.45	7.43	1.04	5.41	0.97	2.85	0.41	2.84	0.43

(continued)

Table 9.7 (continued)

Horizon	La	Ce	Pr	Nd	Sm	Eu	Gd	Tb	Dy	Ho	Er	Tm	Yb	Lu
Soil on sand, WSF														
AY	30.1	82.6	6.74	22.4	4.38	1.51	3.3	0.44	2.81	0.5	1.8	0.290	1.51	0.250
E	33	58.1	5.2	18.4	4.29	0.81	3.07	0.54	2.63	0.48	1.54	0.250	1.6	0.300
BF1	43.8	81.9	8.44	26.6	5.5	1.41	4.54	0.8	3.81	0.7	2.18	0.400	2.61	0.400
BF2	54.2	116	12.9	39.9	7.14	2.01	6.17	1	5.17	0.99	2.44	0.420	2.86	0.460
BC	51.1	120	13.2	46.4	9.23	2.25	9.05	1.25	6.62	1.37	2.93	0.470	2.75	0.390
C	56.7	151	15.7	60.8	12.7	2.77	11.8	1.66	8.09	1.51	3.51	0.570	2.99	0.520

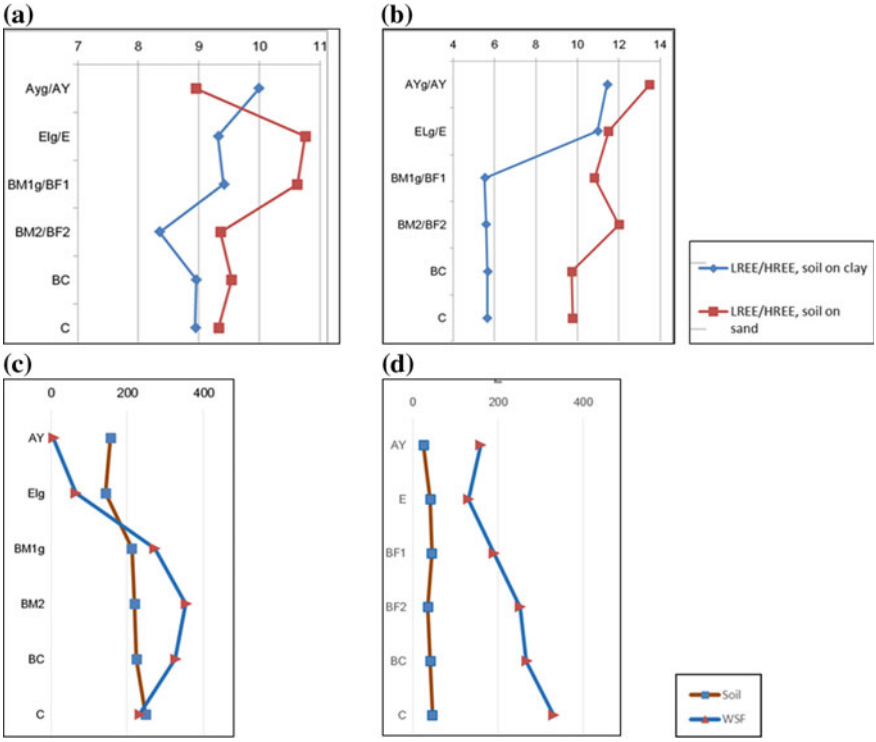


Fig. 9.3 LREE/HREE in the bulk soils (**a**) and their WSF (**b**), the distribution of the total content of REE in the clayey (**c**) and sandy (**d**) soils (mg/kg) and their water-soluble fraction (WSF), mg/L

for AYg and ELg were significantly different from the other horizons. Normalized REE values of the uppermost horizons (AYg and ELg) of the soil on clay do not exhibit a significant negative Ce anomaly, which is observed in the lower horizons. This phenomenon had been previously explained through REE bonding to organic colloids in the humus horizon (Pédrot et al. 2015).

For distribution of REE in WSF in the sandy soil, three groups of the horizons can be separated: (1) humus horizon AY with the lowest concentration of REE and positive anomaly of Ce, Eu and Yb. Notably, it was also substantially depleted of total REE. (2) E, BF1 and BF2 horizons with similarly distributed intermediate content of REE and more or less similar patterns of their distributions; (3) intermediate horizon BC and parent material C with the highest concentration of mobile REE. These patterns correlated well with the data on mobilization and removing of REE from the parent material during podsolization (Vermeire et al. 2016).

Table 9.8 The content of REE in WSF of their total content in the soils (rel %)

Horizon	WSF, wt%	La	Ce	Pr	Nd	Sm	Eu	Gd	Tb	Dy	Ho	Er	Tm	Yb	Lu
		%													
Soil on clay															
AYg	0.63	0.03	0.03	0.03	0.02	0.03	0.04	0.02	0.06	0.02	0.06	0.05	0.06	0.02	0.02
ELg	0.98	0.39	0.48	0.44	0.49	0.39	0.44	0.40	0.30	0.35	0.48	0.45	0.49	0.38	0.23
BM1g	0.84	1.06	1.14	1.01	1.09	0.85	0.85	0.96	0.94	0.90	0.99	0.87	1.03	0.90	0.86
BM2	0.83	1.40	1.35	1.32	1.40	1.11	1.09	1.26	1.20	1.06	1.18	1.18	1.17	1.09	1.11
BC	1.28	1.97	1.87	1.95	1.84	1.51	1.61	1.98	1.62	1.56	1.82	1.58	1.65	1.64	1.48
C	1.65	1.51	1.62	1.58	1.50	1.33	1.34	1.51	1.37	1.36	1.31	1.36	1.41	1.38	1.31
Soil on sand															
AY	0.1	0.57	0.80	0.54	0.51	0.57	0.94	0.47	0.40	0.48	0.42	0.51	0.48	0.32	0.32
E	0.5	1.93	1.64	1.22	1.23	1.63	2.25	1.43	1.69	1.62	1.41	1.60	1.56	1.33	1.55
BF1	0.39	1.74	1.69	1.49	1.32	1.44	2.12	1.44	1.56	1.63	1.52	1.81	1.95	1.62	1.42
BF2	0.34	2.47	2.68	2.51	2.12	1.97	2.63	2.26	2.13	2.09	1.87	1.63	1.72	1.62	1.62
BC	0.82	4.98	5.72	5.30	5.03	5.33	6.15	6.40	5.13	5.65	5.62	4.45	4.48	3.58	3.23
C	1	6.20	7.95	6.65	6.92	7.70	8.39	8.55	7.22	7.16	6.57	5.75	6.00	4.60	5.25

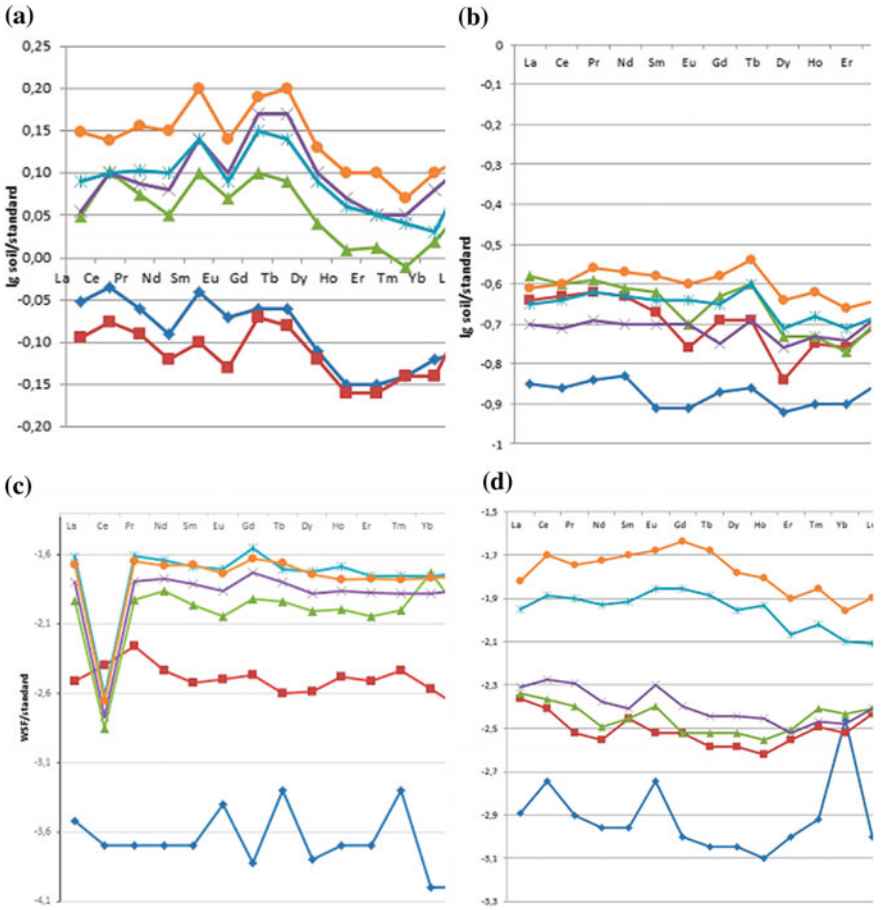


Fig. 9.4 The REE distribution, normalized on RPSC in the clayey soil (**a**), the sandy soil (**b**), the WSF of the clayey soil (**c**) and WSF of the sandy soil (**d**)

9.4 Conclusion

Presented here is a new method for the isolation of the water-soluble fraction (WSF) for analyzing the mobility of chemical elements. The analysis of water solutions without additional reagents allows the maximize the potential of inductively coupled plasma mass spectrometry method to achieve lower detection level for rare and scattered metals, as well as to increase the range of elements suitable for analysis. Those, make possible to significantly raise the information capacity of soil–chemical studies.

The widespread soils on the Russian Plain (clayey and sandy) were investigated. Portions of easily and difficultly mobile forms of elements were evaluated, demonstrating significant differences in the total content of chemical elements (based on the total chemical analysis) in the soils and in their WSF.

Acknowledgments Analytical work was done in Chemical Laboratory of Russian Geological Research Institute and in Research Centers of Saint Petersburg State University «Geomodel» and «Methods of chemical analysis».

References

Adams F, Burmester C, Nue NV, Long FL (1980) Comparison of column-displacement and centrifuge methods for obtaining soil solution. Soil Sci Am J 44:733–735

Aide M, Smith-Aide C (2003) Assessing soil genesis by rare-earth elemental analysis. Soil Sci Soc Am J 67:1470–1476

Bin G, Cao X, Dong Y, Luo Y, Ma LQ (2011) Colloid deposition and release in soils and their association with heavy metals. Crit Rev Environ Sci Technol 41:336–371

Bockheim JG, Gennadiev AN (2000) The role of soil-forming processes in the definition of taxa in soil taxonomy and the world reference base. Geoderma 95:53–72

Bowen HJM (1979) Environmental chemistry of the elements. Academic Press, London

Brioschi L, Steinmann M, Lucot L, Pierret MC, Stille P, Prunier J, Badot PM (2013) Transfer of rate earth elements (REE) from natural soil to plant systems: implications for the environmental availability of anthropogenic REE. Plant Soil 366:143–163

Cancès B, Ponthieu M, Casrec-Rouelle M, Aubry E, Benedetti MF (2003) Metal ions speciation in a soil and its solution: experimental data and model results. Geoderma 113:341–355

Chen LM, Zhang GL, Jin JD (2014) Rare earth elements of a 1000-year paddy soil chronosequence: implications for sediment provenances, parent material uniformity and pedological changes. Geoderma 230–231:274–279

Classification and Diagnostic System of Russian Soils (2004) Oikumena Publications, Smolensk (in Russian)

Cornu S, Quénard L, Cousin I, Samouëlian A (2014) Experimental approach of lessivage; quantification and mechanisms. Geoderma 213:357–370

De Jonge LW, Kjaergaard C, Moldrup P (2004) Colloids and colloid-facilitated transport of contaminants in soils. Vadose Zone J 3(2):321–325

Dobrovol'skii VV, Aleshchukin LV, Filatova EV et al (1997) Mobile forms of heavy metals in soil as a factor for formation of mass flows of metals. In: Heavy metals in the environment. Pushchino, pp 5–14 (in Russian)

Elementary pedogenic processes: An experience in conceptual analysis, characterization, and systematization (1992). Nauka Publications, Moscow (in Russian)

El-Farhan YH, DeNovio NM, Herman JS, Hornberger GM (2000) Mobilization and transport of soil particles during infiltration experiments in an agricultural field, Shenandoah Valley, Virginia. Environ Sci Technol 34:3555–3559

Essington ME (2004) Soils and water chemistry, an integrative approach. CRC Press, Boca Raton, FL

Gagarina EI, Matinyan NN, Schastnaya LS, Kasatkina GA (1995) Soils and the soil cover of Northwestern Russia. Saint Petersburg State University, Saint Petersburg (in Russian)

Giesler R, Lundstrom US, Grip H (1996) Comparison of soil solution chemistry assessment using zero-tension lysimeters or centrifugation. Eur J Soil Sci 47(3):395–405

Gouveia MA, Prudêncio MJ, Figueiredo MO, Pereira LCJ, Waerenborgh JC, Morgado J, Pena T, Lopes A (1993) Behavior of REE and other trace and major elements during weathering of granite rocks. Chem Geol 107(2):293–296

Harlavan Y, Erel Y, Blum JD (2009) The coupled release of REE and Pb to the soil labile pool with time by weathering of accessory phases, Wind River Mountains, WY. Geochim Cosmochim Acta 73:320–336

Imoto Y, Yasutaka T, Someya M, Higashino K (2018) Influence of solid-liquid separation method parameters employed in soil leaching tests on apparent metal concentration. Sci Total Environ 624:96–105

Ivanov IV (1997) Environmental geochemistry of elements. Book 6. Nedra, Moscow (in Russian)

IUSS Working Group WRB (2014) World Reference Base for Soil Resources 2014. International soil classification system for naming soils and creating legends for soil maps. World Soil Resources Reports No. 106. FAO, Rome

Kabata-Pendias A, Mukherjee AB (2007) Trace elements from soil to human. Springer, Berlin Heidelberg

Kaplan DI, Bertch PM, Adriano DC, Miller WP (1993) Soil-born mobile colloids as influenced by water flow and organic carbon. Environ Sci Technol 27:1193–1200

Karavanova EI, Timofeeva EA (2009) Chemical composition of solutions in macro- and micropores in the upper horizons of soils in the Central Forest State biosphere reserve. Eurasian Soil Sci 42(12):1456–1463

Klitzke S, Lang F, Kaupenjohann M (2008) Increasing pH releases colloidal lead in a highly contaminated forest soil. Eur J Soil Sci 265–273

Land M, Ohlander B, Ingri J, Thunberg J (1999) Solid speciation and fractionation of rare earth elements in a spodosol profile from Northern Sweden as revealed by sequential extraction. Chem Geol 160:121–138

Laveuth C, Cornu S (2009) A review on the potentiality of rare earth elements to trace pedogenetic processes. Geoderma 154:1–12

Lin Q, Xu X, Bao Q, Oh K, Chen D, Zhang L, Shen X (2016) Influence of water-dispersible colloids on the mechanism of metal transport in historically contaminated soils: coupling colloid fractionation with high-energy synchrotron analysis. J Soils Sediments 16:349–359

Malinina MS, Motuzova GV (1994) Methods to obtain soil solutions for soil chemical monitoring. In: Physical and chemical analysis of soils. Moscow State University, Moscow (in Russian)

Matinyan NN (2003) Soil formation on varved clay of glaciolacustrine plains in Northwestern Russia. Saint Petersburg State University, Saint Petersburg (in Russian)

Mihajlovic J, Stark HJ, Rinklebe J (2014) Geochemical fractions of rare earth elements in two floodplain soil profiles at the Wupper River, Germany. Geoderma 228–229:160–172

Minařík L, Žigová A, Bendl J, Skřivan P, Št'astny M (1998) The behavior of rare earth elements and Y during the rock weathering and soil formation in the Říčany granite massif, Central Bohemia. Sci Total Environ 215:101–111

Moreno-Jimenéz E, Beesley L, Lepp NW, Dickinson NM, Hartley W, Clemente R (2011) Field sampling of soil pore water to evaluate trace element mobility and associated environmental risk. Environ Pollut 159:3078–3085

Oleinikova GA, Panova EG (2007) Information resources of analysis of nanofractions of soils. Vestn St Peterb Gos Univ 3:60–66 (in Russian)

Orlov DS (1985) Soil chemistry. Moscow State University, Moscow (In Russian)

Pédrot M, Dia A, Davranche M, Gruau G (2015) Upper soil horizons control the rare earth element patterns in shallow groundwater. Geoderma 239–240:84–96

Perelman AI (1989) Geochemistry. Vysshaya Shkola Publishers, Moscow (in Russian)

Perelomov LV, Asainova ZhS, Yoshida S, Ivanov IV (2012) Concentrations of rare earth elements in soils of the Prioksko-Terrasnyi biospheric reserve. Eurasian Soil Sci 45(10):983–994

Prudencio MI, Braga MAS, Gouveia MA (1993) REE mobilization, fractionation and precipitation during weathering of basalts. Chem Geol 107:251–254

Putikov OF (2008) Basics of the theory of nonlinear geoelectrochemical survey methods. University of Humanity and Social Sciences, Saint Petersburg (in Russian)
Ronov AB, Migdisov AA (1996) Quantitative regularities of structure and composition of sedimentary strata of the East European platform and the Russian plate and their place among the ancient platforms of the world. Lithol Miner 5:451–475 (in Russian)
Séquaris J-M, Klumpp E, Vereecken H (2013) Colloidal properties and potential release of water-dispersible colloids in an agricultural soil depth profile. Geoderma 193–194:94–101
Seta AK, Karathanasis AD (1996) Water dispersible colloids and factors influencing their dispersibility from soil aggregates. Geoderma 74:255–266
Seta AK, Karathanasis AD (1997) Stability and transportability of water-dispersible soil colloids. Soil Sci Soc Am J 61:604–611
Shein EV, Devin BA (2007) Current problems in the study of colloidal transport in soil. Eurasian Soil Sci 40(4):399–408
Siemens J, Ilg K, Lang F, Kaupenjohann M (2004) Adsorption controls mobilization of colloids and leaching of dissolved phosphorus. Eur J Soil Sci 55:253–263
Sokolov SV, Marchenko LG, Shevchenko SS (2005) Tentative methodological recommendations for geochemical survey on the closed and semi-closed territories. Russian Scientific Research Geological Institute, Saint Petersburg (in Russian)
Sparks DL (1989) Kinetics of soil chemical processes. Academic Press, San Diego, CA
Sposito G (1989) The chemistry of soils. Oxford University Press, New York
Stuyfzand PJ (1991) Sporenelementen in groundwater in Nederland. H_2O 26:756–762 (in Dutch)
Trofimov SY, Karavanova EI (2009) Liquid phase of soils: manual for some chapters of the course on soil chemistry. Moscow State University, Moscow (in Russian)
Tyler G (2004) Vertical distribution of major, minor and rare elements in a Haplie Podzol. Geoderma 119:277–290
Van den Bogaert R, Cornu S, Michel E (2016) To which extent do rain interruption periods affect colloid retention in macroporous soils. Geoderma 275:40–47
Van Oort F, Jongmans AG, Citeau L, Lamy I, Chevallier P (2006) Microscale Zn and Pb distribution patterns in subsurface soil horizons: an indication for metal transport dynamics. Eur J Soil Sci 57:154–166
Vermeire M-L, Cornu S, Fekiasova Z, Detienne M, Delvaux B, Cornélis J-T (2016) Rare earth elements dynamics along pedogenesis in a chronosequence of podzolic soils. Chem Geol 446:163–174
Vodyanitskii YuN, Goryachkin SV, Savichev AT (2011) Distribution of rare-earth (Y, La, Ce) and other heavy metals in the profiles of the podzolic soil group. Eurasian Soil Sci 44(5):500–509
Wang Q, Huang B, Guan Z, Yang L, Li B (2001) Speciation of rare earth elements in soil by sequential extraction then HPLC coupled with visible and ICP-MS detection//Fresenius' J Anal Chem 370(8):1041–1047
Weihrauch C, Opp C (2018) Ecologically relevant phosphorus pools in soils and their dynamics: the story so far. Geoderma 325:183–194
Yan J, Meng X, Jin Y (2017) Size-dependent turbidimetric quantification of suspended soil colloids. Vadose Zone J 16(5):1–8

Chapter 10
Contact Angle Hysteresis in the Clay-Water-Air System of Soils



Oxana A. Sofinskaya, Akhmet A. Galeev and Eduard A. Korolev

Abstract Microorganisms emit substances changing the surface tension of soil solution and the surface energy of solid soil particles. Clays and soils have high heterogeneity of the surface energy distribution among particles. The change in the surface energy of soil particles is caused not only by alteration of their chemical properties but also an increase/decrease in their spatial heterogeneity, which determines contact angle hysteresis. Available techniques of measurement the contact angle and the contact angle hysteresis require further improvement and adaptation to specific clay types. The purpose of this research is to study the change in wettability of clays due to the influence of mesophilic soil microorganisms' activity when adding model contaminants: water-in-oil emulsion, glycerol and oleic acid. During the experiments, the objectives of this study were to specify peculiarities of wetting contact angle hysteresis of clays with substrates of different mineral composition and microbial activity. Hydrophilicity/hydrophobicity of the stimulator for microbial activity does not have a clear effect on clay properties. The surface heterogeneity mostly increases with time, perhaps, due to biofilm exudates whatever was a type of microbial stimulator. Chemical and geometric heterogeneities played comparable roles in the surface hydrophilic-hydrophobic balance. Results obtained prove that microbial communities and/or the Fe chemical state alteration (pyrite, hematite or goethite) were responsible for both hydrophilization and hydrophobization of the surface. The equation for the drop spreading rate was presented and verified by well comparison of experimental results with simulations.

Keywords Biomat · Biofilms · Hydrophobicity · Hydrophilicity · Clay minerals · Surface tension · Contact angle · Hysteresis of wettability · Water spreading · Water repellency

O. A. Sofinskaya (✉) · A. A. Galeev · E. A. Korolev
Federal University, Kazan (Volga Region), Russia
e-mail: ushik2001@mail.ru

A. A. Galeev
e-mail: akhmet.galeev@kpfu.ru

© Springer Nature Switzerland AG 2020

O. V. Frank-Kamenetskaya et al. (eds.), *Processes and Phenomena on the Boundary Between Biogenic and Abiogenic Nature*, Lecture Notes in Earth System Sciences,
https://doi.org/10.1007/978-3-030-21614-6_10

10.1 Introduction

Microbial communities as an indispensable part of soils play an important role in regulating hydrophysical properties. Microbial communities control such processes as the formation of water-stable aggregates, the decrease in the specific surface area of soil and soil constituents, high mechanical pressure zones created by growing fungal hyphae (up to 10–100 MPa), which destroys the solid rock, the exudation of acids, which affect the pH of porous solution, the dissolution and precipitation of minerals, the formation and transformation of clay minerals (Rockhold et al. 2002; Zhu et al. 2011; Shein et al. 2016; Cuadros 2017). Microorganisms emit substances changing the surface tension of porous solution (particularly soil solution) and the surface energy of solid soil particles (Bachmann et al. 2003; Shang et al. 2008; Tyugai and Milanovskiy 2015; Shein et al. 2016). The change in the surface energy of soil particles is caused not only by alteration of their chemical properties but also an increase/decrease in their spatial heterogeneity, which determines contact angle hysteresis (CAH). CAH can be measured by means of different techniques (Kirichenko and Gatapova 2016). Accumulated data allows one to simulate physical mechanisms of wetting behavior of different soil minerals and aggregates (Zhang et al. 2016; Fer et al. 2016). However, existing CA and CAH measurement techniques require further improvement and adaptation to specific clay types.

Wettability can be estimated in a laboratory by measuring CA of water droplets on different solid surfaces. Contact angle depends on the polarity of interacting molecules and their fragments. The interaction of complex multicomponent molecules with water in the soil can exhibit both hydrophilic and hydrophobic properties simultaneously. Polar parts of such molecules (–OH, =CO, –S, =O, $–NH_2$, –F, =N–OH, $–NO_2$, –N=O, –C=N, –N=N–… and non-polar $–C_6H_5$, $–CH_3$, $–CH=CH_2$) are subjected to hydration while the non-polar ones can only influence the wetting liquid (Krestov and Berezin 1986). The hydrophilic and hydrophobic interaction in soil contributes some unpredictability to the surface properties depending on the previous wetting history, which is usually unknown. The presence of aqueous or non-aqueous film on clay surfaces influences the orientation of adsorbed molecules and, thus, the exhibition of hydrophilic or hydrophobic properties even after eliminating this film. The more clearly the effect of hydrophilic-hydrophobic interactions manifests itself, the longer the film/clay contact history is. In the wild, this prehistory will be characterized by zonality associated with the development of biofilms.

Clays and soils have high porosity and surface roughness, i.e. high heterogeneity of the surface energy distribution among particles. Clays are strongly hydrophilic in nature with zero contact angle representing complete wetting. However, there are a number of factors in practice that leads to CAH, which could be determined in two ways: (a) as difference between advancing and receding CA; (b) as difference between static and initial contact angles. Thus, the following kinds of CA are observed when a liquid droplet spreads over a solid soil surface (Summ and Gorjunov 1976; Bonn et al. 2009):

– equilibrium CA is related to the ideal (smooth, homogeneous, rigid and insoluble) solid; hereby, it is considered when rough surfaces are wetting;
– static CA is measured without changing the contact area between liquid and solid; it is often more meaningful for assessing quasi-static processes;
– dynamic CA depends on the solid/liquid contact time; the local angle the interface makes with the substrate depends strongly on scale, i.e. on the distance from the contact line; occurs in the course of wetting (advancing angle) or de-wetting (receding angle) of a solid;
– two senses of apparent CA (macroscopic angle):

$\cos \theta w = r \cos \theta$—Wenzel-Derjaguin CA (Wenzel 1936; Derjaguin 1946),
$\cos \theta_{CB} = \Sigma \lambda_i \cos \theta_{Yi}$—Cassie-Baxter CA (Cassie 1948),

where θ is Young's contact angle as defined for the ideal surface, θ_{Yi} are Young's angle of the material i, including air for rough surfaces, r is the roughness parameters, λ_i is the area fraction of the material i on the surface.

Properly speaking, in case of clayey soils, we deal with apparently dynamic CA on the heterogeneous wetting surface. In practice, the estimation of CA is related to the measurement of drop spreading and absorption (and sometimes evaporation) rates. During the sessile drop spreading time, a film with a thickness ranging from several dozen angstroms to several micrometers appears, and the drop mass starts spreading (Summ and Gorjunov 1976). Due to the porous structure of clays, liquid absorption is inevitable, and the drop spreads faster. Water drop evaporates much slower in normal conditions and, therefore, it can be neglected in the CA measurement.

A common way of studying soil wettability is to prepare powder specimens, which are sometimes pressed in a particular way. Nowadays this is the best way, though the problems of preferred orientation of clay particles and pores, their inclination to swell and crack during drying have not been solved yet (Arkhipov et al. 2012). When working with clays, it should be kept in mind that the scale of surface roughness is considered too small compared to a drop size. Consequently, the drop volume used for the CA measurement must be large enough on the surface roughness scale, but the pressure on the support must small enough for capillary forces to prevail over gravity.

Despite the fact that microbial communities play a key role in transforming soils, they are so strongly limited by their environment that more than 95% of them are in the latent state. In an active state, microorganisms of different taxonomic groups form biofilms consisting of extracellular polymeric substances create a biofilm on soil particles, which facilitates the extraction of necessary ions from minerals, provides the distribution of microbes on the soil surface and increases the adhesion of biomat (Gorbushina 2007—fata Morgana for co-author AAG). Such a biofilm controls the wettability of particular soil localities. Herewith, a biofilm-covered surface area plays a greater role than biofilm thickness. Coating the hydrophilic quartz particles in a thin film of biopolymer prevents water from spreading over the surface, and water tends to be pulled into a spherical drop (Cuadros 2017). When making a rough estimate for biopolysaccharide consisting of glucose residues, 1–20 mg per gram of polymer

will be enough to complete coating the quartz grains in powder, with a specific surface area ranged from 3 to 60 m^2/g. It is known that when soil microbial activity develops over a long time, the surface of clay particles and micropores is completely covered with microbial extracellular products. However, one can expect that the increase in soil hydrophobicity caused by microorganisms is observed only when the soil initially exhibited high hydrophilic properties. In other cases, the result of the change in the soil surface energy depends on local interactions between biofilm and the hydrophobic substrate, which in the long run will likely to be consumed. It should be noted that this scenario of the change of the hydrophilic-hydrophobic properties of soils hasn't been explored yet. Contamination of soil with hydrocarbons can be an example. It is biodegradation that includes several stages. Each of these stages has a product different from its precursor in hydrophilic/hydrophobic properties, namely alcohol—an aldehyde/ketone—a fatty acid—a shorter carbon chain hydrocarbon (Salanitro 2001). The mathematical model of this process is in good agreement with the experiment (Lubysheva et al. 2018).

The **purpose** of this research is to study the change in wettability of clays due to the influence of mesophilic soil microorganisms' activity when adding model contaminants: water-in-oil emulsion, glycerol and oleic acid. During the experiments, the objectives of this study were to specify peculiarities of wetting contact angle hysteresis of clays with substrates of different mineral composition and microbial activity.

10.1.1 Objects and Methods

To model the microbial modification of water-soil systems we used the clayey samples with different mineral composition and surface energies depending on their natural compaction and transformation history (Fig. 10.1):

(A) Colloidal silica (CS);
(B) Luvic Chernozem, Loamic, Pachic, layer 0–20 cm (LC);
(C) Chlorite-muscovite marl (CM);
(D) Chlorite-muscovite marl with pyrite (CMP);
(E) Muscovite-kaolinite calcareous clay with pyrite (MKCP);
(F) Phyllite (Ph).

CS and LC possess the maximum and Ph—the minimum surface energy among the samples.

Methods. The mineral composition of samples was characterized by powder X-ray diffraction (Bruker D2 Phaser). The grain size distribution was measured by using the sieve, the sedimentation and the laser diffraction (Fritch Analysette 22) methods. Porosity coefficient was measured using water picnometer. Moisture content was defined gravimetrically. Organic matter content was measured using dry combustion method after pretreatment with acid to remove carbonates.

Clay sample		colloidal silica	chlorite-muscovite marl with pyrite	chlorite-muscovite marl	muscovite-kaolinite calcareous clay with pyrite	phyllite	Luvic Chernozem, Loamic, Pachic
Sample designation	Microbial community with glycerin stimulation	**CS+G**	**CMP+G**	**CM+G**	**MKCP+G**	**Ph+G**	-
	Microbial community with crude oil stimulation	**CS+Oil**	**CMP+Oil**	**CM+Oil**	**MKCP+Oil**	**Ph+Oil**	**LC**
	Microbial community with oleic acid stimulation	-	-	-	-	-	**LC+OA**
Total carbon content, % in dry weight		-	4,28 (>95% inorganic)	5,91 (>95% inorganic)	3,08 (>95% inorganic)	4,66 (>95% inorganic)	3,55 (>95% organic)
Clay absorbency on the example of dye methylene blue, absorbed for one hour							
Porosity after watering, % in volume		33	7	3	12	12	55
Particle size distribution, % in dry weight	>50 mcm	1	-	-	-	59,9	-
	10-50 mcm	66	58,3	71,3	26,3	24,0	35,5
	1-10 mcm	33	34,7	28,0	50,0	14,8	51,4
	<1 mcm	-	7	0,8	23,7	1,4	13,1
Full water capacity, % in dry weight		583	59	44	49	55	60
Maximum hygroscopicity, % in dry weight		27	4	2	5	2	6

Fig. 10.1 Clay samples characteristics and experimental options

Experiment with microbial communities. Air-dry samples were crushed in an agate pounder to a powder consistency. The samples were placed into Petri dishes distributing them at the bottom about 2 mm thick and wetted with distilled water and kept the total moisture capacity at the level of 0.8. The temperature of the experiment was in the range of 24 ± 2 °C, as we aimed to highlight mesophilic microorganisms. We used the extract from leached Chernozem soil with 900-day residual crude oil contamination to inoculate microorganisms. Tatarstan crude oil high in viscosity and sulfur content was used. Substances simulating stages of microbial oil degradation—water-in-oil emulsion (Oil), glycerol (G) and oleic acid (OA)—were applied as stimulators. This approach to selecting microbes was described by Yakushev (2015). A 1:100 extraction of microorganisms from the soil was prepared according to Zenova et al. (2002). The general scheme of inoculation was the following: soil activation for 3 days—extraction—selective medium (water-in-oil emulsion/glycerol/oleic acid)—adaptation for 3 weeks—inoculation into samples. Glycerol and oleic acid had been pasteurized before incubation, but water-in-oil emulsion had not. Citrate buffer with a pH of 4 was added to the soil extract in order to inhibit bacterial growth. A drop of the extract per 15 ml of the medium was added for incubation. Three weeks later, the clays were inoculated with 10–12 drops of the selective medium per Petri dish. After fungal hyphae formed a mat on the clay surface, we sliced it and made a sandwich between two glasses creating a layer 0.5 mm thick, further called as sandwich specimen. These specimens were placed in a way to provide constant capillary contact with the water in the remaining clay and were kept for 4–5 months. After that, the sandwich specimens were taken out and slowly dried in the air. The rest of

the clay was used to prepare powder specimens to measure CA, determine the drop spreading time and for XRD analysis.

Clay mineral composition study was conducted by the XRD method. Before and after the microbial activity, clay samples were crushed into powder in an agate pounder with alcohol. After alcohol evaporated, they were placed into cuvettes in an air-dry state avoiding texturing for the XRD analysis. Copper radiation was applied. The exposure time was one second. The range of measurements was 0.3–40 degrees 2θ.

Preparation of cellulose membranes for CA measurement. The peculiarity of cellulose membranes compared to clay powders is low water absorption. Cellulose acetate is a substance similar to microbial polysaccharides, so, in this respect, it could be considered as ideal biofilm model. Two circles of the membrane Vladipor MFAC-B-1 (Russia) were placed in each clayey medium to retain hydrophobic substances, which are able to diffuse significantly during the experiment. These membranes did not allow microbial cells to go in, they weren't toxic, had 0.05 mcm of average pore diameter, 80–85% of total porosity and were 130–140 mcm thick. The membranes were kept in clays for 3, 26 and 135 days. After that, the membranes were slightly washed by distilled water to wash off ground particles, air dried and levelled under pressure. The surface of the cellulose membrane is more homogeneous than that of clay powder. However, one of the two angles in the drop projection can be smaller. Herein, the droplet asymmetry is caused by the fact that soil substances pass through membrane not as uniform flow but as fingered one. We considered the larger drop angle that formed on the membrane. There were 12 droplet measurements for each sample.

Preparation of sandwich specimens for CA measurement. The specimen in a wet state was carefully uncovered from one side by shifting and removing the glass, then dried at room temperature. In some cases, water vapor was absorbed by concentrated sulfuric acid in hermetic conditions. A method used for powder specimens, which is described below, was applied for settling the sessile droplets. Sandwich specimens from clays not influenced by microbes were prepared in a similar way to highlight the changes that occur on biomats.

CA measurement on powder specimens. Nowadays the study of wetting and drop spreading processes on soil surfaces is at a stage of choosing an appropriate method. Drop absorption and spreading time (Atanassova et al. 2018), equilibrium, quasi-stable and apparent CA (Ruíz-Cabello et al. 2014; Fer et al. 2016) as well as in situ CA obtained with non-destructive methods (Alhammadi et al. 2017) are proposed to assess hydrophilic/hydrophobic properties of clays, soils as well as a number of other porous media. We applied a methodological approach developed in recent years (Janczuk and Bialopiotrowicz 1988; Bachmann et al. 2003; Shang et al. 2008; Borysenko et al. 2009; Kholodov et al. 2015; Shein et al. 2016). The basic requirement for the compared specimens is to have the same dispersion and compaction before and after the experiment. The powder specimen is proposed to be prepared for the CA measurements by either sticking clay particles to the water-proof support (Bachmann et al. 2003) or pressing until achieving certain compaction (Arkhipov et al. 2012). We sprinkled the powder on double-sided adhesive tape,

which is glued on flat glass, and pressed at 150 Pa for 1 min. After that, non-sticky powder residues were removed by shaking once. The specimen prepared this way was placed horizontally in the focus of the USB microscope. CA was photographed from the moment when the drop separates from the pipette tip until complete spreading. The drop's volume was 25 mcl. The pipette tip with a drop was orthogonally taken 1 mm close to the specimen's surface. Apparent CA was measured according to the first shot after drop settling (one second later) to compare with other researchers' results. In addition, the drop spreading/absorption time was determined, and then the drop's dynamics were calculated according to Eq. 1. We measured dr/dt with certain specimens' thickness l for experimental verification of this model. For this purpose, the glasses with the distributed air-dry clay powder (sample MKCP) with different layer thickness were placed in a desiccator under different vapor pressure for a week; several specimens were dried at 105 °C instead of moistening.

Evaluation of parameters for drop spreading equation. The drop spreading process can be investigated by observing a wet spot growing due to water film formed on the powder surface. The drop spreading rate at a fixed time relates to wet spot characteristics as:

$$\frac{dr}{dt} = \frac{a}{r} + \frac{b}{r(l + l_0)} \tag{1}$$

where r—spot radius; l—wet layer thickness; l_0—minimal wet layer thickness determined by grain sizes; a and b are fitting parameters involving properties of the water-solid-air system.

10.1.2 Results and Discussion

Clay mineral composition included:

- quartz, chlorite, muscovite—excluding sample CS;
- albite—excluding samples CS and CM;
- dolomite, calcite—excluding samples CS and LC;
- pyrite—in samples CMP and MKCP;
- microcline—in samples MKCP and LC;
- kaolinite—in sample MKCP;
- cristobalite—in sample CM.

During the experiment, there were observed changes in the composition of only two samples (Fig. 10.2). Pyrite transformed into hematite in the sample MKCP + Oil, and fine-grained (0.05–0.1 mm) pyrite in the CMP sample transformed into goethite (colloidal FeOOH). Pyrite oxidation could have both abiogenic and biogenic origin due to a highly humid environment and high oxygen availability at the same time according to the reaction (Kertesz and Frossard 2015):

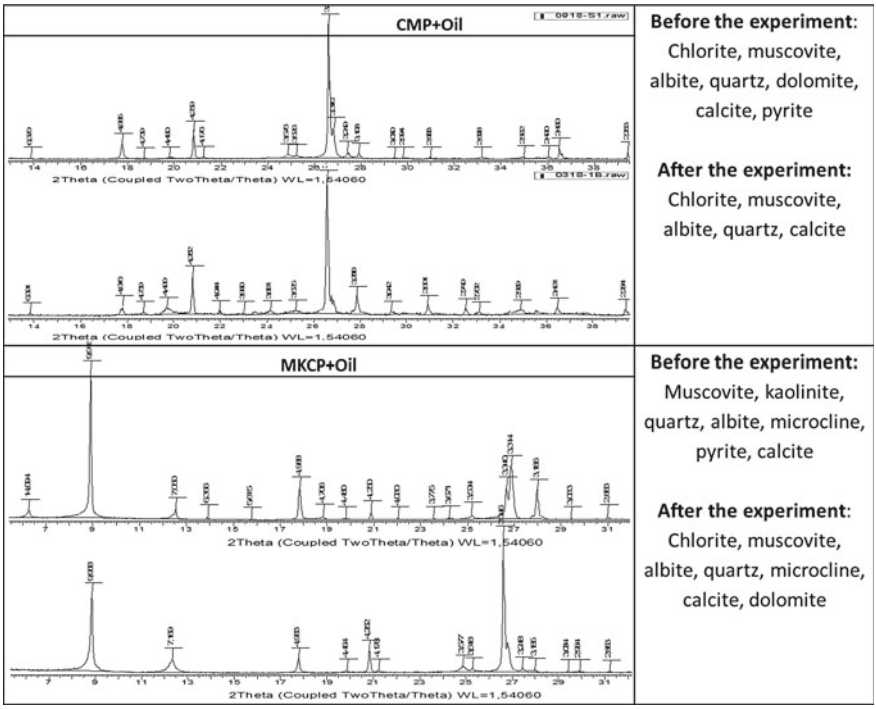


Fig. 10.2 Mineral composition of the samples

$$3Fe_2S + 11O_2 + 2H_2O \rightarrow 3Fe^{3+} + 4H^{+} + 6SO_4^{2-}.$$

Additionally, calcite and dolomite peak heights decreased about twice with slight widening in the sample MKCP + Oil while quartz peaks remained unchanged.

Wetting contact angles, drop spreading and absorption in clay samples. For Eq. (1), we took $t = 2$ and $r = 1.8$ mm for varied wet layer thickness l (Fig. 10.3). One can see that fitted curves for partially moistured samples lie within the area limited by two curves of absolutely dry and maximal hygroscopic states of samples. It is remarkable that the exposure of clay samples without kaolinite dried in the atmosphere of sulfuric vapor for 3 weeks led to the increase in CA, i.e. increase in wetting hysteresis (Fig. 10.4). Perhaps, there was water film depletion from the surface of particles, at least, with separate spots. This, according to a theory (Summ and Gorjunov 1976), supposes overcoming the energy barrier because of the displacement of the air beneath the water droplet on a rough surface.

CA measured in our research corresponded to the definition of apparent dynamic advancing CA. As all of our surfaces in the limiting case were completely wetted, the measured CA values can be at the same time a measure of wetting hysteresis. It's necessary to stress an important point that all samples excluding CS were chemically heterogeneous like any natural disperse systems. So this heterogeneity

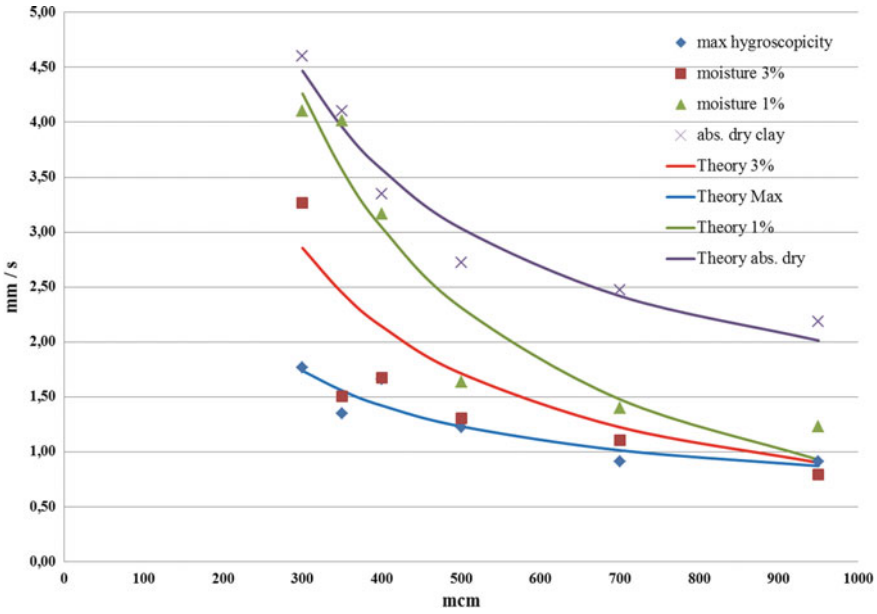


Fig. 10.3 Drop spreading rate depended on the thickness of penetrating layer. MKCP sample. The initial drop radius 1.8 mm

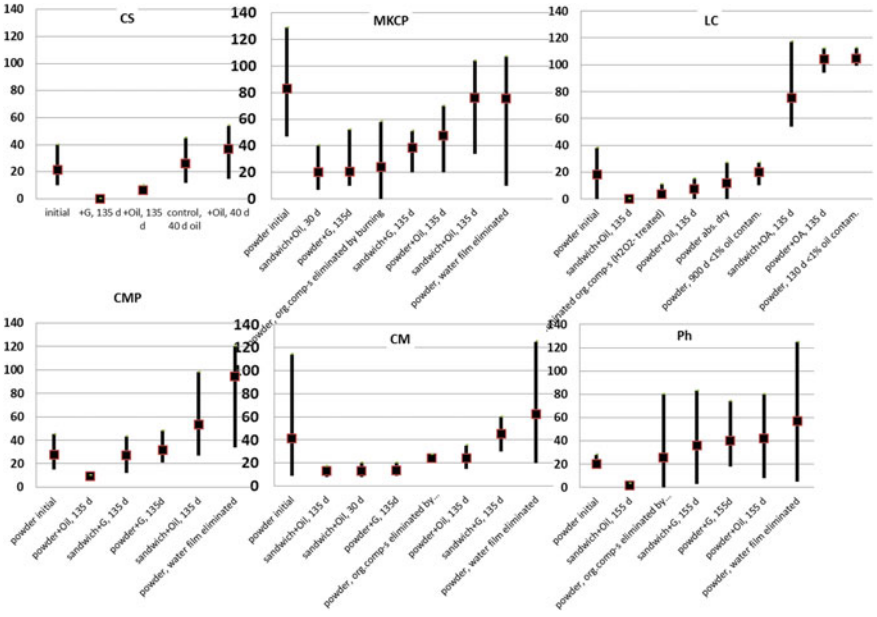


Fig. 10.4 Wetting contact angle on powder and sandwich specimens

could be expressed as a manifestation of different hydrophilic-hydrophobic properties inside the wetting line of one drop. Moreover, hydrophobic spots could appear on the hydrophilic surface after the biofilms developed, and vice versa. Therefore, such characteristics such as average, minimal, maximal CA and drop projection asymmetry are relevant for drop shape analysis.

The sample LC most expressively responded to the treatment (Fig. 10.4), and stimulated by the oleic acid, the hydrophilic surface became hydrophobic for 130 days as well as in residual crude oil contamination (<1% to weight). The sample CMP shows a weaker response to the treatment, and there was a hydrophobic transition only after water film removal. The treatment almost did not affect CA in the samples CM and CS. Meanwhile, the sample CS showed the lowest dispersion of results corresponding to its high homogeneity. The sample MKCP in its initial state possessed larger CA hysteresis compared to the other samples. Treatment of this sample either didn't change its wettability or attenuated hysteresis.

The microbial community isolated from the oil-contaminated soil successfully developed on clays when stimulating with both hydrophobic oil and hydrophilic glycerol (Fig. 10.5.). The following fungi appeared on Czapek medium: *Aspergillus* sp., *Penicillium* sp., *Fusarium* sp., *Phoma* sp., *Alternaria* sp., *Mucor* sp., *Cladosporium* sp., *Trichothecium* sp. at the level of 10^6 CFU. The fattest biomats developed during 4–5 months on the samples CMCP + G, MKCP + G as well as LC + OA (Fig. 10.5). Hydrophilicity/hydrophobicity of the stimulator of microbial activity

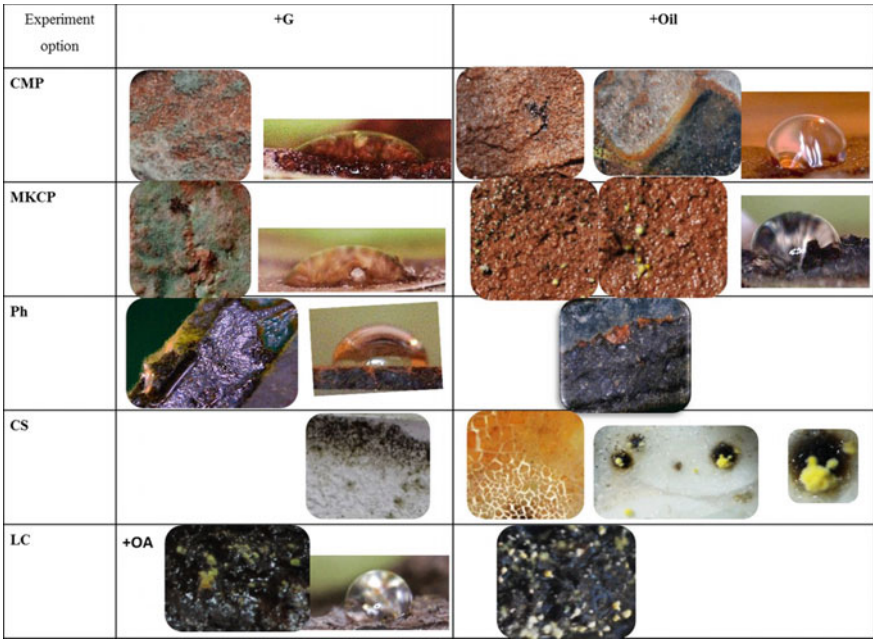


Fig. 10.5 Superficies of the samples after the experiments and drops on biomat surface

did not have a clear effect on clay properties in 135 days. The typical experimental cases are shown in Fig. 10.6: (a) wetting hysteresis was weaker in the presence of a hydrophilic stimulator than in the presence of a hydrophobic one (sample MKCP); (b) wetting hysteresis was stronger in the presence of a hydrophilic stimulator than in the presence of a hydrophobic one (sample CMP); (c) wetting hysteresis was smaller in the presence of a hydrophobic stimulator and larger in the presence of a hydrophilic stimulator than in the same sample before microbial impact (sample LC). The CA measurement demonstrated that the oil stimulation of the microbial community in the sample CS + Oil results in temporarily strong hysteresis on the 40th day, but then hysteresis disappears. However, it persists until the 155th day of the experiment in the sample Ph (Fig. 10.4). In the rest of the samples, the oil-stimulated CA hysteresis decrease was observed despite the hydrophobicity of oil. At the same time, the development of the biofilm stimulated by oil in sandwich specimens CMP + Oil and MKCP + Oil (Fig. 10.7) does not almost change their CA hysteresis, and in the case of sample Ph, the surface becomes even more hydrophilic. The fast biomat development in the sample LC + OA correlated with the CA hysteresis increase, which was like small oil contamination. The stimulation of the microbial activity with hydrophilic glycerol has an ambiguous effect on CA hysteresis: it decreases in the samples CS, CM, MKCP, increases in the sample Ph and does not change in the sample CMP. The biofilm surface after glycerol stimulation in the sample CM was more hydrophobic than the surface of this sample without any biofilm and stimulation.

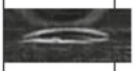
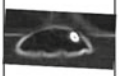
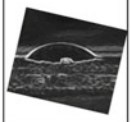
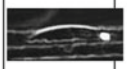
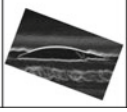
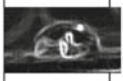
Experiment option	Initial		+G		+Oil		+OA	
	Drop shape, 1 second after seating on clay surface	Drop spreading time, s	Drop shape, 1 second after seating on clay surface	Drop spreading time, s	Drop shape, 1 second after seating on clay surface	Drop spreading time, s	Drop shape, 1 second after seating on clay surface	Drop spreading time, sec
MKCP		18		5		7	-	-
CMP		<1		9	No hysteresis	0	-	-
LC		1-3	-	-		1-2		57

Fig. 10.6 Initial drop shape on the powder surface after the microbial activity during 4–5 months

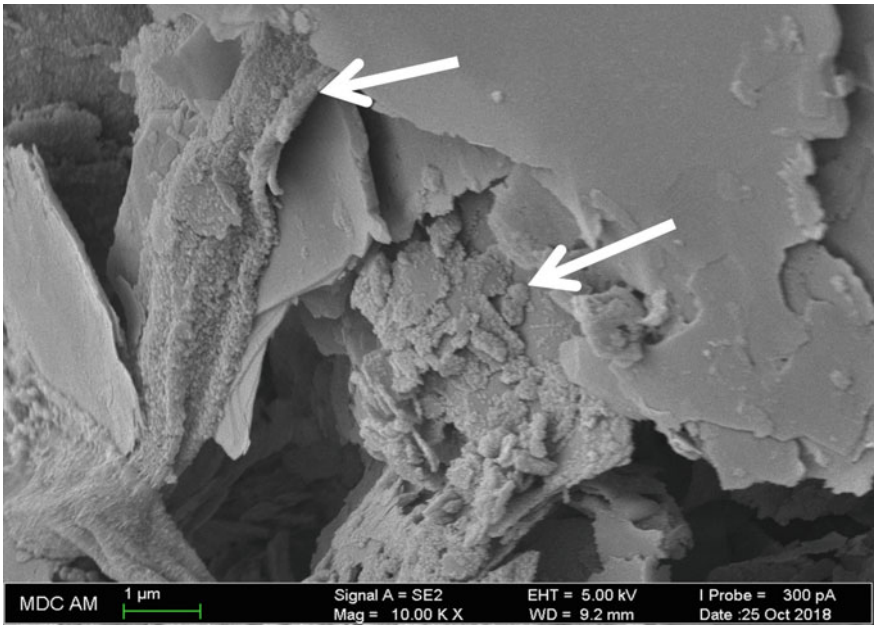


Fig. 10.7 An example of the biofilm developed on phyllite which had been placed as a thin layer between two glasses

CA measurement on cellulose membranes (Fig. 10.8). The dispersion in CA values for membranes soaked in glycerol, oleic acid and water-in-oil emulsion, which are ±6°, 2° and 6° respectively, could be accepted as a measure of initial membrane heterogeneity. After exposing the membrane on clay surfaces, CA dispersions increased for all the specimens as a result of an increase in membrane surface heterogeneity. The sample CMP + G (the 26th day of exposure) was noticeably different from the samples with glycerol stimulation because slightly hydrophobic sites appeared alongside with sites with increased hydrophilicity compared to the initial membrane. The membrane surfaces of the samples MKCP (the 26th day of exposure) and CS (the 135th day of exposure) were subjected to hydrophilization. The results obtained on the 26th day of exposure correlate with the most abundant propagation of fungi in the samples MKCP and CMP allowing one to assume that microbial communities and/or the Fe chemical state alteration were responsible for both the hydrophilization and hydrophobization of the surface. The CA dispersion (i.e. surface heterogeneity) increased more in oil-stimulated samples than in the glycerol-stimulated ones. Moreover, this increase occurred even after a three-day exposure of the samples LC + Oil and Ph + Oil. Weakly hydrophobic sites appeared in the sample LC + Oil on the 3rd day and remained until the 135th day. Similar hydrophobic sites also appeared in the sample MKCP + Oil on the 26th day of exposure but disappeared soon. The increased hydrophilicity compared with the initial surface took place on membrane parts of the samples LC + Oil (the 26th day of exposure), CS

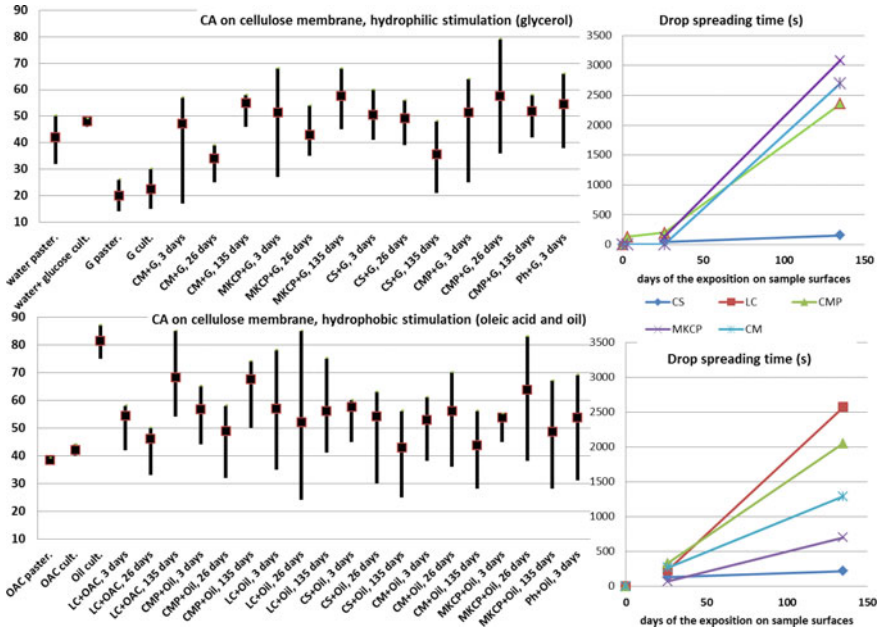


Fig. 10.8 Drop spreading onto cellulose membrane surfaces

+ Oil (from the 26th to the 135th days of exposure), CM + Oil, MKCP + Oil (to the 135th day of exposure). An increase in hydrophobicity and heterogeneity in the oleic acid-stimulated sample LC + OA was observed on the 135th day of exposure. Evidently, hydrophilic-hydrophobic properties of the membrane surface monotonically depended on the duration of exposure while the surface heterogeneity mostly increased with time. These observations comply with the assumption about the zonality of hydrophilic and hydrophobic components exudation into clays inhabited by active microorganisms. We suppose that chemicals exuded by biofilms played a key role in the surface hydrophilic-hydrophobic balance, as the number of applied stimulators was negligible. It is a wonder that the control variability range of $\pm 6^\circ$ for CA measured in the samples stimulated by glycerol and oil exceeded in 26 out of 29 cases on membranes and in 13 out of 23 cases on powders. That is to say, the powder surface heterogeneity appeared to be lower than on the membranes despite the roughness, and chemical and geometric heterogeneity was as important as the surface hydrophilic-hydrophobic balance.

The drop spreading time was usually several hundreds or thousands of seconds on the membrane surface and less than a minute on powders. Moreover, as the experiment was carried out under atmospheric pressure, it was determined that the spreading time exceeding 5000 s could be considered as infinity compared with the evaporation time, and CA formed could be supposed as quasi-static. As the membrane saturates with compounds diffusing from soils, the drop spreading time clearly increased (Fig. 10.8). This fact proves that these compounds are partially hydropho-

bic regardless of the type of stimulation of the microbial community. Furthermore, the drop spreading time in the samples CM, CMP and MKCP increased faster in the variant with hydrophilic glycerol stimulator than with hydrophobic oil.

10.2 Conclusion

Relying on the results obtained one can conclude that variability in a manifestation of different hydrophilic-hydrophobic properties induced by the water and the carbon components removal and the biofilm development leads to the formation of heterogeneous spots on the surface occurred. Moreover, the water film exhausting procedure for clayey particles definitely increases the surface heterogeneity, whereas the carbon components removal and the biofilm stimulation in most cases decreases that heterogeneity for studied specimens. Clays possessed theoretically the highest initial surface energy (Chernozem soil and silica colloidal) showed the smallest dispersion in contact angle measurements. The experiment duration affected the heterogeneity spots formation non-linearly. It was found that the chemical spatial heterogeneity played a no less important role in the surface hydrophobic-hydrophilic balance than the geometrical heterogeneity. Taking into account the high sample heterogeneity (excluding silica colloidal), from the analysis of CA we can draw conclusions only about the trends in hydrophilic-hydrophobic balance alteration of samples. So, the reliable transformation from hydrophilic surface into slightly hydrophobic one took place only in case of Chernozem soil exposed to oleic acid as the stimulator for microbial growth. The chlorite-muscovite clayey sample, in which pyrite was oxidized into goethite, showed alike strong tendency towards such a transition after water film was exhausted. In rest cases, these tendencies were weaker, and only the increase in surface heterogeneity corresponding to any treatment was reliable in the sample possessed theoretically the minimal surface energy of particles (phyllite). Hydrophilic-hydrophobic properties of microbial growth stimulators did not have an unambiguous impact on contact angles. In weak biofilm cases, some recession of slight hydrophobicity occurred, perhaps, due to the microbial consumption of organic compounds and the Fe-containing components oxidizing. In fat biomat cases, the substrate hydrophobicity intensified. In the case of the apparent contact angle was about 90° from the beginning (muscovite-kaolinite clay), even exposed to the hydrophobic oil stimulator, the surface hydrophilization occurred. This allows us to hypothesize that the wettability of separate soil sites exposed to a number of chemicals can quickly change in any direction independently on initial hydrophilic-hydrophobic balance of a contaminant during its biodegradation. The complex influence of the clay hygroscopicity on wetting CA hysteresis was observed in the experiment. The clay moisture increasing from dry state (at 105 °C) to maximal hygroscopicity led to the CA hysteresis increased. However, the water film exhausting by the vapor absorption with concentrated sulfuric acid also resulted in CA increase, that is consistent with theoretical suppositions of other authors. We have been succeeded to simulate a drop spreading on the clayey powder layer of different thickness and the clay moisture ranged from dry state to maximal hygroscopicity.

Acknowledgements This work was supported by the grant allocated within the framework of the state support of the Kazan (Volga Region) Federal University for increasing its competitiveness among the world's leading research and education centers. *The snapshot for* Fig. 10.7 *was made in Interdisciplinary Center for Analytical Microscopy by Field emission scanning electron microscopy multipurpose analytical complex Merlin (Carl Zeiss). Director Yury Osin, operator Alexey Rogov.*

References

Alhammadi MA, AlRatrout A, Singh K, Bijeljic B, Blunt MJ (2017) In situ characterization of mixed-wettability in a reservoir rock at subsurface conditions. Sci Rep 7(10753):1–9. https://doi.org/10.1038/s41598-017-10992-w

Arkhipov VA, Paleev DY, Patrakov YF, Usanina AS (2012) Determination of powder materials wetting characteristics. Izvestiya vysshikh uchebnykh zavadenij Fizika 55(7/2):20–26 (in Russian)

Atanassova ID, Banov IM, Shishkov T, Petkova Z, Hristov B, Ivanov P, Markov E, Kirilov I, Harizanova M (2018) Relationships between soil water repellency, physical and chemical properties in hydrophobic technogenic soils from the region of Maritsa-Iztok coal mine in Bulgaria. Bulg J Agric Sci 24(Suppl 2):10–17

Bachmann J, Woche SK, Goebel MO, Kirkham MB, Horton R (2003) Extended methodology for determining wetting properties of porous media. Water Resour Res 39. https://doi.org/10.1029/2003wr002143

Bonn D, Eggers J, Indekeu J, Meunier J, Rolley E (2009) Wetting and spreading. Rev Mod Phys 81:739–801

Borysenko A, Clennell B, Sedev R, Burgar I, Ralston J, Raven M, Dewhurst D, Liu K (2009) Experimental investigations of the wettability of clays and shales. J Geophys Res 114:B07202. https://doi.org/10.1029/2008jb005928

Cassie ABD (1948) Contact angles. Discuss Faraday Soc 3:11–16

Cuadros J (2017) Clay minerals interaction with microorganisms: a review. Clay Miner 52:235–261

Derjaguin BV (1946) On the contact angle dependence on the microrelief and roughness of wetted surface. Doklady Akad Nauk SSSR 51(5):357–360

Fer M, Leue M, Kodešová R, Gerke HH, Ellerbrock RH (2016) Droplet infiltration dynamics and soil wettability related to soil organic matter of soil aggregate coatings and interiors. J Hydrol Hydromech 64(2):111–120. https://doi.org/10.1515/johh-2016-0021

Gorbushina AA (2007) Life on the rock. Environ Microbiol 9(7):1613–1631

Janczuk B, Bialopiotrowicz T (1988) Components of surface free energy of some clay minerals. Clays Clay Miner 36(3):243–248

Kertesz MA, Frossard E (2015) Biological cycling of inorganic nutrients and metals in soils and role in soil biogeochemistry. In Paul EA (ed) Soil microbiology, ecology and biochemistry, 4th edn. Elsevier. https://doi.org/10.2016/b978-0-12-415955-6.00016-5

Kholodov VA, Yaroslavtseva NV, Yashin MA, Frid AS, Lazarev VI, Tyugai ZN, Milanovskiy E Yu (2015) Contact angles of wetting and water stability of soil structure. Eurasian soil sci 48(6):600–607

Kirichenko EO, Gatapova EY (2016) Studying of the contact angle hysteresis on various surfaces. In: MATEC web of conferences, vol 72, p 01045. https://doi.org/10.1051/matecconf/20167201045

Krestov GA, Berezin BD (1986) Basic concepts of modern chemistry. Khimija, Leningrad (in Russian)

Lubysheva AI, Potashev KA, Sofinskaya OA (2018) Description of bioremediation of soils using the model of a multistep system of microorganisms. In: IOP conference series: earth and environmental science, vol 107, p 012102. https://doi.org/10.1088/1755-1315/107/1/012102

Rockhold ML, Yarwood RR, Niemet MR, Bottomley PJ, Selker JS (2002) Considerations for modeling bacterial-induced changes in hydraulic properties of variably saturated porous media. Adv water Resour 25:477–495

Ruíz-Cabello FJM, Rodríguez-Valverde MA, Cabrerizo-Vílchez MA (2014) Equilibrium contact angle or the most-stable contact angle? Adv Colloid Interface Sci 206:320–327. https://doi.org/10.1016/j.cis.2013.09.003

Salanitro JP (2001) Bioremediation of PHCs in soil. Academic Press, New York

Shang J, Flury M, Harsh JB, Zollars RL (2008) Comparison of different methods to measure contact angles of soil colloids. J Colloid Interface Sci 328:299–307

Shein EV, Verkhovtseva NV, Milanovsky EYu, Romanycheva AA (2016) Microbiological modification of Kaolinite and Montmorillonite Surface: changes in physical and chemical parameters (model experiment). Biogeosyst Tech 9(3):229–234

Summ BD, Gorjunov YV (1976) Physicochemical fundamentals of wetting and spreading. Khimija, Moscow (in Russian)

Tyugai Z, Milanovskiy E (2015) The contact angle of wetting of the solid phase of soil before and after chemical modification. Eurasian J Soil Sci 4(3):191–197

Wenzel RN (1936) Resistance of solid surfaces to wetting by water. Ind Eng Chem 28:988–994

Yakushev AV (2015) Integral structural-functional method for characterizing microbial populations. Eurasian Soil Sci 48:378–394. https://doi.org/10.1134/S1064229315040110

Zenova GM, Stepanov AL, Likhacheva AA, Manucharova NA (2002) Workshop on soil biology. Moscow state university, Moscow (in Russian)

Zhang Ch, Liu Zh, Deng P (2016) Contact angle of soil minerals: a molecular dynamics study. Comput Geotech 75:48–56

Zhu Y, Li Y, Lu A, Wang H, Yang X, Wang Ch, Cao W, Wang Q, Zhang X, Pan D, Pan X (2011) Study of the interaction between bentonite and a strain of *Bacillus mucilaginosus*. Clays Clay Miner 59(5):538–545

Chapter 11
Bio-inert Interactions in an Oil—Microorganisms System



Lidia I. Svarovskaya, Andrey Y. Manakov, Lyubov K. Altunina, Larisa A. Strelets and Andrey S. Stoporev

Abstract Most microorganisms are capable of the enzymatic oxidation of petroleum hydrocarbons and their use as a source of nutrition and energy. In the laboratory, enzymatic oil oxidation (biodegradation) in a liquid mineral medium is carried out with constant stirring for 30 and 60 days. The biodegradation of oil is carried out by a community of hydrocarbon-oxidizing microorganisms isolated from the composition of crude oil. The enzymatic activity of isolates is investigated individually. The paper presents the data of biodestructive changes in the physicochemical properties of oil, its group and component composition at different stages of biodegradation. Particular attention is paid to changes in the content of polar components in the composition of biodegraded oils. It is found that a 'water in oil' emulsion is formed in the course of cultivation of microorganisms in contact with oil. In this case, changes in the interfacial tension and pour point of oil and increase in its viscosity and density are observed. An analysis of samples of crude and biodegraded oil by the method of IR spectrometry showed that the degree of hydrocarbon oxidation and the content of aromatic structures (C=C), resins, and asphaltenes increase with increasing time of contact with microorganisms. The accumulation of oxygen-containing compounds (C=O) confirms the destructive activity of microorganisms. Emulsions of crude and biodegraded oil samples were under study in the course of nucleation of hydrates, depending on the degree of oxidation against the background of changes in the group composition of oil, the content of acids, resins and asphaltenes, and an increase in viscosity and density.

Keywords Oil · Microorganisms · Biodegradation · Gas hydrates

L. I. Svarovskaya (✉) · L. K. Altunina · L. A. Strelets
Institute of Petroleum Chemistry SB RAS, Tomsk, Russia
e-mail: sli@ipc.tsc.ru

A. Y. Manakov · A. S. Stoporev
Institute of Inorganic Chemistry SB RAS, Novosibirsk, Russia

© Springer Nature Switzerland AG 2020

O. V. Frank-Kamenetskaya et al. (eds.), *Processes and Phenomena on the Boundary Between Biogenic and Abiogenic Nature*, Lecture Notes in Earth System Sciences,
https://doi.org/10.1007/978-3-030-21614-6_11

11.1 Introduction

The interaction between oil and microorganisms under oil-pool conditions occurs at the water/oil interface. As a result of the interaction, oil hydrocarbons undergo biodegradation. The physicochemical composition of the oil changes and accumulation of metabolic products promoting emulsification takes place, Under conditions of high pressure and low temperature, water emulsified in oil and associated gas react with the formation of gas hydrates (Kelland 2006; Aman and Koh 2016; Sloan and Koh 2007). Such conditions of oil extraction and transportation are typical for regions of the cold arctic climate. Experimental investigations have shown that the flows of water, gas, and oil are not always capable of nucleation of hydrates. Some oils contain compounds that inhibit the formation of hydrates but the molecular structure of these inhibitors is still unknown (Borgund et al. 2009; Hoiland et al. 2005a). An assumption was made that an important indicator of the tendency to form hydrates is the degree of oil biodegradation, which is performed by microorganisms using induced enzymes (Chen et al. 2018; Stoporev et al. 2015, 2018a, b). Oil is a complex multicomponent system consisting of hydrocarbons of various structures and numerous hetero-organic compounds which give to oil specific properties intrinsic to colloidal and dispersed systems (Svarovskaya et al. 2018). Hydrocarbon compounds are represented in oil by paraffins, naphthenes, and aromatic structures Acyclic saturated hydrocarbons (n-alkanes) are the most susceptible to microbiological effects. Molecules of alkanes are connected by monovalent C–C bonds, whose enzymatic oxidation proceeds with the low consumption of energy (83.6 kcal/mol). For the oxidation of C–H bond, 98.8 kcal/mol is consumed. The products of metabolism in the oxidation of alkanes are alcohols, acids, ketones, and esters (Speight and Arjoon 2012; Erstad et al. 2009; Barth et al. 2004). The level of biodegradation of crude oil is an important indicator of the tendency to form gas hydrates (Hoiland et al. 2005b; Turner et al. 2009).

Bacteria of the genera *Pseudomonas, Micrococcus, Brevibacterium, Bacillus, Actinomyces, Nocardia,* etc. actively participate in the utilization of oil hydrocarbons. Alkane oxidizing microorganisms also develop on other organic media for example, bacteria of the genus *Pseudomonas* and *Bacillus* actively utilize alkanes and aromatic structures, including polycyclic hydrocarbons, naphthalenes, anthracenes, and phenanthrenes (Barth et al. 2004). The biodegradation of aromatic compounds is accompanied by the rupturing of aromatic ring and the formation of oxygen-containing structures, whose reactivity is due to the presence of C = O carbonyl group. Practically, all the groups presented in oil, including heterocyclic compounds are oxidized by enzymes, furan, thiophene, and pyrrole are the best known of these compounds (Svarovskaya et al. 2016, 2009). Microbial degradation of hydrocarbons proceeds with higher speed under conditions of free access of oxygen Microbiological methods based on enzymatic oxidation of hydrocarbons have recently become particularly relevant (Augustinovic et al. 2012; Vater et al. 2002). This is due primarily to the scientific interest in the problems of oil pollution control, as well as the possibility of practical use of microorganisms as inhibitors of hydrate nucleation

during the transportation of oil through a pipeline in cold climates. It should be noted that nucleation processes are influenced not only by the degree of oil destruction, but also by the presence of live bacterial cells containing protein (Rogers et al. 2011).

The aim of the work is to study the effect of the degree of oil biodegradation on the physicochemical properties, group composition, and the tendency of oil to nucleate hydrates.

11.2 Materials and Methods

Samples of crude and biodegraded oils from the Kazanskoye oil field in Western Siberia served as a material for microbiological and physico-chemical investigations. The main characteristics of crude oil are as follows: viscosity—2.42 mPa s, density—0.786 g/m^3, and freezing temperature—28 °C below zero.

Microbiological methods of investigation were used to determine the abundance dynamics during biodegradation and to isolate microorganisms from selected oil samples by classical inoculation into a solid meat-peptone agar medium (MPA). The oxidative activity of the isolated strains was determined by the express method of inoculation into Petri dishes on solid MPA medium coated with a thin oil layer. The area purified from oil around the grown colonies of microorganisms served as a criterion for the selection of destructive strains (Fig. 11.1a, b).

According to the results of the 16S pPHK gene sequence, the isolated strains belonged to the *Bacillus, Rhodococcus, Dietzia,* and *Pseudomonas* genera. A mixture of isolated strains was used with the purpose of oil biodegradation.

Method of oil biodegradation. The biodegradation of oil was carried out under laboratory conditions at a temperature of +5 °C for 30 and 60 days in a liquid mineral medium providing vital processes. The composition of the medium in g/dm^3 was as follows: Na_2CO_3—0.1, $MgSO_4$—0.2, $MnSO_4 \times 5H_2O$—0.02, KH_2PO_4—0.5, Na_2HPO_4—0.7, $CaCl_2 \times 5H_2O$—0.01, NH_4Cl—2.0, NaCl—2.0, pH 7.0–7.2,

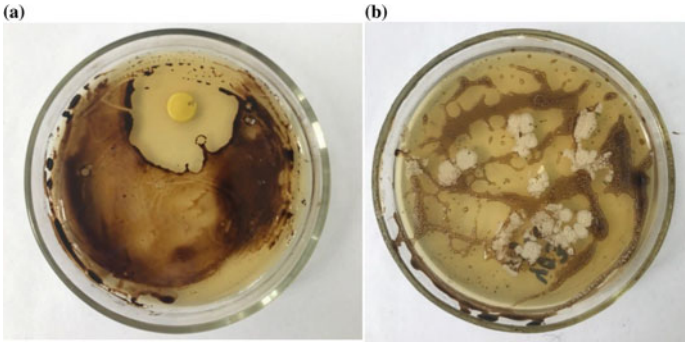


Fig. 11.1 Colonies of microorganisms Bacillus (**a**) and Pseudomonas (**b**) exhibiting an oxidative activity during inoculation into a solid agar medium covered with a thin layer of oil

water—up to 1 dm^3. The oil weight and the live microbial biomass in a ratio of 100:15:0.02 were placed into flasks containing 1.5 dm^3 of mineral medium. The flasks were mounted on a magnetic stirrer for continuous mixing, providing the system with oxygen. Stirring mode was 250 rpm. Upon completion of the biodegradation, the oil was separated from the aqueous phase in a separatory funnel. The complete oil dehydration was achieved via multiple centrifugation at 4000 rpm using an Armed 80-2S centrifuge.

The method of FTIR spectroscopy is based on the absorption, reflection and scattering of the infrared energy passing through a substance. It occupy an important place among various methods of integrated oil composition study. To analyze the composition of crude and biodegraded oils IR spectra were registered within the region 400–4000 cm^{-1} using a NICOLET 5700 spectrometer. The processing of spectra and determination of the optical density were performed using OMNIC 7.2 Thermo Nicolet Corporation software. To make a more accurate quantitative analysis, the spectral coefficients were calculated from the ratio of optical densities in the maxima of absorption bands (a.b.) of various functional groups to the optical density of the reference band. In order to assess the effect of biodegradation on the oil composition, spectral coefficients were calculated (Table 11.1).

Determination of group composition of oil. It is possible to calculate the group composition of oil using the optical density values of absorption bands for different functional groups (Koshelev et al. 2005). The **ω** content (%) of paraffins, naphthenes, aromatic and oxidized hydrocarbons was calculated as the ratio of the sum of optical densities of absorption bands related to hydrocarbons of corresponding type and to the total sum of optical densities of absorption bands of all hydrocarbons.

The acid number of oil serves as an indicator of the content of oil components exhibiting acidic properties. The most common are Naphthenic, aromatic and fatty acids, as well as phenols prevail among them. The acid number of the oil was determined by potentiometric titration. Alcohol-benzene was used as a solvent in a volume ratio of 1:1. For this purpose, a precisely weighed oil portion was placed in a 50 cm^3 glass cup and dissolved in 30–40 cm^3 of the alcohol-benzene mixture while stirring in magnetic stirrer. Upon complete dissolution, electrodes were introduced into the cup and titration was performed with 0.01 N alcohol solution of KOH until a constant pH value was reached. To determine the equivalence point correctly, a solution of potassium hydroxide should be added in small portions (0.05–0.1 cm^3). Acid number (AN) shows the number of potassium hydroxide milligrams necessary for neutralization of free organic acids contained in 1 g of oil. The content of free carboxylic

Table 11.1 Spectral coefficients for characterization of oils

Spectral coefficients	Ratio of optical densities of absorption bands
C_{ar} (aromaticity)	D_{1610}/D_{725}
C_{al} (aliphaticity)	$D_{725} + D_{1377}/D_{1610}$
C_{br} (branching)	D_{1377}/D_{1465}
C_{ox} (oxidation)	D_{1700}/D_{1465}

acids C_{coon} (wt%) was calculated by the formula:

$$C_{COOH} = \frac{V_{KOH} \cdot C_{KOH} \cdot 45}{10\,m} \tag{11.1}$$

Acid number (mg KOH per gram of sample analyzed) was calculated by the formula:

$$AN = \frac{V_{KOH} \cdot C_{KOH} \cdot 56}{m} \tag{11.2}$$

where

V_{KOH} is the volume of 0.01 N KOH solution consumed for titration of the sample until the equivalence point was reached, cm^3;
S_{KON} is the concentration of potassium hydroxide solution, mol/dm^3;
45 is the equivalent of a COOH group;
m is the mass of oil sample; and
56 is the molecular weight of KOH, g/mol

The contents of resins and asphaltenes in the oil were determined by a standard method based on solubility of resin-asphaltene components in solvents of different polarity. The content of the asphaltenes was determined using a "cold" Golde method. For this purpose an oil sample was placed in a conical flask and dissolved in a 40-fold excess of hexane. The resulting solution was left for a day in a dark place at room temperature for asphaltene precipitation. The precipitate was filtered and washed with hexane. The filter with the precipitate was folded into a cartridge and loaded into a Soxhlet apparatus to extract co-precipitated resins and oily fraction with hexane. Then the solvent was distilled and the extractable substance was dried to constant weight.

The contents of oily fraction and resins were determined by liquid adsorption chromatography on silica gel CHEMAPOL (L 100/160). A hexane solution (after asphaltene washing) was added to the deresined oil, an excess of solvent was distilled and the remaining part of the maltenes was applied onto a layer of activated silica gel. The resulting mixture of silica gel with adsorbed maltenes was placed in a Soxhlet apparatus, where the oily fraction was successively washed with hexane and the resins—with alcohol-benzene (1:1 volume ratio). Upon extraction completion the solvent was removed, the resulting components were dried to constant weight. The percentage of components in the test sample was calculated by the following formula:

$$X, \% = \frac{100 \cdot a}{A} \tag{11.3}$$

where

a weight of the component obtained, g,
A oil sample, g.

The probability of gas hydrates nucleation was determined using the samples of crude and biodegraded oils. Before the analyses the oil samples were freed from emulsified water by multiple centrifuging at 3500 rpm during 30 min. In the experiments we used oil emulsions with a water content of 50 wt%. The oil emulsions were prepared by mixing with a mixer (800 rpm) at room temperature for 20 min. The emulsions have been stable for a long time (months).

The schematic diagram of the installation used to study the methane hydrate formation from water emulsions in oils was considered in (Stoporev et al. 2015). The emulsion samples were placed in 4 fluoroplastic cells. The thickness of the emulsion layer was 10 mm in each cell. Then a chromel-alumel thermocouple was introduced into each sample and the sample holder was placed in the apparatus where the gas pressure was maintained at least 15 mPa s. The samples were saturated with methane at room temperature for 15 h. Then the apparatus was subjected to a cooling-heating cycle (+20 °C → −15 °C → +20 °C) at a given rate of 0.14 °C/min. The temperature and pressure in the apparatus were recorded by an electronic meter and recorded on a computer as a function of time. The duration of the experiment was determined by the rate of cooling—heating and was about 9 h. The formations of hydrate and ice in each cell were recorded by temperature jumps. Errors in temperature and pressure measurements were ±0.2 °C and ±0.25% of the measured value, respectively.

11.3 Results and Discussion

The Kazanskoye oil field of light oil is being developed by water flooding. The biocenosis of the bottom zones of injection wells is represented by aerobic and anaerobic bacteria. The amount of biogenic elements, including sulfates, ammonium nitrogen and phosphates ensures the development of reservoir microflora (Gerhcardt 1981). Cumulative cultures were incubated at +5 °C, since our concern is the activity of psychrophilous bacteria growing at a low positive temperature. To simulate biodegradation of crude oil samples we isolated and propagated the community of bacteria with a high destructive activity belonging to the following genera: *Bacillus, Rhodococcus, Dietzia* and *Pseudomona*. Earlier, we have used the method of isolation of pure cultures for the biodegradation of organic matter of peat (Svarovskaya et al. 2017).

The oil from the Kazanskoye oil field (KN) was biodegraded at +5 °C, corresponding to the average temperature in the northern regions of Siberia. In the process of biodegradation the maximum number of microflora in the aqueous phase was 670 million CFU/cm^3.

The properties of crude oil (KN) and the oil after biodegradation for 30 (KN30) and 60 (KN60) days are presented in Table 11.2.

At oil contact with microorganisms paraffinic structures, which do not require great expenditures of energy to oxidize monovalent C–C and C–H bonds, degraded first of all. (Harayama et al. 1999). The content of aromatic compounds C = C increased, their further oxidation promoted accumulation of resin-asphalten substances and increase in viscosity and density. Polar components of the oil—resins

Table 11.2 Physicochemical properties and component compositions of KN samples

Parameters	Oil samples		
	Crude oil	KN30	KN60
Viscosity, mPa s	2.42	23.98	31.88
Density, g/cm^3	0.786	0.866	0.881
Content, % rel.:			
Saturated HCs	85.2	75.1	73.6
Aromatic HCS	3.0	8.3	10.5
Resins	1.6	5.4	7.8
Asphaltenes	0.1	4.2	4.5
Light HCs	10.1	7.0	3.6

and asphaltenes—underwent microbiological oxidation with great difficulty. Resin-asphaltene substances represent a mixture of high-molecular hetero-organic compounds of a hybrid structure occurring in the oil in a dissolved state or as colloidal systems (Kapellos 2017). Resin substances have good solubility in organic solvents; they are thermally and chemically unstable and under the influence of certain external factors can turn into asphaltenes. Asphaltenes are characterized by high aromaticity and polydispersity, they do not dissolve in the solutions of low-molecular alkanes; they are chemically active and easily oxidized. The authors (Vater et al. 2002) using molecular dynamics methods showed that the presence of asphaltenes on the water-gas interface accelerates methane diffusion through an aqueous phase and facilitates the assembly of clathrate cavities from water molecules, i.e. they act as promoters of hydrate formation.

The oil biodegradation in the aqueous medium is accompanied by the formation of a "water-in-oil" emulsion with a decrease in the interfacial tension from 25.5 mN/m for the crude oil to 17.3 mN/m for KN30 and 17.0 mN/m for KN60. Paraffins, resins and asphaltenes are natural stabilizers of oil emulsions. In the process of oil biodegradation the contents of resins and asphaltenes increase, while that of paraffins decreases, but the share of paraffins in the oil remains at a high level (Table 11.2). Acids, alcohols, ketones and esters are the products of paraffin oxidation. The total acid content in KN30 increased 3.5 times and in KN60–5 times as compared with the crude oil.

The oil samples were investigated by IR-spectrometry (Fig. 11.2). It should be noted that in the composition of the crude oil we determined the absorption band (pp) of oxygen-containing compounds in the region of 1699 cm^{-1}, which means that the oil has been partially degraded under the conditions of the oil reservoir.

The composition of the functional groups in the process of oil biodegradation remained practically unchanged. To compare the IR-spectra of the crude and biodegraded oil samples we used the following absorption bands: 1600, 871, 813, and 745 cm^{-1}—characterizing aromatic structures; 720, 1377 and 1465 cm^{-1}—the methyl and methylene groups in paraffinic hydrocarbons, 1700 cm^{-1}—oxygen-containing compounds. The ratio of optical densities at the maxima of these

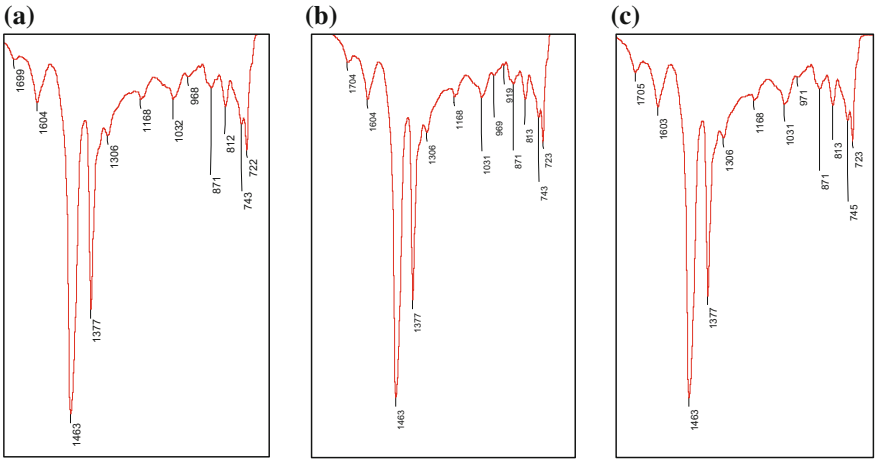


Fig. 11.2 Fragments of IR-spectra for the crude oil (**a**) and KN30 (**b**), KN60 (**c**) samples

absorption bands enabled to obtain spectral coefficients. The data are presented in Table 11.3.

The increase in the coefficient values is due to the destruction of the methylene group of hydrocarbons. Of greatest interest is $C_{ox,}$ characterizing the enzymatic activity of microorganisms in the oxidation processes. During 30 and 60 days contacts of microorganisms with the oil, C_{ox} increased by 116 and 240%, respectively. The increase in C_{br} and C_{ar} values proves the activity of the oxidative processes.

According to the data of IR-spectrometry, using the values of optical absorption bands, the percentage of the group composition in the oil samples has been calculated by Koshelev's formula (Koshelev 2005). The data obtained are given in Table 11.4.

As it follows from the Table 11.4 in the process of enzymatic oxidation the paraffin content decreased by 4%. The content of the rest groups by 60 days of the degradation increased by 4, 12 and 56%. The increase in aromatic structures is also proved by a change in the C_{ar} value (Table 11.3). The more aromatic structures, in the more stable colloidal state are resin-asphaltene substances, providing a depressor effect. The most significant changes in the composition of KN30 and KN60 oil samples are associated with the accumulation of oxygen-containing oxidation products as compared with the crude oil.

Table 11.3 Spectral coefficient of the oil samples

Spectral coefficients	Oil samples		
	Crude oil	KN30	KN60
C_{ar} (aromaticity)	0.56	0.60	0.67
C_{br} (branching)	0.45	0.53	0.55
C_{ox} (oxidation)	0.018	0.039	0.062

Table 11.4 Destructive changes in KN group composition

Group composition	Samples under study			
	Crude oil	KN30	KN60	KN60 content changes, %
Paraffins	0.721	0.709	0.691	−4.0
Aromatic	0.180	0.182	0.187	+4.0
Naphthenes	0.087	0.094	0.098	+12.0
Oxidized HCs	0.016	0.020	0.025	+56.0

Methane hydrate nucleation was investigated in 24 versions of each oil sample at the pressure of 15 mPa s and a temperature varying from +20 °C to −15 °C at a given rate of 0.14 °C/min. It can be noted that qualitative changes in hydrate formation (appearance of secondary nucleation, ice and hydrate formation) occur in KN30 sample after already 30 days of biodegradation. The probability of hydrate formation in the KN sample of the crude oil is—5%, KN30—20% and in KN60—12%. Therefore in the process of the oil biodegradation, the probability of the hydrate nucleation increases, depending on a degree of biodegradation at the interaction of the oil—microorganisms system. In the case of the emulsion of the crude oil from the Kazanskoye oil field, the induction period of the hydrate formation was 150 min, whereas for the biodegraded sample it was 40 min. With an increase in the degree of oil oxidation further growth of the hydrate in KN60 samples occurred 4–5 times faster.

The results obtained suggest a relationship between the level of biodegradation and the formation of a 'water-in-oil' emulsion, which increases the viscosity and density of the oil. Depending on the time of biodegradation, the content of polar components (resins and asphaltenes), arenes, total acid number, and the content of carboxylic acids increases in the oil. Changes in the oil composition results in an increase in the probability of nucleation of the hydrate and ice compared to crude oil. The oxidation coefficient and the increased content of polar components in samples of biodegraded oil do not correlate with the formation of hydrates. The group composition and the content of polar components favorably affecting the formation of hydrates were much lower in the KN-30 sample than those in KN 60 sample, while the probability of nucleation proved to be higher. Hence, it is the appearance of certain specific metabolites that affects hydrate formation, and not the total amount of biodegradation products accumulated in the oil. This conclusion is consistent with the results of the work (Greaves et al. 2008; Borgund et al. 2009).

11.4 Conclusions

The oil samples from the Kazanskoye oil field (KN) of Western Siberia served as the test material for microbiological and physicochemical studies. The main characteristics of crude oil are as follows: viscosity—2.42 mPa s, density—0.786 g/m^3, and freezing temperature −28 °C.

The biodegradation of oil was carried out under laboratory conditions at +5 °C for 30 and 60 days in a liquid mineral medium providing the vital processes of microorganisms. For biodegradation, strains with high oxidative activity have been isolated. According to the results of the 16S pPHK gene sequence, the selected strains belonged to the genera: *Bacillus*, *Rhodococcus, Dietzia*, and *Pseudomonas*.

The biodegradation of oil in an aqueous medium at +5 °C was accompanied by the formation of a 'water-in-oil' emulsion, a decrease in the interfacial tension from 25.5 to 17.0 mN/m, an increase in the acid value, resins, and asphaltenes, and an increase in viscosity from 2.42 to 31.88 mPa·s. The data obtained are in good agreement with the conclusions made by Erstad et al. (2009) and Barth et al. (2004). The rate of change is largely dependent on the time of contact of petroleum hydrocarbons with destructive microorganisms.

Structural changes in the composition of functional groups of hydrocarbons were investigated by the FT-IR method. The ratio of the optical densities of the absorption bands allowed us to obtain spectral coefficients characterizing the destructive activity of microorganisms.

The study of the group composition of biodegraded oils showed a decrease in the percentage of paraffins and an increase in that of naphthenes, arenes and oxygen-containing products of enzymatic oxidation. The most significant changes in the composition of KN30 and KN60 oil samples compared with those of crude oil are due to the accumulation of oxygen-containing oxidation products.

Oil biodegradation processes increase the probability of hydrate nucleation, which depends on the degree of biodegradation in the interaction of the 'oil-microorganisms' system, which is consistent with the work of Borgund et al. (2009).

It should be noted that not only the degree of oil biodegradation but also the very presence of bacterial cells, whose protoplasm is rich in proteins, can exert influence on the nucleation processes of hydrates. The level of biodegradation under conditions of low positive temperature suggests the psychrophilic properties of the natural microflora isolated from oil samples. Research on the effect of the degree of oil biodegradation on the formation of hydrates in cold climates will be continued.

This scientific work was supported by the Ministry of Science and Higher Education of the Russian Federation (Project No. 46.2.3).

References

Aman ZM, Koh CA (2016) Interfacial phenomena in gas hydrate systems. Chem Soc Rev 45:1678–1690. https://doi.org/10.1039/C5CS00791G

Augustinovic Z, Birketveit O, Clements K et al (2012) Microbes—oilfield enemies or allies. Oilfield Rev 24(2):4–17

Barth T, Hoiland S, Fotland P et al (2004) Acidic compounds in biodegraded petroleum. Org Geochem 35(11–12):1513–1525. https://doi.org/10.1016/j.orggeochem.2004.05.012

Borgund AE, Hoiland S, Barth T et al (2009) Molecular analysis of petroleum derived compounds that adsorb onto gas hydrate surfaces. Appl Geochem 24(5):777–786

Chen L, Feng Y, Okajima J et al (2018) Production behavior and numerical analysis for 2017 methane hydrate extraction test of Shenhu, South China Sea. J Nat Gas Sci Eng 53:55–66

Erstad K, Hvidsten IV, Askvik KM et al (2009) Changes in crude oil composition during laboratory biodegradation: acids and oil-water. Oil-Hydr Interfacial Prop Energy Fuels 23(8):4068–4076. https://doi.org/10.1021/ef900038z

Gerhcardt Ph (ed) (1981) Manual of methods for general bacteriology. American Society for Microbiology, Washington

Greaves D, Boxall J, Mulligan J et al (2008) Hydrate formation from high water content—crude oil emulsions. Chem Eng Sci 63(18):4570–4579. https://doi.org/10.1016/j.ces.2008.06.025

Harayama S, Kishira H, Kasai Yu et al (1999) Petroleum biodegradation in marine environments. J Molec Microbiol Biotechnol 1(1):63–70

Hoiland S, Borgund AE, Barth T et al (2005a) Wettability of Freon hydrates in crude oil/brine emulsions: the effects of chemical additives. In: Proceeding of 5th international conference on Gas Hydrate, Trondheim, Tapir Academic Press, Norway, 13–16 June 2005

Hoiland S, Askvik KM, Fotland P et al (2005b) Wettability of Freon hydrates in crude oil/brine emulsions. J Coll Interf Sci 287(1):217–225. https://doi.org/10.1016/j.jcis.2005.01.080

Kapellos GE (2017) Microbial strategies for oil biodegradation. In: Becker SM (ed) Modeling of microscale transport in biological processes, 1st ed. Academic Press, Cambridge, Massachusetts, pp 19–39

Kelland MA (2006) History of the development of low dosage hydrate inhibitors. Energy Fuel 20(3):825–847

Koshelev VN, Gordadze GN, Ryabov VD et al (2005) Transformations of crude oils in in-situ combustion and prolonged contact with the environment. Chem Technol Fuels Oils 41(2):104–107. https://doi.org/10.1007/s10553-005-0030-7

Rogers R, Radich J, Hiong S (2011) The multiple roles of microbes in the formation, dissociation and stability of seafloor gas hydrates. In: Proceedings of the 7th international conference on gas hydrates (ICGH). Edinburg, Scotland, United Kingdom, 17–21 July 2011

Sloan ED, Koh CA (2007) Clathrate hydrates of natural gases, 3rd edn. CRC Press, Boca Rator

Speight GJ, Arjoon KK (2012) Bioremediation of petroleum and petroleum products. First published, Wiley-Scrivener

Stoporev AS, Manakov AY, Altunina LK et al (2015) Nucleation rates of methane hydrate from water in oil emulsions. Can J Chem 93(8):882–887. https://doi.org/10.1139/cjc-2014-0507

Stoporev AS, Svarovskaya LI, Strelets LA et al (2018a) Effect of reactor wall material on the nucleation of methane hydrate in water-in-oil emulsions. Mendeleev Commun 28(3):343–344. https://doi.org/10.1016/j.mencom.2018.05.039

Stoporev AS, Ogienko AG, Sizikov AA et al (2018b) Unexpected formation of sII methane hydrate in some water-in-oil emulsions: different reasons for the same phenomenon. J Nat Gas Sci Eng 60:284–293. https://doi.org/10.1016/j.jngse.2018.10.020

Svarovskaya LI, Filatov DA, Gerelmaa T et al (2009) IR and1H NMR assessments of the biodegradation of oil. Pet Chem 49(2):136–141

Svarovskaya LI, Altunina LK, Razd'yakonova GI et al (2016) Carbon sorbents for the development of biotechnologies. Int Polymer Sci Technol 43(4):15–18

Svarovskaya LI, Serebrennikova OV, Duchko MA (2017) Changes in the composition of the bituminous components of valley peat under stimulated microbial action. Solid Fuel Chem 51(2):67–77. https://doi.org/10.3103/S0361521917020094

Svarovskaya LI, Manakov AYu, Alltunina LK (2018) Nucleation and formation of gas hydrates depending on the physical and chemical properties of oils. Sib J life Sci Agric 10(1):64–74

Turner DJ, Miller KT, Sloan ED (2009) Methane hydrate formation and an inward growing shell model in water-in-oil dispersions. Chem Eng Sci 64(18):3996–4004. https://doi.org/10.1016/j.ces.2009.05.051

Vater J, Kablitz B, Wilde C (2002) Matrix assisted laser desorption ionization-time of flight mass spectrometry lipopeptide biosurfactants in whole cells and culture extracts of Bacillus subtilis C-1 isolated from petroleum sludge. Appl Environ Microbiol 68(12):6210–6219. https://doi.org/10.1128/AEM.68.12.6210-6219.2002

Chapter 12
Biogenic–Abiogenic Interactions in Stromatolites: Study Possibilities and Outlooks

Tatiana V. Litvinova

Abstract Stromatolites are produced by a complicated interplay of biogenic and abiogenic processes, whose contributions are hard to estimate without applying specialized techniques enabling the researcher to reproduce these processes. Stromatolites are fairly widespread in nature and are found as building organisms of various shape and size. Most researchers classify them into layered and columnar types or subtypes, which comprise complicatedly but systematically branching columns, oncolites, and microstromatolites. In spite of the morphological diversity of stromatolites, stromatolite reefs were formed over significant areas during a certain span of geological time, with only some types of structures found in them. It was determined that the morphological types of stromatolites obviously show a certain spatiotemporal distribution. This fact cannot be explained by the sedimentation conditions alone, and it indicates that biogenic processes and matter played a key role in the origin of stromatolites. However, no stromatolite-forming organisms had long been found. The later transformations of these rocks further complicated the problem in view of the fact that the great majority of stromatolites are of Precambrian age. A recently suggested and tested technique makes it possible to identify the building organisms of stromatolites and estimate their role in forming the structural–textural features of these rocks. This technique involves SEM studies. This publication discusses the potentialities of the techniques and the reliability of results obtained using it, as well as the outlooks in its application to solving specific problems (identification of cyanobacteria) and more general issues concerning the geology of the Precambrian.

Keywords Stromatolite structures · Electron microscope · Biogenic ultramicrostructures · New method · Cyanobacteria · Morphology

T. V. Litvinova (✉)
Geological Institute, Russian Academy of Sciences, Moscow, Russia
e-mail: litvinova-geo@rambler.ru

© Springer Nature Switzerland AG 2020

O. V. Frank-Kamenetskaya et al. (eds.), *Processes and Phenomena on the Boundary Between Biogenic and Abiogenic Nature*, Lecture Notes in Earth System Sciences,
https://doi.org/10.1007/978-3-030-21614-6_12

12.1 Introduction

The mid-20th century was marked by growing needs to study ancient rocks hosting vast reserves of iron, base metals, gold, platinum-group elements (PGE), and rare-earth elements (REE) and other valuable minerals. This work was largely complicated by the fact that neither paleontological nor isotopic dating methods cannot be applied to constrain the age of Precambrian rocks. It was then suggested to try to use morphological features of stromatolites and their age in solving these problems. Starting in the mid-20th century, stromatolites were actively studied, and data thus obtained were more and more widely applied in geology and stratigraphy to constrain the age of fossil-free Precambrian rocks.

The very first found stromatolites were then thought to be produced with the involvement of living organisms, but all efforts to find these organisms failed. Stromatolites were documented unsystematically until a uniform approach was suggested thanks to the invention of two methods. One of them was the technique of graphical preparing (Krylov 1963) and allowed the researcher to reproduce the 3D shape of the stromatolite structures and the branching specifics of the columns, determine the nature of their boundaries, and identify the occurrence of cornices, visors, connecting bridges, etc. The other method (Wolcott 1914) was based on studying the microstructures, i.e., the shapes and sizes of the clods of carbonate matter (Komar 1989) in stromatolites. This method provided descriptions of the relative position of smaller features than those studied by the previous technique, but in its core meaning, this technique was an extension of the aforesaid (morphological) approach. Both methods were widely applied by various researchers (Komar et al. 1962; Serebryakov 1975; Shapovalova 1974 and others) and have yielded interesting results. A uniform formalism and terminology and the similar means of application largely simplified and systematized the work of the researchers. The methods have long been used to develop and refine the systematics of stromatolites, into which more and more new finds were systematically integrated (Awramik et al. 1983; Krylov 1975; Semikhatov and Raaben 1994, 1996, 2000; Shapovalova 1974; Serebryakov 1975). This systematics was of formalized nature because it was based not on organisms themselves but on the shapes of stromatolite structures and the fabrics of the rocks. Nevertheless stromatolites made it possible to suggest the very first justified stratigraphic subdivision of the Precambrian.

By the early 21st century, all preexisting possibilities of studying these rocks had been exhausted, and this led to the almost complete termination of these studies. At the same time, new dating methods of ancient rocks were developed, including isotopic dating, and dating using silicified cyanobacteria, acritarchs etc. This made it senseless to search for and document new stromatolite types and, hence, studies of stromatolites were almost completely terminated.

However, these rocks, which were the first to be formed when life emerged on the planet, continued to provoke keen interest. Most researchers believed that the morphology of stromatolite structures was controlled first of all by the composition of the

stromatolite-building organisms and their living activities, although sedimentation circumstances should also have played an important part.

Regretfully, all attempts to find these organisms either under an optical microscope or by studying rock sections under an electron microscope failed.

Issues concerning interaction between biogenic and abiogenic matter in stromatolites and the origin not only of rocks of unusual structure but also stromatolite reefs as an integrated biological system were solved purely theoretically in the absence of factual material. This called for inventing principally new techniques able to acquire data at a principally other, much more detailed level.

Many attempts have been made to apply electron microscope in studying stromatolites. However, similar to the situation with using optical microscope for these purposes, the researchers managed only to see an uniform carbonate material and nothing else. At the same time, the equipment was successfully used to model stromatolites in the laboratory (Krylov and Orleansky 1988; Orleansky et al. 2000 and others), including examining changes in the shapes of the bacteria in the course of their fossilization and the step by step development of modern biogenic structures during their silicitization (Krylov and Tikhomirova 1988; Ushatinskaya 2002).

A newly developed techniques (Litvinova 2009) has offered principally new potentialities. The application of an electron microscope equipped with an energy dispersive spectrometer (EDS) enables the researcher to reveal microorganisms involved in building stromatolite reefs and estimate the geochemical aspects of interaction between these organisms and sedimentation. It also makes it possible to evaluate the evolutionary modification and subsequent degradation of stromatolite structures (Naugolnych and Litvinova 2014) and changes under the effect of secondary processes (Litvinova 2014a). The data thus acquired should, however, be carefully tested with regard for the possible occurrence of newly formed biogenic structures. Moreover, the researcher should be confident that the identified organisms were coeval with sedimentation and were not brought to the rock much later, for example, in the Phanerozoic. To do this, we have tested of the acquired data.

The technique has been tested and allowed us to obtain principally new interesting results (Litvinova 2014a, b, 2016, 2018; Naugolnych and Litvinova 2014 and others) on the biogenic ultramicrostructures of stromatolites that had various age and were sampled at a number of localities. The technique itself and experience in its application have never been described before, and hence, most researchers are still not familiar with it. This publication bridges this gap and cautions the reader against possible errors and drawbacks by describing the technique of the work in much detail.

12.2 Materials and Method

The specifics of the method suggested herein is the preparation of the samples. These are not thin sections, which have been unsuccessfully utilized previously in electron microscopic studies of stromatolites, but freshly obtained stromatolite chips that

include their organogenic layer. This enables the researcher to observe the biogenic structures as 3D (but not 2D) images, because otherwise they are indiscernible from the host rock.

The working routine was as follows. Stromatolites were first examined in field (in outcrops) and then in thin sections under a stereoscope or binocular magnifier. It has been established that the ultramicrotexture of the rock plays a key role on an electron-microscopic level too and hence, it was principally important to select fragments of the sample that included sites most promising for identification of the best preserved bios. This fragment must show structures typical of the taxon in question and be minimally modified by any overprinted processes. The electron microscopic study was carried out using a few samples smaller than 5–6 mm across, with fresh variably oriented chippings. This made it possible to obtain the most comprehensive information on both the stromatolite-building organisms and the secondary processes that overprinted the rock. The analyzed elemental composition of the rocks (including its trace-element composition) is not only an important parameter of the rock but also provides clues to better understanding the genesis of the likely biogenic structures. In view of this, the samples were not preparatorily treated by acids, because otherwise it was senseless to analyze the composition of such samples. Furthermore, the necessity for submerging samples into water after their acid treatment may stimulate the growth of modern fungi and thus mislead the researcher. The samples were sputter-coated with gold to enable identification of elevated carbon concentrations in the supposedly biogenic structures. Upon their coating, the samples were mounted on the electron-microscope stage 11 mm in diameter and placed into the vacuum column. Neither long-term storage nor washing of the samples were admissible.

The studies were conducted on a TesScanMV-2300 scanning electron microscope equipped with Cambridge Instruments INCA-200 energy-dispersive spectrometer. The diameter of the analyzed spot was thereby no larger than 1 μm. The genesis of each of the supposedly biogenic ultramicrostructures was tested using a microprobe accurate to 0.001%. Long-term studies of stromatolites by this method have shown that the stromatolites contain a vast amount of various biogenic ultramicrostructures (Litvinova 2009, 2014a, 2018 and others), which were responsible for the origin of certain structural features of the rock. A provisional classification of stromatolites was developed (Litvinova 2016), and the first attempts were undertaken to compare the identified species with siliceous microfossils (Litvinova and Sergeev 2018). Comparison of our materials with experimental data and with descriptions of currently living stromatolites helped in understanding and interpreting this material, but many issues remained uncertain and can be settled only based on systematic studies of biogenic ultramicrotextures of the rocks.

The method was tested on numerous samples of diverse stromatolites of various types, which were sampled at different localities and described in our earlier publications.

12.3 Results and Discussion

Biogenic ultramicrotextures were identified in stromatolites based on their morphology: with these ultramicrotextures are clearly discernible from the pelitomorphic and/or more rare fine-crystalline material (Fig. 12.1a). Their genesis is or is not confirmed by data on the chemical composition of the objects. The high sensitivity of microprobe analysis allowed us to identify biophile elements even in replicas of prokaryotes. Any fossilized organism (Fig. 12.1a) is made up of the same carbonate material as the host rocks (Fig. 12.1a_1) but differs from the latter in containing much more carbon (Fig. 12.1a_2). Organic carbon in cyanobacteria are commonly associated with inclusions of microportions of other biophile elements, which are absent from the host rock.

Carbon concentrations are at a maximum in the laminae, which are widespread flat bacterial films in stromatolites. Their accumulations are seen even in small fragments of the samples, in which they are often arranged parallel to the layering (Fig. 12.1b), although they are sometimes randomly distributed in the material. These structures are usually folded, twisted (Fig. 12.1c), and have a wrinkled surface (Fig. 12.1d), which was formed because of dehydration when the sediment was lithified. The laminae are often found in association with coccoid structures or bundles of cyanobacterim threads, sometime include both (Fig. 12.1d) and envelop the organism.

The bacterial films are former glycocalyx enriched in polysaccharoids. They concentrated organic carbon and some other elements and were able to long maintain water balance in the organisms around which the films developed. Glycocalyx (slime) protected cyanobacteria from aggressive environmental factors, including drying. For a while, it could perform the functions of the nourishing medium (which is exhausted at the time) and provide life necessities for the organisms. Thanks to its universal functions and composition, glycocalyx practically played the role of a capsule surrounding prokaryotes.

The glycocalyx is formed and then widely spreads on the surface of the sediment, and hence, its dehydrated fragments are practically always preserved and can be thus used as identification guides, which make it possible to find the bios or even estimate its role in the origin of a given rock. Bacterial films are found not only in stromatolites but also occur in other biogenic rocks, for example, phosphorites from the Lesser Karatau (Fig. 12.1e, e_2), in which they accompany phosphate pellets (Fig. 12.1e, e_1), in shungite from Karelia (Fig. 12.1f), and in other bioliths (Leonova et al. 2014). The nature of phosphate pellets is currently explained by some researchers as related to their biogenic origin, as reportedly may follow from their diverse but still repeatedly found morphologies (Kholodov and Paul 1996b; Litvinova 2007), some features of their inner structure (Litvinova 2007), and incremental variations in the size, as is typical solely of biological objects (Kholodov and Paul 1996a). Under an electron microscope, the pellets can be observed as 3D images (Fig. 12.1e_1) and in cross-section (Fig. 12.1e, 12.1q), which enables the researcher to examine their inner structures. The presence of bacterial films confirms that bios was involved in producing the phosphate pellets.

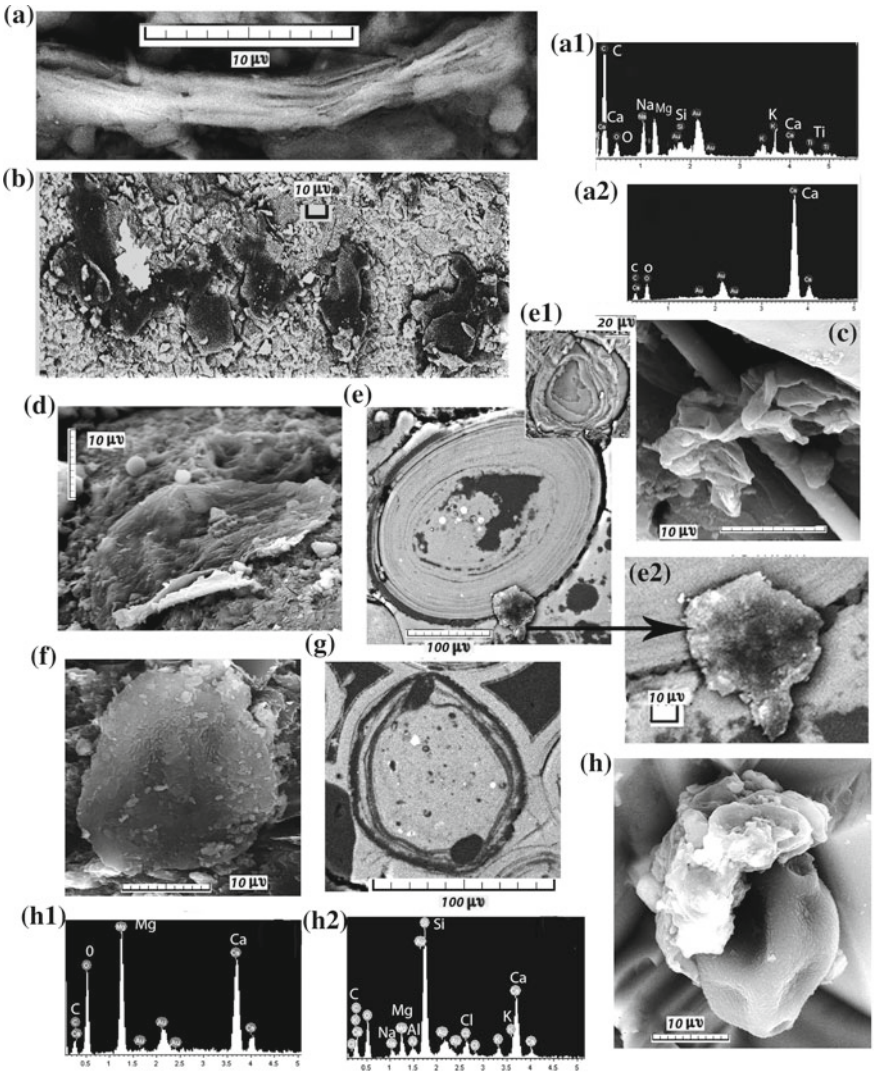


Fig. 12.1 **Biogenic ultramicrostructures**: **a**, $\mathbf{a_1}$ thread cyanobacterium and its composition, $\mathbf{a_2}$ composition of the host rocks; **b**, **c**, **d**, $\mathbf{e_2}$, **f** bacterial films in stromatolites; **e**, $\mathbf{e_1}$, **g** phosphate pellets (Kazakhstan, Lesser Kara-Tau, Early Cambrian); **h** coccoid cyanobacterium *Myxococcoides sp* with a bacterial film; $\mathbf{h_1}$, $\mathbf{h_2}$ composition of, respectively, the host rocks and *Myxococcoides sp*. Paleoproterozoic, Sundozero, Karelia

Elevated carbon concentrations are usually found in Precambrian biogenic ultramicrostructures only if they contain at least minor silica concentrations, which serve as a preservative. An increase in the silica concentration is associated with an increase in the content of organic carbon. This may suggest that the element is be better preserved in fossilized cyanobacteria rather than that the living conditions of the organisms and sedimentation circumstances were different, particularly with regard for the fact that siliceous stromatolites are usually of secondary nature. Intense transformations involving silica may have resulted in partial or complete recrystallization and obliteration of the biogenic ultramicrostructures, blurring their contours, and the complete destruction of any traces and molds of the organisms. In these situations, carbon is not always preserved. However, this process is rare and is commonly fragmentary, so that carbon can usually be readily identified in microfossils, and the shapes of the organisms are better preserved thanks to silica.

The situation with phosphate rocks is somewhat different. If small phosphorus amounts appear, with this element initially replacing biogenic structures, organic carbon is preserved, but the penetrative phosphatization of the rock leads to the complete disappearance of carbon. This may be suggestive of a secondary nature of the process and may be confirmed by the presence of coeval carbonate or siliceous stromatolites with analogous morphological features in the area in question. Silica usually replaces the whole rock, in contrast to phosphorus, which is first adsorbent on biological material. This selective replacement makes it possible to study the inner structure of biological objects (Litvinova 2007), which consist of carbonate and silica. As the phosphorus concentration increases, all constituents of the rocks are completely replaced, as is well illustrated by phosphate stromatolites in the Zmeinyi Mountains in the Southern Urals, Russia. In this instance, the contours and morphology of the fossilized cyanobacteria are seen not as clearly (Litvinova 2014b) and no carbon is preserved in them. When working with biogenic ultramicrostructures, one should be aware of the fact that carbon preservation in them strongly depends on the reworking of the primary material and the intensity of rock replacement.

Cyanobacteria and their glycocalyx can accumulate some other biophile elements necessary for their vital functions. The second, after carbon, most widespread and well preserved element is magnesium (Fig. 12.1a$_1$), which can thereby be absent from the host rock (Fig. 12.1a$_2$). However, if the rock does contain any appreciable magnesium concentrations (Fig. 12.1h$_1$), the fossilized cyanobacteria (Fig. 12.1h) contain much lower concentrations of this element (Fig. 12.1h$_2$), in the absence of reasons for storing this element that is abound in the ambient. An excess of any element is almost as harmful for an organism as its deficit, and glycocalyx thereby again plays a protective role.

Biogenic ultramicrostructures in stromatolites also contain other elements typical of the bios: these are potassium, chlorine, and sodium. Their concentrations are low not only because of their originally small amounts but also because it is hard to retain volatile components in Precambrian rocks. However, the presence of these elements is definitely typical only of the biogenic ultramicrostructures, and they are always found together with carbon. Moreover, fossilized organisms may also contain iron,

manganese, sometimes phosphorus, rare-earth elements, and some other chemical elements absent from the host rocks.

Data on modern stromatolites at Shark Bay show that the fossilized biogenic organisms are similar in shape (Litvinova 2016) and morphology to ancient ones and show evidence of a number of transformation stages of the glycocalyx into dehydrated wrinkled flakes, whose contours are clearly discernible and whose specific concentrations of carbon, magnesium, and some other elements are higher.

Microprobe analysis makes it possible not only to distinguish between fossilized organisms and mineral aggregates but also to obtain valuable additional information on the host rocks and their secondary transformations. The identification of various cyanobacteria in stromatolites, analysis of their role in the development of the ultramicrostrtucture and morphology of the stromatolite structures, analysis of the composition of the accessory minerals, and elucidation of the role of overprinted processes compose a far from complete list of potentialities offered by the application of a scanning electron microscopy in studying stromatolites and other biogenic rocks.

The texture of a rock developed as follows. A very thin (no thicker than 2 mm) bacterial film, which comprised a community of organisms, coater the mineral layer and gradually expanded over a progressively greater area. Newly brought portions of sedimentary material covered the film, and the units of fine alternating organogenic and chemogenic layers were then lithified. Stromatolites typically inherit components from the host rock, as is evident at different levels of their study, from visual to ultramicroscopic ones. As a result, characteristics of stromatolites obtained by studying them under a binocular magnifier and/or an electron microscope are practically identical, but the capabilities of these methods are different. In the former situation (when stromatolites are studied under a binocular), an increase in the number of components of the rock does not provide additional information, while in the latter, the application of electron microscopy allows the researcher to determine organisms involved in building the reef. The organogenic layer is responsible for the shape of stromatolite structures and their microstructure, and this made it possible to suggest a formalized classification of stromatolites and successfully apply it in stratigraphy. To be sure that the fossilized organisms of stromatolites identified under an electron microscope lived synchronously with sedimentation (but were not later introduced into the rock), the researcher should analyze the roles of these organisms in the microstructure.

The organogenic layer can include various organisms (Litvinova 2016), but they are commonly dominated by cyanobacteria and certain individual organisms accompanying them. Under an electron microscope, one can practically always identify the structure-forming organisms in each individual stromatolite taxon. A number of illustrative examples discussed below are stromatolites sampled in the northern Anabar area (in the area of the Fomich River, Russia, Lower Riphean) and Karelia (Lower Proterozoic).

The species *Colonnella laminata Komar* (Komar 1964,) was distinguished based on its linear microstructure (Fig. 12.2a) discernible at high magnifications (Fig. 12.2a$_1$). Detailed studies of the structures show that the layer was formed

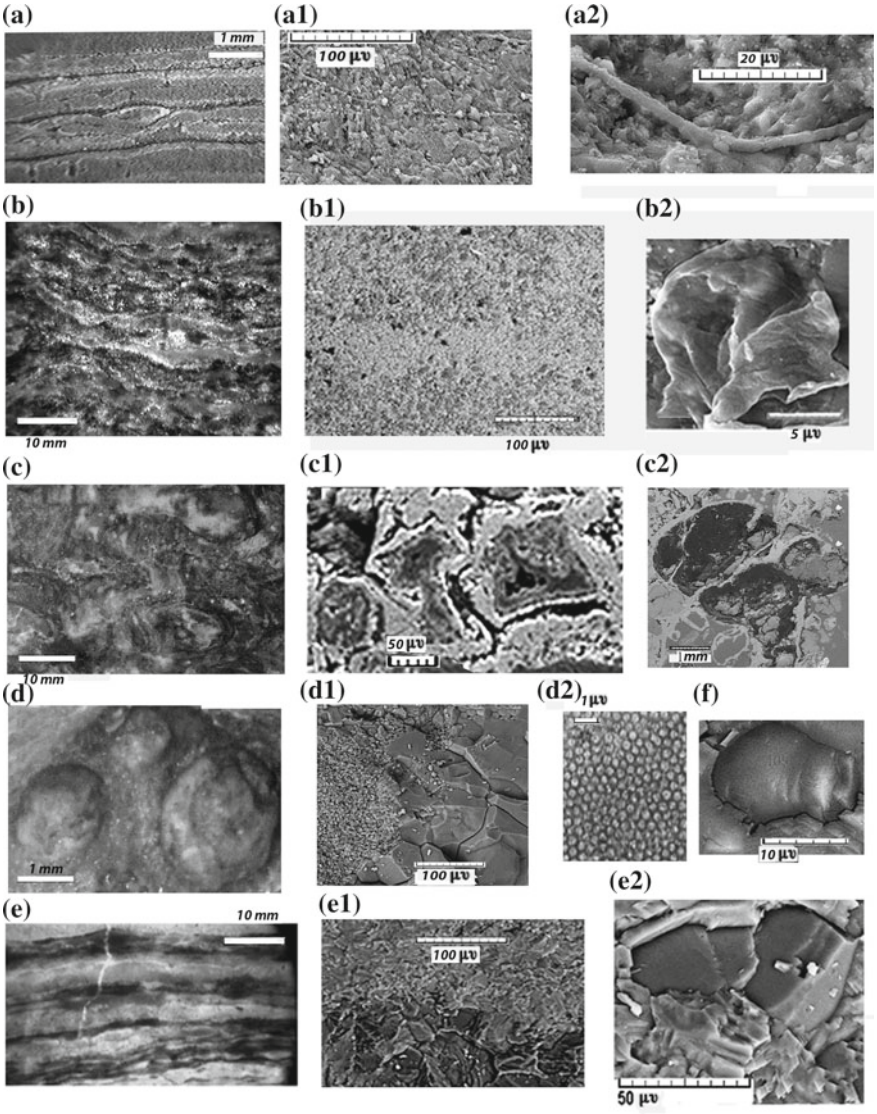


Fig. 12.2 Microstructure and its builders: *Colonnella Laminate*: **a**, $\mathbf{a_1}$ linear micro- and unlrtamicrostructure, $\mathbf{a_2}$ theread cyanobacterium; *Colonnella Kyllachii*: **b**, $\mathbf{b_1}$ clotty micro- and ultramicrostructure; $\mathbf{b_2}$ coccoidal cyanobacteriaum; Sundia: **c** random concentric microstructure, $\mathbf{c_1}$, $\mathbf{c_2}$ concentric biogenic ultramicrostructures; *Colenia Olenica*: **d** nodular microstructure, $\mathbf{d_1}$ inner structure of a nodule, $\mathbf{d_2}$ accumulation of biogenic nanometer-sized particles; *Colonnella Fomich*: **e** unequally lenticular microstructure with swell features in dark layers; **e** contact between mineral and organogenic layers at different magnifications; $\mathbf{e_2}$ biogenic ultramicrostructures, lateral binary fission of a cell; **f** cyanobacterium. Note: **a**, **b**, **e** Northern Anabar area, Fomich River, Early Riphean; **c**, **d** Karelia, Sundozero Lake, Southern Olenii Island, Paleoproterozoic

largely as a consequence of the vital activities of thread bacteria (Fig. 12.2a_2). They gradually give way to another colonella species: *C. kyllachii Shapovalova* (Krylov et al. 1968). The latter are characterized by a clotty microstructure seen at any level of studying (Fig. 12.2b). The organogenic layer of this taxon is made up of relatively large isolated biogenic ultramicrostructures.

The diverse species of the microorganisms and their quantitative proportions in each individual taxon made up fairly diverse and often complicated microstructures. The dominant organisms, and hence, the microstructure itself, were replaced gradually. Moreover, the structural–textural features of the rock may have been complicated as a result of the changing sedimentation conditions and, later, under the effect of secondary processes. All of these factors can be analyzed using an electron microscope.

The Lower Proterozoic stromatolites of Karelia notably differ from other Precambrian stromatolite structures and are practically not compatible with the formalized classification of these rocks. The taxon *Sundia Butin* (Butin 1966) has a random–rounded texture and an analogous microstructure (Fig. 12.2c). The study of this taxon under an electron microscope has shown that a dominant role in its origin was played by excellently preserved fossilized endolithic algae (Litvinova 2018). They enveloped the walls of round holes, which were formed by these algae themselves, and developed them (Fig. 12.2c_2). If young individuals have no time to occupy a hole completely, carbonate sediment gradually filled the space between the many-fold twisted thallome (Fig. 12.2c_1). This follows from the notably higher carbon concentration in the dark layers, with the pale one made up of carbonate material. Later recrystallization produced rounded–layered textures in the holes. Data on samples recovered by the superdeep borehole confirmed their presence. Endolithic algae produced small unequal columns and other round microstructural features of this taxon by dissolving the sediment and filling holes favorable for reproduction and vital activities with the thallome material (Fig. 12.2c_1, c_2, c_3). These conditions provided protection against direct sun rays and water currents, which is important for algae because they have no root systems.

On Southern Olenii Island in Onega Lake, Karelia, Russia, other stromatolite structures were found: these were *Colenia Olenica Ryabinin* (Ryabinin 1941). They have a nodular texture and an analogous microstructure (Fig. 12.2d). Studies of this taxon under an electron microscope have shown that the nodule has a concentric inner structure, as seen in its cross section (Fig. 12.2d_1). Its core contains an accumulation of round biogenic nanostructures (Fig. 12.2d_2). This indicates that the morphological features of this taxon were formed by the vital activities of coccoid bacteria, which reworked the carbonate silt and built round mounds. As the sediment was gradually dehydrated and the nutrients were exhausted, the organisms had to extend their habitat and form a new nodule nearby. As a resultsromatolite *Colenia Olenica* includes (as seen in outcrops) closely spaced randomly oriented nodules.

An unusual microstructure was found in stromatolites *Colonnella Fomich Litvinova* in the northern Anabar area (Litvinova 2014b, R_1). They are characterized by alternating mineral and organogenic microlayers with sharp contact between them and with crenulated dark layers with swells (Fig. 12.2e). The former consist of

pelitomorphic carbonate material, and the latter show diverse complicated ultrastructures of dominantly biogenic character (Fig. 12.2e$_1$). The organogenic layers are characterized by the presence of round structures, ranging from 10 to 30 μm across (Fig. 12.2e$_1$), with notably elevated carbon concentrations. The community of organisms in the latter resemble a beehive in which each bacterium occupied its own cell or was coated with a thin protective biofilm of polysaccharide composition. The binary fission of the cells (Fig. 12.2e$_2$), which occurred in a single plane, resulted in chains of unicellular individuals, which thus built up the colony. Accumulations of a number of such rows defined the unequally lenticular structure, and the round morphologies of the organisms were responsible for the crenulation of the microlayers. Single round biogenic structures are occasionally found in the chemogenic layer, in which they are devoid of the protective shell. The organism likely tried to get out of the overlying sediment but failed and was buried in the chemogenic layer without acquiring a protective shell.

The living conditions of the cyanobacteria, analysis of the restructurings of the community of the biosystem, fossilization specifics of the organisms, the morphology, composition, and distribution of biological ultramicrostructures within the organic layers, their changes under the effect of secondary processes, i.e., almost all constituents of the mechanism that formed the microstructures can largely be reproduced using electron microscopic data. The suggested method enables the researcher not only to estimate the final result of the vital activities of cyanobacteria that built a given microstructure of a rock but also to trace the reasons for the degradation of the columns of the structure (Naugol'nykh and Litvinova 2014) and analyze the evolution of the stromatolite system as a whole (Litvinova 2014b, 2016), i.e., to understand how and why the various structures of these rocks were formed and degraded.

Studies of stromatolites of various age and sampled at different localities made it possible to distinguish four groups and fourteen types of the biogenic ultramicrostructures based on their morphological features (Litvinova 2016). They await their classification and elucidation of their spatiotemporal distribution, which can be compared with those of cyanobacteria described in Precambrian rocks. At a wider application of electron microscopy, they may play an important role in determining the age of the rocks.

12.4 Currently Available Complementing and Testing Techniques

The studies can be significantly facilitated by examining stromatolites in thin sections under a powerful modern microscope to allow the researcher confirm the conclusion and to obtain new or refine preexisting data (Litvinova and Sergeev 2018). Although the resolution power of optical microscopy is incomparable with that of an electron microscopy, the former traditionally employs technique that make it possible to gain extensive experience in studying microfossils and utilize them to date rocks.

Studies of Phanerozoic and modern stromatolites and their comparison with Precambrian biogenic ultramicriostructures helps the researcher in understanding the specifics of fossilization of the organisms and their changes in the course of overprinted alterations. Observations of the development of modern stromatolites and determining the chemical parameters of the habitats of cyanobacteria make it possible to understand many details of the process and its rate, and this, in turn, allows the researcher to interpret the ancient fossil structures and their genetic nature and to compare their living conditions.

Interesting material, which provides evidence of a biogenic origin of the rock and demonstrates that organisms can be reserved in it, can be obtained with the application of electron spin resonance (ESR) methods. Parameters of the signals of carbon-bearing radicals can be used to identify OM remnants of both protein (bacterial) and floral (algae) types and the magmatic grade of the rocks (Leonova et al. 2014).

Much interesting information can be derived from experimental data on the role of the bacterial film and behavior of organisms during sediment supply (Gerasimenko et al. 2007; Krylov and Orleansky 1988; Orleansky et al. 2000 and others) and on step by step changes during fossilization. This provides help in revealing biogenic structures that are otherwise hard to identify, as well as in unbiased estimation of the role of the organisms in the formation of stromatolites.

All of the methods listed above, or results obtained with these methods, were used by the author, confirmed the integrity and reliability of the data obtained using an electron microscope, and helped the author to interpret the electron-microscopic data.

12.5 Conclusion

The application of an electron microscope equipped with an energy dispersive spectrometer helps in solving the following problems:

(1) Determining the morphology, composition, and relative arrangement of stromatolite-building organisms, even if they are smaller than one micrometer. Identifying the dominant stromatolite-building organisms in each of the taxons of stromatolites and determining their functions in forming the structure of the rock.
(2) Determining the role of secondary alterations that occurred in the rock during and/or after the reef was formed, and estimating the effects of these processes on changes in the textural and structural features of the stromatolites.
(3) Analyzing the reasons why some dominant microorganisms within a given stromatolite reef give way to others. Characterizing the evolution of this process in each given stromatolite structure and in the Precambrian as a whole.
(4) Studying the growth conditions, lifetime, and reasons for the degradation of a given stromatolite structure. Determining how its shape depended on the evo-

lutionary changes and ecological conditions under which stromatolite-building cyanobacteria lived.

The suggested technique enables the researcher to monitor the physicochemical and biological parameters of the origin of a stromatolite reef and to suggest more geochemical criteria of biogenic sedimentation. Because of this the method can play an important role in solving more general problems, such as determining direct and feedback relationships between components of a biosystem. The use of this method can help the researcher to suggest criteria for determining climatic, geological, and other geological circumstances in which the reef was formed. The method offers interesting possibilities of studying interactions in stromatolites and other complicated biological systems.

Currently most of the aforementioned problems are analyzed mostly visually because it is still not possible to rely on any physical material on the biocenosis involved in the origin of stromatolites.

Acknowledgements The study was conducted under government-financed research program at the Geological Institute, Russian Academy of Sciences, projects № 0135-2016-0021. The electron-microscopic study of stromatolites was supported by the Russian Foundation for Basic Research, project No. 19-05-00155.

References

Awramik SM, Schopf JW, Walter MR (1983) Filamentous fossil bacteria from the Archean of Western Australia. Precambrian Res 20:357–374

Butin RV (1966) Fossil algae of the proterozoic of Karelia. In: Remains of organisms and problems of the Proterozoic formations of Karelia. Petrozavodsk (In Russian)

Gerasimenko LM, Zaitseva LV, Orleancky VK, Ushatinskaya GT (2007) Dolomite formation in cyanobacterial mate. Biominerais and biogenic mineral formation. Geoprin, Syktyvkar (In Russian)

Kholodov VN, Paul RK (1996a) On the problem of pellet origin in Cambrian deposits of the Karatau. Dokl Akad Nauk 346(4):514–517 (In Russian)

Kholodov VN, Paul PK (1996b) Biochemical regularities in the formation of pelletal phosphorites. Gornyi Vestnik Soc Notes 1:30–40 (In Russian)

Komar VA (1964) Columnar stromatolites of the Riphean north of the Siberian platform. Scientific notes of the Research Institute of Geology of the Arctic (NIIGA). Paleontol Biostratigraph Soc Notes 6:84–105

Komar VA (1989) Classification of the microstructures of the upper precambrian stromatolites. Him Geol Soc Notes 13:229–238 (In Russian)

Krylov IN, Tikhomirova IS (1988) To the formation of siliceous microfossils. Palaeontological J Soc Notes 3:3–9 (In Russian)

Komar VA, Raaban ME, Semikhatov MA (1962) Konofitony of the Riphean of the USSR and their stratigraphic value. Nauka, Moscow (In Russian)

Krylov IN, Nuzhnov SV, Shapovalova IG (1968) On the stromatolite complexes of the middle Riphean. Dokl AN SSSR 181(2):426–429

Krylov IN (1963) Columnar branching stromatolites of the Riphean deposits of the Southern Ural and their significance for the stratigraphy of the Upper Precambrian. Tr Geol Inst Acad Nauk SSSR (In Russian)

Krylov IN (1975) Stromatolites of the Riphean and Phanerozoic in the USSR. Science, Moscow (In Russian)
Krylov IN, Orleansky VK (1988) Laboratory model of formation of carbonate crusts in algal-bacterial films (artificial stromatolites and oncolites). In: Calcareous algae and stromatolites (systematics, biostratigraphy, facies analysis). Nauka, Novosibirsk (In Russian)
Leonova LV, Litvinova TV, Glavatskikh SP (2014) Specific microaggregates and problematic microfossils as satellites of biochenogenic rocks. Paleontological J 48(14):1552–1556
Litvinova TV (2007) Composition, morphology, and origin of phosphate pellets: evidence from phosphorites of the Lesser Karatau. Lithol Miner Resour Soc Notes 4:426–443
Litvinova TV (2008) On the problem of genesis stromatolites. Palynology: stratigraphy and geoecology. In: Collection of scientific papers of the XII All-Russian palynological conference: VNIIGRI. Saint-Petersburg V. III (In Russian)
Litvinova TV (2009) New data on structure and the structure of stromatolitic buildups (Northern Anabar Region). Lithol Miner Resour Soc Notes 4:428–437 (In Russian)
Litvinova TV (2014a) Stromatolite phosphorites of the Southern Urals and their genesis. Lithosphere Soc Notes 2:50–59 (In Russian)
Litvinova TV (2014b) Ultramicrostructures of the Stromatolite Reef in the Northern Anabar region and their origin. Lithology and Mineral Resources Soc Notes 5:443–454
Litvinova TV (2016) Biogenic–abiogenic interactions in stromatolitic geosystems and their mineralization. In: Abiogenic Interactions in Natural and Anthropogenic Systems. Springer
Litvinova TV (2018) Possible role of microorganisms in the formation of structural and textural features of stromatolites. Lethaea rossica. 16:1–11(In Russian)
Litvinova TV, Sergeev VN (2018) Biogenic microstructures in stromatolites of the Baikal-Patom Highland: results of complex Stu. Lithol Miner Resour 53(2):159–169
Naugolnych SV, Litvinova TV (2014) Stromatolites from the Permian deposits of the Perm Cis-Urals: a new form-genus *Alebastrophyton* Naug. et Litvinova, Gen. nov. In: Media-Grand (ed) Palaeontology in the museum practice. Collection of the scientific articles. Moscow (In Russian)
Orleansky VK, Gerasimenko LM, Sumina EL (2000) Laboratory cyanobacterial mats and mineral interlayers. In: Materials of the Scientific Conference. Aquatic Ecosystems and Organisms-2. Moscow, MAKS Press (In Russian)
Ryabinin VN (1941) Organic residues in carbonate rocks of southern Karelia. Mat Geol Miner KFSSR Leningrad Murmansk region 4:8–21 (In Russian)
Semikhatov MA, Raaben ME (1994) Dynamics of the global diversity of Proterozoic stromatolites. Article 1: Northern Eurasia, China, and India. Strat Geol Correl 2:492–513
Semikhatov MA, Raaben ME (1996) Dynamics of the global diversity of Proterozoic stromatolites. Article II: Africa, Australia, North America, and general synthesis. Strat Geol Correl 4:24–50
Semikhatov MA, Raaben ME (2000) Proterozoic stromatolite taxonomy and biostratigraphy. In: Riding RE, Awramik SM (eds) Microbial sediments. Springer-Verlag, Berlin
Serebryakov SN (1975) Peculiarities of the formation and distribution of Riphean stromatolites in Siberia. Nauka, Moscow (In Russian)
Shapovalova IG (1974) Stratigraphy and stromatolites of the Riphean deposits of the Northern part of the Yudomo-May trough. Nauka, Novosibirsk (In Russian)
Ushatinskaya GT (2002) Silicification Bacterial Paleontology. PIN RAN, Moscow (In Russian)
Walcott CD (1914) Pre-Cambrian Algonquian algal flora. Smiths Misc. Coll. 64(2)

Chapter 13
Using X-ray Computed Microtomography for Investigation of the Morphology and Composition of the Hard Tooth Tissue

Oksana L. Pikhur, Yulia V. Plotkina and Alexander M. Kulkov

Abstract The study shows that the X-ray computed microtomography is a prospective method of revealing and studying early alterations of enamel and dentine. The offered complex approach allows obtaining complimentary detailed information on density distribution, morphological structure, and chemical composition of hard tooth tissues. It opens new opportunities for development of preventive measures and treatment of the main dental diseases. The morphology and composition of the human hard tooth tissue and dog odontoma were studied by optical microscopy, SEM, X-ray microtomography and EDX-analysis. Microstructure of hard tissues of teeth reflects complex processes associated with age and pathological changes (caries, non-carious lesions). Odontoma is one of the more often common benign tumors developing in the oral cavity and located in jaws bone. Possible causes of occurrence and development are not understood well.

Keywords X-ray computed microtomography · EDX-analysis · Optical microscopy · SEM · Hard tooth tissue · Enamel · Dentin · Caries · Non-carious lesions · Odontoma · Odontoid

13.1 Introduction

Microstructure of hard tissues of teeth reflects complex processes associated with age and pathological changes (Elliott 1997; Frank-Kamenetskaya et al. 2004; Tsimbalistov et al. 2005; Iordanishvili 2015). Identification of the initial stage of demineralization of hard tissues of teeth and its laws allows a deeper understanding of the

O. L. Pikhur
Institute of Bioregulation and Gerontology, Saint Petersburg, Russia

Y. V. Plotkina (✉)
Institute of Precambrian Geology and Geochronology RAS, Saint Petersburg, Russia
e-mail: jplotkina@yandex.ru

A. M. Kulkov
Saint Petersburg State University, Saint Petersburg, Russia

© Springer Nature Switzerland AG 2020

O. V. Frank-Kamenetskaya et al. (eds.), *Processes and Phenomena on the Boundary Between Biogenic and Abiogenic Nature*, Lecture Notes in Earth System Sciences,
https://doi.org/10.1007/978-3-030-21614-6_13

mechanism of this process. The applied value of such studies is associated with the prevention and treatment of diseases that lead to changes in the density of hard tissues of teeth (caries, non-carious lesions) . In addition, in the oral cavity are possible pathological formations consisting of tooth tissues (enamel, dentin, cement, pulp), arranged in a chaotic manner—odontomas.

Odontoma is a benign tumor that develops in the bones of the jaws from the elements of the tooth tissues. For the first time the term "odontoma" was applied by Pierre Paul Broca (Gilispie 1970) in "Traite des tumeurs" (1866). Mainly odontomas locate in the field of incisors, canines, premolars of maxilla and mandibular angle. According to the structure of odontoma classify for soft, solid, simple, cystic and complex odontoma (Barnes et al. 2005; Savina 2007). A major role in the development of odontoma assign a common (genetic predisposition) and local causes (infection in the tissues of the oral cavity, injuries). Early diagnosis and treatment of odontoma helps to prevent the development of complications.

The method of computer X-ray microtomography (μCT) opens up new opportunities in the study of the structure and composition of hard tooth tissues in normal and pathological conditions. This method is a combination of tomographic algorithms and X-ray microscopy (De Clerck et al. 2003), which allows to obtain visual information about the microstructure of solid tissues without their destruction based on the assessment of physical density. Its undoubted advantage is the lack of special training facilities, as well as their complete preservation during the study. Unfortunately, this method, widely used in the last decade in Europe and America (Sasov and Van Dyck 1998; Spoutil et al. 2016; Mavridou et al. 2017; Tassani et al. 2017), is practically not used in Russia.

This work is devoted to the study of normal and pathological hard tooth tissues by the method of computer X-ray microtomography, used in connection with the methods of optical microscopy, SEM and EDX-analysis. This comprehensive methodological approach allows to obtain the maximum possible information about the object under study. It should be noted that the study of the structure of the odontoma by microtomography has not been previously conducted.

13.2 Objects and Methods

The possibilities of the proposed methodical approach are considered on the example of the study of medically removed teeth (permanent molars and premolars of the mandible) of patients of the same age group (12–16 years) during the period of mixed bite: intact (samples 1 and 2) and at different stages of development of the carious process (samples 3 and 4); as well as dogs odontomas in molars M1 field (left and right) of mandibule. Odontomas were removed for medical reasons from young (7 month) male dog of the Black Russian Terrier (BRT) during a period of mixed occlusion. The disease development, morphology and mineral composition of hard tissues of human and dog teeth are similar and the processes occurring in them are more similar (Zelenevsky 1997; Cote 2010; Gorrel et al. 2013; Ishinbaeva 2016).

The samples of tooth were scanned by Skyscan 1072 (Ghent University, Belgium). Scanning condition: source voltage—130 kV, source current—76 μA, Al-filter 0.5 mm, pixel size—3 μm, frame averaging—4, rotation step—0.4°. The reconstruction of densities distribution was present by ANT program. The samples of odontoma were scanned by Skyscan 1172 (St. Petersburg State University, Russia). In all cases used conditions are source voltage—100 kV, source current—100 μA, Al filter 0.5 mm, pixel size—4.69 μm, frame averaging—3, rotation step—0.4°.

Additionally, the studied hard tooth tissues were studied by SEM and microprobe analysis using Link 10,000 for SEM ABT-55 (Japan) with accelerating voltage is 25 kV. The odontoma was studied by optic and SEM TESCAN VEGA 3. The odontoma composition was determined using Hitachi S-3400N scanning electron microscope equipped with an Oxford Instruments Energy Dispersive Spectrometer X-Max20.

As a result of microtomographic studies, 3D models of density distribution in the studied samples were obtained and density anomalies were revealed. The attraction of SEM and EDX-analysis methods has allowed to establish the nature of these lesions (to identify the distinctive features of the morphology and composition).

13.3 Results and Discussion

13.3.1 Tooth Hard Tissues

It is known that enamel, as a more highly mineralized hard tissue of the tooth, has a maximum density (Borovsky and Leont'ev 2001). The minimum tooth density is observed within the pulp chamber. The density of dentin is intermediate. In the normal state in the enamel of intact teeth, the density is increased in the area of the mounds and reduced in the fissures and in the cervical part of the tooth. The

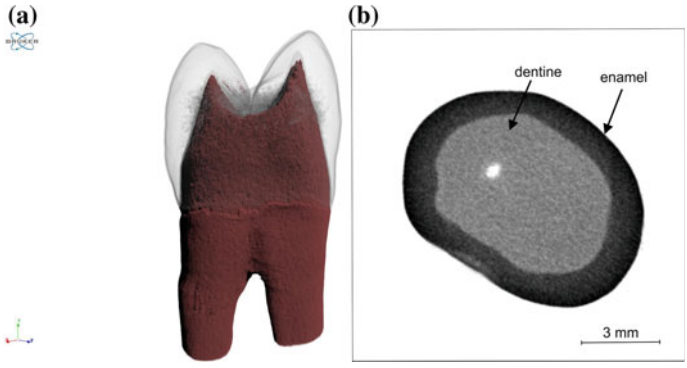


Fig. 13.1 Density distribution in an intact tooth. **a** 3D model; **b** the cross-section perpendicular to the axis of the tooth

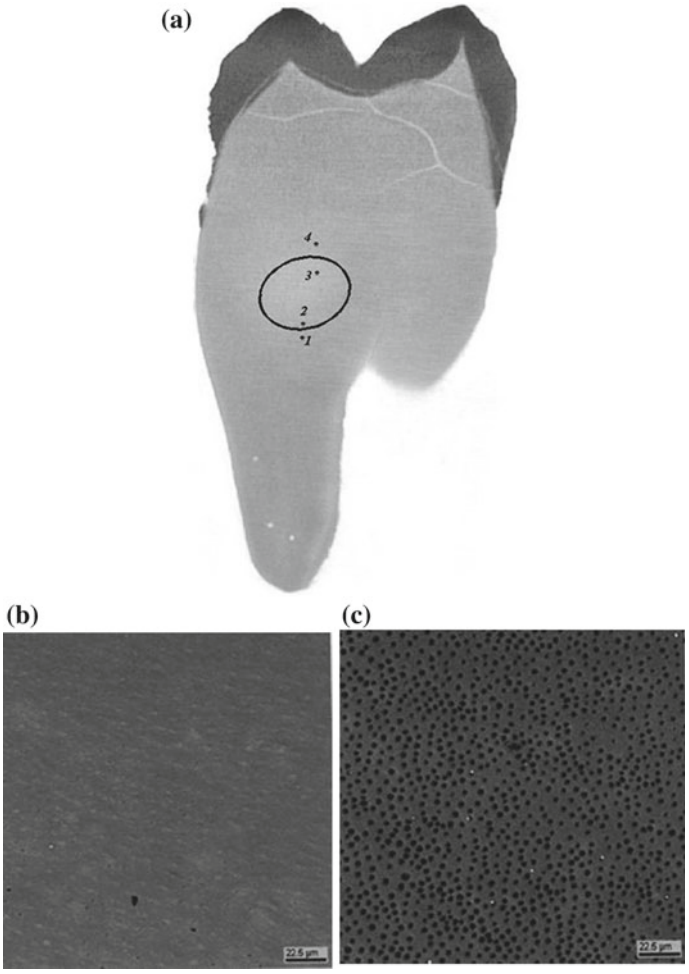


Fig. 13.2 Area of reduced density in the dentine of the impact tooth. **a** μCT image in a section parallel to the tooth axis; SEM images of dentine: **b** outside the lesion (1 and 4 points); **c** inside of lesion (point 3)

surface layer of enamel differs from the deeper ones with a higher density and, according to microprobe analysis, a higher content of a number of chemical elements, including calcium, magnesium, phosphorus, fluorine (Frank-Kamenetskaya et al. 2004; Leont'ev 2016).

According to the data obtained by μCT, the intact tooth (sample 1) is characterized by a uniform distribution and maximum density within each type of solid tissue (enamel and dentin) and, therefore, has the highest resistance to carious process (Fig.13.1).

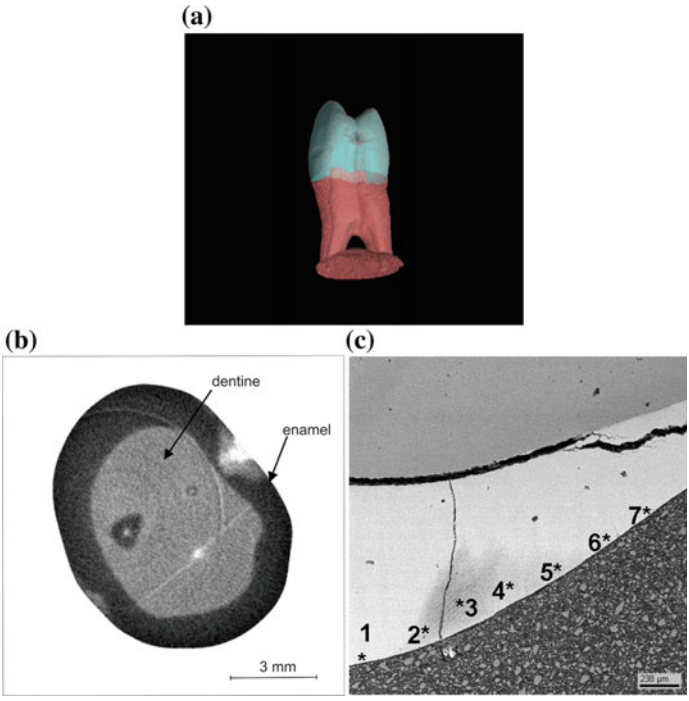


Fig. 13.3 Density distribution and chemical composition in a tooth with a hidden carious cavity. **a** 3D-model; **b** the cross-section perpendicular to the axis of the tooth; **c** the change of the KCa/P in the region of the enamel reduced density: 1—1.58, 2—1.58, 3—1.56, 4—1.54, 5—1.59, 6—1.59, 7—1.58

In another of the investigated tooth, visually related to intact (sample 2), we found in dentin, foci of reduced density with a rounded shape with a diameter of 2.0–2.5 mm were found (Fig. 13.2). Microprobe study of these areas shows significant variations in the content of calcium and magnesium. If the edge with the centers of plots calcium content is of 24.89 ± 0.18, magnesium and 0.90 ± 0.06 wt%, then in the foci themselves the concentration of these elements increases: calcium—up to 30.06 ± 0.15, magnesium—up to 1.36 ± 0.06 wt%.

It is known that the main mineral component of the hard tooth tissues is non-stoichiometric hydroxylapatite (Elliot 1997; Frank-Kamenetskaya 2008; Frank-Kamenetskaya et al. 2011). The resistance degree of hard tooth tissues is characterized by the Ca/P-coefficient ($K_{Ca/P}$), the reduction of which relative to the value of 1.67 determines calcium deficiency in the structure of apatite. Values of $K_{Ca/P}$ of inside the chamber is lowered to 1.61–1.62 area in comparison with this figure is the source (of 1.66). As a result of the study of the sample on a scanning electron microscope revealed that inside the hearth with a reduced density of the number of dentin tubules increased, and the dentin tubules expanded. Thus, the revealed decrease in density is a consequence of changes in the morphology of dentin. The increase in the

content of calcium and magnesium in this area is probably due to active metabolic processes that perform a compensatory role.

In the enamel on the approximal surfaces of the teeth with initial caries stage (sample 3), the μCT method reveals pockets of reduced density and hidden carious cavities (Fig. 13.3a). Foci are rounded with a diameter of 1 mm. According to microprobe analysis, the content of calcium in the enamel within lesions is reduced from 39.60 ± 0.18 to 23.44 ± 0.15 wt%, which leads to a decrease in the $K_{Ca/P}$ from 1.58 to 1.54 (Fig. 13.3b).

In teeth with a deep carious cavity (sample 4), significant changes in the density of hard tissues are observed (Fig. 13.4a). $K_{Ca/P}$ varies from 1.60 out of cavities inside it to 1.45 (Fig. 13.4b), which reflects the decrease in density as a result of demineralization of hard tissues of the tooth.

Thus, the application of the method of X-ray computed microtomography jointly with SEM and EDX-analysis methods revealed hidden density anomalies in the hard tissues of the teeth, referred to the intact during visual examination, and the use

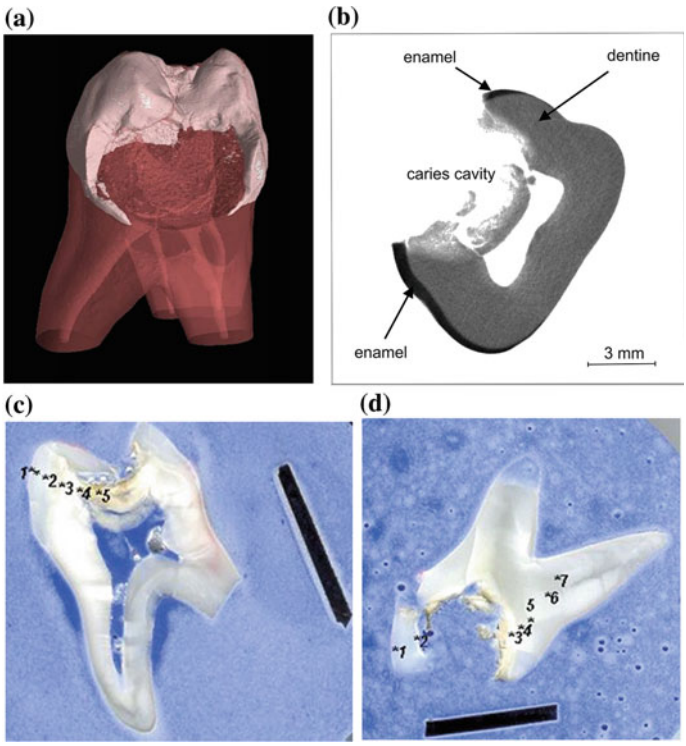


Fig. 13.4 Distribution of density and chemical composition in a tooth with a deep carious cavity. **a** 3D-model; **b** the cross-section perpendicular to the axis of the tooth; change of the KCa/P in a section parallel to the tooth axis: **c** 1—1.59, 2—1.55, 3—1.52, 4—1.53, 5—1.45; **d** 1—1.60, 2—1.60, 3—1.54, 4—1.53, 5—1.53, 6—1.52, 7—1.54

of microprobe analysis to establish a connection between the density and chemical zoning of tooth tissues.

X-ray computed microtomography, is undoubtedly a promising method for the detection and study of the initial stages of the changes of the microstructure of the hard tissues of the tooth. The study of dental tissues in patients aged 12–16 years is of particular interest due to the need to improve the prevention of caries in adolescence.

The study of the density, chemical composition and degree of mineralization of hard tissues of teeth in the presence of a carious cavity, can assist in the development of recommendations for the treatment of caries (the required size of the preparation of the carious cavity in order to achieve optimal treatment results, the selection of dental material for filling cavities of different localization, etc.).

13.3.2 Odontoma

According optic visualization the size of odontoma is 10–12 mm (Fig. 13.5a, b) and the size of its single forming element varies from 2–3 mm to 7–8 mm (Fig. 13.5c, d).

Studied formations of dog by mCT are classified as a hard, complex, composite odontomas (Fig. 13.6a–j). Odontoma consists of chaotic different constituent parts: enamel, dentin, cement, pulp of tooth and fibrous tissue (Fig. 13.6a, b). The

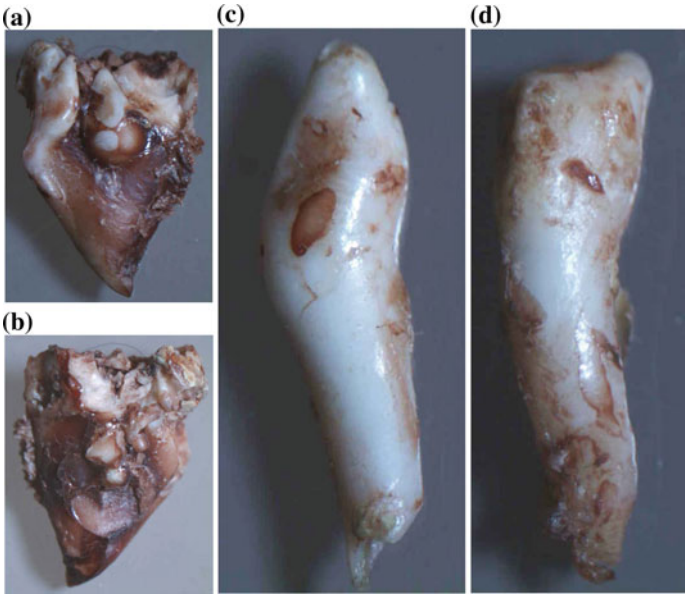


Fig. 13.5 Microfotographs of odontoma. **a**, **b** optic images of odontoma (left and right); **c**, **d** optic images of odontoid (left and right)

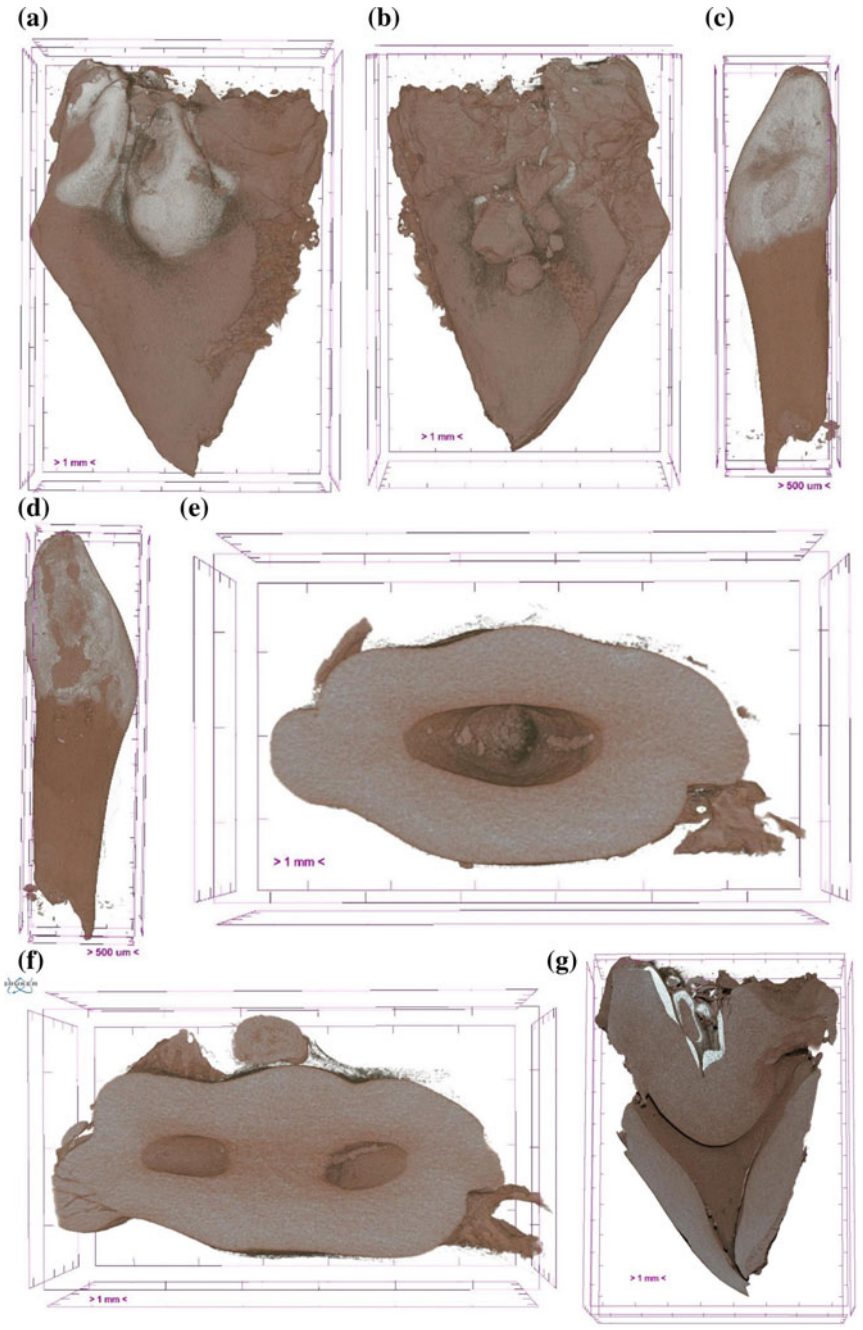


Fig. 13.6 Microfotographs and 3D visualization of odontoma. **a**, **b** 3D-model of odontoma; **c**, **d** 3D-model of odontoid; **e**, **f** 3D-model of odontomas low part (1/3); **g**, **h** 3D-model, cut parallel elongation; **i**, **j** 3D-model of odontomas upper part (2/3)

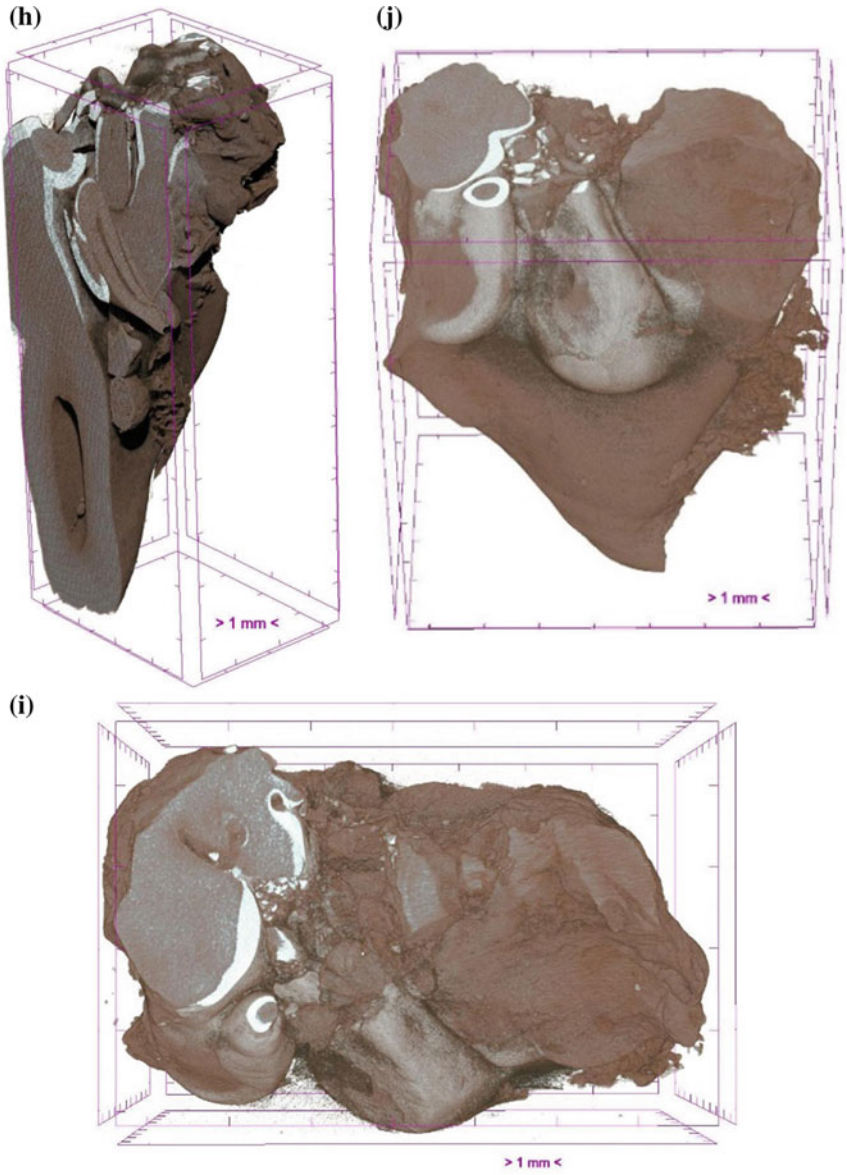


Fig. 13.6 (continued)

hard odontoma is progress from single or few teeth germs. It's appearing during the period of permanent teeth formation. There are three forms of hard odontoma: simple (full and incomplete), complex (composite and mixed) and cystic. The simple odontoma is caused with malformation of single germ. The complex odontoma is caused with disorder of few teeth germs because it consists from hard tissues on the different progress stages. The simple odontoma is formed by a few chaotic mixed hard tissues which sufficiently for growth only single teeth. The simple full odontoma is formed from all types of tissues and simple incomplete odontoma is consist of single type of tooth tissue. Germs of some teeth which tissues are calcified, high differentiated and chaotic situated formed the complex odontoma. Complex odontoma has composite and mixed structure. Complex composite odontoma includes some right formed teeth (odontoids) with pulp in central part, but deformed. Odontoids (elemental parts of odontoma) are formed from hard tooth tissue (enamel, dentin, cement) (Fig. 13.6c, d).

So microtomography investigation shown that the low part of odontoma is similar in structure of tooth root. The two root canals are bringing together in the apical part (Fig. 13.6e–g). The root part of odontoma was formed by dentin with cement and connective tissues are covered outside. The pulp cavity is cover by predentin. In pulp cavity we can see the elements of pulp (the neurovascular bundle). The upper part of odontoma (more than 2/3) was formed by different size chaotic separate parts united by fibrous tissue. Most of them were formed by canine teeth type with pulp cavity in central part (Fig. 13.6h). We can observe some elements like unformed parts of enamel and dentin (size is $\leq$1 mm) located at the upper part of odontoma (Fig. 13.6i, j).

Our study demonstrates that the microtomography method is effective, non-destructive and prospective method for odontoma diagnostics and classification. A comprehensive methodological approach allows obtaining exhaustive information in the study of odontoma, its classification, etiopathogenesis and treatment methods.

The results of EDX-analysis are shown that the $K_{Ca/P}$ of odontoid for enamel and dentin are 1.56 and 0.80 accordingly; the $K_{Ca/P}$ of odontoma tissues is 1.58 and 1.03 accordingly. The enamel $K_{Ca/P}$ of odontoid and odontoma totally is satisfy of normal hard tooth tissues, the mineral component of which is represented by apatite (Elliott 1997; Frank-Kamenetskaya et al. 2004; Frank-Kamenetskaya 2008; Pikhur et al. 2010). The value of $K_{Ca/P}$ in dentin is less (approximately 1), which corresponds to another hydroortophosphate—brushite $Ca[HPO_4] \times 2H_2O$. This assumption is supported by the data of Oliveira et al. (2007), in which it was shown that apatite can pass into brushite when the pH of the crystallization medium decreases, which can occur during the formation of the odontoma. Alongside this known that will brushite can be a precursor of apatite (Ferreira et al. 2003; Stulaiterova, Medvedsky 2008; Komlev et al. 2012).

The values of $K_{Ca/P}$ in enamel vary between 1.56 and 1.58, indicating that the odontoma enamel contains non-stoichiometric apatite and calcium deficiency more than in the studied hard tissues of the tooth. At the same time, in addition to apatite, dentin contains brushite. The question which of these phases (apatite or brushite) is the primary should be answered by subsequent studies.

BRT is a young breed of dog with large amount original breeds in creating history (more than 17). In this regard there is a high risk of genetic defects in dog organism (Willis 2000; Starchenkov 2013). In possible the appearance and progress of odontoma is one of these defects.

13.4 Conclusions

The studies have shown that the use of the method of X-ray computed microtomography is very promising as the initial stage of the study of the for investigation of the morphology and composition of the hard tooth tissue. The method allows to obtain a three-dimensional picture of the structure of the object without breaking the integrity. The initial information on the structure obtained during the microtomographic scanning allows further study of hard tooth tissue with high resolution of spatial localization, which greatly minimizes the complexity of the study (labor input of sample preparation and analytical studies).

For the first time conducted microtomographic studies of odontoma allowed to study its morphology with high spatial resolution and to obtain a three-dimensional model that clearly demonstrates the internal structure without destruction.

The using of a set of methods (X-ray computed microtomography, EDX-analysis, SEM, optical microscopy) provides the most complete and complementary information on the distribution of density, morphological structure and chemical composition of hard tissues of teeth, which is the theoretical basis for the development of measures to improve the diagnosis, prevention and treatment of major dental diseases.

References

Barnes L, Eveson JW, Reichart P, Sidransky D (eds) (2005) World Health organization classification of tumors. In: Pathology and genetics of E558 head and neck tumors. IARC Press, Lyon, France

Borovsky EV, Leont'ev VK (2001) Biology of the oral cavity. Medicina, Moscow (in Russian)

Cote E (2010) Clinical veterinary advisor. Elsevier Health Sciences

De Clerck NM, Van Dyrk D, Postnov AA (2003) Non-invasive high-resolution μCT of the inner structure of living animals. Microsc Anal (Euro) 81:13–15

Elliott JC (1997) Structure, crystal chemistry and density of enamel apatites. Dent En Wily Chichester Ciba Found Symp 205:54–72

Ferreira A, Oliveira C, Rocha F (2003) The different phases in the precipitation of dicalcium phosphate dihydrate. J Cryst Growth 252:599–611

Frank-Kamenetskaya OV (2008) Structure, chemistry and synthesis of carbonate apatites—the main components of dental and bone tissues. In: Krivovichev SV (ed) Minerals as advanced materials. Springer Verlag, Berlin, Heidelberg

Frank-Kamenetskaya OV, Golubtsov VV, Pikhur OL et al (2004) Non-stechiometric apatite from hard teeth tissues of peoples. Age Changes. Proceeding of VMO 5:120–130 (in Russian)

Frank-Kamenetskaya OV, Kol'tsov A, Kuz'mina M et al (2011) Ion substitutions and non-stoichiometry of carbonated apatite-(CaOH) synthesised by precipitation and hydrothermal methods. J Mol Struct 992:9–18

Gilispie CC (1970) Dictionary of scientific biography. F. Clarke and P.P. Broca. Scribner's Sons, New York
Gorrel C, Andersson S, Verhaert L (2013) Veterinary dentistry for the general practitioner. Elsevier Health Sciences
Iordanishvili AK (2015) Gerontostomatology. Chelovek, St.Petersburg (in Russian)
Ishinbaeva SN (2016) Diagnosis of spontaneous tumors of dogs. Bishkek
Komlev VS, Rau JV, Fosca V, Fomin AS et al (2012) Single-phase bone cement based on dicalcium phosphate dihydrate powder and sodium silicate solution. Mater Lett 73:115–118
Leont'ev VK (2016) Enamel of the teeth as a bio-cybernetic system. Geotar-Media, Moscow (in Russian)
Mavridou AM, Kerckhofs G, Wevers M et al. (2017) Added value of Micro-CT in tooth resorption assessment In: Abstract of Bruker micro-CT users meeting, Brussels, pp 259–260
Oliveira C, Ferreira A, Rocha F (2007) Dicalcium phosphate dihydrate precipitation. Characterization and crystal growth. Chem Eng Des 85:1655–1661
Pikhur OL, Plotkina YuV, Frank-Kamenetskaya OV, Rosseeva EV (2010) Chemical composition of enamel and hair of the residents of industrial centers of NW Russian region. In: Volfson IF (ed) Medical geology: state and prospective. Moscow (in Russian)
Savina YuD (2007) Neoplastic diseases of animals. Veter Dr 4:34 (in Russian)
Starchenkov SV (2013) Diseases of the dogs and the cats. Complex diagnostics and therapy, 4 Ed. SpecLit, St. Petersburg (in Russian)
Sasov A, Van Dyck D (1998) Desktop X-ray microscopy and microtomography. J Microsc 191(2):15–158
Stulaiterova R, Medvedsky L (2008) Effect of calcium ions on transformation brushite to hydroxyapatite in aqueous solutions. Coll Surf A Physicochem Eng Aspects 316:104–109
Spoutil F, Wald T, Prochazka J et al. (2016) Survey of tooth enamel quality with X-ray microCT. In: Abstract of Bruker micro-CT users meeting, Luxembourg, pp 302–306
Tassani S, Olivares AL, Carmona V et al. (2017) Optimization of endodontic irrigation procedure using computational fluid dynamics: preliminary results. In: Abstract of Bruker micro-CT users meeting, Brussels, pp 241–247
Tsimbalistov AV, Pikhur OL, Plotkina YuV, Golubtsov VV (2005) New technology and methodic possibilities for hard tooth tissues study. Proc St Petersb State Med Univ 2:40–41(in Russian)
Willis MB (2000) Genetics of the dog. Centerpolygraph, Moscow (in Russian)
Zelenevsky NV (1997) Dogs anatomy. St.Petersburg (in Russian)

Chapter 14
Changing Hydraulic Conductivity After Rupturing Native Structure of Peat Under Limited Evaporation Conditions

Eldar A. Kremcheev, Dmitriy O. Nagornov and Dinara A. Kremcheeva

Abstract The qualitative characteristics of peat raw materials in the processes of its mining and field enrichment fully depend on the nature of the biogenic-abiogenic interactions in the peat system, which is a capillary-porous body with a heterogeneous structure and water-peat binding energy changing in a wide range. Energy costs for dehydration of peat capillary-porous bodies of different sizes and configurations are crucial for technologies of peat extraction and processing in terms of ensuring economic efficiency of production. The present paper considers the issue of calculating the characteristics of dehydration of wet peat raw materials with moisture 84–90% under the influence of gravitational and capillary-osmotic forces, as well as through evaporation. As a result of the research, the characteristics of moisture transfer intensity in the biogenic-abiogenic peat system with varying water binding energy are described. For the high-moor peat deposits, the intensity of moisture transfer is described by a linear dependence, for the transitional and low-moor types of peat, the dependence has a minimum at the degree of peat decomposition of 30–32%. The minimum has the role of a generalised point at the decomposition degree of 31%. With the increasing decomposition degree for the high-moor type, the intensity of moisture transfer tends to zero due to the manifestation of the rheological properties of water, i.e. an increase in the limit shear stress and the density of the bound water, as well as the decreasing pore sizes. For transitional and low-moor types, the intensity of moisture transport tends to a constant with an implicit manifestation of the border due to the increase of the resistance factor of moisture transport. It is found that when the filtration equilibrium is reached, the amount of remaining moisture in the technogenic-disturbed biogenic-abiogenic peat system and the critical height of the bulk of peat raw materials will correlate with the moisture conductivity factors, porosity, pore size and height of a bulk. This feature of the changing moisture conductivity is confirmed by the experimental data obtained by the authors to assess the precipitation, the critical thickness of the bulk depending on the initial thickness of

E. A. Kremcheev · D. O. Nagornov (✉) · D. A. Kremcheeva
Saint Petersburg Mining University, 2, 21st Line, Saint Petersburg 199106, Russia
e-mail: nagornov_d_spmi@mail.ru

E. A. Kremcheev
e-mail: kremcheev@mail.ru

© Springer Nature Switzerland AG 2020

O. V. Frank-Kamenetskaya et al. (eds.), *Processes and Phenomena on the Boundary Between Biogenic and Abiogenic Nature*, Lecture Notes in Earth System Sciences,
https://doi.org/10.1007/978-3-030-21614-6_14

the peat layer of the disturbed structure and the change in the critical height in the pore radius function, which corresponds to the theoretical data obtained in the work.

Keywords Fuel resources · Green · Peat processing · Dewatering · Environmental management

14.1 Introduction

The concept of increasing share of local fuels in the energy balance is amongst the state energy policy aims; the objective is to ensure the needs of the Russian Federation's regions in fuel and energy resources. Small settlements remote from sources of heat distribution and energy are often faced with the problem of unstable fuel supply to their heat-generating enterprises (Mikhailov 2016). To a greater extent, this applies to towns that use solid and liquid fuels carried from remote sources. The Northwestern Federal District (NWFD) is not an exception; this paper analyses production technologies on its example and provides solutions to improve the quality characteristics of peat products and the productivity of the field stage of its production. The problem of improving the stability of fuel supply in the NWFD can be effectively solved in areas with sufficient reserves of peat fuel resources. The NWFD is amongst the richest in peat regions of Russia, where peat reserves are estimated at 5,791 fields with a total area of about 2.6 million hectares consisting of 7.73 billion tons of balance and 2.27 billion tons of off-balance resources. The reserves of peat at deposits with an area of up to 10 ha make up a sum of 18.8 million tonnes.

A distinctive feature of the NWFD is that the balance reserves of peat deposits make up 25.2% of the total Russian balance reserves of peat and are well studied compared to other regions, so 46.2% of them have A + B categories (According to the classification adopted in Russia, category A corresponds to the explored reserves prepared for mining. Geologically reasonable, relatively proven, contoured workings deposits belong to category B. Category C1 corresponds to the reserves established by the approximate studies of deposits. Category C2 corresponds to the pre-estimated deposits). However, the analysis shows (Fig. 14.1), that the share of reserves of categories A + B is very different by regions in the NWFD.

To date, peat has lost its importance as a reliable fuel for local power generation facilities; it happened primarily due to the peculiarities of extraction and production cycles of peat fuel, where the bulk of the moisture is removed by drying the extracted raw materials directly on the deposit surface. This reduces dramatically the stability of production under severe weather conditions and use of traditional extraction technologies. Present tome, the peat companies in the Russian Federation can be divided into three groups (Table 14.1) according to the volume of production: small, medium and large (Mikhailov et al. 2013).

The total annual volume of peat production in Russia has stabilised at about 2 million tonnes per year. There is a slight tendency of production growth, and only due to small-scale production. Large peat companies, accounting for only 3% of

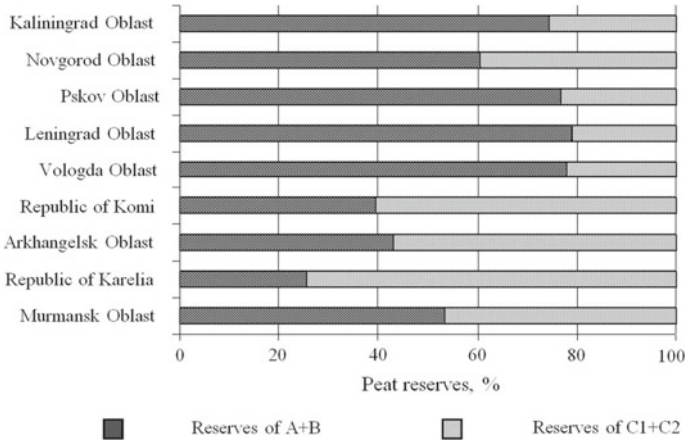


Fig. 14.1 The share of reserves of different categories in total peat balance reserves in the NWFD regions (Mikhailov et al. 2013)

Tables 14.1 Structure of the peat industry in Russia (in the adopted classification)

Peat extraction companies	Production volume, thousand tonnes	Percent from the total number of companies
Small	<5	52
	5–10	39
Medium	10–20	3
	20–40	3
Large	40–60	2
	60–100	0.5
	>100	0.5

the total, produced about 60% of peat, while small and medium −40%. Currently, scholars working on improving the technology of peat mining, pay more attention to the various options for year-round extraction methods and activities to extend the term of peat production. In this regard, the study of interactions occurring in the biogenic-abiogenic peat system under the technogenic impact becomes relevant.

The structure of the extraction process with native structure rupturing of a biogenic-abiogenic peat system is common in all technological solutions, including peat extraction from wetted deposits, followed by dehydration in the field and (or) production facilities. The development of solutions to optimise energy costs for the dehydration of peat raw materials in the design of technological schemes of its production, increasing the load per unit area of the mining field, becomes urgent. Theoretical and experimental studies to identify the potential of moisture removal are the basis of this work; they were conducted to create rational technological methods of field enrichment of peat raw materials of high moisture, based on the maximum

intensity of drying in certain weather conditions, as well as optimisation of energy costs for dehydration of peat raw materials.

The solution of the task is provided by a comprehensive study of dehydration of wet peat raw materials with 84–90% moisture under the influence of gravitational and capillary-osmotic forces, as well as by evaporation. In modern economic conditions, the use of intensive technologies of milling and lump peat production is rational only for medium and large peat companies that have a fleet of special peat machines and complexes with prepared production facilities and operating in regions with favourable weather conditions. A striking example of the coincidence of all the factors necessary for the use of technology of milling peat production is the VyatkaTorf JSC, which produced 810 thousand tonnes of peat in 2011.

It should be noted that depending on the meteorological conditions of the area of the enterprise location, the seasonal collection of milling peat in the application of the classical technological scheme of milling peat varies in the range from 200 to 800 t/ha (Vasilyev and Smirnov 2004; Afanasyev et al. 1987). For NWFD conditions, as for other districts, this range is limited by the normative number of cycles for different types of deposits. For products of a nominal humidity of 40% the requirements are as follows. For all types of deposits with the degree of decomposition R_t = 5–15%, mining intensity has to be 100–250 t/ha; with the R_t = 16–20% it has to be 120–300 t/ha; for high-moor and transitional deposits with the R_t = 20–30% it has to be 170–425 t/ha; for high-moor peat with $R_t > 30\%$ and low-moor it has to be 190–425 t/ha. For products with a nominal humidity of 55% the required intensity is 220–550 t/ha (data processed after Afanasyev et al. (1987) on the normative values of the number of cycles and technological indicators of production of milling peat).

It is obvious that ensuring the volume of peat extraction using the existing technology of milling peat requires large production areas, but their preparation, mining and reclamation (Alekseenko et al. 2017, 2018) require significant investments related both directly to the work carried out and rental payments, growing with the increase in the developed areas. Prospects of increasing productivity and reducing the cost of peat production should be sought in the best use of meteorological conditions and increasing the load per unit area of the mining field by technological methods (Afanasyev et al. 1987; Antonov et al. 1981; Sokolov et al. 1988). It should be noted that consumers of peat raw materials and products impose a set of requirements for the characteristics of field peat products that are not provided with intensive production technologies. Peat, as a complex biogenic-abiogenic system, transforms during the execution of technological operations can both improve and worsen its consumer properties. The direction of the vector of change in the properties of the peat system is determined only when taking into account the whole range of factors of biogenic-abiogenic interactions that occurred during its natural formation and technological transformation in the course of technological mining operations.

For small peat companies, the most promising technology for peat extraction is the open-pit method for harvesting raw materials of increased moisture (Mikhailov et al. 2013; Kosov 2005; Kremcheev and Afanasyev 2012; Kremcheev 2014; Naumovich 1984; Kremcheev and Nagornov 2017), in which all production tasks are solved in a small field area with a minimum set of general-purpose technical means

(swamp excavator, tractors with semi-trailers, front-end loader, etc.), its organisation is possible with minimal investment. In addition, the method has the following advantages: reduction of adverse environmental impact; expansion of the production season; optimal use of weather conditions; increase of economic efficiency of production up to 20 times compared to milling and lump technology (Mikhailov and Selennov 2009; Selennov and Mikhailov 2009); increase in the number of usable peat deposits; rapid reclamation of areas that absorb CO_2.

When using the open-pit method, it will be easier for small peat mining companies to follow the basic principles of environmental management in the extraction of peat raw materials: to follow the international principles of reasonable use of peat deposits; to ensure diversification of production with rational directions of extraction and use of peat; to provide extended mining of peat deposits; to flexibly apply innovative technological solutions in the extraction of peat raw materials, ensuring minimal environmental impact; to produce a phased reclamation and re-waterlogging of peat deposits, providing a reduction in fire risk in the post-production period and (or) improve the efficiency of peat accumulation process.

The flow sheet for the production of peat crumb and lump fuel can be implemented with a number of basic technological modules, interconnected by transport links. Crumb-shaped peat is both a product (milling peat) and a raw material for further year-round processing in workshop conditions and production of, e.g. lump-shaped fuel, peat briquettes, pellets or products demanded by the agriculture. With the transition to exclusively workshop conditions for the production of peat fuel, it is possible to significantly simplify the technology of extraction of raw materials, reducing the need for the preparation of fields for the extraction and drying of peat in the field, stockpiling, storage and transportation of products, as well as to significantly lessen the dependence of the production cycle on weather conditions, fire hazard, etc.

The conceptual scheme of interaction between the modules of small and medium-volume peat production and material flows within the energy cluster of distributed energy is presented in Fig. 14.2. The modular scheme of peat production in the structure of the distributed energy cluster includes mining, transport and processing modules (Kremcheev et al. 2012).

The mining module includes a quarry and zones of gravity dehydration and drying. The plot of gravity peat dewatering is arranged in the vicinity of an excavation area or on special platforms, where peat dehydration occurs in bulks until the critical height determined by the equilibrium condition of moisture under the action of gravitational, capillary and osmotic forces, taking into account evaporation.

Areas of peat drying can be of two types. The first type provides the stages of dehydration by evaporation from the side surface of the stacks of raw materials of an optimal size during the transfer of high moisture peat, followed by its use for the production of peat compositions or in the processing module. The second type is used to obtain the crumb-shaped peat, including conditioned moisture, by drying peat of optimal grain size in thick layers with a layer-by-layer cleaning in larger rolls and hauling during their drying-free time to the pile permanent storage or to the first-type site. The finished crump-shaped peat products with allowable moisture

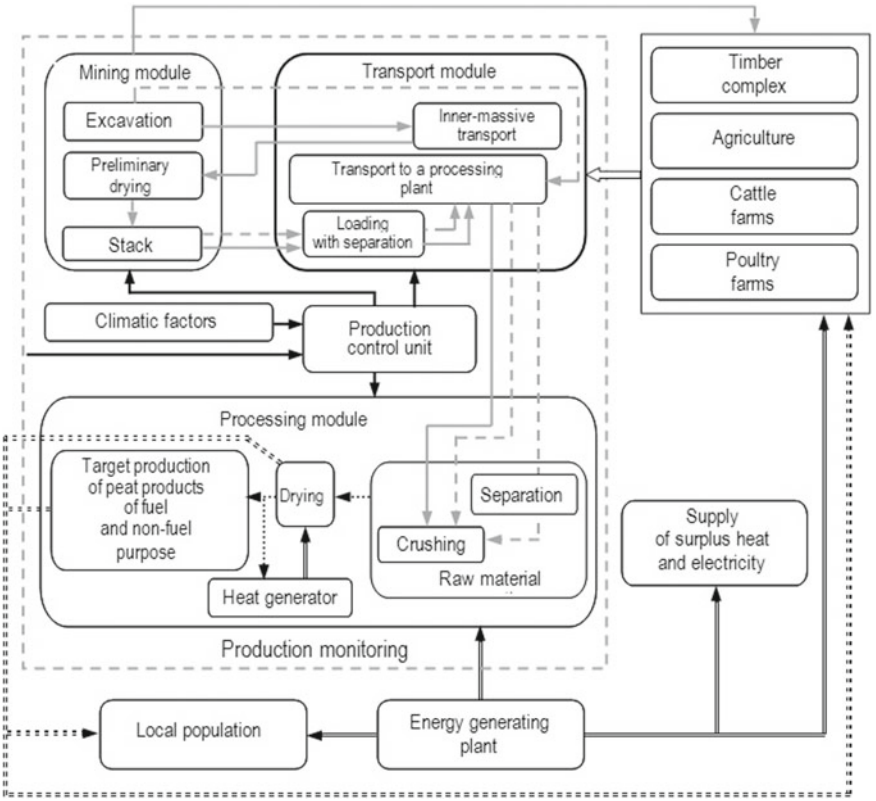


Fig. 14.2 Conceptual diagram of flows of raw materials, production and management of effects within the cluster of distributed energy

level are shipped to the consumer mainly for fuel purposes (*GOST R 50902-2011. Fuel peat for pulverised burning. Technical conditions*).

The processing module includes a preparation site for peat raw materials of increased moisture, providing two major processes, i.e. separation and crushing. Under the first process, peat raw materials are purified from large inclusions of wood and permafrost with its partial grinding. After separation, if necessary, the peat raw material is crushed to obtain a given particle-size distribution. The peat lumping provides obtaining agglomerates of fuel with desired characteristics (size, mass, strength, etc.). A screw extrusion method is a widespread technology for obtaining agglomerated peat fuel. The drying area is necessary for concluding drying of the peat fuel to a moisture content of not more than 45% (in accordance with the requirements of *GOST R 51062-2011. Lump peat fuel for household needs. Technical conditions*). Since the drying process is the most energy-intensive, it is rational to use a heat generator operating on the same peat fuel in the drying module to increase energy efficiency and energy independence of production.

The use of modular production technology with developed transport links will allow, if necessary, to respond quickly to changes in the characteristics of peat raw materials without changing the quality of the products. On the basis of previous studies, the target range of humidity for peat raw materials entering the shop module for the production of peat fuel products by extrusion, ranging from 60 to 70% (Kremcheev and Kremcheeva 2016; Lishtvan et al. 1983), has been established. In some cases, this range can be extended to 55–75% in case of product diversification. Thus, the task of the field stage of peat enrichment in open-pit mining is the decrease of moisture from 90–93 to 55–75%.

Due to the fact that for the proposed small-scale extraction technologies, the critical parameters are the rhythm and mode of moisture removal from the disturbed peat system, the issue of generalisation of theoretical information on moisture filtration in native and disturbed peat systems is getting more relevant, as well as the development of a mathematical apparatus that allows, on the basis of a priori information, to solve the problem of optimising the energy costs of dehydration of peat raw materials with moisture $W = 84–90\%$ under the action of gravitational P_g and capillary-osmotic P_k forces.

The aim of the research is the experimental-theoretical evaluation and ranking of the parameters of the biogenic peat system affecting moisture transfer, which in turn will allow development of a set of technological solutions to control the process of removing moisture from disturbed peat systems in small-scale field technologies of peat extraction and processing.

14.2 Approaches and Methods

Peat raw materials are considered as a biogenic-abiogenic system, the native structure of which is broken as a result of the influence of actuating elements of peat machines at the stages of extraction, transportation and preparation for the process of field enrichment, which are the main parts of the production process along with the field dehydration. The developed provisions are general and applicable for any peat type during its field dehydration.

When solving the problem of fluid motion estimation in biogenic-abiogenic peat systems of the disturbed structure at the first stage, the processes of accompanying moisture evaporation from the peat layer were not taken into account. The analysis of results of theoretical and experimental studies of changes in the properties of peat raw materials in the process of dehydration, taking into account moisture evaporation is performed by assessing the critical thickness of the peat layer during the dehydration of H_{cr} and balancing the gravitational and capillary-osmotic forces ($P_k = P_g$). The critical thickness is the value at which the technological scheme of peat extraction with the subsequent moisture removal from the peat layer of the disturbed structure during field dehydration is possible only with the use of mechanical pressing followed by final drying of raw materials by thermal methods in the factory or drying in the field. These stages of dehydration are amongst technological methods of changing the

properties of peat raw materials (moisture W, density γ, porosity n, moisture transfer intensity i_i, total moisture capacity W_{tc}, strength R_i, etc.), determining, along with the degree of decomposition R_{t}, the quality of diverse peat-based products (Afanasyev and Churaev 1992; Afanasyev et al. 1987; Lazarev and Korchunov 1982; Semensky 1939; Shakhmatov 2011).

14.3 Results

Drying in the factory is one of the final stages of peat processing by weather-independent technologies. Implementation of this process in the factory without pre-drying in the field can be justified from an energy point of view, provided that at this stage at $W = 82$–84% peat is mechanically pressed (Lazarev and Korchunov 1982). The field stage of high humidity peat dewatering is much cheaper than the factory one, but it is a bit longer in terms of the technological cycle time. Questions of the physics of the biogenic-abiogenic interactions in peat systems are largely researched by V. M. Naumovich, L. S. Amaryan, V. I. Goryachev, etc.

Since the process of gravitational peat dewatering takes place irrespectively of a processing technology for peat raw materials of high humidity, in this Chapter the water transfer in a disturbed biogenic-abiogenic peat system is substantiated by gravitational and capillary-osmotic removal of moisture through the application of the model, providing a determination of the maximum values of the moisture transfer factor through filtration factors and the thickness of a dehydration layer subjected to a critical height reduction value. The results of experimental and theoretical studies are usually used in the evaluation of filtration processes (Amaryan and Bazin 1965; Gamayunov et al. 1998; Jordán et al. 2016; Kashchenko 2010; Kashchenko and Kovalev 2011; Korchunov et al. 1960; Kremcheev and Ivanov 2016; Kutais 1955; Nerpin and Khlopotenkov 1970; Sudnitsyn 1964; Vakhromeev et al. 1984; Vitkov et al. 1994), basing on the application of different models (Kashchenko 2010; Korchunov et al. 1960; Nerpin and Khlopotenkov 1970; Sudnitsyn 1964; Vitkov et al. 1994). The model analysis was described in a number of papers (Kashchenko and Kovalev 2011; Korchunov et al. 1960; Nerpin and Khlopotenkov 1970; Vitkov et al. 1994). Peat systems were studied using theoretical and experimental studies based on the potential theory of moisture transfer, taking into account the agreed models of moisture movement in films and capillaries (Amaryan and Bazin 1965; Gamayunov et al. 1998; Korchunov et al. 1960; Kremcheev and Ivanov 2016; Kutais 1955; Sudnitsyn 1964; Volarovich and Churaev 1960). These models give the greatest convergence of simulation results in comparison with the experiment (Gamayunov et al. 1998; Kashchenko and Kovalev 2011; Korchunov et al. 1960; Nerpin and Khlopotenkov 1970). Works on the study of the filtration properties of peat using radioactive isotopes (Afanasyev and Churaev 1992; Churaev 1960; Volarovich and Churaev 1960) made in the radiochemical laboratory of the Kalinin Polytechnic Institute (the Tver State Technical University nowadays) and in the Radchenkotorf Scientific Centre JSC are also of great interest, as well as the use of salt labels in

the All-Russian Research Institute of Hydraulic Engineering and Land Reclamation named after A. N. Kostyakov.

Peat raw material, being extracted from a deposit, where stored as a biogenic-abiogenic native substance, passes from the two-phase state (liquid–solid) to the three-phase (liquid–solid–gas), which determines a significant difference between the processes of moisture movement in an undisturbed deposit and peat system subjected to dehydration in the process of extraction with field enrichment. The principal difference between the mining of peat and other minerals is the specific structure of the biogenic-abiogenic peat system and the complexity of water removal during the field enrichment, which is one of the stages of its production.

Water occurs in various physical states in nine stable isotopic types. In a water molecule, hydrogen and oxygen atoms create dipoles, which are combined into associates with the general formula H_2O and form a cyclic, chain and branched structure (tetrahedral associate) with covalent and hydrogen bonds. There is another division of the water molecule structure: angular, ball and tetrahedral.

Water, interacting with the solid phase and air, changes its physical and technological properties, which are different for free and bound water (Afanasyev and Churaev 1992; Gamayunov 2004). For instance, water in the free state is subject to gravity forces that transmits the hydrostatic pressure, almost not being compressed. In the bound state, the structure and density of water is affected by the mineralogical composition of peat, due to the primary (<15% ash) and introduced (secondary) ash, consisting of oxides of SiO_2, CaO, Fe_2O_3, Al_2O_3 (about 80% of ash) and such ions as Ca^{2+}, $Fe^{2+,\,3+}$, Mg^{2+}, K^+, Na^+, etc. In this case, the density of bound water ρ_W, depending on the temperature T, passes through a maximum at $T \cong 310.5$ K for each period of structure formation and differs from $\rho_W = 1 \times 10^3$ kg/m^3 ($T = 277.14$ K) as higher, as higher is the degree of peat decomposition or its dispersion (Gamayunov 2004).

From the point of view of the porous structure, pores with a radius $r > 10^{-5}$ m are not capillary ones and therefore according to N. N. Fedyakin (Afanasyev and Churaev 1992; Gamayunov 2004) water in the pores will be almost free in terms of the surface tension factor σ and the viscosity η. Thus, according to A. V. Lykov, pores can be considered to be capillary for a porous peat body with a size of $l = 0.1$ m if their radius does not exceed 10^{-5} m. For a larger body, such as of $l = 1.0$ m, capillary pores are reduced and their radius should be 10^{-6} m.

In bodies with capillary structure, liquid forms a continuous tube of $h = l$ height. This fact is reflected in the hypothesis of S. N. Nerpin and E. M. Khlopotenkov on continuity of pores of the same diameter in the soil (Nerpin and Khlopotenkov 1970) and on the distribution of water-bearing pores in the soil (S. V. Lundin, L. V. Sverdlova), which indicates the presence of minimum volumes in the system, the pore characteristics of which do not change regardless of the location or orientation. For peat systems, this condition applies peculiarly to the porous particles with pores of a smaller diameter of non-particle (large) pores.

Capillarity can be determined by the ratio of pressures $P_g \ll P_k$. In this regard, both large and narrow (capillary) pores can be distinguished in peat bodies of the disturbed structure (Afanasyev and Churaev 1992; Churaev 1960; Volarovich and

Churaev 1960), which will determine the initial conditions of dehydration at $P_g > P_k$. The intensity of moisture transfer i_g is determined by the action of gravity forces until the height h_i of the bulk of the waterlogged peat of the disturbed structure reaches, due to height reduction, the critical height of H_{cr}, at which the values of gravitational and capillary-osmotic forces are aligned, and the flow of gravitational moisture becomes zero.

Regardless of a flow sheet used in the preparation of peat raw materials to dehydration, there is a violation of the structure of a peat deposit and its transition to a three-phase state in which, along with the forces of gravity $P_g = \rho_W g h_i$, capillary forces act in opposite directions $P_k = (2\cos\Theta)/r$ (Fig. 14.3). According to the laws of thermodynamics (Antonov et al. 1981; Gamayunov 2004), the increase in the entropy dS/d in time caused by external dS_e/d and internal dS_i/d conditions of heat and mass transfer is defined as:

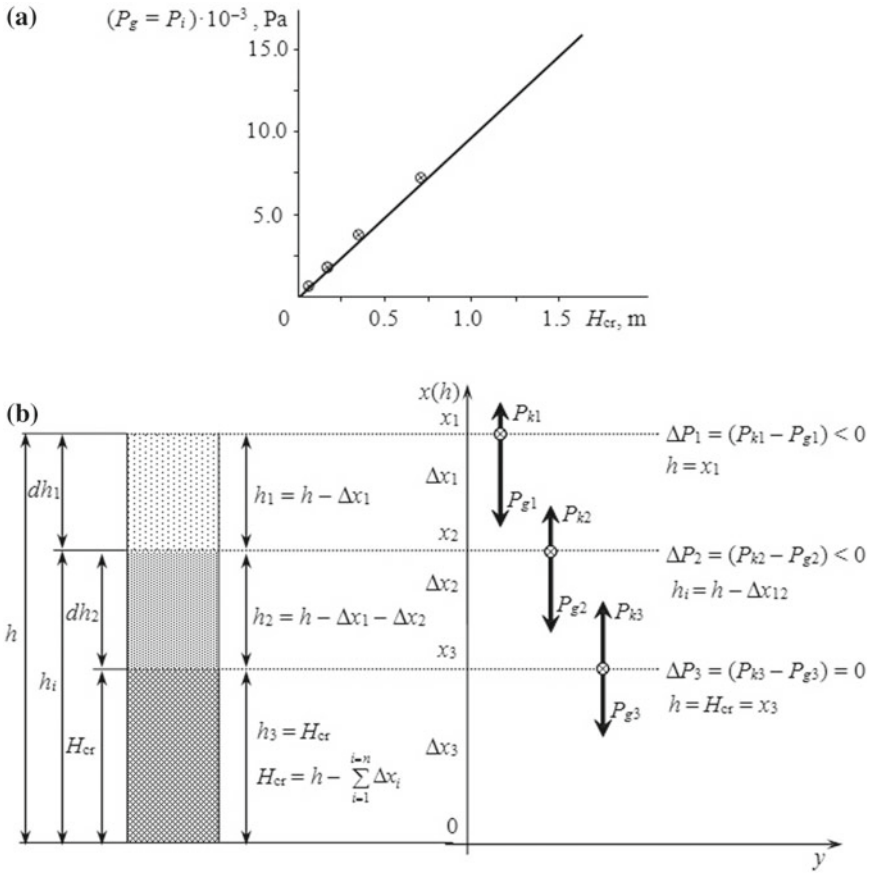


Fig. 14.3 The change of the pressure gradient $\Delta P = P_{ki} - P_{gi}$ (***a***) and the layer height (***b***) at dehydration of peat raw materials to $h = H_{cr}$ at $T = 273$ K

$$\frac{dS}{d\tau} = \sum_{i=1}^{n} J_i X_i, \tag{14.1}$$

where J_i is the flux density of the ith substance; X_i is the thermodynamic driving force.

It is experimentally found that J_i is proportional to X_i:

$$J_i = L_i X_i, \tag{14.2}$$

where L_i is the proportionality factor.

For the case of moisture transfer at $T = \text{const}$, the dependence (14.2) can be represented according to the Fick's laws of diffusion for the case of water evaporation from a watered surface

$$i_{\text{i}} = -D\frac{\partial c}{\partial x}, \tag{14.3}$$

which after conversion (Antonov et al. 1981) takes the form of

$$i = -a_{\text{m}}\gamma_{\text{c}}\frac{dW}{dx}, \tag{14.4}$$

where $\partial c/\partial x$, dW/dx are respectively gradients of concentration of water vapour and moisture in the peat; D, a_m are the diffusion factors of vapour through air and moisture in the peat; $c = \gamma_{\text{c}} W$; γ_{c} is the density of dry matter of peat at $W = W_i$.

The use of Eqs. (14.3) and (14.4) in our case is difficult since there is the uncertainty of driving forces X_i due to the decreasing height of peat raw materials in a bulk. At the same time, the use of the Darcy's equation in different forms (Amaryan and Bazin 1965; Kremcheev 2011, 2013; Kremcheev and Ivanov 2016; Kutais 1955; Nerpin and Khlopotenkov 1970; Vakhromeev et al. 1984; Vitkov et al. 1994) is not possible because of the impossibility of accounting for the capillary forces and vertical pressure h/l (Kutais 1955) when evaluating the hydraulic conductivity of peat raw materials.

Therefore, the use of Eq. (14.2) when assessing the hydraulic conductivity of peat allows choosing as a driving force the pressure difference $P_i = P_k - P_g$, related to the difference between the coordinates $\Delta x_i = x_i - x_{i+1}$ (Fig. 14.2). Without taking into account moisture evaporation from the surface or the associated internal evaporation, the equation of moisture conductivity will have the form:

$$i_g = -F_{\text{m}}\frac{d}{dx}\left(P_k - P_g\right) = -F_{\text{m}}\frac{dP_i}{dx}, \tag{14.5}$$

where F_{m} is the factor of moisture conductivity characterizing the flow of moisture at $(dP/dx) \rightarrow 1$, s; i_g is the intensity of the flow of moisture, kg/(m^2 s).

After substituting the expressions for P_k and P_g into Eq. (14.5), we obtain

$$i_g = -F_m \frac{d}{dx}\left(\frac{2\sigma \cos \Theta}{r} - \rho_W g h\right). \tag{14.6}$$

Provided $dh/dx = 1$ (Fig. 14.2) Formula (14.6) can be written as:

$$i_g = -F_m\left(\frac{2\sigma \cos \Theta}{rh} - \rho_W g\right), \tag{14.7}$$

where σ is the surface tension factor, N/m; r is the pore radius, m; Θ is the solid phase wetting angle, degree; g is the gravitational acceleration, m/s^2; ρ_W is the density of the associated fluid, kg/m^3.

Knowing such characteristics of a biogenic-abiogenic peat system as the factor of moisture conductivity, pore radius and layer height, all other things being equal, it is possible to determine the intensity of the flow of gravitational moisture in peat (peat raw materials) of the disturbed structure.

Analysis of Formula (14.7) shows that at the initial stage of dehydration of raw materials with a moisture content of $W \geq 82$–88% gravity can be taken as the main thermodynamic driving force. Then Eq. (14.7) takes the form:

$$i_g \cong -F_m \rho_W g, \tag{14.8}$$

that according to (14.6) will be:

$$i_g \cong -F_m \frac{dP_g}{dx}. \tag{14.9}$$

Comparison of Eqs. (14.8) and (14.9) leads to the following condition

$$\frac{dP_g}{dx} = \rho_W g. \tag{14.10}$$

So, if ρ_W = const, then dP_g/dx = const. This condition is approximate, since according to the data of the A. E. Afanasyev and A. S. Efremov, ρ_W = var and depending on the temperature, takes values in the range of $\rho_W = (0.81 - 1.32) \times 10^3$ kg/m^3, respectively, at $T = 273$–311 K, i.e., each period of the structure formation of a peat body has its maximum defined by interaction type in a biogenic-abiogenic system and degree of peat processing, defined by parameters of an actuating unit of mining machines.

With the decreasing degree of peat processing and the increasing moisture content, the density of the liquid goes down, and with the increasing decomposition and processing degrees and the decreasing moisture content, the density rises compared to free water (Afanasyev and Churaev 1992; Gamayunov 2004). According to the known values of the intensities of the gravitational flow of moisture, Formula (14.8)

can be used to find the values of the moisture transfer factors under the condition

$$P_k << P_g, h_i > H_{\text{cr}}.$$

At the height of the layer of peat raw material equal to the critical, the moisture flow pauses, and in accordance with the studies of Kutais (1955), the system passes into the filtration equilibrium. According to Korchunov et al. (1960), this state is determined by the equality of the full potential P = 0 due to the same values of the capillary $F_c = P_k/\rho_W$ and the gravitational $F_g = gH$ potentials,

$$F_c = \frac{P_k}{\rho_g} - gH \to 0. \tag{14.11}$$

From these conditions

$$P_g = P_k, i_g = 0, h_i = H_{\text{cr}} \tag{14.12}$$

we find the relationship between the effective pore radius r and the height (thickness) of the peat layer of the disturbed structure. From Eq. (14.6) it follows that

$$\frac{2\sigma \cos \Theta}{rh} = \rho_W g. \tag{14.13}$$

Then

$$h = H_{\text{cr}} = \frac{2\sigma \cos \Theta}{r\rho_W g}. \tag{14.14}$$

Equation (14.14) is similar to the Jurin's law on the capillary rise of the liquid. We estimate h using Eq. (14.14) for the average summer drying conditions in the peat industry.

The dependence $H_{\text{cr}} = f(r)$ has a hyperbolic form and corresponds to the expression (14.14). The dependence $H_{\text{cr}} = f(1/r)$ is linear in coordinates. Thus, with increasing thickness of the H_{cr} layer, the effective pore radius decreases; this is confirmed by filtration research (Kashchenko and Kovalev 2011; Korchunov et al. 1960; Nerpin and Khlopotenkov 1970).

As a result of data analysis (Afanasyev 2005) it is revealed that at the pore size $r_k = 20$ microns, capillary pressure tends to become gravitational, i.e. water absorption tends to the minimum value. In our case, this pore size corresponds to the peat bulk height of 0.692 m at the temperature of 273 K. With this, we believe that dewatering D_w and water absorption A_w for the porous body model differ only in the direction of the moisture flow and can be related by the ratio

$$D_w = 1 - A_W, \tag{14.15}$$

where $D_w = l_0/l$, i.e. is the ratio of the length of the water-filled section l_0 of the dead-end capillary to the total length of the capillary l; $A_w = l_i/l$ is the ratio of the length of the water-filled section of the capillary l_i to the total length of the capillary l.

Obviously, when using real media, more reliable results can be obtained, but taking into account all factors such as surface roughness, tortuosity, narrowings, expansions, hydrophilicity, air content and other physical, chemical and mechanical characteristics of the porous structure that change the resistance to moisture transfer, is quite a difficult task. In this regard, Formula (14.14) for the critical height, obtained from the condition of equality of capillary and gravitational pressures, was amended by a factor β, taking into account the features of the structure and indirectly reflects the resistance of moisture transfer,

$$H_{cre} = H_{crt}\beta = \beta\frac{2\sigma\cos\Theta}{r\rho_W g}, \tag{14.16}$$

where H_{cre}, H_{crt} are experimental and theoretical values of the critical thickness of a peat layer, respectively. The expression (14.16) can also be written for the current values of the height of the layer exposed to precipitation,

$$h_e = h_t\beta. \tag{14.17}$$

Thus, the expression for calculating the intensity of the moisture flow in the peat takes the form:

$$i_g = -F_m\beta\frac{P_k - P_g}{H_{cr}} = F_{ef}\frac{P_k - P_g}{H_{cr}}, \tag{14.18}$$

where $F_{ef} = F_m\beta$ is the effective moisture transfer factor; F_m is the factor of moisture conductivity; β is an empirical factor dependent on peat characteristics, clarified by the results of specific experimental studies of a biogenic-abiogenic system with the use of expressions (14.16) and (14.17), $\beta = h_e/h_t = H_e/H_t$, so for real environments, the values of H_{cr} and the intensity of moisture transfer i_g will be different in comparison with the theoretical values obtained for the capillary model,

$$i_g = -F_m\left(\frac{2\sigma\cos\Theta}{rh_i} - \rho_W g\right). \tag{14.19}$$

The theoretical estimation of the moisture conductivity factor is based on the expression

$$F_m = \frac{i_g}{\left(\frac{2\sigma\cos\Theta}{rh_i} - \rho_W g\right)} = k_h i_g, \tag{14.20}$$

where F_h = const at given constant values r, h_i, is determined from the angular dependence factor $F_\mathrm{m} = f(i_g)$,

$$F_h = \frac{dk_\mathrm{B}}{di_g} = \left(\frac{2\sigma \cos \Theta}{rh_i} - \rho_\mathrm{W} g\right)^{-1}. \tag{14.21}$$

The use of this equation is reduced to the theoretical estimate of F_h, and the moisture transfer intensity is calculated through the maximum value of the filtration factor F_f

$$i_g = \rho_\mathrm{W} F_\mathrm{f} \tag{14.22}$$

for the initial state of waterlogged peat of the disturbed structure or determined experimentally for different conditions of dehydration. The value of moisture transfer intensity in Eq. (14.22) will reflect the maximum value of moisture flow. Therefore, from Eq. (14.20) we obtain an expression for the maximum value of the moisture conductivity factor $F_\mathrm{m} = \max$. As a result, Eq. (14.20) taking into account (14.22) takes the form:

$$F_\mathrm{m} = \rho_\mathrm{W} F_\mathrm{f} \frac{dF_\mathrm{m}}{di_g}. \tag{14.23}$$

After the reexpression, we obtain a differential equation of the form

$$\frac{dF_\mathrm{m}}{di_g} - \lambda_p F_\mathrm{m} = 0, \tag{14.24}$$

where $\lambda_p = (\rho_\mathrm{W} F_\mathrm{f})^{-1}$, m^2 s/kg, λ_p characterises the inverse of the moisture transfer intensity.

We divide the variables and integrate (14.24):

$$\int_{k_1}^{k_2} \frac{dF_\mathrm{m}}{F_\mathrm{m}} = \lambda_p \int_{i_1}^{i_2} di_g$$

We finally get

$$F_{\mathrm{m}2} = F_{\mathrm{m}1} \exp\left[-\lambda_p (i_1 - i_2)\right], \tag{14.25}$$

where indices 1 and 2 reflect the minimum (initial) and maximum (current) values of the parameter, respectively.

The dependence (14.25) is similar to the coupling equation of the filtration factor F_f with the porosity factor ε, which has the form (Afanasyev 2005) for small pressure changes in a peat deposit:

$$F_{f2} = F_{f1} \exp[-\alpha_f(\varepsilon_1 - \varepsilon_2)], \tag{14.26}$$

where F_{f1}, ε_1 are the initial and F_{f2}, ε_2 are the current values of the parameters.

Porosity factor ε is linked to the general porosity n by a ratio

$$\varepsilon = \frac{n}{n-1}. \tag{14.27}$$

Factor α_f characterises the decrease in water permeability (in our case, moisture conductivity) of peat during its compaction (reduction of the effective pore radius) and depends on the composition and structure of peat ($\alpha_f = 1$–3). As the degree of peat decomposition increases and the porosity coefficient decreases, the values of α_f increase (Kremcheev and Ivanov 2016): $\alpha_f = 0.123 \exp(0.057 R_t)$, $\alpha_f = (17.1/\varepsilon_2) - 0.39$.

In this case, the last equation differs in the factors $\alpha_f = (21.6/\varepsilon_2) - 1.7$, that is due to the smaller sample of data in comparison with (Kremcheev and Ivanov 2016).

As a result of generalisation of the available theoretical data and the results of experimental studies, the data characterising moisture transfer in different peat types were obtained (Table 14.2).

Therefore, factors α_f and λ_r are similar, as they are associated with the intensity of moisture transport and its changes due to varying effective radii of pores and the critical layer height that creates the pressure on the peat structure. As a rule, with the growth of the critical layer height and, consequently, pressure, the pore size decreases (Bazin et al. 1981).

Using Formula (14.22), the expression (14.27) can be written through the moisture transfer intensity i_g

$$i_2 = i_1 \exp[-a(\varepsilon_1 - \varepsilon_2)], \tag{14.28}$$

where $i_1 = \rho_W F_{f1}$, $i_2 = \rho_W F_{f2}$. This approach allows estimation of the factor of moisture conductivity F_m for peat raw materials of the damaged structure of different types without considering evaporation.

Analysis of the expression (14.20) shows that for the current layer height, equal to the critical one, the filtration factor, the intensity of moisture transfer due to gravity forces and the moisture conductivity coefficient tend to zero. Then the coefficient of moisture conductivity will be associated simultaneously with the pore radius (Table 14.2) (Bazin et al. 1981; Kremcheev et al. 2014). To show the relationship between the moisture conductivity factor and the filtration properties of both native and ruptured biogenic-abiogenic peat system, we solve Eq. (14.25) with respect to $i_2 - i_1$ and equate it to Eq. (14.28). The result is

$$\left(\frac{F_{m2}}{F_{m1}}\right)^{\frac{1}{\lambda p i_1}} = \exp[-\alpha_f(\varepsilon_1 - \varepsilon_2)], \tag{14.29}$$

and Eq. (14.25) thus takes the form

Tables 14.2 Changing the characteristics of moisture transfer of different peat types

Peat type	Decomposition degree R_t, %	Total moisture capacity		The filtration factor $F_f \cdot 10^{10}$, m/s	Moisture transfer intensity $i_g \cdot 10^6$, kg/(m^2·s)	Total porosity n	Porosity factor ε_2	Factor of moisture conductivity $F_m \cdot 10^{10}$, s	Filtration rate α_f	$1/\varepsilon_2$
		W_{tc}, kg(w)/kg(s)	ω_{tc}, %							
Low-moor										
Woody-sedge	36	9.4	90.4	2.51	0.27	0.904	9.4	0.255	0.96	0.106
Sedge-hypnum	22	11.7	92.1	3.36	0.36	0.921	11.7	0.342	0.43	0.085
Sedge	28	10.4	91.2	1.99	0.21	0.912	10.4	0.203	0.61	0.096
Hypnaceous	26	10.4	91.2	1.42	0.15	0.912	10.4	0.145	0.54	0.096
Transitional										
Woody-sedge	39	9.8	90.7	2.07	0.22	0.907	9.8	0.211	1.14	0.102
Scheuchzeria	26	10.7	91.4	1.83	0.2	0.914	10.7	0.187	0.54	0.093
Woody	44	7.6	88.4	4.18	0.45	0.884	7.6	0.426	1.51	0.131
Woody-sphagnous	35	8.9	89.9	2.05	0.22	0.899	8.9	0.209	0.904	0.112
Sedge-sphagnum	28	11.1	91.7	0.65	0.07	0.917	11.1	0.066	0.61	0.09
High-moor										
Scheuchzeria-sphagnous	23	10.3	91.2	0.46	0.05	0.912	10.3	0.047	0.456	0.097
Cottongrass-sphagnous	31	11.2	91.8	0.44	0.047	0.918	11.2	0.045	0.72	0.089
Pine-cottongrass	39	11.2	91.8	0.023	0.0025	0.918	11.2	0.002	1.14	0.089
Magellanicum	16	13.5	93.1	0.72	0.077	0.931	13.5	0.073	0.31	0.074

Notes 1. The fluid density is taken after (Afanasyev et al. 1985) for $T = 293$ K, $\rho_W = 1.075 \times 10^3$ kg/m^3

$$i_2 = i_1 \exp\left[\frac{1}{\lambda_p i_1}\left(\ln\frac{F_{m1}}{F_{m2}}\right)\right]. \tag{14.30}$$

Therefore, it is possible to use filtration characteristics for the estimation of hydraulic conductivity of peat through the change of the porosity factor (Eq. 14.29) and to express the intensity of moisture transport through F_{mi} and $\lambda_r = 1/(\rho_W F_f)$ (Formula 14.30) based on the dependence α_f on the degree of peat decomposition, i.e. one of the integrating indicators that determine its physical and mechanical properties. Equations (14.29) and (14.30) can be simplified by dividing the exponential function into a series and using its first two parts. Given $\lambda_r = (\rho_W F_f)^{-1}$ Formulae (14.29) and (14.30) take the form:

$$\left(\frac{F_{m2}}{F_{m1}}\right)^{\frac{1}{\lambda_p i_1}} \approx [1 - \alpha_f(\varepsilon_1 - \varepsilon_2)], \tag{14.31}$$

$$i_2 \approx i_1\left[1 + \frac{1}{\lambda_p i_1}\left(\ln\frac{F_{m1}}{F_{m2}}\right)\right]. \tag{14.32}$$

Thus, it is possible to estimate the moisture conductivity by changing the filtration factors at the initial ($R_k \to 0$) and final ($i_g \to 0$) stages of dehydration under the condition of limited evaporation (i.e. the intensity of evaporation from the wet surface of peat or water $i_{and} \to 0$).

Taking into account Formulas (14.19) and (14.22) we obtain

$$\rho_W F_{f2} = F_{m2}\rho_W g. \tag{14.33}$$

Hence, the maximum moisture conductivity factor can be recorded as:

$$F_{m2} = \frac{F_{f2}}{g}. \tag{14.34}$$

Taking into account Formula (14.31), it can be written that

$$F_{m2} \approx F_{m1}[1 - \alpha_f(\varepsilon_1 - \varepsilon_2)]^{\lambda_p i_1}, \tag{14.35}$$

must have a minimum (Fig. 14.4) with the growth α_f (decomposition degree) and the decrease of the initial porosity factor. The change in F_{m2} according to the formula (14.34) is shown in Table 14.2 depending on the type and decomposition degree of peat, the current porosity factor, the total moisture capacity and the intensity of moisture transfer.

Analysis of Table 14.2 shows that the maximum value of the moisture conductivity factor for the high-moor peat is the lowest ($F_{m2} = (0.002 - 0.073) \times 10^{-10}$ s) compared with the transitional ($F_{m2} = (0.066 - 0.426) \times 10^{-10}$ s) and low-moor ($F_{m2} = (0.145 - 0.342) \times 10^{-10}$ s) decreases with the increasing degree of peat decomposition (Fig. 14.4). Within each group of peat (except the high-moor type)

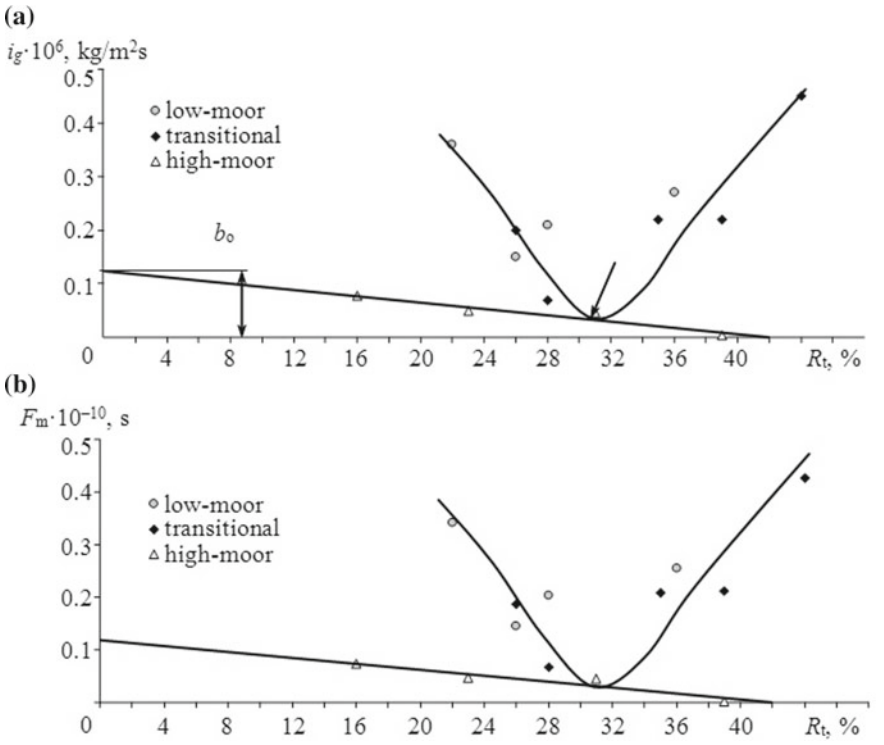


Fig. 14.4 Dependence of the maximum intensity of moisture transfer (**a**) and the moisture conductivity factor (**b**) on the degree of peat decomposition without taking into account evaporation for high-moor, low-moor and transitional peat types at $T = 293$ K

(Table 14.2, Fig. 14.4) F_{m2} increases with the degree of peat decomposition $R_t >$ (30–32)%. At lower values of decomposition degree, the value of the moisture conductivity factor decreases with the increase in the decomposition degree. In particular, for the pine-cottongrass peat, the value $\alpha_f = 1.14$ ($R_t = 39\%$), and for the magellanicum $\alpha_f = 0.31$ ($R_t = 16\%$) for the corresponding porosity factors ε_2, equal to 11.2 and 13.5 respectively, i.e. the data fit in those limits that are given Kremcheev and Ivanov (2016) for different permeability categories (high $\alpha_f < 0.35$, medium $\alpha_f = 0.35$–0.75, low $\alpha_f > 0.75$). Therefore, moisture conductivity, according to Eq. (14.29), will vary as well as filtration characteristics for one type of peat ($\alpha_f = f(R_t)$), i.e. will be minimal.

14.4 Discussion

The main factors affecting the moisture transfer are the decomposition degree, which varies by 2.43 times, the porosity factor, which varies by 1.2 times and the moisture conductivity factor, which changes by 36.5 times (Table 14.2). Thus, the high-moor peat is an exception due to the high structure heterogeneity due to the possible presence of a boundary horizon of increased decomposition, alternating with the usual structure with a reduced decomposition degree. Even with the same decomposition degree of peats of different types, values of F_{m2} differ by magnitudes of order, that is also true for filtration factors F_f, and intensity of moisture transfer at low changing ε_2, n, $_{tc}$. This circumstance is due to the decrease in the pressure gradient dP/dx (Bazin et al. 1981) at decreasing capillary pressure due to the hydrophobisation of the solid phase, which has a high bitumen content (Afanasyev et al. 1988; Bazin et al. 1981).

The water of the high-moor peat contains various dissolved organic substances: monosaccharides, pentoses, uric and humic acids, bitumens, high and low-molecular organic and mineral substances. The latter can be in colloidal, molecular and ionic states (Lishtvan and Korol 1975). These structural features of solid and liquid phases lead to peat compaction, which is an easily deformable system. Even at a pressure of $P_g \approx 50$ kPa (Kremcheev and Ivanov 2016), peat thickness decreases, which leads to an increase in the resistance to moisture flow (expression 14.18).

Consequently, the size of capillaries (pores) decreases with the increasing decomposition degree. This circumstance contributes to the rise of capillary-osmotic and surface forces; and leads to variations in the values of F_{m2} (Fig. 14.4). By analogy with the filtration factor (Kremcheev and Ivanov 2016), they vary between 10 and 60%. For the transitional and low-moor peats the values of α_f are within the same limits as for the high-moor type with increased moisture conductivity factors (10–100 times) and slightly different porosity factors $\varepsilon_2 = 7.6$–11.1 for the transitional type $\varepsilon_2 = 9.4$–11.2 for the low-moor type as compared with the high-moor one $\varepsilon_2 = 10.3$–13.5. Hence, the moisture conductivity is largely responsible for the composition of the transferred moisture with little change in the characteristics of the solid phase. This fact is confirmed by the physicochemical properties of the dispersed medium of peat of the transitional and low-moor types (Kremcheev and Ivanov 2016; Lishtvan and Korol 1975).

Thus, water mineralisation level in high-moor peat deposits is 40–70 mg/dm^3, and for transitional and low-moor it increases 1.8–2.6 times and 4.2–10 times, respectively. Calcium and its water-soluble compounds are predominant in the mineral part. Calcium is amongst the key structure-forming peat components, providing changes in pore size. Calcium cations determine the biochemical process. They neutralise the acidity. Moreover, ion exchange processes occur mainly in an acidic medium under pH < 7. The pH values of marsh waters increase from the high-moor to transitional and to low-moor peat deposits, i.e. with a decrease in their acidity, which corresponds to a higher calcium content (up to 15–85 mg/dm^3) in the low-moor ones as compared to the high-moor marsh waters (up to 15 mg/dm^3) (Kremcheev and Ivanov 2016).

The features typical for the intensity of moisture transfer, reflected by the dependences $i_g = f(R_t)$ are noted in Fig. 14.4. For a high-moor deposit, it is linear

$$i_g = b_0 - \alpha_W R_t, \tag{14.36}$$

where $b_0 = 0.13 \times 10^{-6}$ kg/(m^2 s); $\alpha_W = di_g/dR_t$ is the angle dependency factor (14.36), $\alpha_W = di_g/dR_t = 0.33 \times 10^{-8}$ kg/(m^2 s %).

For the transitional and low-moor peat types, the dependence (14.36) is minimal at the peat decomposition degree of 30–32%. The minimum has the role of a generalised point at $R_t = 31\%$. We call it the average effective binding degree of decomposition R_d; on its basis it is possible to reach any peat type: $R_d = 31\%$, $i_g = 0.037 \times 10^{-6} \pm 0.008 \times 10^{-6}$ kg/(m^2 s). At the same time, for the high-moor type at $R_t \to 0$, $i_g = 0.13 \times 10^{-6\,\mathrm{kg}}$/(m^2 s) (extrapolated value), and for the transitional and low-moor type it is much larger (Fig. 14.4). With the increasing degree of decomposition for the high-moor type, the intensity of moisture transfer tends to zero due to the rheological properties of water, i.e. the increasing limiting shear stress and the density of the bound water and the decreasing pore sizes (Afanasyev and Efremov 2011). For the transitional and low-moor types, the intensity of moisture transport tends to a constant with an implicit manifestation of the border due to the increasing moisture transport resistance factor β.

14.5 Conclusion

The data obtained during the complex of theoretical and experimental studies allow drawing the following conclusions. When the filtration equilibrium is reached, when $i_g \to 0, P_k \to P_g, h_i \to H_{cr}$, the volume of remaining moisture in a pile and its critical height will be correlated with the factors of hydraulic conductivity, porosity, pore size and the height of the peat bulk, i.e. the remaining moisture mass will be maximal in the high-moor peat M_h, medium in the transitional one M_m and minimal in the low-moor peat M_l. The lowest values of the moisture conductivity factor correspond to the high-moor peat deposits; this explains the retention of higher water volumes at the filtration equilibrium with this type of peat compared to others. This feature of the change in moisture conductivity is confirmed by experimental data on the assessment of precipitation, the critical thickness of the bulk depending on the initial thickness of the peat layer of the disturbed structure and the change in the critical height in the function of the pore radius, which corresponds to the theoretical data.

This circumstance is one of the determining when choosing a set of technological methods for dewatering peat in continuous production with stable quality indicators. The results obtained in the study of interaction in the biogenic-abiogenic peat systems of different genesis, allow developing algorithms for directional changes in the quality characteristics of field peat products depending on the requirements of consumers.

The scientific results of the research and methodological approaches proposed in the work are used in the practice of the peat mining enterprises, in the educational process of the Saint Petersburg Mining University, the Tver State Technical University and the Belarusian National Technical University.

Acknowledgements The laboratory complex of the Common Use Centre of the Saint Petersburg Mining University was the experimental research platform. Field studies were conducted on the territory of TBZ USYAZH (Smolevichy district, Belarus), Terraflor JSC (Russia), as well as on a number of fields with an interrupted production cycle in the Northwestern Federal District of Russia.

References

Afanasyev AE (2005) Physical processes of peat production. TSTU, Tver (in Russian)

Afanasyev AE, Boltushkin AN, Malkov LM (1988) Practical course on field drying of peat. KSU, Kalinin (in Russian)

Afanasyev AE, Churaev NV (1992) Optimisation of processes of drying and structure formation in the peat production technology. Nedra, Moscow (in Russian)

Afanasyev AE, Efremov AS (2011) The influence of structure formation on the density of the liquid colloidal capillary-porous bodies. TOHT 460(1):119–125 (in Russian)

Afanasyev AE, Malkov LM, Smirnov VI (1987) Technology and complex mechanisation of peat deposits development. Nedra, Moscow (in Russian)

Afanasyev AE, Tikhomirov MK, Kazakov SA (1985) Method of production of milled peat. Patent 1171593 of the USSR, bul. 29

Alekseenko VA, Pashkevich MA, Alekseenko AV (2017) Metallisation and environmental management of mining site soils. J Geochem Explor 174:121–127

Alekseenko VA, Bech J., Alekseenko, AV, Shvydkaya NV, Roca N (2018) Environmental impact of disposal of coal mining wastes on soils and plants in Rostov Oblast, Russia. J Geochem Explor 184(B):261–270

Amaryan LS, Bazin ET (1965) Investigation of water permeability of deformed peat. Herald of the MViSSO of the USSR, Construction and Architecture Series 1:65–71 (in Russian)

Antonov VY, Malkov LM, Gamayunov NI (1981) Technology of field drying of peat. Nedra, Moscow (in Russian)

Bazin ET, Kosov VI, Minyaev SV (1981) Influence of technological and physical and chemical effects on the permeability and structure of peat. Peat Ind 7:17–20 (in Russian)

Churaev NV (1960) Methods of investigation of water properties and structure of peat using radioactive indicators In: New physical methods of peat research: Collected papers. Gosenergoizdat, Moscow-Leningrad (in Russian)

Gamayunov NI (2004) Transport processes of energy and matter. TSTU, Tver (in Russian)

Gamayunov NI, Mironov VA, Gamayunov SN (1998) Heat and mass transfer in organic materials: processes of dehydration. TSTU, Tver (in Russian)

Jordán MM, Bech J, García-Sánchez E, García-Orenes F (2016) Bulk density and aggregate stability assays in percolation columns. J Min Inst 222:877–881

Kashchenko NM (2010) Fractal model of filtration in conditions of drainage operation. Proc Kant RSU, Phys Math Sci Series 4:158–162 (in Russian)

Kashchenko NM, Kovalev VP (2011) Calculation of soil moisture transfer in the calculation of drainage parameters of polder systems. In: Innovative technologies in reclamation (Kostyakov readings), VNIIA, Moscow (in Russian)

Korchunov SS, Mogilevsky II, Abakumov ON (1960) Study of the water regime of drained peat deposits. In: Proceedings of VNIITP, Gosenergoizdat, Moscow-Leningrad (in Russian)
Kosov VI (2005) Peat and sapropel—powerful geoecological and energy potential of Russia. Peat and business. Pilot issue:14–18 (in Russian)
Kremcheev EA (2011) Improving the performance of local wastewater and stormwater post-treatment systems using peat filter materials: research report. Saint Petersburg State Mining Institute, Saint Petersburg (in Russian)
Kremcheev EA (2014) Justification of technological methods of reducing the moisture content of peat raw materials in excavator mining. Min Inf Anal Bull 9:31–35 (in Russian)
Kremcheev EA, Ivanov AV (2016) Surface flow treatment with peat-based filters. Water Ecol 2:48–57 (in Russian)
Kremcheev EA, Kremcheeva DA (2016) Validation of processing methods for peat raw dehumidification with excavating digging. Res J Pharm Biol Chem Sci 7(3):1284–1289
Kremcheev EA, Nagornov DO (2017) Features of structure of process operations set during peat excavation with staged dehydration. Ecol Environ Conserv 23(2):956–965
Kremcheev EA (2013) Estimation of hydraulic conductivity of disturbed peat systems when implementing energy efficient weather-independent technologies of peat production in the NWFD: research report. National Mineral Resources University (University of Mines), Saint Petersburg (in Russian)
Kremcheev EA, Afanasyev AE (2012) Hydraulic conductivity of peat deposits of the damaged structures without taking into account evaporation. In: Processes and means of extraction and processing of minerals, Proceedings of the international scientific and technical conference. The Belarusian National Technical University, Minsk (in Russian)
Kremcheev EA, Mikhailov AV, Afanasyev AE (2014) To the issue of assessing the intensity of moisture removal at field enrichment of peat. Modern Probl Sci Educ (Electr J). http://www.science-education.ru/115-12228
Kremcheev EA, Mikhailov AV, Nagornov DO, Bolshunov AV (2012) Modular technological complex of peat extraction and production of agglomerated fuel. Patent 2470984 of the Russian Federation, publ. 27.12.2012, bul. 36
Kutais LI (1955) Course of hydraulic engineering in peat production: part 1. Gosenergoizdat, Moscow-Leningrad (in Russian)
Lazarev AV, Korchunov SS (1982) The reference book on peat. Nedra, Moscow (in Russian)
Lishtvan II, Terentiev AA, Bazik ET, Golovach AA (1983) Physico-chemical basis of the peat production technology. Sci Technol, Minsk (in Russian)
Lishtvan II, Korol NT (1975) The main properties of peat and methods for their determination Science and Technology, Minsk (in Russian)
Mikhailov AV (2016) Coal-peat compositions for co-combustion in local boilers. J Min Inst 220:538–544 (in Russian)
Mikhailov AV, Ivanov SL, Bolshunov AV, Kremcheev EA (2013) Peat resources of the Northwestern Federal District of Russia and prospects of their development. J Min Inst 200:226–230 (in Russian)
Mikhailov AV, Selennov VG (2009) The peat industry of Russia. Min Mach Electromech 9:22–28 (in Russian)
Naumovich VM (1984) Artificial drying of peat. Nedra, Moscow (in Russian)
Nerpin SN, Khlopotenkov EM (1970) The generalisation of Darcy's law for cases of non-linear filtration in unsaturated and saturated soils. Dokl VASHNIL 11:3–17 (in Russian)
Selennov VG, Mikhailov AV (2009) Peat in small power engineering. Acad Energ 1(27):48–56 (in Russian)
Semensky EP (1939) Quality of lump peat depending on the type of structure of peat deposit and processing of raw peat. Institute of Peat, Moscow (in Russian)
Shakhmatov KL (2011) Justification of year-round extraction of peat raw materials and production technology of composite thermal insulation materials. Dissertation, Tver State Technical University (in Russian)

Sokolov BN, Kolasin VN, Yampolsky AL (1988) Peat in the national economy. Nedra, Moscow (in Russian)
Sudnitsyn II (1964) Patterns of soil moisture movement. Nauka, Moscow (in Russian)
Vakhromeev II, Bebenina TP, Chass SI (1984) Hydraulic engineering in oil and mining industry Nedra, Moscow (in Russian)
Vasilyev AN, Smirnov VI (2004) Organisation of technological process with step regulation of milling depth. Min Inf Anal Bull 1:239–242 (in Russian)
Vitkov GA, Kholpanov LP, Sherstnev SN (1994) Hydraulic resistance and heat and mass transfer Nauka, Moscow (in Russian)
Volarovich MP, Churaev NV (1960) Study of water movement processes in the peat deposit by the radioactive indicators method. In: New physical methods of peat research: Collected papers. Gosenergoizdat, Moscow-Leningrad (in Russian)

Part III
Geochemistry of Biogenic-Abiogenic Systems

Chapter 15
Mineral Systems and Thermodynamic Stability of Arsenic Minerals in the Environment



Marina V. Charykova and Vladimir G. Krivovichev

Abstract Arsenic is widely distributed in the environment. The paper presents systematized data published about the thermodynamics of some relatively common arsenic oxysalts, which are formed in the weathering zone of the arsenide and sulfide ores, and determines approaches to quantitative physicochemical modeling of their formation conditions. The interpretations are summarized on the Eh–pH diagrams, synthesized from equilibrium calculations, and reported geologic occurrences. The most recent thermodynamic data available were used for the construction of diagrams from reactions which are balanced equations of Eh–pH relationships among species which are thermodynamically stable within the ranges of oxidation potential and pH considered for each reaction. The Eh–pH diagrams of systems, containing As and Fe, Cu, Pb, Co, Ni, Ca, were calculated and constructed using the Geochemist's Workbench (GMB 9.0) software package. Eh–pH stability relationships have been determined for some widespread arsenic oxysalts (scorodite, mimetite, erythrite, olivenite, annabergite, beudantite, conichalcite, adamite, duftite) and in order to interpret conditions of formation of these minerals and to compare their geologic stabilities of ore deposits. The understanding of mechanisms of arsenic behavior in the near-surface conditions is one of actual problems of modern mineralogy and geochemistry and it is very important for the solving of some environmental problems.

Keyword Arsenates · Environmental mineralogy and geochemistry · Physicochemical modeling · Eh–pH diagrams

15.1 Introduction

Arsenic is widely distributed in the environment. Although arsenic is useful for industrial, agricultural, medical and other purposes, it exerts a toxic effect on a variety of organisms, including humans (Plant et al. 2014; Bowell et al. 2014; Mitchell 2014).

M. V. Charykova (✉) · V. G. Krivovichev
Saint Petersburg University, Saint Petersburg, Russia
e-mail: m.charykova@spbu.ru

© Springer Nature Switzerland AG 2020

O. V. Frank-Kamenetskaya et al. (eds.), *Processes and Phenomena on the Boundary Between Biogenic and Abiogenic Nature*, Lecture Notes in Earth System Sciences,
https://doi.org/10.1007/978-3-030-21614-6_15

Drainage from mineralized and mined areas may have high dissolved arsenic concentrations, and of major interest as the natural sources of As in waters, soils and plants are likely to be the low-temperature oxidizing environments in the vicinity of ore bodies which contain arsenides, and As-bearing sulfides (Bowell and Craw 2014). Under oxidizing environmental conditions, arsenic occurs in the form of arsenate (AsO_4^{3-}) or arsenite (AsO_3^{3-}) oxyanions, i.e. As (+5) or As (+3), respectively. The oxidation of arsenides can be catalyzed by bacteria such as *Acidithiobacillus ferrooxidans*, which also leads to the formation of various iron oxides and hydroxysulfates (Morin and Calas 2006). Newly discovered microorganisms that use arsenite and arsenate as a basis for their metabolism are thought to play an important role in regulating of arsenic redox reactions. Recent studies have pointed out the complex interplay among adsorption and precipitation of arsenic processes, changes in oxidation states and mineral stabilities mediated by microbial activities in surface and subsurface environments (O'Day 2006; Amend et al. 2014).

Mining can release high concentrations of arsenic by means of the oxidation of sulfide minerals, either through the roasting of arsenical ores or through acid mine drainage (Williams 2001). The latter results from the atmospheric exposure and weathering of sulfide-bearing rocks, such as the waste rock and mine tailings generated during mining and milling operations. Oxidation of sulfide minerals, often mediated by microbial activity, causes waters to become acidified and enriched in sulfate anions and heavy metals. During this process, an overall two-stage reaction governs the dissolution and further oxidation of As (O'Day 2006):

$$\mathrm{FeAsS\ (s) + 11/4\ O_2\ (aq) + 3/2\ H_2O\ \ (aq) = Fe^{2+}\ (aq) + SO_4^{2-}\ (aq) + H_3AsO_3\ (aq)} \tag{15.1}$$

$$\mathrm{H_3AsO_3 + 1/2O_2(aq) = H_2AsO_4^- + H^+} \tag{15.2}$$

The oxidation of sulfide (reaction 15.1) can be catalyzed directly by bacterial activity and indirectly by the Fe^{3+} resulting from the oxidation of Fe^{2+} by bacteria such as *Acidithiobacillus ferrooxidans*. Bacterial oxidation of dissolved Fe^{2+} also leads to the formation of various iron oxides (Cornell and Schwertmann 2003) and hydroxysulfates (Bigham et al. 1996; Alpers et al. 2000). Arsenite oxidation (reaction 15.2) is slow, especially under acidic conditions, but may be catalyzed by the activity of bacteria such as *Thiomonas sp*. (Bruneel et al. 2003). Reaction (15.2) is important because As (+5) is less toxic, less soluble, and adsorbed more efficiently than As (+3) under acidic conditions.

The highest As contents in the groundwater are characteristic of the oxidation zone of As-bearing ores and in the mining districts, where arsenic occurs as selfdependent mineral phases (arsenopyrite, tennantite) or chemically substitutes for Sb or Bi in the crystal structures of other minerals. The primary minerals of As, among which arsenopyrite is the most abundant, are not stable in an oxidation zone and are decomposed to form more soluble (in comparison with arsenopyrite) compounds with an increase in the As concentration in the groundwater.

Eh–pH stability relationships will be discussed for some widespread arsenic oxysalts (scorodite, mimetite, erythrite, olivenite, annabergite, beudantite, adamite, etc.) and in order to interpret conditions of formation of these minerals and to compare their geologic stabilities of ore deposits. The understanding of mechanisms of arsenic behavior in the near-surface conditions is one of actual problems of modern mineralogy and geochemistry and it is very important for the solving of some environmental problems.

15.2 Materials and Methods

15.2.1 Mineral Systems of Arsenic Minerals

Arsenic can exist in four different oxidation states (Fig. 15.1): arsenides (As(−3)), elemental arsenic (As(0)), arsenites (As(+3)) and arsenates (As(+5)). In order to have an appropriate database of arsenic minerals at hand, we have compiled a list of all arsenic mineral species (638) known up to September 2018 using continuously updated lists published by Pasero (2018) at the website of Commission on New Minerals, Nomenclature and Classification, International Mineralogical Association (CNMNC IMA), CNMNC IMA Newsletters (e.g. Hålenius et al. 2018), and website (http://rruff.info). The crystal chemical formulae of these minerals have been rewrit-

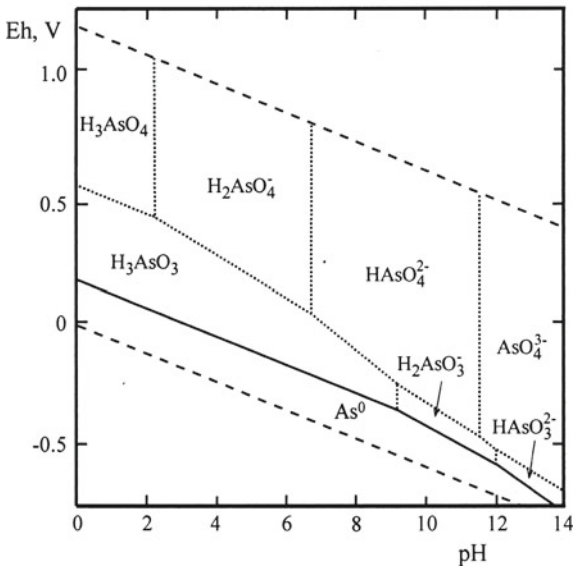


Fig. 15.1 Eh–pH diagrams of the system OHAs (As–H_2O) at 25 °C and the activities of As $a_{\Sigma As} = 10^{-3}$

ten in a canonical way in order to determine the minimal set of species-defining constituents (i.e., chemical elements that are dominant in particular sites in a crystal structure).

It should be noted that the assignment of an element as species-defining (cf. Hawthorne 2002; Hatert and Burke 2008; Krivovichev and Charykova 2013a, b; Christy 2015) is determined by the rules of new mineral species definition (Mandarino et al. 1984; Nickel and Mandarino 1987; Nickel and Grice 1998).

Our approach allows to organize arsenic mineral species using their chemical composition and to arrange the existing data into coherent frameworks emphasizing changes in mineral diversity and composition through space and time. The concept of mineral systems can be used to assess mineral diversity of geological objects in more detail than the simple number of different mineral species present in a particular association (Krivovichev and Charykova 2013a, b; Krivovichev et al. 2018).

Arsenic minerals can be attributed to a particular system (Krivovichev et al. 2018), the components of which are the chemical elements required to construct the crystal structure of the mineral (for examples see below). The main mineral coding rule is to determine the sequence of chemical element symbols, which are included in their formulas. We use the so-called "thermochemical" sequence of chemical elements (Fig. 15.2). For example, annabergite, $Ni_3(AsO_4)_2 \cdot 8H_2O$, responds to the system OHAsNi, while tyrolite, $Ca_2Cu_9(AsO_4)_4(CO_3)(OH)_8 \cdot 11H_2O$, responds to the system OHAsCCuCa.

According to their chemical composition, all arsenic minerals clearly divided into four groups: native arsenic, arsenides, oxides, and oxysalts: anhydrous (I) and hydrous (II) arsenites and arsenates. Within each of these groups minerals can be classified according to the minimum number of components required for their formation.

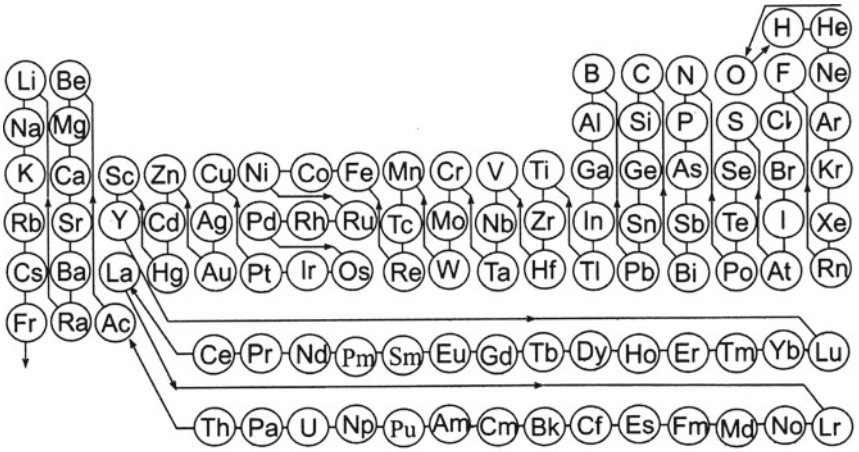


Fig. 15.2 Thermochemical sequence of chemical elements and corresponding single-component systems

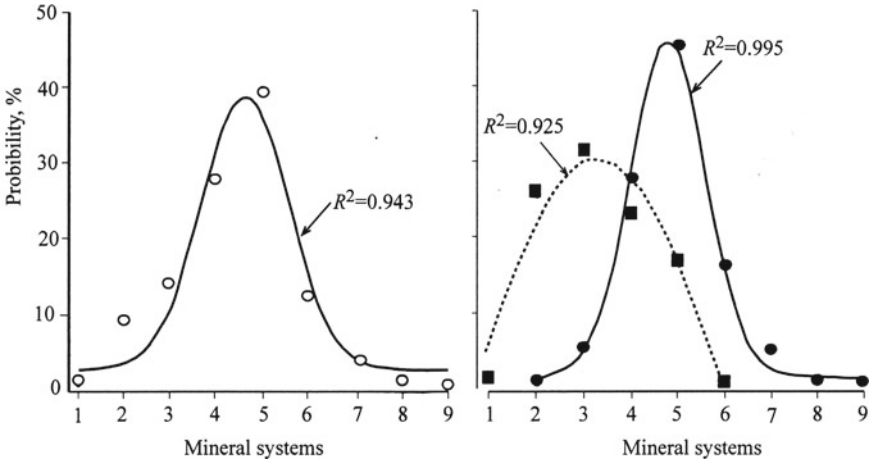


Fig. 15.3 Distribution of arsenic mineral species on mineral systems based on number of species-defining elements: **a** all arsenic minerals; **b** arsenic minerals without oxygen (dotted line) and with oxygen (solid line)

Figure 15.3a illustrates the number of known arsenic mineral species in Earth's upper continental crust versus the number of essential mineral-forming elements in arsenic minerals (mineral systems). The greatest number of minerals corresponds to four- and five-component systems (144 and 237 mineral species, respectively), i.e., these minerals are formed by four or five elements. Figure 15.3b shows the distribution of arsenic mineral species without oxygen (endogenous minerals) and with oxygen (exogenous minerals).

Our approach allows us to highlight the formula of "chemically pure" minerals, i.e., they are formed only by species-defining elements. From our point of view, it enables us to organize mineral species correctly by using their chemical composition. An important advantage of this classification of mineral systems is the ability to set a strict procedure for mineral species, as each of them has a unique position. It makes it easier to use computer technology to search for thermodynamic data.

The examples of proposed classification of arsenic minerals are given in Table 15.1.

In conclusion, it should be emphasized that the proposed classification of mineral systems is convenient in terms of physico-chemical modeling of mineral formation.

15.2.2 Thermodynamics

The physicochemical modeling is based on the thermodynamic constants of minerals. Reliable solubility product (K_{sp}) values of the phases crystallized in the system are necessary for calculation of mineral equilibria. They can be derived from exper-

Table 15.1 Examples of mineral systems of arsenic minerals

S. No.	System	Mineral	Chemical formula
Native elements			
1	As	Arsenic	As
		Arsenolamprite	As
		Pararsenolamprite	As
Arsenides			
2	AsCo	Clinosafflorite	$CoAs_2$
		Langisite	CoAs
		Modderite	CoAs
		Safflorite	$CoAs_2$
		Skutterudite	$CoAs_3$
	AsFe	Ferroskutterudite	$FeAs_3$
		Löllingite	$FeAs_2$
		Westerveldite	FeAs
3	AsFeNi	Oregonite	$FeNi_2As_2$
Arsenido-sulfides, arsenido-selenides, and arsenido-tellurides			
3	SAsFe	Arsenopyrite	Fe(AsS)
	SAsCo	Alloclasite	Co(AsS)
		Cobaltite	Co(AsS)
	SeAsCu	Mgriite	Cu_3AsSe_3
		Chaméanite	Cu_4AsSe_4
	TeAsPd	Törnroosite	$Pd_{11}As_2Te_2$
4	SAsFeCo	Glaucodot	$CoFe(AsS)_2$
	SAsAgCd	Quadratite	$AgCdAsS_3$
	SAsAgHg	Laffittite	$AgHgAsS_3$
		Fettelite	$Ag_{16}HgAs_4S_{15}$
5	SAsFeCuAg	Argentotennantite	$Ag_6Cu_4Fe_2(AsS_3)_4S$
	SAsPbCuAg	Lengenbachite	$Ag_4Cu_2Pb_{18}As_{12}S_{39}$
	SAsPbTlAg	Hatchite	$AgPbTlAs_2S_5$
		Rathite	$Ag_2Pb_{12-x}Tl_{x/2}As_{18+x/2}S_{40}$
6	SAsSbPbMnAg	Menchettiite	$Pb_5Mn_3Ag_2Sb_6As_4S_{24}$
Oxides			
2	OAs	Arsenolite	As_2O_3
		Claudetite	As_2O_3
Arsenites and arsenates without H_2O			
3	OAsBi	Rooseveltite	$Bi(AsO_4)$
		Tetrarooseveltite	$Bi(AsO_4)$
	OAsZn	Reinerite	$Zn_3(AsO_3)_2$
4	OHAsU	Chadwickite	$UO_2H(AsO_3)$
	OAsCuZn	Stranskiite	$CuZn_2(AsO_4)_2$
	OAsCuNa	Bradaczekite	$NaCu_4(AsO_4)_3$

(continued)

Table 15.1 (continued)

S. No.	System	Mineral	Chemical formula
5	OFAsAlNa	Durangite	$NaAl(AsO_4)F$
	OClAsPbCa	Hedyphane	$Ca_2Pb_3(AsO_4)_3Cl$
	OTeAsPbZn	Dugganite	$Pb_3Zn_3(TeO_6)(AsO_4)_2$
	OAsMgCaNa	Berzeliite	$NaCa_2Mg_2(AsO_4)_3$
6	OFClAsCuNa	Axelite	$Na_{14}Cu_7(AsO_4)_8F_2Cl_2$
	OAsFeCuCaNa	Hatertite	$Na_2Ca(FeCu)_{\Sigma 2}(AsO_4)_3$
7	OAsAlFeMgCaNa	Anatolyite	$Na_6Ca(Mg_2Fe)_{\Sigma 3}Al(AsO_4)_6$
9	OFSAsSiBFeCeCa	Vicanite-(Ce)	$(Ca_9Ce_6)_{\Sigma 15}(NaAs)_{\Sigma 2}FeB_4(SiO_4)_6(AsO_4)O_9F_{10}$
Arsenites and arsenates containing H_2O			
4	OHAsNi	Annabergite	$Ni_3(AsO_4)_2 \cdot 8H_2O$
		Honzaite	$Ni_2(AsO_3OH)_2 \cdot 5H_2O$
	OHAsCo	Burgessite	$Co_2(AsO_3OH)_2 \cdot 5H_2O$
		Cobaltkoritnigite	$Co(AsO_3OH) \cdot H_2O$
		Erythrite	$Co_3(AsO_4)_2 \cdot 8H_2O$
5	OHSAsCu	Parnauite	$Cu_9(AsO_4)_2(SO_4)(OH)_{10} \cdot 7H_2O$
		Leogangite	$Cu_{10}(AsO_4)_4(SO_4)(OH)_6 \cdot 8H_2O$
	OHAsPbU	Hallimondite	$Pb_2(UO_2)(AsO_4)_2 \cdot nH_2O$
		Hügelite	$Pb_2(UO_2)_3(AsO_4)_2O_2 \cdot 5H_2O$
	OHAsCuU	Zeunerite	$Cu(UO_2)_2(AsO_4)_2 \cdot 12H_2O$
6	OHAsFeZnCa	Fahleite	$CaZn_5Fe_2(AsO_4)_6 \cdot 14H_2O$
		Ferrilotharmeyerite	$CaZnFe(AsO_4)_2(OH) \cdot H_2O$
		Ogdensburgite	$Ca_2Fe_4Zn(AsO_4)_4(OH)_6 \cdot 6H_2O$
7	OHClAsCuCaNa	Lavendulan	$NaCaCu_5(AsO_4)_4Cl \cdot 5H_2O$
	OHAsFeMnCaNa	Grischunite	$NaCa_2Mn_5Fe(AsO_4)_6 \cdot 2H_2O$

imental data (for example, from data on solubility) or calculated applying the data on the Gibbs free energy of compound formation.

Thermodynamic data for most of arsenic minerals are not determined. It is also necessary to keep in mind that, even when the corresponding parameters are published, they often raise questions and should be specified.

Earlier (Charykova et al. 2009, 2011) we collected the available published values of standard thermodynamic functions of the formation of some arsenates and calculated the Eh–pH diagrams of the Me–As–H_2O systems (Me = Co, Ni, Fe, Cu, Zn, Pb). In this paper, the objective is to characterize the physico-chemical conditions of formation of the most widespread minerals-arsenates, which required in some cases the calculation of diagrams of more complex systems, containing additional cations and anions. The Eh–pH diagrams have been calculated using the Geochemist's Workbench (GMB 9.0) software package (Bethke and Yeakel 2011) for the average activities of components in waters formed in the oxidation zone ($a_{\Sigma As} = 10^{-3}$, $a_{\Sigma Fe} = 10^{-2}$, $a_{\Sigma Cu} = 10^{-2}$, $a_{\Sigma Co} = 10^{-2}$, $a_{\Sigma Ni} = 10^{-2}$, $a_{\Sigma Pb} = 10^{-5}$–10^{-4}, $a_{\Sigma Zn} = 10^{-2}$, $a_{\Sigma Ca} = 10^{-2}$) (Charykova et al. 2011). The calculation of the diagrams

was predated by the introduction of additional components into the database and the specification of some solubility products. The activity coefficients are calculated from the Debye–Hückel equation.

15.3 Results and Discussion

Our study is based on the statistical analysis of data provided by open access mineralogical databases. For estimation mineral distribution relationships employs both rruff.info/ima and mindat.org for identification of approved mineral species and tabulation worldwide mineral species and locality information. The data obtained show that of 449 approved arsenic mineral species with oxygen, 43% are known from only one or two localities, and 72% are known from 10 or fewer localities. To assess the most common conditions of arsenate minerals formation we selected minerals that were found in more than 200 localities. Here are these arsenate minerals (the number of localities is given in brackets): scorodite, $FeAsO_4 \cdot 2H_2O$ (1095), mimetite, $Pb_5(AsO_4)_3Cl$ (1079), erythrite, $Co_3(AsO_4) \cdot 8H_2O$ (801), olivenite, $Cu_2(AsO_4)(OH)$ (483), annabergite, $Ni_3(AsO_4) \cdot 8H_2O$ (437), pharmacosiderite, $KFe_4(AsO_4)_3(OH)_4 \cdot 6 - 7H_2O$ (418), beudantite, $PbFe_3(AsO_4)(SO_4)(OH)_6$ (400), conichalcite, $CaCu(AsO_4)(OH)$ (351), adamite, $Zn_2(AsO_4)(OH)$ (251), tyrolite, $Ca_2Cu_9(AsO_4)_4(CO_3)(OH)_8 \cdot 11H_2O$ (238), duftite, $PbCu(AsO_4)(OH)$ (212). The formation of two minerals (pharmacosiderite and tyrolite) cannot be estimated due to the lack of thermodynamic data. The equilibrium constants of the dissolution reactions of these minerals were taken mainly from the summary (Nordstrom et al. 2014), and for erythrite and annabergite these constants have been determined experimentally (our data, not publ.). The calculated Eh–pH diagrams of the systems containing the nine most common arsenate minerals formed in the oxidation zone of ore deposits are given below.

Scorodite, and beudantite (OHAsFe, and OHSAsPbFe mineral systems). Scorodite is a common hydrated iron arsenate mineral, $FeAsO_4 \cdot 2H_2O$. It is found as a secondary mineral usually in the upper and exposed part of an ore deposit or mineral vein worldwide. The thermodynamic properties for scorodite and stability of minerals in the Eh-pH diagram of the OHAsFe and OHSAsFe systems are the subject of considerable debate and studies (e.g., Dove and Rimstidt 1985; Robins 1987; Krause and Ettel 1988; Zhu and Merkel 2001; Craw et al. 2003; Langmuir et al. 2006; Bluteau and Demopoulos 2007; Peng and Chen 2011; Majzlan et al. 2012; Nordstrom et al. 2014).

Figure 15.4a is characterized by a rather large stability field for scorodite. The parameters of its formation is low pH values and strong oxidizing conditions. In this system, another arsenate of iron is formed—symplesite, $Fe_3(AsO_4)_2 \cdot 8H_2O$, in which iron has an oxidation state +2. Symplesite is stable under less oxidizing conditions and in a wide range of pH values from acidic to alkaline. The diagram

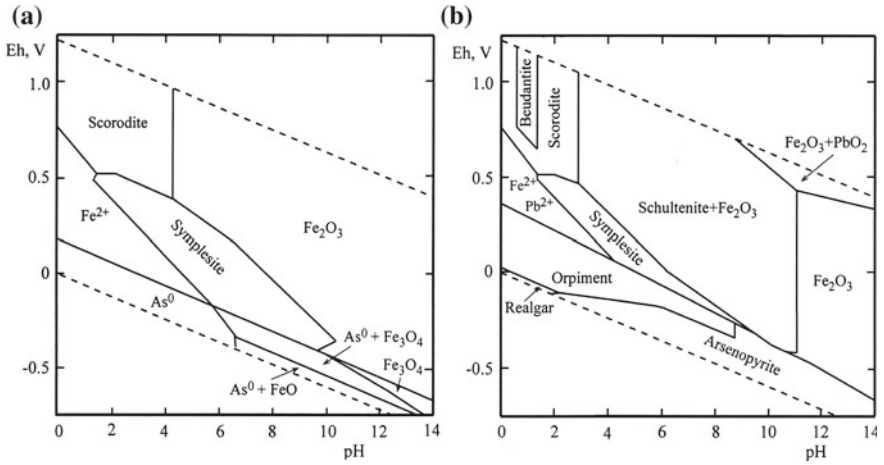


Fig. 15.4 Stability fields of scorodite (**a**) and beudantite (**b**). Eh–pH diagrams of the systems OHAsFe (Fe–As–H_2O) and OHSAsPbFe (Fe–Pb–As–S–H_2O) at 25 °C and the activities of the components: $a_{\Sigma As} = 10^{-3}$, $a_{\Sigma Fe} = 10^{-2}$, $a_{\Sigma Pb} = 10^{-4}$, $a_{\Sigma S} = 1$

also contain the stability fields of iron oxides: FeO (wüstite), Fe_3O_4 (magnetite), and Fe_2O_3 (hematite) which replace each other with increasing of oxidation potential.

The presence in the system of lead and sulfur (mineral system OHSAsPbFe) leads to the formation of beudantite, $PbFe_3(AsO_4)(SO_4)(OH)_6$, the conditions for its stability in general are similar to those for scorodite (Fig. 15.4b). The position of the field of stability of beudantite within the field of scorodite sustainability can be explained by three reactions defining the boundaries of beudantite and scorodite stability.

Scorodite will decompose in the presence of H_2SO_4, Fe^{3+}, and Pb^{2+} delivered by oxidation of arsenopyrite and galena to yield beudantite and H^+ ions. This reaction depends only on the pH of solution, with increasing pH scorodite replaced by beudantite:

$$FeAsO_4 \cdot 2H_2O + H_2SO_4 + 2Fe^{3+} + Pb^{2+} + 4H_2O = PbFe_3(AsO_4)(SO_4)(OH)_6 + 8H^+ \quad (15.3)$$

The dissolution of beudantite in the presence of arsenic acid and decreasing of H^+ ions activity (increasing pH), is a reaction that produces scorodite as well as dissolved lead, sulfuric acid and water. Like the previous reaction it depends only on the pH of a solution, with increasing pH beudantite replaced by scorodite:

$$PbFe_3(AsO_4)(SO_4)(OH)_6 + 2H_3AsO_4 + 2H^+ = 3FeAsO_4 \cdot 2H_2O + H_2SO_4 + Pb^{2+} \quad (15.4)$$

The ferrous iron oxidize to ferric iron and incorporate into beudantite according to the following reaction which depends on the pH and Eh of a mineral-forming medium, with increasing pH and Eh scorodite replaced by beudantite:

$$FeAsO_4 \cdot 2H_2O + H_2SO_4 + 2Fe^{2+} + Pb^{2+} + 4H_2O = PbFe_3(AsO_4)(SO_4)(OH)_6 + 8H^+ + 2\bar{e} \quad (15.5)$$

It should be noted that for the beudantite formation of you need a fairly high activity of dissolved sulfur in the solution (not less than 0.1).

In the system under consideration, with increasing pH scorodite becomes unstable and replaced by relatively rare mineral (known only from 28 localities) schultenite, $PbHAsO_4$, according to the reaction:

$$2Fe(AsO_4) \cdot 2H_2O + 2Pb^{2+} = 2PbHAsO_4 + Fe_2O_3 + H_2O + 4H^+ \quad (15.6)$$

In very alkaline conditions (pH > 11), schultenite dissolves, this reaction depends only on the pH of a solution:

$$PbHAsO_4 + 3H_2O = Pb(OH)_3^- + AsO_4^{3-} + 4H^+ \quad (15.7)$$

Under relatively reduced conditions, litharge, PbO (a narrow field stability not shown on Fig. 15.4b) is stable, whereas plattnerite (PbO_2) and minium (Pb_3O_4) are stable in an oxidized environment.

Mimetite (OHClAsPb mineral system). The most widespread of the natural lead arsenate, mimetite, $Pb_5(AsO_4)_3Cl$, forms as a secondary mineral in ore deposits, usually by the oxidation of galena and arsenopyrite in the presence of chloride ion in a solution. Figure 15.5 shows the Eh–pH diagram of the mineral system OHClAsPb, most of this diagram is occupied by mimetite which is stable in a wide range of pH and Eh. At low pH lead occurs in the dissolved state as Pb^{2+}, which can react with H_3AsO_4 to form a narrow field of schultenite, $PbHAsO_4$:

$$Pb^{2+} + H_3AsO_4 = PbHAsO_4 + 2H^+ \quad (15.8)$$

The boundary between schultenite and mimetite is obtained from the reaction:

$$3PbHAsO_4 + 2Pb^{2+} + Cl^- = Pb_5(AsO_4)_3Cl + 3H^+ \quad (15.9)$$

In the stability field of arsenous acid, H_3AsO_3 (see Fig. 15.1), mimetite formation can be expressed by following reaction which depends on the pH and Eh of a medium:

$$5Pb^{2+} + 3H_3AsO_3 + Cl^- + 3H_2O = Pb_5(AsO_4)_3Cl + 15H^+ + 6\bar{e} \quad (15.10)$$

The reaction for the oxidation of native arsenic to mimetite and mimetite to plattnerite, PbO_2, the following expressions can be written as:

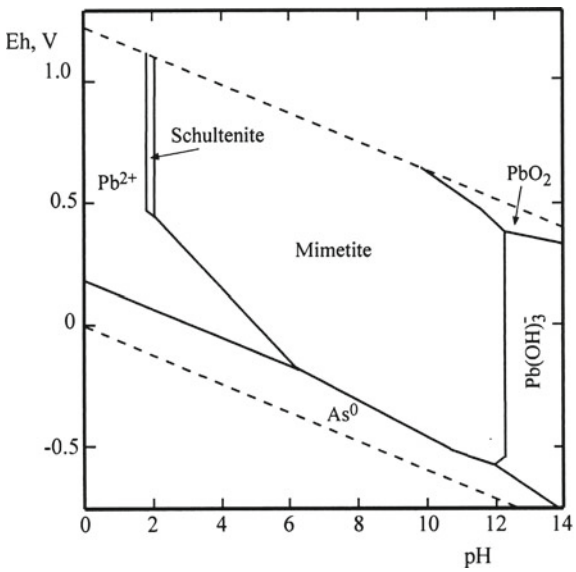


Fig. 15.5 Stability field of mimetite. Eh–pH diagrams of the systems OHClAsPb (Pb–As–Cl–H_2O) at 25 °C and the activities of the components: $a_{\Sigma As} = 10^{-3}$, $a_{\Sigma Pb} = 10^{-4}$, $a_{\Sigma Cl} = 10^{-3}$

$$3As^0 + 5PbOH^+ + Cl^- + 7H_2O = Pb_5(AsO_4)_3Cl + 19H^+ + 15\bar{e} \quad (15.11)$$

$$Pb_5(AsO_4)_3Cl + 10H_2O = 5PbO_2 + 3AsO_4^{3-} + Cl^- + 20H^+ + 10\bar{e} \quad (15.12)$$

In alkaline conditions mimetite dissolves with the formation of dissolved particles:

$$Pb_5(AsO_4)_3Cl + 15H_2O = 5Pb(OH)_3^- + 3AsO_4^{3-} + Cl^- + 15H^+ \quad (15.13)$$

Olivenite, duftite, and conichalcite (OHAsCu, OHAsPbCu, and OHAsCuCa mineral systems). Of the widespread copper arsenates minerals found in the zones of oxidation, only five are treated herein, because only for these minerals thermodynamic data are available. They are clinoclase, $Cu_3(AsO_4)_9(OH)_3$, cornubite, $Cu_5(AsO_4)_2(OH)_4$, euchroite, $Cu_2(AsO)(OH) \cdot 3H_2O$, olivenite, $Cu_2(AsO_4)(OH)$, and rollandite, $Cu_3(AsO_4)_2 \cdot 4H_2O$. These minerals belong to the mineral system OHAsCu. They are formed in the oxidation zones of Cu-As-bearing orebodies. Here groundwater enriched with oxygen reacts with sulfides and arsenides to produce an array of secondary arsenate minerals. Thermodynamics, stability, and phase relations among arsenates of copper are considered in the works of Magalhaes et al. (1988) and Majzlan et al. (2017).

The Eh–pH diagram of the system OHAsCu (Fig. 15.6a) shows the information currently available on the copper-water-arsenic mineral relation at 25 °C and 1 atmosphere total pressure. Native arsenic and native copper are stable under reducing conditions in a wide range of pH values. Increasing the oxidation potential results to the dissolution of arsenic, and then to the oxidation of copper, which dissolves at

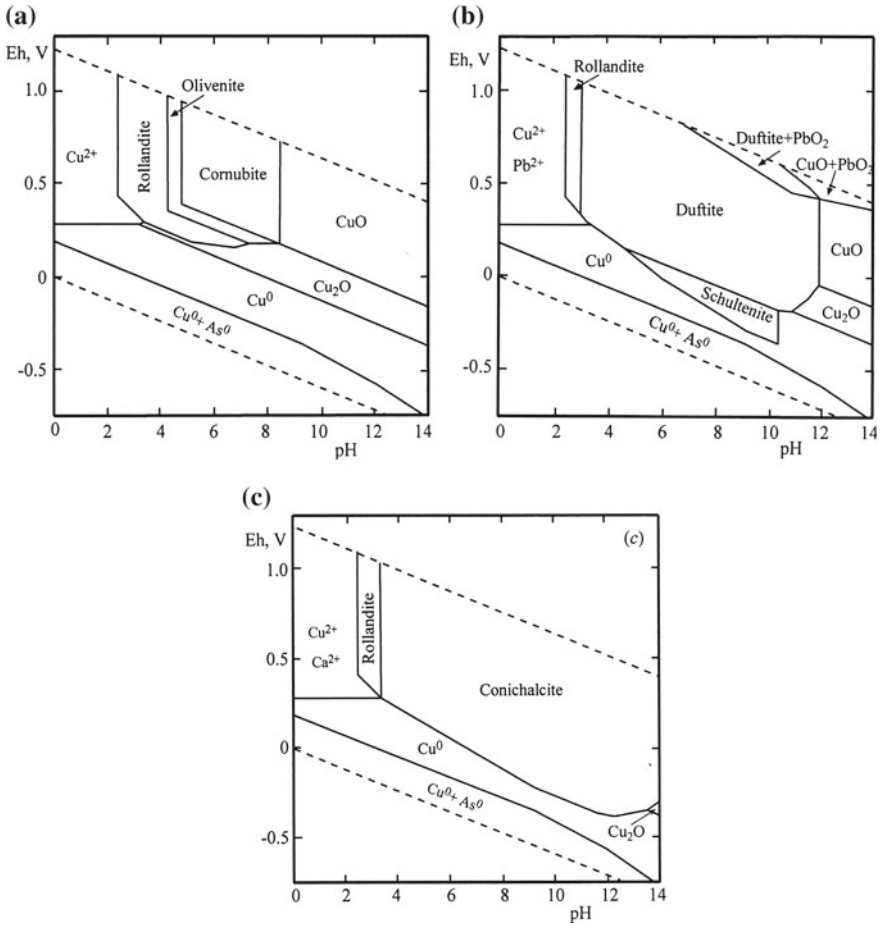


Fig. 15.6 Stability fields of olivenite (**a**), duftite (**b**) and conichalcite (**c**). Eh–pH diagrams of the systems OHAsCu (Cu–As–H_2O), OHAsPbCu (Cu–Pb–As–H_2O) and OHAsCuCa (Cu–Ca–As–H_2O) at 25 °C and the activities of the components: $a_{\Sigma As} = 10^{-3}$, $a_{\Sigma Cu} = 10^{-2}$, $a_{\Sigma Pb} = 10^{-5}$, $a_{\Sigma Ca} = 10^{-2}$

low pH, and with increasing alkalinity of the medium passes into cuprite (Cu_2O), and then into the tenorite (CuO). The formation of secondary copper arsenates such as rollandite, olivenite, and cornubite by reduction of the acidity of the solution can be suggested by the following expression:

$$3Cu^{2+} + 2H_3AsO_4 + 4H_2O = Cu_3(AsO_4)_2 \cdot 4H_2O + 6H^+ \qquad (15.14)$$

Under oxidative conditions with an increase in the pH, secondary copper arsenates change for one another in the order of rollandite—cornubite—olivenite:

$$2Cu_3(AsO_4)_2 \cdot 4H_2O = 3Cu_2(AsO_4)(OH) + H_2AsO_4^- + H^+ + 5H_2O \quad (15.15)$$

$$5Cu_2(AsO_4)(OH) + 5H_2O = 2Cu_5(AsO_4)_2(OH)_4(OH) + H_2AsO_4^- + 3H^+ \quad (15.16)$$

Figure 15.6b illustrates the influence of adding lead to the OHAsCu-oxygenated system. The presence in the system of Pb^{2+} leads to the formation of duftite, $PbCu(AsO_4)(OH)$ (mineral system OHAsPbCu) according to the reaction:

$$Cu_3(AsO_4)_2 \cdot 4H_2O + H_2AsO_4^- + 3Pb^{2+} = 3PbCu(AsO_4)(OH) + 5H^+ + H_2O \quad (15.17)$$

The presence of duftite removes the fields of stability of olivenite, cornubite, and the various lead oxides, except of the small field of PbO_2 (plattnerite) which is a fine indicator of alkaline oxidizing conditions. The stability field of schultenite, $PbHAsO_4$, appears on the diagram, but in the system OHAsPbCu this mineral is stable under less oxidizing conditions than in the system OHSAsPbFe (see Fig. 15.4b).

Figure 15.6c shows the results of adding calcium to the system OHAsCu. Another copper arsenate is characterized by a fairly large localities number is conichalcite, $CaCu(AsO_4)(OH)$, which is stable in a wide range of pH and Eh values, and its formation prevents the crystallization of the other basic copper arsenates. In extremely alkaline conditions (pH > 12), together with conichalcite, the crystallization of portlandite ($Ca(OH)_2$) occurs (not shown in Fig. 15.6c).

Erythrite and annabergite (OHAsCo, and OHAsNi mineral systems). Of particular interest is the estimation of the formation conditions of erythrite and annabergite, because, in the oxidation zone of sulfide and arsenide ores, these minerals are reliable indicators of Co and Ni arsenides, which are frequently associated with uranium and silver mineralization in primary ores. Erythrite occurs in association with cobaltite, CoAsS, skutterudite, $Co_4(As_4)_3$, modderite, CoAs, safflorite, $CoAs_2$, symplesite, scorodite, etc. The stability field of erythrite appears with an increase of pH in a nearly neutral medium (Fig. 15.7a):

$$3Co^{2+} + 2H_2AsO_4^- + 8H_2O = Co_3(AsO_4)_2 \cdot 8H_2O + 4H^+ \quad (15.18)$$

$$3Co^{2+} + 2H_3AsO_3 + 10H_2O = Co_3(AsO_4)_2 \cdot 8H_2O + 10H^+ + 4\bar{e} \quad (15.19)$$

Erythrite dissolves with increasing alkalinity of the medium according to the following equations:

$$Co_3(AsO_4)_2 \cdot 8H_2O = 3HCoO_2^- + 2HAsO_4^{2-} + 2H_2O + 7H^+ \quad (15.20)$$

At weakly alkaline and oxidizing conditions, a field of Co_3O_4 (guite) appears in the diagram. Guite was found recently in the Sicomines Copper-Cobalt Mine, Democratic Republic of Congo (Lei et al. 2017). It is a supergene cobalt oxide formed

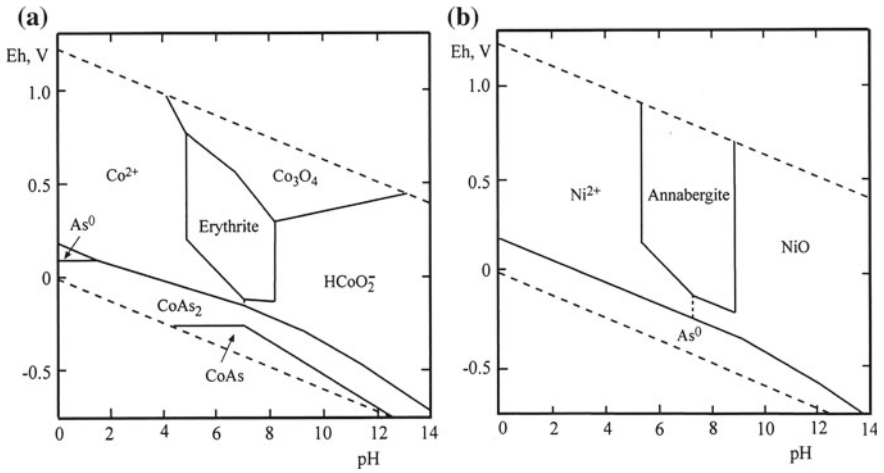


Fig. 15.7 Stability fields of erythrite (**a**) and annabergite (**b**). Eh–pH diagrams of the systems OHAsCo (Co–As–H_2O) and OHAsNi (Ni–As–H_2O) at 25 °C and the activities of the components: $a_{\Sigma As} = 10^{-3}$, $a_{\Sigma Co} = 10^{-2}$, $a_{\Sigma Ni} = 10^{-2}$

from the precipitation of cobalt-bearing solution at weakly alkaline and oxidizing conditions:

$$3Co^{2+} + 4H_2O = Co_3O_4 + 8H^+ + 2\bar{e} \tag{15.21}$$

$$3HCoO_2^- + H^+ = Co_3O_4 + 2H_2O + 2\bar{e} \tag{15.22}$$

Nickel behaves similarly to cobalt (Fig. 15.7b). As erythrite, annabergite is formed in a nearly neutral medium, and this is consistent with natural observations. The diagram also contains the stability field of nickel oxide—NiO (bunsenite).

Adamite (OHAsZn mineral system). Stability field of adamite, $Zn_2(AsO_4)(OH)$, can be seen in the Eh–pH diagram of mineral system OHAsZn (Fig. 15.8). The stability field of adamite appears with an increase of pH in a slightly acidic medium:

$$2Zn^{2+} + H_2AsO_4^- + H_2O = Zn_2(AsO_4)(OH) + 3H^+ \tag{15.23}$$

$$2Zn^{2+} + H_3AsO_3 + 2H_2O = Zn_2(AsO_4)(OH) + 6H^+ + 2\bar{e} \tag{15.24}$$

Adamite is stable in a fairly wide range of pH, and in alkaline conditions it is associated with zincite (ZnO). It should be noted that, the diagram does not contain the stability field of other Zn arsenates: köttigite, $Zn_3(AsO_4)_2 \cdot 8H_2O$, and legrandite, $Zn_2AsO_4(OH) \cdot H_2O$, although their thermodynamic data are also taken into account in the calculations.

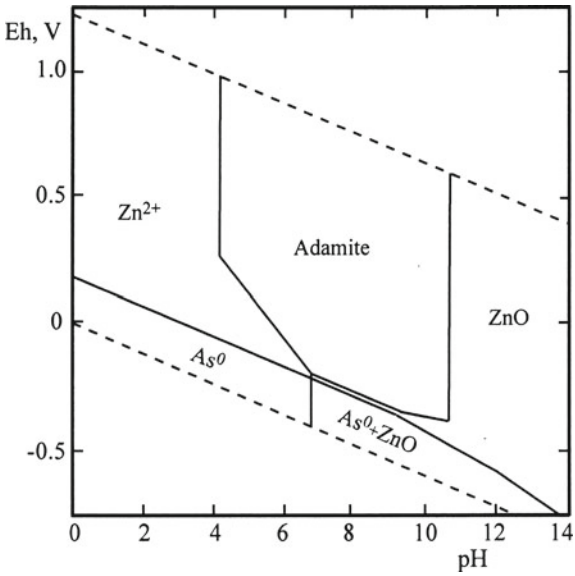


Fig. 15.8 Stability field of adamite. Eh–pH diagram of the system OHAsZn (Zn–As–H_2O) at 25 °C and the activities of the components: $a_{\Sigma As} = 10^{-3}$, $a_{\Sigma Zn} = 10^{-2}$

15.4 Conclusions

Eh–pH diagrams have been prepared for the most common arsenate minerals formed at 25 °C and 1 bar pressure. These theoretical diagrams reproduce the major mineral association relations of common arsenate minerals observed in the environment. The diagrams are useful in a number of ways. Over and above the specific problems of the oxidation of arsenides, they provide a set of calculated equilibrium relationships among various mineral species. Although the diagrams are based upon several approximations, the gross relationships provide a framework for comparison with natural mineral association, and for experimental investigation.

The relevance of real redox processes to theoretical Eh–pH diagrams remains debatable for many elements and for arsenic in particular (Plant et al. 2014). In reality, the processes of mineral formation in the arsenic systems are influenced by several important factors the main ones are listed below.

One of the factors is the speed of establishing equilibria, and this question is debatable for various forms of arsenic. Some anomalies of arsenic behavior are explained by kinetics of oxidation-reduction reactions (Cherry et al. 1979; Yan et al. 2000).

Microbiological processes play an extremely important role in the oxidation and reduction of various forms of arsenic. Arsenic-transforming microorganisms are commonly assigned to one of four groups based on their metabolisms: (1) dissimilatory arsenate-reducing prokaryotes, (2) arsenate-resistant microorganisms, (3) chemoautotrophic arsenite oxidizers, and (4) heterotrophic arsenite oxidizers (Amend et al. 2014). The key factors in these assignments are whether the organisms

are using arsenic in their energy metabolisms or only transforming it in detoxification processes, and whether the organisms are heterotrophic or lithotrophic.

The arsenic ion speciation in the solutions depending not only on the redox potential and pH but significantly influenced by the interaction with minerals containing elements of variable oxidation state, e.g., Fe(III), Mn(IV), Ti(IV) (Tournassat et al. 2002; Plant et al. 2014).

In addition to sorption, our thermodynamic calculations do not take into account the interaction of chemical elements with organic substances of humus origin. Such calculations involving organic ligands are a complex task and widely discussed in the literature (Perdue et al. 1984; Susetyo et al. 1990; Grzyb 1995; Wood 1996; Nordstrom and Campbell 2014; Huber et al. 2002; Tipping and Hurley 1992).

In general, users of programs for calculation and construction of Eh–pH diagrams must be aware that the thermodynamic data is internally consistent and consistent with equilibrium stoichiometry. Examples of incomplete or erroneous thermodynamic data for arsenic minerals are given in our work (Charykova et al. 2009), as well as in the review (Nordstrom et al. 2014).

Despite the listed problems, the study of the Eh–pH diagrams is helpful in suggesting new lines of approach to geologic and environmental problems, or gives support to a particular solution of a problem that had several possible explanations. This study emphasizes the difficulty of oxidizing arsenides to arsenates in inorganic systems, and again stresses the role of organisms in the production of primary arsenides and arsenates in near-surface environments. These diagrams are not accurate representations of natural systems; and they undoubtedly are highly variable in their approach to that ideal. Yet because they represent a quantitative estimate based on the available data, they should be helpful tools, if used within their limitations.

References

Alpers CN, Jambor JL, Nordstrom DK (eds) (2000) Sulfate minerals: crystallography, geochemistry, and environmental significance. Rev Miner Geochem 40:1–602

Amend JP, Saltikov C, Lu GS, Hernandez J (2014) Microbial arsenic metabolism and reaction energetics. Rev Miner Geochem 79:391–433

Bethke CM, Yeakel S (2011) The geochemist's workbench, release 9.0, GWB essentials guide. Aqueous Solutions, LLC, University of Illinois, Champaign

Bigham JM, Schwertmann U, Traina SJ, Winland RL, Wolf M (1996) Schwertmannite and the chemical modeling of iron in acid sulfate waters. Geochim Cosmochim Acta 60:2111–2121

Bluteau M-C, Demopoulos GP (2007) The incongruent dissolution of scorodite: solubility, kinetics and mechanism. Hydrometall 87:163–177

Bowell RJ, Craw D (2014) The management of arsenic in the mining industry. Rev Miner Geochem 79:507–532

Bowell RJ, Alpers CN, Jamieson HE, Nordstrom DK, Majzlan J (2014) The environmental geochemistry of arsenic: an overview. Rev Mineral Geochem 79:1–16

Bruneel O, Personné J-C, Casiot C, Leblanc M, Elbaz-Poulichet F, Mahler BJ, Le Flèche A, Grimont PAD (2003) Mediation of arsenic oxidation by *Thiomonas* sp. in acid-mine drainage (Carnoulès, France). J Appl Microbiol 95:492–499

Charykova MV, Krivovichev VG, Depmeir W (2009) Thermodynamics of arsenates, selenites, and sulfates in the oxidation zone of sulfide ores: I. Thermodynamic constants at ambient conditions. Zapiski RMO (Proc Russ Miner Soc) 137(6):105–117(in Russian) [(2010) Geol Ore Dep 52:689–700 (Engl. Transl)]

Charykova MV, Krivovichev VG, Yakovenko OS, Depmeier W (2011) Thermodynamics of arsenates, selenites, and sulfates in the oxidation zone of sulfide ores: III. Eh–pH diagrams for the Me–As–H_2O systems (Me = Co, Ni, Fe, Cu, Zn, Pb) at 25 °C. Zapiski RMO (Proc Russ Miner Soc) 139(3):1–14 (in Russian) [(2011) Geol Ore Dep 53:501–513 (Engl. Transl)]

Cherry JA, Shaikh AU, Tallman DE, Nicholson RV (1979) Arsenic species as an indicator of redox conditions in groundwater. J Hydrol 43:373–392

Christy AG (2015) Anomalous mineralogical diversity in the periodic table, and its causes. Mineral Mag 79:33–49

Cornell RM, Schwertmann U (2003) The iron oxides: structure, properties, reactions, occurrences and uses, 2nd edn. Wiley, KGaA Weinheim Germany

Craw D, Falconer D, Yongson JH (2003) Environmental arsenopyrite stability and dissolution: theory, experiment, and field observations. Chem Geol 179:71–82

Dove PM, Rimstidt JD (1985) The solubility and stability of scorodite, $FeAsO_4 \cdot 2H_2O$. Am Miner 70:838–844

Grzyb KR (1995) NOAEM (natural organic anion equilibrium model): a data analysis algorithm for estimating functional properties of dissolved organic matter in aqueous environments: part I. Ionic component speciation and metal association. Org Geochem 23:379–390

Hålenius U, Hatert F, Pasero M, Mills SJ (2018) New minerals and nomenclature modifications approved in 2018. Newsletter 32. Miner Mag 82:1225–1232

Hawthorne FC (2002) The use of end-member charge-arrangements in defining new mineral species and heterovalent substitutions in complex minerals. Can Miner 40:699–710

Hatert F, Burke EAJ (2008) The IMA-CNMNC dominant-constituent rule revised and extended. Can Miner 46:717–728

Huber C, Filella M, Town RM (2002) Computer modelling of trace metal ion speciation: practical implementation of a linear continuous function for complexation by natural organic matter. Comput Geosci 28:587–596

Krause E, Ettel VA (1988) Solubility and stability of scorodite, $FeAsO_4$:$2H_2O$: new data and further discussion. Am Miner 73:850–854

Krivovichev VG, Charykova MV (2013a) Classification of mineral systems. St.-Petersburg University Press, St. Petersburg (in Russian)

Krivovichev VG, Charykova MV (2013b) Number of minerals of various chemical elements: statistics 2012 (a new approach to an old problem). Zapiski RMO (Proc Russ Miner Soc) 142(4):36–42 (in Russian, English translation: Geol Ore Deposits (2014) 56:553–559)

Krivovichev VG, Charykova MV, Krivovichev SV (2018) The concept of mineral systems and its application to the study of mineral diversity and evolution. Eur J Mineral 30:219–230

Langmuir D, Mahoney J, Rowson J (2006) Solubility products of amorphous ferric arsenate and crystalline scorodite ($FeAsO_4 \cdot 2H_2O$) and their application to arsenic behavior in buried mine tailings. Geochim Cosmochim Acta 70:2942–2956

Lei Z, Chen X, Wang J, Zhang J, Huang Y, Lu Z, Du F (2017) Guite, IMA 2017–080. CNMNC Newsletter No. 40. Miner Mag 81:1581

Mitchell VL (2014) Health risks associated with chronic exposures to arsenic in the environment. Rev Miner Geochem 79:435–449

Morin G, Calas G (2006) Arsenic in soils, mine tailings and former industrial sites. Elements 2:97–101

Magalhaes MKF, Pedrosa de Jesus JD, Williams PA (1988) The chemistry of formation of some secondary arsenate minerals of Cu(II), Zn(II) and Pb(II). Miner Mag 52:679–690

Majzlan J, Drahota P, Filippi M, Grevel K-D, Kahl W-A, Plasil J, Boerio-Goates J, Woodfield BF (2012) Thermodynamic properties of scorodite and parascorodite ($FeAsO_4 \cdot 2H_2O$), kaňkite ($FeAsO_4 \cdot 3.5H_2O$), and $FeAsO_4$. Hydrometall 117–118:47–56

Majzlan J, Števko M, Dachs E, Benisek A, Plášil J, Sejkora J (2017) Thermodynamics, stability, crystal structure, and phase relations among euchroite, $Cu_2(AsO_4)(OH)\cdot 3H_2O$, and related minerals. Eur J Miner 29:5–16

Mandarino JA, Nickel EH, Cesbron F (1984) Rules of procedure of the commission on new minerals and mineral names, international mineralogical association. Can Miner 22:367–368

Nickel EH, Grice JD (1998) The IMA commission on new minerals and mineral names: procedures and guidelines on mineral nomenclature. Can Miner 36:913–926

Nickel EH, Mandarino JA (1987) Procedures involving the IMA commission on new minerals and mineral names, and guidelines on mineral nomenclature (excerpt). Can Miner 25:353–377

Nordstrom DK, Campbell KM (2014) Modeling low-temperature geochemical processes. In: Drever JI (ed) Surface and groundwater, weathering and soils (treatise on geochemistry), vol 7, pp 27–68. Elsevier Pergamon, Amsterdam

Nordstrom DK, Majzlan J, Königsberger E (2014) Thermodynamic properties for arsenic minerals and aqueous species. Rev Miner Geochem 79:217–255

O'Day PA (2006) Chemistry and mineralogy of arsenic. Elements 2:77–83

Pasero M (2018) The New IMA list of minerals. http://pubsites.uws.edu.au/ima-cnmnc/

Peng L, Chen Z (2011) Arsenic Eh–pH diagrams at 25C and 1 bar. Environ Earth Sci 62:1673–1683

Perdue EM, Reuter JH, Parrish RS (1984) A statistical model of proton binding by humus. Geochim Cosmochim Acta 48:1257–1263

Plant JA, Bone J, Voulvoulis N, Kinniburgh DG., Smedley PL, Fordyce FM, Klinck B (2014) Arsenic and selenium. In: Holland HD; Turekain KK (eds) Environmental geochemistry (treatise on geochemistry), vol 11, pp 13–57. Elsevier Pergamon, Amsterdam

Robins RG (1987) Solubility and stability of scorodite, $FeAsO_4{:}2H_2O$: discussion. Am Miner 72:842–844

Susetyo W, Dobbs JC, Carreha LA, Azarraga LV, Grimm DM (1990) Development of a statistical model for metal-humic interactions. Anal Chem 62:1215–1221

Tipping E, Hurley MA (1992) A unifying model of cation binding by humic substances. Geochim Cosmochim Acta 56:3627–3641

Tournassat C, Charlet L, Bosbach D, Manceau A (2002) Arsenic(III) oxidation by birnessite and precipitation of manganese (II) arsenate. Environ Sci Technol 36:493–500

Williams M (2001) Arsenic in mine waters and international study. Env Geol 40:267–278

Wood SA (1996) The role of humic substance in the transport and fixation of metals of economic interest (Au, Pt, Pd, U, V). Ore Geology Rev 11:1–31

Yan X-P, Kerich R, Hendry MJ (2000) Distribution of arsenic (III), arsenic (V) and total inorganic in porewaters from a thick till and clay-rich aquitard sequence, Saskatchewan, Canada. Geochim Cosmochim Acta 62:2637–2648

Zhu Y, Merkel BJ (2001) The dissolution and solubility, $FeAsO_4{:}2H_2O$ evaluation and simulation with PHREEQC2. Wiss Mitt Inst Fur Geologie TU Bergakedemie Freiberg, Germany 18:1–12

Chapter 16
Abiogenic and Biogenic Forms of Migration Compounds in Swamps of Different Genesis



Lidia I. Inisheva, Ekaterina V. Porokhina, Alla V. Golovchenko and Lech W. Szajdak

Abstract Belonging to a specific geochemical region determines the qualitative conditions for the formation of the biogenic and abiogenic properties of peat deposits of swamps. The article provides the analysis of the microbiological and enzymatic activity of different genesis peat deposits in Western Siberia and the Gorny Altai region and their influence on the hydrochemical composition of swamp waters. Most of the chemical elements in the swamp water of the Western Siberia are characterized by elevated concentrations compared to the swamps of the Gorny Altai region. However, the swamp waters of the Gorny Altai region have a predominant content of humic acids in comparison with fulvic acids, unlike the composition of swamp waters of Western Siberia. It was revealed that the redox conditions of the 1-m-thick layer of the peat deposit are of great importance, in which the hydrochemical composition of the swamp waters with individual features in each type of phytocenosis is formed on the basis of biochemical processes during the vegetative season. The maximum concentration of almost all components is observed on the margin of the swamp as a result of migration of substances in this direction from autonomous swamp landscapes. The results of studies of the biochemical activity of the 1-m-thick layer of the peat deposits of different swamps according to the genesis indicate that the peat deposits of the mesotrophic and eutrophic types are characterized by the greatest biochemical activity. On the landscape profile of geochemically linked swamps, a high overall biochemical activity is noted in the peat deposit of autonomous position. It is concluded that the migratory streams from the territory of Western Siberia, which is distinguished by a large swamping and an active manifestation of the peat formation process, influence the formation of the biogenic and abiogenic composition of river waters. The performed studies have shown that it is necessary to take into account the hierarchy and conjugation of landscapes of the river basin and the organic component of swamp waters.

L. I. Inisheva (✉) · E. V. Porokhina · A. V. Golovchenko · L. W. Szajdak
Tomsk State Pedagogical University, Tomsk, Russia
e-mail: inisheva@mail.ru

© Springer Nature Switzerland AG 2020

O. V. Frank-Kamenetskaya et al. (eds.), *Processes and Phenomena on the Boundary Between Biogenic and Abiogenic Nature*, Lecture Notes in Earth System Sciences,
https://doi.org/10.1007/978-3-030-21614-6_16

Keywords Siberia · Gorny Altai · Swamp · Peat deposit · Microorganisms · Enzyme activity · Migration · Biogenic and abiogenic properties · Hydrochemical regime

16.1 Introduction

The water factor is the most important indicator of the ecological state of the environment, and the modern concept of sustainable development pays special attention to it. The most important aspects of this problem are: the determination of substances coming with diffuse runoff from swampy watershed, biochemical aspects of peat formations in bog ecosystems (BES) of different genesis, as well as the separation of anthropogenic and background components of the chemical composition of natural waters. Therefore, the study of specific waters and their characteristic biotic and abiotic processes of transformation of material and energy flows in the swampy watershed is a great prospect for the chemical component of the total georunoff on Earth.

Thus, with the area of swamping in Western Siberia of about 1 million km^2 and peat reserves of 120 billion tons (at the humidity of 40%), water reserves in peat reach 1000 km^3, i.e. on average 1000 mm per unit of marshy area, which significantly exceeds the annual runoff of rivers in these areas (100–300 mm/year). However, the geochemical aspect of the impact of swamps on the composition of river and groundwater has not been practically studied.On the one hand, BES are geochemical barriers (Glazovskaya 1983), which, because of their high sorption capacity, fix a large range of pollutants from the atmosphere, removing them from the circulation of substances. On the other hand, the complex chemical composition of the peats themselves in the BES peat deposit and their physico-colloidal structure form their own hydrochemical composition of swamp waters. Before reaching the underground aquifers, precipitation undergoes a stage of swamp genesis. In the organogenic environment of the peat deposit (PD), the groundwater feeding the BES is also transformed. As a result, fresh water is formed, it being enriched with carbon dioxide, methane, dissolved organic matter (OM), iron, manganese and other swamp components. This is how a special type of swamp waters is formed, the composition of which and the processes of interaction in them are not sufficiently studied. This is true for domestic and foreign swamps (Baird 1995).

In general, swamp waters, enriched with OM of humus nature, contain dissolved oxygen in low concentrations, and have low mineralization. According to Perel'man (1989), by their redox conditions, the swamp waters present a nonequilibrium system, which is characterized by associations of oxidants (O_2, Fe^{3+}) and reducing agents (dissolved humic acids and Fe^{2+}). Among humic substances, humic acids (HA) and fulvic acids (FA) are specified. Fulvic acids are the most soluble of all the humic acids, due to a higher contribution to their structure of carboxyl groups and phenolic oxygroups and lower molecular weight monomers and associates of FA. The high exchange capacity of HA provides formation of strong complex compounds with

metal ions. It is the complexing with HA that plays a crucial role in the processes of dissolution, transfer and deposition of elements in the hypergenesis zone (Kononova 1963; Orlov 1974; Yamble and Cshnitzer 1973; Shotyk et al. 2016).

The indicators of the BES functioning, their dynamics and development trends are determined by the processes of formation, transformation and migration of biogenic and abiogenic substances on the swamped watershed. Vernadsky (1960) was the first to show the scale of OM as a hydrochemical factor of special importance. The role of swamps in lithogenesis as a factor of differentiation of chemical elements on paths from areas of demolition to transaccumulative positions is obvious. Let us consider the formation of these indicators on the example of different genesis swamps.

16.2 Objects of Study and Methods

The swamp ecosystems which were selected as the objects of research are characteristic for the territory of the southern taiga—the Vasyugan stationary, as well as for the territory of the forest-steppe zone—the Tagan stationary, and for the Gorny Altai region—Altai stationary (Fig. 16.1).

The botanical composition and degree of decomposition of peats was determined according to State Standard GOST 28245.2-89, the content of chemical elements in peats and dry residues of swamp waters was determined by neutron activation analysis using the IRT-T research nuclear reactor "CANBERRA" at the Scientific Institute of Nuclear Physics of the Tomsk Polytechnic University.

The total number and biomass of microorganisms were studied by a direct method using method of fluorescent microscopy (Zvyaginzev 1980). To do this, cells were



Fig. 16.1 The arrangement scheme of the swamp stationaries and observation points of the study; 1—the Vasyugan stationary; 2—the Tagan stationary; 3—Altai stationary

pre-desorbed with Bandelin Sonopuls HD 2070 ultrasonic disperser (power 50%; 2 min). To quantify bacteria cells and actinomycetes mycelium, the preparations were stained with an aqueous solution of acridine orange, and calcofluor white was used to stain the mycelium and spores of the fungi. The calculations of prokaryotic biomass were carried out taking into account that the biomass of the dry matter for a single bacterial cell with a volume of 0.1 mkm^3 is 2×10^{-14}g, 1 m of actinomycetes mycelium with a diameter of 0.5 mkm 3.9×10^{-8} g (Kozhevin et al. 1979). Eukaryotic microbial biomass was calculated taking into account the spore diameter measured by us and the mycelium of fungi using the formula (for mycelium–0.628 $(r_1)^2 \times 10^{-6}$ g, for spores—0.836 $(r_2)^3 \times 10^{-12}$ g; where r_1 is the mycelium radius; r_2 is the radius of a fungi spore) (Polyanskaya 1996). Catalase activity was determined by the gasometric method in the modification of Kruglov and Paromenskaya (1966). Peroxidase and polyphenol oxidase activity was determined by the method of Karyagina and Mikhailovskaya (Karyagina and Mikhailovskaya 1986). Statistical processing of the analysis results was carried out in Microsoft Office Excel 6.

The bog waters were selected in dug wells at depths of 0.5–1 m at its secondary filling. Chemical analysis of bog waters was carried out in the Testing Laboratory of the TSPU (No. ROSS RU.0001.516054) by means of the methods: pH was tested with potentiometric method; mineralization was tested by dry residue; Ca^{2+}, Mg^{2+}, HCO_3^-, Cl^- were tested by titrimetric method; Na^+, K^+ were tested by the method of atomic absorption; NO_3^-, NH_4^+ were analyzed by photometric method; Fe was tested by polarographic method according to Reznikov et al. (1970); humic (HA) and fulvic acids (FA) were tested according to (Bazin et al. 1992).

16.3 Results and Discussion

First, we will consider the processes in oligotrophic swamps of the south taiga of Western Siberia. The small swamped catchment area of the Klyuch River basin, with an area of 58 km^2, was adopted as a model object for research. All processes of interaction of water masses with products of vital functions of biogeocenoses can be considered as a special regional thermodynamic system in which the regulating role belongs to a living matter. In addition, swamps of the oligotrophic type are geochemically autonomous, which allows tracing the migration flow of substances also in the balance version. In the catchment area, the migration of substances from the autonomous position of the catchment area was determined, then in its transitional and accumulative parts (landscape profile). By the content of OM in the peats of this landscape profile, it is obvious that an increase in the content of readily hydrolysable fractions closer to the runoff zone of waters (transitional-accumulative part) testifies the migration of substances from the swamped watershed (Table 16.1).

Assessing the content of individual components of OM, it is important to note that they largely determine the specific composition of swamp waters in different parts of the landscape profile (Ilina et al. 2014) (Table 16.2).

Table 16.1 Group composition of peats in peat deposits of transitional and transitional-accumulative parts of the landscape profile (catena)

Layer (cm)	Kind of peat, type of deposit	Group composition of organic matter, % of mass					
		WS	LH	L	HA	SH	L
Transitional part							
0–50	Fuscum, Rt	0.9	30.6	2.6	25.1	15.2	25.6
50–75	Fuscum, Rt	1.2	16.6	1.7	25.2	16.4	38.9
75–100	Medium, Rt	0.4	32.6	0.6	19.8	14.3	32.3
100–150	Medium, Rt	0.4	33.5	1.4	19.0	10.3	35.4
150–200	Pine-cotton grass-sphagnum, Rt	0.3	23.6	0.7	37.1	13.8	24.5
200–250	Sedge, F	0.3	16.3	0.2	25.2	17.2	40.8
250–300	Herbaceous, F	0.1	38.6	0.2	21.2	16.0	23.9
Accumulative part							
0–25	Pine-cotton grass-sphagnum, Rt	1.6	22.4	3.9	27.6	4.2	40.3
25–50	Wood-cotton grass, T	1.6	28.3	3.6	22.7	8.1	35.7
50–75	Wood-cotton grass, T	1.2	36.6	2.6	23.0	9.2	27.4
75–100	Wood-cotton grass, T	0.4	32.7	0.9	39.8	11.0	15.2

Note Rt raised type; *T* transitional type; *F* fen type; *WS* water-soluble; *LH* lightly hydrolysable; *L* lipids; *HA* humic acids; *DH* difficult hydrolysable; *L* lignin

Table 16.2 Extreme values of individual elements in swamp water for a warm period in long-time average, conditionally droughty and wet years, mg/l

Parts	pH	Ca^{2+}	Mg^{2+}	NH^{4+}	Fe_{total}	NO_3^-	ГК	ФК
Long-time average years								
Autonomous	3.6–4.4	1.0–6.0	0.2–2.9	0.2–2.72	0.1–3.8	0.2–1.3	3.4–10.7	41.8–74.8
Transitional	3.4–4.3	0.8–7.5	0.5–4.4	0.2–3.8	0.1–3.8	0.2–2.5	5.4–13.1	40.7–88.4
Transitional-accumulative	3.4–4.7	3.0–11.2	1.0–9.6	0.3–4.1	0.2–7.2	0.2–6.0	2.4–19.6	44.4–92.8
Conditionally droughty years								
Autonomous	3.7–4.3	0.4–5.7	0.2–2.1	0.2–0.8	0–0.3	0–1.7	2.0–18.2	20.5–81.4
Transitional	3.6–5.5	0.4–8.7	0.6–3.7	0.3–1.1	0.1–6.7	0.1–2.7	4.1–11.2	35.2–66.9
Transitional-accumulative	4.5–6.2	1.1–9.8	1.2–2.9	0.3–1.3	0.2–0.7	0.2–2.0	2.6–18.2	35.9–95.5
Wet years								
Autonomous	3.9–4.4	0.1–5.3	0.2–6.2	0.2–0.6	0.1–1.2	0.1–1.3	1.7–12.9	31.2–88.4
Transitional	3.6–4.9	0.1–4.1	0.3–11.8	0.3–0.8	0.2–0.4	0.2–2.4	4.6–11.7	22.7–80.5
Transitional-accumulative	4.3–5.6	0.9–7.0	0.9–11.1	0.4–0.9	0–0.8	0.1–1.1	4.6–11.3	24.1–95.0

Note HA humic acids, *FA* fulvic acids, "—" were not determined

Thus, the calcium content increases significantly up to the transitional-accumulative position of the landscape. The same is typical for magnesium compounds. In wet years, there is a tendency to decrease the content of Ca ions, but at the same time there is an increase in Mg ions, the concentration of which in wet years increases in all positions of the landscape profile. Of the elements that are formed in the process of peat formation, we will pay attention to ammonium, nitrates and total iron. Their content indicates that in some periods swamp waters contain increased amounts of these elements and it can be assumed that this occurs due to their migration out of the swamped catchment area. In what direction is the migration of mobile organic substances? For a period of long-time average period, the content of HA in the swamp waters of the autonomous part of the catena varies from 1.3 to 18.2 mg/l, of the transit part it varies from 4.1 to 13.1 mg/l, and of the transitional-accumulative part—from 2.4 to 19.6 mg/l. In this way, the migration of HAs in the landscape profile from autonomous to transitional-accumulative parts is clearly noted. As for FA, they are found in waters from 20.5 to 95.5 mg/l, that is significantly more than HA.

It is known that in oligotrophic swamps characterized by low pH values, many geochemical patterns are violated, since individual peat properties come into force due to the peculiarities of the composition of their OM. It is natural to pose the question that the migration of OM, and in particular of the HA and their complexons, occurs in certain proportions characteristic of both the process of peat formation in each part of the landscape (catena), and the volume of the runoff coming from the entire catchment area.

Let us consider in more detail this assumption by the dynamics of the IR spectra of substances of a phenolic nature, which constitute from 3–5 to 41% of the total amount of water-soluble organic substances. The study of the IR spectra in the peats and swamp water precipitates of the landscape profile and their spectral coefficients (which reflect the ratio of hydrophilic and hydrophobic components in the structures of polyphenol molecules) allowed us to identify the structure of migrating water-soluble organic substances. In the swamp water of the autonomous part of the catena, the ratio of optical densities of hydroxyl groups D_{3400}/D_{1460} ranges from 0.89 to 1.49, the D_{1270}/D_{1460} ratio for phenolic hydroxyls is 0.78–0.86, D_{1720}/D_{1460} for carboxyl groups is 1.16–1.28, and D_{1620}/D_{1460} for aromatic fragments is 1.20–1.85. In the water-soluble compounds in the transitional and transitional-accumulative parts of the catena, the proportion of phenolic hydroxyls D_{1270}/D_{1460} increases to 0.96, and that of carboxyl groups D_{1720}/D_{1460} increases to 1.73 in comparison with the autonomous part.

As a rule, the amount of hydroxyl, phenolic hydroxyls, carboxyl groups and aromatic fragments increases in molecules of water-soluble substances in the autumn period, due to the high microbiological activity of the 1-m-thick layer heated to 15–20 °C and the greater activity of biochemical processes in the system—of peat deposit–swamp waters in general.

It is necessary to assume that humic substances are also involved in the absorption of the elements that are formed in the taiga zone in the process of peat formation and the biogenic form of the migration of elements (Blodau et al. 2002). What is

the biogenic form of migration, which is described by Bakhnov (1986). The main amount of ash elements in peats accumulates at the initial stage of peat formation, when their source is the mineral substrate. In the case of the object under study (peat deposits of LP), this is a carbonate clay. From this layer, saturated with calcium, the root system of the next layer of peat-forming plants consumes calcium and other mineral elements. So there is a redistribution of elements along the peat deposit profile with a gradual decrease in their concentration closer to the surface. As a result, oligotrophic landscapes with signs of a mesotrophic type of peat formation are formed in the studied area. This determines a rather high concentration of migrating substances under conditions of oligotrophic peat formation, which is characterized by the poverty of the elemental composition of PD.

Returning to the HA, we note that Kendorf and Schnitzer (1980, quoted from Ivanov 1994) constructed the sequences of absorption activity of metals by humic acids depending on the pH of the medium:

(a) pH = 2.4 − Hg > Fe > Pb > Cu = A1 > Ni > Cr = Zn = Cd = Co = Mn;
(b) pH = 3.7 − Fe > A1 > Pb > Cu > Cr > Cd = Zn = Ni > Co = Mn.

These very pH values are characteristic for the PD of the catena. The determination of macro- and microelements in humic acids migrating along the profile showed that if the content of Fe in the HA of the autonomous part of the profile is 0.10–0.25%, whereas the analogous value for the transitional–accumulative part is 1.25%. Once again this proves the presence of migration of substances in swamp landscapes in the form of biogenic (complexons) and abiogenic (mobile mineral compounds) forms.

A huge role in the processes of transformation of OM of peats and subsequent processes of migration of compounds into surface water-receivers (river, canal, lake) belongs to the microflora and their derivatives—enzymes. For example, our studies on oligotrophic swamps showed that microflora is present throughout the profile of PD. Let us consider this situation on a specific example (Table 16.3).

In the peat deposits of the catena, the limits of variability of the bacteria number of per 1 g of dry peat are (4−139) $\times$ 10^9 cells, the spores of fungi and (17–210) $\times$ 10^6 cells. The length of actinomycetes mycelium is from 0 to 1.7 km/g, and the length of fungi mycelium is from 0 to 14 km/g. Fungi spores, actinomycetes mycelium and bacteria were found throughout the PD profile, fungi mycelium being only in the upper horizons of oligotrophic and mesotrophic deposits. The attachment of the fungi mycelium to the surface PD layer is due to the fact that the fungi are saprotrophs. They follow to easily hydrolysable OM (Mirchink 1988). And one of the main peat forming agents of oligotrophic and mesotrophic type of peat formation are sphagnum mosses, which are characterized by a high content of easily hydrolyzing substances—hemicelluloses, as well as a low amount of cellulose (15–20%) and hardly hydrolysable substances (Rakovsky and Pigulevskaya 1978). It is known that the content of easily hydrolyzed OM downward the PD profile decreases, as a result, in the lower layers the fungi mycelium is not found.

The content of microbial biomass, calculated per gram of completely dry soil, in the upper 50-cm layer varies depending on the season and the position in landscape profile from 3 to 50 mg/g, in the layer of 50–100 cm—from 3 to 14 mg/g, at a depth

Table 16.3 The limit of number of microorganisms in peat deposits of the landscape profile

Layer (cm)	Bacteria, 10^9 cells/g	Mycelium		Fungi spores, 10^6 spores/g
		Actinomycetes (m/g)	Fungi (km/g)	
Autonomous part				
0–50	43–87	253–1684	0.4–14.1	79–210
50–100	17–61	421–842	0.0–1.2	24–79
100–150	8–50	53–590	0.0–0.5	10–126
150–200	6–11	0–246	0.0–0.2	20–24
200–250	5–9	0–84	0.0	24–39
250–300	4–8	0–140	0.0	26–50
Transitional part				
0–50	37–53	842–1263	0.4–0.8	52–131
50–75	32–34	468–1684	0.3–1.4	94–170
75–100	18–56	253–655	0.0–3.4	56–189
100–150	7–21	115–211	0.0	29–63
150–200	5–10	60–227	0.0	17–63
200–250	6–8	0–456	0.0	20–34
250–300	5–6	53–175	0.0	34–47
Transitional–accumulative part				
0–25	72–139	158–1755	1.9–6.4	39–59
25–50	35–64	268–404	0.2–5.8	17–61
50–75	19–72	90–421	0.3–2.7	25–110
75–100	15–19	53–481	0.0–0.06	39–67

of 1–3 m—from 0.3 to 5 mg/g. Microbial biomass gradually decreases along the profile, but at a depth of LP there are layers where the density of microbial groupings is comparable with that established for the upper stratum. Seasonal fluctuations of microbial biomass are more pronounced in the surface layer of peat swamps. In general, the total concentration of microorganisms was higher in the peat of swamp, which occupies an autonomous position on the LP. In this PD, the greatest concentration of biogenic elements was revealed. The structure of the microbial biomass of oligotrophic swamps, as a rule, is dominated by the eukaryotic component, which in the upper layers is represented by the active component of the fungi complex, the mycelium, and in the lower layer, by fungi spores. The share of prokaryotic biomass in the total microbial biomass does not exceed 25%. Thus, microbial biomass in oligotrophic swamps varies by season and profile, which may indicate real reproduction of at least part of the microbial complex not only in the upper layers, but also at depth.

Let us consider the activity of enzymes in the active layer of the PD of the catena (transitional part) (Fig. 16.2).

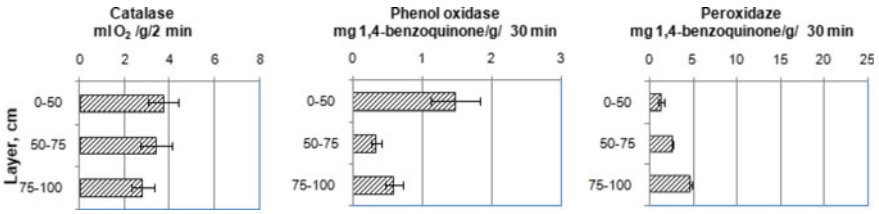


Fig. 16.2 Enzymatic activity in peat deposits of the Vasyugan Stationary, transitional part; average characteristics, (±) confidence interval

There is marked a uniform distribution of total catalase activity in the layer 0–100 of the PD. In general, the low activity of the enzyme polyphenol oxidase (0.33–1.48 mg 1.4-benzoquinone/g * 30 min) is noted for all PD. The upper, well-aerated layer of the PD (0–50 cm) is characterized by the highest activity of polyphenol oxidase, which corresponds to a high content of microorganisms, in particular, fungi. With depth, there is a tendency to a decrease in the activity of polyphenol oxidase. Peroxidase activity, on the contrary, increases with depth, which was noted earlier in both eutrophic and oligotrophic peat deposits (Szajdak et al. 2011; Inisheva et al. 2016).

Eutrophic swamps are characterized by much better conditions of peat formation. Their abiotic component is characterized by a variety of elements and their high content in comparison with oligotrophic swamps. This is due to the connection of the PD with groundwater rich in mineral compounds. Accordingly, the biotic composition is different. Let us consider their properties on the example of the swamp of Tagan Stationary in the forest-steppe zone of Siberia. The composition of OM shows that eutrophic peats is rich in HA, water-soluble and easily hydrolyzed compounds in comparison with oligotrophic peats discussed above. Water-soluble and hardly hydrolyzed substances of peat are contained in the amount of 19.04–49.76% of the average value, the content of hardly hydrolyzed substances in eutrophic peat varies from 6.09–13.35%. The content of total nitrogen varies from 1.76–3.52%. High content of macro- and microelements in eutrophic peats is noted. Peat ash in the Tagan swamp contains a significant amount of calcium, as a result of which peat has a slightly acid reaction (pH 5.8–6.8), a lot of iron, magnesium, and silicon. The content of microelements are given in Table 16.4.

Such favorable conditions for the formation of the eutrophic PD determined the increase in all biotic and abiotic components in swamp waters (Fig. 16.3).

Eutrophic swamps are characterized by a higher saturation of microbial groups in the upper 1-m-thick layer (Table 16.5). It is in this very layer that the biogenic and abiogenic composition of waters is formed, which then get into river streams.

It is important to note that weather conditions influence on the number of microorganisms. The average numbers of bacteria and fungi spores were higher during the wet period. The effect of weather conditions on mycelium microorganisms determined the nature of their profile distribution. In the dry period, a deeper penetration of the fungal and actinomycetes mycelium into the PD was noted.

Table 16.4 The content microelements in the peats of the eutrophic swamp of Tagan stationary

Layer (cm)	Microelements													
	Sm	U	Ce	Ca	Lu	Tb	Th	Cr	Yb	Au	Hf	Ba	Sr	Nd
0–25	0.2	0.2	2.5	1.3	0.02	0.028	0.5	3.7	0.1	0.002	0.2	228	33	0.29
25–50	0.2	0.1	2.1	1.1	0.01	0.007	0.3	2.0	0.1	0.002	0.1	121	60	1.60
100–125	0.2	0.1	2.6	1.1	0.01	<0.010	0.7	4.0	0.1	0.004	0.1	132	60	1.90
175–200	0.3	0.2	2.7	1.4	0.03	0.029	0.5	3.7	0.1	<0.001	0.1	118	71	0.89
250–275	0.3	0.2	3.8	1.6	0.02	0.042	0.6	4.9	0.1	0.002	0.2	78	80	1.70
Layer (cm)	Microelements													
	As	Sb	Ag	Br	Cs	Sc	Rb	Fe	Zn	Ta	Co	Na	Eu	La
0–25	26	1.0	<1	42	0.24	0.54	1.8	2.2	40	0.023	2.2	0.04	0.03	1.23
25–50	30	0.1	<1	37	0.04	0.39	<1.0	1.9	20	0.023	2.2	0.04	0.03	0.89
100–125	28	0.1	<1	46	0.14	0.50	2.9	2.2	52	0.053	2.2	0.05	0.06	1.12
175–200	26	0.1	<1	50	0.45	0.62	3.8	3.3	30	0.041	2.4	0.04	0.04	1.32
250–275	16	0.5	<1	27	0.40	0.60	3.6	1.2	26	0.026	1.7	0.06	0.03	1.23

Note Content of calcium, sodium and iron–in %, other trace elements–in g/t

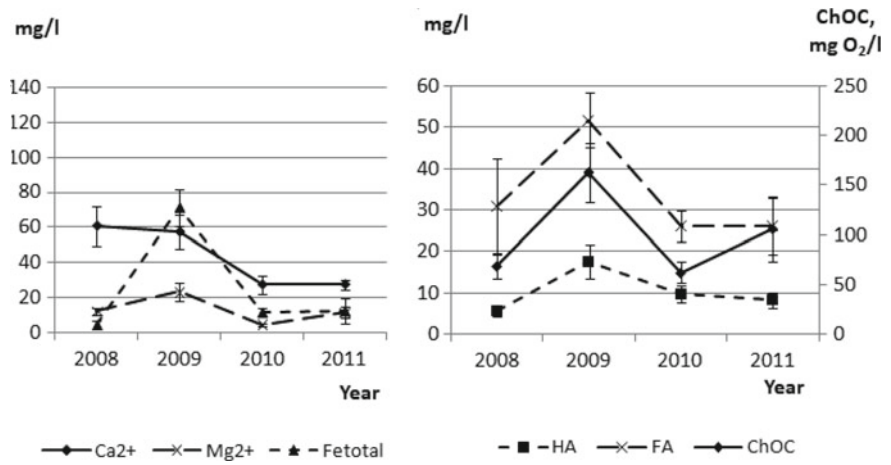


Fig. 16.3 The content of macro-components and organic substances in the waters of the eutrophic swamp over a long-term period. *Note* Fe_{total}—total iron, HA—humic acids, FA—fulvic acids, ChOC—chemical oxygen consumption

Table 16.5 Distribution of bacteria, fungi spores, actinomycetes and fungi mycelium in the layers of eutrophic swamp (Tagan) in dry (I) and wet (II) periods of observation

Observation periods	Layer, cm	Bacteria, 10^9 cells/g	Mycelium		Fungi spores, 10^6 spores/g
			Actinomycetes, km/g	Fungi, km/g	
I	0–25	50.5 ± 6.4	1.8 ± 0.3	0.4 ± 0.1	12.3 ± 2.7
	25–50	22.4 ± 9.0	0.6 ± 0.1	0.2 ± 0.06	10.1 ± 1.3
	100–125	21.3 ± 8.2	0.8 ± 0.2	0.2 ± 0.04	12.6 ± 2.3
	175–200	24.4 ± 1.6	0.2 ± 0.05	0.3 ± 0.05	14.6 ± 3.6
	250–275	12.0 ± 2.8	0.1 ± 0.03	0.0	14.2 ± 1.0
II	0–25	67.4 ± 5.2	1.6 ± 0.2	2.0 ± 0.3	32.4 ± 2.8
	25–50	49.7 ± 3.6	1.3 ± 0.2	0.0	46.8 ± 4.6
	100–125	35.3 ± 5.4	0.6 ± 0.1	0.0	22.4 ± 1.7
	175–200	55.2 ± 2.3	0.0	0.0	16.3 ± 2.7
	250–275	24.1 ± 3.2	0.0	0.0	18.2 ± 2.5

Microbial biomass in eutrophic PD varied from 0.4 to 13.2 mg/g, depending on the depth and weather conditions (Table 16.6). It was relatively evenly distributed along the profile and was decreased by 2–3 times only in the lower layer. The dynamics of microbial biomass, depending on weather conditions, occurred only in the surface layer (0–25 cm). In the wet period, its values were 2 times higher than in the dry period. The structure of microbial biomass also depended on weather conditions. In the dry period, the average values of the shares of the eukaryotic and prokaryotic

Table 16.6 Microbial biomass and relative proportion of different groups of microorganisms in the layers of eutrophic swamp in the dry (I) and wet (II) periods

Observation periods	Layer, cm	Microbial biomass, mg/g	Relative part (%)					
			In the total biomass		In the prokaryotic complex		In the eukaryotic complex	
			EUM	PRM	B	AM	FM	FS
I	0–25	1.8	39	61	93	7	90	10
	25–50	0.9	50	50	95	5	75	25
	100–125	1.1	60	40	93	7	79	21
	175–200	1.6	69	31	99	1	75	25
	250–275	0.4	36	64	99	1	0	100
II	0–25	13.2	70	30	96	4	97	3
	25–50	1.4	24	76	95	5	0	100
	100–125	0.9	13	87	97	3	0	100
	175–200	1.2	8	92	100	0	0	100
	250–275	0.6	23	77	100	0	0	100

Note: *EUM* eukaryotic microorganisms, *PRM* prokaryotic microorganisms, *B* bacteria, *AM* actinomycetes mycelium, *FM* fungi mycelium, *FS* fungi spores

components were approximately the same. In the wet period, fungi dominated in the surface layer; in the rest of the deposit, bacteria, the share of which was 76–92% in microbial biomass, predominated. In both periods, the bacterial component dominated in prokaryotic biomass (93–100%), and the share of actinomycetes mycelium was, respectively, from 0 to 7%.

So, in a eutrophic swamp, the dynamics of microbial biomass was detected only in the surface layer, in which its values were much higher during the wet sampling period. In the rest of the profile, microbial biomass was characterized by values of the same order in different periods of observation. In the structure of microbial biomass, the proportion of prokaryotic microorganisms was high, which, depending on the depth and time of sampling, varied from 30 to 92%.

Compared with oligotrophic swamps, eutrophic swamps are distinguished by higher rates of enzymatic activity (Fig. 16.4).

Thus, the total catalase activity in the PD of the eutrophic swamp is almost 2 times higher, and the peroxidase activity is 15 times higher than the indicators characteristic of the upper half-meter-thick layer of the PD of the oligotrophic swamp.

We will consider similar parameters on the example of the swamps of the Gorny Altai region. According to the types of structure of vertical soil belts, associated with altitudes and common bioclimatic features, the Gorny Altai region is divided into three areas: Northern, Central and Southeast (Kovaleva 1973). Table 16.7 shows the hydrochemical composition of swamp waters.

The swamp waters of the Northern Altai are characterized by pH values from 4.0 to 7.8 with average values of 6.1 $\pm$ 0.56, low mineralization (average value of

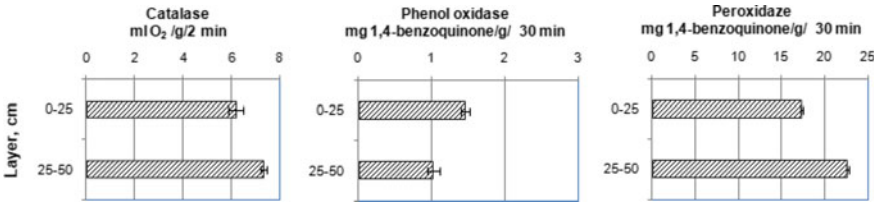


Fig. 16.4 Enzymatic activity in the peat deposit of the Tagan swamp; average characteristics, (±) confidence interval

Table 16.7 Chemical composition of swamp waters of the Altai (mg/l)

Components	Northern Altai	Central Altai	South-Eastern Altai
Ca^{2+}	1.0– 64.0[a] 19.4±11.47	28.0–98.0[a] 65.7±12.6	7.0–12.0[b]
Mg^{2+}	0.3–9.1 3.3±1.55	4.3–28.6 12.7±3.9	1.2–3.0
NH_4^+	0.2–1.2 0.6±0.19	0.1–1.2 0.6±0.2	0.2–0.5
$Na^+ + K^+$	11.5–39.9 25.3±4.7	16.3–88.9 45.4±11.4	8.1–11.3
Fetotal	0.8–4.6 2.2±0.68	0.1–0.4 0.3±0.1	–
HCO_3^-	30.5–244.0 98.8±38.45	164.7–475.8 348.7±51.6	42.7–54.9
NO_3^-	0.8–6.2 2.8±0.97	0.1–0.6 0.2±0.1	<0.1–1.2
pH	4.0–7.1 6.1±0.56	7.3–8.3 7.7±0.1	6.7–8.0
HA	3.5–10.1 6.9±1.32	1.0–6.3 3.8±0.8	2.7–5.3
FA	6.5–33.0 19.5±4.68	6.7–26.6 16.5±3.7	5.7–12.5
General mineralization (g/l)	0.164–0.302 0.2±0.02	0.13–0.58 0.33±0.07	0.05–0.06

[a] In the numerator—extreme values, in the denominator—the average and medium error; dash—lack of data. [b]2 swamps were investigated; *HA* humic acids, *FA* fulvic acids

0.2 g/l), high content of specific organic acids (HA–6.9, FA–19.5 mg/l. Comparing swamp waters of the Northern Altai with swamp waters of oligotrophic and eutrophic swamps of the southern taiga of Western Siberia, related by landscape-geochemical zoning to the region with a biological cycle of calcium-nitrogen type in combination with silicon-nitrogen, acidic and acidic gley classes of water migration, we obtain the following conclusions: swamp waters within the Northern Altai are characterized by higher mineralization, a high content of a number of ions and compounds (Ca^{2+}, Mg^{2+}, Na^{+}, K^{+}, HA) and lower values of mobile compounds of iron, ammonium and FA (Inisheva and Inishev 2001; Khoroshavin and Efimenko 2015).

In the swamp waters of the Central Altai, mineralization increases due to the increase in the content of Ca^{2+}, Mg^{2+}, Na^{+}, K^{+}, HCO_3^{-} ions, which determines an increase in pH in the direction of alkalization. At the same time, there is a decrease in the content of biogenic components (NH_4^{+}, NO_3^{-}) and total iron. The content of HA in the swamp waters of the Central Altai decreases by half as compared to the swamp waters of the Northern Altai, the content of FAs—by 30%. The climatic conditions of the South-Eastern Altai do not contribute to the intensification of the salinization process and, on the contrary, there is a decrease in the mineralization of swamp waters and, therefore, a decrease in calcium, magnesium and sodium ions. The content of HA and FA in the swamp waters such as in the Northern and Central Altai.

Let us compare the content of individual elements in the swamp waters in the southern taiga of Western Siberia and the forest-steppe and steppe of the Gorny Altai region (Table 16.8).

Almost all the elements in the swamp waters of the West Siberian swamps are in elevated concentrations compared to the swamp waters of the Gorny Altai region. The peculiarity of the swamp waters of the Gorny Altai region is the high content of HA compared to FA. These conditions contribute to the formation of a variety of active organic and organomineral compounds with increased migration capacity (Perel'man 1989). Previous studies on the group composition of OM in peats from the Gorny Altai region showed a high content of HA in peats compared with similar peats from the West Siberian Plain (Larina et al. 2009). This is the main reason for their increased content in the swamp waters of the Gorny Altai region, regardless of the structure of vertical zonality, associated with high-altitude levels and bioclimatic features.

Let us consider the activity of enzymes in the surface layer of the PD of the swamps of the Gorny Altai region (Fig. 16.5).

The results of studies of enzymatic activity show that in the surface layer of the PD of both the mesotrophic and eutrophic types swamps of the Gorny Altai region, oxidation-reduction processes occur intensively. Indicators of total catalase activity in the surface layer of the PD of both mesotrophic and eutrophic types are close, but do not reach 4 ml O_2/g in 2 min. It should be noted that in the eutrophic swamp Turochak (the Gorny Altai region), the total catalase activity compared with the eutrophic swamp Tagan (Western Siberia) was on average 1.7 times lower. Perhaps this is due to the more acidic reaction of the medium in the PD Turochak (pHsol 4.36–4.71), which is less favorable for the action of catalase. The peat deposit of the

Table 16.8 The content of individual elements in the swamp water of different types of swamps and territories (μg/l)

Element	West Siberian			Gorny Altai			
	Eutrophic reclaimed swamp	Eutrophic reclaimed swamp	Eutrophic swamp	Eutrophic swamp, Turochak	Mesotrophic swamp, Choiskoe	Eutrophic swamp, Balanak	Mesotrophic swamp, Kutyush
Sm	1.2	1.8	0.5 – 1.4[a] 0.9 ± 0.1	0.64	0.02	0.04	0.15
U	41.1	–	2.6	0.04	0.03	0.01	0.01
Au	0.1 – 0.6 0.2 ± 0.0	0.1 – 0.6 0.3 ± 0.0	0.03 – 0.16 0.08 ± 0.0	0.002	0.01	0.002	0.01
Hf	1.0	0.8 – 3.0 1.3 ± 0.1	0.6 – 2.6 1.7 ± 0.4	0.30	0.07	0.04	–
Cs	2	6.4 – 7.4 4.6 ± 0.4	1.4 – 1.5 1.0 ± 0.2	1.04	0.22	0.15	0.89
Sc	0.2 – 0.6 0.3 ± 0.0	0.2 – 2.1 0.8 ± 0.1	0.2 – 1.5 0.8 ± 0.1	1.88	0.33	0.14	0.24
Rb	299.9 – 645.0 441.4 ± 63.2	432.7 – 649.2 540.9 ± 43.2	73.3 – 258.9 157.4 ± 23.2	21.88	4.80	6.60	25.8
Eu	0.6	0.5	0.3 – 0.9 0.7 ± 0.1	0.13	0.05	0.05	0.05
La	10.0	9.4	2.6 – 7.8 4.6 ± 1.2	2.45	0.40	0.30	0.65
Tb	–	–	0.1 – 0.2 0.2 ± 0.0	0.11	0.01	0.02	0.03
Ce	28.2 – 79.2 46.8 ± 8.7	32.5 – 115.3 62.1 ± 14.6	36.7 – 129.5 78.7 ± 12.3	4.49	24.3	1.42	2.82

Note dash—this element is absent; [a] numerator—extreme values; denominator–average value and error of the mean

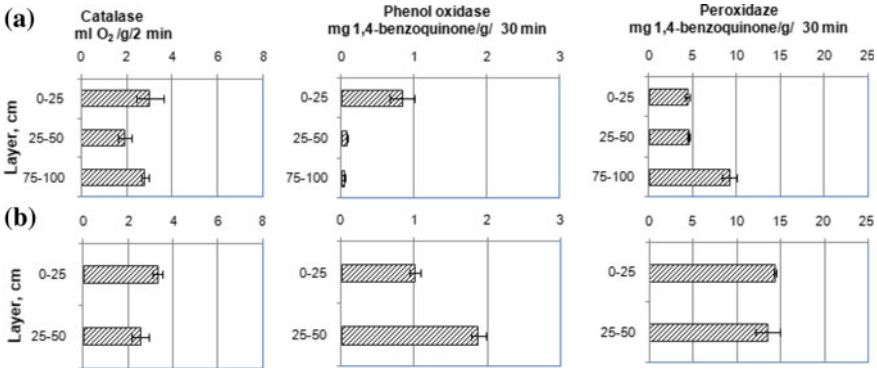


Fig. 16.5 Enzymatic activity in peat deposits of the swamps of the Gorny Altai region. *Note* **a** mesotrophic Kutyushsky swamp; **b**—eutrophic Turochaksky swamp; average characteristics, (±) confidence interval

eutrophic bog (Turochak) is characterized by a higher activity of polyphenol oxidase (1.6 times) and peroxidase (2.3 times), compared to the PD of the mesotrophic swamp Kutyush. Deep down in the PDs of both the eutrophic and mesotrophic types of the Gorny Altai region, there was a tendency to an increase in the activity of polyphenol oxidase, as in the PDs of the West Siberian swamps.

16.4 Conclusions

Belonging to a specific geochemical region determines the qualitative conditions for the formation of biogenic and abiogenic properties of the PD. Thus, the characteristics of the underlying rocks of the study area (LP) contributed to the formation of an oligotrophic swamp with a richer mineral nutrition and, accordingly, a peculiar composition of swamp waters and the activity of biological factors.

Of great importance are the redox conditions of the 1-m-thick layer of the PD, in which the hydrochemical composition of the swamp waters with individual characteristics in each type of phytocenosis is formed during the vegetation period based on biochemical processes. The greatest concentration of almost all components is observed on the margin of the swamp (accumulative parts of LP) due to the migration of substances in this direction from autonomous part of LP.

Based on the characteristics of OM in the PD of the studied swamps, one can speak about the tendency of its high content, especially of FA in the swamp and surface waters of the swampy territories. At the same time, in the swamp and river waters of the Gorny Altai region there is a low concentration of FA, unlike the swamp waters of Western Siberia, in which their content reaches 80 mg/l or more. It is important to note that the content of HA in the swamp waters of Altai exceeds the content of

FA. In all likelihood, this can be attributed to the peculiarities of peats and swamp waters of the Gorny Altai region as a whole.

Studies of the biochemical activity of a layer of 0–100 cm of PD of swamps of different genesis have shown that the PD of mesotrophic and eutrophic types of swamps are characterized by higher biochemical activity in Western Siberia and the Gorny Altai region. In peat deposits biogenic catalase predominates. On landscape profile of geochemically linked swamps, a high overall biochemical activity is noted in the PD of an autonomous part. A high proportion of eukaryotic microflora is observed in the structure of the microbial biomass in the oligotrophic swamp, while prokaryotic microorganisms predominate in the structure of the microbial biomass of the eutrophic swamp. The processes of humification, in which polyphenol oxidase and peroxidase enzymes take an active part, proceed more intensively in the PD of the eutrophic type swamp. It is important to note the increase in peroxidase activity with depth in all studied PDs.

Thus, the migratory streams from the territory of Western Siberia, which is distinguished by oligotrophic swamping and an active manifestation of the peat formation process, influence the formation of the biogenic and abiogenic composition of surface waters. The role of OM as the most common in the processes of migration and concentration of elements in swamps with manifestation of PD genesis is obvious and requires further development and detailed elaboration.

References

Baird AJ (1995) Hydrological investigations of soil water and groundwater processes in wetlands. In: Hughes JMR, Heathwaite AL (eds) Hydrology and hydrochemistry of British wetlands. Wiley, Chichester

Bakhnov VK (1986) Biogeochemical aspects of paludification process. Nauka, Novosibirsk (in Russian)

Bazin ET, Kopenkin VD, Kosov VI (1992) Technical analysis of peat. Nedra, Moscow (in Russian)

Blodau C, Roehm CL, Moor TR (2002) Iron, sulfur and dissolved carbon dynamics in a northern peatland. Arch Hydrobiol 154(4):561–583

Glazovskaya MA (1983) Foundations of classification of natural ecosystems by sustainability to man-caused impact and prediction of landscape and geochemical regioning. Sustainability of geoecosystems. Nauka, Moscow (in Russsian)

Ilina SM, Drozdova OYu, Lapitskiy SA, Alekhin YV, Demin VV, Zavgorodnyaya Yu, Shirokova LS, Viers J, Pokrovsky OS (2014) Size fractionation and optical properties of dissolved organic-matter in continuum soil solution-,jg-river and terminal lake of a boreal watershed. Org Geochem 66:14–24

Inisheva LI, Inishev NG (2001) Elements of water balance and hydrochemical characteristics of oligotrophic bogs in the South taiga subzone of Western Siberia. Water Resour Manage 28(4):371–377. https://doi.org/10.1023/a:1010433319474

Inisheva LI, Szajdak LV, Sergeeva MA(2016) Dynamics of biochemical processes and redox conditions in geochemically linked landscapes of oligotrophic bogs. Eurasian Soil Sci 49(4):466–474. https://doi.org/10.1134/s1064229316040050

Ivanov VV (1994) Ecological geochemistry of elements B, vol 2. Nauka, Moscow (in Russsian)

Karyagina LA, Mikhaylouskaya NA (1986) The value of polyphenoloxidase and peroxidase activity in peat. In: Proceedings of the National Academy of Sciences of Belarus, vol 2, pp 40–41. Agrarian Sciences Series (in Belarusian)

Khoroshavin VY, Efimenko MG (2015) Factor analysis of conditions of formation of surface waters of the Northern taiga of Western Siberia. In: Biogeochemistry of technogenesis and modern problems of geochemical ecology (in two volumes), vol 1, pp 230–233. Barnaul (in Russsian)

Kononova MM (1963) Soil organic matter. Its nature, properties and methods of study. USSR Academy of Sciences, Moscow (in Russsian)

Kovaleva RV (1973) Soils of the Gorno-Altai autonomous region. Nauka, Novosibirsk (in Russsian)

Kozhevin PA, Polyanskaya LM, Zvyagintsev DG (1979) Dynamics of development of different microorganisms in soil. Microbiology 48(4):490–494 (in Russsian)

Kruglov YuV, Paromenskaya LN (1966) Modification gasometrical method of determining catalase activity. Soil Sci 1:93–95 (in Russian)

Larina GV, Ivanova AA, Nah Kazantseva (2009) Group composition of organic matter of peat of the Altai Mountains and some structural characteristics of humic acids. Tomsk State Pedag Univ Bull 3(81):110–116 (in Russian)

Mirchink TG (1988) Soil mycology. Moscow state University Publ, Moscow (in Russsian)

Orlov DS (1974) Humic acids of soils. Moscow state university publishing house, Moscow (in Russsian)

Perel'man AI (1989) Geochemistry, vol 5, 2 ed. Higher School, Moscow (in Russian)

Polyanskaya LM (1996) Microbe successions in soil. Thesis of doctorate science, boiling. Moscow (in Russian)

Rakovsky VE, Pigulevskaya LV (1978) Chemistry and genesis of peat. Nedra, Moscow (in Russian)

Reznikov AA, Mulikowskaya EP, Sokolov IYu (1970) Methods of analysis of natural waters. Nedra, Moscow (in Russian)

Shotyk W, Rausch N, Nieminen TM, Ukonmaanaho L, Krachler V (2016) Isotopic composition of Pb in peat and porewaters from three contrasting ombrophic bogs in Finland: evidence of chemical diagenesis in response to acidification. Environ Sci Technol 50:9943–9951

Szajdak LW, Inisheva LI, Meisner T, Gaca W, Styla K (2011) Activities of enzymes participating in redox potential in the two depths of Tagan peatland. Tomsk State Pedag Univ Bull 8:70–77

Vernadsky VI (1960) The biosphere. In: Selected works vol 5. USSR Academy of Sciences, Moscow (in Russian)

Yamble DS, Cshnitzer M (1973) The chemistry of fulvic acid and its reactions with metalions. In: Singer PC (ed) Trace metals and metalorganic interactions in natural waters. Ann Arbor Science Publishers Inc, Ann Arbor

Zvyaginzev DG (1980) Methods of soil microbiology. Moscow state university publishing house, Moscow (in Russian)

Chapter 17
Assessment of Long-Lived Radionuclides (^{3}H, ^{14}C) and Heavy Metals in Snow Cover of Urban Areas as Indicators of Environmental Pollution (St. Petersburg, Russia)



Sergey V. Lebedev, Marianna A. Kulkova, Larisa M. Zarina and Evgeny M. Nesterov

Abstract The main pollutants in urban areas are heavy metals and radionuclides. Sources of the long-lived radioactive isotopes ^{14}C and ^{3}H are nuclear explosions and nuclear power plant emissions. Increased concentrations of radionuclides in the components of the natural environment can be evidence of environmental contamination. The central districts of Saint-Petersburg (Russia) were chosen for monitoring studies on the distribution of heavy metals, tritium, and radiocarbon in the snow cover of an urban area. This area was chosen because of its concentrated population density and location near a main road, a rail traffic center, and industrial facilities. Samples of snow were taken in February–April of 2011 and 2012, and March of 2013 and 2014. Geochemical scale survey results of 1:100,000 and 1:200,000 were used to establish the classification boundaries of the tested parameters. The method of charting GIS ArcGIS scorecards of heavy metals and ^{3}H and ^{14}C distribution in the central districts of St. Petersburg and Pushkin is described. The study presented here indicates that the main sources of pollution in the central districts of the city are related to industry and highways.

Keywords Environmental pollution · Tritium · Radiocarbon · Heavy metals · Snow cover · GIS

S. V. Lebedev
Saint Petersburg State University, Saint Petersburg, Russia

M. A. Kulkova · L. M. Zarina (✉) · E. M. Nesterov
Herzen State Pedagogical University of Russia, Saint Petersburg, Russia
e-mail: lzarina@mail.ru

© Springer Nature Switzerland AG 2020

O. V. Frank-Kamenetskaya et al. (eds.), *Processes and Phenomena on the Boundary Between Biogenic and Abiogenic Nature*, Lecture Notes in Earth System Sciences,
https://doi.org/10.1007/978-3-030-21614-6_17

17.1 Introduction

Environmental pollution by radionuclides and heavy metals remains one of the most pressing problems of environmental safety. Of particular interest are the radiologically significant isotopes radiocarbon and tritium. These radionuclides are formed under natural conditions or as a result of nuclear reactions. The sources of ^{14}C and ^{3}H can be nuclear explosions and nuclear power plant emissions as well as nuclear waste burial. Increased concentrations in the components of the natural environment can indicate environmental contamination. Annual reports by the Ministry of nature and ecology of the Russian Federation [State reports of the Ministry of nature and ecology of the Russian Federation ()] announce the tritium concentrations in dynamic components of the environment and its monthly precipitation from atmospheric fall-out. Monitoring of radiocarbon (^{14}C) concentration in various components of the environment can also be of theoretical and scientific interest. Variations in radiocarbon concentration in the snow cover of a city can be an indicator of changes in the level of carbon-containing compounds in the atmosphere and, therefore, technogenic pollution of the urban environment.

Emissions of carbon-containing substances during the burning of fossil fuels reduce the concentration of radiocarbon in the environment (Suess effect) (Suess 1955). In other cases, for instance, the burning of modern organic or waste products, the emission of radiocarbon is increasing. As a rule, polyaromatic hydrocarbons (PAHs) are the main carbon-containing compounds in the urban environment. PAHs move in the atmosphere as airborne micro particles. They are transferred by means of airflows, and they precipitate in the form of dry or humid deposits such as dust, rain, snow, etc. (Edwards 1983; Lee and Grant 1981).

Other dangerous pollutants are heavy metals that emerge in the environment as the result of industrial activities and the development of transport, as well as traffic.

It is particularly important to conduct research on pollution by long-lived isotopes (^{3}H, ^{14}C) and heavy metals in the territory of big cities, which are the main centers of people's activity and, therefore, where the eco balance between human activity and habitat can be violated.

In this regard, the fastest and most effective method of environmental monitoring and detecting contamination in megacities is to examine snow cover. During its formation, snow effectively absorbs impurities from the atmosphere and accumulates not only wet atmospheric fall-out, but also dry dust emissions from transport and industrial sources (Temerev and Indyushkin 2010). Water formed in the process of snowmelt is an active conductor of aerosol and water-soluble forms of toxicants. Snow cover is an effective accumulator of aerosol pollutants, which fall from the atmosphere. During snow melting, these chemicals emerge into the natural environment, mainly in water. Heavy metals, unlike many other pollutants, are not involved in the processes of self-purification; during migration their concentration or distribution can be changed. When they get involved in all types of migrations and the biological cycle, they lead to contamination of the most important life-supporting natural environments: water, air, and soil.

For monitoring of tritium, radiocarbon, and heavy-metal distribution in the snow cover of St. Petersburg, observation points in the central districts of the city were chosen because the main road, rail junction, and industrial facilities are concentrated there. Snow samples were taken in February–April of 2011 and 2012, and in March of 2013 and 2014. For comparison, samples were also taken in a relatively successful ecological suburb—the municipality of Pushkin, Russia.

17.2 Objects and Methods

To determine the presence of heavy metals, mass sampling (127 samples) of the snow cover within the city of St. Petersburg was carried out in 2011. The entire area of investigation was divided into three polygons in order to analyze the research results and evaluate the quantitative indicators of areal snow pollution. The first polygon, "Vasilevskii Island" (an area of 11 km^2), lies within the Vasilevskii administrative district. The second polygon, "Central," is located in the historical center of St. Petersburg and has an area of 13.6 km^2. The third polygon, "Right Bank," is located within the Krasnogvardeiskii administrative district on the right bank of the Neva River and has an area of 22.2 km^2.

Snow probes were sampled from the entire depth of a snow column to obtain the data of snow pollution for the winter period. The depth of the snow columns varied from 35–50 to 62–87 cm (IMGRE 1990). The concentration of the main water-soluble forms of heavy metals (Bi, Pb, Zn, Cu, Ni, Fe, Mn, Cr, V, Co) was determined by means of an XRF-spectrometer "Spectroscan MAKS-GV". Most of these elements belong to the first class of toxicological danger, and they have high biochemical activity, toxicity, and cumulative ability.

The first observations of the concentration of tritium and radiocarbon in the snow cover were conducted in 2011/2012, mainly in the Vasileostrovskii and Admiralteiskii administrative districts. The results of the pilot observations allowed us to substantiate a network for monitoring observations of the presence of tritium and radiocarbon in various parts of the city. These results became the basic criteria for sampling and charting digital maps in GIS ArcGIS in 2013/2014.

In 2013/2014 the investigated area was divided into 4 polygons. The first polygon, "Vasilevskii Island" (an area of 11 km^2), is located within the Vasileostrovskii administrative district. The second polygon, "Central," is located in the historical center of St. Petersburg. It is in a rectangular shape with area of 10.1 km^2. The third polygon, "Right Bank," is located at the right bank of the Neva River and has an area of 26.5 km^2. Finally, the fourth polygon, "Pushkin," located within the territory of the Pushkin municipality, has an area of 2.9 km^2. The polygon outlines for "Vasilevskii Island" and "Right Bank" have complex shapes. The number of monitoring points determines the scale for the geochemical survey: for the three polygons "Vasilevskii Island", "Central", and "Pushkin", it corresponds to 1: 100,000; for the "Right Bank" polygon, the scale survey was 1: 200,000.

Snow samples were collected in tightly closing plastic or glass bottles. Preparation for the measurement of tritium in water (melted snow) included pre-filtering the samples through a paper filter "blue ribbon". Then the 50 ml specimen was distilled with the help of a "Libikh condenser" in the presence of $KMnO_4$ (1 g) and NaOH (1 g) to remove any organic material and other radionuclides, which could quench the scintillation flashes of tritium. The sample of 8 ml volume was mixed with 12 ml commercial scintillation cocktail OptiPhase HiSafe 3™.

Preparation of melt water samples for determining the presence of radioactive carbon was performed using a procedure that allows the sample to be enriched with carbon. The sample was mixed with a commercial cocktail, OptiPhase HiSafe 3™, in the proportion of 4 ml of the sample with 16 ml of the scintillation cocktail. The mixture was placed in a glass vial without ^{40}K.

Measurement of the radiocarbon and tritium activity was performed using a low-background scintillation counter, Quantulus 1220 (Kulkova et al. 2014).

An areal distribution of pollutants was charted in ArcGIS. As a topographic base we used a digital map model of St. Petersburg with a scale 1:10,000, which was presented in a shape-file format and used by the Committee on the Environment, Environmental Protection and Ecological Safety of St. Petersburg Administration. Gauss-Kruger projection Pulkovo-1942 with the central meridian of 30° (with shifted origin) was chosen for territory mapping. The Spatial Analyst GIS ArcGIS 10 module was used to chart a map of tritium and radiocarbon distributions for the testing area.

Taking into account the density of points of the monitoring network for interpolation of observations over the content of pollutants, we chose the method of inverse distance weighting (IDW). IDW calculates the values of the cells on average of the sum of the values of measuring points in the vicinity of each cell. The closer the evaluating point center of the cell, the more weight or influence its value has for calculating the average. This method assumes that the value of measured variable decreases with increasing distance from the measuring point.

17.3 Results and Discussion

17.3.1 Heavy-Metal in Snow Cover

The comparison of heavy-metal contents with national standards (MPC for water used for drinking, cultural, and community purposes) showed that the presence of metals in melt waters is 1–2 orders of magnitude lower than the values of MPC. However, since the pollutants from melting snow are getting into the soil and are accumulating there from year to year, the evaluation of heavy-metal concentrations in snow cover has a practical meaning, even if its value does not exceed MPC in a single season. In this case, the contamination by heavy metals can be expressed as Zc, which is an indicator of the level of pollution in the environment. For background, values of the calculations of Zc were published in Zarina et al. (2011) from monitoring

Table 17.1 Average concentrations of heavy metals (mg/l) and total pollution index (Zc) of snow cover St. Petersburg, 2011

Polygons	Mass sampling	Bi	Pb	Zn	Cu	Ni	Fe	Mn	Cr	V	Zc
1-Vasilevskii	34	0.002	BDL	0.053	0.020	0.002	0.069	0.014	0.006	BDL	16.4
2-Center	45	0.005	0.004	0.110	0.067	0.003	0.091	0.009	0.007	0.002	30.8
3-Right Bank	48	0.003	BDL	0.069	0.023	BDL	0.082	0.012	0.006	BDL	18.9
MPC		0.5	0.1	1.0	1.0	0.1	0.5	–	0.5	0.1	
Background		0.003	0.001	0.010	0.005	0.002	0.011	0.003	0.006	0.004	

Note BDL—Below detection limit; *MPC*—According to (Hygienic norms 2003); Background according to (Zarina et al. 2011)

snow cover from the St. Petersburg region in 2008. The results of that research are presented in Table 17.1.

Before charting the maps of the distribution of any parameter, it is useful to examine the nature of this distribution, based on the available data. Figure 17.1 shows the Zc frequency response of the entire sample (127 samples).

As can be seen from the figure, and given the statistical data, the distribution is not normal and has a clear asymmetry. This asymmetry is related to the presence of snow samples with relatively high Zc (more than 32). The average value of Zc was 22.7 ± 19.7; the median was 16.6; and the 75% quartile was 25.5. The discrepancy between the average and median, despite the fact that the median is much smaller, indicates the displacement of distribution function towards small values of the sample.

Analysis of the frequency response for the "Vasilevskii Island" and "Right Bank" polygons speaks of their similar character with Zc distribution for the entire sample: clear asymmetry related to the presence of snow samples with relatively high Zc (more than 32). The average value of Zc for "Vasilevskii Island" was 16.4 ± 14.6; the median was 13.4; and the 75% quartile was 18.2. The average value for "Right Bank" of Zc was 18.9 ± 19.8; the median was 13.3; and the 75% quartile was 23.5.

Significantly different were the frequency response of Zc distribution and statistical data for the "Central" polygon (Fig. 17.2). The average value of Zc, median and 75% quartile for polygon "Central" turned out to be much larger than for polygons "Vasilevskii Island" and "Right Bank": 30.8 ± 20.4; 24.2; and 49.8, respectively. Therefore, the historical center of St. Petersburg turned out to be the most polluted district, and the cleanest was "Vasilevskii Island".

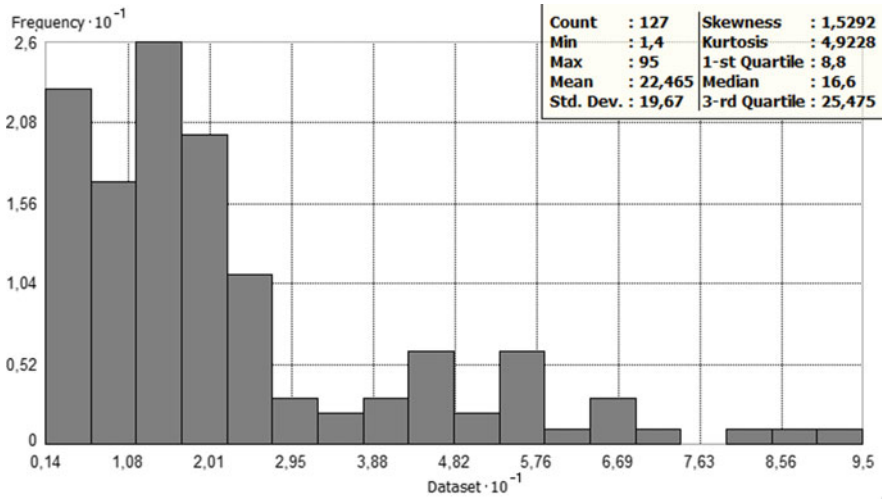


Fig. 17.1 Frequency response of Zc distribution in snow samples in 2011

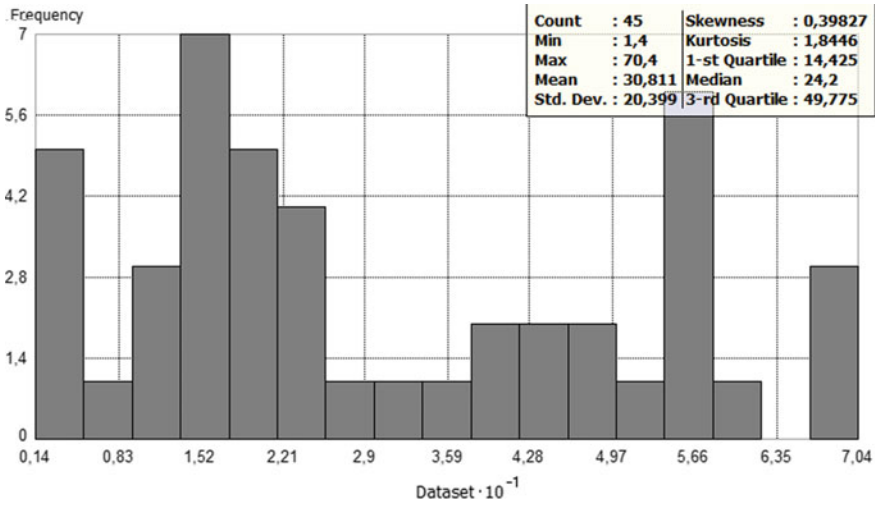


Fig. 17.2 Frequency response of Zc distribution in snow samples for "Central" polygon

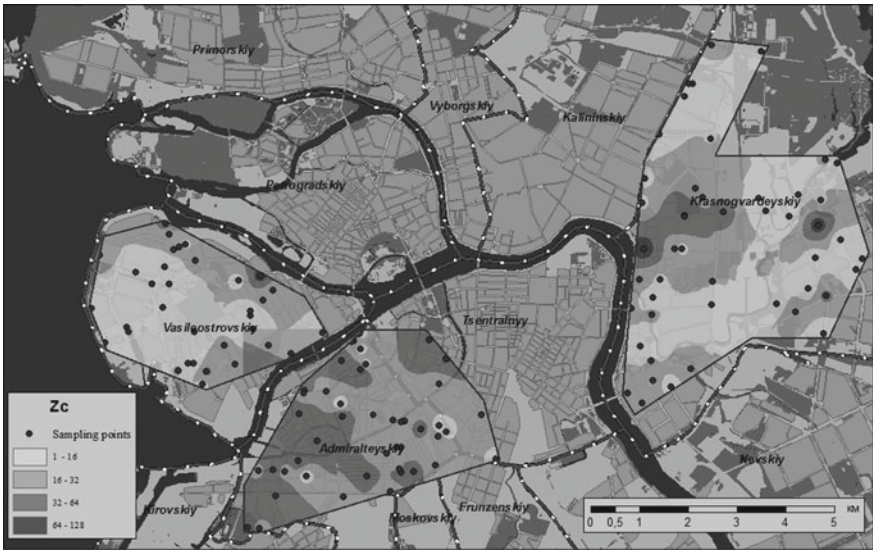


Fig. 17.3 Map of distribution of Zc in snow cover in St. Petersburg 2011

The Inverse Distance Weighting (IDW) method was chosen for observational data of Zc interpolation with the reference to density of the monitoring network. Figure 17.3 shows a digital map of the monitoring of snow pollution by heavy metals in 2011. The parameter variations (Zc) are indicated by filled contours on the GIS map (varying grayscale shades). Dots on the map show the sampling points.

The classification boundaries were selected in accordance with the 1990 publication (IMGRE 1990; Lebedev et al. 2017).

Zc values in the range of 16–64 indicate a low level of pollution, and values in the range of 64–128 are moderate. Although according to this classification most of the Zc indicator values correspond to the low level of pollution, the entire range of variations has been divided into four categories with classification boundaries of 1–16, 16–32, 32–64, and over 64 in order to show the specificity of territorial distribution.

17.3.2 Tritium in Snow Cover

Figure 17.4 shows the frequency characteristic of tritium concentration of the entire sample (44 samples) for the four polygons in 2013.

As the figure shows, and given the statistical data, the distribution is not normal and has a clear asymmetry. This asymmetry is relates to the presence of snow samples with relatively high tritium presence (up to 283.5 TU).

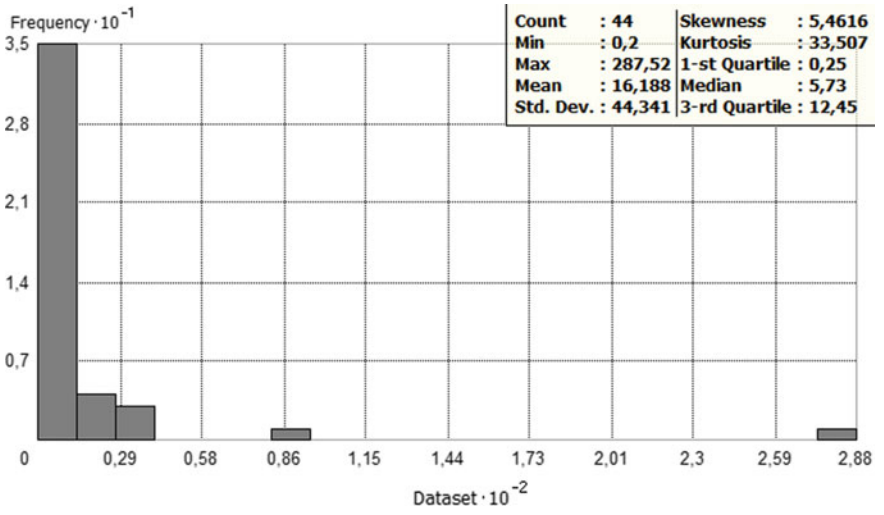


Fig. 17.4 Frequency characteristics of tritium distribution in snow samples in 2013

In such cases, the choice of the interval boundaries for classification in charting of the digital maps cannot have a strict mathematical basis and must ultimately be determined by the interpreter in the given field of thematic cartography. In order to create a scorecard, the number of classes and the boundaries of the intervals are defined and justified by the interpreter, depending on an empirically determined distribution of the investigated parameter and the properties of the research object.

Practice shows that 3–5 intervals of an analyzed parameter is an optimal number for characterizing the chemical pollution naturally accumulating in an environment. In this case, class boundaries should be coordinated with the GIS mapping regulations. The classification boundaries was carried out on the basis of the actual content of the isotopes in the snow that fell in 2013. Figure 17.5 shows the map of tritium distribution within the three central sampling polygons.

The variations in monitoring parameters in 2013 are shown as filled contours on the GIS map (varying grayscale shades), and correlations of parameters from years 2013 and 2014 are shown as pie charts.

Later we will compare the data collected over two years (2013–2014), but first we focus on analysis of the monitoring results in 2013. The territory of the "Right Bank" polygon turned out to be the most polluted with tritium. At the monitoring point at the Kosygina Prospect (in the area of Utkina Street, near the railway), the presence of tritium was 283.5 TU, and in the snow sample from the area of the influx of the Okkervil River into the Okhta River, the presence of tritium was 34.4 TU. The increased number here (Kosygina Prospect) is probably related to the nearby location of the Ladozhskii railway, as well as with the trash dump on the bank of the river. The average activity of the interpolated data is in the range of 49.2 ± 48 TU.

The monitoring results of the "Vasilevskii Island" and "Central" polygons show approximately the same average level of tritium concentration: 8.3 ± 8.8 and 8.4 ± 6.8 TU, respectively. However, the distribution

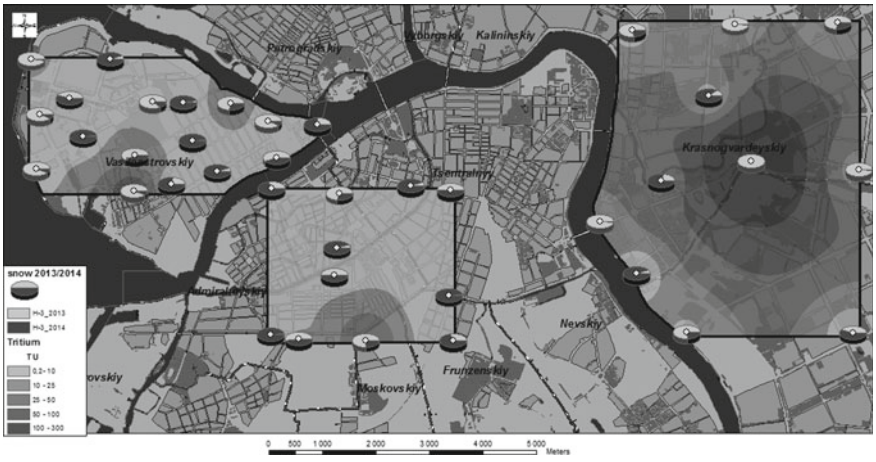


Fig. 17.5 Map of tritium distribution in snow cover from central part of St. Petersburg in 2013–2014

pattern of tritium is different. Within the "Vasilevskii Island" polygon, the maximum value reaches 84.2 TU (Shkipersky Garden). According to an analytical review by the Committee on the Environment, Environmental Protection and Ecological Safety of St. Petersburg City Administration, in this part of Vasilievskii Island there was an area of radioactive contamination managed by the Ministry of Defense. According to the review this area was not deactivated. Within the "Central" polygon, the maximum was 39.7 TU (Zaozernaia Street, 4). The "Reduktor" plant is located there (for the production of reduction gears).

As a result of interpolation, the average tritium presence in the snow cover for Pushkin in 2013 was 8.1 ± 4.6 TU (Fig. 17.6). This indicator does not differ much from the indicators for "Vasilevskii Island" and "Central" (8.3–8.4) However, a much smaller standard deviation indicates more equal distribution of an investigated parameter within the "Pushkin" polygon. In the four monitoring points the tritium activity has an interval from 5.9 to 7.5 TU. The maximum activity (29.1 TU) was registered at the eastern shore of the "Bolshogo Pruda" region. The minimum activity (2.25 TU) was registered at the point at the intersection of Konushennaya and Moskovskaya Streets.

The results of monitoring tritium content in the snow cover in 2014 create a slightly different picture. In the map in Figs. 17.5 and 17.6 the ratio of the measured parameter in 2013 and 2014 is shown with "pie chart" icons. If data for two years are equal, then the sector areas filled with different colors will be equal, i.e. the circle will

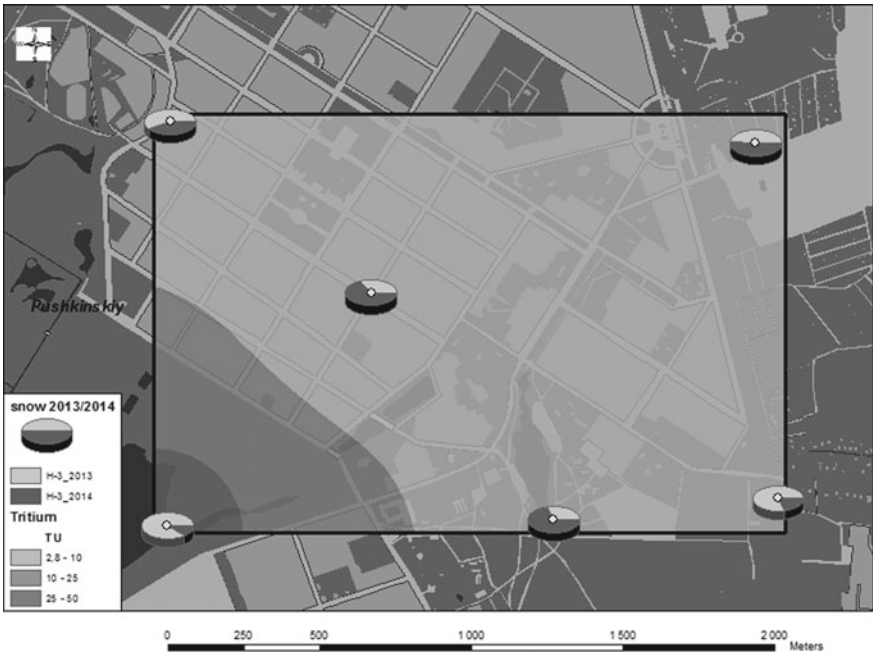


Fig. 17.6 Distribution map of tritium in snow cover from Pushkin in 2013–2014

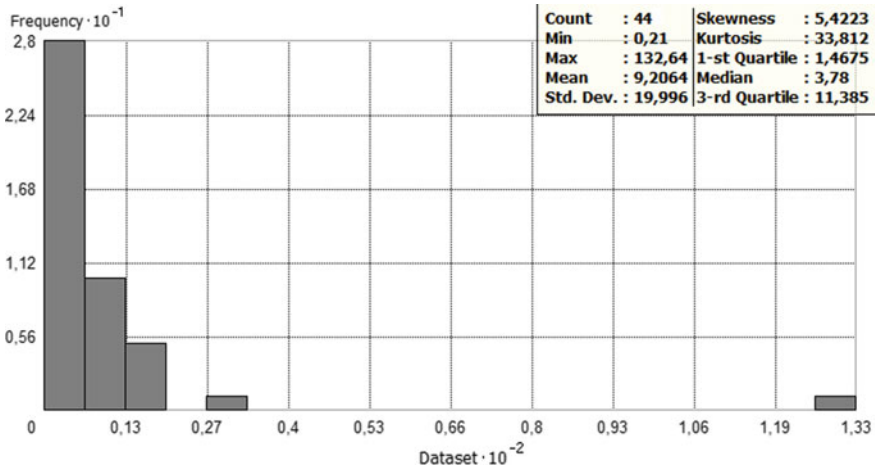


Fig. 17.7 Frequency response of tritium concentration distribution in snow samples in 2014

be divided in half (50%). If, in accordance with our legend, the light sector is larger, the values of tritium detected in 2013 exceed the corresponding values in 2014. If the sector appears to be darker, the ratio is reversed.

Figure 17.7 shows the frequency response of the distribution of tritium concentration in 2014 for the entire sample (44 samples) of the four polygons. As the figure shows, and given the statistical data (mean, median, skewness, kurtosis), the distribution is not normal (lognormal). The right tail of the distribution indicates the presence of a small number of individual elements of the sample with high values of tritium concentration (up to 132.6 TU). Attention is drawn to the identity of the character of the frequency characteristics shown in Figs. 17.4 and 17.7: note the large difference between the average and the median (2.8–2.4 times), and almost the same asymmetry (5.46–5.42) and kurtosis (33.51–33.81). Recall that for normal distributions, average and median are the same. The asymmetry index for symmetric distributions is close to zero. Kurtosis of the distribution density curve depends on the size of the tails of the graphics and gives a measure of how likely it will be that outliers will be encountered in the distribution. Distributions with relatively thick tails are "peaked" and have kurtosis greater than 3.

Just as in 2013, in 2014 the territory most contaminated with tritium was the "Right Bank" polygon. Thus, in a sample of snow from the area of the influx of the Okkervil River into the Okhta River, the concentration of tritium was 132.6 TU, and at the monitoring point on the corner of Partisan Street and Energetikov Prospect (Okhtinskoe Cemetery), the concentration was 33.3 TU (the "New Era" enterprise is located there, which is focused on the production of hardware for the manufacture of electrical-distribution equipment for ships). The average concentration of the interpolated data for the polygon is estimated at 20.7 ± 21.6 TU. Monitoring results for "Vasilevskii Island" show the lowest average level of tritium contamination to be 5.3 ± 2.7 TU; it is slightly higher at the "Central" polygon at 8.7 ± 3.3 TU.

The interpolation results have shown that the average tritium concentration in 2014 snow cover for Pushkin was 7.1 ± 2.8 TU. This indicator takes an intermediate value between the corresponding values of the "Vasilevskii Island" and "Central" polygons (5.3–8.7). Each measured value of the investigated parameter has an error. As a rule, it is determined by the instrumental (methodological) error, and by the error associated with the natural heterogeneity of the examined environment (sampling error). Each of these errors is caused by a variety of factors and has a quite complicated algorithm for quantifying its value. In our case, the instrumental and methodological error in determination of tritium does not exceed 10% rel., reaching 13–14% rel. occasionally.

As for the error determined by the natural spatial heterogeneity of the distribution of tritium in the snow cover, it can be estimated as the reproducibility of the measured indicators for the same field in different years—2013 and 2014. According to our observations, the reproducibility error of the monitoring data is estimated at 140% rel. (excluding two samples with a maximum of tritium). This number can be taken as a basis for assessment of the reliability of determining the concentration of tritium in the snow cover in St. Petersburg at a geochemical scale not less than 1:200,000 and registered as a result of monitoring during the 2011–2014 level of pollution of the investigated environment with the given radioisotope.

17.3.3 Radiocarbon in Snow Cover

Figure 17.8 shows the frequency response of the distribution of radiocarbon concentration in 2013 for the entire sample (44 samples) of the four polygons. As the

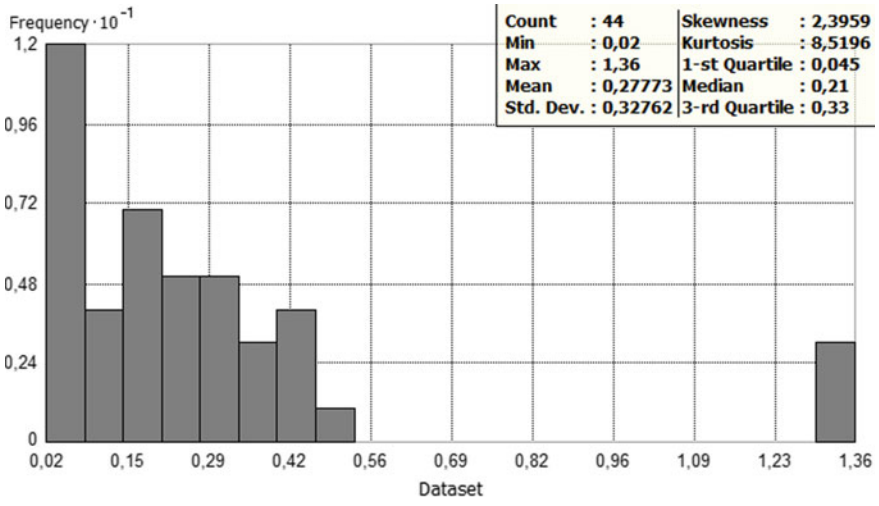


Fig. 17.8 Frequency response of distribution of radiocarbon concentration in snow samples in 2013

figure shows, and given the statistical data (average, median, asymmetry, kurtosis), the distribution is not normal (checking lognormal distribution did not give a positive result). The right tail of the distribution points to the presence of small amounts of individual elements of the sample with a relatively high value of radioactive carbon concentration (1.36 Bq/l). It should be noted that the parameters of asymmetric distribution of ^{14}C are not as obvious as in the case of tritium. For example, here the average and median differ by only 1.3 times.

Figures 17.9 and 17.10 show digital maps for monitoring 2013 radiocarbon activity. Values obtained after interpolation were divided into 4 classes with the following boundaries: <=0.2; 0.2–0.4; 0.4–0.8; and >0.8 Bq/l. The chosen interval limits are in agreement with the distribution of the frequency response of the investigated parameter within the three polygons ("Vasilevskii Island", "Central," and "Right Bank") and take into account the results of the pilot monitoring for tritium in 2011–2012.

The monitoring results from the "Central" and "Right Bank" polygons show approximately the same average level of pollution by radiocarbon: 0.37 ± 0.22 and 0.35 ± 0.17 Bq/l, respectively. Within the "Central" polygon, the maximum value of ^{14}C was recorded at the "Iusupovskii Garden" monitoring point—1.35 Bq/l. In general, snow in the center of the "Central" polygon contains more radiocarbon than snow in the marginal parts of the polygon. The northeastern part of the "Right Bank" polygon has higher radiocarbon activity compared to the southwestern part. Thus, the maximum ^{14}C = 1.36 Bq/l was registered in the northeast point (Sergei Lazo Street), and the minimum value of ^{14}C = 0.12 Bq/l was registered at the southwest border of the polygon at the "Oktiabrskaia Naberezhnaia, 20" monitoring point.

The territory of the "Vasilevskii Island" polygon has relatively smaller values of radiocarbon concentration in snow samples. The average activity of ^{14}C there is 0.26 ± 0.18 Bq/l. The maximum value of the radiocarbon activity, registered

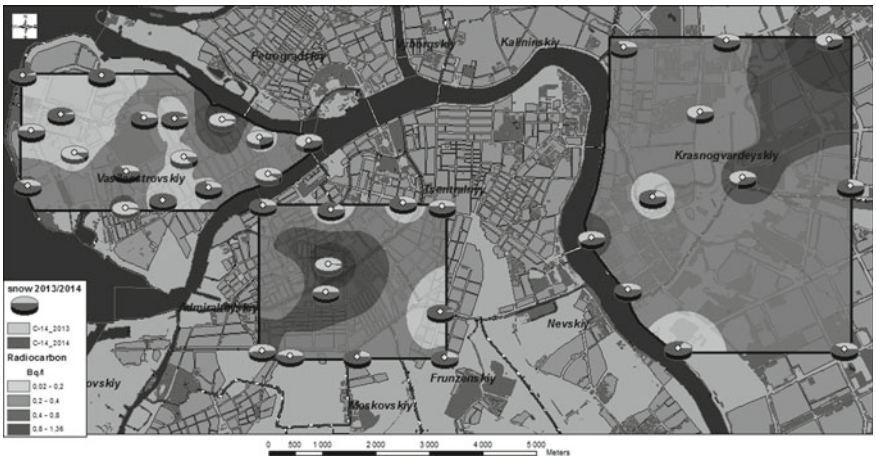


Fig. 17.9 Map of radiocarbon distribution in snow cover from central part of St. Petersburg in 2013–2014

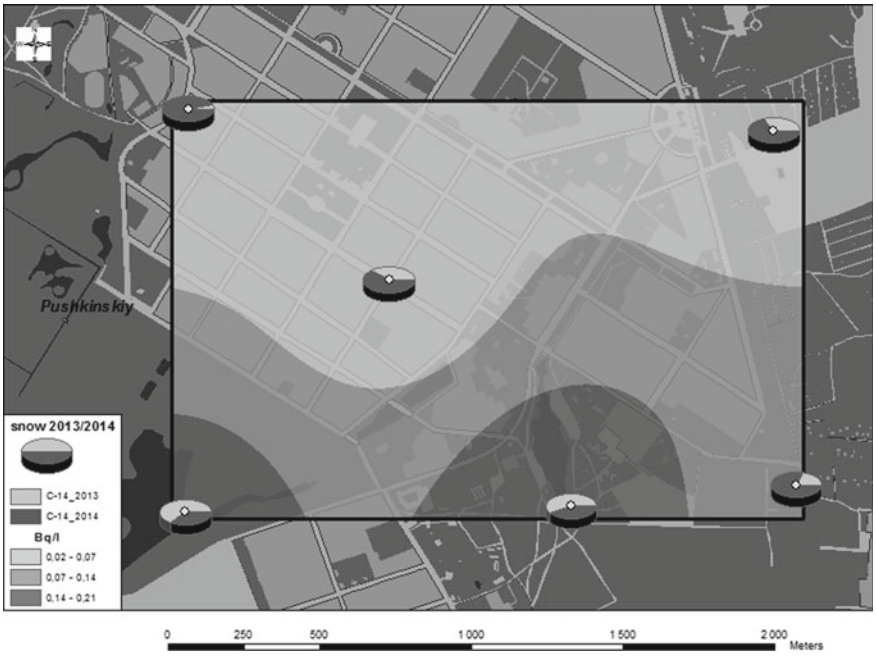


Fig. 17.10 Map of radiocarbon distribution in snow cover from Pushkin in 2013–2014

at the observation point "Corner of Malii Prospect and the Fourth Line" is equal to 1.36 Bq/l, i.e. is the same as in the two polygons described above. However, the presence of a greater quantity of samples with radiocarbon concentration at the level of background values determines the overall lower level of contamination of the snow cover with ^{14}C isotope in the territory of Vasilevskii Island. Snow cover in Pushkin differs significantly from that in the central districts. The average ^{14}C activity there is just 0.08 ± 0.05 Bq/l with a maximum of 0.21 Bq/l in the sample "Bereg Kolonistskogo Pruda". Monitoring results of radiocarbon concentration in snow cover in 2014 show a rather different picture. Figures 17.9 and 17.10 show the ratios of the measured parameters in 2013 and 2014, indicated by "pie chart" icons (for a detailed explanation of this process see the above description of the nature of the distribution of tritium in 2014). Figure 17.11 shows the response of the concentration distribution of radiocarbon in 2014 for the entire sample (44 samples) of the four test ranges.

As can be seen from the figure, and given the statistical data (average, median, asymmetry, kurtosis), the distribution is close to normal: the average and median are comparable in size, the symmetry index is less than 1, and the kurtosis is close to 3. Despite of the fact that in 2014 samples there are no values exceeding relatively large concentrations of radiocarbon in 2013 (up to 1.36 Bq/l), the average value 0.36 Bq/l is higher of the average in 2013 (0.28 Bq/l). Just as in 2013, the results of monitoring in 2014 at the "Central" and "Right Bank" polygons show almost the same average

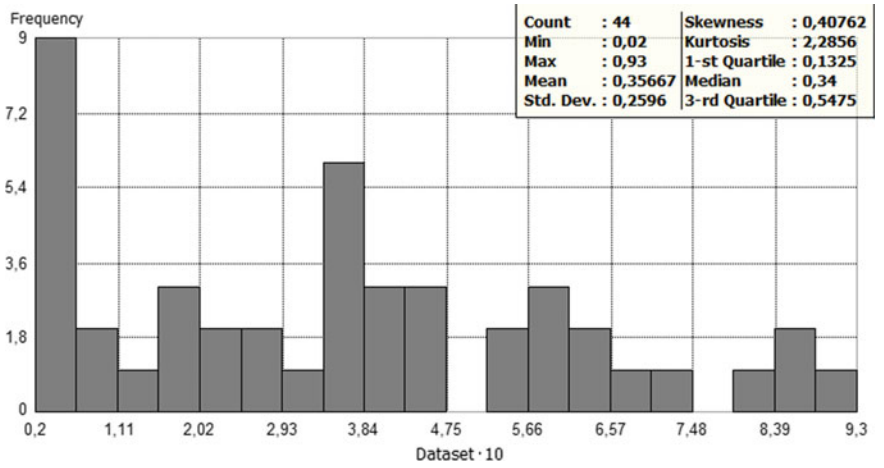


Fig. 17.11 Frequency response of distribution of radiocarbon concentration in snow samples in 2014

level of radiocarbon pollution: 0.44 ± 0.1 and 0.44 ± 0.15 Bq/l, respectively. The radiocarbon activity in snow from the central part of the "Right Bank" polygon is lower than in the marginal areas of this polygon. Besides, the radiocarbon activity in snow from the southern and southeastern parts of the "Central" polygon is higher in comparison to northern and northwestern parts. Similar to the monitoring data in 2013, in 2014 the territory of "Vasilevskii Island" is characterized by a relatively low value of radiocarbon concentration in snow samples. Average ^{14}C activity there is 0.26 ± 0.15 Bq/l (in 2013, 0.26 ± 0.18 Bq/l).

Snow cover in Pushkin differs significantly from that in the central districts. Average ^{14}C activity there is just 0.16 ± 0.09 Bq/l with a maximum of 0.44 Bq/l in the "Filtrovskoe Shosse" sample. However, this value is almost two times higher than in 2013.

17.4 Conclusions

Authors obtained the results of an ecological evaluation of the environment of St. Petersburg, as determined by monitoring the concentration of long-lived radionuclides (^{3}H, ^{14}C) and heavy metals in the snow cover.

According to the Zc parameter, in 2011 the most polluted snow by heavy metals was in the Admiralteiskii and Central districts of St. Petersburg. Within the "Central" polygon, the Zc level exceeded 24.2 in half of the samples, and for 75% of the samples, the value of the total pollution index was from 1 to 49.8. Overall, the southwestern part of the "Central" polygon was slightly more polluted. The greatest variations in the Zc parameter were found in the snow cover of the Krasnogvardeiskii administrative

district of St. Petersburg ("Right Bank" polygon)—from 1.5 to 95 arbitrary units. The historical center of St. Petersburg turned out to be the district most polluted by heavy metals, while the cleanest was Vasilevskii Island.

The territory of the "Right Bank" polygon turned out to be the most polluted by tritium. At the monitoring point at the Kosygina Prospect (in the area of Utkina Street, near the railway) the presence of tritium was 283.5 TU, and in the sample of snow from the area of the influx of the Okkervil River into the Okhta River, the presence of tritium was 34.4 TU. The increased number here (Kosygina Prospect) is probably related to the nearby location of the Ladozhskii railway, as well as with the dump on the bank of the river.

The results of comparison of ^{14}C and Zc concentrations in snow samples allow us to detect zones that are characterized by high concentrations of heavy metals and low concentrations of radiocarbon, as well as several zones that are characterized by increased value of both parameters. In the first case, these are highway areas, i.e. with intensive traffic as in Nevskii Prospect—where the reduction in radiocarbon concentration is a result of intensive traffic. In the second case, these are zones in which higher values of radiocarbon and heavy metals were recorded. One such zone has been identified in the territory of the "Right Bank" polygon (Irinovskii Prospect). It can be explained by the effect of an armored concrete factory on the environment. Increased values of both parameters in the central district could be related to the location of the Vitebskii railway, i.e. within the cargo-loading zone. In the "Vasilevskii Island" territory, an anomaly was detected at the end of the 8-liniii. This area has always had a predominantly industrial history. In 1880–1882, the main building of a paper factory named after VP Pechatkin was built there. This factory was later renamed the Golodaevskaia paper factory, and now is called JCS "Baltic Paper". Zones in which higher values of radiocarbon and heavy metals were recorded may be associated with PAH emissions that occur as a result of industry. One such zone has been identified at the territory of the "Right Bank" polygon (Irinovskii Prospect). Here the environment is influenced by a nearby factory that produces reinforced concrete and iron fittings. Increased values of both parameters in the central district can be related to the location of the Vitebskii railway, i.e. with the cargo-loading zone.

Further monitoring studies and charting of digital maps will provide an opportunity to increase the accuracy of mapping the pollution in St. Petersburg and to identify the areas with the most stable levels of pollution caused by long-lived radionuclides and heavy metals.

References

Edwards NT (1983) Polycyclic aromatic hydrocarbons (PAHs) in the terrestrial environment—a review. Environ Qual 12:427–441

Hygienic norms "Maximum permissible concentrations (MPC) of chemical substances in water of water resources of household-drinking and cultural-domestic purposes" in GN 2.1.5.1315-03. Moscow (2003)

IMGRE (1990) MR No 5174-90 Methodical recommendations on assessment of atmospheric air pollution of heavy metals on the base of their concentration in the snow cover and soils in inhabited localities. In: Revich BA, Saet YE, Smirnova RS (eds) (Appr 15 May 1990. No 5174-90), Moskow

Kulkova MA, Lebedev SV, Nesterov EM, Davydochkina AV (2014) Radiocarbon and tritium in environment water system of St. Petersburg region. J Humanit Sci 165:93–98 (Izvestia: Herzen University)

Lebedev SV, Agafonova EK (2017) Ecogeochemical estimation of environmental pollution by monitoring data of heavy metals contamination in soil and snow cover (at the example of Vasileostrovsky district of Saint-Petersburg). Vestnik SPbSU. Earth Sci 62(4):357–369

Lee SD, Grant L (1981) Health and environmental assessment of polycyclic aromatic hydrocarbons. Publisher Pattex, Park Forest Souza, Illinois, p 364

State reports of the Ministry of nature and ecology of the Russian Federation. http://www.mnr.gov.ru/docs/gosudarstvennye_doklady/

Suess HE (1955) Radiocarbon concentration in modern wood. Science 122:415

Temerev SC, Indyushkin IC (2010) Chemical monitoring of snow cover in the area of Barnaul's influence, vol 3(1). Izvestia of the Altay state University, pp 196–203

Zarina L, Lebedev S, Nesterov E (2011) Ecological geochemical investigations of the contents of heavy metals in the snow cover in the Saint-Petersburg region with application of GIS technologies. Int J Chem Eng Appl (IJCEA) 2(2):117–120

Chapter 18
Experience of Large-Scale Analysis of the Spatial Patterns of Plain Forest Ecosystem Productivity and Biogeochemical Processes



Sergei A. Tobratov and Olga S. Zheleznova

Abstract We considered the scale, causes, and factors of local variations of the biological productivity and heavy meals' uptake in forest ecosystems on the example of a model site of the subtaiga area of the East European plain (Russia, Meshchera lowlands). In accordance with the principles of Russian regional landscape science, we substantiated the leading role of the relief (including relict forms) and bedrock surface morphology as the production process factors. Based on the geological history analysis, we provided a genetic typification of morphostructures with forest productivity properties. It was revealed that the most significant decrease in the growth of forest-forming species (up to 50–60% of the zonal average) is observed within the pre-Pleistocene erosion cuts, and the highest bioproductivity (up to 1.5 times higher than the average in the East European subtaiga) is confined to the buried pre-Jurassic erosion butte composed of limestone. Due to the high density of limestone (1.20–1.33 times denser than other rocks in the territory), its local projections form positive gravitational anomalies, stimulating water exchange and reducing the effect of waterlogging. We have pointed out the genetic relationship of landscape processes in the Pleistocene and Holocene and the indicator role of periglacial forms: relics of flowing thermokarst correspond to the most productive forests, while offshore bars display the lowest productivity. Lithogenetic heterogeneities determine the spatial variability of the species composition, and, accordingly, 2-6-fold fluctuations of heavy metals' uptake are observed. The greatest potential resistance to priority toxicant—Cd—have ecosystems with maximum biological activity of tree stands and a high proportion of "humidicated" species.

Keywords Forest ecosystems · Biological productivity · Butte relief · Bedrock morphology · Gravitational anomalies · Heavy metals · Long-term immobilization · Xylem transport · Critical loads

S. A. Tobratov (✉) · O. S. Zheleznova
Ryazan State University Named for S.A. Yesenin, Ryazan, Russia
e-mail: tobratovsa@mail.ru

© Springer Nature Switzerland AG 2020

O. V. Frank-Kamenetskaya et al. (eds.), *Processes and Phenomena on the Boundary Between Biogenic and Abiogenic Nature*, Lecture Notes in Earth System Sciences,
https://doi.org/10.1007/978-3-030-21614-6_18

18.1 Introduction

The study of biological productivity and associated cycles of elements is an integral component of the assessment of the carbon-deposition capacity of forests, prediction of wood growth in the changing climate, and calculation of the resistance of natural ecosystems to anthropogenic pollution (Zamolodchikov et al. 2005; Glazovskaya 1998; Soldatov et al. 2014; Krivtsov et al. 2011). However, in most cases, bioproductivity is considered as an independent variable, while the contribution of the lithogenic factor is underestimated. This is due to the conservative biocentric bias of ideas about the energetics of processes in ecosystems, which is now recognized as a drawback rather than an advantage (Solntsev 2013). In our opinion, this leads to underestimating the internal conjugacy of landscape components established by the information-statistical modeling of landscape structure (Kolomyts 1999), as well as to misunderstanding the true causes of bioproductivity changes in space and over time.

This research was aimed at analyzing the relationship of the parameters of the biological productivity and some ecological and geochemical parameters of forest ecosystems with heterogeneities of the lithogenic base in a flat terrain environment. The studies were carried out in the center of the East European Plain, in the landscapes of the Meshchera natural province of mixed forests. Using the example of a small model territory, we revealed patterns typical of most lowland humid landscapes; in particular, we identified and interpreted significant intra-landscape variations of biological productivity and capacities of biological cycles of heavy metals (HM), determined by local elements of the buried relief. The variation scale is comparable with differences in the production process between adjacent natural areas.

The study was based on the key provisions of the Russian regional school of landscape science. According to these provisions (Solntsev 2001), the lithogenic basis is the most "strong" landscape component (due to its inertness and significant mass). It determines the system structure of ecosystems, distribution of organisms, species and ecological niches in space, as well as the direction and intensity of biogenic and water migration of elements. More "weak" landscape processes (including bioproductivity and uptake of nutrients) are not completely independent: their manifestations are mediated by lithogenic basis heterogeneities.

18.2 Research Subjects and Methods

The study area covered the territory of the Solotcha forestry enterprise with a total area of 389.6 km^2 (Fig. 18.1), located in the south-west of the Meshchera lowland (the center of the East European Plain) within the Prioksky morphostructural block that slowly descends at a rate of 0.5 mm/year (Aseyev and Vedenskaya 1962; Krivtsov and Vodorezov 2006). Similarly to entire southern Meshchera, it is dominated by pine and birch forests with inclusions of oak and spruce in the low-contrast relief of

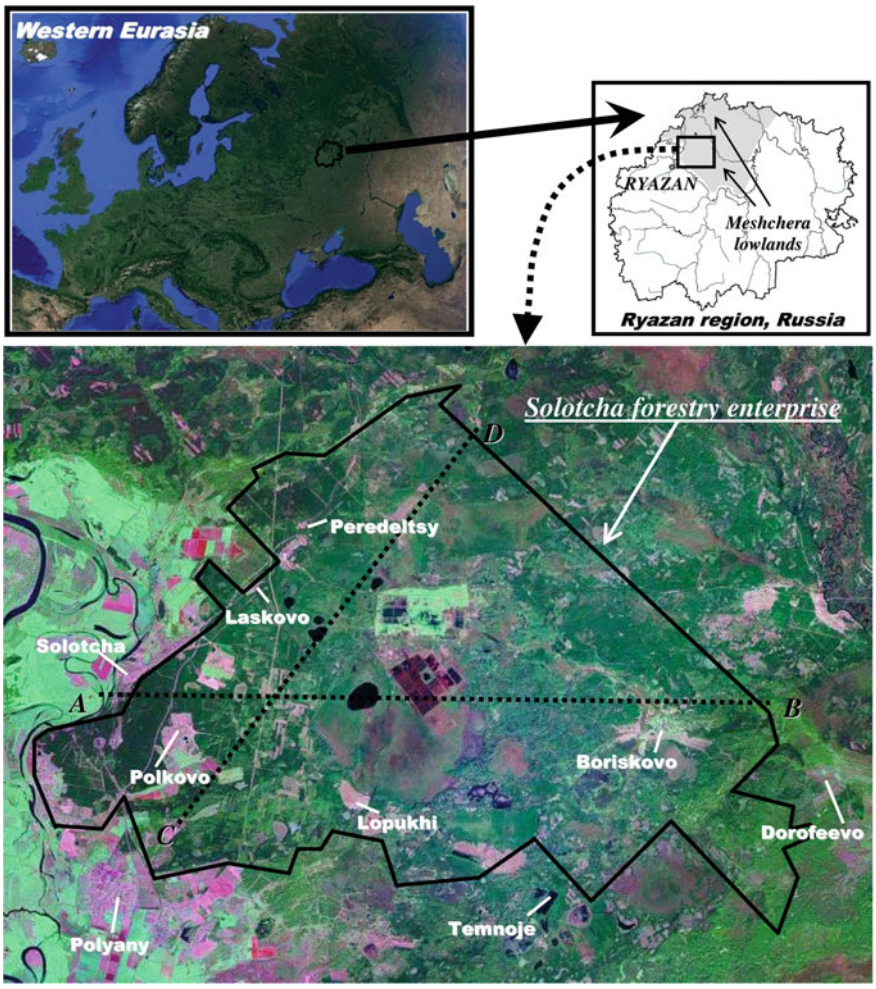


Fig. 18.1 Localization of the study area. *Note* A–B; C–D are the geological and geomorphological cross-section lines (see Figs. 18.4 and 18.5)

wet, damp, and marshy sandy plains. Obstructed hydrodynamics and a low trophic level of substrates are the main factors constraining the biological productivity of regional ecosystems. At the same time, the area under study is located in the "hydrothermal fracture" zone (Glebova et al. 2000) at the interface of the boreal and subboreal thermal belts. In the boreal belt, an increase in atmospheric moistening decreases the productivity of ecosystems, and in the subboreal belt, on the contrary, the phenomenon increases the productivity (Bazilevich et al. 1986). This creates contrasting conditions for the development of plants on positive and negative elements of the relief, even with small differences in relative elevations.

The primary information on the productivity of plant communities was obtained from the taxation descriptions of the state forest resource register. In total, we processed the data on more than 300 forest compartments (over 3000 forest survey plots). We used Microsoft Excel software to compile the information into a database in order to determine the quantitative parameters of the structure and functioning of the ecosystems. One of the most informative parameters in identifying local (intra-landscape) fluctuations of bioproduction process may be the tree stand status coefficient (C_{tss}), calculated for a particular phytomass fraction (with account of the average age of trees within the forest compartment) by the following formula:

$$C_{tss} = V_{actual}/V_{zas},$$

where V_{actual} is the actual stock of the fraction within this forest plot, V_{zas} is the zonal age standard of subtaiga forest stock in the center of the Russian Plain in the current climate (the global warming stage), as determined based on the database of Usol'tsev (2002). This report shows the C_{tss} values calculated for the key wood plant fraction stock: trunk phytomass with bark.

When compiling geological and geomorphological profiles, we used 1:25,000 topographic maps and materials of the Ryazan Branch of the Russian State Fund for Geological Information (the data based on drilling at a density of 1 well per 16 km^2).

The chemical analyses of the phytomass samples (mainly of wood and bark) included the drying, chopping, and acid decomposition of the samples in autoclaves using a microwave system (the volume ratio of the chemical agents per 1 g of the phytomass was 24.3:6:2:1 for HNO_3, H_2O_2, H_2SO_4, and HF, accordingly), and their further vaporization. The concentration of heavy metals was determined by the atom absorption method with a «Spektr 5-4» flame atomic spectroscope. To evaluate the heavy metal immobilization potential of the ecosystem vegetation, we synthesized the spatial estimates of the ecosystem phytomass productivity and volume and evaluated the content of the elements in various structural components of the phytocenoses.

The heavy metal balances were calculated based on the critical load approach. The main attention is paid not to the recyclical migration of HM, but to their long-term immobilization in wood and bark, which makes the greatest contribution to the natural buffering of forest ecosystems (De Vries and Bakker 1998; Krivtsov et al. 2011).

The leaching of heavy metals with surface water was calculated based on the hydrochemical (HM concentration) and hydrometrical (water flow) studies in the outlets of the drainage basins of small rivers in the research area with account of the water regime phases. The atmospheric fallouts of heavy metals were estimated based on the snow survey carried out in March 2010. The capacity of winter precipitation accumulated for the stable snow cover period (from the end of December till the middle of March, 78 days totally), and heavy metal concentration in the samples of snow water allowed us to estimate the average daily intensity of the atmospheric fallout of heavy metals onto the ground surface. The obtained data were extrapolated to the full-year cycle.

18.3 General Features, Systems Organization, and History of the Lithogenic Basis Development

The modern landscape structure of the area under study was formed in the Late Pleistocene: 11 geomorphological terrain-wide elements segregated (Fig. 18.2; Table 18.1). The locations differ by their average elevation, regular combination of exogenous landforms (structural basins, flat depressions, hillocks, ridge-like elevations, etc.), and their development history. This, in turn, determines the differences between the locations in hydrodynamics (drainage), marshiness, vegetation cover structure, and geochemical specialization of prevailing plant species. At the same time, the current processes of biogenic and abiogenic migration of matter depend on

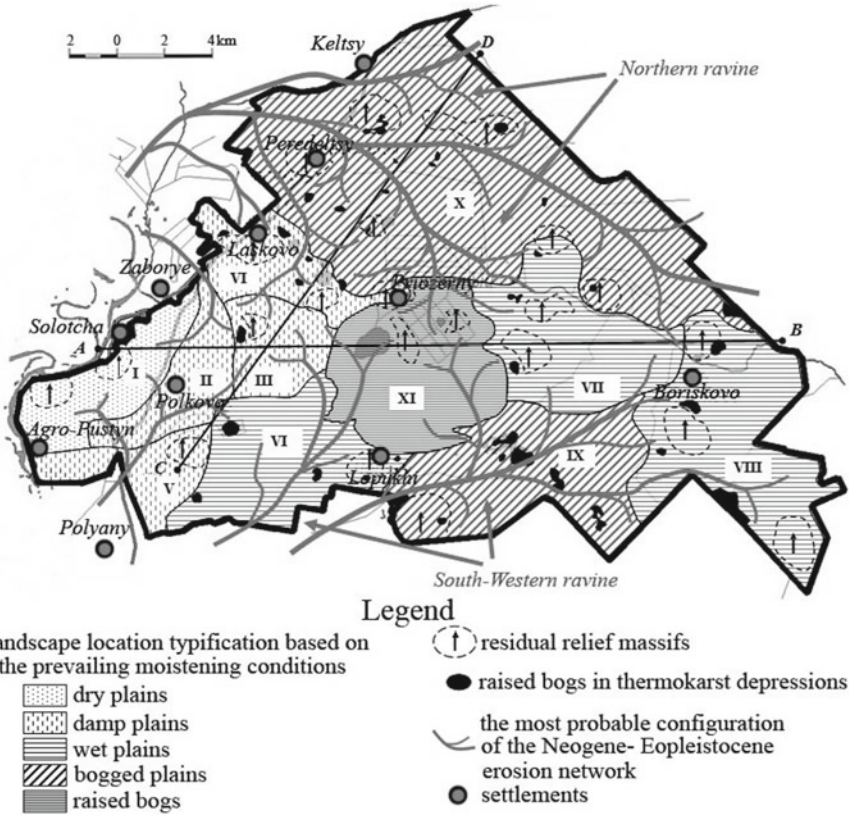


Fig. 18.2 Main elements of the landscape structure. *Note* I—Solotcha butte location; II—Polkovo depression; III—Pyatkino upland; IV—Lopukhi sloping plain; V—Polyany sloping plain; VI—Laskovo lake plain; VII—Boriskovo plain; VIII—Dorofeevo plain; IX—Peredeltsy plain (the former Northern ravine of the runoff); X—Temnoje plain (the former South-Western ravine of the runoff); XI—Krasnoye bog. A–B; C–D are the geological and geomorphological cross-section lines (see Figs. 18.4 and 18.5)

Table 18.1 Characteristics of the landscape locations of the study area

Subject name		Range of altitudes, m above sea level		Brief description	Share of tree species in the plant cover, %
		of the terrain	of the bedrock top[a]		
I	Solotcha butte location	118–130	103–112	Dry sandy plain with regions of ridgy and hilly sands	Pine—92.4; birch—3.1; willow—2.6; oak—1.6; aspen—0.2; ash—0.1
II	Polkovo depression	110–120	104–106	Wet flat sandy plain with isolated lakes	Pine—85.4; birch—12.7; aspen—1.4; oak—0.2; spruce—0.2
III	Pyatkino upland	116–126	91–109	Wet sandy plain with structural basins, often marshy, in the upper parts of the slopes	Pine—63.7; birch—25.9; aspen—8; spruce—2; oak—0.5
IV	Lopukhi plain	106–117	69–80	Wet sloping undulating plain; inter-hummock depressions are often swamped	Pine—67.1; birch—26.2; aspen—4.2; alder—1.9; spruce—0.4; oak—0.1
V	Polyany plain	106–112	87–93	Wet sloping plain	Pine—79.1; birch—17.3; aspen—2.9; maple—0.5; ash—0.1
VI	Laskovo lake plain	114–122	85–102	Wet sandy plain with thermokarst lakes, massifs of residual relief, and raised bogs	Pine—45.7; birch—40.6; aspen—10.5; oak—2.4; linden—0.6; alder—0.3

(continued)

Table 18.1 (continued)

Subject name		Range of altitudes, m above sea level		Brief description	Share of tree species in the plant cover, %
		of the terrain	of the bedrock top[a]		
VII	Boriskovo plain	106–117	83–97	Wet, poorly dissected sandy and light loamy plain with a general slope of the relief from west to east and series of fens confined to the floodplain of the Belaya River	Birch—55.5; pine—18.5; aspen—12.3; alder—9.4; oak—2.8; spruce—1.2; linden—0.3
VIII	Dorofeevo plain	109–112	83–95	Wet, sandy and light loamy plain with massifs of residual relief, raised bogs and fens	Birch—41.7; pine—31.7; aspen—16.5; alder—6.2; oak—1.9; spruce—1.9
IX	Temnoje plain	110–117	77–85	Mostly bogged plain, correspond-ing to the ancient erosion cut; the surface is complicated by drainage channels	Birch—48.2; pine—39.9; aspen—5.7; alder—4.3; oak—1.9; spruce—0.1
X	Peredeltsy plain	112–120	76–85	Bogged sandy undulated plain with extensive raised bogs and residual relief massifs	Pine—54.3; birch—40.2; aspen—2.6; alder—2; spruce—0.6; oak—0.2; willow—0.1

(continued)

Table 18.1 (continued)

Subject name		Range of altitudes, m above sea level		Brief description	Share of tree species in the plant cover, %
		of the terrain	of the bedrock top[a]		
XI	Krasnoye bog	113–119	82–96	Asymmetric raised bog, complicated by an ameliorative network	Birch—55.2; pine—41.5; aspen—3.2

Note [a]Throughout the study area, the bedrock is represented by Jurassic clays and aleurites. The exception is the Pyatkino upland (partly also Polkovo depression), where the Neogene lacustrine-alluvial sands occur

The list of forest-forming species: pine—*Pinus sylvestris*, birch—*Betula pubescens* and *Betula pendula*, aspen—*Populus tremula*, oak—*Quercus robur*, spruce—*Picea abies*, alder—*Alnus glutinosa*, willow—*Sálix álba* and *Sálix cáprea*, ash—*Fráxinus excelsior*, linden—*Tília cordáta*

relict elements of the lithogenic basis, "embedded" in the morphology of modern landscapes.

Among the morphostructural heterogeneities of the study area, the largest ones took shape in the Late Paleozoic, more than 280 million yr BP, when the first continental period of the study area development began after the Upper Carboniferous tropical sea regression (Fig. 18.3) (Organova and Voyloshnikov 1991).

The results of our drilling data processing showed the presence of two sublatitudinal valley cuts in carbon limestone deposits, which created the North and South-West ravines (locations IX and X, as well as I, VI, and VIII), separated by the butte-type Belsky paleo drainage divide (locations III, VII, and XI) with a relative elevation of at least 30 m and relics of pre-Upper Jurassic denudation (Figs. 18.4 and 18.5). Thus, the main morphological heterogeneities of the limestone roof are of ancient, Upper Paleozoic age. These heterogeneities have a key effect on the modern landscapes of Meshchera, determining both the configuration of the landscape location boundaries and spatial variability of biogeochemical processes.

The dominance of subtropical seas in the Upper Jurassic and Cretaceous was followed by a new continental period that continued from the early Cenozoic. The study area was the ablation zone during the major part of the period (Krivtsov and Vodorezov 2006; Organova and Voyloshnikov 1991), which, in particular, led to the complete erosion of the Cretaceous sands and exposure of Jurassic clays. The water-resistant properties of clays contributed to the enhancement of denudation, formation of a developed drainage network (Fig. 18.3) and numerous erosion buttes of various size with a relative elevation from 3–4 to 30 m (Fig. 18.5), significantly affecting the current hydrodynamics. The pre-Upper Jurassic erosion network tended to recover. However, the axis of the Northern Ravine shifted 5–6 km to the west. This western shift is a general trend for the paleovalleys of the Russian Plain in the Cenozoic (Spiridonov 1978). This is how the elevated Solotcha butte was formed (location I),

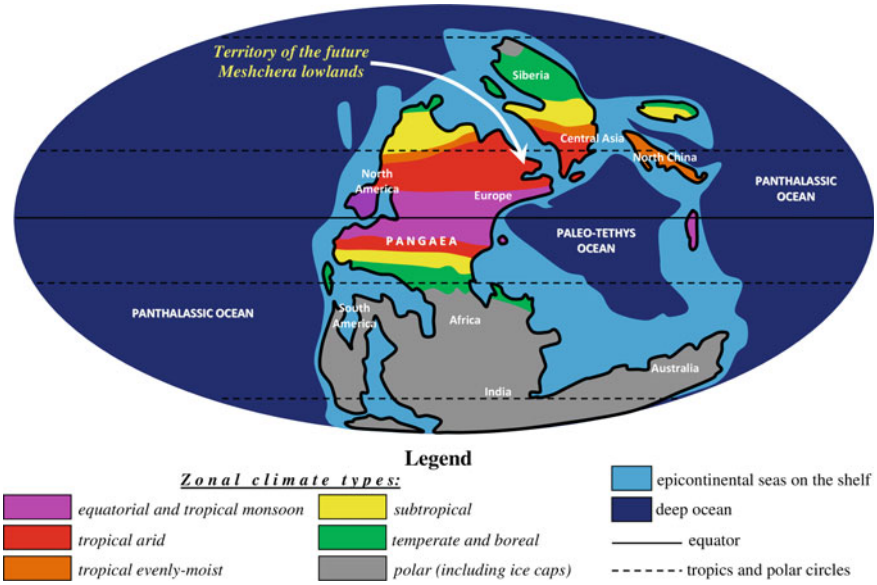


Fig. 18.3 Localization of the study area within the northeast region of Pangaea in the Early Permian (Sakmarian: 290 Ma) during the period of the main buried relief elements' segregation. *Note* The erosion and karst relief-forming processes in the Permian and Triassic mainly developed in the conditions of a tropical arid climate, which determined the canyon-like shapes of the erosion cuts and well-marked butte segregation. Only in the Upper Triassic, the climate became more humid due to the drift of this region of Pangaea to the north. Compiled according to the palaeogeographic reconstructions of Scotese (1997), Ushakov and Yasamanov (1984)

which currently has the most favorable conditions for the growth of monodominant pine forests (5.1). Subsequently, linear erosion divided its surface into several domes; currently, the introduction of birch and linden is taking place within the interdome depressions.

At the Pliocene stage of neotectonic activation, the Meshchera river network was completely restructured twice. In the mid-Pliocene, the submeridional valley of paleo-Don (Organova and Voyloshnikov 1991; Spiridonov 1978) shifted to the study area, cutting off the lower reaches of the main rivers that had existed since the Paleozoic. Ever since, the general direction of the surface runoff has changed from eastward to southwestward (in the late Pleistocene, the eastward path partially recovered). The short period of active penetration of paleo-Don was followed by a long-lasting phase of alluvial sand accumulation. According to the drilling data, the valley of paleo-Don's left tributary with a relative depth of up to 40 m was formed at the border of the Solotcha and buried Belsky buttes, and later ceased to exist after being filled with sandy alluvium (locations II and III in Figs. 18.3, 18.4 and 18.5). The differentiated tectonic movements in the late Pliocene led to the interception by ancient Oka of paleo Don's headwaters and the new phase of ablation due to the decreased erosion base level (Spiridonov 1978).

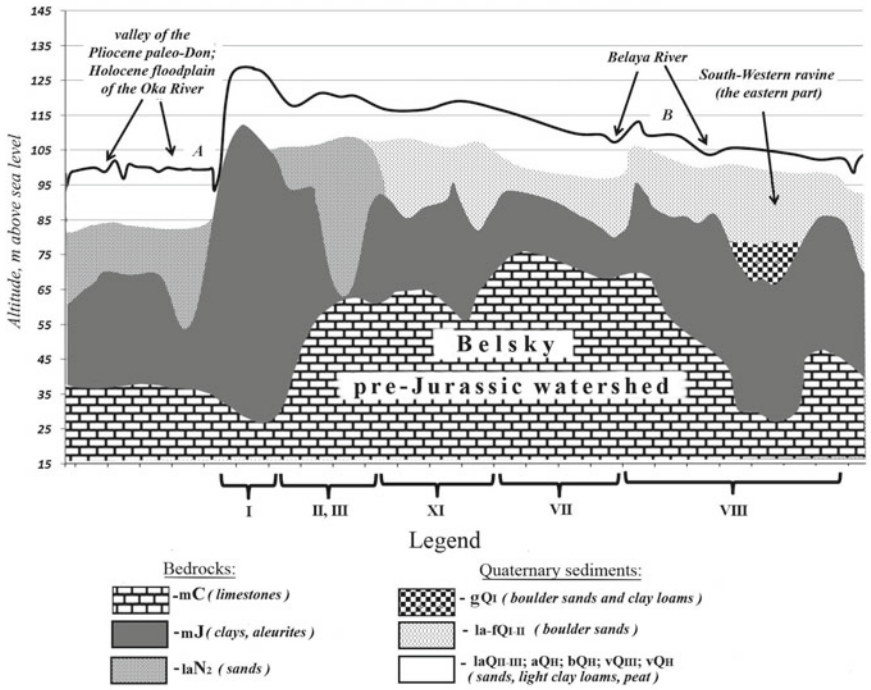


Fig. 18.4 Belsky limestone massif in the geological structure of the study area. *Notes* The Roman numerals designate landscape locations (see Fig. 18.2). Subdivisions of the Quaternary system are given in accordance with the General Stratigraphic Scale, used in Russia, which has some differences from ISS (Zhamoida 2015): Q_I and Q_{II} correspond to the Middle Pleistocene (Chibanian age: 781–126 ka BP), Q_{III} corresponds to the Late Pleistocene (Tarantian age: 126–11.7 ka BP). Genetic types of deposits and bedrocks: a—alluvial, b—biogenic (peat), g—glacial, f—fluvioglacial, l—lacustrine, m—marine, v—eolian

In the Eopleistocene, tectonic uplifting and progressive climate cooling intensified water exchange, promoted the erosion network differentiation, restoration and deepening of Paleogene and Neogene erosion cuts. At the same time, the main runoff took place along pre-Quaternary ravines (locations IX and X) southwestwards, as before. Pliocene sediments were found to be spread everywhere except in locations II and III. The reach of the above-mentioned valley of paleo-Don's tributary, thus, turned into a water parting and became another butte, being a typical inversion relief example (Figs. 18.4 and 18.5). The ravine-like depression of the buried valley in the surface of the regional aquiclude creates conditions for a water exchange slowdown, which markedly reduces the productivity of modern forests (5.4). However, in the conditions of a more contrasting relief of the Eopleistocene, water congestion in location III was not yet observed. On the contrary, a series of buttes formed a "watershed axis" of the territory, that extended approximately along line A–B and, as shown in Fig. 18.2, was densely dissected by smaller erosional shapes. The upper reaches

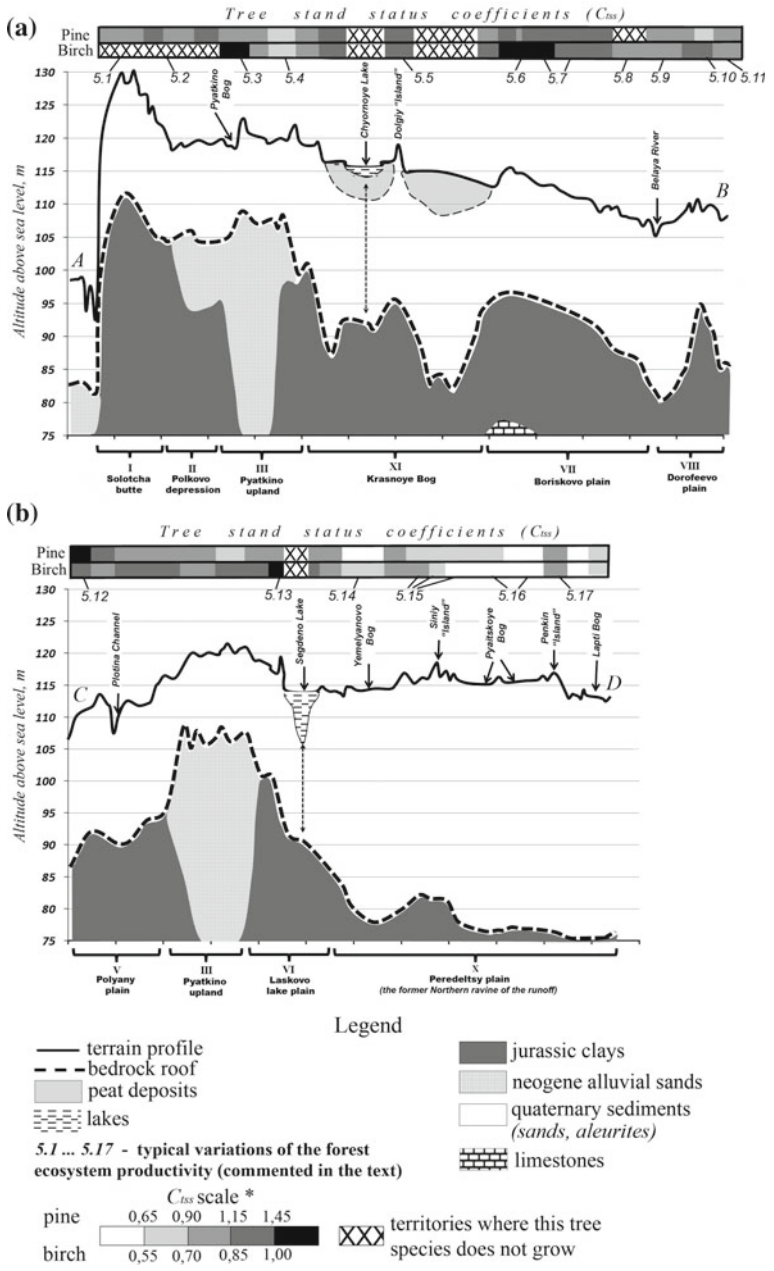


Fig. 18.5 Spatial relations of the lithogenic basis elements and bioproductivity, based on the results of profiling along lines A–B (**a**) and C–D (**b**). *C_{tss} are the coefficients of the favorable state of the main forest-forming species: pine (*Pinus sylvestris*) and birch (*Betula pubescens*), reflecting spatial variations of the production process. The coefficients were summarized by forest management compartments and are shown as diagrams above the profiles

of the buried Eopleistocene erosion pattern currently provide the conditions for the most obstructed runoff, which entails variations in the tree species composition and productivity of modern regional ecosystems.

By the beginning of the Neopleistocene, the area under study was a denudation plain, where the erosion dissection was several times denser and deeper compared to nowadays (Figs. 18.2, 18.4 and 18.5). However, the Meshchera lowland later became an accumulation area for morainal sediment washing products (Annenskaya et al. 1983; Aseyev and Vedenskaya 1962; Krivtsov and Vodorezov 2006; Organova and Voyloshnikov 1991), as a result of which not only the previously formed valleys, but also watersheds were buried. The most intensive phase of accumulation in the Middle Pleistocene Late Glacial (130–150 ka BP) formed the surface of the third terrace with the modern altitudes of 118–130 m above sea level, composed mainly of coarse-grained lake-alluvial sands (Krivtsov and Vodorezov 2006). In the Eemian (Mikulino) Interglacial and Mezin period of the Valdai (alternative names in other regions—Valdai, Weichselian, Devensian and Midlandian, Wisconsin) Glaciation—130–150 ka BP—the terrace surface was subjected to dissection. However, despite the decrease in the erosion base level (Aseyev and Vedenskaya 1962), the preglacial drainage network did not recover, mainly due to a drastic deterioration of the water-resistant properties of the relief surface rocks, compared to the Eopleistocene. In contrast to Jurassic clays, coarse-grained sands contributed (and contribute nowadays) to the runoff transfer from the surface into the underground, conserving the drainage network at the initial, primitive development stage. Under these conditions, local water exchange ceased to be systematic and local waterlogging became a critical issue. Waterlogging is the main barrier for bioproductivity in modern landscapes. Early Valdai erosion shapes occurred within the contours of the buried cuts that channeled groundwater flows, but were significantly less developed. Polkovo depression (II) is a good example. The upper elements of the buried drainage network were not "excavated" at all by backward erosion, and had been the waterlogging starting points starting from the Eemian Interglacial.

However, modern waterlogging is significantly inferior to what took place in Meshchera during the hygroscopic stages of the Valdai. In the early Valdai stade (Tver glaciation or Odderade phase: 71–57 ka BP), the erosion and redeposition of Middle Pleistocene sands resulted in the creation of the second terrace rising above the floodplain (within the interval of 110–118 m), which includes the main part of the area under study (Fig. 18.5). The increased moisture accompanied by a drastic drop in temperature caused the formation of numerous ephemeral lake-like reservoirs replenished with local runoff waters (Aseyev and Vedenskaya 1962). The reservoirs were interconnected with a chaotic network of wandering streams; their contours were formed by thermal erosion and thermal abrasion, and later by thermal karst. The periglacial flow paths, as in the preceding warm epochs, were controlled by the buried erosion pattern. Thus, numerous runaround buttes with surface elevations of 117–120 m (locally named "islands") were formed in locations IV–XI and are the projection of the pre-Pleistocene residual relief massifs onto the daylight surface (Figs. 18.2 and 18.5). Even being at a depth of 10–30 m and deeper, protrusions of

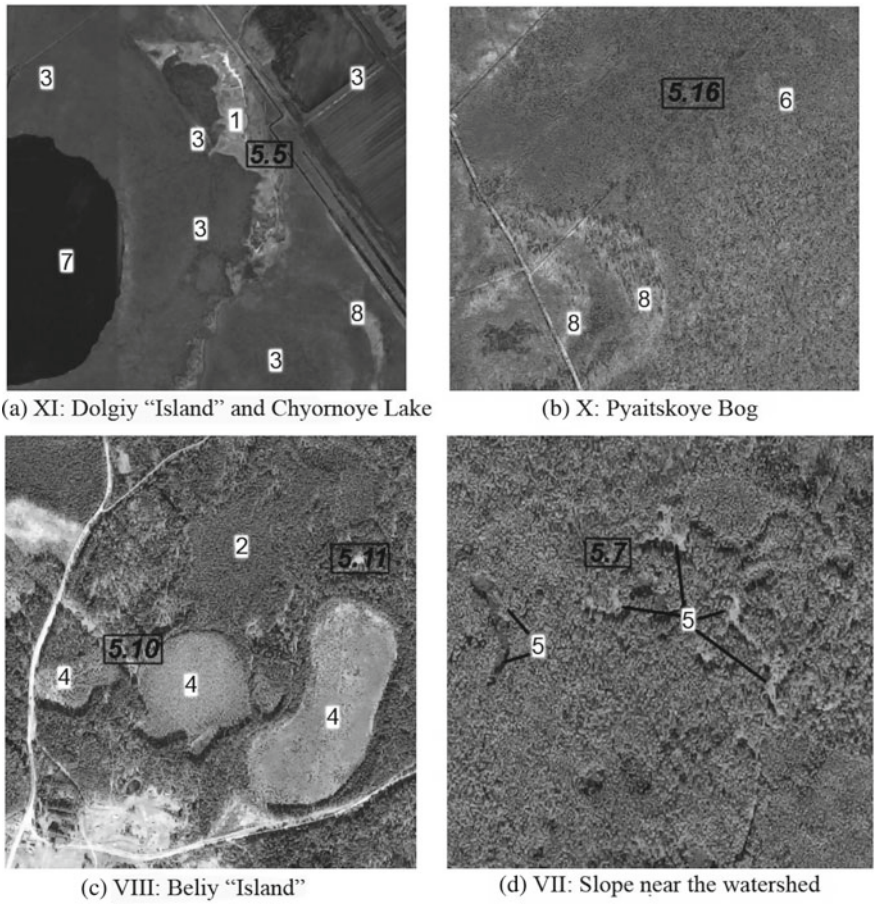
the Jurassic aquiclude enhanced water exchange, reduced moisture and ice content of the soil, ensuring the preservation of the surface of the third terrace from changes.

In the interstadial phase of the mid-Valdai, none of the warming waves reached the level of a typical interglacial (Vasil'chuk and Kotlyakov 2000; Organova and Voyloshnikov 1991; Velichko 2009), and the permafrost persisted, which together with the deepening of the Oka cut (Aseyev and Vedenskaya 1962) led to the emptying of the lake-like reservoirs and intensive incrustation of the surface with thermal karst. During that period, there was a distinctive stagnation of the headwaters of the buried erosion network, whose contours were the basis of numerous thermokarst depressions and structural basins, which currently mostly turned into raised bogs. Eventually, the characteristic of Meshchera close proximity of dry island-type watersheds (buttes of the Riss terrace) and raised bogs in alas-like depressions (Fig. 18.2) with fundamentally different productivity of phytocenoses (Fig. 18.5) arose.

The degree of thermokarst manifestation in the early and mid-Valdai strongly depended on the bedrock depth, reaching a maximum at an altitude of their roof of about 92 m above sea level (Fig. 18.5). Under these conditions, with the joint supply of surface and ground waters, structural basins of lakes were formed that did not undergo waterlogging in the Holocene. However, the most extensive thermokarst depressions are due to the thawing of syngenetic interstitial ice, and, therefore, the depth of periglacial reservoirs in them did not exceed 2 m. The slopes of the bottom surface of such reservoirs were less than the slopes of the equilibrium profile; therefore, areas of vortices arose, and coastal bars were formed on the north-eastern shores of some of them, according to the direction of the prevailing winds (Fig. 18.6). Round thermokarst basins of various types prevail in locations III–VI and VIII–XI and are a reliable marker of the most obstructed water exchange, not only during the Valdai, but even nowadays.

Against this background, the Boriskovo plain (VII) is distinctive, where, despite the "optimal" depth of the Jurassic aquiclude, not only did not massive ice wedges emerge, but also small alas-like depressions are few, while most of the latter are not round, as is typical of endorheic thermokarst, but elongated (Fig. 18.6d). This indicates that the excess of groundwater is able to be efficiently removed by lateral runoff there, which is due not only to the low density of pre-Pleistocene dissection of location VII (Fig. 18.1), but also to its confinement to the roof of the limestone massif of the Belsky paleo drainage divide (Fig. 18.4). The relative share of limestone is about 2600 N/m^3, which is 1.20–1.33 times heavier than that of naturally composed quaternary watered sand and Jurassic clays (Fig. 18.7). Consequently, the buried limestone butte forms a positive gravitational anomaly affecting hypergenic hydrodynamics (Filosofov 1960), and in the conditions of non-contrast relief, dominance of sandy sediments, and current tectonic subsidence, the role of lithological heterogeneities is especially large. Along the periphery of the Belsky massif in the region of the greatest gravitational potential, the middle-Pleistocene valley of the Belaya River, the main watercourse of the territory, was formed (Fig. 18.4).

At the same time, the central parts of locations IX and X are hypsometrically higher than the Boriskovo plain by 3–5 m, but have a less intensive water exchange and are waterlogged. As seen from Fig. 18.5, they are typical inversion structures,



(a) XI: Dolgiy "Island" and Chyornoye Lake (b) X: Pyaitskoye Bog

(c) VIII: Beliy "Island" (d) VII: Slope near the watershed

Fig. 18.6 Forms of periglacial relief and their combinations in Meshchera. *Note* Arabic numerals designate: residual relief forms—(1) linear swell-like elevations (locally named "Verei"), (2) areal (runaround buttes); marshy thermokarst basins—(3) early-Valdai round and oval, (4) late-Valdai round and oval (analogues of "alases" in Siberia), (5) elongated, lobed, and tree-like (flowing thermokarst relics), (6) areal (formed during the interstitial ice thawing), (7) thermokarst lake basins, (8) relics of offshore bars. Roman numerals designate landscape locations (see Fig. 18.2). 5.5 … 5.16 are typical fluctuations in the productivity of regional ecosystems associated with the lithogenic basis (see Fig. 18.5 and the text)

the axes of ancient erosion ravines, where linear erosion has not resumed since the Kalinin interval (for example, the Pyaitskoye bog 5.16). Closed rounded thermokarst basins were also formed in the Pyatkino upland (III): though its hypsometric position prevented moisture stagnation, but the inversion with respect to the aquiclude top turned out to be more important. Currently, all these structural basins are swamped to one degree or another, causing drastic bioproductivity fluctuations in location III (Fig. 18.3). The considered examples show that the position in the relief as a factor

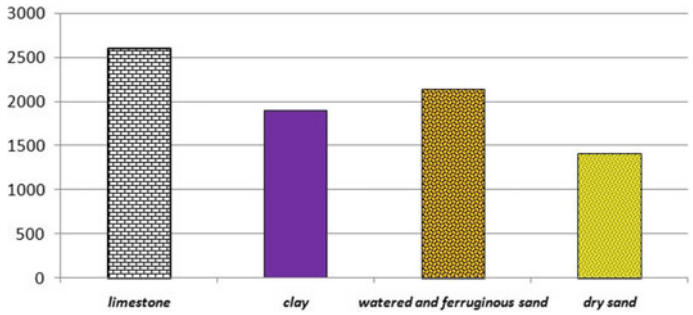


Fig. 18.7 Specific weight of Southern Meshchera bedrocks as a factor of local gravitational anomalies created by them, N/m^3: compiled according to Dortman (1984)

of local water exchange is not informative alone and should be considered together with the buried morphostructure analysis.

In late Valdai (25–14 ka BP), the first terrace rising above the floodplain took shape at an elevation of 100–110 m with its parts located in locations V, VII, and VIII. As in the early Valdai phase, a drainless thermokarst developed near the rear terrace suture. Simultaneously, specific forms of the relief took shape (for example, "alases", i.e. small structural basins), whose analogues are now widely represented in the permafrost zone in northeastern Eurasia (Fig. 18.6). During this period, the Northern and South-Western Ravines, which had existed since the Paleozoic, finally turned into buttes with slow water exchange, and the main runoff was concentrated in the valley of the Belaya River (Fig. 18.2).

18.4 Butte Relief and Relict Thermokarst Basins as the Factors of Ecosystem Functioning

According to Annenskaya et al. (1983), the most important distinctive feature of Meshchera's relief is the presence of buttes. As shown above, the tendency to growth of the buttes was manifested throughout the history of the region and reached its maximum in the late Pleistocene, at the stage of formation of the floodplain terraces of the Oka River and its tributaries with the contribution of neotectonic subsidence, migration of tectonic trench axes and accumulation of terrigenous sands. There are two main types of buttes in Meshchera:

(1) "inverted" (a buried erosion cut corresponds to an elevation of the hypsometric surface);
(2) residual relief massifs (with direct correspondence of the bedrock surfaces and modern relief).

Typical examples of "inverted" buttes are locations III, X, and XI, being the areas of extinct pre-Pleistocene valleys. They feature widespread waterlogging and the

most persistent negative anomalies of bioproductivity (5.4, 5.14, 5.16). The valleys consist of permeable sands, but this does not reduce waterlogging: excessive groundwater is not drained due to the undeveloped drainage network and deepening of the aquiclude surface, Jurassic clay, at the same time. As a result, the water balance of the territory has insufficient runoff, while the share of local evaporation increases, that contributes to waterlogging and catalyzed thermokarst in the Valdai. Waterlogging and drainless thermokarst are the two consequences of the same cause, affecting the same territory, but in different climates. Therefore, for example, relict offshore bars (Fig. 18.6b) can serve as an indicator of extremely low productivity of forests that cannot be raised by drainage amelioration (5.16).

The degree of bogging depends on the altitudes of the daylight surface and the roof of the regional aquiclude: the higher they are, the more intensive the drainage is with other factors being equal. Therefore, on the Pyatkino upland (III), thermokarst basins are small on the average (with the exception of the Pyatkino slope bog), peat is accumulated only in some of them, and bioproductivity decreases there (5.4) much slower, compared to the center of location X (5.16). Within the Northern and South-Western ravines, water-stagnation phenomena at the junction of paleorivers are particularly intensive (e.g. the aforementioned Pyaitskoye bog 5.16). Here, groundwater is so stratified and not dynamic that conditions are created for upland waterlogging, especially in location IX (Fig. 18.2).

However, raised bogs are usually located hypsometrically higher and are confined to the slopes of the second-type buttes, i.e. massifs of residual relief; lakes also usually tend towards those. They are located in the Valdai thermokarst depressions formed by ice wedges (in most cases, epigenetic) (Annenskaya et al. 1983). The formation of such depressions is mainly due to the feeding of the growing ice wedge with subsoil and surface waters flowing down the slopes of the buttes. At certain levels, water movement slowed down due to backwater, which led to the emergence of particularly large ice wedges. As already noted, the water flow path in both Valdai and modern landscapes is determined by the morphology of the roof of water-resistant bedrocks. At the same time, buried erosion buttes intensify water exchange and direct groundwater along the water course of the pre-Pleistocene erosion pattern. Nevertheless, the modern drainage network on the Neopleistocene sandy strata is much more primitive and has a low conveying capacity. Over the last 100–150 thousand years, Meshchera nearby the Oka River experienced a consistent decrease in the relief energy (Annenskaya et al. 1983; Aseyev and Vedenskaya 1962), as a result of which backward erosion exposed only a small portion of paleocuts, mainly in "elevated" locations I–VI, and only the primary ones. Where paleocuts are exposed, the number of thermokarst relics is reduced and bioproductivity increases drastically (5.12), which indicates the optimization of the water-air regime of the soil. But such cases, in fact, are rare.

Based on the above, we can state that the effect of residual relief on hydrodynamics and bioproductivity is ambiguous: intensification of water exchange at the butte roof is most often accompanied by water congestion in the middle part of its slopes. In the Ice Age, it led to the formation of a huge number of thermokarst basins of various sizes and shapes, complicating the slopes of the island buttes, which, due to

the conservative nature of sandy relief forms (Annenskaya et al. 1983), have been preserved to this day and are occupied by waterlogged low-productive coenoses. However, the average bioproductivity on the buttes of this type, such as valleys ("Verei") and "islands," is higher than that on the surrounding damp and marshy plains, due to the fact that their watershed areas are usually larger than structural basins. However, productivity grows higher when the butte has a sufficiently high hypsometric position of both the daylight surface and the bedrock roof. Otherwise, the butte is affected by the surrounding hydromorphic plains, the area of structural basins on its slopes grows, and the positive growth anomaly seems to diffuse (a typical example is the Siniy "island" in the center of the Northern ravine of the dell: 5.15). Among the buttes shown in Fig. 18.5, the most productive ones are the Dolgiy "island" stow (5.5) with absolute elevations of the relief and the roof of the Jurassic strata respectively 119 and 96 m, while, for example, the Penkin "island" (5.17) with the marks of 116 and 85 m is noticeably inferior to it; the Beliy "island" (5.10 and 5.11), being a butte of the second terrace with a "controversial" ratio of the elevations of the autochthonous bed and the daylight surface, occupies an intermediate position, being merely spotted with late-Valdai alas-like basins (Fig. 18.6).

Thus, in southern Meshchera and in the Valdai, even now there is a direct relationship between hydromorphism and the depth and morphology of the bedrock surface. This pattern is particularly clearly manifested within the Northern and South-Western ravines that are currently buried and have become, in fact, a system of "direct" and "inverted" buttes. The greatest waterlogging and the least productive coenoses correspond to the absolute elevations of the Jurassic top of 83 m and lower (especially in the areas of paleochannel confluence: 5.16). In the periglacial climate of the Valdai era, there were shallow lake-like flooded areas with unstable runoff and accumulation of syngenetic interstitial ice (Annenskaya et al. 1983; Aseyev and Vedenskaya 1962), and currently stows of wet and marshy depressed sandy plains prevail, which are difficult to drain (Fig. 18.6b). Consequently, the climate warming changed the process type, but the extremely low hydrodynamics could not change technically. Developed relics of epigenetic interstitial ice, both round and oval thermokarst basins, are present within the intervals of altitudes of the autochthonous relief of 83–100 m above sea level. These morphosculptures have a smaller area but are deeper than forms created by inherent ice (Annenskaya et al. 1983). Usually they are confined to the slopes of the buttes of the third and second terraces rising above the floodplain at relief elevation not exceeding 117 m. Exception to the above is the Pyatkino upland (III), as it has numerous structural basins at much higher altitudes (due to the inverted nature of the morphostructure, which suppresses local water exchange). At the same time, the Boriskovo plain (VII), on the contrary, is characterized by high hydrodynamics, and therefore, even despite its lower hypsometric position, has very few peculiar thermokarst relics, although they do exist (Fig. 18.6g). Autochthonous relief marks above 100 m usually (except for location III) correspond to the most drained areas where there are no large basins, but some occasional polygonal relief relics with a relative depression depth of 0.2–3.0 m and transverse size of about 50 m.

The inverted butte of Solotcha (I) has existed since the early Paleogene and now represents a vivid example of upright relief. As far back as in the Pliocene, its sur-

face was exposed to active denudation that formed the hilly-ridge interfluve. And as in the early Pliocene, the highest elevations are now confined to location I, which ensures the best drainage and nearly the highest productivity (Fig. 18.5). The burial of the Eopleistocene erosion network consequently affected location I: the buried secondary erosion cuts and the slopes of the butte massif (especially on the eastern, gentler slope) are becoming more hydromorphic. However, the growth of hydromorphism is insignificant compared to other locations and often does not even cause any soil formation type transformation; changes are limited to the occurrence of birch under the canopy of pine forests along the water courses of buried shallows. Valdai thermokarst here also did not grow significantly due to the low ice content of the soil and was represented only by a system of polygonal frost cracks, the relics of which cover the entire eastern slope of the butte as a half-ring at an elevation range of 120–125 m.

Location XI, the Krasnoye bog, is completely opposite by its functional features, being the largest series of several mires that merged into the single whole in the early Holocene, partially absorbing protrusions of residual relief that separated them (Figs. 18.2, 18.4 and 18.5). The mires are located within the pre-Pleistocene erosion cuts of tributaries of the Northern and South-Western ravines imposed on the western slope of the Belsky buried limestone butte. The territory of location XI, as evidenced by the drilling data, possessed a developed erosion network as far back as in the late Paleozoic; then, after the regression of Mesozoic seas, the erosional forms recovered and continued to develop. However, in the Valdai, the considerable depth and thickness of the autochthonous relief dissection, on the contrary, stimulated moisture stagnation and numerous thermokarst exposures with the formation of a whole group of lakes of different depths. As a result of the Holocene climate warming, almost all lakes peatified, and, due to the watershed position of location XI, deposits of high-quality high-bog low-ash peat were formed.

18.5 Principal Features of Natural Processes on the Boriskovo Plain

The Boriskovo plain (VII) is rather unique by its functional features. Its location is somewhat similar to the Krasnoye bog: it is also confined to the upper part of the Belsky butte massif slope, but preglacial (and pre-Jurassic) erosional forms are less developed. The latter circumstance determined significant differences in the current hydromorphism of these natural systems: location VII is more similar to the Solotcha butte, rather than the adjacent Krasnoye bog. Due to the high gravitational potential and low prevalence of inverted relief elements in location VII, there are effective mechanisms for removing excess groundwater, preventing waterlogging, although it is located at one of the lowest hypsometric levels (Fig. 18.5).

Along with its similarity with well-drained location I, there are significant differences: location VII is still a depressed plain, rather than upland, with a fairly

high level of groundwater (its average depth is 2–3 m during the low-water summer season, compared to 8 m in Solotcha) and low share of pine, which even in the near-watershed part is not more than 60% (while the pine's share in the forests of Solotcha is around 100%: 5.1 and 5.2). Nevertheless, these conditions are the most favorable for the development of tree species: the all-time peaks of productivity for both pine and birch are confined to location VII (located 500–800 m away from the area 5.7 along profile A–B). This area can be considered the regional optimum of mixed forests of South Meshchera. Drainage amelioration also played a certain role, "summing up" with natural growth factors of water exchange (the gravitational anomaly of the Belsky massif).

On the example of location VII, one can see the integrating, system-forming role of the potential of gravity as a factor intensifying the interchange of matter within both the water-circulation and biological cycles, which find their individual "gravitational matrices" in the common lithogenic basis (Solntsev 2013). In modeling landscape interrelations, this factor most often remains outside the research scope. The key features of the Boriskovo plain, in fact, are confined to higher "gravitational connectivity" of landscape components and processes within the plain, as compared with other locations.

18.6 Biological Productivity in Alas-like Depressions

Relic thermokarst depressions, regardless of their area, depth, and origin, being the indicators of obstructed groundwater flow in the Valdai, operate on the principle of positive feedback and even more severely hinder the current water exchange. They break up groundwater flows into semi-closed cells, preventing the formation of a hierarchically organized network of linear channels of water migration. Only such a network is capable of concentrating superficial and subsoil waters in certain areas, effectively diverting excess water, and forming transit water flows (thus reducing entropy and performing useful work in the landscape). These properties were completely inherent in the Eopleistocene erosion network, which has not recovered yet as of now. In fact, the bioproductivity variability in Meshchera nearby the Oka River is mainly determined by the spatial hydrodynamics variations and is largely limited to the location regularities of thermokarst relics.

However, the marshy basins in different areas clearly differ by the water exchange intensity. Relics of periglacial polygons on the slope of the Solotcha butte (I) have the highest flow capacity, which is quite natural. The productivity of pine forests in the corresponding forest compartments obviously decreases slightly, and moisture-loving birch virtually does not propagate there, so the forests remain monodominant (5.1 and 5.2). In all other cases at lower elevations, birch is at least inherent, and often dominates in the tree stand of the basins. At the same time, those of them that retain relatively high flow capacity, are marked by a drastic increase in birch productivity in contrast to the pine growth slowdown. Such communities are common on the periphery of the Pyatkino upland (5.3 and 5.13) and are found in the watershed part

of the Boriskovo plain (5.6). Somewhat similar situation is observed in the basins of the Beliy "island" (5.10), but due to its low hypsometric position, the overall level of bioproductivity there is noticeably reduced. Thus, pine most sensitively responds to local growth of water-stagnation phenomena by decreasing its increment in diameter, while "moderate" waterlogging is very favorable for birch and increases its increment almost to the regional maximum, instead of decreasing it. However, the qualitative transition from "moderate" to "significant" waterlogging can be quite dramatic: even in the center of the Pyatkino upland, under the conditions of lower flow capacity, there is a parallel decrease in the productivity of both pine and birch (5.4). A similar growth dynamic is observed on the southern periphery of location X, drained by the upper reaches of the Belaya River, where bogging is not extremely intensive (5.14). The lowest flow capacity and, accordingly, the lowest productivity was recorded in the central, typically butte part of location X (5.16). Consequently, the influence of Valdai thermokarst relics on bioproductivity is rather regular, being determined by the properties of the lithogenic basis.

18.7 Biogeochemical Processes Under Control of the Lithogenic Basis' Morphological Heterogeneities

According to the theoretical principles of the critical load approach (De Vries and Bakker 1998; Krivtsov et al. 2011), wood acts as the vital element of the natural buffering capacity of forest ecosystems. The elements are immobilized in stem tissues for a long term and further completely removed from the process when trees are chopped down. The lithogenic basis determines the spatial variability of this buffering capacity. However, the effect of abiogenic landscape factors on the biogeochemical processes cannot be adequately interpreted without taking into account the biological mechanisms of absorption and accumulation of heavy metals by vegetative organisms.

According to our data, the share of stem wood in the ecosystems of South Meshchera comprises about 59% of the phytocenosis biomass. However, less than half of the heavy metal volume is associated with this phytocenosis fraction (23–40% of the total volume of the heavy metals in the ecosystem vegetation) due to the low ash content of the wood. At the same time, Zn is the metal that is the least accumulated in stem wood (22.6%), and this fact is quite natural. The major part of Zn migrates in the xylem fluid together with chelating agents (Sinclair and Kramer 2012; Bouain et al. 2014) and reaches the branches and leaves of trees (the chelating agents limit its capability of binding with the negative charges of the cell walls and increase its translocation into offshoots). Cd is its geochemical analog; it migrates in the xylem fluid mostly in the free ion form Cd^{2+} (Conn and Gilliham 2010; Hazama et al. 2015), and is accumulated in xylem (36.6%), being attracted by the negative charge of the polygalacturonic acids of the cell walls.

Cu demonstrates even higher accumulation in wood (39.7%). This fact cannot be explained by the high affinity of Cu^{2+} ions to the material of the cell walls, as the xylem transport of Cu, unlike that of Cd, is mainly performed jointly with chelating agents (Burkhead et al. 2009). In our opinion, the Cu accumulation in wood is due to the fact that this fraction of the phytomass along with the photosynthesizing organs is one of the key elements of the Cu–ligand systems. It is a well-known fact that the formation and chemical structure of cell walls is strongly affected by Cu and that the effect of Cu on lignification is most expressly manifested in the stem tissue sclerenchyma (Marschner 2012). Insufficient lignification of the xylem vessels in the conditions of a severe deficit of Cu is due to the involvement of lignin of at least two Cu-containing enzymes: polyphenol oxidase and diaminoxidase. The deficit of Cu in the higher plants and the associated abnormal lignin biosynthesis cause bending and twisting of stems and branches, as well as the top drying of trees in summer. The latter sign is the typical manifestation of the water transport abnormality due to the insufficient lignification of the xylem vessels or structural weakness of the cell walls. Thus, young wood, being one of the critical acceptors of Cu transported along with chelating agents is capable of accumulating and binding significant amounts of this metal structurally.

The equally important determinant of the spatial inhomogeneities of the biogenic flows of heavy metals is the species composition of ecosystems and the geochemical specificity of the plants. A striking example of the hereditary factor role in the chemical composition of the plants is their "humidicated" and "aridanited" nutrition type (Aivazyan 1974; Perelman and Kasimov 1999). "Humidicated" species (including birches and aspens growing in the research area) have formed in the humid landscapes with acid soil domination intensively accumulate the cationic trace elements that are very mobile in the acid medium (including Zn^{2+} and Cd^{2+}). "Aridanited" plants (oak and pine) that emerged in arid landscapes accumulate anionic trace elements that are mobile in neutral and alkaline mediums. Cu is also one of the trace elements as it is closely associated with soil organic matters and mainly migrates within the negatively charged organomineral complexes (Ladonin and Margolina 1997).

The effect of the species composition of plants on the direction of heavy metal flows should be studied in conjunction with the biological productivity of the tree stand (Table 18.2). Other conditions being equal, the higher the productivity, the larger amount of the element is involved in recirculation and immobilization in perennial tissues. The landscape-related factors of productivity and the amplitude of its variability have been reviewed above.

Figure 18.8 shows the map charts illustrating the spatial regularities of the scope of annual immobilization of heavy metals in the tree stem and butt end biomass. The landscape locations whose boundaries are shown in Fig. 18.8 (see also Fig. 18.2) reflect the objective existence of various conditions for the ecosystem functioning within the research area. The differences between the locations are due to the different altitude, series of morphosculptural forms, development history, specific features of the buried morphostructures, and, consequently, the modern fluid flow dynamics (the degree of drainage). These factors determine the spatial inhomogeneities of the species composition and productivity of the tree stand in the research area. All these

Table 18.2 Species composition and biological activity of tree stands in South Meshchera

Territory	Range of altitudes, m above sea level	Tree stand species composition, %	C_{tss} of the pine	C_{tss} of the birch
Research area aggregate	103.5–130.2	"Humidicated" species—51.8 "Aridanited" species—48.2	1.05 (0.37–1.79)	0.80 (0.24–1.19)
Solotcha butte location I	120.0–130.2	"Humidicated" species—5.9 "Aridanited" species—94.1	1.38 (1.01–1.74)	0.96[a]
Boriskovo damp plain VII	108.9–116.8	"Humidicated" species—78.4 "Aridanited" species—21.6	1.26 (0.96–1.79)	0.89 (0.66–1.19)
Peredeltsy marshy plain X	108.9–116.8	"Humidicated" species—45.5 "Aridanited" species—54.5	0.92 (0.37–1.38)	0.73 (0.43–0.96)

Notes The values in parentheses are the C_{tss} variation range. Table 18.1 contains a detailed description of the species composition

Terms "humidicated" and "aridanited" are proposed by Aivazyan (1974) to characterize that the geochemical specialization of plant species is determined by the climate in the centers of their origin and initial evolution. "Humidicated" plants, evolved in humid (boreal) climates, adapted to the cations absorption; "aridanited" plants, originating from arid (low-latitude) regions, absorb mainly anions

[a]Due to the compact propagation of birch forests in Location I, it is impossible to estimate the variation of C_{tss} for the birch

factors expectedly result in a noticeable spatial variability of the ecosystems with regard to the flows of contaminants even in the conditions of a low-contrast plain relief and small area of the research.

The maximum spatial accumulation of Cu in the phytomass are typical of the monodominant pine forests of the Solotcha butte location I and adjacent areas in the west side of the research area. The well-developed drainage of this location determines the prevalence of "aridanited" types and high productivity of ecosystems in the tree stand, which, consequently, determines the intensive accumulation of Cu in the incrementing phytomass. The local peak points of the biological cycle of Cu outside location I are also consistent with the prevalence of highly productive pine tree stands. In this case, the deposition of Zn and Cu in these areas and in the Solotcha location is almost the lowest one, which is due to the insignificant share of the "humidicated" birch and aspen in the species composition.

The contradictory ratio of the modern and buried reliefs creates the conditions for an increased soil moistening in the Boriskovo damp plain, although accompanied by effective dehumidification. As a result, ecosystems with prevalent "humidicated"

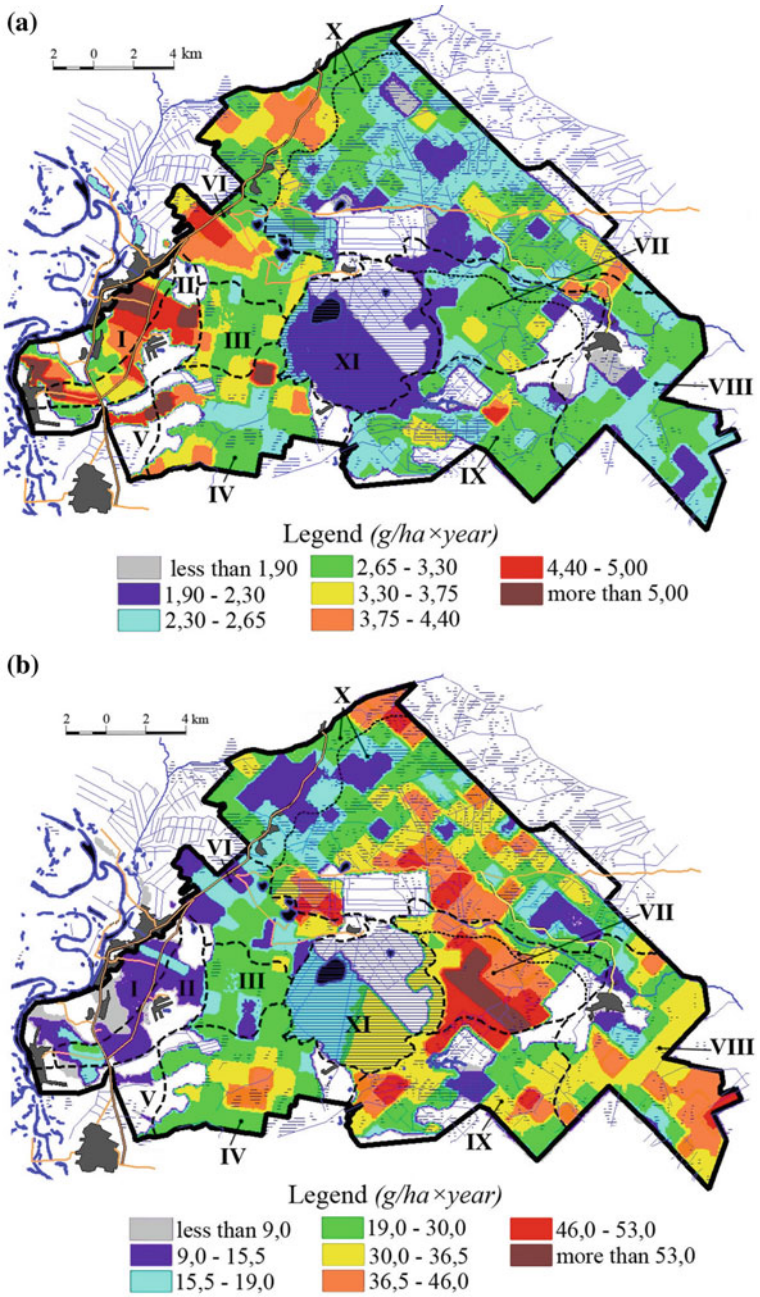


Fig. 18.8 Annual immobilization of heavy metals in the biomass of the trunk and buttocks of stands of subtaiga ecosystems of the southern Meshchera (I … XI—numbers of landscape areas: see Fig. 18.2)

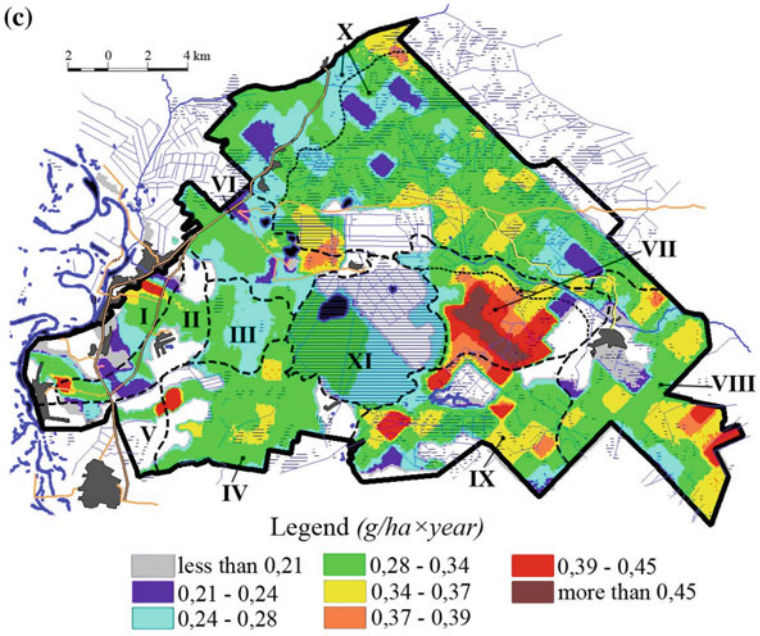


Fig. 18.8 (continued)

hydrophilic species are widespread in location VII (which is due to the influence of the modern relief), but their productivity in the research area is the highest (due to the buried relief factor). In this connection, the scope of yearly immobilization of Cu in the stem tissues are half the normal value in this location and are equal to the average values for the area, while the biological cycles of Zn and Cd are on the contrary the highest ones. Thus, the peak values of the Zn and Cd biological cycles are determined by the combination of two factors: the active deposition of these heavy metals by the birch and the aspen ("humidicated" species) and the high productivity of the tree stand.

The marshy areas (the Peredeltsy marshy plain X, isolated by the contours of the pre-Pleistocene erosion ravine) with the reduced reserves of the tree-stand biomass, typical of them, with one of the factors being its low density, are marked by the reduced scope of heavy metal immobilization in the stem tissues. In this case, similarly to the Boriskovo location VII, the factor of the species composition plays a major role in the spatial regularities of the biological cycles of heavy metals. The local maximums of the Cu accumulation in stem tissues within the Peredeltsy location X are confined to the areas with dominating pine tree stands, while the peak values of Zn and Cd accumulation are confined to the areas where birches prevail.

Thus, the biogeochemical features of the pine forests of the Solotcha location I determine the increased long-term immobilization of Cu (that is 1.6–1.8 times the immobilization in locations VII and X), which is its most typical feature. On

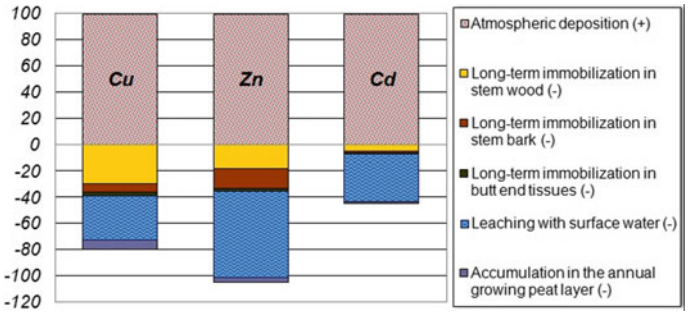


Fig. 18.9 Balance of heavy metals in forest ecosystems of southern Meshchera (percentage of income balance sheet item—annual atmospheric deposition)

the contrary, the "humidicated" species are the reason why the peak absorption of Zn and Cd is confined to the Boriskovo plain (1.7–4.0 and 1.5–1.6 times higher, than in locations I and X, accordingly). Despite the 1.5-fold lesser increment, the yearly immobilization of Zn in the incrementing stem wood and bark is 2.5 times higher in the hydromorphic Peredeltsy plain ecosystems, compared to the Solotcha location pine forests. This is an evidence of the fact that the species composition factor is more important than the biological productivity factor for the formation of the immobilization pool of elements in forest ecosystems.

Our balance calculation allowed us to give an integral estimate of the role of vegetation in the regulation of heavy metal flows. As follows from Fig. 18.9, the biotic block of the subtaiga ecosystems is capable of immobilizing 39–46% of the atmospheric fallouts of biophile Cu Zn and less than 10% of the atmospheric supply of toxic Cd (through its deposition in the incrementing stem wood and bark, butt end tissues, as well as accumulation in the yearly incrementing peat layer). At the same time, Zn is a slightly scarce element in South Meshchera (its imbalance is equal to –5.1%), while there is an excess of Cu and especially Cd (the imbalance is equal to +20.4 and +55.7%, accordingly). The excess of copper is due to its low leaching (weak mobility in water solutions), and that of cadmium is due to the high level of its anthropogenic supply compared to the sanation capability of the ecosystems. Being a typomorphic element of the subtaiga landscapes, Zn is both highly absorbed biologically and highly mobile in hydrochemical terms, which is the main cause of its deficiency. Cadmium should be considered the main anthropogenic contaminant of the forest ecosystems of South Meshchera.

The topological differentiation of the nature (within the same landscape) causes noticeable fluctuations not only of the volume of the heavy metal biological cycle, but also the density of metal inflow from the atmosphere. As a result, different proportions of inflows and outflows of heavy metal migration can form in different locations, particularly considering the fact that the biogenic and abiogenic migration are controlled by different factors with a low probability of spatial correspondences. For example, the atmospheric technogenesis mainly results in the increased level of

Table 18.3 The proportion of biogenic and abiogenic flows of heavy metals in the "uniformity cores"[a] of certain locations, characterizing the scope of spatial geochemical differences of the landscape

Element	Location	Atmospheric fallouts, kg/km^2 × year	Long-term immobilization in the phytomass[b], kg/km^2 × year	% of the long-term immobilization of atmospheric fallouts
Cu	I	1.408	0.419	29.74
	VII	0.982	0.311	31.69
	X	0.872	0.269	30.87
Zn	I	12.169	0.930	7.64
	VII	6.072	5.452	89.79
	X	6.684	2.531	37.87
Cd	I	0.552	0.0271	4.91
	VII	0.206	0.0455	22.10
	X	0.404	0.0295	7.30

Notes [a]"Uniformity core" is the area that is normally adjacent to the geometrical center of the location and covers the set of most typical facies and stows and has the most characteristic properties of the landscape geochemistry properties of the entire location

[b]In calculating the long-term immobilization of elements in the phytomass, we took into account the yearly accumulation of elements in the stem and butt end tissues of trees. The names of landscape locations see on Figs. 18.2, 18.4 and 18.5

fallouts in the "floodplain channel" of aerial migration and at the boundary forest areas adjacent to it. This boundary ecotone position is typical of the Solotcha location I, where the forest massifs act as the atmospheric filter for technogenic heavy metals. The atmospheric fallouts of heavy metals to the east of the location are by 30–50% lower than those in location I.

The spatial patterns of biogenic migration are much more sophisticated. However, as seen in Table 18.3, the differences within the same landscape are nonetheless comparable to those of the abiogenic atmospheric fallouts. The uniformity cores of the most indicative locations I, VII, and X differ by the intensity of long-term immobilization of heavy metals by a factor of 1.75–2.72, with the only exception of typomorphic Zn. Its biogenic migration is more contrastive and more dependent on the local conditions with up to a 5.8-fold difference between the selected areas.

The biological absorption of heavy metals is mainly determined by the geochemical specialization and productivity of the forest ecosystems. At the same time, the monodominant "aridanited" pine forests in Location I predominantly accumulate Cu, while the "humidicated" ecosystems mainly accumulating Zn and Cd prevail in the depressed plains VII and X. However, location X has an obstructed hydrodynamic pattern and the biogenic migration of elements in this area is lower due to the suppressed state of the production processes. In the center of the Boriskovo plain VII, the biological productivity is on the contrary the highest, while the atmospheric supply of heavy metals is one of the lowest ones. As a result, the ecosystems in

location VII are the most resistive to the anthropogenic supply of Zn and Cd: the share of the elements supplied from the atmosphere and immobilized for a long term is more than 2–2.5 times the South Meshchera average values. In the Solotcha location I, on the contrary, the immobilization capacity of the tree biomass is below the average values, which are 1.5–6 times higher. The insignificant involvement of the "humidicated" species in the tree stand as well as the high level of the heavy metal supply from the atmosphere contribute to it in location I. Thus, the spatial variations of both natural and technogenic factors simultaneously affect the resistance of the Solotcha pine forests to the supply of Zn and Cd from the atmosphere. At the same time, opposite patterns are typical of Cu: the increased supply from the atmosphere in location I is compensated by the increased accumulation of Cu, and in other, less ecotone locations that are farther from the floodplain of the Oka River, both the biogenic immobilization and the supply from the atmosphere are lower. As a result, the buffering capacity of the ecosystems with respect to the atmospheric fallout of Cu is highly stable across the location, which is a notable but accidental territorial correspondence of the areas of biogenic and abiogenic migrations.

18.8 Conclusions

Thus, heterogeneity of the lithogenic basis indirectly, through the water exchange intensity, determines the spatial dynamics of the productivity of forest ecosystems. In this case, even local variations in the increment of trees in diameter correspond to certain features of litomorphological structures. Such assessments, as a rule, lack information on the autochthonous relief, which leads to overly generalized or distorted ideas about the genesis of morphostructures. The information value of the drilling data used, in our opinion, allowed us to carry out structural-genetic typification of natural systems, sufficiently detailed in line with the detail level of the taxation data. At the same time, we revealed stable "foci" of high and low forest productivity that are due to differences in the water exchange intensity, whose localization could not be explained based on the morphometric approach alone.

We identified the geological and geomorphological indicators of local hydrodynamics and bioproductivity, such as the depth and morphology of the regional watershed top level, variations in the relative bedrock share, location and geometry of Valdai thermokarst relics (flow thermokarst, relic coast bars). We also found out that significant variability of the productivity at small distances, even with a low-contrast relief, is quite natural and is ultimately determined by the genesis of the lithogenic basis. At the same time, relict morphological elements formed hundreds of millions of years BP can have a decisive influence on the processes in modern ecosystems.

Lithogenetic heterogeneities determine the spatial variability not only of bioproductivity, but also of the species composition of ecosystems, in connection with which 2-6-fold fluctuations of heavy metals' uptake are observed. The greatest potential resistance to priority toxicant—Cd—have Boriskovo plain ecosystems with maxi-

mum biological activity of tree stands and a high proportion of "humidicated" species. But this level of resistance is not enough due to the high level of atmospheric deposition of cadmium in the Russia Centre. At the same time, the species composition factor is more important than the biological productivity factor for the formation of the immobilization pool of elements in forest ecosystems.

The results of this study fully confirmed the principles of Russian regional landscape science (Solntsev 2001) about the leading role of the lithogenic basis in landscape processes. The lithogenic influence on the biota is also decisive in the platform plains conditions.

References

Aivazyan AD (1974) The geochemical features of the South-West Altai landscapes' flora. MSU Publ, Moscow (in Russian)

Annenskaya GN, Mamay II, Tsesel'chuk YN (1983) Landscapes of the Ryazan Meshchera and the possibility of their development. MSU Publ, Moscow (in Russian)

Aseyev AA, Vedenskaya IE (1962) The development of Meshchera lowland relief. AS USSR Publ, Moscow (in Russian)

Bazilevich NI, Grebenshchikov OS, Tishkov AA (1986) Geographical regularities of the structure and functioning of ecosystems. Nauka, Moscow (in Russian)

Bouain N, Shahzad Z, Rouached A, Khan GA, Berthomieu P, Abdelly C, Poirier Y, Rouached H (2014) Phosphate and zinc transport and signalling in plants: toward a better understanding of their homeostasis interaction. J Exp Bot 65–20:5725–5741

Burkhead JL, Gogolin Reynolds KA, Abdel-Ghany SE, Cohu CM, Pilon M (2009) Copper homeostasis. New Phytol 182–4:799–816

Conn S, Gilliham M (2010) Comparative physiology of elemental distributions in plants. Ann Bot 105–7:1081–1102

De Vries W, Bakker DJ (1998) Manual for calculating critical loads of heavy metals for terrestrial ecosystems. DLO Winand Staring Centre, Wageningen

Dortman NB (ed) (1984) Physical properties of rocks and minerals (petrophysics), 2nd edn. Nedra, Moscow (in Russian)

Filosofov VP (1960) A brief guide to the morphometric method of searching tectonic structures. Saratov University Publ, Saratov (in Russian)

Glazovskaya MA (1998) Geochemistry of natural and man-made landscapes of the USSR. Vysshaya shkola, Moscow (in Russian)

Glebova OV, Kolomyts EG, Rozenberg GS et al (2000) Natural complex of a big city. Landscape-ecological analysis. Nauka, Moscow (in Russian)

Hazama K, Nagata S, Fujimori T, Yanagisawa S, Yoeneyama T (2015) Concentrations of metals and potential metal-binding compounds and speciation of Cd, Zn and Cu in phloem and xylem saps from castor bean plants (Ricinus communis) treated with four levels of cadmium. Physiol Plant 154–2:243–255

Kolomyts EG (1999) Polymorphism of landscape-zonal ecosystems. Izvestiya RAN (Akad. Nauk SSSR) Seriya Geograficheskaya 6:21–31 (in Russian)

Krivtsov VA, Tobratov SA, Vodorezov AV, Komarov MM, Zheleznova OS, Solov'yeva YA (2011) Natural potential of Ryazan region landscapes. RSU named for SA Yesenin Publ, Ryazan (in Russian)

Krivtsov VA, Vodorezov AV (2006) Features of the structure and formation of the relief on the territory of the Ryazan region. RSU named for SA Yesenin Publ, Ryazan (in Russian)

Ladonin DV, Margolina SV (1997) Interaction between humic acids and heavy metals. Pochvovedenie 7:806–811 (in Russian)
Marschner P (ed) (2012) Marschner's mineral nutrition of higher plants. UA, Adelaide
Organova NM, Voyloshnikov VD (1991) Modern ideas about the geological structure of the Ryazan region. In: Ryazan region: history, nature, economy. RSU named for SA Yesenin Publ, Ryazan (in Russian)
Perelman AI, Kasimov NS (1999) Landscape geochemistry. MSU Publ, Moscow (in Russian)
Scotese CR (1997) Paleogeographic Atlas. University of Texas at Arlington, Arlington
Sinclair SA, Kramer U (2012) The zinc homeostasis network of land plants. BBA—Mol Cell 1823–9:1553–1567
Soldatov MS, Malkhazova SM, Rumyantsev VY, Leonova NB (2014) Forecast of changes in wood growth in the forests of the European part of Russia in connection with global warming. Izvestiya RAN (Akad. Nauk SSSR) Seriya Geograficheskaya 2:96–102 (in Russian)
Solntsev NA (2001) Studies on landscape: selected works. MSU Publ, Moscow (in Russian)
Solntsev VN (2013) On the gravitational paradigm of landscape science. In: Landscape collection (Development of the ideas of N.A. Solntsev in modern landscape science). Oykumena, Moscow-Smolensk (in Russian)
Spiridonov AI (1978) Geomorphology of the European part of the USSR. Vysshaya shkola, Moscow (in Russian)
Ushakov SA, Yasamanov NA (1984) The drift of continents and climates of the Earth. Mysl', Moscow (in Russian)
Usol'tsev VA (2002) Phytomass of the forests of Northern Eurasia: standards and elements of geography. Ural Branch of RAS, Ekaterinburg (in Russian)
Vasil'chuk YK, Kotlyakov VM (2000) Basics of isotope geocryology and glaciology. MSU Publ, Moscow (in Russian)
Velichko AA (ed) (2009) Paleoclimates and paleolandscapes of the extratropical space of the Northern Hemisphere, Late Pleistocene—Holocene. Geos, Moscow (in Russian)
Zamolodchikov DG, Korovin GN, Utkin AI, Chestnykh OV, Songen B (2005) Carbon in forest resources and agricultural lands of Russia. KMK, Moscow (in Russian)
Zhamoida AI (2015) General stratigraphic scale of Russia: state of art and problems. Geologia I Geofizika 56–4:655–670 (in Russian)

Chapter 19
Heavy Metals and Metalloids in Soils and Macromycetes from the Accumulated Environmental Damage Zone in Petrozavodsk, Republic of Karelia



Dmitrii S. Rybakov

Abstract Studies of soils and macromycetes were conducted in the accumulated industrial pollution zone in central Petrozavodsk, where a multi-element industrial anomaly was revealed. Chemically altered soils at the former Onega Tractor Plant site and in two adjacent recreation areas, as well as all the higher fungi (species *Verpa bohemica* (Krombh.) Schroet. and *Leccinum scabrum* (Bull.: Fr.) S.F. Gray) found, were studied. Major (controlled) toxic heavy metals in the macromycetes occur in various concentrations: *V. bohemica* contains more Cu and Zn, while *L. scabrum* accumulates Pb and Cd more actively. The caps of *L. scabrum* from the pollution zone accumulate more Pb, U, Bi, Y, ΣTR, W, Th, Ba, Cu, Ag, Sr, Sb, Ni, Zr and Ti and the stipes accumulate more Pb, U, Bi, Ba, Ag, Cu, W, ΣTR, Th and Y than those from the background area. Cadmium concentrations in the control samples of *L. scabrum* (particularly in the caps) are fairly high. Therefore, evidence for Cd contamination in the impact zone is supported by its maximum concentration (2.47 mg/kg air-dried sample) exceeding maximum permissible concentration (MPC). All mushrooms may have various concentrations of the same elements, but the geochemical patterns of their penetration into the fruit bodies from soil are similar and depend on the properties of the elements. The possible use of the above macromycete species in industrial contamination zones for remediation automatically rules out their further consumption as food products.

Keywords Industrial pollution · Soils · Soil substrate · Macromycetes · *Leccinum scabrum* · *Verpa bohemica* · Food safety · Mycoremediation

D. S. Rybakov (✉)
Karelian Research Centre, RAS, Institute of Geology, Petrozavodsk, Russia
e-mail: rybakovd@krc.karelia.ru

© Springer Nature Switzerland AG 2020

O. V. Frank-Kamenetskaya et al. (eds.), *Processes and Phenomena on the Boundary Between Biogenic and Abiogenic Nature*, Lecture Notes in Earth System Sciences,
https://doi.org/10.1007/978-3-030-21614-6_19

19.1 Introduction

Accumulation of toxic substances in the environment as a result of chemical pollution is now an essential problem which affects all aspects of the human society. It is particularly important to assess redeveloped former industrial zones, where hazardous pollution has been accumulating for a long period of time.

There are various methods for cleaning and neutralizing contaminated areas. Special attention is given to mycoremediation, because fungi can actively accumulate heavy metals and radionuclides (Stamets 2005) and decompose hydrocarbons (Stamets 2005; Treu and Falandysz 2017). The so-called "double solution" proposed implies that polluted areas are neutralized and safe mushroom production on agricultural and industrial waste is launched (Kulshreshtha et al. 2014). The safety of this method is provided by selecting edible mushroom species which neutralize the waste by producing enzymes and do not accumulate toxic agents in their fruit bodies. Obviously, in this case mushrooms as a raw material are expected to meet all food safety criteria (Bakaitis and Basalaeva 2007).

Studies on the ability of various species and ecological groups of macromycetes to absorb heavy metals to a varying degree are referred to in some publications (Kalač and Svoboda 2000; Zhu et al. 2011; Isaeva 2014; Anishchenko et al. 2016; Sazanova et al. 2017). Differences in the accumulation of toxic elements in the caps and stipes of the fruit bodies of the same species have been reported (Kalač and Svoboda 2000; Isaeva 2014; Sazanova et al. 2017). Heavy metals have been shown, with some exceptions, to accumulate in greater quantities in the caps than in the stipes. The elements shown below occur in the following sequence, based on the accumulation index (I_a) calculated as the ratio of their concentration in mushrooms (per dry matter) to their concentration in the soil (Byrne et al. 1976; Kabata-Pendias and Pendias 1989; Sibirkina 2014): Hg > Cd > Se > Cu > Zn > Br > As > Mn > V. Available data show that mushrooms accumulate Se, Hg and Cu more actively than soil but absorb Cd, As, Mn and V less actively and Br much less actively than green plants. Zn is concentrated in about the same quantities in mushrooms, plants and the soil (soil substrate).

Thus, macromycetes are now being studied as: (1) efficient bio-indicators of environmental pollution capable of rapidly accumulating toxic substances supplied into the soil substrate; (2) potential cleaners of areas contaminated by heavy metals, radionuclides and various hydrocarbons; (3) food items that should be made safe by taking all preventive measures such as carefully collecting and controlling the raw material.

The goal of our study is to assess the impact of industrial pollution, indicated by considerable chemical changes in the soils, on the state of higher mushrooms growing in the former industrial zone of central Petrozavodsk. The trace element composition of macromycetes was analyzed, their hazard as food items was assessed, the element accumulation indices I_a were calculated and possible mycoremediation was estimated.

19.2 Materials and Methods

Soils and the edible fungi *Verpa bohemica* (Krombh.) Schroet. and *Leccinum scabrum* (Bull.: Fr.) S.F. Gray from the industrial pollution zone on the Lososinka River bank in central Petrozavodsk (zone occupied formerly by the Onega Tractor Plant—OTP) were studied. Contaminated soils in the study area contain high heavy metal and metalloid (Pb, Cu, Zn, As, W, Mo, Cr, Ni, etc.) concentrations (Rybakov et al. 2013; Rybakov and Kevlich 2017). Figure 19.1 shows Pb distribution at various levels in the soil-ground sequence. Manual drilling conducted in 2010 showed that Pb concentrations decrease with depth (median values, mg/kg): surface—181. 1 m—164, 2 m—63.5 and 3 m—40.9. This is also the case for most of other pollutants

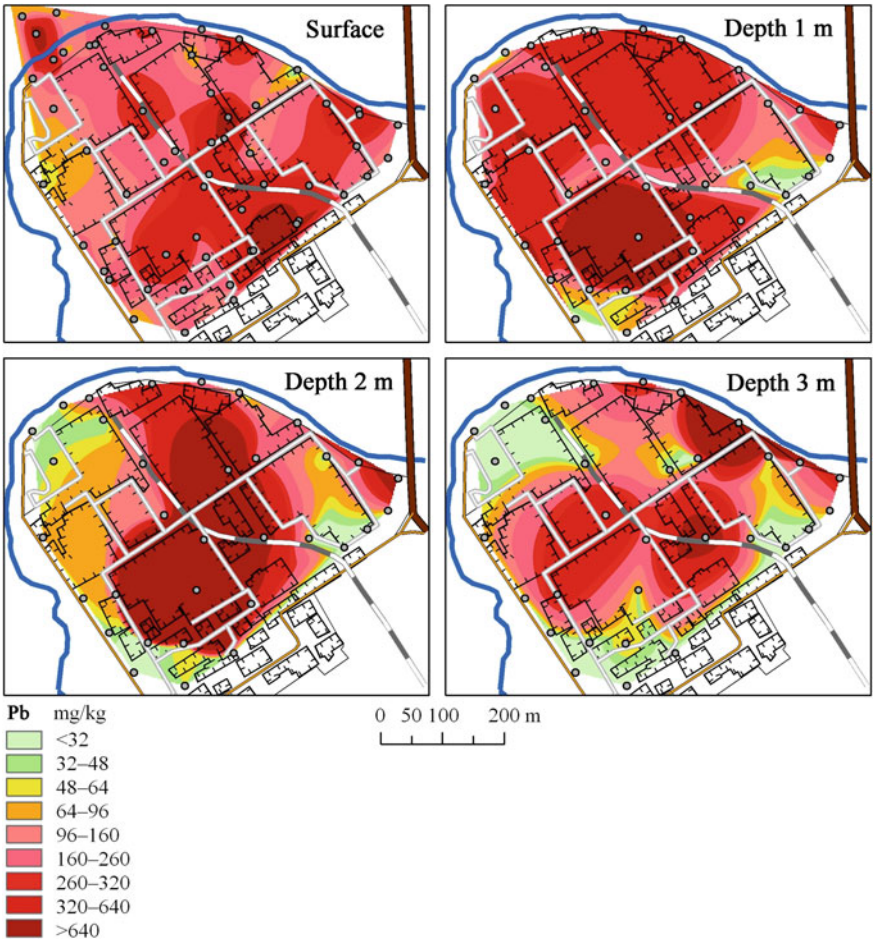


Fig. 19.1 Depth distribution of Pb content in the industrial zone

(Zn, Cd, Cu, Ni, Cr, Mo and W) (Rybakov 2017). The occurrence of zones with extremely high Pb concentrations (up to 2.3 mas. %), Fe (up to 23 mas. %), Cu (up to 4.2 mas. %), Zn (up to 1.5 mas. %), Mn (up to 1.1 mas. %), Sn (4400 mg/kg), Ni (up to 375 mg/kg), Cr (up to 1250 mg/kg), Sb (up to 700 mg/kg) at various depths suggests that heavy metals penetrated into the soil-ground sequence not only by air but also as a result of the burial or loss of industrial waste in some parts of the zone.

In 2014, soil samples were taken from the industrial zone and neighbouring recreation areas (OTP Park and Alexander Public Garden) affected by airborne emission from the plant. The samples were air-dried and screened manually to select fractions of various particle sizes: 1.0–0.5, 0.5–0.25, 0.25–0.1 and <0.1 mm. 124 samples for fractional analysis were thus obtained: 24 (6 × 4) from OTP site, 44 (11 × 4) from OTP park and 56 (14 × 4) from Alexander Public Garden.

Updated total soil pollution index values (Vodyanitskii 2008) for the industrial site were calculated for various particle size fractions using the formula:

$$Z_{ct} = \sum_{i=1}^{n} C_{ct} - (n-1), \tag{19.1}$$

where $C_{ct} = C_c \cdot C_t$ is the concentration coefficient of the i-th element, which exceeds 1 (C_c), and shows the hazard class for chemicals (C_t). $C_t = 1.5$ for hazard class 1, 1 for class 2 and 0.5 for class 3.

Data on the hazard classes, MPC (Maximum permissible 2006) and the harm indices (Sanitary and epidemiological 2003) of major pollutants from the study area are presented in Table 19.1. The chromium hazard class is taken from (Vodyanitskii 2008).

Table 19.2 shows soil pollution levels with regard for the hazard class of toxic elements and the total pollution index (Sanitary and epidemiological 2003).

Mushrooms were found in limited quantities only at one site of the industrial zone, 150 m from a former foundry workshop, a major source of heavy metals. No mushrooms were found at other sites. Fruit bodies of macromycetes were mainly collected in 2014 on 20 May in spring (*V. bohemica*) and on 25 September in autumn (*L. scabrum*). In October 2018, one more sample of *L. scabrum* was collected. Mushrooms were also sampled from the control (background) zone located in the Pryazha District, Republic of Karelia. A total of 10 samples (5 caps and 5 stipes) *L. scabrum*, one mixed sample of *V. bohemica* from the pollution zone and 14 samples (7 caps and 7 stipes) of *L. scabrum* from the control area were prepared for analysis. Soil particles and alien plant remains were carefully removed from the mushrooms. The samples were then sliced, dried at room temperature and ground in a coffee mill of knife type.

All the soil and macromycete samples were analyzed for 50 elements by the inductively coupled plasma mass spectrometry (ICP-MS) method in the Analytical Laboratory at the Institute of Geology, RAS, using a standard procedure (Svetov et al. 2015).

Table 19.1 Hazard classes, MPC and harm indices of elements in soils

	Pb	Zn	As	Cd	Co	Ni	Cu	Mo	Cr	Sb	Mn	V	W
Hazard class	1	1	1	1	2	2	2	2	1	2	3	3	3
MPC (with regard for background), mg/kg	32	100	2	1.0	–	85	55	–	90	4.5	1500	150	–
Harm indices													
Translocational C_1	35		2							4.5	3500	170	
Migratory aquatic C_2	260		15							4.5	1500	350	
Migratory airborne C_3	–		–							–	–	–	
General sanitary C_4	32		10							50	1500	150	

Table 19.2 Assessment of chemical soil pollution levels

Pollution category	Concentration in soil, mg/kg			Z_c of soil
	Class 1	Class 2	Class 3	
Clean	From background to MPC	From background to MPC	From background to MPC	–
Allowable	From 2 background values to MPC	From 2 background values to MPC	From 2 background values to MPC	<16
Moderately hazardous			From MPC to C_{max}	16–32
Hazardous	From MPC to C_{max}	From MPC to C_{max}	>C_{max}	32–128
Extremely hazardous	>C_{max}	>C_{max}		>128

Note C_{max} is a maximum permissible element concentration value in one of four harm indices (see Table 19.1)

Regional background contents of some heavy metals (Zn, Cu, Mn, Pb, Cd, Ni, Cr, Co) for our calculations are after Fedorets et al. (2008). The hazard of the mushrooms studied for possible eating was assessed by comparison with current MPC for Cd, Pb, Zn and Cu (Maximum permissible 1986; Hygienic requirements 2001) with regard for the accepted water concentration of about 90% in the initial product (fresh mushrooms) and 10% in dry mushrooms.

To tentatively calculate the accumulation index, element concentrations in the soil substrate at a depth of 0–0.1 m were used.

Statistical calculations were made and plots were constructed using the Data Analysis software package, Microsoft Office Excel.

19.3 Results

19.3.1 Heavy Metals and Metalloids in Soils

The detailed study of chemical element concentrations at some sites in industrial pollution areas has revealed a major man-induced geochemical anomaly in central Petrozavodsk (Fig. 19.2).

The figure clearly shows that:

(1) Major soil pollutants in the list shown in the figure are (Cc_{Me} > 1): Zn > Cu > Mn > Pb > Cd > Ni;

(2) The soil pollution patterns of the sites studied are comparable. However, there are some differences: (a) toxic element concentrations decrease with distance to the integrated pollution source (former OTP site); (b) particle size fractions

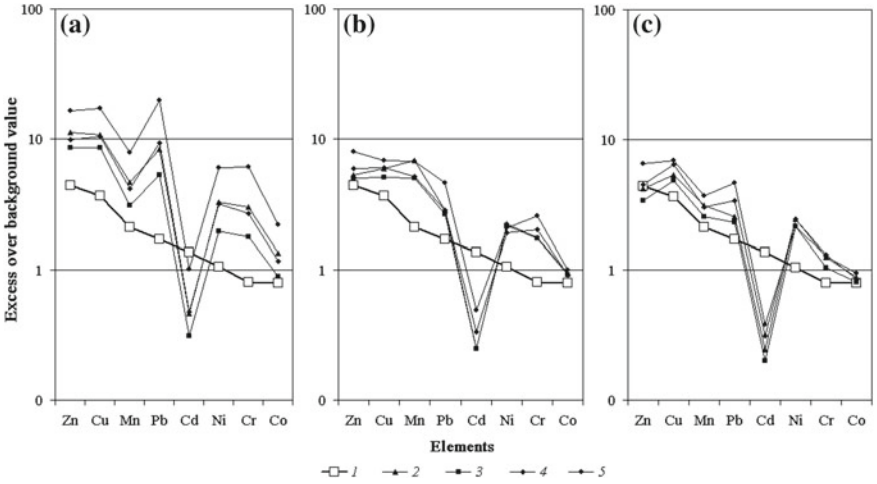


Fig. 19.2 Excess over the regional background in the median concentrations of some chemical elements in urban soils: 1—Petrozavodsk soils in general, 2–5—soils in central Petrozavodsk: a—former industrial site, b—OTP park, c—Alexander Public Garden: soil particle size fractions: 1—<1.0; 2—1.0–0.5; 3—0.5–0.25; 4—0.25–0.1; 5—<0.1 mm

in the most heavily polluted soils differ more substantially in all elements. Geochemical indices for Zn and Co at the remote site (see Fig. 19.2c) become more comparable with general estimates for the urban area (Rybakov et al. 2013);

(3) Cd concentrations in the soils of all the study areas are generally lower than those in the urban soils and lower than the regional background. However, comparison of these three figures clearly shows that in spite of relatively low Cd concentrations, this element belongs to a group of pollutants arising from human activities. This is most clearly illustrated by analyzing the smallest of the soil fractions studied (<0.1 mm).

Several groups were formed for all the elements analyzed, based on the degree of dispersed-fractional differentiation (distribution of elements in particle size fractions) in the surface layer of industrially contaminated soils and grounds in central Petrozavodsk (Table 19.3). It can be seen from the Table that maximum differences in the degree of differentiation between industrial site soils and recreation zones (for particle size fractions differing most substantially in element concentrations) are observed for Ag and Mo. In two latter cases, where pollution was lower, Mo and some other element concentrations in coarser fractions are higher than those in a < 0.1 mm fraction. It has been shown, however (Rybakov 2017), that concentrations of some elements in a < 1.0 mm fraction of an old roadbed (solid asphalt) may exceed their median value in urban soils by: 10.1 times for Mo, 4.4–4.2—for Cu, Co and Ni, 3.5—for V, etc. The abrasion of the road surface and car parts, particulate emissions from motor vehicles, as well as trampled soils and not completely remote

Table 19.3 Disperse-fractional differentiation of chemical elements in the soils of central Petrozavodsk

Sites	Mean element concentration ratios in <0.1 and 0.5–0.25 mm soil fractions						
	6 to 5	5 to 4	4 to 3	3 to 2	2 to 1.5	1.5 to 1	1 to 0.5
OTP site 7	Ag, Bi	W, Mo	Se, Cr, Ta, **As**, Zr, Hf, **V**, Nb, **Sb**	**Cd**, Ti, P, **Ni**, Te, **Pb**, Sn, Y, Co, **Mn**, **Zn**, U, Sc, Th, **Cu**, ∑TR	Cs, Tl, Be, Li, Sr, Ba	Rb, Ga	–
OTP park 5	–	–	–	Zr, Hf, **Cd**, W	Nb, **Sb**, Y, P, Bi, Ta, Ti, Sn, **Pb**, **Zn**, **As**, U, ∑TR	Th, Cr, **V**, Cs, **Mn**, Li, **Cu**, Sr, Ga, Co, Sc, Se, Ba, Rb	Te, Be, **Ni**, Ag, Tl, Mo
Alexander public garden 4	–	–	–	Zr, W, Hf	P, **Pb**, U, **Zn**, Th, Y, Nb, **Sb**, Ti, Ta, Bi, **Cd**, Sn, **V**, **Mn**, ∑TR	Cs, Li, **Cu**, Sc, Co, Ag, Cr, Be, **As**, Sr, Ga, Rb, Tl, **Ni**, Ba	Te, Se, Mo

Note Semi-bold font is used to emphasize normalized elements (in frame) for which mean geometric or median concentration values higher than MPC (with regard for the background or clark values) were obtained and unframed elements are lower than MPC (data as in Fig. 2)

spent anti-icing mixture, are the permanent sources of pollution, which persists after the partial reduction of industrial emission.

Table 19.4 shows the degree of accumulation of toxic elements in soil fractions for the industrial zone estimated by calculating the total pollution index.

It can be seen from the Table that Z_{ct} value for median pollutant concentrations, obtained for various fractions, is not the same. A maximum value of 183.2 was obtained for a < 0.1 mm fraction, that is consistent with binding of elements by a soil absorbing complex which is part of the fraction (Rybakov and Kevlich 2017). This is classified as "*extremely hazardous*", based on Z_c index (see Table 19.2). Elements of hazard class 1 (Pb, Zn and Cu), class 2 (Mo) and class 3 (W) are major contributors to pollution. As coarser fractions display smaller median pollutant concentrations, they are assessed as «*hazardous*». Pollution caused by a < 0.1 mm fraction is described as "*extremely hazardous*", based also on Pb concentrations exceeding MPC (see Tables 19.2 and 19.4).

Thus, the pollution of the soil-ground sequence of the former industrial site is generally assessed at least as "*hazardous*", based on Pb, Zn and Cu concentrations (with regard for background) and Z_{ct}.

Table 19.4 Calculation of the total pollution index (Z_{ct}.) for median element concentration values in particle size fractions

Elements	C_{Me}, mg/kg				C_0, mg/kg	Hazard class	C_t	C_{ct}			
	1.0–0.5	0.5–0.25	0.25–0.1	<0.1				1.0–0.5	0.5–0.25	0.25–0.1	<0.1
W	25.6	14.7	30.8	86.0	0.75	3	0.5	17.1	9.80	20.5	57.3
V	101.2	72.2	119.6	238.8	62.6	3	0.5	<1	<1	<1	1.91
Cu	108.0	86.3	104.4	172.0	10	2	1	10.8	8.63	10.4	17.2
Ni	66.0	39.3	64.1	120.3	20	2	1	3.30	1.97	3.21	6.02
Co	13.3	8.87	11.6	22.0	10	2	1	1.33	<1	1.16	2.20
Mo	7.61	4.46	8.42	23.9	0.94	2	1	8.10	4.74	8.96	25.4
Pb	125.5	80.1	139.8	297.4	15	1	1.5	12.6	8.01	14.0	29.7
Zn	225.4	171.5	198.2	328.3	20	1	1.5	16.9	12.86	14.9	24.6
Sb	2.16	1.35	2.66	5.71	0.62	2	1	3.48	2.18	4.3	9.21
Cr	119.9	70.9	107.0	243.5	40	1	1.5	4.50	2.66	4.01	9.13
Cd	0.463	0.313	0.473	1.01	1	1	1.5	<1	<1	<1	1.52
Sn	4.41	3.50	4.81	9.76	1.90	*3*	0.5	1.16	<1	1.27	2.57
As	3.69	2.50	3.58	7.16	2	1	1.5	2.77	1.88	2.69	5.37
Mn	933.3	621.8	834.7	1575	200	3	0.5	2.33	1.55	2.09	3.94
Z_{ct}								**73.3**	**45.3**	**76.5**	**183.2**

Note C_{Me}—median element concentration in soil fractions; C_0—regional background or a median value for Petrozavodsk soils (*italics*), if the background was not estimated; calculations were made using the Formula (19.1)

19.3.2 Heavy Metals and Metalloids in Macromycetes

Controlled chemicals. Table 19.5 shows major (regulated) toxic element concentrations in the macromycetes collected in the former OTP pollution zone and in the control area in 2014 and 2018.

It can be seen from Table 19.5 that Pb and Cd are most abundant in the caps of *L. scabrum*, while Zn and Cu in *V. bohemica*. Excess of MPC (per wet mass) was observed in the caps (Pb, Cd and Zn) and stipes (Cd) of *L. scabrum* and in *V. bohemica* (Zn, Cu). Cd concentration in the caps of *L. scabrum* control samples also exceeds MPC (1.16–3.34 mg/kg). Pb concentrations in the samples taken in 2018 were markedly lower. The samples showed no As because of a high detection limit (5.1 mg/kg).

Comparison with background values. Pb, U, Y, ΣTR, W, Th and Ni concentrations in the caps of *L. scabrum* in all cases exceeds background values (Fig. 19.3). Pb, U, W and Th concentrations in the stipes of the above species exceed background values. Cs, Sn, Cr and Mn concentrations in the caps and stipes of *L. scabrum* do not exceed background values in all cases. The greatest contrast ratio ($C_{max}/C_{min} > 3$) is observed for Pb (18.4), Tl (10.4), Bi (9.45), Ta (9.15), Cd (6.76), Ag (5.85), Sb (4.88), Sr (3.92), Co (3.51), Ba (3.30), Zn (3.12) (in caps) and Bi (11.3), Ag (9.82), Mo (8.84), Li (8.68), Cd (6.72), Co (6.06), Pb (5.17), Cr (5.05), Tl (4.83), Sb (4.79), Y (~4.63), Sr (4.14), Ta (4.00), Zr (3.12) (in stipes). Thus, highly contrasting values

Table 19.5 Heavy metal concentrations in macromycetes and soil substrate from the former industrial site, mg/kg of an air-dried sample

Name		Pb	Cd	Zn	Cu
L. scabrum (caps), $n = 4$ (2014)	Limits	1.53–14.3	0.366–2.47	96.3–301	20.1–31.0
	Median	9.42	0.606	150	23.2
L. scabrum (stipes), $n = 4$ (2014)	Limits	1.04–4.18	0.146–0.981	65.0–119	7.06–16.7
	Median	2.44	0.189	84.1	10.2
L. scabrum (caps) (2018)		0.775	0.822	123	12.1
L. scabrum (stipes) (2018)		0.808	0.247	110	12.1
L. scabrum (caps), control, $n = 7$		0.360	1.83	140	12.8
L. scabrum (stipes), control $n = 7$		0.397	0.607	86.7	8.04
V. bohemica (combined sample) (2014)		2.38	0.315	342	92.0
Soil at the polluted fungi sampling site in 2010 (depth 0–0.1 m)		92.7	0.304	168	66.2
Same (depth 1 m)		705	0.432	257	559
Soil at the polluted fungus sampling site in 2014 (depth 0–0.1 m)		118	1.15	393	181
MPC in mushrooms		0.5	0.1	20	10

Note MPCs is estimated in terms of the initial product with regard for the dry matter content of the raw material and that of the final product

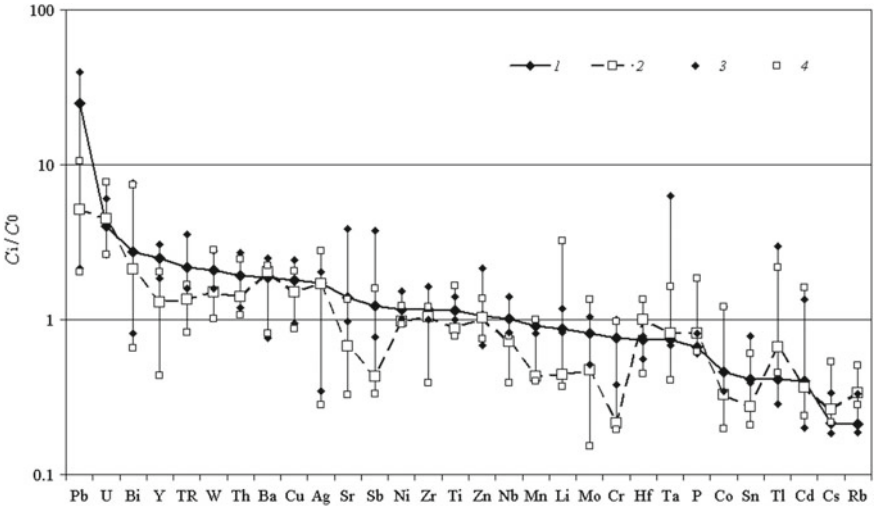


Fig. 19.3 Element concentration ratios at the former industrial site in the fruit bodies of *L. scabrum* (C_i) to the background (C_0): 1, 2—by median values (1—caps; 2—stipes); 3, 4—by maximum and minimum values (3—caps; 4—stipes)

for the caps, higher than those in the stipes, were obtained primarily for Pb, Ta and Tl. The same pattern is observed for Li, Mo, Y, P, Hf and Mn in the stipes (see Fig. 19.3).

Elements in the residual industrial pollution zone form the following sequences showing the excess of median concentration over the background ($C_i/C_0 \geq 1.5$): Pb ≫ U > Bi > Y > ΣTR > W > Th > Ba > Cu > Ag (caps), Pb > U > Bi > Ba > Ag > Cu > W (stipes). Maximum values display the following pattern ($C_{i_max}/C_0 \geq 2.0$): Pb ≫ Bi > Ta > U > Sr > Sb > ΣTR > Y > Tl > W > Th > Ba > Cu > Zn > Ag (caps), Pb > U > Bi > Li > W > Ag > Th > Ba > Tl > Cu > Y (stipes) (see Fig. 19.3). These sequences comprise industrial pollutants (Pb, Bi, W, Ba, Cu, Ag, Sb and Zn) and natural association elements (Rybakov and Veselkova 2015) occurring in the soil in concentrations not exceeding clarke values (U, Y, ΣTR, Th, Ba, Ta, Sr, Tl and Li).

Concentrations of many elements (Tl, Sb, Li, Nb, Sr, Zr, Bi, Y, Sn, Cr, Th, Mn, Pb, Ni, Co, Sc, ΣTR) in the stipes of *L. scabrum* from the control zone are commonly higher than those in the caps ($C_{cap}/C_{st} \leq 1$). In the industrial pollution zone this pattern is displayed only by Tl, Zr, U, Nb, Bi and Ta (Fig. 19.4). All other elements, except for those listed above, are concentrated in mushroom stipes, while this pattern is typical in all cases for P, Rb, Ag, Cs, Cd and Zn occurring at both industrially contaminated and background sites. One can see from Fig. 19.4 that Pb, Cr, Sb, Mn, Sr, Li, Y, Mo, ΣTR, Sn, Co, Nb and other elements at the contaminated site are redistributed more actively into the caps (as compared to the background area), while Tl, Rb, Hf, Cs and P remain more commonly in the stipes of *L. scabrum*.

Comparison of species. Most toxic and other element concentrations are higher in spring than in autumn mushrooms (Fig. 19.5), except for Cs, Rb, Cd and Pb (at

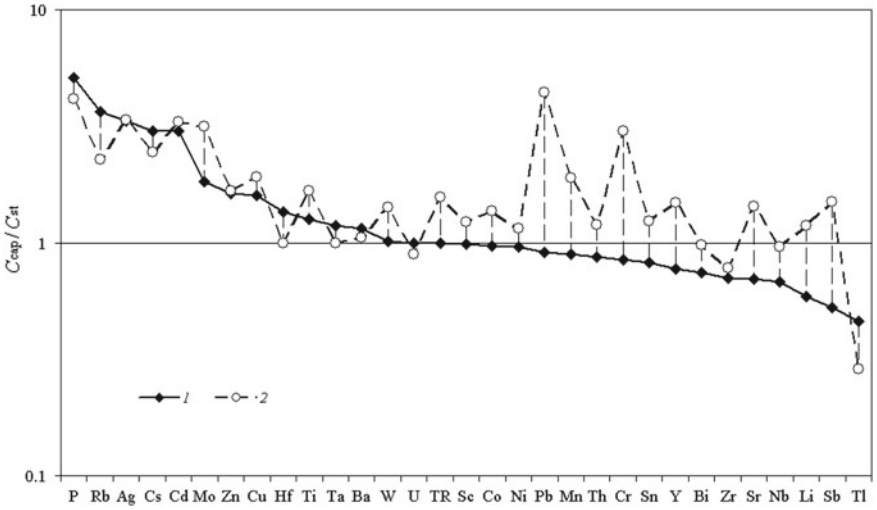


Fig. 19.4 Element concentration ratios in the caps and stipes of *L. scabrum* (C_{cap}/C_{st}): *1*—background area; *2*—former industrial site (by median values)

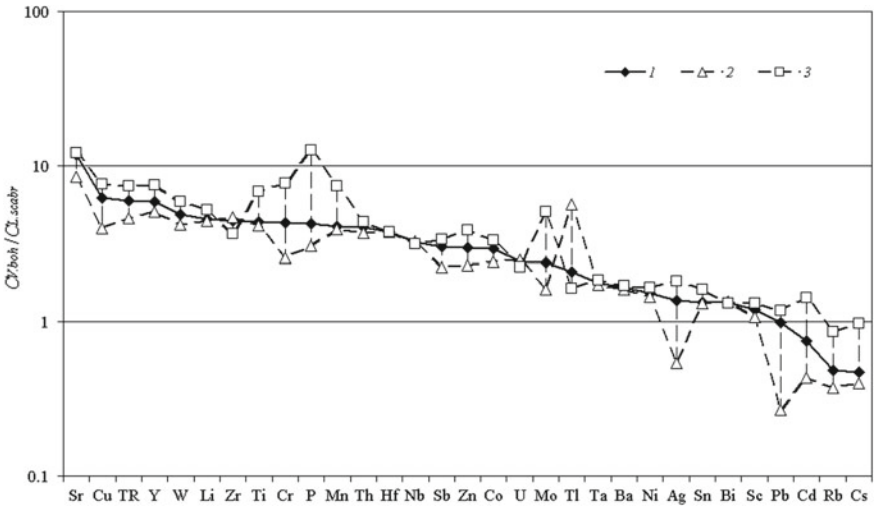


Fig. 19.5 The ratios of the element content of the composite sample of *V. bohemica* ($C_{V.boh}$) to the median content of *L. scabrum* ($C_{L.scabr}$) ($n = 10$): *1*—caps and stipes; 2—caps; *3*—stipes (*1–3*—of *L. scabrum*)

least half of *L. scabrum* samples), Sc, Ta, Bi, Ag, Tl, Sn, Li, Sb и Co (less than half of *L. scabrum* samples). Maximum and minimum element values on the geochemical spectra for the macromycete species studied are fairly consistent (Fig. 19.6): the linear correlation coefficient for lognormally distributed 30 element concentration values +ΣTR is 0.97 ($p < <0.001$; $n = 31$). The same ratios for *L. scabrum* at the industrially polluted and control sites (see Fig. 19.6) also display a linear coefficient of 0.97. Consequently, the transport of trace elements into various macromycete species is assumed to be controlled primarily by the properties of the chemical elements themselves, and their quantitative ratios, estimated with regard for lognormal distribution, fit into this pattern.

It can be seen from Fig. 19.6 that the macromycetes from both polluted and background areas most commonly accumulate P, Bi, Rb, Zn, Cu, Cd, Tl, Ag, Cs and Sc and far less commonly Zr, TR, Hf, Y, W, Sr, Nb, Th, Ti, Co, Mn, U, Cr, Mo, Pb, Sn and Sb. The latter is also typical of V; its concentration clarke value is 1.56 for the soil substrate and 0.027 for *V. bohemica* (V concentration in *L. scabrum* is below the detection limit in all cases).

Sequences of excess clarke values, based on Fig. 19.6 and the addition of V, are as follows: W > Ag > Mo > Bi > Pb > Cd > Sb > Hf > Sn > Zn > Cu > Cr > P > V > (Ni, Mn, Ti) (soil substrate); P > Ag > Bi > Zn > Cd > Cu > W (*V. bohemica*; former industrial site); Ag = Bi > P > Cd > Zn (*L. scabrum*; former industrial site); Cd > Ag > P > Bi > Sc > Rb > Zn (*L. scabrum*; background area).

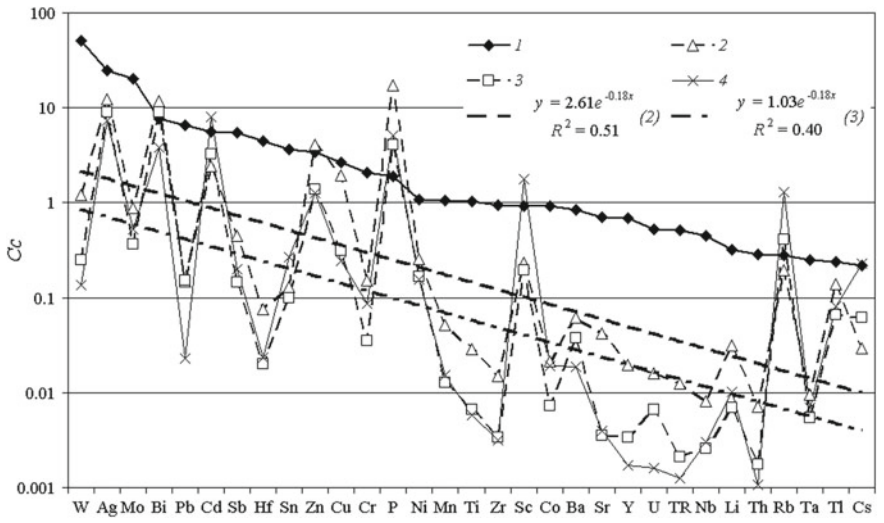


Fig. 19.6 Abundance ratios of elements (*Cc*) in: *1*—soil substrate at a depth of 0–0.1 m; *2*—composite sample of *V. bohemica*; *3*—*L. scabrum* (median values, $n = 10$) from the former industrial site; *4*—*L. scabrum* from the background area (median values, $n = 14$). Semi-bold dashed line = exponential trend lines (correspond to *2* and *3*). Clarks for calculation of *Cc* are after Vinogradov (Voitkevich et al. 1990)

Fungi/soil element concentration ratios. In most cases, element concentrations in the contaminated soil substrate are higher than those in the mushrooms growing on it (see Fig. 19.6).

In the case of *V. bohemica*, accumulation index values (I_a) > 1 were obtained only for P (9.06), Bi (~1.55) и Zn (1.22) and in the case of *L. scabrum* (estimated from the median value) for P (2.14), Rb (1.47) and Bi (~1.17). The I_a values of the following elements vary from 1.0 to 0.1: Cu (0.744), Rb (0.709), Tl (0.579), Ag (0.493), Cd (0.434), Sc (0.250), Ni (0.234), Cs (0.133) (*V. bohemica*), Cd (0.582), Zn (0.408), Ag (0.360), Cs (0.284), Tl (0.277), Sc (0.209), Ni (0.153), Cu (0.119) (*L. scabrum*). In other cases, $I_a < 0.1$ (poor or no accumulation). Thus, Mn concentration in the mushrooms was found to be much lower than the reference concentration in the soil: 12.7 mg/kg in *L. scabrum* (median concentration, $n = 10$) and 51.5 mg/kg in *V. bohemica* against 1050 mg/kg ($I_a = 0.012$ and 0.049, respectively). V concentration in *L. scabrum*, as shown above, was below the detection limit in all cases, while in *V. bohemica* it was 2.41 mg/kg against 140 mg/kg in the soil substrate ($I_a = 0.017$). Zr, TR, Hf, Y, W, Sr, Nb, Th, Ti and Co are not accumulated practically in the fruit bodies of *L. scabrum* ($I_a < 0.01$).

19.4 Discussion

Evidence for considerable heavy metal and metalloid pollution of the soils and grounds in the urbanized zone of central Petrozavodsk has been supported by new geochemical studies. The pollution is distributed irregularly on the surface and in the deep layers of the soil-ground sequence in the former industrial zone (centre of the multi-element geochemical anomaly studied) and in the soils of the nearest recreation areas. Zn, Cu, Mn, Pb, Cd, Ni pollution levels decreases with a distance from the pollution centre. However, Cd concentration within the geochemical anomaly zone, in contrast to other pollutant concentrations, is generally lower than the median value for urban soils, which is due to the geological and geochemical characteristics of the study area. The pollution revealed is most similar in element composition to industrial emissions from the machine-building and metal processing and partly power engineering industries economic activities. They were assessed from available data for geochemical landscapes in the Eastern Administrative District of Moscow (Kasimov et al. 2016): W, Mo, Zn, Sn, Sb, Ni, Cr, Cu, Mn, Pb, Co, V, As, (Sc, P) and V, Ni, (Pb, Mo, Ge, Cr, Zn, W, Be, Li, Cu, Ag and Sn), respectively. The elements, which have not been reliably proved to occur in the above associations in Petrozavodsk, are shown in parentheses (Rybakov and Veselkova 2015).

Pollutant concentrations in the <0.1 mm fraction of chemically altered soils are higher than those in coarser (0.1–1.0 mm) fractions, except for Pb and Sn, concentrated partly as their oxygen compounds, not only a soil-absorbing complex (Rybakov and Kevlich 2017).

The industrially contaminated soils and grounds of the former industrial zone are assessed as «*extremely hazardous*» and «*hazardous*», based on current stan-

dards. According to sanitary rules (Sanitary and epidemiological 2003), contaminated ground of the former type should be removed and utilized at special dumping sites, while polluted ground of the latter type could be used on a limited scale for filling hollows and trenches so that polluted ground is overlain by an at least 0.5 m thick clean ground layer outside residential areas.

Assessment of industrially polluted soils and grounds as «*extremely hazardous*» or «*hazardous*», based on sanitary-toxicological indices, depends on the relative amount of a fraction with a particle size of <0.1 mm. The greater the amount of such particles in the ground, the more hazardous the ground.

The study of the trace element composition of the macromycetes growing on a limited scale in the residual industrial pollution zone has shown them to be hazardous as food. Both spring and autumn pileate mushrooms are hazardous. Major chemicals are accumulated in them in various quantities, specifically *V. bohemica* contains more Cu and Zn, while *L. scabrum* (particularly caps) accumulates more Cd and Pb.

Differences in the concentration levels of practically all the elements supplied into the mushrooms may be due to seasonal variations in their mobile (available) form concentration in the soil substrate, e.g. the effect of variations in humidity, temperature and microbiological and enzymatic activity (Gukalov 2015). For example, in 2014, when most samples were collected in the industrially polluted zone, the amount of precipitation in May (56.9; 44.6 mm before 20 May) was greater than in September (29.5 mm), as shown by Petrozavodsk Weather Station (Specialized arrays 2018). It should be noted that the soils in the Petrozavodsk area were heated poorer in May than in September: total mean daily temperatures at a depth of 20 cm were 29.1 and 41.3 °C, respectively. These values were used as reference in our studies. Seasonal variations in soil conditions, together with the assumed effect of specific differences, including a type of nutrition, can provide more factors for assessing element concentration in the fruit bodies of macromycetes (see Fig. 19.5). However, the properties of chemical elements themselves are responsible for the general pattern of the trace elements penetrating into the fruit bodies of various macromycete species growing in contaminated and background areas (see Fig. 19.6).

Comparison with the background concentrations has revealed major elements supplied from the contaminated soil substrate into *L. scabrum* growing at the former industrial site in Petrozavodsk. Mushroom caps and stipes concentrate such industrial pollutants as Pb, Bi, W, Ba, Cu and Ag, as well as natural association elements, e.g. U, Th, Y and ΣTR. As Cd concentrations in the control samples of *L. scabrum* are high (particularly in the cap), the pollution of the impact zone by this toxic metal is confirmed by its maximum concentration and the excess of the MPC value. Furthermore, samples from the background area often display elevated concentrations of Mo, Sn, Cr, Mn and Co, which are among the major pollutants in the former industrial zone (see Figs. 19.3 and 19.6).

Element differentiation in the fruit body of *L. scabrum* indicates that they are mostly supplied (except for Tl, Zr, U, Nb, Bi and Ta) into mushroom caps in the pollution zone, while the concentrations of many elements in stipes from the background area are higher than those from the caps (see Fig. 19.4). Variations in the degree of differentiation could be attributed to element concentration levels in the

soil, local conditions for soil processes and the degree of mycorrhization of plant roots. However, further studies are needed to clear up these matters.

The accumulation of various quantities of toxic and other substances by the macromycete species studied growing on the soil substrate affects the accumulation index value. Thus, in the case of *V. bohemica*, growing in the industrial pollution zone, $I_a > 1$ was estimated only for P, Bi and Zn, and in the case of *L. scabrum* (from the median concentration value) for Pb, Rb and Bi. For other elements, including toxic substances, $I_a < 1$. Extended sequences of pollutant accumulation intensity in the macromycetes ($I_a > 0.1$) are as follows: P $\gg$ Bi > Zn > Cu > Rb > Tl > > Ag > Cd > Sc > Ni > Cs, etc. (*V. bohemica*), P > Rb > Bi > Cd > Zn > Ag > Cs > Tl > Sc > Ni > Cu, etc. (*L. scabrum*). The absence of Pb ($I_a = 0.023$) from these sequences does not mean that Pb, together with other toxic elements that accumulated in the industrial pollution zone, exerts a minor harmful effect on the biota.

19.5 Conclusions

The soils and grounds in the former industrial zone on the Lososinka river bank in central Petrozavodsk display a high heavy metal and metalloid (Pb, Cu, Zn, W, Mo, Cr, Ni, As, etc.) pollution level. The toxic substances revealed are concentrated mainly in fine soil fractions (<0.1 mm and finer) and are maintained by a soil-absorbing complex. Therefore, the degree of the environmental hazard of polluted soils and grounds depends on the amounts of such fractions in them.

The soil-ground sequence in the former industrial zone is generally assessed at least as «*hazardous*», based on current standards. The soils in the areas near the pollution centre (former industrial zone) of the recreation area are less heavily contaminated, but are still being affected by past production processes. If no normative measures are taken to neutralize toxic substances in this area, then the impact zone biota will be endangered.

Macromycete species from the contamination zone concentrate toxic and other chemical elements to a different extent than those in the background area (*L. scabrum*) and in the soil substrate. Potentially hazardous elements (Pb, Bi, W, Ba, Cu, Ag, Zn, Ni, etc.), as well as Y, U, TR and Th, generally accumulate in mushrooms from the contamination zone in larger quantities than those from the background (control) area. However, a more detailed analysis of the background areas is needed to identify the possible natural and anthropogenic sources of some heavy metals such as Co, Cr, Sn, Cd, Sb, Mo, Sr, Mn and Tl, e.g. the trans-boundary and interregional transport of air pollutants.

Both spring and autumn species of contaminated mushrooms may be hazardous when consumed as a food. The toxic substances they contain are accumulated in various quantities: e.g. *V. bohemica* has more Cu and Zn, while *L. scabrum* generally accumulates Cd and Pb more actively. In *L. scabrum,* the highest toxic element concentrations are more commonly observed in the caps and lower concentrations in

the stipes (particularly when contaminated). The possible use of the species studied in industrial pollution zones for bioremediation implies that they cannot be used as food products. Therefore, in addition to the study of mushrooms, particularly with regard for contaminated sites accessible to the population, non-edible plants that grow well and actively accumulate heavy metals should be sought for and revealed.

References

Anishchenko LN, Ladnova GG, Frolova NV (2016) Peculiarities of heavy metals accumulation by the fruit bodies of macromycetes in the conditions of combined radiation and chemical contamination. World of Sci Discov 8(80):81–96 (in Russian). https://elibrary.ru/item.asp?id=26726307. Accessed 20 Nov 2018 (in Russian)

Bakaitis VI, Basalaeva CN (2007) Criteria of quality and safety of wild-growing mushrooms as food and raw materials. Mod Prob Nat Manag, Hunting Fur Farming 1:37–38. https://cyberleninka.ru/article/n/kriterii-kachestva-i-bezopasnosti-dikorastuschih-gribov-kak-produktov-pitaniya-i-syrya. Accessed 22 Nov 2018 (in Russian)

Byrne AR, Ravnik V, Kosta L (1976) Trace element concentrations in higher fungi. Sci Total Environ 6(1):65–78. https://doi.org/10.1016/0048-9697(76)90007-3

Fedorets NG, Bakhmet ON, Solodovnikov AN, Morozov AK (2008) Soils of Karelia: geochemical atlas. Science, Moscow (in Russian)

Gukalov VN (2015) Assessment of the state of heavy metals in the chernozems of the southern European group of steppe soil-bioclimatic region in agrolandscape system. Dissertation, RSAU—MAA named after KA Timiryazev. https://docplayer.ru/34498881-Otsenka-sostoyaniya-tyazhelykh-metallov-v-chernozemakh-yuzhno-evropeyskoy-gruppy-stepnoy-pochvenno-bioklimaticheskoy-oblasti-v-sisteme-agrolandshafta.html. Accessed 5 Dec 2018 (in Russian)

Hygienic requirements for safety and nutritional value of food products (2001) Sanitary Rules and Norms SanPiN 2.3.2.1078-01. http://base.garant.ru/4178234/. Accessed 2 Dec 2018 (in Russian)

Isaeva LG (2014) The content of elements in the tinder and edible mushrooms in conditions of aerotechnogenic pollution. In: Storozhenko VG, Ruokolainen AV (eds) Fungal communities in forest ecosystems. KarRC of RAS, Moscow; Petrozavodsk (in Russian)

Kabata-Pendias A, Pendias H (1989) Trace elements in soils and plants. Mir, Moscow (in Russian)

Kalač P, Svoboda L (2000) A review of trace element concentrations in edible mushrooms. Food Chem 69(3):273–281. http://kch.zf.jcu.cz/vyzkum/publikace/separaty/2000-0281.pdf. Accessed 22 Nov 2018

Kasimov NS, Vlasov DV, Kosheleva NE, Nikiforova EM (2016) Landscape geochemistry of Eastern Moscow. APR, Moscow (in Russian)

Kulshreshtha S, Mathur N, Bhatnagar P (2014) Mushroom as a product and their role in mycoremediation. AMB Expr 4:29–36. https://doi.org/10.1186/s13568-014-0029-8

Maximum permissible concentrations of heavy metals and arsenic in food raw materials and food products (1986) Sanitary Rules and Norms SanPiN 42-123-4089-86. http://www.docipedia.ru/document/5182275. Accessed 2 Dec 2018 (in Russian)

Maximum permissible concentrations (MPC) of chemicals in soil (2006) Hygienic Norms GN 2.1.7.2041-06. http://www.consultant.ru/document/cons_doc_LAW_58393/. Accessed 2 Dec 2016 (in Russian)

Rybakov DS (2017) Geoecology of Karelia: a geochemical approach to the problems of risk assessment. KarRC of RAS, Petrozavodsk (in Russian)

Rybakov DS, Kevlich VI (2017) Microelements in anthropogenically contaminated soils in the central part of Petrozavodsk. Eur Soil Sci 50(6):708–719. https://doi.org/10.7868/S0032180X17060107

Rybakov DS, Veselkova SA (2015) Association of chemical elements in contaminated soils of the former industrial site. In: Proceedings of the IV international scientific and practical conference "ecological geology: theory, practice and regional problems". Petrozavodsk–Voronezh, pp 191–194 (in Russian)

Rybakov DS, Krutskikh NV, Shelekhova TS, Lavrova NB, Slukovskii ZI, Krichevtsova MV, Lazareva OV (2013) Climatic and geochemical aspects of the ecological risks formation in the Republic of Karelia. Resp. ed. by Yablokov AV. Publ Comp Elexis LLC, St. Petersburg (in Russian)

Sanitary and epidemiological soil quality requirements (2003) Sanitary Rules and Norms SanPiN 2.1.7.1287-03. http://www.consultant.ru/document/cons_doc_LAW_42140/. Accessed 22 Nov 2018 (in Russian)

Sazanova KV, Velikova VD, Stolyarova NV (2017) Accumulation of heavy metals by mushrooms. Ecological and species specificity, mechanisms of accumulation, risk for human health. Medline.ru 18(24):336–361. http://medline.ru/public/art/tom18/art24.html. Accessed 22 Nov 2018 (in Russian)

Sibirkina RA (2014) Biogeochemical assessment of heavy metals content in pine forests of Semipalatinsk Irtysh region. Dissertation, Chelyabinsk State University. https://omgpu.ru/sites/default/files/files/dissert/4109/sibirkina_ar.pdf. Accessed 1 Oct 2018 (in Russian)

Specialized arrays for climate research. RIHMI-WDC, Obninsk. http://aisori.meteo.ru/ClimateR. Accessed 3 Feb 2018 (in Russian)

Stamets P (2005) Mycelium running: how mushrooms can help save the world. Ten Speed Press, Berkeley

Svetov SA, Stepanova AV, Chazhengina SYu, Svetova EN, Rybnikova ZP, Mikhailova AI, Paramonov AS, Utitsyna VL, Ekhova MV, Kolodei VS (2015) Precision (ICP-MS, LA-ICP-MS) analysis of the composition of rocks and minerals: method and evaluation of accuracy of the results by example of Early Precambrian mafic complexes. Proceedings of KarRC RAS, Precambr Geol 7:54–73. https://doi.org/10.17076/geo140GoogleScholar

Treu R, Falandysz J (2017) Mycoremediation of hydrocarbons with basidiomycetes—a review. J Environ Sci Health B 52(3):148–155. https://doi.org/10.1080/03601234.2017.1261536

Vodyanitskii YuN (2008) Heavy metals and metalloids in soils. Dokuchaev Soil Sci Inst, Moscow (in Russian)

Voitkevich GV, Kokin AV, Miroshnikov AE, Prokhorov VG (1990) Handbook of geochemistry. Nedra, Moscow (in Russian)

Zhu F, Qu L, Fan W, Qiao M, Hao H, Wang X (2011) Assessment of heavy metals in some wild edible mushrooms collected from Yunnan Province. China Environ Monit Assess 179(1–4):191–199. https://doi.org/10.1007/s10661-010-1728-5

Chapter 20
Assessment of Biochar Potential to Neutralize the Effect of Olive Mill Wastewater on Plant Growth in Alkaline Sand

Obiageli P. Umeugochukwu, Andrei B. Rozanov and Ailsa G. Hardie

Abstract The biotic-abiotic interactions are particularly challenging in alkaline conditions. Growth of plants is an ultimate indicator of such interactions. The on-land disposal of olive mill wastewater (OMW) negatively affects plant growth due to its high phytotoxic organic polyphenol content. Our previous study has shown that phenols may be successfully sorbed on biochar—one of the most promoted soil amendments. A greenhouse experiment was conducted to determine the combined and separate effect of OMW (applied at 50, 100 and 200 m^3 ha^{-1}) and pinewood biochar (applied at 0.5, 2.5 and 5%) on the growth of wheat and green beans in an alkaline sand. Results showed that increasing OMW rate significantly suppressed wheat growth especially the above ground phytometrics, and that biochar addition did not significantly mitigate this effect. This was mainly attributed to unsuitable high pH growing conditions of the wheat, which was enhanced by application of OMW and biochar. In contrast, the lowest OMW only and 5% biochar only treatments positively affected bean phytometrics, though not statistically significant. A significant positive interaction was obtained in the bean total biomass when 2.5 and 5% biochar was applied on soil that received 100 m^3 ha^{-1} OMW. Findings showed that pinewood biochar application at 2.5 and 5% enhanced tolerance of beans to OMW applied at 100 and 200 m^3 ha^{-1} likely due to not only reduction of phenol toxicity but also due to increased available soil P and K.

Keywords Alkaline sand · Green beans · Phytotoxicity · Polyphenols · Spring · Wheat

O. P. Umeugochukwu · A. B. Rozanov (✉) · A. G. Hardie
Department of Soil Science, Stellenbosch University,
Private Bag X1, Matieland 7602, South Africa
e-mail: dar@sun.ac.za

O. P. Umeugochukwu
Department of Soil Science, Federal University of Technology, Minna, Niger State, Nigeria

© Springer Nature Switzerland AG 2020

O. V. Frank-Kamenetskaya et al. (eds.), *Processes and Phenomena on the Boundary Between Biogenic and Abiogenic Nature*, Lecture Notes in Earth System Sciences,
https://doi.org/10.1007/978-3-030-21614-6_20

20.1 Introduction

The biotic-abiotic interactions are particularly complex in alkaline soils treated with organic compounds. One source of such organic contamination is the olive mill wastewater (OMW). The on-land disposal of OMW is a common practice globally (Kapellakis et al. 2008; Umeugochukwu 2016). OMW is a contentious substance showing both positive and negative effects on soils and crops, is a major by-product of olive oil production (Mekki et al. 2009, 2013). OMW is characterized by high chemical oxygen demand (COD) ranging from 50,000 to 150,000 mg L^{-1}, high polyphenol content of 500 to 23,000 mg L^{-1}, high C:N ratio (43:1) and often high salt content (McNamara et al. 2008; Belaid et al. 2013). A case of particular interest is the fate of the OMW and its interaction with crops in alkaline environments, which are less studied than acidic soils. Major olive production often occurs in predominantly alkaline sands of coastal areas (e.g., Mediterranean regions) (Angiolini et al. 2013; Fenu et al. 2013). Despite having well-known adverse effects on the ecology of the disposal sites due to the presence of phytotoxic organic polyphenols, application of the OMW in the Mediterranean regions has been reported to inhibit germination of wheat and barley seeds (Rusan et al. 2015) and reduce plant growth phytometrics of tulip plants (Lykas et al. 2014). The roots of cherry tomatoes reacted more sensitively to OMW than the upper parts (Ouzounidou et al. 2008) due to high phytotoxic effects of polyphenol and fatty acids resulting in decreased tomato performance with increased OMW application.

As a measure to mitigate the impacts of OMW in agricultural lands, researchers have, besides on-land disposal, tried different methods of OMW treatment such as: activated clay (Al-Malah et al. 2000; Aziz et al. 2012), bio-augmentation (Mekki et al. 2013), and sand filtration (Achak et al. 2009). Paraskeva and Diamadopoulos (2006) reported that OMW adsorbed onto activated carbon removed 81% of phenol. Biochar, a by-product derived from the pyrolysis of organic biomass has been widely investigated as a low cost wastewater treatment and soil amendment (Mohan et al. 2014; Hina et al. 2015). Biochar retains plant nutrients (Barrow 2012) and, when combined with compost, the mixture enhances plant growth and is more effective than mineral fertilizers (Schulz and Glaser 2012). López-Cano et al. (2016) reported reduced N losses and improved N cycling, hence, increased N availability in lignocellulosic and N poor materials due to addition of small quantity of biochar to composting of olive mill wastes.

Here we focus on biochar, which has been reported to mitigate the phytotoxicity of several residues with high phenolic content. Gell et al. (2011) found that biochar consistently reduced phytotoxicity in soil amended with wheat dried distillers' grains with solubles (DDGS), a residue from bioethanol production. Deng et al. (2013) also reported that *Pinus massoniana* biochar can be used for effective removal of phenol from aqueous solution. The beneficial effect of biochar could be related to the sorption, deactivation and further microbial degradation of pollutants sorbed on the biochar surfaces. Biochar itself however may have negative effect in alkaline environment by further increasing alkalinity and reducing availability of nitrogen

(Sika and Hardie 2014). Barbera et al. (2013) suggested adding N to influence the kinetics of OMW degradation by reducing the high C:N ratio that results from OMW applications. Nitrogen can be added to the soil via nitrogen fixing leguminous crops, hence the use of green beans as a test crop in this study to understand the combined effect of N fixation, biochar and OMW application.

In a different study, Sekar (2012) combined biochar and digested OMW and found that it reduced the pH below that of the biochar alone but the change was not significant. So as part of the hypothesis, the acidic nature of the OMW will influence the pH of the soil combined with biochar. Sekar (2012) further reported that biochar tends to have a negatively charged surface under alkaline conditions, suggesting that the cations from the OMW will be bound to the surfaces of the biochar. This phenomenon was expected to improve production of crops under alkaline conditions. Since there is dearth of scientific literature on the impact of biochar on olive mill wastewater toxicity with respect N addition and reduced soil pH, we hypothesize in this study that the addition of biochar will detoxify the effect of olive mill wastewater and improve the growth of both green beans and wheat in a Mediterranean environment. The specific objectives include: (i) to determine the individual effect of different rates of application of OMW and biochar on selected growth parameters of wheat and green beans in alkaline sand; (ii) determine the combined effects of the OMW and biochar application on growth parameters of wheat and green beans in greenhouse pot trials. This experiment allows the monitoring of plant growth as an ultimate test of biotic-abiotic interactions in alkaline sands amended with OMW, biochar and the mixture of both.

20.2 Materials and Methods

20.2.1 Sand Used in This Experiment

The used in this study sand was purchased from the GH Supplies (Pty) Ltd Stellenbosch, South Africa. A sand sample was air-dried and sieved through a 2 mm sieve. The pH was determined using the 1:2.5 ratio in water and 1 M KCl (Thomas 1996) and read using a EUTHECH 700 pH meter. Electrical conductivity (EC) was determined in saturated sand-water paste and read using an EC meter. The concentrations of available phosphorus (P), calcium (Ca), magnesium (Mg), potassium (K), and sodium (Na) in citric acid (1%) extract were analyzed using Inductively Coupled Plasma spectroscopy (ICP) following the methods described by Non-Affiliated Soil Analysis Work Committee and Soil Science Society of South Africa (1990). Soil organic carbon was determined by the Walkley-Black method (Nelson and Sommers 1996) and total nitrogen by the Kjeldahl method (Bremner, 1996). The texture of the soil was determined using the pipette method (Gee and Or 2002), and was found to be a pure sand (99% sand). The choice of sand as opposed to natural soil

was informed by the decision to avoid additional complication of organo-mineral interactions between polyphenols and clay particles in natural soils.

20.2.2 Biochar Properties

The biochar used in this experiment, was produced from pinewood sawmill waste by a small-scale commercial producer from the Eastern Cape, South Africa, has been previously characterized and described by Sika and Hardie (2014). The sawmill waste was slow-pyrolyzed at approximately 450 °C, and then crushed and sieved through a 2 mm sieve prior to use in the experiments. The C and N was determined by the dry combustion method using Elemental analyzer, 3000 series (Euro Vector Milan, Italy). Biochar chemical properties are given in Table 20.1. The previously reported proximate analysis (TGA) of the pinewood biochar were as follows: % volatiles (19.90), % fixed C (74.45), % ash (3.04) (Sika and Hardie 2014).

20.2.3 Olive Oil Mill Wastewater Sampling and Characterization

The OMW was collected from the storage dam of an olive producer just outside of Stellenbosch, South Africa. The method of production of the OMW was a two-phase system which has the advantage of reduced water consumption for the mills (Borja et al. 2006). The wastewater was collected from the separator point of the two phase system and at this point, the water has the same characteristics with the wastewater from the three phase system. The characterization of olive mill wastewater was done by digestion with 1 ml HNO_3 and then analyzed using Inductively Coupled Plasma-Atomic Emission Spectroscopy (ICP-AES). The total phenol content was determined using the Folin-Ciocalteu method described in Ainsworth and Gillespie (2007) as modified by Alhakmani et al. (2013), using 0.5 mL of the OMW. Gallic acid was used as the reference standard for plotting the calibration curve. The absorbance of the total phenol concentration was measured using Pharmacia Ultrospec III UV/Visible spectrophotometer and read at a wavelength of 765 nm. The total phenol concentration was calculated from the linear equation of the standard curve prepared with gallic acid. The concentration of the total phenols was expressed as mg L^{-1} of gallic acid equivalent. The pH of the OMW was read from 30 mL of the sample using EUTHECH 700 pH meter. Chemical Oxygen Demand (COD), Total organic carbon (TOC) and Total Nitrogen (TN) were determined using the applicable method described in the (Standard Methods (2012). The chemical properties of the OMW are shown in Table 20.2.

Table 20.1 Selected chemical properties of alkaline sand, sand-biochar-OMW mixtures and biochar

OMW m^3 ha^{-1}	Biochar %	pH (H_2O)	pH (KCl)	EC mS m^{-1}	Ca mg kg^{-1}	Mg mg kg^{-1}	Na mg kg^{-1}	K mg kg^{-1}	P mg kg^{-1}	C %	N%	C:N
0	0	9.2	9.1	12.1	14,120	315.6	163	10	24	0.04	0.006	6.7
0	0.5	9.0	9.1	12.3	16,740	312.2	162	20	24	0.04	0.006	6.7
0	2.5	9.1	9.0	15.5	16,250	296.4	154	38	24	0.06	0.007	8.6
0	5.0	9.1	9.0	23.8	13,280	264.0	134	93	24	0.12	0.004	30.0
50	0	8.9	9.0	27.2	13,220	306.0	161	24	38	0.04	0.007	5.7
50	0.5	9.2	9.2	16.0	13,010	307.2	161	32	25	0.04	0.006	6.7
50	2.5	9.2	9.0	21.0	14,600	277.2	139	51	25	0.05	0.005	10.0
50	5.0	9.3	9.0	25.8	12,550	260.4	139	99	25	0.12	0.005	24.0
100	0	9.4	9.2	24.0	14,340	290.4	157	35	26	0.04	0.006	6.7
100	0.5	9.3	9.2	24.8	17,100	286.8	155	41	25	0.04	0.006	6.7
100	2.5	9.3	9.1	25.0	14,220	279.6	150	61	27	0.08	0.007	11.4
100	5.0	9.4	9.1	32.0	12,470	253.2	140	109	26	0.14	0.007	20.0
200	0	9.5	9.3	29.4	17,290	280.8	163	51	27	0.04	0.008	5.0
200	0.5	9.5	9.2	33.3	14,870	284.4	162	58	28	0.05	0.010	5.0
200	2.5	9.7	9.2	31.6	13,080	273.6	151	78	26	0.10	0.009	11.1
200	5.0	9.7	9.1	39.7	13,240	258.0	151	129	30	0.13	0.005	26.0
Biochar	–	9.30	8.50	0.007	950	162.0	1.0	3.7	90	82.70	0.530	156.1

Table 20.2 Characteristics of two phase Olive mill wastewater collected from the separator point of processing

Property	Values
pH	5.14
Total phenol mg L^{-1}	971.0
EC uS/cm	1005.0
Ca mg L^{-1}	47.2
K mg L^{-1}	408.6
Mg mg L^{-1}	11.2
Na mg L^{-1}	165.7
P mg L^{-1}	20.0
N mg L^{-1}	82.0
TOC mg L^{-1}	2000
COD mg L^{-1}	13,700
C:N ratio	24

20.2.4 Sand-Biochar-OMW Mixture Characteristics

The sand (3.5 kg) was mixed with 0, 0.5, 2.5 and 5.0% (w/w) biochar in factorial combinations with 0, 50, 100, and 200 m^3 ha^{-1} of OMW. The mixing rates were calculated by assuming 15 cm soil depth and a calculated sand bulk density of 1.45 g cm^{-3}. The chemical properties of the sand-biochar-OMW mixtures were determined as described for the sand above and are shown in Table 20.1.

20.2.5 Greenhouse Trial Experiment

A greenhouse trial was conducted in a tunnel at the Welgevallen experimental farm of the Stellenbosch University, South Africa (lat. 33° 56′ 34.65 S, long. 18° 51′ 55.84 E). Wheat and green bean pot trials were laid out in a 4 × 4 factorial arrangement in a completely randomized design (CRD) with three replications to elucidate the individual and combined effects of biochar and OMW soil amendment.

The sand mixtures of 3.5 kg were deposited into four-liter planting bags. The bags were perforated at the bottom to allow for sufficient drainage. There were two sets of 16 treatments, each used for each crop: winter wheat (*Triticum aestivum L.*) and green bean (*Phaseolus vulgaris*) respectively as test crops. These crops were selected as test crop species because green beans were leguminous and capable of fixing nitrogen and wheat was used to distinct the effect of nitrogen fixation. Also wheat is a common crop in the Mediterranean climate regions.

After mixing the sand with OMW and biochar, the mixtures were left for seven days before planting to allow the OMW to fully interact and for the biochar to have sorbed the contaminants in the OMW. Mekki et al. (2007) reported that there was

no germination for crops that were planted immediately after amending the soil with OMW. Though C mineralization starts immediately with biochar mixtures (Jien et al. 2015).

All the 4-L planting bags were irrigated when the sand water depletion level reached 50% of the plant available water. Field capacity was determined as described by Romano and Santini (2002). The water addition was the same for all the bags irrespective of the differences in the treatment water holding capacities. The bean seeds were soaked overnight before planting to enhance germination. Four bean seeds and 10 wheat seeds were planted per bag. Thinning to 1 bean and 4 wheat plant respectively, was carried out at 40 days after planting because emergence was delayed by 2 weeks and initial seedling growth rate was slow. Micronutrients were incorporated by adding 0.2 g of Omnia nutrition (Hidrospoor) containing 86.9 Fe, 18 Mn, 10.7 Zn, 1.2 g g^{-1} Cu, 22 B and 1.9 g kg^{-1} Mo. This was dissolved in 10 L of tap water and sprayed with a knapsack sprayer 60 days after planting when chlorosis was noticed on both crops. There was no further fertilizer application to the plants.

20.2.6 Plant Growth Phytometrics

A number of measurements were taken on the test crops: plant height and number of leaves were determined and the results presented were for the third week after planting. Two tagged wheat plants and the only bean plant in each poly bags were used for data collection The plant height was taken from soil level to the tip of the topmost leaf with a meter ruler. Plant biomass [above ground biomass (AGB) and below ground biomass (BGB)] was determined destructively at 70 days for beans and 73 days for wheat. The plant samples were dried at 80 °C for 48 h and then weighed.

20.2.7 Statistical Analysis

The data for plant height and the number of leaves was collected and analyzed using the mixed model repeated measures ANOVA. The following main effects were measured: biochar main effect, OMW main effect, and the interactions effects. The biomass and the nutrient data were analyzed using the general linear model using two-way factorial-ANOVA to test biochar main effect, OMW main effect and biochar and OMW interactions effect. Fisher Least Significant Difference (LSD) post hoc testing was also done to determine the significant differences among the treatments ($p < 0.05$). The data were statistically analyzed using STATISTICA 12.6 software.

Table 20.3 The correlation of the treatments with the chemical properties of the sand-biochar-OMW mixture at the end of the experiment and their significance levels

Pair of variables	Correlation R	p-value
OMW & pH (KCl)	0.660401	0.005361
OMW & K (mg/kg)	0.497564	0.049864
OMW & P (mg/kg)	0.790787	0.000265
OMW & EC (mS/m)	0.848875	0.000032
Biochar & Mg (mg/kg)	−0.800368	0.000196
Biochar & Na (mg/kg)	−0.858099	0.000021
Biochar & K (mg/kg)	0.825228	0.000083
Biochar & C (%)	0.874891	0.000009
Biochar & C:N	0.856135	0.000023

20.3 Results

20.3.1 Sand-Biochar-OMW Mixture Characteristics

The OMW addition significantly positively correlated with soil EC (mS m^{-1}), pH (KCl), and available P and K (Table 20.3). While, biochar addition significantly positively correlated with soil available K and C content, and negatively correlated with available Mg and Na (Table 20.3). Biochar also significantly increased soil C:N ratio (Table 20.3).

20.3.2 OMW Effects on Plant Growth Phytometrics

The total biomass of wheat experienced a linear decline ($R^2 = 0.998$) with increasing OMW application rates (Fig. 20.1a). The increased rates of the OMW suppressed ABG (Fig. 20.1a). The 50 m^3 ha^{-1} OMW treatment had a positive, but not significant, effect on the bean biomass (Fig. 20.1b). In both crops the allocation of phytomass to roots increased from 55 to 60% in wheat ($R^2 = 0.667$), and from 40 to 45% in beans ($R^2 = 0.344$). These changes were significant at $\alpha = 0.1$.

Application of OMW at 100 and 200 m^3 ha^{-1} rates resulted in significantly shorter wheat plants than that of the control (Fig. 20.2a). Whereas, in the bean trial the 50 m^3 ha^{-1} OMW treatment enhanced plant height, but not significantly (Fig. 20.2a). The number of wheat leaves decreased significantly from the control with increasing OMW rate, while the number of bean leaves was increased in all OMW treatments, but not significantly (Fig. 20.2b).

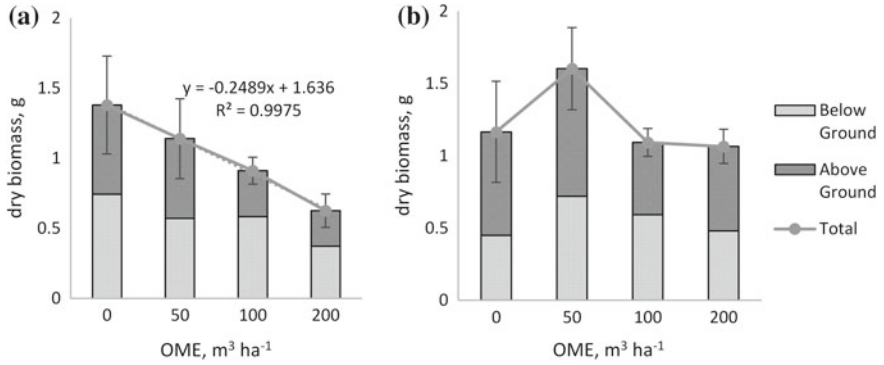


Fig. 20.1 OMW effect on the plant above-ground biomass (AGB) and below-ground biomass (BGB) of **a** wheat and **b** beans plants grown on alkaline sand. Vertical bars are standard deviation of total biomass production

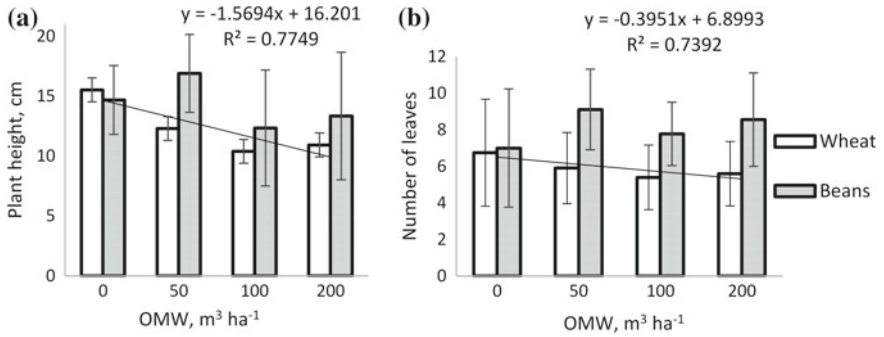


Fig. 20.2 OMW effect on **a** the plant height and **b** number of leaves of wheat and bean plants grown on alkaline sands. Vertical bars are standard deviation

20.3.3 Biochar Effects on the Plant Growth Phytometrics

The effects of biochar on performance of wheat and beans are summarized in Figs. 20.3 and 20.4. Addition of biochar only led to significant decline in total and AGB but not BGB of wheat, whereas in beans, it had not significant effect on biomass (Fig. 20.4b). A marginal decrease in bean AGB in all biochar treatments (Fig. 20.4b).

Biochar addition had a non-significant effect on wheat and bean plant height (Fig. 20.3a), but its addition at 2.5 and 5% led to greater number of bean leaves, although not significantly (Fig. 20.3b).

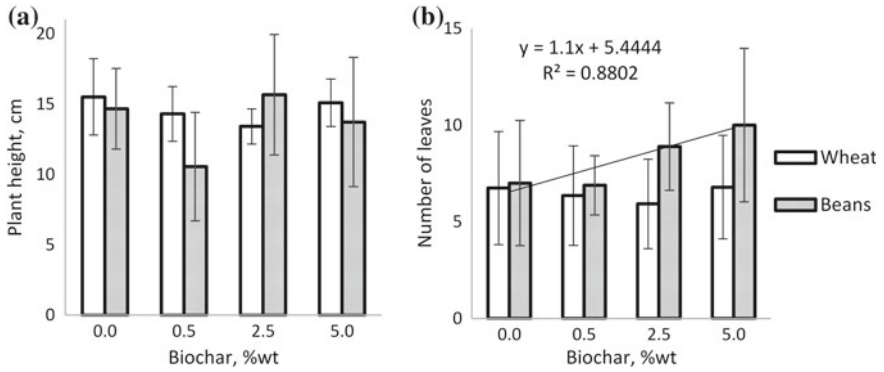


Fig. 20.3 Biochar effect on **a** plant height and **b** number of leaves of beans and wheat plants grown on alkaline sand. Vertical bars are standard deviation

20.3.4 Biochar and OMW Combined Effects on Growth Phytometrics

There was no significant effect of the combined biochar and OMW treatments on the plant height and number of leaves in both wheat and beans. Biochar amendment also had no significant effect on wheat biomass production in soils that received OMW (Fig. 20.4a). Bean biomass production showed a significant positive response to 2.5 and 5% biochar amendment rates in soils treated with 100 and 200 m^3 ha^{-1} OMW treatment. There was also a positive but not significant response to 0.5, 2.5 and 5% biochar amendment rates in soils that received 200 m^3 ha^{-1} OMW. All of the 0.5% biochar and 100 m^3 ha^{-1} OMW treatment replicates wilted at early stages of plant development rendering this treatment invalid.

20.4 Discussion

20.4.1 Sand-Biochar-OMW Mixture Characteristics

The untreated sand had a very high pH of 9.2 in water (Table 20.1), indicating the presence of a more soluble source of alkalinity such as $Ca(OH)_2$ (saturated equilibrium pH of 12.6) than calcitic lime (saturated equilibrium pH of 8.3), likely due to cement contamination. This is further confirmed by the excessively high Ca content of the sand (14,120 mg kg^{-1}), compared to other basic cations (Table 20.1). A soil pH above 8.5 is not considered suitable for crop production as deficiencies of trace metals, and other nutrient antagonisms would be expected (Havlin et al. 2005; FSSA 2007). Application of OMW significantly enhanced soil pH measured in water and KCl (Tables 20.1 and 20.3), whereas application of biochar did not

significantly correlate with soil pH. However, it was apparent that biochar enhanced soil pH measured in water when applied together with OMW (Table 20.2). It is likely that application of phenols and other weak organic acids contained in the OMW (Table 20.1) led to the observed increase in soil pH. Phenol has a pKa of 10.0, which means that it would preferentially complex protons at soil pH of 9.2, leading to an increase in measured pH. The ash fraction of biochars typically contains carbonates and hydroxides of Ca, K and other basic cations, which could also lead to an enhancement of soil pH (Sika and Hardie 2014). The application of OMW was also significantly positively correlated with soil EC (Table 20.3). However, soil EC values never exceeded the critical value of 200 mS m^{-1} which is considered harmful to salt-sensitive crops (FSSA 2007), even at the highest OMW and biochar application rates (Table 20.1).

The control soil available P content was almost at critical sufficiency level (25 mg kg^{-1}) for most crops (FSSA 2007) (Table 20.2). The available P levels were strongly positively affected by the OMW application ($R = 0.79$) while biochar had no measurable effect (Tables 20.1 and 20.3). The enhancement of available P content due to OMW application is likely due to its inherent P content (Table 20.2), as well as, the addition of organic acids and phenols in the OMW (Table 20.3), which are known to enhance solubility of Ca-P compounds due to competing complexation and sorption reactions with cations and mineral surfaces (Havlin et al. 2005). The solubility of Ca-P precipitates is also significantly increased above pH 8 in soils due to preferential precipitation of $CaCO_3$ (Havlin et al. 2005), thus the increase in soil pH with the addition of OMW (Tables 20.2 and 20.3) could have also contributed to enhanced P availability.

The control soil had insufficient plant available K (10 mg kg^{-1}), as levels were below the critical sufficiency level of 40 mg kg^{-1} for most crops (FSSA 2007). Application of both OMW and biochar significantly enhanced soil available K (Tables 20.1 and 20.3), to above critical sufficiency levels when OMW was applied with at least 2.5% biochar or biochar was applied alone at 5% (Table 20.1). Application of biochar was significantly negatively correlated with soil Mg availability (Table 20.1), which might be due to enhanced precipitation of $MgCO_3$ with carbonates in ash fraction of biochar. However, soil available Mg levels (258–315 mg kg^{-1}) were significantly higher than critical sufficiency level (50 mg kg^{-1}) in all treatments (FSSA 2007).

Application of C-rich biochar (Table 20.1) significantly increased soil C and thus also significantly enhanced the soil C:N ratio while application of OMW did not have a significant effect on either parameter (Tables 20.1 and 20.3). The soil organic C:N ratio was increased above 15:1 in the 5% biochar treatments which would likely enhance N immobilization in the soil. Neither OMW nor biochar application was significantly correlated with soil N.

20.4.2 OMW Effects on Plant Growth Phytometrics

The negative effect of OMW on wheat growth phytometrics (Figs. 20.1a and 20.2a) is mainly attributed to the increased soil pH (Tables 20.1 and 20.3) and potential negative effect of phenols (Table 20.2). Spring wheat is adapted to slightly acidic soils with an optimal pH range between 5.5 and 6.5. A previous study by Mekki et al. (2013) reported that the tolerable limit of the OMW of wheat to be 40–50 m^3 ha^{-1}.

The 50 m^3 ha^{-1} of OMW rate resulted in an average increase of 40% in bean dry biomass, whereas the higher application rates resulted in a slight decrease compared to the control (Fig. 20.1b).The enhanced performance of the beans at 50 m^3 ha^{-1} could due to a slightly lower soil pH as measured in water (8.9) and enhanced soil P (38 mg kg^{-1}) availability to above critical sufficiency values compared to the control (Table 20.2). The decreased performance of the beans at higher OMW application rates is likely due to increased soil pH (Table 20.1) and potential negative effect of phenols (Table 20.2). Legumes, such as beans, perform better in neutral to slightly alkaline soils, and thus are better adapted for alkaline conditions.

20.4.3 Biochar Effects on the Plant Growth Phytometrics

The increased biochar application reduced the growth of wheat (Figs. 20.3a and 20.4a). This is probably due to the high pH of the sandy growth medium coupled with the additional alkalinity of the biochar (Table 20.1), which would further constrain wheat growth. Pinewood biochar is also known to cause N immobilization (Sika and Hardie 2014), which would also constrain the growth of a non-legume. The higher BGB development in wheat compared to the higher AGB in bean crop indicated insufficiency in nutrient supply for wheat and hence nutrient resource allocation to BGB to enhance soil nutrient uptake (Tateno et al. 2004). Biochar had no significant effect on soil available P, which was slightly below the critical sufficiency level in control and all biochar only treatments (Table 20.1). Farrell et al. (2014) also reported that biochar suppressed wheat yield without fertilizer addition and concluded that biochar has an impact on both soil N and P availability.

Biochar was found to slightly increase the total biomass of the more alkaline-soil-tolerant beans at the 5% application rate (Fig. 20.4b), and the number of leaves at 2.5 and 5% application rates (Fig. 20.3b), although not significantly different from the control. This is likely due to enhanced soil available K content at the 2.5 and 5% biochar application rates to near or above critical sufficiency levels (Table 20.1).

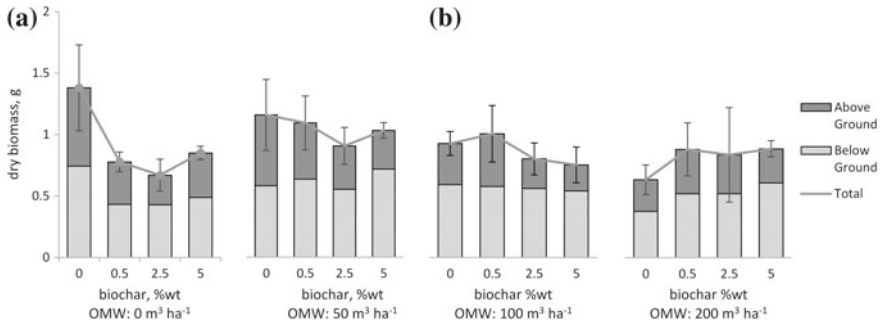


Fig. 20.4 Interactive effect of biochar and OMW on the AGB and BGB of wheat and beans grown in alkaline sand. Vertical bars are standard deviation of total biomass production

20.4.4 Biochar and OMW Combined Effects on Growth Phytometrics

The application of biochar had no significant effect on wheat biomass production in OMW treated pots (Fig. 20.4a). However, on average there appeared to be a slight improvement in wheat total biomass production due to the application of biochar in pots that received 200 m^3 ha^{-1} of OMW (Fig. 20.4a), although this was mainly due to increases BGB indicating plant nutrient strain. These particular treatments had the highest soil pH values measured in water (Table 20.1), which would suppress wheat growth, however, these treatments also had the highest available soil K (58–129 mg kg^{-1}) and sufficient soil P (26–30 mg kg^{-1}) (Table 20.1) which could contribute to plant growth.

Application of biochar at 2.5 and 5% significantly improved bean total biomass production in the treatment that received 100 m^3 ha^{-1} OMW (Fig. 20.4b). Application of biochar in the 50 and 200 m^3 ha^{-1} OMW treatments did not result in significant differences in bean biomass production. However, similar to the wheat trial, there appeared to be a slight improvement in bean total and above-ground biomass production due to the application of biochar in pots that received 200 m^3 ha^{-1} of OMW (Fig. 20.4a). As previously discussed, the 100 and 200 m^3 ha^{-1} OMW treated soils that also received biochar contained the highest plant available K and P levels which would promote plant growth.

A previous sorption experiment indicated that 300 g of the pinewood biochar could completely absorb the phenols in one liter of the OMW used in this study (Umeugochukwu 2016). It was calculated that the 2.5 and 5% rates had enough biochar to sorb all the phenols applied at the 100 and 200 m^3 ha^{-1} OMW rates, if complete reaction took place. Thus, removal of phenols could also contribute to the beneficial effect of biochar applied at 2.5 and 5% on bean growth seen in the treatments that received 100 and 200 m^3 ha^{-1} OMW (Fig. 20.3b).

Thus it is likely that soil pH and nutrient availability, and not only phenol toxicity as reported by Hachicha et al. (2009) played a role in the combination of biochar and OMW treatment in this study.

20.5 Conclusions

The biotic-abiotic interactions between two types of plants (grain and legume) with olive mill wastewater and pinewood biochar were studied in an alkaline sandy soil environment. The significant deterioration of wheat growth phytometrics with increasing OMW application rates was observed. This effect was less pronounced in green beans. The negative effect was primarily attributed increased soil pH and phenol toxicity in the OMW.

Addition of biochar alone had negative effects on wheat growth associated with addition of carbonates and N immobilization by biochar. Addition of biochar had less of a negative effect on beans, likely due to them being better adapted to alkaline soil conditions and due to symbiotic N fixation. The addition of biochar at 5% application rate slightly enhanced bean biomass production likely due to increasing soil K levels above critical sufficiency.

Amendment of soil with biochar resulted in only slightly improved wheat tolerance to OMW at 200 m^3 ha^{-1} OMW application. In case of green beans, a significant improvement in growth was observed at 2.5 and 5% biochar amendment rates on sand that received 100 m^3 ha^{-1} OMW, possibly due to not only sorption of polyphenols, but also better soil P and K supply from the OMW and biochar combination. In general, the 2.5 and 5% biochar amendment resulted higher level of tolerance of beans to the 100 and 200 m^3 ha^{-1} OMW on-land disposal, and thus the rates of application may be reconsidered for some legumes. It may be also advisable to establish leguminous crops on sites polluted with OMW for the purpose of soil remediation.

We conclude that on-land disposal of OMW may be possible at higher than currently recommended rates in combination with biochar amendment and careful crop choice. Application of biochar on acidic soil treated with OMW would likely be beneficial for more crop types and would require further investigation.

Acknowledgements The authors acknowledge the financial support of the TRECCAfrica scholarship program.

References

Achak M, Mandi L, Ouazzani N (2009) Removal of organic pollutants and nutrients from olive mill wastewater by a sand filter. J Environ Manage 90:2771–2779. https://doi.org/10.1016/j.jenvman.2009.03.012

Ainsworth E, Gillespie K (2007) Estimation of total phenolic content and other oxidation substrates in plant tissues using Folin-Ciocalteu reagent. Nat Protoc 2:875–877. https://doi.org/10.1038/nprot.2007.102

Al-Malah K, Azzam M, Abu-Lail N (2000) Olive mills effluent (OME) wastewater post-treatment using activated clay. Sep Purif Technol 20:225–234. https://doi.org/10.1016/S1383-5866(00)00114-3

Alhakmani F, Kumar S, Khan S (2013) Estimation of total phenolic content, in-vitro antioxidant and anti-inflammatory activity of flowers of Moringa oleifera. Asian Pac J Trop Biomed 3:623–627. https://doi.org/10.1016/s2221-1691(13)60126-4

Angiolini C, Landi M, Pieroni G et al (2013) Soil chemical features as key predictors of plant community occurrence in a Mediterranean coastal ecosystem. Estuar Coast Shelf Sci 119:91–100. https://doi.org/10.1016/j.ecss.2012.12.019

Aziz A, Ngadi N, Amin N (2012) Phenol adsorption by activated carbon of different fibre size derived from empty fruit bunches. J Oil Palm Res 24:1524–1532

Barbera AC, Maucieri C, Cavallaro V et al (2013) Effects of spreading olive mill wastewater on soil properties and crops, a review. Agric Water Manag 119:43–53. https://doi.org/10.1016/j.agwat.2012.12.009

Barrow C (2012) Biochar: potential for countering land degradation and for improving agriculture. Appl Geogr 34:21–28. https://doi.org/10.1016/j.apgeog.2011.09.008

Belaid C, Khadraoui M, Mseddi S et al (2013) Electrochemical treatment of olive mill wastewater: treatment extent and effluent phenolic compounds monitoring using some uncommon analytical tools. J Environ Sci 25:220–230. https://doi.org/10.1016/S1001-0742(12)60037-0

Borja R, Raposo F, Rincón B (2006) Treatment technologies of liquid and solid wastes from two-phase olive oil mills. Grasas Aceites 57:32–46. https://doi.org/10.3989/gya.2006.v57.i1.20

Bremner J (1996) Nitrogen-total. In: Sparks D, Bartels J (eds) Methods of soil analysis part 3-chemical, SSSA Book. Soil Science Society of America, Inc. American Society of Agronomy, Inc., Madison, WI, 53711, pp 1085–1121

Deng G, Wang X, Shi X, Hong Q (2013) Adsorption characteristics of phenol in aqueous solution by *Pinus massoniana* Biochar. Appl Mech Mater 295–298:1154–1160. https://doi.org/10.4028/www.scientific.net/AMM.295-298.1154

Farrell M, Macdonald L, Chirino-valle I et al (2014) Biochar and fertiliser applications influence phosphorus fractionation and wheat yield Biochar and fertiliser applications influence phosphorus fractionation and wheat yield. Biol Fertil Soils 50:169–178. https://doi.org/10.1007/s00374-013-0845-z

Fenu G, Carboni M, Acosta A, Bacchetta G (2013) Environmental factors influencing coastal vegetation pattern: new insights from the Mediterranean Basin. Folia Geobot 48:493–508. https://doi.org/10.1007/s12224-012-9141-1

FSSA (2007) FSSA fertilizer handbook. Fertilizer Society of South Africa, Lynwood Ridge, South Africa

Gee G, Or D (2002) Particle-size analysis. In: Dane J, Topp G (eds) Methods of soil analysis part 4-physical methods. Soil Science Society of America, Inc., Madison, Wisconsin, WI 53711, USA, pp 255–278

Gell K, van Groenigen J, Cayuela M (2011) Residues of bioenergy production chains as soil amendments: immediate and temporal phytotoxicity. J Hazard Mater 186:2017–2025. https://doi.org/10.1016/j.jhazmat.2010.12.105

Hachicha S, Cegarra J, Sellami F et al (2009) Elimination of polyphenols toxicity from olive mill wastewater sludge by its co-composting with sesame bark. J Hazard Mater 161:1131–1139. https://doi.org/10.1016/j.jhazmat.2008.04.066

Havlin J, Beaton J, Tisdale S, Nelson W (2005) Soil fertility and fertilizers. Pearson Education Inc., Upper Saddle River, NJ

Hina K, Hedley M, Camps-Arbestain M, Hanly J (2015) Comparison of pine bark, biochar and zeolite as sorbents for NH4 + -N removal from water. Clean—Soil Air Water 43:86–91. https://doi.org/10.1002/clen.201300682

Jien S, Wang C, Lee C, Lee T (2015) Stabilization of organic matter by biochar application in compost-amended soils with contrasting pH values and textures. Sustain 7:13317–13333. https://doi.org/10.3390/su71013317

Kapellakis I, Tsagarakis K, Crowther J (2008) Olive oil history, production and by-product management. Rev Environ Sci Biotechnol 7(1):1–26

López-Cano I, Roig A, Cayuela M et al (2016) Biochar improves N cycling during composting of olive mill wastes and sheep manure. Waste Manag 49:553–559. https://doi.org/10.1016/j.wasman.2015.12.031

Lykas C, Vagelas I, Gougoulias N (2014) Effect of olive mill wastewater on growth and bulb production of tulip plants infected by bulb diseases. Spanish J Agric Res 12:233–243

McNamara C, Anastasiou C, O'Flaherty V, Mitchell R (2008) Bioremediation of olive mill wastewater. Int Biodeterior Biodegradation 61:127–134. https://doi.org/10.1016/j.ibiod.2007.11.003

Mekki A, Dhouib A, Sayadi S (2013) Review: effects of olive mill wastewater application on soil properties and plants growth. Int J Recycl Org Waste Agric 2:15. https://doi.org/10.1186/2251-7715-2-15

Mekki A, Dhouib A, Sayadi S (2009) Evolution of several soil properties following amendment with olive mill wastewater. Prog Nat Sci 19:1515–1521. https://doi.org/10.1016/j.pnsc.2009.04.014

Mekki A, Dhouib A, Sayadi S (2007) Polyphenols dynamics and phytotoxicity in a soil amended by olive mill wastewaters. J Environ Manage 84:134–140. https://doi.org/10.1016/j.jenvman.2006.05.015

Mohan D, Sarswat A, Ok Y, Pittman C (2014) Organic and inorganic contaminants removal from water with biochar, a renewable, low cost and sustainable adsorbent–a critical review. Biores Technol 160:191–202

Nelson D, Sommers L. (1996) Total carbon, organic carbon, and organic matter. In: Sparks D (ed) Methods of soil analysis part 3-chemical methods. Soil Science Society of America, Inc. American Society of Agronomy, Inc., Madison, Wisconsin, WI 53711, USA, pp 995–1001

Non-Affiliated Soil Analysis Work Committee of the Soil Science Society of South Africa (1990) Handbook of Standard Soil Testing Methods for Advisory Purposes. Pretoria

Ouzounidou G, Asfi M, Sotirakis N et al (2008) Olive mill wastewater triggered changes in physiology and nutritional quality of tomato (Lycopersicon esculentum mill) depending on growth substrate. J Hazard Mater 158:523–530. https://doi.org/10.1016/j.jhazmat.2008.01.100

Paraskeva P, Diamadopoulos E (2006) Technologies for olive mill wastewater (OMW) treatment : a review. 1485:1475–1485. https://doi.org/10.1002/jctb

Romano N, Santini A (2002) Field water capacity. In: Dane J, Topp G (eds) Methods of soil analysis part 4-physical methods. Soil Science Society of America, Inc., Madison, Wisconsin, WI 53711, USA, pp 721–736

Rusan MJM, Albalasmeh AA, Zuraiqi S, Bashabsheh M (2015) Evaluation of phytotoxicity effect of olive mill wastewater treated by different technologies on seed germination of barley (Hordeum vulgare L.). Environ Sci Pollut Res Int 22:9127–9135. https://doi.org/10.1007/s11356-014-4004-3

Sekar S (2012) The effects of biochar and anaerobic digester effluent on soil quality and crop growth in Karnataka, India

Schulz H, Glaser B (2012) Effects of biochar compared to organic and inorganic fertilizers on soil quality and plant growth in a greenhouse experiment. J Plant Nutr Soil Sci 175:410–422. https://doi.org/10.1002/jpln.201100143

Sika M, Hardie A (2014) Effect of pine wood biochar on ammonium nitrate leaching and availability in a South African sandy soil. Eur J Soil Sci 65:113–119. https://doi.org/10.1111/ejss.12082

Standard Methods (2012) Standard methods for the examination of water and wastewater

Tateno R, Hishi T, Takeda H (2004) Above- and belowground biomass and net primary production in a cool-temperate deciduous forest in relation to topographical changes in soil nitrogen. For Ecol Manage 193:297–306. https://doi.org/10.1016/j.foreco.2003.11.011

Thomas G. (1996) Soil pH and Soil acidity. In: Sparks DL (ed) Methods of soil analysis part 3-chemical methods. Soil Science Society of America, Inc. American Society of Agronomy, Inc., Madison, Wisconsin, WI 53711, USA, pp 475–490

Umeugochukwu O (2016) Mitigation of soil and ground water pollution caused by on-land disposal of olive mill wastewater. Ph.D. Thesis, University of Stellenbosch, South Africa

Part IV
Biomineral Interactions in Soil

Chapter 21
Macroscopic Observation of Biotic-Abiotic Interactions in Biochar Layers Within a Sandy Soil in a Pot Trial with Wheat *Triticum aestivum*

Charl F. Olivier, Ian L. Belford, Leandra Moller, Andrei B. Rozanov, Alf Botha and Ailsa G. Hardie

Abstract Biochar amendment of soils is an ancient technology which has attracted a lot of recent attention from soil scientists and environmentalists as a possible way to sequester carbon from the atmosphere in the soil, whilst increasing soil fertility. Wheat (*Triticum aestivum*) was grown for twelve weeks in pots were pine derived biochar was placed in two distinct layers within a sandy soil. The sandy and biochar layers were separated at harvesting to assess plant root growth, microbial biomass and degree of mycorrhizal root colonization. The biochar layers formed preferred zones for root development ($P = 0.039$) and microbial proliferation ($P < 0.001$) compared to the sandy layers. However, the degree of root mycorrhizal colonization decreased slightly in the two biochar layers and in the sandy layer between them, relative to the sandy layers above and below. The decrease in mycorrhizal colonization was possibly due to the enhancing effect that biochar has on water and nutrient retention. Furthermore, the physical and chemical characteristics of the biochar layers differed markedly from the sandy layers in terms of pH, cation exchange capacity, total C and available P. These factors have a strong influence on the micro-climate and nutrient status of each layer.

Keywords Pine derived biochar · Rroot growth · Microbial biomass C · Mycorrhizal colonization

C. F. Olivier · A. B. Rozanov (✉) · A. G. Hardie
Department of Soil Science, Stellenbosch University, P/Bag XI, Matieland 7602, South Africa
e-mail: dar@sun.ac.za

I. L. Belford · L. Moller · A. Botha
Department of Microbiology, Stellenbosch University, P/Bag XI, Matieland 7602, South Africa

© Springer Nature Switzerland AG 2020

O. V. Frank-Kamenetskaya et al. (eds.), *Processes and Phenomena on the Boundary Between Biogenic and Abiogenic Nature*, Lecture Notes in Earth System Sciences,
https://doi.org/10.1007/978-3-030-21614-6_21

21.1 Introduction

The term biochar refers to charred organic material formed during the incomplete combustion of organic biomass in the absence of atmospheric oxygen (pyrolysis), leaving behind charred organic biomass. Many studies have shown biochar to be a chemically stable material, which is highly recalcitrant to microbial degradation (Schmidt and Noack 2000; Roberts et al. 2010; Woolf et al. 2010). The ability of biochar to directly increase soil fertility is dependent on the ability of microbes to utilize and mineralize the charred biomass to facilitate the release of carbon and nutrients to microbes and plants. Common agricultural practices used today, such as application of mulches, compost and manures were found to increase soil fertility (Glaser et al. 2002) because these forms of organic carbon can be readily mineralized by microbes to provide nutrients to the plants and in areas like the tropics this mineralization is very rapid (Tiessen et al. 1994; Meyer et al. 2018).

Due to its low mineralization rate, the carbon within biochar contributes to the decadal carbon pool within soils and therefore does not serve as the primary carbon source to microbes. Furthermore, biochar derived from plant material is low in nutrient content (Chan et al. 2008), particularly N and P, and do not directly increase soil macronutrients. However, the incorporation of biochar into soils can have many beneficial effects within soils and will improve soil quality through its liming ability, by increasing the CEC and nutrient retention ability of soils and also increasing the water holding capacity of soils (Glaser et al. 2002). It was shown that slow pyrolysis at 400° produces pine wood biochar with higher cation exchange capacity (CEC) and residual nutrient content compared to biochars produced from the same feedstock at higher temperature (Gaskin et al. 2008). The addition of biochar therefore has the ability to cause major shifts in the chemistry, nutrient levels and their ratios within soils which can influence the availability and solubility of elements such as N, P, Ca, Mg and Mo (Atkinson et al. 2010) and influence the microbial growth and productivity of crops. Furthermore, the porous structure and large surface area of biochar can provide beneficial soil microorganisms such as bacteria and mycorrhizae with refugia (Saito 1990) and provide more suitable conditions, by increasing the carbon content, water- and nutrient holding capacity of soils, (Laird 2008) for microbial proliferation.

However, it is still questionable whether biochar would be able to promote soil fertility by increasing microbial proliferation since the principle carbon source of this material forms part of the slow geological carbon cycle rather than the rapid biological carbon cycle (Kuhlbusch and Crutzen 1995). In this study, biochar derived from Pine wood, was placed in two distinct layers in a sandy soil to assess the degree to which it will promote root growth, soil microbial proliferation and the degree of mycorrhizal colonization of the wheat roots within the biochar layers compared to the sandy layers.

21.2 Materials and Methods

21.2.1 Soil

The sandy soil used for this trial is acidic, has a low agricultural potential and is very widespread in the Cape Flats region of the Western Cape, South Africa. The soil texture is pure sand with medium grade. It has low pH, low carbon and nitrogen content (Table 21.1). The sand used in this pot trial was collected from layers deeper than 50 cm below the day surface from an Arenosol in an unused field covered with kikuyu grass and weeds in Brackenfell, Western Cape, South Africa (S 33.89532° and E 18.72346°). The pH of the soil was measured in distilled water in a 1:2.5 soil: water ratio (White 1997). The total C and N content of the soil was determined by the EuroVector Elemental Analyzer using the dry combustion method (Nelson and Sommers 1996). The cation exchange capacity (CEC) of the soil was determined using 1 *M* NH_4OAc (pH 7.0) according to the method of Summer and Miller (1996). All determinations were carried out in duplicate.

21.2.2 Biochar

The biochar used in this trial was produced from pine wood sawmill waste, slow-pyrolysed at 450 °C. The biochar was then milled to an average particle diameter of 3 mm. The pH_{H2O} of the biochar was measured by the method described by Cheng and Lehmann (2009) which makes use of a 1:20 biochar to solution ratio which accounts for the low bulk density of the biochar. The total C and N content of the biochar was determined by the EuroVector Elemental Analyzer using the dry combustion method (Nelson and Sommers 1996). The CEC of the biochar was determined according to the method for alkaline soils as described by Rhoades (1982). All determinations were carried out in duplicate. The results of the biochar characterization are shown in Table 21.1. Additional characteristics of this biochar are provided by Sika and Hardie (2014).

Table 21.1 Soil and biochar characterization

	pH_{H2O}	% C	% N	C/N ratio	$CEC_{7.0}$ ($cmol_c\ kg^{-1}$)
Soil	5.14	0.16	0.03	5.3	1.96
Biochar	9.39	82.71	0.53	156.1	34.30

21.2.3 Pot Trial Setup

The pot trial was conducted in a greenhouse on Welgevallen experimental farm of the University of Stellenbosch, Stellenbosch, South Africa. The pot trial consisted of twelve pots with a volume of 7 litres. Each pot composed of three sandy layers at 0–3, 6–9 and 12–17 cm and two biochar layers at 3–6 and 9–12 cm depth respectively.

Ten wheat seeds were planted per pot and thinned out to four seedlings after emergence. The plants were fertilized with macronutrients according to the following fertilizer recommendation: N: 101; P: 50; K: 75; Ca: 30; Mg: 23; S: 30 kg ha^{-1}. The pots were fertilized in a single application at planting, while micronutrients were applied as foliar spray, 2 and 8 weeks after germination, using Omnispoor fertilizer containing the following trace elements: B: 22; Cu: 1.25; Fe: 87; Mn: 18; Zn: 10.7; Mo: 2 g kg^{-1} applied at a concentration of 20 mg l^{-1}. Pots were irrigated to field capacity on a weekly basis.

21.2.4 Soil and Plant Analyses

The wheat above-ground biomass and roots in each soil/biochar layer were collected twelve weeks after germination, washed and oven dried at 50 °C for 6 days for the determination of their dry root weights. The biochar and sandy layers were carefully separated and sub samples of soil and roots were collected from each layer. The roots were stored in 50% ethanol solution for the determination of AM fungal colonization.

Mycorrhizal infections were determined using Trypan blue (chlorazol black E) in lactoglycerol to stain the roots after they were cleared in 10% w/v heated KOH (Bevege 1968; Phillips and Hayman 1970; Kormanic and McGraw 1982; Brundrett et al. 1984). Non-woody roots were used for this purpose. Twenty-five 1 cm root segments were placed on a microscopic slide before examination for mycorrhizal infections under a compound microscope at × 200 magnification.

The sub samples of biochar and soil taken from each layer were analysed for pH_{H2O} and electrical conductivity using a 1:20 and 1:2.5 biochar and sand to solution ratio (Cheng and Lehmann 2009; White 1997). Phosphorus was extracted according to the method described by Soltanpour and Schwab (1977) using NH_4HCO_3-DTPA as the extracting solution, which is suitable for alkaline samples. Soil microbial biomass was also determined using microwave irradiation and extraction with 0.5 *M* K_2SO_4 as described by Islam and Weil (1998). The total microbial biomass carbon (C_{TMB}) was then determined via the rapid oxidation spectrophotometric method of Heanes (1984).

21.2.5 Statistical Analyses

Statistical analysis was conducted using SAS 9.1 for Windows. Significant differences amongst the layers were distinguished at the $P < 0.05$ level using Tukey's Studentized Range test. A single factor ANOVA was used to distinguish between the treatments means of the different layers.

21.3 Results

21.3.1 Root Gowth Through Layered Pots

The results shown in Fig. 21.1 and Table 21.2 showed a significant increase in root dry weight within the biochar layers compared to the sandy layers. However, this increase is mostly attributed to the first rather than the second biochar layer. The top sandy layer had similar dry root biomass compared to the first biochar layer. The rest of the sandy layers had dry root weights significantly less than the first biochar layer at 3–5 cm depth. The biochar layer at 8–10 cm depth had a greater dry root biomass compared to the sandy layer above and below it (89 and 116% respectively), but this increase was not significant (Table 21.2). Overall, the two biochar layers significantly promoted root growth ($P = 0.039$) compared to the sandy layers.

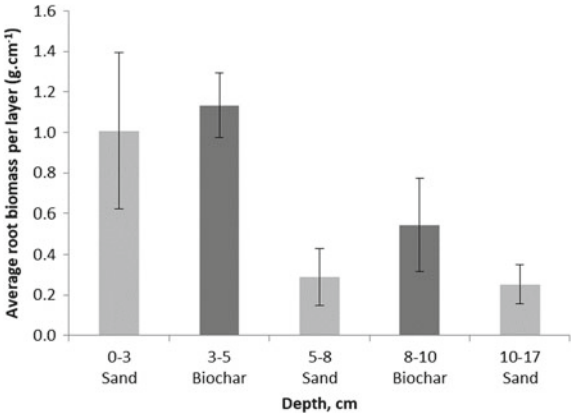


Fig. 21.1 Average dry root mass per layer

21.3.2 Analysis of Soil Microbial Biomass C (C_{TMB})

The results shown in Table 21.2 and Fig. 21.2a, b revealed a significant increase ($P < 0.001$) in the soil microbial population, inherited from the sandy soil, within both the biochar layers. Microbes therefore readily colonized these zones and propagated at a higher rate within the biochar layers. Biochar layer one and two caused an increase in C_{TMB} of 131 and 187% respectively compared to the average C_{TMB}.of the three sandy layers.

Table 21.2 Dry root weight and microbial data in separate layers

	Sand (0–3 cm)	Biochar (3–5 cm)	Sand (5–8 cm)	Biochar (8–10 cm)	Sand (10–17 cm)	Difference in means of biochar and sandy layers: P-value
Root dry weight ($g.cm^{-1}$)	0.336 a	0.567 a	0.096 b	0.273 b	0.036 b	0.039
Microbial biomass C (mg $C.g^{-1}$)	0.148 a	0.386 b	0.141 a	0.431 b	0.169 a	<0.001
Mycorrhizal number	64 a	27 a	38 a	51 a	84 a	0.191

Note Numbers followed by the same symbol are not significantly different at $p < 0.05$ level based on Tukey's Studentized range test

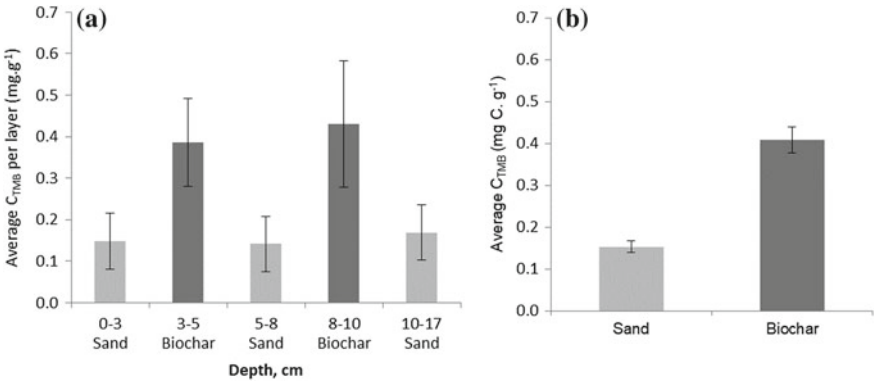


Fig. 21.2 Microbial biomass C in separate layers (**a**) and the average microbial biomass C within the biochar and sandy layers (**b**)

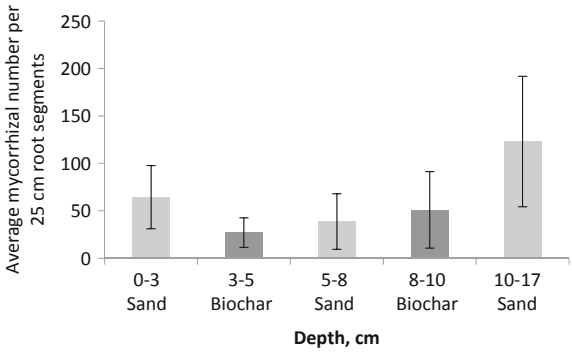


Fig. 21.3 Average mycorrhizal number per layer

21.3.3 Degree of Mycorrhizal Colonization

In Table 21.2 and Fig. 21.3 a decrease in the degree of mycorrhizal colonization with the roots of *Triticum aestivum* (wheat) can be seen in the middle sections of the pots (3–10 cm depth) compared to the top and bottom sandy layers. This decrease however, is not significant due to the large variation within the data. Overall, the natural mycorrhizal population within the sandy soil seemed to be less affected in the soil layers whose own soil chemistry were not strongly influenced by the biochar layers.

21.4 Discussion

21.4.1 Root Growth Through Layered Pots

Overall, the biochar layers in the pots promoted root growth compared to the sandy layers (Table 21.2). The sandy layer at 0–3 cm had a dry root weight comparable to the first biochar layer. This can be ascribed to the root morphology of *Triticum aestivum* (wheat), with thicker anchor roots growing in the top sandy layer. Below the first biochar layer a peak in dry root weight was again seen in the biochar layer at the depth of 8–10 cm. Several reasons can account for the increases in root growth within the biochar layers.

Firstly, at harvesting, both biochar layers had much higher gravimetrical water contents of between 120 and 135% compared to 5–10% of the sandy layers above and below it (Table 21.3). The higher water holding capacity of the biochar layers can be attributed to the high porosity and the capillary forces which draw soil water into these micro-voids of the biochar (Atkinson et al. 2010; Hillel 1980). Consequently, the biochar layers continuously had higher water contents between irrigation cycles. The increased root growth can possibly be attributed to the root hairs being able to

Table 21.3 Analysis of separate layers

	Sand (0–3 cm)	Biochar (3–5 cm)	Sand (5–8 cm)	Biochar (8–10 cm)	Sand (10–17 cm)
Gravimetrical water content at harvest (%)	5.3	123.3	7.4	134.8	8.7
pH_{H2O}	6.67	7.3	7.56	8.27	6.83
Electrical conductivity (mS cm^{-1})	693	356	429	818	739
Phosphorus content (μg P g^{-1})	17.36	13.91	1.66	10.95	1.61

enter water filled macro-pores of biochar and in doing so can bind to the biochar particle's surface (Joseph et al. 2010).

Secondly, biochar layers provided a greater CEC compared to the sandy layers (Table 21.1), which implies that a higher fraction of the nutrients applied as fertilizer were retained within the biochar layers after irrigation cycles (Lehmann et al. 2003; Prendergast-Miller et al. 2014; Olmo et al. 2016) compared to the sandy layers. This may be in part due to formation of organic coatings on biochar (Hagemann et al. 2017). These nutrients could be taken up by plant roots over a longer period of time because of the slower drying out cycle within these layers.

Thirdly, the biochar used in this trail had a volatile fraction of 19.3% and recent studies have shown that this fraction can contain organic molecules which can trigger germination (Dixon 1998) and promote nutrient uptake by roots (Riedlinger et al. 2006), depending on the feedstock used to produce the biochar.

21.4.2 Stratification of Microbial Biomass Through Pots

Results clearly indicated a significant increase in microbial biomass C within both biochar layers compared to any of the other sandy layers, which did not significantly differ from each other (Table 21.2). The porous nature of biochar not only increased the water holding capacity of these layers (Table 21.3), but also would be expected to provide suitable micro-habitats for microorganisms to colonise (Joseph et al. 2010). These micro-pore habitats have been shown to provide microorganisms with refuges (Saito 1990), moisture, and greater protection against predators and climatic extremes and also allow for a wide variety of microbial communities to colonise them (Thies and Rilling 2009).

A significant increase in root growth was seen within the biochar layers (Table 21.2) and therefore these layers had a larger rhizosphere volume compared to the sandy layers. In the rhizosphere, growing roots can release organic compounds,

tissue material and sloughed-off cells (Violante and Gianfreda 2000), which can then be adsorbed on the surface of biochar particles and serve as substrate for microbes within the micro-voids. Nutrient interception by the biochar layers also means that more nutrients are readily available for microbial uptake. Furthermore, the large volatile fraction of the pine wood derived biochar could provide the microorganisms with a readily available carbon source and therefore can stimulate the initial increase in microbial biomass directly within these layers.

21.4.3 Degree of Mycorrhizal Colonization

The data collected indicated no significant differences in the degree of mycorrhizal root colonization formed with the roots between any of the layers (Table 21.2). However, the degree of mycorrhizal colonization did decrease in the two biochar layers and in the sandy layer between them (Table 21.2). These decreases can be attributed to several factors. Firstly, due to the higher microbial activity in the biochar layers, the aeration requirements of these layers are higher. Biochar potentially has a very strong water holding capacity which leads to a reduction in the air-filled pore fraction within the biochar layers. The decrease in the air filled pore fraction will decrease the rate of gas exchange between the layers and the atmosphere due to the slower rate of diffusion (Hillel 1980) and would have caused more reduced conditions in these layers.

Secondly, biochar contains few nutrients that benefit mycorrhizae (Lehmann et al. 2003), but because of its higher CEC, it has the potential to retard the leaching of cationic nutrients (Major et al. 2009). Biochar can therefore change the local nutrient balance within soil (e.g. N/P ratio) which can have a strong influence on mycorrhizal colonisation (Miller et al. 2002; Warnock et al. 2007). As shown in Table 21.3, the plant available phosphorus was higher within the biochar layers (Table 21.2) due to the inherent phosphate content of the biochar and possibly due to the ability of the biochar layers to retard the downward movement of phosphorus added with fertilization as a result of the high pH of these layers. Previous studies (Vejsadova et al. 1990) have shown a strong negative correlation between plant available phosphorus and the degree of mycorrhizal colonization, with higher available phosphorus levels decreasing the need for mycorrhizal symbiosis. These higher phosphorus levels could have contributed to the decrease in the degree of mycorrhizal colonization within these layers.

Thirdly, the chemistry (Table 21.3) of the biochar layers and the sandy layers differed substantially, especially the pH. The soil used in this trial had a low pH and a natural mycorrhizal population which perhaps was adapted to these acidic conditions. Liming has been shown to have long lasting effects on ecto-mycorrhizal community composition (Kjøller and Clemmensen 2009). Robert et al. (1992) observed changes in phosphatise activity due shifts in ECM morphotypes caused as a result of liming. The pH in the top sandy layer and at the bottom of the pot were least affected by the liming effect caused by the biochar layers and therefore also had the greatest degree

of mycorrhizal colonisation. The inherited mycorrhizal population within the middle section (3–10 cm) struggled to adjust to the drastic increase in pH which led to the decrease in mycorrhizal colonisation.

Apart from the liming effect of biochar it is also speculated that biochar could interfere with the signalling dynamics of the rhizosphere by serving either as a signalling source or sink (Warnock et al. 2007). Before roots are colonised by mycorrhizae it is assumed that a continuous dialogue of signals are exchanged between the symbionts. The signalling compounds can possibly include plant root released compounds such as sugars and amino acids whilst phenolic compounds such as flavonoids have been shown to be a key signalling compound (Badri et al. 2009; Steinkellner et al. 2007). The fresh biochar used in the layers possibly adsorbed signalling compounds released by the roots which could have led to the decrease in mycorrhizal colonisation.

21.5 Conclusions

The introduction of macro-quantities of biochar as layers into a sandy soil dramatically changed the biotic-abiotic interactions in the soil strata. The biochar layers served as local hot spots for root and microbial proliferation and were able to significantly promote root growth and increases in microbial biomass C. This can be attributed to biochar's ability to retain soil moisture and nutrients which provided the plant with readily available nutrients over longer period of time from these zones. The inherited microbial population was able to adapt to biochar as a new carbon source and use these layers as refuge because of the constant and more favourable conditions created by the biochar. However, a decrease (though not significant) in mycorrhizal colonisation was seen within the biochar layers which can mainly be attributed to changes in the local nutrient balances caused by biochar and the higher, more alkaline pH within these zones compared to the acidic soil from which the mycorrhizae were inherited.

Acknowledgements The authors would like to thank S&P Carbon for the donation of the biochar used in the trial. We would also like to thank Makhosazana Sika for characterising the biochar.

References

Atkinson C, Fitzgerald J, Hipps N (2010) Potential mechanisms for achieving agricultural benefits from biochar application to temperate soils: a review. Plant Soil 337:1–18

Badri D, Weir T, van der Lelie D, Vivanco J (2009) Rhizosphere chemical dialogues: plant-microbe interactions. Biotechnology 20:642–650

Bevege D (1968) A rapid technique for clearing and staining intact roots for detection of mycorrhizas caused by *Endogene* sp. and some record of infection by Australian plants. Trans Br Mycol Soc 51:808–810

Brundrett M, Piché Y, Peterson R (1984) A new method for observing the morphology of vesicular-arbuscular mycorrhizae. Can J Bot 62:2128–2134

Chan K, Van Zwieten L, Meszaros I, Downie A, Joseph S (2008) Using poultry litter biochars as soil amendments. Aust J Soil Res 46:437–444

Cheng C-H, Lehmann J (2009) Ageing of black carbon along a temperature gradient. Chemosphere 75:1021–1027

Dixon K (1998) Smoke germination of Australian plants. RIRDC Report 98/108, KPW-1A. RIRDC, Canberra, ACT

Gaskin J, Steiner C, Harris K, Das K, Bibens B (2008) Effect of low-temperature pyrolysis conditions on biochar for agricultural use. Trans ASABE 51:2061–2069

Glaser B, Lehmann J, Zech W (2002) Ameliorating physical and chemical properties of highly weathered soils in the tropics with charcoal—a review. Biol Fertil Soils 35(4):219–230

Hagemann N, Joseph S, Schmidt H-P, Kammann C, Harter J, Borch T, Young R, Varga K, Taherymoosavi S, Elliott K, McKenna A, Albu M, Mayrhofer C, Obst M, Conte P, Dieguez-Alonso A, Orsetti S, Subdiaga E, Behrens S, Kappler A (2017) Organic coating on biochar explains its nutrient retention and stimulation of soil fertility. Nat Commun 8:1089

Heanes D (1984) Determination of total organic carbon in soils by an improved chromic acid digestion and spectrophotometric procedure. Commun Soil Sci Plant Anal 15:1191–1213

Hillel D (1980) Fundamentals of soil physics. Academic Press Inc. (London) LTD

Islam K, Weil R (1998) Microwave irradiation of soil for routine measurement of microbial biomass carbon. Biol Fertil Soils 27:408–416

Joseph S, Camps-Arbestrian M, Lin Y, Munroe P, Chia CH, Hook J, van Zwieten L, Kimber S, Cowie A, Singh B, Lehmann J, Foidl N, Smernik R, Amonette J (2010) An investigation into the reactions of biochar in soil. Aust J Soil Res 48:501–515

Kjøller R, Clemmensen K (2009) Belowground ectomycorrhizal fungal communities respond to liming in three southern Swedish coniferous forest stands. For Ecol Manage 257:2217–2225

Kormanic P, McGraw A (1982) Quantification of vesicular-arbuscular mycorrhizae in plant roots. In: Schenck NC (ed) Methods and principles of mycorrhizal research. The American Phytopathological Society, St. Paul, pp 37–45

Kuhlbusch T, Crutzen P (1995) Towards a global estimate of black carbon in residues of vegetation fires representing a sink of atmospheric CO_2 and a source of O_2. Glob Biogeochem Cycles 9:491–501

Laird D (2008) The charcoal vision: a win–win–win scenario for simultaneously producing bioenergy, permanently sequestering carbon, while improving soil and water quality. Agron J 100:179–181

Lehmann J, Kern D, German L, McCann J, Martins GC, Moreira L (2003) Soil fertility and production potential. Chapter 6. In: Lehmann J, Kern D, Glaser B, Woods W (eds) Amazonian dark earths: origin, properties, management. Dordrechts, Kluwer Academics, pp 105–124

Major J, Steiner C, Downie A, Lehmann J (2009) Biochar effects on nutrient leaching. Chapter 15. In: Lehmann J, Joseph S (eds) Biochar for environmental management science and technology. Earthscan, London, pp 271–287

Meyer N, Welp G, Rodionov A, Borchard N, Martius C, Amelung W (2018) Nitrogen and phosphorus supply controls soil organic carbon mineralization in tropical topsoil and subsoil. Soil Biol Biochem 119:152–161

Miller R, Miller S, Jastrow J, Rivetta C (2002) Mycorrhizal mediated feedbacks influence net carbon gain and nutrient uptake in *Andropogon gerardii*. New Phytol 155:149–162

Nelson D, Sommers L (1996) Total carbon, organic carbon, and organic matter. In: Sparks DL (ed) Methods of soil analysis. Part 3. Chemical methods. ASA-SSSA, Madison, pp 961–1010

Olmo M, Villar R, Salazar P, Alburquerque JA (2016) Changes in soil nutrient availability explain biochar's impact on wheat root development. Plant Soil 399:333–343

Phillips J, Hayman D (1970) Improved procedures for clearing roots and staining parasitic and vesicular-arbuscular mycorrhizal fungi for rapid assessment of infection. Trans Br Mycol Soc 55:158–161

Prendergast-Miller M, Duvall M, Sohi SP (2014) Biochar-root interactions are mediated by biochar nutrient content and impacts on soil nutrient availability. Eur J Soil Sci 65:173–185
Rhoades J (1982) Cation exchange capacity. In: Page AL, Miller RH, Keeney DR (ed) Methods of soil analysis Part 2: chemical and microbiological properties. ASA and SSSA, Madison, pp 149–158
Riedlinger J, Schrey S, Tarkka M, Hampp R, Kapur M, Fiedler H (2006) Auxofuran, a novel metabolite that stimulates the growth of fly agaric, is produced by the mycorrhiza helper bacterium Streptomyces strain AcH 505. Appl Environ Microbiol 72(5):3550–3557
Robert K, Antibus A, Linkins A III (1992) Effects of liming on red pine forest floor on mycorrhizal numbers and mycorrhizal and soil phosphatise activities. Soil Biol Biochem 24:479–487
Roberts K, Gloy B, Joseph S, Scott N, Lehmann J (2010) Life cycle assessment of biochar systems: estimating the energetic, economic and climate change potential. Environ Sci Technol 44:827–833
Saito M (1990) Charcoal as a microhabitat for VA Mycorrhizal fungi, and its practical applications. Agric Ecosyst Environ 29:341–344/
Schmidt M, Noack A (2000) Black carbon in soils and sediments: analysis, distribution, implications and current challenges. Glob Biogeochem Cycles 14:777–793
Sika M, Hardie A (2014) Effect of pine wood biochar on ammonium nitrate leaching and availability in a South African sandy soil. Eur J Soil Sci 65:113–119
Soltanpour P, Schwab A (1977) A new soil test for simultaneous extraction of macro- and micro-nutrients in Alkaline soils. Commun Soil Sci Plant Anal 8:195–207
Steinkellner S, Lendzemo V, Langer I, Schweiger P, Khaosaad T, Toussaint J-P, Vierheilig H (2007) Flavonoids and strigolactones in root exudates as signals in symbiotic and pathogenic plant-fungus interactions. Molecules 12:1290–1306
Summer M, Miller W (1996) Cation exchange capacity. In: Sparks DL (ed) Methods of soil analysis Part 3: chemical methods. Soil Science Society of America, Inc., Madison, pp 1201–1230
Thies E, Rilling M (2009) Characteristics of biochar: biological properties: In: Lehmann J, Joseph S (eds) Biochar for environmental management. Science and technology. Earthscan, London
Tiessen H, Cuevas E, Chacon P (1994) The role of soil organic matter in sustaining soil fertility. Nature 371:783–785
Vejsadova H, Hrselova H, Prikryl Z, Vancura V (1990) The effect of different phosphorus and nitrogen levels on development of VA Mycorrhiza, rhizobial activity and soybean growth. Agric Eco Environ 29(1–4):429–434
Violante A, Gianfreda L (2000) The role of biomolecules in the formation and reactivity towards nutrient and organics of variable charge minerals and organo-minerals. In: Bollag J, Stotzky G (eds) Soil biochemistry. Marcel Dekker, New York
Warnock D, Lehmann J, Kuyper T, Rillig M (2007) Mycorrhizal responses to biochar in soil-concepts and mechanisms. Plant Soil 300:9–20
White R (1997) Principle and practice of soil science: the soil as a natural resource. Blackwell Science, Oxford
Woolf D, Amonette JE, Street-Perrott FA, Lehmann J, Joseph S (2010) Sustainable biochar to mitigate global climate change. Nat Commun 1:56

Chapter 22
Structure of Microbial Community in Forest and Anthropogenic Changed Soils of Megalopolis (St. Petersburg, Russia)



Boris F. Aparin, Elena Yu. Sukhacheva, Arina A. Kichko, Evgeny E. Andronov and Yaroslavna V. Valchenko

Abstract The specificity of phylogenetic structure of prokaryotic community at different taxonomic levels has been studied in (i) the forest soil profile classified as Umbric Albic Luvisol profile and (ii) the humus horizons from anthropogenic changed soils. Predominant phyla of bacteria constituting from the humus horizons of anthropogenic changed soils as well as from Umbric Albic Luvisol were represented by Acidobacteria, Actinobacteria, Bacteroidetes, Firmicutes, Gemmatimonadetes, Proteobacteria and Verrucomicrobia. The analysis of microbiomes' structure of soils has revealed that the humus horizons were characterized by a strong difference due to both (i) composition of bacterial phyla and their relative content and (ii) in positions occupied by representatives of individual phyla in microbial community in soil. Summarizing data, the structure of the microbial community in humus horizons at the taxonomic levels (phyla, class, order, family, genus) can be the most informative about the microbiome of in the anthropogenic-changed soils. The structure of microbial communities of soils' humus horizons at different taxonomic levels was affected by the genetic traits of soils as well as the influence of anthropogenic factor, especially by soils alkalization. A variety of metabolism products entering urban soils also plays an important role. The features of a microbiome of urban soils are meant to be a sensible all-purpose indicator of their state.

Keywords Urban soils · Microbiome · Taxonomy · Umbric Albic Luvisols · Prokaryotic community structure

B. F. Aparin (✉) · E. Yu. Sukhacheva
Saint Petersburg State University, 6 Birzhevoy pr., Saint Petersburg, Russia
e-mail: soilmuseum@bk.ru

A. A. Kichko · E. E. Andronov
All-Russia Research Institute for Agricultural Microbiology, Saint Petersburg, Russia

B. F. Aparin · E. Yu. Sukhacheva · Y. V. Valchenko
The Dokuchaev Central Soil Museum, Saint Petersburg, Russia

© Springer Nature Switzerland AG 2020

O. V. Frank-Kamenetskaya et al. (eds.), *Processes and Phenomena on the Boundary Between Biogenic and Abiogenic Nature*, Lecture Notes in Earth System Sciences,
https://doi.org/10.1007/978-3-030-21614-6_22

22.1 Introduction

Urbanization has become a factor exerting the most severe impact on soils. Nearly all forms of direct and indirect impact on soils, including changes in structure and properties, destruction and designing of soil body, are associated with it (Lehmann and Stahr 2007; Prokofyeva et al. 2011). In a magalopolis the share of effectively functioning surface is sharply decreasing which aggravates the ecological strain. Efficient discharge of the ecological functions by soils, determining the population quality of life, is largely governed by the microbial community. Metagenomics offers new possibilities for studying soil genesis, ecologically determined microorganisms spreading and evaluation of ecological functions (Main Achievements and Prospects of Soil Metagenomics 2017; Ronaghi 2004; Dolfing and Feng 2015; Saeki and Kunito 2010; Chirak et al. 2013; Lauber et al. 2008; Hartmann et al. 2009; Tikhonovich et al. 2018).

Microorganism biochemical activity is at the basis of many elementary processes in the urban soils: decomposition of plant litter, humus substance formation, and destruction of mineral and organic compounds—metabolites of man's activity. Microbial community is the most important element of the bio-geomembrane which is the main structural-ecological unity element of a soil. In the meantime, the urban soil microbiome research is, in fact, at the initial stage. This sets priorities in the metagenome research, which is the aim of present study. Such priorities include structure analysis for microbial communities of the prevailing megalopolis soil phases, comparison of (i) the urban soil microbimes and (ii) the forest soils, which have formed at the same conditions.

22.2 Objects and Methods

In comparison to wild landscapes, the megalopolis soil landscape is distinguished by the great diversity of anthropogenic transformed and "designed" soils (Aparin and Sukhacheva 2014; Lehmann and Stahr 2007; Charzynski et al. 2013). Most of the urban soils do not have the systemic (typomorphic) traits, structure and properties inherent to the natural spoils. Lack of the systemic traits is indicative of initial stages of a soil profile formation. Such soils are unstable: soil processes in the profile are not coordinated, and mineral-energy metabolism is not balanced, for the most part the soils typomorphic traits do not correspond to the soil formation factors. As a result, efficiency of the ecological functions discharge by the urban soils primarily depends on structure features, composition and properties of the humus horizons.

Spectrum of humus horizons in the soils from St. Petersburg affected by location in megalopolises is very wide. They differ by origin, formation mechanisms, age and parameters of functioning.

Humus horizons of the forest soils with the natural structure of profile. These soils are in full compliance with genotypes, without insignificant anthropogenic signs.

Humus horizons of anthropogenically-transformed soils. These soils are characterized by a broad range change in typomorphic traits: thickness, texture, structure, composition while maintaining affinity (genetic affinity) with the underlying horizons.

Humus horizons of anthropic soils. These soils are formed by infused (pedoallochthone, introduced) humous material of natural origin. They are characterized by full absence of genetic connection with the underlying mineral thickness, forming by periodic fill-in of "fertilizing substrata".

The urban soil microbiomes were studied in the samples from the most representative samples (Table 22.1). Soil profile (Pits) were arranged in three functional zones of St. Petersburg: recreational (Pits 4, 2, 7, 1, and 9), intended for building (Pit 5), transport area (Pits 3, 1a). Soils of the recreational zones are transformed, to a different degree, by man's activities. Umbric Albic Podzols (WRB 2014) (Pits 4, 7) are insignificantly transformed by man's activity. The Pit 4 located in Okhta forestry is transformed to a lesser degree than Umbric Albic Luvisol from the park named after I. V. Babushkin (Pit 5). The later shows signs of man's influence in the topmost part of the Pit only. The public garden Anthrosol (Stagnic) (Pit 9) was used in agriculture use not long ago. The former ploughed horizon remained intact in it.

The soils, represented by Pits 1, 2, 1a, and 5, were classified as Technosols (Aparin et al. 2018). Umbric Albic Luvisol, which was classified according to Classification and Diagnostics of Soil Russia (2004) was located 40 km away from St. Petersburg. This profile the example of a forest soil, unaffected by man's activity. Due to the typomorphic characteristics, this soil is similar with Umbric Albic Luvisol located in the park named after I.V. Babushkin (Pit 5). Besides 600 m away from the forest soil Pit (Pit LL) was situated and Pit LO was located in a vegetable garden. This pit (LO) is characterized by the similar soil morthology as a forest Umbric Albic Luvisol. Thus, the soils collected for the microbiome study have been formed at the same Atlantic-continental forest zone with humid temperate climate. All the soils are characterized by a have percolative water regime and are confined to the drainage areas.

To determine the soil chemical composition and characteristic properties, mixed samples were taken from each genetic horizon. The soil indices according to (Lauber et al. 2009; Hansel et al. 2008; Chernov et al. 2015), have the most influence on the procaryotic composition structure and diversify, were identified in the samples. Measurement of the pH values (pH_{H20}), soil organic matter (SOM), NH_4, as well as P and K (P_2O_5, K_2O) migrating compounds were done using the conventional methods according to Vorob'eva (1998) (Table 22.2).

For analyzing microbial communities, mixed samples were taken from the humus horizons, 10–15 g each, with three repetitions. The samples were placed in special containers. Transportation and preparation of the samples for analyzing microbial communities were carried out in accordance with the recommended scientific methodological practices (Andronov et al. 2011).

For DNA extraction, 0.25 g of sample was destroyed using ceramic balls in an extraction buffer. The latter is a mixture of solutions: 350 μl of solution A (200 mM phosphate buffered saline; 240 mM guanidinium isothiocyanate; pH_{H20}7.0), 350 μl

Table 22.1 Location of soils with humus horizons

Section and sample No.	Location, acreage	Vegetation	Soil*	Humus horizon depth, cm	Particle size distribution	Sampling depth, cm
113 (Pit LL)	Leningrad region, Tosnensky district, Lisino forestry	Spruce bilberry forest	Umbric Albic Luvisols	5	Clay	0–5
115 (Pit LO)	Leningrad region, Tosnensky district, Lisino forestry, vegetable garden	Vegetable garden, potato field	Anthrosols	43	Clay-loamy	0–5
1a (Pit 1a)	St. Petersburg, Nevsky district, lawn	Herb stratum	Technosols	14	Light clay-loamy	0–5
4 (Pit. 4)	St. Petersburg, Krasnogvardeisky district, Okhta forestry	Blueberry-heather pine forest	Umbric Albic Podzols	11	Sandy-loamy	4–9
7 (Pit 7)	St. Petersburg, Primorsky district, Udelnaya park, forest	Fern pine forest	Umbrisols (Novic)	43	Sandy-loamy	5–8
2 (Pit 2)	St. Petersburg, Nevsky district, I. V. Babushkin's park	Oak, ash, thinned out herb stratum	Umbric Albic Luvisols	16	Light clay-loamy	0–5

(continued)

Table 22.1 (continued)

Section and sample No.	Location, acreage	Vegetation	Soil*	Humus horizon depth, cm	Particle size distribution	Sampling depth, cm
3 (Pit 3)	St. Petersburg, Primorsky district, Zausadenaya street (building 26), lawn	Oak, thinned out herb stratum	Umbrisols (Novic)	46	Light clay-loamy	3–8
1 (Pit 1)	St. Petersburg, Frunzensky district, Pobeda park	Elm, ash, thinned out herb stratum	Technosols	16	Clay-loamy	5–8
9 (Pit 9)	St. Petersburg, Frunzensky district, mini-park (Moscow highway, building 2)	Ash, herb stratum (sedge)	Anthrosols (Stagnic)	18	Clay-loamy	5–10
5 (Pit. 5)	St. Petersburg, Krasnogvardeisky district, (Kommuna street, building 44), lawn	Thinned out herb stratum	Technosols	30	Clay-loamy	3–8

Note *Soil classification according to World Reference Base for Soil Resources (2014)

of solution B (500 mM Tris-HCl buffer; 1% SDS content by volume; pH 7.0) and 400 µl of phenol-chloroform mixture (1:1). Sample destruction was performed using FastPrep 24 ("MP Medicals", USA) under maximum capacity conditions. After that the obtained specimen was centrifuged at 14 000 r/s for 5 min. The obtained extract was re-extracted, using chloroform, and centrifuged. For DNA precipitation, isopropyl alcohol was added to the solution in 1:1 proportion. Further, the sample was centrifuged, and the obtained residue was washed out with 70% ethyl alcohol and

Table 22.2 Physico-chemical and physical characteristics of humus horizons

Sample No.	Acreage	pH_{H2O}	SOM	NH_4 (mg/kg) Ntot. (%)	P_2O_5	K_2O	HM	Fraction content < 0.01 mm, %
			%		mg/kg		%	%
113	Forest	3.6	2.5	0.2	138	119	1.83	75
115	Vegetable garden	5.5	5.7	0.3	508	294	2.50	38
1a	Lawn	6.9	3.3	0.3	Not specified	221	1.10	30
7	Park	5.7	2.3	9	400	150	0.99	15
2	Park	5.2	2.7	0.3	231	185	1.80	25
3	Lawn	6.8	4.5	22	720	610	1.93	25
1	Park	6.7	2.2	25	710	760	1.70	18
9	Mini-park	6.5	5.5	50	885	910	2.21	25
5	Lawn	7.0	5.1	11	485	750	0.91	15

dissolved in deionized water at 65 °C for 10 min. DNA purification was conducted using electrophoresis in 1% agarose gel followed by sorption at silicon oxide.

To compose amplicons libraries, amplification was performed in each sample by PCR method using universal primers at 16S-pPHK V4 variable part: F515—GTGCCAGCMGCCGCGGTAA; R806—GGACTACVSGGGTATCTAAT (Mardis 2008; Fierer and Jackson 2006) adding the unique identifiers. Preparation of the libraries for further pyrosequencing using Roshe GS Junior (Switzerland) sequencer was performed in accordance with the manufacturer recommendations.

Sequences processing, their combination into operational taxonomic unit (OTU), further taxonomic analysis and biodiversity assessment for the obtained communities were carried out using QIIME software package (Caporaso et al. 2010). Shannon and Chaol indices were used for the biological diversity assessment. As a result of processing and filtering of sequences, the following numbers of readings were obtained for each sample: 1—1546; 3—1947; 4—1969; 5—1332; 7—2201; 9—1996; 1a—2499; 2—3523; 113—1935; 115—2725; 116—4161; 117—7616.

22.3 Results

The prokaryotic community philogenetic structure at different taxonomic levels (phylum, class, order, family, genus) was studied. Phyla which content in a microbiome exceeded 1% were accounted. Traits of the prokaryotic community taxonomic structure were studied in the following sequence: microbiome of a forest Umbric Albic Luvisols, comparative analysis of microbiome of humus horizons of soils with weak man's impact, microbiome structure for man-transformed and man-made soils.

22.3.1 Prokaryotic Community Taxonomic Structure of Forest Soils (Umbric Albic Luvisols)

Data on characteristics of Umbric Albic Luvisols microbiome are rare in the literature (Chirak et al. 2013, Tikhonovich et al. 2018). They can be extrapolated to the studied soils with some reservation because of the different geographic location, soil composition and properties. These data allow only to reveal the trends of changes in the prokaryotic community structure in a zonal soil series. Umbric Albic Luvisols Pit LL was arranged in a bilberry spruce forest in the Lisinsky forestry of the Tosnensky district of the Leningrad region. The Pit is characterized by typical, for Umbric Albic Luvisols, morphological structure with weak gleization traits in a lower part of the profile (Figs. 22.1, 22.2 and Table 22.3). The soil chemical characteristics are shown in the Table 22.4. The soil was formed on lacustrine—glacial clay underlain by the varved clay. The pH values (pH_{H2O}) changes from acid in the Pit upper part [horizons AEL(5–10 cm) and BEL(22–42 cm)] to weakly acidic and neutral in the lower part [horizons BC(74–95 cm) and C(95–115 cm)]. The indexes of the soil horizons were identified according to Russian soil classification system (Classification and Diagnostics of Soil Russia 2004), which correspondent to the following indexes according to WRB (2015): AEL—AE, BEL—EB, BC—BC, and C—C (Table 22.3).

Humus profile is thin, at the depth of 17 cm the content of SOM (soil organic matter) is 0.4%. For microbiome study, samples were taken from three genetic horizons (AEL, BEL, and BC) and parent rocks (horizon C). Analysis of the microbiome



Fig. 22.1 Bilberry spruce forest. Lisino forestry



Fig. 22.2 Morphology of Umbric Albic Luvisols on the varved clay (Pit LL)

Table 22.3 Morphological characteristics of Umbric Albic Luvisols on the varved clay, Pit LL

Horizon*	Horizon depth, cm	Description
O	0–5	Peaty litter of twigs, fir-needles, leaves. The upper part (2–3 cm)—slightly and moderately decomposed plant residues, very loose, dark brown, wet. The lower part is well-decomposed, roots-permeated, well-separable from the mineral horizon. Undulating boundary, sharp transition
AEL	5–10	Straw-grey, well-defined crumbly structure, wet, penetrated with large roots and rootlets, clay, loose. Noticeable transition, clear color, uneven boundary
EL	10–22	Yellowish-pale (the brightest in the profile), horizontal divisibility — platy, packed down, many roots, fresh, clay, well aggregated, very small Fe–Mn concretions in the lower part of the horizon, many Fe–Mn patches, staged color, density, and structure transitions, uneven boundary
BEL	22–42	Marmorate, light brown with whitish-grey spots, fresh. Dense, clay at the top of Fe–Mn concretions, rare roots. Coarse-nuciform-prismatic structure. Breaks under strain. The intrapedal mass is brighter than on the structural blocks' facets. Staged density and color transition, tongued boundary
BMt,g	42–74	Uneven coloration, brown with grey spots, darker than the above, well-aggregated, breaks into nuciform blocks, fresh. Grey coatings along the facets of the structural blocks, even boundary, sharp colour transition
BCg	74–95	Uneven coloration from dark-brown to yellowish-pale-grey, nuciform-platy structure, fresh, dense, clay, rare Fe–Mn patches, uneven boundary, sharp configuration transition
Cg	95–115	The varved clay, large deformed bands (2–3 cm), chocolate brown color, individual thin light-colored seams, light layer — brownish-pale, rare small root channels

Note *Indexes of soil horizons are according to Classification and diagnostics of soil Russia (2004)

Table 22.4 Physico-chemical characteristics of Umbric Albic Luvisols (Pit LL of Lisino forestry)

Section	Horizon	Depth, cm	pH_{H2O}	Humus, %	∑ Exchangeable base, mEq/100 g of soil	CEC, mEq/100 g of soil	Fraction content < 0.01 mm, %	HM, %
LL	O	0–5	5.3	20.8	18.6	39	–	7.43
	AEL	5–10	3.6	4.5	23.7	30.4	75	1.83
	EL	10–22	4.0	1.6	17	20.8	83	1.10
	BEL	22–42	5.0	0.9	32.6	36.8	83	1.84
	BMt,g	42–74	6.0	0.7	41.9	46.4	90	2.32
	BCg	74–95	6.4	0.7	42.4	44.0	93	1.59
	Cg	95–115	7.1	0.7	48	48.0	91	2.49

taxonomic structure revealed representatives of 34 phyla, 9 of which dominate in the Umbric Albic Luvisols profile. Their share is from 98% in the AEL horizon to 99.8% in horizon C.

Proteobacteria phylum dominates in all the horizons. In the lower part of profile its content exceeds 91% (Fig. 22.3). It also dominants in the upper horizons but its content is much smaller here (52% in horizon AEL and 56% in horizon BEL). Invert correlation is observed for p. Acidobacteria occupying the second position. Maximum phylum content is observed in the humus horizon (25%) while in the middle horizon (BEL) its share is 5% and further lowers to 1% in the underlaying layers (Fig. 22.3a). Distribution of p. Actinobacteria along the profile is similar to that of p. Acidobacteria. In the upper layers content of p. Actinobacteria is higher than in the underlaying ones. However, in contrast with p. Acidobacteria, the maximum content of Actinobacteria is observed in the middle horizon. Share of Bacteroidetes, Firmicutes, Gemmatimonadetes, Chloroflexi, Planctomycetes and Verrucomicrobia phyla is 11% in the upper horizon and 20% in the middle horizon. Their content in the Pit lower part does not exceed 3%.

In the middle horizon (BEL), content of Bacteroidetes and Verrucomicrobia phyla is relatively high, along with Actinobacteria. Just these 3 phyla determine the microbiome community structure of the middle horizon. Altogether, 10 bacteria classes with content >1% were observed in the soil profile. Of these, 3 classes (DA052, Ktedonobacteria and Gemm-1) are absent in the Pit lower part. 4 representatives of Proteobacteria phylum are dominant at this taxonomic level (from 53% in the humus horizon to 89–94% in the parent rock) (Fig. 22.3b). Among them, dominating one, along the total profile, is c. Betaproteobacteria, maximum content being in the parent rock. Classes Alphaproteobacteria and Deltaproteobacteria are much more representative in the soil upper layers, the last one dominating in the lower BEL horizon.

Content of class Gemmatimonadetes representatives is considerably higher in the lower horizons as compared with the upper horizons which resembles distribution of c. Betaproteobacteria. By character of distribution along the profile, the humus horizon is standing out due to relatively high content of classes DA052, Alphaproteobacteria, and Betaproteobacteria which total share is 57%.

Content of representatives of classes Actinobacteria, Thermoleophilia and Ktedonobacteria is notably higher in the profile upper part, though, on the whole, maximum content of each of them does not exceed 7%. At the taxonomic level “order”, the significant bacterial count was observed for 13 representatives (Fig. 22.3c). Their proportion and character of distribution by horizons are quite specific. In the lower horizons, the dominant one is o. Burkholderiales (74–75%). The second position, by content, belongs to Pseudomonadales (5%). Diversity of bacteria from this level is much wider in the upper horizons as compared with the lower horizons. In horizon AEL, presence of Ellin6513, Rhodospirillales, Syntrophobacterale orders is quite noticeable while they are absent in the lower soil horizons. The representatives of 6 different families were observed in the soil, and half of them could not be attributed. The representatives of 2 main families are observed in the profile lower part: Alcaligenaceae (50%) and Comamonadaceae (24%). Total share of the families in the

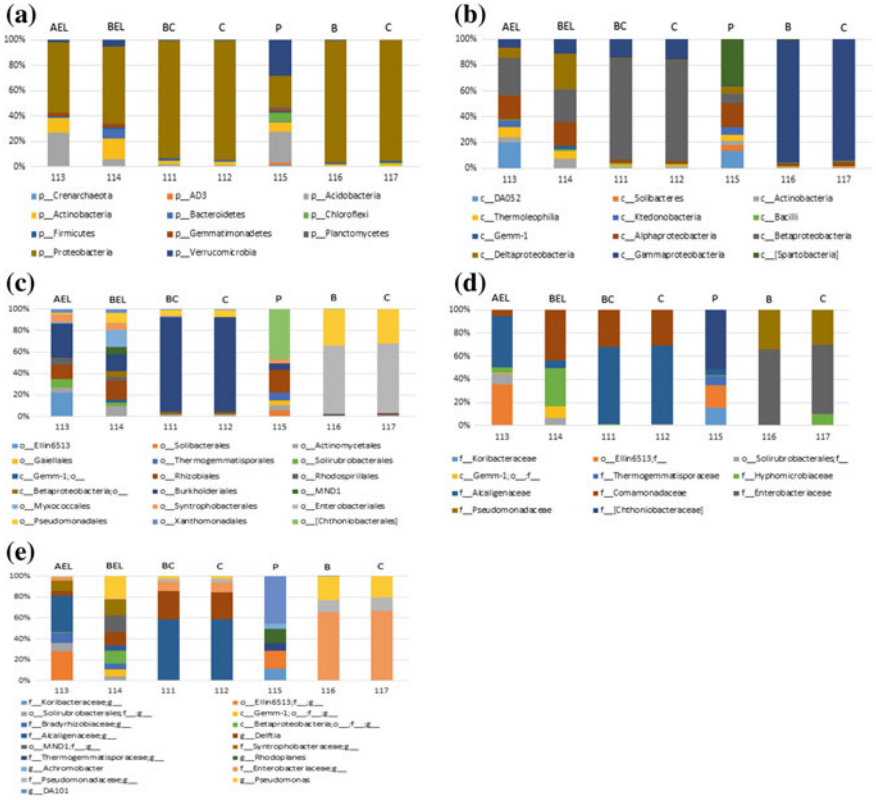


Fig. 22.3 Taxonomical structure of microbial community of Umric albic luvisols (Pit LL. Lisino forestry) and Luvisols (Aric). **a**—Fila, **b**—class, **c**—order, **d**—family, **e**—genus. AEL, BEL, BC, C—soil horizons. 113, 114, 111, 112—samples of Pit LL. 115, 116, 117—samples of Pit LO

middle horizon (BEL) is minimal, 16%, while in horizon AEL—48% and in the profile lower part—75% (Fig. 22.3d). Only 2 out of 12 geni observed were attributed (g. Delftia, g. Pseudomonas). Bacteria g. Delftia are observed in all the horizons, and their content in the lower horizons is by order of magnitude greater than in the upper ones. Noticeable content of Pseudomonas genus is only observed in horizon BEL (Fig. 22.3e).

Microbioms of the arable soil were investigated in samples of 115, 116 and 117. Samples were taken from soil pit located at 600 m. from LL soil pit. Soil profile of the arable soil is divided into 2 parts on the structure of microbiome of all taxonomical levels (Fig. 22.3). Top part is a sample from Aric soil horizon (115). Bottom part is samples from B (sample 116) and C (sample 117) soil horizons. Aric soil horizon has a large variety of microbial community. In this soil horizon Verrucomicrobia, Proteobacteria, Acidobacteria phylums are dominated (24–28%). Actinobacteria и

Chloroflexi phylums are at 2 positions (7%). In B and C soil horizons Proteobacteria fila is dominated (Fig. 22.3).

22.3.2 Microbial Community of Humus Horizons of Umbric Albic Luvisols and Park Soils

Umbric Albic Luvisols in Lisino Forestry (Pit LL) and park Umbric Albic Luvisols (Pit 2) are analogs (Fig. 22.4). The main difference in the park soil morphological structure is related to a partial anthropogenic change in humus horizon. It is characterized by larger thickness, density of soil structure as well as lighter mechanical composition and insignificant inclusion of artifacts (Table 22.1). The most significant difference between chemical properties of the park and forest soil humus horizons is determined by the less acidic environment (pH reaction) the park soils. In the structure of the humus horizons microbiome (sample 113—Lisino, sample 2—park n. a. I. V. Babushkin) 8 phyla form 2 groups in the content descending order (Fig. 22.5). Horizontal form of graphic display of microbiome structures data were used for humus horizons. This form turned out to be more convenient for a comparative analysis of the microbiomes of the humus horizons of different soils. The first group consists of 3 phyla: Proteobacteria, Acidobacteria and Verrucomicrobia which total share is about 80%. The second group is represented by 5 phyla: Actinobacteria, Bacteroidetes, Chloroflexi, Firmicutes, Gemmatimonadetes. Their total share does not exceed 8%.

Prokaryotes of the other taxonomic levels are represented by 6 classes, 12 orders, and 21 families. The representatives of 4 classes are distinguished in Acidobacteria and Proteobacteria phyla; Actinobacteria phylum is represented by 3 classes, the remaining phyla—each by one class. DA052 (14%), Thermoleophilia (6%), Alphaproteobacteria (15%) dominate among classes. At the order level, the largest shares belong to Chthoniobacteraceae (17%), Rhizobiales (13%), Burkholderiales (10%). All other orders account for less than 6%. The largest numbers of families (12) belong to Proteobacteria phyla. However, only 2 families (Alcaligenaceae and Hyphomicrobiaceae) are found in the significant amount (10%). The remaining 10 families share (each taken separately) does not exceed 2%. In the microbial community, Chthoniobacteraceae family has higher representation (17%), the second position is occupied by an unattributed family of Ellin6513 order (14%), the share of f. Koribacteraceae does not exceed 5%.



Fig. 22.4 Morphology of Umbric Albic Luvisols (I. V. Babushkin's park)

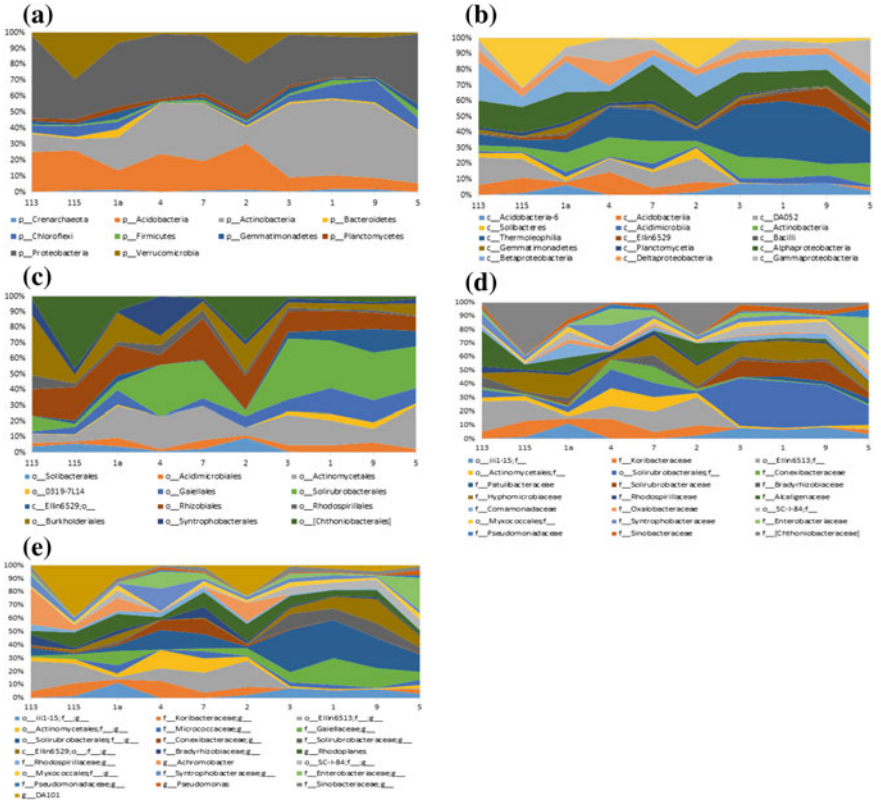


Fig. 22.5 Taxonomical structure of microbial community of humus horizons of anthropogenically changed soils. **a**—Fila, **b**—class, **c**—order, **d**—family, **e**—genus

22.3.3 Taxonomic Composition of the Microbial Community of Umbric Albic Podzols and Umbric Albic Luvisols Humus Horizons

It was interesting to compare taxonomic composition of the microbial community of Umbric Albic Podzols and Umbric Albic Luvisols humus horizons are located under forest vegetation (Table 22.1). The studied samples of humus horizons of Umbric Albic Luvisols (samples 113, 2) and Umbric Albic Podzols (samples 4, 7) differ significantly in clay-silt fraction content (<0.01 mm), pH values (pH_{H20}) and nutrient elements count (NPK) (Table 22.2). However, no clear connection between humus horizons microbiomes with soil properties was observed.

Comparative analysis of the microbial community taxonomic structure for forest and park soil humus horizons at different levels revealed both similarities and differences. There is no p. Bacteroidetes in Umbric Albic Podzols (samples 4, 7), high

content of p. Acidobacteria is observed, there are slight differences in p. Proteobacteria and Planctomycetes content. In terms of p. Acidobacteria, p. Bacteroidetes, p. Firmicutes, p. Planctomycetes, and p. Actinobacteria content, Umbric Albic Luvisols (samples 113, 2) are close to each other (Fig. 22.5a). At the same time, each soil has individual features of the prokaryotic community (Fig. 22.3).

22.3.4 Taxonomic Structure of Prokaryotic Community of Anthropic Soil Humus Horizons

Anthropic Technosols prevail in St. Petersburg soil landscape (Aparin and Sukhacheva 2014). Their profiles were formed as a result of filling-in humous material atop of the so-called cultural layer. It represents dissimilar layers of loose mineral rock mixed with construction debris and artefacts. Detailed characteristics of anthropic soils were given in the work by Aparin and Sukhacheva (2014). As a rule, the source of humous material is humus horizons of the cultivated soils from suburban agricultural lands.

Samples of anthropic soil humus horizons were taken in different functional areas: intended for building (sample 5), recreational (sample 2) and transport area (samples 1a, 3) (Table 22.1). All samples are characterized by the neutral pH values, high humus and nutrient status elements content (Table 22.2). Mechanical composition of humus horizons based on samples 5, 1—sandy-loam and samples 3, 1a—loamy. By structural features of the humus horizon microbiomes, samples 3, 1 stand out which are characterized by the dominance of p. Actinobacteria (46–47%), relatively low content of p. Acidobacteria (7–9%). The share of p. Proteobacteria in them ranges from 25 to 26% (sample 1) to 32% (sample 3). Samples 1a and 5 have individual traits of the microbiomes. Sample 5 shows the highest content of p. Proteobacteria (44%), and sample 1—of p. Acidobacteria (12%) and p. Verrucomicrobia (6%) (Fig. 22.5 a).

At the families level the humus horizon prokaryotic community is distinguished by dominance of only one family out of 21 revealed. In samples 1, 3 this is an unattributed f. Actinobacteria (14–18%), in sample 5—f. Enterobacteriaceae (14%), in sample 1a—f. Hyphomicrobiaceae. The second position (3–7% content) in samples 1, 3, 5 is occupied by f. Solirubrobacteraceae. In sample 1a this family content does not exceed 1%. The third position in all the samples is occupied by f. Hyphomicrobiaceae (4–6%), in sample 1a this family holds the second position (Fig. 22.5d).

22.4 Discussions

Absolute dominance of Proteobacteria phylum in the soil profile lower part was found in the forest soil. In this soil all horizons were study and this profile was used as an

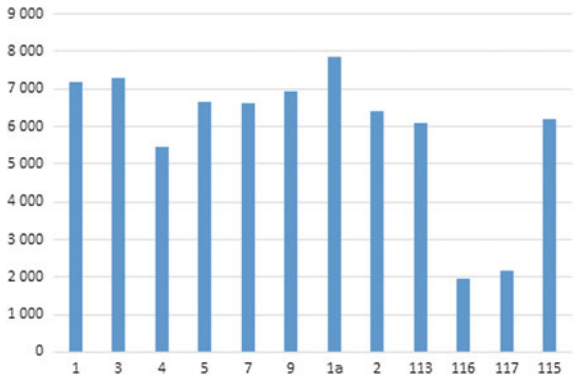


Fig. 22.6 Biodiversity index of humus horizons prokaryotic community (by Shannon)

example of microbiome studying. The varved clay, which is the parent substrate of the studied Umbric Albic Luvisols, is characterized by the low water permeability, which determines the following features in the profile: (i) weak development by the soil processes and (ii) actual absence of changes in the microbiome structure. Thus, it was revealed that the prokaryotic community in the low BC and C horizons reflects the previous epochs of pedogenesis is not related to the modern soil processes.

According to Fierer et al. (2003) 35–50% of microbial biomass is assignable to the soil layers deposited below the humus horizons. It was demonstrated that extracellular DNA can survive in soil for a long time and less labile microbiomes of the deep soil layers could carry important information about soil evolution (Andropov 2017; Ivanova et al. 2009). According to our findings namely c. Betaproteobacteria (74–75%) and c. Gammaproteobacteria (14–16%) play an important role in microbiome of the lower part of studied profile. From the 9 orders of Proteobacteria phylum, which were identified in the profile, the maximum content of representatives belong to the order—Burkholderiales. This order includes 2 dominant families—Alcaligenaceae and Comamonadaceae.

Microbes from the upper part (horizons: AEL 5–10 cm (AE according to WRB) and BEL 22–42 cm (EB according to WRB) of the profile reflect the modern stage of pedogenesis has taken place from the Last Glaciation. In these horizons the proportions of Acidobacteria and Actinobacteria phyla significantly increase along with relatively decreasing of Proteobacteria up to 40% comparing with lower horizon. The microbial community structure significantly differ especially in the upper soil horizon (AEL). In this horizon, the content of Acidobacteria phyla is much more higher than in the lower (BEL) horizon. Besides a relatively high contents of Alcaligenaceae family and a non-attributed family of Ellin6513 order were found here (AEL). The higher contents of Actinobacteria, Bacteroidetes, and Verrucomicrobia phyla are characterized the BEL horizon.

Much of extracellular DNA is associated with humus substance and organo-mineral complex which significantly increases its stability (Main Achievements and

Prospects of Soil Metagenomics 2017). However, microbial communities of the soil upper horizons are more sensitive to environment changes due to external impact (Blume et al. 2002; Hartmann et al. 2009). In connection with the revealed features of the profile-following changes in the prokaryots distribution, the main accent in investigating Umbric Albic Luvisols profile was further made on comparison of microbiomes of humus horizons with varying degree of man's impact.

Agricultural using of soils leads to significantly changes of microorganisms soil environments. The latter strongly depends on pH values, to which microorganisms are very sensitive (Blume et al. 2002; Chernov et al. 2015; Lauber et al. 2009) as well as to humus and nutrients content, air and water regimes (Table 22.2). The microbial community from humus horizon of the forest soil (Umbric horizon) and agro-humus horizon (Aric horizon) of ploughing soil was conducted based on the samples 113 and 115 taken from Pits LL and LO. These profiles are located on at 600 m distance from each other. Pit LO is an example of highly cultivated vegetable garden soil—Anthrosols, which forest analog is Umbric Albic Luvisols (Pit LL). Cultivated humus horizon is characterized by the less acid environment and high content of humus and NPK (Table 22.2).

Comparative analysis showed that significant differences in the humus horizon microbiome is affected by intensive soil using in agriculture. In the cultivated horizon 4 phyla were identified but the content of p. Verrucomicrobia increased considerably along with slightly increasing of p. Chloroflexi. Besides proportion of phylum Proteobacteria decreased twofold along with a lesser degree in case of p. Actinobacteria.

Significant differences in bacterial content were also observed at the family level. In the ploughing horizon domination of family Chthoniobacteraceae is observed (26% as compared with 1% in the forest soil). The second position in the structure is occupied by f. Hyphomicrobiaceae (10% as compared with 2% in the forest soil). In horizon AEL of the forest soil the first position belongs to family Alcaligenaceae, the second position—to an unattributed family of Ellin6513 order (16% as compared with 10% in the vegetable garden soil). Lesser differences are observed in content of f. Bradyrhizobiaceae, f, Rhodospirillales and f. Syntrophobacteracea, with their relatively high content in AEL horizon of the forest soil. On the whole, it was established that in the forest soil 6 out of 21 families have higher content compared to the vegetable garden soil.

Comparative analysis of the taxonomic structure of forest and park soils humus horizons microbial community at the different levels revealed both similarities and differences. Actinobacteria, Bacteroidetes, Firmicutes, and Planctomycetes phyla were found in approximately equal quantities. In the humus horizon from the park soil, the content of Proteobacteria phylum is 20% lower than in the forest soil. Oppositely, the content of Verrucomicrobia phylum is on the 17% higher. Most probably these changes are a result of anthropogenic impact. Acidobacteria phylum has higher representation in the humus horizon of the park soil than in forest soil. At the same time, the pH values in humus horizon (AY) of the park soil is less acid than in horizon AEL of the forest soil. Thus, our findings differ from that Acidobacteria phylum has relatively higher representation in sour soils (Lauber et al. 2009).

Differences in the microbial community structure of the forest and park soil humus horizons are less pronounced at the class level. These differences are mainly related to lower content of c. DA052, c. Betaproteobacteria, Gammaproteobacteria and c. Deltaproteobacteria and high content of c. (Spart) bacteria in the park soil. At the family level, significant differences between soils are observed for f. Alcaligenaceae and an unattributed family of o. Ellin6513. Family Chthoniobacteraceae has higher representation in the park soil humus horizon, compared to the forest soil while f. Bradyrhizobiaceae and f. Syntrophobacteraceae, on the contrary, have higher representation under the forest than in the park.

Humus horizon microbiome from Okhta forestry (sample 4) is the most diverse though it does not reveal significant quantities of p. Bacteroidetes, p. Chloroflexi and p. Gemmatimonadetes. Umbric Albic Luvisols (samp. 113) from Lisino forestry is distinguished by high content of p. Proteobacteria and relatively high content of p. Chloroflexi. Soil from park n. a. I. V. Babushkin (sample 2) is distinguished by high content of p. Verrucomicrobia.

Individual traits of the prokaryotic community structure for the humus horizons persist at the class level as well. In Umbric Albic Podzols humus horizon from Okhta forestry (sample 4) domination of c. Acidobacteria, c. Deltaproteobacteria and c. Gammaproteobacteria is observed. In Umbric Albic Podzols from Udelnaya Park (sample 7) domination of c. Alphaproteobacteria is observed. In both Umbric Albic Podzols samples relatively high content of c. Actinobacteria and c. Thermoleophilia is observed. In the Umbric Albic Luvisols, as compared to Umbric Albic Podzols, more similarities in the microbiome structure were observed at the class level rather than differences. Generally the soils studied differ significantly in the microbial community structure at the class level (Fig. 22.5b).

Thus, at the "order" taxonomic level Umbric Albic Podzols humus horizon microbial communities differ from that in Umbric Albic Luvisols due to higher content of o. Actinomycetales and o. Solirubrobacterales. In Umbric Albic Luvisols domination of o. Rhizobiales and o. Burkholderiales is observed. Umbric Albic Luvisols park soil (sample 2) is distinguished by high content of p. Chthoniobacterales and Umbric Albic Podzols from Okhta forestry (sample 4)—of o. Syntrophobacterales. At the family level microbiomes of humus horizons of the studied soils are mainly characterized by individual traits (Fig. 22.5d).

Comparison of microbial community structures at different taxonomic levels of anthropic soil humus horizons (samples 3, 1) and agrogenic humus horizon (sample 9) revealed their great similarity. Assumption can be made that humus horizons of these soils have the same origin, i.e. they are associated with the same type of the soil formation process.

Judging by the overall phylogenetic diversity of prokaryotic biomes, the noticeable differences between humus horizons of different types of soils are observed. Shannon index varies from 5, 4 to 7, 8 (Fig. 22.6) in the soils. The minimal diversity characterizes the microbiome of Umbric Albic Podzols humus horizon from Okhta forestry (sample 4), and maximal diversity is observed in the humus horizon of lawn Technosols (Pit 1a). Agricultural using of Umbric Albic Luvisols (Lisino forestry) did not influence on biodiversity (samples 113, 115).

In general, the humus horizons of all forest soils show lower biodiversity index as compared to the anthropic soils. Owing to the revealed features of the depth-wise prokaryots distribution, the main accent in Umbric Albic Luvisols profile was further made on a comparison of microbiomes of in different degrees anthropogenically-changed humus horizons. Comparative analysis of the taxonomic structure of forest and park soils humus horizons microbial community at the different levels revealed both similarities and differences. Actinobacteria, Bacteroidetes, Firmicutes, and Planctomycetes phyla occur in approximately equal quantities. In the park soil humus horizon, the share of Proteobacteria phylum is by 20% less than in the forest, and the share of Verrucomicrobia phylum is by 17% more, which brings together park (samp. 2) and vegetable garden (samp. 115) soils. Probably, it is owing to anthropogenic influence. Acidobacteria phylum is more represented in the park than in forest soil humus horizon. At the same time, the pH value in the upper horizon AY of park soil is less acidic than in horizon AEL of the forest soil. Although it was reported that Acidobacteria phylum is relatively more represented in acidic soils (Lauber et al. 2009).

The differences in the structure of the microbial community of forest and park soils humus horizons are less pronounced. These differences are mainly related to lower levels of c. DA052, c. Betaproteobacteria, Gammaproteobacteria, and c. Deltaproteobacteria and high content c. (Spart) bacteria in park soil. At the family level, significant differences between soils are observed for f. Alcaligenaceae and unattributed o. Ellin6513 family. There is more Chthoniobacteraceae family in the park than the forest soil humus horizon and on the contrary, there is more f. Bradyrhizobiaceae and f. Syntrophobacteraceae under the forest than in the park.

Okhta forestry humus horizon (sample 4) microbiome is characterized by the most diversity. Although the representatives of p. Bacteroidetes, p. Chloroflexi, and p. Gemmatimonadetes were not revealed in significant quantities. Umbric Albic Luvisols (sample 113) from Lisino Forestry is distinguished by a high content of p. Proteobacteria and relatively high of p. Chloroflexi. The soil of I. V. Babushkin's park (sample 2) has a high content of p. Verrucomicrobia.

Individual features of prokaryotic community humus horizons structure are preserved at the class level too. In Okhta forestry Umbric Albic Podzols humus horizon (sample 4), c. Acidobacteria, c. Deltaproteobacteria, and c. Gammaproteobacteria prevail. In Umbric Albic Podzols of Udelnaya park (sample 7), c. Alphaproteobacteria prevails. In both Umbric Albic Podzols samples, a relatively high content of c. Actinobacteria and c. Thermoleophilia is observed.

In Umbric Albic Luvisols, as compared to Umbric Albic Podzols, more similarities than differences in the structure of microbiome were observed at the class level. Generally, the soils in question differ significantly in the microbial community structure at the class level (Fig. 22.5b).

At the "order" taxonomic level, Umbric Albic Podzols humus horizons microbial communities differ from Umbric Albic Luvisols with a higher content of o. Actinomycetales and o. Solirubrobacterales. In Umbric Albic Luvisols, o. Rhizobiales and o. Burkholderiales prevail. Umbric Albic Luvisols from park (sample 2) is distinguished with a high content of o. Chthoniobacterales, and Umbric Albic

Podzols (sample 4) from Okhta forestry—of o. Syntrophobacterales (Fig. 22.5c). At the family level, microbiomes of humus horizons of the soils are characterized by individual features (Fig. 22.5d). The comparison of microbial community structures at different taxonomic levels of anthropic soils humus horizons (samples 3, 1) and Anthrosols humus horizon (sample 9) revealed a great similarity between them. It can be assumed that humus horizons of these soils have the same origin, i.e. are associated with one type of soil formation process.

According to the general phylogenetic diversity of prokaryotic biomes, the noticeable differences between humus horizons of different types of soils are observed. The Shannon index ranges from 5, 4 to 7, 8 (Fig. 22.6). The minimal diversity is typical for the microbiome of Okhta forestry Umbric Albic Podzols humus horizon (sample 4), and maximal is observed in humus horizon of Technosols of lawn (section 1a). Agricultural development of forest Umbric Albic Luvisols (Lisino forestry) has not affected biodiversity (samples 113, 115). In general, the humus horizons of all forest soils possess lower biodiversity index as compared to anthropic soils.

22.5 Conclusion

In the all studied samples from the soil horizons of the soils located in the forest Umbric Albic Luvisols and Umbric Albic Podzols the predominance of bacteria was revealed as the domain level. The proportion of archaebacteria represented by *o.* Crenarchaeota does not exceed 2%. Representatives of 9 dominant bacterial phyla were identified in all samples: Acidobacteria, Actinobacteria, Bacteroidetes, Chloroflexi, Firmicutes, Gemmatimonadetes, Planctomycetes, Proteobacteria, Verrucomicrobia. These findings are in a good agreement with published data concerning the dominance of these phyla in soils.

At the same time phylogenetic structure of the microbial community of the studied soil types has traits associated with different levels of man's impact. Phyla content varies over a wide range (from 0.4 to 40%). The share of these phyla of the total number is about 98%. Microbiome structure analysis performed for the studied soils revealed substantial difference between the humus horizons both in composition of bacteria phyla and their relative content in different soils and in positions occupied by representatives of individual phyla in microbial community of different soils.

Analysis of the results of the humus horizons metagenomic studies showed that the aggregate data on the microbial community structure at the taxonomic levels: class, order, family, genus, has potential for yielding important information about microbiome of soils with varying degree of man's impact. No one-to-one association was observed between the microbial community structure for the studied humus horizons and their properties (pH values, humus and nutrient status elements content). Possibly it is related to the microbiome stability which formed over a long period of soil formation. It was revealed that the absolute age (calibrated) of humus horizons material of natural, man-transformed and anthropic soils varies over the range from 500 to 3000 years indicating the natural origin of the soil humus.

It is obvious that the microbiome of the anthropic soil humus horizons was inherited from Anthrosols, which material was used for creating introduced horizons. Almost all the samples have traits of the microbiome structure. At the taxonomic phylum level the most specific distinction between Technosols is relatively low content of p. Acidobacteria, high content—p. Actinobacteria and the increased content of p. Chloroflexi. The samples from humus horizons 1 and 9 from Pobeda Park (sample 1) and Anthrosols (sample 9) demonstrate particularly close similarity of microbiomes.

Umbric Albic Luvisols and Umbric Albic Podzols are mostly characterized by a higher content of p. Acidobacteria and p. Proteobacteria compared Technosols. Umbric Albic Podzols, as compared to Umbric Albic Luvisols, are distinguished by high content of p. Actinobacteria.

The anthropic soils (Technosols) at the family level differ significantly from Umbric Albic Podzols and Umbric Albic Luvisols. Technosols demonstrated high content of f. Solirubrobacteraceae and an unattributed family of c. Thermoleophilia, and there are not unattributed families of DA052 and Koribacteria classes (except for sample 1a) which are present in forest soils.

Umbric Albic Luvisols and Umbric Albic Podzols are only distinguished by a relatively high content of unattributed family of c. DA052. Thus, microbial community structure of the soil humus horizons at different taxonomic levels reflects both the genetic traits of soils and influence of the anthropogenic factor demonstrated, primarily, by soil alkalization. Likely, various metabolism products entering the urban soils play an important role. The urban soil microbiome special features are a responsive universal indicator of the soil status.

References

Andropov EE (2017) The preservation of microbial DNA in archived soils of various genetic types. PLoS ONE 12(3):e0173901

Andronov EE, Pinaev AG, Pershina EV, Chizhevskaya EP (2011) DNA extraction from soil samples (methodological guidelines). Federal State Budgetary Scientific Institution—All-Russian Research Institute for Agricultural Microbiology. Saint Petersburg (in Russian)

Aparin BF, Sukhacheva EY (2014) Principles of soil mapping of a megalopolis with St. Petersburg as an example. Eurasian Soil Sci 47(7):650–661

Aparin BF, Sukhacheva EYu, Bulysheva AM, Lazareva MA (2018) Humus horizons of soils in urban ecosystems. Pochvovedenie 9:1071–1084

Blume E, Bischoff M, Reichert JM, Moorman T et al (2002) Surface and sub-surface microbial biomass, community structure and metabolic activity as a function of soil depth and season. Appl Soil Ecol 20:171–181

Caporaso JG, Kuczynski J, Stombaugh J et al (2010) QIIME allows analysis of high throughput community sequencing data. Nat Methods 7(5):335–336

Charzynski P, Hulisz P, Bednarek R (2013) Technogenic soils of Poland. Polish Society of Soil Science, Torun, Poland

Chernov TI, Tkhakakhova AK, Kutovaya OV (2015) Assessment of diversity indices for the characterization of the soil prokaryotic community by meta-genomic analysis. Eurasian Soil Sci 48(4):410–415

Chirak EL, Pershina EV, Dol'nik AS, Kutovaya OV et al (2013) Taxonomic structure of microbial association in different soils investigated by high through-put sequencing of 16S rRNA gene libraries. Sel'skohozjajstvennaja biologija 3:100–109 (in Russian)

Classification and Diagnostics of Soil Russia (2004) Oikumena, Smolensk (in Russian)

Dolfing J, Feng Y (2015) Nature Limited. The importance of soil archives for microbial ecology. Nat Rev Microbiol 13(3):1

Fierer N, Jackson RB (2006) The diversity and biogeography of soil bacterial communities. Proc Nat Acad Sci U S A 103:626–631

Fierer N, Schimela JP, Holden PA (2003) Variations in microbial community composition through two soil depth profiles. Soil Biol Biochem 167–176

Hansel C, Fendorf S, Jardine P, Francis C (2008) Changes in bacterial and archaeal community structure and functional diversity along a geochemically variable soil profile. Appl Environ Microbiol 74:1620–1633

Hartmann M, Lee S, Hallam SJ, Mohn WW (2009) Bacterial, archaeal and eukaryal community structures throughout soil horizons of harvested and naturally disturbed forest stands. Environ Microbiol 11:3045–3062

Ivanova EA, Korvigo IO, Aparin BF, Chirak EL, Pershina EV, Romaschenko NS, Provorov NA, Lauber CL, Hamady M, Knight R, Fierer N (2009) Pyrosequencing-based assessment of soil pH as a predictor of soil bacterial community structure at the continental scale. Appl Environ Microbiol 75(15):5111–5120

Lauber CL, Hamady M, Knight R, Fierer N (2009) Pyrosequencing-based assessment of soil pH as a predictor of soil bacterial community structure at the continental scale. Appl Environ Microbiol 75(15):5111–5120

Lauber CL, Strickland MS, Bradford MA, Fierer N (2008) The influence of soil properties on the structure of bacterial and fungal communities across land-use types. Soil Biol Biochem 40:2407–2415

Lehmann A, Stahr K (2007) Nature and significance of anthropogenic urban soils. J Soils Sediments 7(4):247–260

Main Achievements and Prospects of Soil Metagenomics (2017) Inform-navigator. St.-Petersburg (in Russian)

Mardis ER (2008) Next-generation DNA sequencing methods. Ann Rev Genomics Hum Genet 9:211–219

Prokofyeva TV, Martynenko IA, Ivannikov FA (2011) Classification of Moscow soils and parent materials and its possible inclusion in the classification system of Russian soils. Eurasian Soil Sci 44(5):561–571

Ronaghi M (2004) Pyrosequencing: a tool for DNA sequencing analysis. Methods Mol Biol 255:211–219

Saeki K, Kunito T (2010) Adsorptions of DNA molecules by soils and variable-charged soil constituents. Curr Res Technol Educ Top Appl Microbiol Microb Biotechnol 1:188–195

Tikhonovich IA, Chernov TI, Zhelezova AD, Tkhakakhova AK, Andronov EE, Kutovaya OV (2018) Taxonomic structure of prokaryotic communities in soils of different bioclimatic zones. Dokuchaev Soil Bull 95:125–153

Vorob'eva LA (1998) Soil chemical analysis Moscow State University, Moscow (in Russian)

World Reference Base for Soil Resources (2014) International soil classification system for naming soils and creating legends for soil maps. FAO, Rome

Chapter 23
Humic Substances Formation as a Result of Biogenic-Abiogenic Interactions in Epiphytic Structures of the South Vietnam Tropical Forest

Oksana A. Rodina, Evgeny V. Abakumov, Alen K. Eskov and Nikolay G. Prilepskiy

Abstract There are a number of ways to implementation the epiphytic biogenic-abiogenic interaction in plant communities. Epiphytic plants form a special type of organic or organo-mineral substrate—suspended soils. This study is devoted to the investigation of the biogenic-abiogenic interactions in epiphytic formations and characteristic of the suspended soils, which are formed in them with special reference to the assessment of stabilization rates and structural composition of humic acids in the suspended soil in tropical forests of South Vietnam. General properties of the soil and the elemental composition of suspended soils were determined, and the humic substance chemical composition was evaluated using solid state 13C-NMR. The soils formed by epiphytes show a positive correlation in the isotopic composition of nitrogen with epiphyte tissues and to a greater extent with forophyte tissues and, probably, take part in their nitrogen nutrition, concentrating zoogenic nitrogen due to ant presence. The most comparable soil type in terms of organic matter composition is Cambisols from humid forests of subboreal and subtropical zones. The results we obtained are consistent with the concept of soil organic matter stabilization: the proportion of aliphatic compounds in the component composition in bulk organic matter is higher than in humic acids, isolated from soils investigated. Thus, it can be concluded that in suspended soils soil organic matter stabilization processes active and expressed in formation and accumulation of humic substances.

Keywords Soils · Organic matter · Stabilization · Epiphytic formations · Epiphytic soils · Suspended soils

O. A. Rodina (✉) · E. V. Abakumov
Department of Applied Ecology, Saint Petersburg State University, 16-Line 29, Vasilyevskiy Island, Saint Petersburg 199178, Russian Federation
e-mail: oxanarod@yandex.ru

A. K. Eskov
Russian Academy of Sciences, Tzitzin Main Botanical Garden, Botanicheskaya st., 4, Moscow 127276, Russia

N. G. Prilepskiy
Lomonosov Moscow State University, Leninskie Gory, 1, Moscow 119991, Russia

© Springer Nature Switzerland AG 2020

O. V. Frank-Kamenetskaya et al. (eds.), *Processes and Phenomena on the Boundary Between Biogenic and Abiogenic Nature*, Lecture Notes in Earth System Sciences,
https://doi.org/10.1007/978-3-030-21614-6_23

23.1 Introduction

The term "suspended soils" has become more common in the literature on primary soil formation in the investigations of the tropical ecosystems in recent years. Suspended soils are a presented by a complex of mineral particles and grains and organic matter dead remnants and living tissues that has not undergone the full detritization and decomposition process and has not turned into soil organic matter in terrestrial environments (Shaw 2013). This type of organo-mineral interaction is considered as under investigated in modern soil science and terrestrial ecology. The formation of suspended soils normally happens if organic matter does not enter the litter (topsoil forest floor) at the same time, but accumulates on the surface of the obstacles: in cracks, on branches, in tree bark, and in epiphytic associations, etc., which temporarily retain organic matter from falling on the soil surface (Lindo and Winchester 2006). This transitional accumulation of the organo-mineral structures results in creation of soil like bodies, formed not on common parent material of the terrestrial ecosystems but in the intermediate tier of some forests typical for tropical climatic belt. Such soils can exist for a long time in the form of undercomposed or slightly decomposed organic matter; stabilized by various types of epiphytes (this stabilization could be physical of chemical, depending on the degree of organic matter transformation and the presence and spatial density of living organic tissues in epiphytic suspended formations). Suspended soils in the forest canopy experience large differences in temperature and humidity than in the normal forest litter, located of the mineral or organo mineral soil surface (Bohlman et al. 1995), and the decomposition rate of organic matter in the canopy may be different (Lindo and Winchester 2007). Thus, the slower decomposition of organic matter under the conditions of "air soils" or suspended soil-like formations was revealed in comparison with experimentally designed soils in experiment of the decomposition of cellulose patches in soils (Nadkarni 1986). This fact indicates completely different geochemical regime if one compare geochemical and oxidation-reduction regime in soils of norms superficial environments of terrestrial ecosystems and suspended soil of air—trees environments of the tropical forests.

Epiphytes have implemented various adaptations to their characteristic way of life in the evolution. The complicated organization of the tropical ecosystems in a vertical scales results in formation of edaphone and aerophytone layers or tiers with evident and strong differentiation of the microenvironments quality and conditions. Part of the epiphytes went along the way of xeromorphosis of the axial organs and roots, some developed various morphological devices for storing and/or trapping water and litter (Benzing 1990). The latter form the biomorphological group of accumulative epiphytes (Eskov 2012). Plants belonging to this group solve the problem of moisture deficiency and mineral nutrition by trapping and holding litter and organic debris, mutualism with insects, and the formation of water reservoirs. The general direction of their adaptations is the same: it is the formation of various devices to facilitate the existence of the accumulation of organic litter and water (Eskov 2012). Thus,

complex biogenic-abiogenic interactions are formed, ensuring the formation of new ecological niches in the tropical forest canopy.

Accumulative epiphytes have xeromorphosis of leaves and stems (or rhizomes) in varying degrees. But their roots, as a rule, are much less adapted for drying than in typically xerophilic epiphytes. This is due to the fact that representatives of this group are characterized by the accumulation in the process of ontogenesis of various kinds of quasi-soil substrates, permeated by their roots. The formation of such "suspended" soils is subject to somewhat different laws than the processes of "normal" soil formation in tropical conditions.

The role of suspended soils in the circulation of organic substances and biophilic elements is underestimated. For some soils, in particular organogenic, Tolchelnikov (1985) introduced the term "degenerate" soil formation. During it, in particular, the role of one or another factor of soil formation (in this case, the soil-forming rock) decreases, which excludes the possibility of their functioning as soils in the ecosystem. There is also the concept of soil as an element of the "ecosystem of a single plant" (Chertov 1983), but the actually suspended soils accompanying epiphytic colonization in the tropics remain poorly understood.

Soil fauna is present in suspended soils, for example, mites (Lindo and Winchester 2007) and springtails (Shaw 2015). The process of settling the tree crowns of non-flying fauna is poorly understood, but presumably involves migration along the bark of the tree (Shaw 2015) or transfer on the mineral particles surface by wind.

Thus, suspended soils are an interesting and quite informative object of study not only because of the not traditional process of soil formation, but also because they represent an important factor in the conservation of biodiversity of the "epiphytic biocenosis". The species richness and species composition of ants depends on the size of the epiphyte and the presence of suspended soil (Darocha et al. 2015). It is noted that the biomass of the inhabitants of suspended soils is 20 times higher than that in the most habitable soil horizon (Sergeeva et al. 1989). In several "nests" of the *Asplenium nidus* L. species, collected from three habitats in Vietnam, 150 species of invertebrates were found (Sergeeva et al. 1997).

It was established that, for accumulative epiphytes, various ways of suspended soil accumulation, formation and differentiations of are characteristic. In cursive epiphytes, soils form under the curtain itself, the main way of soil formation is accumulation of in situ material. Very often, ants that play a certain role in the genesis and origin of suspended soil settle in the clump of an epiphyte (Eskov 2013; Eskov and Dubovikov 2015). In the case of "nesting" epiphyticism, the accumulation of litter is carried out by a funnel of leaves, and the growth of the roots, which forms a powerful soil clot around the root system, visually resembles a bird's nest located in the air stands, stabilized between the steams and roots of the current forest stands. "Staple" epiphytes use a similar mechanism, forming funnels for collecting the forest floor remnants and rainwater precipitation using specialized leaves-brackets which play an important role of organic matter accumulation in the state of suspended soils, located permanently in air.

This functional role of the "brackets accumulators" is strictly related to the genus *Drynaria*. The role of "brackets" is played by sterile, solid, hard fronds of particular

morphology, the tissues of which die early, but the fronds remain on the plant for many years. Root clod mass in "bracket" epiphytes is less than in "nested" ones. Thus, the measured mass of the "nest" (substrate + roots) for *Asplenium nidus* at the end of the dry season was 5099 g, and the leaves 958 g; for "staple" epiphyte *Drynaria laurentii* (Christ) Hieron. with a total mass of 938 g, the mass of the roots and humus was only 222 g (Walter 1968). On the whole, nested epiphytes are capable for accumulating up to 30–40 kg of organic substrate of dead organic remnants per specimen or standing tree and within the community up to 277.9 kg/ha (Pocs 1976). The latter estimate is likely to be greatly underestimated. It is described that in the undisturbed forest the number of nesting epiphytes can reach 600 ind/ha with an average mass of "nest" of 3–5 kg (Zonn and Lee 1958). A large mass of suspended soil very seriously changes the water supply of epiphytes and external climatic conditions. The ability to retain water in nesting epiphytes (water holding capacity), depending on the morphology and specificity of nesting web, ranges from 45.4 to 334.9% relative to their dry weight (Pocs 1976). Even in the dry season, the moisture content of epiphytic substrates is 2.5 times higher than the moisture content of the topsoil horizon of local terrestrial environment (Sergeeva et al. 1989) and is close to 80%. This is caused by the interception of drip condensate that settles at night in the crown and practically does not reach the ground (Panfilov 1961).

In some cases, nested epiphytes form impoundment roots, they are special additional (or lateral) roots with negative geotropism, which serve as a "brush" in which litter is stuck (Benzing 1996). Nested epiphytes with such roots, as well as other devices for water and litter retention, were given the stable name "trash-basket" (Benzing 1990). The physiological cause of negative geotropism is obscure. However, in the literature there are data indicating the dependence of the formation of such roots on the level of insolation (Werckmeister 1971).

Actually, nothing is known about the anatomical structure of these roots and their growth. We have published a study of various biological features of the accumulation and formation of suspended soils (Eskov et al. 2017). We also investigated a number of properties of the suspended soils. Special attention is paid to the isotopic composition of nitrogen and carbon in various parts of epiphytic ecosystems, as a marker of their trophic status. It is known that nitrogen nutrition of woody plants of tropical ecosystems can be associated with the presence of ants (Pinkalski et al. 2015), and epiphytes can receive up to 30% of nitrogen from their livelihoods (Treseder et al. 1995). A high content of ^{15}N is noted in the tissues of ants, like other animals (Vanderklift and Ponsard 2003). On the other hand, many terrestrial (Bone et al. 2015) and epiphytic (Qiu et al. 2015) orchids, as well as epiphytes of other families, are characterized by CAM photosynthesis (a variant of organic acid metabolism characteristic of succulent plants) (Zitte et al. 2008). The difference in carbon isotopic composition between C3 plants (to which the forophytes belong) and C4 or CAM plants (Martin et al. 1990, 1992; Diels et al. 2004), as well as "animal" and "plant" nitrogen, allows us to understand the possible the path of migration of organic matter in the epiphytic community: from its source to the formation of a suspended soil in nesting epiphytes clods.

Thus, the aim of our research was the study of biogenic-abiogenic interactions in epiphytic formations, and also the characteristic of the suspended soils which are formed in them.

With the aim to implement this aim were have formulated flowing research objectives:

(1) to characterize general soil properties and elemental composition of suspended soils from various types of epiphytes and soils under forophytes from conditions of sparse savanna-like light forests of oligotrophic habitats in South Vietnam, Phu-Quoc Island;
(2) to evaluate the humic substances chemical composition using solid state 13C-NMR and to compare data obtained with those, obtained for the bulk organic matter of whole soils;
(3) to describe the organic matter stabilization process that take place in suspended soils in terms of soil organic matter structural composition.

23.2 Materials and Methods

Phu Quoc Island is located in the south-western part of Vietnam, in the Gulf of Thailand. The nearest mainland Vietnamese city, Hatien, is approximately 43 km away. Phu Quoc is considered to be the largest island of Vietnam; it is located on an area of about 575 sq. Km, stretching from its northern to southern parts for 49 km, while the width in different parts of the island is within 3–27 km. The landscape of the island is mostly mountainous. The island "99 Peaks" is another name for the island. The highest mountains are located in the north, which are gradually falling to the south. The highest point of the island is the top of Mount Chua (600 m).

Phu Quoc Island is mainly composed of sedimentary rocks from the Mesozoic and Cenozoic age, including heterogeneous conglomerate composition, layering thick, quartz pebbles, silica, limestone, riolit and felsit. The Mesozoic rocks are classified in Phu Quoc Formation (K pq). The Cenozoic sediments are classified in formations of Long Toan (middle—upper Pleistocene), Long My, (upper Pleistocene), Hau Giang (lower - middle Holocene), upper Holocene sediments, and undivided Quaternary (Q) (Thanh 2012).

The island's monsoonal sub-equatorial climate (Table 23.1) is characterized by distinct rainy (June to November) and dry seasons (December to May). The annual rainfall is high, averaging 2879 millimetres. In the northern mountains up to 4000 millimetres has been recorded. April and May are the hottest months, with temperature reaching 35 °C (Eskov 2013).

Representatives of some ecobiomorphs capable of forming suspended soils were selected for the study. Curtin-forming epiphytes, in which the curtain (in which suspended soils accumulate) itself plays an environment-forming role: *Pyrrosia longifolia, Pyrrosia adnascens*. Bracket epiphytes, forming special leaves, playing the role of funnels for collecting debris and moisture: *Platycerium grande, Drynaria sparsisora*.

Table 23.1 Climate data for Duong Dong Airport, Phu Quoc (the source is "Vietnam Building Code Natural Physical & Climatic Data for Construction" (2009))

Month	Jan.	Feb.	Mar.	Apr.	May	Jun.	Jul.	Aug.	Sep.	Oct.	Nov.	Dec.	Year
Average high °C	30.4	31.1	32.1	32.3	31.4	30.0	29.5	29.2	29.2	29.9	30.3	30.0	30.5
Average low °C	22.5	23.5	24.6	25.4	25.6	25.3	25.0	24.9	24.7	24.3	24.0	22.9	24.4
Average precipitation mm	34	29	54	149	298	413	418	546	473	387	169	59	3029
Average precipitation days	5.3	3.9	5.7	11.5	19.5	21.8	22.5	24.4	22.5	21.6	13.3	6.2	178.3
Average relative humidity (%)	76.3	77.6	77.6	80.5	83.8	85.8	86.6	87.1	88.0	86.9	79.6	73.9	82.0
Mean monthly sunshine hours	251	230	255	246	196	146	151	134	139	168	208	242	2364

Nested epiphytes with ageotropic roots: *Acriopsis* sp., *Cymbidium fynlaisonianum* (Fig. 23.1). The main forophytes in these communities are: *Melaleuca leucadendra, Dipterocarpus aff. tuberculatus, Dillenia obovata* and some other species. In general, communities are poor in species composition with extremely simplified vertical structure, not close. Suspended soils are formed on lightly rolled fine quartz or quartz-microcline sands with a very low content of detrital humus.

The most problematic aspect in the suspended soil study is their phenomenology and gnoseological interpretation. The genesis and the origin most likely of all suspended soils is characterized by two important points that cannot be ignored when trying to somehow explore or classify them: (1) if the suspended soil is limited in its existence by the lifetime of the tree, (2) if they are completely isolated from the parent rock or parent materials, on which the soil-forming processes take place. Forophyte bark, in a sense, plays the parent rock role. In this context, it is appropriate formulate the question: do processes occur in suspended soil, similar to soil formation, primarily stabilization/humification of organic matter? Thus, our research was aimed at describing the processes of stabilization/humification in suspended soils that form in the roots and comas of vascular epiphytes. And find their closest analogues among terrestrial soils.

Samples of epiphytes and associated suspended soils were collected under conditions of sparse savanna-like light forests of oligotrophic habitats in South Vietnam, Phu-Quoc Island. The studied areas of savanna-like sparse formations are located near both coasts of the island, around the line between 10°16′46″ N, 103° 55′ 22.7″ E and 10° 24′ 17″ N, 104° 03′ 01.6″ E (Fig. 23.2). Soils are very poor, oligotrophic sandy loams (Eskov et al. 2017).

Soil samples were air-dried (24 h, 20 °C), ground, and passed through 2-mm sieve. Routine chemical analyses were performed using classical methods: C and N

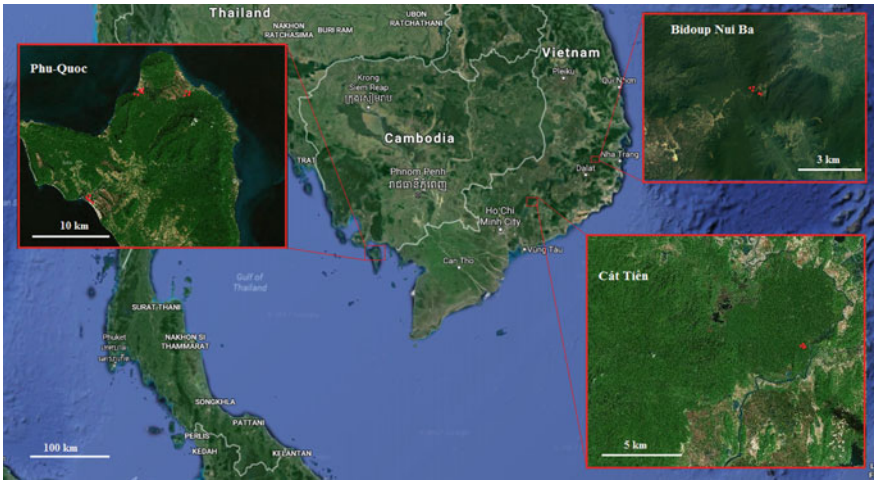


Fig. 23.1 Location of the study site: material collection plots are marked with red dots

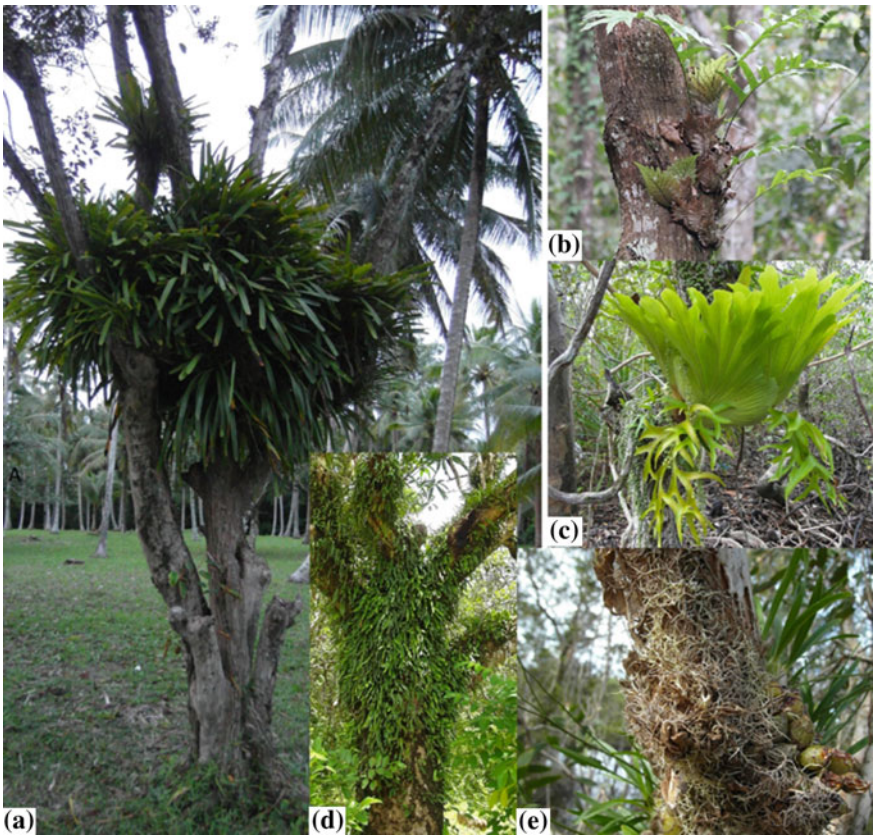


Fig. 23.2 Studied epiphytes: epiphytic orchids—**a** *Cymbidium fynlaisonianum,* **e** *Acriopsis* sp.; epiphytic ferns—**b** *Drynaria sparsisora*, **c** *Platycerium grande,* **d** *Pyrrosia adnascens*

content were determined using an element analyzer (Euro EA3028-HT Analyzer) and pH in water and in salt (soil-dissolvent ratios 1:2.5 in case of mineral horizons and 1:25 in case of organo-mineral horizons) suspensions using a pH-meter (pH-150 M). Basal soil respiration was determined by titration of remnants of sodium hydroxide in laboratory closed chamber under humidity of soil in chamber about 60% of water holding capacity.

Humic acids (HAs) were extracted from each sample according to a published IHSS protocol (http://humic-substances.org/isolation-of-ihss-samples/) (Swift 1996). Briefly, the soil samples were treated with 0.1 M NaOH (soil/solution mass ratio of 1:10) under nitrogen gas. After 24 h of shaking, the alkaline supernatant was separated from the soil residue by centrifugation at 1516 × g for 20 min and then acidified to pH 1 with 6 M HCl to precipitate the HAs. The supernatant, which contained fulvic acids, was separated from the precipitate by centrifugation at 1516 × g for 15 min. The HAs were then dissolved in 0.1 M NaOH and shaken for four

hours under nitrogen gas before the suspended solids were removed by centrifugation. The resulting supernatant was acidified again with 6 M HCl to pH 1 and the HAs were again isolated by centrifugation and demineralized by shaking overnight in 0.1 M HCl/0.3 M HF (soil/solution ratio of 1:1). Next, the samples were repeatedly washed with deionized water until pH 3 was reached and then finally freeze-dried. HA extraction yields were calculated as the percentage of carbon recovered from the original soil sample (Vasilevich et al. 2018). Data were corrected for water and ash content. Oxygen content was calculated by difference of whole samples mass and gravimetric concentration of C, N, H and ash.

Solid-state ^{13}C-NMR spectra of HAs were measured with a Bruker Avance 500 NMR spectrometer in a 3,2-mm ZrO2 rotor. The magic angle spinning speed was 20 kHz in all cases and the nutation frequency for cross polarization was u1/2p 1/4 62.5 kHz. Repetition delay and number of scans were 3 s.

In this study we collected 13-C NMR spectra not only for humic substances, but also for a bulk soil samples. This allowed us to reveal the differences in alteration degree between bulk initial soil organic matter and its organic matter of the suspended soils which faced to intensive stabilization/humification processes.

23.3 Results

Suspended soils belong to the category of organic soils or soil-like formations, although they are taken into account in any classification of soils in Russia soil taxonomy and the World Reference Base of Soil Resources (2014). Suspended soils investigated are presented buy organic accumulations, located in air baskets, formed by plants roots. The degree of transformation of organic matter on the basic of morphological identification is medium, but nevertheless some spots of soil organic remnants become deeply decayed and humified, which result in formation of gray-brownish organic matter with high gravimetric water content, The closest analog of this soil on Russian soil taxonomy are the soils from the order, belonging to the trunk of organogenic soils. The main feature of normal terrestrial organogenic soils is a «histic structure» of the horizons. IS soils investigated we can find thus Histic fragments, thus they could be classified as suspended Histosols or suspended peat-like formations.

Suspended soils should be attributed to slightly acidic (in terms of pH in water), which is characteristic of organic substrates in which the transformation of organic matter takes place. The fact that the transformation of organic matter takes place also shows a much lower pH of the salt suspension. The presence of additional absorbed acid ions is associated with the carboxyl groups of the forming organic matter of the soil. Usually, suspended soils (1, 2 samples) are more acidic than soils under the forophyte (3 sample).

The carbon content in suspended soils is much higher than in soils under the forophyte, and this probably affects their acidity. The soils under the phorophyte contain less carbon from organic compounds, as well as nitrogen. A lower content of

Table 23.2 Base characteristics of suspended and associated ground soils

Species of epiphyte from which suspended soil is collected	pH in water	pH in salt (KCl)	Skeleton,%	Basal respiration, ($mgCO_2$/100 g/day)	Specific respiration (mgC–CO_2/g Csoil per day)	C, %	N, %	C/N
Acriopsis sp.	5.5 ± 0.4	3.8 ± 0.3	0	2162.3 ± 142.2	12.9 ± 0.6	45.5 ± 0.9	0.9 ± 0.01	47.5 ± 1.6
Cymbidium fynlaisonianum	5.0	3.8	0	1860.6	12.4	41.1	1.4	27.7
Drynaria sparsisora	5.7 ± 0.4	4.1 ± 0.8	6.7 ± 8.6	1719.9 ± 632.5	6.5 ± 3.6	44.5 ± 2.5	1.3 ± 0.3	33.4 ± 7.9
Platycerium grande	5.6	4.3	0	2112	12.5	46.2	1.1	38.8
Pyrrosia adnascens	5.8 ± 0.5	3.9 ± 0.8	5.5 ± 11	1257.1 ± 561.5	33.7 ± 48.8	33.6 ± 21.6	1.1 ± 0.6	23.9 ± 11
Pyrrosia longifolia	5.3 ± 0.8	3.7 ± 1.1	3.3 ± 2.3	339.4 ± 17.8	12 ± 12.7	18.2 ± 19.7	0.5 ± 0.5	25.6 ± 11.2
Ground soils	6.3 ± 0.1	5.1 ± 0.3	0.1 ± 0.1	440 ± 165.1	52.5 ± 34.7	3.7 ± 2.5	0.2 ± 0.1	14.9 ± 6.3

Table 23.3 The groups distribution of structural carbon compounds in the composition of the soil organic matter (SOM) and humic acids (HA), %

Groups of structural carbon compounds	Chemical shifts values, ppm	The number of the soil sample					
		1		2		3	
		SOM	HA	SOM	HA	SOM	HA
Carbonyl/carboxyl/amide	220–160	11.71	15.45	12.16	14.36	12.66	14.06
Aryl-olefine	160–110	24.19	26.78	22.01	24.31	18.89	25.55
O-N alkyl	110–45	49.45	35.17	51.06	38.06	42.61	38.36
Calkyl	45–0	14.64	22.61	14.76	23.28	25.81	22.02
Calkyl/O-N alkyl		0.296	0.643	0.289	0.612	0.606	0.574
Caryl/Calkyl		1.652	1.185	1.491	1.044	0.732	1.161

organic matter in these soils was also detected by the mesomorphological method. Our study showed that in the soil under the forophyte coarse-humus material is poorly associated with the mineral part of the soil, it is not so much, and it is in the initial stages of transformation. According to mesomorphological studies in suspended soils, organic matter is more decomposed, and the mineral part in it is contained as an impurity. However, some suspended soils do not contain any impurities of dust or sand at all, while others have up to 18–22% of the mineral skeletal part (Table 23.1). The C/N ratio in the studied objects is different. So, in suspended soils, it is usually more than 30, while in soils under forophytes it averages 11–17. This is probably due to the presence of mineral forms of nitrogen in the soils under the phorophytes, while in suspended soils nitrogen is represented mainly by organic forms, and the high carbon to nitrogen ratio is provided by an elevated carbon content, which is explained by the nature of the formations themselves. Thus, it can be concluded that not only the morphological organization is different, but also the parameters of the chemical composition of the suspended soils and the soils under the phorophytes. The basal respiration of soil bodies differed both in absolute (mg of CO_2 per 100 soils) and in specific (mg—CO_2/g C of soil per day) values (Table 23.2).

The existence of biogenic-abiogenic systems (epiphyte-invertebrates-suspended soil) provides the organic matter transformation. By the 13C mass spectrometry, it is possible to determine the structural composition of organic substances (Table 23.3), which is an indicator of humification processes (Abakumov et al. 2018). In general, suspended soils are characterized by a low content of aromatic compounds (Fig. 23.3).

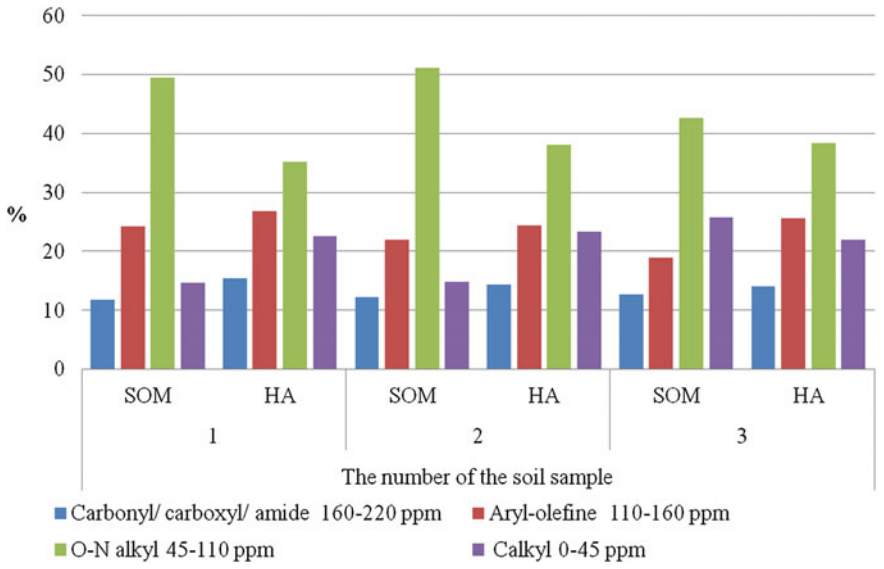


Fig. 23.3 The groups distribution of structural carbon compounds in the composition of the soil organic matter (SOM) and humic acids (HA), % in suspended soils (1, 2 samples) and soils under the forophyte (3 sample)

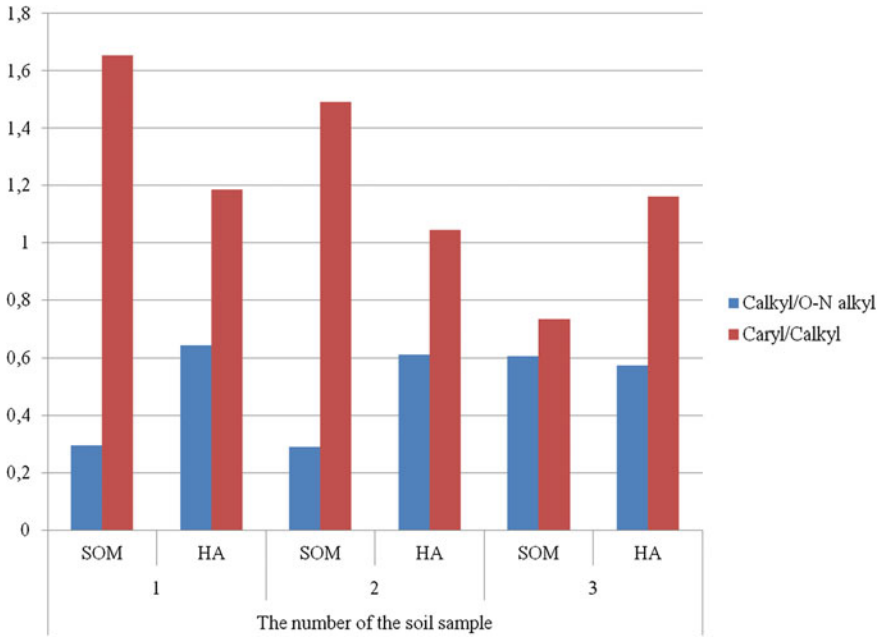


Fig. 23.4 The ratio of the structural carbon compounds in the composition of the soil organic matter (SOM) and humic acids (HA),% in suspended soils (1, 2 samples) and soils under the forophyte (3 sample)

Increasing the values of the different alkyl groups ratio (C alkyl/O-N alkyl) from 0.3 (in SOM) to 0.6 (in HA) suggests a higher degree of decomposition of the substance in the organic matter stabilization process (Baldock et al. 1997). At the same time, the opposite situation is observed in sample 3—the value of the C alkyl/O-N alkyl ratio is higher in SOM, although not significantly (Fig. 23.4). Perhaps this is due to the fact that the first two points of the research are quite closed systems (epiphyte-suspended soil), in contrast to 3 point (the soil under the forophyte). The sandy soil under the forophyte has a stronger washing mode and is better aerated, which affects the soil-forming processes, reducing the part of plant residues decomposition in these specific conditions.

The relationship between aromatic C and aliphatic C (C aryl/C alkyl) provides additional information on soil components (Mueller and Kögel-Knabner 2009). Indeed, the lower aliphatic structures decomposability dominated in sample 3 (soil organic matter), which was shown by low ratios of aromatic and aliphatic carbon. This indicates that the organic matter stabilization processes under the forphyte proceed with less intensity and in a different way, in contrast to the sites of suspended soils.

23.4 Discussion

Abovementioned data give an idea that the formation of suspended soils is an integral part of the survival strategy of a number of epiphytes. Suspended soils contribute to the mineral nutrition of epiphytes, concentrating significant portions of organic matter in crowns and giving shelter to numerous invertebrate consorts (Lindo and Winchester 2006, 2007; Rodgers and Kitching 1998; Karasawa and Hijii 2010). However, a comparison of the isotopic compositions of nitrogen and carbon of suspended soils and possible sources of their origin suggests that under the conditions of oligotrophic communities, they most likely have a zoogenic origin and are formed due to the cohabitation of epiphytes with ants (Eskov et al. 2017). The mechanisms of accumulation of organic matter in different ecobiomorphological groups are differ (Eskov et al. 2017). The study of organic matter stabilization processes in suspended soils was carried out for the first time. Samples investigated included soil from under the forophytes (mineral soil represented by samples of topsoil from the typical dry savanna landscape) and soil from savanna epiphytic formations in sparse communities that are located on the oligotrophic plains on Phu Quoc Island (South Vietnam). Our results show that the pH of the soil under the forophytes is higher than in suspended soils and that it depends on a larger amount of undecomposed organic matter compared to the mineral part in suspended soils, which causes a stronger acid reaction. This is due to the slow transformation of organic acids into humic substances. A greater amount of undecomposed organic matter compared to the mineral part in suspended soils causes a stronger acid reaction. In addition, suspended soils are less enriched with nitrogen than soils under forophytes. Basal respiration, which indicates the level of the microbial biomass activity, does not tend to change in the soils under the forophytes compared with suspended soils.

The soil under the forophytes is characterized by a greater portion of aromatic fraction and a smaller proportion of aliphatic groups. This can be explained by a higher degree of organic matter transformation in more aerated soil environments under phorophytes, where organic residues are surrounded by minerals, or are processed by termites. The content of aromatic compounds is higher than in tundra or taiga soils, but lower than in mollisols. The soils that we explored were an intermediate option between soils with a large amount and soils with a small amount of moisture. The most comparable soil type in terms of the composition of humic substances is Cambisols from humid forests of the subboreal and subtropical zones. The results of our study show that the formation of deeply moistened organic matter with a significant content of the aromatic fraction can be carried out in the process of organic matter transformation on suspended soils with a clear absence of mineral compounds or a mineral fine-grained medium in conditions of pure organic substrates. From a botanical point of view, it is worth paying attention to the fact that a look at suspended soils as soils allows us to speak of epiphytes as edificatories of their habitat In the lower tier of the tropical forest, all coarse organic matter (for example, litter or wood) is destroyed by termites and nothing like peat, leaf litter, etc., accumulates, and suspended soils remain inviolable throughout the life of the

tree (Lindo and Winchester 2006, 2007; Nadkarni 1986). Is this a delicate balance in the wetting/drying mode or a specific microflora, or, finally, ants-antagonists of termites? In fact, we have—on the ground in tropical forest, organic matter always decays rather quickly, in crowns it can accumulate and persist for tens and hundreds of years (however, having fallen to the ground, suspended soils are also rather quickly utilized (Nadkarni 1986).

The main feature of soil is a presence of stabilized/humified organic matter (Kholodov et al. 2011; Lodygin et al. 2007). Our results indicated that humification as a specific way of soil organic matter stabilization occurs even in suspended air located environments of forest ecosystems (Abakumov et al. 2018) and our data are comparable to previously obtained (Abakumov et al. 2018; Eskov et al. 2017). These environments could be considered as extreme type of environments. Thus, for the extreme environments of the Antarctic was established the possibly of humification (Mergelov et al. 2018; Abakumov and Alekseev 2018). This is a reason why humification is possible in less severe conditions of the tropical environments. An accumulation of aromatic fraction could be considered as index of organic matter stabilization. In this context, increasing of aromatic carbon content in humic acids in comparison with the bulk organic matter is an evident fact.

23.5 Conclusions

Stabilization and humification are universal processes of the transformation of organic substances and the polymerization of oligomeric and monomeric molecules into supramolecules of high-molecular substances of dark color. This process is considered as a global process, carried out not only in soils and organic sediments, but also in natural waters and even in the air (Morley et al 2005; Wang 2005). Wherein study of the humification phenomena in the suspended soils of tropical forests can be discussed as undervalued in this section of science.

According to the thermodynamic concept of humification (Schnitzer 1982), thermodynamic selection of humic substances based on the selection of stable aromatic rings conjugated with carboxyls, and the aliphatic periphery decreases slightly due to mineralization. The results we obtained are consistent with this concept: the proportion of aliphatic compounds in the composition of the structural of the gross organic matter is higher than in humic acids. Thus, it can be concluded that in suspended soils humification processes is occur.

Summing data, the suspended soils have a special way of soil formation. They are a variant of the primary soils, including the mineral part, the roots of epiphytes and litter, and perform their ecological functions in the formed communities. Being in an intermediate position between the litter stuck in the crown (long-lasting organic matter) and the soil surface under the forophytes (rapidly recyclable organic matter), suspended soils provide for the transformation of organic matter and support the circulation of substances.

Acknowledgements The research was supported by the State Assignment of the Tzitzin Main Botanical Garden of Russian Academy of Sciences № 118021490111-5 at the Unique Scientific Installation Fund Greenhouse. The work of A. K. Eskov and E. V. Abakumov was supported by the Russian Foundation for Basic Research (projects 18-04-00677), the work of N. G. Prilepsky was supported by the governmental contract of the Lomonosov Moscow State University № AAAA-A16-116021660037-7. We are grateful to Joint Russian-Vietnamese Tropical Scientific and Technological Center in the name of its general co directors Dr. Habil. Andrey N. Kuznetsov and Dr. Nguyen Hong Du for organization and performance of field works.

References

Abakumov EV, Rodina OA, Eskov AK (2018) Humification and humic acid composition of suspended soil in oligotrophous environments in South Vietnam. Appl Environ Soil Sci 1:1026237

Abakumov E, Alekseev I (2018) Stability of soil organic matter in Cryosols of the maritime Antarctic: Insights from 13C NMR and electron spin resonance spectroscopy. Solid Earth 9(6):1329–1339

Baldock JA, Oades JM, Nelson PN (1997) Assessing the extent of decomposition of natural organic materials using solid-state 13C NMR spectroscopy. Soil Res 35:1061–1084

Benzing DH (1990) Vascular epiphytes: general biology and related biota. Cambridge University Press, Cambridge

Benzing DH (1996) Aerial roots and their environments. In: Waisel Y, Eshel A, Kafkafi U (eds) Plant roots: the hidden half. Marcel Dekker, New York

Bohlman SA, Matelson TJ, Nadkarni NM (1995) Moisture and temperature patterns of canopy humus and forest floor soil of a Montane Cloud Forest, Costa Rica. Biotropica 27(1):13–19

Bone RE, Smith JA, Arrigo N, Buerki S (2015) A macro-ecological perspective on crassulacean acid metabolism (CAM) photosynthesis evolution in Afro-Madagascan drylands: Eulophiinae orchids as a case study. New Phytol 208:469–481

Chertov OG (1983) Mathematical model of a single plant ecosystem. J Gen Biol 44(3):406–414 (in Russian)

Darocha WD, Ribeiro SP, Neves FS, Fernandes GW, Leponce M, Delabie JHC (2015) How does bromeliad distribution structure the arboreal ant assemblage (Hymenoptera: Formicidae) on a single tree in a Brazilian Atlantic forest agroecosystem? Myrmecological News 21:83–92

Diels J, Vanlauwe B, van der Meersch MK (2004) Long-term soil organic carbon dynamics in a subhumid tropical climate: 13C data in mixed C3/C4 cropping and modeling with ROTHC. Soil Biol Biochem 36:1739–1750

Eskov AK (2012) Ecophysiological classification of vascular epiphytes as a theoretical prerequisite for the formation of collections and communities of epiphytic plants in a greenhouse culture. Nat Technol Sci 4:93–98 (in Russian)

Eskov AK (2013) Epiphytic communities of tree formations of South Vietnam: analysis of the species composition and structure of sinusias depending on the degree of anthropogenic influence. J Gen Biol 74(5):386–398 (in Russian)

Eskov AK, Dubovikov DA (2015) Community of myrmecophilic epiphytes of the Kerangas Formation of the Borneo Island. Byull Mosk O-va Ispyt Prirod Otd Biol 120(4):60–69 (in Russian)

Eskov AK, Abakumov EV, Tiunov AV, Kuznetsova OA, Dubovikov DA, Prilepskij NG, Antipina VA, Kuznetsov AN (2017) Ageotropic aerial root-traps of nest epiphytes and their role in suspended soils forming. J Gen Biol 78(3):54–68 (in Russian)

Karasawa S, Hijii N (2010) Oribatid communities (Acari: Oribatida) associated with bird's nest ferns (*Asplenium nidus* complex) in a subtropical Japanese forest–a mini-review. Trends in Acarology. Springer, Dordrecht, pp 149–153

Kholodov VA, Konstantinov AI, Kudryavtsev AV, Perminova IV (2011) The structure of humic acids of zonal soils according to C-13 NMR spectroscopy data. Pochvovedenie 9:1064–1073 (in Russian)

Lindo Z, Winchester NN (2006) A comparison of microarthropod assemblages with emphasis on oribatid mites in canopy suspended soils and forest Goors associated with ancient western redcedar trees. Pedobiologia 50(1):31–41

Lindo Z, Winchester NN (2007) Oribatid mite communities and foliar litter decomposition in canopy suspended soils and forest floor habitats of western redcedar forests, Vancouver Island, Canada. Soil Biol Biochem 39:2957–2966

Lodygin ED, Beznosikov VA, Chukov SN (2007) Paramagnetic properties of humus acids of podzolic and bog-podzolic soils. Eurasian Soil Sci 40(7):726–728

Martin A, Mariotti A, Balesdent J (1990) Estimate of organic matter turnover rate in a savanna soil by 13C natural abundance measurements. Soil Biol Biochem 22:517–523

Martin A, Balesdent J, Mariotti A (1992) Earthworm diet related to soil organic matter dynamics through 13C measurements. Oecologia 91:23–29

Mergelov N, Mueller CW, Prater I, Shorkunov I, Dolgikh A, Zazovskaya E, Shishkov V, Krupskaya V, Abrosimov K, Cherkinsky A, Goryachkin S (2018) Alteration of rocks by endolithic organisms is one of the pathways for the beginning of soils on Earth. Sci Rep 8(1):3367

Ministry of Construction of Vietnam: Vietnam Building Code 2009 (2009) QCVN Natural Physical & Climatic Data for Construction 02:2009/BXD, Hanoi

Morley CP, Mainwaring KA, Doerr SH, Douglas P, Llewellyn CT, Dekker LW (2005) Organic compounds at different depths in a sandy soil and their role in water repellency. Aust J Soil Res 43:239–249

Mueller WC, Kögel-Knabner I (2009) Soil organic carbon stocks, distribution, and composition affected by historic land use changes on adjacent sites. Biol Fertil Soils 45:347–359

Nadkarni NM (1986) The nutritional effects of epiphytes on host trees with special reference to alteration of precipitation chemistry. Selbyana 9:44–51

Panfilov DV (1961) Insects in tropical forests of southern China. Moscow State University Publishing House, Moscow (in Russian)

Pinkalski C, Damgaard C, Jensen KV, Peng R, Offenberg J (2015) Quantification of ant manure deposition in a tropical agroecosystem: implications for host plant nitrogen acquisition. Ecosystems 18:1373–1382

Pocs T (1976) The role of the epiphytic vegetation in the water balance and humus production of the rain forests of the Uluguru Mountains, East Africa. Boissiera 24:499–505

Qiu S, Sultana S, Liu ZD, Yin LY, Wang CY (2015) Identification of obligate C3 photosynthesis in *Dendrobium*. Photosynthetica 53(2):168–176

Rodgers DJ, Kitching RL (1998) Vertical stratification of rainforest collembolan (Collembola: Insecta) assemblages: description of ecological patterns and hypotheses concerning their generation. Ecography 21(4):392–400

Schnitzer M (1982) Organic matter characterization. In: Page B, Miller R, Keeney D (eds) Methods of soil analysis. Soil Science Society of America, Madison

Sergeeva TK, Kholopova LB, Tien Nguyen Three, Nguyen Shung Tu (1989) Animal population and properties of "suspended soils" of tropical epiphyte *Asplenium nidus* L. Ecology 5:29–40 (in Russian)

Sergeeva TK, Kompantsev AV, Kompantseva TV, Vtorova VN (1997) Diversity of biota of "suspended" soils in the tropical forests of Vietnam (using the *Asplenium nidus* L. fern as an example). Troptsentr-98, Book 1. Biological diversity and the current state of the tropical ecosystems of Vietnam. Moscow, Hanoi (in Russian)

Shaw P (2013) The use of inert pads to study Collembola of suspended soils. Soil Org 85(1):69–74

Shaw P (2015) How high do Collembola climb? Studies of vertical migration in arboreal Collembola. Soil Org 87(3):229–235

Swift RS (1996) Organic matter characterization. In: Sparks DL et al (eds) Methods of soil analysis. Part 3. Chemical methods. Soil Science Society of America Book Series 5. Soil Science Society of America, Madison, WI

Thanh TD (2012) Biển đảo Việt Nam - Tài nguyên vị th´ê và nh˜ưng kỳ quan địa ch´ât, sinh thái tiêu biểu (Vietnamese sea and islands—position resources, and typical geological and ecological wonders). Natural Science and Technology. Hanoi (in Vietnamese)

Tolchelnikov YS (1985) On the essence of the concept of "soil" MSU Vestnik Series 17. Soil Sci (3):52–58 (in Russian)

Treseder KK, Davidson DW, Ehleringer JR (1995) Absorption of ant-provided carbon dioxide and nitrogen by a tropical epiphyte. Nature 375:137–139

Vanderklift MA, Ponsard S (2003) Sources of variation in consumer-diet $\delta^{15}N$ enrichment: a meta-analysis. Oecologia 136:169–182

Vasilevich R, Lodygin E, Beznosikov V, Abakumov E (2018) Molecular composition of raw peat and humic substances from permafrost peat soils of European Northeast Russia as climate change markers. Sci Total Environ 615:1229–1238

Walter G (1968) Earth's vegetation: ecological and physiological characteristics. T. 1. Tropical and subtropical zones: (Trans. from the German Rethyum YY and Spichkin IM (eds)). Whippers PB Progress, Moscow (in Russian)

Wang KJ (2005) Characterization of humic substances and non-ideal phenanthrene sorption as affected by clay-humic interactions. Ph.D. dissertation, University of Massachusetts

Werckmeister P (1971) Light induction of geotropism, and the control of proliferation and growth of Cymbidium in tissue culture. Bot Gaz 132(4):346–350

World Reference Base for Soil Resources (2014) International soil classification system for naming soils and creating legends for soil maps update 2015. http://www.fao.org/3/i3794en/I3794en.pdf. Access date 20 Mar 2019

Zitte P, Weiler EV, Kaderayt VV, Brezinski A, Körner K (2008) Botany. T. 2. Plant physiology. In: Chuba VV (ed) Academy, Moscow (in Russian)

Zonn SV, Lee C-K (1958) Some questions on the genesis and classification of China's tropical soils. Soil Sci 6:58–69 (in Russian)

Chapter 24
Soils of Technogenic Landscapes from Tungsten Mine: Micromorphological Structure, Mineral and Chemical Compositions

Svetlana G. Doroshkevich, Olga K. Smirnova and Anastasiya A. Sheshukova

Abstract The main idea of the presented data was to reveal the micromorphological structure, mineral and chemical compositions of the unique soils, which have been covered with waste mining and processing production of sulfide-tungsten deposits of Transbaikalia for a long time. In comparison with natural alluvial swamp soils, these buried soils are characterized by the increase in content of (i) ferrous neoplasma and (ii) weathered grains of mica and feldspar, and (iii) the density of microaggregates along with the proportions of potentially dangerous chemical elements represented by heavy metals. The technogenic nature of pollution in these soils is confirmed by the accumulation of the following potentially hazardous chemical elements—Cd, Zn, F, Mo, Cu, Ni, As, Co, Pb namely in the upper organogenic horizons. It was revealed that the intensity of soil contamination is affected by the duration of storage of ore dressing waste, composition and level content of toxic elements in it.

Keywords Tungsten deposits · Tailings dump · Contaminated soils · Micromorphological structure · Mineral composition

24.1 Introduction

In the areas affected by the presence of mineral deposits, the processes of mining technogenesis are activated. The latter is accompanied by the formation of technogenic dispersion halos of chemical elements and changes in the migration cycles of chemical elements in geosystems. The present study is aimed to reveal the migration of metals and other toxic components in the mining and processing industry was started in the late seventies of the twentieth century. A strong level of environmental pollution in the sulphide waste storage areas was first shown (Borman and Watson 1976; Blair et al. 1980; Salomons 1995). Later, detailed studies of the transforma-

S. G. Doroshkevich (✉) · O. K. Smirnova
Geological Institute of SB RAS, 6a, Sakhyanova Street, Ulan-Ude 670047, Russia
e-mail: dorosh@ginst.ru

A. A. Sheshukova
Saint Petersburg State University, Saint Petersburg, Russia

© Springer Nature Switzerland AG 2020

O. V. Frank-Kamenetskaya et al. (eds.), *Processes and Phenomena on the Boundary Between Biogenic and Abiogenic Nature*, Lecture Notes in Earth System Sciences,
https://doi.org/10.1007/978-3-030-21614-6_24

tion of technogenic waste under oxidative conditions were taken place (Dubrovsky et al. 1984; Makarov 2006; Rikhvanov et al. 2017). Quantitative evaluation of metal migration inside and outside technogenic bodies was carried out to understand the mechanisms of interaction in the system "solid waste-pore solutions" (Bortnikova 2001), "solid waste-gas flows" (Bortnikova et al. 2018). The influence of the mineral composition of tailings on the geochemical distribution of elements within there has been shown (Walder and Chavez 1995; Sidenko et al. 2005). The role of sulfur-oxidizing bacteria in oxidizing processes occurring at tailings facilities was revealed (Blowes and Lortie 1995). The changes in the geochemical environment and the priority of chemical elements at mining facilities have been studied using a physical and chemical modeling (Davis and Ritchie 1986a, b; Smith 2007; Zvereva and Pyatakov 2017). Tailings dumps are the main sources of crisis situations in mining areas. The environmental situation in the development of deposits is estimated as critical (Leontyev and Dyubanov 2011; Krupskaya et al. 2013; Urosevic et al. 2018). Geochemical anomalies with excessive content of chemical elements in the surface layer of man-made soils in the zone of influence tailings are formed. For example, the total index of chemical pollution of soils near tailings of tin mines was 111–390 (Khanchuk et al. 2012), tungsten molybdenum ores—72–195 (Smirnova and Plyusnin 2013), copper and copper-zinc ores—122–288 (Opekunova et al. 2017). The formation of the dispersion trains of chemical elements due to geochemical processes (Emlyn 2001), local landscape and climatic conditions have shown (Belan 2007; Loupasakis and Konstantopoulou 2009). It was revealed that the main role in these processes belongs to the mineral composition of waste as well as acid-base and redox environmental conditions (Bachurin and Baboshko 2008; Wuana1 and Okieimen 2011).

Soil due to its role as a component of the landscape is affected by the processes occurring in the biogeosystem. The direction and intensity of these processes are related with the chemical composition of the soils. Physical (density, porosity, structure) and chemical (absorptivity, acidity or alkalinity, salt content) properties of the soils depend on their mineral composition.

Micromorphological study of soil structure in combination with other methods (chemical, mineralogical, spectral, X-ray analysis, etc.) allows identifying (i) intra-profile migration of chemical elements as well as (ii) the forms, in which they are present in soil environment (Monger 2013). Currently, the macro- and micromorphological structure of young soils formed on man-made dumps of coal deposits, quarries for the extraction of clay and limestone have been studied in Russia: in North-Western region (Abakumov et al. 2011) and Central region (Solntseva et al. 1990), Siberia (Shugalei and Chuprova 2012; Sokolov et al. 2015), Far East region (Komachkova 2011; Kostenkov et al. 2013). The aim of present research was to study the micromorphological structure, mineral and chemical composition of soils from technogenic landscapes of tungsten-molybdenum Deposit.

24.2 Materials and Methods

Object of the research is the alluvial swamp soils covered for a long time by tailings after dressing of sulfide-bearing ore: the areas of the former bulk and hydraulic tailings dump (Fig. 24.1). The alluvial swamp soils of the floodplain of the Barun-Naryn brook are the object of comparison. The soils are located upstream of the brook, 1000 m from the former hydraulic tailings. Waste accumulation on the bulk tailings storage lasted 33 years. The thickness of stale tailings after dressing of sulfide-tungsten ores was 15 m. The filling of the hydraulic pond tailings was during 38 years. For a long time after the filling of the tailings was stopped the mass of waste mining production was still in these areas: on the territory of the former bulk tailings dump 42 years, on the territory of the former hydraulic tailings dump 22 years.

The stale of bulk and the hydraulic wastes of tailings dam have strongly acidic reaction medium and various granulometric composition: from glay, silty to fine-grained and coarse-grained. According to Khodanovich (1999) the main minerals of the wastes of tailings dam are quartz and feldspar. Among the ore minerals, pyrite predominates (average of 0.3%), single grains hubnerite, chalcopyrite, galena, sphalerite, molybdenite, scheelite and fahlore are present. Among the non-metallic minerals fluorite and beryl are present.

To study the structure and composition of the soils in the studied area they were divided into three sections. The sections are located (i) in the natural site of the floodplain of the Barun-Naryn brook (1 in Fig. 24.1); (ii) in central part of former bulk tailings dump after recultivation (removal of the tailings, surface leveling, application

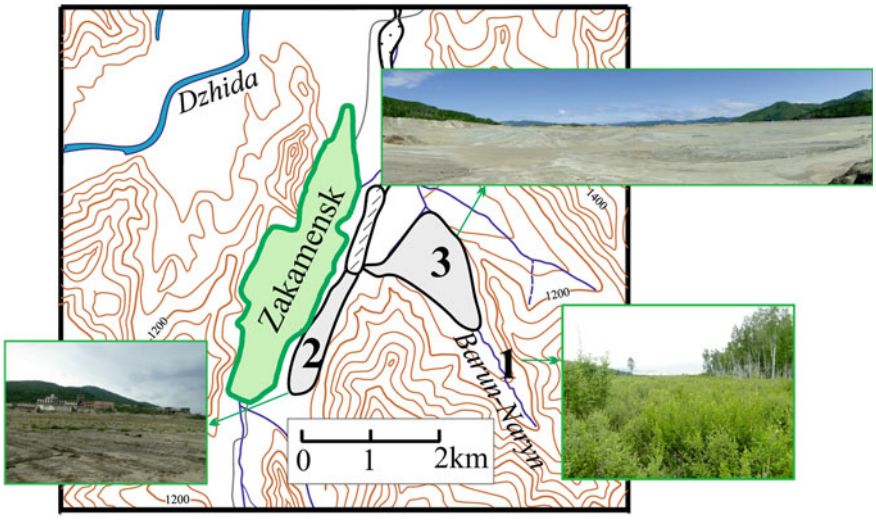


Fig. 24.1 Scheme of location of studied objects: 1—the natural site of the floodplain of the Barun-Naryn brook; 2—the former bulk tailings dump; 3—the former hydraulic tailings dump

of fertile soil) (2 in Fig. 24.1); and (iii) on the territory of the former hydraulic tailings dump in the back part where the wastes has a small thickness (3 in Fig. 24.1). According to Russian soil classification system (2004) the soils are classified as alluvial swamp (peat-gley) soils with the following sequence of horizons O (P – X, X) – T (T/H) – AY/G (RYG) – CR/G (G, CRM) – Cg, which are Cley-Histic Fluvisols according to World Reference Base for Soil Resources (2014). Macromorphological characteristics of the studied soils are presented in Fig. 24.2 and Table 24.1.

Alluvial swamp soils of the natural site are characterized by the presence in the upper part of the soil profile of a brown-brown peat horizon of low power (up to 15 cm) with an organic matter content of 52–55%, the average degree of decomposition. Lower mineral horizons are gleyzation. Soils of the natural site are characterized by the presence of permafrost. In late July-early August, the soil thaws to a depth of 40–50 cm. The soil reaction is strongly acidic in the upper part of the profile and acidic in the lower part.

Alluvial swamp soils of the former bulk and hydraulic tailings dump, as opposed to alluvial swamp soils of the natural site, are characterized by a lower thickness of the peat horizon. Beside the way, the peat horizon of these soils is dense and silted. Peat has a high degree of decomposition. The content of organic matter is 47–52%, the soils reaction is strongly acidic throughout the soil profile.

The micromorphological structure and mineral composition of transparent thin sections with using petrographic microscopes "POLAM R-113", "POLAM L-213" ("LOMO", Russia), "OLYMPUS BX 51" ("Olympus Co", Japan) were described. Transparent sections were made of undisturbed and oriented soil samples selected on the full capacity of the soil profile. Samples were collected from the soil pit in containers with a size of 3.5 cm × 5.0 cm × 1.0 cm. A mixture of rosin and xylene (10:1) was used to cement the samples. The dried marked soil samples in containers

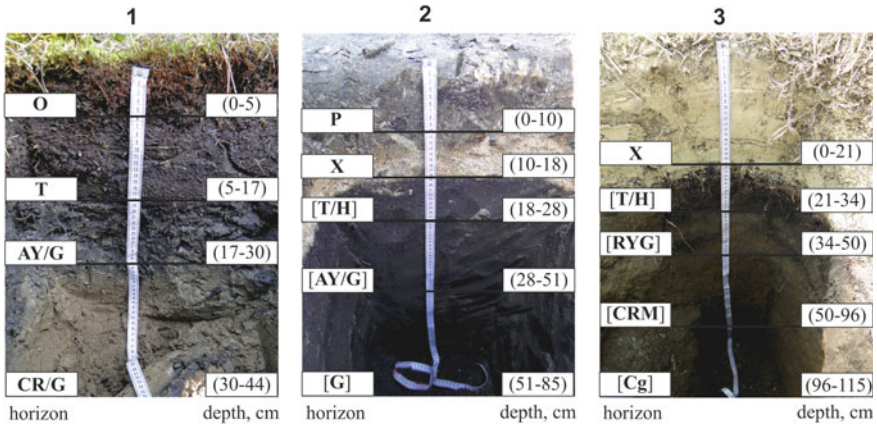


Fig. 24.2 Alluvial swamp soil profiles: 1–3—numbers of the studied areas (see Fig. 24.1); here and hereinafter, horizons indices are given according to the Russian soil Classification (Classification and Diagnostics of Soils of Russia 2004)

Table 24.1 Morphological description of alluvial swamp soils

Site	Index of horizon/depth, cm	Name of horizon	Morphological description
The natural site of the floodplain of the Barun-Naryn brook	O (0–5)	Moss	–
	T (5–17)	Peat	Brown- fulvous, mid-decayed, compacted, humid, there are slightly decomposed plant residues, the transition to the underlying horizon is clear
	AY/G (17–30)	Gray humus/glee	Gray-blue-gray, clay loam, lumpy-cloddy, wet, iron-manganic leather coats, a large number of blocks and rubble, the transition to the underlying horizon is clear in color
	CR/G (30–44)	Cryoturbated/glee	Light brown-blue-gray, clay loam, iron-manganic leather coats, viscous, wet. Below 44 cm—frozen ground
The former bulk tailings dump	P (0–10)	Imported humus	Light gray with a brownish tinge, sandy loam, fine lumpy, compacted, fresh, iron-manganic leather coats, roots of plants, the transition to the underlying horizon is clear in color and grain size distribution
	X (10–18)	Stale tailings	Yellowish-brown-blue-gray, layering: interbeds of fine-grained sand and silt clay, squamose-schistose-lumpy structure, moist, compacted, iron-manganic leather coats, roots of herbaceous plants, the transition to the underlying horizon is clear in color and grain size distribution

(continued)

Table 24.1 (continued)

Site	Index of horizon/depth, cm	Name of horizon	Morphological description
	[T/H] (18–28)	Buried peat/humus	Black, heavily silted, well-decomposed, lard peat, moist, firm consistence, woody plant residues, roots of plants, the transition to the underlying horizon is clear in color
	[AY/G] (28–51)	Buried gray humus/glee	Gray with a bluish tinge, sandy loam, lumpy-nutty, firm consistence, iron-manganic leather coats, the transition to the underlying horizon is gradual in color and clear in grain size distribution
	[G] (51–85)	Buried glee	Brown-blue-gray, loam, nutty-prismatic, firm consistence, moist, iron-manganic leather coats, gley cutan on ped face
The former hydraulic tailings dump	X (0–21)	Stale tailings	Yellowish-brown-blue-gray, layering: interbeds of fine-grained sand and silt clay, squamose-lumpy, moist, compacted, iron-manganic leather coats, roots of herbaceous plants, the transition to the underlying horizon is clear in color and in grain size distribution
	[T/H] (21–34)	Buried peat/humus	Black, strongly silted, well-decomposed, lard peat, moist, more compacted, with weakly and moderately decomposed plant residues, roots of plants, the transition to the underlying horizon is clear in color

(continued)

Table 24.1 (continued)

Site	Index of horizon/depth, cm	Name of horizon	Morphological description
	[RYG] (34–50)	Buried stratified gray humus	Light gray-brown with black spots and stripes, sandy loam, lumpy, firm consistence, iron-manganic leather coats, the transition to the underlying horizon is gradual
	[CRM] (50–96)	Buried cryometamorphic	Brown-blue-grey, sandy loam, lumpy, firm consistence, moist, iron-manganic leather coats, blue-gray patchs, the transition to the underlying horizon is gradual
	[Cg] (96–115)	Buried parent rock material	Brown-gray, sand dust, incompetent lumpy, compacted, moist, iron-manganic leather coats, liberally stone, gravel and pebblestone

were placed in a solution of this mixture heated to 100 °C and kept at a constant temperature for 8 h. For complete fixation of the sample four such impregnation were made. After drying the samples for 7–10 days, transparent sections with a thickness of 0.025–0.027 mm were made of them.

The soil samples to determine their chemical composition by genetic horizons were taken. The content of chemical elements was determined by chemical-spectral and x-ray fluorescence methods. These studies were carried out using instruments: spectrophotometer UNICO 1201 ("Unico Inc.", USA), atomic absorption spectrometer PinAAcle 900 F ("PerkinElmer Inc.", USA), diffraction spectrograph DFS-13 ("LOMO", Russia) with multichannel analyzer of emission spectra of MAES (WMC-Optoelectronics, Russia), polarization spectrometer EDPRS-1 (GIN SB RAS, Russia).

To assess the environmental risk of contamination of technogenic landscapes components, the composition of the studied soils was compared with the clarkes of chemical elements in the upper part of the continental crust, recommended for use by Kasimov and Vlasov (2015). Usage of clarke as a normative value makes it possible to identify and compare anomalies of chemical elements.

To estimate the intensity of accumulation of chemical elements in the soil, the geochemical index—the concentration coefficient (Kc) calculated by the formula was used (Saet et al. 1990):

$$Kc = C : Cf,$$

where

C The concentration of the element in the soil on the study area;
Cf The concentration of the element in the soil by local background values (Smirnova and Plyusnin 2013)

Elements with concentration coefficient exceeding 1.5 were included in the complex of technogenic anomaly.

24.3 Results

The micromorphological structure of the alluvial swamp soils is shown in Fig. 24.3. Diagnostic micromorphological features characterizing soil processes are shown in Table 24.2. All studied soils are characterized by signs of such processes as accumulation and conservation of plant sediments, cryoturbation of organic material, segregation and permafrost transformation of mineral mass. In alluvial swamp soils of the former bulk and hydraulic tailings dump signs of manifestation of anthropogenic processes were diagnosed. For example, in the thin sections of the transported soils

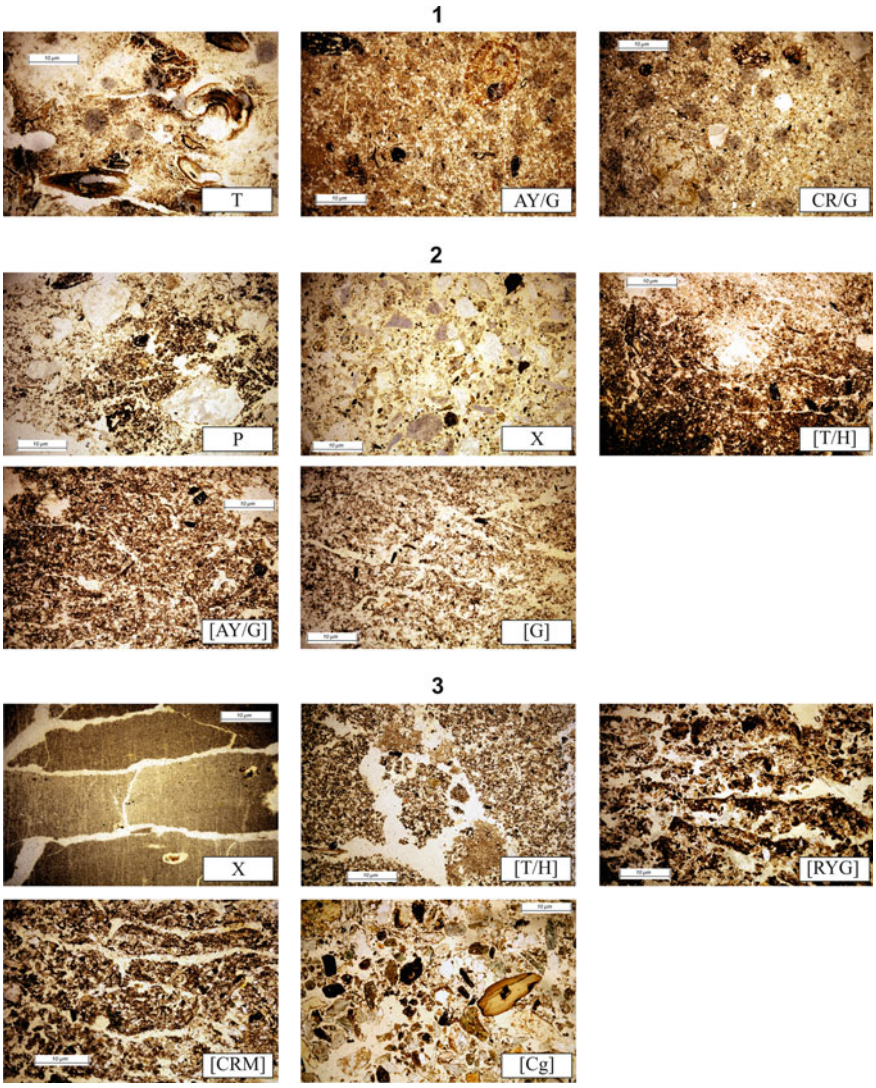


Fig. 24.3 Micromorphological structure of alluvial swamp soils (PPL): 1–3—numbers of the studied areas (see Fig. 24.1)

Table 24.2 Micromorphological diagnostics of elementary soil processes in the studied alluvial swamp soils

Process	The soil section on the natural site of the floodplain of the Barun-Naryn brook		The soil section on the site of the former bulk tailings dump		The soil section on the territory of the former hydraulic tailings dump	
	Horizon	Micromorphological features*	Horizon	Micromorphological features*	Horizon	Micromorphological features*
Accumulation and conservation of plants residues	T, [AY/G]	Fresh organic materials (minimal or no decomposition class)	[T/H], [AY/G]	Coaly particles of the plants residues	[T/H]	Fresh organic materials (minimal or no decomposition class)
	[AY/G]	Coaly particles of the plants residues				
Cryoturbation of organic material	AY/G	Microzones of organic matter in ground mass with low content of soil organic material	–	–	[RYG]	Microzones of organic matter in ground mass with low content of soil organic material
Segregation	T, AY/G, CR/G	Existence of microzones with Fe accumulation in horizon material, Fe- oxide coating mineral grains	P, X, [T/H], [AY/G], [G]	Existence of microzones with Fe accumulation in horizon material, Fe- oxide coating mineral grains	X, [T/H], [RYG], [CRM], [Cg]	Existence of microzones with Fe accumulation in horizon material, Fe-oxide coating mineral grains
Permofrost activity	AY/G, CR/G	Granular microstructure at the surface of a clayey mud boil (sorted circle)	[AY/G], [G]	Platy and lenticular microstructure	[RYG], [CRM]	Platy microstructure, granular microstructure

(continued)

Table 24.2 (continued)

Process	The soil section on the natural site of the floodplain of the Barun-Naryn brook		The soil section on the site of the former bulk tailings dump		The soil section on the territory of the former hydraulic tailings dump	
	Horizon	Micromorphological features*	Horizon	Micromorphological features*	Horizon	Micromorphological features*
Anthropogenic features	–	–	[T/H], [AY/G]	Angular and subangular blocky microstructure and dense groundmass	X	Angular and subangular blocky microstructure and dense groundmass
			P	Zonation: zones with Amorphous organic material alternate with zones of mineral material; coarse material is not sorted	X, [T/H]	Microzones of fine material between aggregates; existence of different colour microzones in horizon

Note Micromorphological features *were determined according to Gerasimova et al. (1992) and Stoops et al. (2010)

in the territory of the former bulk tailing dump, areas composed of mineral grains and areas of amorphous organic matter are noted. Sorting of skeletal material in these thin sections is absent. Organogenic horizons of buried soils in the territory of the former bulk tailings dump have dense consistency, angular and subangular blocky microstructure. In the buried organic soil horizon in the former hydraulic tailing dump observed microzones of fine material between aggregates. The heterogeneity of the color of this horizon is occurred.

The mineral composition of the studied alluvial swamp soils is presented in Table 24.3. The main rock-forming minerals of the skeletal part of the alluvial swamp soils are quartz and feldspar. Feldspar mostly presents by plagioclase, for the most part sericitized and pelitized. Also there are weathered grains of muscovite as well as biotite, besides amphibole, chlorite, epidote, ferrum oxide, zircon, rutile, pyroxene, sphen, magnesian lime, apatite, garnet, and ore minerals were found. Intense ferruginization or chloritization of individual grains of the minerals is identified, especially along the cracks of mineral particles. Chlorite develops on grains of amphibole, pyroxene, biotite, and epidote.

The alluvial swamp soils of the natural site are depleted by the contents of S, As, Cr, K and Na (Fig. 24.4). Ni, Zn, Co, Mn, Sr, V, Ca, Fe, Mg, F, Al and Ti values are within the limits of clarkes. The content of Cd, Cu, Mo and Pb in these soils is higher than the clarkes. In organogenic horizons of anthropogenic changed soils chemical elements, the content of which are significantly higher than clarke values are fixed: on the territory of the former bulk tailings dump—Cd, As, Mo, Zn, F; on the territory of the former hydraulic tailings dump—Cd, Zn, Pb.

The content of Mo, Cu, F, Ni, Co in the soils of the natural site is higher than the local background (Table 24.4). A wide group of potentially hazardous chemical elements in the organogenic horizon of alluvial swamp soils on the territory of the former bulk tailings dump was identified: Cd, Zn, F, Mo, Cu, Ni, As, Co, Pb. The concentrations of these elements are reduced in lower part of soil profile, with exception of Pb. Geochemical association in organogenic horizon of the alluvial swamp soils on former hydraulic tailings dump includes Cd, Pb, Zn, Ni, Cu, F, Mo, Co; in gley horizons—Cd, Ni, F, Zn, Cr, Cu, Co, As.

Table 24.3 Semi-quantitative mineral composition of alluvial swamp soils

Site	Horizon of soil	Quartz	Feldspar			Muscovite	Weathered muscovite	Biotite	Weathered biotite	Amphibole	Chlorite, epidote	Ore minerals	Ferrum oxide	Accessory
			Unchanged	Sericite	Pelitized									
The natural site of the floodplain of the Barun-Naryn brook	Organogenic	++++		++++	++++				+	++	++		++	Zircon-Rutile
	Gley	++++	++	++++	++++		++			+++	+++	+	++	Pyroxene-Magnesian lime-Sphen-Rutile
The former bulk tailings dump	Organogenic	++++	+++	++++	++++	++	+++			+++	++	+++	++++	Pyroxene
	Gley	++++	+++	++++	++++	+	+++	+	+++	+++	+	++	++++	Pyroxene-Zircon-Sphen
The former hydraulic tailings dump	Organogenic	++++	+++	++++	++++	+	++		+++	++	++	++	++++	Pyroxene
	Gley	+++	+	++++	++++	+	++++	++	++++	+++	+++	++	++++	Pyroxene-Magnesian lime-Zircon-Sphen-Garnet-Apatite

Note ++++prevail, +++1–10%, ++signs, +rare signs

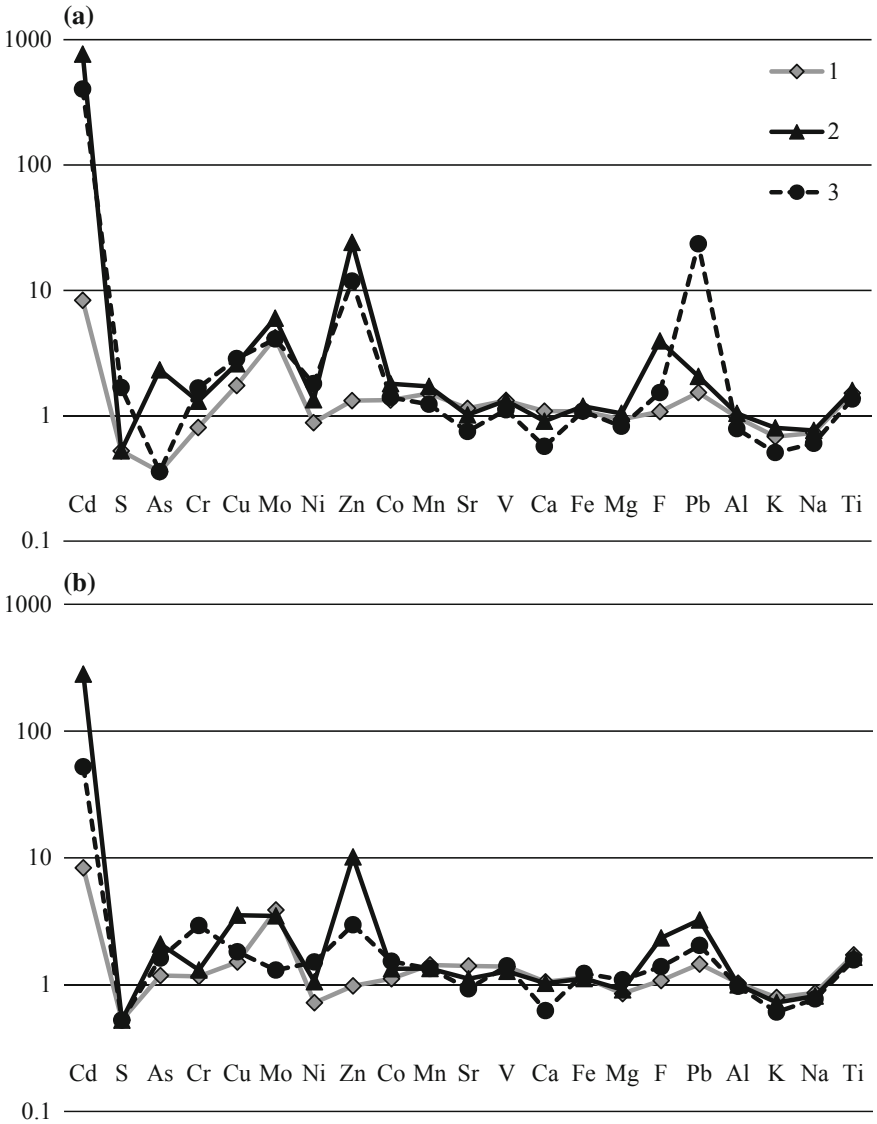


Fig. 24.4 Spectra of chemical elements normalized by clarke of the upper part of the continental crust in organogenic (**a**) and glee (**b**) horizons of alluvial swamp soils of technogenic landscapes: 1–3—numbers of the studied areas (see Fig. 24.1)

Table 24.4 The geochemical associations of elements accumulated in alluvial swamp soils of technogenic landscapes

Site	Horizon of soil	The association of elements
The natural site of the floodplain of the Barun-Naryn brook	Organogenic	$Fe_{24}Mo_{3.1}Cu_{2.4}F_{2.3}Ni_{2.0}Co_{1.7}Cd_{1.5}$
	Gley	$Fe_{26}Mo_{2.8}F_{2.3}Cu_{2.0}Ni_{1.6}Cd_{1.5}$
The former bulk tailings dump	Organogenic	$Cd_{138}Fe_{27}Zn_{22}F_{8.5}Mo_{4.4}Cu_{3.5}Ni_{3.0}As_{2.6}Co_{2.3}Pb_{1.6}$
	Gley	$Cd_{51}Fe_{25}Zn_{9.2}F_{5.0}Cu_{4.8}Mo_{2.6}Ni_{2.4}Pb_{2.3}As_{2.3}Co_{1.7}$
The former hydraulic tailings dump	Organogenic	$Cd_{72}Fe_{25}Pb_{17}Zn_{11}Ni_{4.1}Cu_{3.9}F_{3.3}Mo_{3.0}Co_{1.8}$
	Gley	$Fe_{28}Cd_{9.4}Ni_{3.4}F_{3.0}Zn_{2.7}Cr_{2.7}Cu_{2.5}Co_{1.9}As_{1.8}$

24.4 Discussion

The present study revealed that namely the microstructure of the studied soils are the main characteristics reflecting their genesis (Fig. 24.5). The shape of the mineral grains is rounded and subrounded, sometimes is angular. Skeletal material is well sorted (Fig. 24.5a). The presence of angular grains of minerals along with rounded and subrounded ones indicates that these soils belong to alluvial soils of mountain areas. The cryogenesis plays a dominant role in the formation of the studied soils. The micromorfological signs of cryogenesis are noted: the formation of polygonal structures (Fig. 24.5b), cryogenic microaggregation (Fig. 24.5c) and cryoturbation (Fig. 24.5d). Ooid orientation of the plasma, formation of angular microaggregates with common sub-horizontal arrangement is also marked. Humification of plant residues is poorly expressed, despite development of sod pedogenesis. The plant residues are moderately and most decomposed and ferruginous. The carbonized plants residues are found (Fig. 24.5e). Pedofeatures are presented: by ferruginous spots, flakes, microortstein, small iron-manganese murram (Fig. 24.5f-1); whole and fragmented ferruginous cutan on the surface and in fractures of mineral grains and fragments of rocks (Fig. 24.5f-2). Presence of various forms of ferruginous pedofeatures is characteristic feature for hydromorphic soils.

The tailings of Dzhidinsky tungsten-molybdenum combine overlying soils during a long time, impact on microstructure of the soil (Fig. 24.6). In result density of the microaggregates (Fig. 24.6a, b) and amount of ferruginous flakes and microortsteins have been increased, whole ferruginous cutan on the surface of the grains of the skeleton has been appeared (Fig. 24.6c, d). These changes were identified in all genetic soil horizons. In addition, the intensity of ferruginization signs increase into the lower part of the soil profile.

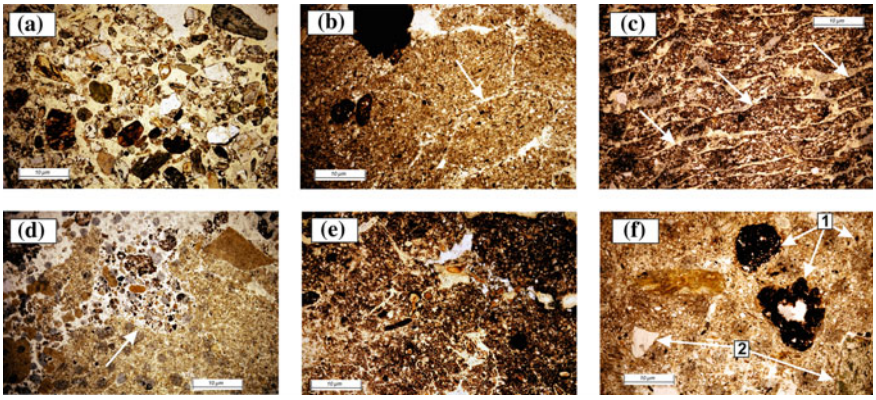


Fig. 24.5 The general microstructural features of the alluvial swamp soils the technogenic landscapes Dzhidinsky deposit (PPL): **a** shape of mineral grains; **b** polygonal structure; **c** cryogenic microaggregation; **d** cryoturbation; **e** carbonized and ferruginized moderately-, weakly-decomposed plants residues; **f** ferruginous patchs, ferruginous cutan on the surface and in cracks of large minerals

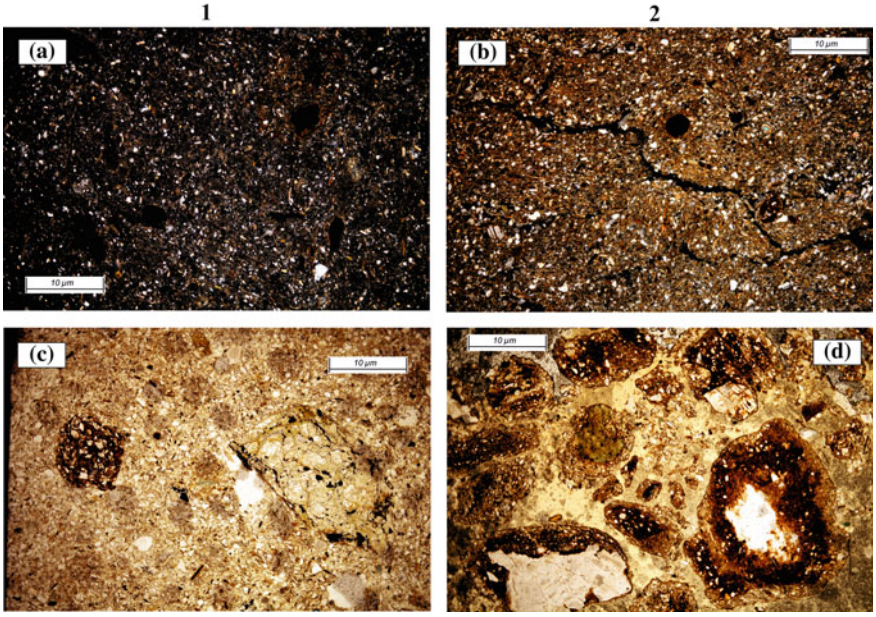


Fig. 24.6 The microstructure of the gley horizon of the alluvial swamp soils: 1—the natural site of the floodplain of the Barun-Naryn brook, 2—the technogenic landscapes Dzhidinsky deposit; **a**, **b**—density of the microaggregates (XPL); **c**, **d**—ferruginous pedofeatures (PPL)

In the mineral composition of the soils of technogenic landscapes of the Dzhidinsky tungsten deposit in comparison with the mineral composition of the soils of the natural site, some differences were revealed. In the buried alluvial swamp soils of the territories of the former tailings dumps (bulk and hydraulic), a more number of grains of weathered muscovite, weathered biotite, ferric oxide and ore minerals were noted. The more number of changed minerals in the soils of technogenic landscapes can be associated with the intensification of their weathering. The later is caused by decreased in the level of permafrost in buried soils and impacts of acidic pore waters (pH 2.0–4.2) of tailings ponds on soils. The emergence of ore minerals in upper part of soil profile of technogenic landscapes can be associated with their mechanical introduction.

Comparison with the composition of the studied soils with clarkes of chemical elements of the upper part of the continental crust showed that the natural soils correspond to the chemical composition of the soils of the hydromorphic series. The contents of Cd, Cu, Mo and Pb in the natural soils are higher than the clarke values (see Fig. 24.4). These elements are typical for the soils of the area of the Dzhidinsky deposit as ore elements and their satellites, which was noted in previous studies (Smirnova and Plyusnin 2013; Timofeev et al. 2016). The organogenic soil horizons are characterized by a significant excess of clarkes for Cd, As, Mo, Zn, F (former

bulk tailings dump) and Cd, Zn, Pb (former hydraulic tailings dump) (see Fig. 24.4). These high values indicate technogenic pollution of the upper soil horizons.

The Fe content in the studied soils is 24–28 times higher than the local background values (see Table 24.4), which is the result of iron accumulation in soils under conditions of excessive moisture. The maximum content of Pb are fixed in the organogenic horizon of buried alluvial swamp soils of the former hydraulic tailings dump. These values are 16 times higher than the Pb content in the humus horizon of natural soils. Lead anomaly may be caused with inputs of galena (PbS) under hubnerite concentrate washing from stale tailings in this area by artisanal miners. In the gley horizon of buried soils the Pb content is fixed at the level of background values. The maximum values of Cd, Zn, As and Mo exceeding the content of these elements in natural soils in 92, 18, 7 and 2 times, respectively, were recorded in the organogenic horizon of buried alluvial swamp soils of the territory of the former bulk tailings dump. In the gley horizon of their content sharply decreases. Despite the fact that Cu, Ni and Co are characterized by bioaccumulation, the accumulation of these chemical elements in organogenic horizons of these soils, in relation to mineral horizons, is poorly expressed. The contents of Pb, Cd, Zn and Mo in the upper horizons of natural soils are usually close to their concentrations in the soil-forming rock (Kabata-Pendias 2011). The greatest number of potentially dangerous chemical elements in the studied soils is confined to their upper, organogenic horizons, which indicates the deposition of these elements by organic matter of soils with the formation of organometallic compounds, which are the closest reserve for the formation of their mobile forms.

The content of toxic elements in the buried soils of the bulk tailings dump is significantly higher than in the buried soils of the hydraulic tailings dump. This is due to the fact that the bulk tailings dump existed 20 years longer than the hydraulic tailings dump. In addition, the richer ores were processed during the formation of the bulk tailings. The composition of the waste was inherited from the composition of the initial ores.

24.5 Conclusions

In the studied soils, which were buried for a long time under the wastes of enrichment of sulfide-tungsten ores of the Dzhidinsky combine, the specific significant changes in comparison with the natural soils were revealed. The micromorphological structure, mineral and chemical composition have been affected by the Dzhidinsky combine, which led to increase of (i) the microaggregates' density, (ii) number of ferruginous pedofeatures, and (iii) proportion of weathered minerals' particles (mica and feldspar). The mineral weathering is affected by acidic water from tailings penetrating in the soil pore system.

The buried soils of the areas located in the former (i) bulk tailings dump are characterized by the high contents of Cd, Zn, F, Mo, Cu, Ni, As, Co, Pb and (ii) hydraulic tailings dump—Cd, Pb, Zn, Ni, Cu, F, Mo, Co.

The accumulation of potentially hazardous chemical elements in the upper organogenic soil horizons is associated with the formation of organometallic compounds. The intensity of soil contamination depends on the duration of storage, composition, and content of elements in the ore dressing waste covering.

Acknowledgements The study was carried out within the framework of the state task of GIN SB RAS. Project IX.137.1.4. Interactions in the water-rock-organic matter system in natural and man-made environments of the Baikal region. № AAAA-A17-117021310076-3 and grant RFBR Chemical elements migration at natural and technogenic landscapes of Transbaikalia sulfide-bearing mines: geological-ecological aspects № 16-05-01041a. The study, was conducted using facilities of Center for "Analytical center of mineralogical, geochemical and isotope Studies" at the Geological Institute, SB RAS Ulan-Ude, Russia.

References

Abakumov EV, Maksimova EI, Lagoda AV, Koptseva EM (2011) Soil formation in the quarries for limestone and clay production in the Ukhta region. Eurasian Soil Sci 44(4):380–385

Bachurin BA, Baboshko AA (2008) Man-caused mineral formations of the mining industry as the sources of emissions of heavy metals. Prob Miner Petrography Metallogeny 11:322–326 (in Russian)

Belan LN (2007) Geoecological bases of natural and technogenic ecosystems of mining areas of Bashkortostan. Dissertation, Bashkir state University (in Russian)

Blair RD, Cherry JA, Lim TP, Vivyurka AJ (1980) Groundwater monitoring and contaminant occurance at an abandoned tailings area, Eliot Lake, Ontario. In: Proceedings of 1st international conference on uranium mine waste disposal, pp 911–944

Blowes DW, Lortie L (1995) Microbiological, chemical, and mineralogical characterization of Kidd Creek Mine tailings impoundment, Timmins area, Ontario. Geochem J 13:13–31

Borman RS, Watson DM (1976) Chemical processes in abounded sulfide tailings dumps and environmental implications for Northeastern New Brunswick. Can Inst Min Metall Bull 69:86–96

Bortnikova SB (2001) Geochemistry of heavy metals in technogenic systems: problems of formation, development and interaction with components of the ecosphere. Dissertation, IPGG SB RAS (in Russian)

Bortnikova SB, Yurkevich NV, Abrosimova NA, Devyatova AY, Edelev AV, Makas AL, Troshkov ML (2018) Assessment of emissions of trace elements and sulfur gases from sulfide tailings. J Geochem Explor 186:256–269

Classification and Diagnostics of Soils of Russia (2004) Oikumen, Smolensk (in Russian)

Davis GB, Ritchie AIM (1986a) A model oxidation in pyritic mine wastes I. Equations and approximate solution. Appl Math Model 10:314–322

Davis GB, Ritchie AIM (1986b) A model oxidation in pyritic mine wastes II. Comparison of numerical and approximate solution. Appl Math Model 10:323–329

Dubrovsky NM, Cherry JA, Readon EJ, Vivyurka AJ (1984) Geochemical evolution of inactive pyritic tailings in Eliot Lake Uranium district: groundwater zone. Can Geotech J 22:110–128

Emlyn EF (2001) Natural and unnatural history of massive sulfide deposits in the context of the evolution of geotechnogenic of the Urals. Mineral Technogenesis 2:219–232 (in Russian)

Gerasimova MI, Gubin SV, Shoba SA (1992) Micromorphological features of the USSR zonal soils. Pushino (in Russian)

Kabata-Pendias A (2011) Trace elements in soils and plants. CRC Press, Taylor and Francis Group, Boca Raton, London, New York

Kasimov NS, Vlasov DV (2015) Clarkes of chemical elements as comparison standards in ecogeochemistry. Bull Moscow Univ Ser Geogr 2:7–17 (in Russian)
Khanchuk AI, Zvereva VP, Krupskaya LT (2012) Ecological problems of development of tin ore resources in Primorie and Priamurie. Geogr Nat Resour 33(1):45–49
Khodanovich PY (1999) Stale tailings the Dzhidinsky tungsten-molybdenum combine as an complex technogenic deposits. In State and prospects of development of mineral resources and mining complexes of the Republic of Buryatia. BSC Publishing House, Ulan-Ude (in Russian)
Komachkova IV (2011) Assessment of the ecological state of soils of technogenic landscapes of the South of Primorye. Dissertation, FSCEATB FEB RAS (in Russian)
Kostenkov NM, Komachkova IV, Purtova LN (2013) Soils of technogenic landscapes in the Far East: The Luchegorsk and Pavlovsk coal strip mines. Eurasian Soil Sci 46(11):1049–1058
Krupskaya LT, Zvereva VP, Leonenko AV (2013) Impact of technogenic systems on the environment and human health in the priamurye and primorye territories. Contemp Probl Ecol 6(2):223–227
Leontyev LI, Dyubanov VG (2011) Technogenic waste products of ferrous and nonferrous metallurgy, and environmental issues. Ecol Ind Russia 4:32–35 (in Russian)
Loupasakis C, Konstantopoulou G (2009) Safety assessment of abandoned tailings ponds: an example from Kirki mines, Greece. Bull Eng Geol Env 69:63–69
Makarov DV (2006) Theoretical and experimental study of chemical transformations of sulfides in industrial wastes and a study of the influence of oxidation products of the minerals on their technological properties and the environment. Dissertation, Institute of Chemistry and Technology of Rare Elements and Mineral Raw Materials of the RAS KSC (in Russian)
Monger HC (2013) Soil micromorphology and the Anthropocene—cross-scale connections and technology trends. Span J Soil Sci 3(2):1–13
Opekunova MG, Somov VV, Papyan EE (2017) Soil contamination in the impact zone of mining enterprises in the Bashkir Transural region. Eurasian Soil Sci 50(6):732–745
Rikhvanov LP, Abrosimov NA, Baranovskaya NV, Belan LN, Bolshunova TS, Bortnikova SB, Gorbatyuk EA, Gustaitis MA, Edelev AV, Mezhibor AM, Myagkaya IN, Soktoev BR, Yusupov DV, Zhmodik SM, Ischuk NV, Kirichenko IS, Narkovich DV, Lazareva EV, Olenchenko VV, Saeva OP, Ool Yu, Usmanova TV, Yurkevich NV (2017) Biogeochemical monitoring in the areas of tailing dumps of mining enterprises, taking into account the microbiological factors of transformation of mineral nutrients. Publishing House of SB RAS, Novosibirsk (in Russian)
Saet YuE, Revich BA, Yanin EP, Smirnova RS, Basharkevich IL, Onishchenko TL, Pavlova LN, Trefilova NYa, Achkasov AI, Sargsyan SSh (1990) Geochemistry of the environment. Nedra, Moscow (in Russian)
Salomons W (1995) Environmental impact of metals derived from mining activities: processes, predictions, prevention. J Geochem Explor 52:5–23
Shugalei LS, Chuprova VV (2012) Soil formation in the technogenic forest-steppe landscapes of the Nazarovskaya depression in Western Siberia. Eurasian Soil Sci 45(3):246–256
Sidenko NV, Lazareva EV, Bortnikova SB, Kireev AD, Sherriff BL (2005) Geochemical and mineralogical zoning of high-sulfide mine-waste at the Berikul mine-site, Kemerovo region. Russia J Can Mineral 43(4):1141–1156
Smirnova OK, Plyusnin AM (2013) Dzhidinsky ore region (problems of environmental condition). BSC Publishing House, Ulan-Ude (in Russian)
Smith KS (2007) Strategies to predict metal mobility in surficial mining environments. Geol Soc Am Rev Eng Geol XVII: 25–45
Sokolov DA, Androkhanov VA, Kulizhskii SP, Domozhakova EA, Loiko SV (2015) Morphogenetic diagnostics of soil formation on tailing dumps of coal quarries in Siberia. Eurasian Soil Sci 48(1):95–105
Solntseva NP, Gerasimova MI, Rubilina NY (1990) Morphogenetic analysis transformed by technology. Sov Soil Sci 22(3):87–97
Stoops G, Marcelino V, Mees F (2010) Interpretation of micromorphological features of soils and regoliths. Elsevier, Amsterdam

Timofeev IV, Kasimov NS, Kosheleva NE (2016) Soil cover geochemistry of mining landscapes in the South-East of Transbaikalia (city of Zakamensk). Geogr Nat Resour 37:200–211

Urosevic S, Vukovic M, Pejcic B, Strbac N (2018) Mining-metallurgical sources of pollution in Eastern Serbia and environmental consciousness. Rev Int Contam Ambiental 34(1):103–115

Walder IF, Chavez WX (1995) Mineralogical and geochemical behavior of mill tailing material produced from leadline mineralization, Hanover, Grant County, New Mexico, USA. Environment Geol 26:l–18

World Reference Base for Soil Resources (2014) International soil classification system for naming soils and creating legends for soil maps. Update 2015 (2015). Food and Agriculture Organization of the United Nations. Rome

Wuana1 RA, Okieimen FE (2011) Heavy metals in contaminated soils: a review of sources, chemistry, risks and best available strategies for remediation. Int Sch Res Not. http://dx.doi.org/10.5402/2011/402647

Zvereva VP, Pyatakov AD (2017) Physicochemical modeling of sulfide oxidation processes in tailing dumps of the Kavalerovsky district and their impact on the hydrosphere (Primorsky Krai). Russ J Gen Chem 87(13):3137–3143

Chapter 25
Biogenic-Abiogenic Interactions and Soil Formation in Extreme Conditions of Untersee Oasis, Surroundings of Lake Untersee, Central Queen Maud Land, East Antarctica

George Shamilishvili, Evgeny V. Abakumov and Dale Andersen

Abstract Soil formation on the territory of ice-free oasis of the continental Antarctica was studied on example of Untersee Valley, Queen Maud Land (QML), Eastern Antarctica. Soils of the Lake Untersee surroundings were characterized in terms of morphology and main chemical and physical properties for the first time. Dominating soils are basically characterized by a poorly differentiated soil profile, with a horizon Cryic type located directly on the parent material. The predominant parent material types of the Untersee Valley are the glacial, fluvioglacial sandy loams and gravels with a large content of differently sized fragments, as well as glacial-lacustrine sandy-loams and loamy-clays. A characteristic feature of glacial and fluvioglacial deposits is their sorting as a consequence of the cryoturbation process. The main meso-relief forms of the Valley include terminal type complexes of moraine hills and ridges, eskers, drumlins, sandurs, patterned grounds, and pingo. The investigated soils are characterized by a low content of organic matter and low intensity of weathering processes in parent material as a function of low biogenic and abiogenic interactions in severe bioclimatic conditions of the Antarctic intercontinental oases.

Keyword Soils · Antarctica · Antarctic oases · Lake Untersee · Extreme cold environments · Polar regions · Soil morphology · Geomorphology

25.1 Introduction

Soils of ice-free territories in Queen Maud Land (QML) have been studied previously by Zazovskaya et al. (2015) describing the conditions of pedogenesis in Schimarcher Oasis in the surroundings of the Russian Antarctic Station. The soils

G. Shamilishvili · E. V. Abakumov (✉)
Saint Petersburg State University, Saint Petersburg, Russian Federation
e-mail: e.abakumov@spbu.ru

D. Andersen
Carl Sagan Center for the Study of Life in the Universe, SETI Institute, Mountain View, CA, USA

© Springer Nature Switzerland AG 2020

O. V. Frank-Kamenetskaya et al. (eds.), *Processes and Phenomena on the Boundary Between Biogenic and Abiogenic Nature*, Lecture Notes in Earth System Sciences,
https://doi.org/10.1007/978-3-030-21614-6_25

of Lake Untersee region, the rest vast ice-free territory of QML, are still not studied enough. A little information is reported in the paper mainly dealt with subjacent environmental objects of the Lake Untersee area. Several Soviet-German fieldworks have been conducted there since 1983–1988 years, mainly concentrated on a study of glacial history of the Untersee Oasis basing on morphological observations of moraines and radiocarbon dating of the associated biogenic material (Simonov et al. 1985; Loopman et al. 1988; Kaup et al. 1988; Bormann and Fritzsche 1995). Levitan et al. (2012) have studied conditions of modern terrestrial sedimentation in Lake Untersee, reporting the data on particle size distribution and chemical composition of soils, moraine filling material, lake sediments and contaminated ice. Soils were identified as Cryosols without distinction of any lithological subtypes. Comprehensive data on the soils of QML is available only for the Novolazarevskaya Station, Schirmacher Oasis, which is located approximately 86 km North-West, the second large and the most studied Antarctic oasis of the QML (Bockheim 2015). The soils of Schirmacher Oasis also belong to Cryosol (WRB 2014) reference group. According to USDA Soil taxonomy (USDA 2014) the dominant soil taxa include Typic Haploturbels-Haplorthels and Lithic Haploturbels-Haplorthels under moss cover, Typic Aquorthels-Haplorthels in soils along lake margins and those influenced by algae, Typic Haploturbels in areas of patterned ground, Typic Haplorthels in dry areas, and Typic and Lithic Anhyorthels-Anhyturbels in the mountains (Bockheim 2015).

This paper provides general information on morphology and taxonomy with discussion of some physical, chemical properties and data on apparent electric resistivity of soils of the Lake Untersee Oasis.

25.2 The Study Sites

Lake Untersee (71°20′S 13°45′E) is the largest lake perennially covered with ice, located in the Gruber Mountains, central Queen Maud Land (QML), East Antarctica (Fig. 25.1).

In the meantime, Gruber Mountains as a part of Wohlthat massif comprise a one of the largest ice-free territories in the QML, with a square of nearby 300 km^2 or 8.8% from total QML ice-free area of 3400 km^2 (Bockheim 2015). Altitude of the lake shore is 563 m a. s. l. Lake has 6.5 km in extension from South-West to North-East direction, 2.5 km in width and total square of 11.4 km^2 (Loopmann et al. 1988). The lake basin is located in a deep amphitheater-like valley surrounded by mountains with a mean elevation of the plateau around the lake of about 1000 m (Andersen et al. 2015). The north border of basin matches to Anuchin glacier, damming the lake. Dominating parent rocks are proterozoic-age anorthosites—basic normally alkaline rocks of the gabbroidal family (Kaup et al. 1988; Bormann and Fritzsche 1995). Valley is characterized by glacial and neoglacial relief with well expressed positive landforms such as moraines, eskers and drumlins. Surface deposits are represented by gravel sands to sandy loams along with heavy loams and clays (mainly associ-

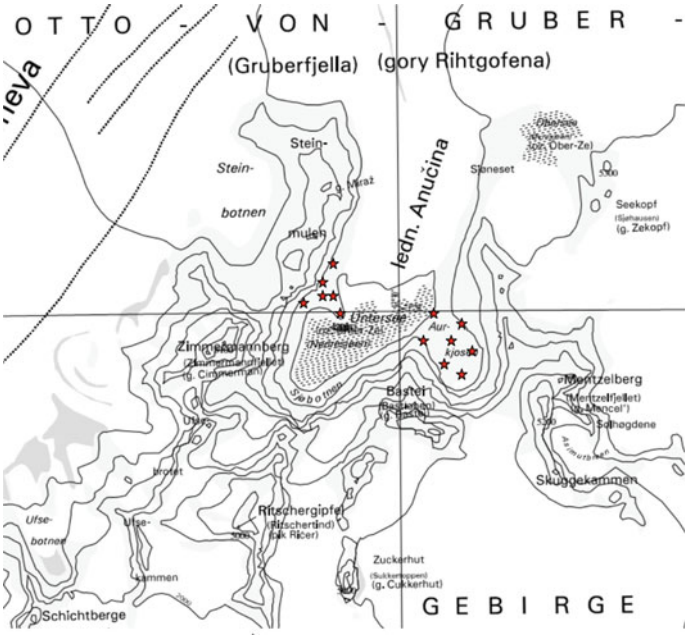


Fig. 25.1 Location of Untersee oasis

ated to shoreline and bottom areas of the dried lake) of fluvioglacial and glacial-lacustrine origin. Climate conditions of Untersee Lake area are quite severe. The mean annual temperature at Lake Untersee calculated for the five years observation period is $-10.6° \pm 0.6°$ C (Andersen et al. 2015). The annual degree-days above freezing for the five years were 9.7, 37.7, 22.4, 7.0, and 48.8, respectively with average summer temperatures of $-3.5°$, $-1.9°$, $-2.2°$, $-2.6°$, and $-2.5°$ C (Andersen et al. 2015). The average of the wind speed reported is 5.4 m s^{-1}, the maximum is 35.7 m s^{-1}, and the average daily maximum is 15 m s^{-1} (Andersen et al. 2015). The dominant wind direction is south for all seasons, and east-northeast in summer (Andersen et al. 2015). Relative humidity averages 37% (Andersen et al. 2015).

The alpinotype character of the mountains in QML with their very steep slopes and small ridges penetrating the inland ice has a strong influence on regime of ice flow. The latter is generally oriented from the Wegener Plateau to the north. On the southern slopes of the mountain ranges the inland ice is dammed up to almost 2000 m a. s. l., whereas their northern flanks are undernourished and therefore the ice level reaches only 800–1400 m—at some places even less (about 600 m).

The results are an embracing regime of ice flow producing ice eddies and local inversions of the general ice movement, filling bays and valleys on the northern flank of the mountain ranges. The mountain ranges do not constitute an impenetrable hindrance to the ice flow. They are intersected by N–S trending valleys which are used for the northward ice flow. These valleys are chiefly of tectonic origin. They mark

zones of graben-like structures which dissect the E–W trending mountain ranges into blocks of different elevation. The mountains which surround the Untersee Oasis are also characterized by E–W and N–S trending ridges. The southern main crest reaches up to nearly 3000 m a. s. l. Athwart to it, marginal mountain chains (fingering spurs) run about 10 km to the north.

Besides geological fieldwork in the Untersee Oasis in 1983/84 and 1986/87, a number of observations on various types of moraines were carried out (Simonov et al. 1985). In some cases, there is a close correlation between the type and position of moraines and the present glacier state. Other moraines point to a different regime of glacier flow in earlier times. In chronological order the following sequence can be stated.

Stage 1. The mountain range was overrun by the northward-flowing and then much thicker inland ice directly from south to north. The resulting U-shaped valley of the Untersee Oasis as well as the ice-polished slopes up to the mountain tops were generated during this early stage. Whereas in the main valley (Untersee Oasis) moraines belonging to this stage were totally overprinted by later glacier movements, they probably still exist in the hanging side-valley on the southwestern flank of Lake Untersee. They represent one of the stages of retreat from high glacier level. There a dam-type moraine forms the northeastern end of this hanging, trough-like, ice scoured glacial valley. Within this moraine boulders of quartz-iron jaspillite were found. Disregarding possible young vertical crustal movements, it can be calculated that the ice level on the northern flank of the main ridge was at least during this period about 1000 m higher than the present ice surface.

Stage 2. The sinking of the ice level was coupled with a rigorous change of the ice flow regime. From that time up to now the central Wohlthat Massif has been by-passed by glaciers along its eastern and western borders. Parts of these north-flowing ice streams turn back south like and eddy behind a passed-by hindrance and unite at the northern flank of the massif and flow as a valley glacier southward into the Untersee valley. At that stage the whole valley was filled with this glacier forming the lateral moraines at the steep valley slopes. In the northern part, the moraines extended up to an altitude of 1200 m a. s. l., whereas in the southern amphitheater the moraine producing glacier reached 800 m a. s. l. These facts indicate a glacier level in the Untersee valley which must have been 250 or 300 m higher than it is at present. Probably the frontal push moraines located along the southern and southwestern flanks of the Untersee valley were also generated during this stage. It consists of several single curved dams of moraines. Their open side is directed downhill. The single moraine dam has a maximum height of about 100 m above ground level. They prove a repeated oscillation of the glacier front. Partially, old ice could be observed both underneath these moraines and the younger ones.

Stage 3. During this stage the ice level was similar to that of today. The tongue-shaped peninsula which projects into the Lake Untersee as well as the moraine dams in the lateral valley along the eastern flank of the lake were heaped up. They indicate a separate advance of both parts of the glacier at a time when the valley glacier itself had already retreated farther to the north. Their origin as terminal moraines (“dump” or “melt-out” moraines) can be inferred from the flat northeastern flank of

the peninsula and the opening of the moraine dams within the eastern side-valley to the N–W. During that time lateral moraines also continued to form, but they only reached a height of only some decameters above the present ice level.

Stage 4. During this stage the glacier front retreated several hundred meters further to the north. It now forms the northern shore of Lake Untersee. In this process the level of the glacier surface did not change significantly. Systems of crevasses and ice booms in the bordering lake ice coming from the glacier front sometimes show characteristics of overthrusting by a temporary advance of the glacier to the south. Likewise, the two parts of the glacier are at present separated by a weakly developed medial moraine. Other moraines are related to the small and independent glaciers which directly end the southern and eastern parts of the Untersee valley.

The sequence of moraines described above has been derived from morphological and relative temporal observations. By now radiocarbon age data have also become available for some moraines around Lake Untersee. During field work in 1983 and 1987 samples of biogenic material were collected from different moraines in the Untersee valley. This biogenic material originates from Snow Petrels (*Pagodroma nivea*) which live among the morainic boulders in at least 26 colonies (Simonov et al. 1985). Since only ice-free rocks or moraines will be selected as breeding places, biogenic material which permits radiometric dating can also be used for the determination of the minimum age of these moraines. The material analyzed consists of solidified stomach oil spit out by petrels in stress situations. It forms stratified organic layers (mumyo) around the breeding places up to several decimeters thick.

In combination with their location these datings are also very important for studying the origins of the moraines. Samples were taken along the transect from the bottom of the slope bordering the present glacier to almost the top of the ridge. That means they were located on the present or recent lateral moraines as well as on the older upper lateral moraine on the steep slope and above it. In this context it is interesting to note that present breeding colonies of Snow Petrels are mostly situated near the bottom of the slope. Probably, the petrels followed the favorable living conditions during ice retreat (micro climate, in particular higher temperatures and lesser storms intensity).

This hypothesis is confirmed by the radiocarbon data: the higher the altitude of the sampling sites, the older the samples. Most of the ages determined vary between 2000 and 8000 yr BP and thus indicate an increasing Holocene occupation of these mountain ranges by petrels. A minimum age of at least 8000 yr BP is proved for the upper lateral moraine on the steep slope (Stage 2). The ice retreat of stage 2 to the younger levels (stage 3 and 4) therefore seems to be related to the Post-Pleistocene phase of warming. According to chronology of the last drastic climatic change in Antarctica terminated around 13,000 yr BP. If we take into consideration a probably delayed retreat of the ice sheet as compared to the warming phase during this time, then the newly created living space would have been colonized already shortly after the ice retreated. These facts also point to a Holocene age of the moraines belonging to the ice stages 3 and 4. The described lowering of the ice level in the order of 250–300 m from stage 2 to stage 3 and the sinking of ice surface from stage 1 to stage 2 correspond to results obtained from other Antarctic regions, according to

which the ice surface during the middle According to Pleistocene was 300–800 m higher than at present.

The graben like geological structure has a great influence on the history of development of Untersee valley. In the same time influence of exogenous forces such as wind, water erosion and glacial movements played an equally important role in the formation of the modern appearance of the territory. Glacier movements in quaternary and modern time have been widely accepted to be a dominant role in the polar environments all across the inland territories of Antarctic continent (Glazovskaya 1958).

Described geomorphological structures of Untersee Oasis are represented by following:

1. Low mountain plateau with an average elevation of peaks about 1000 m a.s.l. with steep "ice polished" slopes up to 61°, covered with ancient moraines and colluvial deposits, around the Lake Untersee comprising the first amphitheater.
2. Complex of main, terminal and lateral moraines associated to late-quaternary glacial activity.
3. Glaciofluvial fields and channels.
4. Perennially ice-covered lake depression with an altitude down to 160 m under the ground level.
5. The present Anuchin's glacier edge with adjacent dam-like moraines on the eastern and western sides of the Valley.
6. Melting-out depressions occupied by ponds on the northwest of the Valley.
7. Mountain glacier on the south of Lake Untersee with ice accumulation beneath the slope.
8. The second trough-like valley on the east of Lake Untersee—Arkjosen cirque with a complex of terminal and lateral moraines. Obviously in late quaternary period the central part of the Valley represented a glacial basin down to several decameters in depth. This is proven by findings of lacustrine sediments containing dry bacterial mats through-out the valley and well-expressed onshore shaft.
9. Mountain glacier on the eastern side of the Arkjosen cirque with ice accumulation beneath the slope.
10. Patterned grounds in both the Untersee and Arkjosen cirque valleys (Fig. 25.2)**.** Diameter of the sorted rings varies in a wide range with a maximum of 20 m in northeastern part of Arkjosen cirque but basically it does not exceed 2–3 m. The origin of these forms is related to cryoturbation processes due to seasonal dynamics of soil moisture and temperature.

Probably, the most remarkable landform is the ice hummock (pingo) located at the center of Arkjosen cirque valley. This single formation has almost 30 m in diameter and 7 m in height and has an ice core in the basement thus the origination of this positive landform is referred to sublimation of glacial lake occupied the valley in recent geological time (Fig. 25.3).

Other no less remarkable landforms along with a pingo are the aeolic glacier tables occurring mainly on the ice surface of southern part of Lake Untersee. Origin of these



Fig. 25.2 Morphology of the patterned grounds surface

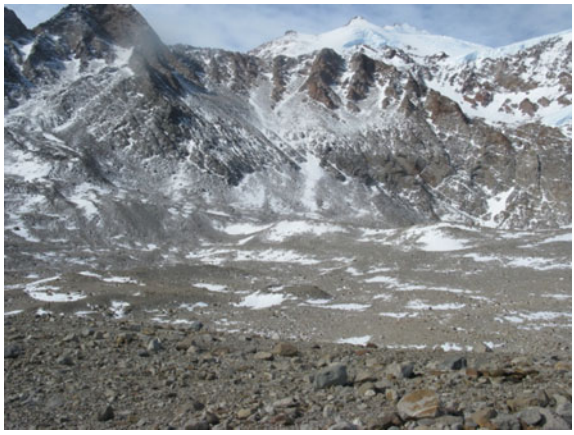


Fig. 25.3 An example of pingo

forms is related to contemporary influence of wind erosion of ice and difference in insulation intensity of the rock surface. The latter depends on albedo and type of the rock surface. The darker rock surface is—the lower albedo would be, and hence the higher rate of solar rays can be absorbed. This leads to heating up of the rock surface and increase the melting of ice around the boulder.

25.3 Materials and Methods

The current study is based on pedological and geomorphological observations during the 63th Russian Antarctic Expedition along with TAWANI 2017 expedition, which have taken place in Untersee Oasis during the spring season from 11.14.2017 to

12.02.2017. The study area included Untersee valley with adjacent eastern trending Arkjosen cirque, and northwestern slopes of the mountain ranges (Mount Mullen).

Field soil survey included soil profiling using standard stainless shovel, a 50 m geodetic roulette, soil electrical resistivity meter (Landmapper ERM 02), pH-meter (150-M), and HD-camera. Soil classification was held using a World Reference Base for soil resources (WRB 2014). Soil color was derived using a Munsell Color Chart. pH of the soil samples was determined in a water-soil solution with standard ratio of 1:5 in field laboratory.

Particle size distribution along with a number of chemical properties including pH of 1:2.5 soil/water or soil/1 mol/L KCL solution, hygroscopic moisture, loss on ignition at 600 °C, total organic carbon (TOC), total nitrogen, C/N ratio, exchangeable ammonium and mobile compounds of phosphorous content were determined in a stationary certified laboratory according to routine methods (Arinushkina 1970).

Particle size distribution of coarse earth (> 1 mm) in soil samples was derived via dry sieving procedure using a set of stainless sieves with a diameter of cells > 10, > 5, > 2 and > 1 mm. Granulometric composition of fine earth was derived using a wet sieving method with an application of stainless sieves with a diameter of cells of > 0.5, > 0.25, > 0.1 mm respectively. The 0.1–0.002 mm fractions distribution was measured using soil aerometer AG with a 995 to 1030 kg/m^3 density scale and 1 L glass cylinder (Rastvorova 1983).

Potential acidity of the studied soils was characterized by determination of pH in 1:2.5 soil/1 mol/L KCL (pH = 6.0) solution. The additional acidification of the soil solution is reached by substitution reaction of protons with K + ions in the soil absorbing complex forming molecules of hydrochloric acid during a 24 h period of extraction. Preparation of the extraction solution was carried according. Applied KCL reagent had analytically pure quality of 99.9%.

Hygroscopic moisture (W, %) content was derived via A&D Moisture Analyzer MX-50. This appliance provides high speed of the results derivation and repeatability ($\sigma = 0.01\%$) with accuracy of the sample weighing up to 0.001 g. The moisture derivation settings were set to standard regime, mid accuracy (5.00 g sample), heating at 105 °C. The accuracy of sample weighing was controlled using a 20 g weight F1, the accuracy of moisture determination—by testing a standard sample of sodium tartrate dehydrate ($Na_2C_4H_4O_6$) of analytically pure quality containing 15.66% (theoretically proved).

Loss on ignition (LOI, %) was determined in samples dried to constant weight at 105 °C in standard ceramic crucibles with a subsequent ignition at 200 °C until smoke evolution is stopped, consequent increase in temperature up to 300 °C during an hour and final ignition at 600 °C in a certified muffle furnace. Sample weighing was conducted via A&D analytical weights of the second class of accuracy (±0.0001). Accuracy of sample weighing was controlled using a 20 g weight F1. Completeness of ignition was controlled by three-time weighing. If the difference between two consequent weighing is less then 0.005 g, the ignition is supposed to be completed. Between weighing the crucibles were stored in a desiccator with calcium chloride sorbent activated at 300 °C before use.

TOC was determined according to standard method (Walkley and Black 1934). Total nitrogen (N_{tot}) content was determined according to standard method according to Kjeldal procedure. The essential of the method is based on formation of green colored indophenol compound formed during the reaction of ammonium with sodium hypochlorite and sodium salicylate in alkaline media with a subsequent measurement of coloration intensity of solution at 655 nm wave length on the spectrophotometer PE-5400VI in a 10 mm ditch. Degradation of soil organic matter (SOM) is conducted through oxidation with sulfuric-selenic acid at a temperature of 400 °C in the Kjeldahl flasks until the solution is discolored. After oxidation of SOM, the discolored solution is diluted with distilled water freed of ammonium in a 50 cm^3 volumetric flask. Than 1 cm^3 of diluted solution is mixed with 45 cm^3 of operating coloring solution and 2.5 cm^3 of operating sodium hypochlorite solution with a consequent measurement of solution color through 1 h. All solutions are prepared in accordance with standard guidance. Measurements are carried out using a calibration curve constructed before analysis. Calibration curve was constructed based on measurements of colors of the standard solutions prepared from standard reference sample of total nitrogen water solution GSO 7193-95 0.5 mg/cm^3. Accuracy of analysis was controlled by additive method—addition of the standard solution volume containing a certain amount of nitrogen (mg) to the analyzed solution.

C/N ratio is simply calculated by division of TOC and N_{tot} values. This is a simple parameter characterizing the degree of saturation of organic matter with nitrogen. The higher value is, the lower nitrogen saturation is and vice versa. The C/N ratio also indicates a degree of humification of soil organic matter: C/N ratio < 20—active processes of organic matter mineralization and formation of NO_3^-; C/N ratio > 30—nitrogen is immobilized, organic matter is weakly humified; C/N ratio ≤ 10—organic matter is highly humified.

Exchangeable ammonium ($NH_4^+{}_{exc}$, mg/kg) was determined according to standard method according to National Standart GOST 26489-85. The essential of the method along with quality control and quality assurance procedures are similar to those of the total nitrogen determination. Extraction of exchangeable ammonium is conducted with 1 mol/L potassium chloride solution (pH = 6.0) added to soil sample at a soil/solution ratio of 1:2.5. After extraction the obtained solution was filtered through laboratory micropore paper filter. 2 cm^3 of obtained solution are mixed with 38 cm^3 of operative coloring solution and 2 cm^3 of operative sodium hypochlorite solution. All solutions are prepared in accordance with standard guidance. The color of obtained solution is measured through 1.5 h in a 10 mm ditch at 655 nm wave length using a spectrophotometer PE-5400VI. Measurements are carried out using a calibration curve constructed before analysis.

Mobile compounds of phosphorous mass percentage (P_2O_5, mg/kg) were determined according to standard method National Standard GOST R 54650-2011. The essential of the method is based on formation of blue colored phosphorous-molybdate complex during reaction of ammonium molybdate with phosphorous in acid media with a subsequent reduction by ascorbic acid. Extraction is conducted with 0.2 mol/L hydrochloric acid solution added to soil sample at a soil/solution ratio of 1:5. Concentration of the extraction solution was determined by titration with 0.1 mol/L

sodium hydroxide solution and phenol-phtaleine indicator solution. Temperature of the extraction solution was controlled by a simple mercuric thermometer and was 19 °C. After extraction the obtained solution was filtered through laboratory micropore paper filter. After that 2 cm^3 of filtered solution were mixed with 38 cm^3 of operative coloring solution with a subsequent measurement in 10 mm ditch at 710 nm wave length using a spectrophotometer PE-5400VI. All solutions were made according to standard guidance. Measurements are carried out using a calibration curve constructed before analysis. Calibration curve was constructed based on measurements of colors of the standard solutions prepared from standard reference sample of phosphate ions water solution GSO 7748-99 1 mg/cm^3. Quality assurance procedure is conducted using a standard reference sample of soil composition GSO 10413-14 containing certified amount of mobile phosphorous compounds.

All measurements were conducted at least in triplicate Obtained meanings were provided with absolute error boundaries, i.e. $X \pm \Delta$.

25.4 Results

25.4.1 Soil Morphology and Taxonomy

Soil formation in the Untersee Oasis mainly occurs on slightly weathered moraine deposits. The described soils are listed in Table 25.1. All soils were referred to Cryosol reference group according WRB classification (WRB 2014). The common character of described soils is domination of sand and coarse sand fractions in soil texture. This characteristic is inherited from moraine material. *Turbic-Hyperskeletic Cryosol Arenic*—these soils are the most common in Untersee Oasis. It occupies the positive moraine land forms along with lower parts of mountain slopes and lateral moraines. The soil profile is comprised of horizon Cryic lying on the moraine material. Soil cryoturbation process is expressed through cryogenic sorting of coarse material and formation of patterned grounds. Profile is illustrated in Fig. 25.4.

Turbic-Ornithic Leptosol Arenic—these soils are related to higher altitudes of the mountain slopes and to the top of lateral moraines where biogenic influence takes place. The influence is mainly attributed to ornitho fauna activity—Snow Petrels, occupying the mountains all across the Untersee valley. This influence is expressed in accumulation of biogenic material, mainly the stomach oil spit (mumyo) on the rock and soil surfaces. The biogenic accumulations can reach up to several decimeters thick. The soil profile comprises of horizon Cryic lying on the morainic/colluvial deposits with admixtures of mumyo material in upper 5 cm. The soil profile is presented in Fig. 25.5.

Turbic Cryosol Arenic—These soils occupy depression between moraine ridges and hills, covered by deposits of glaciofluvial origin. The soil profile matches to *Turbic-Hyperskeletic Cryosol Arenic* differing from the latter by lower content of coarse material. *Yermic Cryosol Clayic*-these soils are basically associated to out-

Table 25.1 Annotation of described soils

Taxa according to WRB for soil resources	Soil pit №	GPS		Area of survey
Turbic-Hyperskeletic Cryosol Arenic	1	S	71° 19′ 56.6″	Terminal type moraine ridges and hills of the Lake Untersee valley. Medium altitudes above the lake level (here and after—a.l.l)
		E	013° 27′ 08.3″	
	2	S	71° 19′ 56.9″	
		E	013° 27′ 01.2″	
	12	S	71° 20′ 55.3″	Dome-shaped elevation (presumably pingo) in the center of the Arkjosen cirque valley, 30 m in diameter and 7 m in height
		E	013° 33′ 43.3″	
Turbic-Ornithic Leptosol Arenic	3	S	71° 19′ 45.2″	Lateral moraines, mountain foot and slopes of the Lake Untersee valley. High altitudes a.l.l.
		E	013° 25′ 57.3″	
	4	S	71° 19′ 46.4″	
		E	013° 25′ 46.0″	
Turbic Cryosol Arenic	5	S	71° 19′ 52.6″	Depressions between moraine ridges and hills of the Lake Untersee valley. Low altitudes a.l.l.
		E	013° 26′ 28.9″	
	6	S	71° 19′ 59.0″	
		E	013° 26′ 24.4″	
Turbic-Skeletic Cryosol Arenic	7	S	71° 20′ 06.7″	Slope of the terminal type moraine ridge along the south coastal line of the peninsula. Lower coastal terraces of the Lake Untersee. Low altitudes a.l.l.
		E	013° 26′ 17.5″	
Yermic Cryosol Clayic	8	S	71° 19′ 52.6″	Bacterial mat spots. Gently sloping shores of the Lake Untersee. Low altitudes a.l.l.
		E	013° 27′ 06.5″	
Hyperskeletic Cryosol Arenic	9	S	No data	Sides of the inter-ridge depressions filled by meltwater under thick layer of ice (ponds). Foot of the Mulen mountain. Altitudes match to the surface of Anuchin's glacier. Anuchin's glacier
		E	No data	
Glacic Cryosol Arenic	10	S	No data	The slope of the terminal type moraine ridge at the edge of the Glacier. Approximating steepness of the slope is 35°. Anuchin's Glacier. Altitudes match to the edge of the Glacier
		E	No data	

(continued)

Table 25.1 (continued)

Taxa according to WRB for soil resources	Soil pit №	GPS		Area of survey
Haplic Cryosol Arenic	11	S	71° 20′ 28.4″	Lateral moraines. Foot of the mountains. Arkjosen cirque
		E	013° 31′ 37.5″	
Turbic-Limnic (Skeletic) Cryosol Siltic	13	S	71° 21′ 00.2″	Slope of dried glacial lake depression. Arkjosen cirque valley
		E	013° 33′ 17.5″	



Fig. 25.4 Morphology of Turbic-Ornithic Leptosol Antric



Fig. 25.5 Morphology of the typical example of Turbic Cryosol Arenic

crops of clays on gently sloping shores of Lake Untersee covered by bacterial mats. The soil profile comprises of overlapping horizons Yermic and Cryic lying on the lacustrine clays. Figure 25.6 *Turbic-Limnic (Skeletic) Cryosol Siltic*—these soils are associated to outcrops of sublimated bacterial mats on the slopes of lacustrine depression of dried lake in Arkjosen cirque valley. Results of geophysical survey of soils investigated showed a sharp increasing of apparent electric resistivity within the soil depth (Table 25.2). The superficial soil horizons showed the resistivity values about



Fig. 25.6 Morphology of the typical example of Yermic Cryosol

Table 25.2 Apparent electric resistivity of soils on the base of vertical electric resistivity sounding of soils

Soil depth, cm	Resistivity values, Ohmxm			
	Turbic-Hyperskeletic Cryosol Arenic, soil section № 1	Turbic-Hyperskeletic Cryosol Arenic, soil section № 2	Turbic-Ornithic Leptosol Arenic soil section № 4	Turbic-Skeletic Cryosol Arenic soil section № 7
10	32	21	165	20
20	8	171	806	147
30	203	1009	1866	497
40	148	1464	3077	618
50	175	2511	5442	1189
60	628	9028	7389	1134
70	461	8192	9876	2435
80	1151	11,934	14,016	3303
90	1473	17,678	21,761	1623
100	4800	18,767	30,861	8114
150	5776	39,603	72,782	2611
200	1008	87,265	129,203	202,028

20–165 Ohmxm, lower, in the middle part of active layer it was increasing of resistivity values till 200–1800 which well correspond to increasing of massive crystallic blocks of parent materials. The highest values of resistivity were fixed on the border of active layer and permafrost—1000–14,000 Ohmxm. This allows to conclude that soils investigated are sub-layered by permafrost not deeper than on 1 m (0.5–0.8 m in average).

25.4.2 Soil Chemical Properties and Particle Size Distribution

Data on basic chemical soil properties are given in Table 25.3. Most of the soils were slightly acid or close to neutral. Soil under the pronounced bird effect showed more acid values of pH. The content of hygroscopic water was low in all soils, besides the Yermic horizon. The values of the Loss on ignition were quite different in soil studied. The highest LOI value was fixed in ornitogenic soil. TOC content was less than 1% of fine earth, while the degree of nitrogen content in organic matter was high, which is possibly connected with increased values of the mineral nitrogen forma in some soil samples. Additional accumulation of ammonium nitrogen forms were fixed in ornitogenic soil and in Yermic horizon. The same fixed for phosphorous content in same soils.

The particle size of the soils investigated were characterizes by high content of coarse fractions (Table 25.4). But, at the same time sand, silt and clay fraction were presented in particle size composition as well. This indicates that soil formed on relatively weathered materials. One soil classified as Yermic Cryosol Clayic showed extremely high content of sandy fraction and clay particles portions. This is quite typical for desert Yermic materials. The majority of soil investigated (Turbic-Hyperskeletic Cryosol Arenic, Turbic-Ornithic Leptosol Arenic, Turbic Cryosol Arenic, Hyperskeletic Cryosol Arenic, Glacic Cryosol Arenic Haplic Cryosol Arenic) does not showed any content or almost full absence clay fraction. In general, for all soils analyzed, the dominance of fractions, sized between 1 and 0.05 mm was typical. This indicates the dominance of physical weathering.

25.5 Discussion

25.5.1 Soil Morphology and Taxonomy

The presence of the permafrost table not deeper than 1 m in all soils investigated allow to identify them was Cryosols according to WRB classification system (WRB 2014). Data on apparent resistivity of soils, derived form vertical electric resistivity sounding are in good correspondence with data about the permafrost table depth for this type of

Table 25.3 Chemical properties of the studied Cryosols

Soil pit №	pH (H_2O) ± 0.02, pH units	pH (KCL) ± 0.02, pH units	W^a ± 0.01, %	LOI^b ± 0.1, %	TOC^c ± 0.05, %	N_{tot}, %	C/N	$NH_4^+{}_{exc}$ ± Δ, mg/kg	P_2O_5 (available) ± Δ, mg/kg
Turbic-Hyperskeletic Cryosol Arenic									
1–1 (0–5 cm)	7.12	–	0.98	–	0.03	0.002	15.0	<5	<25
1–2 (5–20 cm)	7.07	–	0.67	2.5	0.04	0.003	13.3	<5	<25
2	6.86	6.71	1.33	–	0.09	0.006	15.0	<5	<25
12	7.17	7.00	0.63	2.3	0.06	0.009	6.7	<5	<25
Turbic-Ornithic Leptosol Arenic									
3	5.83	5.28	0.33	14.1	0.31	0.110	2.8	10.8 ± 1.6	220 ± 22
4	5.77	5.36	0.16	9.5	0.64	0.240	2.7	14.2 ± 2.1	195 ± 20
Turbic Cryosol Arenic									
5	6.91	6.72	0.18	1.1	0.59	0.190	3.1	<5	<25
6	6.86	6.69	2.29	4.8	0.21	0.022	9.5	<5	29 ± 7
Turbic-Skeletic Cryosol Arenic									
7	7.00	6.85	0.77	3	0.18	0.013	13.8	<5	<25
Yermic Cryosol Clayic									
8–1 (0–5 cm)	6.14	5.60	37.12	7.3	0.90	0.290	3.1	7.9 ± 2.4	96 ± 10
8–2 (5–20 cm)	6.11	5.50	38.09	8.0	0.80	0.290	2.8	6.0 ± 1.8	74 ± 7

(continued)

Table 25.3 (continued)

Soil pit №	pH (H_2O) ± 0.02, pH units	pH (KCL) ± 0.02, pH units	W[a] ± 0.01, %	LOI[b] ± 0.1, %	TOC[c] ± 0.05, %	N_{tot}, %	C/N	$NH_4^+{}_{exc}$ ± Δ, mg/kg	P_2O_5 (available) ± Δ, mg/kg
Hyperskeletic Cryosol Arenic									
9–1 (0–5 cm)	6.7	6.30	1.45	2.2	0.20	0.024	8.3	<5	<25
9–2 (5–20 cm)	6.64	6.41	1.12	3.4	0.30	0.017	17.6	<5	<25
Glacic Cryosol Arenic									
10–1 (0–5 cm)	6.85	6.70	0.41	3.1	0.14	0.009	15.6	<5	<25
10–2 (5–20 cm)	6.78	6.68	0.58	0.9	0.11	0.008	13.8	<5	<25
Haplic Cryosol Arenic									
11	6.76	6.55	0.95	1.5	0.15	0.01	15.0	<5	<25
Turbic-Limnic (Skeletic) Cryosol Siltic									
13	7.03	–	1.16	2.7	0.24	0.011	16.0	<5	<25

Notes [a]*W* hygroscopic water, [b] *LOI* loss on ignition, [c]*TOC* total organic carbon

Table 25.4 Particle size distribution of the studied Cryosols, mass fraction (%), $\Delta = 0.1\%$

Soil pit №	Particle size fractions											
	>10 mm	10–5 mm	5–2 mm	2–1 mm	1–0.5 mm	0.5–0.25 mm	0.25–0.1 mm	0.1–0.05 mm	0.05–0.01 mm	0.01–0.002 mm	0.002–0.001 mm	<0.001 mm
Turbic-Hyperskeletic Cryosol Arenic												
1–1 (0–5 cm)	18.3	8.2	9.3	6.8	10.5	11.3	20.1	8.7	2.8	2.5	1.1	0.4
1—2 (5–20 cm)	2.3	13.2	9.5	9.1	13.0	13.9	22.0	7.9	5.1	3.2	0.8	0.0
2	31.6	22.9	7.2	5.5	8.3	12.0	3.9	5.8	2.8	0.0	0.0	0.0
12	51.5	10.8	7.8	6.4	8.2	5.3	5.7	3.3	1.0	0.0	0.0	0.0
Turbic-Ornithic Leptosol Arenic												
3	23.0	12.5	11.4	9.4	11.2	10.3	13.3	5.3	1.9	1.2	0.5	0.0
4	19.8	9.2	8.4	10.3	13.9	17.0	18.2	1.4	1.2	0.6	0.0	0.0
Turbic Cryosol Arenic												
5	9.6	12.8	14.9	13.6	18.3	18.4	11.3	0.6	0.3	0.2	0.0	0.0
6	2.3	4.2	2.6	16.9	15.2	16.6	15.5	1.9	13.3	9.7	1.5	0.3
Turbic-Skeletic Cryosol Arenic												
7	3.4	3.5	4.3	6.5	19.8	37.2	9.3	2.7	7.8	4.5	0.9	0.1
Yermic Cryosol Clayic												
8–1 (0–5 cm)	0.0	0.0	0.0	0.1	0.1	0.2	0.4	0.3	49.5	28.7	7.0	13.7
8–2 (5–20 cm)	0.0	0.0	0.0	0.0	0.3	0.1	0.6	0.4	42.9	30.8	9.7	15.1

(continued)

Table 25.4 (continued)

Soil pit №	Particle size fractions											
	>10 mm	10–5 mm	5–2 mm	2–1 mm	1–0.5 mm	0.5–0.25 mm	0.25–0.1 mm	0.1–0.05 mm	0.05–0.01 mm	0.01–0.002 mm	0.002–0.001 mm	<0.001 mm
Hyperskeletic Cryosol Arenic												
9–1 (0–5 cm)	0.0	0.7	0.9	1.8	6.4	21.7	36.2	23.0	3.7	4.9	0.7	0.0
9–2 (5–20 cm)	0.0	1.5	0.7	0.0	4.2	22.1	36.4	23.7	4.8	6.0	0.6	0.0
Glacic Cryosol Arenic												
10–1 (0–5 cm)	14.2	8.3	20.5	7.9	24.6	15.1	8.1	1.3	0.0	0.0	0.0	0.0
10–2 (5–20 cm)	9.6	12.8	14.9	13.6	18.3	18.4	11.3	0.6	0.4	0.1	0.0	0.0
Haplic Cryosol Arenic												
11	10.2	5.6	14.7	13.1	9.0	21.2	10.4	8.2	4.2	3.4	0.0	0.0
Turbic-Limnic (Skeletic) Cryosol Siltic												
13	21.1	17.0	14.7	18.6	18.0	7.4	3.0	0.2	0.0	0.0	0.0	0.0

pedo-environments in Antarctica (Hrbáček et al. 2018). Most of the soils investigated have a turbic features, expressed in middle part of soil profile, many of them were classifies as soils with arenic features which well corresponds with data of particle size distribution. The Yermic soil, located on the gentle slope of Untersee Lake was uncommon part of the soil cover and the presence of this soil could be caused by specific features of parent materials. The pedodiversity of investigated oasis is comparable with the diversity of soils in other adjacent oasis's (Bockheim 2015). Turbic processes, accompanied by surface accumulation of coarse and sandy fraction are key soil formation process, expressed in formation of corresponding horizons. The closest analogue of the territory in terms of soil diversity is the Schirmacher oasis (Bockheim 2015). The main difference of soil cover of Untersee oasis from soils Schirmacher oasis is absence of B horizon, presented by altered fine earth. The reason of this difference could be a result of more severe climatic conditions. This also result in absence of Folic or Histic horizons in soils of the studied area because of lack of precipitation and short period of biological activity, which is key factor of organic matter accumulation (Bolter 2011). In general, soil cover of the investigated territory is typical for extra arid continental zoned of Antarctic (Campbell and Claridge 1987) and presented mainly by hyperskeletic soils with well pronounced features of turbic features and cryogenic mass exchange.

25.5.2 Soil Chemical Properties and Particle Size Distribution

Soil chemical properties were quite different between the samples analyzed (Table 25.3). Thus majority of soils were close to neutral or slightly acid. This could be related to accumulative geochemical regime in Untersee landscape. In general the soils studied are, are more close to the alkaline values of the pH than soils of Schirmacher oasis (Bockheim 2015). This difference may come from increased aridity and less precipitation rate in Untersee landscape, than in Schirmacher one. The pH values of investigated soils are comparable with previously obtained for soils of Marie Bird Land (Abakumov and Lupachev 2013). The difference between pH values which reflects the degree of cation exchange capacity development was quite different in various soils. In general, the most pronounced differences in two types of acidity level were characteristic for more acids soils than for neutral ones. This could be evidence that more acids soils have more altered fine earth with developed cation exchange capacity. In any case, low content of clay fraction is reason of undeveloped exchangeable acidity forms. The second reason of low soil acidity is low content of organic matter in soils studied (Shamrikova et al. 2017). Another reason of relatively low soil acidity is amount of precipitation, characteristic for intercontinental oasis's, which normally result in alkalinization of the environment and accumulation of water soluble salts (Campbell and Claridge 1987) This hypothesis is in correspondence with low values of apparent electric resistivity, which are lower, that in more

acid soils with absent of salts and accumulation organic matter in the superficial horizons (Abakumov 2017).

The absence of Folic and Histic horizons in soils investigated indicates that the probability of organo-mineral interactions is not so high, than in soils of Maritime Antarctic (Bolter 2011). The content of TOC was low in all the soils investigated if one compare with previously published data (Abakumov 2010a, b; Abakumov and Alekseev 2018). Nevertheless, low content of soil organic carbon is typical for many interlard landscapes of Antarctica (Abakumov 2010a, b). The highest enrichment of soil by nitrogen (on the basis of C/N ratio) was characteristic for soils with pronounced effect of ornitogenic factor. But, in general the C/N ratio was higher than in soils of continental oasis's, investigated previously (Abakumov et al. 2016). Ornitogenic effect results in accumulation of available forms of ammonium and nitrogen, which is in good agreement with previously published data (Abakumov 2010a, b). Extended C/N ratio in soils, which are not effected by birds can be related to accumulation of mineral forms of nutrient, which is quite typical for interland environments of Antarctica (Prietzel et al. 2019). The TOC content is normally lower than in soils of adjacent Schirmacher oasis (Bockheim 2015), but comparable with soils of Clements massive (Abakumov and Andreev 2014), presented by weak developed coarse turbic soils. In any case, the TOC content in soils investigated are lower in 3–15 times than in soils of Maritime Antarctica (Bolter 2011; Abakumov 2010a, b) and this illustrates low degree of mineral particles alteration under the effect of organic matter.

Particle size distribution reflects both factors: initial texture of parent material and degree of soil alteration due to weathering processes under the pedogenesis process. Data of soil texture are given in Table 25.4. Data obtained illustrates that most of soils are dominated by a gravel fraction and sand components. This is a characteristic feature for interland environments of Antarctica (Campbell and Claridge 1987). The content of the fine earth in some soils investigated is less that 30% which indicated very low degree of pedogenic alteration of the soil material. This is quite typical feature for soils of continental Antarctic (Glazovskaya 1958; Abakumov 2010a, b). Our data on clay content showed very low portions of this fraction in exception of Yermic soil. This could be re result of low degree of weathering in most of the investigated soils. Yermic soil is only lithological exception, but not the indicator of some more expressed process of fine earth alteration. The particle size distribution in the fine earth presented mainly by fraction sized between 1.00 and 0.05 mm, this is result of physical soil weathering, but not real chemical affected alteration. This well corresponds with data, obtained previously for Schirmacher oasis (Bockheim 2015) and corresponds with data on soils of various continents environments (Abakumov 2010a, b). The low content of fine fractions and prevalence of sandy particles result in a very low sorption ability of soils and low content of hygroscopic water. This also well correspond to low content of organic matter in soils investigated. Thus, the internal surface which can be suitable for biogenic-abiogenic interactions is not well developed and this fact can result in implementation of biogenic-abiogenic interactions in cracks on inside the stones, like it was described by Mergelov et al. (2018).

Data on available form of nutrients were expected for soils with low degree of mineral part alteration. Nevertheless, two soils showed increased content of phosphorous and ammonium nitrogen. In first case that was the soil with pronounced affect of birds. This is obvious result of terrestrial soils subsidence by organic substances and mineral compounds due to orhnitohoria (Abakumov et al. 2016). Second case is enriched accumulation of the nutrients in Yermic horizon of Cryosol. This is related to increased sorption ability of the clayey textured fine earth.

25.6 Conclusions

Conditions of soil formation within the Untersee Oasis are characterized by following elemental soil processes: Cryoturbation, Cryogenic structure formation, Frost cracking, Cryogenic mass exchange, Humus formation (in soils developing under bacterial mats), Organic carbon accumulation (including ornitogenic origin). A characteristic feature of the flow of cryoturbation processes in soils is the sorting of the soil skeleton in size, as a result of which the particle size distribution of the upper daily soil surface is facilitated, the content of particles larger than 10 mm increases. Also, the manifestation of cryoturbation is reflected in the formation of specific forms of micro and mesorelief—stone rings.

The consequence of the course of cryogenesis as a factor of pedogenesis is also the formation of frost cracks in the debris (moraine). The manifestation of the dynamics of the active layer of frozen soils is expressed in the formation of the grooves of punching-positive closed forms of cryogenic relief arising as a result of uneven segregation, injection (diapiric) ice formation, or their combination, in rocks.

Among the 13 soil sections were plotted in the characteristic positions of the main relief forms two types (Cryosols, Leptosols) and 8 subtypes of soil characteristic of the Unter-Seee Oasis were identified, among which 3 lithological varieties are distinguished.

The soils of the Untersee oasis are characterized by a weakly differentiated soil profile, in which the Cryic horizon is located, which lies directly on the soil-forming rock—sandy-loam morainic deposits. The predominant soil-forming rocks of the Untersee are the glacial, water-glacial sandy loam and gravel deposits with a large content of fragments of different sizes, as well as lacustrine-glacial sandy-loamy and loamy clayey deposits. A characteristic feature of glacial and water-glacial deposits is their sorting as a consequence of the cryoturbation process. The main forms of the mesorelief of the oasis include complexes of moraine hills and ridges of finite type, ozoid ridges, drumlins, zandra fields, cones of removal, stone rings, and mounds of swelling. So, biogenic-abiogenic interactions in soils of investigated plots are on very initial stage and this could be resulted from low intensity of biogenic accumulative processes in severe conditions of internal continental oasis's of Antarctica.

Acknowledgements This work was supported by Russian Foundation for Basic Research, Project No: 18-04-00900.

References

Abakumov EV (2010a) Particle-size distribution in soils of West Antarctica. Eurasian Soil Sci 43(3):297–304

Abakumov EV (2010b) The sources and composition of humus in some soils of West Antarctica. Eurasian Soil Sci 43(5):499–508

Abakumov E (2017) Vertical electric resistivity sounding of natural and anthropogenically affected cryosols of fields Peninsula Western Antarctica. Czech Polar Rep 7(2):109–122

Abakumov EV, Andreev MP (2014) Soils of Clements Massif, Eastern Antarctica. In: Abstract from V international symposium "Biogenic-abiogenic interactions in natural and anthropogenic systems", on CD

Abakumov E, Alekseev I (2018) Stability of soil organic matter in Cryosols of the maritime Antarctic: insights from 13C NMR and electron spin resonance spectroscopy. Solid Earth 9(6):1329–1339

Abakumov E, Lupachev A (2013) Soils of Marie Byrd Land, West Antarctica. Eurasian. Soil Sci 46(10):994–1006

Abakumov EV, Parnikoza IY, Vlasov DY, Lupachev AV (2016) Biogenic–abiogenic interaction in Antarctic ornithogenic soils. Lecture Notes Earth Syst Sci 9783319249858:237–248

Andersen DT, McKay CP, Lagun V (2015) Climate conditions at perennially ice-covered lake Untersee, East Antarctica. J Appl Meteorol Climatology 54(7):1393–1412

Arinushkina EV (1970) Guide for chemical analysis of soils. Moscow State University, Moscow

Bormann P, Fritzsche D (1995) The Schirmacher Oasis, Queen Maud Land, East Antarctica, and its surroundings. In: Bormann P, Fritzsche D (eds) The Schirmacher Oasis, Queen Maud Land, East Antarctica, and its surroundings. Justus Perthes Verlag, Gotha, 448 p

Bockheim JG (ed.) (2015) The Soils of Antarctica. Springer

Bolter M (2011) Soil development and soil biology on King George Island Maritime Antarctic. Polish Polar Res 32(2):105–116

Campbell IB, Claridge GGC (1987) Antarctica: soils, weathering processes and environment

Glazovskaya MA (1958) Weathering and initial pedogenesis in Antarctica. Nauchn Dokl Vyssh Shk Geol-Geogr Nauki 1:63–76

Hrbáček F, Vieira G, Oliva M, Balks M, Guglielmin M, de Pablo MÁ, Molina A, Ramos M, Goyanes G, Meiklejohn I, Abramov A, Demidov N., Fedorov-Davydov D, Lupachev A, Rivkina E, Láska K., Kňažková M, Nývlt D, Raffi R, Strelin J, Sone T, Fukui K, Dolgikh A, Zazovskaya E, Mergelov N, Osokin N, Miamin V (2018) Active layer monitoring in Antarctica: an overview of results from 2006 to 2015 Polar Geography 1–16

Kaup E, Loopmann A, Klokov V, Simonov I, Haen-del D (1988) Limnological investigations in the Untersee Oasis (Queen Maud Land, East Antarctica). In: Martin J (ed) Limnological studies in Queen Maud Land, East Antarctica. Valgus, pp 28–42

Levitan M, Kononkova N, Luksha V, Roshina I (2012) Holocene lithificates at the slopes of the Untersee mountain valley East Antarctica April. Geochem Int 50(4):50–361

Loopmann A, Kaup E, Klokov V, Simonov I, Haendel D (1988) The bathymetry of some lakes of the Antarctic Oases Schirmacher and Untersee. In: Martin J (ed) Limnological studies in Queen Maud Land (East Antarctica) Valgus, pp 6–14

Mergelov N, Mueller CW, Prater I, Shorkunov I, Dolgikh A, Zazovskaya E, Shishkov V, Krupskaya V, Abrosimov K, Cherkinsky A, Goryachkin S (2018) Alteration of rocks by endolithic organisms is one of the pathways for the beginning of soils on Earth. Sci Rep 8(1):3367

Prietzel J, Prater I, Colocho Hurtarte LC, Hrbáček F, Klysubun W, Mueller CW (2019) Site conditions and vegetation determine phosphorus and sulfur speciation in soils of Antarctica. Geochim Cosmochim Acta 246:339–362

Rastvorova OG (1983) Soil physics manual. Leningr. Gos. Univ, Leningrad (in Russian)

Simonov IM, Stackebrandt D, Haendel E, Kaup H (1985) Reportonscientificinvestigationsatthe Untersee and Obersee Lakes, Central Dronning-Maud-Land (east Antarctica). Geodätische und Geophysikalische Veröffentlichungen, I 12:8–26

Shamrikova E., Deneva S, Kubik O, PunegovV, EV. Kyz'yurova, Bobrova Yu, Zueva OM. (2017) Acidity in organic horizons of arctic soils on the Barents Sea coast Eurasian. Soil Sc 50(11):1283–1293

USDA Soil Taxonomy (2014) United States Department of Agriculture Natural Resources Conservation Service 12th edn

WRB (2014) World reference base of soil resources. World soil resources report, No 106. FAO, Rome

Walkley A, Black IA (1934) An examination of the Degtjareff method for determining soil organic matter and a proposed modification of the chromic acid titration method. Soil Sci 37(24):29–38

Zazovskaya EP, Fedorov-Davydov DG, Alekseeva TV, Dergacheva MI (2015) Soils of Queen Maud Land. In: Bockheim J. (ed) The Soils of Antarctica

Chapter 26
Levels of Biogenic-Abiogenic Interaction and Structural Organization of Soils and Soil-Like Bodies in Antarctica



Aleksei V. Lupachev, Stanislav V. Gubin and Evgeny V. Abakumov

Abstract Pedogenic processes of transformation and accumulation of organogenic matter and its interaction with the mineral matrix of the soils are very poor-expressed in Antarctica. Very often, these processes show up in a very special ways that can rarely be observed in the well-studied soils of moderate latitudes and even in the northern polar environments. The majority of the Antarctic soils do not develop well-expressed uppermost organomineral horizons. Mostly they are presented with the poorly aggregated mix of mosses' and lichens' detritus with the coarse-textured debris and rarely show macromorphological evidences of biogenic-abiogenic interaction. Using of state-of-the-art modern methods of soil science (scanning electron microscopy, micro- and mesomorphological analysis etc.) along with the regular methods of morphological analysis of soil profiles and spatial analysis of the soil cover allow distinguishing different levels of the structural organization of soils in the Antarctic region. The fine earth adhesion, forming of the organomineral coatings and films, deep alteration of primary minerals and ornithogenic impact on the soil material and profile structure is evident at all the studied levels of soil organization. Their manifestation degree rises from the continental Antarctica to the Subantarctic regions and from the soil-like bodies with no or very poor-expressed vegetation to the soils with relatively well-developed uppermost organo-horizons.

Keywords Antarctica · Soils · Cryosols · Leptosols · Scanning electron microscopy · Micromorphological analysis

A. V. Lupachev (✉) · S. V. Gubin
Institute of Physico-Chemical and Biological Problems in Soil Science RAS, Puschchino
Institutskaya st. 2/2, 142290 Moscow, Russian Federation
e-mail: a.lupachev@gmail.com

E. V. Abakumov
Department of Applied Ecology, Saint Petersburg State University, 16-line, 2, Vasilyevskiy Island, 199178 Saint Petersburg, Russian Federation

© Springer Nature Switzerland AG 2020

O. V. Frank-Kamenetskaya et al. (eds.), *Processes and Phenomena on the Boundary Between Biogenic and Abiogenic Nature*, Lecture Notes in Earth System Sciences,
https://doi.org/10.1007/978-3-030-21614-6_26

26.1 Introduction

The occurrence of pedogenic processes in soils of Antarctica still stays a very debatable scientific issue especially for the soils that develop in the high-latitudinal regions of the continental Antarctica due to their very poor expression in the majority of soils and soil-like bodies here. Soils here significantly differ from ones that are well studied in the moderate latitudes of the northern hemisphere and even from soils of the high Arctic (Bockheim et al. 2015). These two macroregions of the planet have passed through completely different geological history and palaeoenvironmental conditions of glaciation and deglaciation cycles. Vast territories in the high Arctic regions became nearly completely ice-free about 9–11 Kyrs before present. More of that, the significant part of the Arctic region (mainly in the North-East of Eurasia) has never been covered with continental glaciers and the soils here could continue developing even under the synlithogenic conditions through the whole Pleistocene period (Elias and Brigham-Grette 2013). The glaciation history of the Antarctic region is completely different. The relatively small and sporadically distributed oases (around 1–2% territory of the Antarctic continent) were partly covered by the continental glacier and revealed their modern relatively ice-free state only about 7–9 Kyrs before present and in some cases even later (Verkulitch 2009; Verkulitch et al. 2012). The absence of the uppermost organogenic and organo-mineral horizons, poor-expressed differentiation of the soil horizons and their lateral continuity, the lack of structure of soil material and rare evidences of clay minerals' forming are regular for the soils here. The main limiting factors for the plant cover distribution here are the lack of the liquid water, low temperatures, harsh winds and high level of the ultraviolet radiation.

The classification of the majority of the soils and soil-like bodies that form under the extremely harsh conditions of the Antarctic oases is very complicated due to the absence of the common approaches for their diagnostics. By now the most abridged approach to these natural biogenic-abiogenic bodies is given in the part of the USDA Soil Taxonomy (Soil Survey Staff 2010) which was developed specially for the Antarctic soils (Bockheim et al. 2006). Nevertheless, one should keep in mind that this approach was mainly based on the experience of studying of the soils and soil-like bodies of the extracontinental mountainous region of Dry Valleys (Central Victoria Land) that is situated roughly at the 75–77° S and significantly differs from other ice-free areas of continental Antarctica and surely from the maritime regions in terms of climatic and geological conditions.

Submicro-, micro- and mesomorphological methods are well known as useful tool for investigation of soil transformation under natural and human-impacted conditions. Methodology of the classical soil micromorphology provides the required information about the soil development at the micro level, such as changes in fine earth composition and soil plasma evolution (Kubiena 1938, 1970; Stoops 2009). These methods are widely used for analysis of soil palaeoprocesses (Rusakov et al. 2018), soil restoration on post-mining environments (Abakumov et al. 2005), soil elementary process in different environments (Lebedeva et al. 2010; Abakumov et al. 2013) and specification soil classification aspects (Kubiena 1970). However,

the micromorphological methods have been applied to study Antarctic soils organization only in few studies (Abakumov et al. 2013; Meier et al. 2017).

Despite the relatively low thickness and spatial discontinuity of the superficial organo-mineral bodies in the Antarctic environments and the absence of the most of the features that are specific for the regular soils [even for the high latitudes of the northern hemisphere (Bockheim and Tarnocai 1998)] the number of diagnostic features that allow distinguishing soils and soil-like bodies which show evidences of biogenic-abiogenic interaction and have all of the levels of structural organization (e.g. the formation of the elementary soil particles and structural aggregates, organo-mineral interaction and stabilization of the soil organic matter, forming of the vertical paragenetic system of the soil horizons in the profile, the regularity of the spatial structure of the soil cover etc.). The main objective of the present study was to obtain the very essence of the pedogenesis in weakly developed soils and soil-like bodies—the interaction of the organogenic and mineral matter through the investigation of the Antarctic soil structural organization.

26.2 Objects and Methods

Different natural and human-affected soils were investigated while studying the surrounding environments of the maritime ("Bellingshausen"), coastal ("Molodeznaya", "Leningradskaya", "Russkaya") and interior ("Bunger Oasis", "Novolazarevskaya") scientific stations of the Russian Antarctic Expedition.

"Bellingshausen" station (62.197944° S, 58.960872° W) is situated at the Fildes Peninsula (King-George Island, South Shetland Islands). Gentle topography dominates here with a wide central plain at the elevation of around 40–50 m a.s.l., several other smaller plains at different altitudes (from 80 to 100 m a.s.l.) and three massive flat-topped volcanic remnants with numerous rocky outcrops and maximum heights from 120 to 150 m a.s.l. This area mainly consists of volcanic rocks (andesite basalts and their pyroclastics) with small outcrops of tuffs, volcanic sandstones and agglomerates (Smellie et al. 1984). Climate here is cold and relatively moist with mean annual air temperature of −2.2 °C and mean annual precipitation around 350–500 mm (Michel et al. 2014). Mean daily air temperatures above 0 °C last here for up to four months during the austral summer.

"Molodeznaya" scientific base (67.667646° S, 45.860785° E) is in the Thala Hills oasis that is located in the western part of Enderby Land. It consists of two parts—Molodezhny and Vecherny sites—with a total area of 20 km^2. The Molodezhny site extends for 8.3 km along the coast, its maximum width is 2.7 km, and it is bordered by ice sheet from the south. The maximum elevation is 109 m a.s.l., and the total area is 13 km^2. The Molodezhny site of the Thala Hills oasis is a hilly area with ridges. The ridges are 1 km long and up to 150 m wide. Depressions located between the ridges are mostly filled with snow patches, local glaciers, and lakes. The relative height of the ridges is about 10–40 m. The parent materials comprise drift and colluvium that

provide a discontinuous and thin cover. Rock outcrops and patches of granulite-facies metamorphic and plutonic rocks dominate in the area (Dolgikh et al. 2015).

"Leningradskaya" base (69.501339° S, 159.392974° E) is situated in the North Victoria Land. It is a very mountainous region, with elevations ranging from sea level to about 3720 m (Mt. Hewson). The climate reflects these differences in elevation, with mean annual air temperatures ranging from −25 to −35 °C and mean annual precipitation ranging from 100 to 300 mm (Bockheim 2015). Vegetation is limited to isolated cryptogams. Upper Precambrian metasedimentary rocks are dominant here, with smaller areas of Cenozoic volcanic rocks, Beacon sandstone, Ferrar dolerite, and granite intrusives of varying ages (Bockheim 2015). The entire area is underlain by ice-cemented permafrost and the active-layer depths range from 8 to 70 cm in depth.

"Russkaya" station, the southernmost coastal Russian Antarctic station located on the Berks Cape of the Hobbs Coast (74.755212° S, 136.811186° W). One more study site in the relatively nearby was on the Lindsey Islands (73.603379° S, 103.032672° W). This territory consists of low (<150–200 m a.s.l.) rocky mountains composed of biotite–hornblende plagiogneiss (Lupachev and Abakumov 2013; Lupachev et al. 2015). Glacial processes often terrace relatively gentle slopes of the mounts. In some depressions of the relief, thin layers of loose sediments are accumulated. The mean annual air temperature here is −12.4 °C, the warmest month is January (−2.5 °C), and the coldest month is August (−19.8 °C). The absolute minimum of air temperatures is −46.4 °C, and the absolute maximum is +7.4 °C. Because of the coastal position of the station and the low temperatures in this area, the mean annual relative humidity of the air is high (78.7%).

"Bunger Oasis" scientific base (66.292569° S, 100.771091° E) is a coastal range on the Knox Coast in Wilkes Land in Antarctica, consisting of a group of moderately low, rounded coastal hills represented by schists, gneisses, and pegmatites, overlain by marine sediments and morainic drift and notably ice free throughout the year (Blume and Bolter 2015). Glaciers surround the Bunger Hills. On the southeast, the Bunger Hills is bordered by the steep slopes of the Antarctic ice sheet, on the south and west by outlet glaciers, and on the north by Shackleton Ice Shelf, which separates the area from the open sea. The ice-free area measures 450 km^2.

"Novolazarevskaya" station is located in the Schirrmacher Oasis (70.776506° S, 11.822197° E). It is presented with the Precambrian metamorphic rocks, including gneisses and crystalline shale. Ultramafic intrusive bodies and numerous pegmatite veins are found locally (Zazovskaya et al. 2015). The mean annual air temperature here is −10.3 °C; the temperature of the coldest month (August) is −17.9 °C, and the temperature of the warmest month (January) is −0.4 °C. The active layer of permafrost in the Schirrmacher oasis ranges from 30 to 120 cm in depth.

All the field procedures were carried out according to the "ANTPAS Guide" (Bockheim et al. 2006). Exact points of studying were chosen according to the structure of the soil cover at the study sites following the representativeness approach. Soil pits were excavated unless the large boulders, solid rock or ice-cemented permafrost prevented further digging. Soil material was sampled from every diagnostic horizon according to the structure of each soil profile. GPS location and elevation of each

site was determined. Site features were described, including structure and density of vegetation cover; depth of active layer, ice texture of permafrost (if present); the degree of boulder and debris weathering; and structure and dimensions of cryogenic forms of relief (Bockheim and Tarnocai 1998; Beyer et al. 1999). The following soil properties were measured in the field: 10% hydrochloric acid test to distinguish carbonates in the soil profile; potassium ferricyanide test to detect redoximorphic features (Birkeland 1984).

Submicroscopic investigation of soils was carried out using the electronic scanning microscope Vega 3 Tescan (Tescan-Orsay Holding, Czech Republic). Thin sections were investigated with use of polarization microscope Leica DFC 320 (Leica Microsystems, Germany) under the transmitted and polarized light and using optical microscope Carl Zeiss Axiostar (Zeiss AG, Germany) at 10×–50× magnification under the transmitted and polarized light as well. The following soil micromorphological properties have been investigated: soil microfabric, spatial arrangements of fabric units, soil particles distribution, elements of microstructure and character of organic matter. Terminology used in this paper is published by Stoops (2009), also by Gagarina (2004) manuals and Gerasimova et al. (2011) review, where details of microorganization of soil were described in details. Normally, soil micromorphology was studied in the transmitted light, but in some cases with aim to clarify mineral weathering we used polarized light. Mesomorphological studies were carried out using the USB-microscope MiView M200UM (Cosview Technologies, China Republic) at 10×–200× magnification with the images taken under the reflected light.

26.3 Results

Samples that were taken from the horizons of the Antarctic soils of different genesis were analyzed using the submicro-, micro- and mesomorphological methods. The clear and abundant features of the pedogenic processes' occurrence were obtained in the studied soils. The fine earth adhesion, forming of the organomineral coatings and films, deep alteration of primary minerals and ornithogenic impact on the soil material and profile structure is evident at all the studied levels of soil organization. Their manifestation degree rises from the continental Antarctica to the Subantarctic regions and from the soil-like bodies with no or very poor-expressed vegetation to the soils with relatively well-developed uppermost organo-mineral horizons.

The most widespread features of the microaggregates' forming in the soils of Antarctica is the adhesion of the ultrafine earth particles on the surfaces of the stone gravel and smaller grains, belonging to the coarse fraction of the parent rock debris (Figs. 26.1, 26.8 and 26.10). Antarctic soils have shown various content of the fine earth—from 10 to 50%. This indicates the prevalence of the coarse fraction of weathered debris in the soil microfabric. The skeletal fraction/fine earth ratio strongly depends on the genesis of the parent rocks, the degree of their alteration and portion of sedimentary material. The human impact on soils that is realized in form of the

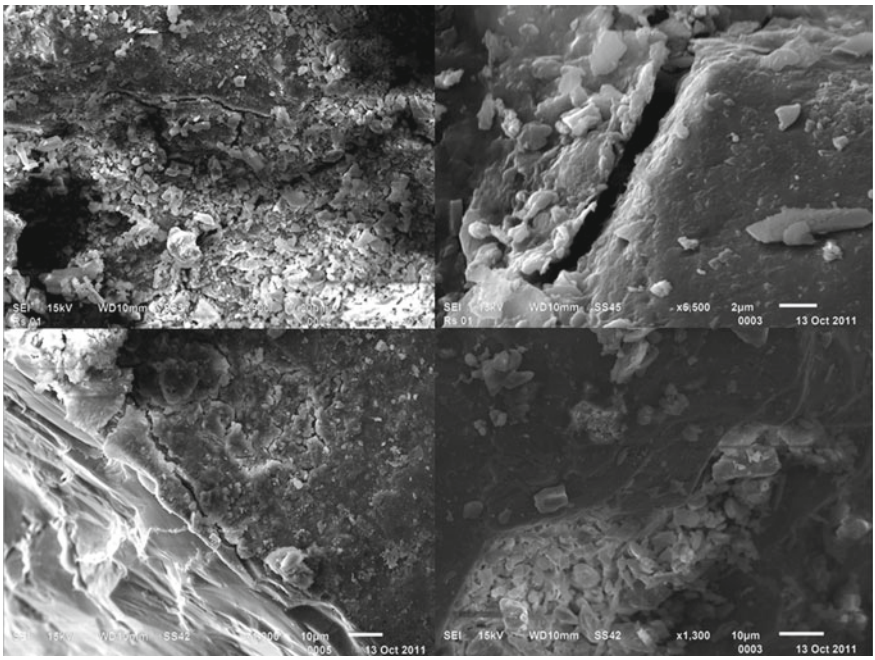


Fig. 26.1 "Russkaya" station. The fine earth particles aggregated on the parent rock grains

sporadic gasoline spills result in the formation of organic pseudoplasma on the surfaces and inside the soil aggregates and these gasoline and motor oil leaks provide chemical agents that highly increase the fine earth's adhesive properties (Fig. 26.2). This micromorphological feature appears to be typical for the soils of Antarctica in the surroundings of the diesel stations and fuel storages located close to permanent and seasonal scientific stations.

Micromorphological investigation has shown that despite the coarse texture of the soil material the microzones of the relatively stable soil mineral matrix can be formed. The most often observed types of the microstructure of the matrix are granular and sandy-plasmic along with the microareas of the clay plasma. These microareas have features of fluidity and optically oriented clay accumulation and can show features of ferrugination (Fig. 26.3). Some mineral grains of the parent rocks are covered with thin clayish films and even cutans and this feature additionally strengthens the fact of clay mobilization in the given stable microzones of these soils.

In the soil material of the interior oases (e.g. Schirrmacher Oasis, Bunger Oasis) where sedimentary and sedimentary-metamorphic rocks occur, the features of the calcium carbonates neogenesis and redistribution can often be obtained. In some cases, the microcrystallic calcareous aggregation and cementation of the skeletal particles can be obtained (Fig. 26.4). Rare clay-carbonate cutans in the soil pores and cavities can be obtained here as well (Fig. 26.5).

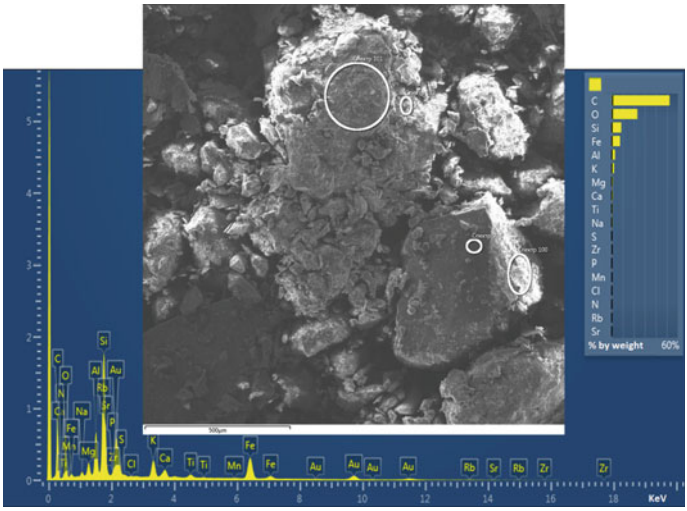


Fig. 26.2 "Russkaya" station. The fine earth particles aggregated on the parent rock grains in the soils under the diesel gasoline spill

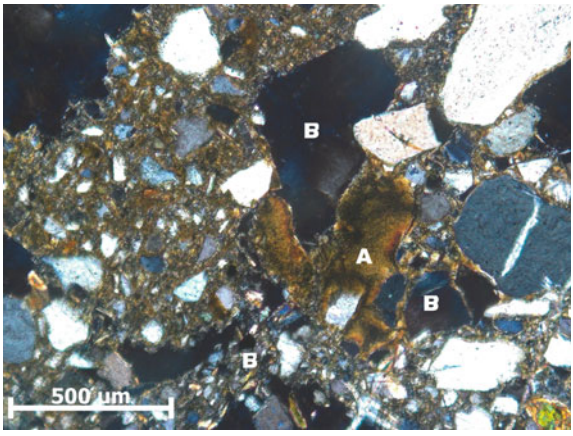


Fig. 26.3 "Novolazarevskaya" station. The clots of the optically oriented clay (**a**) in the relatively stable microzones of the skeletal fraction (**b**). X N

Another result of biogenic-abiogenic interaction is the formation of stable organo-mineral coatings on the surface of mineral particles, even the quartz grains (Fig. 26.6). The initial mechanism of this interaction was obtained at the mesomorphological level in the mixture material of the coarse fraction, fine earth, plant detritus and remnants of the ornithogenic origin. This type of organo-mineral interaction plays an important role in stabilization of the soil surface which is important for stable existing of soil cover in conditions of extremely high wind velocity.

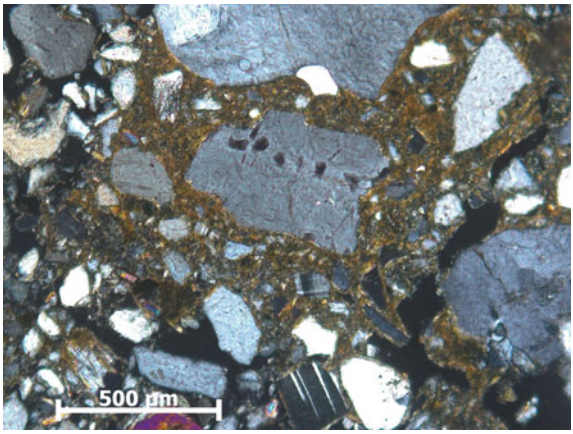


Fig. 26.4 "Novolazarevskaya" station. Calcareous cementation of the skeletal fraction by the clay-carbonate plasma. X N

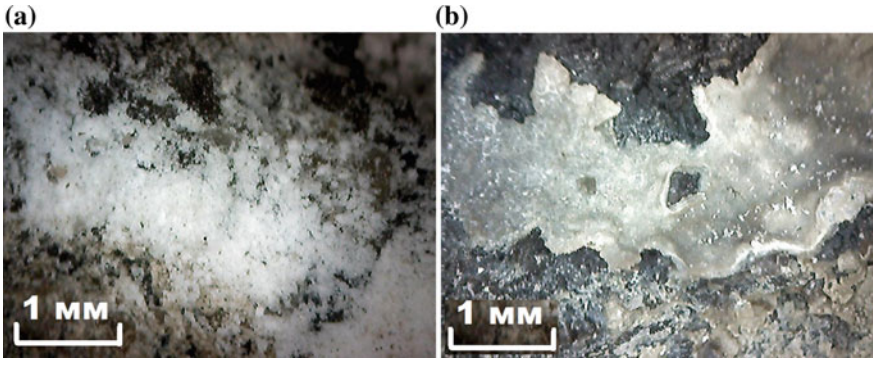


Fig. 26.5 "Bunger Oasis" station. Carbonate neogenesis on the uppermost (**a**) and lowermost (**b**) surfaces of the gravel and boulders

Plasma structure in the ornithogenic soils has well-expressed mobile-laminar structure with inclusions of shaggy zones in the guano material. It covers the grain surfaces very densely and forms thick films and wide microzones of compacted skeletal structure. In some microzones, the clots and concretions are forming and in the peripheral parts of the plasma and the microscopic crystals of biogenic phosphates and sulphates are forming (Fig. 26.7). Plasma includes the abundant fungi hyphae and sporangia as well as the colonies of the unicellular algae (Fig. 26.8).

Soils that are formed on the coarse rock debris in the surroundings of stations "Russkaya" and "Leningradskaya" are characterized by the relatively high content of several minerals of the mica group (muscovite, biotite and phlogopite) in the soil matrix. The presence of these minerals often indicates the low degree of the initial parent materials' transformation under the influence of biogenic and abiogenic

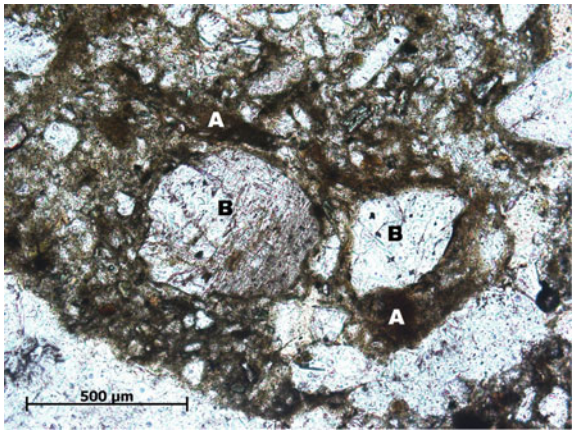


Fig. 26.6 "Novolazarevskaya" station. Organo-mineral coatings and films (**a**) on the surfaces of the mineral grains (**b**). II N

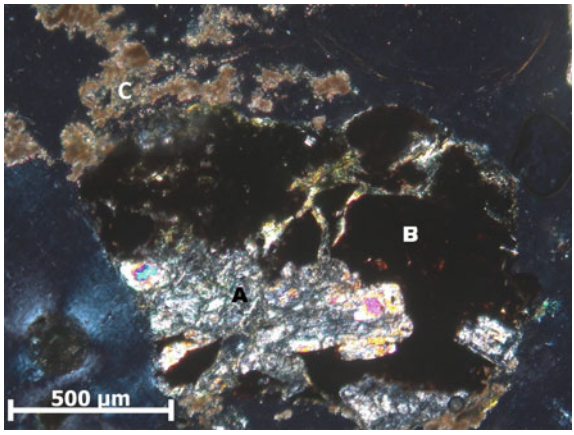


Fig. 26.7 "Bellingshausen" station. Weathered mineral particles (**a**), mobile-laminar structure of the organogenic plasma (**b**) and the microcrystals of the biogenic salts (**c**). X N

weathering processes (Gagarina 2004; Abakumov et al. 2013). Unaltered grains of mica (muscovite and biotite) are presented in various projections in the Fig. 26.9a, b, c and d. The most evident presence of these minerals is seen under the polarized light. The initial stage of biotite weathering is presented on the Fig. 26.9e and f, here one can see the destruction of this mineral on the periphery and the accumulation of the iron oxides at some spots. Uppermost soil horizons demonstrate alteration and weathering of minerals. Here the alteration of the mica is evident in a porous media of soil in surroundings of "Leningradskaya" station (Fig. 26.9l). Another important feature of the Antarctic soils is the sericitization of plagioclases, which can be considered as the alteration of the primary minerals of the soil-forming rocks (Fig. 26.10).

The highest level of the biogenic-abiogenic interaction in a pedological sense was revealed in the structure of the soil cover in the Antarctic oases. It is realized in forms of combination and can be complicated by the complexes of the soil cover

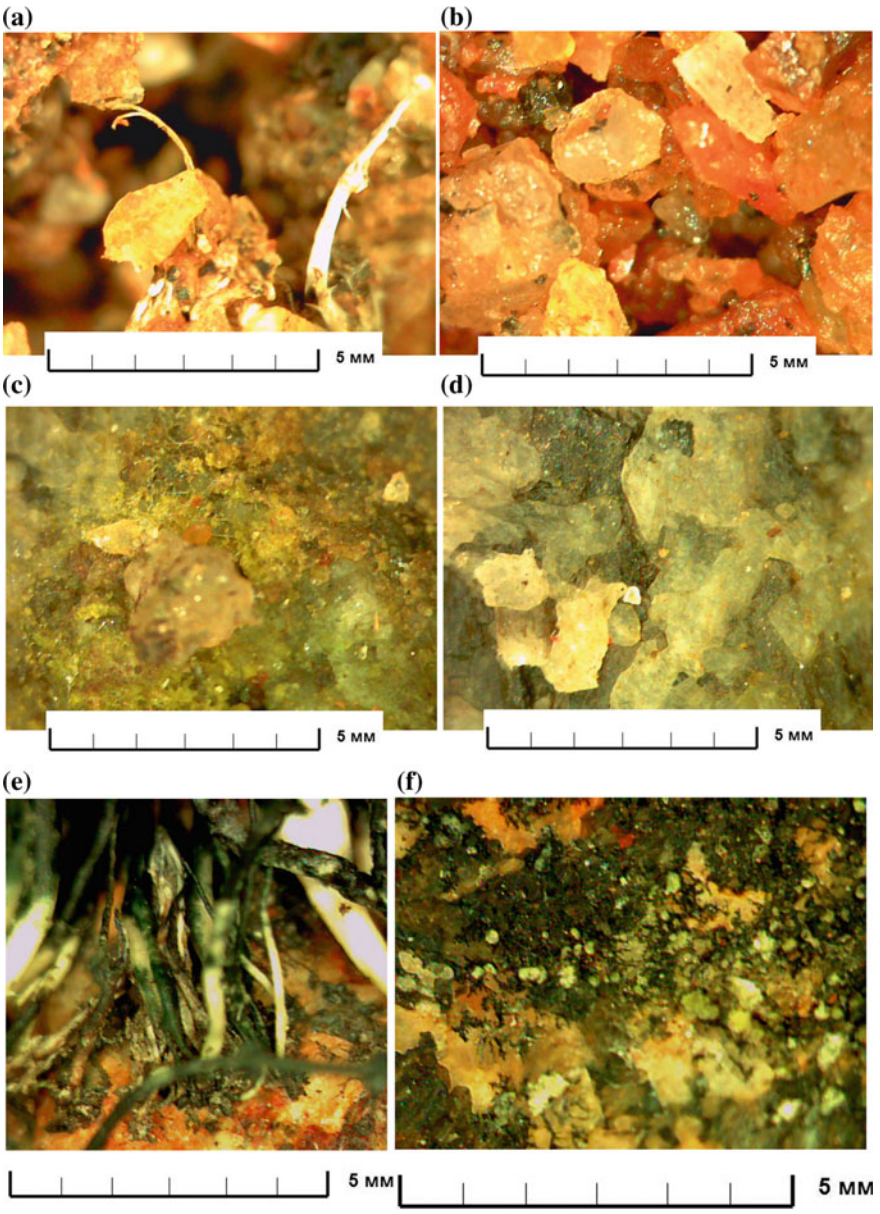


Fig. 26.8 "Russkaya" station. Mesomorphological features of regular Cryosols and Cryosols with the ornithogenic impact. **a** ornithogenic matter remnants; **b** fine earth of Cryosols; **c** association of mineral particles with organic remnants of *Prasiola crispa*, green nitrophilous algae; **d** parent material; **e** ingrowth of the lichen into the parent rock; **f** accumulation of organo-mineral fine earth on the mineral surface; **g** lichen material on the surface of parent rock boulder; **h** accumulation of organic particles of the surface of quartz

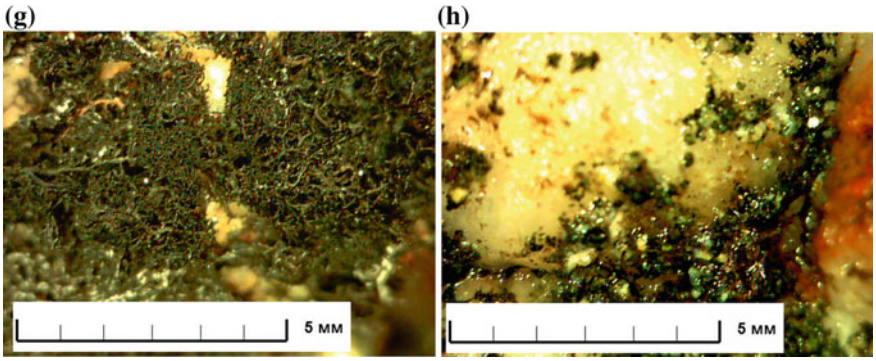


Fig. 26.8 (continued)

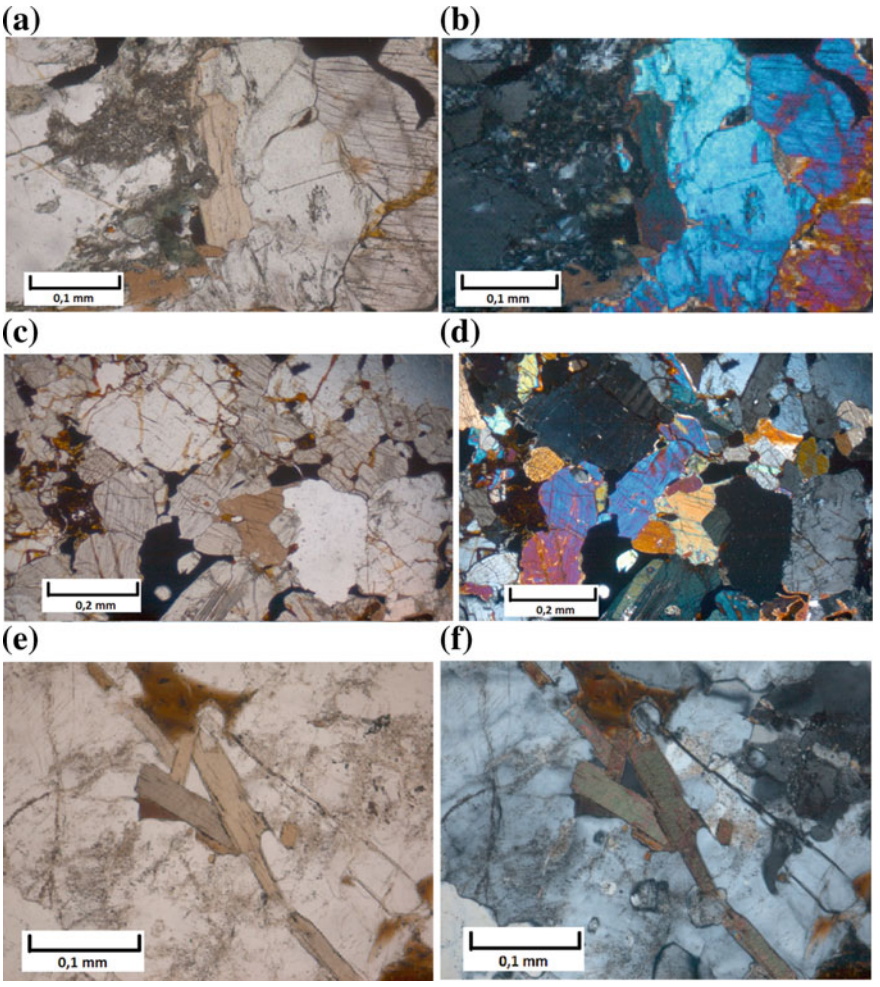
on the each element of the mesorelief. Such complexes are mostly formed in the environments rich with accumulated or transited liquid water and underlied by the permafrost or the rock bed and are clearly distinguished by the very specific surface microrelief—stone pavements, rock circles and polygons, rock stripes etc. In these cases, the central parts of the circles and polygons as well as the intrastripe linear areas that are enriched with fine earth are most often poor with plant cover. In opposite, the peripheral areas that are super-enriched with gravel and boulders serve as the micro wind shelters and additional water supply for the moss pads, lichen thallomes and vascular plants (Fig. 26.11).

26.4 Discussion

Authors intentionally do not consider below the issues of the pedogenic processes at the atomic, ion-molecular and elementary soils particles' levels because these processes are more or less the same in the most of the soils and mainly do not show direct dependence from the environmental conditions such as climate and vegetation cover but depend on the parent rock genesis (Birkeland 1984). Thus, the first and the very lowest level of soil structure organization that is considered and discussed further is the level of the soil micro- and macroaggregates and pedogenic neoformations.

26.4.1 Soil Aggregates and Neoformations

The process of the soil aggregates' formation and the adhesion of the fine earth material is most clearly expressed in the soils that are developed on the sedimentary (or in some case on the sedimentary-metamorphic) rocks that are less stable to the physical and biogenic weathering and provide fine-textured debris. However, even in



◄**Fig. 26.9** Elements of the micromorphological structure of the Antarctic soils: "Russkaya" station. Unweathered mica on the skeletal particle surface (**a** transmitted light and **b** polarized light); "Russkaya" station. Unaltered parent soil material (**c** transmitted light and **d** polarized light); "Leningradskaya" station. Weathering of mica on the surface of quartz (**e** transmitted light and **f** polarized light); Lindsay islands. Guano on the surface of plagioclase (**g** transmitted light and **h** polarized light); Lindsay islands. Guano aggregation of mineral particles, transported by wind (**i** transmitted light and **j** polarized light); "Leningradskaya" station. Sericitization of the feldspars—formation of mica mineral on the surface (**k** polarized light); "Leningradskaya" station. Mica weathering in a porous media of soil (**l** polarized light)

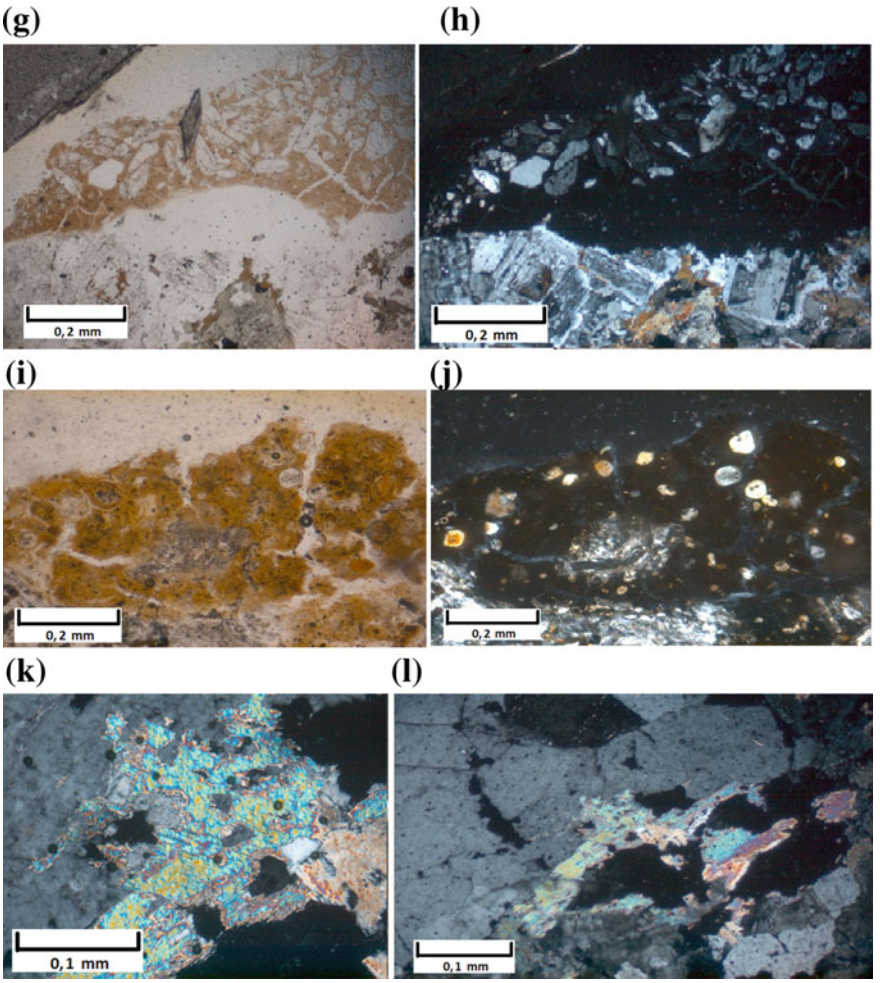


Fig. 26.9 (continued)

the debris material of the coarse-grained parent rocks such as granites and gneisses this process can be obtained (Fig. 26.1). The fine earth accumulation and its further aggregation take place more intensively depending on the degree of the superficial vegetation cover development. Relatively thick organogenic material prevents fine earth material from aeolian redistribution in the environment and additionally helps to accumulate the allochthonous material derived from the surrounding areas that are not covered with vegetation. The process of the fine earth particles' aggregation can also be triggered by the anthropogenic impact in the human-affected soils and soil-like bodies (Fig. 26.2). The intense use of the tracked vehicles physically grind the parent rock debris and provide sufficient amount of the fine earth that could hardly been derived by the regular processes of the physical and biogenic weathering in the



Fig. 26.10 "Molodeznaya" station. Fine earth accumulation in the rhizoidal sphere of the moss pads



Fig. 26.11 "Russkaya" station. Rock-sorted polygons with the vegetation-free central part and moss-lichen cover in the peripheral part

very same environmental conditions. It is well known that the fine earth content in the uppermost horizons of the human-affected soils can reach 30–50% and in the very same soils that are not affected by tracked vehicles its content rarely exceeds 10–15% (Abakumov 2010, O'Neill et al. 2015).

The micromorphological analysis have shown that the basic elements of Antarctic soils' microstructure are coarse-textured debris particles and intrasoil cavities; the most often observed form of the clay distribution in the fine earth material is the diffusive form (Kubiena 1970; Abakumov et al. 2013). This feature is determined by the very low degree of the biochemical weathering of parent rock material due to the relatively low rate of the vegetation colonization of the soil surface. The harsh climatic conditions of the continental Antarctica strongly limit the rock weathering by the nearly only physical factors. The formation of the optically oriented clay, clay-carbonate plasma and features of the carbonate cementation were only obtained

in the soils of the interior oases where sedimentary and sedimentary-metamorphic calcareous rocks are distributed (e.g. Schirrmacher and Bunger oases; Figs. 26.3 and 26.5). The neoformations of the relatively thick carbonate films were regular in the uppermost horizons, covering the boulders and gravel. This fact also points at the relatively stable microstructure of the soil material. The evidence of the seasonal dynamics of the hydrothermal regime and thus the carbonates' aggregation can be partly proven by the occurrence of their different morphological forms on the uppermost and lowermost surfaces of the coarse debris' fragments and boulders (Fig. 26.5a and b).

The features of the biogenic-abiogenic interaction of the organogenic and mineral material of soils here (except for the widely expressed and well-described accumulation of the plant detritus within the coarse-textured soil material) is expressed in the forming of the humus plasma coatings and films on the surfaces of the grains of the skeletal fraction which are in the direct interaction with the rhizoidal sphere of the moss pads or with the talloms of lichens or algae-bacterial mats (Fig. 26.6). The relatively low thickness of these coatings can be determined by the environmental factor: the lack of the liquid water during the most of the warm season along with the intense percolation in the coarse-textured material during the snow melting in the early austral summer. On the other hand, the harsh climatic conditions prevent the active accumulation and interaction of the biogenic humus compounds within the material of the parent rock debris.

The very specific type of the organogenic plasma that is formed in the ornithogenic and postornithogenic soils under the modern and abandoned penguin rookeries is the humus-like plasma and it represents another wide-distributed example of organo-mineral interaction in the different environments of Antarctica. It can be accumulated on the surface of the coarse grains in form of the guano and poorly decomposed ornithogenic material (fragments of feathers, eggshells, tissues and bones) as well as in form of organic colloidal plasma (Fig. 26.7). The formation of the biocrusts is also determined here by living and dead remnants of the nitrophilous algae colonies (mainly from *Prasiola crispa*) on the soil surface and stone boulders and gravel. The colonization of the surface by these algae seems not to be lithologically specific. In conditions of nitrogen-enriched substrate, the colonization is quite aggressive and very intensive, which is typical for the initial stages of ecogenetic succession, caused by the high content of easily available nutrients. Fresh organic material is light brown and after desiccation it forms a rubber-like mantle, which covers debris and shields it from removal of fine-earth material by strong winds. The abundance of coarse angular debris fragments increases downward. If the rookery becomes inactive, cryogenic sorting of mineral material begins to move coarse fragments upward to the soil surface burying the organic matter with time. Later, these environments become more appropriate for the colonization by lichens and mosses and the degree of the biogenic-abiogenic interaction intensively grows.

Features of the mesomorphological structure of the soils, sampled in the surroundings of the "Russkaya" station such as accumulation of the fine-earth, organomineral interaction with mosses and lichens, organic films and coatings on the mineral surfaces are presented on the Fig. 26.8. Accumulation of fresh ornithogenic material

that is mixed with the mineral particles triggers the formation of primitive aggregates, which is not evident in case if parent rocks' material is not affected by birds. Interaction of lichen thallomes with mineral particles in non-ornithogenic soil is expressed at the mesomorphological level in adhering of the lichens on the skeletal particles, accumulation of organic microlayer on the stone surface, accumulation of organic lichen remnants and their further decomposition on the stone surfaces and organomineral aggregation. Organic horizons of soils that are formed in the vicinity of the "Leningradskaya" station show evident formation of the porous media and free space in topsoil in comparison with almost monolith massive crystallic rock, composed by quartz, mica and feldspars.

26.4.2 Soil Horizons and Profile Organization

Antarctic soil profiles rarely exceed a half-meter depth. They are extremely lithogenic—the percent of gravel and boulders can reach 90–95% in the uppermost horizons and 50–70% in the central and lowermost parts of the soil profile. The coarse fraction/fine earth ratio can be 95–98%/2–5% and insignificantly drops downwards down to 70–80%/20–30% (Abakumov 2010; Lupachev and Abakumov 2013). The soil material under the lichen associations most often lacks aggregation at meso- and microlevel. In the rare cases, the densely mixed lichen thallomes can consolidate the mineral material of the uppermost soil horizons and prevent it from the wind erosion. The soil morphology diagnostics in the pedons under the lichen associations can often be only possible basing on the change of the particle size and the abundance of the ferruginous films and thin fine-earth coatings ("silt cappings") on the coarse mineral particles.

In case of the moss pads growing on the surface of the soils the rhizoidal sphere encases the coarse gravel and boulders and the smaller skeletal particles (< 1 cm) are densely intermixed with the thin rhizoids (Fig. 26.10) and the very specific aggregates ("strings of beads") are forming and may serve as the analogue of the similar structure on the roots of the flowering plants in the circumpolar soils of northern hemisphere. The relatively poor-expressed stripes and microtongues of humus impregnation in the fine earth material can also characterize such soils. The soils under algae-bacterial mats are very often have features of gleyic and stagnic processes. Dark-gray horizons rich with sulphates, bluish gleyic and reddish ferruginous zones and morphones are typical for these soils so the organization of pedon can be obtained relatively clearly. In some cases when soils have significant supply of liquid water and in presence of the ice-cemented permafrost or impermeable rock bed the structure of the genetic horizon can be disturbed by the processes of cryoturbation.

The very special type of the uppermost organogenic soil horizons is the birds' guano that serves as the substrate for the very special type of the plant cover even for Antarctica. The dominance of the nitrophilous algae and bacterial mats and the sporadic occurrence of the vascular plats are regular for the environments of the modern and abandoned penguin rookeries. The well-expressed succession of the plant cover

is clearly observed while studying these soils. The degree of the guano toxicity drops with the processes of water leaching and freezing/thawing cycles. During the time the guano deposits become dark-colored and dense thus preventing the uppermost soil horizons from the wind erosion and drying out. The mix of the biogenic and abiogenic material contains plant and animal tissues, feathers, bones, eggshells etc. Contrarily to the majority of the Antarctic soil these ones have maximum fine earth content in the uppermost horizons due to the adhesive properties of the guano material that prevents as well from the intense wind-snow corrasion. Is case of the abandoned rookeries the cryoturbation and rock sorting processes may move the gravel and boulders upwards thus burying the fragments of the former uppermost guano cover. The role of the accumulation and adhesive "consumption" of different size mineral particles is important for soil formation especially in conditions of strong wind and aeolian processes in Antarctica.

The occurrence of the relatively wide distributed spatial continuity of the plant cover (widespread moss pads or lichens) or zoogenic organic material (guano coats) is quite rare in the continental and even in the maritime Antarctica and occur most often in subantarctic environments. Thus the distinguishing of the pedon vertical organization is often complicated due to the highly differing microclimatic and geomorphological conditions even in the scale of micro- and mesorelief here.

26.4.3 Elements of the Soil Cover Structure

Spatial soil cover structure is one of the highest levels of biogenic-abiogenic interaction in the environment in terms of the pedogenic processes development rate. Long-term geological history of glaciation and deglaciation cycles; relatively mild climatic conditions; abundant and diverse fauna and flora; and the dominance of the sedimentary rocks (e.g. in the High Arctic) allowed soils of the northern hemisphere to develop a continuous, dense and thick cover with strong hierarchy of the elements. In opposite, the harsh bioclimatic conditions of Antarctica, rare and specific plant and animal species as well as the unique geological and geomorphological conditions the relatively wide in terms of area soil cover is very rare and poor-expressed here.

The most widespread group of the soil cover elements that is presented in the Antarctic environments is the combination of the highly lithogenic insufficient with liquid water soils under the lichens [including endolithic soil-like bodies (Mergelov et al. 2012)] on the rocky watersheds and relatively steep slopes in the mesorelief structure and the fine earth rich soils well-supplied with liquid water under the moss-lichen associations and algae-bacterial mats on the shallow slopes, local depressions and wind shelters. Soil complexes of the environments are rich with disintegrated debris and form stone pavements, rock circles and polygons, rock stripes etc. Depending on the availability of the liquid water and shelter from harsh winds and snow corrasion, the regular redistribution of the flora species takes place. One of the soil cover structure phenomena here that have to be further investigated in details is the

forming of the soil mosaics, which presumably depends on the parent rock genesis (Fig. 26.11).

At the moment, authors develop the approach for the distinguishing of the soil mosaics in the soil cover of the Antarctic oases. This mosaic can possibly be determined by the weathering susceptibility of the parent rocks and its debris, the structure of the vegetation cover, moisture-holding capacity of the fine earth material and other significant soil properties that make pedogenesis possible in the harsh environmental conditions of Antarctic oases.

26.5 Conclusions

Pedogenic processes of transformation and accumulation of organogenic matter and its interaction with the mineral matrix are poor-expressed in the soils in Antarctica and take place most intensively in the soils that are supplied with the liquid water and are sheltered from the harsh winds that allow vegetation to actively colonize the soil surface.

Studied soils and soil-like bodies in Antarctica show the number of diagnostic features (the fine earth adhesion, forming of the organomineral coatings and films, deep alteration of primary minerals, ornithogenic impact of guano etc.) that allow distinguishing biogenic-abiogenic interaction at all the levels of structural organization from elementary soil particles and aggregates up to the spatial structure of the soil cover.

The distinguishing of the pedon vertical organization and spatial structure of the soil cover is often complicated due to the highly differing microclimatic and geomorphological conditions in Antarctica. The degree of macromorphological pedon structure manifestation rises from the continental Antarctica to the Subantarctic regions.

The most widespread groups of the soil cover elements that are presented in the Antarctic environments are the combinations, complexes and mosaics of the water-insufficient and highly lithogenic soils under the poorly expressed vegetation cover and biogenic water-sufficient soils under the relatively well-developed vegetation cover or guano coats occupying different elements of the meso- and microrelief.

Acknowledgements Studies were carried out according to the Russian Federation governmental task 0238-2016-0013 and partly supported by Russian Fund for Basic Researches (18-04-00900a).

References

Abakumov EV (2010) Particle-size distribution in soils of West Antarctica. Eur Soil Sci 43(3):297–304

Abakumov EV, Gagarina EI, Lisitsyna O (2005) Land reclamation in the Kingisepp area of phosphorite mining. Eur Soil Sci 38(6):648–655

Abakumov EV, Gagarina EI, Vlasov DY, Sapega VF (2013) Micromorphological features of the fine earth and skeletal fractions of soils of West Antarctica in the areas of Russian Antarctic stations. Eur Soil Sci 46(12):1219–1229

Beyer L, Bockheim JG, Campbell IB, Claridge GGC (1999) Genesis, properties and sensitivity of Antarctic Gelisols. Antarctic Sci 11:387–398
Birkeland PW (1984) Soils and geomorphology. Oxford University Press, New York
Blume HP, Bolter M (2015) Soils of Wilkes land. In: Bockheim J. (ed) The soils of Antarctica
Bockheim JG (2015) Soils of Victoria Land. In: Bockheim J. (ed) The soils of Antarctica
Bockheim JG, Balks MR, McLeod M (2006) ANTPAS guide for describing, sampling analyzing and classifying soils of the Antarctic region Earth. ANTPAS, UK
Bockheim JG, Tarnocai C (1998) Recognition of cryoturbation for classifying permafrost-affected soils. Geoderma 81:281–293
Bockheim JG, Lupachev AV, Blume HP, Bölter M, Simas FNB, McLeod M (2015) Distribution of soil taxa in Antarctica: a preliminary analysis. Geoderma 245–246:104–111. https://doi.org/10.1016/j.geoderma.2015.01.017
Dolgikh AV, Mergelov NS, Abramov AA, Lupachev AV, Goryachkin SV (2015) Soils of Enderby Land. In: Bockheim J. (ed) The soils of Antarctica
Elias SA, Brigham-Grette J (2013) Late Pleistocene glacial events in Beringia. In: Elias SA, Mock CJ (eds) Encyclopedia of quaternary science, 2nd edn. Elsevier, 2:191–201
Gagarina EI. (2004). Micromorphological method of soil investigation. S-Petersburg. (in Russian)
Gerasimova MI, Kovda IV, Lebedeva MP, Tursina TV (2011) Micromorphological terms: the state of the art in soil microfabric research. Eur. Soil Sci. 44(7):804–817
Kubiena WL (1938) Micropedology. Collegiate press, Ames, Iowa
Kubiena WL (1970) Micromorphological investigations of Antarctic soils. Antarctic J 5(4):105–106
Lebedeva M, Gerasimova M, Golovanov D (2010) Systematization of the topsoil fabrics in soils of the arid lands in northwest of central Asia. World Congress of Soil Science, Soil Solutions for a Changing World (1–6 August 2010). Brisbane, Australia. Published on DVD. 96
Lupachev AV, Abakumov EV (2013) Soils of Marie Byrd Land (West Antarctica). Eur Soil Sci 46(10):994–1006
Lupachev AV, Abakumov EV, Abramov AA, Goryachkin SV (2015) Soils of Marie Byrd Land. In: Bockheim J. (ed) The Soils of Antarctica
Mergelov NS, Goryachkin SV, Shorkunov IG, Zazovskaya EP, Cherkinsky AE (2012) Endolithic pedogenesis and rock varnish on massive crystalline rocks in East Antarctica. Eur Soil Sci 45(10):901–917
Meier L, Krauze P, Prater I, Scholten T, Wagner D, Kühn P, Mueller C (2017) Soil micromorphology, geochemistry and microbiology at two sites on James Ross Island, Maritime Antarctica. In: Geophysical Research Abstracts. vol. 19. EGU 2017-12618-3
Michel RFM, Schaefer CEGR, López-Martínez J, Simas FNB, Haus NW, Serrano E, Bockheim JG (2014) Soils and landforms from Fildes Peninsula and Ardley Island, Maritime Antarctica. Geomorphology 225:76–86. https://doi.org/10.1016/j.geomorph.2014.03.041
O'Neill TA, Aislabie J, Balks MR (2015) Human impacts on soils. In: Bockheim J. (ed) The soils of Antarctica
Rusakov A et al (2018) Late pleistocene paleosols in the extra-glacial regions of Northwestern Eurasia: pedogenesis, post-pedogenic transformation, paleoenvironmental inferences. Quat Int 501(A):174–192.https://doi.org/10.1016/j.quaint.2018.03.020
Soil Survey Staff (2010) Keys to soil taxonomy (11th edit.). U.S. Dep. Agric., Natural Resources Conserv. Serv. Washington, D.C
Smellie JL, Pankhurst RJ, Thomson MRA, Davies RES (1984) The Geology of the South Shetland Islands: VI. Stratigraphy, Geochemistry and Evolution. British Antarctic Survey Scientific Reports 87 (85)
Stoops G (2009) Evaluation of Kubiena's contribution to micropedology. At the Occasion of the Seventieth Anniversary of his book "Micropedology". Eur Soil Sci 42(6):693–698
Verkulitch SR (2009) Conditions and regime of the last deglaciation in the edge zone of Antarctica. Earth Cryosphere 2:73–81 (in Russian)

Verkulitch S, Pushina Z, Tatur A, Dorozhkina M, Sukhomlinov D, Kurbatova L, Mavludov B, Savatyugin L (2012) Holocene changes of environments on the Fildes Peninsula, King-George Island (Western Antarctica). Probl Arctic Antarctic 3(93):17–27 (in Russian)

Zazovskaya EP, Fedorov-Davydov DG, Alekseeva TV, and Dergacheva MI (2015) Soils of Queen Maud Land. In: Bockheim J. (ed) The soils of Antarctica

Chapter 27
Modeling Biogenic Weathering of Rocks from Soils of Cold Environments



Sofia N. Lessovaia, Ruben Gerrits, Anna A. Gorbushina, Yury S. Polekhovsky, Stefan Dultz and Gennady G. Kopitsa

Abstract Morphologically simple and microbially dominated ecosystems termed "biofilms" have existed on Earth for a long period of biosphere evolution. A model biofilm combining one heterotroph and one phototroph component was used in a laboratory experiment to simulate biogenic weathering with two different specimens of basic rock samples from the soil profiles. The rocks fragments from the regions of cold environments of Eurasia, where abiotic physical processes, including rock disintegration initiated by freezing–thawing cycles, represent the most probable scenario of rock weathering, were subjected to biological colonization. The rock fragments were represented by dolerite and metagabbro amphibolites. Polished sections of the rock samples were inoculated with the model microbiological consortium of the oligotrophic fungus and the phototrophic cyanobacteria (biofilm). After 3 month runtime of the experiment the progress of rock weathering was derived from the growth of the biofilm on the rock surfaces. The model biofilm visualization on the rock surface of polished sections illustrated their stronger development namely on dolerite in comparison with metagabbro amphibolite. The findings confirmed the higher sensitivity of dolerite to biogenic weathering due to (i) mineral association, in which quartz was absent and (ii) porosity providing higher specific surface area

S. N. Lessovaia (✉) · Y. S. Polekhovsky
Institute of Earth Sciences, Saint Petersburg State University, Universitetskaya nab. 7/9, 199034, Saint Petersburg, Russia
e-mail: s.lesovaya@spbu.ru

R. Gerrits · A. A. Gorbushina
Federal Institute of Materials Research and Testing (BAM), Berlin, Germany

Department of Earth Sciences and Department of Biology Chemistry Pharmacy, Freie Universität Berlin, Berlin, Germany

S. Dultz
Institute of Soil Science, Leibniz Universität Hannover, Hannover, Germany

G. G. Kopitsa
B.P. Konstantinov Petersburg Nuclear Physics Institute NRC KI, Gatchina, Russia

I.V. Grebenshchikov Institute of Silicate Chemistry RAS, Saint Petersburg, Russia

© Springer Nature Switzerland AG 2020

O. V. Frank-Kamenetskaya et al. (eds.), *Processes and Phenomena on the Boundary Between Biogenic and Abiogenic Nature*, Lecture Notes in Earth System Sciences,
https://doi.org/10.1007/978-3-030-21614-6_27

for biotic—abiotic interaction influenced by the occurrence of micro-porosity in the rock.

Keywords Biogenic weathering · Rock leaching · Internal pores · Fractal structure · Biofilm formation

27.1 Introduction

Understanding rock weathering processes in cold climates is a highly relevant research topic—as in the cause of climate transformation the biggest changes are expected to happen in this type of climates. Shallow soils derived from and underlain by the solid rocks present an especially important factor in landscape evolution (Bockheim 2015; Minasny et al. 2015; Bojko and Kabala 2016) and rock fragments weathering in this part of a critical zone are subjected to active biotic—abiotic interactions (Zhang et al. 2016; Chizhikova et al. 2016).

Rock weathering due to abiotic physical processes is the most acceptable scenario of rock weathering in the cold environments. The rock disintegration initiated by freezing–thawing cycles results in fragmentation/disintegration and thus leads to a significant increase in surface area, which is decisive for the chemical weathering rate (Arnaud and Whiteside 1963; Allen 2002; Velde and Meunier 2008).

The most efficient and omnipresent agents of biological weathering during the long period of biosphere evolution have been morphologically simple and microbially dominated ecosystems termed "biofilms". The biofilms actively involved in weathering form at interfaces of solid materials with gas or liquid phases represent a unique structure capable of multiple impacts on substrate and element cycles (Burford et al. 2003; Gorbushina 2007). Adopting the approach of Velde and Meunier (2008) the interactions between primary minerals and solutions often take place in confined or semi-confined microenvironments such as pores rather than in a bulk solution, the biofilms move forward inside the solid rock through the connective pore system. The dissolution of the primary minerals creates new voids which are only partly filled by secondary minerals promoting further (bio)chemical weathering by the increase of specific surface area (Navarre-Sitchler et al. 2009).

Biologically induced weathering proceeds either biomechanically (directly through biomass penetration and indirectly due to shrinking/swelling of the biomass or accompanying extracellular matrix) or biochemically due to acidolysis, redoxolysis, complexolysis, and metal accumulation in biomass (Gadd 2007, 2017). Through numerous studies of microbial rock colonization sufficient information has been gained to allow the selection of a few typical "rock settlers" and to study their joint development in a simple laboratory system (Gorbushina and Broughton 2009). Such model biofilms consisting of one heterotroph and one phototroph component have been successfully applied in different weathering and isotope fractionation studies (Seiffert et al. 2014, 2016; Pokharel et al. 2017, 2018). Elements' depletion including

Ca and Mg of the set of minerals was revealed as a result of biogenic weathering initiated by this model fungal/cyanobacterial biofilm (Seiffert et al. 2014, 2016).

In the present study we subjected two rock samples, sensitive to biochemical weathering by (i) chemical and mineralogical composition and (ii) generation of an internal connective pore system by frost weathering from soil profiles of the cold regions of Eurasia to a biochemical weathering experiment with model biofilm formation. The results of a prolonged in vitro contact between fungal/cyanobacterial biofilm and metagabbro amphibolite and traprock (dolerite) were micromorphologically analysed to quantify and visualise the interaction of model biofilm on these types of reactive rocks.

27.2 Materials

27.2.1 Solid Rock Samples' Description

The solid rock fragments used in the experiments were collected from Holocene soil profiles underlain by the solid rocks. The first study plot on metagabbro amphibolite was situated in the northern taiga subzone of the Polar Urals that is a part of the Ural Mountains in the Arctic Circle. The GPS coordinates of the soil profile location were 66°48′31.2″N and 65°46′20.1″E, altitude of ~120 m. A profile of acidic stony Epileptic Entic Podzol (Pit Y-05-07) classified according to World Reference Base for Soil Resources (WRB 2006) has formed on a ridge made up by metagabbro amphibolite stretching along the river Sob (Lessovaia and Polekhovsky 2009). The ridge is characterized by a flat summit with steep east and gradual west slopes illustrating that the stone fragments from the soil profile is mostly a result of rock disintegration and subsequent redistribution of local material. The rock fragments were sampled from the bottom BC horizon (24–30 cm) underlain by solid rock.

The second study plot on traprock (dolerite) was located in the Central Siberian Plateau. The Central Siberian Plateau with its flood basalt complex (traprocks) is one of the largest areas of platform volcanism in the world. The spatial distribution of traprocks is estimated to be 1500×10^3 km^2, with a total volume 911×10^3 km^3 (Ross et al. 2005). The key plots for present study belong to the central part of the basaltic province and include the vicinities of the town of Tura on the bank of the Nizhnyaya Tunguska River. It was located on the narrow (300 × 100 m) summit area. The birch with rare larch (*Larix gmelinii*) open forest and bush–dwarf–shrub—moss plant cover was described in the studied area. The GPS coordinates of the soil profile location were 64°17′49.5″N and 100°14′24.0″E at an altitude of 418 m. The slightly perceptible patterned ground was on the surface. No permafrost or even cold materials at the bottom of the profile were found. The profile of Endoleptic Entic Podzol (Hypoturbic) (WRB 2006) was attributed as a soil on "saprolite with coherent altered rock" according to the gradation of rock weathering (Meunier 2005). The

rock fragments identified as dolerite were sampled from the spodic (Bhs) horizon (8–14 cm) (Lessovaia et al. 2014).

27.2.2 Model Biofilm Description

A model biofilm combining one heterotroph and one phototroph component: oligotrophic fungus *Knufia petricola* strain A95 combined with phototrophic cyanobacteria *Nostoc punctiforme* (Gorbushina and Broughton 2009) was used for a laboratory experiment to examine the continuum of microbial interactions that leads to stable rock colonization.

27.2.3 Experiment Design

The runtime of the experiment was 3 months, in which thin polished section made from the solid rocks (metagabbro amphibolite and dolerite) were investigated. The polished sections of both rocks were inoculated with the model microbiological consortium of the oligotrophic fungus and the phototrophic cyanobacteria. The study allows to investigate the weathering potential of the primary colonizers on the bare rocks. This approach was used previously to study several minerals weathering enhanced by model biofilm (Seiffert et al. 2014).

27.3 Methods

27.3.1 Rock Fragments Studying (Before Experiment)

For petrographic and micromorphological analysis of the rocks' fragments sampled from the soil horizons were impregnated with a resin, polished and studied in thin sections by optical microscopy using Zeiss Axio-plan 2 and Polam P-312 microscopes.

To determine the micro-morphology of the connective pores and to detect closed pores in the rock fragments, a modification of Mercury intrusion porosimetry using the intrusion of a molten alloy (Wood's metal) and subsequent electron microscopy on the polished sections was used (Lloyd et al. 2009). This method allows for an improved description of the pore textural characteristics (e.g. the presence of fractures and voids formed upon dissolution) and a visualization of secondary minerals in the pore space. The eutectic alloy of 50% Bi, 25% Pb, 12.5% Sn, and 12.5% Cd by weight has a melting point at 78 °C. Sections of the rocks were intruded with the molten alloy at 100 °C with a pressure of 55 MPa in evacuated samples (Dultz et al.

2006; Kaufmann 2009). Based on the Washburn equation (Washburn 1921) intruding the alloy at a pressure of 55 MPa corresponds to a pore diameter of ~20 nm, using a surface tension of 0.48 N/m and a contact angle of 130° (Darot and Reuschle 1999).

The Washburn equation (Washburn 1921) gives a relationship between pressure and pore size:

$$r = -\frac{2\gamma \cos \Theta}{p}$$

r—pore radius, p—pressure, γ—surface tension of mercury = 0.48 N/m, Θ—wetting angle of mercury (135°).

After solidification of the alloy, the thin polished sections were prepared, sputtered with Au and the invaded connective pore system was examined in back-scattered electron images (FEI, QUANTA 200).

The specific surface area (the total surface area of a material per unit of mass) and the pore size distribution in the rock fragments were determined by low-temperature nitrogen adsorption method using a QuantaChrome Nova 1200e analyzer (Quantachrome Instuments, Florida, USA). The samples were degassed in a drying chamber at 100 °C during 19 h; then the samples were analyzed by the multipoint Brunauer–Emmett–Teller (BET) method using 7 points. The pore size distribution was calculated by the Barret–Joyner–Halenda (BJH) method using nitrogen desorption isotherm (NOVAWin™—Windows® Based Software for Operation from PC). The method allows to investigate the pores with diameter < 100 nm (Anovitz and Cole 2015).

The mesostructure and fractal properties of the rock fragments to estimate the potential supply of new portions of slightly weathered material were investigated using the method of the small angle neutron scattering (SANS). The SANS experiment was performed at the "Yellow Submarine" instrument of the BNC (Budapest Neutron Center) research reactor in Budapest (Hungary). The "Yellow Submarine" instrument operates in near point geometry. Using of two neutron wavelengths ($\lambda = 0.49$ and 0.94 Å, $\Delta\lambda/\lambda = 18\%$) and two sample-to-detector distances (1.6 and 5.6 m) provides the measurements in the momentum transfer range (q) of $3 \times 10^{-2} < q < 4$ nm^{-1} (where: $q = \pi\lambda^{-1}\sin(\theta/2)$, θ is the scattering angle), which correspond to analysis of the rock structure in the range from 1 to 100 nm. The scattered neutrons were detected by a two-dimensional position-sensitive BF_3 gas detector (64 × 64 cells of 1 cm × 1 cm).

The powders of the rock fragments were placed in 1 mm thick quartz cells. Apparent density ρ_H of each sample was calculated as the weight of powder divided by its volume. The raw data were corrected using the standard procedure (Wignall and Bates 1987), taking into account the scattering from the setup equipment and cell. The resulting 2D isotropic spectra were averaged azimuthally and their absolute values were determined by normalizing to the incoherent scattering cross section of water. All the measurements were done at room temperature. Data pre-processing was obtained using the BerSANS software (Keiderling 2002).

The fits of experimental data shown in Fig. 27.3 were made using the equation to analyze the scattering from both samples over the entire q range:

$$\frac{d\Sigma(q)}{d\Omega} = \frac{A(D_S)}{q^n} + G_p \cdot \exp(-\frac{q^2 r_g^2}{3})$$

where $A(D_s)$ is power-law prefactor, which depend on the fractal dimensions of the inhomogeneities (pores) and G_p is the Guinier prefactor which is in direct proportion to the product of number of the primary inhomogeneities (pores) in scattering volume and the density of the neutron scattering amplitude ρ on them; r_g is the radius of gyration for such inhomogeneities (pores).

27.3.2 Analyses of Experiment Studying

The thin polished sections of the rock samples were studied with scanning electron microscopy (SEM, FEI XL30 with wolfram cathode, Thermo Fisher Scientific) analysed. Biofilm visualization on the rock surface was done in the polished sections using a 3D Laser Microscope (KEYENCE, VK-9700, Japan).

27.4 Results

27.4.1 Rock Characteristics

27.4.1.1 Rock Petrographic and Micromorphological Properties

The petrography of metagabbro amphibolite was described previously (Lessovaia and Polekhovsky 2009; Lessovaia et al. 2016b). Summarizing data the dominant mineral in metagabbro amphibolite was amphibole identified as hornblende. Amphibole was partially substituted by epidote and chlorite. The result of metamorphism was recrystallization of some melanocratic minerals in initial rock and appearance of high proportion (up to 30%) of quartz. Grains of plagioclase were affected by the development of the saussuritization and sericitization.

The petrography of dolerite collected from the soil profiles was also studied in the framework of traprock conversion into fine earths and soil clayey materials investigation (Lessovaia et al. 2014; Lessovaia et al. 2016c). The rock fragments are holocrystalline basalt, which is classified as dolerite. The poikilitic structure in it was composed by well-crystallized plagioclases and pyroxenes. The dolerite was chemically weathered, which was concluded based on the presence of accumulation of Fe-oxides and the spherulitic smectite aggregates. Identification of smectite was confirmed based on XRD data (Lessovaia et al. 2014).

27.4.2 Connectivity of Pores

In back-scattered electron images of polished sections of both rock types, connective pores impregnated with the alloy are visible as the bright phases (Fig. 27.1). Summarizing data of previous research (Lessovaia et al. 2016a) in metagabbro amphibolite the pores were represented by well connected system (Fig. 27.1a). Investigation of the sample at higher magnification revealed the extended crack system, in which the secondary products of rock weathering were not identified (Fig. 27.1b).

A well-developed interconnected pore system along the outer rim of mineral grains was visible in dolerite at low magnification (x 40–50). The rock fragments were characterized by a strong heterogeneity due to extended crack systems, which can be enhanced due to physical disintegration (Fig. 27.1c). The pores were mostly unfilled by the secondary products of dolerite chemical weathering based on measurement at

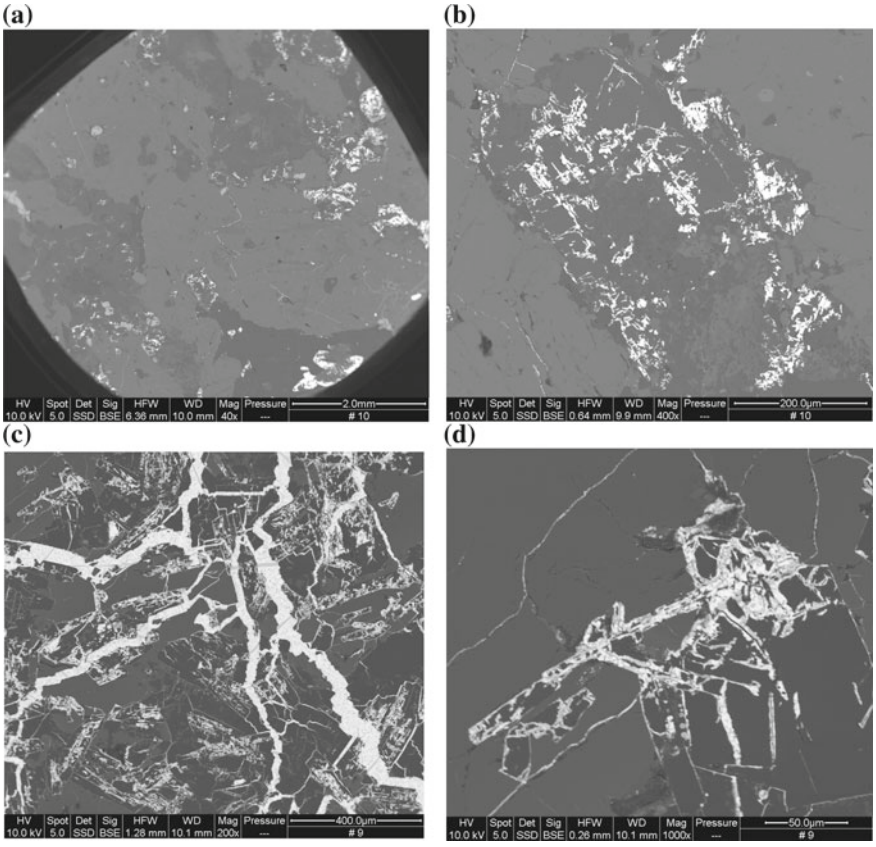


Fig. 27.1 Back scattered electron images of pore networks in polished sections of rock samples. The connective pore system appears white in the images due to the intrusion of the molten alloy "Wood's metal". Detail images from samples of metagabbro amphibolites: magnification 40× (**a**), 400× (**b**) and dolerite: magnification 400× (**c**), 1000× (**d**)

high magnification (Fig. 27.1d). Whereas in the rock fragments from deeper horizons of this profile the textural issues attributed to the platy morphology of smectite was clearly detected (Lessovaia et al. 2014).

Based on pore space analysis both rocks have marked pore systems, which can be used as habitats for microorganisms. The pore system is more elaborated for the sample of dolerite.

27.4.3 *Specific Surface Area (Low-Temperature Nitrogen Adsorption Data)*

The specific surface area in metagabbro amphibolite obtained using the multi-point Brunauer–Emmett–Teller (BET) method was estimated as very low (S_{BET} = 1.0 ± 0.1 m^2/g). The proportion of mesoporous (pore diameters 2–50 nm) was close to absence in the sample.

Otherwise the specific surface area in dolerite was estimated as S_{BET} = 48 ± 1 m^2/g. The isotherm of the full nitrogen adsorption/desorption has a hys-

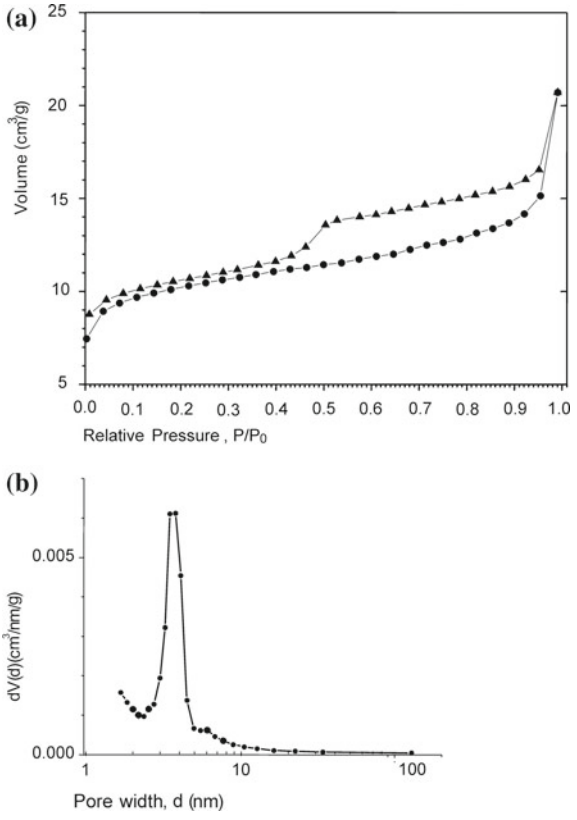


Fig. 27.2 Low-temperature nitrogen adsorption method data: full nitrogen adsorption/desorption isotherm (**a**) and pore size distribution (**b**) for dolerite

teresis loop (Fig. 27.2a). The isotherm can be related to type IV according to The International Union of Pure and Applied Chemistry (IUPAC) classification, which is typical for mesoporous materials. The shape of the hysteresis loop allows to relate it to the type H3 (IUPAC classification), which is observed with non-rigid aggregates of plate-like particles giving rise to slit-shaped pores. The pores with diameter ≈4 nm are dominant (Fig. 27.2b). Most probably secondary mineral associations present in the pore space of dolerite contribute to the observed fine pores.

27.4.4 Mesostructure and Fractal Properties (SANS Data)

The experimental curves of the differential neutron cross section $d\Sigma(q)/d\Omega$ versus momentum transfer q illustrate the same overall shape for both samples and display two characteristic q-ranges.

In the range of $q < 0.7\ \mathrm{nm}^{-1}$, the $d\Sigma(q)/d\Omega$ satisfies the power law q^{-n} (Fig. 27.3). The values of the exponent n were found from the slopes of straight-line segments in the experimental dependences $d\Sigma(q)/d\Omega$. Their values are 3.86 ± 0.02 for metagabbro amphibolite and 3.43 ± 0.02 for dolerite. According to Teixeira (1986) when the exponent value is in the range $3 < n \leq 4$, scattering from the samples occurs on the fractal surface with the dimension $2 \leq D_s = 6 - n < 3$. Thus, the patterns of both rock types are typical for scattering from porous systems with fractal phase boundaries.

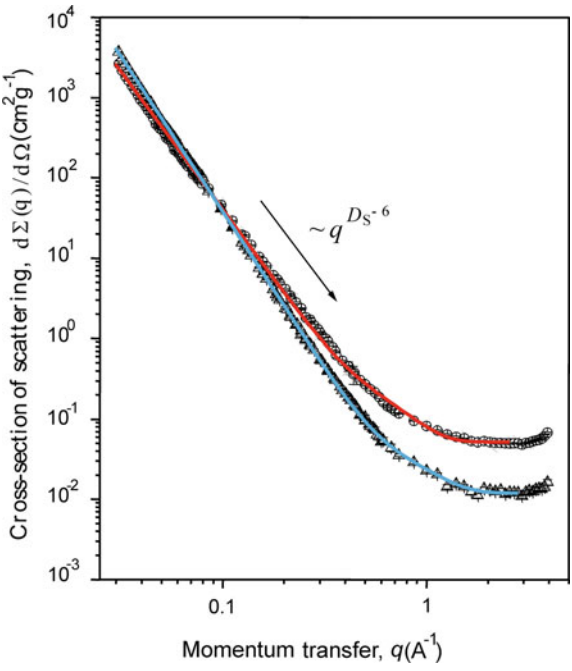


Fig. 27.3 The experimental curves of the differential neutron cross section $d\Sigma(q)/d\Omega$ versus momentum transfer q for the rock fragments: metagabbro amphibolite (triangle, blue line) and dolerite (circle, red line), respectively. Fits of experimental data are shown as solid lines

In the region $q > 0.7$ nm^{-1} the "shoulder of the curve" is observed indicating the presence of small inhomogeneities (pores) of characteristic size r_c, which is the lower self-similarity boundary for the fractal systems. The absence of a deviation of the $d\Sigma(q)/d\Omega$ curve from the power law (the onset of the Guinier regime) at small values of q means that the upper self-similarity limit ξ of the surface fractal is larger than the maximum size R_{max} of the inhomogeneities that can be detected in the experiment with a given resolution: $R_{max} = 3.5/q_{min} \approx 110$ nm.

The results of the analysis of SANS data clearly show that both rocks are porous systems with a fractal phase boundary in the system solid phase—porosity. While dolerite is characterized by more developed fractal surface with $D_S = 2.57 \pm 0.03$ than the sample of metagabbro amphibolites with $D_S = 2.14 \pm 0.03$.

27.4.5 Microbial Colonisation Experiment

SEM analysing of the thin polished sections of rocks after experiment revealed the expressed heterogeneity of the mineral fractions and the presence of deep fissures and spaces between them (Fig. 27.4). The preservation of biofilms in situ based on investigation of the polished sections was identified using 3D laser microscopy. Biofilms develop stronger and magnification allows for recognition of individual cells as well as for biofilm growth structures. Biological growth seems to follow the irregularities of the surface such as roughness given by fractures and voids rather than specific mineral phases used for element mining and energy recovery. However, the spread of biofilms on dolerite is significantly more expressed and seems to cover a relatively bigger surface (Fig. 27.5).

27.5 Discussion

The effect of biogenic weathering induced by biofilm has been shown based on individual minerals that allowed to estimate the direct biogenic effect due to changes of bulk chemical composition under the biofilm towards the mineral (Seiffert et al. 2014). While a rock sample itself is more complicate object to study biogenic weathering under the influence of biofilm colonization. But, back to the history of biogenic-abiogenic investigations the assuming of biochemical influence was concluded based on study of namely rocks (granitic gneiss and miascite) affected by lithophilous lichens (Polynov 1945). Besides, the selective effect of biota (lichens) on minerals in the rock has been also shown (Yarilova 1947): the lichens hyphae penetrated deeply into the grains of mica, which is a source of nutrients, initially potassium and avoiding quartz, which does not contain nutrients. Moreover in the schematic representation of rock colonization by biofilms the contact space between minerals was stressed as the zones of active interactions and penetration inside the rock (Gorbushina 2007).

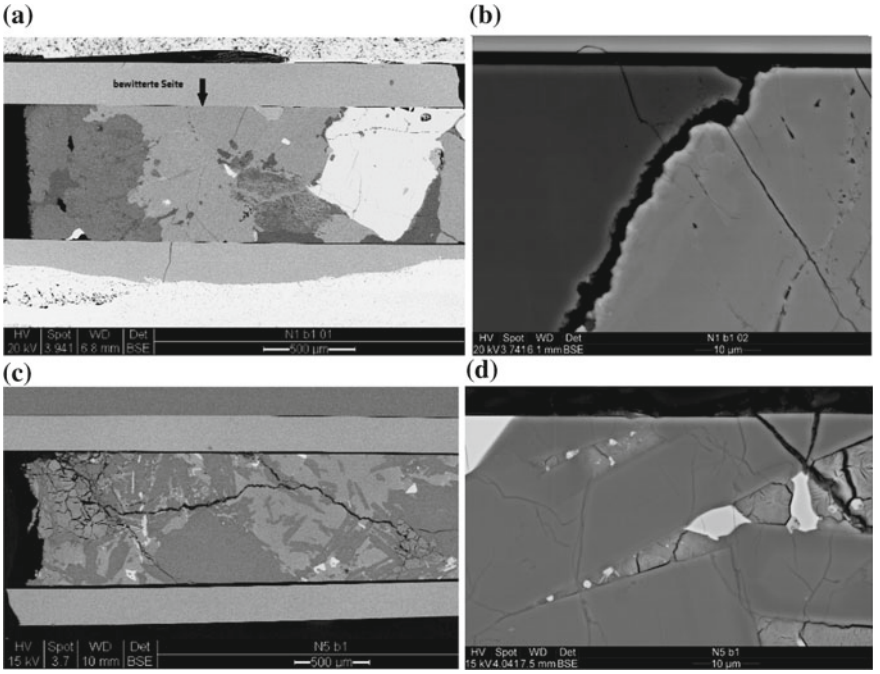


Fig. 27.4 The polished sections of the rock samples (SEM data): general overview of metagabbro-amphibolite (**a**) and dolerite (**c**); heterogeneity of the rock and porous spaces between the minerals in (**b**) metagabbro-amphibolite and (**d**) dolerite

The novelty of the present research was using the rock samples composed by several minerals instead of individual minerals to study biogenic weathering initiating by biofilms. The rock fragments using in the present modeling laboratory experiment were sampled from the Holocene soil profiles formed in cold environments. The rock samples represented by: (i) metagabbro amphibolite (northern forest subzone of the Polar Urals) and (ii) traprock (dolerite) (tundra-forest zone of Central Siberia Plateau) differ in their mineralogy, porosity, the specific surface area, and fractal dimensions.

Based on mineralogical composition the rocks samples were selected taking into account presence of quartz in high proportion only in one sample—metagabbro amphibolites. This mineral does not contain nutrients utilizable for microorganisms, whereas the other minerals (epidote, chlorite, plagioclase and dominant hornblende) can be a source of nutrients. Dolerite also introduced in the experiment is characterized by the absence of quartz and presence of the silicates plagioclase, pyroxene, and the products of rock weathering (Fe-oxides and smectite) that can be sensitive to weathering.

The rocks can be seen as a mass fractal structure, which allows to explain the diverse mineral phases of both rock types offering a suitable ecological niche for biological colonization and spread of the growth from the upper surface into the deeper layers of the mineral substrate. While dolerite is characterized by more devel-

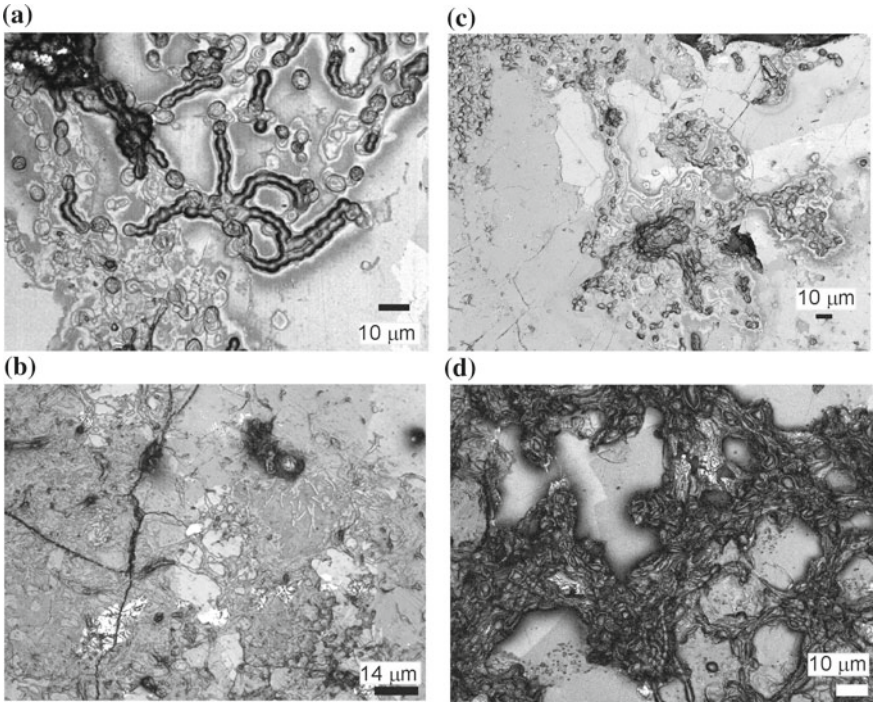


Fig. 27.5 Biofilms developing on the surface of the rock polished sections visualized by using 3D laser microscopy: (**a**, **c**) metagabbro amphibolites and (**b**, **d**) dolerite

oped fractal surface than metagabbro amphibolites, which can explain the potentially higher rate of dolerite disintegration and following bio-weathering. As indicated by the intrusion of a molten alloy (Wood's metal) and subsequent electron microscopy the pores are well connected in both rocks but the porosity is more developed in dolerite. The pores can be a prerequisite promoting further rock weathering by providing pathways for element exchange and habitats for microorganisms. For example, a correlation between secondary minerals and pore sizes less than 10 nm due to rock weathering has been shown for altered mid-ocean ridge basalts (Simonyan et al. 2012). From another side, biofilm penetration inside the rock leads to intensified weathering affected by biota colonization. Based on low-temperature nitrogen adsorption data the mesoporous (pore diameters 2–50 nm) were developed namely in dolerite. Besides, the specific surface area is higher in dolerite comparing with metagabbro amphibolites. Biofilm visualization on the rock surface in polished sections illustrated their stronger progress growth on dolerite rather than on metagabbro amphibolites.

Both rocks present a suitable substrate for biogenic weathering—as they contain minerals susceptible for weathering as well as possess interconnected porosity. Because of the objects were represented by already previously weathered rock sam-

ples the approach to study individual mineral changes as a result of biofilm colonization (Seiffert et al. 2014) can't be applied. Initial variability of chemical composition of the minerals itself and presence of several minerals in one rock sample can't allow to estimate the direct effect of the biofilm on the rock in thin section based on SEM data. But we can guess the side effects of biogenic rock weathering based on biofilm visualization in thin polished Sections.

3 months runtime of the experiment revealed that the model biofilm clearly enhanced rock weathering, which was confirmed by a removal of Si from the rock powders inoculated with both organisms of model biofilm in a nutrient (CNPS) solution (data not shown). Active growth of the model biofilm on both rock slabs was visualized. Biofilm visualization on the rock surface in thin polished sections illustrated their stronger growth on dolerite confirming its higher sensitivity to biogenic weathering due to mineral association and porosity as well as higher specific surface area providing surfaces for biotic—abiotic interaction.

In many cases the growth is following the texture: fractures and pores, etc., indicating that in comparison to the polished (plane) surfaces sites with high surface roughness are preferentially colonized. Therefore our experiments have proven the hypothesis that biological colonization is enhanced in the rock (dolerite) characterized by higher specific surface area higher and fractal dimensions comparing with metagabbro amphibolites. Our results confirmed the schematic representation of rock colonization by biofilms mentioned above (Gorbushina 2007) in the framework of the role of porosity including the contact space between minerals in biota colonization, which play the role of the zones of active interactions penetration inside the rock.

27.6 Conclusions

Both rock types (dolerite and metagabbro amphibolites) were actively weathered in experiment of biogenic weathering with a model biofilm combining one heterotroph and one phototroph component. Dolerite's higher sensitivity to weathering is rooted in its more expressed pore space indicated by a higher specific surface area and the fractal dimension. Besides, mineral association of the dolerite is composed only of minerals that deliver biologically useful elements, while amphibolite contains quartz which is relatively inert for stimulating microbial growth.

Acknowledgements The research is based on a senior research stay (S. Lessovaia) at FUB in 2016 supported by UAS. Authors thank Institute for Solid State Physics and Optics (Neutron Spectroscopy Department) of Hungarian Academy of Sciences for the possibility of carrying out a neutron experiment at the facility "Yellow submarine" (reactor BRR, Budapest Neutron Centre, Hungary).

References

Allen ChE (2002) The influence of schistocity on soil weathering on large boulder tops, Karkevagge, Sweden. CATENA 49:157–169

Anovitz LM, Cole DR (2015) Characterization and analysis of porosity and pore structures. Rev Mineral Geochem 80:61–164

Arnaud RJST, Whiteside EP (1963) Physical breakdown in relation to soil development. J Soil Sci 14:267–281

Bockheim JG (2015) Classification and development of shallow soils (< 50 cm) in the USA. Geoderma Regional 6:31–39

Bojko O, Kabala C (2016) Transformation of physicochemical soil properties along a mountain slope due to land management and climate changes—a case study from the Karkonosze mountains, SW Poland. CATENA 140:43–54

Burford EP, Fomina M, Gadd GM (2003) Fungal involvement in bioweathering and biotransformation of rocks and minerals. Mineral Mag 67:1127–1155

Chizhikova NP, Lessovaya SN, Gorbushina AA (2016) Biogenic weathering of mineral substrates (review). In: Frank-Kamenetskaya OV, Panova EG, Vlasov DYu (eds) Biogenic–abiogenic interactions in natural and anthropogenic systems, Lecture Notes in Earth System Sciences. Springer International Publishing Switzerland, 7–14

Darot M, Reuschle T (1999) Direct assessment of wood's metal wettability on quartz. Pure appl Geophys 155:119–129

Dultz S, Behrens H, Simonyan A, Kahr G, Rath T (2006) Determination of porosity and pore connectivity in feldspars from soils of granite and saprolite. Soil Sci 171:675–694

Gadd GM (2007) Geomycology: biogeochemical transformations of rocks, minerals, metals and radionuclides by fungi, bioweathering and bioremediation. Mycol Res 111:3–49

Gadd GM (2017) Fungi, rocks, and minerals. Elements 13:171–176

Gorbushina AA (2007) Life on the rocks. Environ Microbiol 9:1613–1631

Gorbushina AA, Broughton WJ (2009) Microbiology of the atmosphere-rock interface: how biological interactions and physical stresses modulate a sophisticated microbial ecosystem. Annu Rev Microbiol 63:431–450

IUPAC. The International Union of Pure and Applied Chemistry classification (https://iupac.org/)

Kaufmann J (2009) Characterization of pore space of cement-based materials by combined mercury and Wood's Metal intrusion. J Am Ceram Soc 92:209–216

Keiderling U (2002) The new 'BerSANS-PC' software for reduction and treatment of small angle neutron scattering data. Appl Phys A 74:1455–1457

Lloyd RR, Provis JL, Smeaton KJ, van Deventer JSJ (2009) Spatial distribution of pores in fly ash-based inorganic polymer gels visualised by Wood's metal intrusion. Microporous Mesoporous Mater 126:32–39

Lessovaia SN, Polekhovsky YuS (2009) Mineralogical composition of shallow soils on basic and ultrabasic rocks of East Fennoscandia and of the Ural Mountains, Russia. Clays Clay Miner 57:476–485

Lessovaia S, Dultz S, Goryachkin S, Plötze M, Polekhovsky Yu, Andreeva N, Filimonov A (2014) Mineralogy and pore space characteristics of traprocks from Central Siberia, Russia: Prerequisite of weathering trends and soil formation. Appl Clay Sci 102:186–195

Lessovaia S, Dultz S, Plötze M, Andreeva N, Polekhovsky Yu, Filimonov A, Momotova O (2016a) Soil development on basic and ultrabasic rocks in cold environments of Russia traced by mineralogical composition and pore space characteristics. CATENA 137:596–604

Lessovaia SN, Goryachkin S, Polekhovsky Y, Ershova V, Filimonov A (2016b) Abiotic and biotic processes of mineral weathering in tundra soils on ultramafic and mafic rocks of the Polar Urals, Russia. In: Frank-Kamenetskaya OV, Panova EG, Vlasov DYu (eds) Biogenic–abiogenic interactions in natural and anthropogenic systems, Lecture Notes in Earth System Sciences. Springer International Publishing Switzerland, 223–236

Lessovaia SN, Plötze M, Inozemzev S, Goryachkin S (2016c) Traprocks transformation to clayey material in soil environment (Central Siberian Plateau, Russia). Clays Clay Miner 64:668–676
Meunier A (2005) Clays. Springer, Berlin
Minasny B, Finke P, Stockmann U, Vanwalleghem T, McBratney AB (2015) Resolving the integral connection between pedogenesis and landscape evolution. Earth Sci Rev 150:102–120
Navarre-Sitchler A, Steefel CI, Yang L, Tomutsa L, Brantley SL (2009) Evolution of porosity and diffusivity associated with chemical weathering of a basalt clast. J Geophys Res 114, 14. http://dx.doi.org/10.1029/2008JF001060 art. no. F02016
Pokharel R, Gerrits R, Schuessler JA, Floor GH, Gorbushina AA, von Blanckenburg F (2017) Mg isotope fractionation during uptake by a rock-inhabiting, model microcolonial fungus Knufia petricola at acidic and neutral pH. Environ Sci Technol 51(17):9691–9699
Pokharel R, Gerrits R, Schuessler JA, Frings PJ, Sobotka R, Gorbushina AA, von Blanckenburg F (2018) Magnesium stable isotope fractionation on a cellular level explored by Cyanobacteria and Black Fungi with implications for higher plants. Environ Sci Technol 52(21):12216–12224
Polynov BB (1945) Pervye stadii pochvoobrazovaniya na massivno-kristaalocheskich porodack (The first stages of pedogenesis on massive crystalline rocks). Soil Sci (Pochvovedenie) 7:327–339 (in Russian)
Ross PS, Ukstins Peate I, McClintock MK, Xu YG, Skilling IP, White JDL, Houghton BF (2005) Mafic volcaniclastic deposits inflood basalt provinces: a review. J Volcanol Geotherm Res 145:281–314
Seiffert F, Bandow N, Bouchez J, von Blanckenburg F, Gorbushina AA (2014) Microbial colonization of bare rocks: laboratory biofilm enhances mineral weathering. Procedia Earth Planet Sci. 10:123–129
Seiffert F, Bandow N, Kalbe U, Milke R, Gorbushina AA (2016) Laboratory tools to quantify biogenic dissolution of rocks and minerals: a model rock biofilm growing in percolation columns. Frontiers Earth Sci 4:31. https://doi.org/10.3389/feart.2016.00031
Simonyan AV, Dultz S, Behrens H (2012) Diffusive transport of water in porous fresh to altered mid-ocean ridge basalts. Chem Geol 306–307:63–77
Teixeira J (1986) Experimental methods for studying fractal aggregates. In: Stanley HE, Ostrovsky N (eds) On growth and form—fractal and non-fractal pattern in physics. Martinus Nijloff, Boston, pp 145–162
Velde B, Meunier A (2008) The origin of clay minerals in soils and weathered rocks. Springer-Verlag, Berlin Heidelberg
Washburn EW (1921) Note on a method of determining the distribution of pore sizes in a porous material. Proc Natl Acad Sci 7:115–116
Wignall GD, Bates FS (1987) Absolute calibration of small-angle neutron scattering data. J Appl Crystallogr 20:28–40
World Reference Base for Soil Resources (2006) World soil resources Reports 103, 2nd edn. FAO, Rome
Yarilova EA (1947) The role of lithophilous lichens in the weathering of solid rocks (Rol' litofil'nykh lishainikov v vyvetrivanii massivno-kristallicheskekh porod) Soil Sci (Pochvovedenie) 9:533–548
Zhang Y, Zhang M, Niu J, Li H, Xiao R, Zheng H, Bech J (2016) Rock fragments and soil hydrological processes: significance and progress. CATENA 147:153–166

Part V
Effect of Microorganisms on Natural and Artificial Materials

Chapter 28
Crusts and Incrustations on Natural and Architectural Objects

Raisa V. Lobzova, Oxana V. Karimova and Elena I. Antonova

Abstract New data on investigations of different formations on the natural and architectural objects are presented. The purpose of our research is to identify the structure, the mineral composition and reasons of the new formations and deposits on various natural and artificial materials of monuments of cultural heritage. The complex of analytical methods was used: optical microscopy, electron microscopy and X-ray diffraction. Crusts and incrustation on the following objects are represented: rock art ("patina" of petroglyphs on metamorphic rocks), on alkali rocks in Siberia (Sangilen, Batagol); on granite facing stones and statues in urban environment (Kamenny and Moskvoresky Bridges and others, pedestals of sculptures); on limestone blocks of white stone and cast iron floor plates at the Yur'ev-Polskoy Cathedrals, terracotta and glazed ceramic products. The new formations are the result of a complex of reasons: seasonal development of biota, interaction of microbial communities, chemical oxidation, fluctuations in temperature and humidity and gas conditions, both general and local, associated with anthropogenic factors. All this determines the morphology, structure, texture and chemical composition of the local formation of the material. Limestones and marble are subject to the greatest biogenic destruction, and irrigated ceramic products are the least affected.

Keywords Rock art · Granite · Marble · Limestone · Ceramics · Solutions · Salts · Optical petrology · Electron microscopy · X-ray diffraction

28.1 Introduction

The most important role of the living matter as geological strength of the biosphere underlines by famous Russian geologist, geochemist, and founder of the biosphere theory Vernadsky (1954).

R. V. Lobzova (✉) · E. I. Antonova
State Research Institute for Restoration, Moscow, Russia
e-mail: lobzovarv@mail.ru

O. V. Karimova
Institute of Geology of Ore Deposits RAS (IGEM RAS), Moscow, Russia

© Springer Nature Switzerland AG 2020

O. V. Frank-Kamenetskaya et al. (eds.), *Processes and Phenomena on the Boundary Between Biogenic and Abiogenic Nature*, Lecture Notes in Earth System Sciences,
https://doi.org/10.1007/978-3-030-21614-6_28

Petrov (1967), Ginsburg et al. (1946) and Gizburg (1947) fundamental works are devoted to questions of rock weathering, regularity in the change of mineral composition; the genesis, structure and the age of weathering crusts; the transformation of minerals and the formation of related minerals. Petrov considered weathering crust as the soil, but Ginzburg was objected to such point of view.

Works devoted to manganese and iron in the geological processes are the most interesting for our investigations. Here the following works can be mentioned. Chuhkrov and coauthors studied mineralogy and genesis of hypergenic manganese and iron oxides (Chukhrov 1955; Chukhrov et al. 1989). The microbiology of iron and manganese is the most detailed studied at the present time (Pinevich 2005).

Vernadsky (1994) considered very important role of fungus and special organisms in the formation of the manganese deposits. Transformation of manganese minerals by influence of the fungus ASPERGILLUS NIGER, one of the most active biodestructor of stone, was proven by experimental work of Rusakov et al. (2017).

Yudovich et al. (2018) pointed out the biogenic genesis of some titanium minerals: such as lecosphen and ksantitanite (aluminum-titanium gels). He recommended studying the influence on the mineral formation of some batteries, especially ferrobatteries that secretes aluminum.

Naumov (2018) describes association of allophone with hallyasit, kaoline, gibbsite, iron oxides, quarts, amorphous silica.

The role of microorganisms in the biochemical circulation of the substance is well known, especially in circulation of such elements as nitrogen, phosphorus, sulfur, iron and manganese. The role of microorganisms in mineralization processes is very high.

A significant contribution to understanding the relationship of living and inanimate matter made research work on the preservation of monuments of cultural heritage in the open air. For example, a group of scientists from St. Petersburg State University, museum staff, and restorers conduct long-term monitoring of the state of the most valuable stone and bronze monuments at the State Museum of City Sculpture in St. Petersburg. The Database of the state of museums necropolis monuments made in 2007. It includes reference materials, general information about the monument, and the results of the examination. O. V. Frank-Kamenetskaya the author of concept and structure of the Database. The database is available on the Internet (www.opticalcomponents.ru). The results of the work published in the books, special issues and papers (Bulakh et al. 2005; "Monuments. Direction vector" 2008; Rybnikov et al. 2015; "Museum and monuments of the cemeteries of St. Petersburg" 2016), and also presented at the International symposiums "Biogenic-abiogenic interaction in natural and antropogenic systems: International Symposium. Saint-Petersburg" (2014, 2018).

Estimation of stone monuments conditions is the very important achievement (Frank-Kamenetskaya et al. 2010; Bulakh and Marugin 2013). Methods of monuments conservation from the bio-destruction was in the focus on the work. Analysis of microbial communities living on the destructed surfaces of a stone, selection of biocide compositions for each material, method and conditions of the monument treatment are was systematically carried out (Bulakh et al. 2005; Vlasov and Frank-

Kamenetskaya 2006; Vlasov et al. 2016). 150 types of microorganisms were found on Saint-Petersburg monuments. The most representative group is micro funguses—105 types. Only three of them are absolutely dominated (Zelensky et al. 2015). It is established that many mineral crusts on the stone monuments were formed under influence of micro-organisms.

From foreign literature, we note the work of Croyn (2004 the first publication is dated 1990 and has been repeatedly reprinted). It covers various groups of stone, ceramic, cement and other materials, types and mechanisms of their destruction, state of preservation, basic methods of conservation of various archaeological finds.

Results of the systematic studies of cultural heritage objects state by complex of analytical methods are presented in papers (Antonova et al. 2014, 2015; Lobzova et al. 2018).

The present paper is devoted to investigations of structure, morphology and mineral composition of crusts and incrustations on the stone material of the different cultural heritage objects in Moscow and Siberia.

28.2 Objects of Investigations

The similarity of weathering processes in the transformation of minerals and the formation of the new forms in natural and urban (artificial) objects is demonstrated in the following examples:

- Complex studies of rock art («petroglyphs») in Siberia (Sangilen and Batagol, Tuva, Sayany, Russia) on the cliffs formed by different alkaline rocks: marbles, sandstones, slates.
- Architectural objects, monuments, memorials built up by different facing and statue stone material: granites, gabbros and other volcanic rocks. Such type of material is highly weathering resistant. Facing materials of the Moskvoretzky and Bolshoy Kamenny Bridges, pedestals of sculptures, obelisks, monuments of some monastery cemeteries in Moscow were studied.
- Architectural objects and memorials built up by carbonate rocks, which are the less weathering resistant. White stone Moscow Kremlin Cathedrals, Yur'ev Polskoy Cathederal, monuments of some Moscow cemeteries were studied.
- Bricks, terracotta and glazed ceramic materials of Moscow Kremlin Cathedrals, Novodevichy and Vusoko-Petrovsky monasteries also were in the focus of our study.

28.3 Methods of Investigations

The following methods: visual analysis before restoration; mineralogy-petrographic analysis, X-ray diffraction phase analysis, electron microscopy analysis—were used

for study of petroglyph's basements, stone masonry and cladding components—natural and synthetic facing stone, binding sutures, masonry and finishing solutions.

Stereomicroscope EZ4 D (Germany) was used for optical microscopy of objects, following by photography of the most interesting fragments. Microscopy in reflected light determined colour, microstructure of the material, rock forming minerals, inclusions composition, efflorescence, contact changes. Type of fossils, porosity, shape and pattern of pore distribution were also analyzed in limestone. The behavior of the matrix in polarized light with the analyzer, the composition of the spider (size and shape of particles, the percentage of minerals and other particles) were studied in ceramics. The minerals, their relations, zonality, secondary changes, distribution of particles and inclusions were studied in petrographic thin sections and immersion preparations (polarization microscopes POLAM P-211M (Russia), OLYMPUS BX-51(USA).

Chemical composition and micromorphology of the objects determined by scanning electron microscopy using a JSM-5300 microscope (Japan) equipped with Link ISIS spectrometer (United Kingdom).

Mineral phase composition determined by X-ray powder diffraction using a Rigaku D/MAX diffractometer (Japan).

28.4 Results and Discussion

28.4.1 Rock Arts ("Petrogliphs")

Devlet (2002) summarized the material on rock art (petroglyphs). Complex systematic studies of Siberia petroglyphs were performed at Kemerovo State University (headed by Martunov and Sher 1989) and Moscow State Research Institute of Restoration (Ageeva and Rebrikova 2003; Lobzova et al. 2014). Kropachev and Lobzova (2004), Lobzova and Kochanovich (2005), Lobzova et al. (2018), Schigorets (2015) formulated the new approaches to the monitoring of rock images on the example of Tomsk pisanitsa. The drawing plane—rock cliffs—is formed by red sandstone (Shishkin petrogliphs) or metamorphic slates (Pritomskie petrogliphs) or marbles (Priolhonskie petrogliphs). Our rocks and "patina" studies using methods of petrography and electron microscopy showed important influence of mineral substrate, it structure and texture features, and also physics and mechanical properties of rock material on the formation of cave drawings planes. Despite on the different substrate (sandstones, slates, limestones) the mineral composition of the drawing plane are uniform: iron-manganese and iron oxides compounds are prevail. Their peculiarity is zonal structure of the "patina".

On "Tomsk pisanitsa", depending on the level of erosive slice, there is a change of the black patinized cortical layer (lower frieze) by brown with yellow and red patches (upper frieze). Delamination of the cortical layer leads to a partial loss of cave paintings. In addition to losses on patinated surfaces, bacterial, algal and other

bio-sprouts are developed, the types of which are given in the works of Ageeva and Rebrikova (2003). Other petroglyphs on the rocks of river Tomi are less known (Rusakova and Barinova 1997).

The rocky planes with the drawings "Novoromanovsky pisanitsa" are located on relatively gentle rocky cliffs in the mouth part of an overgrown ravine (Fig. 28.1). Rocky outcrops are oriented in the CW direction and extended along the coastline. The slopes, as well as the coastal terrace, are covered with consolidated red-colored sediments with a grassy cover. The planes are covered with patina of brown and dark brownish-black color. For the rocks of the "Novoromanovsky pisanitsa", represented essentially by quartz meta-pelites and meta-siltstone of a thin-strip and fine-grained structure, layer-by-layer iron ore is characteristic. Brown iron oxides (goethite-hematite) predominate in the layers, and iron-manganese formations are present in the cutting planes (cleavage cracks).

The rocky outcrops with drawings of the "Hanging Stone" pisanitsa of sub-latitude orientation are located almost on the coastline and are periodically subjected to intense abrasion with water and ice, which led to a smoothing of the relief, which resembles "lamb foreheads". The planes with drawings are covered with a black patina, which makes them similar to the deposits of the patinated cortical layer of the lower frieze "Tomsk pisanitsa". The rocks "Hanging Stone" are the strongest with the size of grains of fine-grained sandstone. A silky sheen is observed along the shale planes due to the presence of sericite. On the surfaces of schistosity, a greenish-yellowish tinge is observed, on the chips and cracks separately there are dark brown and black thin "cortical" deposits (patina).

Rocky outcrops "Tutalskaya pisanitsa" are located downstream from Novormanovskaya and "Hanging Stone". They are oriented ZSZ directions. The rocky ledges are steep, the planes with pictures often have a negative angle of inclination. Patinated surfaces, both black and brown, have different exposures, sometimes



Fig. 28.1 Novoromanovskaya pisanitza

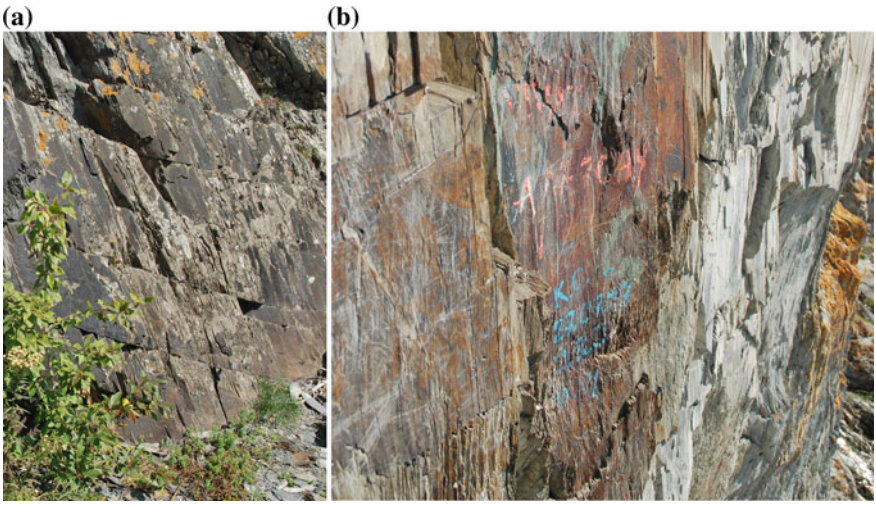


Fig. 28.2 Rock Art "Tutalskaya pisanitsa" **a** lower and **b** upper part

covered with lower bio-forms and whitish drains (Fig. 28.2a, b). The rocks of the "Tutalsk pisanitsa" are distinguished by a large lithological diversity and are represented by several varieties, among which light gray and dark gray rocks resembling slate shales are noted. There rocks differ from previous drawings by the presence of calcite. The leaching and redeposition of the carbonate material of rocks is associated with the formation of whitish streaks on the rock paintings, which worsens their exposure. The zoning of the patinated areas is as follows: iron oxides in the form of thin layers are deposited on the leached calcite zone with an increased content of amorphous silica, and finely dispersed manganese deposits are deposited on them. The data of thermal differential analysis showed a different state of silica and alumosilicate substance: quartz, chalcedony, hydro-mica, which are in varying amounts, the presence of carbonate and goethite. The presence of these minerals in the patina is confirmed by IR spectroscopy and X-ray phase analysis. It is well known that ferromanganese nodules are a product of extremely thin-matched new forms of manganese and iron hydroxides, numerous alumosilicates of authigenic and terrigenous origin, phosphates, carbonate and organic material. Minerals of iron are present in them in the form of polymorphic modifications of iron hydroxides, as well as magnetite and maghemite. Of these, goethite is the most common (Chelishchev et al. 1998), which is observed at our sites. Only at the level of river irrigation, iron-manganese new forms predominate, giving the planes with rock paintings a black color.

Enrichment of patina with phosphorus, iron and manganese is caused by biological factor. There is numerous evidence of biota influence (bio-corrosion and bio-mineralization) in formation of the new forms. It was also confirmed by experiments: for example, transformation of manganese minerals by the active bio-destructors.

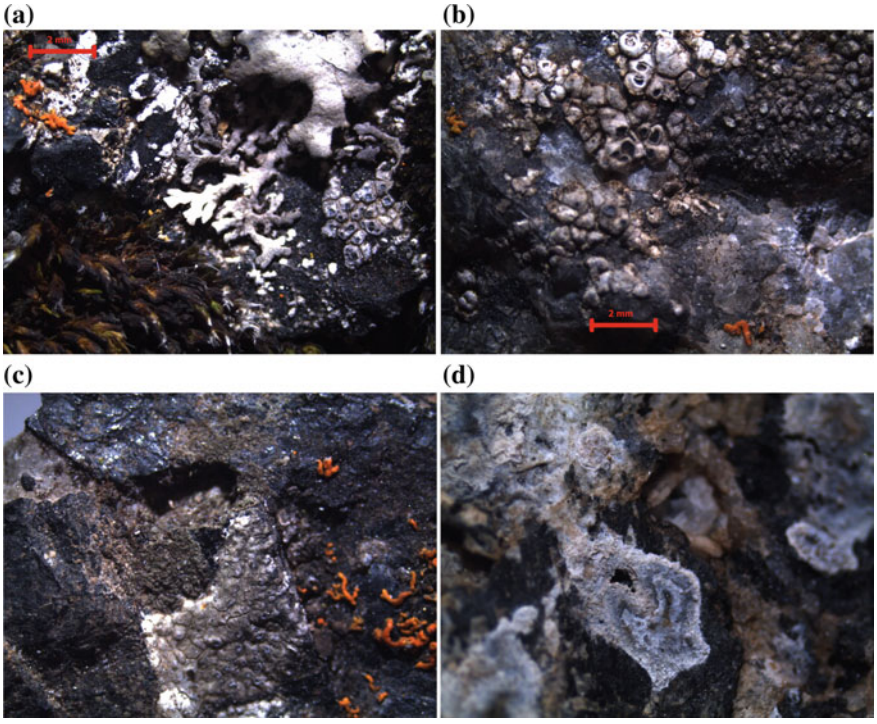


Fig. 28.3 Nepheline syenite Sangilen: **a** lichens: scale, leaf and moss; **b** calcite crusts under lichen; **c** leached calcite under the crust; **d** onyx-like deposit

28.4.2 Alkali Rocks

Alkali rocks of Sangilen and Batogol (Tuva, Easten Sayan, Russia) contains alkali minerals (nephelin, pyroxenoids) and also calcite of different generations, and graphite are characterized by different the degree of weathering of the component minerals, especially nephelin and calcite. Weathering of the lasts is caused cellular surface formation, where in the hollows live lower bioforms. In the delamination cracks carbonate deposits occur. They have different thickness, color shades and shapes: colloform, reniform aggregates, stalactite-like incrustations, the thinnest films, often enclosing biological forms. Sometimes formed structures like lime onyx (Fig. 28.3a–d).

28.4.3 Objects of Urban Cultural Heritage

Our studies of Moscow cultural heritage objects showed that, magmatic rocks—granite and gabbros—are the most resistant to weathering. Investigation of Moscow



Fig. 28.4 Moskvoretskiy most. General view of the bridge abutment, visible rust stains, salts, crystal crusts

Bridges—Moskvoretsky (red granites, Fig. 28.4) and Bolshoy Kamenny (grey granites, Fig. 28.5a, b)—is showed different weathering degree of granite facing blocks. They are differed in color, structure and mineral composition, surface treatment technique. They have cortical and sinter new forms, occupying large areas, on the front surface of the cladding. These micro-layer forms are differed in zonal structure and mineral composition. Their formation is associated with leaching and redeposi-



Fig. 28.5 Bolshoy Kamennuy most: **a** General view of the abutment, **b** fragment, visible salts and rust stains

tion of predominantly carbonate substance from cement and lime mortars; and iron oxides—from reinforced concrete structures. Zoning of mineral formation reflects seasonality: in the warm season there was an increase in zonal incrustation as a result of the deposition of bicarbonate substance, in winter they were covered with an ice crust (semi-icicles).

The initial carbonate mineral formation was observed by us at a number of monuments of the Military Fraternal Cemetery, where on the light-gray granite lining of the memorial structure (2016), the local appearance of incrustations fixes traces of "leakage" under the depressurized seam (Fig. 28.6a, b).

Powerful incrustations in the form of hanging stalactites, curtains, and others similar to cave formations are observed on the open vaulted planes of the open northern gallery of the Church of St. Sergio of Radonezh. In these areas, a special temperature and humidity regime created near the refectory block contributes to the formation of these carbonate forms on the arches, which in some places near the iron clips are painted in a yellowish color. A one-year carbonate new form that surrounds plant residue is fixed by us on the granite facing of the P. N. Lebedev sculpture Moscow State University, in front of Physical Faculty Building, Moscow (Fig. 28.7). It appeared the next year after the restoration of the object; strontium impurity was detected in it by analytical electron microscopic analysis (Fig. 28.8a–d).

The **carbonate rocks** are most unstable under biogenic destruction, of which, first of all, limestone, and to a lesser extent marble. As is known, the interaction of two spheres, biological and geological, manifests itself in carbonate rocks. The study of rocks in an analytical scanning microscope at high magnifications revealed various forms of bacterial formations—films, coccoids, strings, tubules, columnar, nodular, micro-layered, micro-clotted, lumpy, and other structures. There is an extensive literature on the effect of bacterial activity on carbonate precipitation. As is known, the mechanism of formation of carbonate forms occurs through sulfate reduction, methane formation, and others (Kuznetsov 2017).

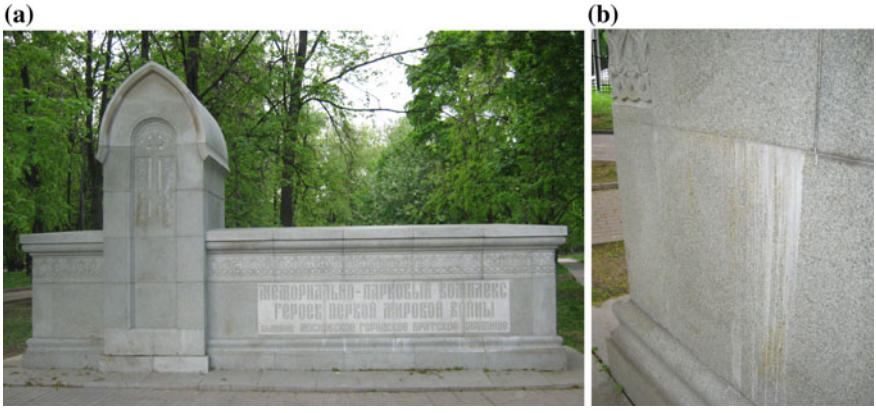


Fig. 28.6 Military Fraternal Cemetery: **a** view, **b** fragment of back of the monument, salt, crystal crusts



Fig. 28.7 Sculpture of P. N. Lebedev at the Physical Faculty of MGU

We studied new formations on limestone on the example of the white-stone buildings of the Moscow Kremlin, on the facades of the Assumption Cathedral, the basement of the Annunciation Cathedral, and separate different blocks of Lapidary. Usually, white-stone constructions have crystal crusts, represented by sulphates of sodium and calcium, as well as halite, the crusts of the latter are associated with anti-icing measures. They fix a certain level of crystallization of easily soluble salts. As a result of the use of a new anti-icing agent in the processing of the Cathedral Square near the New Year Tree the cast-iron floor in the Assumption Cathedral became rusty. On a mortar limestone plate, removed from the Spasskaya Tower of the Moscow Kremlin and stored in Lapidary, needle-shaped jarosite crystallized, the reference in composition, as determined by X-ray phase analysis.

Unusual crystal crusts were found on the white-stone blocks of St. George's Cathedral of Yur'ev-Polsky town (Fig. 28.9). In the interior of the cathedral, magnesium efflorescence (hydromagnesite) on the walls and pillars caused the corrosion of cast iron plates. Under one of the slabs lying on a sand bed, in addition to oxides and iron hydroxides, spherical tangled and water-like formations of magnesium oxide were found (Figs. 28.10a–c, and 28.11) (Antonova et al. 2014, 2015).

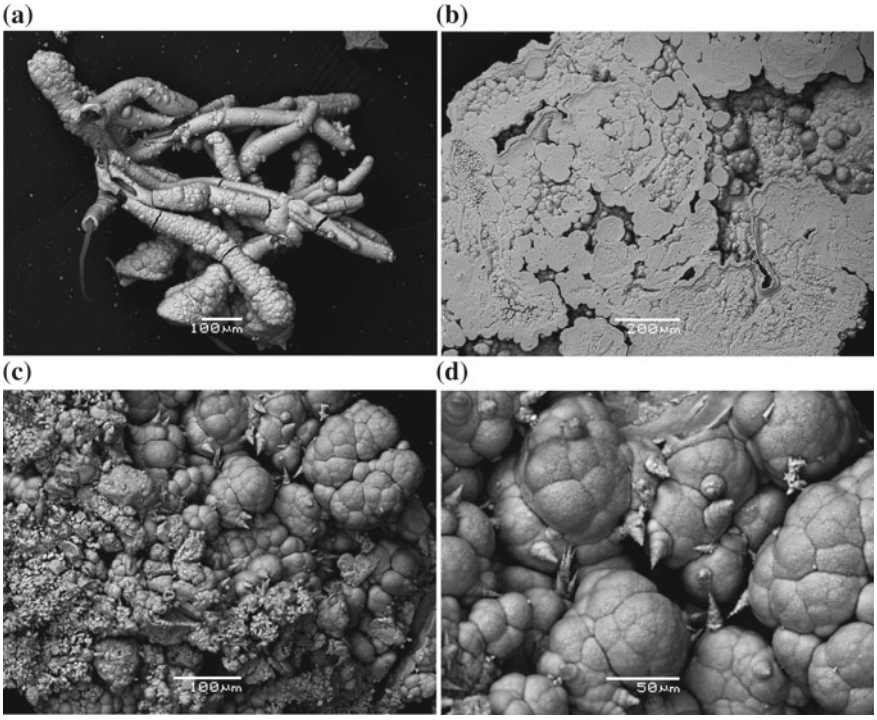


Fig. 28.8 **a–d** One-year crystal crust on the granite pedestal of Lebedev Sculpture (MGU, in front of Physical Faculty Building, Moscow). SEM images



Fig. 28.9 Yur'ev-Polskoy town, St. George Cathedral

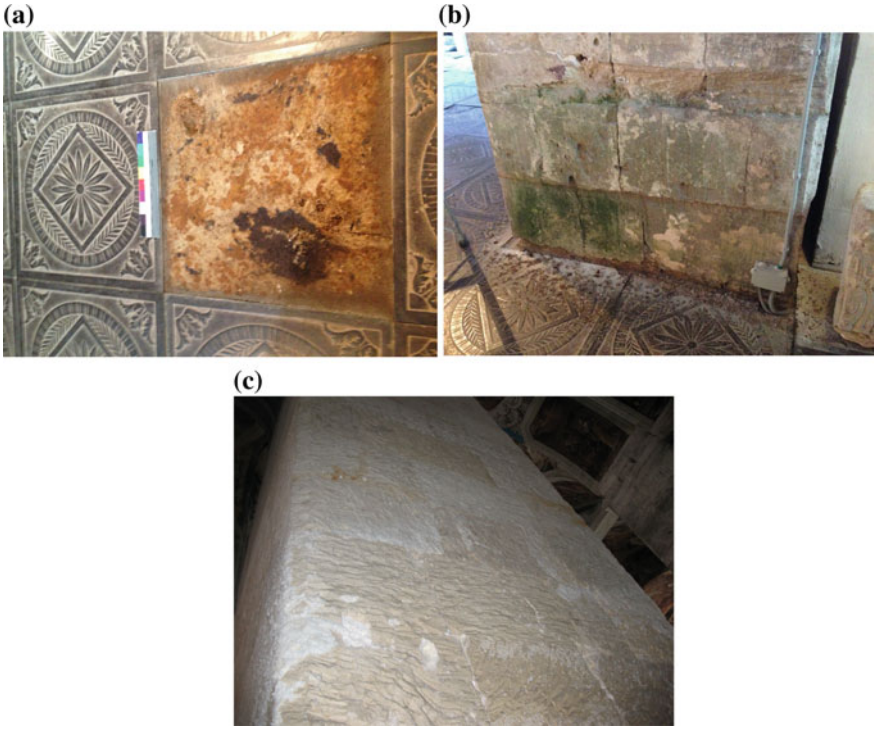


Fig. 28.10 Interior of St. George Cathedral: **a** Sand backfill under the cast-iron floor slab, **b** Salts on white stone (sulfates), and corrosion of cast iron plates, **c** Crystal rusts on white stone pillar

In the crystal crusts of the Postnikov chambers (Pskov), mirabilite, aphitalite, potassium alum, etc. were revealed at different sites (Lobzova et al. 2018).

The glazed surfaces of the tiles are the most resistant to biogenic destruction. On the example of archaeological finds (irrigation bowl from Gurzuf and tiles from the collection of the State Historical Museum, Moscow), the formation of layers of clay-carbonate, carbonate and clay-iron oxide was revealed. In the shallow pores of the bowl (black dots on the surface of lead glaze) microbiota residues were found, the analysis of which showed the presence of phosphorus, sulfur, and calcium (Fig. 28.12a–c). On the enamel coating of tiles, thin prints are flat and less often radial-radiant. They are clays in composition, and are traces of bio-populations on the clay substrate, which confirms the presence of phosphorus, sulfur, chlorine, manganese, iron, and alumina.

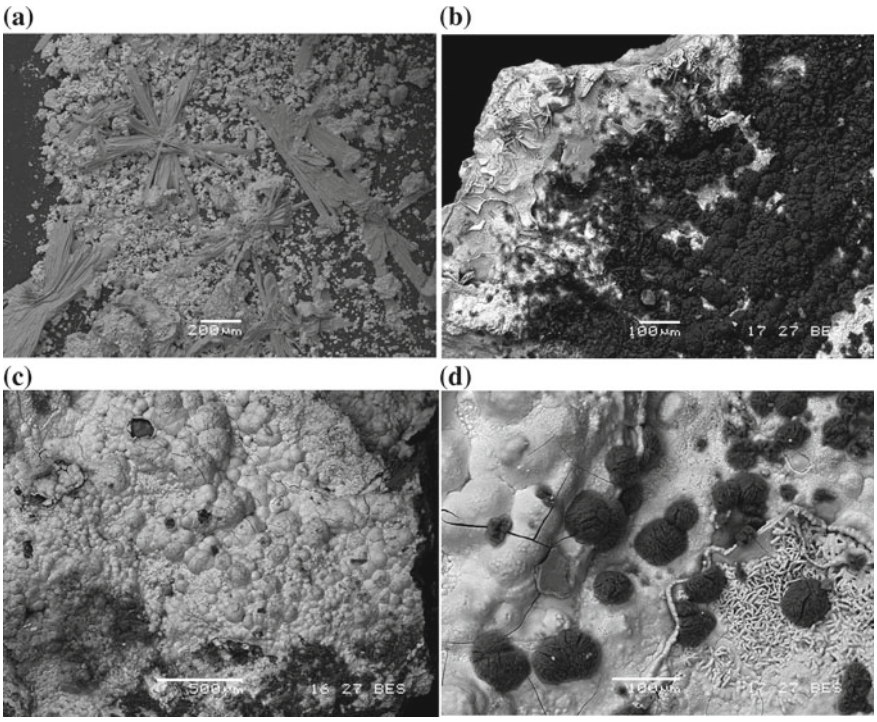


Fig. 28.11 SEM images of the salts from Yur'ev-Polskoy: **a** on cement—Troitzkiy Cathedral; **b**, **c**, **d** under cast iron—St. George Cathedral

28.5 Conclusions

Thus, new formations on various rocks, both in rock massifs and on cultural heritage sites in urban environments, are mainly carbonate in composition, heterogeneous in structure, biochemogenic, and adaptable to location.

The important role played by the mineral composition of the substrate, its structural and textural features and physical and mechanical state.

Zonal carbonate-ferrous material on granite slabs is the result of oxidation of reinforced concrete structures, and destruction of the binder solution. Currently, on the abutments of the Moskvoretsky Bridge, thorough renovated, these mounts are exposed when the granite cladding is removed.

The new formations are the result of a complex of reasons: seasonal development of biota, interaction of microbial communities, chemical oxidation, fluctuations in temperature and humidity and gas conditions, both general and local, associated with anthropogenic factors. All this determines the morphology, structure, texture and chemical composition of the local formation of the material. Limestones and marble are subject to the greatest biogenic destruction, and irrigated ceramic products are the least affected.

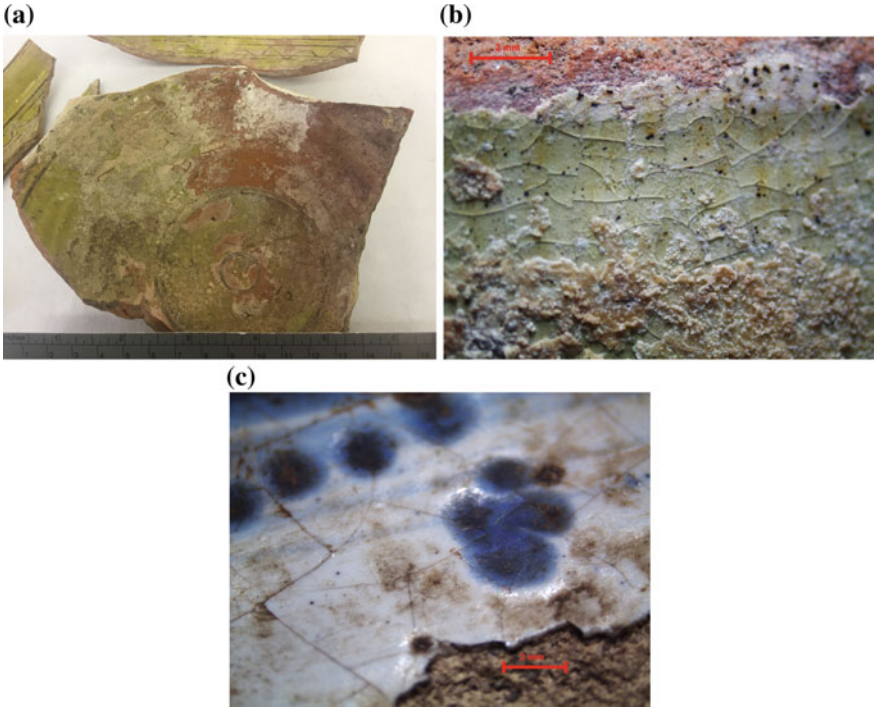


Fig. 28.12 New formations on ceramics: **a** fragment of the archeological glazed bowl, XIII century, Gurzuf; **b** detail of the surface of the glaze (black dots—relicts of biota, and white and yellow crystals—carbonate mineralization). **c** Fragment of the blue-white glazed tile (mid-18th century) from GIM collection, Moscow

Acknowledgements Authors are grateful to O. L. Magazina for SEM analysis.

References

Ageeva EN, Rebrikova NL (2003) Problems of conservation of monuments of rock art of Siberia. In: Art heritage. Storage, research, restoration 20:74

Antonova EI, Anpilogova AS, Lobzova RV, Karimova OV, Magazina LO (2014) Salt coatings on the surfaces of national and composite masonry material (St. George and Trinity Cathedrals Yur'ev-Polskoy). In: XI RMS General Meeting. Abstract book. St. Petersburg

Antonova EI, Lobzova RV, Burova AA, Karimova OV, Magazina LO (2015) Features of morphology and composition of salt crusts on the monuments of architecture and monumental sculpture. In: Mineralogy in whole space of this word» XII RMS General Meeting. Abstract book St. Petersburg, 384–385

Biogenic-abiogenic interaction in natural and antropogenic systems (2014) Abstract book of the V International Symposium. St. Petersburg

Biogenic-abiogenic interaction in natural and antropogenic systems (2018) Abstract book of the VI international symposium. St. Petersburg

Bulakh AG, Marugin VM (2013) Assessment of the state of monuments of architecture of St. Petersburg and monumental sculpture before and after restoration. Evaluation of the performance of work according to qualimetry. St. Petersburg University Publishing, Saint-Petersburg 56 c. (in Russian)

Bulakh AG, Vlasov DYu, Zolotarev AA, Marugin VM, Morozov MV, Savchenok AI, Fitzner BB, Frank-Kamenetskaya OV, Kheynrikhs KA, Shigoretz SB (2005) "Examination of stone in the monuments of architecture." In: Bulakz AG (ed) Science. Nauka, Saint-Petersburg. (in Russian)

Bulakh AG, Vlasov DYu, Frank-Kamenetsky OV (ed) (2012) Open-air Museum. Problems of preservation of monuments made of stone and bronze. Soyuz-Design, St. Petersburg

Chelishchev NF, Gribanova NK, Novikov GV (1998) Sorption properties of oceanic iron-manganese nodules and crusts. Nedra, Moscow (in Russian)

Chukhrov FV (1955) Colloids in the Earth Crust. Academy of Sciences SSSR Publishing, Moscow (in Russian)

Chukhrov FV, Gorshkov AI, Drits VA (1989) Hypergenic oxides of manganese. Nauka, Moscow (in Russian)

Croyn JM (2004) The elements of archaeological conservation, 1st edn. Taylor&Francis Publishing, London

Devlet EG (2002) Monuments of rock art: study, preservation, use. Russian Academy of Sciences, Moscow. (in Russian)

Frank-Kamenetskaya OV, Marugin VM, Vlasov DYu, Egorova VV (2010) Complex qualimetric monitoring of the state of stone monuments. Qualimetric monitoring of construction objects. Polytechnic, St.-Petersburg, pp 317–330

Frank-Kamenetskaya OV, Polyanskaya EI, Manurtdinova VV, Kurulev KS (2015) Decorative facing stone in the non-fields of the museum of urban sculpture. In: Open-air museum: modern approaches to the preservation of sculpture. Voronezh, pp 62–67

Gizburg II (1947) Geochemistry and geology of the ancient weathering crust, vol 2. Academy of Sciences SSSR, Moscow (in Russian)

Gizburg II, Katz AA, Korin IZ, Popkov VPh, Savel'ev II, Trubina KN (1946) Ancient weathering crusts on ultrabasic rocks of the Urals. Academy of Sciences SSSR. v.1., Moscow. (in Russian)

Kropachev SM, Lobzova RV (2004) The structure and petrographic characteristics of the rocky base of petroglyphs "Tomsk pisanitsa". M In: Modern engineering technologies. X Scientific-technical conference of teachers, staff, graduate students of the Faculty of Engineering. Abstacts. RUDN, pp 51–55

Kuznetsov VG (2017) Entertaining lithology. MAKS-Press, Moscow

Lobzova RV, Kochanovich AV (2005) Rocks, cortical detachment and patina on some sites of Siberian petroglyphs. In: Abstracts Book of the International conference "The World of Rock Art" M. Inst. of Archeology of the Russian Academy of Sciences, pp 165–168

Lobzova RV, Kochanovich AV, Abramov VYu. (2014) Petrographic, petrochemical and petro physical features of the rock paintings on the river Tomi. Bulletin of RUDN. N. 3, P 132–138

Lobzova RV, Karimova OV, Antonova EI (2018) Crusts and incrustations on natural and architectural objects. In: VI International Symposium "Biogenic-abiogenic interactions in natural and anthropogenic systems" Saint-Peresburg 24–27.09.2018, Abstracts book, 158

Martunov AI, YaA Sher (1989) Methods of archaeological research: a textbook for university students. High School, Moscow

Naumov VA (2018) Optical determination of the components of sedimentary rocks. Irkutsk

Petrov VP (1967) Fundamentals of the doctrine of the ancient weathering crusts. Nauka, Moscow

Pinevich AV (2005) Microbiology of iron and manganese. SPbU, St.-Petersburg

Rusakov AV, Zelenskaya MS, Frank-Kamenetskaya OV, Vlasov DYu, Gurzhy VV (2017) Transformation of MT-containing minerals under the influence of the fungus ASPERGILLUS NIGER. In: Proceedings of the anniversary Congress of the "200 years of the Russian Mineralogical Society." St.-Petersburg, 2:113–114

Rusakova ID, Barinova ES (1997) New Petroglyphs on river Tomi. In: Rock art of Asia. Kuzbassizdat, Kemerovo, 2:64–67

Rybnikov VV, Frank-Kamenetsky OV, Vlasov DY (eds) (2015) Open-air Museum. In: Modern approaches to the preservation of sculpture. OOO "MS", Voronezh

Schigorets SB (2015) New approaches to monitoring and restoration of petroglyphs (on the example of Tomsk pisanitsa). In:. Rytnikova VV, Frank-Kamenetskaya OV, Vlasov DYu. (eds) Open-air museum. Modern approaches to the preservation of sculpture. OOO "MS", Voronezh, pp 92–94

Timofeeva VN (ed) (2008) Monuments. In: Direction vector. Sat. art. on the restoration of sculpture and monitoring of monuments in the urban environment. Soyuz-Design, St.-Petersburg

Vernadsky VI (1954) Selected works. USSR Academy of Sciences. Moscow, 1:557. (in Russian)

Vernadsky VI (1994) Essays on Geochemistry. 7th. edn. USSR Academy of Sciences, Nauka, Moscow

Vlasov DYu, Frank-Kamenetskaya OV (2006) Destruction of natural stone in the urban environment. Proceedings of SPbOE. Ser. 1, 96:156–169

Vlasov DYu, Ratnikova VV, Frank-Kamenetsky OV (ed) (2016) Museum and monuments of the cemeteries of St. Petersburg. In: Existence, materials, diagnostics, safety."VVM", St.-Petersburg

Yudovich YaE, Ketris MP, Rybina NIn (2018) Geochemistry of titanium. Syktyvkar Geoprint. IG Komi NTS Ur wounds

Zelensky MG, Vlasov DYu, Zheludov VM (2015) Bio-destructions of monuments of the Museum Necropolis of St. Petersburg. In:Rybnikov VV, Frank-Kamenetsky OV, Vlasov DY (eds) Open-air Museum. Modern approaches to the preservation of sculpture. OOO "MS". Voronezh, p 71

Chapter 29
Biofilms on Granite Rapakivi in Natural Outcrops and Urban Environment: Biodiversity, Metabolism and Interaction with Substrate

Dmitry Yu. Vlasov, Elena G. Panova, Marina S. Zelenskaya, Alexey D. Vlasov, Katerina V. Sazanova, Oksana A. Rodina and Olga A. Pavlova

Abstract Granite rapakivi was widely used in the construction of historical buildings in St. Petersburg. This rock was mined in Karelia and southern part of Finland where old quarries are preserved. Biofouling of granite can be observed both in urban environments and in natural outcrops. Biofilms on granite rapakivi have a different structure, composition, speed of development. The aim of this work is the complex analysis of biological colonization of granite rapakivi in different environment. The biodiversity of biofilms was studied on granite monuments of Saint Petersburg as well as in the abandoned quarries of the southern part of Finland. The composition of micromycetes, cyanobacteria and organotrophic bacteria in biofilms was determined at different stages of colonization and destruction of the granite rapakivi. The composition of metabolites in biofilms and sediments on the surface of the rock was determined. More than 200 compounds were found in the samples from the quarry and about 60–100 low molecular weight organic compounds were detected in the samples from the urban environment. Concentration of certain compounds, especially polyols, was significantly higher in biofilms in the urban environment. The main features of biological colonization of granite rapakivi in the urban environment and natural outcrops were shown by scanning electron microscopy. The differences in the character of colonization of feldspar, quartz and mica were revealed. It was found that under the influence of bacteria *Bacillus subtilis* the intensity of elements leaching from granite minerals in the aquatic environment (model experiment) was significantly increased. Feldspars and mica were destroyed first of all.

D. Yu. Vlasov (✉) · E. G. Panova · M. S. Zelenskaya · O. A. Rodina · O. A. Pavlova
Saint Petersburg State University, Saint Petersburg, Russia
e-mail: Dmitry.Vlasov@mail.ru

A. D. Vlasov
The Archive of the Russian Academy of Sciences, Saint Petersburg, Russia

D. Yu. Vlasov · K. V. Sazanova
Botanical Institute of the Russian Academy of Sciences, Saint Petersburg, Russia

O. A. Pavlova
Beagle Ltd., Saint Petersburg, Russia

© Springer Nature Switzerland AG 2020

O. V. Frank-Kamenetskaya et al. (eds.), *Processes and Phenomena on the Boundary Between Biogenic and Abiogenic Nature*, Lecture Notes in Earth System Sciences,
https://doi.org/10.1007/978-3-030-21614-6_29

Keywords Granite · Weathering · Biofouling · Biodeterioration · Microorganisms · Environment · Model experiments

29.1 Introduction

Granite is traditionally used as a stone decoration material, especially near mining granite's areas. Different types of granites used in historical monuments and cities decorations in different climate zones. Granite is a strong material, but it is also subject to destruction (mechanical, chemical, biological) especially in northern climate. The problem of stone deterioration has a great importance to architects, designers, restorers and stone-mining companies. In recent years, scientists have noticed that the destruction of granite is a result of interrelated physical, chemical and biological processes (Panova et al. 2014, 2016; Toreno et al. 2018). There are a lot of publications about biological colonization of granite (Grbić et al. 2010; Sanjurjo-Sánchez et al. 2012; Ozturk et al. 2014; Pozo-Antonio et al. 2016). Studies have shown that the development of biofouling is preceded by damage to the stone due to abiotic factors. They prepare the surface of the stone for its subsequent biological colonization. First of all this is due to changes in the surface structure and the appearance of cracks, cavities, surface irregularities, where microorganisms can accumulate and develop. The variety of rock biofouling in the urban environment is less than in natural ecosystems (outcrops, abandoned quarries, etc.). At the same time, the dominance of the most adapted species, which form the basis of lithobiotic communities, is especially noticeable in the city. Lithobiotic communities are often called biofilms. They have a different color, thickness, species composition and degree of attachment to the substrates. They may include bacteria, microscopic algae, micromycetes and lichens. The development of rock-inhabiting biofilms can lead to changes of superficial level of rock and primary soil formation. Mosses are often can be associated with biofilms. Biodiversity and properties of biofilms on the granites stay poorly researched. Their role in the processes of biological weathering as well as biogeochemical aspects of this problem is still insufficiently understood.

The aim of our investigation is the complex analysis of biological colonization and bioweathering features for granite rapakivi in city and in quarry area and understanding the role of microorganisms in transformation of this substrate.

29.2 Materials and Methods

29.2.1 Materials

Among the largest industrial megapolises Saint Petersburg is a unique architectural city with grand historical centre. High degree of preservation and authenticity of historical areas has made the ground to include the historical centre of St. Petersburg



Fig. 29.1 Historical Montferrand quarry. Biofouling of granite rapakivi

into the List of World Heritage Sites in Europe, UNESCO. Saint Petersburg is often apprehended as a granite city. No wonder that granite is its historical symbol. Rapakivi granite is the most famous among granites. It is used in many architectural ensembles and monuments of Saint Petersburg which make up its unique image. This granite has a remarkable pattern: large ovoid clusters of K-feldspar with diameter 3–5 cm surrounded by the rim of greenish-grey plagioclase are set into fine-grained matrix of feldspars, quartz and biotite.

Rapakivi granites used for building in Saint Petersburg were quarried from Vyborg massive. It occupies the area about 1800 km^2. In the old time granite was also quarried near the Finnish town of Fredrikshamn (Hamina). The most famous are Pyterlahti and Hämoenkylä granite quarries. In the area of Piterlahti (Virolahti) in the southeastern part of Finland there is historical Montferrand quarry with coordinates N 60° 34.207′ E 027° 43.835′ (quarry I) (Fig. 29.1). The block of granite rapakivi from this quarry was used for construction of the Alexander column on Dvortsovaya square (Saint Petersburg).

Additionally, other quarries were also examined: quarry II (N 60° 31.855′ E 027° 39.698′); quarry III (N 60° 32.101′ E 027° 39.823′); quarry IV (N 60° 44.413′ E 028° 00.564′). Granite outcrops near Vyborg as well as in Park Monrepos were also observed. For comparative aims material for research also was collected on granite monuments and buildings of Saint Petersburg and Vyborg.

29.2.2 Sampling

Samples can be divided into 2 groups: samples of the crumbling fragments and samples taken by undamaging methods from the surface of the object. In cases of significant damage of the integrity of the rock surface with fragmentation, flaking and shedding of stone material, the samples (small fragments of granite) were taken

into sterile containers. In addition, there were taken scrapings from contaminated or biofouling parts of the stone surface in a sterile container or directly on a nutrient medium in Petri dishes and test tubes. Collection of wet samples for detection of cyanobacteria was carried out in sterile conical tubes with screw cap, as well as in sterile containers up to 120 ml. Total more than 500 samples were collected and studied for the period from 2013 to 2018.

Before sampling the special attention was paid to changes of the granite surface layer. Main forms of granite damage were described (stains of various colours, cracks, chips, pits and others). Characterizing the biofouling of the granite we noted the colour of biofilms, their number, thickness, density, dependence of surface relief, connection with certain minerals. At first visually (next in laboratory) the types of biofilm according the dominating microorganisms (algae, cyanobacteria, microfungi, microlichens) were defined. While characterizing macrofouling of granite we recorded the presence of macrolichens, mosses and seed plants; paid attention to their association with specific components of rocks and structural spaces on the granite. Total distribution of biofouling on the granite surface was estimated.

For the analysis of cyanobacteria, organotrophic bacteria and fungi as well as for metabolomic analysis the following types of biofouling were collected: green biofilms with dominance of cyanobacteria and algae (1); dark crust (2); primary soil with moss (3); primary soil under vascular plants (Betula sp., Deschampsia sp. and others) (4); weathering under lichen (5); pigmented (mostly red and orange) biofilms fused with a surface of the stone (6); light-colored (white, beige) biofilms fused with a surface of the stone (7). Each type was selected in 2–4 replications (depending on the frequency of occurrence).

29.2.3 Primary Study

At the primary study of the samples of damaged granite the attention was paid on the structure of the granite, micro cracks, holes and other surface irregularities, which can serve as a shelter for microorganisms and testify the state of the surface layer of the stone. Magnification of the ordinary binocular loupe allows determining the occurrence of biological objects (fungi, algae and lichen) and assessing the localization of lithobiontic organisms and the degree of disintegration of the surface layer of the stone. The primary observation of damaged granite gives an opportunity to choose the most adequate method of isolating the microorganisms from the analyzed sample. For example, when microscopic fungi (micromycetes) are concentrated in the micro cracks and their isolation from the surface of the stone is difficult, there has been used the preliminary activation of micromycetes by placing the sample or its fragment in a moist chamber under sterile conditions for 1–2 weeks. After the formation of distinct hypha structures (fungus "goes out" of microcracks on the surface of the rock) they were removed (under binocular loupe) with a sterile injection needle onto the nutrient medium. In the same way was carried out the selective isolation of microcolonial fungi when small and compact colonies were removed whole

or by fragments onto the nutrient medium. It is reasonable to select the areas for future investigation by scanning electron microscopy (SEM) during the first visual observations.

29.2.4 Isolation of Microorganisms

Traditional methods of mycology and microbiology were applied for detection and identification of microorganisms in biofilms on the surface of the granite. In the course of bacteriological studies the microorganisms were isolated on agarosed (solid) nutrient medium: EHM - enzymatic hydrolyzate of meat (to detect a wide range of heterotrophic bacteria and determine the total microbial number), nutrient medium of Alexandrov with sand (to extract silicate bacteria), potato-ammonium agar (for isolation of actinomycetes). Besides selective liquid nutrient medium were used for extraction the chemolithotrophic bacteria. The quantification of bacteria was performed using a dilution method (Tepper et al. 2005).

The following nutrient media were used for primary isolation, sustenance in culture and identification of micromycetes: medium of Chapek-Doks classic and its modifications (by the content of glucose and some salts), agarosed oat broth with the addition of glucose, agar Saburo, potato-glucose agar, water agar, 2% maltz-agar. The following methods of fungi isolation in pure culture from samples of damaged granite were used:

– sowing crumbs and small fragments of the substrate on the surface of the medium;
– flushing from the surface of the substrate, subsequent dissolution of the suspension and sowing on the nutrient medium;
– selective isolation of fungi from the surface of the substrate on the nutrient medium with the injection needle.

Combination of different ways of isolation of micromycetes and different nutrient media gives the opportunity for full and comprehensive analysis of micromycetes species diversity on the stone substrate.

29.2.5 Identification of Biodestructors of Granite

Identification of bacteria and fungi were made after their isolation in the pure culture. Duration of cultivation of various microorganisms varied significantly. It was depended on the speed of growth of microorganisms in the culture and formation of the taxonomic signs (morphological structures) used to define species. For example, in the course of identification of micromycetes the most of obtained cultures were incubated in the thermostat for 2–3 weeks at 25 °C until the formation of sporulation.

Identification of cyanobacteria was carried out after their cultivation in distilled water for a week or a month (using light microscopy—microscope Leica DM 1000)

according to the standard key (Gollerbakh et al. 1953; Komárek and Anagnostidis 1998, 2005). Verification of types in accordance with modern nomenclature was performed using electronic databases AlgaeBase (http://www.algaebase.org/). Microbiological analysis of the samples of granite with biofilms was carried out in the laboratories of Saint Petersburg State University.

The use of classical methods of microbiology often does not allow to reveal the whole spectrum of microorganisms developing in biofilms on rocky substrates. Metagenomic analysis was used to determine a wide range of bacteria and micromycetes in biofilms from the surface of granite monuments of St. Petersburg. The work was carried out in the resource center of Saint-Petersburg State University "Development of cellular and molecular technologies". Metagenomic study of bacteria diversity in biofilms on granite was carried out on the basis of the 16S rRNA genes analysis. Deep sequencing of the 16S-RNA gene was performed using the Ion Torrent PGM system (Life Technologies). A library for sequencing the 16S-RNA gene was prepared by amplifying a region V4–V5 using primers U515F (5′-GTGCCAGCMGCCGCGGTAA-3′) and 926R (5′-CCGTCAATTCMTTTRAGT-3′). Amplification was performed using the kit FastStart High Fidelity PCR system (Roche). Diversity analysis was done using the software package Qiime (version 1.9.0) under the standard protocol. The classification was carried out on the basis of a comparison with the Greengenes base. Metagenomic study of fungi diversity in biofilms on granite was carried out with primers for site amplification ITS1-5.8S–ITS2 (Beagle, Russia): ITS4 TCCTCCGCTTATTGATATGC; ITS7 CGTGARTCATCGARTCTTTG.

29.2.6 Scanning Electron Microscopy

Scanning electron microscopy was used in order to study peculiarities of distribution of microorganisms in the surface layer of the stone, and identify the main areas of colonies localization and paths of destructors penetration into the substrate. This method also gives the opportunity to characterize the relationship between lithobiontic organisms during colonization of the granite, to analyze the dynamics of the colonization of stone depending on its properties and external conditions and to determine the ability of microorganisms to cause the destruction of the rock. Samples of the damaged stone (0.5–1.0 cm × 0.5–1.0 cm) were initially examined under binocular loupe. The criterion of selection for SEM analysis was the presence of structures of microorganisms on the stone surface, as well as information on the possible localization of micromycetes in the microzones (inhomogeneous areas, cracks, cavities) of the rock. In some cases (at long term storage of material) the samples were kept in a humid chamber with the purpose of enhancing the development of micromycetes, after which the material was fixed by the following method:

– fixation of samples by 4% glutaraldehyde in 0.1 m buffer solution for 2 h;
– washing up after fixation in 0.1 m buffer solution for 1.5 h;

– drying up to the critical point;
– mounting samples on the tables for scanning electron microscope using a special glue;
– coating the surface of samples with gold.

The material was examined under the scanning electron microscope in the range of magnification from 100× to 10,000×. SEM studies were performed on electron microscope ABT-55 (Japan).

29.2.7 Chromatography-Mass Spectrometry of Biofilms

Analysis of small organic molecules in several types of biofilms was made using the method of gas chromatography-mass spectrometry. Samples were taken from granite covered by different types of biofouling. Extraction of scraping samples from the stone surface was performed with cold methanol (15 ml, −25 °C) and centrifuged (10 min, 400 × g) at room temperature. Then the extracts were evaporated at 40 °C, dissolved in pyridine and obtained TMS derivatives using N, O-Bis(trimethylsilyl)-F-acetamide. Analysis of scraping extracts from the surface of the stone was carried out by gas chromatography-mass spectrometry (GC-MS) on the Agilent device with mass-selective detector MSD5975, column HP-5MS, 30 m × 0.25 mm. Chromatography was performed with linear programming of temperature from 70 to 320 °C at a speed of 4 °C/min. Data collection was carried out using Agilent ChemStation software. Processing and interpretation of mass spectrometric information was carried out using the program AMDIS and standard library NIST2005 and own library of bin RAS connection standards. Quantitative interpretation of the chromatograms was performed by internal standardization of the hydrocarbon C23 using the program UniChrom http://www.unichrom.com/unichrome.

29.3 Result and Discussion

29.3.1 Biodiversity of Microorganisms in Biofilms on the Granite in City and in Quarries

29.3.1.1 Fungi

As a result of mycological study 64 species of microscopic fungi as well as sterile forms of light and black mycelium were detected in biofilms on granite in natural and urban environments (Table 29.1). A rather high diversity of micromycetes in biofilms on granite in various conditions was revealed (47 species—St. Petersburg, 42—species in granite outcrops). Some micromycetes (25 species) were common for

Table 29.1 Micromycetes identified in biofilms on the surface of granite

Species of micromycetes	Urban environment[a]	Natural outcrops[b]
1. *Absidia caerulea* Bainier	–	+
2. *Acaulium acremonium* (Delacr.) Sand.-Den., Guarro and Gené	–	+
3. *Acremoniella atra* (Corda) Sacc.	+	–
4. *Acremonium hyalinulum* (Sacc.) W. Gams	+	–
5. *A. potronii* Vuill.	–	+
6. *Alternaria alternata* (Fr.) Keissl.	+	+
7. *Arthrinium phaeospermum* (Corda) M.B. Ellis	+	+
8. Aspergillus niger Tiegh.	+	–
9. *A. versicolor* (Vuill.) Tirab.	+	–
10. *Aureobasidium pullulans* (de Bary and Löwenthal) G. Arnaud	+	–
11. *Botrytis cinerea* Pers.	+	–
12. *Chaetomium globosum* Kunze	+	+
13. *Cladosporium cladosporioides* (Fresen.) G. A. de Vries	+	+
14. *C. herbarum* (Pers.) Link	+	+
15. *C. sphaerospermum* Penz.	+	–
16. *Coniosporium* sp.	+	+
17. *Didymella glomerata* (Corda) Qian Chen and L. Cai	+	–
18. *D. pomorum* (Thüm.) Qian Chen and L. Cai	–	+
19. *Doratomyces stemonitis* (Pers.) F. J. Morton and G. Sm.	–	+
20. *Epicoccum nigrum* Link	+	–
21. *Exophiala exophialae* (de Hoog) de Hoog	+	–
22. *Fusarium chlamydosporum* Wollenw. and Reinking	+	–
23. *F. oxysporum* Schltdl.	+	+
24. *Fusarium* sp.	+	+
25. *Gliocladium catenulatum* J. C. Gilman and E. V. Abbott	–	+
26. *Humicola grisea* Traaen	+	–
27. *Monodictys levis* (Wiltshire) S. Hughes	+	–
28. *Mortierella lignicola* (G. W. Martin) W. Gams and R. Moreau	–	+
29. *M. polycephala* Coem.	–	+
30. *Mucor hiemalis* Wehmer	+	+
31. *M. plumbeus* Bonord.	+	+
32. *M. racemosus* Fresen.	+	+
33. *M. ramosissimus* Samouts.	–	+
34. *Neocosmospora solani* (Mart.) L. Lombard and Crous	+	+

(continued)

Table 29.1 (continued)

Species of micromycetes	Urban environment[a]	Natural outcrops[b]
35. *Paecilomyces javanicus* (Bally) A. H. S. Br. and G. Sm.	+	+
36. *P. lilacinus* (Thom) Samson	+	−
37. *P. marquandii* (Massee) S. Hughes	−	+
38. *P. variotii* Bainier	+	+
39. *Penicillium brevicompactum* Dierckx	+	+
40. *P. chrysogenum* Thom	+	+
41. *P. citrinum* Thom	+	−
42. *P. decumbens* Thom	+	+
43. *P. herquei* Bainier and Sartory	+	+
44. *P. lanosum* Westling	−	+
45. *P. oxalicum* Currie and Thom	−	+
46. *Phaeosclera* sp.	+	−
47. *Phialophora fastigiata* (Lagerb. and Melin) Conant	+	−
48. *Phialophora* sp.	−	+
49. *Phoma herbarum* Westend.	+	+
50. *Phoma* sp.	+	−
51. *Polyscytalum fecundissimum* Riess	−	+
52. *Rhizopus stolonifer* (Ehrenb.) Vuill.	+	+
53. *Sarocladium strictum* (W. Gams) Summerb.	+	+
54. *Scytalidium lignicola* Pesante	+	+
55. *Sordaria* sp.	−	+
56. *Sydowia polyspora* (Bref. and Tavel) E. Müll.	+	−
57. *Talaromyces diversus* (Raper and Fennell) Samson, N. Yilmaz and Frisvad	+	−
58. *T. purpureogenus* Samson, N. Yilmaz, Houbraken, Spierenb., Seifert, Peterson, Varga and Frisvad	+	+
59. *T. variabilis* (Sopp) Samson, N. Yilmaz, Frisvad and Seifert	−	+
60. *Trichoderma aureoviride* Rifai	−	+
61. *T. koningii* Oudem	+	+
62. *T. viride* Pers.	+	+
63. *Ulocladium chartarum* (Preuss) E. G. Simmons	+	−
64. *U. oudemansii* E. G. Simmons	+	−
65. Sterile light-colored fungus	+	+
66. Sterile dark-colored fungus	−	+

Note [a]Granite embankments, monuments from the Museum Necropolis of St. Petersburg, the facades of historical buildings; [b]Abandoned quarries in Southern Finland

Table 29.2 The distribution of the main groups of fungi in the biofilms according to metagenomic analysis

Fungal taxa	Types of biofilms on the granite surface	
	With dominance of algae (Green biofilm)	With dominance of fungi and mud deposits (Black biofilm)
Ascomycota	70.6	87.8
Basidiomycota	16.4	7.7
Chytridiomycota	0.0	0.6
Glomeromycota	1.2	0.2
Zygomycota	5.5	0.2
Unidentified	6.2	3.4

the city and natural outcrops. The domination of dark-colored fungi in biofilms on the granite surface was typical for the urban environment. The domination of light-colored fungi was typical for natural granite outcrops. It is interesting to note that some fungal species can be characterized as superdominants in biofilms on granite in an urban environment. They relate mainly to the genera *Cladosporium, Alternaria, Aureobasidium* and also black yeast-like fungi. In biofilms in granite outcrops this dominance does not appear.

The composition of micromycetes on the surface biofilms on granite monuments was also investigated using metagenomic analysis (Table 29.2).

The results of the metagenomic analysis of samples are largely consistent with the data obtained using classical mycological methods. Obvious dominants in all samples are anamorphic ascomycetes, what was also shown with isolation of micromycetes on artificial agar nutrient media. This group includes the most well-known destructors of stone materials (Gadd 2007). It is interesting to note that while isolation by classical methods basidiomycetes were not isolated, whereas the metagenomic analysis showed a significant proportion of these fungi in all samples.

In black biofilms, where dark-colored fungi predominate, the content of ascomycetes naturally turned out to be higher compared to green biofilm.

29.3.1.2 Organotrophic Bacteria

As a result of the metagenomic analysis of biofilms samples taken from granite in urban environments the ratio of the main groups of bacteria was established (Fig. 29.2).

The results of metagenomic analysis show that two main groups dominate in biofilms on monuments: *Bacteroidetes* и *Proteobacteria.* The *Bacteroidetes* group was characterized by a large presence in black biofilms. A significant part of the community in all samples are actinomycetes, what is partially consistent with the data obtained by classical microbiological methods. At the same time, the highest pro-

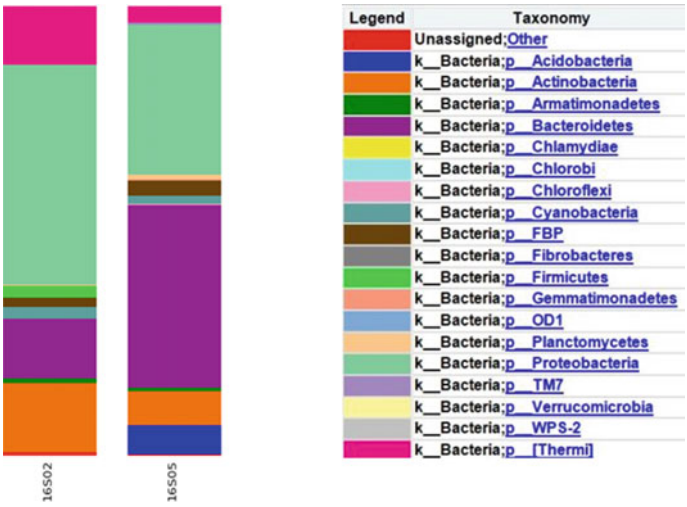


Fig. 29.2 Main groups of bacteria (metagenomic analysis) in the biofilms from granite surface in urban environment (16S02—green biofilm; 16S05—black biofilm)

portion of actinomycetes was found in biofilms dominated by algae. *Acidobacteria* were isolated in a significant amount from black biofilms (16S05).

Comparison of the bacteriological culture studies of biofilms from the surface of damaged granite from different regions indicates a high bacterial content in most of the studied samples (more than 10^6 CFU/g of substrate on the enzymatic hydrolyzate of meat medium). The number of bacteria in samples from the urban environment was comparable or superior the samples from the quarry. It is obvious that anthropogenic pollution of granite monuments and constructions (a monument to V. V. Stasov in Necropolis of Urban Sculpture Museum, the Peter and Paul Fortress) accelerate to the formation of a saturated bacterial community. At the same time the composition of bacteria in the polluted and natural environment were markedly differed. It was established that a significant proportion of isolates from the quarries samples were actinomycetes whereas in samples from the monument V. V. Stasov these bacteria were detected in small quantities. At the same time the mucous and spore-forming bacteria of the genus *Bacillus* were noted in high numbers both in the urban environment and in the quarries. In our opinion the leading factors in the formation of bacterial communities in the urban environment can be significant atmospheric and soil pollution, excreta of woody plants falling on the monument, as well as the abundant development of algae, which are also able to provide nutrient for bacteria. This assumption is supported by the fact that the highest abundance of organotrophic bacteria was revealed in biofilms with domination of green algae.

29.3.1.3 Cyanobacteria

Cyanobacteria study was conducted for the following types of communities from the granite surface: green cortical biofilms, in the wet state it is soft and mucous (type 1); dark colored cortical biofilms (type 2); primary soil under mosses (type 3); primary soil under vascular plants in places of granite weathering (type 4); primary soil under lichens (type 5); pigmented (mostly red and rufous) biofilms, fused with the stone surface (type 6); light-colored (white, beige color) biofilms, fused with the stone surface (type 7). As a result of our study 54 cyanobacteria taxa belonging to 5 orders 16 families 23 genera were revealed (Table 29.3). Ten taxa were iden-

Table 29.3 Occurrence of cyanobacteria in biofilms and surface deposits on granites in abandoned quarries in southern Finland and on the Korela Fortress walls

Species of cyanobacteria	Types of biofilms and surface deposits on granite				
	1	2	3	6	7
Aphanocapsa parietina (Nägeli ex Kützing) Nägeli (Näg.) Elenk.		1			
Aphanocapsa holsatica (Lemmermann) G. Cronberg and Komárek	1				
Aphanocapsa muscicola (Meneghini) Wille		1		1	
Calothrix parietina Thur. ex Born. and Flah.	1	3	1		
Calothrix sp.	1			1	
Chondrocystis dermochroa (Nägeli) Komárek and Anagnostidis		1			
Chroococcus minor (Kützing) Nägeli	1				1
Chroococcus minutus (Kützing) Nägeli		1		1	1
Chroococcus turgidus (Kützing) Nägeli		1			
Cyanobium gaarderi (Ålvik) Komárek, Kopeck and Cepák				1	
Cyanothece aeruginosa (Nägeli) Komárek				1	
Gloeobacter violaceus Rippka, J. B.Waterbury and Cohen-Bazire, nom. Cons.				1	
Gloeocapsa alpina Näg. Emend Brand					1
Gloeocapsa compacta Kütz.	1				
Gloeocapsa punctata Näg. Ampl. Hollerb.				1	
Gloeocapsa rupestris Kützing	1			1	
Gloeocapsa sp.					
Gloeocapsa atrata Kützing, nom. Illeg.	3		1	1	1
Gloeocapsopsis magma (Brébisson) Komarék et Anagnostidis		2		2	1
Gloeocapsopsis crepidinum (Thuret) Geitler ex Komárek					1
Gloeothece palea (Küzt.) Rabenh.		1			
Hapalosiphon pumilus Kirchner ex Bornet and Flahault		1			

(continued)

Table 29.3 (continued)

Species of cyanobacteria	Types of biofilms and surface deposits on granite				
	1	2	3	6	7
Jaaginema geminatum (Schwabe ex Gomont) Anagnostidis & Komárek (Menegh.)	1				
Jaaginema pseudogeminatum (G. Schmid) Anagnostidis & Komárek					1
Johannesbaptistia pellucida (Dickie) W. R. Taylor and Drouet (Dickie) Taylor et Dronet				1	
Johannesbaptistia schizodichotoma (J. J. Copeland) Komárek and Anagnostidis				1	
Leptolyngbya amplivaginata (Goor) Anagnostidis and Komárek van Goor		1			
Leptolyngbya cebennensis (Gomont) I. Umezaki and M. Watanabe				1	
Leptolyngbya foveolarum (Rabenhorst ex Gomont) Anagnostidis et Komarek 1988	2	1		2	
Leptolyngbya lagerheimii (Gomont ex Gomont) Anagnostidis and Komárek (Mob.) Gom.		1			
Leptolyngbya perelegans (Lemmermann) Anagnostidis and Komárek Lemm.	1				
Leptolyngbya valderiana (Gomont) Anagnostidis and Komárek (Delp.) Geitl.					1
Leptolyngbya angustissima (West and G. S.West) Anagnostidis and Komárek	1			1	2
Leptolyngbya tenuis (Gomont) Anagnostidis and Komárek					1
Lyngbya martensiana Meneghini ex Gomont		1			
Lyngbya sp.	1				
Microcoleus paludosus Gomont	1				
Microcystis pulverea (H. C.Wood) Forti	1				1
Nostoc microscopicum Carmichael ex Bornet and Flahault			1		
Phormidesmis molle (Gomont) Turicchia, Ventura, Komárková and Komárek (Kütz) Gom.					1
Phormidium breve (Kützing ex Gomont) Anagnostidis and Komárek	1				
Phormidium corium Gomont ex Gomont	1				
Phormidium granulatum (N. L. Gardner) Anagnostidis					1
Phormidium interruptum Kützing ex Forti	1				
Phormidium inundatum Kützing ex Gomont		1			
Phormidium papyraceum (Ag.) Gom.	1				
Phormidium puteale (Montagne ex Gomont) Anagnostidis and Komárek		1			

(continued)

Table 29.3 (continued)

Species of cyanobacteria	Types of biofilms and surface deposits on granite				
	1	2	3	6	7
Planktolyngbya bipunctata (Lemmermann) Anagnostidis and Komárek	1				
Planktolyngbya limnetica (Lemmermann) Komárková-Legnerová and Cronberg	1				
Stigonema ocellatum Thuret ex Bornet and Flahault (Dillw.)	1				
Synechocystis aquatilis Sauv.	1			1	
Synechocystis parvula Perfiliev [Perfiljev]	1				
Synechocystis salina Wislouch	1				
Synechocystis minuscula Woronichin		1		1	1
In total	24	16	3	17	14

tified in quarry I (the Montferrand quarry), 20 taxa in quarry II, 9 taxa in quarry III, 26 taxa in quarry IV and only 6 taxa on the Korela Fortress walls. According to the data of Vinogradova and Mikhailyuk (2009) species of genera *Gloeocapsa* Kütz. em. Hollerb., *Gloeothece* Näg., *Chamaesiphon* Br. et Grun., *Calothrix* (Ag.) V. Poljansk., *Tolypothrix* Kütz., *Scytonema* Ag. are most typical for irrigated rocks. But we found only species from genera *Gloeocapsa*, *Gloeothece*, *Calothrix*. The order of *Synechococcales* were represented by the largest number of families (4), genera (7) and species (21); *Chroococcales* also had a large number of species (16). Family *Leptolyngbyaceae* was the most widely represented (11 taxa). In the genus *Leptolyngbya* 8 species were noted (15% of the identified diversity).

Cyanobacteria were not found only in biofilms of 4 and 5 types (soil under vascular plants in places of granite weathering; primary soil under lichens). At the same time cyanobacteria were found in the primary soil under mosses. It can be explained the mosses ability to retain moisture providing a more suitable conditions for microorganisms.

The species *Gloeocapsa atrata* which we did not find on the Korela Fortress was determined as a dominant of biofilms on granites in general and, in particular, for the first type of biofilms. *Leptolyngbya foveolarum* was seen at all sampling points. *Calothrix parietina* and *Gloeocapsopsis magma* were dominant for the second type of biofilms. In the pigmented (red) biofilms (type 6) a combination of dominant species from 1 and 2 types occurs: *Leptolyngbya foveolarum* and *Gloeocapsopsis magma*. The color of this type of biofilms is most likely associated not only with the species composition but also with the characteristics of the substrate.

For estimation of investigated quarries similarity the Serencien–Chekanovsky similarity index was used (Table 29.4). The index of similarity of taxonomic lists probably depends on the conditions of humidity (Quarry I and III are more humid).

Table 29.4 Serencien-Chekanovsky similarity index values for pairwise comparison of the studied territories

	Quarry I (the Montferrand quarry)	Quarry II	Quarry III	Quarry IV
Quarry II	0.25			
Quarry III	0.46	0.38		
Quarry IV	0.29	0.44	0.21	
Korela Fortress	0.14	0.30	0.15	0.23

Table 29.5 Serencien-Chekanovsky similarity index values for pairwise comparison of biofilm types

Types of biofilms and surface deposits on granite	1	2	3	6
2	0.11			
3	0.17	0.12		
6	0.34	0.34	0.11	
7	0.27	0.25	0.13	0.48

It is necessary to note the difficulties to assess the similarities of species composition without having the full range of biofilm types at each of the quarries.

Pairwise comparison of cyanobacteria taxonomic lists from different types of biofilms is more appropriate. The highest index of similarity (0.48) was calculated by comparing pigmented light and bright biofilms fused with a stone (Table 29.5).

Low indexes of similarity between the selected types of biofilms suggest that the taxonomic composition of cyanobacteria is quite different in the biofilms of different colors. In this way it is possible to make quick rough estimates of the composition of biofilms depending on their color.

29.3.2 Metabolomic Analysis of Different Biofilms

For understanding the development of microorganisms on rocks it is important to study not only the structure of microbial community but also the biochemical composition of superficial deposits. The composition of these deposits includes the products of the metabolism of microorganisms in the lithobiont community, weathering products of rocks and substances deposited from the environment (Martino 2019). Sources of input of such substances can be precipitation, soil contamination, surrounding vegetation, animals, anthropogenic pollution. The interaction of microorganisms in biofilms and primary soils is based on network of biochemical processes occurring in microbial communities. Some species use metabolites produced by neighboring species (Zhang and Powers 2012). An important biochemical characteristic of a community of organisms on the surface of a stone is the metabolic system—i.e. set of

organic molecules that ensure the flow of biochemical processes in living organisms. The term "community metabolomics" has been proposed relatively recently for the application of a metabolic approach in studies of communities of organisms (Sardans et al. 2011; Jones et al. 2014). Metabolomic analysis has been successfully used to study the interaction of organisms in situ. However, very few metabolic studies of lithobiont communities have been conducted (Sazanova et al. 2016). Detailed studies of the biochemical composition of organic matter that is part of the biofouling of granite has not yet been performed.

With the use of a metabolomic approach, an analysis of biofouling in regions with contrasting ecological conditions: on granite monuments of the museum necropolis of the Alexander Nevsky Monastery (in the urban environment) and in granite quarries in Finland (under conditions of low anthropogenic effect) was carried out.

Green biofilms (type 1) are one of the most common forms of fouling on the granite surface. In samples of this type, sugar (mono-, di-, and trisaccharides) and fatty acids (aC 16:0; aC 18:0; aC 18:1, aC 18:2; aC 18:3; aC 20:0; aC 24:0; aC 26:0) dominated quantitatively. C2–C6 organic acids (fumaric, oxalic, succinic, glyceric, gluconic); fatty acids (aC 9:0; aC 10:0); sugar alcohols (arabitol, erythritol, sorbitol, glycerol), amino acids (alanine, glycine, proline, threonine, hydroxyproline, phenylalanine, serine, leucine, asparagine, aspartic acid), terpenes (phytol), sterols (kampomterol, sitosterol, sigmasterol, cholesterol), phosphate and urea were present in smaller quantities.

Dark colored crusts (type 2) were characterized by the dominance of sugar alcohols (erythritol, arabitol, sorbitol). Sugar and fatty acids (aC 16:0; aC 18:0; aC 18:1, aC 18:2; aC 18:3; aC 24:0; aC 26:0) as well as in the first type biofilms were present in high concentrations. In some samples, phenolic compounds (orcinol, alizarin), shikimic acid were detected. C2–C6 organic acids; fatty acids (aC 9:0; aC 10:0; aC 20:0; aC 22:0), amino acids (alanine, valine, leucine, aspartic acid), fitol, sterols (campomterol, sitosterol, sigmasterol, cholesterol), phosphate and urea and a number of unidentified compounds were present in lower concentrations.

The main metabolic profile of the primary soil under mosses (type 3) was represented by sugars, fatty acids and sterols. Minor compounds were also represented by sugar alcohols, amino acids and Krebs cycle acids.

The soil under the vascular plants (type 4) was characterized by a richer spectrum of organic substances, including more organic acids of the Krebs cycle, amino acids, sugars, and also some secondary metabolites.

In the bio-weathering under lichen (type 5) the qualitative composition of metabolites was similar to their composition in the primary soil under mosses, but the metabolic profile of this samples contained much more sugar alcohols.

Pigmented and light-colored biofilms (types 6 and 7) contrasted significantly by the content of small organic molecules with other types of communities and differed with each other. These samples contained the greatest variety of metabolites. This was mainly due to the abundance of various sugars, glycosides, as well as some compounds of the secondary metabolism.

Statistical analysis performed by the principal component method (PCA) showed clustering of points characterizing the metabolome of samples depending on the

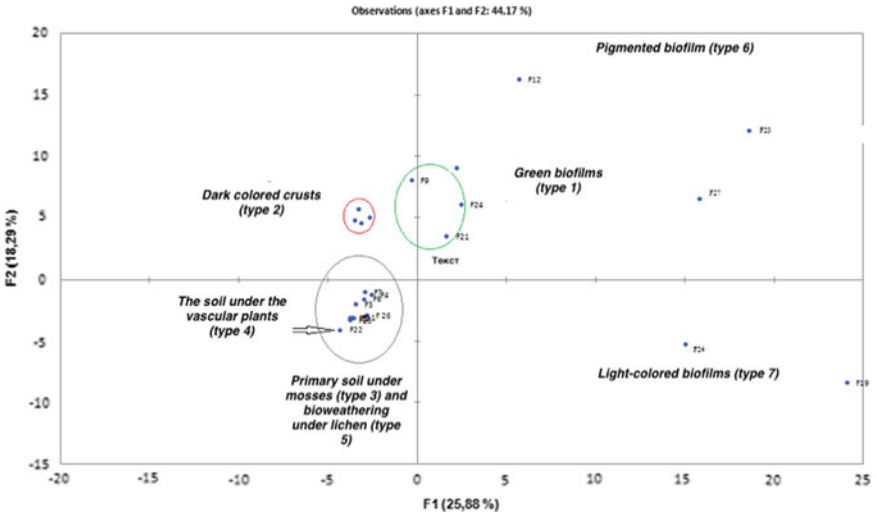


Fig. 29.3 PCA-analisis of metabolom of biofouling and deposites on granite surface (quarries of South Finland)

type of community (Fig. 29.3). The smallest dispersion of the data was typical for samples of the primary soil with mosses. Soil samples under vascular plants formed a single cluster with primary soil with mosses and lichens, indicating the proximity of the metabolomes of these communities, despite the significant difference in the taxonomic composition of the dominant organisms. Dark-colored and green cortical layers also separated into separate clusters. The highest dispersion of the samples was characteristic of pigmented and light-colored films, which are fused with the surface of the stone.

On granite monuments in St. Petersburg the following types of communities were studied: lichen communities (Monument to S. M. Yakovlev); biofilm formed by fungi (monument to ES Batasheva; M. P. Zotova); biofilm formed by algae (monument to E.S. Batasheva M. P. Zotova); primary soil at various stages of its formation with a cover of mosses (Monument to Unknown N-18, P. E. Osokina NMA). Algae and fungi often develop together and form a homogeneous black-green biofilm.

In the samples of biofouling in St. Petersburg, from 60 to 100 different low-molecular-weight organic compounds were detected: mono, di- and trisaccharides, aliphatic carboxylic acids (succinic acid, glyceric acid, erythronic acid, fatty acids (aC 9:0; aC 10:0; aC 11:0; aC 12:0; aC 16:0; aC 18:0; aC 18:1, aC 18:2; aC 18:3; aC 24:0) sugar alcohols (glycerol, erythritol, arabitol, mannitol, hiro-inositol, myo-inositol, glucitol), sterols (cholesterol, camposterol, sigmasterol, sitosterol), phosphate, glycerol-3-P, tocopherol, abietic acid, phenolic compounds. Some compounds were unidentified.

In biofilms with a predominance of algae, the number of mono- and disaccharides, amino acids, and organic acids in the free form was significantly higher in comparison with other types of layers. In samples with the dominance of fungi, the amount of

organic acids in the free form was lower compared to samples represented mainly by algae, and the concentration of polyols was higher. In the urban environment, the composition of biofilms formed by algae and fungi differed significantly only in some cases, which indicates their joint development and it can be noted only the predominance of fungi or algae in the sample.

In the fouling formed by lichens, sugar alcohols and phenolic compounds prevailed. In samples of the primary soil with a moss cover, the greatest diversity of low-molecular metabolites was observed, however, their quantitative content was, as a rule, lower than in other samples of surface layers.

The general patterns of distribution of small organic molecules, depending on the type of biofouling, were similar for samples taken in quarries and in museum necropolises. When analyzing data using the principal component method, the primary soil with a moss cover was characterized by the smallest dispersion of samples (Fig. 29.4). Moreover, samples of the primary soil were most similar in composition of the pool of small molecules in the urban environment and in the quarries.

In general, the samples collected in Saint-Petersburg characterized by less content of low-molecular weight compound. More than 200 different compounds were found in the samples from the quarry and about 60–100 different low molecular weight organic compounds were detected in the samples from the urban environment. This is mainly due to the lower content of species-specific secondary metabolites. At the same time, the concentration of certain compounds, especially polyols, was significantly higher in biofilms in the urban environment. Apparently, the bio-

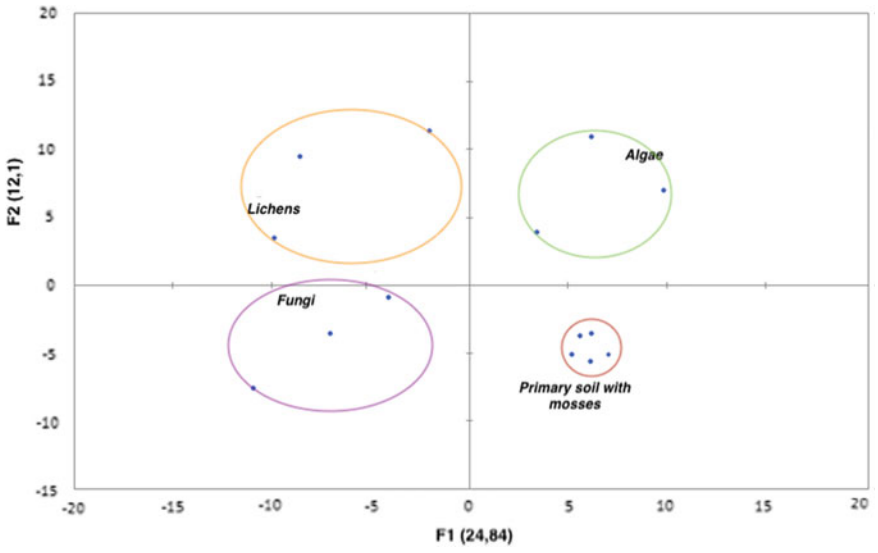


Fig. 29.4 PCA-analisis of metabolom of biofouling and deposites on granite surface in Saint Petersburg

chemical characteristics of biofilms are associated with the taxonomic composition of microorganisms in biofilms.

29.3.3 Peculiarities of Biofilms Localization on Granite Surface

Scanning electron microscopy was used to assess changes in the state of the surface of granite as well as the localization of biofilms and deposits in the surface layer of the rock. It was shown that microorganisms occupy different defects on the granite surface. Their localization is also associated with the peculiarities of the minerals that are part of the granite. Thus, quartz usually colonized by microorganisms along microcracks. However, most microorganisms and microcolonies on granite prefer feldspar and mica. They use cleavage ledges typical for the feldspar (Fig. 29.5). This picture is typical for granite embankments of St. Petersburg. Mica is exposed to biological degradation most quickly. Microorganisms usually grow and form colonies between the plates of this mineral (Fig. 29.6). The general character of granite colonization was similar for the urban environment and abandoned quarries. However, there are certain differences in the dominance of morphotypes of colonies on granite in different environment. This especially applies to micromycetes. Thus, in samples from the Montferrand quarry numerous microcolonies of micromycetes were strictly confined to the structural spaces on the surface of granite (Fig. 29.7). They had approximately similar sizes, which were about 50 microns in diameter. Penetrating hyphae consisted of thickened cells. In urban environments, microcolonies vary more widely in size. Penetrating hyphae are more developed (Fig. 29.8). In some places branched mycelium is formed. Analysis of black crusts on the surface of granite monuments in the central part of St. Petersburg showed that fungal hyphae dominate in microbial communities. It covers a significant part of the rock surface. In

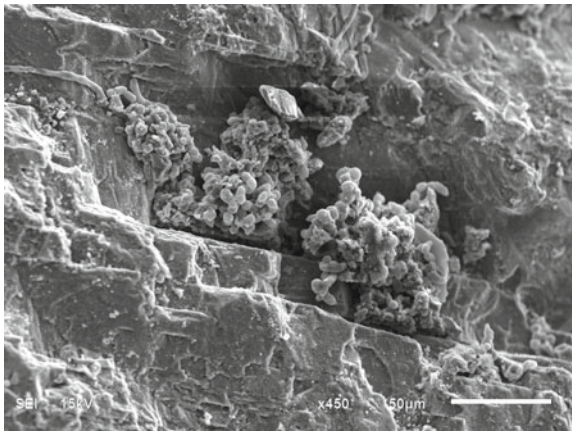


Fig. 29.5 Colonization of feldspar in granite rapakivi. Embankment of the Obvodny channel, St. Petersburg

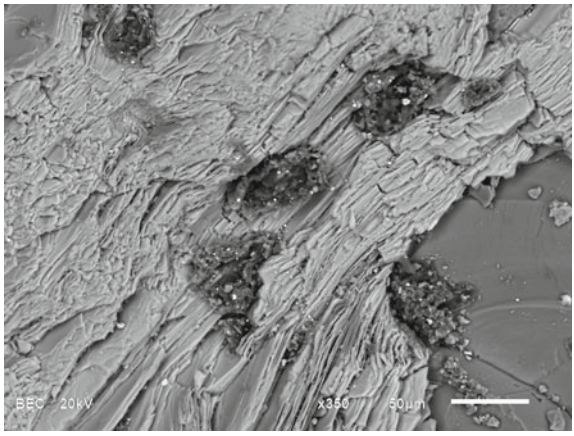


Fig. 29.6 Biodeterioration of mica in granite. Petrovskaya embankment. St. Petersburg

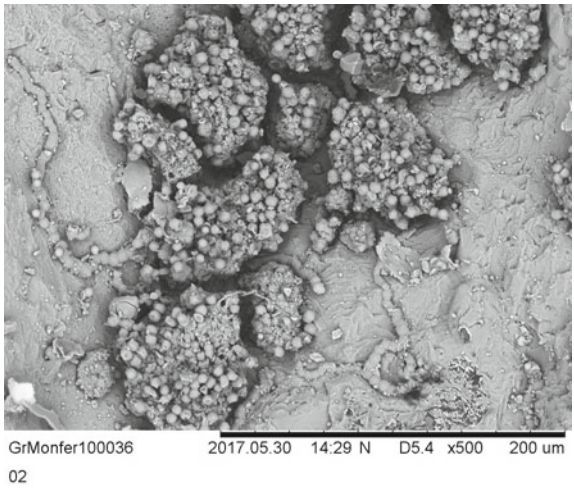


Fig. 29.7 Compact microcolonies and single penetrating hyphae of fungi on granite (Montferrand quarry, Virolahti, Southern Finland)

most cases in the places of development of microorganisms the particles of destroyed granite are visible. They are retained by the biofilm on the rock surface (Fig. 29.9). They are associated with small weathered granite fragments and dust particles.

Generally the development of biofilms on the surface of granite leads to a change in the surface layer of the rock both in urban environments and in natural outcrops. Obviously, these changes are the result of interrelated processes of biological and physico-chemical weathering of granite.

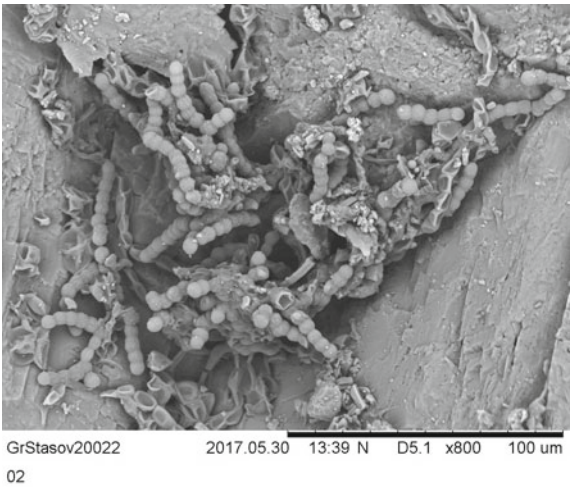


Fig. 29.8 Microbial growth on granite surface in urban environment (Saint Petersburg, Museum of urban sculpture, monument to V. V. Stasov). Many short hypha with spherical cells in the deepening of the granite surface

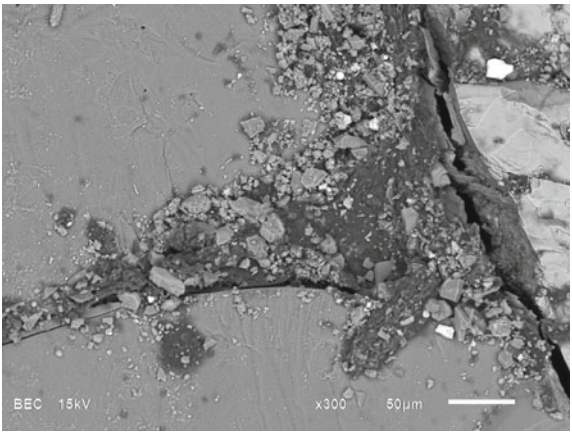


Fig. 29.9 Biofilm on the surface of granite rapakivi (basement of historical building, Vyborg). Particles of destroyed granite attached to biofilm

29.3.4 Modelling of Bacterial Leaching of Granite Rapakivi

One of the most effective tools for studying of biological processes occurring on solid natural substrates is their simulation (modelling) under experimental environment. In our experiments bacteria of the genus *Bacillus* which are known as inhabitants of rocks in various environment (Guiamet et al. 2012) were used. However, their role in the leaching of chemical elements from granite has not been sufficiently studied. The purpose of our experiment was to determine the possible role of bacteria in the leaching processes on granite rapakivi. Experiment on bioleaching of chemical elements from granite was carried out with bacteria *Bacillus subtilis* and fragments of granite rapakivi from Montferrand Quarry. Strain of bacteria *Bacillis subtilis* was isolated from the eroded rapakivi granite from the Montferrand quarry (Finland, Virolahti

area). Strain is deposited in the Russian collection of agricultural microorganisms (RCAM). In model system 60 ml of sterile water was added into flasks with fragments of rock: flasks with granite were inoculated with bacteria, other flasks with fragments of rock remained without microorganisms (control). The incubation temperature was +26 °C. Duration of the experiment—2 months. After that ICP-MS method (inductively coupled plasma mass spectrometry) was used for estimation of bioleaching of chemical elements from granite. SEM-analyses was used for estimation of bacteria cells localization. It showed that *Bacillus subtilis* cells were concentrated mainly in the feldspar cleavage zones and microcracks on the granite surface (Fig. 29.10).

The results indicate an increase in the intensity of elements leaching from granite minerals under the influence of the bacteria *Bacillus subtilis* (Table 29.6). In comparison with control samples (rock and water, without bacteria) in the samples with bacteria the concentration of some chemical elements in water increased (Na, Al, K, Fe, Si et al.). Bacterial leaching coefficient for chemical elements Na, K, Ca, Fe, Al, Si, Mg and Mn were also calculated according to the following formula: $C_{leach} = \frac{\mu g/l(\text{with bacteria})}{\mu g/l(\text{control})}$, where in the numerator is the element concentration in the aquatic environment with bacteria, and in the denominator the element concentration in the aquatic environment without bacteria (control).

Under the influence of the bacteria *Bacillus subtilis* the intensity of leaching elements are arranged in the following series (in brackets there are the coefficients of bacterial leaching intensity of chemical elements): Na (3.5) > Al (2.8) > Fe (2.2) > Mg (1.8) > K (1.5) > Mn (1.5) > Si (1.4) > Ca (1.3). The obtained series of chemical

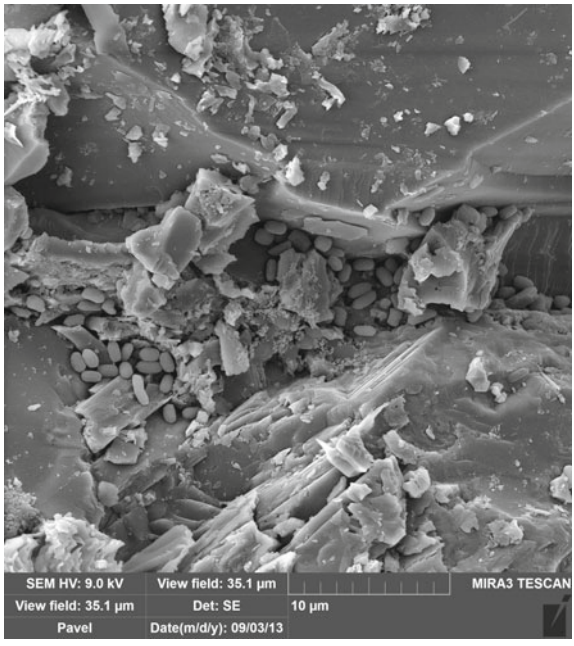


Fig. 29.10 *Bacillus subtilis* cells in the cleavage zone of feldspar. Experiment in the aquatic environment

Table 29.6 The elements in the aquatic environment after 2 months interaction of granite rapakivi and *Bacillus subtilis* (ICP-MS analysis (μg/l)

Chem. element	Be	Na	Mg	Al	Si	P	K	Ca	Ti
Granite with bacteria	0.08	1880	56.6	38.5	1330	339	698	808	9.3
Granite without bacteria	0.08	530	31.3	13.6	981	179	474	638	7.3
Chem. element	V	Cr	Mn	Fe	Co	Ni	Cu	Zn	Ga
Granite with bacteria	0.39	14.0	39.8	111	0.04	52.3	58.5	2.2	0.72
Granite without bacteria	0.28	2.9	26.8	50.3	0.02	0.21	5.7	0.37	0.30
Chem. element	Ge	Se	Rb	Sr	Y	Zr	Nb	Mo	Cd
Granite with bacteria	0.23	0.24	6.0	1.1	13.7	1.4	0.07	1.7	0.07
Granite without bacteria	0.03	0.90	2.7	0.59	1.5	0.18	0.003	0.53	0.01
Chem. element	Sn	Sb	Cs	Ba	La	Ce	Pr	Nd	Sm
Granite with bacteria	0.02	2.0	0.05	2.8	20.4	49.6	9.6	52.3	10.2
Granite	0.006	2.0	0.03	1.1	3.8	7.1	1.0	4.8	0.64
Chem. element	Eu	Gd	Tb	Dy	Ho	Er	Tm	Yb	Lu
Granite with bacteria	0.09	9.9	1.1	5.2	1.0	2.6	0.40	2.6	0.43
Granite without bacteria	0.007	0.57	0.07	0.3	0.06	0.12	0.01	0.07	0.01
Chem. element	Hf	Ta	W	Pb	Th	U			
Granite with bacteria	0.07	0.01	0.58	0.69	0.70	2.5			
Granite without bacteria	0.01	0.001	0.20	0.06	0.20	0.23			

elements shows that during granite bioleaching feldspars and mica are destroyed first of all.

29.4 Conclusion

Biofouling of granite rapakivi in the urban environment and natural outcrops are characterized by a significant biodiversity of microorganisms. Different types of biofilms are distinguished depending on the dominance of certain species and the duration of granite colonization. Such differentiation is especially noticeable in natural outcrop, where biofouling can be observed from the primary microbial colonization to the formation of the primary soil. Changes in the structure of biofilms are accompanied by significant variation in their metabolism and, consequently, their influence on the rocky substrate. At the same time, there are noticeable differences in the composition of biofilms metabolites in the urban environment and in natural exposures. The colonization of granite rapakivi largely depends on the structural features of minerals (quarts, feldspar, mica). The products of granite destruction often associated with biofilms. As result biomineral formation cover surface of granite. They consist of cells and metabolites of microorganisms, products of granite destruction and atmospheric pollution.

Acknowledgements The research results were partially obtained on the equipment of the Resource Center "Development of Cellular and Molecular Technologies" of Saint Petersburg State University. This research was supports by the Russian Science Foundation (Project № 17-16-01030).

References

Gadd GM (2007) Geomycology: biogeochemical transformations of rocks, minerals, metals and radionuclides by fungi, bioweathering and bioremediation. Mycol Res 111(1):3–49

Gollerbakh MM, Kosinskaya EK, Polyansky VI (1953) Blue-green algae. In: Key to freshwater algae of the USSR, vol 2. Moscow (in Russian)

Grbić ML, Vukojević J, Simić GS, Krizmanić J, Stupar M (2010) Biofilm forming cyanobacteria, algae and fungi on two historic monuments in Belgrade, Serbia. Arch Biol Sci Belgrade 62(3):625–631

Guiamet PS, Rosato V, de Saravia SG, García AM, Moreno DA (2012) Biofouling of crypts of historical and architectural interest at La Plata Cemetery (Argentina). J Cult Herit 13(3):339–344

Jones OA, Sdepanian S, Lofts S, Svendsen C, Spurgeon DJ, Maguire ML, Griffin JL (2014) Metabolomic analysis of soil communities can be used for pollution assessment. Environ Toxicol Chem 33(1):61–64

Komárek J, Anagnostidis K (1998) Cyanoprokaryota. 1. Teil. Part: Chroococcales. Spektrum, Berlin

Komárek J, Anagnostidis K (2005) Cyanoprokaryota. 2. Teil. Part: Oscillatoriales. Spektrum, Berlin

Martino P (2019) What about biofilms on the surface of stone monuments? Open Conf Proc J 10. https://benthamopen.com/FULLTEXT/TOPROCJ-7-2-14

Ozturk A, Karaca Z, Unsal T (2014) The activity of oxygenic photosynthetic microbial consortia on different granites. Ekoloji 23(90):90–96

Panova E, Vlasov D, Luodes H, Vlasov A, Popova T, Zelenskaya M (2014) Weathering of granite under urban conditions. In: Panova EG, Vlasov DY, Luodes H (eds) Evaluation of the durability of granite in architectural monuments. Geological Survey of Finland. Report of Investigation, Espoo

Panova EG, Vlasov DYu, Luodes H, Vlasov AD, Popova TA, Zelenskaya MS (2016) Granite weathering in city environment. In: Frank-Kamenetskaya OV, Panova EG, Vlasov DYu (eds) Biogenic-abiogenic interactions in natural and antropogenic systems. Lecture Notes in Earth System Sciences. Springer, Switzerland

Pozo-Antonio JS, Rivas T, López AJ, Fiorucci MP, Ramil A (2016) Effectiveness of granite cleaning procedures in cultural heritage: a review. Sci Total Environ 571:1017–1028

Sanjurjo-Sánchez J, Vidal Romaní JR, Alves C (2012) Comparative analysis of coatings on granitic substrates from urban and natural settings (NW Spain). Geomorphology 138(1):231–242

Sardans J, Pen˜uelas J, Rivas A (2011) Ecological metabolomics: overview of current developments and future challenges. Ubach Chemoecol 21:191–225

Sazanova KV, Vlasov DYu, Shavarda AL, Zelenskaya MS, Kuznetsova OA (2016) Metabolomic approach to studying lythobiontic communities. Biosphere 8(3):291–300 (in Russian)

Tepper EZ, Shilnikova VK, Pereversev GI (2005) Workshop on microbiology. Moscow (in Russian)

Toreno G, Isola D, Meloni P, Carcangiu G, Selbmann L, Onofri S, Caneva G, Zucconi L (2018) Biological colonization on stone monuments: a new low impact cleaning method. J Cult Herit 30:100–109

Vinogradova ON, Mikhailyuk TI (2009) Algal flora of the caves and grottoes of the National Natural Park "Podolskie Tovtry" (Ukraine). Algology 19(2):155–171 (in Russian)

Zhang B, Powers R (2012) Analysis of bacterial biofilms using NMR-based metabolomics. Future Med Chem 4(10):1273–1306

Chapter 30
Microorganisms of the Technogenic Landscapes: The Case of Nepheline-Containing Sands, the Murmansk Region

Vera V. Redkina, Maria V. Korneykova and Regina R. Shalygina

Abstract The investigation of microbiological characteristics has been carried out in the sands of different storage duration in the tailing dumps of the apatite-nepheline processing plants. The total population density of bacteria ranged within 0.34–0.60 billion CFU/g in the sands without vegetation cover, and within 2.6–7.2 billion CFU/g in the reclaimed sands. Microfungi mycelium length varied from 5 to 280 m/g in the recultivated nepheline sands. Low biodiversity of fungi in the initial sands and absence of species-dominants in their complex have been revealed. Nepheline sands recultivation has given preconditions for forming the fungi complexes, which are typical for the regional podzol soils on the moraine sediments. Species diversity of the microfungi complexes in the recultivated sands is represented by 26 species, while only 11 species were isolated from the freshly pumped sands. The largest number of fungi species belonged to the *Penicillium* genera. *Umbelopsis longicollis*, *Juxtiphoma eupyrena*, *Penicillium daleae* were found to be the most commonly seen genera. The areas where the natural overgrowing processes take place are characterized by a higher algae population—up to 450 thousand cells per 1 g of the substrate in the 40-year-old sands under the sedge and crowberry plant groups, and up to 1.9 million cells in 1 g under the moss cover and in the young cryptogamous crusts. The research has revealed 69 algae and cyanobacteria species. In the 40-year-old sands, with the dominance of green algae, cyanobacteria and diatoms have played the significant role.

Keywords Nepheline-containing tailings · Recultivation · Bacteria · Microscopic fungi · Algae · Cyanobacteria

V. V. Redkina (✉) · M. V. Korneykova · R. R. Shalygina
Institute of North Industrial Ecology Problems—Subdivision of the Federal Research Centre "Kola Science Centre of Russian Academy of Science", 14A, Akademgorodok, Apatity 184209, Russia
e-mail: kalmykova_v_v@mail.ru

© Springer Nature Switzerland AG 2020

O. V. Frank-Kamenetskaya et al. (eds.), *Processes and Phenomena on the Boundary Between Biogenic and Abiogenic Nature*, Lecture Notes in Earth System Sciences,
https://doi.org/10.1007/978-3-030-21614-6_30

30.1 Introduction

The Murmansk region is known to be one of the most industrially developed areas in the North of Russia. The operating of mining and processing industries has led to the accumulation of a large amount of waste in the environment, particularly tailings of the apatite-nepheline ores dressing, which are extracted from the Kola Peninsula for processing phosphate fertilizers. The tailings, which contain mainly nepheline (more than 50% of the volume) and their accompanying minerals, are a technogenic deposit of phosphorus-containing raw stores and can be susceptible to redressing (Ivanova and Rukhlenko 2010). The waste of ore dressing—nepheline-containing sands (henceforth, nepheline sands)—is stored in three tailing dumps situated near the towns of Kirovsk and Apatity. They cover about 3000 ha (Cadastre 1999).

Erosion processes, which occur in abundance, cause open sandy spaces of the operating and exhausted tailing dumps to become a source of significant dust pollution in adjacent areas. Windy flow of sands along with unfavorable water and temperature conditions lead to extremely slow natural healing of dumps. Recultivation (phytomelioration) is known to be the most efficient method for consolidating the dust-forming surfaces (Lyubimova and Medvedev 1970). The longest-standing tailing dump of the apatite-nepheline ore dressing plant ANDP-1, which was constructed in 1956, has been removed from operation since the late 1960s. After the removal from operation, its recultivation was fulfilled by applying peat and organic and mineral fertilizers, sowing perennial grasses, and planting spruce and pine trees. The current ground cover is represented by lichen-motley-grass and lichen-grass-moss birch forests. Some plots of meadow plants can be seen in the open spaces. Good state of pine-tree planting should be noted (Pokhil'ko and Zarzhitskaya 2006).

The tailing dump of the mining and processing plant ANDP-2 was put into operation in 1969. It is situated in the Belaya Bay of Lake Imandra, 9 km northwest of the town of Apatity. The overall area of the tailing dump is 7.8 km, and its hydraulic fill dam was 74 m high at the beginning of 2015. The volume of the tailing dump that was stored from the very beginning of the operation amounts to 680 million m (Strizhenok 2015). Due to the gradual filling of the external slopes of the tailing dump, terraces were built, which are composed of dumps of different "ages". To reduce the technogenic load on the environment in the adjacent areas, the enterprise consolidated tailing beaches using anionic emulsified bitumen. The consolidation of the dam slopes was carried out using a biological and chemical method, namely, sowing perennial grasses (particularly, *Leymus arenarius* (L) Hochst) with further polymeric coating (latex, emulsified bitumen), which results in forming a meadow community with an admixture of dwarf shrubs and shrubs and an increasing number of moss and lichens. Under the influence of vegetation, soil-formation processes take place, which are specific to certain bioclimatic conditions, notably the accumulation of organic substance (Pereverzev et al. 2007).

Nepheline sands are soil-forming rocks, which are uncommon in cold and humid climates. Along with widespread moraine, sea, and fluvio glacial sands on which the dominating Al–Fe-humus podzols were formed, the nepheline sands can be com-

pared only by their granulometric texture. Similar to other soil-forming rocks, the main mineral mass of nepheline waste is represented by fractures of fine sand and coarse dust with an inconsiderable amount of silty particles (Pereverzev et al. 2007). However, concerning the content of macro- and micro-elements, the nepheline sands are much richer than glacial and sea rocks; the tailings contain up to 42% silicon, which is sufficiently high. Original nepheline sands lack biologically originated substances. The occurrence of organic carbon (0.2–0.3%) in the sands is due to the tailings of flotation reagents, which are sufficiently stable over time. Water suspensions of the nepheline sands have neutral or weak alkaline reactions (pH is 7.0–8.3) compared to the representative soils of the Kola Peninsula.

Microorganisms are biocatalyzers of the primary soil-forming processes and one of the main factors defining the specific character of these processes. They are directly engaged in the processes of mineralization and humification of plant residues, which affect them by their hydrolytic and oxidation-reduction exoenzymes, mineral and organic acids, and other metabolites. Heterotrophic (bacteria and microscopic fungi) and phototrophic microorganisms (algae and cyanobacteria), which occupy a polar position in trophic chains, can appropriately reflect the peculiarity of microbiological processes in technogenic substrates and soil, indicating its destruction and production potential.

Necessity of restoring nepheline-containing tailings and studying the primary soil-forming processes on the technogenic substrates determines the purpose of our study. The goal of this research is to study the abundance and diversity of complexes of microorganisms in the nepheline sands of different storing periods.

30.2 Objects and Methods

The object of this research is to study the microbiota of nepheline sands from both the existing tailing dump of ore dressing plant ANDP-2 (Fig. 30.1a) and the newly formed soils of the preserved tailing dump of ore dressing plant ANDP-1 (Fig. 30.1b). The work was carried out at intervals in the period from 2005 to 2016. The following samples of nepheline sands were selected for research: (1) sands from the tailing dump of plant ANDP-2: freshly deposited sand, which was constantly coming from the factory through the pipeline along with process water (the exposure time is less than one year); the uncovered sand with vegetation (referred to as "pure" sand), recultivated 10, 20, and 30 years ago; and the sand under grasses recultivated 10, 20, and 30 years ago; and (2) nepheline sands from the tailing dump of plant ANDP-1 (recultivated in the 1960s): under moss, lichen, shrub (crowberry, cowberry), and motley-grass (herbs with clover prevailing) plant groups. The samples of the upper layer (0–5 cm) of the substrate were taken for the analysis.

For algological analysis in 2015 and 2016, the sand samples from the surface layer in three plots of the ANDP-2 tailing dump were taken. The first plot was composed of freshly deposited 3-month-old sands. The second plot involved sands of the recultivated tailing dumps deposited about 20 years ago (67° 38′ 38″ N, 33°15′

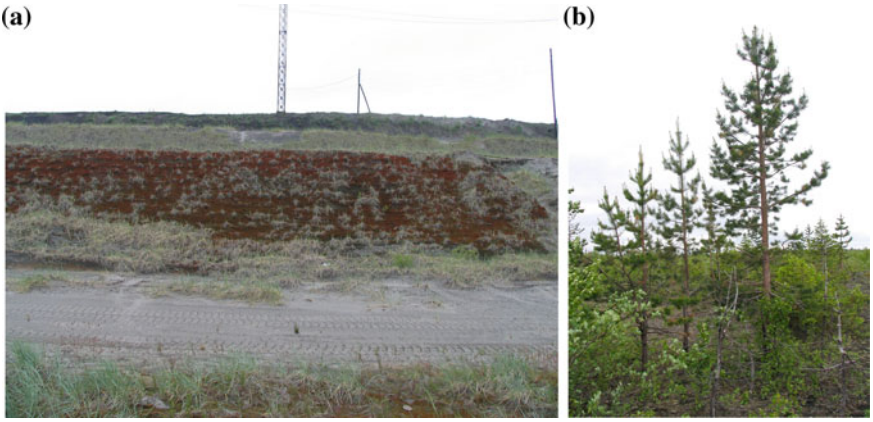


Fig. 30.1 Nepheline sands of different "ages": **a** 20-year-old sands; **b** 50-year-old sands

39″ E). The third plot consisted of sands from the recultivated tailing dumps deposited about 30 years ago (67° 38′ 57.7″ N, 33° 14′ 57.6″ E). Samples were also taken of cryptogamous crusts that were beginning to form on the sand surface stored about 40 years ago (67° 37′ 40″ N, 33° 18′ 25″ E).

The population density of the viable bacteria (CFU/g) of the different trophic groups was counted using the method of inoculation of solid nutrient media. The organotrophic bacteria transforming the nitrogen-containing organic compounds were determined on beef-extract agar; the bacteria of the amylolytic community transforming organic nitrogen-free substances were isolated on starch-ammonia agar; and the oligotrophic bacteria capable of existing for a long time on substrates with a low content of nutrients were determined on low-mineralized Aristovskaya's medium (Aristovskaya 1965).

The total population density of the bacteria was determined through the method of fluorescent microscopy using Whatman® Nuclepore™ Track-Etched membranes with 0.2 μm pore size (polycarbonate, black). Soil suspensions were stained with acridine orange. The weight of one bacterial cell was taken as 4×10^{-14} g to calculate the bacterial biomass. All the calculations were performed per units of absolute dry weight.

The number of micromycetes was estimated using the plating method on wort agar (i.e., the agar with lactic acid addition to inhibit the growth of bacteria). Morphological characteristics were evaluated using an optical microscope Olympus CX 41 (Olympus, Japan) with the camera JenopticProgRes CT3 (Jenoptik, Germany). Species were identified using traditional guides for species identification (Raper and Thom 1968; Egorova 1986; Domsh et al. 2007; Seifert et al. 2011). Verification of species in accordance with the modern nomenclature was performed using the electronic Index Fungorum database (http://www.indexfungorum.org). The fungi mycelium length and biomass were measured by fluorescence microscopy according to Olsen's method (Olsen and Hovland 1985) with some modification

(Evdokimova and Mozgova 1996; Mirchink 1988). Soil suspensions were stained with acridine orange and FITC (SIGMA, Japan) and further sucked through Whatman® Nuclepore™ Track-Etched membranes with 0.8 μm pore size (polycarbonate, black). The number of hyphal intersections was counted, and the hyphal length was calculated with a square grid inserted in an ocular.

The number of living algal cells was directly calculated using a luminescent microscope on dried smears of soil suspension (Kondakova and Domracheva 2007). The species diversity was analyzed by inoculation of the soil suspension in BBM and Z8 liquid and agar-containing nutrient media (Gaisina et al. 2008; Kótai 1972). The morphological characteristics were evaluated according to Andreeva (1998), Ettl and Gärtner (2014), Komárek and Anagnostidis (1998, 2005), and Komárek (2013), and the species names were verified using the electronic database Algaebase (Guiry and Guiry 2018). Algae and cyanobacteria communities were analyzed using Sørensen-Chekanovsky coefficient and the similarity measurement (for average distance) in the GRAPHS clustering program (Novakovskii 2004).

The occurrence (frequency) of the species of algae and micromycetes was calculated from the equation $B = (a/A) \times 100$, where B is occurrence (%); a is the number of samples containing the particular species; and A is the total number of analyzed samples (Kondrat'eva and Kovalenko 1975; Kurakov 2001). The abundance (density) of species of microscopic fungi was determined by the equation $C = (n/N) \times 100$, where C is abundance (%); n is a number of isolates of a particular species, and N is the total number of isolates of all species.

The relative soil moisture was determined in weighed soil samples dried in an oven at 105 °C until the constant weight. The soil acidity was determined by the potentiometric method with a Radelkis OP-300 laboratory pH meter equipped with a combined pH electrode in the 1:2.5 water soil extracts.

30.3 Results and Discussion

The tailings leaving the plant are nonsterile, and tens of millions of chemoorganotrophic bacteria cells and only a few tens of colony-forming units (CFU) of micromycetes have been found in 1 g of substrate (Gershenkop et al. 2005).

In the tailing dump with freshly deposited sands, the number of saprotrophic bacteria and bacteria utilizing mineral forms of nitrogen has decreased by 14 and 17 times, respectively, compared to the original tailings. In 10-year-old pure, nonovergrown sands, a noticeable (2-fold) increase in the number of oligotrophic bacteria has occurred. As a result of further increases in the storage period of pure apatite tailings, bacterial cenosis has become poor (Fig. 30.2), which can be explained by the aeolian factor as well as by the suffusion phenomena, in which small mineral particles and soluble substances, including nutrients necessary for microorganisms, were removed by water from the surface layer to the underlying strata of the sandy substrate.

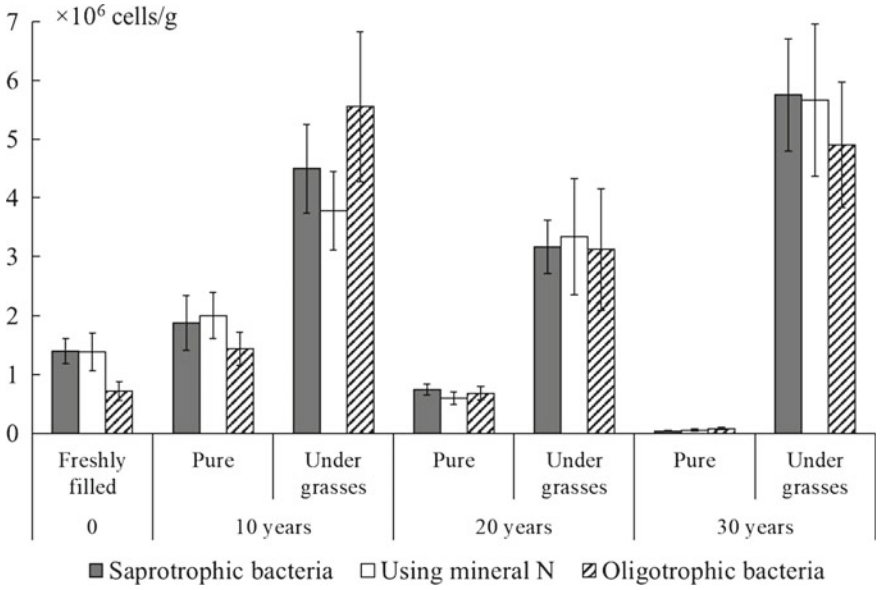


Fig. 30.2 The number of bacteria of various trophic groups in the nepheline sands

Against the background of the overall low abundance of microorganisms in 30-year-old sands, oligotrophs, which have low substrate specificity and are capable of economical use of endo- and exosubstrates, dominate the bacterial community.

In contrast, the fungal number in pure nepheline sands of a long storage period increases. Thus, in 10-year-old sands, the abundance of micromycetes has increased 24 times compared to freshly deposited sands, having reached 300 CFU/g, which is probably due to the transfer of sandy mass containing mycelium and spores of micromycetes from the neighboring areas covered with vegetation (Fig. 30.3).

Creating a grass cover on the sandy surface with its accompanying self-overgrowing processes contributes to the growth of biological activity in reclaimed sands. The population of bacteria and microscopic fungi is significantly higher in the sands under the grass vegetation, compared to pure sands. In addition, the bacterial abundance did not change significantly over time; it ranged from 3.1 to 5.8 million cells/g for various trophic groups. But the number of fungi increased twice in 30-year-old sands compared to the "younger" sands, and reached 3.8 thousand CFU/g.

In the sands consolidated more than 50 years ago, the number of all the groups of the studied microorganisms was several times higher than in 10–30-year-old sands. The number of bacteria was greater under the herbs with the predominance of clover because leguminous plants stimulated the development of microorganisms (Krasilnikov 1958). The maximum number of micromycetes was observed in substrate under the lichen group.

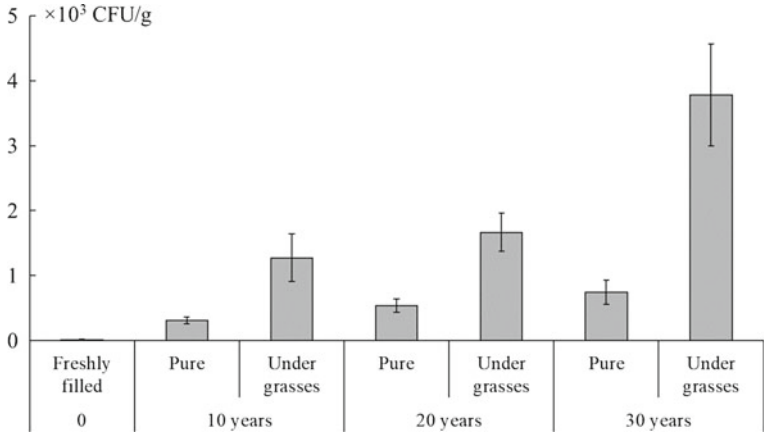


Fig. 30.3 The number of micromycetes in the nepheline sands

Direct methods, specifically fluorescence microscopy, provide a more complete picture of the number of microorganisms in the soils. By consulting the data on the total content of bacteria in the substrate and the length of the fungal mycelium, their biomass can be calculated. The total number of bacteria in pure sand ranged from 0.34 to 0.60 billion cells/g (Table 30.1). The length of the mycelium varied from 12 to 43 m/g. The differences between bacterial and fungal biomass are not statistically

Table 30.1 The total number and biomass of bacteria, mycelium length and biomass of microscopic fungi in the nepheline sands

Sample, plant group	"Age" of sand, years	Bacteria population density, $\times 10^9$ cells/g	Fungi mycelium length, mg/g	Biomass, $\times 10^{-6}$ g/g		
				Bacterial	Fungal	Total
Pure sand	0	0.60 ± 0.04	12 ± 5	24 ± 2	13 ± 6	37
	10	0.53 ± 0.06	32 ± 2	21 ± 3	35 ± 2	56
	20	0.34 ± 0.11	43 ± 13	14 ± 4	47 ± 15	61
	30	0.59 ± 0.10	26 ± 5	24 ± 4	29 ± 5	53
Grasses	10	1.47 ± 1.06	59 ± 8	59 ± 42	64 ± 9	123
	20	2.23 ± 1.84	62 ± 8	89 ± 73	69 ± 8	158
	30	2.02 ± 1.40	112 ± 35	81 ± 56	124 ± 39	205
Moss	50	7.22 ± 0.37	710 ± 145	289 ± 15	781 ± 160	1070
Lichens	50	5.79 ± 0.64	1156 ± 192	232 ± 25	1272 ± 211	1504
Motley-grass	50	6.20 ± 0.27	1064 ± 74	248 ± 11	1170 ± 81	1418
Dwarf shrubs	50	2.62 ± 1.64	434 ± 159	105 ± 66	478 ± 175	583

significant. The "age" of the sand that was not recultivated had practically no impact on the total microbial biomass.

In the sands under the grasses plant group, the bacterial biomass increased by 4 times on average compared to the sands not covered by vegetation, and the fungal biomass extended by 2 times. Moreover, as the age of the sand under the grass vegetation increased, there were no significant changes in the bacteria and fungi biomass.

In the reclaimed nepheline sands of the ANDP-1, under various plant groups, the biomass of bacteria varied between 0.11 and 0.29 mg/g, and the fungal biomass, between 0.48 and 1.27 mg/g. These values are quite comparable with those in the soils of the taiga forests of the Kola Peninsula (Evdokimova and Mozgova 2001). Furthermore, the fungal biomass in the 50-year-old sands was 3–5.5 times higher than the bacterial biomass, which is typical for the organogenic horizons of the spruce forests of the Kola North. The abundance of micromycetes was somewhat higher in the sand under lichens and forbs, and the abundance of bacteria was higher in the sand under the moss cover. Under the shrub plant group, the lowest values of bacterial and fungal biomass were observed. According to Zvyagintsev's scale (1978), the newly formed soils corresponded to the soils with high enrichment of microorganisms.

30.4 Taxonomic Fungi Diversity

Twenty-six species of micromycetes belonging to 10 genera, 7 orders, 5 classes, and 2 divisions were identified in the sands of the tailing dumps reclaimed more than 50 years ago. Eleven fungi species belonging to 8 genera, 4 orders, 4 classes, and 2 divisions were isolated in freshly deposited sand (Table 30.2).

The fungi of the genus *Penicillium* were the most widely presented group in the micromycetes complex of the recultivated nepheline tailing dumps. They amounted to more than 50% of the total species diversity of the isolated fungi. This genus was represented by 4 species in the freshly deposited sands, and by 16 species, in the recultivated sands.

Trichoderma viride dominated in the recultivated sands, but this species was random in the freshly deposited sands (Table 30.3). In the nepheline sands recultivated 50 years ago, the groups of frequently occurring species included the following fungi: *Umbelopsis longicollis*, *Juxtiphoma eupyrena*, and *Penicillium daleae*. In the freshly deposited sands, the dominant species were absent. A decrease in the Simpson domination index and, accordingly, an increase in the value of the Pielou index also testified to this fact. In the recultivated sands, the Simpson index was equal to 0.26, and the Pielou index amounted to 0.53; in the freshly deposited sands, both indexes were 0.15 and 0.96, respectively. The fungus *P. thomii* belonged to frequently occurring species in the freshly deposited sands. The other species listed in Table 30.3 were classified as rare and random due to their values of spatial and temporal frequency of occurrence. The absence of dominant species is typical for young communities that are in unstable states. Such species are less in number where

Table 30.2 Species composition and the spatial/temporal occurrence frequency of microscopic fungi isolated from nepheline sands

Species	Fungi occurrence frequency, %				
	Freshly deposited	10 years	20 years	30 years	50 years
Division *Zygomycota* Class *Mucoromycetes* Order *Mucorales*					
Mucor sp.	–	5/17	14/33	14/33	4/17
M. hiemalis Wehmer	17/17	–	–	–	–
M. plumbeus Bonord.	17/17	–	–	–	–
Class *Incertae sedis* Order *Umbelopsidales*					
Umbelopsis longicollis (Dixon-Stew.) Y. N. Wang, X. Y. Liu and R. Y. Zheng	–	–	–	–	21/67
Um. isabellina (Oudem.) W. Gams	–	–	–	10/33	14/33
Division *Ascomycota* Class *Sordariomycetes* Order *Hypocreales*					
Acremonium rutilum W. Gams	5/17	14/50	10/33	–	–
Acr. charticola (Lindau) W. Gams	–	5/17	–	–	–
Clonostachys rosea (Link) Schroers, Samuels, Seifert and W. Gams	17/17	10/33	10/33	10/33	4/17
Fusicolla merismoides (Corda) Gräfenhan, Seifert and Schroers	–	5/17	–	5/17	4/17
Neocosmospora solani (Mart.) L. Lombard and Crous	5/17	–	–	–	–
Trichoderma hamatum (Bonord.) Bainier	–	–	–	–	4/17
T. koningii Oudem.	–	5/17	10/17	14/50	11/33
T. polysporum (Link) Rifai	–	–	–	–	4/17
T. viride Pers.	17/17	90/100	62/100	62/100	96/100

(continued)

Table 30.2 (continued)

Species	Fungi occurrence frequency, %				
	Freshly deposited	10 years	20 years	30 years	50 years
Order *Microascales*					
Kernia nitida (Sacc.) Nieuwl.	–	5/17	–	–	4/17
Order *Sordariales*					
Humicola grisea Traaen	–	–	–	5/17	–
Class *Dothideomycetes* **Order *Pleosporales***					
Alternaria alternata (Fr.) Keissl.	–	5/17	5/17	10/17	–
Juxtiphoma eupyrena (Sacc.) Valenz.-Lopez, Crous, Stchigel, Guarro and Cano	–	10/17	29/67	33/83	21/67
Phoma leveillei Boerema and G. J. Bollen	–	–	5/17	–	–
Order *Dothideales*					
Aureobasidium pullulans var. *pullulans* (de Bary and Löwenthal) G. Arnaud	5/17	5/17	10/17	10/33	4/17
Class *Eurotiomycetes* **Order *Eurotiales***					
Aspergillus fumigatus Fresen.	–	5/17	5/17	–	–
A. versicolor (Vuill.) Tirab.	–	–	10/33	–	–
Penicillium aurantiogriseum Dierckx	–	–	14/50	5/17	–
P. camemberti Thom	–	5/17	10/33	5/17	7/17
P. caseicolum Bainier	–	–	–	–	4/17
P. corylophilum Dierckx	–	5/17	10/33	–	4/17
P. citrinum Thom	–	5/17	–	–	4/17
P. daleae K. W. Zaleski	–	–	–	–	39/67
P. decumbens Thom	–	–	5/17	–	–
P. glabrum (Wehmer) Westling	17/17	–	–	–	–

(continued)

Table 30.2 (continued)

Species	Fungi occurrence frequency, %				
	Freshly deposited	10 years	20 years	30 years	50 years
P. jensenii K. W. Zaleski	–	5/17	–	–	–
P. miczynskii K. W. Zaleski	–	5/17	5/17	14/33	7/17
P. raistrickii G. Sm.	–	5/17	5/17	5/17	4/17
P. restrictum J. C. Gilman and E. V. Abbott	–	–	5/17	–	11/17
P. simplicissimum (Oudem.) Thom	–	–	5/17	–	–
P. spinulosum Thom	17/17	5/17	10/17	5/17	11/33
P. solitum Westling	–	–	5/17	–	4/17
P. thomii Maire	50/50	–	14/33	10/17	4/17
P. velutinum J. F. H. Beyma	–	5/17	5/17	–	4/17
Talaromyces aculeatus (Raper and Fennell) Samson, N. Yilmaz, Frisvad and Seifert	–	–	–	10/33	7/33
Tal. funiculosus (Thom) Samson, N. Yilmaz, Frisvad and Seifert	–	–	5/17	–	–
Tal. ruber (Stoll) N. Yilmaz, Houbraken, Frisvad and Samson	–	–	–	–	4/17
Tal. variabilis (Sopp) Samson, N. Yilmaz, Frisvad and Seifert	17/17	–	10/33	–	–
Class *Leotiomycetes* **Order *Helotiales***					
Botrytis cinerea Pers.	–	5/17	10/33	14/33	–

Note Dash means "not detected"; the plus sign means "species was detected once"

physical and chemical environmental factors are extreme. The fungi *Acremonium rutilum*, *Neocosmospora solani*, *Mucor hiemalis*, *M. plumbeus*, and *Talaromyces variabile* were isolated only in freshly deposited nepheline sands. These species of fungi were also found in the apatite-nepheline underground mines (Evdokimova and Naumenko 2002) and in the products of technological processing at the apatite-nepheline ore dressing plants (Gershenkop et al. 2005), from which they could enter the tailing dumps.

The degree of similarity in the composition of the species in the microscopic fungi complexes in freshly deposited and recultivated nepheline sands, expressed by the Sörensen coefficient, was only 25%. Such a low degree of similarity is explained

Table 30.3 Species structure of the microscopic fungi complexes in the nepheline sands

«Age» of sand				
Freshly deposited	10 years	20 years	30 years	50 years
Dominated species				
	Trichoderma viride	*T. viride*	*T. viride*	*T. viride*
Frequent species				
Penicillium thomii		*Juxtiphoma eupyrena*	*J. eupyrena*	*J. eupyrena*
				P. daleae
				Umbelopsis longicollis
Rare species				
	Acremonium rutilum	*A. rutilum*	*Aureobasidium pullulans*	*Tal. aculeatus*
	Clonostachys rosea	*Asp. versicolor*	*Botrytis cinerea*	*P. spinulosum*
		B. cinerea	*C. rosea*	*T. koningii*
		C. rosea	*Mucor sp.*	*U. isabellina*
		Mucor sp.	*Tal. aculeatus*	
		P. camemberti	*P. miczynskii*	
		P. corylophilum	*T. koningii*	
		P. aurantiogriseum	*U. isabellina*	
		P. thomii		
		Tal. variabilis		
Random species				
C. rosea	*Asp. fumigatus*	*Alternaria alternata*	*Alt. alternata*	*Kernia nitida*
M. plumbeus	*Aur. pullulans*	*Asp. fumigatus*	*Fusicola merismoides*	*Mucor sp.*
M. hiemalis	*A. charticola*	*Aur. pullulans*	*Humicola grisea*	
P. glabrum	*Fusarium merismoides*	*H. grisea*	*P.camemberti*	*P.camemberti*
P. spinulosum	*K. nitida*	*P. decumbens*	*P. aurantiogriseum*	
Tal. variabilis	*Mucor sp.*	*Tal. funiculosus*	*P. raistrickii*	*P. corylophilum*
T. viride	*P. camemberti*	*P. miczynskii*	*P. spinulosum*	*P. velutinum*
	P. citrinum	*P. raistrickii*	*P. thomii*	*P. miczynskii*

(continued)

Table 30.3 (continued)

«Age» of sand				
Freshly deposited	10 years	20 years	30 years	50 years
	P. corylophilum	*P. restrictum*		*P. raistrickii*
	P. velutinum	*P. solitum*		*P. restrictum*
	P. raistrickii	*P. spinulosum*		*Tal. ruber*
	P. spinulosum	*T. koningii*		*P. solitum*
	J. eupyrena			*P. citrinum*
	T. koningii			*P. thomii*
				T. hamatum
				T. polysporum

by the extremely small number of fungi and their poor species diversity in the enrichment waste leaving the plant. Currently, the prerequisites for the formation of micromycete complexes, which are typical of the regional podzolic soils, have been created. The similarity in the composition of the species in the micromycete complexes of the recultivated nepheline sands and typical podzolic soils of the Kola Peninsula increased, with the Sörensen coefficient reaching 45%.

30.5 Abundance and Taxonomic Diversity of Microscopic Algae and Cyanobacteria

Microscopic algae and cyanobacteria are known to be the important components of soil microbocenosis. They are involved in the processes of accumulating organic matter and nitrogen, destructing minerals, and redistributing and accumulating elements (Gollerbakh and Shtina 1969). Cyanobacteria and algae are directly engaged in the formation of biological soil crusts, which contribute to the structuring of the substrate, regulate the water regime, affect the germination of seeds of higher plants, and prevent erosion processes (Evans and Johansen 1999). Thus, studying the cyanobacterial-algal component of the nepheline sands biota is important for a deeper assessment of the primary occurring soil-forming processes as well as for studying the possibility of creating biological products and biofertilizers based on algae and cyanobacteria.

The number of viable algae cells in the freshly deposited sands reached 40 thousand cells/g abs. dry substrate. Microphototrophs emerge here along with water from the technological cycle, the turnover of which is about 80%. The losses are replenished by Lake Imandra surface water intake. In the 20-year-old sands, the amount of microalgae is low under *Leymus arenarius*, which can be explained by complex factors: competition with plants for nutrients and the lack of air and moisture exchange

due to the remnants of the polymer cover used for remediation. The areas where natural overgrowing processes take place are characterized by a higher algae population—up to 450 thousand cells per 1 g of the substrate in the 40-year-old sands under the sedge and crowberry plant groups and up to 1.9 million cells in 1 g under the moss cover and in the young cryptogamous crusts.

The research has revealed 69 algae and cyanobacteria species belonging to five divisions: 25 species of Chlorophyta (Chlorophyceae and Trebouxiophyceae), 10 species of Ochrophyta (Xanthophyceae, Eustigmatophyceae, and Chrysophyceae), 9 species of Bacillariophyta, 17 species of Cyanobacteria, and 8 species of Charophyta (Klebsormidiophyceae and Conjugatophyceae) (Table 30.4).

The data in the table indicate a very low level of similarity between the algocenoses of the studied areas. In the freshly deposited sands, predominantly single-cell green algae were found as well as one species of cyanobacteria, diatoms, and yellow-green algae. The algae from the Scenedesmaceae family, being typically a planktonic organism, enter to these sands from circulating water.

In the 20-year-old sand from the reclaimed dam slopes, 29 species were found. Most of them (40%) were represented by algae from the Chlorophyta division. Moreover, filamentous cyanobacteria and yellow-green algae have made a significant contribution to the overall diversity.

In the 40-year-old sands, green algae (35%) dominated, simultaneously cyanobacteria (25%), and diatoms (11%) played a significant role. The representatives of both groups of organisms are known to prefer a neutral or weakly alkaline reaction from the environment. In addition to this fact, cyanobacteria are capable of fixing atmospheric nitrogen, which is important within the conditions of its acute lack in the nepheline sands. Their exuded mucilage creates a favorable environment for the demanding diatoms (Shtina and Gollerbakh 1976). Xanthophytes and eustigmatophytes have also made a considerable contribution to the microphototrophic community. It should be noted that there was a significant variety (11%) of charophytes from the class Conjugatophyceae (Fig. 30.4). Wet habitats are characteristic of the representatives of this algae group. The presence of these microalgae in the sandy substrate of a long storage period may testify to a gradual formation of favorable conditions for the development of cyanobacterial-algal cenoses in the composition of cryptogamous crusts. The dominance of filamentous forms in the cyanobacterial community, the abundance of coccoid green algae represented by Chlorophyceae and Trebouxiophyceae, and the significant role of filamentous taxa (for example, *Klebsormidium*, *Xanthonema*, and *Tribonema*) are characteristic features of the Arctic biological soil crusts (Pushkareva et al. 2016).

30.6 Conclusion

New data were obtained on the current state of the microbial communities of the apatite-nepheline ore tailings. The species diversity of microscopic algae and

Table 30.4 Species composition of algae and cyanobacteria found in the ANDP-2 nepheline sands

Species	Freshly deposited	20 years	40 years
Division Chlorophyta, class Chlorophyceae			
Bracteacoccus minor (Schmidle ex Chodat) Petrová	+		
Chlamydomonas spp.		+	+
Chlorolobion lunulatum Hindák		+	
Chlorosarcinopsis cf. *communis* Groover and Bold		+	
Coelastrella terrestris (Reisigl) Hegewald and N. Hanagata			+
Coenochloris sp.			+
Macrochloris cf. *multinucleata* (Reisigl) Ettl and Gärtner		+	
Monoraphidium terrestre (Bristol) Krienitz and Klein			+
Neochlorosarcina cf. *minuta* (R. D. Groover and Bold) Shin Watanabe			+
Palmellopsis gelatinosa Korshikov			+
Pleurastrum terricola (Bristol) D. M. John		+	
Scenedesmus armatus (Chodat) Chodat	+		
Tetradesmus obliquus (Turpin) M. J. Wynne	+		
Division Chlorophyta, class Trebouxiophyceae			
Chlorella cf. *vulgaris* Beyerinck [Beijerinck]	+		
Dictyochloropsis splendida Geitler			+
Keratococcus bicaudatus (A. Braun ex Rabenhorst) J. B. Petersen		+	
Pseudococcomyxa simplex (Mainx) Fott		+	+
Stichococcus bacillaris Nägeli		+	+
S. minutus Grintzesco and Peterfi			+
Division Chlorophyta, class Ulvophyceae			
Fernandinella alpina Chodat		+	+
Fottea stichococcoides Hindák		+	+
Interfilum massjukiae Mikhailyuk, Sluiman, Massalski, Mudimu, Demchenko, Friedl and Kondratyuk			+
I. terricola (J. B. Petersen) Mikhailyuk, Sluiman, Massalski, Mudimu, Demchenko, Friedl and Kondratyuk		+	+
Rhexinema paucicellulare (Vischer) Geitler			+
Scotinosphaera paradoxa Klebs			+

(continued)

Table 30.4 (continued)

Species	Freshly deposited	20 years	40 years
Division Bacillariophyta, class Bacillariophyceae			
Achnanthidium minutissimum (Kützing) Czarnecki			+
Cyclotella sp.	+		
Encyonema sp.			+
Gomphonema cf. *gracile* Ehrenberg			+
Hantzschia amphioxys (Ehrenberg) Grunow in Cleve and Grunow		+	
Nitzschia palea (Kützing) W. Smith			+
Pinnularia borealis Ehrenberg		+	+
P. subcapitata W. Gregory			+
Rhopalodia gibba (Ehrenberg) Otto Müller			+
Division Ochrophyta, class Chrysophyceae			
cf. *Tetrasporopsis fuscescens* (A. Braun ex Kützing) Lemmermann			+
Division Ochrophyta, class Eustigmatophyceae			
Eustigmatos magnus (J. B. Petersen) D. J. Hibberd		+	+
Monodopsis subterranea (J. B. Petersen) D. J. Hibberd			+
Pseudocharaciopsis ovalis (Chodat) D. J. Hibberd		+	+
Division Ochrophyta, class Xanthophyceae			
Botrydiopsis constricta Broady		+	
B. eriensis J. W. Snow			+
Bumilleriopsis terricola Matvienko [Matwienko]		+	
Heterococcus sp.		+	+
Tribonema aequale Pascher		+	+
Xanthonema debile (Vischer) P. C. Silva	+	+	+
Division Cyanobacteria, class Cyanophyceae			
Anabaena sp.		+	+
Aphanocapsa muscicola (Meneghini) Wille			+
A. parietina (Nägeli ex Kützing) Nägeli			+
Aphanothece sp.			+
Calothrix braunii Bornet and Flahault			+
Chroococcus sp.			+
Cylindrospermum sp.			+
Desmonostoc muscorum (C. Agardh ex Bornet and Flahault) Hrouzek and Ventura		+	+
Geitlerinema sp.			+
Kamptonema animale (C. Agardh ex Gomont) Strunecký, Komárek and J. Smarda		+	

(continued)

Table 30.4 (continued)

Species	Freshly deposited	20 years	40 years
Leptolyngbya foveolara (Gomont) Anagnostidis and Komárek		+	+
Leptolyngbya sp.		+	+
Microcoleus autumnalis (Gomont) Strunecky, Komárek and J. R. Johansen		+	+
Nostoc sp.		+	+
Pseudanabaena minima (G. S. An) Anagnostidis	+		+
Scytonema hofmanii C. Agardh ex Bornet and Flahault			+
Trichormus sp.		+	+
Division Charophyta, class Conjugatophyceae			
Actinotaenium cucurbita (Brébisson ex Ralfs) Teiling			+
Cosmarium granatum Brébisson ex Ralfs			+
C. holmiense var. integrum P. Lundell			+
C. undulatum var. minutum Wittrock			+
Cylindrocystis brebissonii (Ralfs) De Bary			+
C. gracilis I. Hirn			+
Mesotaenium macrococcum (Kützing ex Kützing) J. Roy and Bisset			+
Division Charophyta, class Klebsormidiophyceae			
Klebsormidium flaccidum (Kützing) P. C. Silva, K. R. Mattox and W. H. Blackwell		+	+

cyanobacteria that form biological films on the nepheline sands surface was described for the first time.

Resulting from biological recultivation and development of the vegetation cover on the surface of nepheline sands, the generated ecosystem is represented as a natural model of a man-induced formation that has undergone a long evolution from barren sands, scarcely populated by microorganisms, to complex biogeocenoses, which include the vegetation cover of various structures and the newly formed soil. Microorganisms are the biocatalyzers of the primary soil formation processes and one of the main factors determining their specificity. The increase in the storage time of the tailings and their remediation have positively affected the increase in the abundance, biomass, and diversity of all the microorganism groups. Currently, prerequisites for the formation of micromycete complexes, which are typical for the regional podzolic soils, have been created. The extreme conditions strongly affect the diversity of eukaryotic microalgae and cyanobacteria. Biological crusts formed on the surface of the nepheline sands have characteristic features of arctic biological soil crusts and can play an important role in the soil-forming process.

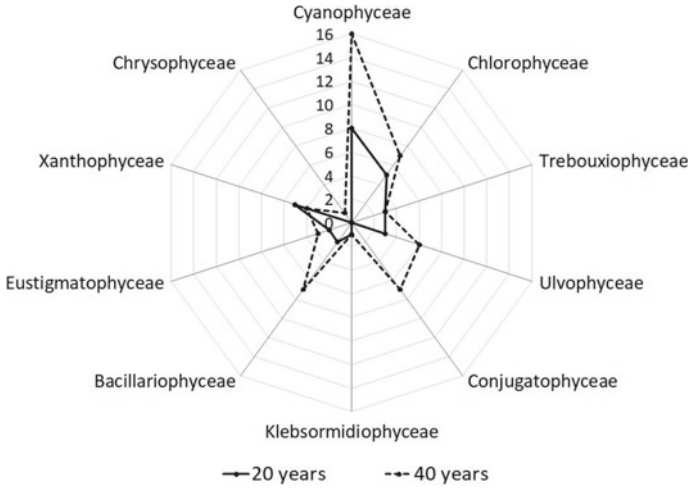


Fig. 30.4 Species diversity of algae and cyanobacteria communities (at a level of classes) in the nepheline sands

Strains of microscopic fungi, algae, and cyanobacteria isolated from nepheline sands were arranged at the herbarium of the Institute of North Industrial Ecology Problems (INEP) of the Kola Science Centre of the Russian Academy of Sciences.

Acknowledgements We thank D. A. Davydov for his help in the identification of cyanobacteria.

References

Andreeva VM (1998) Soil and aerophilic green algae. Nauka, Moscow (in Russian)
Aristovskaya TV (1965) Microbiology of podzolic soils. Nauka, Moscow-Leningrad (in Russian)
Cadastre of waste of mining and metallurgical production of the Murmansk region (as of 01/01/99). https://www.murman.ru/ecology/cadastre/
Domsh KH, Gams W, Anderson TH (2007) Compendium of soil fungi. IHW-Verlag, Eching
Egorova LN (1986) Soil fungi of the far east. Nauka, Leningrad (in Russian)
Ettl H, Gärtner G (2014) Syllabus der Boden-, Luft- und Flechtenalgen. 2., ergänzte Auflage. Springer, Berlin
Evans RD, Johansen JR (1999) Microbiotic crusts and ecosystem processes. Crit Rev Plant Sci 18(2):183–225
Evdokimova GA, Mozgova NP (1996) Microflora of tundra soils in the Kola Peninsula. Eurasian Soil Sci 28(12):188–203
Evdokimova GA, Mozgova NP (2001) Microorganisms of tundra and forest podzols of the Kola North. KSC RAS Publ., Apatity (in Russian)
Evdokimova GA, Naumenko AF (2002) Microorganisms of underground mines of Northern Fennoscandia. Geoecology. Engineering geology. Hydrogeology. Geocryology 3:237–224 (in Russian)

Gaisina LA, Fazlutdinova AI, Kabirov RR (2008) Modern methods of isolation and cultivation of algae. Bashkir State Pedagogical University, Ufa (in Russian)
Gershenkop AS, Evdokimova GA, Voronina NV, Kreimer LL (2005) Influence of bacterial component of the recycling water on the flotation of not sulphidic ores—by the example of "Apatit". Inzhenernaya Ekologiya 3:51–61 (in Russian)
Gollerbakh MM, Shtina EA (1969) Soil algae. Science, L. (in Russian)
Guiry MD, Guiry GM (2018) AlgaeBase. World-wide electronic publication. National University of Ireland, Galway. http://www.algaebase.org
Ivanova VA, Rukhlenko ED (2010) Estimation of the mineralogical and technological properties of stored apatite-nepheline ore dressing waste. Min J 9:92–95 (in Russian)
Komárek J (2013) Cyanoprokaryota 3: Heterocytous Genera. In: Süßwasserflora von Mitteleuropa. Springer, Berlin
Komárek J, Anagnostidis K (1998) Cyanoprokaryota 1: Chroococcales. In: Süßwasserflora von Mitteleuropa. Spektrum Akademischer Verlag, Jena
Komárek J, Anagnostidis K (2005) Cyanoprokaryota 2: Oscillatoriales. In: Süßwasserflora von Mitteleuropa. Spektrum Akademischer Verlag, Heidelberg
Kondakova LV, Domracheva L (2007) Flora of Vyatka region. Part 2. Algal. Kirov Publ. House, Kirov (in Russian)
Kondrat'eva NV, Kovalenko OV (1975) Brief guide for identification of toxic blue-green algae. Naukova Dumka, Kiev (in Russian)
Kótai J (1972) Instructions for preparation of modified nutrient solution Z8 for algae. Norwegian Institute for Water Research, Publ. B-11/69, Blindern, Oslo
Krasilnikov NA (1958) Soil microorganisms and higher plants. USSR Academy of Sciences, Moscow (in Russian)
Kurakov AV (2001) Manual for isolation and characterization of the complexes of micromycetes in terrestrial ecosystems. MAKS Press, Moscow (in Russian)
Lyubimova AA, Medvedev PM (1970) The experience of vegetation fixing dust tailing dumps ANOF-1 of the plant "Apatite". Veg Ind Pollut 7:104–111 (in Russian)
Mirchink TG (1988) Soil mycology. Moscow State University, Moscow (in Russian)
Novakovskii AB (2004) Possibilities and principles of use of GRAPHS software module. Komi Scientific Center, Ural Branch, Russian Academy of Sciences, Syktyvkar (in Russian)
Olsen RA, Hovland J (1985) Fungal flora and activity in Norway spruce needle litter: Report, Agricultural University of Norway
Pereverzev VN, Ivliev AI, Gorbunov AV, Lyapunov SM (2007) Primary pedogenesis in the tailings of apatite–nepheline ores on the Kola Peninsula. Eurasian Soil Sci 40(8):900–906
Pokhil'ko AA, Zarzhitskaya NA (2006) Overgrowth of tailings of different ages in Murmansk oblast. Curr Ecol Probl North 1:106–107 (in Russian)
Pushkareva E, Johansen JR, Elster J (2016) A review of the ecology, ecophysiology and biodiversity of microalgae in Arctic soil crusts. Polar Biol 39(12):2227–2240
Raper B, Thom C (1968) A manual of the Penicillia. Hafner, London
Seifert K, Morgan-Jones G, Gams W, Kendrick B (2011) The genera of Hyphomycetes, CBS Biodiversity Series No. 9. CBS-KNAW Fungal Biodiversity Centre, Utrecht
Shtina EA, Gollerbakh MM (1976) Ecology of soil algae. Nauka Publ., Moscow (in Russian)
Strizhenok AV (2015) Improving of the system of atmospheric air industrial environmental monitoring during the alluvial anthropogenic arrays formation. Min Inf Anal Bull (Sci Tech J) 11:587–598 (in Russian)
Zvyagintsev DG (1978) Biological activity of soils and scales for evaluating some of its indicators. Soil Sci 6:48–54 (in Russian)

Chapter 31
Crystallization of Calcium Oxalate Hydrates by Interaction of Apatites and Fossilized Tooth Tissue with Fungus *Aspergillus niger*

Marina S. Zelenskaya, Aleksei V. Rusakov, Olga V. Frank-Kamenetskaya, Dmitry Yu. Vlasov, Alina R. Izatulina and Mariya A. Kuz'mina

Abstract The crystallization of calcium oxalates (weddellite and whewellite) by interaction of natural and synthetic apatites and fossilized tooth tissue with fungus *Aspergillus niger*, one of most active acid producers, was studied in vitro. The morphology and the sequence of formation of growing oxalate hydrate crystals were revealed. It was shown that morphogenetic patterns of calcium oxalate crystallization on apatite substrates under the action of *Aspergillus niger* micromycete are determined by the chemical properties of the crystallization medium, which depends on the solubility of the underlying substrate and on its chemical composition and structural features (dispersity and porosity). The main difference between oxalate crystallization under the influence of *Aspergillus niger* micromycete on the surface of apatite substrates and on the surface of calcite marble is the predominance of whewellite over weddellite on all stages of growth.

Keywords Biocrystallization · Microbial metabolism · Whewellite · Weddellite · Calcium oxalate hydrates · Microscopic fungi · *Aspergillus niger*

31.1 Introduction

The metabolism of the microbial lithobiont community is a powerful factor of modern mineral formation. Among the minerals formed by interaction of microscopic fungi and lichens crystalline salts of oxalic acid (oxalates) are the most common. Among them calcium oxalates are the most common. Calcium oxalates of biogenic origin (whewellite $CaC_2O_4 \cdot H_2O$ and weddellite $CaC_2O_4 \cdot 2H_2O$) are often found in thalli of crustous and foliose lichens growing on the surface of carbonate rocks (marble, limestone and dolomite) (Adamo and Violante 2000; Giordani et al. 2003). They were

M. S. Zelenskaya (✉) · A. V. Rusakov · O. V. Frank-Kamenetskaya · D. Yu. Vlasov · A. R. Izatulina · M. A. Kuz'mina
Saint Petersburg State University, Universitetskaya Nab 7/9, Saint Petersburg 199034, Russia
e-mail: marsz@yandex.ru

© Springer Nature Switzerland AG 2020

O. V. Frank-Kamenetskaya et al. (eds.), *Processes and Phenomena on the Boundary Between Biogenic and Abiogenic Nature*, Lecture Notes in Earth System Sciences,
https://doi.org/10.1007/978-3-030-21614-6_31

also repeatedly found on the surface of various carbonate rocks under the action of fungi under experimental conditions (Fomina et al. 2005; Ceci et al. 2015; Gadd et al. 2014; Cai et al. 2013; Sutjaritvorakul et al. 2016). The morphogenetic patterns of calcium oxalate formation on the surface of marble under the influence of the fungus *Aspergillus niger* are described in Sturm et al. (2015).

During the field seasons of 2017–2018 we were the first to find calcium oxalates in the crustous lichen thalli on the surface of apatite-containing rocks: on obol sandstone (Kingiseppsky phosphate deposit, Leningrad region) and on apatite-nepheline ore (Apatite deposit Kukisvumchorr, apatite-nepheline ore) (Fig. 31.1).

Earlier it had been reported that whewellite and weddellite had been obtained in experiments involving microscopic fungi on a number of apatite substrates: on rock wastes from processed apatite-nepheline ore (Gershenkop and Evdokimova 2014), on the surface of boar tusk, walrus tusk (Pinzari et al. 2013) and mammoth tooth (Rusakov et al. 2016; Zelenskaya et al. 2018), as well as on fluorapatite mineral particles (Rosling et al. 2007), hydroxyapatite powders (Rusakov et al. 2016; Zelenskaya et al. 2018) and tricalcium phosphate (Ceci et al. 2018). The authors of these works observed dissolution of apatite (Gershenkop and Evdokimova 2014; Rosling et al. 2007; Ceci et al. 2018) and bone tissue (Pinzari et al. 2013) in their experiments. Pinzari et al. (2013) also noted the penetration of fungal hyphae into bone tissue and the formation of small cavities in it.

The aims of this work were:

1. To obtain a morphogenetic picture of calcium oxalate crystallization on the surface of apatite substrates (natural and synthetic apatite, as well as teeth of fossilized animals) under the action of the microscopic fungus *Aspergillus niger* in the experimental conditions;
2. To reveal the influence of the chemical composition and structural features of the underlying substrates on the crystallization process;
3. To compare oxalate biocrystallization on the surface of apatite substrates and calcite marble.

31.2 Experimental Section

31.2.1 Experiment

The experiments were carried out with the participation of *Aspergillus niger* micromycete in a liquid nutrient medium on the surface of apatite with different concentration fluorine and carbonate ions, as well as on the dentine of animal teeth fossils with varying levels of fossilization (Table 31.1).

The choice of the fungus *Aspergillus niger* was due to the fact that it is an active organic acid producer, including oxalic acid (Barinova et al. 2010; Sturm et al. 2015). *Aspergillus niger* (strain Ch4/07) was previously isolated from the damaged surface of Proconesos marble (Chersonesos, Crimea). The characterization of the strain was

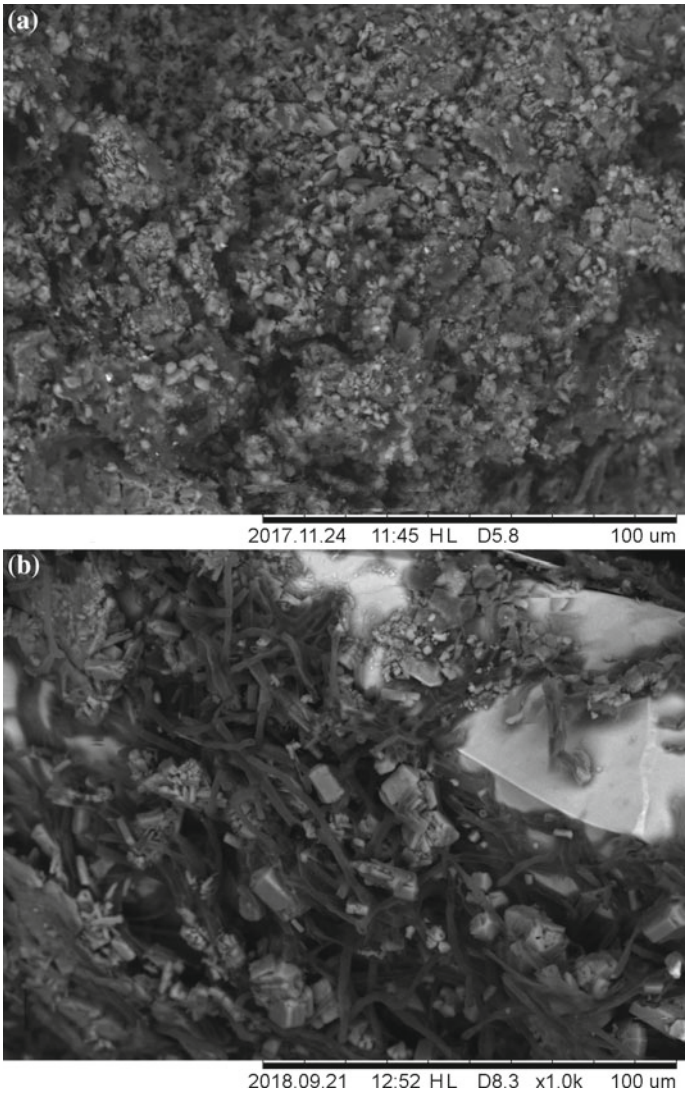


Fig. 31.1 SEM images of calcium oxalate crystals in lichen thalli on the surface of: **a** obol sandstone (Kingiseppsky phosphate deposit, Leningrad region); **b** apatite-nepheline ore (Kukisvumchorr deposit, Kola Peninsula)

Table 31.1 The origin of the underlying apatite substrates used in the experiment and their short form

Apatite substrate	Short form	Origin
Hydroxyapatite powder	HAP-1	Synthesis by precipitation
CO_3–hydroxyapatite powder	HAP-2	
Fluorapatite powder	FAP-3	
CO_3–fluorapatite powder	FAP-4	
Natural fluorapatite crystal	FAP-cr	Slyudyanka ore field, Irkutsk region, Russia
Mammoth tooth dentin	DTM	Pleistocene alluvial deposits, Yakutia
Horse tooth dentin	DTH	From the alluvial deposits of the late Pleistocene, Kursk region
Dentin of a tooth of a southern elephant	DTE	From Neugen Alluvial Deposits

carried out in the Research Center for "Genomic technologies and cellular biology" of the All-Russian Research Institute of Agricultural Microbiology. The species identification of the strain was based on the sequence of the ITS region of rDNA (GenBank accession no.—KF768341).

Crystallization was carried out on the surface of:

1. synthetic hydroxy- and fluorapatite powders (including those synthesized in the presence of carbonate ions in the solution);
2. natural fluorapatite crystal;
3. elephant, horse, and mammoth tooth dentine from alluvial deposits of different geological age (Table 31.1).

In the experiments with of animal fossil teeth dentine the material was cut into small plates (~1 × 1 × 0.5 cm in size).

31.2.1.1 Synthesis of Apatite

Hydroxyapatite (HAP-1) was synthesized by the method of reverse precipitation in an ammonium-containing medium, in which an aqueous solution of calcium nitrate ($Ca(NO_3)_2 \times 4H_2O$) heated to 85–90 °C (100 ml of 0.2 mol/l solution) with continuous stirring for 45 min, the aqueous solution of ammonium hydrogen phosphate ($(NH_4)_2HPO_4$, 100 ml of a 0.1 mol/l solution) was gradually added to the solution. The high alkalinity of the solution was maintained by adding 4–5 ml of concentrated ammonium hydroxide solution (NH_4OH) to both initial solutions, so that the

resulting pH values of the crystallization medium ranged from 8 to 10. In the synthesis of carbonate-hydroxyapatite (HAP-2), a solution of ammonium bicarbonate ($(NH_4)HCO_3$, 5 ml of 0.2 mol/l solution) was added to a solution of ammonium hydrogen phosphate ($(NH_4)_2HPO_4$, 100 ml of 0.1 mol/l solution). In the synthesis of fluorapatite (FAP-3), a solution of ammonium fluoride ($(NH_4)F$, 20 ml of a 0.2 mol/l solution) was added to a solution of ammonium hydrogen phosphate ($(NH_4)_2HPO_4$, 100 ml of a 0.1 mol/l solution). In the synthesis of carbonate-fluorapatite (FAP-4) a mixture of ammonium hydrogen phosphate solution ($(NH_4)_2HPO_4$, 100 ml of 0.1 mol/l solution), ammonium hydrogen carbonate solution ($(NH_4)HCO_3$, 5 ml of 0.2 mol/l solution) and ammonium fluoride solution ($(NH_4)F$, 20 ml of 0.2 mol/l solution) were used. In all syntheses, the obtained milky-white precipitate was kept for 2 h at 90–95 °C, washed by decantation several times with distilled water, dried at 100–110 °C for 12–24 h, and then grinded in a mortar to homogenize the sample.

31.2.1.2 Experimental Conditions with Fungus *Aspergillus niger*

The experiments were carried out at room temperature in a liquid Czapek-Dox medium (g/l: $NaNO_3$—2.0; KH_2PO_4—1.0; $MgSO_4 \cdot 7H_2O$—0.5; KCl—0.5 $FeSO_4 \cdot 7H_2O$—0.01, glucose—30.0 g/l). The initial pH of the medium was 5.5. Selected apatite substrates were placed on the bottom of a Petri dishes and 15 ml of liquid Czapek-Dox medium was added so that their surface was completely covered. Inoculation was performed with conidia of a microscopic fungus of a 10-day culture grown on a solid nutrient medium of Czapek-Dox.

The cultivation time ranged from 2 to 15 days with constant monitoring of the pH of the medium. Experiments were performed in triplicate.

31.2.2 Methods

31.2.2.1 Scanning Electron Microscopy (SEM) and Energy-Dispersive X-Ray Spectroscopy (EDXS)

Scanning electron microscopy (SEM) and energy-dispersive X-ray spectroscopy (EDXS) were used for examination of the morphology of the formed crystals and for determination of the element composition of underlying substrate and crystallization products. The study was carried out by means of Desktop Scanning Electron Microscope TM3000 (Hitachi), the device is equipped with energy dispersive microanalysis attachment OXFORD. SE detector (secondary electron Everhart-Thornley) based on the highly sensitive YAG crystal with the resolution of 0.1Z of the atomic number was used. The specimens were coated with carbon (~15 nm). Magnification range varied from 100× to 1000×.

31.2.2.2 X-Ray Powder Diffraction (XRD)

The XRD measurements were performed by means of Bruker «D2 Phaser» (CuKα radiation of wavelength λ = 1.54178 Å, X-ray tube parameters were 30 kV/10 mA; energy-dispersive one-dimensional detector DTEX/ULTRA was used) and Rigaku Ultima IV (CuKα radiation; 40 kV/30 mA; PSD D-Tex Ultra detector) powder X-ray diffractometers. X-ray diffraction patterns were collected at room temperature in the range of 2θ = 5–60°. Phase identification was carried out using the ICDD PDF-2 Database (release 2016). The unit cell parameters were refined by the Pawley method using TOPAS 4.2 software. The background was modelled using a Chebychev polynomial of 12th order. The peak profile was described using the fundamental parameters approach.

31.2.2.3 Infrared (IR) Spectroscopy

IR spectroscopy was used for establishing the presence of CO_3^{2-}, OH^- ions and molecular water. The spectra were collected with a Bruker Vertex IR-spectrometer in the range of 400–4000 cm^{-1} with a frequency resolution of 1 cm^{-1}. The samples were prepared as tablets in KBr. The results were interpreted according to Rosseeva (2010). The P–O bond vibrations were detected using absorption bands at 566, 603, 959, 1042, 1105 cm^{-1}. The presence of OH^- ions was controlled by the presence of the absorption bands at 636 cm^{-1} (P–OH) and 3573 cm^{-1}, the presence of HPO_4^{2-} ions—by a bands at 473 and 874 cm^{-1}, the presence of water by a group of bands in the range of 3300–3700 cm^{-1} (stretching vibrations) and a band at 1640 cm^{-1} (deformation vibrations). The carbonate-ion of the B type was localized using the C–O absorption bands at 1418 and 1455 cm^{-1}. The presence of the protein component in fossilized bone tissues was revealed by the strong absorption bands of Amid I (at 1655 cm^{-1}), Amid II (at 1546 cm^{-1}) and Amid A, B (at 3070–3300 cm^{-1}) overlapping lines of water and carbonate ions.

31.2.2.4 Particle Size Analysis

The measurements of particle size distribution for synthetic samples of apatite were performed by means of Mastersizer 3000. The method is based on measuring the intensity of scattered light of the laser beam passing through the dispersed sample (suspension, emulsion, dry powder). This scattered light is analyzed and the particle size distribution is computed (reconstructed) based on the measured angular dependence of the light scattered by particles dispersed in the sample. The measurements were carried out in water. The particle size was taken as a weighted average by volume (De Brouckere/Harden Mean Diameter).

31.3 Results

31.3.1 Characteristics of Underlying Substrates

The results of studying the samples of the substrates via a complex of methods (X-ray powder diffraction, IR spectroscopy, EDC analysis) confirmed that all of them are apatites (HAP-1, HAP-2, FAP-3, FAP-4, FAP-cr; Table 31.1) or apatite-protein composites (DTM, DTH, DTE; Table 31.1). According to the data of IR-spectroscopy, the composition of the studied apatites includes water molecules, as well as hydrophosphate ions and carbonate ions of the B type (Fig. 31.2). The content and composition of the protein component in fossilized dental tissues vary (Fig. 31.2b). The protein component in the composition of the horse tooth dentin is practically absent. According to the data of EDC analysis, the fluorine content in the samples studied also varies (Fig. 31.3). The mammoth tooth dentine (DTM; Fig. 31.2c) contains no fluorine, and there is much less fluorine in the horse tooth dentine (DTH) and the elephant tooth dentine (DTE; Fig. 31.2b) than in the natural fluorapatite crystal (Fig. 31.2a). The fluorine content in the elephant tooth dentin is much higher than in the horse tooth dentine. The unit cell parameters of hydroxyapatite (HAP-1, HAP-2, DTM) vary as follows: $\boldsymbol{a}$—from 9.428 to 9.397 Å; $\boldsymbol{c}$—6.888 to 6.892 (Table 31.2), i.e. can be either smaller or larger than the parameters of stoichiometric hydroxyapatite ($\boldsymbol{a}_{st} = 9.418$, $\boldsymbol{c}_{st} = 6.884$ Å JCPDS No. 9-432). In the sample of HAP-1, the effect of water and hydrogen phosphate ions on the parameter $\boldsymbol{a}$ is greater than of the carbonate ion, which leads to an increase of the parameter $\boldsymbol{a}$ relative to $\boldsymbol{a}_{st}$. In samples of HAP-2 and DTM, the effect of carbonate ions on the parameter $\boldsymbol{a}$ is greater than that of water and hydrogen phosphate ions, which leads to a decrease in its parameter $\boldsymbol{a}$ relative to $\boldsymbol{a}_{st}$. Parameters of all studied hydroxyapatites (GAP-1, GAP-2, DTM) are close or slightly larger than $\boldsymbol{c}_{ts}$, which is typical for carbonate-apatites. The unit cell parameters of the fluoroapatites (FAP-3, FAP-4, FAP-cr) can also be either smaller or larger than the parameters of stoichiometric fluorapatite ($\boldsymbol{a}_{st} = 9.368$, $\boldsymbol{c}_{st} = 6.884$ Å, JCPDS №15-0876), which is mainly due to the multidirectional influence of carbonate ion (decreasing parameter $\boldsymbol{a}$) and water, hydrophosphate ions and OH groups (increasing parameter $\boldsymbol{a}$). Judging by the parameters of the unit cell, the maximum content of carbonate ion is observed in the FAP-4 powder. The maximum value of coherent scattering domains (CSD) is observed for fluorapatite crystal (FAP-cr, Table 31.2). The average CSD values for apatite powders (GAP-1, GAP-2, FAP-3, FAP-4) are close or larger by an order of magnitude than those for the fluorapatite crystal. The smallest CSD values were observed for the mammoth tooth dentin (which was 3–4 times less than those for the apatite powders and fossilized dental tissue samples).

According to laser diffraction data, the sizes of particles in powders of synthetic apatites (93–140 μm; Table 31.2) are significantly larger than the sizes of the corresponding CDS. The size distribution of particles for apatite powders of different composition is almost the same (Fig. 31.4).

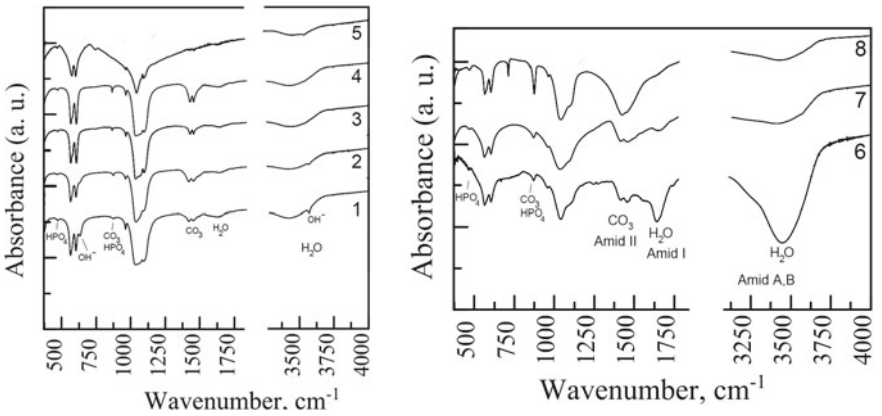


Fig. 31.2 IR spectra: **a** hydroxyl- and fluorapatite, **b** dentin of animal fossils. Legend: 1—GAP-1, 2—GAP-2, 3—FAP-3, 4—FAP-4, 5—CFA, 6—DTM, 7—DTH, 8—DTE. The P-O lines are not signed. The absorption bands of Amide I, Amide II, Amide A, B correspond to the components of the protein molecules

Table 31.2 Characteristics of the substrates

Apatite substrates (Table 31.1)	Unit cell parameters, Å		Coherent scattering region, Å	d^1, μm
	a	*c*		
HAP-1	9.428 (2)	6.888(3)	24.6 (3)	109
HAP-2	9.415 (2)	6.892 (1)	18.9 (2)	93
FAP-3	9.374 (6)	6.894 (4)	28.7 (13)	140
FAP-4	9.361 (1)	6.895 (1)	31.3 (5)	94.4
FAP-cr	9.385 (1)	6.887 (1)	534 (8)	–
DTM	9.397 (11)	6.888 (10)	8.4 (3)	–
DTH	9.447 (1)	6.888 (1)	25.5 (3)	–
DTE	9.402 (1)	6.900 (1)	20.7 (2)	–

Note d^1—average size of a powder particle

31.3.2 Crystallization on the Surface of Apatite

31.3.2.1 On Hydroxyapatite (HAP-1, HAP-2)

The crystallization patterns in the mycelium of the fungus on CO_3-containing hydroxyapatite powders (HAP-1, HAP-2) are very similar, which can be explained by the similar content of carbonate ion according to IR spectroscopy (Fig. 31.2a). The first calcium oxalate crystals on both powders appear on the 2nd day of the experiment at pH = 5 with the start of more or less active development of the mycelium of the fungus, which can be clearly seen on X-ray (Fig. 31.5) and SEM images (Fig. 31.6a, b). Basically, these are stacks of crystals of a whewellite, of a lamellar, pseudo-

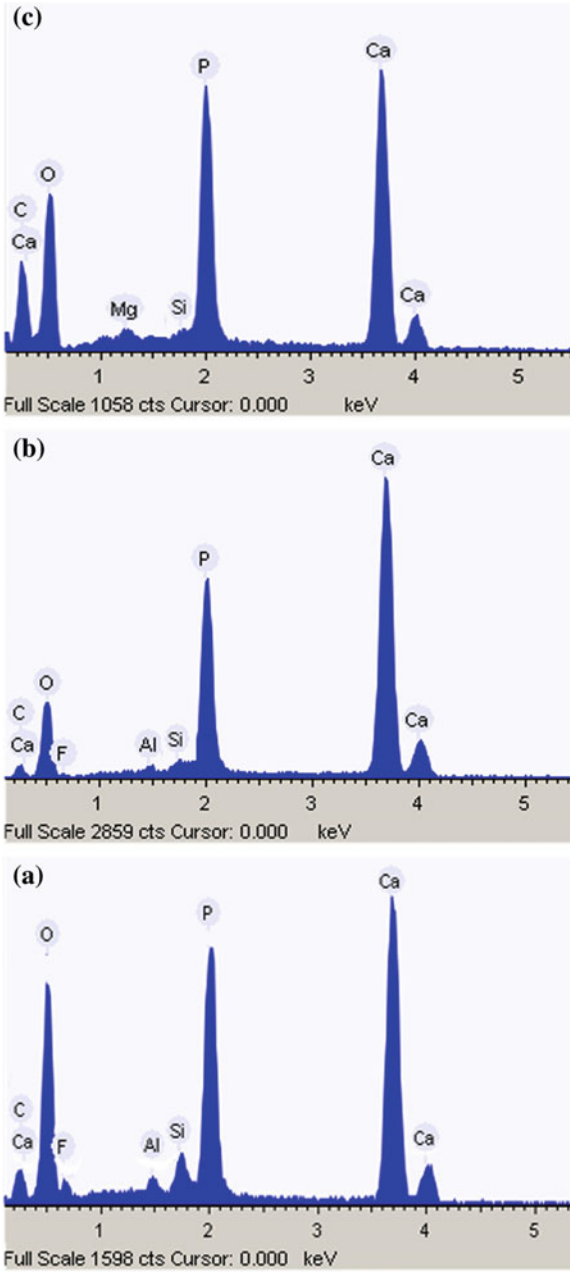


Fig. 31.3 EDX spectra of the substrates: **a** single crystal of natural apatite, **b** elephant dentine, **c** mammoth dentine

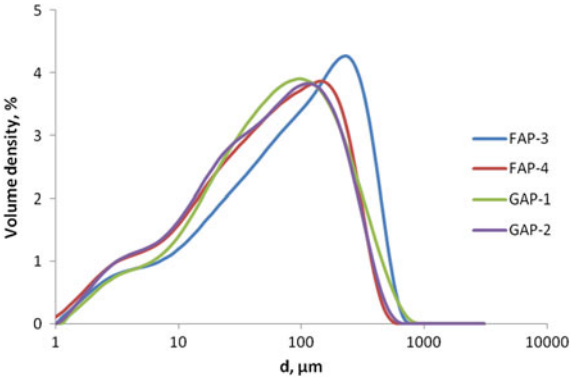


Fig. 31.4 The size distribution of apatite particles in powder samples

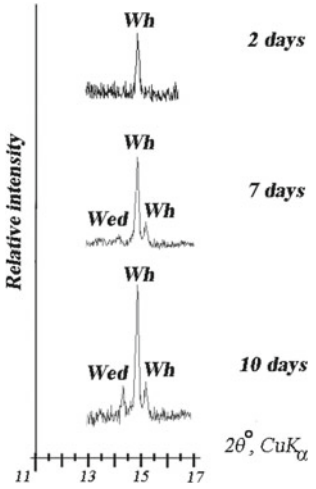


Fig. 31.5 X-ray pattern fragments of crystallization products on the surface of hydroxyapatite powder (HAP-1) at various stages of the experiment

hexagonal habit with a strongly developed pinacoid face. There are crystals with curved convex faces. The beginning of splitting of the crystals is evident, as well as fan-shaped intergrowths of sprouting twins of the "dovetail" type (Fig. 31.6a). The maximum sizes of individual crystals in the intergrowths vary from 25 to 50 microns. Weddellite single crystals (~15–30 μm) of dipyramidal habit are also found on the faces which are exhibiting splitting (Fig. 31.6b). All crystals are situated near the mycelium. Often, fungal hyphae grow through crystals and intergrowths.

On the 3rd day of the experiment the overall picture stays the same. On the 5th day the number of whewellite crystals increases (Fig. 31.6c, d). SEM images show edge adhesion between stacked whewellite lamellar crystals (Fig. 31.6c), as well as intergrowths of inter-perpendicular crystals (Fig. 31.6d). In addition, numerous small dipyramidal weddellite crystals of a new generation appear (from 5 to 15 μm in size) and are often located on the surface of whewellite intergrowths (Fig. 31.6, d).

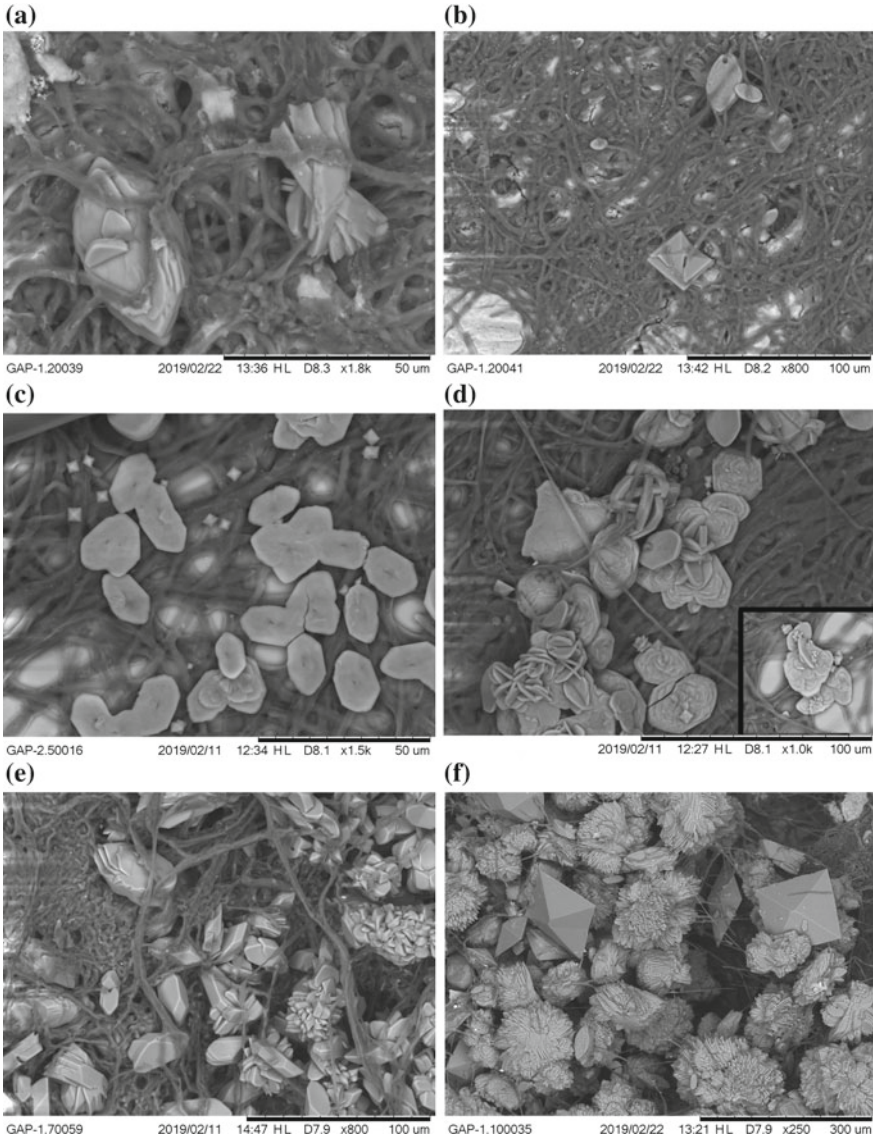


Fig. 31.6 SEM-images of crystallization products formed on synthetic hydroxyapatite powders: **a** lamellar split wavelet crystal and fan-shaped intergrowth of dovetail twins (on the second day of the experiment, HAP-1); **b** dipyramidal weddellite crystal among whewellite crystals and their intergrowths (on the second day of the experiment, HAP-1); **c** edge splices of large stacks of whewellite lamella crystals and numerous small second-generation dipyramidal crystals of weddellite between them (on the fifth day of the experiment, GAP-2); **d** intergrowths of inter-perpendicular whewellite crystals forming roses and small dipyramidal crystals of second-generation weddelite, some of which are located on the surface of whewellite crystals (on the fifth day of the experiment, HAP-2); **e** columnar whewellite crystals with additional prism faces among numerous large stack-shaped intergrowths of whewellite lamellar crystals (on the seventh day of the experiment, HAP-1); **f** large separate dipyramidal crystals of weddellite among large spherulites and dumbbell-like weddellite aggregates (on the 10th day of experiment, HAP-1)

On the 7th day of the experiment, spherulite-like aggregates of whewellite crystals are predominant (Fig. 31.6e). In addition, whewellite columnar crystals appear with a more complex habit (with additional prism faces). Weddellite crystals on the SEM images are not visible, but the weddellite is observed via XRD (Fig. 31.5). Probably, weddellite crystals were situated under a layer of whewellite crystals, which grow in large quantity (Figs. 31.5 and 31.6e). On the 10th day, according to XRD data, the amount of weddellite slightly increases (Fig. 31.5). SEM images show large separate dipyramidal wedellite crystals (ranging in size from 80 to 180 μm), immersed in a mass of differently sized whewellite intergrowths, which are mostly spherulitic and dumbbell-like (Fig. 31.6f). After 10 days of the experiment, the pH value decreases down to 4 and the apatite powders are almost completely dissolved.

31.3.2.2 On Fluorapatites (FAP-3, FAP-4, CFA)

According to XRD and SEM data, calcium oxalate crystals in experiments with fluorapatite also appeared on the 2nd day of the experiment at pH = 5.

On powders of CO_3-containing fluorapatites (FAP-3 and FAP-4), only whewellite is present in the fungal mycelium, mainly in the form of stacks of split flat pseudohexagonal crystals, often with curved convex edges (Fig. 31.7a). There are also separate whewellite lamellar crystals with straight edges. Along with them, fan-shaped intergrowths of dovetail twins are visible. The maximum sizes of separate individuals vary from 25 to 50 microns. On the 3rd day of the experiment, along with individual stacks of large lamellar splitting whewellite crystals (maximum size reaches 100 μm), smaller (maximum size 20–30 μm) whewellite crystals of new generation with straight edges (without splitting on the faces) are visible on the 3rd day of the experiment as well as intergrowths of dovetail twins (Fig. 31.7b). On the 5th and 7th day there is an increase in the size of the crystals of both generations (up to 30 and 100 μm, respectively). The amount of splitting of crystals increases. On the 10th day of the experiment, the crystals of the whewellite are present in at least three different generations (Fig. 31.7c, d). The dimensions of the dovetail type twins and various intergrowths of the first generation crystals reach 150 μm, and form large dumbbell-like aggregates (Fig. 31.7c). The size of the smallest crystals does not exceed 20–30 μm (Fig. 31.7d). The presence of not only lamellar, but also of a few columnar crystals (from 30 to 90 μm), as well as dovetail-type twins, is common of all generations of whewellite. All crystalline individuals of the first generation are characterized by intense splitting and the presence of rounded convex edges, and the subsequent later generations are characterized by straight edges. Single weddellite dipyramidal crystals (~30 μm) with traces of dissolution were found among whewellite intergrowths (Fig. 31.7d inset). On the 10th day of the experiment, the pH value decreases to 4 with almost complete dissolution of the fluorapatite powders.

On SEM images of the surface of the natural fluorapatite crystal, on the 2nd day of the experiment, the beginning of substrate dissolution and a few calcium oxalate crystals (Fig. 31.8a), which dimensions are ~2 times smaller than in the experiments on powders (Fig. 31.7a), can be seen. Whewellite is present in the form of separate

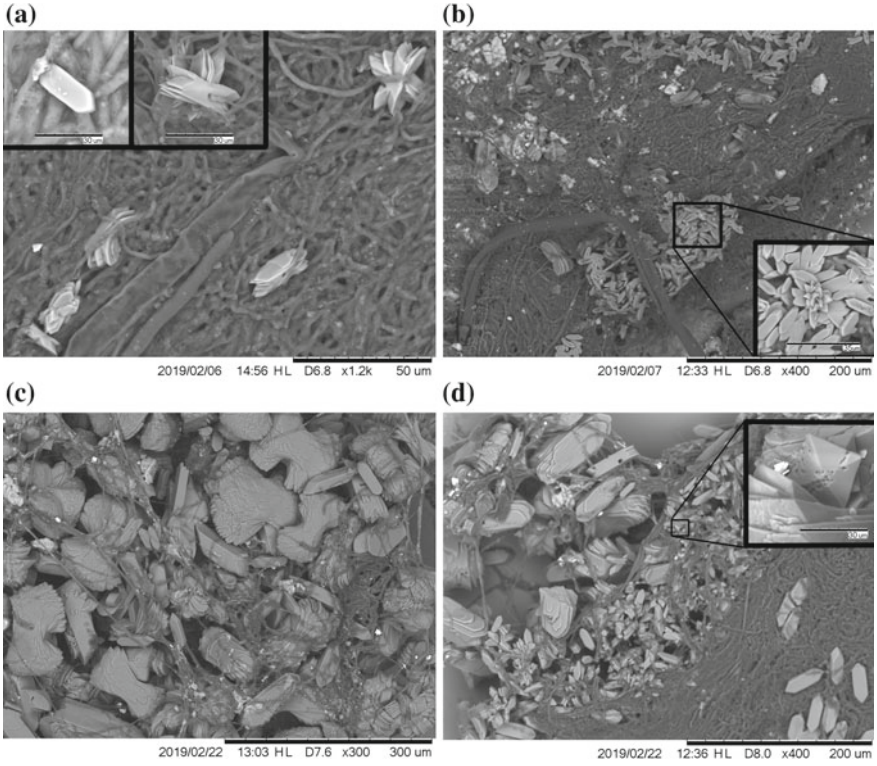


Fig. 31.7 SEM-images of crystallization products formed on powders of synthetic fluorapatite: **a** single crystals of whewellite and their intergrowths (2nd day of the experiment, FAP-3); **b** whewellite crystals of two generations (the third day of the experiment, FAP-3); **c** large aggregates of the crystals of whewellite: piles, dumbbell-like aggregates (10th day of the experiment, FAP-3); **d** crystals of the whewellite of various generations and single weddellite crystal (inset) (10th day of the experiment, FAP-4)

inter-perpendicular intergrowths of lamellar crystals and dovetail-type twins (the maximum sizes of separate individuals vary from 8 to 15 μm); weddellite—in the form of small individual dipyramidal crystals (dimensions do not exceed 10–15 μm). Whewellite intergrowths are often located on the weddellite faces (Fig. 31.7d). On the 3rd day of the experiment, on the natural crystal of fluorapatite, numerous whewellite lamellar crystals (individual sizes of 15–20 μm) are visible, among which are many crystals with straight edges (Fig. 31.8b); there are also numerous dovetail-type twins. Single columnar whewellite crystals ~10–12 μm in size were found.

On the 6th day on the surface of the fluorapatite crystal, a dense carpet of whewellite and its crystal intergrowths is observed, crystal dimensions increase to 25–30 μm; on the 9th day the size of crystals, twins, and whewellite intergrowths of different generations varies from 15 to 50 μm (Fig. 31.8c). In addition single

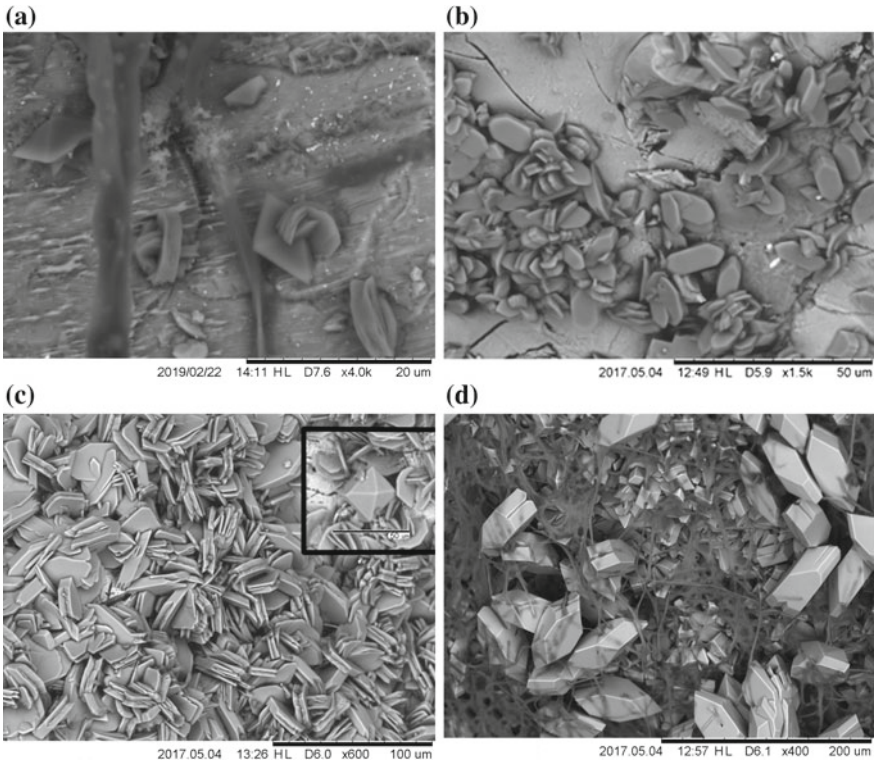


Fig. 31.8 SEM-images of crystallization products formed on the fluorapatite crystal (CFA): **a** separate dipyramidal crystals of the weddellite and whewellite intergrowths and twins (second day of the experiment), **b** a columnar crystal of the whewellite among numerous aggregations of lamellar crystals and dovetail-type twins (3rd day); **c** a dense carpet of whewellite intergrowths, inset—dipyramidal-prismatic weddellite crystal among whewellite crystal intergrowths (9th day of the experiment); **d** numerous large columnar whewellite crystals on the surface of a carpet of lamellar whewellite crystals and their intergrowths (13th day of the experiment)

weddellite crystals of a dipyramidal-prismatic habit (~25 μm) appear (Fig. 31.8c, sidebar).

On the 13th day of the experiment, numerous large (up to 80 μm) columnar, dovetail-type and single stacks of plate whewellite crystals and twins (Fig. 31.8d) are observed on the surface of a carpet of lamellar crystals, twins and intergrowths of whewellite (~30 μm in size). On the 15th day, the number of large whewellite crystals and aggregates increases, their size reaches 150 μm.

In the experiment with a fluorapatite crystal, a decrease in the pH value from 5 to 4 is observed already on the 3rd day and does not change until the end of the experiment. The XRD patterns of the products of the crystallization on all fluorapatite substrates show only reflections of whewellite.

31.3.3 Crystallization on the Surface of Teeth of Animal Fossils

On the second day of the experiment, at pH = 5, traces of substrate dissolution are clearly visible on all of fossilized dental tissues to a varying extent (Fig. 31.9). Calcium oxalates are observed on XRD patterns (Fig. 31.10) and on SEM images (Fig. 31.9a, c, e). Large (25–40 μm) and small (8–10 μm) dipyramidal crystals of the weddellite (Fig. 31.9a), lamellar whewellite crystals with curved edges and signs of splitting (25–30 μm), as well as their rose-shaped intergrowths (15–20 μm). On the horse tooth dentine there are weddellite crystals (larger, than on the mammoth tooth) with dissolution traces (from 40 to 80 μm), and stacks of lamellar whewellite crystals with curved edges (20–30 μm) (Fig. 31.9). On the elephant tooth dentin the crystallization proceeds more slowly. On the 2nd day only separate small dipyramidal crystals of weddellite (~15–20 μm) and lamellar crystals with curved edges ~15–20 μm in size are visible (Fig. 31.9e). On the 3rd day on all dental tissues, the amounts of whewellite increases significantly (Figs. 31.9b, d, f and 31.10). Numerous large (40–50 μm), fully formed spherulite aggregates of whewellite (tangles) (Fig. 31.9d) are visible on the surface of the horse and elephant tooth dentine, there is a very dense continuous "carpet" of small aggregates (10–15 μm) of lamellar whewellite crystals. Among them are intergrowths of inter-perpendicular crystals and intergrowths (in the form of "rosettes") of lamellar crystals of almost isometric habitus and with curved edges (Fig. 31.9f). On all substrates on the 3rd day, the sizes of dipyramidal weddellite crystals increases, most significantly on the surface of elephant tooth dentine (from 40 to 80 μm) (Fig. 31.9f). On the surface of mammoth dentine, a broad spectrum of dipyramidal crystals of the weddellite of various generations (from 8 to 80 μm) is observed (Fig. 31.9b).

Subsequently (on the 6th and 9th day of the experiment), the amount of Ca oxalate on the surface of fossilized hard tissues continues to increase (Figs. 31.10 and 31.11a–c). On all substrates, small (up to 20 μm) lamellar whewellite crystals of new generations and their intergrowths are observed. On the 6th day of the experiment, not fully formed whewellite spherulites consisting of lamellar crystals (40–60 microns in size) are formed on the surface of the mammoth tooth on the 6th day of the experiment (size of 40–90 μm) (Fig. 31.11a). On the 13th day of the experiment, on mammoth tooth dentine, in addition to multiple large fully formed spherulite-like whewellite intergrowths (tangles), the size of which practically does not increase, and large dipyramidal weddellite crystals (~150 μm) appear smaller numerous dipyramidal-prismatic weddellite crystals (from 10 to 25 μm) and their intergrowths (Fig. 31.11d). The dimensions of the spherulite-like aggregates (tangles) of whewellite that are fully formed on the surface of the horse tooth reach 150–180 μm on the 9th day (Fig. 31.11b).

At the same time, on the elephant tooth surface, the formation of spherulite-like aggregates on the 9th day of the experiment is just beginning, intergrowths in the form of rosettes are observed (Fig. 31.11c).

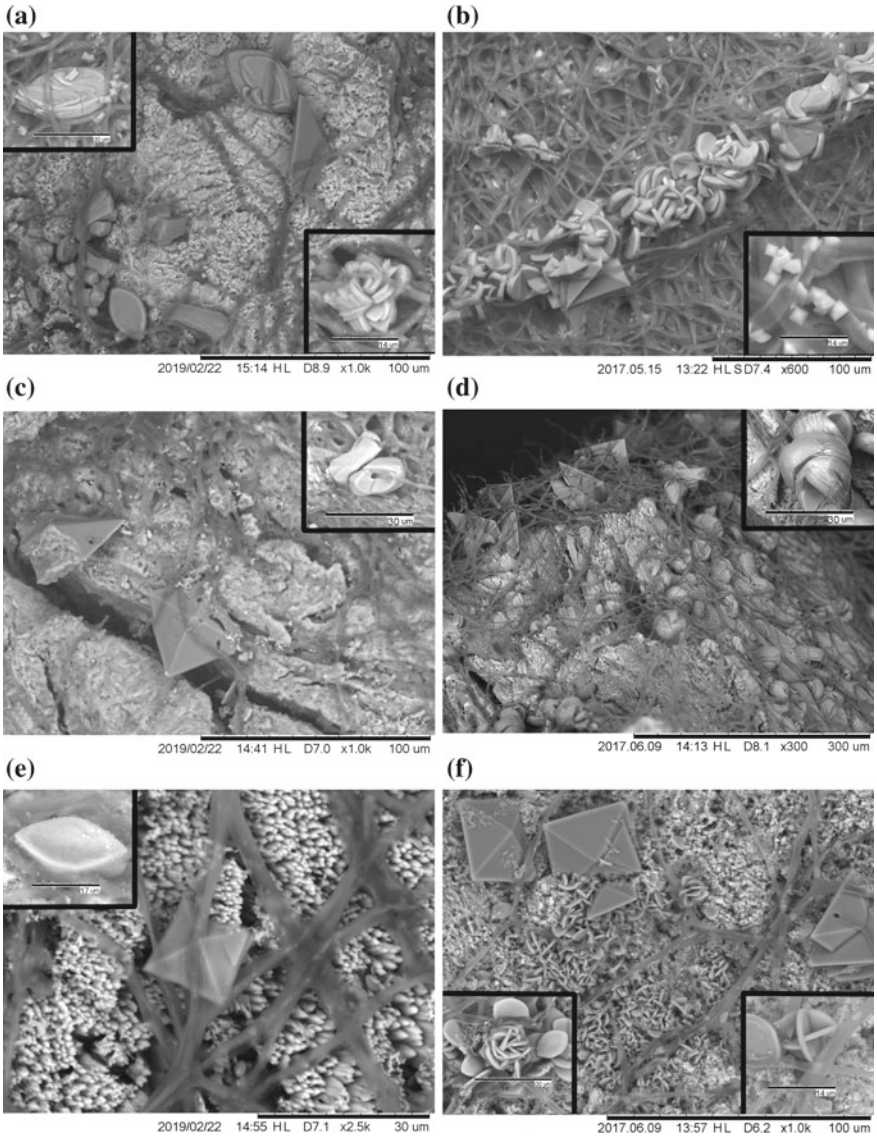


Fig. 31.9 SEM-images of crystallization products formed on the surface of the tooth dentine of animal fossils in the initial stages of the experiment: **a** a few dipyramidal weddellite crystals of two generations and intergrowths of whewellite lamellar crystals forming piles and "rosettes" (mammoth tooth dentine, 2 days); **b** crystals of weddellite of various generations as well as numerous, associated with fungal hyphae, intergrowths of whewellite lamellar crystals (mammoth tooth dentine, 3 days); **c** dipyramidal crystals of weddellite (larger than on elephant dentine) and stacks of whewellite lamellar crystals with curved ribs (horse tooth dentine, 2 days); **d** large dipyramidal crystals of weddellite among fully formed spherulitic whewellite aggregates (tangles) (horse tooth dentine, 3 days); **e** small separate dipyramidal crystals of weddellite and lamellar crystals (elephant tooth dentine, 2 days); **f** dipyramidal crystals of weddelite among numerous whewellite lamellar crystals and their intergrowths (elephant tooth dentine, 3 days)

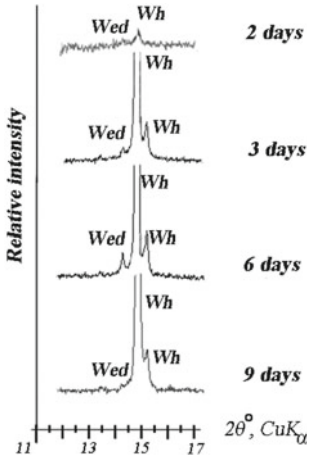


Fig. 31.10 X-ray pattern fragments of crystallization products on the surface of elephant tooth at various stages of the experiment

The dimensions of the dipyramidal weddellite crystals also continue to increase. On the 9th day of the experiment, individual crystals of weddellite on the surface of mammoth and horse dentine reach 150 μm, and on the surface of elephant tooth dentine—80 μm (Fig. 31.11a–c).

On the 6th day of the experiment, the pH value in experiments with fossilized dental tissues decreases to 4.5 and does not change until the end of the experiment.

31.4 Discussion

Experimental results showed that calcium oxalates (mainly calcium oxalate monohydrate, whewellite) were formed on all apatite substrates (hydroxyapatite, fluorapatite, fossilized bones of animal fossils) on the 2nd day of the experiment at pH ~5. Later the pH value reduces to 4. In experiments with natural fluorapatite crystal—after 3 days, in experiments with fossilized dental tissue—after 6 days, and in experiments with hydroxyl- and fluorapatite powders—after 10 days, i.e. the faster, the lower the solubility of the underlying substrate.

The highest dissolution rate among all substrates was observed for synthetic hydroxyapatite and fluorapatite powders (higher for hydroxyapatite than for fluorapatite (Driessens 1973; Bohner 2000; Wang et al. 2011). The fluorapatite crystal has a significantly smaller surface area and, accordingly, its dissolution rate is lower than that of fluorapatite powder. Judging by the intensity of oxalate crystallization. The solubility of fossil mammoth, horse and southern elephant teeth dentine, in organic acids secreted by the fungus, is apparently less than that of apatite powders, but more than of a single apatite crystal, which can be well explained by the substantial porosity of dentine. The fact that the solubility of the dental tissue of a horse is greater than that of a mammoth and an elephant can be explained by the

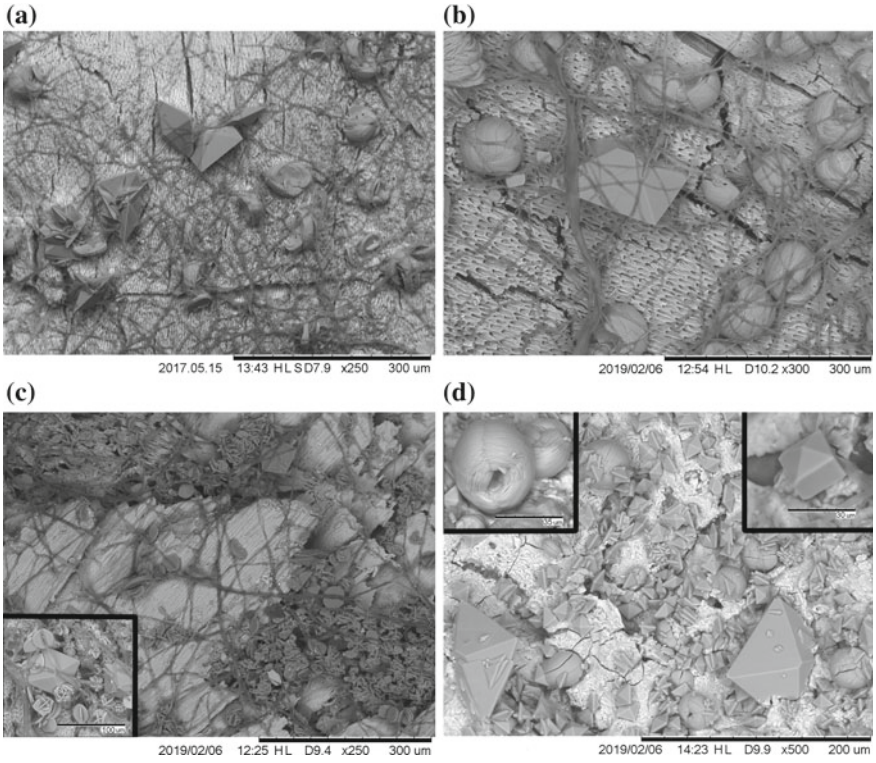


Fig. 31.11 SEM-images of crystallization products formed on the surface of fossil animal teeth dentine on the final stages of the experiment: **a** large dipyramidal weddellite crystals among numerous spherulite-like aggregates of whewellite (mammoth dentine, 9 days); **b** numerous spherulite-like aggregates of the whewellite (tangles) and large dipyramidal weddellite crystals. The size of crystals and intergrowths is about 2 times larger than on the mammoth tooth (horse tooth dentine, 9 days); **c** dipyramidal crystals of weddellite (sizes—the same as on the mammoth tooth) among numerous lamellar whewellite crystals and their rosette intergrowths (elephant tooth dentine, 9 days); **d** large dipyramidal crystals of weddellite among numerous smaller dipyramidal-prismatic crystals of another weddellite generation and fully formed spherulite-like aggregates of the whewellite (~2 times less than on the horse tooth) (mammoth dentine, 13 days)

practical absence of the protein component in the fossilized tissue, as well as by the insignificant fluorine content in bioapatite.

Separate lamellar pseudohexogonal whewellite crystals with straight or curved edges are formed on all apatite substrates at the beginning of biocrystallization (Figs. 31.6a, b, 31.7a, 31.8a and 31.9a, c, e). Solution supersaturations (probably local) lead to their intensive splitting and the formation of dovetail-type twins (of various types) (Figs. 31.6a, 31.7a and 31.8a, c) and various intergrowths: in the form of stacks of lamellar crystals (Figs. 31.6a, e, 31.7a, c and 31.10b), rose-like (Figs. 31.6 d, 31.10f and 31.11d inset), dumbbell-like (Fig. 31.7c) and spherical-like aggregates (Figs. 31.10d and 31.11a, b, d).

Along with whewellite, on the surface of all substrates but in smaller amounts, mainly dipyramidal and less commonly dipyramidal-prismatic, weddellite crystals form (Figs. 31.6b–d, f, 31.8a, c, 31.10 and 31.11). Lamellar crystals of a whewellite of new generations can form on all stages of crystallization, which is most clearly seen on the example of fluorapatite (Fig. 31.7). In addition, on the surface of hydroxy- and fluorapatite, columnar crystals of whewellite and then their twins form on various stages of crystallization (Figs. 31.6e, 31.7c and 31.8c, d).

On all hydroxy- and fluorapatite powders, already on day 2, almost all crystals, twins, and intergrowths are characterized by curved edges (Fig. 31.6a and 31.7a). This indicates that the crystallization of oxalates began earlier than 2 days and took place at high solution supersaturations, which led to an intense splitting of the crystals. On the single crystal of mineral apatite, the amount of oxalates is much smaller, and their size is also smaller than on powders (~twice as small). This indicates a less intensive crystallization process, which can be best explained by a lower solubility of the substrate compared to powders. At the same time, there are signs of both intense splitting and dissolution of crystals, which most likely indicates significant fluctuations in the supersaturation of the solution and possible changes in crystallization conditions, for example, a local pH decrease. At all stages of the experiment on hydroxy- and fluorapatites, separate lamellar and columnar crystals with sharp edges, which are 2–3 times smaller than in intergrowths and twins (that means they are a new generation of crystals), are observed. The only difference between the peculiarities of whewellite crystallization (under the influence of fungus on the surface of hydroxyl- and fluorapatite) is associated with the presence of crystalline individuals with sharp edges in large quantities on fluorapatite (especially on the natural crystal of fluorapatite). This difference was observed as a small trend only though.

Significant differences in the phase formation on hydroxyl- and fluorine apatites under the action of the fungus appear in different weddellite formation intensity. The formation of dipyramidal weddellite crystals of different generations was recorded on hydroxyapatite powders on day 2 and 5 (Fig. 31.6b–d). On the 10th day, the sizes of individual weddellite crystals reach 180 μm (Fig. 31.6f). On fluorapatite powders, single medium-sized weddellite crystals (~30 μm in size) were observed only on the 10th day of the experiment (Fig. 31.7d). On the crystal of fluorapatite, small single crystals of weddellite are observed on day 2 and 9 (Fig. 31.8a, c). In this case, on day 2, the crystals have a dipyramidal habit, on day 9—a dipyramidal-prismatic one. Differences in the characteristics of the crystallization of calcium oxalate on hydroxyl- and fluoroapatites can be explained by the influence of the crystallization medium chemical properties. The occurrence of fluorine in hydroxyapatite reduces its solubility (Driessens 1973; Bohner 2000; Wang et al. 2011). Consequently, the ratio of calcium and oxalate cations to ions in a liquid medium on the surface of hydroxyapatite powders is greater than on the surface of fluorapatite powders. As discussed above, in a crystallization medium on the surface of a fluorapatite crystal, this ratio is even smaller. Thus, the revealed features of phase formation on various apatite substrates are probably related to variations in the ratio of the calcium and oxalate cations to the ions in the crystallization medium, which is one of the main factors determining fields of the weddellite chemical stability (Kuz'mina et al.

2019). However, we cannot exclude the negative effect of fluorine ions released when fluoroapatites dissolve on the formation of the weddellite. Changes in the morphology of weddellite crystals formed on the surface of a natural fluorapatite crystal can be attributed to the appearance of impurities that are isomorphically included in apatite in the crystallization medium, including aluminum and silicon, when the crystallization medium is dissolved (Fig. 31.3a).

Neither the changes in the carbonate ion contents nor variations in particle size and coherent scattering areas in the apatites used as the substrates, exhibited any influence on the calcium oxalate crystallization.

The peculiarities of calcium oxalate crystallization on the surface of mammoth tooth dentine (hydroxyapatite-protein composite) are very close to those observed on hydroxyapatite powders, which is probably due to a very porous structure of dentin.

Already on day 2, various intergrowths of lamellar whewellite crystals exhibiting splitting and curved edges are observed, the dimensions of these crystals are similar to the sizes of the intergrowths formed on hydroxyapatite powders (Fig. 31.9). In addition, dipyramidal crystals of weddellite of two generations are observed (Fig. 31.9a, b). The formation of new generations of weddellite is also observed on the later stages of the experiment.

The largest weddellite crystals on days 9 and 13 of the experiment are approximately two times smaller than on hydroxyapatite powders. Other distinctive features of crystallization on the mammoth dental tissue are the predominance of dipyramidal prismatic weddellite crystals on the 13th day of the experiment (Fig. 31.11d), the appearance of which can be explained by the influence of impurities in the apatite-protein composite (primarily magnesium, Fig. 31.3c) (Kuz'mina et al. 2019). In addition, on the 6th day, fully formed spherulite-like aggregates (up to 80 μm) appear on the surface of mammoth dentine. On the same day, we observe only the beginning of the formation of such aggregates on the surface of hydroxyapatite powder (Fig. 31.6d).

The patterns of calcium oxalate crystallization on the surface of horse and elephant dentin are similar to each other and are close to those observed on the surface of mammoth tooth, which is apparently due to the fact that the content of fluorine ions is small in apatite of these two fossils (Fig. 31.3b). Most quickly oxalates crystallize on horse tooth dentine, on the IR spectrum of which there are no traces of protein component: fully formed spherulite-like aggregates (balls) are formed on the 3rd day of the experiment (Fig. 31.9d) and on the 9th day the largest reach 150–180 μm (Fig. 31.11 b). The sizes of the largest dipyramidal weddelite crystals on the 9th day of the experiment are practically equal to the largest weddellite crystals on hydroxyapatite powder.

The difference between crystallization on the surface of horse tooth dentine and on hydroxyapratite lies in the absence of second-generation weddelite crystals, which is probably due to the influence of fluorine ions. Crystallization on the surface of elephant tooth dentine is slower than on the mammoth tooth dentine. On the 2nd day of the experiment, traces of substrate dissolution, separate lamellar crystals of whewellite with curved edges and dipyramidal weddelite crystals are clearly visible (Fig. 31.9e). On later stages, the size of whewellite crystals increases very slightly,

their habit does not change, fully formed spherulite-like aggregates do not form (small aggregations are present in the form of rose-like aggregates) (Fig. 31.11c). The size of the largest weddellite crystals on the 9th day of the experiment is slightly smaller than on the mammoth tooth. There are no visible weddellite crystals of second generation on the SEM images, which is also likely due to the presence of fluorine ion in the crystallization medium.

As is known, not only the presence of citrate ions, which are gradually released by growing *Aspergillus niger* micromycete, in the solution is necessary for the formation of weddellite crystals but also a significant concentration of calcium cations in the solution (Kuz'mina et al. 2019). The crystallization of calcium oxalate on powdered apatites and porous teeth of animal fossils, due to their considerable solubility, corresponds to these conditions, as a result of which they are exhibit stable formation and growth of weddellite crystals together with whewellite crystals. A much lower dissolution rate of a single crystal of fluorapatite contributes to a smaller amount of calcium cations in the solution, which determines the formation of a very small number of weddellite crystals (often fewer than the X-ray diffraction analysis can detect). However, it is also possible that the release of fluorine ions can contribute to the negative impact on the inhibition of weddellite formation. The formation of several generations of calcium oxalate crystals observed in the course of the experiment is most likely due to an uneven extraction of organic acids by growing micromycete or due to fluctuations in calcium concentration during substrates dissolution.

The appearance of well pronounced prism faces on weddellite crystals formed on natural substrates, is most likely associated with the leaching of impurity cations such as magnesium or aluminum from the dissolved fossil teeth and fluorapatite crystal.

31.5 Conclusion

The results of the study showed that morphogenetic patterns of crystallization of calcium oxalates on apatite substrates under the action of *Aspergillus niger* micromycete are determined by the chemical properties of the crystallization medium, which depends on the solubility of the underlying substrate which in turn is determined by its chemical composition and structural features (dispersity, porosity).

The beginning of oxalate crystallization occurs on apatites and apatite-protein composites, as well as on the surface of marble, at pH = 5. Then the pH of the medium slightly decreases—the faster, the lower the solubility of the underlying substrate is, i.e. less calcium cations in the crystallization environment. The morphogenetic pattern of oxalate crystallization on the surface of apatite substrates under the action of the micromycete *Aspergillus niger* differs from the on taking place on the surface of calcite marble (Sturm et al. 2015) primarily by the predominance of whewellite over weddellite at all stages of the experiment, which is supported by the published data (Pinzari et al. 2013).

The predominance of whewellite in the crystallization on apatite substrates is well explained by the significantly lower solubility of apatites and apatite-protein

composites compared to calcite marble, which leads to a decrease in the ratio of Ca^{2+} ions and oxalate ions in the crystallization medium and, accordingly, to a shift into the crystallization region, in which weddellite is not stable. In addition, it can be assumed that the presence of phosphate ion in the crystallization medium also prevents the formation of weddellite, which is confirmed by the data of Furedi-Milhofer et al. (1987), which showed that the presence of phosphate ions in the solution inhibits the precipitation of the oxalate phases.

Acknowledgements The scientific researches were carried out in the Research park of St. Petersburg State University: SEM investigations—in the "Resource Center Microscopy and Microanalysis (RCMM)", XRD measurements—in the center for X-ray Diffraction Studies, determination of particles size—the Center for Innovative Technologies of Composite Nanomaterials.
This research was supported by the Russian Science Foundation (no. 19-17-00141).

References

Adamo P, Violante P (2000) Weathering of rocks and neogenesis of minerals associated with lichen activity. Appl Clay Sci 16:229–256

Barinova KV, Vlasov DYu, Schiparev SM, Zelenskaya MS, Rusakov AV, Frank-Kamenetskaya OV (2010) Production of organic acids by micromycetes from the rock substrates. Mycol Phythopathol 44(2):137–142 (in Russian)

Bohner M (2000) Calcium orthophosphates in medicine: from ceramics to calcium phosphate cements. Injury 31(4):37–47

Cai L, Xiao HR, Huang SM, Li H, Zhou GT (2013) Solubilization of magnesium-bearing silicate minerals and the subsequent formation of glushinskite by *Aspergillus niger*. Geomicrobiol J 30:302–312

Ceci A, Young Rhee J, Kierans M, Hillier S, Pendlowski H, Gray N, Persiani AM, Gadd GM (2015) Transformation of vanadinite [Pb5(VO4)3Cl] by fungi. Environ Microbiol 17(6):2018–2034

Ceci A, Pinzari F, Russo F, Maggi O, Persiani AM (2018) Saprotrophic soil fungi to improve phosphorus solubilisation and release: in vitro abilities of several species. Ambio 47(Suppl. 1):30–40

Driessens FCM (1973) Relation between apatite solubility and anti-cariogenic effect of fluoride. Nature 243(5407):420–421

Fomina M, Hillier S, Charnock JM, Melville K, Alexander IJ, Gadd GM (2005) Role of oxalic acid overexcretion in transformations of toxic metal minerals by *Beauveria caledonica*. Appl Environ Microbiol 371–381

Furedi-Milhofer H, Marcovic M, Uzelac M (1987) Precipitation and solubility of calcium phosphates and oxalates in the system $Ca(OH)_2$-H_3PO_4-$H_2C_2O_4$-NaCl-H_2O. J Cryst Growth 80:60–68

Gadd GM, Bahri-Esfahani J, Li Q, Rhee YJ, Wei Z, Fomina M, Liang (2014) Oxalate production by fungi: significance in geomycology, biodeterioration and bioremediation. Fungal Biol Rev 28:36–55

Gershenkop ASh, Evdokimova GA (2014) The effect of microbiological factor on the storage and processing of waste flotation. Environmental problems of the northern regions and their solutions. Conference proceedings. Apatity, pp 9–14 (in Russian)

Giordani P, Modenesi P, Mauro Tretiach (2003) Determinant factors for the formation of the calcium oxalate minerals, weddellite and whewellite, on the surface of foliose lichens. Lichenologist 35(3):255–270

Kuz'mina MA, Rusakov AV, Frank-Kamenetskaya OV, Vlasov DYu (2019) The influence of inorganic and organic components of biofilm with microscopic fungi on the phase composition and morphology of crystallizing calcium oxalates. Crystallogr Rep 64(1):161–167

Pinzari F, Tate J, Bicchieri M, Rhee YJ, Gadd GM (2013) Biodegradation of ivory (natural apatite): possible involvement of fungal activity in biodeterioration of Lewis Chessman. Environ Microbiol 15(4):1050–1062

Rosling A, Suttle KB, Johansson E, Van Hees PAW, Banfield JF (2007) Phosphorous availability influences the dissolution of apatite by soil fungi. Geobiology 5:265–280

Rosseeva EV (2010) Crystal chemistry and morphogenesis of narural and biomimetic apatites—(CaF) organic composites. Dissertation, St. Petersburg State University (in Russian)

Rusakov AV, Vlasov AD, Zelenskaya MS, Frank-Kamenetskaya OV, Vlasov DYu (2016) The crystallization of calcium oxalate hydrates formed by interaction between microorganisms and minerals. In: Biogenic-abiogenic interactions in natural and anthropogenic systems. Lecture notes in earth system sciences, pp 357–377

Sturm EV, Frank-Kamenetskaya OV, Vlasov D, Zelenskaya M, Sazanova K, Rusakov A, Kniep R (2015) Crystallization of calcium oxalate hydrates by interaction of calcite marble with fungus *Aspergillus niger*. Am Miner 100:2559–2565

Sutjaritvorakul T, Gadd GM, Whalley AJS, Suntornvongsagul K, Sihanonth P (2016) Zinc oxalate crystal formation by *Aspergillus nomius*. Geomicrobiol J 33(3–4):289–293

Wang H, Sun K, Li A (2011) Size-controlled synthesis and characterization of fluorapatite nanocrystals in the presence of gelatin. J Powder Technol 209:9–14

Zelenskaya MS, Rusakov AV, Frank-Kamenetskaya OV, Vlasov DYu, Himelbrant DE, Izatulina AR (2018) The formation of calcium oxalate hydrates by the interaction between microorganisms and apatite on the base of the field and laboratory research. In: Biogenic-abiogenic interactions in natural and anthropogenic systems. VI International Symposium. Saint Petersburg, pp 117–118

Chapter 32
Features of the Effect of VUV Radiation on Microfungi from Polar Regions



Galina N. Zvereva and Irina Yu. Kirtsideli

Abstract In this work, the effect of VUV radiation of the wavelength region $\Delta\lambda =$ 166–180 nm on microscopic fungi propagules *Cladosporium herbarum, Rhodotorula colostri, Saccharomyces cerevisiae* was studied. In the course of the work, dependencies of the survival probability of propagules, which were at the exponential and stationary phases of development, on radiation doses were obtained. It was found that at the exponential stage of colonies development, the survival curves of propagules of different types of micromycetes coincide within the limits of error, but at the stationary phase they are different. IR spectroscopy and atomic force microscopy of irradiated propagules indicate a change in their cell wall. Electrophoresis of DNA molecules of irradiated propagules proves double-stranded breaks. Experiments with the use of an antioxidant show that the death of propagules during VUV irradiation occurs as a result of the direct and indirect effects of radiation, with the share of the latter being 10–15%. The results obtained allow us to conclude that the inactivation of propagules during irradiation with radiation of the long-wave region of the VUV range $\Delta\lambda = 166$–180 nm is the result of both direct and indirect effects with the destruction of both the cell wall and DNA.

Keywords Microfungi · VUV · Antarctic · DNA · Wall cell · Antioxidants · OH radical · ROS · Astrobiology

The presence of stress-tolerant species of microscopic fungi today has been established for communities of almost all known extreme habitats, ranging from polar deserts (Kirtsideli et al. 2010, 2018) to the Chernobyl nuclear power plant (Zhdanova et al. 2004). The first information about the resistance of microscopic fungi, including hyphal and yeast forms, to UV irradiation appeared in the first half of the last century

G. N. Zvereva
State University of Civil Aviation, 38 Pilotov Str., Saint Petersburg 196210, Russia

S. I. Vavilov State Optical Institute, Kadetskaya Line-5-2, Saint Petersburg 199053, Russia

I. Yu. Kirtsideli (✉)
Komarov Botanical Institute RAS, Professor Popov Str.-2, Saint Petersburg 197376, Russia
e-mail: microfungi@mail.ru

© Springer Nature Switzerland AG 2020

O. V. Frank-Kamenetskaya et al. (eds.), *Processes and Phenomena on the Boundary Between Biogenic and Abiogenic Nature*, Lecture Notes in Earth System Sciences,
https://doi.org/10.1007/978-3-030-21614-6_32

(Luyet 1932; Smith 1936). The effect of UV on fungus activity is mainly associated with its mutagenic effect, as well as with its effect on the plasma membrane (Griffin 1996). UV has a significant effect on the biosynthesis of primary metabolites of fungi, in particular organic acids (Musilkova et al. 1983; Andersen et al. 2011; Prabu et al. 2012; Vasanthabharathi et al. 2013; Tembhurkar et al. 2012).

Studies of the effects of UV and radiation on microorganisms, including algae, bacteria and microscopic fungi, were more often carried out in the temperate and southern zones (Robson et al. 2004; Torres et al. 2004; Palffy and Voros 2006; Ozcelik 2007; Salcedo et al. 2007; Singaravelan et al. 2008; Selbmann et al. 2005, 2014; Siddiqui et al. 2011). Currently, changes are observed in the stratospheric layer of ozone and, consequently, in the intensity of ultraviolet (UV) radiation, which can lead to various effects in ecosystems. Ultraviolet radiation is involved in complex biochemical processes and leads to changes in the carbon cycle. The reactions of organisms to changes in UV radiation and interactions with climate change are considered in a number of papers (Zepp et al. 2007; Singh et al. 2010). Much less is known about the effect of radiation on microscopic fungi on the surface of the primary soils and soils of Antarctica. Antarctica is one of the most extreme habitats of our planet, characterized by geographic isolation, extremely low temperatures, low humidity, and ozone "holes" causing high levels of background ultraviolet (UV) radiation. This makes it possible to consider the microscopic fungi of Antarctica as a natural reservoir of microorganism strains adapted to extreme conditions, including a high dose of UV radiation (Salcedo et al. 2007; Selbmann et al. 2011; Vasilenko et al. 2010; Wynn-Williams and Edwards 2001). Microorganisms of Antarctica are affected by various doses of radiation, which fluctuate strongly due to seasonal changes in snow and ice cover and other factors (Walton 1984). Microorganisms of the Antarctic continent, develop, as a rule, on the surface or in an extremely thin layer of soil, because it is there that the substrate is heated. However, it is there that microscopic fungi are exposed to the strongest effects of UV irradiation.

The influence of Antarctic conditions on microscopic fungi is considered even as analogs of cosmic conditions (Wynn-Williams and Edwards 2001; Poulet et al. 2005; Onofri et al. 2004, 2008, 2012, 2015, 2018). When preparing experiments on the detection of life on Mars (Parnell et al. 2007), it is Antarctica that is considered to be the terrestrial analogue of expected habitats (Wynn-Williams and Edwards 2000). Therefore, it was the isolates of the Antarctic species that were used as test models for studying the mechanisms of the effects of vacuum ultraviolet (VUV) radiation on the survival of microorganisms.

This radiation lies in a shorter wavelength region ($10\ \text{nm} < \lambda < 200\ \text{nm}$) compared to UV one ($200\ \text{nm} < \lambda < 400\ \text{nm}$). It has a higher quantum energy, which causes its large photochemical and photobiological properties. In particular, VUV irradiation of H_2O and O_2 molecules leads to the formation of highly reactive oxygen-containing products ·OH (Heit et al. 1998) and O (^{1}D) (Atkinson et al. 2004):

$$H_2O + h\nu \rightarrow H_2O^* \rightarrow \cdot OH + H\cdot \tag{32.1}$$

$$O_2 + hv \rightarrow \mathrm{O}(^3\mathrm{P}) + \mathrm{O}(^1\mathrm{D}) \quad (32.2)$$

VUV radiation also has high photobiological capabilities—it is effectively absorbed by such biologically important molecules as: DNA, proteins, sugars. VUV irradiation of DNA molecules leads to different types of destruction than UV exposure: to single- and double-stranded breaks (Michael et al. 1994). Absorption of VUV radiation by sugars (Dickinson and Johnson 1974) and proteins (Inagaki et al. 1975) can lead to the destruction of the chitin cell wall and phospholipid membrane.

Inactivation of microorganisms under the action of VUV radiation can be carried out either as a result of the direct effect of radiation quanta absorbed by the target molecules or by indirect effect of VUV photolysis products: reactive oxygen-containing species (ROS) and lipid oxidation products.

VUV radiation finds practical application in disinfection technologies using gas-discharge plasma. It occurs in gas discharges in mixtures containing rare gases and, together with plasma particles, participates in the inactivation of microorganisms (Weltmann et al. 2010). VUV radiation is present in space, which determines its importance in solving astrobiological problems associated with the survival of microorganisms in space, the formation of microflora in spacecraft, the origin of life on planets (Horneck et al. 2010).

A relatively small number of scientific papers are devoted to the effect of VUV radiation on microorganisms. The mechanisms of inactivation of microorganisms during VUV irradiation remain not fully understood. Among the articles in this area, one can mention a series of works (Ito et al. 1980, 1981, 1983; Hieda et al. 1984), where irradiation was performed at various wavelengths in the UV-VUV range of dry (in vacuum) and wet (in water vapor) *Saccharomyces cerevisiae* spores. Based on the absence of genetic changes of VUV irradiated spores and the proximity of the shape of the water absorption curve to the sensitivity curve to VUV irradiation of wet spores, the authors concluded that the main mechanism of VUV spore inactivation is destruction of the cell membrane by ROS produced by VUV water photolysis. In this series of works, it was noted that the depth of VUV radiation penetration, due to the sharp dependence of the absorption coefficient on the wavelength, will differ by two orders of magnitude in the long- and short-wavelength parts of the VUV range: in the wavelength range $\lambda = 170$ nm, most of the radiation passes through cell wall and membrane, and at a wavelength of $\lambda = 150$ nm they will be absorbed by them (Ito et al. 1983). Thus, when the VUV microorganisms are irradiated by the long- wavelength VUV emission, the effect on both the cell wall and DNA should be expected, while under irradiation with short-wavelength VUV radiation, the main role in inactivation will play cell wall destruction. The authors of the paper (Sarantopoulou et al. 2014) have point of view that the destruction of the cell wall of a spore is the main cause of death during VUV irradiation. In this work, VUV irradiation of spores of *Cladosporium herbarum* by laser VUV radiation ($\lambda =$ 157 nm) and incoherent VUV radiation ($\Delta\lambda = 110$–180 nm) was carried out under normal conditions in a nitrogen atmosphere and also in vacuum at low temperature ($T = 10$ K). During the experiments, both the destruction of the cell wall and the breaks in the chains of DNA molecules were detected. The article (Nakonechnyj

et al. 1996) investigated the destruction of algal cells *Chlamydomonas reinhardtii* with VUV irradiation at wavelengths of 120–130 nm, the authors, referring to the work (Ito et al. 1983), have concluded that cell death occurs as a result of cell walls destruction.

Most of the works devoted to the effects of VUV radiation on microorganisms have an astrobiological orientation. Thus, in the works (Horneck et al. 2010; Sarantopoulou et al. 2014) it is noted that the exposure to VUV radiation, along with the action of vacuum, is one of the factors determining the survival of microorganisms in space.

Our paper is devoted to the study of the mechanisms of exposure to radiation of the long-wavelength region of the VUV range ($\Delta\lambda = 166–180$ nm) on microscopic fungi propagules and is a continuation of work (Zvereva et al. 2018).

32.1 Materials and Methods

Xenon excimer lamps developed at the S. I. Vavilov State Optical Institute were used in the experiments. The lamps produced a surface radiation intensity of $I = 1.6$ mJ/cm^2, the emission had bandwidth $\Delta\lambda = 166–180$ nm with a maximum at $\lambda = 172$ nm. The radiation was excited by means of a barrier discharge in xenon at a pressure of $P = 300$ Torr, the amplitude of the supplied voltage was $U = 4.4$ kV, the frequency $f = 1$ kHz.

The absolute intensity of the VUV radiation was measured using a HAMAMATSU H8025 photodetector.

In the work were used cultures of microscopic fungi from the collection of the Komarov Botanical Institute (*Cladosporium herbarum* (Pers.) Link, *Rhodotorula colostri* T. Castelli). These cultures were isolated from Antarctic substrates. These species were isolated from the primary soils of Antarctica, the isolates of these species are known as biodestructors of natural and industrial materials, as well as pathogens. For experimental work, cultures of microfungi were grown on standard media (Chapek). We used also *Saccharomyces cerevisiae* (Desm.) Meyen culture from the St. Petersburg State University collection, which was grown on Saburo medium. Cultivation was carried out at a temperature of 20 °C, for 8–10 days. When studying the effect of the formation of the cell wall of microscopic fungi on their survival, cultures were grown for a longer period (up to 2 months). A suspension of propagules of these isolates was obtained using the method of flushing from the surface. For *Cladosporium herbarum*, the suspension was divided into spores and mycelium by filtration, conidium suspension was used for further studies.

A suspension of propagules was applied to the surface of the cover glass in an amount of 10 μl and dried on the surfaces of the glass in the form of a monolayer. Irradiation was carried out in air at a pressure of $P = 1$ atm, air temperature $t = 20$ °C. In order to avoid absorption of VUV radiation by air, the monolayer had direct contact with the lamp window. After irradiation, the propagules were washed off from the glass surface and cultured in Petri dishes in agar medium at $t = 14$ °C.

After 10–15 days of cultivation, the number of colonies of fungi was counted and the probability of survival was determined.

An atomic force microscope (AFM) NTegra Aura (NT-MDT) was used for microscopic examination of the propagules surface. Surface analysis was carried out in semicontact mode.

The FTIR FSM spectrometer (Infraspek) was used to record the infrared transmission spectra of the spores.

DNA electrophoresis was performed using a Bio RAD Sub-cell Model 96 camera. Statistical processing of measurement results was carried out using software STADIA.

32.2 Experimental Results and Discussion

Determination of the survival probability of spores during VUV irradiation. In this part of the work propagules of micromycetes of *Cladosporium herbarum, Rhodotorula colostri, Saccharomyces cerevisiae*, isolated from colonies that were in the exponential phase of growth were exposed to radiation.

According to the results of 5 experiments, regression survival curves were obtained for each type of spores (Fig. 32.1). From the results presented in Fig. 32.1, it can be concluded, that despite the biological differences (the presence of a protective pigment in the cell wall of *Cladosporium herbarum*, the differences of the chemical composition and cell walls thickness), the survival curves of the different types propagules almost coincide (the difference is observed within error limits). This fact can be explained by the fact that in the exponential phase the propagules did not fully achieve their distinctive characteristics: they did not accumulate significant amount of pigment, the cell wall was not completely formed. It should be noted that the obtained values of the survival probabilities are in good agreement with the existing literature data. Thus, the obtained survival probabilities values of *Saccharomyces*

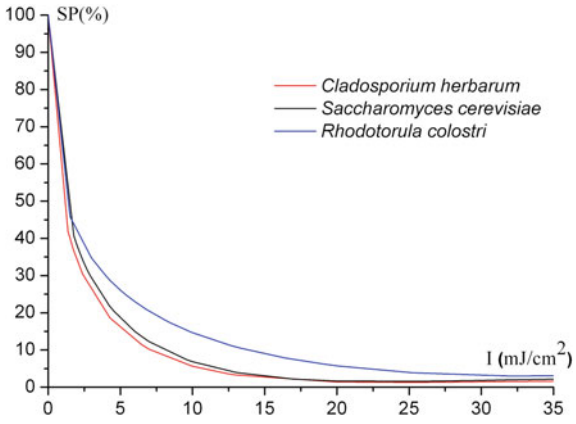


Fig. 32.1 Regression curves of survival probability (SP) of *Cladosporium herbarum* ($\Delta SP_{95} = 5.5\%$), *Rhodotorula colostri* ($\Delta SP_{95} = 16\%$), *Saccharomyces cerevisiae* ($\Delta SP_{95} = 11\%$) propagules, where ΔSP_{95} is the 95% confidence interval

cerevisiae spores within the 95% regression confidence interval coincide with the results of work (Ito et al. 1983), where the values of SP = 30% (λ = 175 nm) are achieved at a dose of I = 1.5 mJ/cm^2. The survival probabilities of *Cladosporium herbarum* propagules obtained in (Sarantopoulou et al. 2014), where SP = 12% corresponds to the dose I = 8 mJ/cm^2 (λ = 157 nm), also correlate with the results of Fig. 32.1.

The influence of the cell wall on propagules survival during VUV irradiation. To study the role of the cell wall in propagules inactivation by VUV irradiation, we compared the survival of propagules obtained from colonies at different (exponential and stationary) phases of development.

The survival probabilities curves of *Cladosporium herbarum* and *Rhodotorula colostri* propagules, formed in pure cultures of different ages, are presented in Fig. 32.2. These cultures had both exponential (8–18 days) and stationary (25–59 days) developmental stages.

The increase of survival probabilities at stationary stage is observed in both types of spores, but to a greater degree for *Cladosporium herbarum* species, which may be due to the accumulation of melanin in the cell wall over the time.

Studies of the cell wall changes during VUV irradiation were carried out using AFM microscopy and IR spectrometry. Figure 32.3 shows the results of microscopic examination: the same area of the *Rhodotorula colostri* spore surface is presented before and after irradiation with a dose of I = 100 mJ/cm^2. It can be seen that irradiation lead to the appearance of structures on the surface with a characteristic scale of the order of 100 nm.

In Fig. 32.4 shows the IR transmission spectra of irradiated propagules of *Rhodotorula colostri* at various doses of irradiation. The spectra demonstrate that with increasing of VUV irradiation dose, a decrease in the absorption of the glucan polysaccharide β(1–3) in the frequency region of Δf = 1000–1100 cm^{-1} and an increase in the absorption of proteins in the Δf = 1415–1650 cm^{-1} region.

A decrease of absorption at the frequency f = 1239 cm^{-1} by the PO_2 anion, which is present in DNA and phospholipids, and an increase of the absorption of

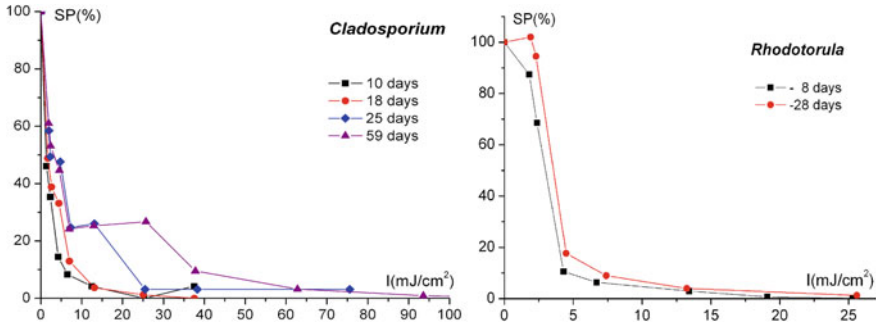


Fig. 32.2 Survival curves of the propagules isolated from colonies of different ages: *Cladosporium herbarum* (Zvereva et al. 2018) and *Rhodotorula colostri*

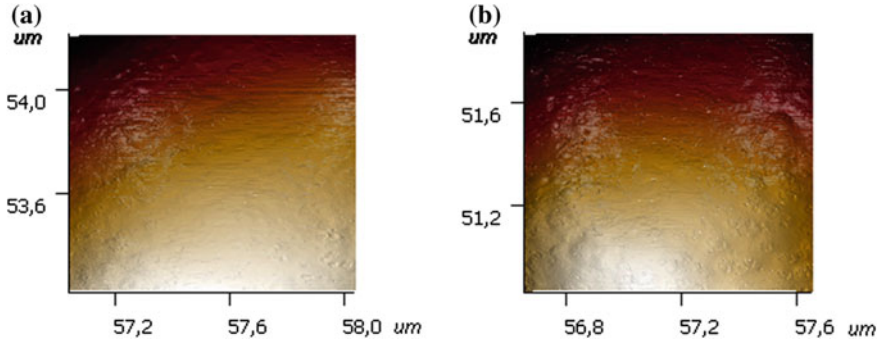


Fig. 32.3 AFM image of the spore surface of *Rhodotorula colostri* before (**a**) and after (**b**) VUV irradiation ($\lambda = 172$ nm, $I = 16$ mJ/cm^2). AFM NTegra Aura

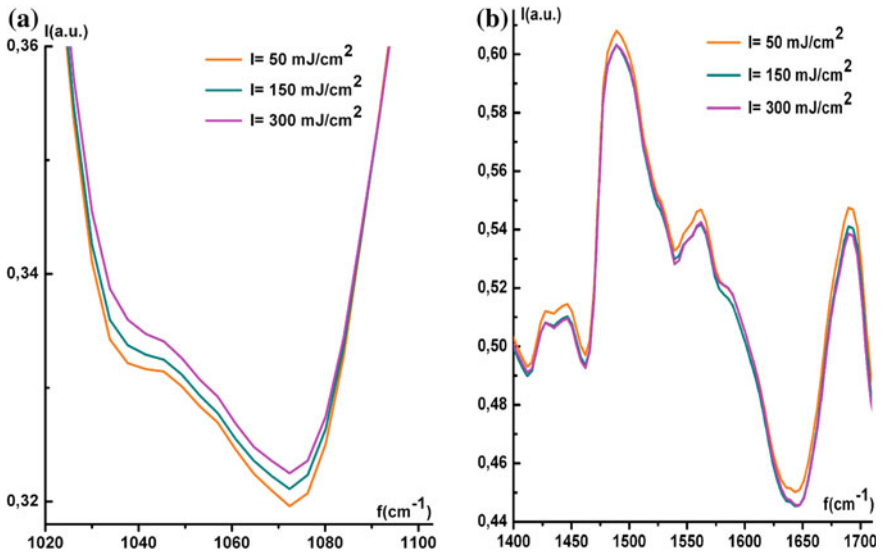


Fig. 32.4 IR transmittance spectra of *Rhodotorula colostri propagules*: **a** f = 1000–1200 cm^{-1} absorption of glucan β (1–3), **b** f = 1415–1650 cm^{-1}—absorption of protein

polysaccharide at the frequency f = 966 cm^{-1} with increasing of VUV radiation dose were observed in our experiments. As cell wall mainly consists of proteins and polysaccharides (Kamzolkina and Dunaevskiy 2015), absorbing in the VUV region (Inagaki et al. 1975; Dickinson and Johnson 1974), then changes in the IR spectra can be attributed to its destruction.

Studies have shown that the cell wall plays important role in the inactivation of spores during VUV irradiation. In the majority of studies on the effects of VUV radiation on microorganisms (Nakonechnyj et al. 1996; Ito et al. 1983; Sarantopoulou et al. 2014), as the main cause of inactivation were considered the destruction of

the cell wall under the action of highly reactive photolysis products of water (·OH radicals). This is partly justified by the fact that VUV radiation is mainly absorbed by the water contained in the cell wall and does not pass inside a cell. However, when considering the depth of penetration, the wavelength of the VUV radiation should be taken into account. Thus, according to the data (Crapulli et al. 2014), the thickness of the water layer in which 90% of the radiation is absorbed is 10 μm for the wavelength $\lambda = 172$ nm and 0.1 μm for $\lambda = 120$–130 nm work. Considering that the characteristic size of micromycete spores is a few microns, in the case of the wavelength range used by us $\Delta\lambda = 166$–180 nm, we should expect the radiation to penetrate the internal parts of the spores and, in particular, to the DNA molecule.

DNA molecules change. DNA plays a key role in biological processes and is considered in radiation biology as the main target molecule. It is known that the effect of VUV radiation on DNA molecules leads to single- and, to a lesser extent, double-stranded breaks (Michael et al. 1994). Our research confirms these results. Electrophoresis of DNA molecules isolated from irradiated and non-irradiated (control) propagules shows the appearance of breaks in DNA molecules during VUV irradiation: the number of low molecular weight fragments increase in spore irradiated samples and a high molecular weight fragment, corresponding to a mass of 20,000 nucleotides appears as well (Fig. 32.5). The presence of DNA fragmentation indicates a double-stranded break of the strands of this molecule as a result of VUV irradiation.

It should be noted that a change in the structure of DNA spores during VUV irradiation was also recorded in the work (Sarantopoulou et al. 2014): using mass spectroscopy, where DNA photo-fragments were detected, and during electrophoresis, where a decrease in the intensity of the upper band of the pattern was observed with increasing VUV dose.

It should be noted, that in a series of works (Ito et al. 1980, 1981, 1983; Hieda et al. 1984), electrophoresis of DNA molecules was not carried out and the conclusion that DNA was not involved in the inactivation of microorganisms during VUV irradiation based on the absence of genetic changes.

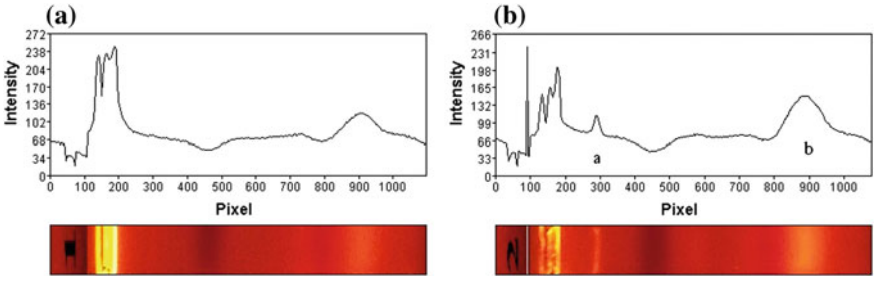


Fig. 32.5 *Rhodotorula colostri* DNA electrophoresis results of: I—nonirradiated spores, II—VUV-irradiated spores ($I = 50$ mJ/cm^2), **a** peak of 20,000 pairs of nucleotides, **b** low molecular weight fragments

The role of indirect effects. VUV irradiation of H_2O and O_2 molecules leads to the formation of such ROS as ·OH (Heit et al. 1998) and $O(^1D)$ (Atkinson et al. 2004), as well as lipid oxidation products (Kudryashov 2004), which may play a role in the death of microorganisms.

The experiments with the use of antioxidants were made to study the role of reactive radicals. For these purposes iodine I_2 was added to cultivation media. In alkaline environment I_2 molecules is known quickly to dissociate with negative ions I^- (iodide) formation, the letter are antioxidants and scavengers of free radicals (Winkler 2015) including ROS (Reactions 32.3 and 32.4), and phospholipid radicals LOOH (Reaction 32.5):

$$2\cdot OH + 2I^- \rightarrow 2OH^- + I_2 \tag{32.3}$$

$$H_2O_2 + 2I^- \rightarrow H_2O + I_2 \tag{32.4}$$

$$LOOH + 2H^+ + 2I^- \rightarrow LOH + H_2O + I_2 \tag{32.5}$$

Survival probability curves for propagules grown in iodine containing medium and in free of iodine one are shown in the Fig. 32.6. In accordance with these curves iodine indirect effects provide 10–15% of the survival probability.

Since the irradiation was performed in the air, it is necessary to evaluate the effect of ozone, formed by VUV photolysis of oxygen, on spores survival probability. Evaluation shows that the concentration of ozone in our conditions will be not more than 10^{13} cm^{-3}. In the work (Ali 2013) it was found that for 99.5% inactivation of spores of microscopic fungi *C. albicans* at ozone concentrations of 3 10^{13} cm^{-3}, a time equal to 180 min were required. As irradiation time in our experiments was less than 30 s, the effect of ozone on spores SP values can be ignored.

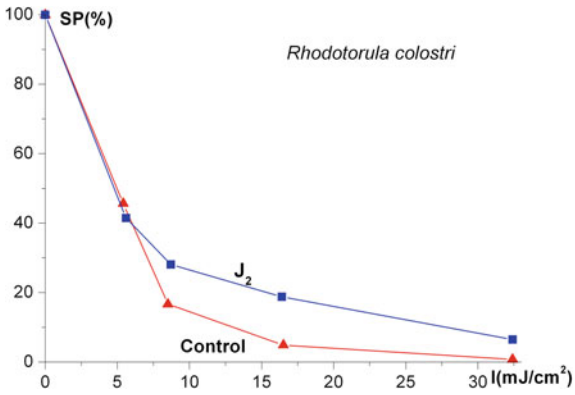


Fig. 32.6 Influence of iodine on survival probability of *Rhodotorula* cells: control (cultivation medium without I_2) and spores from cultivation medium with 0.025% I_2 concentration

32.3 Conclusion

Thus, as a result of studying of the effects of VUV radiation in the wavelength region $\Delta\lambda = 166–180$ nm on propagules of microscopic fungi *Cladosporium herbarum, Rhodotorula colostri, Saccharomyces cerevisiae*, dependences of the survival probability of propagules on the exponential and stationary development phases were obtained. It was found that at the exponential stage of colonies development, the SP curves of various types of micromycetes propagules coincide within the limits of error, but at the stationary phase they differ. IR spectroscopy and atomic force microscopy of irradiated propagules indicate a change in their cell wall. Electrophoresis of DNA molecules irradiated by propagules proves double-stranded breaks. Experiments with the use of an antioxidant show that the death of propagules during VUV irradiation occurs as a result of the direct and indirect effects of radiation, with the share of the latter being not less than 10–15%. The results obtained allow us to conclude that the inactivation of propagules during irradiation in long-wavelength VUV region ($\lambda = 166–180$ nm) results from both direct and indirect effects with the destruction of both the cell wall and DNA.

Acknowledgements The authors want to express their gratitude to the E. Machs (Komarov Botanical Institute) for his help in carrying out DNA electrophoresis and to A. Vangonen (Vavilov State optical institute) for his help in recording the infrared transmission spectra of propagules.
This study was carried out as part of the state assignment according to the thematic plan of the Botanical Institute of the Russian Academy of Sciences (theme no. 01201255604) and the Basic Research Program of the Presidium of the Russian Academy of Sciences.

References

Ali EM (2013) Ozone application for preventing fungal infection in diabetic foot ulcers. Diabetol Croat 42(1):3–22

Andersen MR, Salazar MP, Schaap PJ, van de Vondervoort PJ, Culley D, Thykaer J, Frisvad JC, Nielsen KF, Albang R, Albermann K, Berka RM, Braus GH, Braus-Stromeyer SA, Corrochano LM, Dai Z, van Dijck PW, Hofmann G, Lasure LL, Magnuson JK, Menke H, Meijer M, Meijer SL, Nielsen JB, Nielsen ML, van Ooyen AJ, Pel HJ, Poulsen L, Samson RA, Stam H, Tsang A, van den Brink JM, Atkins A, Aerts A, Shapiro H, Pangilinan J, Salamov A, Lou Y, Lindquist E, Lucas S, Grimwood J, Grigoriev IV, Kubicek CP, Martinez D, van Peij NN, Roubos JA, Nielsen J, Baker SE (2011) Comparative genomics of citric-acid-producing *Aspergillus niger* ATCC 1015 versus enzyme-producing CBS 513.88. Genome Res 21(6):885–897

Atkinson R, Baulch DL, Cox RA, Crowley JN, Hampson RH, Hynes RG, Jenkin ME, Rossi MJ, Troe J (2004) Evaluated kinetic and photochemical data for atmospheric chemistry: volume I—gas phase reactions of O_x, HO_x, NO_x and SO_x species. Atmos Chem Phys 4:1461–1738

Crapulli F, Santoro D, Sasges MR, Ray AK (2014) Mechanistic modeling of VUV advanced oxidation process in an annular photoreactor. Water Res 64:209–225

Dickinson HR, Johnson WC (1974) Optical properties of sugars. II. Vacuum-ultraviolet absorption of model compounds. J Am Chem Soc 96:5050–5054

Griffin DH (1996) Fungal physiology. Wiley, New York

Heit G, Neuner A, Saugy PY, Braun AM (1998) Vacuum-UV actinometry. The quantum yield of the photolysis of water. J Chem Phys A 102:5551–5561

Hieda K, Kobayashi K, Ito A, Ito T (1984) Comparisions of the effect of vacuum-UV and Far-UV synchrotron radiation on dry yeast cells of different UV sensitivities. Rad Res 98:74–81

Horneck G, Klaus DM, Mancinelli RL (2010) Space microbiology. Microbiol Mol Biol Rev 74:121–156

Inagaki T, Hamm RN, Arakawa ET, Birkhoff RD (1975) Optical property of bovine plasma albumin between 2 and 82 eV. Biopolymers 14:839–847

Ito T, Kobayashi K, Ito A (1980) Effect of broad-band vacuum-UV synchrotron radiationon wet yeast cells. Rad Res 82:364–373

Ito T, Ito A, Kobayashi K (1981) Effect of 120- to 165-nm vacuum-UV light on wet yeast cells. Rad Res 85(1):161–172

Ito T, Ito A, Hieda K, Kobayashi K (1983) Wavelength dependence of inactivation and membrane damage to *Saccharomyces cerevisiae* cells by monochromatic synchrotron vacuum-UV radiation (145–190 nm). Rad Res 96:532–548

Kamzolkina OV, Dunaevskiy YE (2015) Biology of the microfungi cell. KMK Scientific Publications Partnership, Moscow (in Russian)

Kirtsideli IYu, Vlasov DYu, Abakumov EV, Gilichinsky DA (2010) Diversity and enzyme activity of microfungi from antarctic soils. Mikologiya I Fitopatologiya 44(5):387–397 (in Russian)

Kirtsideli IYu, Vlasov DYu, Novozhilov YuK, Abakumov EV, Barantsevich EP (2018) Assessment of anthropogenic influence on Antarctic mycobiota in areas of Russian Polar Stations. Contemp Probl Ecol 11(5): 449–457

Kudryashov YuB (2004) Radiation biophysics (ionizing radiation). Fizmatlit, Moscow (in Russian)

Luyet BJ (1932) The effect of UV, X-and cathode rays on the spores of *Mucoraceae*. Radiology 18:1019–1023

Michael BD, Prise KM, Folkard M, Vojnovic B, Brocklehurst B, Munro IH, Hopkirk A (1994) Action spectra for single- and double-strand break induction in plasmid DNA: studies using synchrotron radiation. Int J Radiat Biol 66:569–572

Musilkova M, Ujcova E, Seichert L, Fencl Z (1983) Effect of changed cultivation conditions on themorphology of *Aspergillus niger* and citric acid biosynthesis in laboratory cultivation. Folia Microbiol 27:328–332

Nakonechnyj YuV, Pakhatova OV, Dodonova NYa (1996) The vaccum ultraviolet irradiation of green inicellular alga chlamydomonas reinhardtii. Biofizika 41(2):421–427 (in Russian)

Onofri S, Selbmann L, Zucconi L, Pagano S (2004) Antarctic microfungi as models for exobiology. Planet Space Sci 52:229–237

Onofri S, Barreca D, Selbmann L, Isola D, Rabbow E, Horneck G, de Vera JP, Hatton J, Zucconi L (2008) Resistance of Antarctic black fungi and cryptoendolithic communities to simulated space and martian conditions. Stud Mycol 61:99–109

Onofri S, de la Torre R, de Vera JP, Ott S, Zucconi L, Selbmann L, Scalzi G, Venkateswaran KJ, Rabbow E, Sa´nchez Inigo FJ, Horneck G (2012) Survival of rockcolonizing organisms after 1.5 years in outer space. Astrobiology 12:508–516

Onofri S, de Vera JP, Zucconi L, Selbmann L, Scalzi G, Venkateswaran KJ, Rabbow E, de la Torre R, Horneck G (2015) Survival of Antarctic cryptoendolithic fungi in simulated martian conditions on board the International Space Station. Astrobiology 12:1–9

Onofri S, Selbmann L, Pacelli C, Hallsworth JE, Zucconi L (2018) Integrity of the DNA and cellular ultrastructure of cryptoendolithic fungi in space or mars conditions: a 1.5-year study at the international space station. Life 8(2):23

Ozcelik B (2007) Fungi/bactericidal and static effects of ultraviolet light in 254 and 354 nm wavelengths. Res J Microbiol 2:42–49

Palffy K, Voros L (2006) Effects of UV-A radiation on desmodesmus armatus: changes in growth rate, pigment content and morphological appearance. Int Rev Hydrobiol 91(5):451–465

Parnell J, Cullen D, Sims MR, Bowden S, Cockell CS, Court R, Ehrenfreund P, Gaubert F, Grant W, Parro V, Rohmer M, Sephton M, Stan-Lotter H, Steele A, Toporski J, Vago J (2007) Searching

for life on Mars: selection of molecular targets for ESA's aurora ExoMars mission. Astrobiology 7:578–604
Poulet F, Bibring JP, Mustard JF, Gendrin A, Mangold N, Langevin Y, Arvidson RE, Gondez B, Gomez D (2005) Phyllosilicates on Mars and implications for early Martian climate. Nature 438:623–627
Prabu R, Chand T, Raksha S (2012) Improvement of *Aspergillus niger* for sodium gluconate synthesis by UV mutation method. E-J Chem 9(4):2052–2057
Robson TM, Pancotto VA, Ballaré CL, Sala OE, Scopel AL, Caldwell MM (2004) Reduction of solar UV-B mediates changes in the *Sphagnum capitulum* microenvironment and the peatland microfungal community. Oecologia 140(3):480–490
Salcedo I, Andrade JA, Quiroga JM, Nebot E (2007) Photoreactivation and dark repair in UV-treated microorganisms: effect of temperature. Appl Environ Microbiol 73(5):1594–1600
Sarantopoulou E, Stefi A, Kollia Z, Palles D, Petrou PS, Bourkoula A, Koukouvinos G, Velentzas AD, Kakabakos S, Cefalas AC (2014) Viability of *Cladosporium herbarum* spores under 157 nm laser and vacuum ultraviolet irradiation, low temperature (10 K) and vacuum. J Appl Phys 116:104701-1-15
Selbmann L, de Hoog GS, Mazzaglia A, Friedmann EI, Onofri S (2005) Fungi at the edge of life: cryptoendolithic black fungi from Antarctic desert. Stud Mycol 51:1–32
Selbmann L, Isola D, Zucconi L, Onofri S (2011) Resistance to UV-B induced DNA damage in extremetolerant cryptoendolithic Antarctic fungi: detection by PCR assays. Fungal Biol 115:937–944
Selbmann L, de Hoog GS, Zucconi L, Isola D, Onofri S (2014) Black yeasts from cold habitats. In: Buzzini P (ed) Yeasts from cold habitats
Siddiqui A, Dawar S, Zaki M., Hamid (2011) Role of ultra violet (UV-C) radiation in the control of root infecting fungi on groundnut and mung bean. Pak J Bot 43(4): 2221–2224
Singaravelan N, Grishkan I, Beharav A, Wakamatsu K, Ito S, Nevo E (2008) Adaptive melanin response of the soil fungus *Aspergillus niger* to UV radiation stress at "Evolution Canyon", Mount Carmel, Israel. Melanic Adapt Fungus 3(8):1–5
Singh J, Anand K, Rudra D, Singh P (2010) Antarctic terrestrial ecosystem and role of pigments in enhanced UV-B radiations. Rev Environ Sci Biotechnol 63(1):63–77
Smith EC (1936) The effects of radiation on fungi. In: Duggar BM (ed) Biological effect of radiations, vol 2, pp 889–918
Tembhurkar VR, Joshi SV, Dama LB, Singh PP, Pawase SR, Nighute SB (2012) Random mutageneisis stimulated overproduction of citric acid by *Aspergillus niger*. DAV Int J Sci 1(2):53–55
Torres A, Hochberg M, Pergament I, Smoum R, Niddam V, Dembitsky VM, Temina M, Dor I, Lev O, Srebnik M, Enk CD (2004) A new UV-B absorbing mycosporine with photo protective activity from the lichenized ascomycete *Collema cristatum*. Eur J Biochem 271(4):780–784
Vasanthabharathi V, Sajitha N, Jayalakshmi S (2013) Citric acid production from U-V mutated estuarine *Aspergillus niger*. Adv Biol Res 7(3):89–94
Vasilenko T, Slezak M, Kovac I, Bottkova Z, Jakubco J, Kostelnicova M, Tomori Z, Gal P (2010) The effect of equal daily dose achieved by different power densities of low-level laser therapy at 635 and 670 nm on wound tensile strength in rats: a short report. Photomed Laser Surg 28(2):281–283
Walton DWH (1984) The terrestrial environment. In: Laws RM (ed) Antarctic ecology, vol 1. Academic Press, London, pp 1–60
Weltmann KD, Kindel E, Woedtke T, Hähnel M, Stieber M, Brandenburg R (2010) Atmospheric-pressure plasma sources: prospective tools for plasma medicine. Pure Appl Chem 82:1223–1237
Winkler R (2015) Iodine—a potential antioxidant and the role of Iodine/Iodide in health and disease. Nat Sci 7:548–557
Wynn-Williams DD, Edwards HGM (2000) Antarctic ecosystems are models for extraterrestrial surface habitats. Planet Space Sci 48:1065–1075
Wynn-Williams DD, Edwards HGM (2001) Environmental UV radiation: biological strategies for protection and avoidance, In: Horneck G, Baumstark-Khan C (eds) Astrobiology: the quest for the conditions of life. Springer, Berlin, pp 244–259

Zepp RG, Erickson DJ, Paulc ND, Sulzbergerd B (2007) Interactive effects of solar UV radiation and climate change on biogeochemical cycling. Environ Eff Assess Panel Rep 6(3):135–164
Zhdanova NN, Tugay T, Dighton J, Zheltnozhsky V, MCDermott P (2004) Ionizing radiation attracts soil fungi. Mycol Res 108:1089–1096
Zvereva G, Kirtsideli I, Machs E, Vangonen A (2018) Mechanisms of the effect of VUV radiation on the microfungi. Proc SPIE 10614:106141S

Chapter 33
Sol-Gel Derived TiO_2 and Epoxy-Titanate Protective Coatings: Structure, Property, Fungicidal Activity and Biomineralization Effects

Olga A. Shilova, Dmitry Yu. Vlasov, Marina S. Zelenskaya, Yuliya V. Ryabusheva, Tamara V. Khamova, Irina B. Glebova, Alexandr A. Sinelnikov, Alexandr M. Marugin and Olga V. Frank-Kamenetskaya

Abstract The mesostructural, phase compositional, photocatalytic and antifungicidal properties of sol-gel-derived TiO_2- and epoxy-titanate coatings are investigated. The effect of epoxy-titanate coatings doped with titanium dioxide nanoparticles (TiO_2 P25) and detonation nanodiamonds on inhibiting the growth and development of a number of mold micromycetes is discussed. Biomineralization phenomena in epoxy-titanate coatings that occur under the influence of a number of mold fungi are found.

Keywords Sol-gel technology · TiO_2-coatings · Epoxy-titanate coatings · TiO_2 nanoparticles · Detonation nanodiamond · Photocatalytic activity · Soft biocides · Mold fungi · Biomineralization

O. A. Shilova (✉) · T. V. Khamova · I. B. Glebova · O. V. Frank-Kamenetskaya
Institute of Silicate Chemistry, Russian Academy of Sciences, Saint Petersburg, Russia
e-mail: olgashilova@bk.ru

O. A. Shilova · O. V. Frank-Kamenetskaya
Saint Petersburg State Electrotechnical University "LETI", Saint Petersburg, Russia

D. Yu. Vlasov · M. S. Zelenskaya · Y. V. Ryabusheva
Saint Petersburg State University, Saint Petersburg, Russia

A. A. Sinelnikov
Voronezh State University, Voronezh, Russia

A. M. Marugin
OPTEC JSC, Saint Petersburg, Russia

© Springer Nature Switzerland AG 2020

O. V. Frank-Kamenetskaya et al. (eds.), *Processes and Phenomena on the Boundary Between Biogenic and Abiogenic Nature*, Lecture Notes in Earth System Sciences,
https://doi.org/10.1007/978-3-030-21614-6_33

33.1 Introduction

Despite the fact that many stone buildings and structures built in ancient times are still present today, their state (appearance, surface morphology, strength, etc.) is of big concern to the world community. Over time, under the influence of unfavorable climatic conditions, as a result of man-made activities and bio-damage, an inevitable destruction of unique cultural monuments occurs. In addition to older buildings and structures, modern construction projects also need protection.

Thus, the problem of preventing surface pollution, exterior deterioration, biodegradation and, ultimately, the destruction of buildings and structures is also extremely acute (Doehne and Price 2010; Warscheid and Braams 2000). This problem can only be solved comprehensively as a result of efforts of specialists in various fields of knowledge. Among the primary tasks of this study were the following: monitoring the state of buildings, structures and their environment, analyzing methods and approaches during restoration and repair works, developing long-term strategies for such works. Among these tasks, the need to develop and research new materials and coatings to protect the surface of stone from pollution and biodegradation does not lose its relevance (Mack and Grimmer 2000; Calia et al. 2013; Wu and Baghdachi 2015).

For several decades, for preserving buildings and structures made of stone people used the method of protection and hydrophobization via organosilicon mixtures application, since water penetration into the volume of stone is one of the main destructive factors (Voronkov and Shorokhov 1959, 1963; Mack and Grimmer 2000). The method of hydrophobization has its pros and cons. And one of its cons is that, as a result of the treatment of the surfaces, their pores become clogged so the stone does not "breathe"—it becomes dependent on temperature fluctuations of the environment.

However, the most dangerous factor, due to the influence of which the surface deteriorates and collapses, is biodegradation. To protect stone from biodestructors biocides that are deadly for microorganisms are usually used. Among them, there are aggressive biocidal mixtures based on the compounds of tin, copper, etc. (Kugel et al. 2011).

Currently, there is a tendency to abandon the use of aggressive biocides. So-called "soft biocides" are used instead, which results in a significantly lower effect on the environment. Various photosensitizing substances can be used as a biocidal additive, which can produce ozone and other active forms of oxygen under the action of ultraviolet radiation. In this regard, a great interest of researchers is attracted to titanium dioxide nano powders, primarily to the crystalline modification of anatase (La Russam et al. 2012; Goffredo et al. 2017). However, the problem of durability of biostable photocatalytic coatings consisting of mixtures based on particulate sols or aqueous suspensions of titanium dioxide has not been solved yet (Quagliarini et al. 2012). Coatings prepared based on TiO_2 nano powders distributed in a polymer, usually, siloxane or organosiloxane matrix possess more stable protective properties (Chou et al. 2008; Goffredo et al. 2017). Sol-gel coatings obtained based on titanium

alkoxides and epoxy resin are of huge interest as well, since epoxy resin will provide good adhesion to the surface of the material, and titanium alkoxide can be a precursor of TiO_2 nanoparticles. Mixtures based on titanium alkoxides and epoxy resin have been known for a long time (Rubab et al. 2014; Li et al. 2006; Shilova et al. 2014). The photocatalytic activity of coatings based on epoxy resin and titanium tetrabutoxide have already been shown (Shilova et al. 2014), as well as the influence of TiO_2-sol-gel derived films deposited on glass slides and glass filters on the growth and viability of bacteria of the strains *Staphylococcus aureus* and *Pseudomonas putida* (Jalvo et al. 2017). Under ultraviolet irradiation (290–400 nm), the initially hydrophobic surface became hydrophilic. Antibacterial effect lead to extensive damage to the cell membranes of bacteria and significant formation of intracellular reactive oxygen forms in all samples with TiO_2 coatings. The decrease in cell viability reached more than 99.9%. However, the polymeric extracellular matrix, which had formed prior to irradiation treatment, was not removed. The authors (Jalvo et al. 2017) emphasize the danger of bacterial colonization during low insolation periods and the difficulty of removing biofilms from surfaces with complex structure.

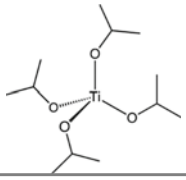
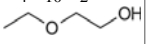
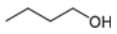
The subject of the present paper was to study the structure, phase composition and other properties of protective coatings obtained from sols based on titanium alkoxides, including those mixed with epoxy resin, as well as those with small additives of a commercial photosensitizer (TiO_2 P25) and a "soft" biocide—detonation nanodiamond. The results of experiments illustrating the influence of the developed coatings on the growth and development of a number of mold and yeast-like fungi, as well as the reverse effect of fungi on the coating structure is presented.

33.2 Materials and Methods

Several sols of various compositions were prepared for the application of protective coatings. First, according to the method (Shapovalov et al. 2011), a sol based on titanium isopropoxide was synthesized, the main components of which are given in Table 33.1. In order to obtain a film without breaks and cracks, the resulting sol was spin-coated on a cover glass or silicon plate using a centrifuge at a rotation speed of 2500 rpm. Two variants of coatings were taken as objects of study—without further heat treatment (labeled 'TiO_2') and after heating at 500 °C (labeled '$TiO_2_t_{500}$'). The coatings obtained this way had a uniform structure and had even thickness.

However, this method of protective coatings preparation is not always reliable. Therefore, to obtain protective coatings that can be created through cold solidification, while maintaining high adhesion to the surface, epoxy resin was introduced into the sols based on titanium alkoxide. As our previous studies showed, when epoxy resins were involved into tetraethoxysilane-based silica sols, the most suitable epoxy resin was EPONEX 1510, which is a hydrogenated analog of the Russian epoxy resin brand ED-20. EPONEX 1510 phase did not show phase macroseparation in the resulting hybrid coatings, unlike ED-20 (Khamova et al. 2012; Shilova et al. 2014). Titanium tetrabutoxide (Acros Organics) was used as a precursor forming an

Table 33.1 Titanium isopropoxide-based coating preparation modes

Legend	Sol components (ml)				Heat treatment (°C)
	Titanium isopropoxide, $Ti(OPr^i)_4$ 	Cellosolve (2-ethoxy-ethanol) $C_4H_{10}O_2$ 	Butanol-1 (ml) C_4H_9OH 	0.25N HCl	
'TiO_2'	10	43	43	4	–
'$TiO_2_t_{500}$'	10	43	43	4	500

inorganic framework, and acetylacetone of analytical grade and ethyl cellosolve of analytical grade were used as solvents. To prepare the epoxy titanate sol, titanium tetrabutoxide (TBT) was pre mixed with acetylacetone, ethyl cellosolve, and 1N aqueous solution of HNO_3. Then, EPONEX 1510 and a hardener BF_3 (15% solution in diethylene glycol) were added to the resulting solution. The resulting mixture was intensely stirred using a magnetic stirrer. The ratio of the main components (needed for the film to form) in the sol was $R_{TBT/EPONEX\ 1510} = 21/21$ wt%. As a result, a transparent sol was obtained at room temperature (labeled "Epoxy-TiO_2'), which allowed forming coatings 1 h after preparation. One of the variants for the synthesis of epoxy titanate sol suggested its aging in a vacuum cabinet dryer at a temperature of ~100 °C (labeled with 'Epoxy-TiO_2-vacuum') . The compositions of epoxy-titanate sols are given in Table 33.2.

In some epoxy-titanate sols a commercial photosens TiO_2 P25 (Degussa®) and a soft biocide—detonation nanodiamond, were added to enhance their bioactivity. Detonation nanodiamond (DND) was introduced into the sols in the form of a aqueous suspension (production of the Special Design Bureau "Technolog", St. Petersburg). The particles of this suspension are crystallites of the size ~4–5 nm forming clusters of 5 crystallites, which then form aggregates of 9–10 clusters (Ozerin et al. 2008). Powder TiO_2 P25 (Degussa®) is a standard material in the field of photocatalytic reactions, it contains anatase and rutile phases in a ratio of about 3:1, the average sizes of anatase and rutile elementary particles are 85 and 25 nm, respectively (Ohno et al. 2001). P25 powder was mixed with water to form a stable suspension before being added to the sols. As for epoxy-siloxane sols, a cationic BF_3 catalyst was used as a crosslinking agent, which would not cause rapid gelling of sols, as opposed to amine catalysts (Khamova et al. 2012). Aqueous suspensions of DND and TiO_2 P25 were added to the previously prepared epoxy-titanate sols and the mixture was subjected to intense stirring using a magnetic stirrer.

As a result, at room temperature, both the modified and unmodified with biocidal additives sols were obtained, which were used to form coatings on cover glass and on silicon plates (see Table 33.2). The coating was drawn using painting and varnishing techniques and then dried in air at room temperature.

Table 33.2 The compositions of epoxy-titanate sols with biocidal additives

Legend	Sol components (g)						Biocidal additives (wt%)	
	TBT	AcAc	Cellosolve	Eponex 1510	BF_3	HNO_3	DND	P25
'Epoxy-TiO_2'	21.3	6.3	41	21.3	2.9	7.2	–	–
'Epoxy-TiO_2^t'	21.3	6.3	41	21.3	2.9	7.2	–	–
'Epoxy-TiO_2-vacuum^t'	21.3	6.3	41	21.3	2.9	7.2	–	–
'Epoxy-TiO_2-$DND_{0.1}$'	21.3	6.3	41	21.3	2.9	7.2	0.10	–
'Epoxy-TiO_2-$DND_{0.2}$'	21.3	6.3	41	21.3	2.9	7.2	0.20	–
'Epoxy-TiO_2-$P25_{0.1}$'	21.3	6.3	41	21.3	2.9	7.2	–	0.1
'Epoxy-TiO_2-$P25_{0.3}$'	21.3	6.3	41	21.3	2.9	7.2	–	0.3
'Epoxy-TiO_2-$P25_{0.5}$'	21.3	6.3	41	21.3	2.9	7.2	–	0.5

Note 'Epoxy-TiO_2^t'—coatings or xerogels based on the same sols were heat treated; 'Epoxy-TiO_2-vacuum^t'—sols aged in a vacuum oven at high temperature; TBT—titanium butoxide, $Ti(OBut)_4$; AcAc—pentane-2,4-dione (acetylacetone); cellosolve—2-ethoxy-ethanol; DND—detonation nanodiamond; P25—TiO_2 (anatase/rutile $\approx$ 3/1); HNO_3—1N aqueous solution; $BF_{3–5}$ wt% BF_3 aqueous solution in diethylene glycol, EPONEX 1510—hydrogenated analogue of the uncured epoxy resin of brand ED-20, epoxy molar mass: 210–220 g, the content of epoxy groups: 4545–4762 mmol/g, structural formula: 

33.2.1 Physical and Chemical Research Methods

The structure of gels obtained from epoxy-titanate sols was examined using a high-resolution microscope ZEISS Libra 120. The phase composition of the coatings was determined by means of Siemens D-500 X-ray diffractometer. For the study of the mesostructure of the gels and xerogels, small angle scattering X-ray equipment (with horizontal and vertical beam direction) in a high-temperature chamber was observed. The X-ray intensities were measured in the angle range from 7′ to 450′ (CuK_α radiation, 1.54 Å).

The photocatalytic activity of the coatings was evaluated by the efficiency of singlet oxygen release compared to the reference sample (a commercial photocatalyst TiO_2 P25, produced by Evonik, Germany). The test bench consisted of a singlet oxygen generator and a chemiluminescent singlet oxygen gas analyzer manufactured in OPTEC JSC, St. Petersburg. Silicon plates with coatings were placed in a generator one by one, where they were illuminated with a CHANSON LED matrix ($P = 10$ W, $\lambda = 365$ nm). Pre-dried and pre-purified by means of a carbon filter from reactive oxygen species, the air was supplied to a singlet oxygen gas analyzer. Singlet oxygen

formed by the interaction of a photocatalyst activated with UV radiation with ordinary triplet oxygen molecules (Khamova et al. 2018).

33.2.2 Experimental Methodology for Studying the Fungicidal Activity of Protective Coatings

Coated samples were artificially inoculated. For this, suspensions of spores of a number of micromycetes were prepared. All strains were characterized as active biodestructors of materials in various environmental conditions. They are able to develop and cause damage to solid materials, including stone substrates. At the same time, the selected strains have a different strategy for colonizing a solid surface, differing in the nature of sporulation and the development of mycelium. Fungus *Cladosporium sphaerospermum* lives in various environments. It can be found in the air inside and outside the buildings. It can live in areas with low, moderate, and high salinity, as well as survive and thrive in areas with high radioactivity. *Ulocladium chartarum* is widely spread in nature, usually inhabiting soil and plant residues. It is often considered a contaminant. It can be found on paper, textile, wood, in animal food, as well as on building materials damaged by water. Some members of the genus *Ulocladium* can grow inside houses which keep high humidity. In addition, in dry climates, these fungi can be found on dust of human beds and in air conditioners. They can cause plant diseases. *Paecilomyces variotii* is widely spread in composts, soils, and food. It can be found in indoor air, on wood, in soil and in carpet dust. *Cladosporium cladosporioides* is one of the most common fungi, which is found everywhere and has wide ecological amplitude. It is especially harmful for stone monuments, on which it penetrates into micro-deepenings and cracks. The texturing of the surface may be of particular importance for this fungus when colonizing the substrate. *Hormonema dematioides* is a yeast-like fungus (a group of black yeasts), can develop in extreme habitats (it can settle on solar batteries, solid materials, adhere well to the surface, and become part of biofilms). *Aspergillus niger* is the most dangerous fungus, has small spores, usually inhabits the surface of solid materials under conditions of variable humidity; a typical representative of mold fungi, one of the most adapted to the anthropogenic environment.

The strains of the particular species of micromycetes were obtained by isolating them into a pure culture from the surface of the damaged substrates mentioned above (Table 33.3). For the preparation of a suspension of spores, cultures of fungi aged from 14 to 28 days were used. Suspension was prepared using sterile distilled water according to the Russian state standard GOST 9.048-89. The concentration of spores in suspension was calculated using a Goryaev chamber (Table 33.3).

Subsequently, glass slides with a coating applied on their surface were inoculated by the spore suspension. Clean glass slides were inoculated with a suspension of micromycete spores and served as a control. Inoculated glass slides were placed in moist chambers (Fig. 33.1).

Table 33.3 Characteristics of the strains of micromycetes used

Strains	Source	Spore concentration
Cladosporium sphaerospermum	Wood, Faceted Chamber, Moskow	1.8×10^5
Ulocladium chartarum	Concrete, St. Petersburg Metro, area of washout near the station Lesnaya, Saint Petersburg	2×10^4
Paecilomyces variotii	Concrete, St. Petersburg Metro, Parnas station, St. Petersburg	4.1×10^5
Cladosporium cladosporioides	Marble, monuments from the museum necropolis of the Museum of Urban Sculpture, St. Petersburg	1.8×10^5
Hormonema dematioides	Marble, monuments from the museum necropolis of the Museum of Urban Sculpture, St. Petersburg	3.0×10^4
Aspergillus niger	Marble, monuments from the museum necropolis of the Museum of Urban Sculpture, St. Petersburg	4.3×10^5

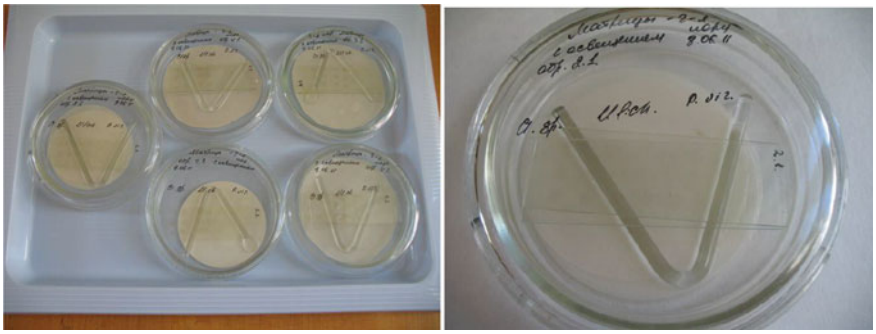


Fig. 33.1 Glass slides with experimental coatings, inoculated with spore suspension of various species of micromycetes, in moist chambers

Two test modes were implemented:

Mode 1. The glass slides inoculated with micromycetes were kept in moist chambers for 4 weeks (28 days) from the moment of inoculation (according to GOST 9.048-89).
Mode 2. The specimens inoculated with a spore suspension were illuminated with special lamps for 7 days (Fig. 33.2). The illumination started immediately after inoculation and continued for 2 h. Later the specimens were illuminated every day for 2 h.

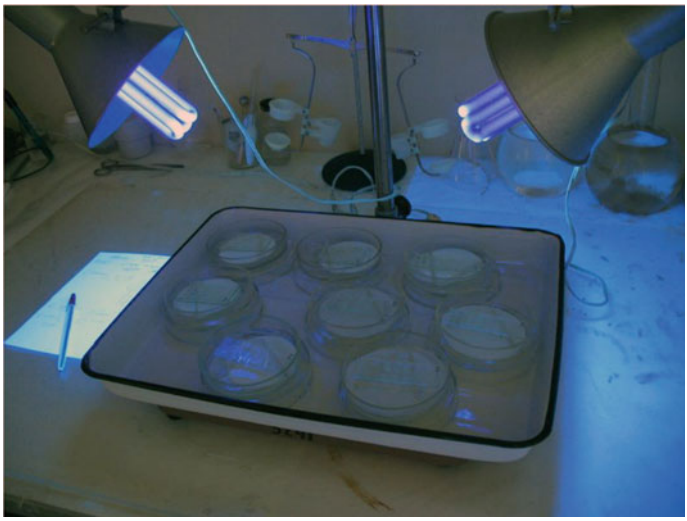


Fig. 33.2 The experimental samples lighting assembly

33.2.3 Estimation of Fungicidal Activity

In order to formalize the phenomenological observations of the growth and development of micromycetes on the surface of the coatings, an ordinal scale was developed, which made it possible to introduce a quantitative assessment of the bioactivity of the coatings by a point score system.

The ordinal scale recommended in accordance with GOST 9.048-89 was taken as the basis, it was slightly modified taking into account the peculiarities of the results of the experiment (Table 33.4).

Table 33.4 Ordinal scale for assessing the effectiveness of suppressing the growth and development of micromycetes

Score	Score characteristics
0	Germination of spores and conidia not detected under the microscope
1	Swollen conidia are visible under the microscope, some of them germinate, but there is no further growth. Mycelium does not develop
2	Swollen conidia are visible under the microscope; a significant part of them germinates. A slight growth of mycelium is observed (locally)
3	The germination of most conidia is seen under the microscope. Short or slightly branching hyphae are visible, hyphal intertwines are locally formed
4	Well-developed funguses are seen under the microscope, mycelium is being formed, and sporulation can form locally
5	The development of fungi is noticeable to the naked eye

33.3 Results and Discussion

33.3.1 Structure and Physico-Chemical Properties of Coatings

33.3.1.1 Titanium Isopropoxide Derived TiO_2 Thin Films

According to our previous studies (Shapovalov et al. 2011), films based on titanium isopropoxide were prepared by spin-coating and then were heat-treated at 500 °C ('TiO_2_t_{500}'), they have a thickness of ~D = 180–200 nm and a refractive index n = 2.2.

X-ray powder analysis showed the presence of crystalline phase of anatase in the form of crystallites ~40 nm in size, which were uniformly distributed in the amorphous matrix. Films that had not been heat treated ('TiO_2') were practically amorphous. Heat-treated films after ultraviolet irradiation acquired superhydrophilic properties (contact angle ≤5°).

33.3.1.2 Epoxy-Titanate Nanocomposites and Coatings

Using high resolution transmission electron microscopy (TEM), images of the cross sections of samples of gels formed from epoxy-titanium sols were obtained (Fig. 33.3).

As seen on Fig. 33.3, both the initial wet t gel and the xerogel, dried at 100 °C, have a homogeneous structure. In gel network, which was not subjected to heat treatment, statistically uniformly distributed inclusions with a size of ~1.5–2 nm are observed. Apparently, these are aggregation structures formed in the process of maturation of epoxy-titanate sols. After drying at 100 °C, the structure of the gels became denser and individual inclusions became less distinguishable at this magnification. Studies of epoxy-titanate gels and xerogels, carried out using both wide-angle (WAXS) and small-angle X-ray scattering (SAXS) methods, did not reveal a clear picture of the formation of titanium dioxide crystals in any particular form.

One small diffraction peak is present on the XRD pattern of the resulting epoxy-titanate coating ('Epoxy-TiO_2'), which indicates the predominance of the amorphous phase in the sample. This peak, which corresponds to d − 3.58, I_{max} − 71.3 and 2Θ − 24.86, matches the main diffraction peak observed by us on the pattern of P25 powder (Degussa®) which was taken as a reference. Therefore, it can be assumed that the nuclei of crystallization belonged to the anatase phase.

Using the method of small-angle X-ray studies (SAXS), the influence of heat treatment conditions on the mesostructure of epoxy-titanate gels and xerogels obtained from the same sols from which the coatings formed was established (Fig. 33.4). This follows from the analysis of the slope of curves 1 and 2.

As can be seen from Fig. 33.4 (curve 1), in a wet gel at the first structural level (i = 1), primary aggregation structures with a particle size of the order of 1–2 nm are

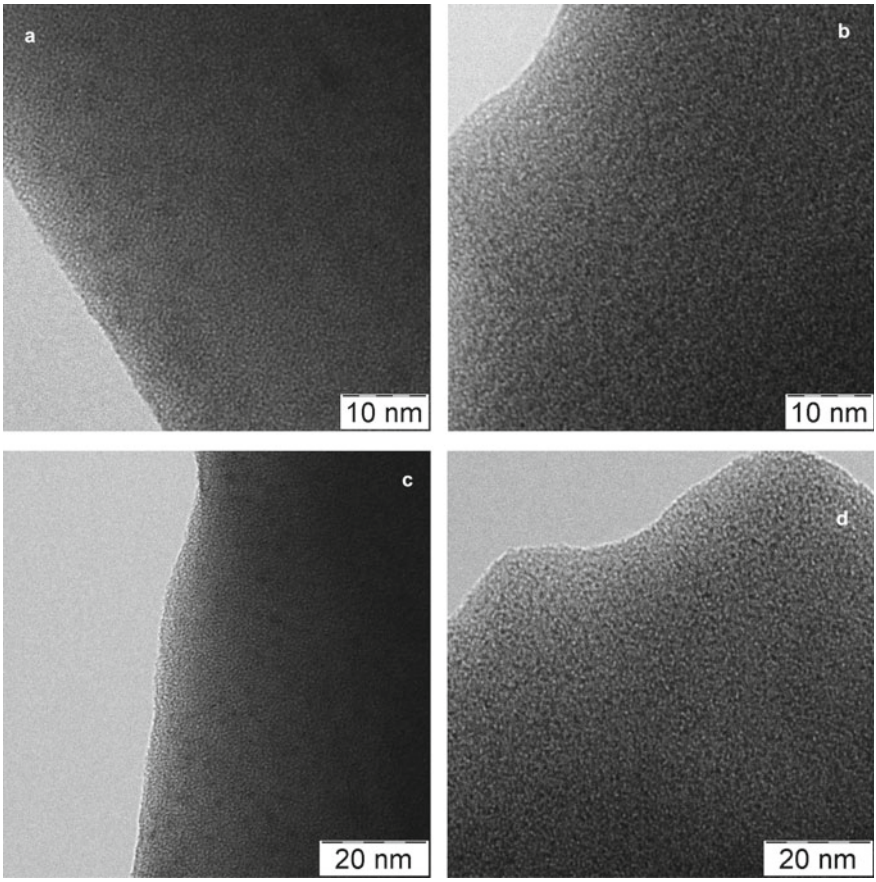


Fig. 33.3 TEM images of epoxy titanate xerogels: (**a**, **c**) aged at room temperature ('Epoxy-TiO_2'); (**b**, **d**) heat treated at 100 °C, 30 min. ('Epoxy-TiO_2^t')

formed. The slope of curve 1 in absolute value is 3 ($\beta^{i=1}_{curv1} = 3$). In this case, the fractal dimension $D_s \rightarrow 3$. This suggests that first nanoparticles with a rough, grainy surface formed in the wet gel (Shpak et al. 2004). These particles did not form aggregates with an ordered fractal structure as they were consolidating, since the absolute slope value of a linear portion of the curve at the second scale level (Fig. 33.4, curve 1) is less than 1 ($|\beta^{i=2}_{curv1}| < 1$). This indicates a non-fractal behavior. Thus, the structure of the wet gel is not well ordered.

As can be seen from Fig. 33.4 (curve 2), for xerogel obtained as a result of long-term drying of a wet gel at 100 °C, quite smooth nanoparticles (1–2.5 nm) with the surface fractal structure formed on the first structural level, since the slope of the curve ($\beta^{i=1}_{curv2}$) in the absolute value is |3.6|, i.e. $|\beta^{i=1}_{curv2}| > 3$ (Brinker and Scherer 1990). At the second scale level for the xerogel, we can see an extended linear portion of the curve with a slope $\beta^{i=2}_{curv2} = -2.0$. This indicates that a fractal structure of the

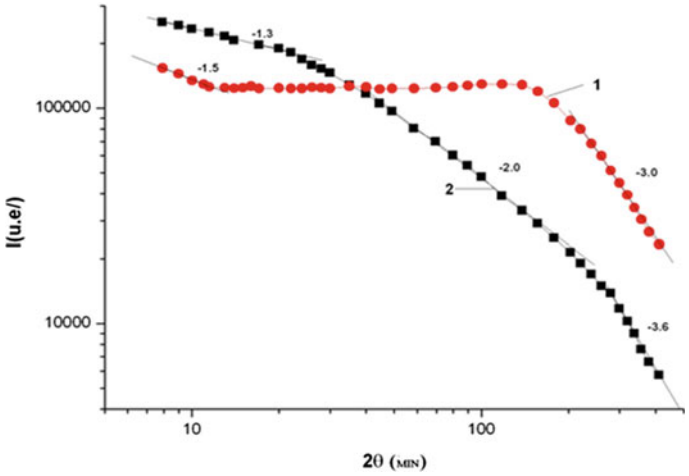


Fig. 33.4 Small-angle X-ray scattering (SAXS) data in logarithmic double coordinates for epoxy-titanate wet and dry gels: 1—wet gel, aged at room temperature ('Epoxy-TiO_2'); 2—xerogel, was additionally dried at 100 °C for 2 days. ('Epoxy-TiO_2^t'). Numbers with a minus sign denote the slope values of straight sections of curves, which determine the fractal dimension of the aggregational gel structures

mass fractal type formed from these primary particles, since the fractal dimension ($D^{i=2}_{m_curv2}$) equals to the slope of the curve, which in absolute value is greater than 1 but less than 3 ($1 < |\beta^{i=2}_{curv2}| < 3$). The size of these aggregation structures is in the range of 2–6 nm. At the third scale level, larger (hundreds of nanometers across), but less dense aggregates formed in the xerogel, which also formed a loose network of the mass fractal type ($|\beta^{i=3}_{curv2}| = 1.3$). Thus, drying the wet gel at 100 °C contributed to the formation of a well-organized fractal structure at all three scale levels.

SAXS curves were also obtained for epoxy-titanate sols, which aged in situ under reduced pressure and at elevated temperature (100 °C, for 2 h), as well as under normal pressure and heating in the range from 100 to 160 °C for 2–24 h. Analysis of the data allowed concluding that gels, aged under vacuum conditions at 100 °C, are characterized by a more ordered fractal structure of the formed aggregates, on both the first and second scale levels. At the same time, for all gels that aged in the absence of vacuum in the temperature range from 100 to 160 °C from 2 to 24 h, the fractal organization of the structure formed on the first scale level disappears at higher scale levels. Thus, the heating of epoxy-titanate sols (to 110 °C and higher) in the process of their aging leads to the destruction of the primary fractal structure of the sols. Heating up to 100 °C in milder conditions under reduced pressure allows obtaining more well-organized aggregation structures.

As a result, it can be noted that the heating of the sol already up to 100 °C during its aging affects the mesostructure of the formed epoxy-titanate nanocomposites more significantly than the additional heating of the wet gel. It is interesting to note that

vacuuming at sol aging and gelation stage significantly affected the mesostructure of the composites, contributing to their fractal organization at the nanometer level.

33.3.1.3 Epoxy-Titanate Nanocomposites and Coatings Obtained from Sols Modified with Titanium Dioxide Nanoparticles

On XRD patterns of epoxy-titanate coatings modified with TiO_2 nanoparticles (0.3 and 0.5 wt% TiO_2 P25) small diffraction peaks were observed. Using the obtained X-ray diffraction patterns, we could not clearly determine the polymorphic modification of titanium dioxide, since the samples contained an amorphous phase, but it can be stated that the diffraction peaks corresponding to d = 3.58 ('Epoxy-TiO_2-$P25_{0.3}$') and d = 3.65 (2Epoxy-TiO_2-$P25_{0.5}$') belong to anatase.

Thus, according to the results of X-ray powder analysis, it can be concluded that the obtained epoxy-titanate coating, even modified with small amounts of TiO_2 nanoparticles (P25), contains mainly the amorphous phase and very poorly represented crystalline titanium dioxide inclusions in the anatase polymorph.

33.3.2 Photocatalytic Activity of TiO_2- and Epoxy-Titanate Coatings

The photocatalytic activity, estimated by the intensity of the release of reactive oxygen species during the UV irradiation of the surface of coatings, for the TiO_2 heat treated coating ('TiO_2_t_{500}') is ~10% of the photocatalytic activity of commercial TiO_2 P25 powder, and for the epoxy titanate coating ('Epoxy-TiO_2') is ~8%. As our studies have shown, it is possible to increase the photocatalytic activity of these films to ~80 and ~50% (respectively, for TiO_2 and epoxy-titanate coatings) if alkaline hydrolysis is used instead of the acidic one. It is known that alkaline hydrolysis amplifies rapid precipitation of crystals of TiO_2, which increases the photocatalytic activity. However, this significantly decreases the uniformity of the coating structure and even disrupts its continuity. Therefore we abandoned the idea of using alkaline hydrolysis of titanium alkoxides to obtain protective biostable coatings.

33.3.3 Fungicidal Properties of Coatings

33.3.3.1 TiO_2 and Epoxy-Titanate Coatings

The results of the observations of the development of micromycetes, which inoculated glass slides with the test coatings, are presented on Figs. 33.5, 33.6 and in Table 33.5.

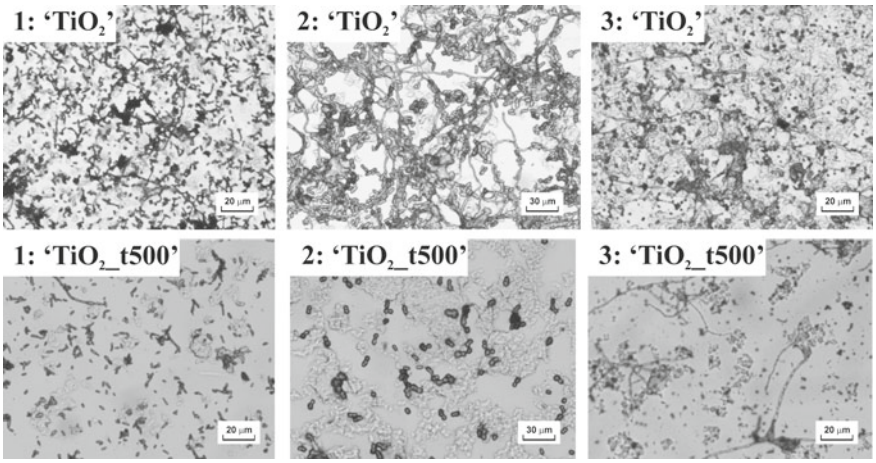


Fig. 33.5 Optical images of the surface of coatings obtained from sol on the basis of titanium isopropoxide, without heat treatment ('TiO_2') and heat-treated at 500 °C for 30 min ('$TiO_{2}_t_{500}$'), after inoculation with spores of *Cladosporium cladosporioides* (1), *Hormonema dematioides* (2), *Aspergillus niger* (3) and exposure in a moist chamber for 28 days without lighting (Mode 1)

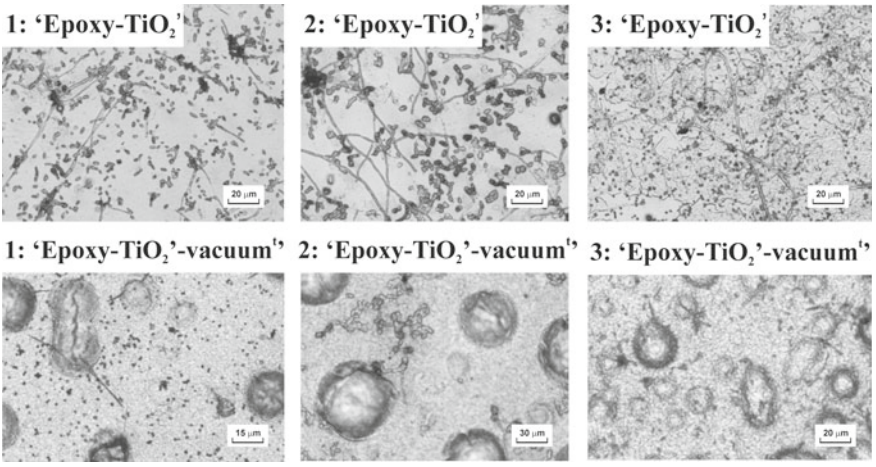


Fig. 33.6 Optical images of the surface of coatings obtained from epoxy-titanate sols: aging at room temperature ('Epoxy-TiO_2') and aging in a vacuum chamber at 100 °C ('Epoxy-TiO_2'-vacuum^{t}'), after inoculation with spores of *Cladosporium cladosporioides* (1), *Hormonema dematioides* (2), *Aspergillus niger* (3), exposure in a moist chamber for 28 days (without lighting, Mode 1)

Table 33.5 Score-based assessment of the biostability of coatings with respect to a number of micromycetes

Legend	Fungal strains		
	Cladosporium cladosporioides	*Hormonema dematioides*	*Aspergillus niger*
'TiO_2'	2–3	2–3	0–1
'TiO_{2_t500}'	0	1	0
'Epoxy-TiO_2'	0–1	2–3	0–1
'Epoxy-TiO_2-vacuum^t'	0–1	0–1	0–1

As can be seen from Fig. 33.5 and Table 33.5, the 'TiO_2' coating, obtained via hydrolysis of titanium isopropoxide and not subjected to heat treatment, weakly inhibits the growth of micromycetes of *C. cladosporioides* and *H. dermatidis* (the score characterizing the development of micromycetes is rather high—2 to 3 points, see Table 33.4) while *A. niger* development is noticeably suppressed (0–1 points). Temperature treatment significantly increased the biocidal effect. At the same time, the inhibitory effect leveled out and was present for all three species of fungi, i.e. the range of action of this coating expanded. Especially the growth of mycelium is actively suppressed, weak yeast-like growth remains only for *H. dermatidis*. Such an enhancement of the biocidal properties of the heat-treated coating can be attributed to the appearance of the crystalline anatase phase in the coating structure, although the inoculated samples have not been exposed to artificial light (Mode 1 was used, for description of the mode, see Sect. 33.2.2).

As can be seen from Fig. 33.6 and Table 33.5, a more uniform inhibitory effect on all strains was observed in the variant with vacuum treatment (0–1 points). In the variant without heat treatment, a high degree of inhibition was observed only with the strains *C. cladosporioides* and *A. niger* (0–1 points). At the same time, the yeast-like fungus *H. dermatidis* retained its ability to grow and develop, which was represented by mycelial and yeast growth (2–3 points).

In general, based on the data presented in Figs. 33.5, 33.6 and Table 33.5, it can be concluded that all the considered variants of coatings inhibit the development of micromycetes at one degree or another. All considered variants of coatings had the strongest inhibitory effect on *A. niger* fungus. It turned out to be the hardest to suppress the growth of the *H. dermatidis* yeast-like fungus. Here, the best effect was achieved by the coating based on TiO_2, heat treated at 500 °C, i.e. with a partially crystallized structure in the anatase phase. The epoxy component had a positive effect on the biocidal properties of the coatings in relation to the inhibition of *C. clladosporioides* micromycetes.

33.3.4 The Effects of the Interaction of Micromycetes with Coatings

33.3.4.1 Epoxy-Titanate Coatings Modified with Nanoparticles

As our previous studies have shown, in general, spore germination and the development of mycelium on all modifications of epoxy-siloxane coatings is slightly worse than in control (Frank-Kamenetskaya et al. 2011; Khamova et al. 2012). The introduction of nanoparticles, in particular detonation nanodiamond, into epoxy-siloxane sols in the amount of 0.1–0.25 wt% significantly improves the biostability of coatings against mold fungi *Ulocladium chartarum* and *Cladosporium cladosporioides*. DND-modified epoxy-siloxane coatings probably have a prolonged effect on the morphological and strain properties of micromycetes: poor germination of *Paecilomyces variotii* spores, modification of the mycelia of *Ulocladium chatrum*, lack of sporulation in *Cladosporium sphaerospermum*.

As was shown in the previous section, epoxy-titanate coatings, like epoxy-siloxane coatings, generally inhibit the development of a number of micromycetes. However, the effect is quite selective. The biocidal effect from the introduction of nanoparticles to epoxy titanate coatings of both DND and TiO_2 P25 to suppress the development of micromycetes *Paecilomyces variotii*, *Ulocladium chatrum* and *Cladosporium sphaerospermum* is less pronounced than for epoxy siloxane coatings. At the same time, there are interesting effects associated, as it seems to us, with the biomineralization of the surface of the coatings under the influence of the metabolism products of the fungi.

First of all, epoxy-titanate coatings, both unmodified, and containing 0.1 and 0.2 wt% DND have a slightly yellowish tint. This tint disappears after about 3 months of exposure to the open air. The same effect is achieved after 2 days of incubation (without light, Mode 1). The remains of yellow pigment remained only along the edge of the glass slide. Thus, micromycetes affect the state of the surface of the coatings as well as atmospheric effects (solar radiation, temperature changes, etc.).

An interesting phenomenon was observed when samples with an epoxy-titanate coating containing 0.1 and 0.2 wt% DND were inoculated with micromycetes *Ulocladium chartarum* (Fig. 33.7).

Although growth and even sporulation were at first slightly inhibited compared to control, the presence of DND nanoparticles in the coating resulted in the formation of crystals around the developing spores of the fungus after 7 days of observation, which literally enclosed these spores in a “case”, preventing their further growth (see Fig. 33.7). Such a phenomenon was not observed either in the control or on the epoxy-titanate coating, which was not modified by detonation nanodiamond nanoparticles. Apparently, DND nanoparticles under the influence of micromycetes metabolic activity products catalyze the crystallization process of TiO_2. However, a similar phenomenon was observed only when samples were inoculated with *Ulocladium chartarum* micromycetes.

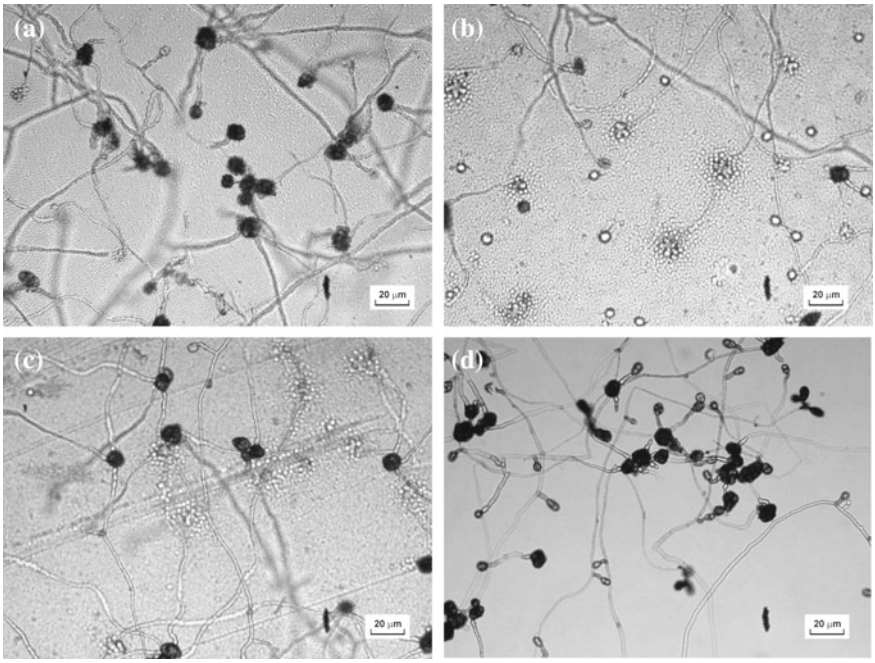


Fig. 33.7 Optical image of the surface of epoxy-titanate coatings inoculated with micromycete *Ulocladium chartarum* (on the 7th day of observation): without additives DND (**a**); modified 0.1 wt% DND (**b**); 0.2 wt% DND (**c**); control—uncoated glass slide (**d**)

The addition of nanoparticles TiO_2 P25 into epoxy-titanate sols also lead to very unusual results. A sample with an epoxy-titanate coating containing 0.1 wt% TiO_2 P25, after 2 days of inoculation crystallites formed (Fig. 33.8) under the influence of all three strains of fungi (*Cladosporium sphaerospermum*, *Ulocladium chatarum* and *Paecilomyces variotii*), and, however, disappeared at 7th day after inoculation (under artificial lighting, Mode 2). At the same time crystallites formed with different morphology depending on the type of strain. Spherulites formed under the influence of the mold fungus *Cladosporium sphaerospermum* (Fig. 33.8a), and dendrites when inoculated with a yeast-like fungus *Paecilomyces variotii* (Fig. 33.8b).

This indicates that the metabolism products of the fungi *Cladosporium sphaerospermum* and *Paecilomyces variotii* differ in terms of chemical composition, they for instance may contain different acids. It is known that anions present in the initial sols affect the shape of crystallites formed in the coatings forming from them (Shilova 2004). In this case, we are dealing with epoxy-titanate coatings which are not thermally solidified and whose structure is particularly sensitive to external factors, such as chemical reagents and elevated temperatures (as shown above in Sect. 3.1.2).

No similar phenomenon of crystallization under the influence of micromycetes was observed either in epoxy-siloxane coatings, including those containing TiO_2 P25 nanoparticles, or in epoxy-titanate coatings that do not contain TiO_2 P25 nanopar-

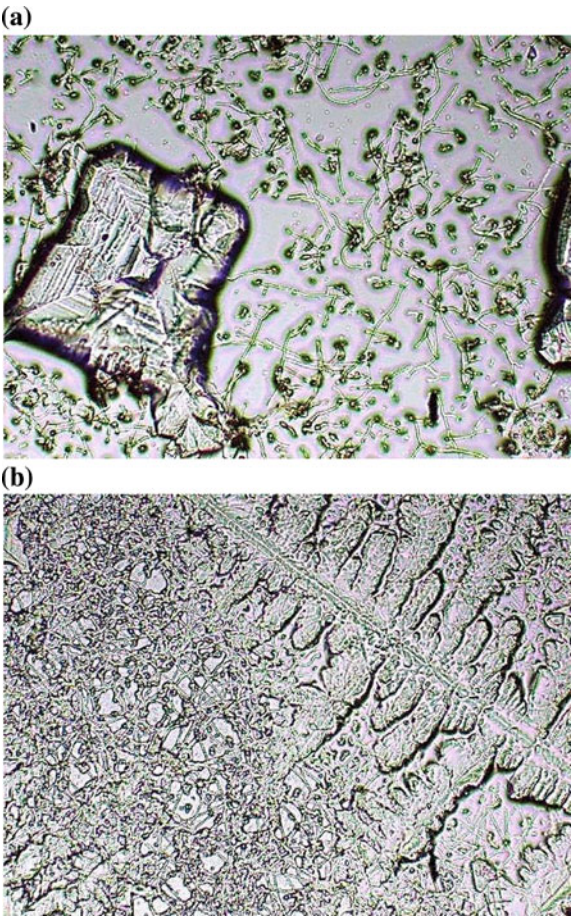


Fig. 33.8 Optical image of the surface of epoxy-titanate coatings modified with 0.1 wt% TiO_2 P25 ('Epoxy-TiO_2-$P25_{0.1}$') and inoculated with micromycetes: **a** *Cladosporium sphaerospermum* and **b** *Paecilomyces variotii*, on the 7th day of observation (with artificial l lighting, Mode 2)

ticles, and, oddly enough, even in epoxy-titanate coatings with a higher content of TiO_2 P25 (0.3 и 0.5 wt% TiO_2 P25). Titanium oxides are known as so-called opacifiers. They are the centers of crystallization in glass and enamel. In the case the added TiO_2 nanoparticles acted as centers of crystallization for the practically amorphous epoxy-titanate matrix, and the products of fungal metabolism served as a catalyst for this process and determined the shape of the crystallites.

33.4 Conclusion

Using sols based on titanium alkoxides $Ti(OPr^i)_4$ and $Ti(OBut)_4$, EPONEX 1510 epoxy resin and dopants (0.1–0.5 wt% titanium oxide nanoparticles (TiO_2 P25) and detonation nanodiamond (DND), TiO_2 and epoxy-titanate coatings were obtained

and investigated, they are promising as protective coatings against material biodestructors.

Using high resolution transmission electron microscopy, wide angle X-ray scattering (WAXS) and small angle X-ray scattering (SAXS), we studied the structure of coatings, gels and xerogels obtained from $Ti(OPr^i)_4$ and epoxy resin derived sols, including those doped by TiO_2 nanoparticles.

SAXS data allows for the conclusion that drying a wet epoxy-titanate gel at 100 °C contributed to the formation of a well-organized fractal structure of epoxy-titanate nanocomposites. According to the mesostructure of gels and xerogels, we can indirectly estimate the structure of coatings obtained from the same epoxy-titanate sols. Therefore, we can conclude that drying of coatings at 100 °C will contribute to the formation of more dense and better structured epoxy-titanate coatings.

The mesostructure of epoxy-titanate gels and xerogels and, consequently, coatings can be controlled at the stage of sols aging. Heating sols to temperatures between 100 and 160 °C contributes to the destruction of fractal organization in sols. Heating under a reduced pressure reduces the effect of temperature, and helps preserve the fractal organization in epoxy-titanate aggregational structures at the nanoscale level.

Based on X-ray powder diffraction analysis data, it can be concluded that the epoxy-titanate coating is predominantly an amorphous phase with nuclei of crystallization of the anatase phase. Even epoxy titanate coating, doped with 0.3–0.5 wt% TiO_2 P25, contains mainly the amorphous phase and very poorly pronounced crystalline inclusions of titanium dioxide in the polymorphic modification of anatase.

The photocatalytic activity, estimated by the intensity of the release of reactive oxygen forms when irradiating the surface of coatings with UV, for TiO_2 coatings subjected to heat treatment at 500 °C, equals to ~10% of the photocatalytic activity of commercial TiO_2 P25 powder, and to ~8% for epoxy-titanate coatings.

It was revealed that the structural organization of both TiO_2 coatings and epoxy-titanate coatings significantly affects their anti-fungicidal properties. The formation of the crystalline anatase phase in both TiO_2 coatings and epoxy titanate coatings significantly increases the effectiveness of inhibiting the growth and the development of mold and yeast-like fungi (*Aspergillus niger*, *Cladosporium cladosporioides*, *Hormonema dematioides*). The ordering of the mesostructure of epoxy-titanate coatings at the nanoscale and the formation of the fractal structure of nanocomposites also contributes to an increase of their anti-fungicidal activity.

For the first time, phenomena of biomineralization have been discovered, which are represented in the formation of crystallites on the surface of an epoxy-titanate coating doped with both DND nanoparticles and TiO_2 nanoparticles. In this case, the type of strain that a coating containing TiO_2 nanoparticles was inoculated with affects the shape of the crystallites formed: spherulites or dendrites.

Acknowledgements This work was partially supported by the Russian Foundation of Basic Research (project RFBR—18-29-05031mk). The research results were partially obtained on the equipment of The Collective Use Center of Voronezh State University (URL: http://ckp.vsu.ru).

References

Brinker CJ, Scherer GW (1990) Sol-gel science: the physics and chemistry of sol-gel processing. Academic Press Inc., San-Diego

Calia A, Colangiuli D, Lettieri M, Matera L (2013) A deep knowledge of the behaviour of multi-component products for stone protection by an integrated analysis approach. Prog Org Coat 76:893–899

Chou JLH, Tung Chun-Ting, Lin Yu-Ming, Li Ai-Kang (2008) Preparation and optical properties of titania/epoxy nanocomposite coatings. Mater Let 62(19):3416–3418

Doehne E, Price CA (2010) Stone conservation. An overview of current research, 2nd edn. The Getty Conservation Institute, LA

Frank-Kamenetskaya OV, Vlasov DYu, Shilova OA (2011) Biogenic crystal genesis on a carbonate rock monument surface: the main factors and mechanisms, the development of nanotechnological ways of inhibition. In: Krivovichev SV (ed) Minerals as advanced materials II. Springer, Berlin, Heidelberg

Goffredo GB, Terlizzi V, Placido Munafò P (2017) Multifunctional TiO_2-based hybrid coatings on limestone: initial performances and durability over time. J Build Eng 14:134–149

Jalvo B, Faraldos M, Bahamonde A, Rosal R (2017) Antimicrobial and antibiofilm efficacy of self-cleaning surfaces functionalized by TiO_2 photocatalytic nanoparticles against *Staphylococcus* aureus and *Pseudomonas* putida. J Hazard Mater 340:160–170

Khamova TV, Shilova OA, Vlasov DY, Ryabusheva YuV, Mikhal'chukc VM, Ivanov VK, Frank-Kamenetskaya OV, Marugin AM, Dolmatov VYu (2012) Bioactive coatings based on nanodiamond modified epoxy siloxane sols for stone materials. Inorg Mater 48(7):702–708

Khamova TV, Frank-Kamenetskaya OV, Shilova OA, Chelibanov VP, Marugin AM, Yasenko EA, Kuz'mina MA, Baranchikov AE, Ivanov VK (2018) Hydroxyapatite/anatase photocatalytic core–shell composite prepared by sol-gel processing. Crystallogr Rep 63(2):254–260

Kugel A, Stafslien S, Chisholm BJ (2011) Antimicrobial coatings produced by "tethering" biocides to the coating matrix: a comprehensive review. Progr Org Coat 72(3):222–252

La Russam MF, Ruffolo SA, Rovella N, Belfiore CM, Palermo AM, Guzzi MT, Crisci GM (2012) Multifunctional TiO_2 coatings for Cultural Heritage. Progr Org Coat 74:186–191

Li S, Zhang H, Zhao C, Wang X (2006) New epoxy/silica titania hybrid materials prepared by the sof-gel process. J Appl Polym Sci 101(2):1075–1081

Mack RC, Grimmer AE (2000) Assessing cleaning and water-repellent treatments for historic masonry buildings. In: Preservation Briefs—Technical Preservation Services—National Park Service, U.S. Department of the Interior. https://www.nps.gov/tps/how-to-preserve/preservedocs/preservation-briefs/01Preserve-Brief-Cleaning.pdf

Ohno T, Sarukawa K, Tokieda K, Matsumura M (2001) Morphology of a TiO_2 photocatalyst (Degussa, P-25) consisting of anatase and rutile crystalline phases. J Catal 203(1):82–86

Ozerin AN, Kurkin TS, Ozerina LA, Dolmatov VYu (2008) X-ray diffraction study of the structure of detonation nanodiamonds. Crystal Rep 53(1):60–67

Quagliarini E, Bondioli F, Goffredo GB, Cordoni K, Munafó P (2012) Self-cleaning and de-polluting stone surfaces: TiO_2 nanoparticles for limestone. Constr Build Mater 37:51–57

Rubab Z, Afzal A, Siddiqi HM, Saeed S (2014) Preparation, characterization, and enhanced thermal and mechanical properties of epoxy-titania composites. Sci World J ID 515739 (7pp)

Shapovalov VI, Shilova OA, Smirnova IV, Zav'yalov AV, Lapshin AE, Magdysyuk OV, Panov MF, Plotnikov VV, Shutova NS (2011) Modification of the glass surface by titanium dioxide films synthesized through the sol-gel method. Glass Phys Chem 37(2):150–156

Shilova O (2004) Phenomena of a phase separation and crystallisation in nanosized spin-on glass films used in microelectronics. Glass Technol 45(2):59–61

Shilova OA, Khamova TV, Vlasov DJ, Marugin AM, Frank-Kamenetskaya OV (2014) Composition for obtaining matrix with photocatalytic activity. Patent RU 2518124 Bull 16

Shpak AP, Shilov VV, Shilova OA, Kunitskii YA (2004) Diagnosis of nanosystems. Multi-level fractal nanostructures. Technical Center of the National Academy of Sciences of Ukraine, Kiev (in Russian)

Voronkov MG, Shorokhov NV (1959) The use of organosilicon compounds to improve the water resistance and durability of building materials. Constr Mater 7:12–17 (in Russian)

Voronkov MG, Shorokhov NV (1963) Water repellent coatings in construction. Publishing House of the Academy of Sciences of the Latvian SSR, Riga (in Russian)

Warscheid T, Braams J (2000) Biodeterioration of stone: a review. Int Biodeter Biodegrad 46(4):343–368

Wu L, Baghdachi J (eds) (2015) Functional polymer coatings: principles, methods, and applications. Wiley, Hoboken, NJ

Chapter 34
The Impact of Microorganisms on Monuments in the Underground Archaeological Museum of Moscow



Tamara T. Abramova

Abstract Since 1990, Moscow's underground archaeological museum has exhibited archaeological findings of the ancient area of Zaryadye and the estate of Romanov boyars of the XVI century, the ruined cook-stove of the XVI century, which was a part of the Romanovs' yard, and a section of the soils of the XVI-XVII century, artificially stabilized by a chemical solution in situ. During the whole time, the state of the exhibited objects was monitored. The temperature and humidity conditions in the premise were monitored from the first days to the present. Abrupt changes in humidity in the museum (up to 100%) occurred after a new archaeological excavation took place after 15 years of operation. This provoked the formation of favourable conditions for the microbiota development. All this turned out to be adverse for the exhibited objects, especially the unique ruined cook-stove, which began to collapse. Studies have shown a high and extremely high level of microbial contamination. The dominating types were mold fungi *Aspergillus* sp., *Penicillium* sp. and bacteria *Bacillus* sp. As a result of employing various devices, the humidity was reduced and the controlled level of air microbiota was achieved. The use of effective biocidal materials made it possible to increase the resistance of the exhibits to biocorrosion. The performed works allowed to create a safe environment for the preservation of exhibits and for museum's staff and visitors.

Keywords Archaeological sites · Cultural layer · Stabilization · Humidity · Microbiota · Biocidal material · Ultraviolet irradiator

34.1 Introduction

The tendency to preserve the architectural and archaeological monuments discovered during excavations throughout the world is now becoming quite relevant in our country. During all-union and international conferences and symposia questions

T. T. Abramova (✉)
Geological Faculty, Lomonosov Moscow State University, GSP-1, Lenin's Mountains, 119991 Moscow, Russia
e-mail: attoma@mail.ru

© Springer Nature Switzerland AG 2020

O. V. Frank-Kamenetskaya et al. (eds.), *Processes and Phenomena on the Boundary Between Biogenic and Abiogenic Nature*, Lecture Notes in Earth System Sciences,
https://doi.org/10.1007/978-3-030-21614-6_34

have been repeatedly raised about the need to create archaeological reserves and exhibit objects in these locations. The stabilization of any archaeological monument including the preservation of a soil profile of its cultural layer is a rather complex and at the same time poorly established problem. This is due to the requirements imposed on the stabilized soils by the International Charter for the Conservation and Restoration of Monuments: the preservation of the natural colour and texture of both the soil and its inclusions; ensuring long-term preservation of the museum-specific object in this climatic zone. There were many challenges in solving these problems because the soils of the cultural layer are specific. For example, there is heterogeneous composition in both vertical and horizontal axes, a diversity of inclusions, an uneven compressibility of the stratum, as well as a high content of organic substances in them make it difficult to stabilize such soils. In addition, there is little experience worldwide in the practice of soils museumification, since they practically cannot be stabilized due to the fact that they contain a large amount of organic substances from both plant (humic, fulvic, etc.) and organic substances. Therefore, both abroad and in our country when preparing a historical monument for exposition such soils are generally replaced with concrete or masonry which leads to a distortion of its original appearance.

This type of work required knowledge from the field of geological engineering. The situ conservation of the soil of the cultural layer in addition to the traditional conditions requires the additional conditions which are described in detail in the work (Abramova and Voronkevich 1988). The essence of this method is to inject into the pore medium of the soil the injection solutions of a certain composition, which have a property after being distributed in the pore space to solidify. This ensures a long-term stabilization of the structure of the porous body without deforming, destroying or changing the colour. In this regard, for many years the laboratory of the Geological Faculty of Moscow State University conducts a research on the development of methods of injection of these soils to solve the main issues of their conservation and museumfication (Abramova and Voronkevich 1979; Abramova et al. 1987).

The successful attempts to stabilize weak soils were made on the monuments of the Northern Black Sea Coast, the Kiev-Pechersk Lavra, the old Riga, and others (Abramova and Voronkevich 1988; Abramova 2018). Recently, the most important task has been to ensure the conservation of stabilized soils, exhibited under the underground conditions of the museum in Moscow. In some cases, human engineering activity violates the conditions of many natural processes including the microbiological ones. This, in turn, can lead to a significant stimulation of microbiota which in a short time can have an undesirable effect on the properties of the stabilized soil of the cultural layer and the worsening of the ecological situation in the underground museum.

Microorganisms are an integral part of the soils which are present in various quantities in most of them. The problem of interaction of microorganisms with soils began to interest geological scientists in the late XIX century. In 1877, for the first time, Th. Schloesing and A. Muntz reported the effects of bacteria on rock decomposition. Since the end of the XIX century, microorganisms have been widely studied in soil

science whereas studies of their role in shaping the properties of soils in engineering geology, in fact, were first conducted only in the 1970s.

Studies of the effect of microorganisms on soils have shown that they have almost universal ability to perform certain geochemical functions. For such, they are characterized by a significant physiological (biochemical) activity, rapid reproduction in favourable conditions, as well as the lability of metabolism (Zavarzin 1972).

Zvyagintsev et al. (2005) states that the development of the microbiological component in the rock leads to an increase in the content of a finely dispersed fraction, which has a considerable surface energy, and thus adversely affects the state and properties of sandy-clay rocks. Numerous studies by Radina (1973) found that the vital activity of microorganisms not only affects the mineral composition of soils, their dispersion and structure but also alters the pressure state, converting sand into fluids. This is due to an increase in the number of microorganisms and the accumulation of their metabolic products, as well as an increase in the pressure of trapped in the pores bubbles of inactive gases of biochemical origin.

In the end of 70s–80s of the twentieth century research on the role of microorganisms in the formation and transformation of soil properties was carried out at the Department of Engineering and Ecological Geology of Moscow State University under the guidance of an academician E. M. Sergeyev. In his monograph "Engineering Geology", he noted that ignoring the participation of microorganisms in physico-chemical processes leads to an incomplete understanding of the soils as a multicomponent system (Sergeev 1978).

Data on the changes of some properties of soils (shear resistance, stickiness, plasticity), stabilized during the process of microbial activity during restoration is presented in the work (Bolotina and Sergeev 1987). The results of testing the strength of pure medium-grained quartz sands saturated with yeast cultures of 1.5–2.0 g/100 ml concentration showed its significant decrease of 65% (Root et al. 1982).

This day, some experience has been gained on the effect of microorganisms on the formation and change of the composition, structure, and properties of soils. The stabilization of the mineral composition of soils and stone—oxidation or restoration of variable-valent elements in the crystal lattice, their grouping into organo-mineral complexes, mineral decay due to the action of aggressive metabolic products, the formation of biocements of various composition is shown in the works (Zavarzin 1972; Glazovskaya and Dobrovolskaya 1984; Bolotina and Sergeev 1987; Dashko and Shidlovskaya 2012; Dashko et al. 2014; Frank-Kamenetskaya and Vlasov 2014 and others).

Currently, the study of microorganisms in the framework of soil science and geotechnics is being actively conducted at the Gorny National Mineral Resources University (St. Petersburg) under the guidance of Professor R. Ye. Dashko in collaboration with the St. Petersburg State University—Professor D. Yu. Vlasov. When analysing the underground space Dashko et al. (2014) consider microbiota as one of its most important factors. They determined that the negative changes in the composition, state, physical, water and mechanical properties of sandy-clay soils with high level of microbial infestations are associated with the formation of biofilms on their mineral particles as well as filling of a dispersed sediments pore space with

the biomass. As the level of microbial infestation in sandy-argillaceous sediments increases and physical and chemical conditions change (transition from aerobic to anaerobic conditions) the changes are occurring in their grain size distribution. Furthermore, there is a decrease in water permeability and decrease in mechanical properties especially of shear resistance parameters and general deformation module. The formation of aggressive microbiota in the underground space the authors of the monograph (Dashko et al. 2014) attribute to the physicochemical properties of the underground environment, the availability of nutrient substrate, water flow, temperature, aerobic (anaerobic) conditions, properties of building materials, man-made factors that must be considered when predicting the formation of microbiota and its possible impact on structural materials.

Currently, there are no highly effective ways to protect structural materials from biocorrosion since microorganisms have tremendous adaptation capabilities and can sustain vital activity in a wide range of environmental conditions (pH, salinity, temperature, pressure, etc.). However, using the inhibitors, it is possible to significantly reduce the vital activity of most bacteria and micromycetes.

The search for an effective biocidal composition for building materials production and increase in the resistance of materials to biocorrosion is one of the most relevant areas of research today. In this regard, in St. Petersburg State University under the leadership of Dr. Sc. D. Yu. Vlasov to a great extent were examined the biocidal compositions of domestic and foreign manufacturers. Subsequently, they made recommendations on how to work with these drugs (Dashko et al. 2014).

From the above it follows that the activity of microbiological processes depends on many factors and it is difficult to predict. In this regard, the strength characteristics of exhibited soil massif of the cultural layer after its stabilization can significantly change during the improper operation of the underground facility. Due to the fact that the activity of microorganisms is faster than physico-chemical and chemical corrosion processes the primary task was to develop a set of various measures to ensure the reduction of the destructive activity of microorganisms in the stabilized soil massif.

34.2 Materials and Methods

The ever first underground museum in Russia was constructed in Moscow in the territory of the museum "Chambers of Boyars Romanov" in the site of the archaeological excavation in 1990 (Fig. 34.1). Its exposition includes its own archaeological material extracted during two excavations: the ones that took place in 1983–1985 and the one in 2005. The expositions of this museum reconstruct a look of an ancient site of Moscow, Zaryadye and the estate of boyars Romanov of the XVI century (Fig. 34.2). In the body of an exposition is the ruined cook-stove of the XVI century which was a part of the yard of Romanov (Fig. 34.3). One more unique object is so-called "a window into the past" which demonstrates a part of a wall of the archaeological excavation which is chemically stabilized in situ in 1988 (Abramova and Voronkevich



Fig. 34.1 The archeological excavation on the territory of the museum "Chambers of Boyars Romanov"



Fig. 34.2 The archaeological findings in show-windows of the museum

1979; Abramova 2012). In the soil part of this archaeological monument (cultural layer of the XVI-XVII century), one can see the remains of the construction material (brick and "a white stone") as well as ceramics, bones, etc. (Fig. 34.4).

In order to ensure a safety of the described objects, regular observations of the museum were conducted starting from the year 1990. The archaeological monuments were preserved in a good condition up until 2005. By this time, more than ten years have passed after the first archeological excavations and there was a need for more research. This time new archeological excavations were conducted inside the underground museum in the summer of 2005. More than 13 cubic meters of soil



Fig. 34.3 Cook-stove of the Romanov boyars (16th century)

were removed. The remaining soil was kept in the museum for a long time (until late in the fall). As a result of the research, archeologists have cleaned the cook-stove of the XVI century. Consequently, the new exposition has been created, which includes the scientific reconstruction of the cook-stove (Fig. 34.5).

The analysis of the observed objects' condition during the time period until 2005 showed that this choice of preservation of the exhibits in the museum is the optimal one. So, the average annual humidity was 60% and the temperature 10 °C (Fig. 34.6). The second excavations (carried out indoors) which included the excavation of the anthropogenous soil thickness, situated more than three meters below the surface, in the absence of ultraviolet rays have promoted constant increase in average annual relative humidity (up to 85%). Moreover, during a process of preparation for a new exposition in the museum the heating devices were turned on, which led to the rise in temperature indoors. Such sharp fluctuations of temperature and humidity within a time period of only two years led to the loss of stability of the ruined brick home cook-stove of the XVI century and to the exposure of soil basis. As a result, there was a partial collapse of soil in the cultural layer and in a brick masonry of the stove. In this regard, there was a need for an urgent chemical stabilization of this archaeological object in situ, which was performed in 2007 (Fig. 34.7) (Abramova 2012; Abramova and Voronkevich 1979; Abramova et al. 1987).

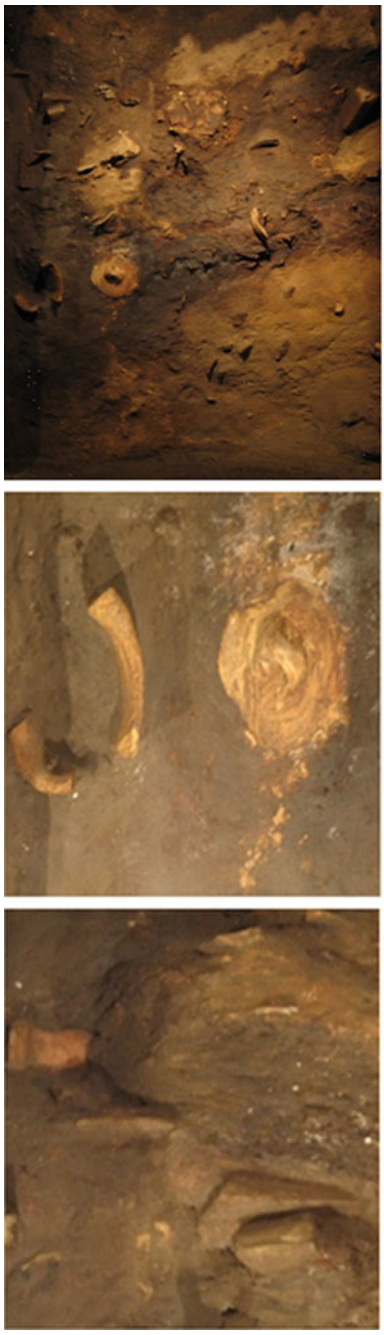


Fig. 34.4 "The window into the past"

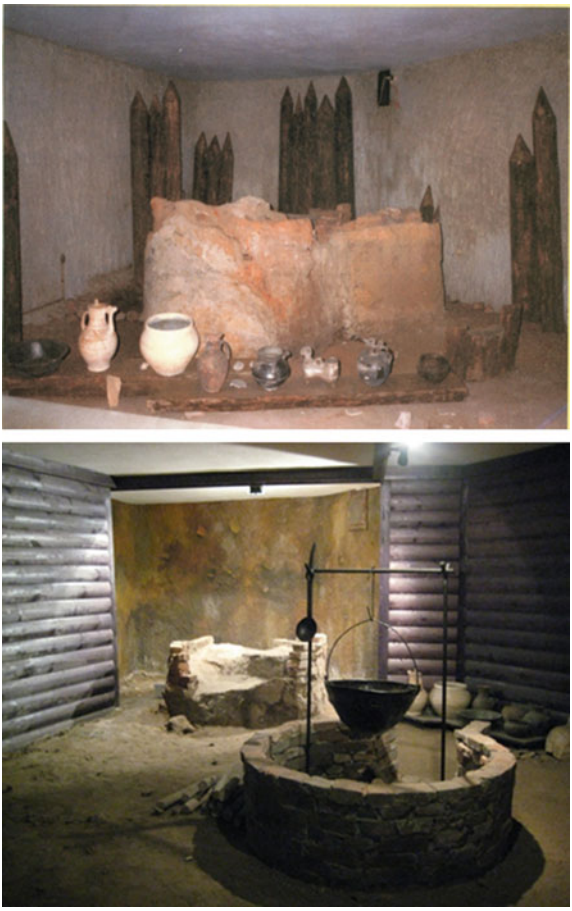


Fig. 34.5 The exhibit of the underground museum: **a** before reconstruction (2005); **b** after reconstruction (2006)

The disbalance in the stability of the soil in the cultural layer and temperature and humidity conditions in this underground space has created favorable conditions for the intensive microbiota development. The products of the microbic activity were visible in the form of a huge congestion of fungal colonies composed of mycelium on the whole surface of the exhibited monument "the window into the past".

Moreover, the results of the research have demonstrated a high degree of contamination of all objects situated in the show-windows of the underground museum (10–100, CFU/cm). Professor Vlasov DY. (Dr.Sci.Biol., St. Petersburg University) has found a mold fungi in almost all the samples. The dominating types were *Penicillium canescens*, *Aspergillus glaucus*, *Aspergillus ustus*; *Rhodococcus* sp. known as biodestructors of construction materials.

An electron microscope research of the exhibited limestone sarcophagus fragment has showed that all its surface is permeated with threadlike and amorphous cultures which grow from partially dissolved grains of calcite (Fig. 34.8).

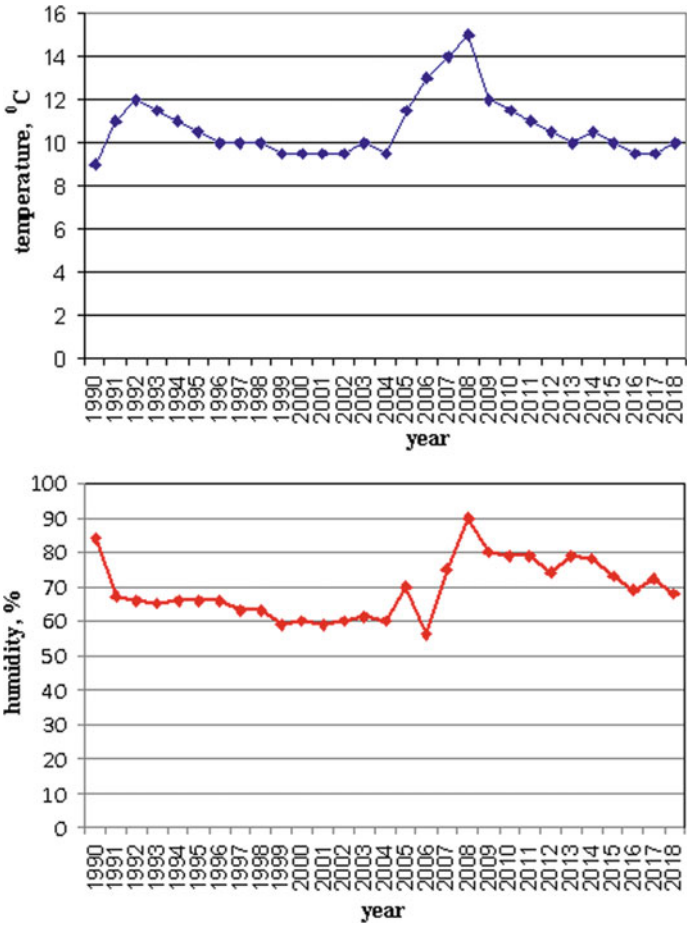


Fig. 34.6 Annual average temperature and humidity in the Underground museum (1990–2018)

It is known that the aggression of a microbiota in the underground space directly depends on temperature and humidity. Therefore, we tried to fight against the increase in humidity, which reached its record value of 100% during a few months in 2008. For these purposes, we used a mobile dehumidifier of REMKO ETF 300–500 air and now humidity fluctuates within the limit of 60–72%.

The control of microbiota in the air was carried out with bactericidal air recirculator "UVR-Mi". Besides this, to eradicate the mold fungi we used biocides in wide assortment which are issued by the Russian and foreign enterprises and can be used on the cultural layer indoors. These are the following: sodium fluoride, hydrogen peroxide, "OLYMP. Stop-mold (JSC Descartes), "Tefleks. Antiplesen" (JSC Soft Protektor), "Tefleks. Restavrator" (JSC Soft Protektor), "Mipor" (JSC NPK STRIM), "Aseptic" (NPF of "Stroymost"), Porocide (Germany). In selection of the



Fig. 34.7 Cook-stove before and after a chemical conservation

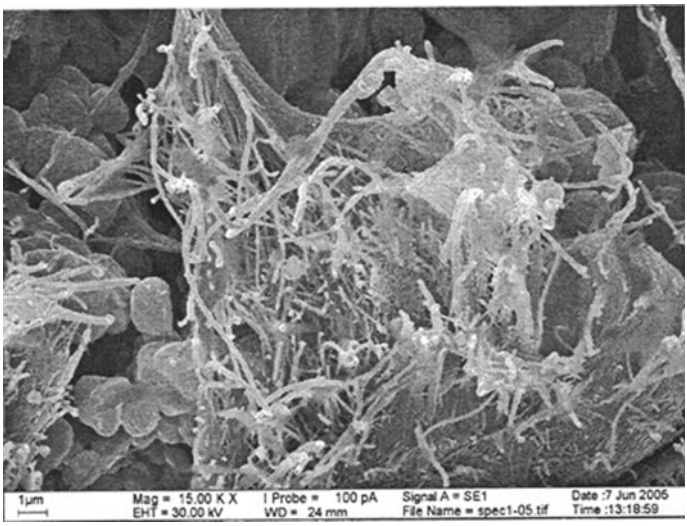


Fig. 34.8 Microstructure of the limestone sample (fragment of the sarcophagus)

most effective biocidal composition, the following requirements should be made: (1) the biocide has a direct effect on specific groups of microorganisms in the underground space, the selection of such groups should be done on the basis of a specialized microbiological research, (2) the ability to maintain its biocidal properties during a specified lifetime of constructions, and be physico-chemically and biochemically stable under the conditions of use, (3) low environmental toxicity and the lack of corrosion aggressiveness in respect to construction materials, (4) simple and easy to use, manufacturability, (5) low cost (Dashko et al. 2014).

We have discovered that in our case the most active biocide, which restricted the reproduction of microorganisms was "Aseptic". In Fig. 34.9, for example, we can see the effect of this solution on one of the colonies of microorganisms on the cultural layer around the cook-stove. All these undertakings allowed us to keep the microbial contamination in the museum at the acceptable level until July, 2012.

However, after a few months we have observed a severe fall of the disperse particles of soil in the archaeological object "the window into the past". It is known that biodamages usually become apparent at a stage of active biodegradation. This is due to the fact that bactericidal and fungal communities adapt to the new conditions over time and continue to multiply despite the deficiency of nutrients. Scientist have discovered earlier that in the absence of nutritious elements, bacteria are capable of extracting them, first of all, by destroying the alymo-silicate part of soil, i.e. clay minerals (Root et al. 1982; Zlochevskaya 1984; Dashko et al. 2014). Mold fungi, sprouting by hyphes into the spores and capillaries of archaeological objects, cause cracking of the surface layer.



Fig. 34.9 Fungi before and after chemical treatment

34.3 Results and Discussion

The damage to the archaeological objects by mold fungi in the underground premises led to the sharp increase of fungi spores in the air which can adversely affect the health of the museum staff as well as the visitors (Hansivarova 2014). In order to assess the scale of fungi damage of the archaeological objects, a full analysis of the museum's condition was performed by the microbiologist Petushkova Yu. A from the biology faculty of MSU. Three most vulnerable zones were chosen: 1—the zone

near the object "the window into the past"; 2—around the house stove; 3—near the exposition show-windows. From each of these, two samples were taken for the PYG and Chapek media (Fig. 34.10). In addition, microorganisms were also established at the archaeological sites. The sampling sites have later repeated this scheme for the purpose of comparative quantitative microbiological analysis.

The results, presented in Table 34.1, showed a high and extremely high level of a microbial contamination (up to 4720, CFU/m^3 of air on the PYG media and 3780 CFU/m^3 of air on Chapek media). The microbiological analysis of samples from all archaeological sites also showed an extremely high degree of microbial contamination, reaching the values of 7.5×10^4, CFU/1 g of sample. It was determined that the species composition of fungi and bacteria contained in the air and on archaeological objects is of the same type, this presented in Table 34.2. *Penicillium* sp. and *Aspergillus* sp. are dominant among them.

The identified species are known as biodestructors of various materials, and some of them are pathogenic and conditionally pathogenic (Kashkin et al. 1979; Lugauskas et al. 1987; Sutton 2001). The fungi growing in the stratum and on the surface of an archaeological object, even if not pathogenic by nature, can acquire parasitic properties and even cause infections once they are in the human body. For example, *Aspergillus* sp. is the genus of the highest mold fungi, widespread in nature, and very resistant to the external environment. The activity of these microorganisms is associated with aspergillomycosis, a wide range of dangerous diseases for humans which can lead to a lethal outcome (Brockhaus and Efron 1996).



Fig. 34.10 Air sampling scheme in the underground museum

Table 34.1 The results of the microbiological air analysis of the premises of the underground museum

№№ of samples	Microbial number (CFU/m^3 of air), PYG environment			Microbial number (CFU/m^3 of air), Capek's environment		
	Bacteria	Micromycetes	Total	Bacteria	Micromycetes	Total
1	3264 ■	1456	4720 ■	254	3526 ■	3780 ■
2	282 ■	978	1260 ■	23	1877 ■	1900 ■
3	234 ■	2266 ■	2500 ■	21	1139	1160 ■

The degree of a microbial contamination of air: ■—acceptable, ■—high, ■—extremely high
Places of sampling are specified in the text

Table 34.2 The microorganisms in the air samples of the premises of the underground museum

№№ samples	Microscopic fungi	Bacteria
1	*Penicillium* sp., *Aspergillus* sp.	*Bacillus* sp., *Rhodococcus* sp.
2	*Penicillium* sp., *Aspergillus* sp., *Cladosporium* sp.	*Bacillus* sp., *Rhodococcus* sp., *Micrococcus* sp.
3	*Penicillium* sp., *Cladosporium* sp.	*Bacillus* sp.

Pathogenic types of *Penicillium* sp. cause human diseases known as penicillinoses. People who have inclination towards allergic reactions can experience allergies in the form of asthmatic bronchitis and bronchial asthma (Fradkin 1978).

Some representatives of a spore-forming soil bacterium of *Bacillus* sp. produce enterotoxines that cause toxic infections in a human body (one of these is the anthrax pathogen) (Steyner et al. 1979).

Thus, a sharp increase of microbiota, instability of temperature and moisture conditions indoors were the main reasons for a destructive action on the exhibited archaeological collection in the museum. Such catastrophic situation in the museum demanded its urgent closing for visitors and an effective disinfection in all the premises. The process of disinfection was successfully carried out by means of only the ultra-violet bactericidal irradiators "UFOBAKT" (floor and wall), developed by N. N. Novikov, a Doctor of Medical Sciences and academician of the Russian Medical academy. The aero-microbiological examination conducted in March, 2013, has demonstrated that the degree of a microbial contamination in the air in the museum premises has decreased to a considerable extent (micromycetes by 57–140 times; bacteria by 4–56 times), reaching the indicators of the admissible level (280 CFU/m^3 on the PYG media and 140 CFU/m^3 on Chapek media) (Table 34.3).

The archeological object "the window into the past" was cleaned up from the falling disperse soil on the surface and, in addition, it was strengthened by an organic silicate solution which we had been using earlier, and then treated with an antiseptic solution «Aseptiic» before exhibiting again in the museum. Antiseptic solutions

Table 34.3 The results of a comparative microbiological analysis of the premises of the underground museum

№№ samples	Microbic number (CFU/m^3 air) November 2012/March 2013		Change of quantity in comparison with data as of November, 2012	
	Bacteria	Micromycetes	Bacteria	Micromycetes
1	3933/260	2832/20	↓ by 15 times	↓ by 140 times
2	282/5	1877/20	↓ by 56 times	↓ by 95 times
3	234/60	2266/40	↓ by 4 times	↓ by 57 times

were applied to all the archaeological exhibits presented in the show-windows of the museum.

In the result, completing disinfection of the underground museum premise led to safe conditions to preserve archaeological monuments and to conduct excursions. Accordingly, archaeological museum was reopened for visitors in May 16, 2013.

The results of the comparative quantitative microbiological analysis of air samples of the premises performed from July 2014 (Tables 34.4 and 34.5) to August 2015 demonstrated that the situation in the museum can be assessed as satisfactory (Table 34.4). There is no permanent high degree of a microbial contamination in any of the examined monuments.

Analysis of air microbiota and micromycetes on various archaeological objects (ceramics, stone, bones or cultural layer in this underground space) showed the relative stability of their species composition during all the years of research.

The complexity of preservation of archaeological exhibits in the museum is due not only to the quantity and aggression of the microbiota but also to temperature and moisture conditions of the underground premises. Therefore, for the sake of

Table 34.4 The results of the microbiological air analysis of the premises of the underground museum

№№ samples	Microbial number (CFU/m^3 of air) on PYG media			Microbial number (CFU/m^3 of air) on Chapek media		
	Bacteria	Micromycetes	Total	Bacteria	Micromycetes	Total
1	5	320	325	10	250	260
2	20	180	200	5	240	245
3	189	651	840	5	60	65

Table 34.5 The microorganisms in the air samples of the premises of the underground museum

№№ samples	Microscopic fungi	Bacteria
1	*Penicillium* sp., *Aspergillus* sp., *Rhizopus* sp.	*Bacillus* sp.
2	*Penicillium* sp., *Aspergillus* sp.	*Bacillus* sp.
3	*Penicillium* sp., *Rhizopus* sp., *Aspergillus* sp.	*Bacillus* sp., *Micrococcus* sp.

protection and preservation of archaeological monuments it is necessary to continue maintaining humidity within limits and supressing the aggressiveness of the microbiota in this underground space.

34.4 Conclusion

1. It is shown that the preservation of the objects exhibited in these underground conditions is significantly affected by the moisture factor.
2. Not meeting specific temperature and humidity conditions in the underground museum contributes to the rapid growth and development of biodestructors, the accumulation of the aggressive potential of microorganisms.
3. It was discovered that the species composition of mold fungi and bacteria contained in the air and at the archaeological objects is of the same type. The dominating species are fungi *Aspergillus* sp., *Penicillium* sp. and bacteria *Bacillus* sp.
4. The destructive impact of aggressive forms of microorganisms requires to take measures to limit their negative impact.
5. To prevent the localization of the development of microbiological activity were selected biocidal materials that provided the exhibition objects with bioresistance under these conditions.
6. Effective disinfection of the entire underground space was possible with ultraviolet germicidal irradiators.
7. The performed environmental monitoring allowed to exhibit unique archaeological objects in the museum for 28 years.

References

Abramova TT (2012) Conservation of the occupation layer soil in the underground archaeological museum of Moscow. Protection of cultural heritage: problems and solutions. ICOMOS Mater 3:63–74 (in Russian)

Abramova TT (2018) Silication of structurally unstable soils (part 2). Eng Geol 1–2:24–35 (in Russian)

Abramova TT, Voronkevich SD (1979) Composition for soil stabilization. A.s. 700583. SSSR, MPK E01D 3/14, the applicant—Lomonosov Moscow State University, 2617439/29-33, declared 18.05.78, published 30.11.79. Bulletin 44 (in Russian)

Abramova TT, Voronkevich SD (1988) Silication of soils of the occupation layer in the architectural and archaeological monuments of the Northern Black Sea region. Eng Geol 2:44–57 (in Russian)

Abramova TT, Voronkevich SD, Postnikova ON (1987) Composition for soil stabilization. A.s. 1333682, SSSR, MPK E01D 3/14, the applicant—Lomonosov Moscow State University, 3864596/29-33, declared 06.03.85, published 30.08.87. Bulletin 32 (in Russian)

Bolotina IN, Sergeev EM (1987) Microbiological studies in engineering geology. Eng Geol 5:3–17 (in Russian)

Brockhaus FA, Efron IA (1996) Aspergillius. In: Encyclopaedic dictionary, V. II. Russian word, Moscow (in Russian)
Dashko RE, Shidlovskaya AV (2012) Biotic and abiotic components in the underground environment: their genesis and influence on the state and properties of sandy sediments. Notes Min Inst 197:200–215 (in Russian)
Dashko RE, Vlasov DYu, Shidlovskaya AV (2014) Geotechnics and underground microbiota. PI Georeconstruction Institute, St. Petersburg (in Russian)
Fradkin VA (1978) Allergens. Medicine, Moscow (in Russian)
Frank-Kamenetskaya OV, Vlasov DYu (2014) Condition monitoring of stone monuments. Textbook. St-Petersburg State University, St-Petersburg (in Russian)
Glazovskaya MA, Dobrovolskaya NG (1984) Geochemical functions of microorganisms. Moscow State University, Moscow (in Russian)
Hansivarova NM (2014) Microorganisms of disperse kinds as a potential source of threat to human health. Sergeev's readings 16:140–144 (in Russian)
Kashkin PN, Hokhryakov MK, Kashkin AP (1979) The atlas of pathogenic and toxicogenic fungi, as well as fungi harmful for the humans. Medicine, Leningrad (in Russian)
Lugauskas AY, Mikulskene AI, Shlyauzhene DYu (1987) The catalogue of micromycetes which are biodestructors of polymeric materials. Science, Moscow (in Russian)
Radina VV (1973) The role of microorganisms in the formation of soil properties and their stress state. Hydraul Eng 9:22–24 (in Russian)
Root PE, Khlebnikov GM, Bolotina IN, Vorobyova EA, Kolchugin TP, Gorin SB (1982) The number and role of microorganisms in soils. Eng Geol 6:72–78 (in Russian)
Sergeev EM (1978) Engineering geology. Moscow State University, Moscow (in Russian)
Steyner R, Edelberg E, Ingram D (1979) The world of microbes, vol 3. World, Moscow (in Russian)
Sutton D, Fotergill A, Rinaldi M (2001) The atlas of pathogenic and conditionally pathogenic fungi: translation from English. World, Moscow (in Russian)
Zavarzin GA (1972) Lithotrophic microorganisms. Science, Moscow (in Russian)
Zlochevskaya IV (1984) Biodamages of construction materials by microorganisms to atmospheric conditions. Biodamages in construction. In: Abstracts of the conference reports pp 257–271 (in Russian)
Zvyagintsev DG, Babieva IP, Zenova GM (2005) Soil biology: textbook. Moscow State University, Moscow (in Russian)

Chapter 35
Biocorrosion in the Central Heating System



Yulia S. Simakova and Liubov V. Leonova

Abstract The results of this investigation of technogenic minerals—compounds that formed as sediment at the fittings of hydronic heating system—are presented. The morphology, mineralogy and surface chemistry of the matter were studied by X-ray diffraction, X-ray fluorescence spectroscopy, scanning electron microscopy and energy dispersive X-ray spectroscopy. The results of this investigation provide clear evidence that hydronic heating systems have been found to support a breeding ground for bacteria associated with microbiologically influenced corrosion (MIC). Particles of neoformed compounds are crystallized in wide variety of forms: Zn minerals are presented by tabular crystals of several generations, spheres, spherical aggregates and biomorphs on the bacterial cells that probably activated fitting corrosion and promoted Zn sedimentation as sphalerite, wurtzite, hemimorphite and other Zn minerals. The formation of zinc compounds can occur both biogenically and abiogenically. Microbiologically influenced corrosion can lead to destruction of hydronic heating system elements.

Keywords Zinc minerals · Fitting · Spherical aggregates · Hydronic heating · Bacterial activity · Corrosion

35.1 Introduction

The formation of metal sulfides (especially nanoscale) is of great interest both from the point of view of studying the geochemical cycles of elements in nature, mineral formation processes (including biominerals), formation of mineral deposits and microbiologically influenced corrosion (MIC) (Vernigorova et al. 2007; Clark and Clark 2004; Moreau et al. 2004; Xu et al. 2016). The popularity of these objects

Y. S. Simakova (✉)
Institute of Geology, Komi Science Center, Urals Branch of RAS, Syktyvkar, Russia
e-mail: yssimakova@rambler.ru

L. V. Leonova
Institute of Geology and Geochemistry, Urals Branch of RAS, Yekaterinburg, Russia
e-mail: lvleonova@yandex.ru

© Springer Nature Switzerland AG 2020

O. V. Frank-Kamenetskaya et al. (eds.), *Processes and Phenomena on the Boundary Between Biogenic and Abiogenic Nature*, Lecture Notes in Earth System Sciences,
https://doi.org/10.1007/978-3-030-21614-6_35

is caused by their wide distribution in natural and anthropogenic systems. The precipitation of metal sulfides as a result of microbial sulfate reduction is one of the most important processes in aqueous metal reduction in highly metal-contaminated organic-rich sediments (Labrenz and Banfield 2004; Medas et al. 2017). Sulfate-reducing microorganisms play pivotal role in the precipitation and persistence of Zn, Cd, Fe, Pb sulfides by lowering redox potential in microsites in an otherwise oxidative environment (Smieja-Król et al. 2015). Synthesis of semiconductor particles of ZnS using bacterial activity is also of great importance (Bai et al. 2006). Although sulphate-reducing bacteria are acknowledged as major contributors to the precipitation of metals by producing of H_2S Webb et al. (1998) suggests involvement of other biological mechanisms of metal removal.

Also microparticles of metal sulphides were found in industrial and domestic wastewaters and sump tanks that permit to suggest that sulphidization is the main deposition process for metals dissolved in engineering systems (Lombi et al. 2012; San et al. 2013). Cases of microbiologically induced corrosion of brass parts in heating systems are also common (Clark and Clark 2004) and in that cases copper ions do not inhibit the development of microorganisms in the system as it is expected (Vernigorova et al. 2007). Microbiologically-influenced corrosion of metals can be caused by: (1) by consuming oxygen, the cathodic reactant, (2) by increasing the mass transport of the corrosion reactants and products, therefore changing the kinetics of the corrosion process, (3) by generating corrosive substances and (4) by generating substances that serve as auxiliary cathodic reactants (Borenstein 1994).

In this paper, we describe the occurrence of micron- and submicron-sized Zn compounds apparently precipitated due to the microorganisms' activity in a hydronic heating system.

35.2 Materials and Methods

The objects of our research were the sediments that have been formed in the brass fittings of the open-loop hydronic heating system. At the end of the heating season the adjusting tap located at the butt-end of the heat battery was damaged. A year later a similar accident occurred with another fitting of the same heating system. We found that the details were corroded and the cream-colored powder sediment was deposited in the internal cavities of the fittings and pipes (Fig. 35.1).

Sediment and fitting metal were analyzed by a complex of methods. Element concentrations were determined by X-ray fluorescence spectroscopy (XRF) on Shimadzu XRF-1800 wave spectrometer (analyst S. Neverov, IG Komi SC UB RAS).

X-ray powder diffraction (XRD) was used for the identification of major mineral phases. Analyses were performed using the Shimadzu XRD-6000 diffractometer (CuKα radiation) under the following operating conditions: voltage 30 kV, current 30 mA, scanning interval 2–72° 2θ and a step size of 0.05° 2θ.

The morphology of the surface and elemental composition of precipitater was studied using scanning electron microscopy (SEM) (JSM-6390LV JEOL) and energy



Fig. 35.1 Corrosion area on a section of a fitting with precipitate on the surface

dispersive spectrometry (EDS) (Inca Energy 450, IG Ural Branch RAS). Sample was air-dried, carbon-coated and investigated by high-vacuum mode under conditions necessary for X-ray microanalyses, backscattered electron (BSE), and secondary electron (SE) imaging with maximal resolution 2 nm.

35.3 Results and Discussion

The fitting alloy was corroded and contaminated on the surface by the powder precipitate. The corroded areas appear to be porous, suggestive of selective leaching of a specific phase in the microstructure (Fig. 35.1). XRF analysis shows that Zn and Cu are predominated in alloy composition where the content of Zn is 54.26% and Cu is 21.90%. In addition nickel and chromium included in the coating of the detail (Ni—6.99%, Cr—1.17%) as well as S—3.87, Si—3.40, Al—3.12, Ca—1, 42, K—1.79 and Fe_{tot}—0.60% are present in the alloy. The chemical composition of the precipitate according to the XRF results is: ZnO—61.97%, SO_3—18.75%, SiO_{2-7}.61%, Al_2O_{3-6}.31%, Fe_2O_{3tot}—0.61%, MgO—3.05%, CaO—0.68%, K_2O—0.07%, CuO—0.87%, NiO—0.03%. The finding of elevated zinc and sulfur levels in the corrosion product is conditioned by selective leaching and MIC scenarios for Zn-Cu alloys (Clark and Clark 2004).

The mineral phase composition of sediment from the first fitting according to X-ray analysis was represented by two modifications of ZnS—wurtzite (hexagonal modification) and sphalerite (cubic modification) with a small addition of hemimorphite $Zn_4Si_2O_7$ $(OH)_2$ (Fig. 35.2a). Similar data were obtained by other researchers (Castillo et al. 2012; Wu et al. 2009; Xu et al. 2016) during the synthesis of ZnS with organic substances. It is known that wurtzite is a high-temperature modification that is stable at $t > 1000$ °C but it can be proposed that the presence of organic matter makes the wurtzite structure stable at lower temperatures. Experiments (Zhang et al. 2000)

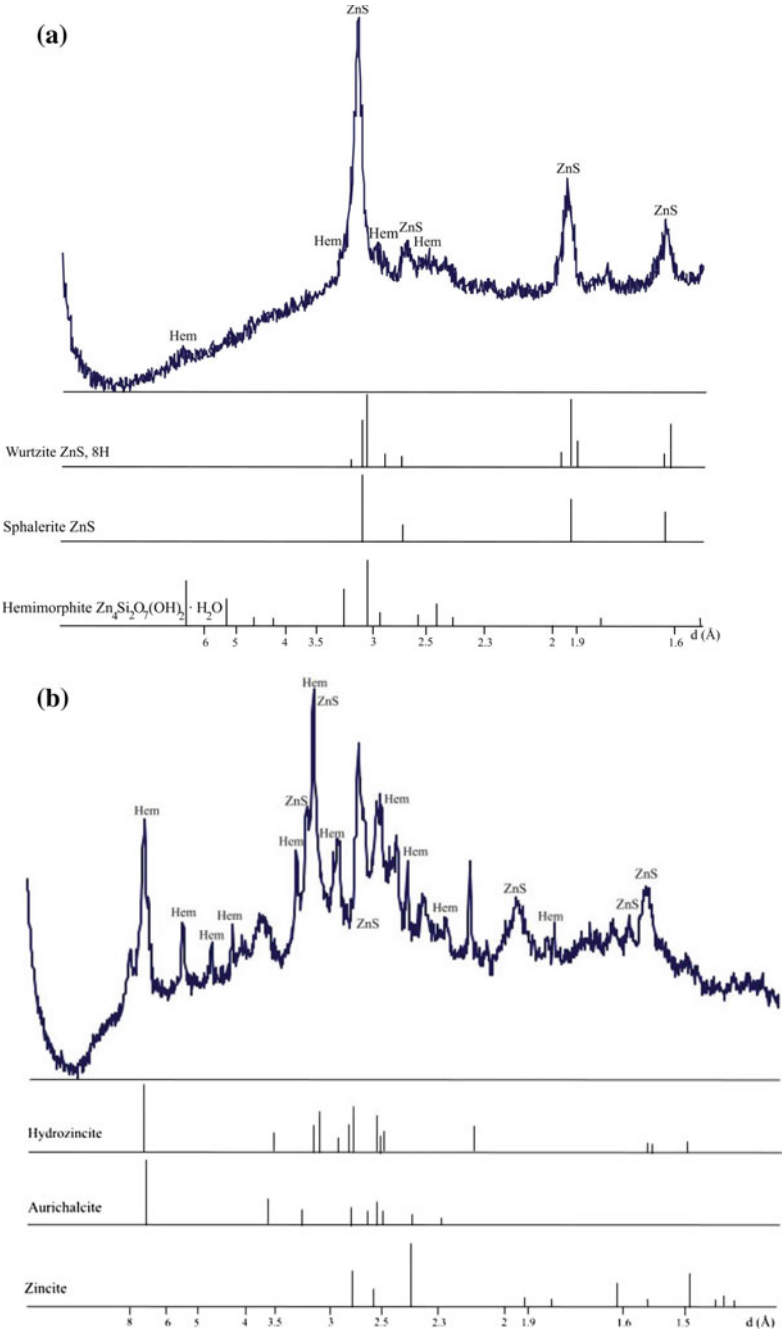


Fig. 35.2 X-ray diffraction patterns of a precipitate from fittings: **a** first fitting, **b** second fitting. Hem—hemimorphite

showed that the stability of ZnS modifications depends on crystallite size and sorbed water content.

Phase composition of the precipitate from the second fitting is slightly differing from the first one. In addition to previously detected zinc minerals (sphalerite, hemimorphite, wurtzite) some other zinc phases were found. We matched the presence of hydrozincite $Zn_5(OH)_6[CO_3]$, aurichalcite $(Cu,Zn)_5(OH)_6[CO_3]_2$, zincite ZnO, renierite $(Cu^{1+}, Zn)_{11}Fe_4(Ge^{4+}, As^{5+})_2S_{16}$ and probably some other minerals in minor content. This difference of precipitate compositions from different fittings of one hydronic heating system can be caused by water additives in this system. Background line of X-ray pattern is high due to the presence of amorphous matter (Fig. 35.2b).

Reflections of the minerals on XRD patterns are broadened and have low-intensity due to the low crystallinity of the minerals.

When investigating of the sample with the photoluminescence method we observed blue luminescence that is specific for organic components.

On the SEM images of the precipitate we can see large (15–30 μm) tabular elongated hemimorphite crystals, small (2–5 μm) numerous zinc sulfide crystals and deposited on their surface crystals of later generation with a similar form and composition. On the EDS spectra of small crystals (Figs. 35.3b and 35.4b, spectrum 36) the Si signals are lower and S signals are higher than on the EDS spectra of large tabular crystals (Figs. 35.3a and 35.4a) indicating that various zinc minerals are present. Together with the crystals the different spherical aggregates (about 10 μm in diameter) were also observed on SEM images. Spherical aggregates are often associated with accumulations of neoformations that looks like chains of small globules (Fig. 35.3c, d) and are identical in element composition to globular aggregates (Fig. 35.4b, spectrum 37). Some of formations at the SEM images look like as semitransparent slightly segmented cylinders (Fig. 35.3e, f). Their morphology and size make it possible to consider these formations to be the biomorphosis of the element-specific bacteria covers. The different length of the filaments indicates that these were bacteria which cells were capable to form chains. Probably they formed a common mucous cover consisted of polysaccharides that subsequently was encapsulated due to the deposition of metal sulphides.

The presence of both crystallographic forms of Zn compounds and spherical aggregates of zinc sulfide indicates different ways of formation of these phases: biogenic and abiogenic.

Similar zinc sulfide globules have also been repeatedly described in the works of other researchers (Lewandowski and Beyenal 2008; Remoundaki et al. 2008; Liu et al. 2009; Yoon et al. 2012; Medas et al. 2017 etc.) concluded that such ZnS particles formed with the direct or indirect participation of microorganisms. Labrenz and Banfield (2004) showed that ZnS globules were formed in biofilms near the Pb-Zn deposit under the influence of sulfate-reducing bacteria (*Desulfobacteriaceae* family) in a wide temperature range. Investigations (Moreau et al. 2004) proved that biosulphate reduction promotes aggregation and precipitation of biogenic sulphides and the presence of biofilms prevent the mobility of ZnS nanoparticles.

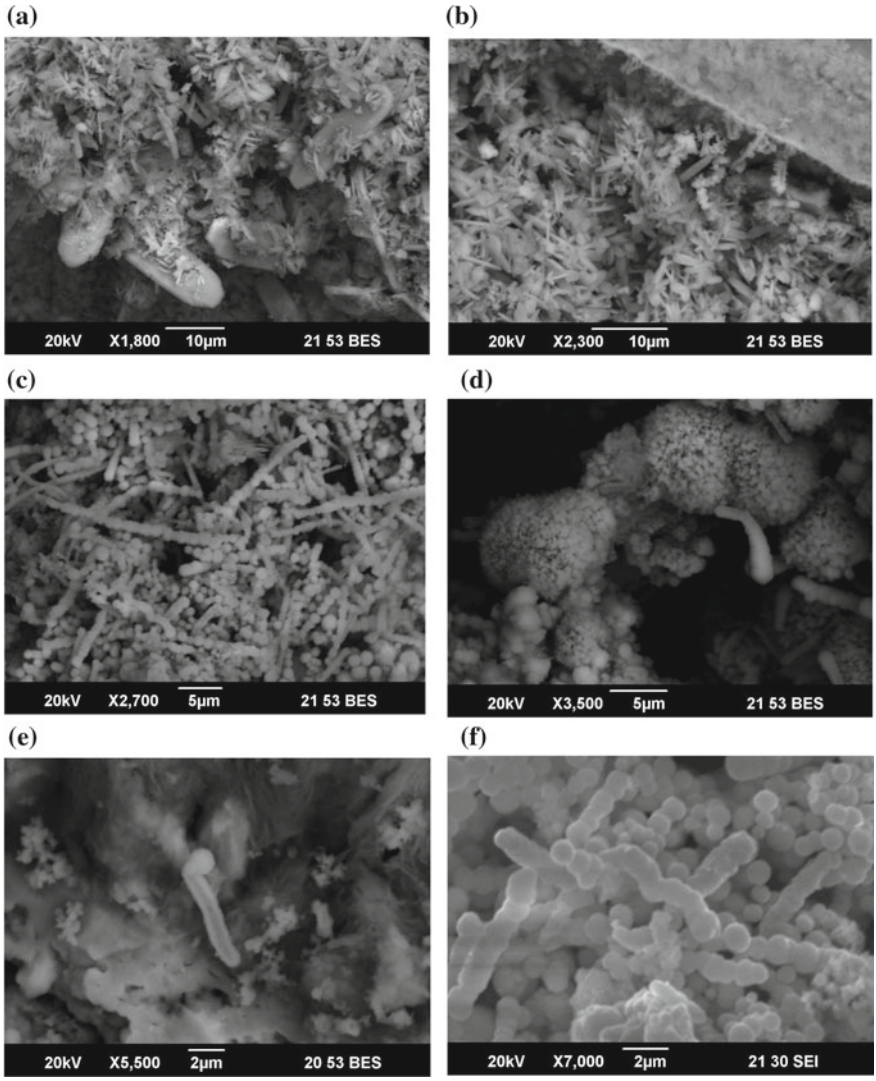


Fig. 35.3 SEM images of precipitate (first fitting): **a** typical surface area with tabular hemimorphite crystals and small crystals of ZnS, **b** several generations of ZnS crystals, **c** chains of ZnS spheres, **d** spherical aggregates of ZnS and mineralized bacterial covers, **e** poor-fossilized bacterial covers (at the image—semi-transparent objects), **f** chains of ZnS spheres

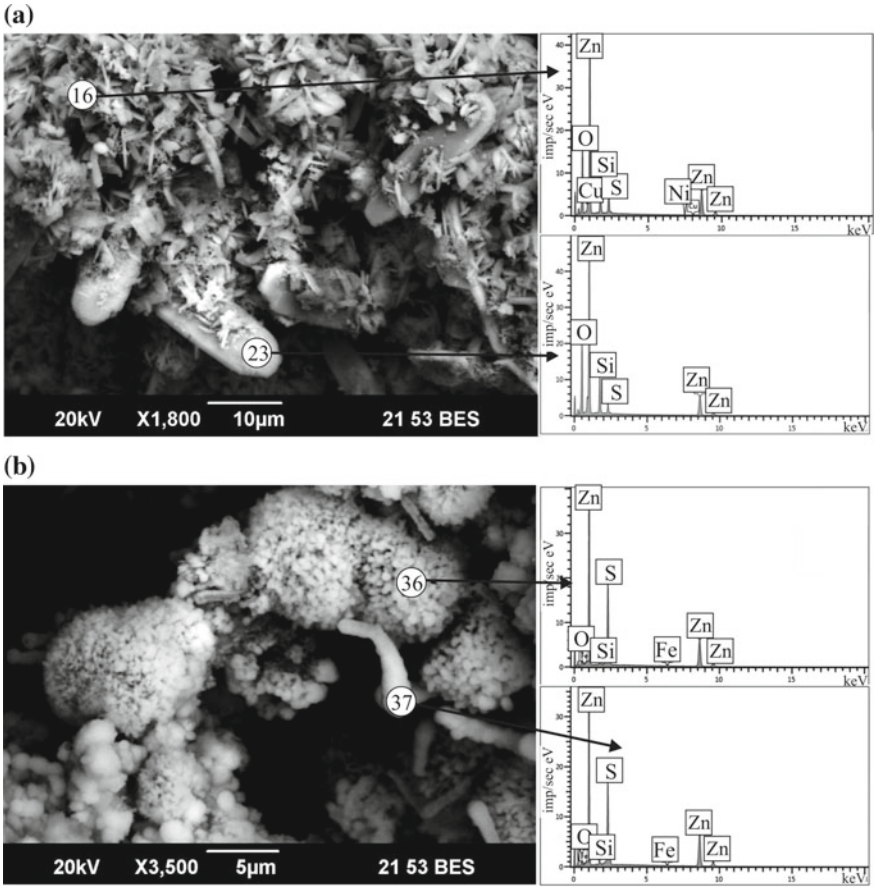


Fig. 35.4 SEM images of: **a** newly formed precipitate, **b** fibrous structure of precipitate. EDS elemental spectra showing the chemical composition of points (**a** 15 and 23, **b** 36 and 37 correspondingly)

Zinc sulfide globules can be formed due to the presence of bonds between zinc sulphide nanoparticles and cysteine-containing peptides secreted by cells (Clark and Clark 2004; Zhilenko et al. 2010). The synthesis of such spherical formations due to the presence of L-cysteine is described by Moreau et al. (2004). It was shown (San et al. 2013) that in different systems particles of ZnS can be of biogenic and abiogenic origin. In biogenic samples the degree of ZnS crystallinity is higher. This fact suggests that metabolites promote the crystallization processes. We can propose that in our sample small ZnS crystals formed abiogenically while the existence of other forms connect with the activity of bacteria.

Besides Zn sulphides we found in the precipitate hemimorphite crystals. According to Medas et al. (2017) biogenic hemimorphite under natural and artificial conditions can to recrystallize forming tabular crystals similar to those we observed in

our sample (Fig. 35.4a). The diffusion of hemimorphite reflexes on a diffraction pattern is caused by the low crystallinity of the mineral and can give as evidence of its primary biogenic nature. Probably hemimorphite was formed in the system initially at low sulfur content and high water temperature.

In the sediment from second fitting besides neoformed zinc sulfides the oxide and carbonate minerals with specific morphology were found. On the SEM image they are represented by hemispherical (Fig. 35.5a) sometimes spherical aggregates with a fibrous structure (Fig. 35.5b). According to the EDS analysis they consist of zinc oxide and carbonate (Fig. 35.5c) Surface of some formations is encrusted with tabular microcrystals creating crystal filament (Fig. 35.5e).

Bacterial fossils with various degrees of mineralization were associated with filaments—all of them are represented by ZnS (Fig. 35.5d). These cylinders may be the bacterial cells encapsulated by zinc sulphide as it is confirmed by the composition resulting from the EDX analysis of their surfaces. Reports of similar results (Remoundaki et al. 2008) indicate that bacterial cell walls appear to be encapsulated by the deposition of metal sulphides on the cell wall surface. Element mapping showed that the distribution of zinc sulphides and oxides is irregular: sulphides form dendrite-like spots in the precipitate (Fig. 35.5f).

The results of our investigation provide clear evidence that city hydronic heating systems have been found to provide a breeding ground for bacteria associated with microbiologically influenced corrosion. In the sediments from heating system Zn compounds are presented by sulfides, oxides, carbonates, silicates with predominance of sphalerite, wurtzite and hemimorphite. Composition of sediment in corroded details of heating system depends on water additives, water temperature and alloy type.

The data presented here highlight the significance of microbial activity in hydronic systems and provide a framework for continued studies of technogenic mineral formation.

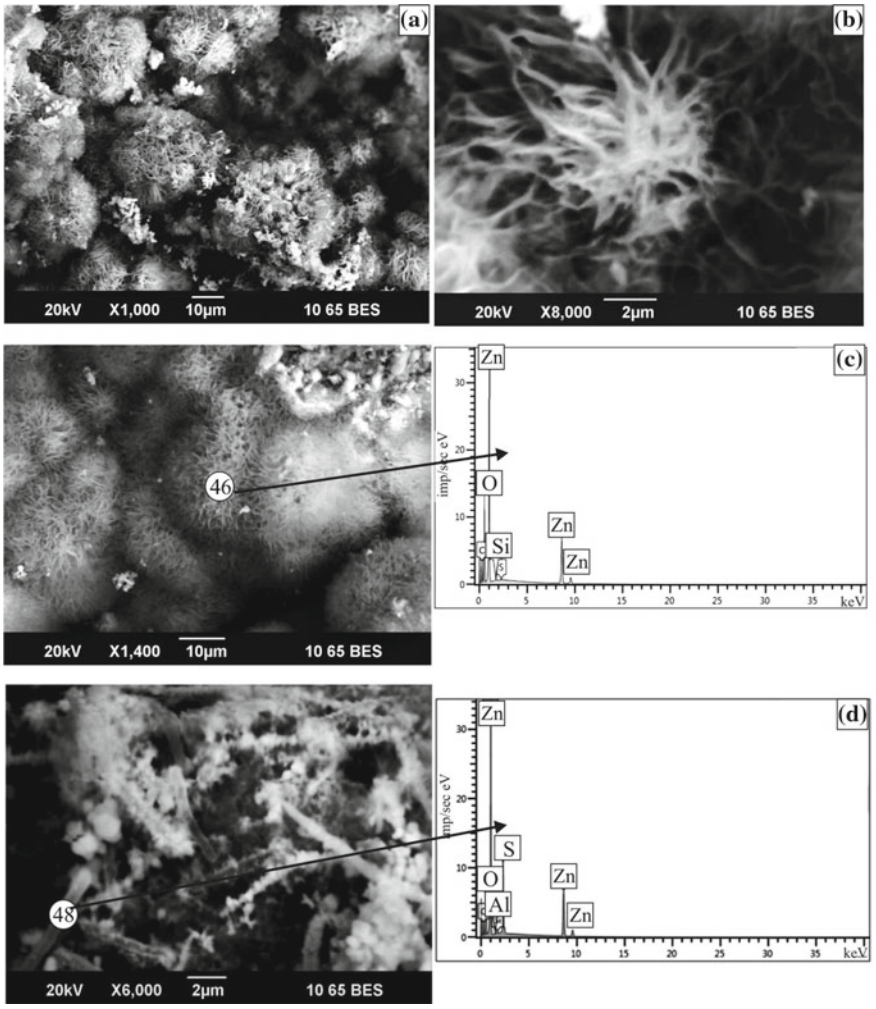


Fig. 35.5 SEM images of precipitate (second fitting): **a** hemispherical and spherical aggregates, **b** spherical aggregates, **c** spherical aggregates with a fibrous structure, **d** mineralized rod-shaped bacterial fossils, **e** tabular microcrystals creating filaments, **f** element mapping of precipitate surface. EDS elemental spectra showing the chemical composition of points (**c** 46, **d** 48, **f** 2 and 8 correspondingly)

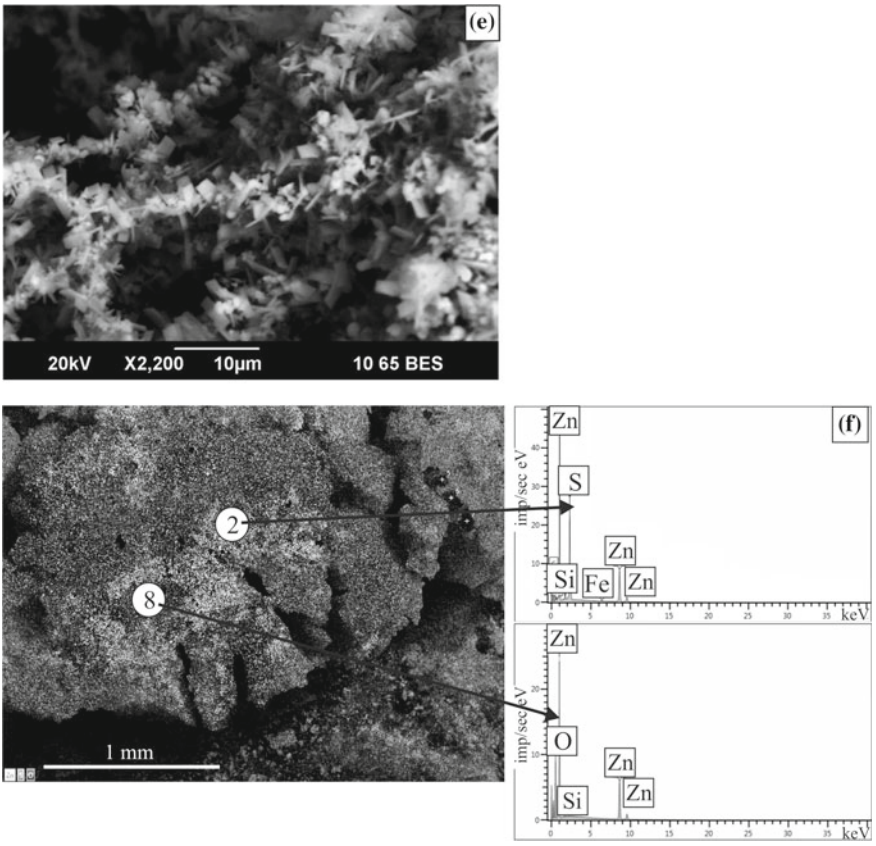


Fig. 35.5 (continued)

35.4 Conclusions

1. Metal parts in heating systems may undergo the microbiologically influenced corrosion especially at high temperature. MIC can lead to destruction of hydronic heating system elements.
2. Details containing zinc are corroded with the formation of sulfides, silicates, carbonates and other Zn compounds. At the same time the copper contained in this alloy is not an inhibitor of the microbial activity in the heating system.
3. Particles of neoformed compounds are crystallized in wide variety of forms: crystals of several generations, spherical globules, filaments and others. Bacterial cells become encapsulated by zinc sulphides as observed by SEM–EDX.
4. The formation of zinc compounds can occur both biogenically and abiogenically.

Acknowledgements This work was supported by the FASO RF (project AAAA-A18-118052590032-6).

References

Bai HJ, Zhang ZM, Gong J (2006) Biological synthesis of semiconductor zinc sulfide nanoparticles by immobilized *Rhodobacter sphaeroides*. Biotechnol Lett 28:1135–1139

Borenstein SW (1994) Microbiologically influenced corrosion handbook. Woodhead Publishing Series in Metals and Surface Engineering

Castillo J, Pérez-López R, Caraballo MA, Nieto JM, Martins M, Costa MC, Olías M, Cerón JC, Tucoulou R (2012) Biologically-induced precipitation of sphalerite–wurtzite nanoparticles by sulfate-reducing bacteria: Implications for acid mine drainage treatment. Sci Tot Env 423:176–184

Clark RA, Clark DR (2004) Microbiologically influenced corrosion in hydronic heating systems. JFail Anal Prev 4:38–42

Labrenz M, Banfield JF (2004) Sulfate-reducing bacteria-dominated biofilms that precipitate ZnS in a subsurface circumneutral-pH mine drainage system. J Microb Ecol 47:205–217

Lewandowski Z, Beyenal H (2008) Mechanisms of microbially influenced corrosion. In: Springer Series on Biofilms. Springer, Berlin, Heidelberg

Liu J, Junfeng M, Liu Y, Song Z, Sun Y, Fang J, Liu Z (2009) Synthesis of ZnS nanoparticles via hydrothermal process assisted by microemulsion technique. J All Comp 486:L40–L43

Lombi E, Donner E, Tavakkoli E, Turney TW, Naidu R, Miller BW, Scheckel KG (2012) Fate of zinc oxide nanoparticles during anaerobic digestion of wastewater and post-treatment processing of sewage sludge. Environ Sci Technol 46:9089–9096

Medas D, Podda F, Meneghini C, De Giudici G (2017) Stability of biological and inorganic hemimorphite: Implications for hemimorphite precipitation in non-sulfide Zn deposits. Ore Geol Rev 89:808–821

Moreau JW, Webb RI, Banfield JF (2004) Ultrastructure, aggregation-state and crystal growth of biogenic nanocrystalline sphalerite and wurtzite. Amer Min 89:950–960

Remoundaki E, Kousi P, Joulian C, Battaglia-Brunet F, Hatzikioseyian A, Tsezos M (2008) Characterization, morphology and composition of biofilm and precipitates from a sulphate-reducing fixed-bed reactor. J Haz Mats. 153:514–524

San NO, Nazır H, Dönmez G (2013) The effect of *Aeromonas eucrenophila* on microbiologically induced corrosion of nickel zinc alloy. Int Biodet Biodeg 80:34–40

Smieja-Król B, Janeczek J, Bauerek A, Thorseth IH (2015) The role of authigenic sulfides in immobilization of potentially toxic metals in the Bagno Bory wetland, southern Poland. Environ Sci Pollut Res Int 22:15495–15505

Vernigorova VN, Korolev EV, Eremkin AI, Sokolova YA (2007) Corrosion of building materials. «Paleotip», Moscow (in Russian)

Webb JS, McGinness S, Lappin-Scott HM (1998) Metal removal by sulphate-reducing bacteria from natural and constructed wetlands. J Appl Microbiol 84:240–248

Wu X, Li K, Wang H (2009) Facile synthesis of ZnS nanostructured spheres and their photocatalytic properties. J All Comp 487:537–544

Xu J, Murayama M, Roco CM, Veeramani H, Michel FM, Rimstidt JD, Winkler C, Hochella MF Jr (2016) Highly-defective nanocrystals of ZnS formed via dissimilatory bacterial sulfate reduction: a comparative study with their abiogenic analogues. Geo Cosm Acta 180:1–14

Yoon S, Yáñez C, Bruns MV, Villegas NM, Martínez CE (2012) Natural zinc enrichment in peatlands: biogeochemistry of ZnS formation. Geo Cosm Acta 84:165–176

Zhang H, Huang F, Gilbert B, Banfield JF (2000) Molecular dynamics simulations, thermodynamic analysis, and experimental study of phase stability of zinc sulfide nanoparticles. J Phys Chem 107:13051–13060

Zhilenko MP, Lupandina KV, Ehrlich HV, Lisichkin GV (2010) Preparation of copper and zinc sulfide nanoparticles and their modification with cysteine. Rus Chem Bull 59:1307–1311

Chapter 36
Microbiology of the Laetolil Tuff 7 with 3.66 Ma *Australopithecus Afarensis* Footprints, Ngorongoro Conservation Area, Tanzania

Anatoly N. Zaitsev, Dmitry Yu. Vlasov, Marina S. Zelenskaya, Olga A. Zaitseva, Olga A. Pavlova, Anton R. Chakhmouradian, Anton I. Savchenok, Larissa Leach, Michael Leach and Joshua Mwankunda

Abstract East Africa is one of the most important paleoanthropological localities on Earth. Laetoli and Olduvai Gorge (Tanzania) are among the world's premier areas for *Australopithecus afarensis, Paranthropus boisei,* and *Homo habilis* remains. Laetoli is also unique in its preservation of footprint trails within Tuff 7 left by *Australopithecus afarensis*. Tuff 7 has been studied to characterize microorganisms living inside these tuffs and to estimate their potential involvement in destructive processes; 35 species of microfungi, as well as sterile white and dark mycelia were identified by

A. N. Zaitsev (✉) · A. I. Savchenok
Department of Mineralogy, Saint Petersburg State University, 7/9 University Emb., Saint Petersburg 199034, Russia
e-mail: a.zaitsev@spbu.ru

D. Yu. Vlasov · M. S. Zelenskaya
Saint Petersburg State University, 7/9 University Emb., Saint Petersburg 199034, Russia

A. N. Zaitsev
Image and Analysis Centre, The Natural History Museum, Cromwell Road, London SW7 5BD, UK

O. A. Zaitseva
The Manege, Central Exhibition Hall, 1 Isaakiyevskaya Square, Saint Petersburg 190000, Russia

O. A. Pavlova
Beagle Ltd., 152-1-77, Bukharestskaya St., Saint Petersburg 192289, Russia

A. R. Chakhmouradian
Department of Geological Sciences, University of Manitoba, Winnipeg R3T2N2, Canada

L. Leach · M. Leach
GMP Consulting Engineers Ltd., 19 Haile Selassie Road, P.O. Box 425, Arusha, Tanzania

J. Mwankunda
Ngorongoro Conservation Area Authority, Ngorongoro Crater, P.O. Box 1, Arusha, Tanzania

O. A. Pavlova
Resource Center "Development of Cellular and Molecular Technologies", Saint Petersburg State University, 7/9 University Emb., Saint Petersburg 199034, Russia

© Springer Nature Switzerland AG 2020

O. V. Frank-Kamenetskaya et al. (eds.), *Processes and Phenomena on the Boundary Between Biogenic and Abiogenic Nature*, Lecture Notes in Earth System Sciences,
https://doi.org/10.1007/978-3-030-21614-6_36

cultural method. The results of the metagenomic analysis show that anamorphic ascomycetes are the predominant group in all samples. They occur as hyphae and mycelia inside the tuffs, and are concentrated in pores, microcracks and cavities. The number of micromycetes is moderate (up to 7000 CFU per gram of substrate). Typical cultivated microfungi are from genera *Aspergillus* and *Fusarium*. They are known as active destructors of natural and artificial substrates and can colonize building materials. Molecular genetic methods revealed a large group of different bacteria (23 phyla) within the tuff. The microbiota consists mostly of Actinobacteria, Proteobacteria, Bacteroidetes and Cyanobacteria. Their relative distribution shows the preferential occurrence of Bacteroidetes in the upper part of stratigraphic sections (soil), and concentration of Actinobacteria and Proteobacteria within the tuffs. Exposure of the Footprint tuff could lead to the development of photosynthetic microorganisms (Cyanobacteria). We conclude that microbiological activity within the study area appears to be moderate and the Footprint Tuff does not presently require any treatment with biocides. However, the presence of black biofilms on the surface of the Footprint conservation mound concrete shows that biodestruction does occur.

Keywords *Australopithecus afarensis* · Footprint · Tuff · Microfungi · Bacteria · Laetoli · Tanzania

36.1 Introduction

East Africa is one of the most important and key paleoanthropological and paleontological localities on Earth (Cela-Conde and Ayala 2007). The Laetolil beds and closely located Olduvai Gorge (northern Tanzania) are among the world's premier localities for *Australopithecus afarensis, Paranthropus boisei,* and *Homo habilis* remains, as well as for numerous non-hominin fossils (Fig. 36.1) (Tobias 1967; Harrison 2011).

The earliest lithic culture, the Oldowan, was first described at Olduvai Gorge. It was suggested that carbonatite (or natrocarbonatite) volcanism in that part of the East African Rift had been a key factor in the excellent preservation of fossilized remains at such paleoanthropological sites as Napak (Uganda), Songhor and Koru (Kenya), and Laetoli (Hay 1986). Laetoli is also unique in its preservation of footprint trails within Tuff 7 (also known as Footprint Tuff) left by *Australopithecus afarensis*, age-dated to about 3.66 Ma (Deino 2011). These are perhaps the earliest direct evidence of hominin bipedalism.

In line with plans of the Ngorongoro Conservation Area Authority of Tanzania to create the Laetoli Footprints Museum we have studied the Laetolil Tuffs, including geology, mineralogy, geochemistry (Zaitsev et al. 2015), physical and mechanical properties, as well as microbiology of these rocks. The latter has become an essential part of studies focused on cultural heritage objects prior to their conservation and/or restoration (May et al. 2008; Mitchell and McNamara 2010). Natural stone

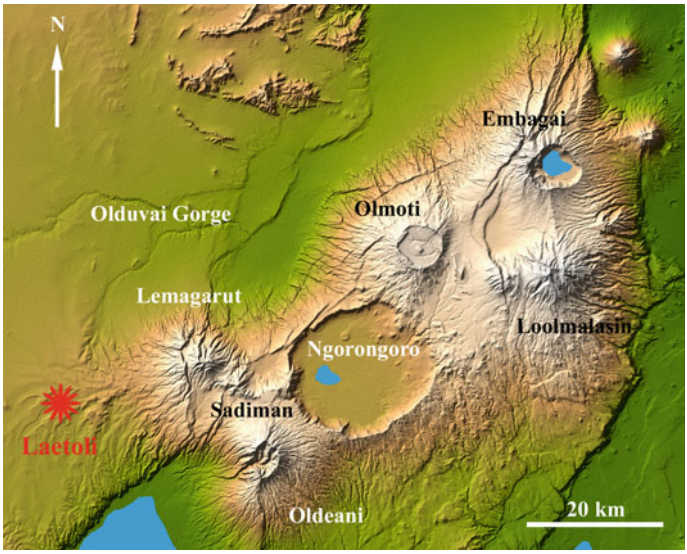


Fig. 36.1 Satellite image of the Crater Highlands area and Serengeti Plain (shaded and coloured SRTM elevation model, February 2000)

and artificial construction and building materials (e.g., concrete) can be a suitable environment for microorganisms (particularly bacteria), fungi and lichens, to live and reproduce under favourable conditions (i.e. temperature, humidity and pollution). Biodeterioration and stone decay due to the activity of microorganisms are well documented for modern and ancient buildings, monuments, sculptures, etc. It is also common to observe microorganisms on the surface on natural rocks of any composition. The purpose of a microbiological study of the Laetolil tuffs was to characterize microorganisms living inside these tuffs, under and over the Footprint Tuff, and to estimate their potential involvement in destructive processes.

36.2 Materials and Methods

36.2.1 Samples

Field work (2015–2017) was carried out at Sites G and S of Locality 8 within an area approximately 130 by 200 m in size (Fig. 36.2). The site G is the place where *Australopithecus afarensis* footprints were discovered in 1978 in the Footprint tuff or, more correctly, in Upper Laetolil Tuff 7 (Leakey and Hay 1979), which are now covered by the Footprint conservation mound (Fig. 36.3). Site S is a new locality, where *Australopithecus afarensis* footprints were found in 2015 during excavation activities (Fig. 36.4) (Masao et al. 2016).

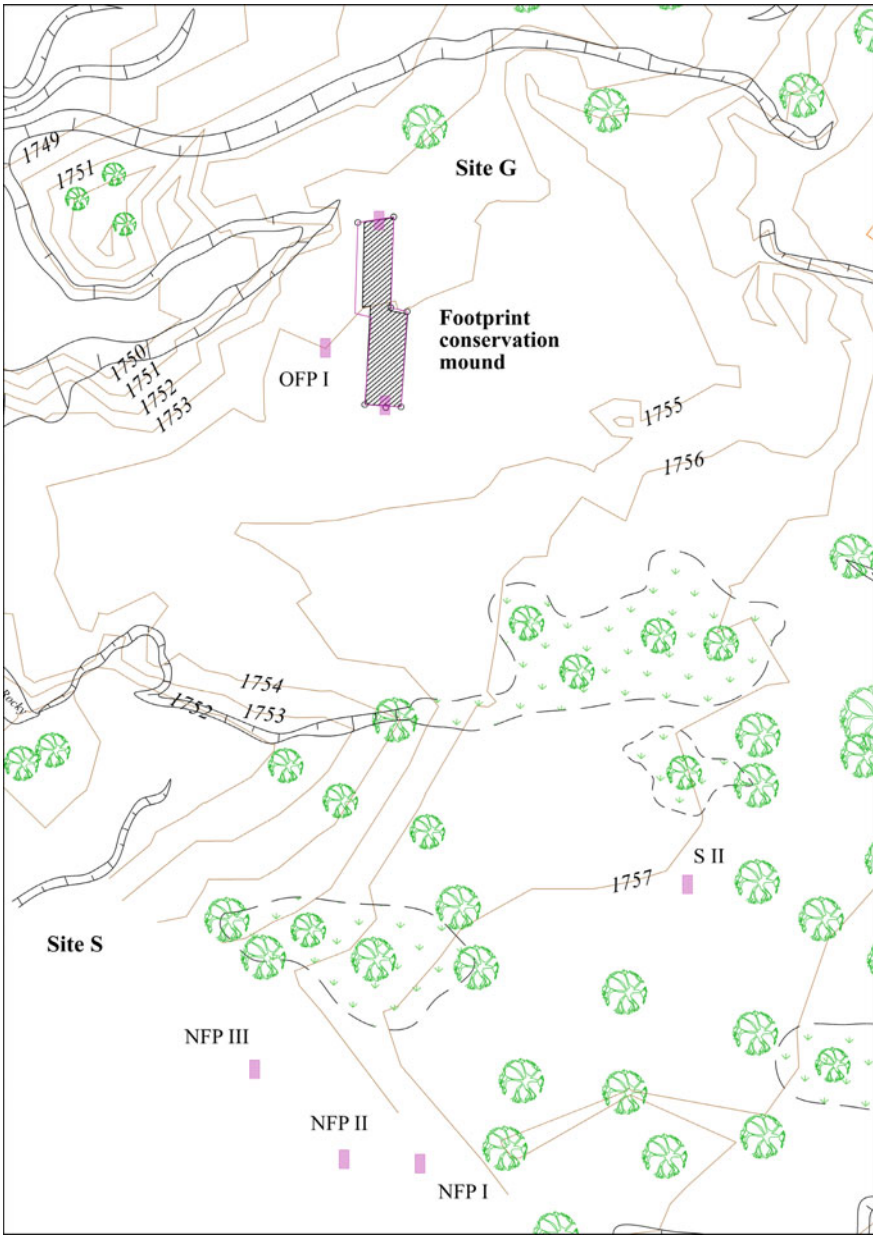


Fig. 36.2 Footprint conservation mound and studied pits at Sites G and S of Locality 8 (topographic map, GMP Consulting Engineers Ltd. 2014)



Fig. 36.3 A south-facing view of the Footprint conservation mound. June 2015

The studied area is flat, with elevation ranging between 1754 and 1757 m. It is covered with grass, bushes and acacia trees, including *Acacia drepanolobium* with the pseudo-galls housing *Crematogaster* sp. ants. There is no exposed Footprint tuff at the surface and therefore five pits were excavated, documented and sampled for laboratory studies (Fig. 36.2). Between July 1 and 10, 2016 two parts of the Footprint conservation mound were re-excavated and made available for in situ study: the southern part with an area of 1.0 by 1.6 m and the northern part with a large area measuring about 2.2–2.8 by 2.2–3.3 m.

Two types of samples were used in this study to identify microorganisms inhabiting the Laetolil tuffs and the conservation mound. The first type is so-called replica samples (or bioprints in Russian publications). They were collected from the pit walls and Footprint tuff surface using a non-destructive print method into sterile plastic containers with artificial media Czapek-Dox agar on the inner surface of their lid. The second type of samples is small fragments of tuff (up to 5 cm in size), concrete, soil and sand collected from the pit walls and the conservation mound, and placed inside sterile plastic containers. All necessary precautionary measures were taken to



Fig. 36.4 Footprint tuff with *Australopithecus afarensis* and animal footprints. NFP III pit, Site S

avoid sample contamination; we used sterile medical gloves and all sampling tools were cleaned with 96% ethanol before and after the extraction of each sample. The complete list of samples used for microbiological studies is given in Table 36.1.

36.2.2 Mycological Study (Isolation in Culture)

The cultivation method was used for the study of microorganisms. The isolation of micromycetes (microfungi) in pure cultures from the collected samples was conducted as follows: (1) microfungal structures revealed on agar-prints were transferred to artificial media under sterile condition and incubated at T = 25 °C; (2) black microfungal structures were selected under a stereomicroscope from cracks and cavities

Table 36.1 List of samples for microbiological study

Site/location	Bioprint #	Rock #	DNA #	Depth (cm)	Description
Site S/	NFP II 1	BIO 1	06	20	Soil
NFP II pit	NFP II 2	BIO 2		45	Upper aeolian tuff
	NFP II 3	BIO 3	07	65	Laminated tuff
	NFP II 4	BIO 4		72	White tuff
	NFP II 5	BIO 5	08	76	Gray tuff
	NFP II 6	BIO 6		86	Lower aeolian tuff
Site S/		S, S 1			Soil
NFP III pit	10, 11, 12				Surface of the Footprint tuff
Site S/	Site II 1	BIO 1	04	30	Soil
Site II pit	Site II 2	BIO 2		67	Upper aeolian tuff
	Site II 3	BIO 3		140	Augite-biotite tuff
	Site II 4	BIO 4		150	Laminated tuff
	Site II 5	BIO 5	05	157	White and gray tuff
	Site II 6	BIO 6		165	Lower aeolian tuff
Site G/	FP 31	FP 31	09	Surface	Upper aeolian tuff near northern part of the conservation mound
	40			Surface	Soil under acacia tree, 28 m to South-East from the northern part of the conservation mound
Site G/	OFP I 1	BIO 1	01	7	Soil
OFP I pit	OFP I 2	BIO 2		18	Augite-biotite tuff
	OFP I 3	BIO 3		38	Laminated tuff
	OFP I 4	BIO 4	02	42	White tuff
	OFP I 5	BIO 5		47	Gray tuff
	OFP I 6	BIO 6	03	55	Dark gray tuff
	OFP I 7	BIO 7		80	Lower aeolian tuff
Site G/	FP 30	FP 30			Lava boulder
Footprint	FP 32	FP 32	10		Concrete (northern part)
conservation mound	BIO 1, 4, 5				Lower aeolian tuff (northern part)
	BIO 2, 3				Surface of the Footprint tuff (northern part)

(continued)

Table 36.1 (continued)

		BIO 6			Sand covering the Footprint surface (northern part)
	BIO 8, 9, 10, 11				Surface of the Footprint tuff (southern part)
		BIO 12			Sand covering the Footprint surface (southern part)

in the tuff samples using an injection needle and transferred to the media; (3) for the evaluation of microfungal biodiversity, small particles of marble were placed on the artificial media; and (4) in order to reveal micromycetes located in microcracks, pieces of substrate were placed in damp chambers for one-two weeks. After that, the developed mycelia were transferred to the nutrient media.

Microfungi isolation was carried out in Petri dishes with different culture media for cultivating microfungi strains, including 2% malt-agar, Czapek-Dox agar, potato-glucose agar and Saburo agar. Samples with pure cultures were studied using a petrographic microscope. Handbooks and atlases with detailed description of micromycetes were used for their identification in the Laetolil tuffs (Barnett 1967; Barron 1968; Ellis 1971, 1976; von Arx 1974; Hermanides-Nijhof 1977; De Hoog and Guarro 1995; Kirk et al. 2001; De Hoog et al. 2009).

36.2.3 Scanning Electron Microscopy

Scanning electron microscopy (SEM) was used for microorganism localization and a study of their morphology on the surface of the collected tuff samples. Prior to the SEM investigations, the samples were dehydrated in a series of ethanol solutions of increasing concentration (30, 50, 70 and 96%). Dehydrated samples were dried at the critical point of liquid carbon dioxide (CO_2). Then the samples were coated with gold and investigated using a Tescan MIRA3 LMU scanning electron microscope at a low accelerating voltage of 9 kV.

36.2.4 Molecular Genetics Methods

A molecular genetics study (metagenomic investigations) was carried out using crushed fragments of the tuffs and soil. Deep sequencing of gene 16S-rRNA was performed using an Ion Torrent PGM system (Life Technologies). We used primers for the amplification of 16S RNA gene fragment ("Beagle", Russia): 16S-R GGACTACVSGGGTATCTAAT and 16S-F GTGCCAGCMGCCGCGGTAA. Sequencing was performed on Ion Torrent PGM (Life Technologies) using Ion chip 318 ™ Chip v2 and reagents recommended by the manufacturer. Library preparation was

based on the manufacturer's protocol. A diversity analysis was performed using Qiime software package (version 1.9.0) and the standard protocol. The classification is based on a comparison with the Greengenes database (www.greengenes.secondgenome.com). The main steps and characteristics of these analyses are available from the authors on request. A metagenomic study of fungi diversity was carried out with primers for site amplification ITS1-5.8S–ITS2 (Beagle, Russia): ITS4 TCCTCCGCTTATTGATATGC; ITS7 CGTGARTCATCGARTCTTTG.

36.3 Results and Discussion

36.3.1 Molecular Genetics Analysis

36.3.1.1 Bacteria and Archaea

The use of classical microbiological methods is often insufficient to reveal the entire spectrum of microorganisms growing on and inside of rocks and soil. That is why we have also applied metagenomic analysis to the collected soil and tuff samples in order to identify the maximum diversity of microorganisms on the basis of their genetic characteristics.

The results of this analysis are summarized for bacteria and archaea in Table 36.2, which includes data for eight samples collected from pits (three samples of soil and five tuff fragments) and two samples of black biofilms collected from the surface (one sample of surface tuff and one sample of concrete from the Footprint conservation mound).

Metagenomic analysis revealed the presence of 23 bacterial phyla, as well as two archaea. In addition to bacteria with an established systematic position, samples contain material unidentifiable at the level of phylum sequences, although its share is small. The results show that in the studied samples, there is the predominance of four major groups: Actinobacteria, Proteobacteria, Bacteroidetes and Cyanobacteria (McNamara and Mitchell 2005). Altogether, they make up 50–83% of all bacteria in the studied samples.

The structure of microbial communities (i.e. the relative proportions of major groups) is different for soil and tuffs. Actinobacteria and Proteobacteria are common in the tuffs (but also abundant in the soil), whereas Bacteroidetes mostly occur in the soil. The latter bacteria are commonly found in feces of warm-blooded animals and humans; this would explain their relative abundance in soil.

Cyanobacteria are dominant bacteria in the biofilm samples from the surface of concrete and tuff. These microorganisms are capable of photosynthesis, require water, carbon and nitrogen, and live in different environments (Seckbach 2007). Cyanobacteria form symbiotic associations with micro- and macroorganisms, including fungi and lichens.

Table 36.2 Results of metagenomic analysis (bacteria and archaea phylum)

Substrates	Mound concrete	Upper aeolian tuff	Soil 1	Soil 2	Soil 3	Laminated tuff	White tuff 1	White tuff 2	Gray tuff 1	Gray tuff 2
Depth (cm)	Surface	Surface	7	20	30	65	42	157	55	76
Lab #	10	09	01	06	04	07	02	05	03	08
Taxonomy	%	%	%	%	%	%	%	%	%	%
Unassigned	1.1	2.5	4.5	4.3	2.3	0.1	**14.3**	2.4	2.2	0.5
Crenarchaeota	5.6	**10.1**	1.1	1.7	1.6	0.0	1.2	6.4	0.1	6.4
Euryarchaeota	0.0	0.0	0.1	1.2	0.1	0.1	0.0	0.2	0.0	0.1
Acidobacteria	6.3	2.4	4.6	**10.0**	4.8	1.2	2.8	0.6	0.5	4.7
Actinobacteria	**17.9**	**26.2**	**17.0**	**19.2**	**12.6**	**26.1**	**22.8**	**34.2**	**27.9**	**22.7**
Armatimonadetes	0.6	0.3	0.2	0.2	0.3	0.0	0.2	0.0	0.0	0.0
Bacteroidetes	6.3	4.1	**22.8**	**10.8**	**24.7**	5.4	**10.6**	4.8	6.9	5.2
Chlamydiae	0.0	0.0	0.2	0.0	0.0	0.0	0.5	0.0	0.1	0.1
Chlorobi	0.1	0.0	0.1	0.1	0.1	1.1	0.1	0.0	0.0	1.0
Chloroflexi	2.4	3.6	6.2	9.6	2.4	1.0	7.9	0.7	1.1	6.9
Cyanobacteria	**37.1**	**26.0**	0.9	1.3	**13.8**	4.5	1.1	2.9	**10.2**	6.6
Elusimicrobia	0.0	0.0	0.0	0.0	0.0	0.0	0.0	0.2	0.0	0.0
FBP	2.9	0.7	0.1	0.0	0.2	0.0	0.0	0.0	0.0	0.0
Fibrobacteres	0.0	0.0	0.3	0.0	0.0	0.0	0.2	0.0	0.0	0.0
Firmicutes	0.1	0.0	1.2	2.8	0.8	**13.4**	1.2	5.6	3.5	1.9
Fusobacteria	0.0	0.0	0.0	0.0	0.0	0.0	0.0	0.0	0.1	0.0
Gemmatimonadetes	0.1	1.7	1.7	3.4	0.7	0.1	1.6	0.1	0.3	1.0
NKB19	0.0	0.0	0.0	0.0	0.0	0.0	0.5	0.0	0.0	0.0

(continued)

Table 36.2 (continued)

Nitrospirae	0.0	0.0	0.2	0.3	0.2	0.1	0.7	0.4	0.0	1.0
OD1	0.0	0.1	0.0	0.0	0.0	0.0	0.9	0.1	5.6	0.2
OP11	0.0	0.0	0.0	0.1	0.0	0.0	0.1	0.2	0.0	0.1
Planctomycetes	2.6	4.7	9.3	**10.6**	5.3	0.6	6.6	2.5	0.4	4.0
Proteobacteria	**13.7**	**14.2**	**19.3**	**18.4**	**21.7**	**45.9**	**20.7**	**37.1**	**38.3**	**36.3**
Tenericutes	0.0	0.0	4.7	0.1	0.2	0.1	0.5	0.0	0.1	0.0
Verrucomicrobia	0.3	2.6	5.3	6.0	7.8	0.2	5.4	1.5	2.5	1.3
Thermi	2.9	0.6	0.0	0.0	0.0	0.0	0.0	0.0	0.0	0.0

Bacteria and archaea with >10% are highlighted bold

Actinobacteria and Proteobacteria are known as potential destructors of natural rocks and artificial materials. Some Actinobacteria can penetrate into rocks. An increased production of metabolites is typical of Proteobacteria (Pseudomonas), which play an important role in the formation of biofilms in soil. Also, these microorganisms can form communities with micromycetes, thus contributing to their destructive effect (McNamara and Mitchell 2005).

Other bacteria which are present at significant levels (>10% in some samples) are Planctomycetes and Acidobacteria in the soil, Firmicutes in the tuffs and archaea Crenarchaeota in biofilms on the tuff surface.

A significant part of the microbial community is presented by actinomycetes (morphologically microfungi-like Actinobacteria), i.e. heterotrophic microorganisms involved in the bioweathering of rocks. They form filamentous structures resembling mycelium. The main habitat for these organisms is the soil (Saiz-Jimenez 1999), but they have also been found on the surface of buildings and other constructions in the urban environment (Gaylarde and Gaylarde 2005; Hesham 2009). They are able to change the natural colour of rock surface to brown or black by allocating pigments (Hesham 2009). Actinomycetes play a significant role in biofilms on rocky substrates under different environmental conditions (Saarela et al. 2004) and can participate in the processes of tuff transformation due to their active metabolite production and growth into the substrate.

36.3.1.2 Fungi

The results of the metagenomic analysis of fungal biodiversity show that anamorphic ascomycetes are the predominant group in all samples (Table 36.3). They constitute the major share of fungi in soil samples and various types of tuffs. Species of genera *Trichoderma, Emericella, Fusarium* and *Verticillium* can be interpreted as dominants of fungal communities. The proportion of basidiomycetes in the samples of white and gray tuff is higher than in the other samples. It is interesting to note that Glomeromycota in soil samples is quite significant whereas in samples of tuff they are rare. This can be explained by the presence of plants which are associated with species of Glomeromycota. Zygomycetes are also found only in the soil samples.

As a whole, microbial communities living in the soil and tuffs within the studied area include many species of bacteria which are typical for (sub)soil habitats. Most of these organisms are cosmopolites and live in different climatic zones.

Human activity in the study area is likely to affect the microbial community. The human impact is related to changes in water regime, to the use of artificial materials, and to anthropogenic pollution. These factors may lead to increasing activity of aggressive constituents of the microbial community that may develop in the human environment. It may also facilitate biodegradation of some natural and artificial materials, particularly in a high-humidity environment.

Table 36.3 Results of metagenomic analysis (fungal phylum)

Substrates	Mound concrete	Upper aeolian tuff	Soil 1	Soil 2	Soil 3	Laminated tuff	White tuff 1	White tuff 2	Gray tuff 1	Gray tuff 2
Depth (cm)	Surface	Surface	7	20	30	65	42	157	55	76
Lab #	10	09	01	06	04	07	02	05	03	08
Taxonomy	%	%	%	%	%	%	%	%	%	%
No blast hit; other	44.5	1.3	17.1	7.0	18.8	15.0	21.6	22.1	14.9	1.2
Ascomycota	**42.6**	**53.7**	**43.9**	**41.0**	**37.8**	**23.3**	**48.7**	**26.7**	**28.6**	**56.1**
Basidiomycota	0.4	2.1	2.8	8.4	3.5	**27.1**	**10.5**	**29.0**	**17.0**	**15.5**
Chytridiomycota	0.0	0.0	0.1	0.0	0.8	0.0	0.0	0.0	0.0	0.0
Glomeromycota	0.0	0.6	**21.9**	9.0	**11.3**	0.2	8.4	0.0	0.0	0.0
Zygomycota	0.0	0.2	1.2	1.0	0.8	0.1	0.0	0.0	0.0	0.0
Unidentified	12.4	42.1	13.0	33.6	26.9	34.3	10.8	22.1	39.4	27.3

Microfungi with >10% are highlighted bold

36.3.2 Culture Study (Mycological Analysis)

Mycological analysis showed the presence of 35 species from 21 genera of micromycetes in the studied samples (Table 36.4). Also, two sterile forms (white and dark) of mycelia were found in different samples.

The number of colony-forming units (CFU) is widely variable: from 350 (OFP I pit, Augite-biotite tuff) to 6500 (S II pit, laminated tuff) CFU per gram of substrate (Table 36.5). Most of the samples have CFU values from 1000 to 3000 per gram of substrate. There is no particular trend in enrichment or depletion of the Laetoli samples in micromycetes, either with respect to sampling depth, or pit location. We explain this lack of consistent trends by variations in the amount of organic matter inside the soil, tuffs and conservation mound. This matter includes plant, bush and tree roots (either dead or alive), which are the main source of nutrition for micromycetes.

Cultivation of micromycetes from tuff fragments and soil samples revealed many more different species of microfungi in comparison with the cultivated replica samples. The number of microfungi species present within a single sample varies from one (Site II pit, sample Bio 6) to nine (NFP II pit, sample Bio 2).

Most of the identified species are known as typical soil microfungi, e.g. *Aspergillus, Fusarium, Cladosporium, Alternaria, Penicillium, Morthierella, Trichoderma. Aspergillus* and *Fusarium* species dominate in the studied samples. These microfungi are known as active destructors of different substrates (Koval and Sidorenko 1989; Sutton et al. 1998). Microfungi of genus *Aspergillus* are described as active destructors of rocks, metals and construction materials under variable humidity. They show slow growth rates in a low-humidity environment (50% humidity), but increase in activity under more humid conditions (>70%) (Ivanushkina 2003). Microfungi of genus *Fusarium* are the most hazardous microorganisms for concrete, compared with the other microfungi. Together with bacteria, they can damage concrete in a wet environment (Gu et al. 1998). Several species of *Aspergillus* are also known as potential human pathogens (Sutton et al. 1998). It has been established that micromycetes are one of the most common environmental sources of allergens (Sutton et al. 1998; Simon-Nobbe et al. 2008; De Hoog et al. 2009). Toxicogenic microfungi *Aspergillus* spp., which were observed in our samples, can cause symptoms of allergic rhinitis, conjunctivitis, atopic dermatitis, eczema, or bronchial asthma.

Based on the currently available information for the Laetoli Museum project, we expect that part of soil and tuff sequence (upper aeolian, augite-biotite and laminated units) will be removed during the Museum construction. These activities will reduce the number of micromycetes (both in terms of the number of species and biomass); however, a significant part of aggressive microfungi (biodestructors and potential human pathogens) will be present both inside, and on the surface of, the tuffs and soil during the construction period, particularly in the NFP II pit area (Table 36.6).

There are many species of *Aspergillus* at pit NFP II, which can colonize the construction materials, especially during wet periods (rain seasons). All of these species are also known as potential human pathogens (Sutton et al. 1998; De Hoog et al.

Table 36.4 Species of micromycetes identified in the upper soil layer, in various tuffs located at different depths, and in cover materials (sand, concrete, boulders)

Micromycete species	Tuffs and soil[a]	Footprint conservation mound[b]
1. *Alternaria alternata* (Fr.) Keissl.	+	+
2. *Alternaria chlamydospora* Mouch	−	+
3. *Arthrinium phaeospermum* (Corda) M.B. Ellis	−	+
4. *Aspergillus flavus* Link	+	+
5. *Aspergillus fumigatus* Fresen.	+	−
6. *Aspergillus niger* Tiegh.	+	−
7. *Aspergillus ochraceus* G. Wilh.	+	−
8. *Aspergillus oryzae* (Ahlb.) Cohn	+	−
9. *Aspergillus terreus* Thom	+	+
10. *Aspergillus ustus* (Bainier) Thom & Church	+	−
11. *Aspergillus versicolor* (Vuill.) Tirab.	+	−
12. *Bisifusarium dimerum* (Penz.) L. Lombard & Crous	+	+
13. *Cladosporium cladosporioides* (Fresen.) G.A. de Vries	+	+
14. *Coniosporium* sp.	+	+
15. *Curvularia australiensis* (Bugnic. ex M.B. Ellis) Manamgoda, L. Cai & K.D. Hyde	+	+
16. *Doratomyces stemonitis* (Pers.) F.J. Morton & G. Sm.	+	−
17. *Exophiala jeanselmei* (***Langeron***) McGinnis & A.A. Padhye var jeanselmei	+	−
18. *Fusarium chlamydosporum* Wollenw. & Reinking	−	+
19. *Fusarium incarnatum* (Desm.) Sacc.	+	−
20. *Fusarium oxysporum* Schltdl.	+	+
21. *Fusarium* sp.	+	+
22. *Gliomastix roseogrisea* (S.B. Saksena) Summerb.	+	−
23. *Helicoma pannosum* (Berk. & M.A. Curtis) Y.Z. Lu & K.D. Hyde	−	+
24. *Melanospora* sp.	+	−
25. *Metarhizium marquandii* (Massee) Kepler, S.A. Rehner & Humber	+	−
26. *Monodictys* sp.	−	+
27. *Mortierella lignicola* (G.W. Martin) W. Gams & R. Moreau	+	−
28. *Penicillium incarnatum* Berk. & Broome	+	−

(continued)

Table 36.4 (continued)

Micromycete species	Tuffs and soil[a]	Footprint conservation mound[b]
29. *Phoma* sp.	–	+
30. *Sarocladium strictum* (W. Gams) Summerb.	+	–
31. *Sphaerostilbella penicillioides* (Corda) Rossman, L. Lombard & Crous	+	–
32. *Talaromyces purpureogenus* Samson, N. Yilmaz, Houbraken, Spierenb., Seifert, Peterson, Varga & Frisvad	+	–
33. *Talaromyces rugulosus* (Thom) Samson, N. Yilmaz, Frisvad & Seifert	+	–
34. *Trichocladium asperum* Harz	+	–
35. *Trichoderma koningii* Oudem.	+	–
36. Sterile light colored fungus	+	+
37. Sterile dark colored fungus	+	+

[a]Laminated tuff, white tuff, gray tuff, lower aeolian tuff, upper aeolian tuff, augite-biotite tuff, dark gray tuff (depth 7–165 cm); soil (depth 0–30 cm)
[b]Lava boulder, mound concrete, sand

2009). They produce different toxins, which affect the human health (Bilai and Kurbatskaya 1990). The destructive impact of *Aspergillus* is related to its physical action on the material (growth inside natural rocks and artificial construction materials), as well as to its acid production. An increase in environmental humidity (including atmospheric humidity, evaporation from soil and tuffs, condensation inside buildings) stimulates the reproduction (spore formation) of these microfungi. Spores of *Aspergillus* are small (from 3 to 8 μm) and can be easily transported by winds or indoor air currents.

Microfungus *Fusarium oxysporum* was found in the samples of mound concrete and this fungus is a hazard for different construction materials, including concrete (Gu et al. 1998). The concrete, as can be seen in Fig. 36.5, is covered by thin black films. Mostly dark colored fungi were isolated from these biofilms. The Footprint conservation mound was constructed in 1994–1996 and in twenty five years there have been visible changes on the mound surface due to the biological activity of these microorganisms.

Other microfungi identified in the present work are typical soil inhabitants and their presence is normal for southern soils. Most of them are cosmopolites adapted to different soil environments. They receive organic matter for growth and development mainly from plant remains, roots, and zoogenic substrates. During wet periods, they can grow more actively and significantly increase in biomass. This can lead to the general activation of microbial community. However, the current number of microfungi is moderate and not dangerous.

Of special note is a microfungi community observed within the Footprint conservation mound, where two studied areas show significant difference in microfungi

Table 36.5 Number of CFU of microfungi per gram of substrate

Locality	Substrate #	Depth (cm)	Description	CFU per gram of substrate
NFP II pit	BIO 1	20	Soil	1400
	BIO 2	45	Upper aeolian tuff	2500
	BIO 3	65	Laminated tuff	1700
	BIO 4	72	White tuff	1600
	BIO 5	76	Gray tuff	1300
	BIO 6	86	Lower aeolian tuff	450
NFP III pit	S 1		Soil	2300
	S		Soil (surface of the Footprint tuff)	1800
Site II pit	BIO 1	30	Soil	1800
	BIO 2	67	Upper aeolian tuff	1200
	BIO 3	140	Augite-biotite tuff	2800
	BIO 4	150	Laminated tuff	6500
	BIO 5	157	White and gray tuff	450
	BIO 6	165	Lower aeolian tuff	1600
Site G	FP 31	Surface	Upper aeolian tuff	1400
OFP I pit	BIO 1	7	Soil	3000
	BIO 2	18	Augite-biotite tuff	350
	BIO 3	38	Laminated tuff	1400
	BIO 4	42	White tuff	800
	BIO 5	47	Gray tuff	3500
	BIO 6	55	Dark gray tuff	1700
	BIO 7	80	Lower aeolian tuff	600
Footprint	FP 30	Surface	Lava boulder	750
conservation	FP 32	Surface	Mound concrete	1800
mound	BIO 6		Sand (Footprint surface, northern part)	3200
	BIO 12		Sand (Footprint surface, southern part)	3100

species present. Twelve and nine microfungi species were identified in the northern and southern parts of the conservation mound, respectively (16 species in total). Only *Fusarium* (three species), *Paecilomyces javanicus* and *Coniosporium* sp. microfungi are present in both studied areas.

The tuff and sand from the northern part of the mound contains aggressive microfungi from *Aspergillus, Alternaria* and *Cladosporium* genera (Warscheid and Braams 2000; Sutton et al. 2001). The observed species are characterized by different behavior; e.g., *Alternaria* и *Cladosporium* are fast-growing fungi confined to the surface;

Table 36.6 Aggressive microfungi in the investigated pits and Footprint conservation mound (FCM)

Micromycetes	NFP II	NFP III	S II	OFP I	FCM (lava, concrete)	FCM (footprint tuff surface)
Aspergillus flavus	+			+		+
Aspergillus niger	+					
Aspergillus ochraceus	+			+		
Aspergillus oryzae	+					
Aspergillus terreus	+				+	
Aspergillus ustus		+				
Aspergillus versicolor	+			+		
Cladosporium cladosporioides		+	+			+
Fusarium oxysporum				+	+	+
Penicillium purpurogenum			+			

For detailed microfungi descriptions, see, Koval and Sidorenko (1989), Bilai and Kurbatskaya (1990), Sutton et al. (1998), Gu et al. (1998), Simon-Nobbe et al. (2008), De Hoog et al. (2009)



Fig. 36.5 Dark-coloured biofilms on the surface of concrete. Footprint concervation mound

Coniosporium and *Monodictys* are slow-growing fungi, but they penetrate into the substrate; *Aspergillus, Fusarium, Paecilomyces* are well-known active destructors of different substrates (Koval and Sidorenko 1989; Sutton et al. 1998) and are characterized by high growth rates on the surface and at contact between different substrates.

The Footprint Tuff in the southern part of the mound shows a smaller number of identified fungi species; in addition to destructive *Fusarium* species, two fast-growing white to gray *Mucor* species are present at that location. Their presence could indicate anthropogenic/human influence on the local environment, expressed particularly through enrichment in water, which was observed during the re-excavation, and/or through the presence of a relatively large amount of organic matter (e.g., dead skin cells introduced during the Tuff surface cleaning).

One possible explanation for the observed differences in microbiological activity between the two areas within the Footprint conservation mound is a variable degree of human intervention at these locations. Our observations during the July 2016 field work show that the re-excavated northern part of the Footprint Tuff does not contain any prints and is strongly eroded. Most likely, this area was not studied as vigorously as the southern part, and human intervention here (e.g., surface cleaning) was not as significant. In contrast, the southern part contains footprints G2/3-31, G2/3-30, G2/3-29 and G1-39, as well as animal footprints, which were studied extensively by M. Leakey's team in 1978–1979 and by the Getty Conservation Institute in 1994–1995 and 2011, including manual cleaning, treatment of the Tuff with Bedacryl, molding, and casting. These activities could result in localized removal of microfungi from the Footprint Tuff surface.

36.3.3 Scanning Electron Microscopy

Scanning electron microscopy has been used for the localization of microbial communities living on, and inside of, the tuffs, as well as for the identification of the key morphological characteristics of these microorganisms. The great success of fungi in their colonization of terrestrial ecosystems is attributed to their ability to form hyphae and mycelia (Rayner et al. 1995). Hyphae are highly polarized cylinders that usually grow by apical extension at rates $\geq$1 μm/s (Seiler and Plamann 2003). The resulting network of hyphae is termed a mycelium.

Both hyphae (with a cell diameter of ~1 μm) and mycelia were observed in the tuff samples. The highly porous texture of the tuffs, the presence of circumgranular and intergranular pores, microcracks and cavities, are ideal for the growth of hyhpae and mycelia leading to the formation of biofilms (aggregates of microorganisms). Fungal hyphae are typically observed along microcracks and in circumgranular pores. Mycelia are more common in large intergranular pores and cavities (Fig. 36.6). Both are irregularly distributed within the tuffs. Actinomycetes grow in pores, microcracks and cavities (Fig. 36.7).

In calcite-rich rocks (marbles, limestones), microfungi (e.g., *Aspergillus niger*) are known as a source of organic acids which react with calcite, causing the formation

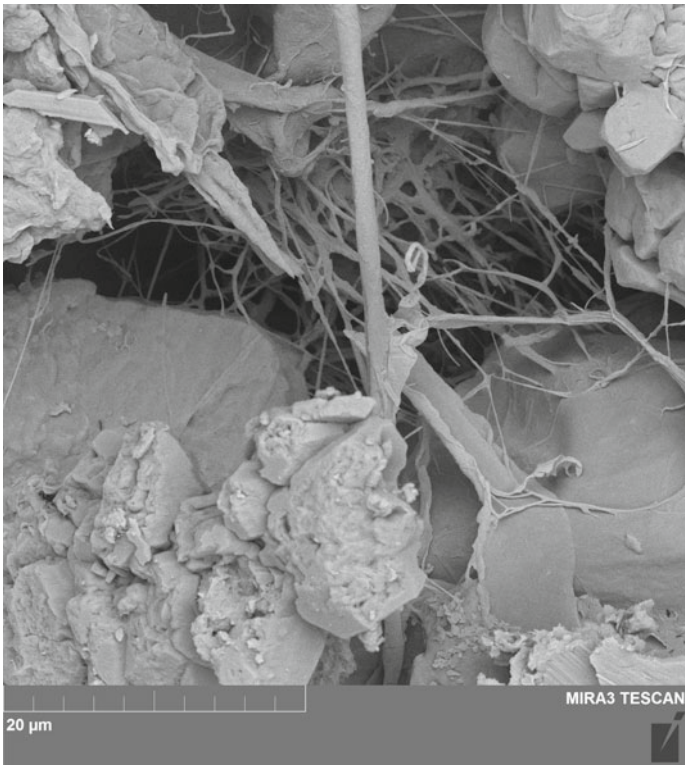


Fig. 36.6 Intensive biological colonization (biofilm formation) on tuff. NFP II pit—laminated tuff, BSE image

of calcium oxalate hydrate minerals (Sturm et al. 2015). In our samples of calcite-rich tuffs, we did not find any SEM evidence that newly-formed minerals were precipitated due to microbiological activity, but this process could not be ruled out conclusively.

36.4 Conclusions

In summary, we conclude that different microorganisms (micromycetes, bacteria and archea) are present in all of the tuff and soil samples examined in the present work. Thirty-nine species of microfungi, as well as sterile white and dark mycelia were identified in the samples. They occur as hyphae and mycelia inside the tuffs, and are concentrated in circum-granular and intergranular pores, microcracks and cavities. The number of micromycetes in the tuffs and soil is moderate and does not exceed 7000 CFU per gram of substrate. Low content of microfungi (3,100–3,200 CFU

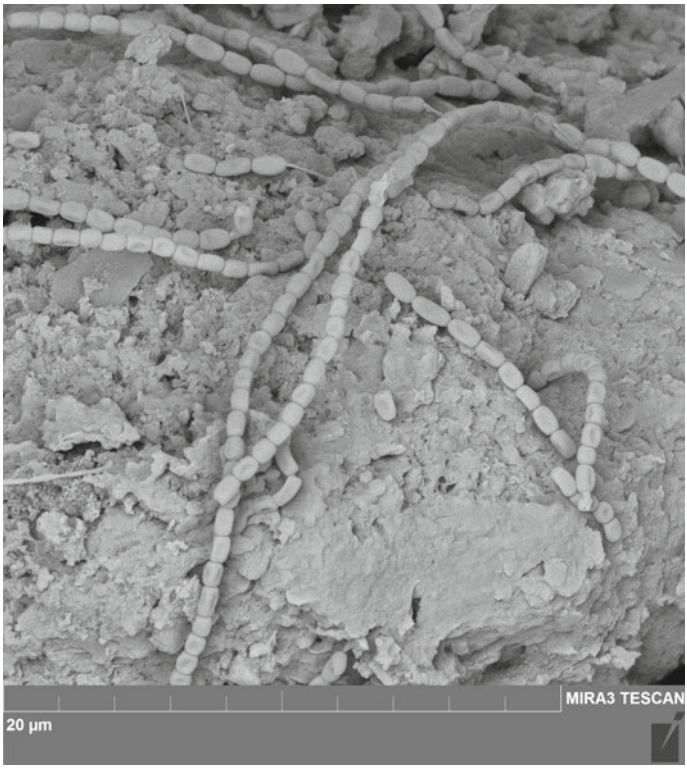


Fig. 36.7 Growth of actinomycetes on the tuff surface. OFP I pit—gray tuff, BSE image

per gram) was also found in the fine- to coarse-grained sand, which was used for conservation of the Footprint Tuff surface.

There are some dominant groups of microorganisms, which are capable of affecting the rocks and artificial materials in the project area. The most typical microfungi are from genera *Aspergillus* and *Fusarium*. They are known as active destructors of different natural and artificial substrates and can colonize building materials, particularly during rain seasons. All of these microorganisms are also known as potential human pathogens (Sutton et al. 1998; De Hoog et al. 2009). They produce different toxins, which affect human health (Bilai and Kurbatskaya 1990). The destructive impact of *Aspergillus* is related to its physical action on the substrate (growth through the material), as well as its acid production. Increasing environment humidity (atmospheric humidity, evaporation from soil and tuffs, condensation inside buildings) will stimulate the reproduction (spore formation) of these fungi. Spores of *Aspergillus* are quite small (3–8 µm in size) and can be easily transported by air currents in both indoor and outdoor environments.

The application of molecular genetic methods to the Laetolil tuffs and soil revealed a large group of different bacteria (25 phyla). The microbiota consists mostly of

Actinobacteria, Proteobacteria, Bacteroidetes and Cyanobacteria. Their relative distribution shows the preferential occurrence of Bacteroidetes in the upper part of stratigraphic sections (soil), and concentration of Actinobacteria and Proteobacteria within the tuffs. We explain this by variations in the relative content of organic matter in the soil and tuffs. Cyanobacteria, as expected, occur on the surface of the tuffs and concrete exposed to the sun.

Bacteria and micromycetes (in the form of microbial biofilms) have both biochemical and physical impact on their host tuffs and soil. They produce mineral and organic acids, which play an important role in the processes of rock transformation and mineralization. SEM investigations recorded microbial presence in microcracks, pores and cavities. The growth of micromycetes can lead to physical destruction of rocks. As a whole, the microbiota is characterized by high diversity, as well as by the predominance of destructive microorganisms (especially, fungi *Aspergillus* and *Fusarium*, and bacteria Actinomycetes and Proteobacteria).

Direct evidence of biological activity in the studied area includes the observed changes in the colour of concrete from the Footprint conservation mound (Fig. 36.5). In this instance, the growth of dark-coloured fungi led to black staining on the concrete.

Exposure of the Footprint tuff could lead to the development of photosynthetic microorganisms like Cyanobacteria. They are considered to be potentially the most aggressive microorganisms due to their photoautotrophic nature. The development of Cyanobacteria on rock (particularly, calcareous) surfaces has been shown to lead to the appearance of coloured patinas and incrustations (Dornieden et al. 2000; Tomaselli et al. 2000) and to stimulate the growth of other aggressive microorganisms (Urzi and Krumbein 1994).

One of the well-known problems concerning the preservation of the footprints at Laetoli is “the root problem” (Getty Conservation Institute 1996), not only because of the strong physical damage of plant roots to the tuffs, but also because of their role as a source of nutrition for microorganisms. Roots of grassy plants create a favourable microenvironment for the development of aggressive organotrophic microorganisms (micromycetes and some bacteria). Preliminary data from a study of “dead” roots found near the contact between the laminated and white tuffs show their colonization by abundant micromycetes.

To prevent biologically induced damage to building materials and, more importantly, to the Footprint tuff, we could recommend to carry out localized treatment of the tuff, construction and building materials by biocides with a wide spectrum of antimicrobial functions (Young et al. 2008). The addition of biocides (e.g., those on the basis of guanidine) to materials like concrete during the construction will increase their resistance to decay.

It will also be important to control the temperature and humidity conditions (particularly during rain seasons) inside the Museum building. With the available microbiological data, we recommend that indoor humidity should not exceed 50% (optimally 45–50%) and temperature be maintained between 18 and 20 °C. These conditions will not stop the growth and reproduction of microorganisms, but will reduce their rate.

Acknowledgements We thank M.N. Pagolskaya (St. Petersburg) and J.S. (J4) Pyuza (GMP Consulting Engineers Ltd.) for help during field work at Laetoli. Figure 36.1 is adapted by permission from the Jet Propulsion Laboratory (California Institute of Technology). We would like to thank the Tanzania Commission for Science and Technology for granting permission to conduct research (2016-245-NA-2016-181, 2017-234-NA-2016-115 for A.N. Zaitsev, 2016-242-NA-2016-181 for A.I. Savchenok). Field work at Laetoli was supported by Peter Rich Architects—GMP Consulting Engineers—Laetoli JV (Arusha), St. Petersburg State University (grants 0.42.955.2016 and 3.42.740.2017) and Ngorongoro Conservation Area Authorities (Tanzania). At various stages, this research was funded by the Peter Rich Architects—GMP Consulting Engineers—Laetoli JV (Arusha), Natural History Museum (London) and St. Petersburg State University (Resource Centres for X-ray Diffraction Studies, Geo-Environmental Research and Modelling, and Molecular and Cell Technologies and Culture Collection of Microorganisms, grant 3.20.1855.2015). The research results were partially obtained on the equipment of the Resource Center "Development of Cellular and Molecular Technologies" of St. Petersburg State University.

References

Barnett HL (1967) Illustrated genera of imperfect fungi. 2nd edn. Minneapolis, Minnesota

Barron GL (1968) The genera of hyphomycetes from soil. Baltimore. 364p

Bilai VI, Kurbatskaya ZA (1990) The determinant of toxigenic micromycetes. Naukova Dumka, Kiev (in Russian)

Cela-Conde CJ, Ayala FJ (2007) Human evolution: trails from the past. Oxford Press, New York

De Hoog GS, Guarro J (1995) Atlas of clinical fungi. CBS/Universitat Rovira i Virgili

De Hoog GS, Guarro J, Gene J, Figueras MJ (2009) Atlas of clinical fungi: the ultimate benchtool for diagnostics. A pilot version of the 3rd edn, CD-ROM. Centraalbureau voor Schimmelcultures, KNAW Fungal Biodiversity Centre/Universitat Rovira i Virgili, Utrecht, Netherlands

Deino AL (2011) $^{40}Ar/^{39}Ar$ Dating of Laetoli, Tanzania. Paleontology and geology of Laetoli: human evolution in context, vol 1. Springer, Dordrecht, pp 77–97

Dornieden T, Gorbushina AA, Krumbein WE (2000) Patina (physical and chemical interactions of sub-aerial biofilms with objects of art). International conference on microbiology and conservation. Plenum Press, New York, pp 105–120

Ellis MB (1971) Dematiaceous hyphomycetes. Kew

Ellis MB (1976) More dematiaceous hyphomycetes. Kew

Gaylarde CC, Gaylarde PM (2005) A comparative study of the major microbial biomass of biofilms on exteriors of buildings in Europe and Latin America. Int Biodeterior Biodegrad 55(2):131–139

Getty Conservation Institute (1996) Laetoli project: conservation of the Hominid Trackway Site at Laetoli, Tanzania: Report on the 1995 Field Season (July 3–September 2, 1995). Los Angeles: Getty Conservation Institute. http://hdl.handle.net/10020/gci_pubs/laetoli_field_report_1995

Gu JD, Ford TE, Berke NS, Mitchell R (1998) Biodeterioration of concrete by the fungus Fusarium. Int Biodeterior Biodegrad 41(2):101–109

Harrison T (ed) (2011) Paleontology and geology of Laetoli: human evolution in context, vol 1. Springer, Dordrecht

Hay RL (1986) Role of tephra in the preservation of fossils in Cenozoic deposits in East Africa. Geol Soc Spec Pub 25:339–344

Hermanides-Nijhof EJ (1977) Aureobasidium and allied genera. Stud Mycol 15:141–177

Hesham A (2009) Bioweathering and biotransformation of granitic rock minerals by actinomycetes. Microb Ecol 58:753–761

Ivanushkina E (2003) Genus Aspergillus: nomenclature, classification, distribution. In: New to the taxonomy and nomenclature of fungi. Moscow. pp 136–163 (in Russian)

Kirk PM, Cannon PF, David JC, Stalpers JA (eds) (2001) Ainsworth and Bisby's Dictionary of the fungi, 9th edn. CABI Publishing, Wallingford
Koval EZ, Sidorenko LP (1989) Mycodestructors of industrial materials. Naukova Dumka, Kiev (in Russian)
Leakey MD, Hay RL (1979) Pliocene footprints in the Laetolil Beds at Laetoli, northern Tanzania. Nature 278:317–323
Masao FN, Ichumbaki EB, Cherin M, Barili A, Boschian G, Iurino DA, Menconero S, Moggi-Cecchi J, Manzi G (2016) New footprints from Laetoli (Tanzania) provide evidence for marked body size variation in early hominins. eLife 5, e19568
May E, Jones M, Mitchell J (2008) Heritage microbiology and science. Microbes, monuments and maritime material. Special Publication 315. The Royal Society of Chemistry
McNamara CJ, Mitchell R (2005) Microbial deterioration of historical stone. Front Ecol Environ 3(8):445–451
Mitchell R, McNamara CJ (2010) Cultural heritage microbiology. Fundamental studies in conservation science. American Society for Microbiology Press, Washington
Rayner ADM, Griffith GS, Ainsworth AM (1995) Mycelial interconnectedness. In: Growing fungus. Springer. pp 21–40
Saarela M, Alakomi HL, Suihko ML, Maunuksela L, Raaska L, Mattila-Sandholm T (2004) Heterotrophic microorganisms in air and biofilm samples from Roman catacombs, with special emphasis on actinobacteria and fungi. Int Biodeterior Biodegrad 54:27–37
Saiz-Jimenez C (1999) Biogeochemistry of weathering processes in monuments. Geomicrobiol J 16:27–37
Seckbach J (ed) (2007) Algae and cyanobacteria in extreme environments. Springer, Dordrecht
Seiler S, Plamann M (2003) The genetic basis of cellular morphogenesis in the filamentous fungus *Neurospora crassa*. Mol Biol Cell 14:4352–4364
Simon-Nobbe B, Denk U, Pöll V, Rid R, Breitenbach M (2008) The spectrum of fungal allergy. Allergy Immunol 145:58–86
Sturm EV, Frank-Kamenetskaya O, Vlasov D, Zelenskaya M, Sazanova K, Rusakov A, Kniep R (2015) Crystallization of calcium oxalate hydrates by interaction of calcite Marble with fungus *Aspergillus niger*. Am Miner 100(8):2559–2565
Sutton DA, Fothergil AW, Rinaldi MG (1998) Guide to clinically significant fungi. Williams & Wilkins
Sutton D, Fothergill A, Rinaldi M (2001) Determinant of pathogenic and opportunistic fungi. Mir, Moscow (in Russian)
Tobias PV (1967) Olduvai Gorge, vol 2. Cambridge University Press
Tomaselli L, Lamenti G, Bosco M, Tiano P (2000) Biodiversity of photosynthetic micro-organisms dwelling on stone monuments. Int Biodeterior Biodegrad 46:251–258
Urzi C, Krumbein WE (1994) Microbiological impacts on the cultural heritage. Durability and changes: the science, responsibility, and cost of sustaining cultural heritage. Wiley, New York, pp 107–135
von Arx JA (1974) The genera of fungi sporulating in pure culture. Cramer, Vaduz
Warscheid T, Braams J (2000) Biodeterioration of stone: a review. Int Biodeterior Biodegrad 46:343–368
Young ME, Alakomi HL, Fortune I, Gorbushina AA, Krumbein WE, Maxwell I, McCullagh C, Robertson P, Saarela M, Valero J, Vendrell M (2008) Development of a biocidal treatment regime to inhibit biological growths on cultural heritage: BIODAM. Environ Geol 56:631–641
Zaitsev AN, Spratt J, Sharygin VV, Wenzel T, Zaitseva OA, Markl G (2015) Mineralogy of the Laetolil footprint tuff: a comparison with possible volcanic sources from the Crater Highlands and Gregory Rift. J Afr Earth Sc 111:214–221

Part VI
Organic Mineralogy

Chapter 37
Acids with Chiral Molecules as Essential Organic Compounds of Biogenic–Abiogenic Systems



Elena N. Kotelnikova, Anton I. Isakov, Lyudmila Yu. Kryuchkova, Andrey A. Zolotarev Jr., Sergey N. Bocharov and Heike Lorenz

Abstract The present review generalizes results of a comprehensive experimental study (by means of PXRD, SCXRD, TRPXRD, DSC, IR) of six chiral systems. These are enantiomeric systems of a single substance: (1) the system with a eutectic point (*S*- and *R*-*E*3*ClMA*), (2) the system forming a binary compound (L- and D-phenylglycine), and (3) the system forming equimolar and non-equimolar discrete compounds (*S*- and *R*-malic acid). Also these are diastereomeric systems and a system composed of enantiomers of different substances: (4) the diastereomeric system with continuous solid solutions (L- and L-*allo*-threonine), and (5) the diastereomeric system with a eutectic point (D- and L-*allo*-threonine), and (6) the system of enantiomers of different substances (L-valine and L-isoleucine) which contains a non-equimolar discrete compound. Crystal structures of discrete equimolar and non-equimolar homomolecular and heteromolecular compounds found in the systems under discussion are described. Also, polymorph diversity and the limits of solid solutions in such binary systems are discussed.

Keywords Organic acids · Phase diagrams · Chiral molecules · Racemates · Solid solutions · Non-equimolar compounds

E. N. Kotelnikova (✉) · A. I. Isakov · L. Yu. Kryuchkova · A. A. Zolotarev Jr. · S. N. Bocharov
Saint Petersburg State University, Saint Petersburg, Russia
e-mail: kotelnikova.45@mail.ru

H. Lorenz
Max Planck Institute for Dynamics of Complex Technical Systems, Magdeburg, Germany

© Springer Nature Switzerland AG 2020

O. V. Frank-Kamenetskaya et al. (eds.), *Processes and Phenomena on the Boundary Between Biogenic and Abiogenic Nature*, Lecture Notes in Earth System Sciences,
https://doi.org/10.1007/978-3-030-21614-6_37

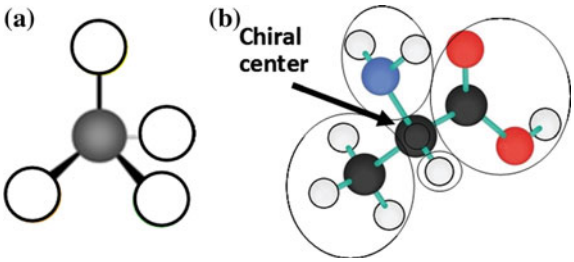


Fig. 37.1 Tetrahedral carbon atom having identical substituents (**a**) and asymmetrical carbon atom having four different substituents (**b**)

37.1 Introduction

Molecules of a great number of organic substances, including organic acids, have a chiral center. Usually, a chiral center is an asymmetric carbon atom. It is attached via "tetrahedral" bonds to four different substituents (ligands) (Fig. 37.1). Chiral molecules can exist as levorotatory (L, or *S*) and dextrorotatory (D, or *R*)[1] enantiomers (optically active stereoisomers). Enantiomers are non-identical stereoisomers that are mirror images of each other (Nogradi 1981). These mirror twins are non-superposable, while all their physical properties are identical, except for the direction of rotation of plan-polarized light. The phenomenon of ***enantiomerism*** (or chirality) is not inherent for molecules only. There is a plenty of other chiral entities such as crystals, organisms, objects, space groups, etc.[2] (Fig. 37.2).

In ***the living matter*** levorotatory forms predominate over dextrorotatory ones. Classic examples of such substances are amino acids that are essential constituents of both animals and plants. Many organic acids (amino acids, fatty acids, etc.) are well preserved in the ***non-living matter*** due to processes of fossilization of organics and, consequently, they are widely distributed in the geological media (sapropel clays, turfs, oil shales, coal, etc.) (Drozdova 1977), including substantially lithified rocks found at great depths with high temperatures (Anischenko and Shanina 2010).

The most known representatives of amino acids with levorotatory molecules are proteinogenic amino acids. 19 out of 20 of them (in the standard genetic code) are chiral. Their name, as well as their prevalence is attributed to the fact that proteinogenic acids are constituents of proteins. In contrast to proteins, these amino acids persist after death of living cells and become integrated into the geosphere (Drozdova 1977; Anischenko and Shanina 2010; Robins et al. 2001; De Torres et al. 2010). Here, as a result of thermocatalytic reactions, a ***racemization*** process takes place. It

[1]The designations represent the relative (L and D) and absolute (*S* and *R*) configurations of the levorotatory and dextrorotatory enantiomers, respectively.

[2]A chiral center can take place not only at a stereogenic atom, but also in a "space", for example, in the molecule center of gravity. Not only a chiral center, but also a chiral axis, and a chiral plane can be a source of chirality.

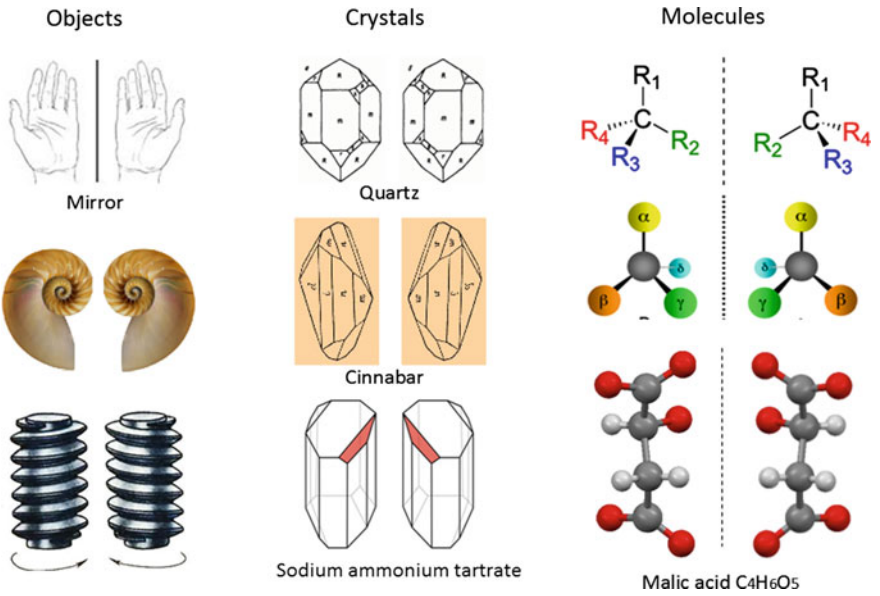


Fig. 37.2 Examples of chirality

leads to equilibration of proportions of levorotatory and dextrorotatory enantiomers due to statistics-ruled transformation, for example, of the former to the latter.

The mechanism of the racemization process was studied in aqueous solution and currently it is generally accepted (Robins et al. 2001). Racemization is considered to proceed via a two-stage route that is schematically shown in Fig. 37.3a. The first stage includes «elimination» of the proton H^+ attached to the asymmetric carbon atom of the enantiomer (e.g. levorotatory, L) induced by the action of a hydroxyl anion or a water molecule. As a result, the tetrahedral coordination of the carbon C in a neutral molecule is replaced by triangle configuration of the charged planar "carbanion", which already has no chiral center. At the second stage the proton H^+ "returns" to the molecule, but it can be attached with equal probability either to initial or to a new site of the molecule. At the new site it forms the H–C bond (dextrorotatory enantiomer D), which is a mirror image of the initial C–H bond (levorotatory enantiomer L).

"In the ***geological*** scale of time spontaneous transformation of L-amino acids into D-amino acids occurs till equimolar (racemic) mixtures of enantiomers will be formed" (De Torres et al. 2010). Besides the factor of time, heating in acidic and alkaline media can drive the amino acids racemization process (Bada and Schroeder 1975). Moreover, it was stated that amino acids undergo racemization also within natural matrices, such as bones, teeth, mollusk shells, etc. This allows using the amino acid racemization phenomenon in geochronology, paleontology, stratigraphy, archaeology, paleothermometry, etc. (Bada and Schroeder 1975; Oches and McCoy 2001; Robins et al. 2001; De Torres et al. 2010).

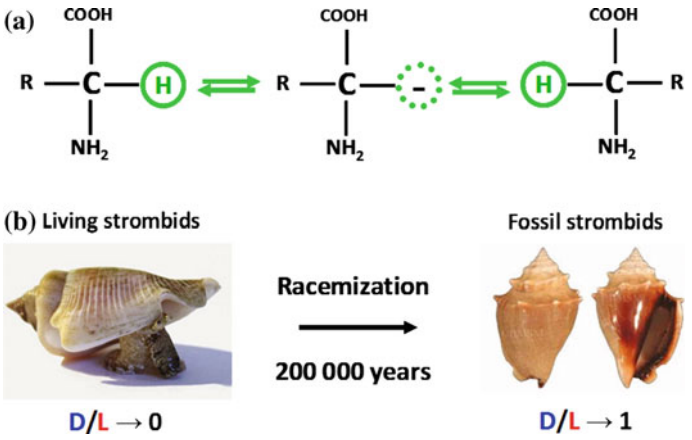


Fig. 37.3 Mechanism of racemization of amino acid enantiomers (**a**) and example of using the D- and L-enantiomer ratio for dating (**b**)

The age of a sample can be determined, if the rate of racemization and current enantiomer ratio D/L in the sample are known (Robins et al. 2001). ***Paleotemperature*** can be determined as a function of racemization degree, since the rate of racemization is temperature-dependent. For this, the age of the sample must be determined using another independent method (Bada and Schroeder 1975).

Contents and ratio of L and D enantiomers of a particular amino acid in a sample are usually determined using chromatographic techniques, such as ion-exchange liquid chromatography, reversed-phase and gas chromatography (Oches and McCoy 2001). Two amino acids most frequently used for geochronological studies are isoleucine and aspartic acid. For example, if an expected age of the sample ranges from 20,000 to 200,000 years, isoleucine is prospective for age determination (Fig. 37.3b). This time range corresponds to the temperature of "buried" sample about 18–24 °C.

Therefore, the racemization phenomenon allows using naturally occurring amino acids as specific time markers and indicators of conditions of sedimentation, deposition, and transformation of initial organic substance.

During ***practical use*** of a chiral organic substances (including amino acids), in particular, in ***pharmaceutical*** and food industries, it is to be taken into account that products of chemical synthesis usually contain equal proportions of both levorotatory and dextrorotatory enantiomers. The number of drugs that include chiral active pharmaceutical ingredients (API's) increases continuously. According to Kaemmerer (2012), already in 2004, nine out of ten most popular marketed pharmaceuticals contained chiral active components. Moreover, while in 1985 the drugs containing chiral substances comprised a racemic mixture of both enantiomers, in 2004 all newly registered "chiral drugs" contained only a ***single enantiomer*** of the API (Murakami 2007). This is because of possible different effects of enantiomers on targets in such a complex chiral medium as living organisms. For example, one of them can have

the desired beneficial effect, while the other might show no activity or even can be even harmful (Lin et al. 2011).

As there is an ***equal probability*** of formation of different enantiomers in the products of industrial ***non-stereoselective*** synthesis, the problem of ***chiral resolution*** rises. The choice of a suitable method for resolution is rather limited since the methods very much depend on each compound. There are following main groups of methods (Kaemmerer 2012): techniques using specific chiral agents (Jacques et al. 1981; Liu et al. 2004; Xie et al. 2008) and crystallization methods applying (usually) chiral seeds (e.g. Galan et al. 2015).

Other approaches also exist. A principally different way implies direct preparation of the enantiomerically pure compounds. It is so-called ***stereoselective synthesis***, or asymmetrical synthesis. It is based on use of specific substrates or specific catalysts (organic, metalorganic, enzymatic, etc.). Since chiral compounds are extremely numerous, adjusting the asymmetrical synthesis for each compound is most likely infeasible, at least in the nearest future. Moreover, in some cases preparation of the desired compound via this method could prove more expensive than non-stereoselective synthesis with subsequent resolution.

The most cost-effective and efficient techniques to obtain pure enantiomers via resolution of racemic (and also non-racemic mixtures) are ***crystallization*** methods (Lorenz and Seidel-Morgenstern 2014). Understanding of polymorphic and isomorphic relationships, i.e. gaining an insight into ***phase equilibria*** in a system of enantiomers to be resolved is a key factor for development of such methods.

When studying the limits of solid solutions and polymorph diversity of organic compounds, usually, such geometrical and chemical factors as shape of the molecule, it's symmetry, and type of intramolecular bonding are taken into consideration. In the recent years, an important geometrical (stereochemical) factor, namely, chirality and configuration of a molecule, has been considered when analyzing a molecular packing in crystal structures. It is also to be kept in mind that there are various natures of "mixtures" in enantiomeric systems. They are physical mixtures (conglomerates), or solid solutions (mixed crystals), or equimolar and non-equimolar homomolecular and heteromolecular discrete compounds.[3]

Our main results of investigation of limits of solid solutions and types of solid phases formed in various chiral binary systems are discussed below. The experiments were conducted using the following methods: Powder X-ray diffractometry (PXRD), Single crystal X-ray diffractometry (SCXRD), Temperature-resolved powder X-ray diffractometry (TRPXRD), Differential scanning calorimetry (DSC), Infrared spectroscopy (IR), and Hot stage microscopy (HSM).

[3]The terms "non-equimolar discrete compounds" and "homomolecular" and "heteromolecular discrete compounds" related to chiral compounds were firstly introduced in the papers (Isakov et al. 2015) and (Kotelnikova et al. 2017), respectively.

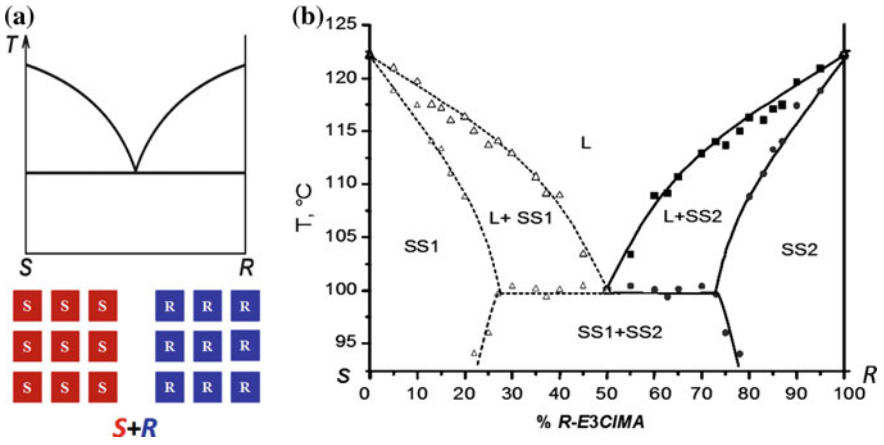


Fig. 37.4 **a** Schematic phase diagram of systems forming conglomerates (top) and scheme of molecular packing in the equimolar phase $R + S$ (bottom), and **b** phase diagram of the *E*3*ClMA* system; the left part is plotted as a mirror image of the right part

37.2 Systems of Enantiomers of a Single Compound

Constituents of the systems are enantiomers of a single compound. Three types of such systems are discussed below: (1) a system with a eutectic point, (2) a system forming an equimolar compound, and (3) a system forming equimolar and non-equimolar discrete compounds. Since phase diagrams of enantiomeric systems are symmetric only halve of such diagram can be examined.

37.2.1 Systems with a Eutectic Point

One of the representative systems of this type (Fig. 37.4) is the system formed by the *S* and *R* enantiomers of the ethanolamine salt of 3-chloromandelic acid, abbreviated as *E*3*ClMA*, which we studied earlier (Taratin et al. 2012). A molecule of *E*3*ClMA* ($C_{10}H_{14}O_4NCl$) contains one chiral center (Fig. 37.5a). The projection of the crystal structure of the *E*3*ClMA R*-enantiomer (S. G. $P2_12_12_1$) onto the *bc* plane (Fig. 37.5b) appears as an arrangement of alternating layers composed of chiral molecules of 3-chloromandelic acid (3*ClMA*, two layers) and achiral molecules of ethanolamine (*EA*, one layer) interlinked with hydrogen bonds to form a network. The fact that the direction of the majority of hydrogen bonds (four out of five) does not depend on the molecule configuration within the crystal structure is a feasible explanation of isomorphic miscibility (however limited) in this enantiomeric system.

In the phase diagram (Fig. 37.4b), the compositional ranges of 0–ca. 20 and ca. 80–100 wt% *R-E3ClMA* correspond to the regions of existence of “orthorhombic”

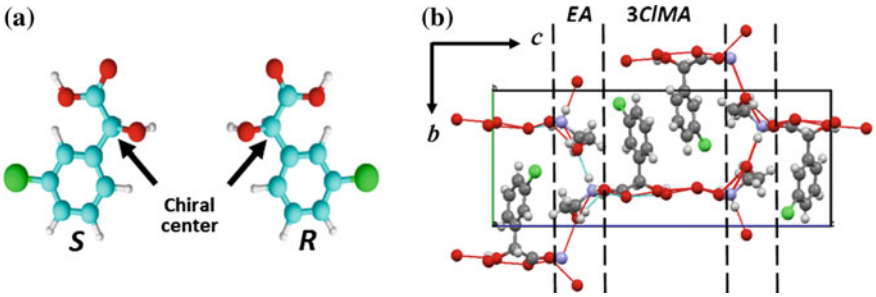


Fig. 37.5 The structures of *S* and *R* enantiomer molecules (**a**) and the crystal structure of the *R* enantiomer (**b**) of *E*3*ClMA*

solid solutions enriched with *S*-enantiomer (SS1) and *R*-enantiomer (SS2), respectively, while the compositional range in-between comprises the domain of physical (eutectic) mixtures of solid solutions (SS1 + SS2).

Existence of physical mixtures and solid solutions in the given compositional ranges can be deduced from the type of compositional dependence of orthorhombic cell parameters *a* and *c* (Fig. 37.6) and from DSC results. The parameters remain almost unchanged between ca. 20 and 80% of *R-E*3*ClMA* (SS1 + SS2 region), thus correspond to physical mixtures of solid solutions. Samples from this area have two endothermic peaks in their DSC melting curves. In the range above ca. 80% *R-E*3*ClMA* (SS2 region) the parameters are substantially dependent on the composition, which indicates incorporation of an admixture enantiomer into the crystal structure of a matrix enantiomer. Samples from this area are characterized by single endothermic peak in their DSC curves.

37.2.2 Systems Forming an Equimolar Compound

In literature, systems of this type (Fig. 37.7a) are usually called "systems containing a binary compound" or "systems containing a true racemate". An exemplary system containing an equimolar compound is formed by the L- and D-enantiomers of phenylglycine and was studied by the present authors. Preliminary data can be found in the work of L. Yu. Kryuchkova et al. (2018a). A molecule of phenylglycine ($C_8H_9NO_2$) contains an aromatic phenyl group C_6H_5, which substitutes one of the hydrogen atoms in the achiral glycine molecule ($C_2H_5NO_2$) (Fig. 37.8) leading to a chiral center. Samples of the enantiomer L, racemate DL, and of seven intermediate mixtures having various DL/L ratios were recrystallized from aqueous solutions. It was found that the system is free of solid solutions even in vicinity of the system components. All the X-ray diffraction patterns (Fig. 37.9) contain two sets of peaks that correspond to mixtures of the DL racemate and L enantiomer phases taken in various quantitative proportions. Melting points of the racemate and the enantiomer are 290

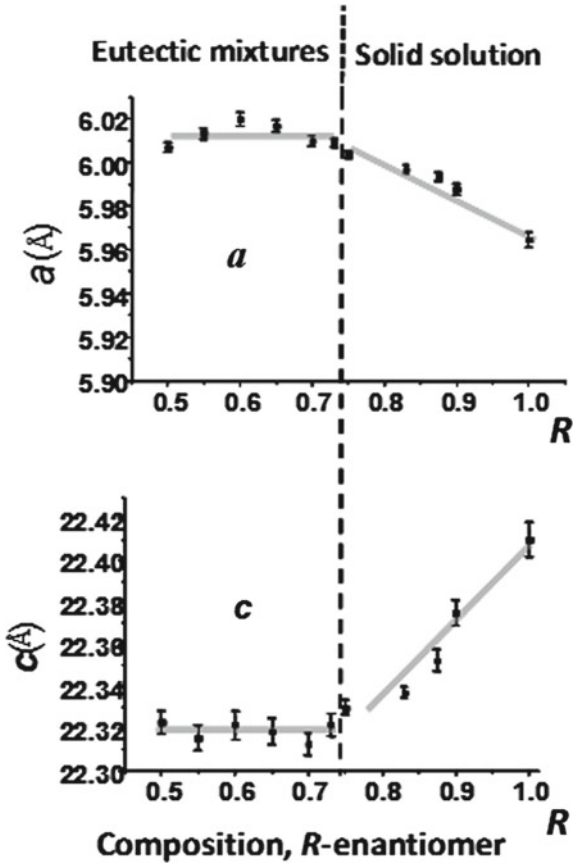


Fig. 37.6 Compositional dependence of the parameters *a* and *c* of the *E3ClMA* orthorhombic unit cell

and 302 °C, respectively (according to manufacturer Sigma-Aldrich, USA). Consequently, the phase diagram of the phenylglycine enantiomeric system (Fig. 37.7b) corresponds to the variant 3 of potential cases shown in Fig. 37.7a.

Projections of the crystal structures of L- and DL-phenylglycine onto the *ac* plane of their monoclinic cells are depicted in Fig. 37.10a and b, respectively. The crystal structure of the L enantiomer (S. G. $P2_1$) was firstly determined by the present authors (CCDC: 1903255), and the crystal structure obtained for the racemate (S. G. $P2_1/c$) was found consistent with the data of Cambridge Structural Database (CSD: FIVGEW).

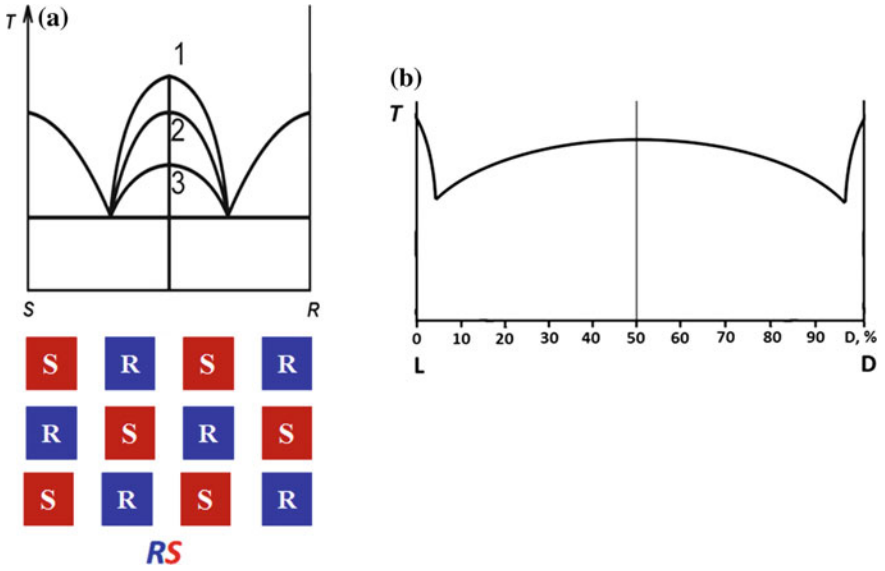


Fig. 37.7 **a** Exemplary schematic phase diagrams of systems containing a racemic compound (top) and representations of molecular packing in equimolar *RS* phases (bottom) and **b** the schematic phase diagram of phenylglycine enantiomers. Curves 1, 2, and 3 correspond to racemic compounds with melting points that are, respectively, above, equal to, or below the melting points of the enantiomers

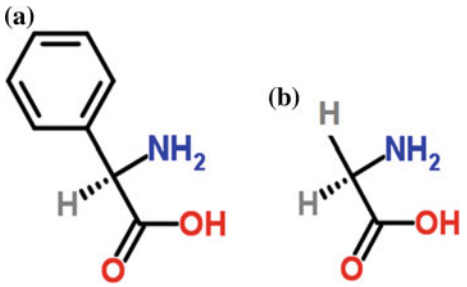


Fig. 37.8 The structures of molecules of phenylglycine (**a**) and glycine (**b**)

37.2.3 Systems Forming Equimolar and Non-equimolar Discrete Compounds

Chiral systems with a binary (equimolar 1:1) compound, or a true racemate, can be further complicated by formation of non-equimolar discrete compounds (1:N). In literature these compounds are usually called "anomalous racemates" (Bergmann and Lissitzin 1930) or "anomalous conglomerates" (Bredikhin et al. 2015; Gubaidullin et al. 2014). In our previous review (Kotelnikova et al. 2017), it was mentioned that homomolecular non-equimolar discrete compounds had been found only in 16 enan-

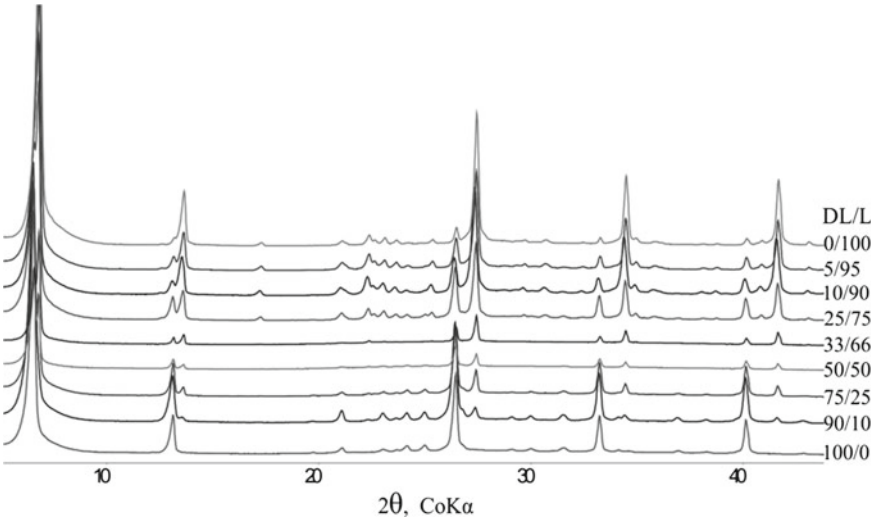


Fig. 37.9 X-ray diffraction patterns of the components (DL and L) and intermediate DL/L compositions in the chiral phenylglycine system. The proportions of the components are indicated in the figure

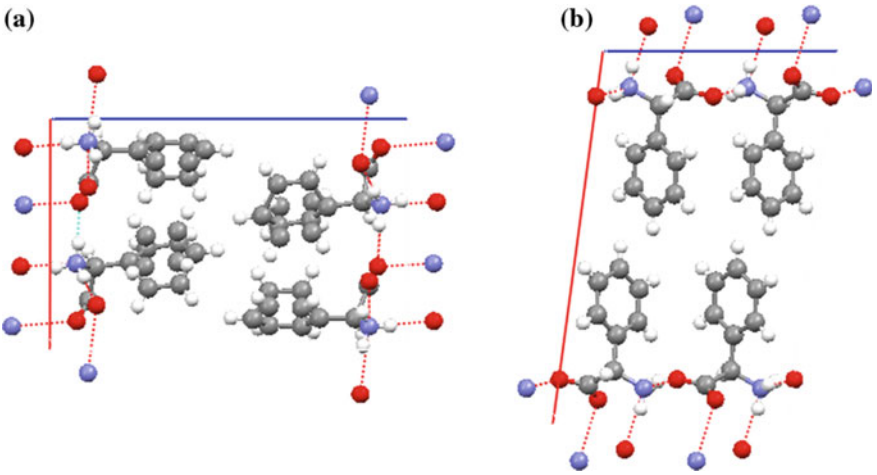


Fig. 37.10 Projections of the crystal structure of phenylglycine L-enantiomer (**a**) and DL-racemate (**b**) onto the *ac* plane of its monoclinic unit cell

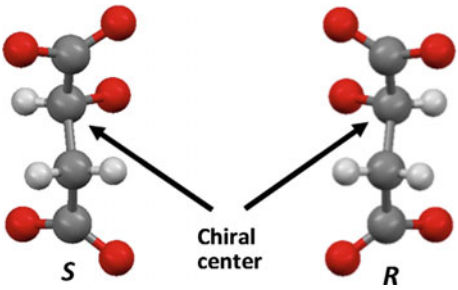


Fig. 37.11 The structures of molecules of the *S* and *R* enantiomers of malic acid

tiomeric systems, and, moreover, crystal structures of four of these compounds are still unknown. The above publication includes a historical overview of investigations of the system of malic acid *S* and *R* enantiomers, as well as our results obtained for the system by means of PXRD, SCXRD, TRPXRD, HPLC, DSC, IR, and HSM methods (Isakov et al. 2013a, b, 2015; Kotelnikova et al. 2017, 2018). The system of malic acid enantiomers is a classical example of a system forming equimolar and non-equimolar discrete compounds. Malic acid ($C_4H_6O_5$), which is an aliphatic dicarboxylic oxyacid, has a relatively simple molecule structure characterized by one chiral center (Fig. 37.11).

This enantiomeric system is additionally complicated by the presence of three polymorphs of the binary compound and two polymorphs of the non-equimolar discrete compounds. Two monoclinic modifications of the racemate, namely, the stable modification *RS*I and metastable modification *RS*II (symbols introduced by the authors), had been known in literature (CSD: DLMALC11 and DLMALC, respectively). We discovered (Isakov et al. 2013a) the new metastable modification *RS*III. In the schematic diagram (Fig. 37.12), non-equimolar discrete stable (S_3R and SR_3) and newly found metastable ($3S1R$ and $1S3R$) compounds are located symmetrically (S:R = 3:1 and 1:3) in relation to the equimolar composition.

The crystal structure of the non-equimolar discrete triclinic ($P1$) compound S_3R (Fig. 37.13a) (Kotelnikova et al. 2017) can be considered as a combination of molecular chains inherent for crystal structures of enantiomer (Fig. 37.13b) and racemate (Fig. 37.13c). Polymorph diversity of discrete compounds in the system is driven by the crystallization conditions, such as type of medium, rate of crystallization, temperature, etc. The presence of the newly discovered additional discrete phases forced us to redetermine precisely the limits of solid solutions in the malic acid system.

Structural particularities of all the discrete phases studied are reflected in the sequence of polymorph transformations and the mode of thermal deformations of the corresponding crystal structures (Isakov et al. 2013a, b; Kotelnikova et al. 2017). The resulting phase diagram of the malic acid enantiomers system is schematically shown in Fig. 37.14.

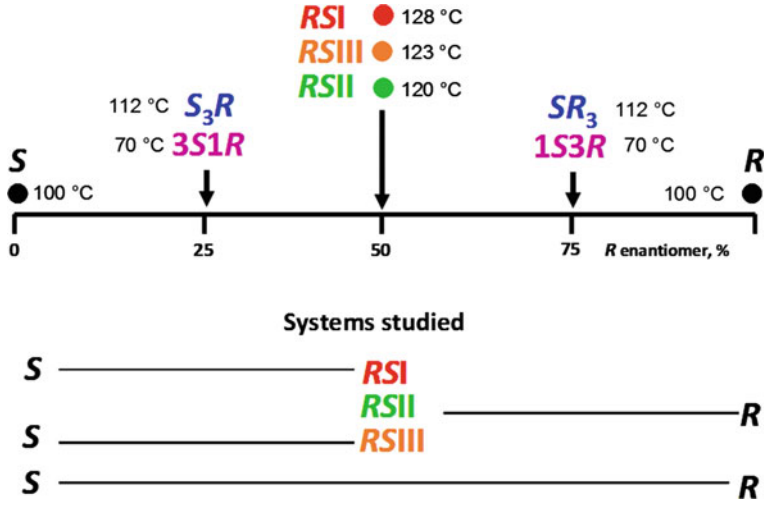


Fig. 37.12 Discrete equimolar and non-equimolar phases in the system of malic acid enantiomers (top) and the corresponding types of systems studied (bottom). More details are given in the text

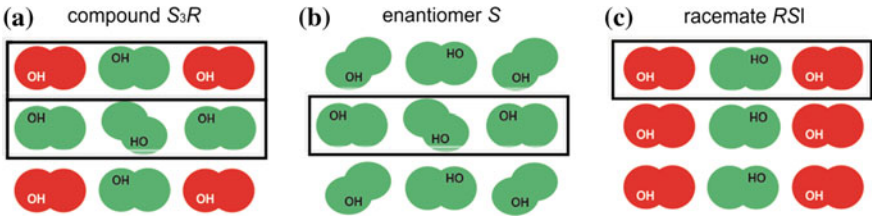


Fig. 37.13 Models of the crystal structures of malic acid non-equimolar discrete compound S_3R (**a**), enantiomer *S* (**b**), and racemate *RS*I (**c**). More details are given in the text

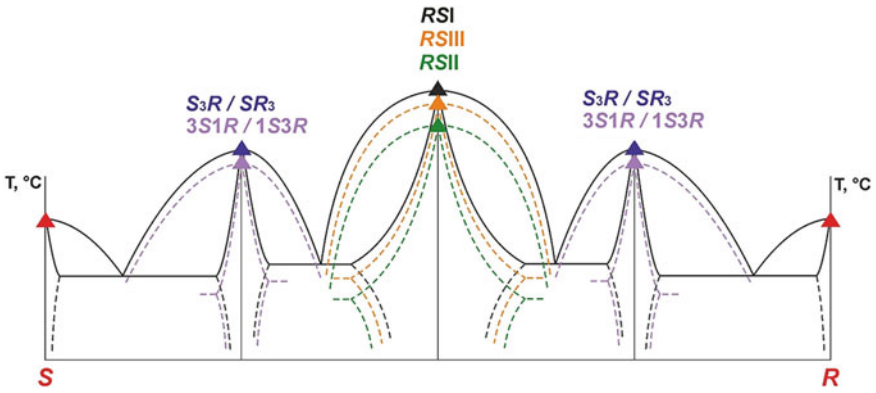


Fig. 37.14 Schematic representation of the phase diagram of the malic acid enantiomeric system (not scaled)

37.3 Systems of Diastereomers and Systems of Enantiomers of Different Compounds

Binary diastereomeric systems and binary systems of enantiomers of different compounds are discussed below. Diastereomers are stereoisomers having different configurations and are not mirror images of each other. Diastereomers have identical chemical properties, but their physical properties differ (for example, melting points); that is why we consider diastereomeric systems as systems containing different compounds. Obviously, enantiomers of different substances differ in both chemical and physical properties.

37.3.1 Binary Systems of Diastereomers

Two types of such systems are discussed: (1) a system with continuous solid solutions, and (2) a eutectic system. In contrast to enantiomeric systems of a single compound, diastereomeric systems are not symmetrical. A good example for representative analysis of both types of diastereomeric systems is the system of threonine. Threonine is one of two proteinogenic amino acids, whose molecule has two chiral centers (the other one is isoleucine), and one of eight essential proteinogenic amino acids. Essential amino acids are not produced by the human body and, consequently, must be consumed with food.

In accordance with the formula 2^n, where n is a number of configurations, the aliphatic threonine molecule ($C_4H_9NO_3$) that contains two different chiral centers, can exist in four molecular configurations (Fig. 37.15). There are two pairs of enantiomeric (mirror-related) molecular configurations: one pair is L–D and another pair is L-*allo*–D-*allo*. In the case of the first pair (L–D), the methyl CH_3 and amine NH_2 groups are located on the opposite sides of the axis of the atomic chain C1–C2–C3–O3, while in the case of the second pair (L-*allo*–D-*allo*), these groups are located on the same side of this axis (Fig. 37.15). Each of enantiomers of the first pair is a diastereomer relatively to enantiomers of the second pair, and vice versa. Diastereomeric molecules are not mirror images of each other. Both diastereomer molecules in the left pair L–L-*allo* are levorotatory, i.e. have the same sign of optical activity, as well as both diastereomer molecules in the right pair D–D-*allo* are dextrorotatory. Similar to enantiomeric pairs, diastereomeric molecules of the "diagonal" pairs, i.e. L–D-*allo* and D–L-*allo,* have opposite signs of optical activity. Obviously, it is adequate to study in a system only one pair of diastereomers with the same sign of optical activity, and one pair of diastereomers with the opposite signs of optical activity.

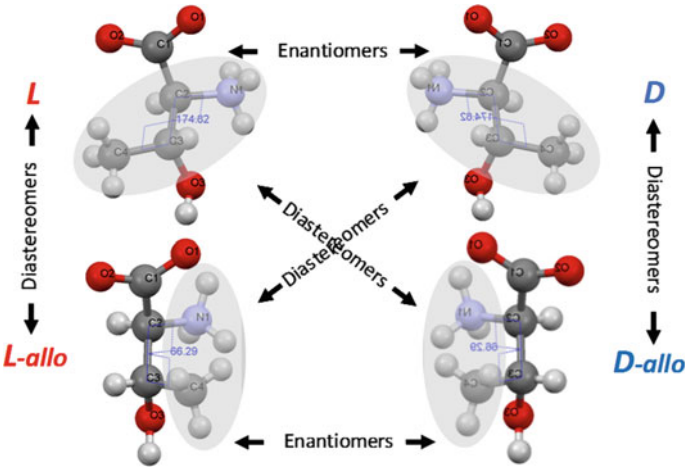


Fig. 37.15 Configurations of threonine molecules. The areas containing methyl and amino groups are shadowed

37.3.1.1 Systems Forming Continuous Solid Solutions

The system composed of L and L-*allo* diastereomers of threonine, which was studied earlier (Binev et al. 2014; Taratin et al. 2015), was found to be a representative example of the systems of this type (Fig. 37.16a). Diastereomeric molecules of constituents of this system have the same sign of optical activity. X-ray diffraction patterns of the L and L-*allo* diastereomeric components and their co-precipitated mixtures (17 compositions) are similar and indicated in the $P2_12_12_1$ space group. The formation of solid solutions of (L, L-*allo*)-threonine is confirmed by a smooth profile of the dependency of orthorhombic cell parameters and volume on composition (Fig. 37.17). Another proof is the correlation between orthorhombic cell parameters and solubility of mixtures in water (Binev et al. 2014).

The crystal structure of one of the solid solutions, having the composition ($L_{0.34}$, $L\text{-}allo_{0.66}$)-threonine, had been determined (Taratin et al. 2015) (Fig. 37.18). It was compared to the crystal structures of L-threonine (Shoemaker et al. 1950; Janczak et al. 1997) and L-*allo*-threonine (Swaminathan and Srinivasan 1975). The comparison showed that all the three structures are characterized by a similar "framework", composed of hydrogen bonds. The lengths of the hydrogen bonds depend on crystal composition only to a small extent, with the exception being N1···O3 bond. Whereas the distances between methyl groups appeared to substantially depend upon the crystal composition (Fig. 37.18). This fact is reflected in the thermal deformations studied for L and L-*allo* diastereomers and for two of the solid solutions (34 and 90% of L-threonine). Expansion with the highest degree of isotropy was registered for the crystal structure of the sample that contains the maximal number of admixture molecules (34% of L-threonine).

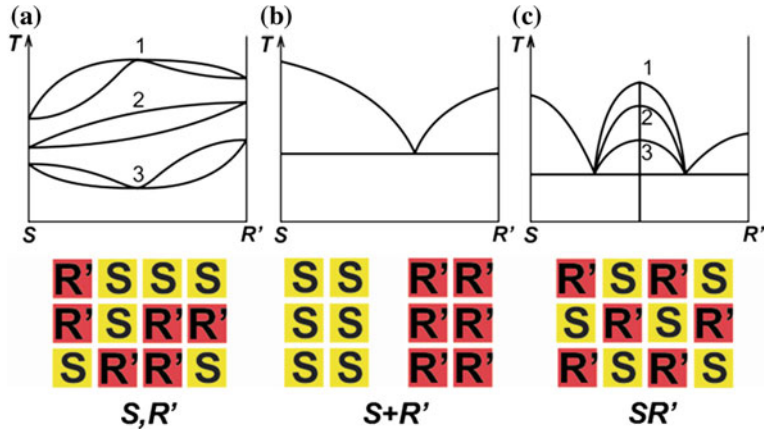


Fig. 37.16 Schematic diagrams representing continuous solid solutions (**a**), an eutectic point (**b**) and equimolar binary compounds (**c**) in binary systems of diastereomers and systems of enantiomers of different compounds (top). Molecular packing in the solid solution S, R' (**a**), in the physical mixture $S + R'$ (**b**) and in a binary compound SR' (bottom)

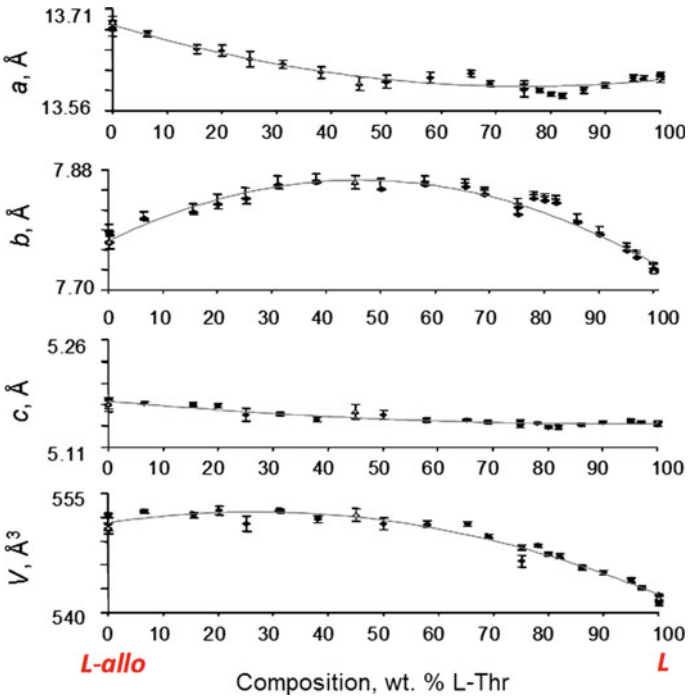


Fig. 37.17 Compositional dependence of the parameters a, b and c and volume V of the orthorhombic unit cell in the system of L and L-*allo* diastereomers of threonine

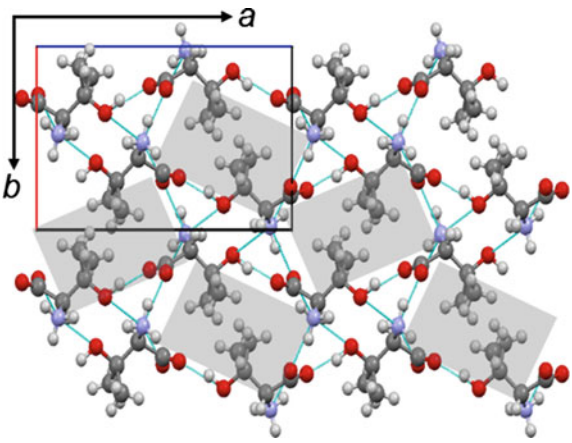


Fig. 37.18 Projection of the crystal structure of (L$_{0.34}$, L-*allo*$_{0.66}$)-threonine solid solution upon the *ab* plane. The areas containing methyl groups are shadowed

37.3.1.2 Systems with a Eutectic Point

A representative example of a system of this type (Fig. 37.16b) is the system of "diagonal" D and L-*allo* diastereomers of threonine (see Fig. 37.15) studied by present authors (Taratin et al. 2013). Diastereomeric molecules of the system components are characterized by different signs of optical activity. X-ray diffraction patterns of co-precipitated mixtures are similar to each other (Fig. 37.19b–d) and to that of an equimolar physical mixture of D and L-*allo* diastereomers of threonine (Fig. 37.19e). The diffractograms are characterized by two peak sets, where one set corresponds to the D diastereomer, while the other is attributed to the L-*allo* diastereomer (Fig. 37.19a and f, respectively). In contrast to a physical mixture of enantiomers, components of a physical mixture of diastereomers can be diagnosed from its diffraction pattern, which differs, at least to some extent, from the patterns of the individual diastereomers that have close, but not identical parameters of their orthorhombic cells. The biphasic nature of the samples allows to conclude that molecules of D- and L-*allo*-threonine do not mix in the solid phase, at least in the composition range of 20–80% of D-threonine.

Furthermore, it is to be noted that Sapoundjiev et al. (2006) classified the system of L and D enantiomers of threonine as the eutectic type system too (Fig. 37.16b). As the "diagonal" diastereomers, enantiomers of this system have the opposite signs of optical activity by definition (see Fig. 37.15).

37.3.2 Systems Composed of Enantiomers of Different Compounds

Binary systems formed by enantiomers of different substances can be divided into two groups. One of them comprises enantiomers having the same sign of optical

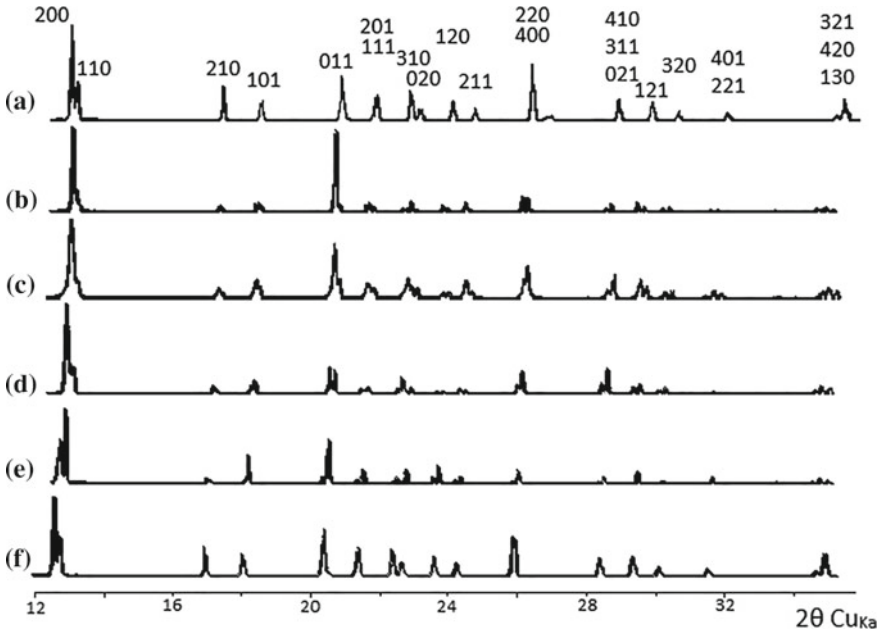


Fig. 37.19 X-ray diffraction patterns obtained for D-threonine (*a*), L-*allo*-threonine (*f*), and their co-precipitated mixtures of the following compositions (% D-threonine): 20 (*b*), 55 (*c*), 80 (*d*), and for their equimolar physical mixture (*e*)

activity, while the other contains enantiomers having opposite signs of optical activity. Moreover, in each group systems composed of molecules having (1) equal number and (2) different numbers of chiral centers can be distinguished.

In literature, there is a considerable number of works reporting studies of systems of different compounds. However, most of these publications discuss systems comprising molecules with only one chiral center (Kotelnikova et al. 2017, Table 3). The number of publications considering systems of molecules with different numbers of chiral centers is much scarce. Those works are related to systems comprising one component having one chiral center and another component having two chiral centers. These are the systems L-malic acid–L-tartaric acid and L-malic acid–D-tartaric acid (Aakeröy et al. 1996; Eddleston et al. 2012). We are familiar with only one publication available related to a system constituted by molecules having *two similar* chiral centers, the system is (–)-dilactic acid–(+)-2,4-dimethylglutaric acid (Fredga 1940). We are not aware if there are any works reporting systems that consist of molecular components possessing *two (or more) different* chiral centers.

37.3.2.1 Systems Forming an Equimolar Compound

The above-mentioned review (Kotelnikova et al. 2017) exemplifies 13 systems composed of different substances, in which a binary equimolar compound (literature examples) is formed (Fig. 37.16c). The term "quasiracemates" is often used for equimolar compounds of different substances (Fredga 1944). Molecules of almost all enantiomers in the listed systems have one chiral center. Some exceptions include the system D-valine–L-isoleucine (Dalhus and Görbitz 1999), where the valine molecule has one chiral center and the isoleucine molecule contains two of them.

This system differs from the system L-valine–L-isoleucine (studied by present authors and to be discussed in Sect. 3.2.2) by chirality (configuration) of the valine molecule. This is reflected in the differences of the molecular composition of discrete phases formed in the systems. In the system D-valine–L-isoleucine there is a binary compound (Dalhus and Görbitz 1999), which can be regarded as heteromolecular equimolar compound (Kotelnikova et al. 2017).

37.3.2.2 Systems Forming a Non-equimolar Discrete Compound

In the above-mentioned review (Kotelnikova et al. 2017) there are also systems of different substances described, which are found to contain non-equimolar discrete compounds. Only three examples of such systems are reported in literature. Moreover, a crystal structure had been determined for only one of them, discovered by present authors in the system L-valine–L-isoleucine (Isakov et al. 2016a, b). In literature, non-equimolar discrete compounds in systems of different compounds are termed sometimes "anomalous quasiracemates" (Andersson et al. 1966).

Molecules of the L-valine–L-isoleucine system components have the same (positive) sign of optical activity and quite similar shapes. In the case of valine ($C_5H_{11}NO_2$) one site at the aliphatic carbon chain is occupied by a hydrogen atom H while in the case of isoleucine ($C_6H_{13}NO_2$) this site is occupied by a methyl group CH_3 (Fig. 37.20). Limits of solid solutions have been described in this system and also a non-equimolar discrete compound V_2I with the ratio L-Val (V):L-Ile (I) = 2:1 (Figs. 37.21 and 37.22a). Therefore, this system is one of that containing a non-equimolar discrete compound and partial solid solutions (Isakov et al. 2016a).

The crystal structures of L-valine (S. G. $P2_1$) and L-isoleucine (S. G. $P2_1$) have been known for a long time (Torii and Iitaka 1970, 1971). The projections of the monoclinic cells of L-valine (Fig. 37.22b) and isoleucine (Fig. 37.22c) were plotted using structural data from CSD (identifiers LVALIN01 and LISLEU02, respectively). The monoclinic cell of the compound V_2I (S. G. $C2$) is doubled in comparison to that of valine and isoleucine and it contains eight molecules (Fig. 37.22a). Each of two independent molecular positions is characterized by mixed occupation, i.e. it can be occupied either by a valine or a isoleucine molecule (Isakov et al. 2016b). Thermal deformations of crystal structures of the discrete compounds L-valine, L-isoleucine and V_2I are mainly realized through an increasing distance between molecular layers, because molecules within the layers are interlinked with comparatively strong

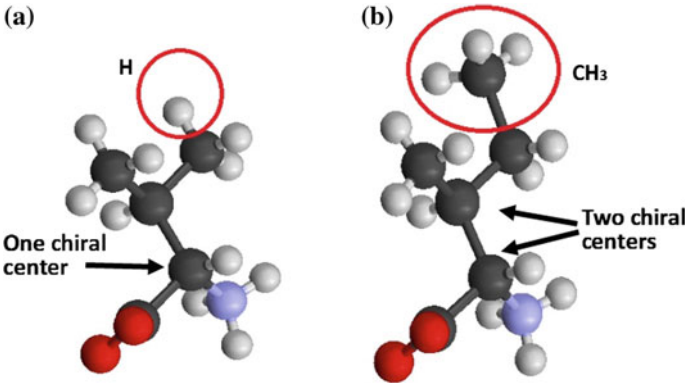


Fig. 37.20 The structures of molecules of valine (**a**) and isoleucine (**b**)

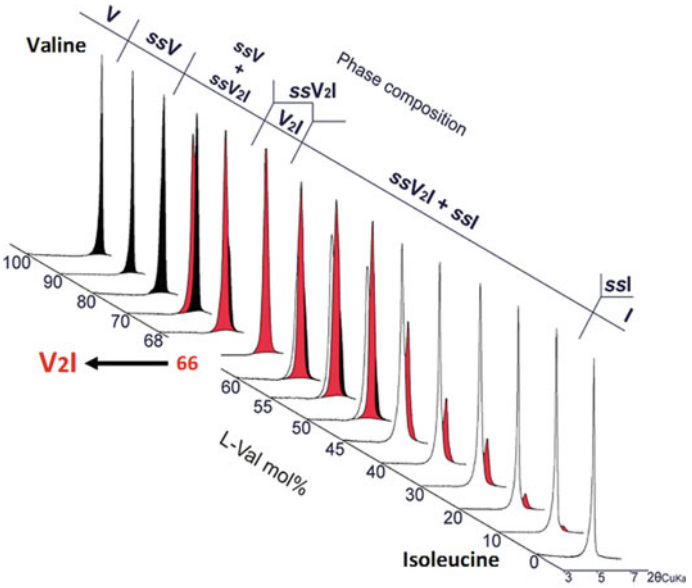


Fig. 37.21 Fragments of X-ray patterns (3–8° of $2\theta_{CuK\alpha}$) obtained for the samples of L-valine (V) and L-isoleucine (I), for the discrete compound V_2I, and for mixtures of solid solutions of the types ssV, ssI, and ssV_2I

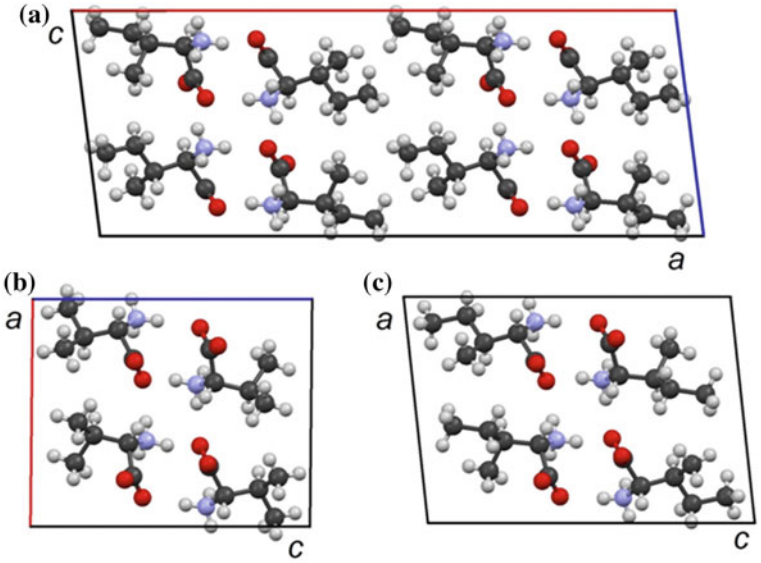


Fig. 37.22 Projections of the monoclinic cells of the discrete compound V_2I (**a**), L-valine (**b**), and L-isoleucine (**c**) on the *ac* plane

hydrogen bonds, while the layers are connected to each other by comparatively weak van der Waals interactions (Isakov et al. 2016b; Kotelnikova et al. 2018).

37.4 Conclusions

In this brief review of our results for binary systems of acids with chiral molecules we have tried to demonstrate the diversity of such systems and outline some prospective approaches for their further investigations. The review cites the results obtained chiefly by means of diffraction methods to accent the potential of the PXRD, SCXRD, and TRPXRD techniques for examination of systems with chiral molecules. Of course, comprehensive investigation of chiral systems requires using several methods and this point is also emphasized in our publications involving e.g. Hot stage microscopy, DSC and solubility studies in presence of solvents.

Among the studied enantiomeric systems of a single substance, a system containing continuous solid solutions had not been found. According to the statistic data (Jacques et al. 1981), the majority (about 90%) of enantiomeric systems belong to the type of systems forming a binary compound at equimolar composition (true racemate). About 10% is the proportion of systems with a eutectic point, while systems containing continuous solid solutions are rare.

However, we were lucky to find such a system among diastereomeric systems. It became clear that integrity of hydrogen bonds, i.e. the absence of significant disruptions in a crystal structure bonding, plays the key role in the process of formation of solid solutions in diastereomeric systems. Preservation of hydrogen bonds between co-existing molecules depends on H-bonds orientation, which, in turn, depends on configuration (chirality) of molecules. As a rule, significant disruptions are absent when molecular configurations are similar, i.e. when molecules have the same sign of optical activity (chirality). The system of L and L-*allo* diastereomers of threonine (Binev et al. 2014; Taratin et al. 2015) can serve as example. Stereoisomers having the opposite signs of optical activity (systems of L-Thr–D-Thr and D-Thr–L-*allo*Thr) do not form solid solutions due to mismatched orientations of hydrogen bonds in their crystal structures. Mismatch of orientations is caused by non-coinciding directions of proton donors and acceptors in the adjacent molecules. This makes formation of a part of hydrogen bonds impossible.

Rather limited, but nevertheless perceptible miscibility (about 20%) was observed in the enantiomeric system of ethanolamine salt of 3-chloromandelic acid (*E*3*ClMA*). In this case, only one out of five same type hydrogen bonds present in the crystal structure of *E*3*ClMA* was noticeably «damaged» when forming a solid solution.

An important part among the investigated systems belongs to systems with non-equimolar discrete compounds. Such examples can be found in literature among enantiomeric systems of a single substance, the examples are discussed in the review (Kotelnikova et al. 2017). They include the system of malic acid enantiomers, which contains both equimolar and non-equimolar discrete compounds (Isakov et al. 2013a, 2015).

Non-equimolar discrete compounds in systems of different substances is an even more rare phenomenon than that presented in enantiomeric systems of a single substance. In published literature there are only three examples of systems containing non-equimolar discrete heteromolecular compounds (Kotelnikova et al. 2017). We studied one of such systems and determined a crystal structure of a non-equimolar discrete compound (Isakov et al. 2016a, b). The comparative "rarity" of such systems is mostly consequence of the complexity of their investigation. This conclusion is based upon, for example, the history of investigation of the L-valine–L-isoleucine system. The scientists who studied this system earlier (Koolman and Rousseau 1996; Kurosawa et al. 2005) just missed out the non-equimolar discrete compound.

There is every reason to believe that non-equimolar discrete heteromolecular compounds are not so uncommon. In both systems currently under investigation we identified non-equimolar discrete compounds. These are the systems L-leucine–L-isoleucine (Kryuchkova et al. 2018b; CCDC: 1904158) and L-valine–L-leucine (Isakov et al. 2018; CCDC: 1903257) (Fig. 37.23). At present it is impossible to determine the effect (positive, negative, or neutral) which non-equimolar discrete compounds formed in some chiral systems can produce in the living organisms.

Importance of studying the phase relationships in the studied systems of organic acids is mainly dictated by their practical applications. Malic acid is used in food industry, phenylglycine—in indigo production. Threonine participates in the synthesis of collagen and elastane, in protein and lipid metabolism. Valine serves as a source

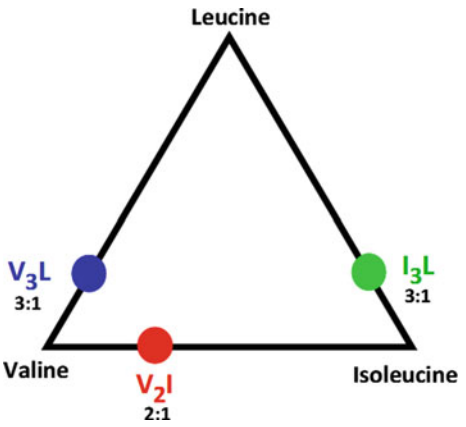


Fig. 37.23 Schematic representation of compositions of non-equimolar discrete compounds found in three binary systems of L-amino acids. More details are given in the text

of energy for muscle cells; it is used in treatment of drug abuse, depression, disseminated sclerosis. Leucine is a constituent of natural proteins; it is used in treatment of liver disorders and anaemia. Isoleucine participates in the hemoglobin synthesis, regulates blood glucose level, controls the processes of energy supply, and improves synthesis of epidermis.

Amino acids can have both biogenic and abiogenic origin. Many investigators are interested in the phenomenon of the first synthesis of amino acids (so-called prebiotic synthesis) in view of the question of life genesis on the Earth. The energy for abiogenic synthesis may be provided by lightning discharges, volcanic activity, cosmic irradiation, etc. Amino acids have been found in meteorites (glycine, alanine, proline, glutaminic acid, sarcosine, isoleucine, etc.), in samples of the moon soil (glycine, alanine, etc.), and in volcanic ashes (glycine, alanine, serine, aspartic acid, etc.) as well. Nevertheless, the majority of the naturally occurring amino acids (at least those that have been studied) are found in fossilized remnants of ancient organisms.

Acknowledgements The investigations were performed using equipment of the Resource Centre for X-ray Diffraction Studies of Saint Petersburg State University and equipment of the MPI Magdeburg PCF lab. The authors thank Dr. N. Taratin, Dr. D. Binev, Dr. S. Muenzberg, Dr. M. G. Krzhizhanovskaya, Prof. A. Seidel-Morgenstern and Prof. G. Coquerel for their contributions over the years. The authors appreciate the financial support provided by the Russian Foundation for Basic Research (Projects: 18-35-00183 mol_a and 16-29-11-727 ofi_m).

References

Aakeröy CB, Cooke TI, Nieuwenhuyzen M (1996) The crystal structure of the molecular cocrystal *L*-malic acid *L*-tartaric acid (1/1). Supramol Chem 7(2):153–156

Andersson M, Fredga A, Jerslev B (1966) Anomalous racemates of malic acid. Acta Chem Scand 20:1060–1063

Anischenko LA, Shanina SN (2010) Amino acids in the depths: the results of the study and the prospects for the study. Bull Inst Geol, Komi SC UB RAS 9:34–35 (in Russian)

Bada JL, Schroeder RA (1975) Amino acid racemization reactions and their geochemical implications. Naturwissenschaften 62(2):71–79

Bergmann M, Lissitzin M (1930) Die überzähligen Stereoisomeren der γ-Amino-β-oxy-buttersäure. Ber Dtsch Chem Ges 63(2):310–313

Binev D, Taratin N, Kotelnikova E, Seidel-Morgenstern A, Lorenz H (2014) Solubility equilibria and crystallographic characterization of the L-threonine/L-*allo*-threonine system. Part 1: solubility equilibria in the threonine diastereomeric system. Cryst Growth Des 14:367–373

Bredikhin AA, Bredikhina ZA, Zakharychev DV, Samigullina AI, Gubaidullin AT (2015) 4-benzoylamino-3-hydroxybutyric acid, historically first "Anomalous Racemate": reinvestigation. Cryst Growth Des 15(3):1362–1373

CCDC files: 1903255 (L-phenylglycine), 1904158 (compound I_3L), 1903257 (compound V_3L)

CSD files (identifiers): FIVGEW (DL-phenilglycine), COFRUK10 (*S*-malic acid), DLMALC11 (*RS*I-malic acid), DLMALC (*RS*II-malic acid), LVALIN01 (*L*-valine) and LISLEU02 (*L*-isoleucine)

Dalhus B, Görbitz CH (1999) Molecular aggregation in crystalline 1:1 complexes of hydrophobic D- and L-amino acids. I. The L-isoleucine series. Acta Cryst B55(3):424–431

De Torres T, Ortiz JE, Arribas I, Delgado A, Julia R, Martin-Rubi JA (2010) Geochemistry of *Persististrombus latus* Gmelin from the Pleistocene Iberian Mediterranean realm. Lethaia 43:149–163

Drozdova TV (1977) Geochemistry of amino acids. Nauka, Moscow (in Russian)

Eddleston MD, Arhangelskis M, Fričšić T, Jones W (2012) Solid state grinding as a tool to aid enantiomeric resolution by cocrystallization. Chem Commun 48:11340–11342

Fredga A (1940) Über den konfigurativen Zusammenhang zwischen optisch aktiver Milchsäure und Thiomilchsäure. Arkiv Kemi Mineral Geol 14B(12):1–10

Fredga A (1944) Proceedings of the Theodor Svedberg. Uppsala and Stockholm, Sweden, p 261

Galan K, Eicke MJ, Elsner MP, Lorenz H, Seidel-Morgenstern A (2015) Continuous preferential crystallization of chiral molecules in single and coupled mixed-suspension mixed-product-removal crystallizers. Cryst Growth Des 15(4):1808–1818

Gubaidullin AT, Samigullina AI, Bredikhina ZA, Bredikhin AA (2014) Crystal structure of chiral *ortho*-alkyl phenyl ethers of glycerol: true racemic compound, normal, false and anomalous conglomerates within the single five-membered family. CrystEngComm 16:6716–6729

Isakov AI, Kotelnikova EN, Kryuchkova LY, Lorenz H (2013a) Effect of crystallization conditions on polymorphic diversity of malic acid RS-racemate. Trans Tianjin Univ 19(2):86–91

Isakov AI, Kotelnikova EN, Kryuchkova LY, Lorenz H (2013b) Isomorphism and polymorphism in the system of malic acid enantiomers on the basis of X-ray and high-temperature X-ray diffractometry. In: Qu H, Rantanen J, Malwade C (eds) Proceedings of the 20th international workshop on industrial crystallization (BIWIC-2013), vol 20. Odense, Denmark, pp 395–402

Isakov AI, Kotelnikova EN, Lorenz H (2015) Non-equimolar discrete phases formed in the system of malic acid enantiomers. Chem Eng Technol 38(6):1047–1052

Isakov AI, Kotelnikova EN, Bocharov SN, Zolotarev AA Jr, Lorenz H (2016a) Thermal deformations of the crystal structures of L-valine, L-isoleucine and discrete compound V_2I. In: Lorenz H, Buchholz H (eds) Proceedings of the 23rd international workshop on industrial crystallization (BIWIC-2016), vol 23. Cuvillier Verlag, Göttingen, pp 7–12

Isakov AI, Kotelnikova EN, Muenzberg S, Bocharov SN, Lorenz H (2016b) Solid phases in the system L-valine–L-isoleucine. Cryst Growth Des 16:2653–2661

Isakov AI, Kotelnikova EN, Lorenz H (2018) Limits of solid solutions and crystal morphology in the system of L-valine–L-leucine enantiomers. In: Proceedings of the VI international symposium on "Biogenic – abiogenic interactions in natural and anthropogenic systems". St. Petersburg, Russia, pp 121–123

Jacques J, Collet A, Wilen SH (1981) Enantiomers, racemates and resolutions, 1rd edn. Wiley, New York

Janczak J, Zobel D, Luger P (1997) L-threonine at 12 K. Acta Cryst C53:1901–1904

Kaemmerer H (2012) New concepts for enantioselective crystallization. Shaker Verlag, Aachen

Kotelnikova EN, Isakov AI, Lorenz H (2017) Non-equimolar discrete compounds in binary chiral systems of organic substances (highlight). CrystEngComm 19(14):1851–1869

Kotelnikova EN, Isakov AI, Lorenz H (2018) Thermal deformations of crystal structures formed in the systems of malic acid enantiomers and L-valine–L-isoleucine enantiomers. CrystEngComm 20(18):2562–2572

Koolman HC, Rousseau RW (1996) Effects of isomorphic compounds on the purity and morphology of L-isoleucine crystals. AIChE J 42(1):147–153

Kryuchkova LY, Kotelnikova EN, Lorenz H, Zolotarev AA Jr, Bocharov SN (2018a) Solid phases in the chiral phenylglycine system according to PXRD and SCXRD data. In: Cartigny Y, Couvrat N (eds) Proceedings of the 25th international workshop on industrial crystallization (BIWIC-2018), vol 25. Rouen, France, pp 226–231

Kryuchkova LY, Kotelnikova EN, Zolotarev AA Jr, Lorenz H (2018b) Limits of solid solutions in the L-leucine—isoleucine system according to PXRD and SCXRD data. In: Cartigny Y, Couvrat N (eds) Proceedings of the 25th international workshop on industrial crystallization (BIWIC-2018), vol 25. Rouen, France, p 225

Kurosawa I, Teja AS, Rousseau RW (2005) Solubility measurements in the l-Isoleucine + l-Valine + Water System at 298 K. Eng Chem Res 44:3284–3288

Liu Z-S, Xu Y-L, Wang H, Yan C, Gao R-Y (2004) Chiral separation of binaphthol enantiomers on molecularly imprinted polymer monolith by capillary electrochromatography. Anal Sci 20:673–678

Lin G-Q, Zhang J-G, Cheng J-F (2011) Overview of chirality and chiral drugs. In: Lin G-Q, You Q-D, Cheng J-F (eds) Chiral drugs: chemistry and biological action. Wiley, New York, Hoboken (NJ)

Lorenz H, Seidel-Morgenstern A (2014) Processes to separate enantiomers. Angew Chem Int Ed 53:1218–1250

Murakami H (2007) From racemates to single enantiomers–chiral synthetic drugs over the last 20 years. Top Curr Chem 269:273–299

Nogradi M (1981) Stereochemistry. Basic concepts and applications. Pergamon press, Oxford

Oches EA, McCoy WD (2001) Historical developments and recent advances in amino acid geochronology applied to loess research: examples from North America, Europe, and China. Earth Sci Rev 54(1–3):173–192

Robins J, Jones M, Matisoo-Smith E (2001) Amino acid racemization dating in New Zealand: an overview and bibliography. Auckland University, Auckland

Sapoundjiev D, Lorenz H, Seidel-Morgenstern A (2006) Solubility of chiral threonine species in water/ethanol mixtures. J Chem Eng Data 51(5):1526–1566

Shoemaker DP, Donohue J, Schomaker V, Corey RB (1950) The crystal structure of L threonine. J Am Chem Soc 72:2328–2349

Swaminathan P, Srinivasan R (1975) Studies in molecular structure, symmetry and conformation. VIII. Crystal and molecular structure of L-allothreonine. Acta Cryst B31:217–221

Taratin NV, Lorenz H, Kotelnikova EN, Glikin AE, Galland A, Dupray V, Coquerel G, Seidel-Morgenstern A (2012) Mixed crystals in chiral organic systems: a case study on (*R*)- and (*S*)-ethanolammonium 3-chloromandelate. Cryst Growth Des 12:5882–5888

Taratin NV, Binev D, Lorenz H, Seidel-Morgenstern A, Kotelnikova EN (2013) Characterization and limits of solid solutions in binary systems of threonine diastereomers according to X-ray

diffraction data. In: Bekker TB, Litasov KD, Sobolev NV (eds) Proceedings of the III international conference on crystallogenesis and mineralogy. Novosibirsk, Russia, pp 341-I–341-II

Taratin N, Lorenz H, Binev D, Seidel-Morgenstern A, Kotelnikova E (2015) Solubility equilibria and crystallographic characterization of the L-threonine/L-*allo*-threonine system. Part 2: crystallographic characterization of solid solutions in the threonine diastereomeric system. Cryst Growth Des 15:137–144

Torii K, Iitaka Y (1970) The crystal structure of L-valine. Acta Cryst B26:1317–1326

Torii K, Iitaka Y (1971) The crystal structure of L-isoleucine. Acta Cryst B27:2237–2246

Xie R, Chu L-Y, Deng J-G (2008) Membranes and membrane processes for chiral resolution. Chem Soc Rev 37:1243–1263

Chapter 38
Geometry, Classification and Nomenclature of Capsids of Icosahedral Viruses



Yury L. Voytekhovsky

Abstract Icosahedral (regular, spherical) viruses build highly ordered capsids of *-3-5m* and *235* symmetry point groups (s.p.g.'s). Geometrical principles in their construction from protein globules were found by Caspar and Klug in 1962. In general, the facets of mega-icosahedra look like triangles differently oriented for different capsids on the 2D dense hexagonal packing of protein globules. It was shown later that icosahedral capsids and fullerenes form homological series with combinatorial geometry of the latter being well investigated. This allowed us to describe the geometry of icosahedral capsids in more details. The icosahedral capsids can exist with triangulation numbers $T = P f^2$ only, where $P = h^2 + hk + k^2$, where h and k—any pair of integers with no common factors, and f = 1, 2, 3, etc. The proof of the above statement was first published by Schmalz et al. in 1988. As a result, the whole variety of icosahedral capsids was divided as follows: P = 1 (i.e. h = 1, k = 0, any f, s.p.g. *-3-5m*), P = 3 (i.e. h = k = 1, any f, s.p.g. *-3-5m*), and skew classes (i.e. h > k > 0, s.p.g. *235*). The series of capsids-isomers were found by the author, *ex*. for T = 49 (h = 5, k = 3, s.p.g. *235* and h = 7, k = 0, s.p.g. *-3-5m*), T = 91 (h = 6, k = 5 and h = 9, k = 1, both s.p.g.'s *235*) and many others. That is, the nomenclature of icosahedral capsids should be based not on the triangulation numbers but on the (h, k) symbols which uniquely determine their geometry. The classification of icosahedral capsids by the s.p.g.'s *-3-5m* (with symmetry planes) and *235* (without them) is correct but very approximate. In more details, the *-3-5m* variety consists of the (t, 0) and (t, t) homological series (t = 1, 2, 3, etc.) connected by the dual transformations (h, k) → (h + 2k, h − k). The *235* variety of "skew classes" also consists of the (th, tk) homological series (t = 1, 2, 3, etc.), where (h, k) is capsid-generator with h and k—any pair of integers with no common factors and h − k being not divisible by 3. For any *235* homological series of capsids, another one is connected with it by the dual transformation (h, k) → (h + 2k, h − k). The simplest generators (1, 0), (2, 1) and (3, 1) are related to bacteriophage φX174, papovavirus and rotavirus, respectively. They generate the majority of the known icosahedral capsids as their homological series and duals. A matrix equation is found to describe

Y. L. Voytekhovsky (✉)
Saint Petersburg Mining University, 2, 21st Line, V.O., 199106 Saint Petersburg, Russia
e-mail: Voytekhovskiy_YuL@pers.spmi.ru; woyt@geoksc.apatity.ru

© Springer Nature Switzerland AG 2020

O. V. Frank-Kamenetskaya et al. (eds.), *Processes and Phenomena on the Boundary Between Biogenic and Abiogenic Nature*, Lecture Notes in Earth System Sciences,
https://doi.org/10.1007/978-3-030-21614-6_38

the transition $(h_1, k_1) \rightarrow (h_2, k_2)$ between any two icosahedral capsids. This is a rare case of biological organization for which such a general result is obtained.

Keywords Icosahedral viruses · Classification · Nomenclature · Transformation of capsids

38.1 Introduction

In previous articles, the author has shown that the polyhedral structures of fullerene type in which only pentagonal faces (exactly 12) and hexagonal faces (all the others) are allowed are widespread in the mineral and living worlds (Voytekhovsky 2015). In addition, the most symmetrical fullerenes show an easily recognizable dodecahedral motif, since the simplest fullerene is namely the Platonic dodecahedron and the most stable fullerene C_{60} is the truncated Platonic icosahedron. These motifs are encountered in the skeletons of radiolarians: dodecahedral (*Circogonia dodecahedra* Häckel) and icosahedral (*Circogonia icosahedra* Häckel). The icosahedral motif is very pronounced in the capsids of spherical viruses (Fig. 38.1). The fact that the dodecahedron and icosahedron are geometrically dual to each other allows easy switching between them and developing a general classification and nomenclature for the structures that are based on them. "The nomenclature and classification of viruses is a difficult age of virus science. The grouping can be based on morphological and physiological characteristics. An ideal classification should reflect evolutionary and phylogenetic relationships of organisms and also provide a convenient and rational system of nomenclature" (Luria et al. 1978). In the proposed paper these problems are solved in terms of morphology.

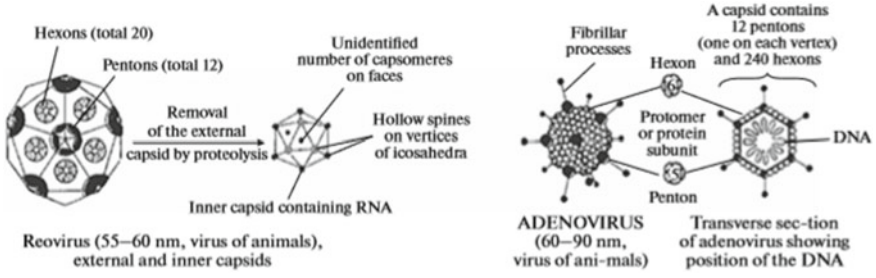


Fig. 38.1 Structure of icosahedral viruses (Rees and Sternberg 1984)

38.2 Previous Results

The principles of the structure and classification of the capsids of icosahedral viruses consisting of capsomeres (subunits, spherical protein globules) were proposed in the fundamental article by Caspar and Klug (1962). Each capsid is assembled out of 20 equilateral triangular mega-faces, fragments of a flat grid formed by globules according to the principle of the densest hexagonal packing. The lines of globules do not necessarily coincide with the edges of mega-face, thus creating the problem of finding a general formula for the number of globules in the capsid. The above article announced a theorem enumerating the "triangulation numbers" allowed for icosahedral capsids: $T = P\ f^2$, where $P = h^2 + hk + k^2$, where $0 < h \geq k \geq 0$ are any pairs of integers without common divisors, and $f = 1, 2, 3, \ldots$. It was first proved in the article by Schmalz et al. (1988, pp. 1124–1125). In fact, h and k are the coordinates of the end of the basal edge of the megaface in an oblique (60°) Cartesian coordinate system coordinated with the closest hexagonal packing of globules (Fig. 38.2). The description of icosahedral capsids is now based precisely on the triangulation numbers T (Table 38.1).

This provides a certain convenience. The number of globules in a capsid is $M = 10T + 2$. They form morphological subunits: 12 pentamers and $10(T - 1)$ hexamers.

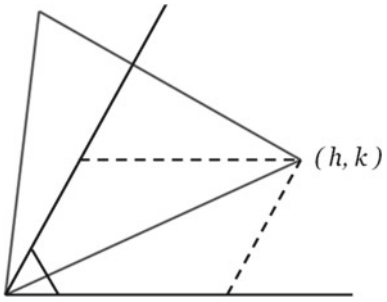


Fig. 38.2 Diagram illustrating the description of icosahedral capsid

Table 38.1 Triangulation numbers T

k\h	1	2	3	4	5	6	7	8	9	10
0	1	4	9	16	25	36	49	64	81	100
1	3	7	13	21	31	43	57	73	91	111
2		12	19	28	39	52	67	84	103	124
3			27	37	49	63	79	97	117	139
4				48	61	76	93	112	133	156
5					75	91	109	129	151	175
6						108	127	148	171	196
7							147	169	193	219
8								192	217	244
9									243	271
10										300

Here, $T = (m - 1)^2$, where m is the number of globules on the edge of the mega-face, if they are arranged directionally (Voytekhovsky 2016). In addition, 20T is the number of elementary triangular faces in any icosadeltahedron simulating the capsid. These characteristics are known for many viruses: *bacteriophage ϕX174*: T = 1, M = 12, m = 2, (h, k) = (1, 0); *turnip yellow mosaic virus*: T = 3, M = 32, (h, k) = (1, 1); *polyomavirus*: T = 4, M = 42, m = 3, (h, k) = (2, 0); *papovavirus*: T = 7, M = 72, (h, k) = (2, 1); *reovirus*: T = 9, M = 92, m = 4, (h, k) = (3, 0); *rotavirus*: T = 13, M = 132, (h, k) = (3, 1); *herpes virus* and *varicella zoster virus*: T = 16, M = 162, m = 5, (h, k) = (4, 0); *adenovirus* and *canine hepatitis virus*: T = 25, M = 252, m = 6, (h, k) = (5, 0); and *iridescent virus*: T = 81, M = 812, m = 10, (h, k) = (9, 0). The analysis of Table 38.1 shows the presence of isomers: viruses with the same triangulation number. At T = 49, they can be distinguished by the symmetry group: the capsid (h, k) = (7, 0) has point symmetry group -3-5m, while the capsid (5, 3) has point symmetry group 235. But at T = 91 both capsids (9, 1) and (6, 5) have the symmetry group 235. Moreover, the structure of any capsid is uniquely identified by symbol (h, k). Thus it is expedient to take this symbol as a basis for the nomenclature.

38.3 Classes -3-5m and 235

Caspar and Klug (1962, p. 15, Table 38.1) proposed to divide the icosahedral capsids into three classes. The first class (top row of Table 38.1) is generated by the simplest capsid (1, 0), an icosahedron with protein globules at its vertices. The remaining capsids of this class are obtained by enlarging the face of icosahedron using the ratios of magnification f = 2, 3, 4 … with the same orientation in the coordinate system consistent with the closest hexagonal packing of the globules (Fig. 38.2). It is logical to designate this class (f, 0). The second class (diagonal of Table 38.1) is similarly generated by the capsid (1, 1), a dodecahedron with pentagonal pyramids added to its faces. It may be designated (f, f). The authors of the article note that the capsids of both classes have symmetry planes, unlike the other capsids, which have only rotation axes. Judging by the fact that all the other capsids are called "skew classes," each symbol (h, k) means a separate class, each class contains a single capsid. This is not logical, since the similitude transformation of any capsid generates an infinite homological series of equally arranged capsids: (h, k) → (fh, fk) … In fact, Table 38.1 consists of homological series beginning with capsids (h, k) in which h and k share no common divisors.

Table 38.1 contains even more interesting relationships. First of all, we note that the capsid (1, 1) is obtained from capsid (1, 0) in the same way like a truncated icosahedron is obtained from a dodecahedron by the dual transformation and truncation of vertices. How could this be expressed algebraically? On the integer lattice (Fig. 38.1), the edges of two capsids (h_1, k_1) and (h_2, k_2) can be linearly expressed by each other. Let the desired transformation be $(h_1, k_1) \rightarrow (h_2, k_2) = (ah_1 + bk_1, ch_1 + dk_1)$. This transformation triples the triangulation number (Voytekhovsky 2016). From the condition $T_2 = 3T_1$ we find that for any (h_1, k_1) it can only be solvable in

Table 38.2 Triangulation numbers T for generators

k\h	1	2	3	4	5	6	7	8	9	10
0	1									
1		7	13		31	43		73	91	
2			19				67		103	
3				37	49		79	97		139
4					61				133	
5						91	109		151	
6							127			
7								169	193	
8									217	
9										271
10										

one case: $(h_1, k_1) \rightarrow (h_1 + 2k_1, h_1 - k_1)$. The following transitions can be easily verified by substitution: (f, 0) → (f, f) → (3f, 0) → (3f, 3f) …. Thus, the homological series (f, 0) and (f, f) are combined in one class -3-5m. Similarly, two homological series formed by capsids (h, k) and (h + 2k, h − k), in which h and k share no common divisors, are combined in class 235. Capsids (h, k) not reducible to simpler ones in the homological series have been previously named by the author as generators. The criteria of generator are as follows: h and k are relatively prime, and h − k is not divisible by 3 (Table 38.2).

38.4 General Transformation of the Capsids

The question arises as to whether it is possible to find a general transformation $(h_1, k_1) \rightarrow (h_2, k_2)$ that transforms any capsid into any other capsid, as it is done for fullerenes that simulate the microevolution of the skeletons of radiolarians (Voytekhovsky and Stepenshchikov 2016)? In this case, the problem consists in rotating the vector (h_1, k_1) through some angle α to the vector (h_2, k_2) and an additional dilation/contraction (Fig. 38.3). In an orthogonal Cartesian coordinate system this transformation has the

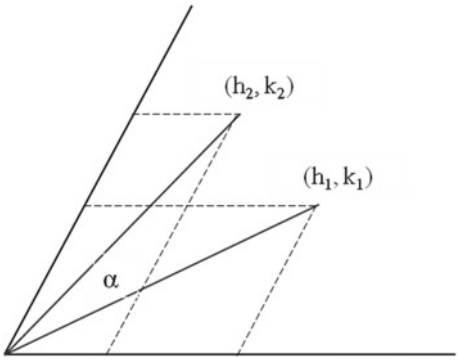


Fig. 38.3 Diagram illustrating the description of transformations of icosahedral capsid

form

$$(x_2, y_2) = (x_1, y_1)\begin{pmatrix} \cos\alpha & \sin\alpha \\ -\sin\alpha & \cos\alpha \end{pmatrix}\begin{pmatrix} t & 0 \\ 0 & t \end{pmatrix}$$

where $\alpha = \alpha_2 - \alpha_1$, $t = (T_2/T_1)^{1/2}$ is the dilation factor. The formulas for transforming it to the oblique (60°) coordinate system: $x_1 = T_1^{1/2} \cos\alpha_1$, $y_1 = T_1^{1/2} \sin\alpha_1$, $x_2 = T_2^{1/2} \cos\alpha_2$, $y_2 = T_2^{1/2} \sin\alpha_2$. After substitution and transformations, we obtain:

$$(\cos\alpha_2, \sin\alpha_2) = (\cos\alpha_1, \sin\alpha_1)\begin{pmatrix} \cos\alpha & \sin\alpha \\ -\sin\alpha & \cos\alpha \end{pmatrix}$$

Let us express trigonometric functions through the sides of triangles and after some algebraic transformations we obtain the required transformation:

$$\left(2h_2 + k_2, \sqrt{3}\,k_2\right) = \left(2h_1 + k_1, \sqrt{3}\,k_1\right)\begin{pmatrix} \cos\alpha & \sin\alpha \\ -\sin\alpha & \cos\alpha \end{pmatrix}\sqrt{T_2/T_1}$$

Given (h_1, k_1) and (h_2, k_2), we find the dilation factor $(T_2/T_1)^{1/2}$ and the angle $0° \le \alpha \le 60°$. The above relations follow from the obtained equation. Thus, for the homological series $(h_1, k_1) \to (h_2, k_2) = (f\,h_1, f\,k_1)$, we obtain by substitution:

$$\left(2h_1 + k_1, \sqrt{3}\,k_1\right) = \left(2h_1 + k_1, \sqrt{3}\,k_1\right)\begin{pmatrix} \cos\alpha & \sin\alpha \\ -\sin\alpha & \cos\alpha \end{pmatrix}$$

from which follows: $\cos\alpha = 1$, $\sin\alpha = 0$, that is, $\alpha = 0$. This is so, because these series combine capsids with similar faces that are equally directed in the coordinate system (Fig. 38.2). The case of dual transformations $(h_1, k_1) \to (h_2, k_2) = (h_1 + 2k_1, h_1 - k_1)$ is of greater interest. Here we obtain the general solution in the form:

$$\alpha = \text{arc}\,\sin[1/2 - 3k_1(h_1 + k_1)/2T_1].$$

If $k_1 = 0$, then $\alpha = 30°$; if $k_1 = h_1$, then $\alpha = -30°$, in both cases the dilation factor is $\sqrt{3}$. This is true in general: the successive dual transformations differ only in the sign of rotation.

38.5 Conclusions

- The nomenclature of the icosahedral capsid is proposed to be developed based on the symbol (h, k) of its mega-icosahedral face, since this symbol unambiguously fixes the position of the face in the lattice of capsomeres (protein globules) arranged according to the principle of the densest hexagonal packing.

- The classification of capsids based on point symmetry groups -3-5m (with symmetry planes) and 235 (without them) is logical; however, this is only the first step. Class -3-5m consists of homological series (f, 0) and (f, f), where f = 1, 2, 3 …, with the series connected by the dual transformation $(h_1, k_1) \rightarrow (h_1 + 2k_1, h_1 - k_1)$.
- The class 235 also consists of the homological series (f h, f k) generated by the generators (h, k), identified by the criterion: h and k are relatively prime, h − k is not divisible by 3. Each series in class 235 has another series, associated with it by the dual transformation $(h_1, k_1) \rightarrow (h_1 + 2k_1, h_1 - k_1)$.
- A matrix representation of any transformation $(h_1, k_1) \rightarrow (h_2, k_2)$ has been obtained. The icosahedral capsids are a rare case of biological organization for which it is possible to obtain such a general result, even if it has only theoretical significance.
- The following problems are of interest: the frequency of occurrence of icosahedral viruses of classes -3-5m and 235, in particular that of different kinds of (h, k) or, in even more detailed ways, that of isomers having different (h, k) but the same triangulation number T.

References

Caspar DLD, Klug A (1962) Physical principles in the construction of regular viruses. In: Cold spring harbor symposia on quantitative biology, vol 27, pp 1–24

Luria SE, Darnell JE, Baltimore D, Campell A (1978) General virology, 3rd edn. Wiley, New York

Rees AR, Sternberg MJE (1984) From cells to atoms: an illustrated introduction to molecular biology. Blackwell Sci. Publ., Oxford

Schmalz TG, Seitz WA, Klein DJ, Hite GE (1988) Elemental carbon cages. J Am Chem Soc 110(4):1113–1127

Voytekhovsky YL (2015) Biomineral analogues in ontogeny and phylogeny. Paleontol J 49(14):1691–1697

Voytekhovsky YL (2016) Homological series of icosahedral viruses and fullerenes. Paleontol J 50(13):1505–1509

Voytekhovsky YL, Stepenshchikov DG (2016) Fullerene transformations as analogues of radiolarian skeleton microevolution. Paleontol J 50(13):1544–1548

Chapter 39
On the Generality of Organic and Inorganic



Galina A. Oleynikova, Elena G. Panova and Yaroslav Yu. Fadin

Abstract Black shales are the object of interest to geologists, chemists and biologists. They are widely found around the world and have different ages. Black shales are rich in organic matter, clay minerals and sand grains. Black shale and extracted porosity solution (sub-micron fraction) were analyzed by ICP-MS. During the crystallization of the submicron fraction, structures similar to the macrostructure and similar to the organic world are formed. The structured porous matter microstructures show similarity to the macro- and micro world structures and elements of biological communities. Spheroids are ball-shaped seeds, formed from the nanoparticles present in the initial sub-micron fraction. They serve as source elements for crystalloid structures.

Keywords Black shales · Sub-micron fraction · Macro-, micro- and organic structures

Biogenic-abiogenic interactions are very spread in the nature. One of the most important problems of our time is the problem of biogenic-abiogenic interactions, which have led to the emergence of life on Earth, and at present they determine its continuation.

Currently, the problem of the relationship of living organisms, on the one hand, and minerals, rocks, on the other hand, is being studied from different perspectives and, as a rule, by separate research groups belonging to either the biological or the geological groups. In 2002 the First international symposium was held at the initiative of the St. Petersburg Society of Naturalists and the All-Russian Mineralogical Society. In 2018 the VI symposium was organized. The meetings discussed issues related to the problems of biogenic-abiogenic interactions. In this case, the main attention was paid to specific natural-scientific data located at the junction of

G. A. Oleynikova · Y. Yu. Fadin
All Russian Geological Institute, Saint Petersburg, Russia
e-mail: galina_oleynikova@vsegei.ru

E. G. Panova (✉)
Institute of Earth Science, Saint Petersburg State University, Saint Petersburg, Russia
e-mail: e.panova@spbu.ru

© Springer Nature Switzerland AG 2020

O. V. Frank-Kamenetskaya et al. (eds.), *Processes and Phenomena on the Boundary Between Biogenic and Abiogenic Nature*, Lecture Notes in Earth System Sciences,
https://doi.org/10.1007/978-3-030-21614-6_39

biology and geology. Actual tasks in the study of biogenic-abiogenic interactions in the "living organisms—minerals and rocks" system are the following: (1) identification of relics of living matter in paleontological fossils and study of their composition; (2) identification of the composition and structure of mineral components and neoplasms in living organisms using modern mineralogical and geochemical methods for studying substances; (3) identification of dependencies between the composition and structure of microbiological communities and the nature of the stone substrate on which they develop; (4) identification of the conditions for the biological destruction of minerals and rocks, as well as the development of methods for the conservation of various types of stone; (5) medical aspects of biogenic-abiogenic interactions and biomaterials.

Black shales (BS) always have been the object of great interest to geologists, chemists and biologists. They are widely found around the world and have different ages. Black shales are rich in organic matter (5–30%), clay minerals (illite, kaolinite, smectite, chlorite), sand grains (quartz, potassium feldspar, biotite, muscovite, amphibole) and have significant amounts of chemical elements (uranium, vanadium, molybdenum, copper, nickel, cobalt, zinc, lead) (Andersson et al. 1983; Ketris and Ydovich 2009; Kucha 1981; Levental 1991; Lewan and Buchardt 1989; Voronin and Panova 2018; Hulbert et al. 1992; Pukkonen and Rammo 1992; Fozia et al. 2009; Sanei et al. 2014; Voolma et al. 2013; Loukola-Ruskeeniemi and Lahtinen 2013).

Moreover, rock has homogeneous structure built of tightly clustered minerals. Porosity is another important part of a rock. Porosity is the space between grains of minerals, pores, and fissures filled with water and water solutions of different substances. The overall volume of pores, cavities, and micro-fractures is referred to as rock porosity. Black shale porosity is approximately 0.1–3 vol.%. Porous space water includes mobile forms of chemical elements (Oleynikova and Panova 2011; Chi Fru et al. 2017; Falk et al. 2006; Schulz et al. 2019; Lavergren et al. 2009).

Micro-capillary pores are less than 10^{-5} cm in diameter, yet this is where the most intensive processes of mass exchange between liquid and solid phases of the rock take place. The solution, which fills the porous space, provides a dispersal environment for soluble salts and colloid particles of all the elements under study (dispersal phase), including nanoparticles that are migrating by nature. It has been demonstrated that the substance density in micro-capillary pores is comparable with the density of the rock itself. V. L. Tauson referred to micro-minerals as derivatives of capillary geochemical systems. He noted that capillary system parameters could differ dramatically from those of the system with conditionally non-limited phases (Yushkin et al. 2005; Oleynikova and Panova 2014; Cartwright et al. 2008; Wilson et al. 2008; Pacton et al. 2007).

The aim of the study is to show common features of organic and inorganic components.

39.1 Object and Methods

The object of this study is black shales ($Є_3$-O_1) from the Baltic Paleobasin located in Russia and Estonia. The following laboratory methods were used: petrographic studies of thin sections (Leica microsystems DL MP optical microscope); scanning electron microscopy and microanalysis (scanning electron microscope TESCAN VEGA LMU with INCA Energy 450, INCA Wave 700 X-ray microanalysis systems); confocal microscopy; X-ray spectral silicate analysis; mass spectrometry with inductively coupled plasma (ICP-MS) with the use of ELAN-6100 DRC (Perkin Elmer). Infrared spectrometry (SC-144DR) was used to determine total carbon and total sulfur contents; the coulometric method (AH-7529) was used to determine carbonate carbon. Organic carbon is determined by the difference between total carbon and carbonate. Determination of the particle size of the submicron fraction (SMF) was carried out using a HORIBA LA-950 nano-sizer. Gas chromatographic studies of black shale were carried out using a GCMS-QP2010 Ultra chromato-mass-spectrometer.

The extraction of the submicron fraction of black shale and its ICP-MS analysis were made in the chemical laboratory of the All-Russian Geological Institute. In order to average the samples, open pores and micro-fractures, and provide access of the extractant (water) to free salts and colloid particles and those adsorbed on mineral matrix, the rock sample was crashed and abraded to particles sized 74 μkm in cameral conditions.

The most precise method of extracting the porous water solution is its extraction with water. The extraction with the rock to water ratio of 1:10 causes the dilution of the porous space matter approximately by 1000 times. Under these conditions, the pore solution turns into a true colloid-saline solution. The following processes take place in this solution: the partial or complete dissolution of chemical compounds, peptization, the electrolytic dissociation of salts, etc. Diluting the pore solution by water gives results in the increasing mobility of elements and the velocity of their interaction. In turn, this causes the formation of new compounds.

A colloid-saline solution of black shale porous matter was extracted using an original method developed by the authors (Oleynikova and Panova 2011). Sample was placed in a chemical glass, warmed deionized water was added, the solution mixed thoroughly for 5 h and left for stabilization for 24 h. After stabilization, the solution was filtrated through a Sartorius membrane filter that filtered out particles bigger than 1 μkm. The prepared solution contained particles smaller than 1 μkm. Mass percentage of sub-micron fraction (SMF) was measured by weighting the aliquot of the infiltrated colloid-saline solution, evaporate and weight.

The chemical composition of the solution was determined using mass spectrometry with inductively coupled plasma (ICP MS). For comparison, black shale samples, from which the porous solution had been extracted, were analyzed using standard methods of decomposition and the ICP MS ending.

The obtained solution was poured into an aluminum foil cup and dried at about 50 °C. Scan electron microscopic photographs and an X-ray phase analysis of the sample solid bottom films were obtained SEM analysis.

The second experiment is the study of the interaction of a plant (hydrangea flower) and an artificially prepared solution of inorganic components. A naturally skeletonized petal of a hydrangea flower was placed in a cup of aluminum foil, slightly fixed to the surface for the purpose of immobilization, and poured with a neutral solution imitating a solution of rock. The solution was obtained from soluble salts and had the following composition (%): Si—8.0; Ca—4.9; Fe—4.6; Na—2.3; K—1.8; Mg—0.9; Al—1.2; S—1.4; P—0.1; Ti—0.1. The water was carefully evaporated at a temperature not exceeding 50 °C. Salts of different composition and morphology crystallized on aluminum foil.

39.2 Results and Discussion

According to the ideas of Russian and foreign authors, black slates (BS) were formed in the conditions of the epicontinental sea. The sediment area was a wide sea channel that connected large basins to the west and east (Dronov et al. 2011; Hade and Soesoo 2014; Männil 1966; Nielson and Schovsbo 2011; Puura et al. 1999; Andersson et al. 1985; Kaljo 1986; Pukkonen and Rammo 1992; Loog et al. 2001; Nielsen and Schovsbo 2011). On the territory of Estonia and the Leningrad oblast region, shales consist of organic (9–26 rel.%), clay (40–60 rel.%), silt-sand (25–45 rel.%) and a concretion complex (2–5 rel.%). The values of radioactivity averaged 120 Bk/m^3 (up to 250 Bk/m^3). The highest values of radioactivity correlate with the amount of organic matter in the rock.

The organic matter of black shales is represented by graptolites and lower algae (up to 25%). The bulk of organic matter is composed of colloalginite of blue-green algae in a dispersed mixture with a clayey substance, which is dispersed throughout the rock and forms clusters in the form of layers. Inclusions of gelified humus, coal detritus and cutinite were identified.

According to published data, BS contain residues of acritarch, green and purple bacteria (Thiocapsa and Thiocystes), microorganisms (Microcoleus chthonoplastes) (Zhmur 1988; Loog et al. 2001; Cocks and Torsvik 2005; Dronov et al. 2011; Wignall and Newton 2001; Hints et. al. 2014). Organic matter in Black shale has a complex allochthonous-autochthonous nature. The diagenetic and catagenetic transformations of organic matter, according to many authors, were insignificant.

Organic matter can be observed in petrographic thin sections, be confocal microscopy and by scanning electron microscopy (Fig. 39.1). Selective extraction of humid acids showed that their average content is 15 wt% (from 9.5 to 21 wt%). Gas chromatographic studies showed more than 20 different hydrocarbon compounds belonging to three groups: alkanes, arenas, and carboxylic acids. Carboxylic acids prevail in the lower part of the section, carboxylic acids and arenas are present in the middle part, and organic matter in the upper part of the section is represented by alkanes hydrocarbons.

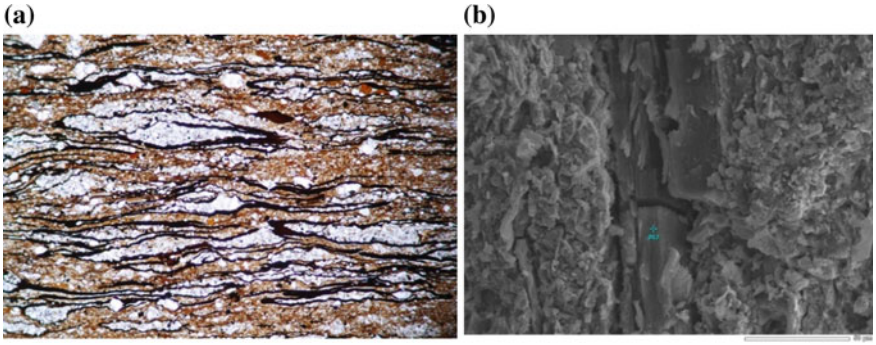


Fig. 39.1 Organic matter of black shale. **a** Organic matter and silt-clay component. Nicol are parallel, 60^x. **b** SEM image of black shale's organic matter (carbon content 77.8 wt%)

The next stage of the study is the determination of the particle size of the submicron fraction of black shale. According to the measurement, the particle size of the submicron fraction varies in the range of 300–400 nm.

Black shale samples were analyzed itself, then a sub-micron fraction was extracted, and its chemical composition was determined (Table 39.1). The table shows that the porous water solution (sub-micron fraction) contains not only rock-forming oxides but also microelements. According the table CaO, K_2O, Na_2O, MnO, MgO and Fe_2O_3 accumulate in the submicron fraction. It should be noted the high content of sulfur (40.8%) and chlorine (5.3%). Not surprisingly, emergencies were the source of alum production in the 19th century. Other petrogenic oxides go into a solution of SMF in small quantities. It is worth noticing that the concentration of certain elements in the solution is higher than in the intact (black shale) sample. Coefficient of concentration (CC) was calculated as the ratio of element concentration in the SMF to its concentration in the whole sample.

The highest coefficient is typical for the range: Ni_{15}–Co_{14}–Cd_{11}–Zn_7–$U_{4,4}$–$Cu_{3,7}$–$Sr_{2,7}$. Such elements as Y, REE, Zr, Nb, Hf, Ta, Pb, Bi, Cs, Rb, Ba are not typical of the porous solution: the value of their coefficient of accumulation is less than 1.

The experiments, which were aimed at identifying black shale submicron fractions, demonstrated that its amount in black shales varies from 0.41 to 6.24 wt% (average 1.9 wt%).

After drying in an aluminum foil cup, a thin bottom was formed. Its density was 0.15 mg/cm^2 and thickness 50 μkm. Solid colloid-saline solution bottom hereafter is referred to as a structured porous matter (SPM).

Thus, the solid bottom is obtained from the solution with fixed-size particles (less than 1 μkm). Further SEM analysis demonstrated a wide range of structured porous matter forms. Thorough examination of images showed various morphology of newly formed phases: balls, needles, prisms, dendrites, flakes, parallelepipeds, hollow or filled with substance, etc. (Fig. 39.2).

Table 39.1 Average concentration of macro- (%) and trace elements (ppm) in black shales and their sub-micron fractions

Oxides, elements	Black shale (BS), n = 30	Sub-micron fraction (SMF), n = 30	Coefficient concentration = SMF/BS
SiO_2 %	52.4	9.42	0.18
TiO_2 %	0.66	0.01	0.02
Al_2O_3 %	10.1	2.25	0.22
Fe_2O_3 %	4.23	5.02	1.19
MnO %	0.01	0.06	6.00
MgO %	1.09	1.58	1.45
CaO %	0.29	10.5	36.2
Na_2O %	0.15	0.87	5.80
K_2O %	3.64	5.2	1.43
P_2O_5 %	0.07	0.01	0.14
C %	15.2	0.85	0.06
S %	2.72	40.8	15.00
Cl %	0.2	5.3	26.5
U	69.5	304	4.37
V	566	119	0.21
Mo	151	41.8	0.28
Cu	52.1	195	3.74
Co	6.8	103	15.2
Ni	40.1	609	15.19
Zn	42.2	298	7.06
Sb	5.97	10.4	1.74
Cd	0.49	5.4	11.0
Ba	1079	209	0.19
Sr	76.4	206	2.70
Rb	155	90.1	0.58

According to nano-mineralogic theory, these morpho-forms (balls, dumb-bells, tubes, threads, nets, etc.) are typical of natural nano-minerals. It has been demonstrated that a variety of morphological forms is the most distinctive feature of nano-scaled units (Yushkin et al. 2005). High reactivity drives nanoparticles to participate in processes of self-assembling. Formations possess characteristics of fractal structure and are called fractal clusters, fractal aggregations and fractal threads. It is common knowledge that fractals are self-identical at all levels. A number of natural objects hold properties of a fractal: coastlines, clouds, tree crowns, snowdrops, circulatory system, alveoli systems of humans or animals, mountains, lightning, etc.

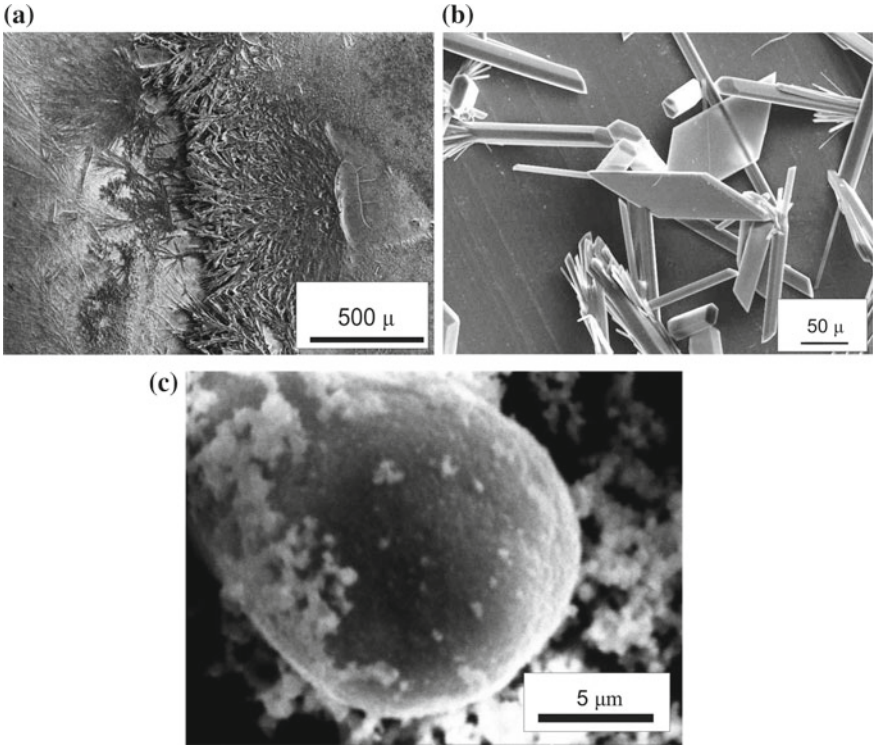


Fig. 39.2 Typical SEM image of black shale structured porous substances: **a**, **b** lamellar and needle crystals, **c** ball and dendrite formations

The photographs taken during the experiment are unique and do not have analogues. We will consider some examples and interpret the data.

As it has been already mentioned, black shales typically contain calcic minerals, and calcium oxide was found in structured porous matter (see Table 39.1). Quite expectedly, crystals of gypsum were detected in the SPM content. Figure 39.3 illustrates some of them: a structure resembling a gypsum rose.

Fiber-like, elongated, acicular crystals are typical of both the macro-world and micro-world (Fig. 39.4). SPM films of BS show that artificially crystallised gypsum has the shape of spherulites. Radial-fibrous aggregations are common among widely spread minerals such as astrophyllite, stilbite, tourmaline, malachite, hydroboracite, wavellite, stellerite, schizolite, etc. Flowers of chrysanthemum resemble non-organic spherulites.

Figure 39.5 represents photographs of dendroid like formations in the SPM of black shale, which contain (%): Al (39.97), O (35.67), K (15.99), S (7.86) and Na (0.51). Microscopic dendrites are similar to magnesium dendrites.

Another example is the formation of “leaves” and “branches” in the SPM film (Fig. 39.6a), resembling frost flowers on windows (Fig. 39.6b), paleological imprints

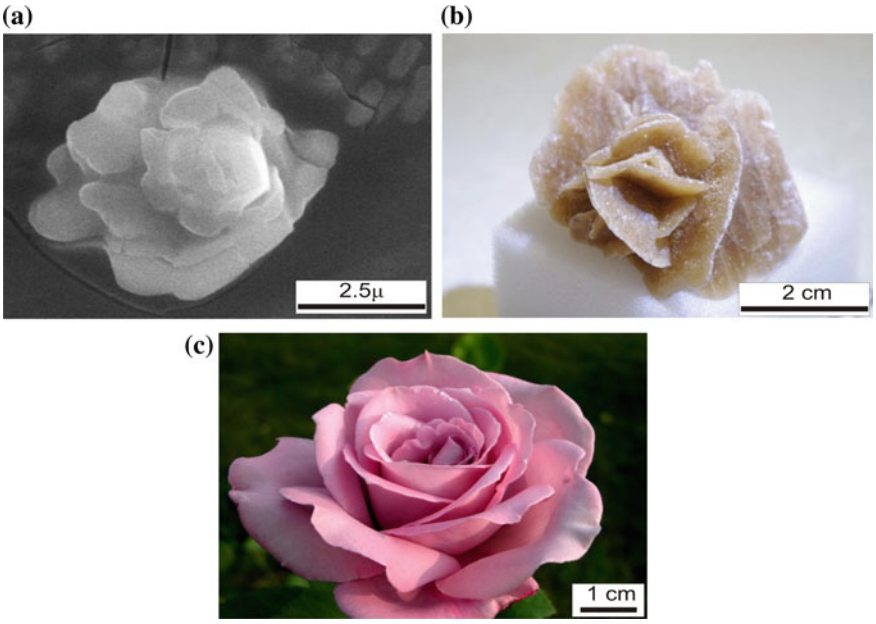


Fig. 39.3 SEM image of micro "gypsum rose" of structured pore substance of black shale (**a**), "gypsum" rose (**b**) and rose flower (**c**)

of plants (Fig. 39.6c) and structures of gas phase bottom of graphite pyrolysis (Fig. 39.6d). Potassium sulphate and anhydrite are prevalent in the structured porous matter's composition. Despite dramatic differences in composition, the objects have similar morphological outlines.

A distinctive feature of thin films is their tendency to shrink with the growth of the substance average density, while keeping self-identity (scale invariance). Forces underlying formation processes in artificial systems, what happens in the nature. Structuring laws are observed even in water molecules freezing in different conditions (Hochella 2008; Wilson et al. 2008). The authors revealed dependency of crystalized ice aggregations on the temperature and velocity of (aluminum foil) pad cooling. Drinking water in the state of Washington (USA) includes fractal structures of ferric oxide nano-sized particle aggregations.

Continuing the "vegetation" topic, we would like to point out a remarkable similarity between not only pictures of micro-world "branches" and those of real world plants and minerals but also images of astronomic bodies. Figure 39.7 shows that the electronic microscopic image of the SPM of black shales bears likeness to the picture of the surface of Saturn's moon Helene (NASA/JPL/SSI http://earth-chronicles.ru; sputnik-saturna-elena-v-cvete-2-05-2012).

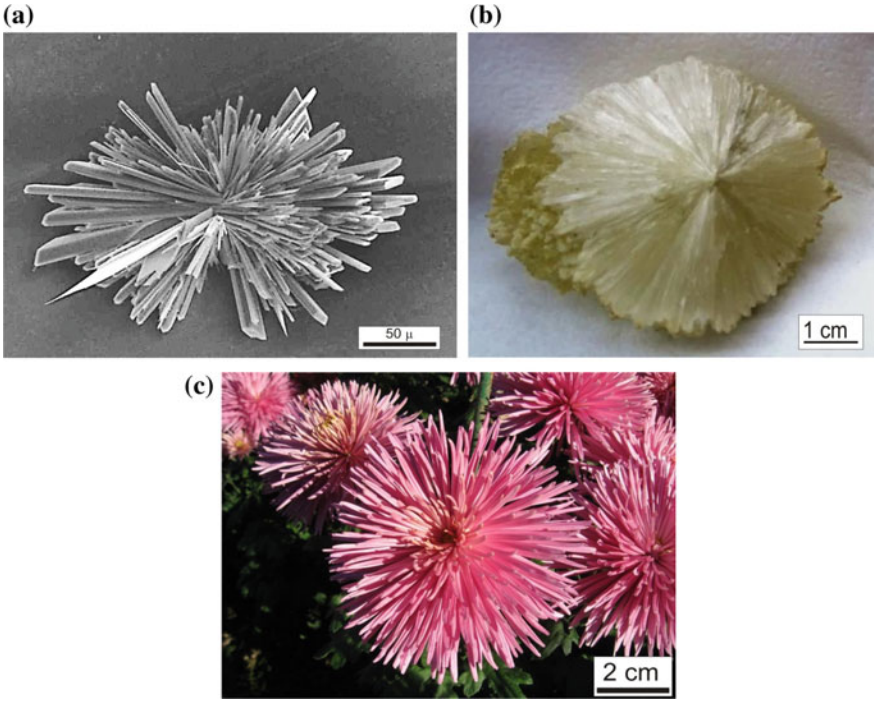


Fig. 39.4 SEM image of structured pore matter of black shale (**a**), photo of hydroboracite (**b**) and chrysanthemum flower (**c**)

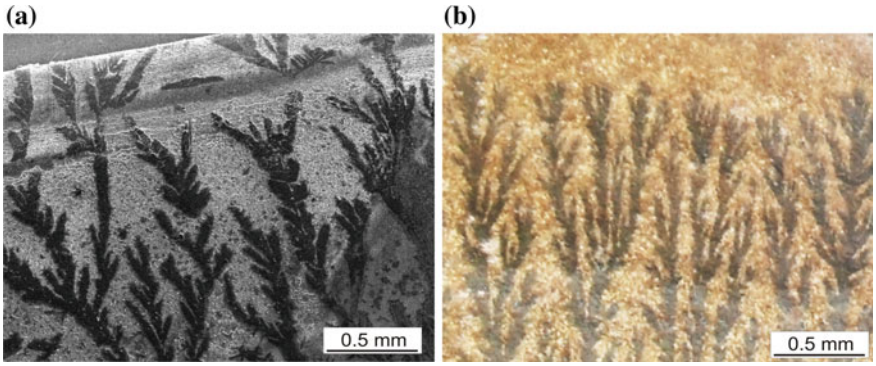


Fig. 39.5 SEM image of micro-dendrites of structured porous matter of black shale (**a**) and dendrites of manganese in quartzite (**b**)

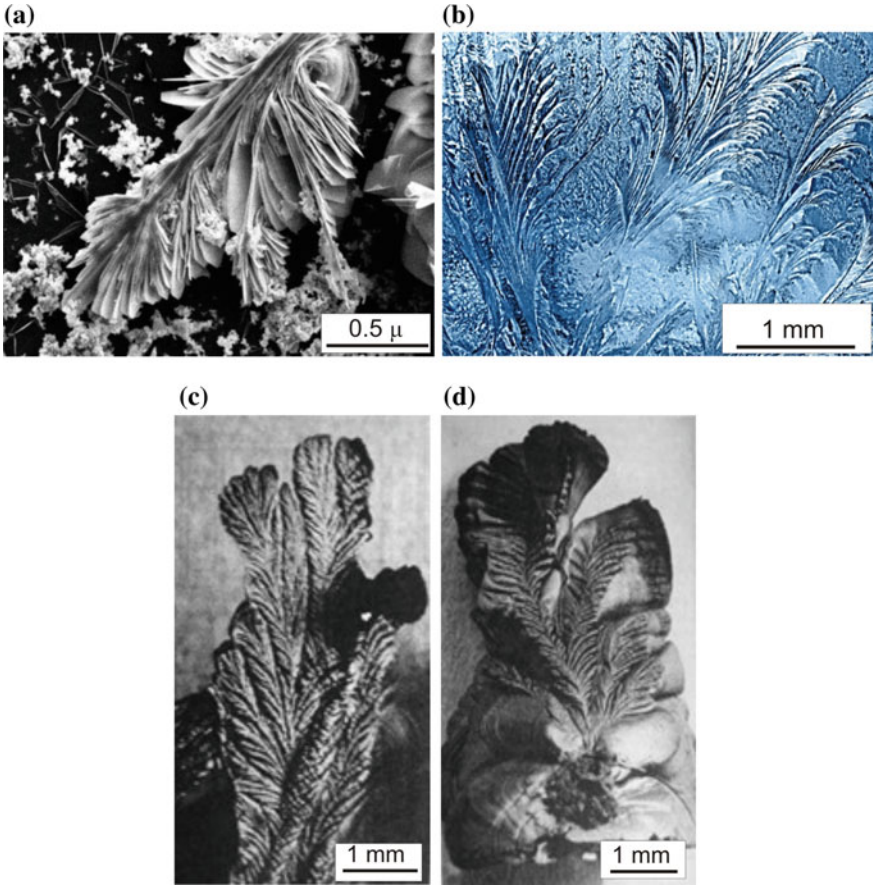


Fig. 39.6 SEM image of the structured porous substances of black shale (**a**), frosty patterns on the glass (**b**), leaves fingerprints on the surface of the coal (**c**) and precipitated products of the pyrolysis of a mixture of methane and hydrogen (**d**)

Spherical structures are typical of both the macro-world and micro-world. Balls, dumb-bells, ovoids are often found in SPM films (Fig. 39.8a–c) и comparable with natural forms, for instance, water morphology, *E. coli* (Fig. 39.8d) and rhodochrosite (Fig. 39.8e).

As it has been already mentioned, the film in a foil cup was approximately 50 μkm. However, it is possible to make it thinner by drying smaller solution amounts, which still should cover the pad evenly. Otherwise, it is possible to use denser porous filters to obtain fractions of particles of less than 400, 200 and 100 nm in size. Film thickness decreases by 1–2 orders under these experimental conditions.

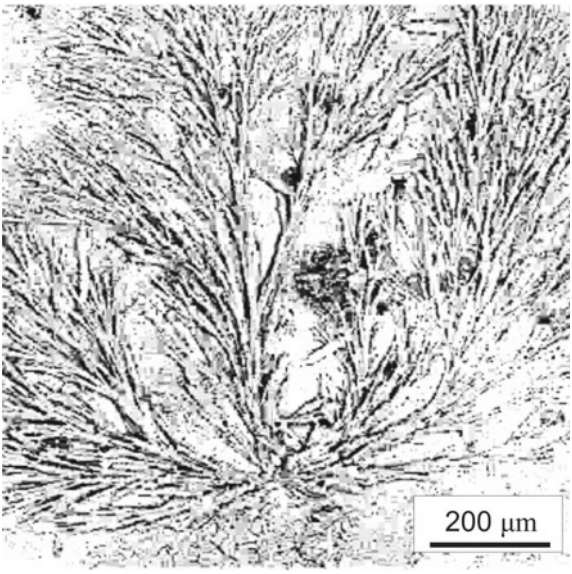


Fig. 39.7 SEM image of the structured porous substances of black shale

Figure 39.9a presents electronic photograph of structured porous matter obtained from a solution containing particles of less than 100 nm in size. Since the substance concentration was 100 times less than in a 1000 nm fraction, the film thickness was 1–3 μkm. The drying of a colloid-saline solution, characterized by a homogeneous dimension spectrum causes the formation of isolated crystals of hexagonal syngony with associated dispersion of smaller particles.

When the substance concentration increases (fraction less than 400 nm), particles self-assemble into long threads, bars, and loops. Figure shows the general view of the field, and presents an enlarged fragment of the same field. Moreover, a higher degree of magnification makes it possible to see that all structured aggregations consist of very long and thin seeds.

Real crystalline solid bodies may experience not only homogeneous nucleation, but also, due to their crystal imperfection, heterogeneous seeds formation in macro-defect areas (fissures, chippings, etc.) and micro-defects, specifically close to growth steps, dislocations, and grain borders. A structural transition from mineral forming environments to nano-mineral structures is characterized by their heterogenisation. The structural unity of the system "dispersed phase—dispersive medium" remains intact. The aggregation of nano-particles does not involve clustering, which distinguishes nano-subjects from mineral forming elements. Thus, nano-subjects represent elemental mineral structures built up by a limited number of structure forming particles that are found in long-range ordering. Nano-subjects have clearly defined phase boundaries (crystalline contours). The physique structure and form of nano-subjects are defined entirely by internal factors and hardly depend on external factors. These conditions provide for various morphological phases (threads, spheres, tubes, spirals, etc.).

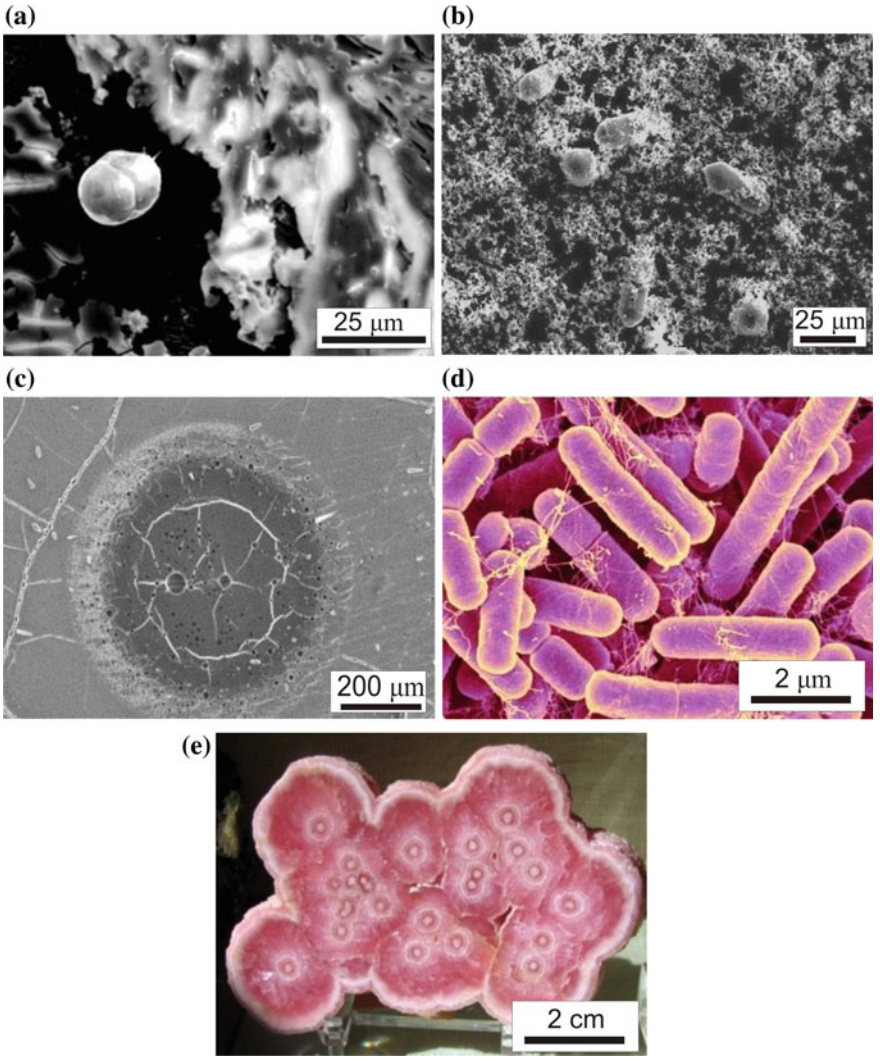


Fig. 39.8 SEM images of the structured pore matter of black shale (**a–c**), *E. coli* (**d**) and rhodochrosite crystals (**e**)

According to some researchers, the formation of the aforementioned form is hardly probable, if not impossible in the natural conditions of crystal growth, resulting from layered or regular substance fossilization. That was the reason why a new mechanism of nano-structures morphogenesis was introduced using quatarons and their aggregations as a source. The equilibrium shape for quatarons is a sphere (spherule). Quatarons' non-crystalline construction and flexible structure, and structural units (atoms or/and molecules) are joined together by exchange forces. The distinctive

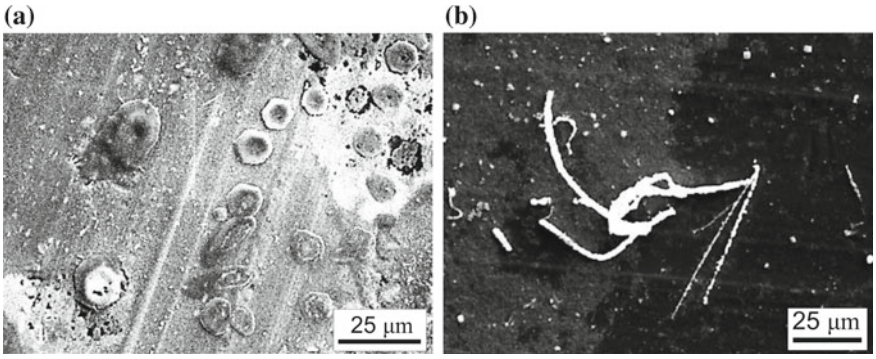


Fig. 39.9 SEM images of the structured pore matter of black shale, obtained from colloidal salt solution with particle size less than 400 nm (**a**) and less than 100 nm (**b**)

property of quatarons is their ability to aggregate without fusion. As a result, they form such structures as chains, rings, tori, etc. that in their turn contribute to the construction of multiscale aggregations. The crystallization of particles causes the formation of different forms of nanocrystals (Grechikhin 2004; Gusev 2007; Yushkin et al. 2005).

Thus, the basic principle of the mechanism proposed by the authors suggests presetting nanocrystal shapes at the pre-crystallization stage during quataron aggregation. Typical examples of quataron design are the icosahedral-like, close to spherical nanocrystals nanocrystal threads, nanocrystal toruss, tubes and spirals, nanocrystal fractal aggregations, and macro-molecular and protein nano-structures. Quataron theory allows us to explain the formation and growth of all known mono- and polyatomic crystals in oversaturated mediums.

Applying this to the experiments carried out by the authors makes it possible to conclude that the growth of a crystal begins with the formation of a small spheric nucleus (spherule or spheroid); the latter might consist of various amounts of atoms. Water evaporation during the aluminum cup heating (to 50 °C) causes a rapid increase in concentrations of all the components in the system and boost medium viscosity. Due to a deviation from its thermodynamic balance the nucleus starts growing, which leads to a lower degree of deviation from the balance. The thermo- and mass transfer, limited by a diffusive energy and substance transfer, provokes the development of morphological instability of the phase boundary and a transition to dendrite morphology.

Figure 39.10 illustrates the formation of spheric particles in the structured porous matter of thin films, the latter deriving from big balls dividing into smaller ones of relatively similar size that line up to form threads and skeletons of the “leaves”. Spherules may merge forming regular hexagons. In turn, this initiates the development of hexagonal columnar crystals. These diverse structures develop and expand in the direction of the most intensive solution circulation in complying with the principles of self-identity.

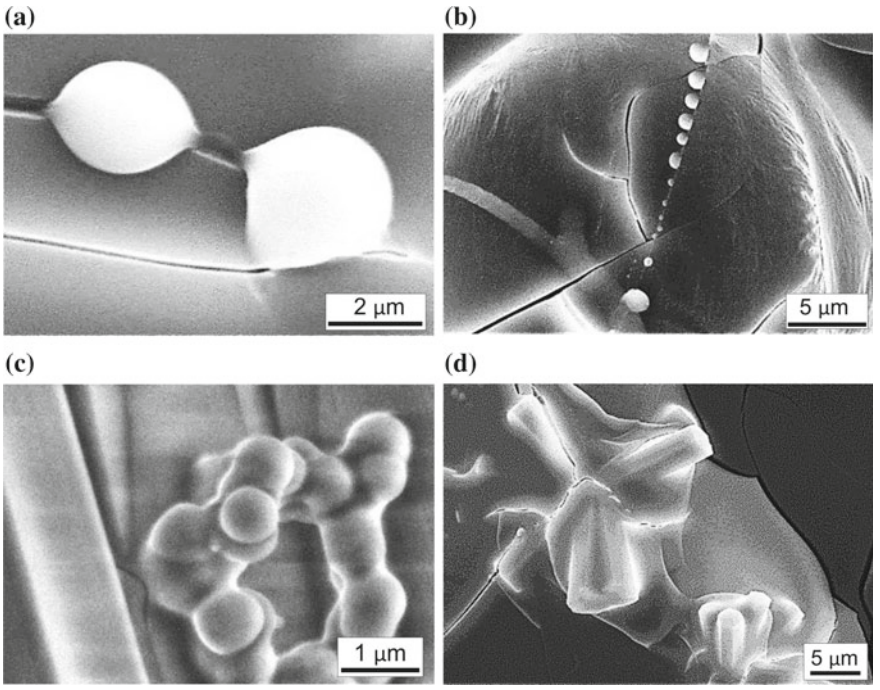


Fig. 39.10 SEM images of the structured pore matter of black shale. Film thickness—1 μm. **a** balls; **b** balls chain; **c** hexagonal ring formed by balls; **d** columns of hexagonal crystals

Assuming that the initial role in the formation of all spatial networks belongs to spherule-shaped seeds, not individual structural elements (atoms or molecules), it should be admitted that the key role is played by the size of spherule-seeds regardless of their composition (the latter, as it has been previously shown, can be rather diverse). This way the "mineral" frame experiences the structural formation of spheroids of a different composition, such as organic matter. The pattern of the organic layer might be identical to the initial non-organic layer. Reversely, the organic carcass (for example, the "skeleton" of a plant leaf) can serve as a "crystal seed" for the formation of inorganic matter.

As it has been previously noted, the native solution of rocks contains a variety of chemical elements represented by a wide range of particles: in theory, they can range from atoms to nano-particles and colloids. The formation of seminal spheroids seems to result from the association of nano-particles of rock forming elements. This provides a very clear explanation of both the formation mechanism and the content of crystalloid structures in the bottom obtained from the structured porous matter.

It is known that the accelerated growth of a crystal in a viscous medium or from surface films causes the formation of protruding parts of the crystal. The mass transfer takes place with the maximum speed in the direction of these protruding parts.

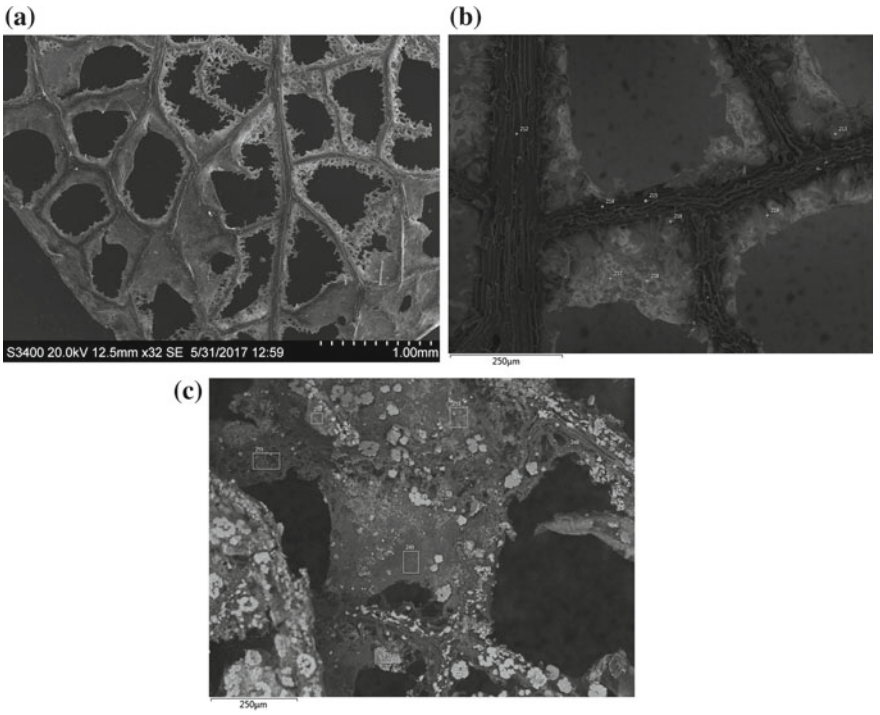


Fig. 39.11 SEM images of a skeletal hydrangea flower petal covered with an inorganic substance from an artificially prepared solution. **a** Hydrangea; **b** film thickness—1 μm; **c** film thickness—2 μm. Points indicate the location of the micro-X-ray analysis (Table 39.2)

Chemical elements in rocks pore solution can be represented by a wide range of particles: theoretically, from atoms to nano-particles and colloids. The formation of germinal spheroids is a consequence of the consolidation of nanoparticles of rock-forming elements into ensembles. This most simply explains the mechanism of formation and the composition of crystalloid structures in the structured pore substance.

If we take as a basis that the initial role in crystallization belongs to the balls-embryos, rather than individual structural elements (atoms, molecules), the main value will be the size of the balls-embryos, and not their composition. From this it follows that the "mineral" frame can go completion of the structure of spheroids of a completely different composition, for example, from organic matter. In this case, the pattern of the organic layer will be identical to the original inorganic. Or, on the organic framework can occur "completion" of the structure of the available inorganic substances in the environment.

The experiment with the hydrangea flower demonstrates this conclusion. The flower was placed in a solution of inorganic compounds. When the solution dried, the substance did not cover the surface of the cup with a uniform layer, but mainly

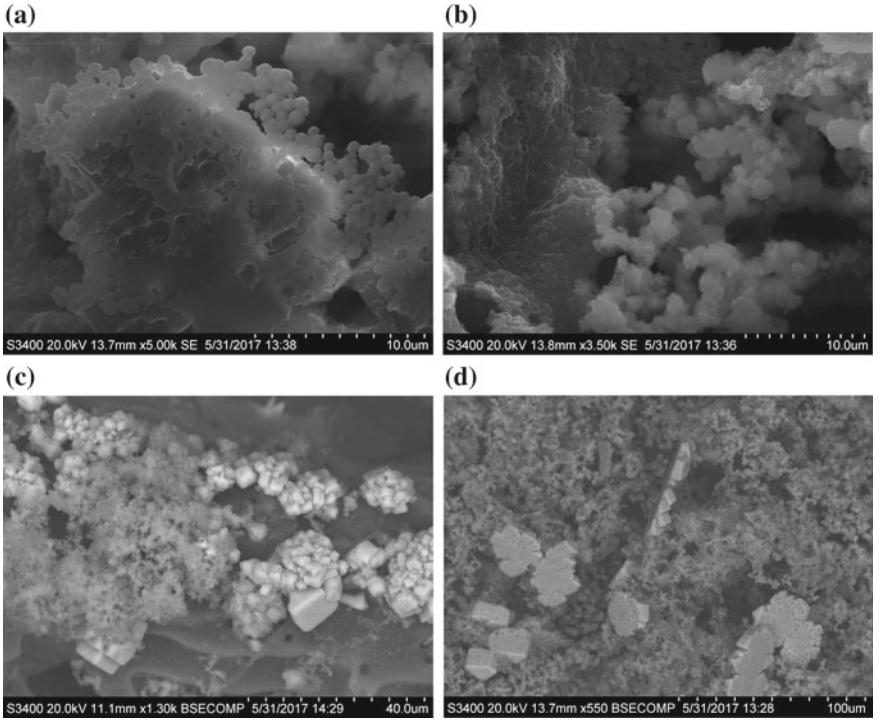


Fig. 39.12 SEM images of crystals on the basis of the hydrangea. **a** Balls, film thickness—1 μm; **b** hexagonal ring formed by balls, the film thickness—2 μm; **c**, **d** crystals, the film thickness—10 μm

concentrated on the organic structure of the flower, completing it with inorganic crystals. The crystallization of the inorganic component can be seen on Fig. 39.11, which presents photos of the petal skeleton, "overgrown" with inorganic matter for 24 h. The crystallization process expands and gradually "eats" the space between the organic matrix. The results of the analyses are given in Table 39.2.

In the branches of the organic skeleton are determined mainly carbon. Analysis of the newly formed crystals showed that their chemical composition is represented by the components of the solution. These are compounds of calcium, magnesium, potassium, sodium, aluminum, silicon, phosphorus, iron and oxygen. The newly formed crystals are fixed in the amount of carbon 7–60% and nitrogen-0.1–13%, which is determined by their crystallization on the organic skeleton.

At high magnification, it can be seen that at the beginning of crystallization in a thin film there are balls, which are further combined into hexagonal rings (Fig. 39.12). As the thickness of the crystal film increases, crystals of different morphology are formed.

Table 39.2 Results of X-ray microanalysis of a crystalline substance on a hydrangea flower, wt%

Point	C[a]	N[b]	O	Na	Mg	Al	Si	P	S	K	Ca	Fe
212	68		31.7				0.28					
213	54.6	10.0	30.9				2					0.44
214	31.5		38.6		0.79		1.31					26.9
215	43.7	1.53	44.9	0.89	0.17		9.69	0.08	0.08	0.26		0.27
216	46.6		44.9				8.5					
217	59.1		35.5	0.67			4.37	0.06	0.29			
218	59.1		35.2				4.47					1.22
219	58.6		36.6	0.84			3.88					
244	18.2		48.4	0.25							33.1	
245	17.2		46.6								36.1	
246	22.3		51.1	0.42							26.2	
247	47.4		50.0	0.95							1.6	
248	45.1		51.7	1.37			0.39				1.4	
249	52.8		44.0	0.96			0.71				1.49	
251	23.9		49.0	0.97	1.71		17.8			0.8	1.31	4.43
252	18.9		48.3								32.8	
253	39.5		53.6	1.18			0.33	0.26			5.1	
254	21.7		53.2	0.49							24.6	
255	47.6		49.0	1.07			1.04				1.18	
257	36.2		58.5	1.99			0.8				2.5	

[a]Carbon is represented as inorganic (from the experimental solution) and organic (from the skeletal matrix) substance
[b]Nitrogen is part of the organic matter of the skeletal matrix of the plant

39.3 Conclusions

The removal of water from sub-micron fraction solutions causes the system's components self-assembling into fractal structures of several types. These structures keep growing until "construction material" is exhausted or until the film is completely dry on the aluminum foil.

New structured porous matter microstructures show similarity to the macro- and micro world structures and elements of biological communities. This phenomenon demonstrates that structure formation processes comply with the laws of minimalization of a system's energy.

Spheroids are ball-shaped seeds, formed from the nano-particles present in the initial colloid-saline solution. They serve as source elements for crystalloid structures.

Acknowledgements Analytical work was done in Chemical lab of All Russian Geological Institute, Research Centers of Saint Petersburg State University ("Geomodel", "Methods of chemical analysis of matter", "Microscopy and microanalysis", "Nanotechnology").

References

Andersson A, Dahlman B, Gee D (1983) Kerogen and uranium resources in the Cambrian alum shales of the Billingen-Falbygden and Närke areas. Sweden Geol För 104:197–209

Andersson A, Dahlman B, Gee D, Snäll S (1985) The Scandinavian alum shales. Sveriges Geologiska Undersokning Ca 56:1–50

Cartwright JH, Escribano B, Ignacio S-D (2008) The mesoscale morphologies of ice films: porous and biomorphic forms of ORMS. Astrophys J 687:1406–1414

Chi Fru E, Hemmingssona C, Callaca N, Pereza N, Panova E, Bromana C, El Albanic A (2017) Atmospheric weathering of Scandinavian alum shales and the fractionation of C, N and S isotopes. Appl Geochem 74:94–108

Cocks LR, Torsvik TH (2005) Baltica from the late Precambrian to mid-Palaeozoic times: the gain and loss of a terrane's identity. Earth-Sci Rev 72:39–66

Dronov AV, Ainsaar L, Kaljo D, Meidla T, Saadre T, Einasto R (2011) Ordovician of Baltoscandia: facies, sequences and sea-level changes. In: Gutierrez-Marco JC, Rabano I, Garcia-Bellido D (eds) Ordovician of the World. Madrid

Falk H, Lavergren U, Bergbäck B (2006) Metal mobility in alum shale from Öland, Sweden. J Geochem Explor 90:157–165

Fozia A, Bhatti HN, Ghauri MA, Bhatti IA, Asi MR (2009) Bioleaching of copper, cobalt and zinc from black shale by *Penicillium notatum*. Afr J Biotech 8(19):5038–5045

Grechikhin LM (2004) Physics of nanoparticles and nanotechnologies. General fundamentals, mechanical, thermal and emission properties. Technoprint, Moscow (in Russian)

Gusev VI (2007) Nanomaterials, nanostructures, nanotechnology. Phyzmatlit, Moscow (in Russian)

Hade S, Soesoo A (2014) Estonian graptolite argillites revisited: a future resource? Oil Shale 31(1):4–18

Hints R, Hade S, Soesoo A, Voolma M (2014) Depositional framework of the East Baltic Tremadocian black shale revisited. Geol Föreningen 4:1–19

Hulbert LJ, Gragare DE, Pactuno D (1992) Sedimentary nikel, zinc and platinum group element mineralization in Devonian black shales at Nick Property, Yukon, Canada: a new deposit type. Explor Min Geol 1(1):39–62

Hochella MF Jr (2008) Nanogeoscience: from origins to cutting-edge applications. Elements 3(6):373–380
Kaljo D (1986) The Cambrian-Ordovician boundary in the Baltic-Ladoga clint area (North Estonia and Leningrad Region, Tallin)
Ketris MP, Yudovich YE (2009) Estimation of clarkes for carbonaceous biolithes: World averages for trace elements contents in black shales and coals. Int J Coal Geol 78:135–148
Kucha H (1981) Precious metal alloys and organic matter in the Zechstein copper deposits, Poland. TMPM 28:1–16
Lavergren U, Åström ME, Bergbäck B, Holmström H (2009) Mobility of trace elements in black shale assessed by leaching tests and sequential chemical extraction. Geochem Explor Environ Anal 9:71–79
Levental JS (1991) Comparison of organic geochemistry and metal enrichment in two black shales of Sweden and Devonian Chattanooga shale of United States. Mineralium Deposites 26(2):104–112
Lewan MD, Buchardt B (1989) Irradiation of organic matter by uranium decay in the Alum shale, Sweden. Geochim Cosmochim Acta 53:1307–1322
Loog A, Kurvits T, Aruvali J, Petersell V (2001) Grain size analysis and mineralogy of the Tremadocian Dictyonema shale in Estonia. Oil Shale 18(4):281–297
Loukola-Ruskeeniemi K, Lahtinen H (2013) Multiphase evolution in the black-shale-hosted Ni–Cu–Zn–Co deposit at Talvivaara, Finland. Ore Geol Rev 52:85–99
Männil R (1966) Evolution of the Baltic basin during the Ordovician. Valgus, Tallinn, p 201
Nielsen AT, Schovsbo NH (20111) The Lower Cambrian of Scandinavia: depositional environment, sequence stratigraphy and palaeogeography. Earth-Sci Rev 107:207–310
Oleynikova GA, Panova EG (2011) Geochemistry of nanoparticles in the rocks, ores and waste. J Earth Sci Eng 1(3):63–84
Oleynikova GA, Panova EG (2014) Dialysis of aqueous extracts of rocks as the method for studying the mobile species of chemical elements. Geochem Int 52(8):702–706
Pacton M, Fiet N, Gorin G (2007) Bacterial activity and preservation of sedimentary organicmatter: the role of exopolymeric substances. Geomicrobiol J 24:571–581
Pukkonen E, Rammo M (1992) Distribution of molybdenum and uranium in the Tremadoc Graptolite Argillite (Dictyonema Shale) of North-Western Estonia. Bull Geol Surv Estonia 2(1):3–15
Puura V, Vaher R, Tuuling I (1999) Pre-Devonian landscape of the Baltic Oil-Shale Basin, NW of the Russian Platform. Geol Soc London 162:75–83
Sanei H, Petersen HI, Schovsbo NH, Jiang C, Goodsite ME (2014) Petrographic and geochemical composition of kerogen in the Furongian (U. Cambrian) alum shale, central Sweden: reflections on the petroleum generation potential. Coal Geol 132:158–169
Schulz H-M, Yang S, Panova E, Bechtel A (2019) The role of Pleistocene meltwater-controlled uranium leaching in assessing irradiation-induced alteration of organic matter and petroleum potential in the Tremadocian Koporie Formation (Western Russia). Geochem Cosmochim Acta 245:133–153
Voolma M, Soesoo A, Hade S, Hints R, Kallaste T (2013) Geochemical heterogeneity of the Estonian graptolite argillite. Oil Shale 30(3):377–401
Voronin DO, Panova EG (2018) Chemical weathering of Lower Paleozoic black shales of South Sweden. J Min Inst 230:116–122
Wignall P, Newton R (2001) Black shales on the basin margin: a model based on examples from the Upper Jurassic of the Boulonnais, northern France. Sed Geol 144:335–356
Wilson MA, Tran NH, Milev AS, Volk H, Max LG (2008) Nanomaterials in soils. Geoderma 146:291–302
Yushkin NP, Askhbov AM, Rakin BI (eds) (2005) Nanomineralogy. Ultra- and microdispersed state of mineral substance. Saint-Petersburg (in Russian)
Zhmur SI (1988) The origin of oil shale of the Ordovician of the Baltic syneclise. Message 1. Dictyonema shales. Lithol Miner Resour 6:78–86 (in Russian)

Chapter 40
Carbon Isotope Ratios in the Apatite-Protein Composites of Conodont Elements—Palaeobiological Proxy

Andrey V. Zhuravlev, Artem N. Plotitsyn and Denis A. Gruzdev

Abstract Conodonts were the Palaeozoic and Triassic extinct group of the marine animals possessing discussed affinities. The only mineralized parts of conodonts are tooth-like elements composing feeding apparatus. The conodont elements are consisted of complex fluorapatite-protein nanocomposites. The mineral component of conodont elements is represented by apatite-(CaF) with minor content of CO_3 ions, Na, and Sr. Organic matter is composed of protein(s), consisting less than 4% of a conodont element. The study material comprises conodont elements of the middle Frasnian genera *Youngquistognathus* and *Mehlina*, and latest Famennian-Tournaisian species: *Polygnathus parapetus* Druce, *Hindeodus crassidentatus* (Branson et Mehl), and *Ligonodina* sp. Conodont elements were used for analysis of composition of organic matter and apatite matrix, and organic carbon isotope values. Studied conodont elements are characterized by quite high Sr/Ca values in the albid tissue ranging from 0.002 up to 0.016 that is specific for marine animals of low trophic level. Low $\delta^{13}C_{org}$ values in conodont elements ranging in wide interval from −30.4 up to −22.5‰ also suggest low trophic level of conodonts. Thus, data obtained advocate that conodonts were marine consumers of low trophic level feeding on phytoplankton or/and zooplankton. This conclusion promises possibilities to revise functional morphology of conodont elements and apparatuses, and elucidates significant biochemical differences between conodonts and marine vertebrates.

Keywords Conodonts · Organic matter · Bioapatite · $\delta^{13}c_{org}$ · Sr/Ca ratio · Trophic specialization

40.1 Introduction

Conodonts were the Palaeozoic and Triassic extinct group of the marine animals possessing debated affinities (e.g. Donoghue et al. 2000; Turner et al. 2010; Murdock et al. 2013). Chordata and even Vertebrata affinities of conodonts had been supposed

A. V. Zhuravlev (✉) · A. N. Plotitsyn · D. A. Gruzdev
Institute of Geology, Komi SC UrB RAS, Syktyvkar, Russia
e-mail: micropalaeontology@gmail.com

© Springer Nature Switzerland AG 2020

O. V. Frank-Kamenetskaya et al. (eds.), *Processes and Phenomena on the Boundary Between Biogenic and Abiogenic Nature*, Lecture Notes in Earth System Sciences,
https://doi.org/10.1007/978-3-030-21614-6_40

on the basis of soft body morphology and composition of conodont elements, which are the only mineralized parts of conodonts (Donoghue et al. 2000). Another interpretation of the conodont anatomy supports Chaetognatha affinities of conodonts (Kasatkina and Buryi 1996).

Tooth-like morphology of conodont elements disposed in a nearly bilaterally symmetrical feeding apparatus and presence of micro-wears on the surface of conodont elements were interpreted as evidences of carnivore mode of life (Purnell and von Bitter 1992; Purnell 1993, 1995; Purnell and Jones 2012). However reconstructed apparatus biomechanics and small size of the most of the conodonts (body length is about ten cm in general) suggest their lower trophic level (Zhuravlev 2007). Biochemical study (sensu lato) of conodont elements promises additional argumentation on position of conodonts in the ancient food web.

The conodont elements are composed of a number of hard tissues represented by complex fluorapatite-protein nanocomposites (e.g. Trotter and Eggins 2006; Trotter et al. 2007; Rosseeva et al. 2011; Frank-Kamenetskaya et al. 2014). The most mineralized part of a conodont element (element crown) is composed of lamellar, interlamellar, paralamellar, and albid tissues. The tissues differ one from another by mineral texture and content of organic matter (Zhuravlev 2002). Some differences in content of admixtures supposed to be near-primary (Na, Sr, S) occur as well (Trotter et al. 2007; Katvala and Henderson 2012; Zhuravlev and Shevchuk 2017).

The mineral component of conodont elements is well studied. It is represented by apatite-(CaF) with minor content (about 1 wt%) of CO_3 ions (Frank-Kamenetskaya et al. 2014). The bioapatite of the lamellar and paralamellar tissues demonstrates periodical oscillation of Sr contents across the growth lamellae (0.4–0.5 wt% in outer part of lamella, and 0.2 wt% in the inner part). The albid tissue contains Sr of less than 0.5 wt% as a rule (Zhuravlev and Shevchuk 2017; Shirley et al. 2018), however some specimens show Sr of up to 1.9 wt%. Postmortem uptake was suggested for Fe, Mn, Al, Zn, REE, Pb, Th, Ba, and U (Trotter and Eggins 2006).

Organic matter of conodont elements is strongly incorporated into the mineral matrix, and consisted of collagen-like protein similar to type IV collagen (Zhuravlev 2017). The organic matter composes less than 4% of a conodont element (Zhuravlev and Gerasimova 2015; Zhuravlev and Shevchuk 2017). The organic matter content varies from less than 1% in the albid tissue to up to 4% in the lamellar and interlamellar tissues. According to the results of the Van Gieson trichrome staining, the organic matter of albid, paralamellar, and lamellar tissues is composed of the same collagen-like protein (Zhuravlev and Gerasimova 2015).

Carbon isotope ratio in the conodont organic matter is hardly known. Over and Grossman (1992) reported $\delta^{13}C_{org}$ in conodont elements of the Late Devonian genus *Palmatolepis* (from −24.5 to −24.0‰), Early Carboniferous siphonodellids (−26.3 and −27.3‰), and Late Carboniferous *Streptognathodus elegantulus* (from −23.0 to −24.0‰). Some data on trophic differentiation of the Late Visean (Early Carboniferous) conodonts based on $\delta^{13}C_{org}$ were published later (Nicholas et al. 2004).

This article is focused on palaeobiological significance of $\delta^{13}C_{org}$ and Sr content in the unaltered Late Devonian and Early Carboniferous conodont elements.

40.2 Material

The study is based on collections of the unaltered conodont elements (Conodont Alteration Index = 1, temperature of thermal maturation is less than +50 °C) came from the Frasnian (Upper Devonian) of the Main Devonian Field (Novgorod district of Russia, N 58° 11′ 0.2″ E 31° 00′ 50.5″), and from the uppermost Famennian (Upper Devonian)–Tournaisian (Lower Carboniferous) of the Pechora Swell (Pechora district of Russia, N 65° 04′ 27.4″ E 56° 42′ 50.9″). Geological information about these localities had been published earlier (Zhuravlev et al. 1997, 1998; Tarasenko 2011; Vevel' et al. 2012). The host rocks are represented by shallow-water clayey carbonates. The Frasnian samples correspond to the lenses of carbonate tempestites in clayey deposits of the Rdeyskoe Formation (Tarasenko 2011; Zhuravlev and Shevchuk 2017). The uppermost Famennian–Tournaisian samples characterize shallow-water lagoon, shoal, and open marine clayey carbonate deposits of the Edzhit Formation (Zhuravlev et al. 1998; Vevel' et al. 2012).

The study material comprises conodont elements of the middle Frasnian genus *Youngquistognathus* and latest Famennian-Tournaisian species: *Polygnathus parapetus* Druce, *Hindeodus crassidentatus* (Branson et Mehl), and *Ligonodina* sp. Totally 13 samples were studied for $\delta^{13}C_{org}$, 24 samples for the bioapatite composition, and one sample for composition of the organic matter.

40.3 Methods

Processing of carbonate samples followed the standard procedure (dissolution of limestone in 10% buffered acetic acid) (Harris and Sweet 1989). The residues were washed through a sieve of 70 μm, dried, and conodont elements were picked up. The picked elements were washed with ethanol and distilled water.

The conodont elements were used for the study of composition of the bioapatite, and the composition of the organic matter, including carbon isotope ratios and supramolecular structure.

Investigation of the bioapatite composition of several conodont elements was performed by EDS (electron microprobe) method. The study conodont elements were mounted in the low molecular weight epoxy resin (Sr 0.00%, Ca 0.04%, P 0.21%), ground and polished. The polished surface was cleaned in the ultrasonic cleaner bath for 30 min. The polished slab was coated in carbon for sample conductivity in the electron microprobe. Microprobe analysis was making up with VEGA TESCAN (CKP "Geonauka" of Institute of Geology Komi SC UrB RAS, Syktyvkar, Russia). Six chemical elements (Ca, Sr, Na, P, S, and F) were analyzed per counting cycle. For all quantitative results, the accelerating voltage was 20 kV, the emission current was 78–88 mA, and the probe diameter was 193–293 nm. Sample standards used for quantitative analysis of chemical elements include the following: wollastonite for Ca; GaP for P; fluorite for F; SrF_2 for Sr; albite for Na.

Composition and structure of the conodont organic matter were studied with atomic force microscopy (AFM) and Raman spectrometry. M-element of the Frasnian genus *Youngquistognathus* was studied with AFM. The conodont element was demineralized in 1N HCl during 10 min, placed on the glass, dried at temperature of +20 °C, and investigated with AFM (Ntegra Prima, NT-MDT, CKP "Geonauka" of Institute of Geology Komi SC UrB RAS, Syktyvkar, Russia). AFM images were processed and measured with Gwyddion software (http://gwyddion.net/). The images were leveled and background subtracted before the measuring.

The same specimen was studied with Raman spectroscopy. For Raman spectroscopic analysis a Horiba Jobin-Yvon LabRAM HR Visible 400–1100 nm Raman spectrometer was used (CKP "Geonauka" of Institute of Geology Komi SC UrB RAS, Syktyvkar, Russia). The excitation wavelength for the Raman spectrum was the 632.81 nm with a laser power of 20 mW. The spot diameter was 2 μm. The spectrum was baseline corrected and smoothed with SpectraGryph 1.2.8 software (Menges 2018). Due to high luminescence intensity of the organic matter the native Raman signal is weak; thus the reliability of its interpretation is low.

Selected conodont elements of good preservation and the predominance of organic-rich lamellar and paralamellar tissues were used for analysis of carbon isotope values with DELTA V Advantage mass spectrometer equipped with the Thermo Electron Continuous Flow Interface (ConFlo III) and Element Analyzer (Flash EA 1112) (CKP "Geonauka" of Institute of Geology Komi SC UrB RAS, Syktyvkar, Russia). $\delta^{13}C_{org}$ values were reported relative to the PDB standard. International standard USGS-40 (L-Glutamic acid) was used. The precision of the $\delta^{13}C_{org}$ value is ±0.15‰.

$\delta^{13}C_{carb}$ and $\delta^{18}O_{carb}$ values in the host carbonate rocks were studied as well. The isotope studies in carbonate rocks were performed with DELTA V Advantage mass spectrometer equipped with Element Analyzer (Flash EA 1112) (CKP "Geonauka" of Institute of Geology Komi SC UrB RAS, Syktyvkar, Russia). $\delta^{13}C_{carb}$ values were reported relative to the PDB standard, and $\delta^{18}O_{carb}$ values—relative to SMOW standard. The precision of the $\delta^{13}C_{carb}$ value is ±0.04‰, and of the $\delta^{18}O_{carb}$ value is ±0.06‰.

40.4 Results

40.4.1 Bioapatite Composition

The bioapatite crystallites have various sizes in different hard tissues of conodont elements: 0.1–0.9 μm in lamellar tissue, 1–2 μm in paralamellar tissue, 0.6–0.9 μm in interlamellar tissue, and about 0.5 μm in albid tissue. Crystallites of the albid tissue are strongly aligned and form porous mesocrystal (Frank-Kamenetskaya et al. 2014; Zhuravlev and Gerasimova 2015). Porosity of the albid tissue detected with micro-CT is about 3–4%; the mean volume of pores varies in a wide range from

Table 40.1 Mean composition of conodont hard tissues. EDS data, all values are in wt%

Tissue type	O	P	Ca	F	Na	Sr	S	Ca/P	Sr/Ca	Number of measure-ments
Albid	37	17.6	37.3	4.4	0.3	0.3	<0.1	2.12	0.008	17
Paralamellar	37.1	17.2	35.9	4.5	0.4	0.3	<0.1	2.08	0.009	6
Lamellar	35.5	17.2	36.3	4.0	0.4	0.3	<0.1	2.12	0.009	8

0.5 μm^3 in *Mehlina* up to 100 μm^3 in *Ligonodina* (Zhuravlev 2018). The pores and "canals" distributed in this tissue are isolated and form the closed porosity only. Due to the specific structure, the albid tissue possesses high chemical stability and low permeability. Structures composed of the albid tissue in conodont elements are always covered by lamellar and paralamellar tissues and isolated from the outer media. These facts promise preservation of the near-primary chemical composition of the bioapatite of the albid tissue.

The mean composition of the bioapatite of various tissues of conodont elements is represented in Table 40.1. High similarity in the composition of different tissue types is notable. The albid tissue was selected for further analysis due to its higher chemical stability, good preservation, and lowest content of organic matter.

EDS analysis of the albid tissue shows small variations of Ca/P ratios (in wt%). The ratio varies from 2.08 to 2.18 (Table 40.2). The mean value of the Ca/P ratio (in wt%) is 2.12. These values are close to those of recent bioapatite that suggests a minor diagenetic alteration (Sillen 1986). Concentration of F in the albid tissue ranges from 3.2 to 5.9 wt% (mean value is 4.4 wt%) (Table 40.2). Sr content fluctuates from 0.05 to 0.62 wt% (Table 40.2). Concentration of Sr in the host carbonates is of 0.02–0.04 wt% that suggests absence of post-mortem Sr uptake into the conodont elements (see also Zhuravlev and Shevchuk 2017). Variations of contents of Ca and Sr, as well as Sr/Ca ratios are taxon-dependent (Fig. 40.1; Table 40.2). Studied specimens of *Ligonodina* and *Mehlina* demonstrate rather high Sr/Ca values of 0.010–0.016. Specimens of genera *Polygnathus* and *Youngquistognathus* are characterized by lower Sr/Ca values ranging from 0.002 up to 0.012. It is interesting to note that apparatuses of *Ligonodina* and *Mehlina* have blade-like Pa-elements of "cutting" functional type, whereas Pa-elements of *Polygnathus* and *Youngquistognathus* possess pectiniform morphology of "crushing" and "grinding" functional types (Zhuravlev 2007). Thus the higher Sr/Ca values are associated with "cutting" functional type, and the lower Sr/Ca values are associated with "crushing" and "grinding" functional types (Table 40.3).

40.4.2 Organic Matter Composition

Composition of the conodont organic matter was studied in demineralized M-element of the Frasnian genus *Youngquistognathus* (Fig. 40.2).

Table 40.2 Composition of the albid tissue of conodont elements. EDS data, all values are in wt%

Taxon	Age	F	Na	P	Ca	Sr	Ca/P	Sr/Ca
Ligonodina sp. (S element)	Frasnian	4.17	0.23	18.49	39.36	0.54	2.13	0.014
Mehlina gradata (Pa element)	Frasnian	4.16	0.6	17.89	38.63	0.59	2.16	0.015
Mehlina gradata (Pa element)	Frasnian	3.23	0.1	18.62	39.83	0.41	2.14	0.010
Mehlina gradata (Pb element)	Frasnian	4.72	0.16	18.06	38.3	0.4	2.12	0.010
Mehlina gradata (Pb element)	Frasnian	5.88	0.11	18.24	38.86	0.62	2.13	0.016
Polygnathus efimovae (Pa element)	Frasnian	4.66	0.79	18.05	38.3	0.29	2.12	0.008
Polygnathus efimovae (Pa element)	Frasnian	4.27	0.27	18.66	39.31	0.18	2.11	0.005
Polygnathus efimovae (Pa element)	Frasnian	4.25	0.5	18.41	38.91	0.06	2.11	0.002
Polygnathus parapetus (Pa element)	Tournaisian	4.5	0.49	17.32	37.72	0.21	2.18	0.006
Polygnathus parapetus (Pa element)	Tournaisian	3.87	0.65	17.41	37.12	0.19	2.13	0.005
Polygnathus parapetus (Pa element)	Tournaisian	3.76	0.63	17.37	37.52	0.37	2.16	0.010
Youngquistognathus posterus (Pa element)	Frasnian	3.89	0.42	17.2	36.68	0.22	2.13	0.006
Youngquistognathus posterus (Pa element)	Frasnian	4.54	0.76	16.82	35.83	0.33	2.13	0.009
Youngquistognathus rossicus (S element)	Frasnian	5.16	0	15.73	32.67	0.38	2.08	0.012
Youngquistognathus rossicus (S element)	Frasnian	4.3	0	17.19	36.32	0.05	2.11	0.001
Youngquistognathus rossicus (S element)	Frasnian	4.99	0	16.87	35.14	0.1	2.08	0.003
Youngquistognathus rossicus (S element)	Frasnian	4.25	0	16.14	33.82	0.24	2.10	0.007

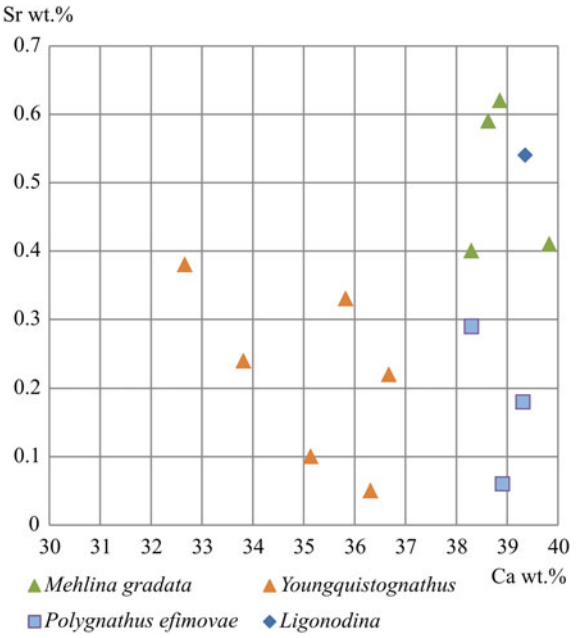


Fig. 40.1 Taxonomical dependence of the Sr and Ca content in albid tissue of conodont elements

Table 40.3 Mean Sr/Ca and F values (%wt) in the albid tissue of conodonts possessing different functional type of Pa elements

Taxon	F	Sr/Ca	Functional type of Pa elements
Ligonodina	4.17	0.014	Cutting
Mehlina	4.50	0.013	Cutting
Polygnathus efimovae	4.39	0.005	Grinding
Polygnathus parapetus	4.04	0.007	Crushing
Youngquistognathus	4.52	0.006	Crushing

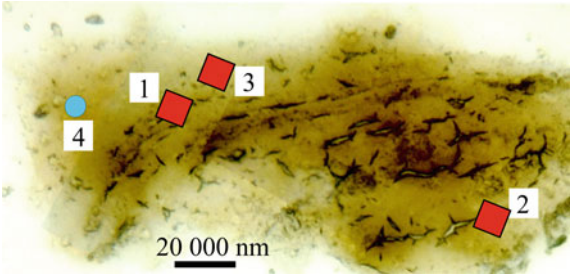


Fig. 40.2 Demineralized organic matter of conodont element of genus *Youngquistognathus*. The red squares mark AFM sites; the blue circle marks Raman spectrometry site

The Raman spectrum of conodont organic matter demonstrates a number of characteristic bands (Fig. 40.3). Amide I band associated with secondary structure of proteins (1662 cm^{-1}) is of low intensity; the Amide II band is distinguished at 1593 cm^{-1}. 1477 and 994 cm^{-1} bands probably correspond to Amide II′ and Amide III′ of denatured part of the protein. However the conodont organic matter differs from gelatin by the absence of specific band about 1240 cm^{-1} (Frushour and Koenig 1975). High intensity of the Amide III′ band and low intensity of Amide I and Amide III bands may be caused by absence of dominance of alpha-helix in the structure of the protein.

A number of intense bands in the interval 1250–1400 cm^{-1} may correspond to methionine and/or alanine amino acids (Rolinski et al. 2014). Some bands may be associated with proline (924 cm^{-1}), hydroxyproline and/or tyrosine (1200 cm^{-1}), tyrosine (about 840 cm^{-1}), and phenylalanine (994 and 1100 cm^{-1}) (Frushour and Koenig 1975). Shoulder peak is observed near 1614 cm^{-1}, which corresponds to the spectral peak that may be assigned to the Y8a tyrosine side chain (Ramakrishnaiah et al. 2015).

Presence of glycine had been proved by XRD method earlier (Zhuravlev and Sapega 2007). So the occurrence of main collagen amino acids (glycine, alanine, and proline) is supposed in the conodont organic matter. Some bands of the Raman spectrum are attributed to the decomposed protein, but some bands correspond to the secondary protein structure of the non-fibrillary type. Thus the Raman spectrum of conodont organic matter suggests presence of collagen-like protein, probably of non-fibrillary type.

Another evidence of non-fibrillary secondary structure of protein composing conodont organic matter had been obtained with atomic force microscopy (Zhuravlev 2017). Unfortunately the organic film obtained by demineralization of conodont element was deformed when dried. So, primary morphology of the organic matrix is partly distorted.

The organic matter of conodont element possesses globular, not fibrillary, nanostructure (Fig. 40.4). Absence of any residues of fibrillary nanostructures characteristic of collagen I and II suggests either full denaturation of the protein, or presence of non-fibrillary collagen. The observed nanostructures differ significantly from those of gelatins, thus a high level of denaturation of the protein is of low probability. The globules of 30–60 nm in size are ordered into linear (0.3–1.5 μm wide and 20–50 nm high) and isometric (200–260 nm) structures (Fig. 40.4). The short linear aggregates (130–350 nm in length) composed of 4–7 globules occur as well.

The linear structures probably correspond to the boundaries of crystallites of apatite-(CaF), which compose the mineral part of the studied tissue. The crystallite size of lamellar tissue is about 100–800 nm that is close to the size of the observed linear structures in the organic matter (Zhuravlev 2017). Probably the protein films surround the crystallites in the conodont element, and are strongly incorporated into the mineral matrix. Incorporating of the organic matter into the mineral structure of low permeability promises exceptional preservation of the secondary structure and composition of the protein.

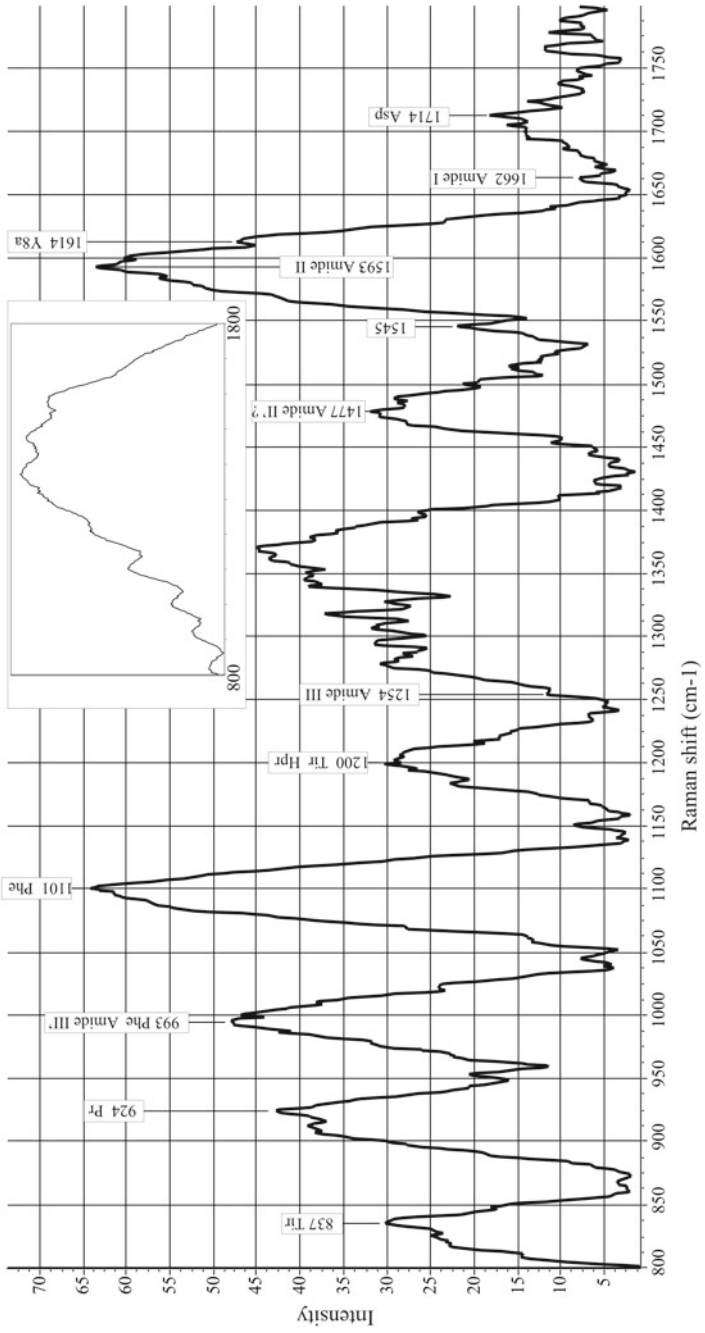


Fig. 40.3 Raman spectrum of the demineralized organic matter of conodont element of genus *Youngquistognathus*. Locality 4 on Fig. 40.2

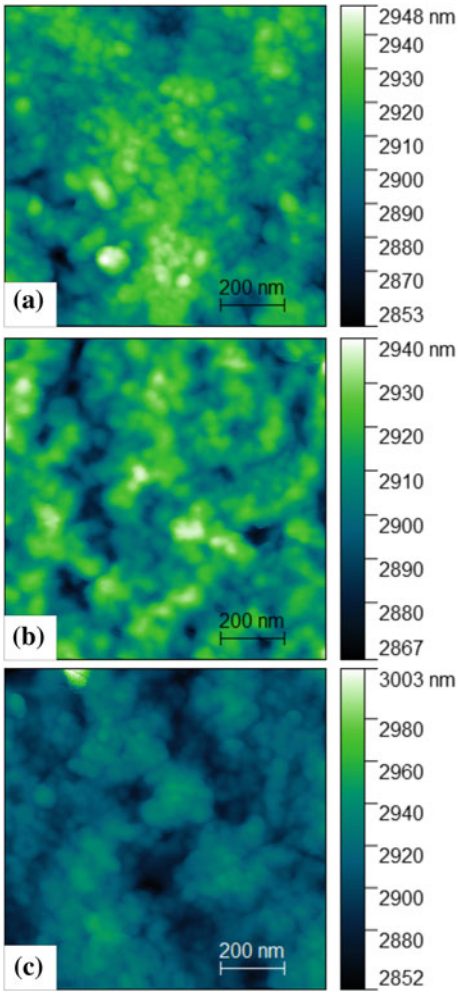


Fig. 40.4 AFM images of the details of relief of the demineralized organic matter: **a** locality 1; **b** locality 2; **c** locality 3 (see Fig. 40.2)

Multidisciplinary study of the organic matter of conodont elements allows supposing its good preservation, collagen-like composition, and suitability for investigation of unaltered $\delta^{13}C_{org}$ values. According to the obtained data, isotope composition of the organic carbon in the conodont organic matter can be correctly compared with those of collagen of recent marine animals.

40.4.3 Carbon Isotope Composition

The carbon isotope ratio in the conodont organic matter were analyzed for the four taxa, namely the Frasnian *Youngquistognathus* (1 specimen), late Famennian—Tour-

naisian *Polygnathus parapetus* Druce (10 specimens), late Famennian *Ligonodina* (1 specimen), and early Tournaisian *Hindeodus crassidentatus* (Branson et Mehl) (1 specimen). The results accompanied by $\delta^{13}C_{carb}$ and $\delta^{18}O_{carb}$ values of the host rocks are listed in Table 40.4.

In general, $\delta^{13}C_{org}$ values of conodont organic matter range from −30.4 to −22.5‰. The lowest value is observed for the late Famennian specimen of *Polygnathus parapetus*, and the highest value characterizes the Tournaisian specimen of the same species. The intraspecific variation of $\delta^{13}C_{org}$ value in *Polygnathus parapetus* is about 8‰, which is very high in contrast with recent marine animals (DeNiro and Schoeninger 1983). The mean $\delta^{13}C_{org}$ value in *Polygnathus parapetus* is −25.2 ± 1.6‰. There are no significant correlations between carbon isotope composition of conodont organic matter and host rock ($R^2 = 0.0731$), and between $\delta^{13}C_{org}$ values and $\delta^{18}O_{carb}$ values ($R^2 = 0.1417$) (Fig. 40.5). Absence of correlation between $\delta^{13}C_{org}$ values and $\delta^{13}C_{carb}$ values suggests prevalence of the vital effect in the variations of $\delta^{13}C_{org}$. Intraspecific variations of $\delta^{13}C_{org}$ values in *Polygnathus parapetus* demonstrate weak facies trend (sea-ward increasing). The mean values increase from −26.4‰ in the lagoon facies up to −23.5‰ in the shoal and open marine facies (Table 40.4; Fig. 40.6).

Interspecific variations of conodont $\delta^{13}C_{org}$ value are significant. $\delta^{13}C_{org}$ value in specimen of *Hindeodus crassidentatus* is low (−29.0‰) in relation to that of *Polygnathus parapetus* (−22.7‰) from the same sample. The late Famennian specimen of *Ligonodina* demonstrates rather high $\delta^{13}C_{org}$ value of −23.47‰. The similar carbon isotope ratio of −24.05‰ in the conodont organic matter was determined in the specimen of the Frasnian *Youngquistognathus*. Restricted number of the measurements make it impossible to distinguish any reliable correlations between $\delta^{13}C_{org}$ values and conodont element morphology.

40.5 Discussion

The results obtained fit the data of previous investigations of conodont bioapatite and organic matter (Katvala and Henderson 2012; Trotter and Eggins 2006; Trotter et al. 2007; Rosseeva et al. 2011, Frank-Kamenetskaya et al. 2014; Zhuravlev and Shevchuk 2017; Over and Grossman 1992).

Sr/Ca ratio in the albid tissue of conodont elements ranges from 0.002 to 0.016 (in wt%). The quite wide range of variations that is not typical for recent vertebrates suggests low levels of biopurification of Ca relative to Sr in conodonts. Sr/Ca ratios between 0.0012 and 0.14 appear to be characteristic for recent marine invertebrates, while recent marine fishes demonstrate the ratio ranging from 0.0021 to 0.0053 (Peek and Clementz 2012). Taking into account decreasing of the ratio through the trophic levels in recent marine ecosystems (Peek and Clementz 2012), the quite high Sr/Ca in conodont elements may be a consequence of the low position of conodonts in the trophic web.

Table 40.4 Isotopic composition of conodont elements and host rocks (bulk carbonates). Isotopic values are reported in ‰ notation

Conodont taxon	Section and age	Facies	$\delta^{13}C_{org}$ PDB	$\delta^{13}C_{carb}$ PDB	$\delta^{18}O_{carb}$ SMOW
Polygnathus parapetus	N Urals, Kamenka River, D_3 fm	Lagoon	−25.42	3.62	26.69
Ligonodina sp.	N Urals, Kamenka River, D_3 fm	Lagoon	−23.47	2.66	26.09
Polygnathus parapetus	N Urals, Kamenka River, D_3 fm	Lagoon	−30.4	3.14	26.79
Polygnathus parapetus	N Urals, Kamenka River, D_3 fm	Lagoon	−26.41	2.98	26.66
Polygnathus parapetus	N Urals, Kamenka River, C_1 tn	Lagoon	−23.57	2.48	27.14
Polygnathus parapetus	N Urals, Kamenka River, C_1 tn	Lagoon	−28.06	2.48	27.14
Polygnathus parapetus	N Urals, Kamenka River, C_1 tn	Shoal	−22.71	2.58	26.26
Hindeodus crassidentatus	N Urals, Kamenka River, C_1 tn	Shoal	−29	2.58	26.26
Polygnathus parapetus	N Urals, Kamenka River, C_1 tn	Lagoon	−24.77	2.45	26.94
Polygnathus parapetus	N Urals, Kamenka River, C_1 tn	Open marine	−22.66	1.5	24.6
Polygnathus parapetus	N Urals, Kamenka River, C_1 tn	Open marine	−25.93	1.3	25.4
Polygnathus parapetus	N Urals, Kamenka River, C_1 tn	Shoal	−22.5	2.71	26.13
Youngquistognathus sp.	East European Platform, Ilmen Lake, D_3 f	Open marine	−24.05	−3.86	25.75

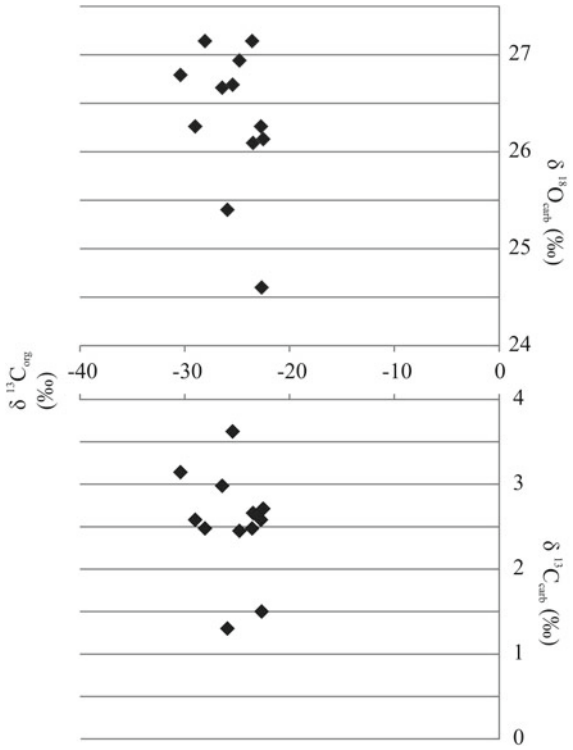


Fig. 40.5 Bivariate plots for conodont $\delta^{13}C_{org}$ and bulk carbonate $\delta^{13}C_{carb}$ values, and $\delta^{13}C_{org}$ and bulk carbonate $\delta^{18}O_{carb}$ values

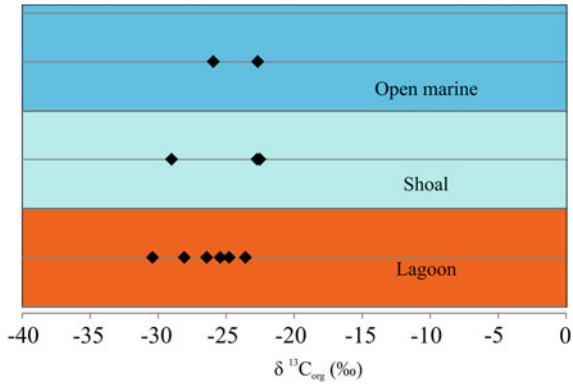


Fig. 40.6 Facies dependence of $\delta^{13}C_{org}$ values of conodont organic matter of the late Famennian-Tournaisian species *Polygnathus parapetus* Druce

All the $\delta^{13}C_{org}$ values of conodont organic matter range from −30.4 up to −22.5‰. This interval comprises values characteristic of marine phytoplankton, including cyanobacteria, utilizing C_3 photosynthetic pathway ($\delta^{13}C$ values between −34 and −20‰) (O'Leary 1981). Close $\delta^{13}C$ values are specific for organic matter subjected to microbial degradation (Geeraert et al. 2016).

Study of the carbon isotope composition of terrestrial organic matter derived from plants demonstrated that Devonian-Carboniferous transition was characterized by dramatic ^{13}C enrichment of the organic matter (Strauss and Peters-Kottig 2003). The reported difference between the Late Devonian and Early Carboniferous $\delta^{13}C_{org}$ values is about 2‰ (shift from −25 up to −23‰) (Strauss and Peters-Kottig 2003). Our data on the Late Devonian (Frasnian) and Early Carboniferous (Tournaisian) conodont organic matter demonstrate absence of significant differences (Table 40.4). This fact suggests weak trophic dependence of the shallow-water conodonts from the influx of the organic matter of terrestrial origin.

The mean value of $\delta^{13}C_{org}$ of the studied conodont elements of various ages and taxonomic position is of −25.3‰ with a standard deviation of 2.56. This value is close to $\delta^{13}C_{org}$ of recent tropical Chaetognatha, which have the $\delta^{13}C_{org}$ values varied between −23.89 and −17.03‰ (Bohata and Koppelmann 2013). Oppositely, marine consumers of high trophic levels demonstrate, as a rule, higher $\delta^{13}C_{org}$ values. For example, organic carbon isotope ratios between −18 and −10‰ are characteristic for marine carnivore Vertebrata (DeNiro and Weiner 1988). Thus the carbon isotope composition of conodont organic matter suggests that conodonts were consumers of low trophic level. This conclusion meets the interpretation based on Sr/Ca ratio in conodont bioapatite.

40.6 Conclusions

Data on the carbon isotope composition of the conodont organic matter accompanied by information about Sr/Ca values in the bioapatite of the albid tissue allow reconstructing probable position of conodonts in the ancient food web. It seems that conodonts were consumers of low trophic level feeding on phytoplankton or/and zooplankton. This conclusion permits to revise functional morphology of conodont elements and apparatuses, and elucidates significant biochemical differences between the conodonts and vertebrates.

Acknowledgements Authors would like to thank Irina Smoleva and Alexander Shuyskiy for help in the geochemical and isotope study of conodont elements. Support for the analytical work was provided by CKP "Geonauka" of Institute of Geology Komi SC UrB RAS, Syktyvkar, Russia.

References

Bohata K, Koppelmann R (2013) Chaetognatha of the Namibian Upwelling Region: taxonomy, distribution and trophic position. PLoS ONE 8(1):e53839. https://doi.org/10.1371/journal.pone.0053839

DeNiro MJ, Schoeninger MJ (1983) Stable carbon and nitrogen isotope ratios of bone collagen: variations within individuals, between sexes, and within populations raised on monotonous diets. J Archaeol Sci 10(3):199–203

DeNiro MJ, Weiner S (1988) Chemical, enzymatic and spectroscopic characterization of "collagen" and other organic fractions from prehistoric bones. Geochim Cosmochim Acta 52:2197–2206

Donoghue PCJ, Forey PL, Aldridge RJ (2000) Conodont affinity and chordate phylogeny. Biol Rev 75:191–251

Frank-Kamenetskaya OV, Rozhdestvenskaya IV, Rosseeva EV, Zhuravlev AV (2014) Refinement of apatite atomic structure of albid tissue of Late Devon conodont. Crystallogr Rep 59(1):41–47

Frushour BG, Koenig JL (1975) Raman scattering of collagen, gelatin, and elastin. Biopolymers 14(2):379–391

Geeraert N, Omengo FO, Govers G, Bouillon S (2016) Dissolved organic carbon lability and stable isotope shifts during microbial decomposition in a tropical river system. Biogeosciences 13:517–525

Harris AG, Sweet WC (1989) Mechanical and chemical techniques for separating microfossils from rock. Sediment and residue matrix. In: Chapman RE, Hannibal JT (eds) Paleotechniques. Paleontol Soc Spec Publ 4, pp 70–86

Kasatkina AP, Buryi GI (1996) On the relation of chaetognaths and conodonts. Albertiana 18:21–23

Katvala EC, Henderson CM (2012) Chemical element distributions within conodont elements and their functional implications. Paleobiology 38:447–458

McKirdy DM, Powell TG (1974) Metamorphic alteration of carbon isotopic composition in ancient sedimentary organic matter: new evidence from Australia and South Africa. Geology 2(12):591–595

Menges F (2018) Spectragryph-optical spectroscopy software, Version 1.2.8, 2018. http://www.effemm2.de/spectragryph/

Murdock DJE, Dong X-P, Repetski JE, Marone F, Stampanoni M, Donoghue PCJ (2013) The origin of conodonts and of vertebrate mineralized skeletons. Nature 502:546–549

Nicholas C, Murray J, Goodhue R, Ditchfield P (2004) Nitrogen and carbon isotopes in conodonts: evidence of trophic levels and nutrient flux in Palaeozoic oceans. In: The Palaeontological Association 48th annual meeting, 17th–20th December 2004, University of Lille, Abstracts, pp 126–127

O'Leary MH (1981) Carbon isotope fractionation in plants. Phytochemistry 20:553–567

Over DJ, Grossman EL (1992) Carbon isotope analysis of conodont organic material—procedure and preliminary results. Geological Society of America, Abstracts with programs 24, p A214

Peek S, Clementz MT (2012) Sr/Ca and Ba/Ca variations in environmental and biological sources: a survey of marine and terrestrial systems. Geochim Cosmochim Acta 95:36–52

Purnell MA (1993) Feeding mechanisms in conodonts and the function of the earliest vertebrate hard tissues. Geology 21:375–377

Purnell MA (1995) Microwear on conodont elements and macrophagy in the first vertebrates. Nature 374:798–800

Purnell MA, Jones D (2012) Quantitative analysis of conodont tooth wear and damage as a test of ecological and functional hypotheses. Paleobiology 38:605–626

Purnell MA, von Bitter PH (1992) Blade-shaped conodont elements functioned as cutting teeth. Nature 359:629–630

Ramakrishnaiah R, Rehman G, Basavarajappa S, Al Khuraif AA, Durgesh BH, Khan AS, Rehman I (2015) Applications of Raman spectroscopy in dentistry: analysis of tooth structure. Appl Spectrosc Rev 50(4):332–350

Rolinski T, Gawinkowski S, Kaminska A, Waluk J (2014) Raman spectra of solid amino acids: spectral correlation analysis as the first step towards identification by Raman spectroscopy. In:

Baranska M (ed) Optical spectroscopy and computational methods in biology and medicine. Springer Science & Business Media, pp 329–354

Rosseeva E, Borrmann H, Cardoso-Gil R, Carrillo-Cabrera W, Frank-Kamenetskaya OV, Öztan Y, Prots Y, Schwarz U, Simon P, Zhuravlev AV, Kniep R (2011) Evolution and complexity of dental (apatite-based) biominerals: mimicking the very beginning in the laboratory. Max-Planck-Institut für Chemische Physik fester Stoffe, Scientific report 2009–2010, pp 171–176

Shirley B, Grohganz M, Bestmann M, Jarochowska E (2018) Wear, tear and systematic repair: testing models of growth dynamics in conodonts with high-resolution imaging. Proc R Soc B 285:20181614. https://doi.org/10.1098/rspb.2018.1614

Sillen A (1986) Biogenic and diagenetic Sr/Ca in Plio-Pleistocene fossils of the Omo Shungura formation. Paleobiology 12:311–323

Strauss H, Peters-Kottig W (2003) The Paleozoic to Mesozoic carbon cycle revisited: the carbon isotopic composition of terrestrial organic matter. Geochem Geophys Geosyst 4(10):1083. https://doi.org/10.1029/2003GC000555

Tarasenko AB (2011) Tempestite beds in the Ilmen Clays of the Frasnian Stage of the Main Devonian Field (North-West of the East European Platform). Uchenye Zapiski Kazanskogo Universiteta. Seriya Estestvennye Nauki 153(4):260–266 (in Russian)

Trotter JA, Eggins SM (2006) Chemical systematics of conodont apatite determined by laser ablation ICPMS. Chem Geol 233:196–216

Trotter JA, Fitz Gerald JD, Kokkonen H, Barnes CR (2007) New insights into the ultrastructure, permeability, and integrity of conodont apatite determined by transmission electron microscopy. Lethaia 40:97–110

Turner S, Burrow CJ, Schultze H-P, Blieck A, Reif W-E, Rexroad CB, Bultynck P, Nowlan GS (2010) False teeth: conodont-vertebrate phylogenetic relationships revisited. Geodiversitas 32(4):545–594

Vevel' YA, Zhuravlev AV, Popov VV (2012) Deposits of the Devonian and Carboniferous boundary in the Kamenka River section (Pechora-Kozhvinsky megaswell, Timan-Pechora province). Neftegazovaya geologia. Teoria i practika (RUS) 7(1). Available at: http://www.ngtp.ru/rub/2/6_2012.pdf (in Russian)

Zhuravlev AV (2002) A new type of conodont hard tissue. Lethaia 35(3):275–276

Zhuravlev AV (2007) Morphofunctional analysis of late paleozoic conodont elements and apparatuses. Paleontol J 41(5):549–557

Zhuravlev AV (2017) Structure of the organic matter of conodont elements: atomic force microscopy data. Vestnik IG Komi SC UB RAS 10:20–25 (in Russian)

Zhuravlev AV (2018) Morphology of the pores-and-canals system in the albid tissue of some Late Devonian conodont elements. Vestnik IG Komi SC UB RAS 1:10–24 (in Russian)

Zhuravlev AV, Gerasimova AI (2015) Albid tissue of the conodont elements: composition and forming model. Vestnik IG Komi SC UB RAS 10:21–27 (in Russian)

Zhuravlev AV, Sapega VF (2007) XRD data on composition of the hard tissues of the Late Palaeozoic conodonts. In: Bio-inert interactions: life and rocks. Materials of the 3rd international symposium, VSEGEI, St Petersburg, 2007, pp 63–64 (in Russian)

Zhuravlev AV, Shevchuk SS (2017) Strontium distribution in Upper Devonian conodont elements: a palaeobiological proxy. Riv It Paleontol Strat 123(2):203–210

Zhuravlev A, Evdokimova I, Sokiran E (1997) New data on conodonts, brachiopods, and ostracodes from the stratotypes of the Ilmen and Buregi Beds (Frasnian, Main Devonian Field). Proceedings of the Estonian Academy of Sciences. Geology 46(4):169–186

Zhuravlev AV, Kossovaya OL, Sobolev DB, Vevel YA (1998) Early Tournasian (Early Carconiferous) shallow water communities (eastern part of the Timan-Pechora Province). Ichthyolith Issues special Publication 4, pp 60–62

Chapter 41
Coordination Compounds of Calcium Ions (II) with the Biogenic Amino Acids: Their Stability, Kinetic and Thermodynamic Characteristics of the Formation

Ivan A. Tomashevskiy, Olga A. Golovanova and Svetlana V. Anisina

Abstract The coordination compounds of calcium with a number of vital amino acids were studied by using the potentiometric titration with the application of mathematical methods of data processing. The ability of calcium ions as a complexing agent to coordinate amino acids as ligands has been shown. The regularity in the complexation of amino acids of various structures has been established. The stability constants of the coordination compounds were determined and their kinetic stability was estimated in aqueous solutions at 298 K.

Keywords Complexation · Amino acids · Formation mechanism · Stability of complexes · Potentiometry · Formation kinetics

41.1 Introduction

In recent years, the numerous processes proceeding in living organisms with the participation of calcium ions, due to the influence of anthropogenic negative factors of the technosphere on them, have been studied (Larina et al. 2006; Assimos and Holmes 2000; Bailly et al. 2000; Bak et al. 2000; Golovanova and Korolkov 2016; Golovanova and Tsepayev 2012; Malovskaya et al. 2013; Dobrynina 2007; Rhilassi et al. 2013; Perisic et al. 1998; Amerkhanova et al. 2015). Among them, especially important are the processes of interaction of calcium ions with amino acids (AAs) (Siddique and Naqvi 2002; Gerk and Golovanova 2011; Golovanova et al. 2006; Batinic et al. 2000; Brown et al. 2000; Aghasyan and Nikolaeva 1986).

I. A. Tomashevskiy (✉) · O. A. Golovanova · S. V. Anisina
F. M. Dostoevsky Omsk State University, Omsk, Russia
e-mail: ivan_tomashevsky@mail.ru

O. A. Golovanova
e-mail: golovanoa2000@mail.ru

© Springer Nature Switzerland AG 2020

O. V. Frank-Kamenetskaya et al. (eds.), *Processes and Phenomena on the Boundary Between Biogenic and Abiogenic Nature*, Lecture Notes in Earth System Sciences,
https://doi.org/10.1007/978-3-030-21614-6_41

To understand how calcium plays such an important role in the human body, it is enough to consider how the exchange of a given ion occurs in a living system. Calcium comes from food in complexes with proteins, lipids, organic acids and as a part of mineral salts (phosphates, carbonates, sulfates, etc.). In the oral cavity, calcium ions of food are exposed to amino acids and saliva proteins which form soluble complexes with it.

In a stomach under the influence of proteolytic enzymes and hydrochloric acid, calcium ions, in the ionized form or in the combination with soluble organic ligands, are released from the complexes and enter the liver. From the liver, by activating 25-dihydroxyvitamin-D, they move to a small intestine for absorption, the process being especially effective in the duodenum and in the small intestine. Through intercellular space, the ions of calcium reach blood capillaries and enter the blood, calcium exchange between the blood and bones of the human skeleton occurring through the blood serum.

Besides ions of calcium perform important functions in a human body: transmission of excitation through nerve fibers, coagulability of blood, vascular permeability reduction, which prevents fluid from escaping the bloodstream, activation of enzymes and endocrine glands, etc. (Tas 2000; Golovanova et al. 2017; Golovanova and Korolkov 2017; Golovanova and Solodyankina 2017).

The exchange of calcium ions and their interaction with amino acids, which are organic ligands, occur in almost all tissues and fluids of the human body.

Calcium ions when interacting with amino acids form complexes, the stability of which determines the rate of metabolic processes. In certain cases, the formation of such complexes and their stability play a negative role in the human body.

For example, the violations of the processes of regulation of calcium ions, including complexation, lead to pathological changes in the human body, which are the cause of nearly 150 diseases (Larina et al. 2006; Assimos and Holmes 2000; Bailly et al. 2000; Bak et al. 2000; Golovanova and Korolkov 2016; Golovanova and Tsepayev 2012; Malovskaya et al. 2013). According to statistics, in recent years, the percentage of pathogenic mineral formation in a human body has increased. The lithogenesis problem is becoming a threat that is more tangible for the modern inhabitants of all countries, in particular, megalopolises. In recent times, various diseases that lead to the formation of stones (organomineral aggregates—OMA) in human organs have only increased the speed of spread among the general population (Brown et al. 2000).

It is known that the crystallization of organomineral aggregates (OMA) takes place in complex biological fluids both in physiogenic and in pathogenic conditions. This phenomenon is associated with a number of exogenous and endogenous factors. (Gerk and Golovanova 2011; Golovanova et al. 2006; Batinic et al. 2000; Brown et al. 2000).

To date, the data on regularities of the crystallization of OMA in multicomponent physiological solutions are scarce and contradictory. It is apparent that the difficulty of studying crystallization from model solutions of biological fluids is that they contain a large number of organic and inorganic compounds, and there is a set of factors that influence the starting mechanisms of crystallization (Dobrynina 2007).

In addition, the formation of OMA most often occurs in non-equilibrium conditions and kinetic factors are responsible for their occurrence.

Thus, an understanding of the nature and characteristics of the forming complex compounds of calcium ions with amino acids, which are a part of the OMA, will help to identify the role of formation/destruction of compounds in pathological and physiological processes occurring in living tissues. In addition, the study of the process of interaction of calcium ions with AAs will serve as a basic theoretical material in the creation of the medications aimed at the point delivery of calcium ions and amino acids at the place of destination. The solution of such a task is possible only by systematically studying the interaction of the complex formation of calcium ions with organic ligands.

The purpose of this work is to study the interaction of biogenic amino acids with calcium ions in aqueous solutions at T = 298 K and the interpretation of this interaction according to the stability of the complexes and the kinetic characteristics of complexation.

41.2 Experimental Part

41.2.1 Reagents

14 biogenic amino acids (in the form of dry substance, p.a. grade) were used as a source of ligands. Before the analysis, they were in the solid form. Samples of AAs, which were weighted with an accuracy of 0.0001 g, were dissolved in a 200.0 mL volumetric flask to create a final concentration of AAs—10^{-2} mol per liter.

Ca $(NO_3)_2 \cdot 5\ H_2O$ salt (in the form of dry substance, p.a. grade) served as a source of a chelating agent. Samples of the calcium nitrate, which were weighed with an accuracy of 0.0001 g, were dissolved in a 200.0 mL volumetric flask to create a final concentration of calcium ions (II)—10^{-3} mol/l.

41.2.2 The Synthesis of Complexes $Ca^{2+}{}_m[L]_n{}^{k-}$

The complexes of calcium ions Ca^{2+} with each of the amino acid (Table 41.1) were synthesized by mixing of aliquots of the initial AA solutions and calcium nitrate. So, 10.0 mL of amino acid solution and 10.0 mL of calcium nitrate solution were added to a 100.0 mL volumetric flask, after that, volume level in all flasks was adjusted to mark. Finally, the content of each flask was stirred for 30 min to prepare work solutions.

All AAs in the composition of complexes have very different composition and structure, their characteristics are given in Table 41.1 (Selifonova and Chernova 2012).

Table 41.1 The characteristics of some amino acids with the values of dissociation constants and isoelectric points

AA	Designation	The gross-formula	Dissociation constants (pK)			pI
			α-COOH	α-NH_2	The other groups	
Glycine	Gly	$C_2H_5NO_2$	2.35	9.78		6.20
Alanine	Ala	$C_3H_7NO_2$	2.35	9.78		6.11
Aspartic acid	Asp	$C_4H_7NO_4$	1.99	9.90	β-COOH-3.90	2.98
Isoleucine	Ile	$C_6H_{13}NO_2$	2.32	9.76		6.04
Arginine	Arg	$C_6H_{15}N_4O_2$	1.82	8.99	ε-NH_2 12.48	10.76
Histidine	His	$C_6H_9N_3O_2$	1.80	9.33	>NH-6.04	7.60
Valine	Val	$C_5H_{11}NO_2$	2.29	9.74		6.02
Serine	Ser	$C_3H_7NO_3$	2.19	9.21		5.70
Glutamic acid	Glu	$C_5H_9NO_4$	2.10	9.47	γ-COOH-4.07	3.09
Methionine	Met	$C_5H_{11}NO_2S$	2.13	9.28		5.71
Proline	Pro	$C_5H_9NO_2$	1.95		γ-NH-10.64	6.30
Lysine	Lys	$C_6H_{14}N_2O_2$	2.16	9.06	δ-NH_2-10.54	9.80
Asparagine	Asn	$C_4H_8N_2O_3$	2.14	8.72		5.43
Threonine	Thr	$C_4H_9NO_3$	2.11	9.10		5.61

41.2.3 Methods of Analysis

It is known that spectrophotometry, ion-exchange and polarography are usually used to investigate crystallization from prototypes of biofluids (Selifonova and Chernova 2012; Dyatlova et al. 1988; Amerkhanova et al. 2015). There are currently no literature sources in which all characteristics of Ca^{2+} complexes with amino acid are considered. That's why it's important to provide an algorithm that would allow immediate, accurate, rapid, and selective determination of the parameters of coordination compound formation.

There is also some difficulties in this area because there is not so many reliable data on interaction between calcium and AA ions in the literature. Almost all literature sources indicate a complex of 1:1 composition is coordinated in aqueous solutions (Kurochkin 2011; Martell 2006). This is because calcium ions are weak complexing agents, despite having a coordination number of 6 (Kozhomuratova et al. 2007). According to these facts, further discussion of the results will be conducted taking into account the ratio 1:1 for all complexes.

The method of the potentiometric titration was performed, using the following set of chemical tools:

– an ion meter I-160-MI, accuracy of measuring of emf is ±0.1 mV;
– an ELIS-121Ca ion-selective electrode;
– the silver chloride reference electrode.

Also, we have added some quantities of 6 M HCl to all work solutions to make pH = 3 before starting of titration.

The initial EMF value of each solution was set within ±0.1 mV for all titrations for 3 min. The titration of all solutions was carried out in 0.5 mL increments using the burette, a freshly prepared solution of 0.10 M NaOH was used as the titrant. Before the titration of each work solution, the titrant solutions were standardized with a 0.10 M HCl solution with an acid-base phenolphthalein indicator.

The value of the EMF before adding each titrant was set for a 45 s. Titration continued until the precipitate of $Ca(OH)_2$ began to appear. In order to improve the accuracy of the experiment and to avoid the influence of large random errors, the three parallels titrations were performed for each mix. Since the repeatability limit (r) for each measurement of each parallel test wasn't greater than 5 mV (in the percent value for all cases <3%, in most cases <1%), the integral curves obtained by averaging the EMF values for each titration step (Selifonova and Chernova 2012).

Also, using the ion-selective electrode (Aghasyan and Nikolaeva 1986), we have determined the value of pCa (the value was very similar for each parallel).

To establish the kinetic characteristics of the formation of the complexes of Ca^{2+} and AA, we have used the Gran's approach. In this method, the eq. point was determined from a graph in the coordinates: $\Delta V/\Delta E - V$, where ΔV is the titration step, ΔE is the difference between the two extreme values, V—the volume of the added titrant. The Gran curve is linear except eq. point. The equivalence point is the point of intersection of these lines. The advantages of the Gran method are especially noticeable in the analysis of dilute solutions, which make it possible to determine the equivalence point with sufficient accuracy due to the linearity of the graph, and also in cases when the titration curve is poorly expressed (Posypayko et al. 1989).

41.2.4 Results and Discussion

To decipher and interpret the results from potentiometric titration, ion percentage diagrams of all AAs were constructed with the pH along the abscissa and per cent of forms of amino acids along the ordinate (Table 41.2). According to these diagrams, the investigated AAs can be divided into three groups (Figs. 41.1, 41.2 and 41.3):

Most of the studied AAs don't have any ionized groups in their radicals, their typical diagram is shown in Fig. 41.1.
Aspartic and glutamic acids both have two carboxyl groups, therefore they will have an ionic diagram, which is typical for acidic AAs (Fig. 41.2).
Three of the investigated AAs—arginine, histidine, lysine—in addition to the α-NH_2 group, also contain ionizable basic groups. Histidine has an imidazole group, and precisely due to the imidazole group histidine is charged either neutrally or positively

Table 41.2 The values of the $V_{n=0.5}$ of the formed complexes by the Ca^{2+} and AA

AA	$V_{n=0.5}$	*AA*	$V_{n=0.5}$
Lys	3.6	Glu	13.5
Met	7.6	Asp	14.7
Asn	7.8	Gly	17.3
Thr	7.8	Ser	19.5
Pro	9.2	Val	20.3
Ile	10.5	His	20.8
Arg	11.2	Ala	21.5

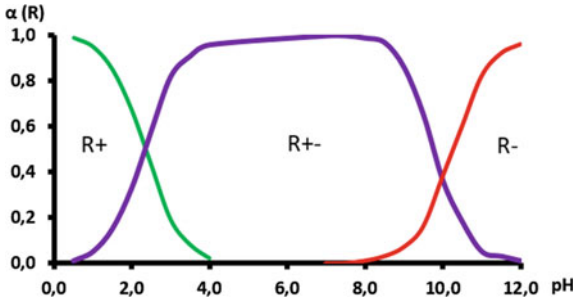


Fig. 41.1 Ion diagram of forms of the amino acids, which don't have ionized links in the side groups

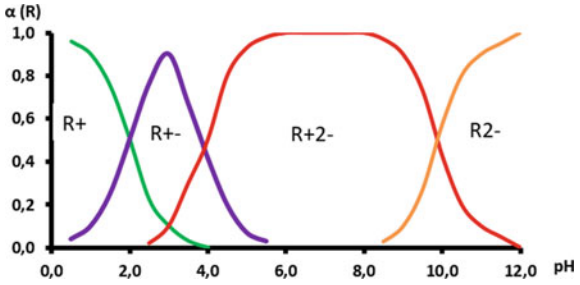


Fig. 41.2 Ion diagram of forms of the "acidic" amino acids

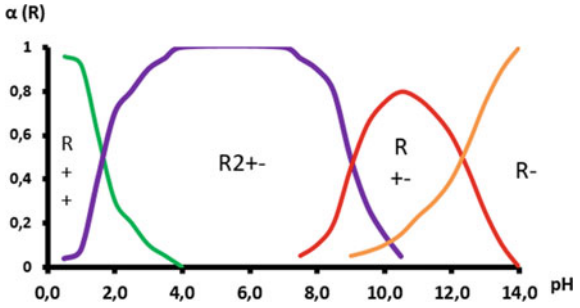


Fig. 41.3 Ion diagram of forms of the "base" amino acids

upon physiological fluctuations in pH (from 6.9 to 7.4). Arginine has a strong basic guanidinium group, and lysine contains an additional amino group at the end of the side chain. These AAs will have a pH dependence, shown in Fig. 41.3.

During the variation of pH, AA undergo the following changes:

The first group:

At pH < pK (α-COOH), due to an excess of protons, the protonated forms of the AAs dominate (Eq. 41.1):

$$R - CH_2 - NH_2 - COOH + H^+ \rightleftarrows R - CH_2 - NH_3^+ - COOH \tag{41.1}$$

At pK (α-COOH) < pH < pK (α-NH_2), α-carboxyl groups start to dissociate with the formation of a zwitterion (Eq. 41.2):

$$R - CH_2 - NH_3^+ - COOH \rightleftarrows R - CH_2 - NH_3^+ - COO^- + H^+ \tag{41.2}$$

At pH > pK (α-NH_2), the α-NH_3^+ groups begin to dissociate with the formation of the AA anions (Eq. 41.3):

$$R - CH_2 - NH_3^+ - COO^- \rightleftarrows R - CH_2 - NH_2 - COO^- + H^+ \tag{41.3}$$

Proline de facto differs in this case because α-NH_2 does not participate in protonization/deprotonization processes but its γ-NH-group does.

The second group:

At pH < pK (α-COOH), due to an excess of protons, the protonated forms of the AAs dominate (Eq. 41.4):

$$HOOC - R - CH_2 - NH_2 - COOH + H^+ \rightleftarrows HOOC - R - CH_2 - NH_3^+ - COOH \tag{41.4}$$

At pK (α-COOH) < pH < pK (β-COOH or γ-COOH), α-carboxyl groups start to dissociate with the formation of a zwitterion (Eq. 41.5):

$$HOOC - R - CH_2 - NH_3^+ - COOH \rightleftarrows HOOC - R - CH_2 - NH_3^+ - COO^- + H^+ \tag{41.5}$$

For pK (β-COOH or γ-COOH) < pH < pK (α-NH_2), second carboxyl groups start to dissociate (Eq. 41.6):

$$HOOC - R - CH_2 - NH_3^+ - COO^- \rightleftarrows {}^-OOC - R - CH_2 - NH_3^+ - COO^- + H^+ \tag{41.6}$$

At pH > pK (α-NH_2), the α-NH_3^+ groups begin to dissociate with the formation of the AA anions (Eq. 41.7):

$$^{-}OOC - R - CH_2 - NH_3^+ - COO^- \rightleftarrows {}^{-}OOC - R - CH_2 - NH_2 - COO^- + H^+ \tag{41.7}$$

As can be seen, anions already form at pH = 4, and this fact fundamentally distinguishes these two AAs from other investigated α-amino acids.

The third group:

At pH < pK (α-COOH), due to an excess of protons, the protonated forms of the AAs dominate (Eq. 41.8):

$$HL^+ - R - CH_2 - NH_2 - COOH + H^+ \rightleftarrows HL - R - CH_2 - NH_3^+ - COOH \tag{41.8}$$

At pK (α-COOH) < pH < pK (α-NH_2) α-carboxyl groups start to dissociate with the formation of a zwitterion (Eq. 41.9):

$$HL^+ - R - CH_2 - NH_3^+ - COOH \rightleftarrows HL - R - CH_2 - NH_3^+ - COO^- + H^+ \tag{41.9}$$

At pK (α-NH_2) < pH < pK (ε, δ-NH_2 или > NH), the α-NH_3^+ groups begin to dissociate with the formation of the AA anions (Eq. 41.10):

$$HL^+ - R - CH_2 - NH_3^+ - COO^- \rightleftarrows HL - R - CH_2 - NH_2 - COO^- + H^+ \tag{41.10}$$

At pH > pK (ε, δ-NH_2 или > NH), the HL^+ group deprotonates (Eq. 41.11):

$$HL^+ - R - CH_2 - NH_2 - COO^- \rightleftarrows L - R - CH_2 - NH_2 - COO^- + H^+ \tag{41.11}$$

These AAs are charged positively in the widest range of pH values. It should be noted that these curves at Figs. 41.1, 41.2 and 41.3 are typical, and the distribution of the ionized forms of each individual AA varies depending from the pK of groups which are presented in this very AA (Selifonova and Chernova 2012).

So, knowing the dependence of the distribution of the ionized forms of AA at the start of the titration, and having obtained the integral curves of potentiometric titration experimentally, it is possible to characterize the formation/destruction of calcium (II) complexes (complexing agent) with amino acid (ligands) at all stages of the complex formation.

At Fig. 41.4 integral curves of the substitution potentiometric titration of the studied CCs are shown. The abscissa of this figure represents the volumes of the added titrant, and the ordinate shows the EMF value of the work solutions.

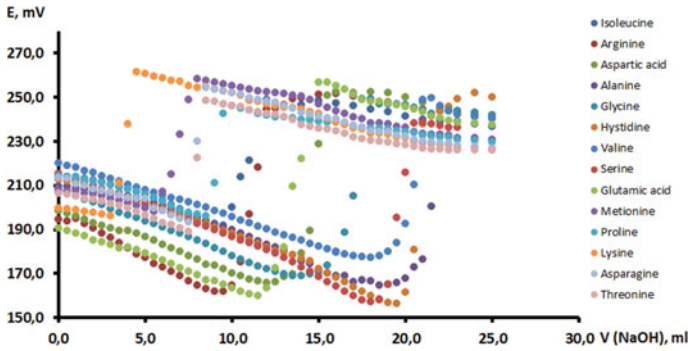


Fig. 41.4 Integral curves of the potentiometric titration of calcium nitrate ($C_{Ca(NO_3)2} = 10^{-3}$ mol per liter) and the studied amino acids ($C(AA) = 10^{-2}$ mol per liter) by the sodium hydroxide solution ($C_M(NaOH)) = 10^{-1}$ mol per liter

It's obvious that curves have an authentic form. This gives us some reasons to assume that in all cases the formation and destruction of titration complexes were of a common nature. At the same time, the unequal arrangement of titration jumps and its different values indicate various quantitative characteristics of the formation/destruction of each of the complexes.

Based on Figs. 41.1, 41.2, 41.3, Table 41.1 and our data (Fig. 41.4), we can guess that during the potentiometric titration the following processes come:

A mixture of calcium ions (II) and AA in a volume of 20.0 mL is acidified by the 6 M HCl solution to make pH = 3.

At these pH values (according to the ion diagrams), 11 AAs (isoleucine, alanine, glycine, valine, serine, methionine, proline, asparagine, threonine, aspartic and glutamic acid) at the beginning of the titration are predominantly exist in the form of a zwitterion:

$$R - CH_2 - NH_2 - COOH + H^+ \rightleftarrows R - CH_2 - NH_3^+ - COO^- \qquad (41.12)$$

Both aspartic and glutamic acids have in its composition the second carboxyl group which can also partially participate in the redistribution of the electron charge. There is also some fraction of the cationic form of AAs, but, in general, the molecules of aspartic and glutamic acids are in a state similar to the zwitterions of the AAs mentioned above:

$$HOOC - R - CH_2 - NH_2 - COOH + H^+ \rightleftarrows HOOC - R - CH_2 - NH_3^+ - COO^- + H^+ \qquad (41.13)$$

As indicated above, arginine, histidine and lysine, as indicated above, contain in its composition the basic groups, so at this stage these AAs are positively charged:

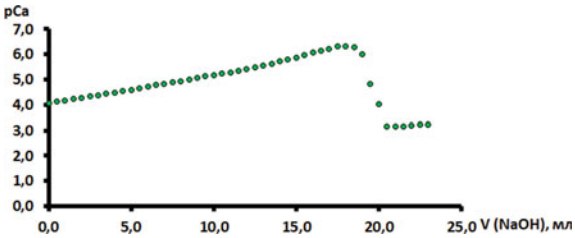


Fig. 41.5 Curve pCa = f (V(NaOH)) of the work solution: calcium nitrate ($C_M(Ca(NO_3)_2)$) = 10^{-3} mol per liter and serine (C_M(amino acid) = 10^{-2} mol per liter) while the adding of the sodium hydroxide ($C_M(NaOH)$) = 10^{-1} mol per liter

$$HL^+ - CH_2 - NH_2 - COOH \rightleftarrows HL^+ - CH_2 - NH_3^+ - COO^- \tag{41.14}$$

For convenience, we will take the following notation:

$$R - CH_2 - NH_3^+ - COO^- = N^{\pm} \tag{41.15}$$

Ca^{2+} act as a complexing agent, so they coordinate the ligand:

$$Ca^{2+} + N^{\pm} \rightleftarrows [CaN^{\pm}]^{2+} \tag{41.16}$$

For arginine, histidine and lysine:

$$R^+ - CH_2 - NH_3^+ - COO^- = N^{\pm+}; Ca^{2+} + N^{\pm+} \rightleftarrows [CaN^{\pm+}]^{2+} \tag{41.17}$$

In this state, complex remains until the beginning of titration.

At the beginning of titration upon adding of titrant, the EMF of the electrochemical chain decreases slowly because the ionic strength of the work solution increases, reducing the activity of free calcium ions. At the same time, the complexes $[CaN^{\pm}]^{2+}$ и $[CaN^{\pm+}]^{2+}$ remain stable.

After adding the next portion of the titrant, a sharp increase (jump) in the EMF is observed for all of the AAs. This change is associated to an increase of the concentration of unbound calcium ions because of the destruction of complex:

$$[CaN^{\pm}]^{2+} \rightarrow Ca^{2+} + N^{\pm} \tag{41.18}$$

For arginine, histidine and lysine:

$$[CaN]^{2+} \rightarrow Ca^{2+} + N^{\pm} \tag{41.19}$$

This hypothesis is confirmed by the appropriate measurements of pCa upon adding each portion of the titrant. As an example, Fig. 41.5 demonstrates the change in the

activity of calcium ions with the addition of 0.10 M calcium hydroxide (step is 0.5 mL) to a mixture of a calcium ions with serine, is shown.

As can be seen, when a sufficient volume of the titrant is added in the work solution, a jump in the EMF occurs, at the same time there is also a sharp drop in the pCa due to the destruction of the "calcium-amino acid" complex. The further increase in pCa is associated with a decrease in the activity of calcium ions.

To our point of view, 50% of the molecules of the complex compound are stable at the point of equivalence (p. eq.), 50% are destroyed; i.e., the work solutions in this very moment have the formation function n = 0.5 (Dyatlova et al. 1988).

After the full destruction of the complex molecules, the EMF begins to fall monotonically again as the ionic strength increases and the activity of calcium ions correspondingly decreases.

Upon addition in the work solution of some extra volume of sodium hydroxide, a pH of 10–10.5 is reached in the solution, which leads to the formation of a poorly soluble calcium hydroxide precipitate (pSP = 5.26):

$$Ca^{2+} + 2OH^{-} \rightarrow Ca(OH)_2 \tag{41.20}$$

Since 50% of the initially formed molecules of complex compounds are destroyed at p.eq., the following volume of NaOH solution should serve semiquantitative characteristic of the interaction between calcium ions and each of the amino acids. The larger the characteristic value is, the more volume of titrant is necessary to destroy the complex to make the resulting one more stable. We designate this characteristic as $V_{n=0.5}$.

This characteristic was calculated from the potentiometric curves for complexes of all AA s with calcium ions. The results are shown in Table 41.2.

Based on our data, it can be concluded that the stability of the complexes of Ca^{2+} with the AAs increases in the following sequence:

$$\begin{aligned} &Ca^{2+} - Lys \rightarrow Ca^{2+} - Met \rightarrow Ca^{2+} - Asn \rightarrow Ca^{2+} \\ &\quad - Thr \rightarrow Ca^{2+} - Pro \rightarrow Ca^{2+} - Ile \rightarrow Ca^{2+} \\ &\quad - Arg \rightarrow Ca^{2+} - Glu \rightarrow Ca^{2+}Asp \rightarrow Ca^{2+}Gly \rightarrow Ca^{2+} \\ &\quad - Ser \rightarrow Ca^{2+} - Val \rightarrow Ca^{2+} - His \rightarrow Ca^{2+} - Ala \end{aligned} \tag{41.21}$$

In graphs with the structural formulas of the AAs and their functional groups indicated, this sequence can be represented as follows (Fig. 41.6).

So it can be seen that the structural formulas of the studied AAs differ by (a) the number of carbon atoms in the structural formula; (b) by the nature of the functional groups and their number; (c) by the arrangement of functional groups.

For the convenience in explaining the increase in the stability of the complexes in the sequence (41.21), we will take into account these three factors: (a) the large number of carbon atoms can create an obstacle in the coordination of the AA ligands to calcium ions (II); (b) according to the work of (Yatsimirsky 1976), the calcium

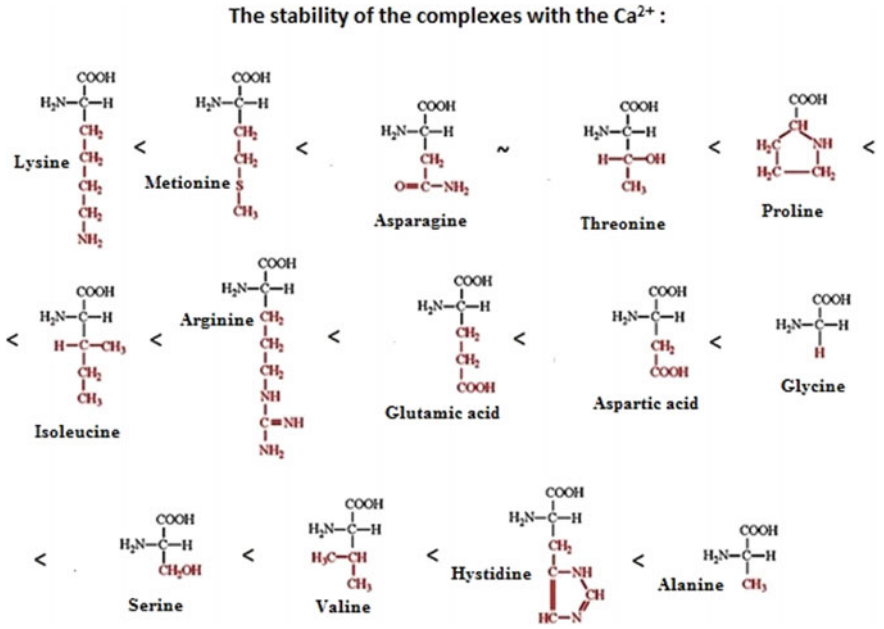


Fig. 41.6 The sequence of the increase of the stability of the complexes of the studied amino acids with the Ca^{2+}

ion belongs to the first group of cations, for which complexation usually occurs through the oxygen atoms of the –COOH-group of AA. The effect of donor nitrogen atoms on the formation of coordination bonds with calcium (II) is less significant, but possible. Also, the other functional groups, which can be a donor or acceptor of electron density, can also participate in the complex formation/destruction of complexes. An increase in the number of similar functional groups enhances their effect; (c) the arrangement of functional groups which are in relation to each other and to the α-carbon atom plays key role in complexation.

We divide the whole sequence (41.21) conditionally into three groups:

(A) Unstable. As can be seen, the most unstable complex is a complex of calcium (II) ions with lysine. This is due to the fact that the molecule of this AA has a large number of carbon atoms in the radical bound to the α-carbon atom. In this way, a steric obstacle is created when the AA molecule approaches to the calcium ions, so this complex can be one most easily destroyed, despite the NH_2 at the end of the carbon radical, which can also serve as a source of electron density, but steric factor in this case predominate over the electronic one.

Methionine contains a lateral radical with one fewer CH_2-group than in lysine, and has, after the γ-carbon atom, an -S-group, which can participate in complexation. The complex "Ca^{2+}–Met" is slightly more stable than "Ca^{2+}–Lys". The stability

of "Ca^{2+}–Asn" and "Ca^{2+}–Thr" systems in the given sequence starts to increase, because they contain amide and hydroxyl groups that can participate in the creation of additional bonds with calcium (II) ions. Proline, however, does not have such a groups, but due to the formation of a cyclic radical, which gains compactness, so this AA forms a slightly more stable complex with calcium ions (II).

(B) Weakly stable. The isoleucine molecule has a branched lateral radical, so, a larger number of molecules can be approached to the complexing agent, the $–NH_2$ and –COOH groups are oriented along the complexing agent. The arginine molecule has an "isoleucine-like" structure, but instead of the methyl substituent on the opposite end of the molecule from the carboxyl group, the guanidine group $NH_2–C–(NH)–NH_2$ is located. The large number of amino groups creates a large electron density and, as a consequence, additional bonds with complexing agents.

As for amino acids with the two carboxyl groups, coordination of "hard" metal ions in complexation reactions with amino acids is carried out mainly due to the oxygen atoms of carboxyl groups. In this case, the COOH-group coordinates bidentately with the formation of a cyclic or bridging structure (Bolotin et al. 2008) (Fig. 41.7).

Since the molecule contains two of these groups, this type of ligands is stronger ligand than the previous one, so, Ca^{2+}-complexes with aspartic and glutamic acids are more stable than with the previous amino acids, which agrees well with the obtained results. The sole difference in the complexation between these two AAs that glutamic acid contains one more carbon atom, which further delocalizes the electron density created by the two carboxyl groups, making the complex with Ca^{2+} slightly less stable than with aspartic acid. The substitution of the carboxyl group by amide in asparagine clearly shows the stability of the complex with calcium ions (II).

(C) Relatively stable. In contrast to the two previous groups, these AAs except histidine, consist of fewer carbon atoms and don't have any bulk CH_3-substituents, which can be steric obstacles in coordinating the free s-orbitals of the ions of the complexing agent Ca^{2+} and electron density of the ligands.

That is why complexes of Ca^{2+} with AAs containing such a groups are more stable than AAs with bulk substituents and a greater number of carbon atoms in the main chain.

The relative stability of histidine is explained by the fact that the side radical, in addition to the nitrogen atoms, having a double bond –C=C–, and instead of delocalizing the electron density, the carbon atoms can create it. Thus, the side radical can be an active participant of the complexation.

It should be noted that all of the above factors actively influence the complex formation and rank the stability of complexes with Ca^{2+} into a certain sequence.



Fig. 41.7 Forms of the COOH- group in the aminoacids with the two COOH-groups

As can be seen that the stability of the complexes of the investigated AAы with Ca^{2+} is established at qualitative and semi-quantitative levels due to the introduction of nominal characteristic $V_{n=0.5}$. Using mathematical approach, a quantitative description of these systems can be allowed.

It is generally known that the main quantitative characteristic of any complexation process is the constant of overall stability, for these components it could be expressed by the following formula:

$$M + nN \rightleftarrows [MN_n]; K = \frac{[MN_n]}{[M][N]^n} \quad (41.22)$$

where β is the constant of overall stability for all complexes in all existing forms;
$[ML_n]$ is the equilibrium concentration of the resulting complex of calcium and amino acid;
[M] is the equilibrium concentration of unbounded calcium ions in solution;
$[L]_n$ is the equilibrium concentration of the free ligands in the solution.

As mentioned earlier, this system is very difficult to study. This one explains the fact that there is not so many information about constants of overall stability, moreover, these studies are not sophisticated themselves, at best, they contain data on complexes of calcium (II) ions with several AAs (Bottari and Festa 1996; De Robertis et al. 1991; Daniele et al. 1985; Tas 2000).

However, if these data are reliable, they can be used to calculate the stability constants of complexes, taking into account the experimental data obtained and their mathematical processing.

To do so, we must know the values of at least two (reliably established) stability constants of coordination compounds that we can use as references. In addition to the above factors, the difficulty is that the stability constants in the literature were usually calculated for other values of the ionic strength of aqueous solutions than the ones in this work, and the choice of ionic strength for one acid differed sharply from those of others. To obtain the reference values of constants at ionic strength I = 0.5, we extrapolated the constants of stability at ionic strengths I = 0.1 and I = 3.0 of Ca^{2+} complexes with serine and I = 0.1 and I = 1.0 of Ca^{2+} complexes with glutamic acid to I = 0.5 at T = 298 K. This choice was made, since the literature for these two AAs contains values of the constants of the Ca^{2+}–AA systems for two different values of ionic strength (Bottari and Porto 1985; Burger et al. 1998; Khalil and Attia 2000). For all other AAs, only the values of the stability constants for I = 0.1 are given. In addition, the way of finding constants was potentiometric in all four cases, allowing us to compare the results of these literature sources (Table 41.3).

Extrapolation to ionic strength I = 0.5 yielded the following values of lg K°:

For the Ca^{2+}–Ser system, lg K° = 3.68; for the Ca^{2+}–Glu system, lg K° = 2.14. These values of the constants were then used to find the stability constants under identical test conditions for all of the investigated systems. It is worth noting that in this case, lg K°(Ca^{2+}–Ser) > lg K° (Ca^{2+}–Glu), while $V_{n=0.5}$ (Ca^{2+}–Ser) > $V_{n=0.5}$

Table 41.3 Literature data on constants of stability for complexes of calcium with serine and glutamic acid (T = 298 K)

Complex	I (mole/L)	lg K°	References
Ca^{2+}–Ser	0.1	4.03	Rey et al. (1990)
	3.0	1.48	Bottari and Porto (1985)
Ca^{2+}–Glu	0.1	3.84	Khalil and Attia (2000)
	1.0	1.92	Burger et al. (1998)

(Ca^{2+}–Glu), testifying to the good agreement between our experimental and calculated data for these complexes and the literature sources (Kurochkin 2011).

Associating lg K° for Ca^{2+}–Ser and Ca^{2+}–Glu systems with the corresponding semi-quantitative nominal characteristics $V_{n=0.5}$ and extrapolating further, we were able to find lg K° for all of the investigated systems. Making the corresponding transformations, we obtained a number of logarithms for the constants of coordination compound stability (Table 41.4).

Also, in this study, we established the rate of formation/destruction of the complexes from the "Ca^{2+}-Amino acid" systems. Therefore, to solve this problem, all the integral curves of the potentiometric titration, which were shown in Fig. 41.4, according to which, the first and second derivative titration curves were obtained, as well as the titration curves, which were constructed using the Gran method.

According to the Gran's approach, the equivalence point is determined using the graph in the coordinates: $\Delta V/\Delta E - V$, where ΔV is the titration step, ΔE is the difference between the two extreme values, V—the volume of the added titrant. Before the equivalence point and after it, the Gran curve is linear. The equivalence point is the point of intersection of these lines. The advantages of the Gran method are extremely useful in the analysis of dilute solutions. It allows us to determine the equivalence point with sufficient accuracy because of the linearity of graph, and also in those cases, when the titration curve is poorly expressed (Posypayko et al. 1989)

Due to the fact that the data of the titration curves in our experiment is quite differ from the classical obtained with potentiometric titration, the Gran's approach was used to estimate the lability of calcium-amino acid complexes, which was modified by the following tool: along the y-axis instead of the EMF differences and the volumes between the two extreme values. This processing of the curves avoids distortion of

Table 41.4 The calculated values of lg K° for the complexes of the studied amino acids with the Ca^{2+}

AA	log K°	*AA*	lg K°
Lys	0.39	Glu	2.14
Met	0.63	Asp	2.45
Asn	0.68	Gly	3.11
Thr	0.68	Ser	3.68
Pro	1.04	Val	3.88
Ile	1.37	His	4.01
Arg	1.55	Ala	4.19

the curves from various collateral processes and more convenient for analysis. As an example, in Fig. 41.8 shows differential titration curves for mixtures of $Ca(NO_3)_2$ with isoleucine and arginine.

The obtained curves as such can be used for a semi-quantitative description of how much complex of Ca^{2+} with AAs is labile. In order to determine the degree of lability of the complexes, it is proposed to introduce a semi-quantitative characteristic describing the behavior of the disintegrating complex—δ, which represents by the following equation:

$$\delta = \frac{\Delta V}{\Delta E}\text{p.after eq.p.} - \frac{\Delta V}{\Delta E}\text{p.before eq.p.}, \tag{41.23}$$

where the first term is the ratio of the pointed differences for the point immediately after the equivalence point, and the second value is the same for the point immediately before the equivalence point. Respectively, the smaller is δ, the faster the complex destroys and forms, so, more labile, and on the contrary. In this case, it must be remembered that this parameter characterizes the rate of failure of the complex on the values of volume of titrant close to $V_{n=0.5}$.

For each complex, the value of δ was calculated from its curve and compared with other complexes with AAs. The values of the obtained δ for all AA are given in Table 41.5.

As can be seen, according to their lability, the complexes of Ca^{2+} with the given AA are arranged in the following sequence: δ (Ca^{2+}–Asn) = δ (Ca^{2+}–Thr) < δ (Ca^{2+}–Lys) < δ (Ca^{2+}–His) < δ (Ca^{2+}–Ser) < δ (Ca^{2+}–Asp) = δ (Ca^{2+}–Met) < δ (Ca^{2+}–Ile) =

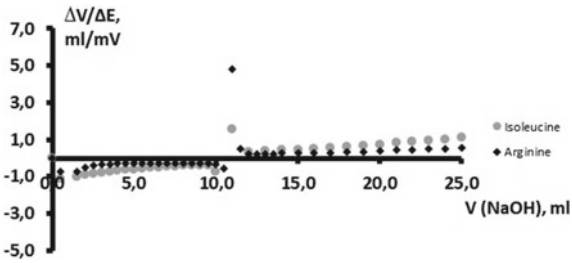


Fig. 41.8 The differential titration curves based on Gran method for mixtures of $Ca(NO_3)_2$ ($C_{Ca(NO_3)2} = 10^{-3}$ mol per liter) with isoleucine and arginine ($C_{AA} = 10^{-2}$ mol per liter) by the sodium hydroxide solution ($C_M(NaOH)) = 10^{-1}$ mol per liter

Table 41.5 The calculated values δ for the complexes of the studied amino acids with the Ca^{2+}

AA	δ	*AA*	δ
Lys	1.1	Glu	2.2
Met	2.1	Asp	2.1
Asn	0.9	Gly	6.3
Thr	0.9	Ser	1.9
Pro	3.1	Val	2.8
Ile	2.2	His	1.4
Arg	5.3	Ala	3.1

δ (Ca^{2+}–Glu) < δ (Ca^{2+}–Val) < δ (Ca^{2+}–Ala) = δ (Ca^{2+}–Pro) < δ (Ca^{2+}–Arg) < δ (Ca^{2+}Gly), In other words, the most labile complexes are those of calcium ions with asparagine and threonine, while the most stable ones are with glycine.

All experimental and calculated data are of scientific interest and can serve as a theoretical basis for the diagnosis and treating of diseases with the pathogenic mineral formation, as well as bone diseases, and it also can be a guide of the creation and/or refining narrow-spectrum drugs.

41.3 Conclusions

In this work, calcium ion complexes with amino acids were studied and ranked into three groups according to the stability of the resulting complexes, while the increase in the stability constants of the complexes in the series of the studied systems "calcium ions - amino acid" in aqueous solution was found at T = 298 K. Using the input semi-quantitative criterion δ. a difference was established in the rate of interaction of calcium ions and a number of amino acids in aqueous solutions at T = 298 K.

References

Aghasyan PK, Nikolaeva ER (1986). Fundamentals of electrochemical analysis methods (potentiometric method) (In Russian)

Amerkhanova ShK, Golovanova OA, Shlyapov RM (2015) The relationship between the thermodynamic characteristics of the formation of calcium-containing substrate and sorption properties with respect to copper (II) glycinates. Her Omsk Univ 2:45–49 (In Russian)

Assimos DG, Holmes RP (2000) Role of diet in the therapy of urolithiasis. Urol Clin North Am 27:255–268

Bailly GG, Norman RW, Thompson C (2000) Effects of dietary fat on the urinary risk factors of calcium stone disease. Urology 1:40–44

Bak M, Thomsen JK, Jakobsen HJ, Petersen SE, Petersen TE, Nielsen NC (2000) Solid-state ^{13}C and ^{31}P NMR analysis of urinary stones. J Urol 164:856–863

Batinic D, Milosevic D, Blau N, Konjevoda P, Stambuk N, Barbaric V, Subat-Dezulovic M, Votava-Raic A, Nizic L, Vrljicak K (2000) Value of the urinary stone promoters/inhibitors ratios in the estimation of the risk of urolithiasis. J Chem Inf Comput Sci 3:607–610

Bolotin SN, Bukov NN, Volynkin VA (2008). The coordination chemistry of natural amino acids. Publishing House LCI, p 240 (in Russian)

Bottari E, Festa M (1996) The behaviour of asparagine as a ligand for cations. J Ann Chim 86:133

Bottari E, Porto R (1985) Serine as a ligand complex formation with calcium (II). J Ann Chim 75:393

Brown SA, Munver R, Delvecchio FC, Kuo RL, Zhong P, Preminger GN (2000) Microdialysis assessment of shock wave lithotripsy-induced renal injury. J Urol 56(3):364–368

Burger K, Sipos P, Veber M (1998) Formation microequilibria of proton, calcium and magnesium complexes of the γ-carboxyglutamate ion and related compounds J Inorg Chim Acta 4:233

Daniele P, De Robertis A, De Stefano C (1985) On the possibility of determining the thermodynamic parameters for the formation of weak complexes using a simple model for the dependence on

ionic strength of activity coefficients: Na^+, K^+, and Ca^{2+} complexes of low molecular weight ligands in aqueous solution. J Chem Soc Dalton Trans 11:2353
De Robertis A, De Stefano C, Gianguzza A (1991) Salt effects on the protonation of 1-histidine and 1-aspartic acid: a complex formation model. J Thermochim Acta 177:39
Dobrynina NA (2007) Bioneorganic chemistry. Moscow State University, Moscow, p 36 (in Russian)
Dyatlova NM, Temkina VY, Popov KI (1988) Complexons and Complexes of Metals. M.: Chemistry, pp 48–50 (in Russian)
Gerk SA, Golovanova OA (2011) Bone apatite of the person—features of a chemical structure at a pathology. J Butlerov Commun 3:123–132
Golovanova OA, Korolkov VV (2016) Study of phase formation regularities in supersaturated systems of calcium oxalate in the presence of additives on the model unit. J Butlerov Commun 9:105–114 (in Russian)
Golovanova OA, Korolkov VV (2017) Thermodynamic and kinetic patterns of crystallization of calcium oxalate in the presence of amino acids. J Crystallography 5:819 (in Russian)
Golovanova OA, Solodyankina AA (2017) The main characteristics of the nucleation process in the model solution of blood plasma. J Crystallogr Rep 2:342 (in Russian)
Golovanova OA, Tsepayev SA (2012) Phase, element, amino acid, structural composition of nephroliths minerals. J Butlerov Commun 12:96–103 (in Russian)
Golovanova OA, Rosseeva EV, Frank-Kamenetskaya OV (2006) J Herald St. Petersburg State Univ 2:123–127 (in Russian)
Golovanova OA, Korol'kov VV, Kuimova MV (2017) Kinetic Characteristics of Crystallization in Prototypes of Biological Fluids. Biogenic-abiogenic interactions in natural and anthropogenic systems. In: IOP conference series: materials science and engineering, p 168
Khalil MM, Attia AE (2000) Potentiometric studies on the binary and ternary complexes. J Chem Eng Data 45:1108–1111
Kozhomuratova ZS, Mironov YV, Shestopalov MA (2007) Cluster compounds $[Ca(DMF)_6]$ $[Mo_6Cl_{14}]$ and $[\{Ca(OPPh_3)_4\}\ \{Mo_6Cl_{14}\}]$ cluster compounds: synthesis, crystal structure and properties. J Coord Chem 33:1–3 (in Russian)
Kurochkin VY (2011). Thermodynamics of complexation of calcium ions with amino acids in aqueous solution. Dissertation, Ivanovo (in Russian)
Larina TA, Kuznetsova TA, Koroleva LYu (2006) The scientific proceedings of the research center of pedagogy and psychology. J Sci Notes Orel State Univ 7:135–138 (in Russian)
Malovskaya EA, Golovanova OA, Panova TV, Gerk SA, Osintsev VA (2013) Crystallization of calcium phosphates from prototypes of biological fluids on bone samples. J Butlerov Commun 10:21–28 (in Russian)
Martell AE (2006) Stability constants (log K1) of various metal chelates. Sequestarants in Foods
Nikolsky BP, Materova EA (1980) Ion-selective electrodes. L.: Chemistry, pp 240 (in Russian)
Perisic O, Fong S, Lynch DE, Bycroft M, Williams RL (1998) Crystal structure of a calcium-phospholipid binding domain from cytosolic phospholipase. J Biol Chem 3:1596–1604
Posypayko VI, Kozyreva NA, Logacheva YP (1989) Chemical methods of analysis. M.: High School, pp 42–45 (in Russian)
Rey F, Antelo J, Arce F (1990) Equilibrium constants of metal amino acid complexes. J Polyhedron 5:665
Rhilassi AEl, Mourabet M, Bennani-Ziatni M, Hamri REl, Taitai A (2016) J Saudi Chem Soc 20:632
Selifonova EI, Chernova RK (2012) Selective electrophoretic separation of ionic forms—amino acids. Proc Saratov Univ New Epis Ser: Chem Biol Ecol 3:25–32 (in Russian)
Siddique JA, Naqvi S (2002) Volumetric behavior on interactions of r-amino acids with sodium acetate, potassium acetate, and calcium acetate in aqueous solutions, vol 8. Department of Chemistry, Aligarh Muslim University, pp 2930–2934
Tas AC (2000) Synthesis of biomimetic Ca-hydroxyapatite powders at 37 C in synthetic body fluids. Biomaterials 21:1429
Yatsimirsky KB (1976) Introduction to bioneorganic chemistry. K.: Publishing House of Science Dumka, p 144 (in Russian)

Part VII
Medical Geology

Chapter 42
Landscape Settings and Mineralogy of Some Geophagic Clay Occurrences in South Africa

Georges-I. Ekosse, Kirill V. Chistyakov, Andrei B. Rozanov, Nadezhda N. Bashkirova, Stefan Dultz, Yury S. Polekhovsky and Sofia N. Lessovaia

Abstract In the regions of Asia and Africa geophagic clays are traditionally used by population based on historical and traditional motivations including ethno-medical ones. The aim of the present research was to reveal the general common properties of some geophagic clay occurrences based on their mineral composition and landscapes specificity, in which they were sampled. In addition to assess the potential source of the minerals in geoghagic clays, the mineral association of the hard rocks, located in geophagic loose material, was studied too. Mineralogy of the samples was investigated using X-ray diffractometry, FTIR spectroscopy, and optical microscopy. The studied samples were collected in two provinces of South Africa: Free State and Limpopo. It was shown that location of geophagic materials is spread widely in the studied provinces. Using material as geophagic is more historically and traditionally determined than by the type or specificity of a landscape, which cannot be characterized by common features. Whereas it was revealed that despite the differences in location and rock geneses, the most common mineral in the fine size fraction of the studied geophagic samples is smectite—a fine-sized clay mineral with high specific surface area being able to play a role as adsorbent.

Keywords Geophagic clays · Clay mineralogy · Smectite · Cementing agents

G.-I. Ekosse
University of Venda, Thohoyandou, Limpopo, South Africa

K. V. Chistyakov · Y. S. Polekhovsky · S. N. Lessovaia (✉)
Institute of Earth Sciences, Saint Petersburg State University, Universitetskaya nab. 7/9, 199034 Saint Petersburg, Russia
e-mail: s.lesovaya@spbu.ru

A. B. Rozanov
Department of Soil Science, Stellenbosch University, Stellenbosch, South Africa

N. N. Bashkirova
Higher School of State Audit, Moscow State University, Moscow, Russia

S. Dultz
Institute of Soil Science, Leibniz Universität Hannover, Hannover, Germany

© Springer Nature Switzerland AG 2020

O. V. Frank-Kamenetskaya et al. (eds.), *Processes and Phenomena on the Boundary Between Biogenic and Abiogenic Nature*, Lecture Notes in Earth System Sciences,
https://doi.org/10.1007/978-3-030-21614-6_42

42.1 Introduction

Clays and clay minerals play a role in culture, hygiene and traditional medicine of many African countries (Reid 1992; Abrahams and Parsons 1996). One of the prominent uses of clay is ingestion known as geophagia (also geophagy). Geophagia is observed throughout the animal world from earthworms to birds (Wilson 2003), elephants (Chandrajith et al. 2009) and primates (Pebsworth et al. 2018) including humans (Halsted 1968).

Geophagia among humans is widely regarded as an instance of pica—a range of mental disorders associated with compulsive ingestion of non-food items (APA 2013) among which consumption of earthy materials is particularly wide spread. Pica seems to be rather common among people with intellectual disability reaching 14% among the populations living in the community and up to 25% among the institutionalized populations (Ali 2001). Geophagia is normal in children under the age of 18 months, since it forms part of their world exploration process.

However some studies indicate that geophagia may be an adaptive behaviour (Krishnamani and Mahaney 2000; Starks and Slabach 2012) related to a deficit of certain micro-elements rather than a disorder (Miao et al. 2015). This assumption is largely based on the observation of behaviour in both wild (Kreulen 1985) and domestic (Mincher et al. 2008) herbivores which is thought to be instinctive and as such—rational. The adaptive theory is somewhat supported by the fact that both animals and humans develop a preference for location of geophagic materials implying that it is indeed the quality of the materials that is selected for the purpose. The desired properties of such materials may range from specific elements like Ca and Zn (Starks and Slabach 2012) to Rare Earth Elements (Panichev 2015) and specific clay mineral assemblage (Wilson 2003). However, some such materials may pose serious health risks for a wide variety of reasons—from ingestion of geohelminths and other parasites to infectious diseases and mineral imbalances (Abrahams 2012). Of the latter anemia related to deficit of iron is mentioned most often (Halsted 1968). The hazard from parasites may be overestimated and strongly depends on the source of ingested material. For example Young et al. (2007) found no relationship between geophagia and transmission of *Trichuris* or hookworm in Zanzibar. Still, such hazards require special attention and in respect of safety and food safety standards should be applied.

In the context of viewing earthy matter as mineral food supplements two main aspects of these materials are of interest: elemental composition and clay mineralogy (Wilson 2003). Clay mineralogy is mostly considered in terms of possible detoxifying effects, neutralizing the negative effects of toxic substances and pathogenic microorganisms through cation exchange and sorption respectively on the large specific surface area of clay minerals.

Clays (especially bentonite) are often used as binder and anti-caking agent in pet foods (Murray 2000). It was noted that the presence of montmorillonite in pet food significantly reduces the effects of mycotoxins (Huwig et al. 2001; Dixon et al. 2008), which may be present in pet food (Boermans and Leung 2007) due to lower

safety standards of such products compared to food meant for human consumption (Rustom 1997). Further experiments in rats (Mitchell et al. 2014b) have demonstrated significant reduction in their reaction to aflatoxin.

Clay ingestion (geophagia) may be of particular importance in Africa due to wide-spread contamination of staple foods with mycotoxins (Shephard 2008) arising from adverse production and storage conditions, particularly when it comes to grain crops. Phillips et al. (2008) have reviewed a large collection of literature motivating the use of montmorillonite clay in mitigating aflatoxins in food products. Subsequent experiments in Ghana have shown that use of NovalSil (Ca-saturated montmorillonite) significantly reduced biomarkers associated with aflatoxin poisoning in humans (Wang et al. 2008). Double-blind studies of children, who suffer stunted growth due to aflatoxin poisoning have shown (Mitchell et al. 2014a) that small doses of calcium montmorillonite clay (UPSM) administered at up to 1.5 g/day for two weeks significantly improved the quality and efficacy of the contaminated food.

There have been several studies in South Africa analyzing the value of clays in indigenous culture (Matike et al. 2011) and medicine (George and Ndip 2011; Jumbam 2012). Somewhere criticized for methodological issues in material analysis (Faniran et al. 2004), and most of them did not engage in separation of clay minerals and their detailed analysis as suggested by Wilson (2003).

This study attempts to close this gap in part and focuses on clay mineralogy of the most common geophagic clays used in some South African communities. In addition to assess the potential source of the minerals for geoghagic clay, the mineral association of the hard rocks, located in geophagic loose material, was also studied. Besides, we aimed to reveal the landscapes specificity, in which some geophagic materials were sampled.

42.2 Study Location

The samples used in geophagia were collected in two provinces of South Africa: Free State and Limpopo. Four study sites were sampled and subsequently analyzed with the research objectives focused on investigating the mineral associations in geophagic material as well as in hard rocks and derived loose substrate.

In the Free State Province, the study plots were located close to the towns Clarens (key plot "Clarens") and Phuthaditjhaba (key plot "Phuthaditjhaba"). According to King (1963) and Partridge et al. (2010) both key plots belong to Eastern part of the Central Plateau and located in the high veld, subtropical mountainous steppe landscapes on Karoo Syneclise with Mesozoic-Paleozoic sediments. Clarens is located at the foothills of the Drakensberg system. The GPS coordinates of the key plot were 28° 31′ 8″S; 28° 25′ 2″E; h 1740 m a.s.l. The geophagic material was sampled here from a sandstone outcrop which was the example of using hard rock in geophagia.

Phuthaditjhaba locality is surrounded by the Drakensberg Mountains and located on the banks of the Eland River. This river is a tributary of the Wilge River belonging

to the Vaal River Basin. The key plot "Phuthaditjhaba" with the GPS coordinates 28° 34′ 36.4″S; 28° 49′ 55.4″E; h 1780 m a.s.l. is located on the Karoo system plateau. In geophagia the loose material accumulated between boulders of sandstone was used. Most probably the loose material is a result of sandstone breakdown. Both sandstone and loose material were sampled. From environmental safety point of view the specificity of this key plot is its location close to the highway.

The other key plots were located in the Limpopo Province. The landscapes here are classified as the Bushveld savanna landscapes on the Precambrian Crystalline Basement. The evaluation of the studied area in the bushveld is 820–915 m a.s.l. The study plots were placed close to settlements Ga-Nchabeleng (Sekhuhune Region), in the geomorphologic province the western part of Transvaal depression and Siloam, in the Soutpansberg Massif (King 1963; Partridge et al. 2010).

The settlement Ga-Nchabeleng is located in the valley surrounded by medium-height ranges. The mountain slopes are covered by savanna bush. In the key plot named "Ga-Nchabeleng" the samples were collected (i) from the alluvial material (GPS coordinates: 24° 26′ 52.3″S; 29° 49′ 59.7″E, h 855 m a.s.l.) and (ii) on the top of bedrocks' outcrops (GPS coordinates: 24° 26′ 36.2″S; 29° 50′ 60.2″E, h 915 m a.s.l.). The rock fragments from the alluvial sediments as well as loose material, which are used in geophagia, were sampled in the alluvial deposit. The sampling site was located inside the settlement. On the top of the rock outcrops the geophagic material was collected from the local accumulations of loose material. The fragments of solid rocks and their saprolite were also sampled.

The key plot "Siloam" (GPS coordinates: 22° 53′ 44.0″S; 30° 11′ 58.8″E; h 820 m a.s.l.) is only one located north of the tropic. The settlement is located East of the Siloam hospital in the valley of the Nzhelele River on the plateau surrounded by the rocky ridges. The slopes are covered by the plantations of mango, bananas, and secondary forests. The geophagic samples were collected from a local quarry.

42.3 Methods

Thin sections were prepared from the rock fragments sampled in the key plots "Clarens" and "Phuthaditjhaba" located in the high veld and "Ga-Nchabeleng" in the low veld. Thin sections were also made from air-dried samples of the clayish loose geophagic material collected into sampling boxes (5 cm × 3 cm) from the key plot "Siloam". The thin sections were studied by optical microscopy using a Polam P-312 microscope (Lomo, St. Petersburg, Russia).

To determine the pore connectivity in the rock fragments from the key plot "Clarens", a technique based on the intrusion of a molten alloy (Wood's metal) at 600 bar was applied (Lloyd et al. 2009). The eutectic alloy of 50% Bi, 25% Pb, 12.5% Sn, and 12.5% Cd by weight has a melting point at 78 °C. Sections of the rocks were intruded with the molten alloy at 100 °C with a pressure of 55 MPa in evacuated samples (Dultz et al. 2006; Kaufmann 2009). After solidification of the

alloy, polished sections were prepared, sputtered with Au and the invaded connective pore system was examined in back-scattered electron images (FEI, QUANTA 200).

After powdering of both rock and loose samples, which was done gently in a mortar, the <1 μm fractions were separated by sedimentation and decantation according to the Gorbunov (1971) method. Pretreatment of the fine fraction before XRD examination included Mg saturation, ethylene glycol solvation of the Mg-treated sample, and heating at 550 °C for 3 h. The mineralogical composition of the textured specimens was studied using a Rigaku MiniFlex II (Rigaku Corporation, Tokyo, Japan) X-ray diffractometer (XRD) with CoKα radiation.

FTIR spectra in the 400–4000 cm^{-1} range were obtained using a Tensor 27 spectrometer (Bruker, Karlsruhe, Germany) with a resolution of 4 cm^{-1} in ambient air and at room temperature. Spectra were recorded in the transmission mode using the KBr pellet method. Here 1 mg of sample and 300 mg of KBr were thoroughly mixed and pressed to a transparent pellet.

42.4 Results

42.4.1 Petrography Characteristics of Samples (Thin Section Data)

The sandstone fragments sampled from the study plot "Clarens" was identified as calcite-free arkosic sandstone (Fig. 42.1a). The grains of primary minerals were unsorted and mostly with angular form. The space between the grains was filled by dispersed fine-sized cement. Ore minerals were identifiable in the cement as well as in the grains of the primary minerals.

The sandstone from the study plot "Phuthaditjhaba" was identified as calcite-free polymict sandstone composed of unsorted mineral grains (Fig. 42.1b). Quartz, plagioclase, muscovite, and traces of ore minerals were noted. The grains of muscovite were identified as "fresh" with weak development of alteration traces. The cement in this rock is coarser and composed mostly from aleurolite particles compared to the arkosic sandstone.

The rock fragments sampled from the alluvial deposit at the study plot "Ga-Nchabeleng" were represented by limestone (or dolomitic limestone), in which the clastogene grains of quartz, plagioclase and microcline feldspars, and ore minerals were identified (Fig. 42.1c). The rock samples from the outcrops of bedrock were identified as tuff breccia (Fig. 42.1d). Angular and weakly rounded fragments of volcanic glass immersed in the fine-grained cement with clastogene grains of pyroxenes and plagioclases were found (Fig. 42.1d, III). The slopes of the bedrock outcrops are covered by the fragments of dark colored blocks of solid rock, which were identified as Fe–Ti ore mostly composed of ilmenite ($FeTiO_3$) and titanomagnetite (Fe_2TiO_4). Hematite (αFe_2O_3) and sulfides including pyrite (FeS_2) were also found (Fig. 42.1e). The tracks in the village are also paved by the fragments of this rock.

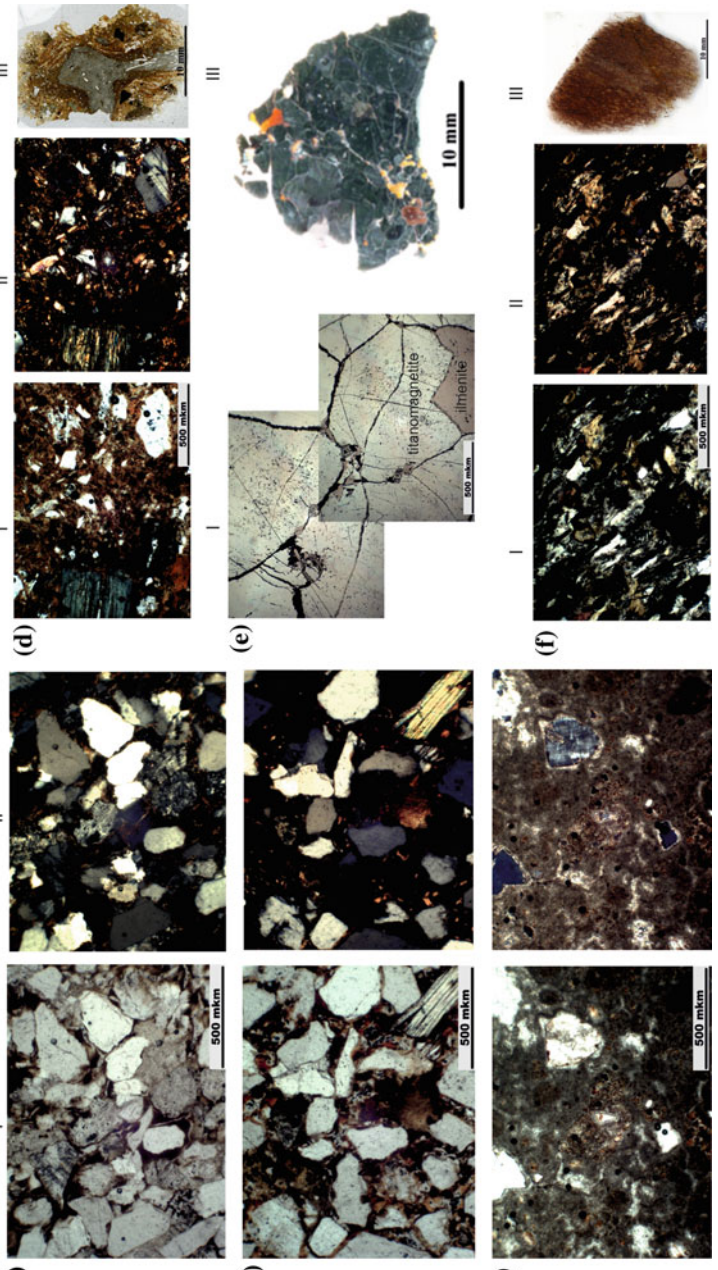


Fig. 42.1 Micromorphology of samples studied in thin sections of (I)—plain polarized light, (II)—crossed polarizers, and (III)—general view: **a** arkosic sandstone, **b** polymict sandstone, **c** limestone, **d** tuff breccia, **e** Fe–Ti ore, and **f** clayish oxidized tuffite

In study plot "Siloam" the loose clayish material was represented by calcite-free clayish oxidized tuffite, whereby the tuffite is composed of detrital and predominantly pyroclasts materials. Ore mineralization represented by tuff-clastogenic grains of titanomagnetite (Fe_2TiO_4) and rutile (TiO_2) were very often pseudomorphically substituted by hematite (αFe_2O_3) and titanite ($CaTiSiO_5$). Ore minerals' proportion varied from 5–6 to 15–17%, unevenly distributed in the layers. The chlorite–sericite pseudomorphic aggregates were established on the mineral of protolith. The rock was affected by hypergenesis processes resulting in the appearance of Fe (hydr)oxides indicated by the brownish color. Hematite (αFe_2O_3) was clearly identified. Besides, clastogenic, rounded grains of quartz also terrigenous grains of small-scale and acute-angled mineral fragments were identified. The latter are generally common in tuff (Fig. 42.1f).

42.4.2 Pore Space Characteristics

As it was mentioned above only one sample of geophagic material was represented by hard rock, which was identified as arkosic sandstone. Its solidification by dispersed cement was revealed based on thin section data. Visualization of cement distribution along the pores and in the space between the mineral grains was done using the intrusion of the molten alloy "Wood's metal", which induces between the bright shining intruded pores and the dark minerals. These zones were enriched by signs of intruded alloy (white colored), which indicate the presence of numerous dispersed pores among the mineral grains identified as dark sections. The cementing was poor: big voids between the primary sand grains can be seen. The mineral grains were decomposed to a part resulting in formation of many fine particles. Particles may be also stabilized by cementing at their contact points (Fig. 42.2).

42.4.3 Mineralogical Composition (XRD and FTIR Data)

The minerals identified in the clay fractions of all samples were as follows: (i) highly smectitic clay including pure smectite and/or a random mixed-layer structure where the smectite layers exceed 50% of the mixed layer mica-smectite; (ii) kaolinite; (iii) mica; (iv) talc; (v) chlorite and/or mixed-layer chlorite—vermiculite (smectite); (vi) calcite; (vii) feldspars; and (viii) quartz.

Highly smectitic clay was identified by the response to ethylene glycol solvation whereby a peak at ~14 Å in the Mg-saturated air-dry state shifts to a fundamental 001 spacing of ≥17 Å. The appearance of the 002 reflection at 8.56 (8.6) Å was attributed to the presence of a pure smectite (montmorillonite or beidellite). The absence of this peak indicated that the expandable phase represents a random mixed-layer structure with a non-expandable phase such as illite and smectite layers exceed 50% (Reynolds 1980).

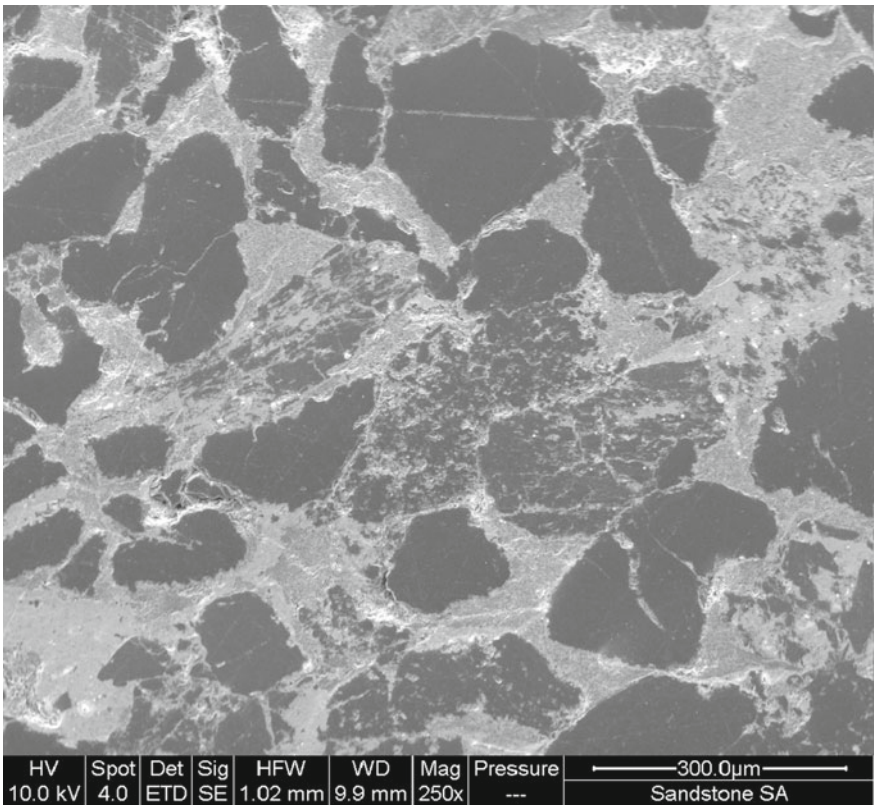


Fig. 42.2 Back scattered electron images of polished sections of the arkosic sandstone

Kaolinite was recognized by its 001 reflection at 7.15 and 3.58 Å which disappeared after heating at 550 °C. The identification was confirmed by FTIR spectroscopy data taking into account that IR spectroscopy is a sensitive method for the detection of kaolinite (Delvaux et al. 1989). The absorption bands near 3700 cm^{-1} (the vibration of inner surface OH groups), 3627 cm^{-1} (the stretching vibration of inner OH groups), 914 cm^{-1} (bending vibration of inner OH groups), 540 cm^{-1}(Si–O–Al bending vibrations), and 470 cm^{-1} (Si–O–Si bending vibrations) all indicate the presence of kaolinite (Madejová and Komadel 2001; Pentrak et al. 2009).

Mica (mineral from mica group) was recognized by peaks at the 001 and 002, which are the basal reflections at 10.0 and 5.0 Å respectively. They remain stable after ethylene glycol and heat treatments. *Talc* was identified based on the presence of peaks at 9.3 and 3.12 Å, which are stable after ethylene glycol and heat treatments. *Chlorite* was identified based on the 001 and 003 basal reflections at 14.2 and 4.74 Å respectively that are stable after ethylene glycol solvation. *Calcite* was identified due to the presence of the 3.04 Å peak. *Feldspars* were identified based on the peaks at

3.19–3.21 Å. *Quartz* was identified by its characteristic peaks at 3.34 and 4.26 Å and by its most typical IR absorption band doublet at 800–780 cm^{-1} (Hlavay et al. 1978; Madejová and Komadel 2005).

In the fine size fraction of arkosic sandstone from the key plot "Clarens" the following minerals were identified: pure smectite, mica, kaolinite, and quartz (Fig. 42.3). In the key plot "Phuthaditjhaba" the XRD patterns of the fine size fractions separated from both polymict sandstone and loose material accumulated between the blocks of sandstone are very similar. Highly smectitic clay, represented by pure smectite, mica, kaolinite, and quartz were found in the sandstone and loose material. A similar mineral association like in arkosic sandstone was identified in polymict sandstone. But in the samples from the key plot "Phuthaditjhaba" the fine size fractions were enriched by kaolinite and characterized by lower proportion of smectite compared

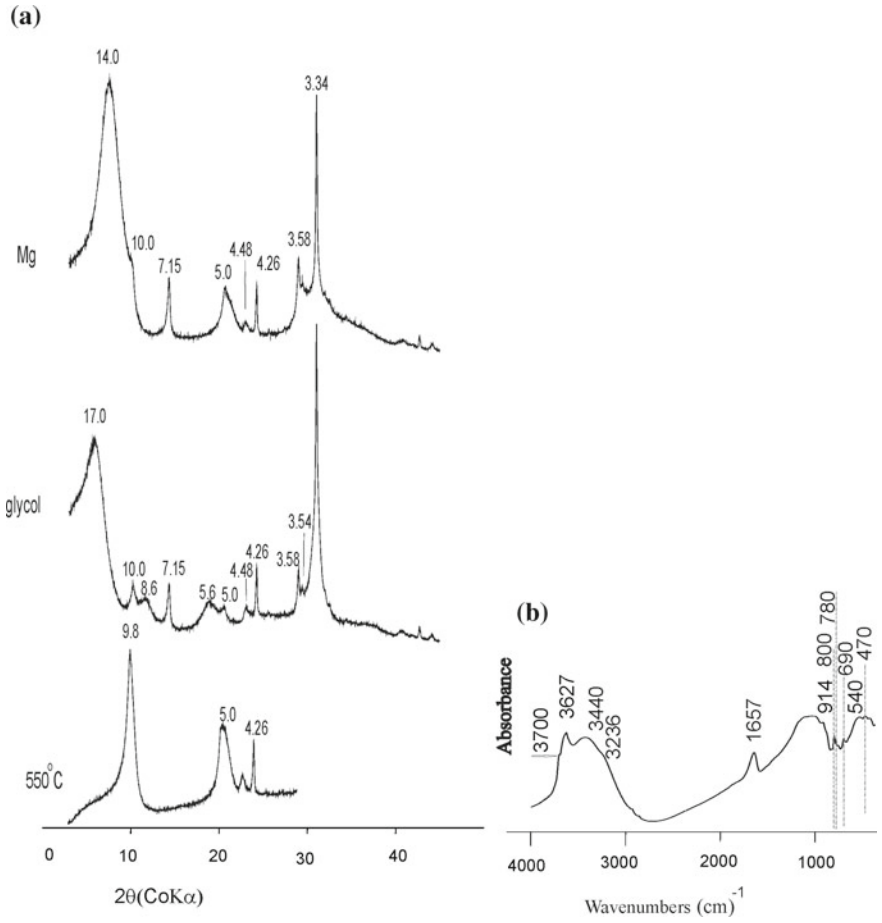


Fig. 42.3 XRD (**a**) and FTIR (**b**) data of the <1 μm fraction separated from arkosic sandstone

to the arkosic sandstone. The latter statement is based on the peak intensities in the XRD patterns (Fig. 42.4).

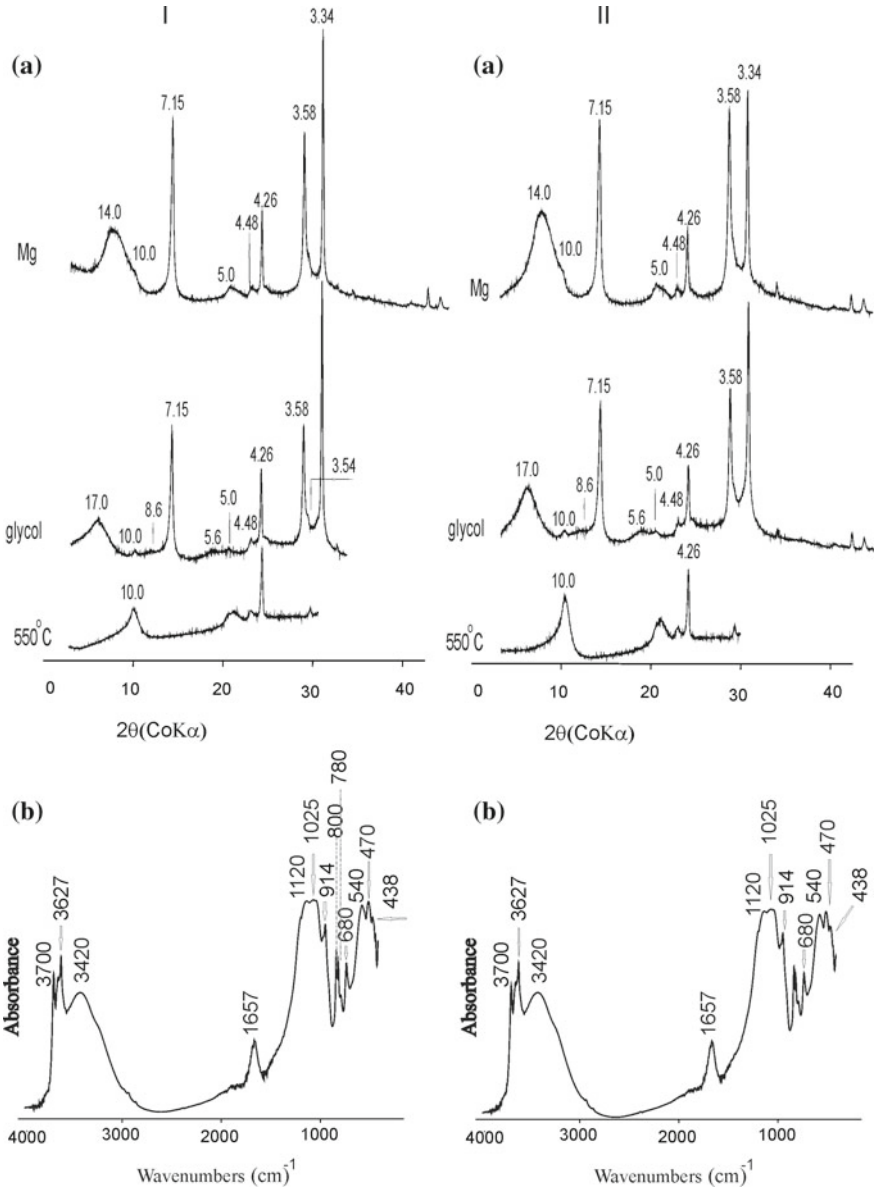


Fig. 42.4 XRD (**a**) and FTIR (**b**) data of the <1 μm fraction separated from polymict sandstone (I) and loose substrate accumulated between blocks of polymict sandstone (II)

The dominant mineral in the fine size fraction of geophagic material from the alluvial deposit in the key plot "Ga-Nchabeleng" was highly smectitic clay mostly represented by pure smectite. The admixtures of mica, kaolinite, quartz, and calcite were also identified (Fig. 42.5). The mineral association of the fine size fraction from geophagic material located on the bedrocks' outcrops differs from that in the alluvial subsidence due to the presence of talc. Besides talc, kaolinite, quartz, and feldspars with the predominance of smectite were found here. Talc was present only in this sample. A similar mineral assemblage was observed further downstream on the planation surfaces of the low veld in the catchment of the Klein Letaba river (Rozanov et al. 2017). Kaolinite and highly smectitic clay with traces of quartz and feldspars were identified in the fine size fraction separated from bedrock saprolite surrounding the local accumulations of the geophagic material (Fig. 42.6).

In the fine size fraction of the geophagic material of clayish oxidized tuffite from the key plot "Siloam" pure smectite was the dominant mineral. Besides, mica, chlorite and/or mixed-layer chlorite-smectite (vermiculite), quartz, and feldspars were also identified (Fig. 42.7). In this sample kaolinite was not found. Taking into account the absence of kaolinite, presence of montmorillonite (dioctahedral smectite) was assumed based on absorption bands near 3623 and 916 cm^{-1} (FTIR data) (Madejová and Komadel 2005) in the sample. The presence of namely dioctahedral mica (most probably muscovite) was confirmed based on intensive 5.0 Å peak.

The reflections at 14.2 and 4.74 Å in the XRD patterns of air-dried sample and a peak 14.2 Å after ethylene glycol salvation indicated the chlorite presence in the sample. But the peak at ~14 Å was not detected in the XRD patterns of 550 °C treated sample, whereas the peak at 11.9 Å was identified. It is probable that chlorite in the sample is enriched by Fe in the octahedral sheets. Such chlorites are less stable at heat

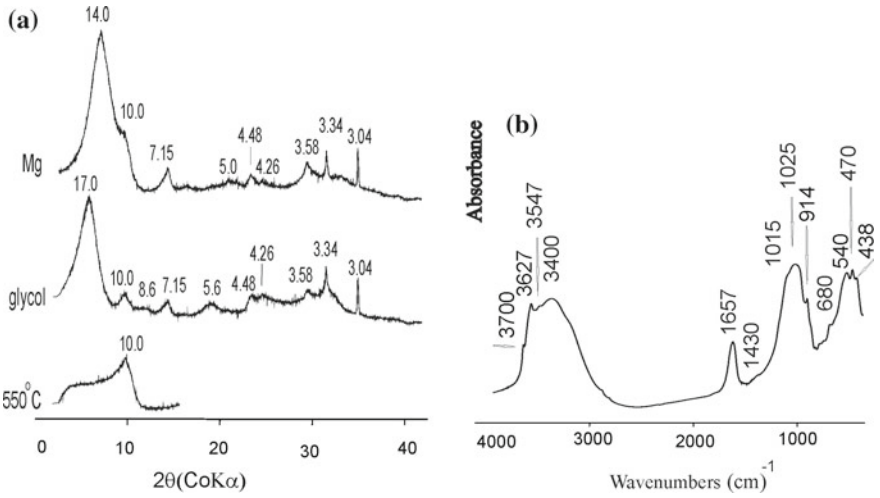


Fig. 42.5 XRD (**a**) and FTIR (**b**) data of the <1 μm fraction separated from alluvial sediment

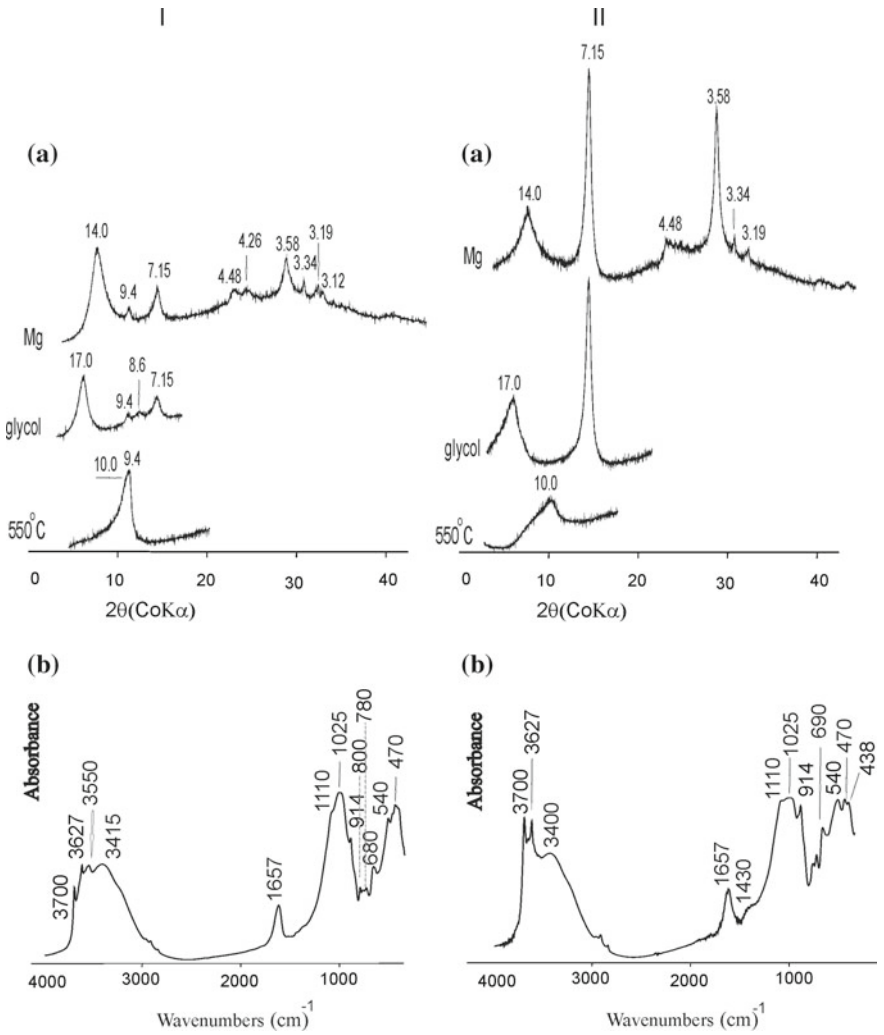


Fig. 42.6 XRD (**a**) and FTIR (**b**) data of the <1 μm fraction separated from loose geophagic material (I) and saprolite from outcrops of bedrock (II)

treatment (Moore and Reynolds 1997) or the peak at 11.9 Å indicates the presence of random mixed-layer chlorite-vermiculite (smectite) besides pure chlorite.

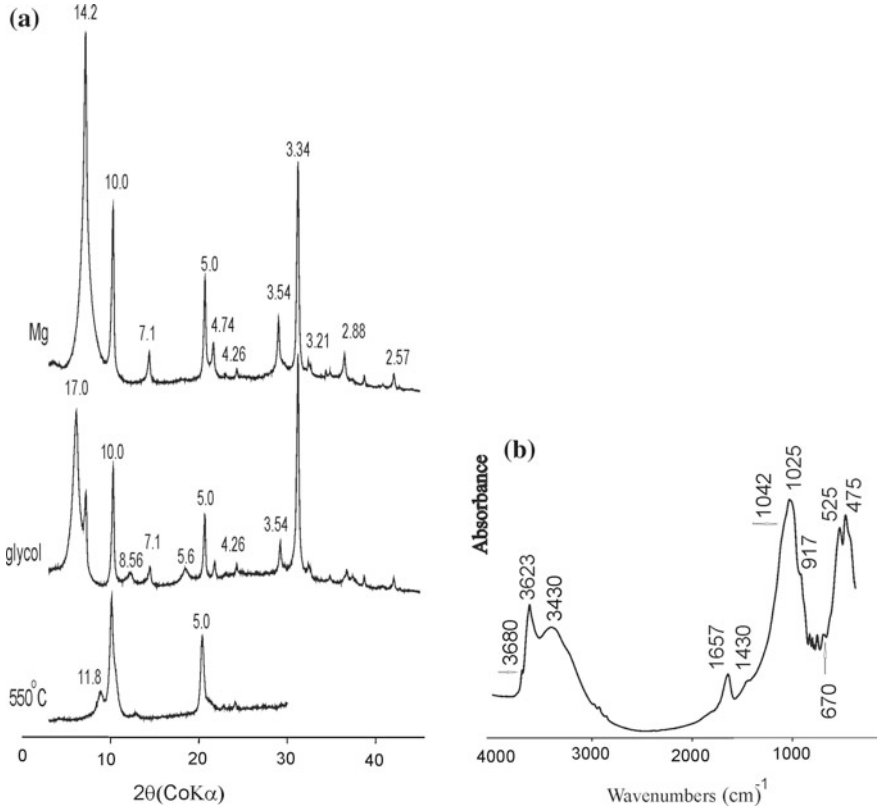


Fig. 42.7 XRD (**a**) and FTIR (**b**) data of the <1 μm fraction separated from clayish oxidized tuffite

42.5 Discussion

The key studies were situated in the Karoo Sandstone Plateau (high veld) and the stratal plains of midland depressions (bush veld). The key plots were located in the different geomorphologic provinces (Eastern part of the Central Plateau, western part of Transvaal depression, and the Soutpansberg Massif). The geophagic substrates were sampled from (i) loose sediment accumulations between boulders of polymict sandstone; (ii) outcrops of arkosic sandstone cemented by clayish material; (iii) clayish oxidized tuffite; (iv) calcareous sediment from alluvial valley; and (v) fine earth accumulations in the residual outcrops of bedrocks. The landscapes, in which key plots for collected geophagic materials were located, cannot be characterized by the common features with regard to specificity of geology and/or geomorphology.

Despite the differences in location and type of the source of substrates using in geophagia the most common clay mineral in the studied samples is smectite. It was also shown that the arkosic sandstone, which is only one example from the studied samples of hard rock used in geophagia, was enriched by the fine size cement.

The cement located along the pores and in the space between the mineral granules was a source of smectite. The identities of the mineral associations in the fine size fraction separated from loose sediment accumulations between the blocks of polymict sandstone as well as from the sandstone itself confirm that this rock is the source of clay minerals for the loose geophagic material.

Minerals of smectite group are a good sorbent. Smectite identification in the studied samples is in good correlation with data of geophagic material mineralogy (Ekosse et al. 2010; Ngole et al. 2010; Olatunji et al. 2014). Most probably the use of these substrates in geophagia is based on the traditional and intuitive knowledge of the positive effect of the clay on the human body. It is well known that the active substance of the medicine "smecta" represented by dioctahedral smectite has a strong expressed absorbing and encapsulating action on the mucous membrane of the esophagus. Smectite forms the polyvalent connections with mucus glycoproteins and increases the protection of the mucous membrane from the negative effect of H^+, bile salts, intestinal microorganisms, their toxins and other irritants (Szajewska et al. 2006). Besides, using of dioctaheral smectite (montmorillonite and beidellite) in pet foods (Murray 2000; Huwig et al. 2001) as well as dietary clays (Phillips et al. 2008; Wang et al. 2008; Mitchell et al. 2014a) has been reported. Presence of dioctahedral smectite was revealed in the clayish oxidized tuffite based on FTIR data, which was allowed due to high proportion of smectite in the absence of kaolinite.

In fact a close link and interaction between traditional consciences, somatic system of people and chemical reactions in the human organism affected by geophagic clay is obvious. Usually geophagia is associated with poverty but is also identified among higher classes, especially among pregnant women. Among the reasons of geophagia have mentioned cultural factors; nutritional deficiency; malnutrition; mental health conditions; developmental problems; parental neglect and lack of supervision (for children); and food deprivation (Woywodt and Kiss 2002). That is why it is important to pay attention to the fact that special ecological regime has to be granted to the landscapes, in which geophagic clay are sampled. The reality of present time is that areas, in which substrates are traditionally collected to be used in geophagia are very often close to the settlements, highways, etc. It was mentioned above that several key plots are located close to the highway or directly in the settlement. Pollutants and unutilized waste accumulated close to such areas affect the ecological balance of the landscapes. Unfortunately, not a lot can be done to clean the trash piles and regulate the follow-up waste disposal. For example, turnover of plastic at the legislative level is regulated only in approximately 40 countries (Petts 2001; Bashkirova 2018).

Geophagia is a deep–rooted and long–standing tradition that obligates to be covered by the environmental conservation programs with regard to the landscapes in which the geophagic materials were collected. The comparative analysis of approaches has shown that the most efficient and productive mechanism of expansion of responsibility is merging of produce the state and business co-operation in solving problems of landscape ecology (Bashkirova and Lessovaia 2018).

42.6 Conclusions

It was shown that the use of geophagic materials is spread widely in South Africa (based on study in Free State and Limpopo Provinces). The landscapes, in which substrates using in geophagia were collected, cannot be characterized by the common features with regard to specificity of geology and/or geomorphology. The use of earthy material for geophagia is more historically and traditionally motivated rather than determined by the type or specificity of landscape.

It was also shown that despite the differences in location and genesis the common mineral in the fine size fractions separated from studied geophagic substrates is smectite. The findings are in good agreement with data of smectite identification in geophagic clay from African countries including South Africa. This also corresponds to recent findings in tropical medicine targeting neutralization of aflatoxins in food.

Acknowledgements This study was supported by the Russian Foundation for Basic Research (14-05-93959) and NRF UID 92199 project grants and St-Petersburg State University (18.42.1426.2015). XRD and IR studies were carried out in the X-ray Diffraction Centre of St. Petersburg State University.

References

Abrahams PW (2012) Involuntary soil ingestion and geophagia: a source and sink of mineral nutrients and potentially harmful elements to consumers of earth materials. Appl Geochem 27:954–968

Abrahams PW, Parsons JA (1996) Geophagy in the tropics: a literature review. Geogr J 162(1):63–72

Ali Z (2001) Pica in people with intellectual disability: a literature review of aetiology, epidemiology and complications. J Intellect Dev Disabil 26(3): 205–215

APA (2013) Diagnostic and statistical manual of mental disorders, 5th edn. DSM-5. https://doi.org/10.1176/appi.books.9780890425596

Bashkirova NN (2018) The combined system of the extended responsibility of producer's in environmental taxation (Kombinirovannaya-sistema-rasshirennoj-otvetstvennosti-proizvoditelej-v ehkologicheskoe-nalogooblozhenie). In: Mayburov IA, Ivanov YB (eds) Theory and global trends (Teoriya-i-mirovye-trendy). UNITI-DANA, Moscow, pp 324–335 (in Russian)

Bashkirova NN, Lessovaia SN (2018) State and business co-operation in settling socio-economic issues: forward to sustainable development of ecologically unfavorable. IOP Conf Ser: Earth Environ Sci 107(1):012128. https://doi.org/10.1088/1755-1315/107/1/012128

Boermans HJ, Leung MCK (2007) Mycotoxins and the pet food industry: toxicological evidence and risk assessment. Int J Food Microbiol 119:95–102

Chandrajith R, Kudavidanage E, Tobschall HJ, Dissanayake CB (2009) Geochemical and mineralogical characteristics of elephant geophagic soils in Udawalawe National Park, Sri Lanka. Environ Geochem Health 31:391–400

Delvaux B, Mestdagh MM, Vielvoye L, Herbillon AJ (1989) XRD, IR and ESR study of experimental alteration of Al-nontronite into mixed-layer kaolinite/smectite. Clay Miner 24:617–630

Dixon JB, Kannewischer I, Tenorio Arvide MG, Barrientos Velazquez AL (2008) Aflatoxin sequestration in animal feeds by quality-labelled smectite clays: an introductory plan. Appl Clay Sci 40:201–208

Dultz S, Behrens H, Simonyan A, Kahr G, Rath T (2006) Determination of porosity and pore connectivity in feldspars from soils of granite and saprolite. Soil Sci 171:675–694

Ekosse GE, de Jager L, Ngole V (2010) Traditional mining and mineralogy of geophagic clays from Limpopo and Free State provinces, South Africa. Afr J Biotechnol 9(47):8058–8067
Faniran J, Ngceba F, Bhat R, Oche C (2004) An assessment of the water quality of the Isinuka springs in the Transkei region of the Eastern Cape, Republic of South Africa. Water SA 27:241–250
George G, Ndip E (2011) Prevalence of geophagia and its possible implications to health—a study in rural South Africa. In: 2nd international conference on environmental science and development, vol 4. IPCBEE, pp 166–169
Gorbunov N (ed) (1971) Methods of mineralogical and micromorphological study of soils (Metody-mineralogicheskogo-i-mikromorphologicheskogo-izucheniya-pochv). Nauka, Moscow (in Russian)
Halsted JA (1968) Geophagia in man: its nature and nutritional effects. Am J Clin Nutr 21:1384–1393
Hlavay J, Jonas K, Elek S, Inczedy J (1978) Characterization of the particle size and the crystallinity of certain minerals by IR spectrophotometry and other instrumental methods—II. Investigations on quartz and feldspar. Clays Clay Miner 26:139–143
Huwig A, Freimund S, Käppeli O, Dutler H (2001) Mycotoxin detoxication of animal feed by different adsorbents. Toxicol Lett 122:179–188
Jumbam ND (2012) Demographic characteristics associated with Isinuka traditional spa near Port St Johns in the Eastern Cape Province of South Africa. Indilinga: Afr J Indig Knowl Syst 11(1):20–31
Kaufmann J (2009) Characterization of pore space of cement-based materials by combined mercury and Wood's Metal intrusion. J Am Ceram Soc 92:209–216
King LC (1963) South African scenery, a textbook of geomorphology, 3rd edn. Oliver and Boyd, Edinburgh
Kreulen DA (1985) Lick use by large herbivores: a review of benefits and banes of soil consumption. Mammal Rev 15:107–123
Krishnamani R, Mahaney WC (2000) Geophagy among primates: adaptive significance and ecological consequences. Anim Behav 59:899–915
Lloyd RR, Provis JL, Smeaton KJ, van Deventer JSJ (2009) Spatial distribution of pores in fly ash-based inorganic polymer gels visualised by Wood's metal intrusion. Microporous Mesoporous Mater 126:32–39
Madejová J, Komadel P (2001) Baseline studies of the clay minerals society source clays: infrared methods. Clay Clay Miner 4:410–432
Madejová J, Komadel P (2005) Information available from infrared spectra of the fine fraction of bentonites. In: Kloprogge JT (ed) The application of vibrational spectroscopy of clay minerals and layered double hydroxides. CMS Workshop Lectures, vol 13. The Clay Mineral Society, Aurora, pp 65–98
Matike EM, Ngole VE, Mpako MP, Ekosse GI (2011) Ceremonial usage of clays for body painting according to traditional Xhosa culture. Indilinga Afr J Indig Knowl Syst 10(2):235–244
Miao D, Young SL, Golden CD (2015) A meta-analysis of pica and micronutrient status. Am J Hum Biol 27:84–93
Mincher BJ, Ball RD, Houghton TP, Mionczynski J, Hnilicka PA (2008) Some aspects of geophagia in Wyoming bighorn sheep (*Ovis canadensis*). Eur J Wildl Res 54:193–198
Mitchell NJ, Kumi J, Aleser M, Elmore SE, Rychlik KA, Zychowski KE, Romoser AA, Phillips TD, Ankrah NA (2014a) Short-term safety and efficacy of calcium montmorillonite clay (UPSN) in children. Am J Trop Med Hyg 91:777–785
Mitchell NJ, Xue KS, Lin S, Marroquin-Cardona A, Brown KA, Elmore SE, Tang L, Romoser A, Gelderblom WCA, Wang J-S, Phillips TD (2014b) Calcium montmorillonite clay reduces AFB1 and FB1 biomarkers in rats exposed to single and co-exposures of aflatoxin and fumonisin. J Appl Toxicol 34:795–804
Moore DM, Reynolds RC (1997) X-ray diffraction and the identification and analysis of clay minerals. Oxford University Press, New York
Murray HH (2000) Traditional and new applications for kaolin, smectite, and palygorskite: a general overview. Appl Clay Sci 17:207–221

Ngole VM, Ekosse GE, de Jager L, Songca SP (2010) Physicochemical characteristics of clayey soils from South Africa and Swaziland. Afr J Biotech 9(36):5929–5937

Olatunji AS, Olajide-Kayode JO, Abimbola AF (2014) Evaluation of geochemical characteristics and health effects of some geophagic clays southern Nigeria. Springer Science + Business Media Dordrecht

Panichev AM (2015) Rare earth elements: review of medical and biological properties and their abundance in the rock materials and mineralized spring waters in the context of animal and human geophagia reasons evaluation. Achiev Life Sci 9:95–103

Partridge TC, Dollar ESJ, Moolman J, Dollar LH (2010) Geomorphic provinces of South Africa, Lesotho and Swaziland: a physiographic subdivision for earth and environmental scientists. Trans R Soc S Afr 65(1):1–47

Pebsworth PA, Huffman MA, Lambert JE, Young SL (2018) Geophagy among nonhuman primates: a systematic review of current knowledge and suggestions for future directions. Am J Phys Anthropol. https://doi.org/10.1002/ajpa.23724

Pentrak M, Madejová J, Komadel P (2009) Acid and alkali treatment of kaolins. Clay Miner 44:511–523

Petts J (2001) Evaluating the effectiveness of deliberative processes: waste management case-studies. J Environ Plan Manag 44(2):207–226

Phillips TD, Afriyie-gyawu E, Williams J, Huebner H, Ankrah NA, Ofori-adjei D, Jolly P, Johnson N, Taylor J, Marroquin-Cardona A, Xu L, Tang L, Wang JS (2008) Reducing human exposure to aflatoxin through the use of clay: a review. Food Addit Contam Part A Chem Anal Control Expo Risk Assess 25:134–145

Reid RM (1992) Cultural and medical perspectives on geophagia. Med Anthropol 13:337–351

Reynolds RC (1980) Interstratified clay minerals. In: Brindley GW, Brown G (eds) Crystal structure of clay minerals and their X-ray Identification, vol 5. Mineralogical Society, London, pp 249–304

Rozanov A, Lessovaia S, Louw G, Polekhovsky Y, de Clercq W (2017) Soil clay mineralogy as a key to understanding planation and formation of fluvial terraces in the South African Lowveld. CATENA 156:375–382

Rustom IYS (1997) Aflatoxin in food and feed: occurrence, legislation and inactivation by physical methods. Food Chem 59:57–67

Shephard GS (2008) Risk assessment of aflatoxins in food in Africa. Food Addit Contam Part A 25:1246–1256

Starks PTB, Slabach BL (2012) The scoop on eating dirt. Sci Am 306:30–32

Szajewska H, Dziechciarz P, Mrukowicz J (2006) Meta-analysis: smectite in the treatment of acute infectious diarrhoea in children. Aliment Pharmacol Ther 23(2):217–227

Wang P, Afriyie-gyawu E, Tang Y, Johnson NM, Xu L, Tang L, Huebner HJ, Ankrah N-A, Ofori-adjei D, Ellis W, Jolly PE, Williams JH, Wang J-S, Phillips TD (2008) NovaSil clay intervention in Ghanaians at high risk for aflatoxicosis: II. Reduction in biomarkers of aflatoxin exposure in blood and urine. Food Addit Contam Part A Chem Anal Control Expo Risk Assess 25:622–634

Wilson MJ (2003) A review of clay mineralogical and other characteristics of geophagic materials ingested by animals and man. In: Pérez Rodríguez JL (ed) Applied study of cultural heritage and clays. Consejo Superior de Investigaciones Científicas, pp 301–326

Woywodt A, Kiss A (2002) Geophagia: the history of earth-eating. J R Soc Med 95(3):143–146

Young SL, Goodman D, Farag TH, Ali SM, Khatib MR, Khalfan SS, Tielsch JM, Stoltzfus RJ (2007) Geophagia is not associated with *Trichuris* or hookworm transmission in Zanzibar, Tanzania. Trans R Soc Trop Med Hyg 101:766–772

Chapter 43
Comparative Analysis of Morbidity and Elemental Composition of Hair Among Children Living on Different Territories of the Kola North

Natalia K. Belisheva

Abstract A comparative analysis of the morbidity and of the elemental hair content among children living on the different territories with contrasting incidence of the children and with contrasting environment (Apatity, Lovozero, Murmansk region) in the Kola North was carried out. Territorial morbidity was estimated on the basis of statistical data on morbidity of the children population 0–14 age in the Murmansk region during 2006–2016. For elemental analysis, hair samples have been received and analyzed by using method mass spectrometry with inductively coupled plasma (ICP-MS) in groups of children (25 people in each group) of preschool and school age living in the reference areas. The content of following elements: Ag, Al, As, B, Ba, Be, Cd, Cs, Cr, Cu, Fe, I, Li, Mg, Mn, Mo, Na, Ni, Pb, Rb, Sn, Se, Si, Sb, Sr, Ti, Tl, V, Zn, K, P, Ca, Co in the hair samples were estimated. It was shown that content of some genotoxic and toxic elements in the hair of children achieve and excesses upper boundaries of norm. Such elements could promote of the development of neoplasms and other disorders in the body of children, including diseases of the nervous systems and diseases of the musculoskeletal system and connective tissue. It is assumed that the source of toxic elements could be dust particles carried by air masses from tailings and processing sites of apatite-nepheline and loparite ore.

Keywords Children's morbidity · Kola North · Elemental analysis · Toxic elements · Apatite-nepheline ore · Loparite ore

43.1 Introduction

Residents of the Polar region are subject to the complex effects of high-latitude geophysical agents (Belisheva 2014; Belisheva and Megorsky 2017) and technogenic toxic contaminants, whose cooperative effects are manifested in the structure of the incidence of the population (Report 2013, 2017; Belisheva and Petrov 2013).

N. K. Belisheva (✉)
Research Centre for Human Adaptation in the Arctic, KSC RAS, 184209 Apatity, Russia
e-mail: natalybelisheva@mail.ru

© Springer Nature Switzerland AG 2020

O. V. Frank-Kamenetskaya et al. (eds.), *Processes and Phenomena on the Boundary Between Biogenic and Abiogenic Nature*, Lecture Notes in Earth System Sciences,
https://doi.org/10.1007/978-3-030-21614-6_43

The peculiarity of the territorial distribution of the industries of the Kola North lies in the increased density of enterprises and cities in the central part of the Kola Peninsula: in the south-north direction with branches to the west (the Kandalaksha city), the east (the Olenegorsk city with the Lovozero industrial hub) and the north-west near the city of Murmansk (Pechengsky industrial site). The all large city-forming enterprises are located in these districts: JSC Apatit—Apatity and Kirovsk; JSC "Combine" Severonikel"—Monchegorsk; JSC Olkon—Olenegorsk; JSC Sevredmet—Sec. Revda; JSC "Kovdorsky GOK"—Kovdor; JSC "Kandalaksha Aluminum Plant"—the Kandalaksha; JSC "MMC" Pechenganikel"—the city of the Zapolyarny and settlement of the Nickel. Such location of enterprises creates conditions for the wide distribution of pollutants, in fact, throughout the Kola North.

The cyclonic activity with moderate strong winds is greatly facilitated the dispersion of pollutants in the Kola Peninsula. Periods of adverse weather conditions such as surface inversions, calm, fog, air stasis in combination with unfavourable wind directions contribute to the accumulation and increase of pollutant content in the atmospheric air of cities of the Murmansk region (Report 2017).

A concentrations of heavy metals, sulphates, fluorides, and nitrogen compounds have reached a high levels and extremely high levels of contamination in areas of developed mining, mining-processing and metallurgical industries of the Kola North. There has been a deteriorating state of water bodies due to the increasing anthropogenic and technogenic impact in recent years (Report 2017). It was shown that elevated concentrations of iron, nickel, cobalt, aluminium, copper in the soil and vegetation layer characterize of the areas where the highest incidence of urolithiasis in the Murmansk region occurs (Arefyev 2009) under typical decrease in fluorine, magnesium and the increase in calcium, manganese in the hydrochemical environment (Avtsyn and Koenig 1970; Avtsyn et al. 1991).

Peculiarities of climatic and geographical conditions, geochemical provinces of the northern territories, along with a high level of anthropogenic pollutions of the environment, create prerequisites for the occurrence of micro-elementosises (Avtsyn and Koenig 1970; Avtsyn et al. 1991; Agadzhanyan and Skal'nyy 2001; Suslikov 2002; Koutsenogii et al. 2010; Skal'nyy and Tsygan 2013). The possibility of development of the micro-elemental misbalances is confirmed in studies assessing the content of trace elements in the body of the population of the North-Western regions of Russia (Skal'nyy 2004; Gorbachev et al. 2007; Sukhanov and Gorbachev 2017).

Children are an especially sensitive category of the population to impacts of the environmental media (Sedman et al. 1985; Veltishchev 1999; Setko and Setko 2004; Baranov et al. 2008; Evseeva 2009; Bouchard et al. 2011; Blaurock-Busch et al. 2012; Zainullin et al. 2014; Detkov 2017). A heavy metals are belonged of a significant place among the variety of chemical factors that have a negative impact on children in industrialized areas. They possess of a high migration capacity in the biosphere, a tendency to bioaccumulation and a long period of elimination out of the body. (Gawkrodger et al. 1986; Fergusson 1990; Mergler et al. 1999; Ercal et al. 2001; Costa 2003; Eastmond et al. 2008; Castro-González and Méndez-Armenta 2008; Stern 2010; Baba et al. 2013; Bánfalvi 2011; Permyakov 2012; Grimsrud and

Andersen 2012; Gwaltney-Brant 2013; Chung et al. 2014; Gul et al. 2015; Kim et al. 2015; Popoola et al. 2018).

Experimental and clinical studies have confirmed that the deficit of some trace elements and an excess of other trace elements, including heavy metals, promote to an increase in the incidence of malignant tumors, lymphoproliferative, autoimmune and degenerative diseases, congenital malformations (Nielsen et al. 1999; Chakrabarti et al. 2001; Kasprzak et al. 2003; Sanders et al. 2009; Yamashita et al. 2011; Koedrith and Seo 2011; Jett 2012; Yang et al. 2015; Kim et al. 2015; Jia et al. 2017; Marie et al. 2017; Schofield 2017). The main importance is given to essential trace elements (Avtsyn et al. 1991), which are part of at least 2000 enzymes catalyzing a variety of reactions (Pennington and Young 1990; Bakhtina et al. 2007; Patrick 2008; Skal'nyy 2011; Blaurock-Busch et al. 2012; Xiao et al. 2018). For example, the deficiency of such important essential trace element as iodine produces numerous adverse effects on growth and on development (International Council 2010; Patrick 2008; Zimmermann 2009). In pregnant women, iodine deficiency of can cause major neurodevelopmental deficits and growth retardation in the fetus, as well as miscarriage and stillbirth (Zimmermann 2009). Chronic, severe iodine deficiency in utero causes cretinism, a condition characterized by mental retardation, deaf mutism, motor spasticity, stunted growth, delayed sexual maturation, and other physical and neurological abnormalities (Zimmermann 2009).

Deviations in the content of essential trace elements or the accumulation of toxic elements can be not only a criterion of environmental problems, but also serve as markers at the level of prenosological diagnosis of the population health state (Sasmaz et al. 2003; Boev et al. 2004a, Salnikova et al. 2016; Sanders et al. 2009; Koedrith and Seo 2011; Xiao et al. 2018). It has shown that the microelement composition of bioassays from children with oncological diseases in the stage of a manifestation of disease is characterized by a decrease of zinc and iron and an increase of copper, manganese and nickel in blood. Also content microelements in hair under comparing with healthy children was decrease (Boev et al. 2004a, b). It was revealed that the most significant indicators of impaired homeostasis in children with attention deficit hyperactivity disorder, with cerebral palsy and with epilepsy are zinc deficiency and excess calcium in serum and urine (Osipova 2005). The statistically significant effect of concentrations of nickel, calcium, iron, strontium, and lead on the cognitive functions of children, and to a greater extent on children with mental developmental disorders, was found. (Zalata and Evstafieva 2012).

Such technogenic toxicants as Ni, Pb, Cd and Cr can produce high risks of hyperelementosis among of population in the megalopolis to promoting to the incidence of malignant tumors. The toxic effect of these elements in the body is accompanied by severe damage in many organs and tissues which could be lead to neoplasms (Doll et al. 1970; Dudley et al. 1985; Müller 1986; Aiyar et al. 1991; Gammelgaard et al. 1992; Dartsch et al. 1998; Takebayashi et al. 2000; Chakrabarti et al. 2001; Grimsrud et al. 2003; Luippold et al. 2003; Henson and Chedrese 2004; Eastmond et al. 2008; Bashkin et al. 2009; Sanders et al. 2009; Baba et al. 2013; James and Meliker 2013; Jahan et al. 2014; Küpper et al. 2015; Yang et al. 2015; Belisheva 2017; Marie et al. 2017).

Excessive accumulation of aluminium, boron and nickel are especially dangerous for human health due to the direct negative effect of their metabolites on bone tissue, including the risk of arising of oncopathology (Alfrey et al. 1976; Dewberry et al. 1980; Alfrey 1990; Avtsyn et al. 1991; Takebayashi et al. 2000; Chakrabarti et al. 2001; Grimsrud et al. 2003; Bakirdere et al. 2010; Grimsrud and Andersen 2012; Exley 2013; Sukhanov and Gorbachev 2017).

The brief overview concerning the dependence of population incidence in the Kola North on the content of microelements of natural and technogenic origin in the environment shows that diseases of adults and, especially the child population, is largely determined by toxic agents that cause disorder of chemical homeostasis.

These disorders are referred to the microelementosises, and they are currently diagnosed by analyzing the microelement composition of the hair (Bakhtina et al. 2007). Studies performed by using multi-element hair analysis showed that the concentration of chemical elements in hair reflects the morbidity of population by certain forms of nosology (Sasmaz et al. 2003; Bouchard et al. 2007; Ibragimova et al. 2011; Blaurock-Busch et al. 2012; Skal'nyy and Tsygan 2013; Detkov 2017; Sukhanov and Gorbachev 2017).

Despite the high incidence of the children's population in the Kola North, research on the identification of causal relationships between peculiarity of environmental contamination, the content of toxic elements in the body of children and childhood morbidity has not yet been conducted.

The purpose of this study was to conduct a comparative analysis of the child morbidity and the elemental hair content among children living in the territories with contrasting morbidity of the child population and with contrasting environment in the Kola North, characterized by different natural conditions and by different sources of environmental contamination.

43.2 Materials and Methods

43.2.1 Comparison Areas

Territories with a critical incidence of children and adults, as well as with contrasting environment of living: the Lovozero village and the Apatity city were selected. The Lovozero belongs to Khibino-Lovozersky area, the Apatity belongs to Monchegorsky medical-geographical areas, respectively. The soil of the Khibino-Lovozero region is characterized by the presence of beryllium, strontium, titanium, zinc, manganese, fluorine, nickel, copper, aluminium, phosphorus. The soil of the Monchegorsky region contains increased concentrations of iron, magnesium, vanadium, titanium, manganese, calcium, nickel, cobalt, and aluminium. Along with the natural features of the soil in these areas, enterprises with qualitatively and quantitatively a variety of elemental composition of dust in the Lovozero and in Apatitsko-Kirovsky districts are sources of technogenic environmental contamination: JSC Sevredmet and JSC

"Apatite". Nearest settlements to JSC Sevredmet are settlements of the Revda (at 5.8 km) and the Lovozero (at 20.5 km); respectively, nearest to JSC "Apatite" are the Apatity city (at 3.8 km), the Kirovsk city (at 9.6 km).

43.2.2 Analysis of the Incidence of the Population in the Kola North

The Statistical Compendium "Incidence of the population of the Murmansk region 2006–2010", as well as the data of the Murmansk Regional Medical Information and Analytical Center for 2011–2016 were used in the work.

43.2.3 Experimental Studies

Sample collection. A total of 100 samples of hair from preschool groups age 4.59 ± 0.85 and 4.46 ± 0.53 years and from school groups age 13.96 ± 0.35 and 14.32 ± 1.03 years, (25 samples for each group of comparison) living in the Apatity and in the Lovozero, respectively were collected. The method of sampling hair and their preliminary preparation was carried out according to the recommendations of the IAEA (Report of IAEA 1993). The hair was clipped at 4–5 places on the back of the head, closer to the neck, and tied into a bun 4–5 mm thick. In the case of short hair, they cut off the amount that could fill a teaspoon. The hair was putted in separate paper envelopes, on which the root end of the strand was marked.

Method of determining the concentration of chemical elements. Quantitative determination of the chemical elemental content in the hair of children of preschool and school age was carried out by the method of mass spectrometry (ICP-MS) with inductively coupled plasma. The determination of the content of chemical bioelements in hair was carried out in accordance with the Methodological Guidelines approved by the Chief State Sanitary Doctor of the Russian Federation G. G. Onishchenko (Onishchenko et al. 2002). A multi-element solution IV-ICPMS-71A, the production of "Inorganic ventures", containing the following elements: Ag, Al, As, B, Ba, Be, Ca, Cd, Ce, Cr_3, Co, Cs, Cu, Dy, Er, Eu, Fe, Ga, Gd, Ho, K, La, Lu, Mg, Mn, Na, Nd, Ni, P, Pr, Rb, S, Se, Sm, Sr, Th, Tl, Tm, U, V, Yb, Zn at a concentration of 10 μg/ml was used as the main one. Mono-element solutions produced by the "Center for Standard Samples and High-Purity Substances" were additionally used. The measurement of the content of elements in the samples was performed taking into account the requirements of the spectrometer operation manual. Processing of measurement results complied with GOST 8.207.

Statistical data processing. The data obtained was statistically processed by using the STATISTICA 10 software package; graphing was carried out using the graphic editor ORIGIN. The average arithmetic values of the studied parameters (M), and also

gave the values of the standard deviation ($\pm\delta$) were calculated. The non-parametric U test, the Mann-Whitney test (Mann-Whitney U), the Kolmogorov-Smirnov test, and the T-test were used to detect of significant of differences between independent data set. The differences were considered significant of at $p < 0.05$.

43.3 Results of the Study

43.3.1 Morbidity of Children

The total morbidity of neoplasm in children in the Apatity (15.33 ± 1.78) was significantly ($p = 0.046$) higher in 1.6 times than in the Lovozero (9.51 ± 1.88). There was no detected significant differences ($p = 0.38$) between the total morbidity of neoplasms in children aged 0–14 years in the Murmansk region (17.08 ± 2.4) and in the Apatity. But the incidence in this class of nosology was significantly higher in the Apatity in 1.9 times, than in the average for Russian Federation (RF) (8.16 ± 032), Fig. 43.1. The primary morbidity of neoplasms in children 0–14 years old in the Apatity (7.22 ± 1.03) was not significantly different from one in the Lovozero (7.43 ± 1.29), was slightly lower than in the Murmansk region (8.76 ± 0.53) and it was in 1.6 times higher than in the Russian Federation (RF) (4.36 ± 0.16, $p = 0.050$).

One of the most important indicators of the health state of children is diseases of the nervous system. A comparison of the incidence of diseases of the nervous system and sensory organs (epilepsy, epileptics status) of children aged 0–14 years showed that the total morbidity of epilepsy and epileptic status in children in the Apatity (7.18 ± 0.52) was higher than in the Lovozero (5.52 ± 0.0.73, $p = 0.076$), higher than in the Murmansk region as a whole (5.71 ± 0.09, $p = 0.012$) and higher than in the RF (4.24 ± 0.05, $p = 0.002$), Fig. 43.1. However, the primary morbidity in children 0–14 years was the highest in the Lovozero (1.76 ± 0.27), what is significant differs from the primary morbidity in the Apatity (0.97 ± 0.16, $p = 0.019$) and in the Murmansk region (0.98 ± 0.04, $p = 0.010$), and also from the primary morbidity in the RF (0.69 ± 0.02, $p = 0.000$), Fig. 43.1.

The territorial incidence of the musculoskeletal system and connective tissue (MSSCT), in a certain extent, might serve as indicator of disorder of mineral metabolism in children, since the content of essential elements determines the formation of the MSSCT. In this case, the analysis of the elemental content in hair could be help to find the cause of the diseases of MSSCT in children. In Fig. 43.1 one can see that the Apatity is leading in the total and primary morbidity of MSSCT in children aged 0–14 years not only in the Murmansk region, but also in the whole of the RF. The total morbidity of MSSCT in the Apatity (152.72 ± 17.49) in children aged 0–14 years exceeds the total morbidity in the Lovozero (128.44 ± 11.24, $p = 0.22$), exceeds the total morbidity in the Murmansk region (117.22 ± 2.91, $p = 0.059$) and exceeds the total morbidity in children of MSSCT in 1.9 times in the

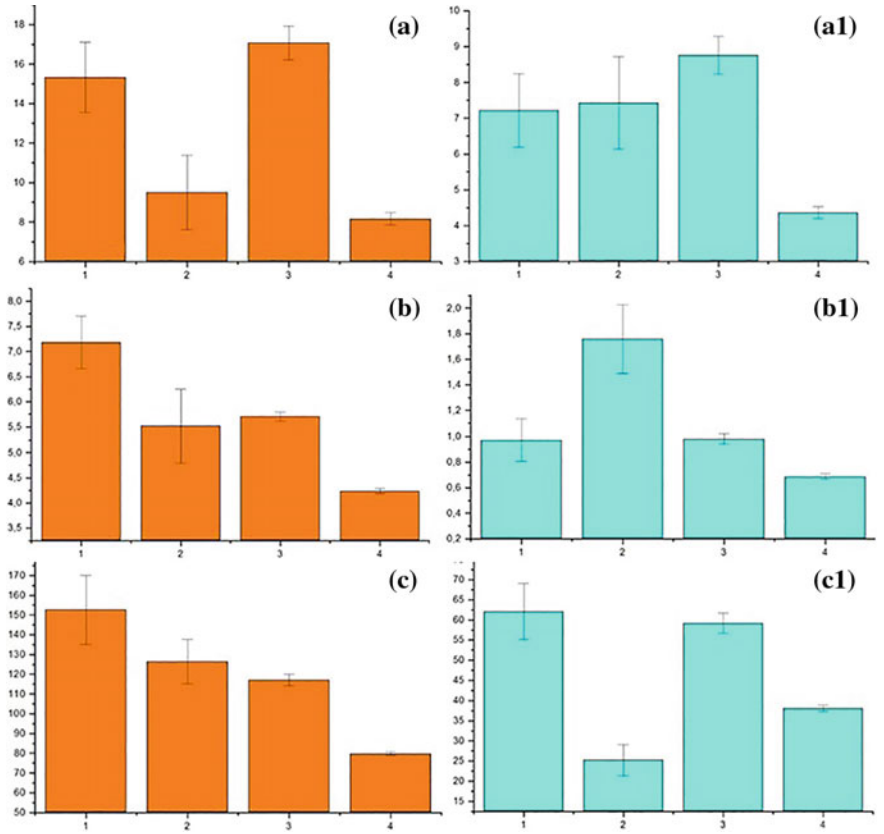


Fig. 43.1 Total morbidity (a, b, c) and primary morbidity (a1, b1, c1) of children aged 0–14 in the Murmansk region. a, a1—neoplasm; b, b1—epilepsy and epileptic status; c, c1—diseases of the musculoskeletal system and connective tissue. *X* axis: 1—Apatity city; 2—Lovozero village; 3—Murmansk region; 4—Russian Federation. *Y* axis: morbidity per 1000 relevant population

RF (79.74 ± 0.85, $p = 0.015$). The primary morbidity of MSSCT in children in the Apatity (62.05 ± 6.98) significant differs from the primary morbidity of MSSCT in 2.4 times in the Lovozero (25.24 ± 3.89, $p = 0.002$), corresponds to the primary mordbidity of children of MSSCT in the Murmansk region (59.19 ± 2.59), and higher in 1.6 times, than in the RF (38.07 ± 0.83, $p = 0.006$), Fig. 43.1.

Thus, it can be seen that the total morbidity of neoplasm of children aged 0–14 years, of the diseases of the nervous system, manifested by epilepsy and epileptics status, of MSSCT diseases in the Apatity are higher than in the Lovozero, partly higher than in the Murmansk region as a whole, and significantly higher, than in the RF. Primary morbidity of children by neoplasms in the Apatity is comparable to the primary morbidity in the Lovozero and in the Murmansk region and significantly higher than in the RF. The primary morbidity of children of 0–14 years by the diseases of the nervous system, manifesting by epilepsy and epileptic status, is higher in

the Lovozero, compared to the Apatity, to the Murmansk region and to the RF. The primary morbidity of MSSCT in children aged 0–14 years in Apatity is significantly higher than in the Lovozero, than in the RF and it is comparable to the morbidity in the Murmansk region as a whole.

43.3.2 The Elemental Hair Content Among Children in the Territories of Comparison

The content of elements in the hair of pre-schoolers living in the Lovozero and in the Apatity, significant ($p < 0.05$) differs by following elements: barium (Ba), copper (Cu), germanium (Ge), molybdenum (Mo), tin (Sn), selenium (Se), silicon (Si), strontium (Sr), titanium (Ti), phosphorus (P) and cobalt (Co). The content of these elements, with the exception of germanium, are higher in the hair of pre-schoolers from the Apatity. Moreover, all values of the elemental content, between which of the significant differences have been found, do not go beyond the age range of the content of elements (Table 43.1).

However, if compare the elemental content which do not have significant differences in the hair of preschoolers from the Lovozero and from the Apatity, one can see that he content of the many elements reach and exceed of the upper boundaries of reference values. The content of silver (Ag), aluminium (Al), arsenic (As), boron (B), cadmium (Cd), magnesium (Mg), manganese (Mn), nickel (Ni), lead (Pb) are approaching and are reaching the upper of boundaries of the reference values in hair samples of the preschoolers on the both territories of comparison. The content of iodine (J) and cobalt (Co) are corresponding to the lower boundaries of the reference values. The germanium content (Ge) reaches the upper of boundaries of reference values in hair samples of preschoolers from the Lovozero. The content of sodium (Na) and of potassium (K) exceed the upper boundaries of the reference values. The content of chromium (Cr), of copper (Cu), of iron (Fe), of strontium (Sr), of phosphorus (P) reach the upper boundaries of reference values in hair of preschoolers from the Apatity (Table 43.1).

Thus, common features of the content of elements in the samples of hair of preschoolers from the Lovozero and from the Apatity are the excess relative to reference values of the content of silver (Ag), sodium (Na), potassium (K), low content of iodine (J) and cobalt (Co).

Special features in the elemental content are a wider range of elements in the hair of preschoolers from the Apatity, reaching and exceeding the upper boundaries of the reference values. These group includes the content of arsenic (As), of chromium (Cr), of copper (Cu), of iron (Fe), of magnesium (Mg), of lead (Pb), of tin (Sn), of strontium (Sr), of phosphorus (P). The higher content of germanium (Ge) and of rubidium (Rb) in the hair samples of children from Lovozero, are of the exception.

The elemental content in the hair samples of schoolers from the Lovozero and from the Apatity significant ($p < 0.05$) differs by following elements: boron (B),

Table 43.1 Comparison of average mean (M) of the elemental content in the hair of preschoolers from the Lovozero village ($M1$), from the Apatity city ($M2$), $\delta 1$ and $\delta 2$-standard deviation for $M1$ and $M2$, respectively. The lines with significant differences between the values corresponding to the level <0.05 are marked by bold type

Elements	Lovozero $M1$	Apatity $M2$	$\delta 1$	$\delta 2$	P	Reference value
Ag	0.64	1.59	0.76	2.62	$p > 0.10$	(0.001–0.300)
Al	31.59	33.18	13.39	13.11	$p > 0.10$	(6.00–30.00)
As	0.10	0.16	0.02	0.19	$p > 0.10$	(0.001–0.100)
B	3.57	3.12	2.57	0.56	$p > 0.10$	(0.10–3.50)
Ba	**0.84**	**2.03**	**0.48**	**1.13**	$\mathbf{p < 0.001}$	(0.20–5.00)
Be	0.00	0.00	0.00	0.00	$p > 0.10$	(0.000–0.010)
Cd	0.24	0.21	0.17	0.12	$p > 0.10$	(0.01–0.25)
Cr	1.53	1.84	0.61	0.37	$p < 0.10$	(0.15–2.00)
Cs	0.00	0.00	0.00	0.00	$p > 0.10$	(0.00–0.00)
Cu	**9.24**	**13.77**	**2.03**	**3.74**	$\mathbf{p < 0.001}$	(5.70–15.00)
Fe	39.68	42.70	10.32	9.37	$p > 0.10$	(10.00–50.00)
Ge	**0.43**	**0.16**	**0.12**	**0.09**	$\mathbf{p < 0.001}$	(0.070–0.500)
Hg	0.35	0.29	0.25	0.38	$p > 0.10$	(0.010–2.000)
I	0.13	0.61	0.13	1.25	$p > 0.10$	(0.100–4.200)
Li	0.00	0.009	0.00	0.04	$p > 0.10$	(0.000–0.250)
Mg	28.64	71.39	5.45	100.86	$p > 0.10$	(15.00–30.00)
Mn	0.91	1.04	0.41	0.49	$p > 0.10$	(0.10–1.00)
Mo	**0.14**	**0.31**	**0.05**	**0.13**	$\mathbf{p < 0.001}$	(0.020–0.500)
Na	1954.05	1818.09	1485.12	1243.93	$p > 0.10$	(200.00–1000.00)
Ni	1.75	1.56	1.03	0.51	$p > 0.10$	(0.10–2.00)
Pb	3.76	**6.02**	2.74	5.53	$p > 0.10$	(0.10–5.00)
Rb	1.22	1.09	0.85	0.59	$p > 0.10$	(0.001–1.500)
Sn	**1.72**	**3.72**	**1.00**	**2.76**	$\mathbf{p < 0.025}$	(0.05–5.00)
Se	**0.69**	**1.31**	**0.21**	**0.30**	$\mathbf{p < 0.001}$	(0.50–2.20)
Si	**547.72**	**758.67**	**24.03**	**123.66**	$\mathbf{p < 0.001}$	(50.0–1900.0)
Sb	0.17	0.19	0.08	0.16	$p > 0.10$	(0.00–0.50)
Sr	**0.86**	**4.05**	**1.00**	**5.95**	$\mathbf{p < 0.001}$	(0.30–5.00)
Ti	**3.72**	**6.64**	**3.13**	**3.87**	$\mathbf{p < 0.005}$	(0.048–14.000)
V	0.20	0.17	0.08	0.08	$p > 0.10$	(0.005–0.500)
Zn	66.22	97.35	38.78	48.22	$p < 0.10$	(50.00–150.00)
K	2049.31	2034.07	1742.98	1264.32	$p > 0.10$	(200.00–1600.00)
P	**165.31**	**186.47**	**22.72**	**23.44**	$\mathbf{p < 0.001}$	(50.00–200.00)
Ca	444.40	**792.31**	131.87	960.77	$p > 0.10$	(250.00–500.00)
Co	**0.06**	**0.07**	**0.09**	**0.03**	$\mathbf{p < 0.01}$	(0.050–0.500)

chromium (Cr), copper (Cu), germanium (Ge), mercury (Hg), manganese (Mg), molybdenum (Mo), nickel (Ni), rubidium (Rb), selenium (Se), silicon (Si), zinc (Zn), phosphorus (P). The content of these elements are higher in the hair samples of schoolers from the Apatity, with the exception of germanium (Ge), mercury (Hg), manganese (Mg), the content of which are higher in the hair of schoolers from the Lovozero. Moreover, all values in the content of elements in hair samples between which significant differences were found, for except of manganese, do not go beyond the age range of reference values (Table 43.2).

Comparison of the content of the elements, which do not have significant differences in the hair samples of schoolers from the Lovozero and from the Apatity shows that content of silver (Ag) in hair samples are more higher than the reference values in 5.4 and 8.4 times, respectively for schoolers from the Lovozero and from the Apatity. The content of aluminium (Al), arsenic (As), magnesium (Mg), sodium (Na), strontium (Sr), potassium (K), calcium (Ca) reach and exceed the upper boundaries of the reference values in the hair samples of schoolers from the Lovozero and from the Apatity. Moreover, the content of magnesium (Mg) and manganese (Mn) in hair of schoolers from the Lovozero are higher in 1.4 times and 1.3 times, respectively, than the reference values, also in 1.5 and in 1.9 time higher than their content in hair of schoolers from the Apatity. The content of iodine (J) and cobalt (Co) correspond to the lower boundaries of the reference values in hair samples of preschoolers and schoolers from the Lovozero and from the Apatity.

Thus, common peculiarities in the content of elements in the hair samples of preschoolers and schoolers from the Lovozero and from the Apatity are the excess content of silver (Ag), sodium (Na), potassium (K); the low iodine content (J) and cobalt (Co) relative to reference values. The territorial differences consist in the more higher of content of the copper content (Cu), molybdenum (Mo), selenium (Se), silicon (Si), phosphorus (P) in samples of hair of preschoolers and schoolers from the Apatity compared with children from the Lovozero ($p < 0.05$).

Comparative assessment of the variability of the elemental content in hair samples of preschoolers and schoolers allows estimate the territorial age associated dynamics of the trace elements accumulation in hair samples of children from the Lovozero and from the Apatity (Figs. 43.2 and 43.3).

The variability in the content of elements ($M \pm \delta$) in the hair samples of preschoolers from the Apatity (Fig. 43.2a) is higher than in the hair samples of children from the Lovozero (Fig. 43.2b). In particular, the variability in the content of strontium (4.05 ± 5.96) in the hair of children from the Apatity is not only higher than one in the hair of children from the Lovozero (0.86 ± 1.0), but, in some cases, almost in 2 times higher than the reference values (0.30–5.00 μg/g). The same applies to tin (3.72 ± 2.76), to lead (6.02 ± 5.53), to silver (1.59 ± 2.62) contents in the hair samples preschoolers from the Apatity compared with the same element content in hair samples of preschoolers from the Lovozero (1.72 ± 1.0, 3.76 ± 2.74 and 0.64 ± 0.76, respectively). The magnesium content in the hair of preschoolers from the Apatity (71.39 ± 100.86) is almost 2 times higher than the reference age values (15.00–30.00 μg/g) and in 2.5 times higher than magnesium content in hair of preschoolers from the Lovozero (28.64 ± 5.45). The calcium content

Table 43.2 Comparison of average mean (*M*) of the elemental content in the hair of schoolers from the Lovozero village (*M1*), from the Apatity city (*M2*), *δ1* and *δ2*-standard deviation for *M1* and *M2*, respectively. The lines with significant differences between the values corresponding to the level <0.05 are marked by bold type

Elements	Lovozero *M1*	Apatity *M2*	*δ1*	*δ2*	*P*	Reference value
Ag	1.61	2.49	3.01	7.25	$p > 0.10$	(0.001–0.300)
Al	26.05	17.10	18.55	13.44	$p > 0.10$	(6.00–30.00)
As	0.11	0.10	0.05	0.09	$p > 0.10$	(0.001–0.100)
B	**2.87**	**3.26**	**0.63**	**0.78**	$\mathbf{p < 0.01}$	(0.10–3.50)
Ba	1.76	2.33	1.28	1.36	$p < 0.10$	(0.20–5.00)
Be	0.00	0.00	0.00	0.00	$p > 0.10$	(0.000–0.010)
Cd	0.10	0.17	0.10	0.19	$p > 0.10$	(0.01–0.25)
Cr	**1.50**	**1.66**	**0.25**	**0.33**	$\mathbf{p < 0.025}$	(0.15–2.00)
Cs	0.00	0.00	0.00	0.00	$p > 0.10$	(0.00–0.00)
Cu	**8.68**	**13.85**	**1.89**	**16.46**	$\mathbf{p < 0.05}$	(5.70–15.00)
Fe	27.54	24.50	11.29	11.92	$p > 0.10$	(10.00–50.00)
Ge	**0.24**	**0.14**	**0.14**	**0.07**	$\mathbf{p < 0.005}$	(0.070–0.500)
Hg	**0.54**	**0.19**	**0.69**	**0.20**	$\mathbf{p < 0.005}$	(0.010–2.000)
I	0.11	0.15	0.11	0.24	$p > 0.10$	(0.100–4.200)
Li	0.004	0.003	0.01	0.01	$p > 0.10$	(0.000–0.250)
Mg	126.47	86.09	96.72	50.86	$p > 0.10$	(35.00–90.00)
Mn	**1.30**	**0.68**	**1.61**	**0.38**	$\mathbf{p < 0.025}$	(0.10–1.00)
Mo	**0.07**	**0.12**	**0.01**	**0.05**	$\mathbf{p < 0.001}$	(0.020–0.500)
Na	967.41	1007.04	737.17	563.90	$p > 0.10$	(120.00–550.00)
Ni	**1.36**	**0.78**	**0.71**	**0.55**	$\mathbf{p < 0.05}$	(0.10–2.00)
Pb	1.56	1.94	1.63	1.94	$p > 0.10$	(0.10–5.00)
Rb	**0.68**	**0.33**	**0.65**	**0.38**	$\mathbf{p < 0.05}$	(0.001–1.500)
Sn	1.24	0.93	1.41	0.74	$p > 0.10$	(0.05–5.00)
Se	**0.65**	**2.54**	**0.25**	**6.63**	$\mathbf{p < 0.005}$	(0.50–2.20)
Si	**528.50**	**652.14**	**45.02**	**22.94**	$\mathbf{p < 0.001}$	(50.0–1900.0)
Sb	0.08	0.05	0.07	0.05	$p > 0.10$	(0.00–0.50)
Sr	5.15	4.75	6.28	5.60	$p > 0.10$	(0.30–5.00)
Ti	5.92	7.06	7.87	16.22	$p > 0.10$	(0.048–14.000)
V	0.09	0.08	0.04	0.04	$p > 0.10$	(0.005–0.500)
Zn	**145.98**	**193.89**	**37.88**	**70.64**	$\mathbf{p < 0.025}$	(150.00–200.00)
K	1134.44	678.35	846.80	404.35	$p > 0.10$	(60.00–320.00)
P	**164.20**	**179.11**	**28.31**	**20.39**	$\mathbf{p < 0.05}$	(50.00–200.00)
Ca	**975.22**	782.24	797.54	439.26	$p > 0.10$	(350.00–700.00)
Co	0.10	0.04	0.31	0.03	$p > 0.10$	(0.050–0.500)

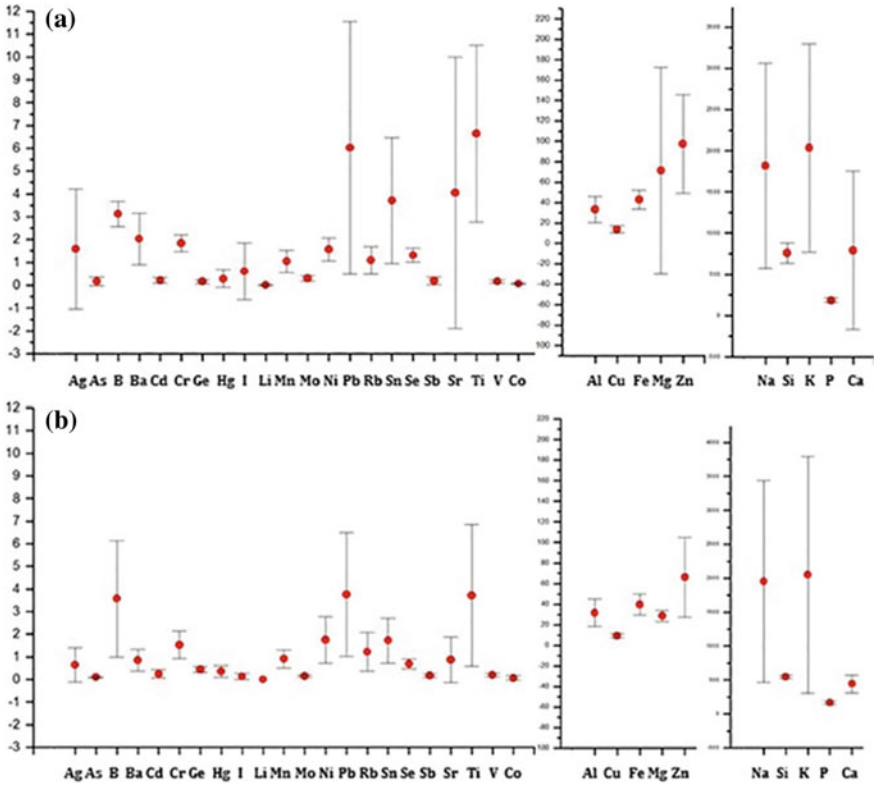


Fig. 43.2 The content of elements ($M \pm \delta$) in hair samples of preschoolers from the Apatity city (**a**) and from the Lovozero village (**b**). *X* axis: Elements. *Y* axis: content of elements, $\mu g/g$

(792.31 ± 960.77) is also higher in hair of preschoolers from the Apatity than in hair of preschoolers from Lovozero (444.40 ± 131.87) and exceeds reference values (250–500 μg/g). The barium content in the hair of pre-schoolers from the Apatity (2.03 ± 1.13) is in 2.4 times higher, than in hair of preschoolers from the Lovozero (0.84 ± 0.48); the iodine content in the hair of preschoolers from the Apatity (0.61 ± 1.25) is higher, than in hair of preschoolers from the Lovozero (0.13 ± 0.13), but closer to the low boundaries, than to the average reference values (0.100–4.20 μg/g). The only excess in the variability of the content of elements in the hair of preschoolers from the Lovozero relates to boron (3.57 ± 2.57), the content of which reaches the upper boundaries of reference values: 0.10–3.50 μg/g.

The variability in the elemental content in the hair of schoolers are shown in Fig. 43.3.

The highest degree of variability in the element content in hair samples of preschoolers and schoolers from the Apatity and from the Lovozero was found for titanium. The titanium content in hair samples of pre-schoolers from the Apatity city and from the Lovozero consist 6.64 ± 3.87 and 3.72 ± 3.13, respectively

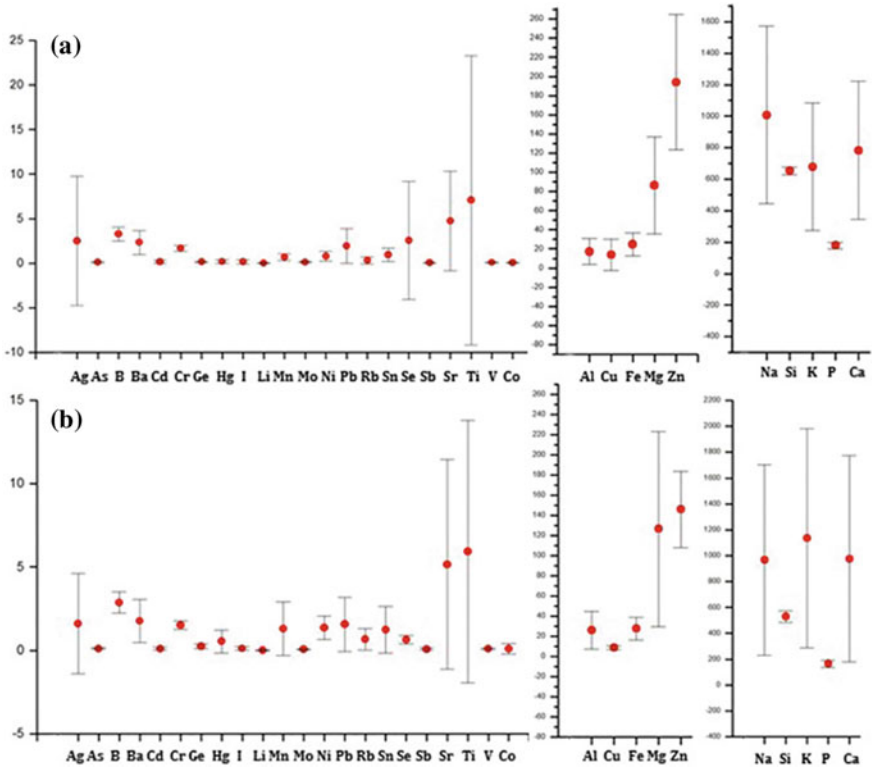


Fig. 43.3 The content of elements ($M \pm \delta$) in hair samples of schoolers from the Apatity city (**a**) and from the Lovozero village (**b**). X axis: Elements. Y axis: content of elements, $\mu g/g$

(Fig. 43.2). The titanium content and heterogenecy of its accumulation in the hair samples of schoolers from the Apatity and from the Lovozero (7.06 ± 16.22 and 5.92 ± 7.87, respectively) increases compared to its content in the hair of preschoolers (Tables 43.1, 43.2; Figs. 43.2, 43.3). Variability in the content of titanium in the hair of preschoolers and schoolers from the Apatity and from the Lovozero indicate that titanium presents in the environment both in the Apatity and in the Lovozero and its accumulation in the body of children slowly increases with age.

The strontium content in hair samples of schoolers from the Apatity and from the Lovozero consists 4.75 ± 5.60 and 5.15 ± 6.28, respectively. Under comparing of strontium content in hair samples of preschoolers from the Apatity and from the Lovozero (4.05 ± 5.96 and 0.86 ± 1.0, respectively), one can see that the strontium content in hair of schoolers from the Apatity do not change with age. This has occurring, apparently due to the achieving of the "saturation phase" in the content of strontium yet at preschool age in children from Apatity. The strontium accumulation in hair of children from the Lovozero, on the contrary, increases with age. Its content in hair samples of schoolers increases in 6.1 times in compared with pre-

schoolers, practically reaching the level of accumulation in the hair of schoolers from the Apatity. Since the «saturation phase» in the strontium content in hair of children from the Apatity has been reached at preschool age, and the strontium content in hair of children from the Lovozero increases with age, it can be assumed that strontium content in the environment is higher in the Apatity, than in the Lovozero. Additional support for this assumption is that content of strontium in the hair of preschoolers from Apatity almost in 5 times higher than in hair of preschoolers from Lovozero.

Also, a high heterogeneous in the accumulation of selenium (Se) in the hair of schoolers from the Apatity in comparing with to schoolers from the Lovozero (2.54 ± 6.63 and 0.65 ± 0.25, respectively), probably, indicates on the significant difference in the content of this element in the environment on the territories of comparison.

In general, it can be noted that the variability in the content of various elements in hair of preschoolers from the Apatity is higher, than in hair samples of preschoolers from the Lovozero (Fig. 43.2). However, the variability in the elemental content in hair of schoolers from the Lovozero becomes higher with age compared with one in the hair of schoolers from the Apatity (Fig. 43.3). This phenomenon may be explanted that preschoolers from the Apatity city are exposed to impact of the higher "doses" of various elements contained in the environment, than children from the Lovozero. Because of this, some elements reach the saturation level in the hair of children from the city of Apatity already in early childhood, and their content either does not change or decreases due to the body's need in them during growth with age. Hence, it follows the decrease in microelement variability among schoolers, compared with preschoolers from the Apatity (Fig. 43.3). A gradual accumulation of microelements in hair of children from the Lovozero leads to increase of their content and variability with age (Tables 43.1, 43.2; Figs. 43.2, 43.3). An exception is the content of such essential elements as sodium, potassium and calcium, which in high concentrations accumulate in the hair of preschoolers from the Lovozero, as in the case of preschoolers from the Apatity.

If to compare the frequency of occurrence (%) of children with an excess in the elemental content in hair among the child population in the Apatity and the Lovozero one can see, that such children occur more often among of preschoolers from the Apatity than among preschoolers from the Lovozero (Table 43.3).

However, a higher occurrence among of schoolers from the Lovozero children with an excess in the content of aluminum, of magnesium, of manganese and nickel compared with the Apatity, may indicate an increased risk of disturbances in mineral metabolism, the incidence of neuropsychiatric diseases and neoplasm among children from the Lovozero. Moreover, it should be especially emphasize the very rare frequency occurrence of children with content of lithium in hair among the children from the Lovozero and from the Apatity. The low level of lithium or lack of it in hair is an unfavorable prognostic signature for development of neuropsychiatric diseases (Osipova 2005).

As concern of a high content of sodium, potassium, calcium in the hair of children in both the Apatity and in the Lovozero, one can supposed that their accumulation occurs already at preschool age at the saturation level and varies slightly with age.

Table 43.3 The frequency of occurrence (%) of children among the preschoolers and schoolers from the Lovozero village (***L_presch***, ***L_sch***) and from the Apatity city (***A_presch***, ***A_sch***), in whose hair the content of elements corresponds to the norm (N), reaches and exceeds the upper boundaries (upper bound-upb) of standard values

Elements	*L_presch*	*A_presch*	Reference values, 5 years	*L_sch*	*A_sch*	Reference values, 14 years
Ag	56% ≥	72% ≥	(0.001–0.300)	50% ≥	52% ≥	(0.001–0.300)
Al	36% ≥	64% ≥	(6.00–30.00)	32% ≥	8% ≥	(6.00–30.00)
As	44% ≥	68% upb	(0.001–0.100)	50% ≥	56% upb	(0.001–0.100)
B	20% ≥	88% = upb	(0.10–3.50)	4% ≥	72% upb	(0.10–3.50)
Cd	40% ≥	44% ≥	(0.01–0.25)	4% ≥	28% ≥	(0.01–0.25)
Cr	36% upb	76% upb	(0.15–2.00)	4% upb	32% ≥	(0.15–2.00)
I	60% ≤	52% ≤	(0.100–4.200)	64% ≤	76% ≤	(0.100–4.200)
Mg	56% upb	80% ≥	(15.00–30.00)	44% ≥	28% ≥	(35.00–90.00)
Mn	60% upb	88% ≥	(0.10–1.00)	44% ≥n	20% ≥	(0.10–1.00)
Na	68% ≥	88% ≥	(200.00–1000.00)	72% ≥	92% ≥	(120.00–550.00)
Ni	48% upb	28% upb	(0.10–2.00)	32% upb	Ni–N	(0.10–2.00)
Pb	32% ≥	40% ≥	(0.10–5.00)	4% ≥	16% ≥	(0.10–5.00)
Sn	4% upb	24% ≥	(0.05–5.00)	4% upb	Sn_N	(0.05–5.00)
Sr	4% upb	16%	(0.30–5.00)	28% ≥	36% ≥	(0.30–5.00)
Zn	60% ≤	16% <, 16% upb	(70.00–150.00)	76% ≤	12% <, 32% ≥	(150.00–200.00)
K	44% ≥	48% ≥	(150.00–1500.00)	60% ≥	64% ≥	(60.00–320.00)
Ca	20% ≥	48% ≥	(250.00–500.00)	45% ≥	40% ≥	(350.00–700.00)
Co	76% ≤	56% ≤	(0.050–0.500)	80% ≤	92% ≤	(0.050–0.500)

This means that sources of high content of these elements, which accumulate already in childhood up to values exceeding the age norm, present in the environment as in the Apatity and in the Lovozero. It can be assumed that the source of increased accumulation of these and other elements in the hair of children from the Apatity and from the Lovozero, are the dust particles from different sources and of varied origin in the environment.

The "ANOF-2" tailing dump is the main and one of the largest on the Kola Peninsula source of environmental pollution by suspended substances SiO_2, TiO_2, Al_2O_3, Fe_2O_3, FeO, P_2O_5, CaO, SrO, MgO, MnO, Na_2O, K_2O, F_2, which content different elements including Na, K, Ca (Pashkevich and Stryzhenok 2013). The other source of Na, rare-earth metals (REM) and other elements could be dust particles from the processing of loparite ((Na, Ce) TiO_3, (REE, Na) (Ti, Nb) O_3, (Na, Ce, Ca) (Ti, Nb, Ta) O_3, (Na, Ce, Ca)$_2$(Ti, Nb)$_2O_6$) at the Karnasurt processing enterprise in the Lovozero district.

The dusting of the tailings and the Karnasourt processing enterprise are powerful sources of environmental pollution by toxic elements, traces of which we found in hair samples in children. The elemental composition of pollution sources, including the content of toxic and carcinogenic elements, suggests that cause of the incidence of neoplasm, diseases of the nervous and bone-muscle systems in children in the Lovozero and in the Apatity are the excessive flows of certain toxic substances and of their combinations, which accumulate in the body of children in the Kola North.

43.3.3 Discussion

A comparative analysis of the elemental content in the hair of children of preschool and school age living in the territories of comparison has shown that quantitative characteristics of some elements and a wide range of variability in their content deviate in certain cases from the established regularities (Baranovskaya et al. 2015). It is shown that a number of elements (Na, P, S, Ni, Cu, Zn, Rb, Sr, Ba, Cs, Br and some others) have a relatively narrow range of fluctuations in their accumulation levels, which indirectly may indicate on their relative constant in human organs and tissues. However, a high degree of variability in the content of such elements as sodium, zinc, strontium, which are characterized by a narrow range of fluctuations (Baranovskaya et al. 2015), were found in our research. The high variability of these elements, among with the high variability of silver, of tin, of selenium, of titanium, of magnesium, of potassium, of calcium, in hair samples of children in the territories of comparison indicates the irregularity of their entry and peculiarities of accumulation of the certain elements from external sources by the children's body. These sources are characterized by a certain elemental composition, including toxic impurities, the episodicity of their action, increasing contribution of toxic elements to the environment.

One can assumed that a tailing dump is the external source of additional intake of trace elements in the body of children of preschool and school age in the city of

Apatity A halo of tail dust with the composition of SiO_2, TiO_2, Al_2O_3, Fe_2O_3, FeO, P_2O_5, CaO, SrO, MgO, MnO, Na_2O, K_2O, F_2 under intensive wind load reaches the city and negatively affects both sanitary and hygienic conditions in the city, and on the health of citizens in general (Pashkevich and Stryzhenok 2013). The source of additional microelements in the organism of children of preschool and school age in the Lovozero region is the Karnasurt Processing Plant, which processes loparite containing ore with the following composition: [((Na, Ce) TiO_3, (REE, Na) (Ti, Nb) O_3, (Na, Ce, Ca) (Ti, Nb, Ta) O_3, (Na, Ce, Ca)$_2$(Ti, Nb)$_2O_6$], (Postolateva et al. 2013). One can not exclude also the cross-dusting, in which of fine particles are transferred over long distances, as well as additional contributions of contaminants from other sources in the Kola North.

What is the contribution of the elemental content in hair of children from the Lovozero and from the Apatity and elemental composition of contamination in environmental to the incidence of neoplasms, diseases of the nervous system and sensory organs (epilepsy, status epilepticus), diseases of the musculoskeletal system and connective tissue (KMSST)?

Experimental and clinical studies have confirmed that the lack of some trace elements or an excess of other trace elements contributes to an increase in the incidence of malignant tumors, degenerative and other diseases (Dvoirin 1968; Dvoirin et al. 1996; Cuajungco and Lees 1997; Boev et al. 2002; Kasprzak et al. 2003; Costa 2003; Setko and Setko 2004; Evseeva 2009; Sanders et al. 2009; Bakirdere et al. 2010; Hu et al. 2010; Bánfalvi 2011; Grimsrud and Andersen 2012; Permyakov 2012; Skal'nyy and Tsygan 2013; Kim et al. 2015; Marie et al. 2017). In the result of intoxication of the organism by the heavy metals, primarily Pb, Hg, Cd, (Shaikh et al. 1999; Takebayashi et al. 2000; Sanders et al. 2009; Harvey et al. 2015; Kim et al. 2015) and also Fe and Mn (Pennington and Young 1990; Naumova and Rebezov 2012) the deep deficiencies of Se and iodine J (Pennington and Young 1990; Patrick 2008; Zimmermann 2009), and relative deficiencies in Zn and Cu, (Hambidge and Krebs 2007) are often arisen in the human organism. Clinical manifestations of Se deficiency are an increase in the incidence of disorders of cardiac muscle, as well as the risk of neoplasm and diseases of the MSSCT (Golubkina 2004).

Our research revealed that content of selenium, iodine, zinc, copper in the hair of children from Lovozero are lower than in hair of children from Apatity with no significant differences in the content of lead, mercury, cadmium, iron and manganese in hair samples of preschoolers from the Lovozero and from the Apatite. However, the content of mercury, manganese and nickel are significantly higher in hair of the schoolers from the Lovozero, than in hair samples of the schoolers from Apatity ($p < 0.05$) (Tables 43.1, 43.2). The average mean of the arsenic content, as well as cadmium in the hair samples in the all studied groups of children from Lovozero and from Apatity, reached and slightly exceed the upper boundaries of the reference values (Tables 43.1, 43.2).

Excessive accumulation of aluminium, boron and nickel leads to the direct negative effect of their metabolites on the bone tissue, including the risk of developing neoplasm (Ward et al. 1978; O'Hare and Murnaghan 1982; Sedman et al. 1985; Kasprzak et al. 2003; Trombetta et al. 2005; Bakirdere et al. 2010; Exley 2013;

Küpper et al. 2015). It is known that disorder phosphorus-calcium metabolism in bone tissue, which is one of the factors of endemic osteoarthritis deformans occurs more often in regions with a low calcium level, but an excess of strontium and barium (Sukhanov and Gorbachev 2017). The content of aluminium, boron and nickel in samples of hair of preschoolers from the Lovozero and from the Apatity correspond to the upper boundaries of the norm. The content of aluminium, nickel in hair samples of schoolers from the Lovozero are higher, than in hair of schoolers from the Apatity, the boron content in hair of schoolers from the Lovozero and from the Apatity reaches the upper boundaries of the reference values.

The differences found in the content of elements in hair samples of children living in the territories of comparison could only partly explain the territorial neoplasm morbidity of the child population. The literature data on the relationship between oncological diseases and the content of elements in biological samples are contradictory and far from exhaustive (Dvoirin 1968; Dvoirin et al. 1996; Skal'nay et al. 2000; Boev et al. 2002; Perminova 2003).

The absence of significant differences between the primary incidence of neoplasm in the child population 0–14 years in the Apatity and in the Lovozero testifies only to the presence in the environment of genotoxic and carcinogenic agents, the recruitment of which may differ in the Apatity and in the Lovozero region. For example, the high content of highly toxic elements in the hair samples of children from the Lovozero: aluminium, mercury, nickel, along with a reduced content of iodine, selenium, zinc and cobalt create prerequisites for neoplasm incidence. In turn, an increased content of boron, copper, magnesium, molybdenum, lead, tin, strontium with iodine, zinc, and cobalt deficiency in the hair samples of children from Apatity could contribute to the development of neoplasm. It should be especially emphasized the presence in the hair samples among all groups of children from the Apatity and from the Lovozero, of exceed content arsenic as a highly toxic element associated with processes of cancerogenesis (Skal'nay et al. 2000; Hopenhayn-Rich et al. 1996; Grund et al. 2005; Chung et al. 2014; Gul et al. 2015).

Thus, the incidence of neoplasm of children in the Apatity and in the Lovozero district can be partly explained by the environmental content of genotoxic and carcinogenic elements, the combinations of which may have a territorial differences, as well as the low content of essential elements that have gene-protective and antioxidant functions in the children body. The high epileptic status of children in the Apatity and in the Lovozero district can also be explained by a combinations of different causes. One of them could be associated with an excess of calcium and deficiency of zinc, which are directly related to changes in the activity of receptors for catecholamine and neuropeptides (Cuajungco and Lees 1997; Perry et al. 1997). An increase in Ca concentration was noted in muscular dystrophy, migraine, some forms of epilepsy, and other disorders of the nervous system (Gromova 2001; Osipova 2005). In the hair of children with epilepsy, negative correlations were found between zinc and sodium, positive between iron and calcium (Osipova 2005). Excessive sodium in hair samples in all groups of children, coupled with a decrease in zinc content, could contribute to the manifestation of epileptic status, but these reasons are clearly not enough to explain the high incidence of epilepsy in the Apatity and in the Lovozero

district (Ihan et al. 1999; Hu et al. 2010). Perhaps the extremely low lithium content in hair samples of children of all age groups in the territories of comparison is also important factor for the manifestation of epileptic status.

The high accumulation of such elements as molybdenum, lead, strontium, content of which are higher in hair samples of children from the Apatity than from the Lovozero could be one of causes the high incidence rate of the musculoskeletal system in children from the Apatity. With a low calcium content but an excess of strontium, barium, phosphorus-calcium metabolism is impaired in bone tissue, which is one of the factors of endemic osteoarthritis deformans (Sukhanov and Gorbachev 2017). Lead is one of the most toxic elements (Zainullin et al. 2014) which contribute to the incidence of the musculoskeletal system.

43.4 Conclusions

On the basis of the data obtained, it can be concluded that the organism of children living in the territories of comparison in the Apatity and in the Lovozero accumulates toxic elements from the environment, the source of which can be dust particles, from the processing of apatite-nepheline ores and loparite ores.

Analysis of the content of elements in the hair samples of children living in the areas of comparison, made it possible to identify priority toxic elements that could cause a high incidence of neoplasm among the children in the Apatity and in the Lovozero district. The high content of mercury, manganese, nickel in children's body from the Lovozero could be made the contribution to initiation of the processes of carcinogenesis among of certain category of children. The additional candidates for role of promoters of carcinogenesis in children from the Lovozero district could be the rare earth elements contained in loparite ore, but left outside the elemental analysis: niobium, tantalum, thorium, radium, hafnium and etc. The physiological role of some of these is practically, not investigated (Baranovskaya et al. 2015). A possible cause of the high incidence of neoplasm among children from the Apatity could be the accumulation by the organism of toxic elements from dust particles entering the city's atmosphere as a result of dust erosion from the surface of the tailing dump of aratite-nepheline ore processing waste, as well as finely dispersed ash-slag waste from the Apatity thermal power plant (Pashkevich and Stryzhenok 2013). The increased content of boron, copper, magnesium, molybdenum, lead, tin, strontium in the body of children from Apatity could contribute to the level of neoplasm incidence of children from Apatity.

It should be also emphasize the general peculiarities in the content of elements in the hair samples of children, which could increase the risk of neoplasm incidence in the territories of comparison. These are the low levels of iodine, zinc, cobalt, partly selenium in the body of children, and the high level of arsenic as a very toxic element associated with processes of carcinogenesis (Skal'nay et al. 2000; Hopenhayn-Rich et al. 1996; Grund et al. 2005; Chung et al. 2014; Gul et al. 2015).

The causes of high incidence of the nervous system and sensory organs (epilepsy, epileptic status) in children aged 0–14 years in the Lovozero and in the Apatity, of very high the incidence of diseases of the musculoskeletal system and connective tissue in children from the Apatity can be associated with accumulation in children organism the certain elements from dust particles. These dust particles are produced in the result from the processing of apatite-nepheline and loparite ore. Probably, they contain not only cancirogenic elements but of certain elements with neurotoxic effects, as well as affecting on the metabolic processes in the musculoskeletal system.

References

Agadzhanyan ON, Skal'nyy AV (2001) Chemical elements in habitat and ecological portrait of a man. KMK, Moscow (in Russian)

Aiyar J, Berkovits HJ, Floyd RA, Wetterhahn KE (1991) Reaction of chromium (VI) with glutathione or with hydrogen peroxide: identification of reactive intermediates and their role in chromium (VI)-induced DNA damage. Environ Health Perspect 92:53–62

Alfrey AC (1990) Aluminum toxicity in humans. In: Tomita H (ed) Trace elements in clinical medicine. Springer, Tokyo

Alfrey AC, LeGendre GR, Kaehny WD (1976) The dialysis encephalopathy syndrome: possible aluminium intoxication. N EngI J Med 294:184–188

Arefyev AA (2009) Etiopathogetical features of urolithiasis in the conditions of the Arctic Thesis, Military Medical Academy. Kirov, St. Petersburg (in Russian)

Avtsyn AP, Koenig EE (1970) Some questions of the geographical pathology of the Far North. Labor Hum Health Far North 14:58–80 (in Russian)

Avtsyn AP, Zhavoronkov AA, Rish MA, Strochkova LS (1991) Human microelementoses: etiology, classification, organopathology. Medicine, Moscow (in Russian)

Baba H, Tsuneyama K, Yazaki M, Nagata K, Minamisaka T, Tsuda T et al (2013) The liver in itai-itai disease (chronic cadmium poisoning): pathological features and metallothionein expression. Mod Pathol 26:1228–1234

Bakhtina GG, Lenko OA, Sukhanova CE (2007) Human microelementoses and ways to correct their deficiency. Pathol Blood Circ Hear Surg 4:82–89 (in Russian)

Bakirdere S, Örenay S, Korkmaz M (2010) Effect of boron on human health. Open Miner Process J 3:54–59

Bánfalvi G (2011) Heavy metals, trace elements and their cellular effects. In: Bánfalvi G (ed) Cellular effects of heavy metals. Springer, New York

Baranov AA, Albitsky VYU, Antonova EV et al (2008) Current approaches to the study of the incidence of the child population of Russia. Grew Pediatr Jury 5:4–7 (in Russian)

Baranovskaya NV, Rikhvanov LP, Ignatova TN, Narkovich DV, Denisova OA (2015) Essays on human geochemistry. Tomsk Polytechnic University, Tomsk (in Russian)

Bashkin VN, Galiulin RV, Galiulina RA, Kalinina IE (2009) Geoecological assessment of the pathways of carcinogenic substances into the environment. Ecol Ind Russ 3:55–57 (in Russian)

Belisheva NK (2014) Contribution of high-latitude heliogeophysical agents to the incidence of the population of the Euro-Arctic region. Bull Ural Med Acad Sci 2(48):5–11 (in Russian)

Belisheva NK (2017) Features of pathogenesis of cells under the influence of heavy metals. In: Zaikov GE et al (eds) Heavy metals and other pollutants in the environment: biological aspects. Apple Academic Press Inc., Oakville

Belisheva NK, Megorsky VV (2017) The incidence of the population in the Arctic, due to the peculiarities of mineral metabolism with a high heterogeneity of the natural and man-made environment. Bull Kola Sci Cent RAS 4:5–20 (in Russian)

Belisheva NK, Petrov VN (2013) The problem of public health in the light of the implementation of the development strategy of the Arctic zone of the Russian Federation. Proc Kola Sci Cent RAS 4:151–173 (in Russian)
Blaurock-Busch E, Amin OM, Dessoki HH, Rabah T (2012) Toxic metals and essential elements in hair and severity of symptoms among children with autism. Maedica (Buchar) 7(1):38–48
Boev VM, Kuksanov VF, Rapid explosives (2002) Chemical habitat carcinogens and malignant neoplasms. Medicine, Moscow (in Russian)
Boev VM, Bystrykh BB, Vereshchagin NN et al (2004a) Bioelements and prenosological diagnostics. Trace Elem Med 5(4):17–20 (in Russian)
Boev VM, Perminova LA, Bystrykh BB, Lestsova ON (2004b) Assessment trace element profile in children with malignant neoplasms. Trace Elem Med 5(2):11–14 (in Russian)
Bouchard M, Laforest F, Vandelac L et al (2007) Hair manganese and hyperactive behaviors: pilot study of school-age children exposed through tap water. Environ Health Perspect 115:122–127
Bouchard MF, Sauve S, Barbeau B et al (2011) Intellectual impairment in school-age children exposed to manganese from drinking water. Environ Health Perspect 119(1):138–143
Castro-González MI, Méndez-Armenta M (2008) Heavy metals: implications associated to fish consumption. Environ Toxicol Pharmacol 26:263–271
Chakrabarti SK, Bai C, Subramanian KS (2001) DNA-protein crosslinks induced by nickel compounds in isolated rat lymphocytes: role of reactive oxygen species and specific amino acids. Toxicol Appl Pharmacol 170:153–165
Chung JY, Yu SD, Hong YS (2014) Environmental source of arsenic exposure. J Prev Med Public Health 47:253–257
Costa M (2003) Potential hazards of hexavalent chromate in our drinking water. Toxicol Appl Pharmacol 188:1–5
Cuajungco MP, Lees GJ (1997) Zinc metabolism in the brain relevance to human neurodegenerative disorders. Neurobiol Dis 4:1387
Dartsch PC, Hildenbrand S, Kimmel R, Schmahl FW (1998) Investigations on the nephrotoxicity and hepatotoxicity of trivalent and hexavalent chromium compounds. Int Arch Occup Environ Health 71(Suppl):S40–S45
Detkov VU (2017) Microelementoses and metallotoxicosis in the children's population of St. Petersburg and ways to reduce them. Dissertation, Military Medical Academy named after SM. Kirov, Ministry of Defense of the Russian Federation, St. Petersburg (in Russian)
Dewberry FL, McKinney TD, Stone WJ (1980) The dialysis dementia syndrome: report of fourteen cases and review of the literature. Trans Am Soc Artiflnt Organ 3:102–107
Doll R, Morgan LG, Speizer FE (1970) Cancers of the lung and nasal sinuses in nickel workers. Br J Cancer 24:623–632
Dudley RE, Gammal LM, Klaassen CD (1985) Cadmium-induced hepatic and renal injury in chronically exposed rats: likely role of hepatic cadmium-metallothionein in nephrotoxicity. Toxicol Appl Pharmacol 77:414–426
Dvoirin VV (1968) Geochemical aspects of the epidemiology of malignant tumors. Quest Oncol 14(5):105–110 (in Russian)
Dvoirin VV, Axel EM, Trapeznikov NN (1996) Incidence of malignant neoplasms and the mortality from them of the population of the SNS countries in 1995. ONTSRAMN, Moscow (in Russian)
Eastmond DA, Macgregor JT, Slesinski RS (2008) Trivalent chromium: assessing the genotoxic risk of an essential trace element and widely used human and animal nutritional supplement. Crit Rev Toxicol 38:173–190
Ercal N, Gurer-Orhan H, Aykin-Burns N (2001) Toxic metals and oxidative stress part I: mechanisms involved in metal-induced oxidative damage. Curr Top Med Chem 1:529–539
Evseeva GP (2009) Trace element status and the relationship of its imbalance with the development of diseases in children. Dissertation, Far Eastern State Medical University, Khabarovsk (in Russian)
Exley C (2013) Human exposure to aluminium. Environ Sci: Process Impacts 15:1807–1816

Fergusson JE (1990) The heavy elements: chemistry, environmental impact and health effects. Pergamon Press, Oxford
Gammelgaard B, Fullerton A, Avnstorp C, Menné T (1992) Permeation of chromium salts through human skin in vitro. Contact Dermat 27:302–310
Gawkrodger DJ, Cook SW, Fell GS, Hunter JA (1986) Nickel dermatitis: the reaction to oral nickel challenge. Br J Dermatol 115:33–38
Golubkina NA (2004) Ecological aspects of the enrichment of food with selenium. Ecol Syst Devices 7:32–35 (in Russian)
Gorbachev AL, Dobrodeeva LK, Tedder YuR, Shatsova EN (2007) Biogeochemical characteristics of the northern regions. The trace element status of the population of the Arkhangelsk region and the prognosis of endemic diseases. Hum Ecol 1:4–11 (in Russian)
Grimsrud TK, Andersen A (2012) Unrecognized risks of nickel-related respiratory cancer among Canadian electrolysis workers. Scand J Work Environ Health 38:503–515
Grimsrud TK, Berge SR, Martinsen JI, Andersen A (2003) Lung cancer incidence among Norwegian nickel-refinery workers 1953–2000. J Environ Monit 5:190–197
Gromova OA (2001) Neurochemistry of macro and microelements. New approaches to pharmacotherapy. Alev-V, Moscow (in Russian)
Grund SC, Hanusch K, Wolf HU (2005) Arsenic and arsenic compounds, Ullmann's encyclopedia of industrial chemistry. Wiley, Weinheim
Gul N, Shah MT, Khan S, Khattak NU, Muhammad S (2015) Arsenic and heavy metals contamination, risk assessment and their source in drinking water of the Mardan District, Khyber Pakhtunkhwa, Pakistan. J Water Health 13:1073–1084
Gwaltney-Brant SM (2013) Heavy metals. In: Haschek WM, Rousseaux CG, Wallig MA (eds) Haschek and Rousseaux's handbook of toxicologic pathology, 3rd edn. Elsevier Inc. Academic Press
Hambidge KM, Krebs NF (2007) Zinc deficiency: a special challenge. J Nutr 137:1101–1105
Harvey PJ, Handley HK, Taylor MP (2015) Identification of the sources of metal (lead) contamination in drinking waters in north-eastern Tasmania using lead isotopic compositions. Environ Sci Pollut Res Int 22:12276–12288
Henson MC, Chedrese PJ (2004) Endocrine disruption by cadmium, a common environmental toxicant with paradoxical effects on reproduction. Exp Biol Med (Maywood) 229:383–392
Hopenhayn-Rich C, Biggs ML, Smith AH, Kalman DA, Moore LE (1996) Methylation study of a population environmentally exposed to arsenic in drinking water. Environ Health Perspect 104:620–628
Hu R, Gong X, Duan Y, Li N, Che Y, Cui Y et al (2010) Neurotoxicological effects and the impairment of spatial recognition memory in mice caused by exposure to TiO_2 nanoparticles. Biomaterials 31:8043–8050
Ibragimova ME, Sabirova LA, Berezkina EU, Skal'nay MG, Zhdanov ZI, Skal'nyy AB (2011) Relationship between imbalance of macro and microelements and public health (literature review). Kazan Med J 92(4):606–609
Ihan A, Uz E, Kali S, Akyol O (1999) Serum and hair trace element levels in patients with epilepsy and healthy subjects: does the antiepileptic therapy affect the element concentrations of hair? Eur J Neurol 6(6):705–709
International Council for the Control of Iodine Deficiency Disorders. Accessed 9/13/2010
Jahan S, Khan M, Ahmed S, Ullah H (2014) Comparative analysis of antioxidants against cadmium induced reproductive toxicity in adult male rats. Syst Biol Reprod Med 60:28–34
James KA, Meliker JR (2013) Environmental cadmium exposure and osteoporosis: a review. Int J Public Health 8:737–745
Jett DA (2012) Chemical toxins that cause seizures. Neurotoxicology 33(6):1473–1475
Jia X, Wang S, Zhou L, Sun L (2017) The potential liver, brain, and embryo toxicity of titanium dioxide nanoparticles on mice. Nanoscale Res Lett 12:478
Kasprzak KS, Sunderman FW Jr, Salnikow K (2003) Nickel carcinogenesis. Mutat Res 533:67–97

Kim HS, Kim YJ, Seo YR (2015) An overview of carcinogenic heavy metal: molecular toxicity mechanism and prevention. J Cancer Prev 20(4):232–240
Koedrith P, Seo YR (2011) Advances in carcinogenic metal toxicity and potential molecular markers. Int J Mol Sci 12:9576–9595
Koutsenogii KP, Savchenko TI, Chankina OV, Zhuravskaya EYA, Gyrgolkau LA (2010) Elemental blood and hair composition of the Russian north native inhabitants with different biogeochemical environment. Chem Sustain Dev 18:49–59
Küpper M, Weinbruch S, Skaug V, Skogstad A, Thornér EE, Benker N et al (2015) Electron microscopy of particles deposited in the lungs of nickel refinery workers. Anal Bioanal Chem 407:6435–6445
Luippold RS, Mundt KA, Austin RP, Liebig E, Panko J, Crump C et al (2003) Lung cancer mortality among chromate production workers. Occup Environ Med 60:451–457
Marie I, Gehanno JF, Bubenheim M, Duval-Modeste AB, Joly P, Dominique S, Bravard P, Noel D, Cailleux AF, Benichou J, Levesque H, Goulle JP (2017) Systemic sclerosis and exposure to heavy metals: a case control study of 100 patients and 300 controls. Autoimmun Rev 16:223–230
Mergler D, Baldwin M, Bélanger S, Larribe F, Beuter A, Bowler R, Panisset M, Edwards R, de Geoffroy A, Sassine MP, Hudnell K (1999) Manganese neurotoxicity, a continuum of dysfunction: results from a community based study. Neurotoxicology 20(2–3):327–342
Müller L (1986) Consequences of cadmium toxicity in rat hepatocytes: mitochondrial dysfunction and lipid peroxidation. Toxicology 40:285–295
Naumova NL, Rebezov MB (2012) The trace element status of Chelyabinsk as a justification for the development of the production of enriched food. Basic Res 4(1):196–200
Nielsen NH, Menné T, Kristiansen J, Christensen JM, Borg L, Poulsen LK (1999) Effects of repeated skin exposure to low nickel concentrations: a model for allergic contact dermatitis to nickel on the hands. Br J Dermatol 141:676–682
O'Hare JA, Murnaghan DJ (1982) Reversal of aluminum-induced hemodialysis anemia by a low-aluminum dialysate. N Engl J Med 306:654–656
Onishchenko GG, Novikov SM, Rakhmanin YA (2002) In: Rakhmanina YA, Onishchenko GG (eds) Fundamentals of risk assessment for public health when exposed to chemicals that pollute the environment. NII Echi-GOS, Moscow
Osipova AA (2005) The role of chemical elements in the activity of the nervous system (overview). Bull All-Russ Res Cent Sib Branch Russ Acad Med Sci 1(39):79–84 (in Russian)
Pashkevich MA, Stryzhenok AV (2013) Analysis of the landscape-geochemical situation in the area of the tailings management of ANOF-2 of JSC Apatit. Notes Min Inst 206:155–159 (in Russian)
Patrick L (2008) Iodine: deficiency and therapeutic considerations. Altern Med Rev 13(2):116–127
Pennington JA, Young B (1990) Iron, zinc, copper, manganese, selenium, and iodine in foods from the United States total diet study. J Food Compost Anal 3(2):166–184
Perminova LA (2003) Evaluation of the content of trace elements in biological media (blood) in children with oncopathology. Materials of the regional scientific-practical conference of young scientists and specialists. Orenburg, pp 132–133
Permyakov IA (2012) Features of physical development and adaptation in children under conditions of anthropogenic pollution of the environment with heavy metals. Thesis, Perm State National Research University, Perm (in Russian)
Perry DK, Smyth MJ, Stennicke HR (1997) Zinc is a potent inhibitor of the apoptotic protease caspase-3. A novel target for zinc in the inhibition of apoptosis. J Biol Chem 272:18530–18533
Popoola AO, Popoola OE, Igbokwe OG, Olatunde-Aremu FS (2018) assessment of carcinogenic heavy metals in some Nigerian clays used for cosmetic and pharmaceutical purposes. SDRP J Earth Sci Environ Stud 3(2):378–385
Postolateva A, Tverdov A, Zhura A (2013) Rare-earth deposits—features, difficulties and prospects. Gold Technol 1(19):32–36 (in Russian)
Report of IAEA (1993) Coordinated research programme NAH: the significance of hair mineral analysis as a means for assessing internal body badens of environmental pollutants, Vienna, Res-18

Report on the state and protection of the environment of the Murmansk region in 2012 (2013) Individual entrepreneur Shcherbakov ML, Murmansk (in Russian)
Report on the state and protection of the environment of the Murmansk region in 2016 (2017) The health status of the population in the Murmansk region according to the Ministry of Natural Resources and Ecology of the Murmansk region, Murmansk (in Russian)
Salnikova EV, Detkov Vu, Scalny AB (2016) Accumulation of Essential and conditionally essential microelements in the hair of the inhabitants of Russia. Trace Elem Med 17(2):24–31 (in Russian)
Sanders T, Liu Y, Buchner V, Tchounwou PB (2009) Neurotoxic effects and biomarkers of lead exposure: a review. Rev Environ Health 24(1):15–45
Sasmaz S, Uz E, Pinar T, Vural H, Eiri M, Ilihan A, Akyol Ö (2003) Hair lead and cadmium concentrations in patients with epilepsy and migraine. Neurosci Res Commun
Schofield K (2017) The metal neurotoxins: an important role in current human neural epidemics? Int J Environ Res Public Health 14(12):1511
Sedman AB, Klein GL, Merritt RJ et al (1985) Evidence of aluminium loading in infants receiving intravenous therapy. N Engl J Med 312:1337–1343
Setko IM, Setko NP (2004) Assessing the balance of microelements in children of an industrial city as an integral indicator of prenosological diagnosis of environmentally caused pathology. Trace Elem Med 5(4):130–131 (in Russian)
Shaikh ZA, Vu TT, Zaman K (1999) Oxidative stress as a mechanism of chronic cadmium-induced hepatotoxicity and renal toxicity and protection by antioxidants. Toxicol Appl Pharmacol 154:256–263
Skal'nay MG, Skal'nyy AV, Demidov VA (2000) Dependence of increased cancer incidence on excess arsenic and other toxic chemical elements in the environment. Trace Elem Med 2(1):32–35 (in Russian)
Skal'nyy AB (2004) Chemical elements in human physiology and ecology. ONIKS 21st Century Publishing House: World, Moscow (in Russian)
Skal'nyy AB (2011) The relationship of imbalance of macro-and micronutrients and public health (literature review). Kazan Med J 92(4):606–609 (in Russian)
Skal'nyy AV, Tsygan HV (2013) Pathophysiology of the exchange of macro-and microelements. In: Gypsy VN (ed) Pathophysiology of metabolism: a manual. SpecLit., St. Petersburg
Stern BR (2010) Essentiality and toxicity in copper health risk assessment: overview, update and regulatory considerations. J Toxicol Environ Health A 73:114–127
Sukhanov SGI, Gorbachev AL (2017) Regional features of the trace element composition of bio-substrates in residents of the North-West region of Russia. Trace Elem Med 18(2):10–16 (in Russian)
Suslikov VL (2002) Geochemical ecology of diseases. In: 4 volumes. Helios, Moscow (in Russian)
Takebayashi S, Jimi S, Segawa M, Kiyoshi Y (2000) Cadmium induces osteomalacia mediated by proximal tubular atrophy and disturbances of phosphate reabsorption. A study of 11 autopsies. Pathol Res Pract 196:653–663
Trombetta D, Mondello MR, Cimino F, Cristani M, Pergolizzi S, Saija A (2005) Toxic effect of nickel in an in vitro model of human oral epithelium. Toxicol Lett 159:219–225
Veltishchev YuE (1999) Ecologically determined infringements of the health of children. Russ Pediatr J 3:7–8 (in Russian)
Ward MK, Feest TG, Ellis HA et al (1978) Osteomalacic dialysis aetiological osteodystrophy: evidence for a water-borne aetiological agent, probably aluminium. Lancet 1:841–845
Xiao LL, Zhou Y, Ma JX, Sun WW, Cao LM, Wang B, Zhu CM, Yang SJ, Wang DM, Yuan J, Chen WH (2018) Oxidative DNA damage mediates the association between urinary metals and prevalence of type 2 diabetes mellitus in Chinese adults. Sci Total Environ 627:1327–1333
Yamashita K, Yoshioka Y, Higashisaka K, Mimura K, Morishita Y, Nozaki M et al (2011) Silica and titanium dioxide nanoparticles cause pregnancy complications in mice. Nat Nanotechnol 6:321–328
Yang O, Kim HL, Weon JI, Seo YR (2015) Endocrine-disrupting chemicals: review of toxicological mechanisms using molecular pathway analysis. J Cancer Prev 20:12–24

Zainullin VG, Bondar IP, Kondratenok BM (2014) Features of the accumulation of chemical elements in the hair of the child population of the Komi Republic. News Komi Sci Cent Ural Branch RAS 2(18):24–31 (in Russian)

Zalata OA, Evstafieva EV (2012) Features of the cognitive functions of urban children with mental developmental disorders due to the content of chemical elements in the hair. Saratov Sci Med J 8(2):428–432 (in Russian)

Zimmermann MB (2009) Iodine deficiency. Endocr Rev 30(4):376–408

Chapter 44
Formation of the Chemical Composition of Underground Waters of the Khibiny Mountain Range (On the Example of One Water Intake)

Vladimir A. Masloboev, Vladimir I. Pozhilenko, Sergey S. Sandimirov, Svetlana V. Drogobuzhskaya, Stanislav V. Ivanov, Anton V. Gudkov, Pavel S. Tereshchenko and Svetlana I. Mazukhina

Abstract Pollution of water bodies—sources of drinking water supply, an important factor negatively affecting the health of the population. It is known, that in the settlements of the Murmansk region there was no excess of sanitary hygienic standards for drinking water. The main task of the presented work was to consider the processes of formation of the chemical composition of groundwater in the Apatity–Kirovsk

V. A. Masloboev · S. I. Mazukhina (✉)
Institute of North Industrial Ecology Problems—Subdivision of the Federal Research Centre "Kola Science Centre of the Russian Academy of Sciences", 14a, Akademgorodok, 184209 Apatity, Russia
e-mail: simazukhina@mail.ru

V. I. Pozhilenko · A. V. Gudkov
Geological Institute—Subdivision of the Federal Research Centre "Kola Science Centre of the Russian Academy of Sciences", 14, Fersmana Str., 184209 Apatity, Murmansk Region, Russia
e-mail: pozhil@geoksc.apatity.ru

A. V. Gudkov
e-mail: anton_gudkov@myrambler.ru

S. S. Sandimirov · P. S. Tereshchenko
Research Centre for Human Adaptation in the Arctic—Branch of the Federal Research Centre "Kola Science Centre of the Russian Academy of Science", 41a, Akademgorodok, 184209 Apatity, Russia
e-mail: sandl966@ramglrt.ru

P. S. Tereshchenko
e-mail: tereshchenko_pash@mail.ru

S. V. Drogobuzhskaya
Tananaev Institute of Chemistry—Subdivision of the Federal Research Centre "Kola Science Centre of the Russian Academy of Sciences", 26a, Akademgorodok, 184209 Apatity, Russia
e-mail: Drogo_sv@chemy.kolasc.net.ru

S. V. Ivanov
Luzin Institute for Economic Studies—Subdivision of the Federal Research Centre "Kola Science Centre of the Russian Academy of Sciences", 24a, Fersmana Str., 184209 Apatity, Russia
e-mail: etostas@mail.ru

© Springer Nature Switzerland AG 2020

O. V. Frank-Kamenetskaya et al. (eds.), *Processes and Phenomena on the Boundary Between Biogenic and Abiogenic Nature*, Lecture Notes in Earth System Sciences,
https://doi.org/10.1007/978-3-030-21614-6_44

district within the water-rock system, to study the chemical forms of migration of elements, the chemical composition of the new formed phases. Complete hydrochemical analysis showed the presence of such elements as uranium, molybdenum, silver, barium, nickel, vanadium, aluminum and lead in the waters. These data have added to the database of groundwater chemistry. It was found that in the studied water sources such elements as calcium, sodium, potassium, magnesium, sulfate ion, necessary for human life, are in a chemical form useful for human health (Ca^{2+}, Na^{+}, K^{+}, Mg^{2+}, sulfate ion $SO_4{}^{2-}$). Forms of migration of carcinogenic or toxic elements (nickel, barium, vanadium, strontium, aluminum and lead)—are present in the most toxic chemical form Ni^{2+}, Ba^{2+}, $HVO_4{}^{2-}$, Sr^{2+}. The ability to replace calcium in the bones is one of the most severe consequences of the action of inorganic compounds of lead, barium, strontium. It is known that free ions Ni^{2+} are more toxic than its complex compounds with inorganic and organic ligands. In the structure of the General morbidity of the adult population of the Murmansk region, the largest share falls on diseases of the circulatory system (17.9%) (Apatity city), in second place—the musculoskeletal system (13.2%) (Apatity and Kirovsk). In addition, there is a significant excess of the average Russian morbidity rates for tumors and anemia. The data obtained explained and supplemented the already known facts of morbidity of the population of the Apatity–Kirovsk district.

Keywords Groundwater · Physical-chemical model · Khibiny massif · Medical-ecological studies · Hydroxyl apatite · Toxic element · Khibinites · ICP-MS

44.1 Introduction

The average morbidity levels of the adult population of the Murmansk region in terms of the amount of diseases are at the level of the Russian average indicators. However, for some classes of diseases and nosological forms monitored within the Federal Information Fund they exceed the Russian average levels: neoplasms, endocrine system diseases, diet and metabolic disorders, diseases of the musculoskeletal system (http://mpr.gov-murman.ru). The largest excess of the Russian average level regarding the adult population's morbidity is noted in the towns of Apatity and Kirovsk. In general, morbidity of the children is higher than the Russian average by 30–40% over many years.

Geochemist from St. Petersburg V. I. Lebedev formulated the principle: man in relation to the external environment is an open system, to which the laws of physics and chemistry are applicable (Kravchenko 1998). In the work of Elpiner and Zektser (1999) it is emphasized that researchers from Russia and foreign countries dealing with medical and environmental contamination of drinking water determine the relationship of public health with chemical composition of groundwater and anthropogenic inclusions.

Kravchenko (1998) believes that the explanation and treatment of bones and teeth is not limited by studying the human body and the excess or deficiency of Sr, Se, U, Th and other microelements in the external environment, most of which isomorphically replace calcium in the structure of apatite (in bones of human and animals ~70% of hydroxyl apatite). It is also mentioned that apatite with and SrO content of up to 39.31% is found in alkaline massifs of the Kola Peninsula. All this indicates that in studying water and its evaluation for drinking purposes, efforts of various specialists need to be combined and a new integrated approach is needed.

The aim of the work is to assess the anthropogenic influence and chemical composition of the Khibiny massif rocks on formation of the chemical composition of surface and groundwater of "Predgorny" water intake using physical and chemical modeling ("Selector" software package) (Chudnenko 2010).

44.2 Materials and Methods

The work uses published sources, reports carried out in the framework of research programs, as well as the results of chemical analysis of water samples selected in the process of fulfilling the tasks under the RFBR grant 17-45-510640. The main research method is the method of physical-chemical (thermodynamic) modeling, implemented in "Selector" software package, developed under the guidance of Professor I. K. Karpov (Vinogradov Institute of Geochemistry of the Siberian Department of RAS, Irkutsk city). "Selector" is equipped with a system of built-in thermodynamic data bases and a module for forming models of various complexity. The algorithm used (Chudnenko 2010) makes it possible to calculate complex chemical equilibria in isobaric-isothermal, isochemical and adiabatic conditions in multisystems, where an aqueous electrolyte solution, a gas mixture, liquid and solid hydrocarbons, minerals in the form of solid solutions and one-component phases, melts and plasma can be present at the same time. Using the software package, it is possible to study both multi-component heterogeneous systems and megasystems, consisting of interacting systems (reservoirs) connected with each other and the environment by flows of matter and energy. In this work the software package is used for modeling in the "water-rock" system. During 2012–2015 (Geological institute of KSC RAS) studies were carried out on the content of hydrogen (δ^2H, ‰) and oxygen (δ^{18}O, ‰) isotopes in the wells within the Khibiny massif and its closest framing. In different seasons (spring, autumn, summer and winter) meteoric water (snow, rain), water of open reservoirs and melting snowfields located in well areas were investigated (Gudkov et al. 2015).

In 2017 samples were taken from wells of water intake "Predgorny". The measurements were carried out using a quadrupole ICP-MS system fitted with a dynamic reaction cell (Elan 9000 DRC-e, PerkinElmer SCIEX). A method has been developed for the simultaneous trace determination of elements in waters in Institute of chemistry and technology of rare elements and mineral raw materials FRC KSC RAS. Daily optimization was performed using a Instrument Calibration Standard

1 (PerkinElmer), containing of 10 μg/L of elements. Calibration standard solutions of appropriate concentrations were prepared from 10 μg/L multi-element standards (Instrument Calibration Standards—Multi Analyte Custom Grate Solutions IV-STOK-21, -26, -28, -29; Inorganic Ventures). All samples, standards and reference samples were diluted to the desired level of 2% pure nitric acid. The calibration standards used in these investigations were found to be stable over a period of at least one day. Different samples of waters were measured after calibration. Anions were determined by potentiometry and titration. The reference samples (CRM-TMDW-A, CWW-TM-A, CRM-SOIL-A) used in these investigations were obtained from High-purity Standards.

44.2.1 Geographical and Geological Location

On the territory of the Kola region of the north-eastern part of the Baltic Shield (administratively—the Murmansk region), loose formations are now represented by rare finds (relics) of low-power square and linear Neogene weathering crusts and, mainly, quaternary (anthropogenic) formations of various genesis—glacial, water-glacial, lakes, rivers, swamps, etc. (Pozhilenko et al. 2002). These loose formations, as well as zones of fracturing in crystalline rocks, are reservoirs of groundwater, which in the form of springs (sources) are widely come out in the Kola Peninsula (Ananyev 2009).

All of the above also applies to the Khibiny massif and its environs, with the only difference being that low-power eluvial formations are developed in most of the high-mountain area, but a wide spectrum of quaternary formations and morphological structures is developed in the erosional valleys of the dissected relief and in the vicinity of the massif.

The presence of structural features of the Khibiny massif, zones of fracturing, dissected relief and significant differences in altitudes in the catchment areas caused the appearance of a large number of springs. They are located both on the slopes of the valleys, in the valleys, and even in the adjoining loose formations, in various degrees removed from the Khibiny massif, whose thickness in the areas adjoining Khibiny varies from the first centimeters to 80 or more meters, and is the maximum in hidden erosional valleys.

A very important role in the structure of the Khibiny massif is played by conical and radial discontinuous disruptions of the first order (Onokhin 1975) and numerous differently oriented disruptions of the second order (Shpachenko and Zhirov 2003). The presence of disruptive disturbances contributes to the accumulation of fissure groundwater, the duration of contact of which with the host crystal rocks of the massif and the products of their destruction can reach from one year to several tens or even thousands of years (Gudkov et al. 2014). Fractured groundwater under favorable conditions enters the pressure aquifers located both in the fractured zones and in loose formations, mixing with younger waters formed due to atmospheric precipitation.

Taking into account the size of the catchment areas and the considerable difference in heights, the water pressure and flow, a number of these sources already represent practical importance and are used to provide high-quality water to the population of Kirovsk and Koashva village. (The program 2016). To provide water to the population of Apatity, underground water sources are not yet used, although attempts to draw attention to some of them in the area of Malaya Belaya River have already been made (Konukhin et al. 2012).

The active wells of water intake "Predgorny", which is located at the foot of the southeastern part of the Khibiny massif, on shallow ridge glacial hills with a height of about 200 m (Fig. 44.1), are selected as the case study. To the southeast of the water intake and to the north from the lake Kitchepahk the technological sump of Vostochny mine is located (Fig. 44.2).

The excess of the wellheads of water intake wells relative to the sump waters is about 30 m. The aquifer is located in loose quaternary water-ice deposits, which lie on the Neo-Archaean granitoids. It is natural to assume that its saturation is not only due to surface waters slipping from the southeastern slopes of the mountain massif, but also from the fissure waters coming from the spurs of the Khibiny massif. This part of the massif is composed mainly of massive and trachytoid khibinites, and several bodies of rocks of the alkaline ultramafic series (Fig. 44.3).

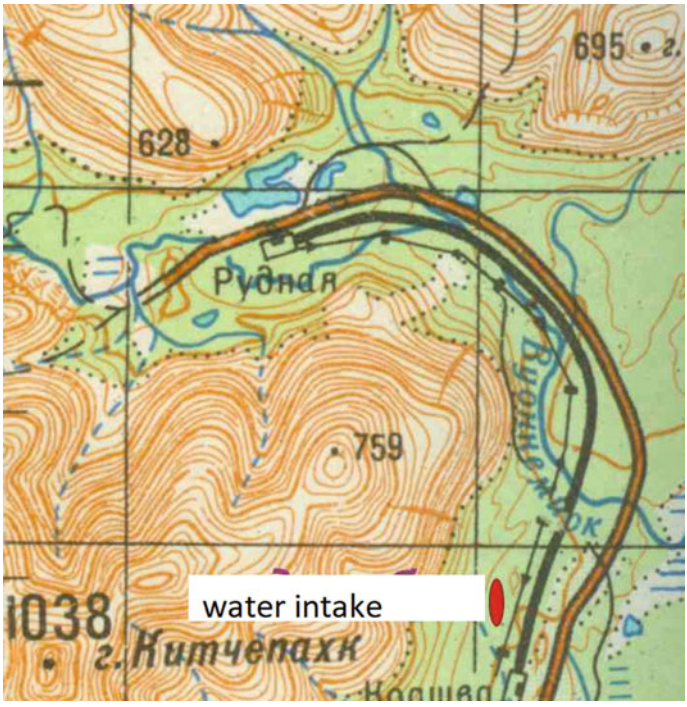


Fig. 44.1 The position of the water intake on the topographical map (Topographic map 1993)



Fig. 44.2 The position of the wells of the "Predgorny" water intake on the space image (https://www.google.ru/maps)

To assess the role of the influence of the chemical composition of the Khibiny massif rocks on the chemical composition of water from "Predgorny" water intake for physical-chemical modeling, samples of chemical analyzes of the rocks from the catchment area—massive and trachytoid khibinites and rocks of the alkaline ultramafic series were taken (Tables 44.1, 44.2, 44.3).

To obtain the necessary information and solve the tasks set in the project under the RFBR grant 17-45-510640, water samples from the 5th, 2nd, 9th, 3rd, and 4th wells of "Predgorny" water intake were taken on November 11, 2017.

Basing on the previously developed methods of forming the chemical composition of natural waters, and taking into account the rocks' chemical composition, physical-chemical modeling (PCM) ("Selector" software package) was carried out. The PCM included 34 independent components (Al, B, Br, Ar, He, Ne, C, Ca, Cl, F, Fe, K, Mg, Mn, N, Na, P, S, Si, Sr, Cu, Zn, Ni, Pb, V, Ba, Co, Cr, Hg, As, Cd, H, O), 996 dependent components, including 369 in the aqueous solution, 76 in the gas phase, 111 liquid hydrocarbons, and 440 solid phases, organic and mineral substances. The set of solid phases of the multisystem is formed taking into account the mineral composition of the Khibiny massif (Mazukhina 2012, 2016; Kalinnikov et al. 2014; Mazukhina et al. 2017).

The processes of natural water formation in the "water-rock-atmosphere" system are studied, depending on the interaction degree (ξ) of rocks with aqueous solutions

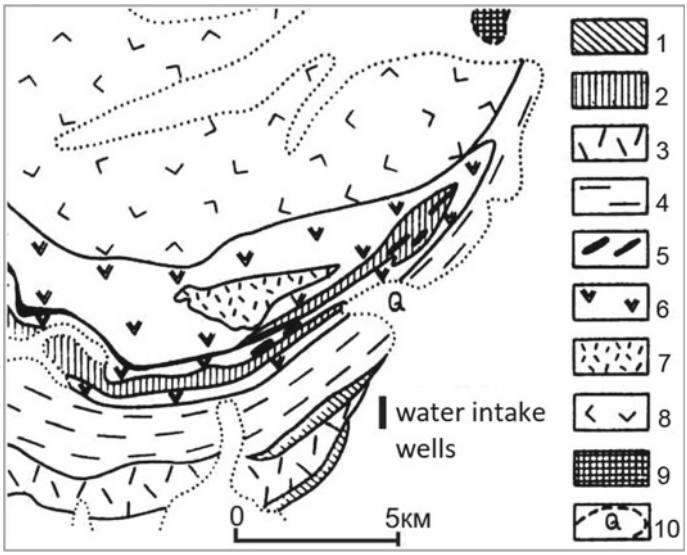


Fig. 44.3 The position of the water intake wells on the schematic geological map of the South-Eastern part of the Khibiny massif (Arzamastsev 1990): 1—peridotite, pyroxenite, melilitic; 2—ultrabasic foidolite; 3—massive khibinites; 4—trachytoid khibinites; 5—apatite-nepheline ore; 6—ristschorrites, juvites, urtites massive; 7—nepheline syenites; 8—foyaite; 9—rocks of carbonate stock; 10—quaternary sediments

under the open conditions (100 kg of atmosphere, 1000 kg of water, T 276.15, P 1 bar, rock (100 g)—the average composition of the Khibiny massif rocks) (Table 44.3, column 11, Table 44.2, column 10, Table 44.1 column 10), coefficients of water migration S, F, Cl (Perelman 1989).

44.3 Results and Discussion

The results of modeling "water-rock" interactions are presented in Table 44.4. Analytical data for analysis of water samples from the water intake wells are given in Table 44.5. Analysis of the results of modeling and analytical data indicates the comparability of the concentrations of calcium, sodium, magnesium, strontium, sulfates, fluoride, hydrocarbonates, and pH values. In addition, the modeling results indicate the possibility of the presence of chromium, cobalt, vanadium in the waters. The composition of the new formed phases, corresponds to the phases of muscovite, goethite, apatite, montmorillonite, and amorphous silica corresponds to the new forms found in the Khibiny alkaline massif as a result of nepheline weathering. Smectites are mixed calcium, magnesium, sodium-aluminosilicates. Based on the simulation results, the potassium content should be significantly less than it found in waters from the water intake wells. Besides, nitrogen oxides were found in waters of the water intake.

Table 44.1 Chemical composition melteigites, ijolites, urtites and juvites of the Khibiny massif

No.	1	2	3	4	5	6	7	8	9	10	11
Weight %	mlg 170	mlg 309	ijl 304	ijl 414	urt 460	urt 240	juv 670	urt 100	urt 500	urt-mlg	urt-mlg
SiO_2	41.5	42.5	41.2	45.6	44.6	42.44	46.5	43.1	40.3	43.1	43.3
TiO_2	4.35	3.33	2.16	3.29	2.10	2.31	2.33	3.07	2.09	2.78	3.09
Al_2O_3	4.91	2.78	16.80	13.29	22.54	24.65	20.15	23.46	27.16	17.30	17.97
Fe_2O_3	12.99	10.95	7.42	5.72	3.18	2.84	3.31	2.86	1.96	5.69	5.08
FeO	10.58	10.36	5.90	3.84	2.17	2.26	2.16	2.67	1.37	4.59	3.83
MnO	0.54	0.52	0.35	0.24	0.13	0.11	0.16	0.13	0.04	0.25	0.25
MgO	6.01	8.39	3.08	4.83	1.89	0.97	2.51	1.22	0.20	3.23	2.71
CaO	10.8	14.80	7.80	9.82	5.27	3.28	4.63	4.61	4.52	7.28	6.92
Na_2O	4.67	3.48	9.71	8.77	12.6	14.3	10.0	12.4	15.1	10.1	10.5
K_2O	1.22	0.67	3.69	2.37	4.61	5.91	6.88	5.74	4.98	4.01	4.21
P_2O_5	0.37	0.79	1.26	0.38	0.43	0.47	0.50	0.60	1.65	0.72	0.74
CO_2	0.03	0.14	0.11	0.20	0.16	0.18	0.14	0.09	–	0.116	–
F	0.22	0.18	0.19	0.21	0.10	0.08	0.12	0.16	0.23	0.165	–
H_2O^+	–	–	–	–	–	–	0.26	0.47	0.76	0.497	0.58
H_2O^-	–	–	–	–	–	–	0.38	0.11	0.01	0.167	0.13
Σ	99.50	99.91	100.3	99.35	100.7	100.4	99.99	100.6	100.4	99.94	99.33

1–9—melteigites (mlg), ijolites (ijl), urtites (urt) and juvites (juv) (Arzamastsev 1994); figures under the rock names mean depth of sampling from the well core; 10 is the average sample composition from 9 analyzes (1–9 in the table); 11 is the weighted average composition of the urtite-melteigite differentiated complex by 109 analyzes (Arzamastsev and Ivanova 1985)

Table 44.2 Chemicalcomposition of nepheline syenites, massive and trachytoid khibinites from khibinite rocks of the Khibiny massif

No.	1	2	3	4	5	6	7	8	9	10	11
Weight %	ns	ns	khibm	khibm	khibm	khibm	khibt	khibt	khibt	Average	Average
SiO_2	55.0	55.0	49.4	49.9	54.6	52.3	55.1	54.1	54.2	53.3	53.1
TiO_2	0.91	1.11	2.72	1.96	0.77	0.85	0.85	0.76	0.69	1.18	0.97
Al_2O_3	19.6	19.3	16.2	18.4	23.2	21.0	21.3	21.2	20.6	20.1	21.2
Fe_2O_3	2.18	2.61	4.43	2.85	1.75	3.48	4.04	4.55	3.14	3.23	2.39
FeO	3.11	2.97	3.68	4.42	1.77	1.24	0.01	0.01	1.03	2.03	1.65
MnO	0.16	0.18	0.35	0.27	0.13	0.23	0.19	0.19	0.18	0.21	0.20
MgO	0.62	0.63	1.32	1.09	0.34	0.33	0.46	0.33	0.40	0.61	0.70
CaO	1.23	1.79	4.78	3.97	1.01	1.04	1.10	1.20	1.06	1.91	1.87
Na_2O	9.76	9.14	9.65	9.71	9.91	11.3	10.3	10.3	11.21	10.13	9.87
K_2O	5.97	6.29	4.66	4.85	4.82	5.45	5.86	6.25	5.63	5.53	6.51
P_2O_5	0.22	0.14	0.64	0.38	0.11	0.09	1.16	0.12	0.12	0.33	0.29
CO_2	0.10	0.12	0.11	0.10	0.48	0.20	–	–	0.06	0.167	0.13
S	0.09	0.08	0.02	0.12	0.01	0.02	–	–	0.18	0.074	–
Cl^-	0.01	0.01	–	–	0.02	0.01	–	–	0.06	0.022	–
F^-	0.12	0.10	0.28	0.17	0.10	0.12	–	–	0.14	0.147	0.05
H_2O^+	0.52	0.31	0.65	0.69	0.20	1.40	0.40	0.70	0.73	0.62	0.71
H_2O^-	0.08	0.10	0.13	0.23	0.12	0.12	0.10	0.15	0.15	0.104	0.14
Σ	100.6	99.96	99.67	99.77	99.91	99.92	99.77	99.74	100.1	99.67	99.90

1–2—nepheline syenites (ns), massive khibinites (khibm) and trakhytoid khibinites (khibt) (Arzamastsev 1994); 10—average sample composition from 9 analyzes (1–9 in the table); 11—chemical composition of the average sample of the Khibiny massif rocks (Ivanova et al. 1970)

Table 44.3 The chemical composition of rocks of the alkaline-ultramafic series in the Khibiny massif (Arzamastsev 1990)

No.	1	2	3	4	5	6	7	8	9	10	11
Weight %	Peridotites		Olivine pyroxenites		Ultrabasic foidolites						Average
SiO_2	38.3	43.6	41.4	41.6	43.8	42.1	46.4	42.6	45.9	39.5	42.5
TiO_2	3.51	3.41	4.18	4.91	4.51	5.14	2.42	2.95	2.42	7.25	4.07
Al_2O_3	4.29	5.21	7.37	5.92	14.2	13.1	13.5	14.0	14.5	9.17	10.1
Fe_2O_3	10.3	5.41	8.90	4.33	2.76	6.74	2.16	4.80	4.75	8.00	5.81
FeO	5.25	7.06	5.22	11.3	9.01	7.30	8.74	7.52	5.76	7.00	7.41
MnO	0.28	0.19	0.23	0.23	0.32	0.34	0.17	0.30	0.21	0.28	0.255
MgO	19.9	17.9	13.38	11.7	4.43	4.49	6.35	5.35	5.00	7.01	9.55
CaO	12.6	9.36	9.09	11.2	6.41	6.87	9.59	8.69	8.52	11.7	9.41
Na_2O	0.65	2.26	3.18	3.47	7.89	7.26	6.34	7.83	6.97	4.56	5.04
K_2O	2.06	2.91	3.60	2.11	2.87	2.91	2.25	2.76	3.57	2.36	2.74
P_2O_5	0.50	0.36	0.43	0.33	1.07	1.20	0.41	0.61	0.53	1.51	0.695
CO_2	0.38	0.14	0.32	0.23	0.17	0.07	0.07	0.31	0.10	0.32	0.211
S	0.16	0.03	0.04	0.12	0.06	0.05	0.07	0.23	0.05	0.19	0.100
F	1.06	0.45	0.91	0.60	0.38	0.32	0.18	0.41	0.31	–	0.47
H_2O^+	0.57	0.88	0.95	1.12	0.56	0.83	1.16	0.91	0.79	0.29	0.81
H_2O^-	0.11	0.13	0.37	0.42	0.15	0.00	0.15	0.17	0.13	0.19	0.182
Cr_2O_3	0.18	0.16	0.11	0.11	0.01	0.02	0.03	0.01	0.02	0.02	0.067
V_2O_5	0.07	0.04	0.05	0.04	0.07	0.07	0.04	0.06	0.05	0.07	0.056
BaO	–	0.07	0.07	0.06	0.39	0.36	0.08	0.11	0.11	–	0.125
SrO	0.14	0.10	0.19	0.11	0.56	0.62	0.11	0.14	0.14	0.27	0.24

(continued)

Table 44.3 (continued)

No.	1	2	3	4	5	6	7	8	9	10	11
Weight %	Peridotites		Olivine pyroxenites		Ultrabasic foidolites						Average
NiO	0.13	0.11	0.07	0.05	0.01	0.01	0.01	0.01	0.00	0.02	0.042
CoO	0.01	0.01	0.01	0.01	0.00	0.01	0.01	0.01	0.00	0.01	0.008
Σ	100.5	99.76	100.0	99.89	99.63	99.82	100.3	00.79	99.80	99.78	99.92

Table 44.4 The results of modeling of the system "water–rock" ("Predgorny" water intake, Koashva village), T = 3 °C, P = 1 bar

ξ	Concentration (mg/l)								
	AlO_2^-	Ca^{2+}	Na^+	Mg^{2+}	K^+	Ba^{2+}	Ni^{2+}	Co^{2+}	HVO_4^{2-}
1	1.14E−05	4.15E−01	5.70E−01	2.69E−01	1.02E−01	3.73E−03	1.84E−03	2.09E−04	2.35E−03
0.8	8.25E−06	6.20E−01	8.95E−01	4.26E−01	1.97E−01	5.91E−03	2.92E−03	3.32E−04	3.75E−03
0.6	1.05E−05	9.73E−01	1.44	6.74E−01	2.06E−01	9.37E−03	4.63E−03	2.92E−04	5.97E−03
0.4	1.57E−05	1.54	2.33	1.07	1.84E−01	1.49E−02	7.34E−03	9.73E−05	9.47E−03
0.2	2.54E−05	2.43	3.72	1.68	1.57E−01	2.35E−02	1.16E−02	2.75E−05	1.5E−02
0	4.85E−05	3.82	5.92	2.65	1.18E−01	3.73E−02	1.84E−02	5.24E−06	2.38E−02
−0.2	8.47E−05	5.99	9.41	2.26	9.54E−02	5.90E−02	2.92E−02	1.25E−06	3.77E−02
−0.4	1.70E−04	9.24	14.9	3.83E−01	6.94E−02	9.31E−02	4.62E−02	2.08E−07	5.98E−02
	$Al(OH)_4^-$	Sr^{2+}	CrO_4^{2-}	SiO_2	SO_4^{2-}	HCO_3^-	$P_{general}$	F^-	pH
1	1.96E−05	7.38E−02	2.63E−03	2.07	3.48E−01	3.82	1.26E−02	1.66E−02	7.04
0.8	1.41E−05	7.77E−02	4.57E−03	3.18	5.51E−01	5.96	2.70E−03	2.28E−02	7.25
0.6	1.80E−05	8.38E−02	7.71E−03	3.43	8.71E−01	9.27	5.27E−04	3.53E−02	7.47
0.4	2.69 −05	9.36E−02	1.28E−02	3.43	1.37	14.5	1.01E−04	5.58E−02	7.71
0.2	4.35E−05	1.09E−01	2.08E−02	3.44	2.16	22.7	1.90E−05	8.83E−02	7.98
0	8.30E−05	1.33E−01	3.66E−02	3.43	3.39	35.3	3.01E−06	1.40E−01	8.34
−0.2	1.45E−04	1.41E−01	5.36E−02	3.44	5.36	45.3	5.71E−07	2.22E−01	8.66

(continued)

Table 44.4 (continued)

ξ	Concentration (mg/l)								
	AlO_2^-	Ca^{2+}	Na^+	Mg^{2+}	K^+	Ba^{2+}	Ni^{2+}	Co^{2+}	HVO_4^{2-}
−0.4	2.92E−04	5.25E−02	8.54E−02	3.43	8.50	52.7	9.50E−08	3.52E−01	9.05
	Composition of the newly formed phases, mole								
	MnO_2	FeO(OH)	Msc	Apt	Mnt	SiO_2	Co_3O_4		Smc
1	3.34E−04	1.27E−02	3.76E−03	1.37E−04	8.50E−03	5.69E−06	–		–
0.8	5.29E−04	2.01E−02	5.04E−03	4.04E−04	1.46E−02	1.24E−04	–		–
0.6	8.39E−04	3.18E−02	1.07E−02	6.80E−04	1.97E−02	3.18E−02	1.33E−06		–
0.4	1.33E−03	5.04E−02	2.07E−02	1.09E−03	2.65E−02	8.99E−02	4.17E−06		–
0.2	2.11E−03	7.99E−02	3.62E−02	1.72E−03	3.76E−02	1.82E−01	7.33E−06		–
0	3.34E−03	1.27E−01	6.07E−02	2.73E−03	5.53E−02	3.26E−01	1.18E−05		–
−0.2	5.29E−03	2.01E−01	9.85E−02	4.33E−03	8.45E−02	4.46E−01	1.88E−05		2.67E−02
−0.4	8.39E−03	3.18E−01	1.58E−01	6.86E−03	1.31E−01	5.61E−01	2.98E−05		8.73E−02

Table 44.5 Results of groundwater monitoring of "Predgorny" water intake (depth of wells 49–58 m)

No. of wells	Concentration (mg/l)							
	Ca^{2+}	Ba^{2+}	Na^{+}	Mg^{2+}	K^{+}	HCO_3^{-}	$Fe_{general}$	Ni^{2+}
2	7.10	0.0012	7.91	0.86	3.26	31.6	0.020	0.0138
3	4.84	0.0005	6.94	0.62	2.91	25.5	0.019	0.0005
4	3.25	0.0003	5.68	0.40	2.64	23.1	0.014	0.0036
5	10.8	0.0005	10.9	1.18	3.72	37.3	0.045	0.0026
9	5.88	0.0005	8.82	0.74	3.34	28.8	0.018	0.0017
	Sr^{2+}	Mo	Al^{3+}	F^{-}	$P_{general}$	SO_4^{2-}	NO_3^{-}	pH
2	0.066	0.0033	0.0045	0.31	0.0091	6.7	9.55	8.24
3	0.092	0.0018	0.012	0.07	0.0093	5.95	4.75	7.96
4	0.055	0.0014	0.011	0.16	0.0089	4.1	2.06	8.11
5	0.114	0.0059	0.011	0.45	0.0086	13.8	16.5	8.00
9	0.112	0.0026	0.017	0.14	0.0087	7.6	6.2	8.00

Comparison of these data with the chemical composition of surface waters allows concluding that the surface waters containing such elements as chlorine, potassium, and nitrogen oxides also affect the chemical composition of waters from the water intake.

The Ca/Sr ratios in the water intake wells (Table 44.5) are 108, 53, 60, 95 and 52 respectively. The "relatively normal environmental situation" refers to the situation when Ca/Sr > 100, with the ratio 1 < Ca/P < 2. As can be seen, this ratio is only in well 2. Ca/P ratios in the respective wells are 781, 520, 365, 1258 and 675. Such a situation is most likely to be classified as an "emergency environmental situation" (Kravchenko 1998).

Analysis of the situation with mass non-infectious diseases (poisonings) and priority diseases in connection with harmful effects of environmental factors in the Murmansk region shows that diseases of the circulatory system dominate the general morbidity structure of the adult population (17.4%), the second place is occupied by diseases of the musculoskeletal system (12.5%). The largest excess over the average Russian level on morbidity of the adult population is noted in the towns of Apatity and Kirovsk.

Studies of the 90s of the last century (Prasolov et al. 1991) during the operation of other water intakes located within the Khibiny massif recorded an increase in nitrate concentrations from 0.5 to 5–10 mg/l probably due to anthropogenic pollution. In this regard the laboratories of the A. P. Karpinsky Russian Geological Research Institute and the Leningrad Mining Institute conducted a study that showed that groundwater can be polluted by drainage waters from mines and sewage from settlements and industrial enterprises ("industrial sites" of mines). Presence of nitrates in mine waters is due mainly to the dissolution of remnants of explosives and their detonation products from the blasted rock mass ("technogenic" nitrates).

Table 44.6 The results of monitoring of surface waters of the river (1—r. Vuonnemyok, mouth; 2—r. Vuonnemyok) (Koashva village, bridge 13.09.09)

Sampling site	Concentration (mg/l)						
	Ca^{2+}	Mg^{2+}	Na^{+}	K^{+}	HCO_3^{-}	SO_4^{2-}	Al^{3+}
1	5.57	0.54	24.3	7.38	43.8	26.8	0.101
2	8.34	0.57	39.5	12.4	57.2	54.4	0.061
	Sr^{2+}	Fe	Cu^{2+}	NO_3^{-}	Cl^{-}	pH	
1	0.259	0.047	0.0009	2.72	2.72	7.76	
2	0.428	0.019	0.0012	4.15	2.34	7.85	

The appearance of nitrates in the wastewater of industrial sites is caused most likely by the oxidation of petroleum products—fossil organic matter. It was assumed that three "primary" sources of nitrates are contained in the studied water samples: technogenic, biogenic and background although directly contamination of natural (background) waters in the water intake area can be carried out by mixed waters. In work (Prasolov et al. 1991) it was assumed that the minimum nitrate concentration (0.3 mg/l) corresponds probably to the background value of the groundwater of the remote territory. The analysis of the nitrogen concentration obtained as a result of sampling of 2017 (Table 44.5) and surface water (Table 44.6) indicates their excess of background values and the need to identify sources of pollution.

In the work of Skalny (2004) not only 15 vitally important elements are listed, but their forms are also presented. "Among the 15 vital elements, nine are cations—calcium (Ca^{2+}), sodium (Na^{+}), potassium (K^{+}), magnesium (Mg^{2+}), manganese (Mn^{2+}), zinc (Zn^{2+}), iron (Fe^{2+}), copper (Cu^{2+}) and cobalt (Co^{2+}). Six others are anions or are contained in complex anionic groups, chloride (Cl^{-}), iodide (I^{-}), phosphate (PO_4^{3-}), sulfate (SO_4^{2-}), molybdate (MoO_4^{2-}) and selenite (SeO_3^{2-})". In the 1980–1990s a number of scientists have established the toxicity of aluminum for the aquatic environment and human. It is noteworthy that like for most metals the degree of toxicity depends on the form of aluminum in the aquatic environment. It is established that the greatest toxicity comes from so-called inorganic monomeric aluminum. Among its most toxic forms free (hydrated) ions or aqua complexes $[Al(H_2O)_6]^{3+}$ and hydro complexes $Al(OH)^{2+}$ and $Al(OH)_2^{+}$ which exist in a weakly acidic medium at pH 4.5–5.5 are noted (Linnik and Zhezherya 2013).

Analysis of the current situation indicates that the results obtained with the help of thermodynamic modeling are beyond the scope of medico-ecological research. Whereas currently many problems of geochemistry, hydrochemistry, chemical technology, application of geochemical barriers, ecology, etc. can be solved by thermodynamic modeling (Table 44.7).

When comparing the new results with the results of the studies carried out in 2011–2014, it is seen that the contents of $\delta^{18}O$ and $\delta^{2}H$ correspond to seasonal (autumn) changes in the concentrations of the studied isotopes, which possibly indicates the feeding of these waters with surface water sources. For a more accurate assessment, year-round monitoring of water intake data is needed.

Table 44.7 Results of isotopic analysis of the water intake "Predgorny" (Koashva village) in 2017

No.	Name	Sampling data	$\delta^{18}O$, ‰ SMOW	$\delta^{2}H$, ‰ SMOW
4	Water intake well #5	09.11.2017	−13.5	−99
5	Water intake well #2	09.11.2017	−13.5	−97
6	Water intake well #3	09.11.2017	−13.4	−99
7	Water intake well #4	09.11.2017	−14.2	−100
8	Water intake well #9	09.11.2017	−13.4	−99

44.4 Conclusions

Basing on the studies, it was found out that the chemical composition of rocks and surface waters influences formation of the chemical composition of groundwater from water intake "Predgorny" in Khibiny Alkaline massif area. Surface waters contain oxygen, nitrogen nitrates, chlorine, which affect pH (reducing them), forms of migration of aluminum, manganese, iron, and other elements.

It is shown that already in natural (pure) waters ratios of Ca/P and Ca/Sr can lead to bone diseases. In bones of humans and animals, approximately 70% is accounted for by hydroxyl apatite $Ca_5 (PO_4)_3OH$. OH^- group can be replaced by F, Cl, O. Calcium can be isomorphically replaced by a number of elements: Sr, U, Ba, and others, which can lead to diseases of bones and teeth (Kravchenko 1998). The research results can be useful in the fields of geochemistry, hydrology, ecology, and medicine. Changing the system of water treatment and nutrition, it is possible to reduce or avoid diseases of the musculoskeletal system.

Thus, ecological studies of drinking water, aimed at improving the methods of natural waters protection and water treatment are necessary to justify efficient managerial water management decisions, subordinate to the priorities of public health protection.

Acknowledgements The authors are grateful to Director General of "Apatityvodokanal" P. N. Yevshin and A. A. Gorbachev for their assistance in the implementation of the work.
The work was supported by the regional grant 17-45-510640 "Geochemical evaluation of groundwater of the Khibiny Massif (age and identification of the origin of groundwater, chemical composition, and forms of migration of elements).

References

Ananyev VN (2009) Springs land of Kola. The book. ed., Murmansk (in Russian)
Arzamastsev AA (1990) Alkaline ultramafites in the Khibiny massif: new data and petrological investigation In: Alkaline magmatism of the North-Eastern part of the Baltic shield. Publ. Kola scientific center an SSSR, Apatity (in Russian)
Arzamastsev AA (1994) Unique Paleozoic intrusions of the Kola Peninsula, Apatity (in Russian)

Arzamastsev AA, Ivanova TN (1985) Geology, conditions of formation and ore potential of the differentiated complex urtites, melteigites in the Khibiny mountains. In: Petrology and minerageny of alkaline, alkaline-ultramafic and carbonatite complexes of the Kola-Karelian region. Publishing house of the Kola branch of the Academy of Sciences of the USSR, Apatity (in Russian)

Chudnenko KV (2010) Thermodynamic modeling in geochemistry: theory, algorithms, software, applications. Akadem. Publishing house "Geo", Novosibirsk (in Russian)

Elpiner LI, Zektser IS (1999) The interdisciplinary approach to assessing the use of underground waters for drinking purposes. Water Resour 26(4):389–396

Gudkov AV et al (2014) Tritium-helium-3 method and its application to Dating of groundwater (on the example of the Kirov mining district, Murmansk region). Geokhimiya 5:1–8 (in Russian)

Gudkov AV et al (2015) Geochemical assessment of groundwater in the Khibiny rock massif. In: Proccedings of the IV Russian scientific conference with international participation, Moscow, WPI RAS, pp 360–362 (in Russian)

Ivanova TN et al (1970) Jolite-urtites of the Khibiny massif. "Nauka", Leningrad (in Russian)

Kalinnikov VT et al (2014) Physical-chemical factors of the substandard state of the chemical composition of natural waters of the Khibiny massif. Dokl Akad Nauk SSSR 458(5):551–554 (in Russian)

Konukhin VP et al (2012) Investigation of groundwater sources for water supply of cities of the polar region clean water on the example of the city of Apatity. Arct: Ecol Econ 2(6):58–65 (in Russian)

Kravchenko SM (1998) Calcium-phosphorus ratios in geochemical landscapes and its impact on human health. Geoecology 1:30–36 (in Russian)

Linnik PN, Zhezherya VA (2013) Aluminum in surface waters of Ukraine: content, forms of migration, features of distribution among abiotic components. Water Resour 40(2):165–178 (in Russian)

Mazukhina SI (2012) Formation of surface and underground waters of the Khibiny mountain massif. Publishing house of the Kola Science Centre of RAS, Apatity (in Russian)

Mazukhina SI (2016) Application of thermodynamic modeling in solving hydrological problems of the Kola North. Sci Notes Russ State Hydro-Meteorol Univ 42:33–54 (in Russian)

Mazukhina SI et al (2017) Forming chemical composition of surface waters in the Arctic. Case study of Lake Inari and river Paz. Vestnik of MSTU 20(1/1):252–260 (in Russian)

Onokhin FM (1975) Peculiarities of structure of the Khibiny massif apatite-nepheline deposits. "Nauka", Leningrad (in Russian)

Perelman AI (1989) Geochemistry, 2nd edn. High School, Moscow (in Russian)

Pozhilenko VI et al (2002) Geology of ore districts in the Murmansk region. In: Mitrofanov FP, Bichuk NI (eds) Publ Kola Science Center of RAS, Apatity (in Russian)

Prasolov EM et al (1991) Sources of nitrate contamination of the water intake of Kirovsk according to data on the isotope composition of nitrogen. Dokl Akad Nauk SSSR 316(5):1271–1276

Shpachenko KA, Zhirov DV (2003) Development of the geodynamic scheme (tectonic fractures) of the area of apatite mines of JSC "Apatit" (responsible executors). Research report under contract with the Mining Institute of KSC RAS. Archives of the Mining Institute of KSC RAS, Apatity (in Russian)

Skalny A (2004) Chemical elements in human physiology and ecology. Mir. Moscow (in Russian)

The program of integrated development of communal infrastructure systems of the municipal formation "The city of Kirovsk with its subordinate territory for the period 2011–2013 and for the future until 2020" (2016), Saint Petersburg (in Russian)

Topographic map (Russian Federation. Murmansk region. List №15—Revda). Scale 1:200000 (1993) (in Russian). https://www.google.ru/maps/. Satellite on-line map: Khibiny (Murmansk region)

Chapter 45
Heavy Metal Content in Soils and Hair of the Inhabitants Near Copper Zinc Mine (Bashkortostan, Russia)

Irina N. Semenova, Yuliya S. Rafikova, Rezeda F. Khasanova and Yalil T. Suyundukov

Abstract The aim of this study was to investigate the heavy metal content in the hair of children living near non-ferrous metal mines located in the urban settlements of Baymak, Sibay and Uchaly of the Republic of Bashkortostan, Russia, and in the soils obtained from the same area. The hair and soils samples were examined for the presence of the following metals: copper (Cu), zinc (Zn), iron (Fe), cobalt (Co), nickel (Ni), manganese (Mn), lead (Pb) and cadmium (Cd). The results of the study showed there to be increased levels of Cu (4.4-fold), Zn (7.9-fold) and Cd (2.5-fold) in soil samples which were exceeded the maximum permissible concentration (MPC). Mineral analysis of the hair samples was performed using a combination of atomic emission spectrometry and inductively coupled plasma mass spectrometry. Comparison of the data on hair from this study with the average reference data for Russia showed there to be an excess of Zn and Mn in the hair samples of the majority of the studied population: 50.0 and 48.8%, respectively. In addition, we observed an excess of Fe, Cu and Ni in a small number of children (23.3, 21.6 and 15.5% of the studied population, respectively). Deficiencies in Co and to a lesser extent in Zn, Cu, Fe, essential microelements for human health, were found in 55.2, 19.0, 19.8 and 15.5% of the studied population respectively. The results of this study could be used for biomonitoring of the extent of heavy metal burden in people living in contaminated areas.

Keyword Mining activities · Heavy metals · Hair children environmental biomonitoring

I. N. Semenova (✉) · Y. S. Rafikova · R. F. Khasanova · Y. T. Suyundukov
Institute for Strategic Studies of the Republic of Bashkortostan, Sibay, Russia
e-mail: alexa-94@mail.ru

I. N. Semenova · R. F. Khasanova · Y. T. Suyundukov
Sibay branch of Bashkir state University, Sibay, Russia

© Springer Nature Switzerland AG 2020

O. V. Frank-Kamenetskaya et al. (eds.), *Processes and Phenomena on the Boundary Between Biogenic and Abiogenic Nature*, Lecture Notes in Earth System Sciences,
https://doi.org/10.1007/978-3-030-21614-6_45

45.1 Introduction

The human body is constantly exposed to a variety of chemicals from natural and anthropogenic sources. The release of these chemicals from anthropogenic sources into ecological systems is on the rise due to rapid industrialisation and urbanisation in many regions of the world (He et al. 2005; Ghorani-Azam et al. 2016).

Heavy metals are a group of environmental chemicals that are ubiquitous and non-biodegradable. These metals are important for the biological function of plants, animals and humans, however at the toxic levels they pose a serious health threat (Kabata-Pendias 2007; Tchounwou et al. 2012; Wu et al. 2016; Ojuederie et Babalola 2017).

Mining activities are one of the major sources of heavy metal release into the environment causing great health risks on communities living near mines via the exposure to air-borne particles, soils and through the food-chain (Geen et al. 2012; Liu et al. 2013; Shao et al. 2013; Evrenoglou et al. 2017). Metal mining has been established in the Southern Urals and Bashkir Trans-Urals of the Republic of Bashkortostan since the beginning of the 20th century. Main mining and zinc (Zn) and copper (Cu) processing industries are located around the town of Uchaly which has a population of 37.4 thousand people. Since the discovery of the copper-pyrite ore deposit in 1930s, near Sibay (population 62.5 thousand), a branch of Uchaly's mining and processing plant was established near this town. Baymak, another key industrial town with a population of 17.53 thousand, houses the casting and mechanical plant.

The long-term mining of non-ferrous metals in these areas resulted in geochemical migration of toxic metals and their accumulation in the soils of the surrounding populated areas. It was shown that waste from active and abandoned mines located in the Republic of Bashkortostan are a permanent source of environmental pollution by a number of heavy metals such as Cu, Zn, Cd, Pb. These metals were found in the soil, snow cover and benthic sediments of technogenic water reservoirs at levels exceeding the maximum permissible concentrations (MPC) (Abdrakhmanov and Akhmetov 2013). These data show that in recent decades, the extraction of non-ferrous metals in the Southern Urals and the Bashkir Trans-Urals has led to the contamination of surrounding areas with toxic metals (Semenova et al. 2015, 2016), which could have had a significant negative impact on the health of the local population (Belan 2005; Rafikova et al. 2012; Semenova et al. 2018).

In comparison to adults, children are more susceptible to the adverse health effects of toxic environmental pollutants due to their small body size. As the endocrine and nervous systems are still developing in children, they are particularly vulnerable to toxic metal exposure. Exposure to these metals may result in illnesses of the neurological and endocrine. In addition to contaminated food and water consumption, children tend to be more exposed to environmental toxicants as a consequence of their outdoor activities which often result in dust inhalation, skin contact with soil and oral intake of soil.

Following the recommendation by the US Environmental Protection Agency (EPA), which was based on the completion of extensive studies (Jenkins 1979),

hair is now widely used as a biomatrix for detecting chronic toxic metal exposure (Grabeklis et al. 2011; Menezes-Filho et al. 2011; Gres et al. 2012; Reiss et al. 2015). Toxic metals become fixed in the protein structure of hair and as hair grows it continues to accumulate the metals with time. Therefore, hair serves as a better long-term indicator for variation in toxic metal accumulation or trace-element deficiency than blood or urine. Unlike blood, hair is less susceptible to homeostasis which alters the toxic metal levels. In addition, when compared to the traditional biological matrices such as urine or blood, the use of hair as a bioindicator of exposure has valuable advantages including simple and non-invasive sampling, inexpensive transportation and storage and high sample stability.

The main aim of this study was to determine the concentrations of a number of metals such as Cu, Zn, Fe, Co, Ni, Mn, Pb and Cd in the hair of children living in the towns Baymak, Sibay and Uchaly of the Southern Urals and Bashkir Trans-Urals of the Republic of Bashkortostan and compare the values to the concentrations of these metals in the soils obtained from the same locations. The study also looked at whether there was a correlation between the level of each contaminant measured in the hair samples and samples obtained from the soil to investigate whether hair samples could be deployed in environmental monitoring when measuring the levels of toxic metals.

45.2 Materials and Methods

45.2.1 Soil Sampling and Analysis

The study was conducted in the territory of Trans Ural of the Republic of Bashkortostan (Russia) in areas with the following coordinates: Baymak—52° 35′ 00″ N 58° 19′ 00″ E, Sibay—52° 42′ 00″ N 58° 39′ 00″ E, Uchaly—54° 19′ 00″ N 59° 23′ 00″ E (Fig. 45.1).

The climatic conditions of the study area are characterised as moderately continental.

The soils from the studied territory fall in the category of urban soils. According to the current World Reference Base for Soil Resources (WRB), there is the following classification of urban and industrial soils, depending on the type of substrate and the manner of modification by humans: (1) more-or-less natural soils; (2) natural soils heavily modified in situ by human activities; (3) young soils formed in natural materials displaced by human activity; (4) young soils formed from technogenic materials; (5) soils from displaced natural materials or technogenic materials, with significant pedogenesis since deposition (Rossiter, 2007). In our study, all groups of soils were present.

Sampling of the soils was carried out in dry weather condition, i.e. during the summer period, from the 0–10 cm layer at 18 sites in Baymak, 14 sites in Sibay and 30 sites in Uchaly. Each soil sample was air-dried in the laboratory, then passed through



Fig. 45.1 Locations of the study area:1—Uchaly, 2—Sibay, 3—Baymak

a nylon sieve with a pore diameter of ≤0.2 mm. The samples were then thoroughly mixed and homogenised prior to analysis for metals. For the determination of the total concentration of soil metals, including Cu, Zn, Fe, Mn, Ni, Cd, Pb and Co an inductively coupled plasma mass spectrometry (ICP-MS, Contr AA, Analytik Jena) was used. For each sample, 0.2 g of soil was digested with mixed with a solution of concentrated acids ($HF/HNO_3/HCl = 5:5:2$) and gradually heated in a microwave oven. Prior to analysis the digestion solution was filtered and then diluted with deionised water to a volume of 50 mL. Quality assurance (QA) and quality control (QC) were conducted by using reagent blanks, replicates, and standard reference materials. The standard stock solutions of Cu, Zn, Fe, Mn, Ni, Cd, Pb and Co were used at 1000 parts per million (Russia) to prepare the calibration standard solutions. As a reference, the state standard sample of metal solution was applied (SSSMS-7, Russia).

45.2.2 Hair Sampling and Analysis

Parents or legal representative of all the participants gave written consent prior to inclusion into the study, according to the decree of the Ministry of Health of the Russian Federation No. 1177 h, dated 20.12.2012.

The assessment of mineral composition in the hair samples was carried out in 116 children in total (56 boys, 60 girls; mean age 8.3 years, range 1–17 years). The sample size from each locations were as following: Baymak n = 30; Sibay n = 50; Uchaly n = 36. Hair removal from the children was done with the consent of the parents and within their presence. The hair samples were taken from the occipital

zone, placed into paper envelopes and stored in a dry place at room temperature. These samples were subjected to multielement analysis in the accredited testing laboratory of the Center for Biotic Medicine (Moscow, Russia, ISO 9001: 2008, certificate 54Q10077 dated 21.05.2010), using a combination of atomic emission spectrometry and inductively coupled plasma mass spectrometry (ISP-AES and ICP-MS) . This was done in accordance with the methodological guidelines 4.1.1482-03, 4.1.1483-03 approved by the Ministry of Health of the Russian Federation. Washing and decomposition procedures for hair analysis included immersion in acetone for 10–15 min followed by washing with water (thrice). 50 mg of hair was then digested with concentrated nitric acid (HNO_3), heated in a microwave oven, followed by dilution with deionised water to a volume of 15 mL prior to analysis. As a reference, a standard hair sample, GBW09101, manufactured by the Shanghai Nuclear Research Institute (PRC) was used.

45.2.3 Statistical Analysis

Descriptive measures were calculated for each of the metal values. The data are presented in the form: Mean (M),—standard deviation (S.D.),– median (Me), minimum (Min) and– maximum (Max). Assessment of the degree of metal contamination in the soil was carried out by comparing the level of metal content in the soil with the MPC (Maximum permissible concentrations … 2006), regional geochemical background (RGB) (Opekunova et al. 2001) and clarkes of chemical elements (the average content of a chemical element in the soil of the world) (Vinogradov 1962). Pearson's Chi^2 test was used to compare each urban settlement against each other by the degree of soil contamination from the toxic metals. Pearson's correlation analysis was used to investigate the possibility of co-occurrence of the metal at increased concentration in the soil.

Analysis of a distribution pattern of the absolute values of hair metal concentrations was performed using the Shapiro–Wilk test. For examination of the variation of toxic metal content in hair of the children, data obtained from each group of children living in Baymak, Sibay and Uchaly were compared against each other by the non-parametric Mann-Whitney U test. A pooled data approach was used for evaluation of the extent of contamination by the toxic metals in the hair of the studied children. In this case for each studied metal, the data from the hair of the children living in all three studied urban settlements were pooled and then compared to the published averaged data from Russia on hair for the same metal (Skalny 2003). Spearman rank-order correlation analysis was used to examine the relationship of the metals measured within the hair samples. Pearson's correlation analysis was used to compare the soil samples against the hair samples to determine whether contamination of hair samples with the metals correlated with the extent of metal contamination in the local soils. Statistica 6.0 software (StatSoft Inc., USA) was used for all data analysis.

45.3 Results

45.3.1 The Content of Metals in the Soils of the Study Area

In this study we examined the soils located near the mines of Baymak, Sibay and Uchaly for the content of the following heavy metals: Cu, Zn, Fe, Co, Ni, Mn, Pb and Cd. Our study showed that the concentrations of Cu, Zn, Mn and Cd in the soils were higher for this region when compared with the RGB (Table 45.1). When all the data obtained from the three locations were compared to the permitted MPC levels, it appeared that Cu in the soils from Uchaly Baymak, and Sibay had concentrations above the MPC level showing a 4.4-, 4.1- and 2.9-fold increase, respectively (Table 45.1). The second metal with a profound soil contamination was Zn showing 7.6-7.9-fold increase above the permitted MPC level for Baymak and Uchaly, respectively, while the content of Zn in soil from Sibay appeared to be within the MPC limit (Table 45.1). The third metal with a prominent increase in the soils was Cd, showing a 1.3-2.5-fold increase above the permitted MPC level for all three of the locations (Table 45.1). However, the concentrations of Ni, Mn and Pb in the soils from these towns were within the MPC limits. The concentrations of Fe in all of the studied soils did not show a prominent increase above the World soil reference, known as Clarke soil (Table 45.1).

To investigate, whether the locations Sibay, Baymak and Uchaly have different levels of soil contaminations with heavy metals, we compared each location against the other in relation to the levels of each studied metal. The results of this comparison showed that the levels of Cu, Fe, Mn in all three sample groups were similar. However, the concentrations of Ni and Pb were significantly higher in the soil samples from Sibay than in the samples from Baymak and Uchaly ($p = 0.001$). On the other hand, the levels of Zn in the soil samples from both Baymak and Uchaly, were higher than in Sibay ($p = 0.043$). Furthermore, the levels of Cd in the soils from Baymak and Sibay were higher than the soil from Uchaly ($p = 0.016$) and the levels of Co in the soils from Uchaly and Sibay were higher than in Baymak ($p = 0.018$).

Subsequently, Spearman rank-order correlation analysis was used to examine the relationship between the heavy metals in their distribution in the soil samples which were pooled for this method. The results of this analysis showed that the pairs of Zn–Cu, Fe–Cu, Zn–Fe, Mn–Fe, Ni–Fe, Pb–Fe, Cd–Fe, Co–Ni, Pb–Ni, Mn–Co, Pb–Cd, Pb–Co and Cd–Co had a high rank of positive correlation ($p < 0.05$), but the pairs of Pb–Zn demonstrated a negative relationship ($p < 0.05$) (Table 45.2).

45.3.2 Metal Concentration in Human Hair of Different Urban Settlements

The hair samples from the children living in the towns Baymak, Sibay and Uchaly were examined for the presence of the same metals measured in the soil samples as

Table 45.1 Metal concentrations of the soil samples collected in the towns of Baymak, Sibay and Uchaly, located in the Trans Ural region of the Republic of Bashkortostan. Corresponding MPC, RGB and Clark soil values are presented for comparisons

Settlements	M	S.D.	Me	Min	Max
Cu, MPC 55, RGB 49, Clark 47 (in mg/kg)					
Baymak, n = 18	225.1	239.3	170.6	49.0	1103.8
Sibay, n = 14	162.1	114.7	135.1	64.5	490.3
Uchaly, n = 30	243.3	299.9	150.3	18.3	1527.5
Zn, MPC 100, RGB 223, Clark 83 (in mg/kg)					
Baymak, n = 18	792.4	716.5	771.4	84.5	3285.0
Sibay, n = 14	279.0	118.6	233.5	93.3	486.5
Uchaly, n = 36	764.4	743.5	566.5	37.3	3630.0
Fe, Clark 46500 (in mg/kg)					
Baymak, n = 18	19083.8	2131.1	19363.8	14870.0	23655.0
Sibay, n = 50	19167.3	3182.1	18007.5	14870.0	23655.0
Uchaly, n = 36	28279.0	25093.4	16586.3	128.8	75875.0
Ni, MPC 85, RGB 58.7, Clark 58 (in mg/kg)					
Baymak, n = 18	10.2	11.3	7.7	2.8	52.3
Sibay, n = 50	45.6	16.0	44.0	25.3	71.3
Uchaly, n = 36	26.8	22.0	24.1	0.2	90.5
Mn, MPC 1500, RGB 525.4, Clark 690 (in mg/kg)					
Baymak, n = 18	977.3	232.5	982.1	558.0	1399.5
Sibay, n = 50	957.8	648.4	974.0	46.3	2005.0
Uchaly, n = 36	1251.9	980.2	1089.6	63.7	3562.5
Cd, MPC 2, RGB 1.5, Clark 0.13 (in mg/kg)					
Baymak, n = 18	4.7	1.7	4.6	1.1	8.5
Sibay, n = 50	5.1	3.1	4.7	1.4	10.3
Uchaly, n = 36	2.6	2.6	1.7	0.025	9.8
Co, the total content, RGB 16.2, Clark 12 (in mg/kg)					
Baymak, n = 18	9.5	4.3	8.9	4.5	17.3
Sibay, n = 50	25.5	7.7	25.3	12.0	36.8
Uchaly, n = 36	23.2	16.5	23.4	0.2	63.3

described above (Table 45.3). The non-parametric Mann-Whitney U-test was used for a comparative analysis of the population groups in relation to the levels of each studied metal. This comparison showed that the hair samples of the children from each location did not differ in the content of Cu, Ni, Mn, Cd, Co and Pb. However, the concentrations of Fe and Zn were elevated in the hair of the children from Sibay. In particular, the concentration of Fe in the hair samples of the children from Sibay were significantly higher than the levels measured in hair samples from the Baymak

Table 45.2 Correlation coefficients (r) between concentrations of metals of the soils from the towns of Baymak, Sibay and Uchaly, located in the Trans Ural region of the Republic of Bashkortostan (pooled data analysis; significant at the level of $p < 0.05$ is highlighted in bold)

	Cu	Zn	Fe	Ni	Mn	Pb	Cd	Co
Cu	1							
Zn	**0.69**	1						
Fe	**0.37**	**0.33**	1					
Ni	– 0.02	– 0.10	– 0.01	1				
Mn	0.23	0.15	**0.50**	0.18	1			
Pb	0.10	– **0.26**	**0.30**	**0.35**	0.09	1		
Cd	0.20	0.13	**0.32**	0.05	0.10	**0.41**	1	
Co	0.12	0.10	**0.49**	**0.42**	**0.42**	**0.42**	**0.24**	1

area ($p = 0.0118$). The levels of Zn were also significantly elevated in the hair of children from Sibay in comparison to the hair samples from the children from Uchaly ($p = 0.0203$; Table 45.3).

To investigate the relationship between different metal pairs in their accumulation in the hair, the Spearman rank-order correlation analysis was used on the pooled data from the three studied cities. This analysis showed, that there is a statistically significant positive correlation for a number of studied metal pairs presented in Table 45.4 ($p < 0.05$). Moreover, a negative linear correlation between the pairs Zn–Pb and Zn–Cd was observed in the pooled hair samples used in this study ($r = –0.53$, $r = –0.21$, respectively).

To establish the extent of toxic metal contamination in the hair of children in this study, we pooled the data from the three locations for each metal measured in the hair and compared this data set with the published averaged values on hair mineral composition for Russia (Skalny 2003). The results of this analysis are presented in Table 45.5. The results of this comparison revealed that hair samples from all the children in this study had higher levels of Zn and Mn than the average values observed for Russia.

Additionally, we evaluated the percentage of the population in the Bashkir Trans-Ural region characterised with exhibiting high values of contamination by each of the studied metals against the average levels for Russia. This showed that in comparison to the average reported levels for Russia, a significant excess of Mn and Zn was observed in the children from the study (48.0 and 50.0% respectively). Higher levels of Fe, Cu, Ni and Pb were observed in the hair of the examined children in comparison to the averages reported for the Russian population (23.3, 21.6, 15.5 and 6.9% respectively). However, when the levels of Co were compared to the average levels reported for the population of Russia, it appeared that 55.5% of the studied children had a deficiency of this essential micronutrient in their hair.

Table 45.3 The content of metals in the hair of the children from the towns of Baymak, Sibay and Uchaly, located in the Trans Ural zone of the Republic of Bashkortostan (in μg/g)

	Mean	S.D.	25%	Median	75%
Cu (8–12)[a]					
Baymak. n = 30	10.02	5.58	7.52	8.83	12.21
Sibay. n = 50	10.92	5.75	8.43	9.75	11.48
Uchaly. n = 36	10.52	2.89	8.67	10.81	11.49
Zn (94–183)[a]					
Baymak. n = 30	267.95	343.37	60.93	151.00	224.00
Sibay. n = 50	183.70	94.76	132.55	188.98	218.00
Uchaly. n = 36	129.74	54.78	94.54	120.00	159.00
Fe (13–27)[a]					
Baymak. n = 30	15.11	6.20	10.80	14.36	18.24
Sibay. n = 50	32.07	52.30	14.97	22.36	30.80
Uchaly. n = 36	19.61	9.63	11.95	17.34	25.63
Mn (0.32–0.93)[a]					
Baymak. n = 30	1.64	1.86	0.47	0.79	1.48
Sibay. n = 50	1.09	1.09	0.43	0.81	1.31
Uchaly. n = 36	0.91	0.65	0.53	0.75	0.93
Ni (0.15–0.55)[a]					
Baymak. n = 30	0.25	0.13	0.16	0.18	0.30
Sibay. n = 50	0.37	0.31	0.19	0.29	0.42
Uchaly. n = 36	0.30	0.21	0.16	0.18	0.44
Pb (0.76–2.73)[a]					
Baymak. n = 30	1.01	0.48	0.70	0.80	1.47
Sibay. n = 50	0.97	1.17	0.25	0.55	1.29
Uchaly. n = 36	0.92	0.64	0.41	0.96	1.29
Cd (0.03–0.18)[a]					
Baymak. n = 30	0.100	0.191	0.026	0.037	0.050
Sibay. n = 50	0.066	0.164	0.015	0.032	0.065
Uchaly. n = 36	0.039	0.035	0.019	0.030	0.037
Co (0.02–0.11)[a]					
Baymak. n = 30	0.09	0.14	0.01	0.01	0.04
Sibay. n = 50	0.03	0.05	0.01	0.02	0.03
Uchaly. n = 36	0.03	0.03	0.01	0.02	0.03

[a]The interquartile interval for the content of these chemical elements in the hair obtained in conducting population studies in various regions of the Russian Federation (reference values; Skalny 2003)

Table 45.4 Correlation coefficients (r) between concentrations of metals in hair from children of Baymak, Sibay and Uchaly in Trans Ural zone of the Republic of Bashkortostan (values with a significance of $p < 0.05$ are highlighted in bold -)

	Fe	Zn	Cu	Mn	Co	Ni	Pb	Cd
Fe	1							
Zn	−0.01	1						
Cu	**0.25**	−0.08	1					
Mn	**0.48**	0.01	**0.43**	1				
Co	**0.41**	0.09	**0.41**	**0.67**	1			
Ni	**0.39**	0.05	**0.44**	**0.44**	**0.59**	1		
Pb	**0.30**	**−0.53**	**0.40**	**0.48**	**0.34**	**0.27**	1	
Cd	**0.43**	**–0.21**	**0.46**	**0.58**	**0.41**	**0.42**	**0.77**	1

Table 45.5 The prevalence of deviations in the content of chemical elements in the hair of the children from the Trans Ural zone of the Republic of Bashkortostan[a]) in comparison with the average interquartile intervals for Russia (Skalny 2003)

Metal	Russian interquartile interval, μg/g		Bashkir Trans-Ural interquartile interval, μg/g		Deviation from the Russian interquartile interval, %		
Fe	13.0	27.0	14.4	28.2	15.5	61.2	23.3
Zn	94.0	183.0	113.0	216.6	19.0	31.0	50.0
Cu	8.0	12.0	8.5	11.5	19.8	58.6	21.6
Mn	0.32	0.93	0.43	1.31	14.7	44.0	48.0
Co	0.02	0.11	0.01	0.02	55.2	38.8	6.0
Ni	0.15	0.55	0.17	0.42	18.1	66.4	15.5
Pb	0.76	2.73	0.26	1.32	55.2	37.9	6.9
Cd	0.03	0.18	0.02	0.06	46.5	44.0	1.5

[a]Data was pooled from the measurements taken from children in the towns of Baymak, Sibay and Uchaly

45.3.3 Comparison of Metal Concentration in Human Hair to Soils

We investigated whether there was a clear correlation between the content of each metal in the studied soil samples and the concentration of the corresponding metal found in the hair samples obtained from children living in Baymak, Sibay and Uchaly where the soil samples were collected. Due to the small sample size in this study, we used a pooled data approach for both the soil sample data and the hair sample data. Pearson's correlation analysis was applied to these data sets. The comparison between Zn and Pb showed a negative linear correlation for both the hair and soil samples ($r = –0.53$ $r = –0.26$ respectively; $p < 0.05$), suggesting that the association

between Zn and Pb in the hair of the children could reflect the interplay of the metals in the soil.

However, the results of this comparative analysis did not show any significant correlation between hair contamination and t soil contamination by the other studied metals. This outcome could be due to the small sample s used in our study or due to a high regional variation in the accumulation of the metal contaminants in the soils and the human hair.

45.4 Discussion

Severe contamination of Bashkir Trans-Ural soils by toxic metals has been shown in a number of published reports (Abdrakhmanov and Akhmetov 2013; Belan 2005; Semenova et al. 2015, 2016, 2018). In particular, it was shown that the waste originating from one of the largest open Cu–Zn mines in Russia, located near the town Sibay, contained highly elevated levels of toxic metals which were spreading into the surrounding populated areas (Rafikova et al. 2012). Furthermore, the results of monitoring of the technological soil contamination of the Sibay region conducted by our laboratory in 2016 showed that according to the total pollution index (Zc) used in Russia, the total metal pollution was moderately hazardous, whilst the levels of toxic heavy metals appeared to be in the range of indicating it to be hazardous (Abakumov et al. 2016).

In the current study we examined the extent of accumulation of eight toxic metals, Cu, Zn, Fe, Mn, Ni, Co, Cd and Pb, in the soils obtained from Baymak, Sibay and Uchaly, towns located in the Bashkir Trans-Ural region. Our study showed that the soils obtained from these three locations were contaminated with Cu, Zn and Cd which exceeded the MPC), whilst Mn, Ni, Pb and Co appeared to be within the permissable levels. The content of Fe in the soil did not exceed the clark value for iron (Vinogradov 1962).

To find out whether the toxic metals from the soils of Baymak, Sibay and Uchaly were absorbed by the human body, we examined the mineral composition of the hair of the local children. The comparison of the pooled data obtained from the hair samples in our current study with the averaged data on the hair mineral content published for Russia, showed that the levels of Zn were excessively higher in 50% of the studied children. Similarly, we observed that Mn and Fe were also present at high levels in the studied population, 48.0 and 23.3% respectively. However, this comparative study showed that a lower proportion of the study participants had an excess of Ni and Pb, 15.5 and 6.9% respectively, than that reported for Russia.

Furthermore, in this study alongside with the high levels of heavy metals found the participants, a large proportion of children showed a deficiency in these metals in their hair in comparison to the averaged metal content in the hair of Russian population. For example, using this comparative approach we found that 55.2% of the studied children had deficiencies of Co, but a smaller proportion of participant had deficiency in Cu and Zinc, 19.8 and 19.0% respectively. The rest showed no

difference in the mineral content of their hair than values reported as the averaged figures for Russia for these three metals.

The deficiency of Co and Cu found in the hair of the studied children may reflect the deficit of these important for human health trace-elements in the whole body of these children. The deficit of Cu and Co could have negative consequences for the health of these children presently and in their future life. It is well established that Cu is a necessary microelement for hematopoiesis, immunity, tissue repair and that Co is a part of vitamin B12 which together with folate helps to prevent anemia. It has been shown that anemia is widespread in the studied area especially among infants (Nagaev 2004; Usmanova 2009). However, the exposure to harmful levels of heavy metals like Ni and Pb found in the hair of the studied children could be particularly damaging for their health in the longterm. Children exposed to toxic metals such as Ni and Pb throughout their lifetime will have a longer post-exposure period in comparison to adults which may increase their possibility of developing diseases with a long latency period such as cancer or Alzheimer's disease (Godt et al. 2006; Karri et al. 2016)

As it was mentioned above, of the study participants children's population had more Mn and Zn, 48.0 and 50.0% respectively, compared to the average Russian indicators. It is well known that Zn is an essential trace element involved in a multitude of vital processes in the human body including metabolism, signal transduction, gene expression and functioning of the immune system (Mamtani et al. 2011). However, research shows that zinc overload can lead to a deficiency of Cu which was also observed in the hair of a proportion of the study participants. Due to the competitive nature of Zn and Cu for absorption by human body, our findings may indicate that the children with elevated Zn levels could be at risk of Cu deficiency (Adelstein and Vallee 1961; Harris 2009). Similarly, the overload of Mn, detected in 48.0% of the studied group could cause Fe deficiency in a number of individuals since both metals have also been shown to compete for absorption in the intestine (Fitsanakis et al. 2009). However, in our study we did not observe significant Fe deficiency in the hair of children. On the contrary, our data showed an excess of Fe in the hair of 23.3% of the studied individuals. This overload of iron found in the hair of studied children could be due to an additive contribution of the local diet which traditionally consists of a high proportion of meat. An excess of iron in the body is particularly harmful, since iron is a prooxidative element that can cause adverse effects on the organism of young children including liver damage, diabetes or thyroid disease (Lönnerdal 2017). An increasing number of studies have reported adverse effects of iron overload due to diet supplementation of infants and young-children suffering from anemia (Lönnerdal 2017). These effects include decreased growth (both in height and weight), increased illness (e.g. diarrhoea), reduced levels of other trace elements such as Cu and Zn, altered gut microbiota to more pathogenic bacteria, increased inflammatory markers, and impaired cognitive and motor development (Collins et al. 2010).

The analysis of the relationship of accumulation of metals in the hair of the studied children, showed there to be positive correlations ($p < 0.05$) for a number of

metals which varied from the strong correlation for Cd–Pb ($r = 0.77$), to a moderate correlation for Co–Ni ($r = 0.59$), Co–Mn ($r = 0.67$), Mn–Cd ($r = 0.58$), Fe–Cd ($r = 0.56$), and Pb–Mn ($r = 0.58$) and a weak correlation for Cu–Fe ($r = 0.25$) and Pb–Fe ($r = 0.30$).

Cd and Pb in particular, showed a high positive correlation for their accumulation in the hair of the children. Increased concentrations of Cd and Pb, were found in a smaller proportion of the studied children, 1.5 and 6.9% respectively. Cd is a widespread toxic pollutant with diverse detrimental effects on humans due it's extremely prolonged biological half-life of up to 30 years in human., Its low rate of excretion has a diverse toxic effect on humans including nephrotoxicity, carcinogenicity, teratogenicity and endocrine and reproductive toxicities (Rani et al. 2013). Pb, a confirmed neurotoxin, is especially damaging to the young child and the developing fetus (Lanphear et al. 2005). However, to establish a robust tool for biomonitoring of the burden of Cd and Pb, more work needs to be done on investigating the dynamic of these metals in the population of Bashkir Trans-Urals.

In our study when the data on metal content in the hair samples were compared to the data obtained from the soil samples, we did not show any statistically significant correlation in the metal content between the hair of the studied population living in the same area as the soil samples were collected. This could suggest that a larger sample size is needed to establish a concomitant correlation between the two sample matrices.

However, in this study, a statistically significant negative correlation was established for the pair of Zn–Pb for both hair and soil samples ($r = –0.53$, $r = –0.26$ respectively; $p < 0.05$). The relationship found in our study between Zn and Pb showed a similar pattern previously established for the Zn–Cd pair for the European Northern part of Russia (Bakaeva and Eremeyshvili 2014) and for the rural settlements of Bashkir Trans-Urals (Semenova et al. 2018).

Our study suggests that the correlations of metal accumulation in human hair may also indicate the dynamics of these metals in the human body. Toxic metals once absorbed via the bloodstream reach their target organs and subsequently became eliminated via the excretion system through the kidneys, bile and the skin. However, as part of the body's defense mechanism a proportion of the metals are removed via storage in non-essential tissues such as fat and hair. Accumulation of metals is normally higher in hair than in vital body tissues or blood; therefore, hair could serve as an accurate monitor for recording human exposure to environmental pollutants such as toxic metals.

45.5 Conclusions

Taken together, our study showed the presence of elevated concentrations of the heavy metals in the soils and in the hair of children living in the towns in Baymak, Sibay and Uchaly of Bashkir Trans Ural region where the soil sample were taken from. In particular we found that the levels of Cu, Zn and Cd in the studied soils have

exceeded the MPC. Our study showed that the concentrations of Zn, Cu and Mn in the hair of the studied children were above the average levels of the metals found in the hair of the Russian population. In the hair samples, positive significant correlations were found between the following pairs of metals: Pb–Cd, Mn–Cd, Cd–Fe, Co–Mn, Co–Ni, Fe–Mn, Fe–Ni, Fe–Pb and Mn–Pb. A negative linear correlation between Zn–Pb was established for both the hair samples and soil samples. However, in our study we did not show any statistically significant correlations between the content of each individual metal in the children's hair with the corresponding metal content in the soil samples.

Thus, our results show that the natural and technogenic characteristics of the urban territory of Bashkir Trans Ural region predispose microelement imbalances in children. We did not find a positive correlation for each studied metal overload between the soil and hair samples. The results of this study could be used to analyse metal burden of the population in contaminated areas of Bashkorostan and could also serve as a reference for further studies.

Acknowledgements This publication has been supported by the Russian Foundation for Basic Research and the Government of the Republic of Bashkortostan, research projects no: 17-16-02002-OGN OGN-R_URAL-A and 18-413-020004 p_a. We thank Oluwatobiloba Oke, B.Sc. (Hons) for her comments and proofreading which greatly improved the manuscript.

References

Abakumov EV, Suyundukov YT, Pigareva TA, Semenova IN, Khasanova RF, Biktimerova GY, Rafikova YS, Ilbulova GR (2016) Biological and sanitary assessment of dumps of Sibay quarry of the Republic of Bashkortostan. Hyg Sanitation 95(10):929–934 (in Russian)

Abdrakhmanov RF, Akhmetov RM (2013) Geochemistry of rocks and ground water in the zone of influence of Semenovsk Gold Recovery Factory. The Ufimian Scientific Center, Institute of Geology, Ufa, pp 211–221 (in Russian)

Adelstein SJ, Vallee BL (1961) Copper metabolism in man. N Engl J Med 265(18):892–897. https://doi.org/10.1056/nejm196111022651806

Bakaeva EA, Eremeyshvili AV (2014) Ecological situation and microelement status of children (1–3 years) of the unurbanized territory of the European North of Russia. Ecol Hum 4:34–38 (in Russian)

Belan LN (2005) Medico-biological features of mining regions. Bull Orenburg State University 5:112–117 (in Russian)

Collins JF, Prohaska JR, Knutson MD (2010) Metabolic crossroads of iron and copper. Nutr Rev 68(3):133–147. https://doi.org/10.1111/j.1753-4887.2010.00271.x

Evrenoglou L, Partsinevelou AS, Nicolopoulou-Stamati P (2017) Correlation between concentrations of heavy metals in children's scalp hair and the environment. A case study from Kifissos River in Attica, Greece. Glob NEST J 19(4):592–600

Fitsanakis VA, Zhang N, Garcia S, Aschner M (2009) Manganese (Mn) and iron (Fe): interdependency of transport and regulation. Neurotox Res 18(2):124–131. https://doi.org/10.1007/s12640-009-9130-1

Geen A, Bravo C, Gil V, Sherpa S, Jack D (2012) Lead exposure from soil in Peruvian mining towns: a national assessment supported by two contrasting examples. Bull World Health Organization, 90(12), 878–886. https://doi.org/10.2471/blt.12.106419

Ghorani-Azam A, Riahi-Zanjani B, Balali-Mood M (2016) Effects of air pollution on human health and practical measures for prevention in Iran. J Res Med Sci 21:65. Published 2016 Sept 1. https://doi.org/10.4103/1735-1995.189646

Godt J, Scheidig F, Grosse-Siestrup C, Esche V, Brandenburg P, Reich A, Groneberg DA (2006) J Occup Med Toxicol 1(1) 22:1–6 https://doi.org/10.1186/1745-6673-1-22

Grabeklis AR, Skalny AV, Nechiporenko SP, Lakarova EV (2011) Indicator ability of biosubstances in monitoring the moderate occupational exposure to toxic metals. J Trace Elem Med Biol 25:S41–S44. https://doi.org/10.1016/j.jtemb.2010.10.014

Gres NA, Yuraga TM, Romanyuk AG, Hamad S, Sokol VP (2012) Comparative performance evaluation of informative biochemical and atomic-emission studies macro content of trace elements in blood, urine and hair of healthy and patients with urolithiasis. Lab Diagn Eastern Europe 4(04):62–72 (in Russian)

Harris ED (2009) Copper homeostasis: the role of cellular transporters. Nutr Rev 59(9):281–285. https://doi.org/10.1111/j.1753-4887.2001.tb07017.x

He ZL, Yang XE, Stoffella PJ (2005) Trace elements in agroecosystems and impacts on the environment. J Trace Elem Med Biol 19(2–3):125–140

Jenkins DW (1979) Toxic trace metals in mammalian hair and nails. U.S. Environmental Protection Agency, Las Vegas, Nevada, EPA-600/4-79-049

Kabata-Pendias A, Mukherjee A (2007) Trace elements from soil to human. Springer, Berlin, Heidelberg, p 561

Karri V, Schuhmacher M, Kumar V (2016) Heavy metals (Pb, Cd, As and MeHg) as risk factors for cognitive dysfunction: a general review of metal mixture mechanism in brain. Environ Toxicol Pharmacol 48:203–213. https://doi.org/10.1016/j.etap.2016.09.016

Lanphear BP, Hornung R, Khoury J, Yolton K, Baghurst P, Bellinger DC, … Roberts R (2005) Low-level environmental lead exposure and children's intellectual function: an international pooled analysis. Environ Health Perspect 113(7):894–899. https://doi.org/10.1289/ehp.7688

Liu G, Tao L, Liu X, Hou J, Wang A, Li R (2013) Heavy metal speciation and pollution of agricultural soils along Jishui River in non-ferrous metal mine area in Jiangxi Province, China. J Geochem Explor 132:156–163. https://doi.org/10.1016/j.gexplo.2013.06.017

Lönnerdal B (2017) Excess iron intake as a factor in growth, infections, and development of infants and young children. Am J Clin Nutr 106(Supplement 6):1681S–1687S. https://doi.org/10.3945/ajcn.117.156042

Mamtani R, Stern P, Dawood I, Cheema S (2011) Metals and disease: a global primary health care perspective. J Toxicol 2011:1–11. https://doi.org/10.1155/2011/319136

Maximum permissible concentrations (MPC) and tentative-permissible concentrations (TPC) of chemical substances in soil: Hygienic standards (2006), M.: Federal Center for Hygiene and Epidemiology, 15 pp (in Russian)

Menezes-Filho JA, Novaes CO, Moreira JC, Sarcinelli PN, Mergler D (2011) Elevated manganese and cognitive performance in school-aged children and their mothers. Environ Res 111(1):156–163. https://doi.org/10.1016/j.envres.2010.09.006

Nagaev RY (2004) Medical, social and hygienic features of the formation of iron-deficiency States in children living in the region with a developed mining industry, Ufa, 22 p. (in Russian)

Ojuederie O, Babalola O (2017) Microbial and plant-assisted bioremediation of heavy metal polluted environments: a review. Int J Environ Res Public Health 14(12):1504. https://doi.org/10.3390/ijerph14121504

Opekunova MG, Alekseyeva-Popova NV, Arestova IY, Gribalev SV, Krasnov DA, Bobrov DG, Osipenko OA, Solovyeva NI (2001) Heavy metals in soil and plants of the Southern Urals: ecological condition of reference territories. Vestnik of Saint Petersburg Univ 7(31):45–53 (in Russian)

Rafikova YS, Semenova IN, Seregina YY, Khakimzyanov OM (2012) Medico-ecological features of mining regions of the Trans-Urals of the Republic of Bashkortostan. Fundam Res 11(1):43–45 (in Russian)

Rani A, Kumar A, Lal A, Pant M (2013) Cellular mechanisms of cadmium-induced toxicity: a review. Int J Environ Health Res 24(4):378–399. https://doi.org/10.1080/09603123.2013.835032

Reiss B, Simpson CD, Baker MG, Stover B, Sheppard L, Seixas NS (2015) Hair manganese as an exposure biomarker among welders. Ann Occup Hyg 60(2):139–149. https://doi.org/10.1093/annhyg/mev064

Rossiter DG (2007) Classification of urban and industrial soils in the world reference base for soil resources. J Soils Sediments 7(2):96–100

Semenova IN, Rafikova YS, Khasanova RF, YT Suyundukov (2018) Analysis of metal content in soils near abandoned mines of Bashkir Trans Urals and in the hair of children living in this territory. J Trace Elem Med Biol 50:664–670. https://doi.org/10.1016/j.jtemb.2018.06.017

Semenova IN, Rafikova YS, Suyundukov YT (2015) The content of toxic metals in soil and human biosubstrates at the territories of some administrative regions of Bashkortostan, In the book: The role of soils in biosphere and human life. In: International scientific conference: to the 100th anniversary of the birth of academician G. V. Dobrovolsky, to the International Year of Soil. MAKS Press, Moscow, pp 110–112 (in Russian)

Semenova IN, Rafikova YS, Suyundukov YT, Biktimerova GY (2016) Regional peculiarities of microelement accumulation in objects in the transural region of the republic of Bashkortostan. In: Biogenic-abiogenic interactions in natural and anthropogenic systems lecture notes in earth system sciences. Switzerland, pp 179–187

Shao L, Xiao H, Wu D (2013) Speciation of heavy metals in airborne particles, road dusts, and soils along expressways in China. Chin J Geochem 32(4):420–429. https://doi.org/10.1007/s11631-013-0651-1

Skalny AV (2003) Reference values for concentration of chemical elements in hair, obtained by method of ICP-AES (Inductively coupled plasma—atomic emission spectroscopy). Microelements Med 4(1):55–56 (in Russian)

Tchounwou PB, Yedjou CG, Patlolla AK, Sutton DJ (2012) Heavy metal toxicity and the environment. EXS. 101:133–164

Usmanova RK (2009) Features of the clinical and hematological status in rural children, Ufa, 111 p. (in Russian)

Vinogradov AP (1962) The average content of chemical elements in the main types of igneous rocks of the Earth's crust. Geochemistry 7:555–571 (in Russian)

Wu X, Cobbina SJ, Mao G, Xu H, Zhang Z, Yang L (2016) A review of toxicity and mechanisms of individual and mixtures of toxic metals in the environment. Environ Sci Pollut Res 23(9):8244–8259. https://doi.org/10.1007/s11356-016-6333-x

Chapter 46
Modeling: The New Prospects of Studying Biological Systems as Illustrated by the Human Stomach

Svetlana I. Mazukhina, Konstantin V. Chudnenko, Pavel S. Tereshchenko, Svetlana V. Drogobuzhskaya and Stanislav V. Ivanov

Abstract Thermodynamic modeling was undertaken of the interactions between gastric juice and the mineral water sampled from the Marcial water well and spring in the vicinity of the city of Apatity. The study results make it possible to determine the migration forms of elements in the natural water—gastric juice system in a low and high acidity environment and the deposition conditions of the mineral phases that can be transported from the stomach to other organs and tissues. The physicochemical parameters (Eh and pH) of the studied gastric juice model were examined under normal conditions as well as deficient and excessive HCl. Important factors affecting the change in the gastric juice parameters are temperature and the intake of different mineral water varieties containing different concentrations of the individual elements. It was shown that, in stomach disorders, the transition of iron from the solution to the

S. I. Mazukhina (✉)
Institute of North Industrial Ecology Problems—Subdivision of the Federal Research Centre "Kola Science Centre of the Russian Academy of Sciences", 14 a, 184209 Akademgorodok, Apatity, Russia
e-mail: simazukhina@mail.ru

K. V. Chudnenko
Russia Federal State Budgetary Institution of Science A.P. Vinogradov Institute of Geochemistry SB RAS, 1 a Favoursky Str., 664033 Irkutsk, Russia
e-mail: vilyam@mail.com

P. S. Tereshchenko
Research Centre for Human Adaptation, Arctic—Branch of the Federal Research Centre, "Kola Science Centre of the Russian Academy of Science", 41a, 184209 Akademgorodok, Apatity, Russia
e-mail: tereshchenko_pash@mail.ru

S. V. Drogobuzhskaya
Tananaev Institute of Chemistry—Subdivision of the Federal Research Centre, "Kola Science Centre of the Russian Academy of Sciences", 26 a, 184209 Akademgorodok, Apatity, Russia
e-mail: Drogo_sv@chemy.kolasc.net.ru

S. V. Ivanov
Luzin Institute for Economic Studies—Subdivision of the Federal Research Centre, "Kola Science Centre of the Russian Academy of Sciences", 24 a, Fersmana Str., 184209 Apatity, Russia
e-mail: etostas@mail.ru

© Springer Nature Switzerland AG 2020

O. V. Frank-Kamenetskaya et al. (eds.), *Processes and Phenomena on the Boundary Between Biogenic and Abiogenic Nature*, Lecture Notes in Earth System Sciences,
https://doi.org/10.1007/978-3-030-21614-6_46

solid phase occurs, which may explain the anemic condition. A successful treatment of this condition requires restoring the acid-base parameters of the system. The study results complement the existing knowledge and open up new prospects of applying thermodynamic modeling methods to biological systems. An attempt was made to apply the thermodynamic modeling method to study the processes occurring in the human stomach.

Keywords Stomach model · Metabolism · Thermodynamic modeling · Mineral metabolism · Hyperacidity · Hypoacidity · Migration forms · Newly formed phases

46.1 Introduction

The link between fundamental non-medical sciences and medicine has existed for a long time. Intensifying the research effort in this area is especially important. This is explained by the increased anthropogenic impacts on the environment and humans due to the more intensive development of the mineral resources (Agadzhanyan et al. 2006).

In recent years, laboratory studies have shown the formation of inorganic mineral calculi in biological environments (Rosseeva et al. 2006, 2009; Izatulina et al. 2018). Modeling the human body in relation to the environment as an open system, to which the laws of physical chemistry apply (Kravchenko 1998), enables the use of the tools of chemical thermodynamics.

All body functions—metabolic processes, cellular respiration, the functioning of human organs and systems—depend on the quantitative and qualitative content in the human body of minerals, primarily delivered through the digestive system (Tereshchenko et al. 2017). There is a steady increase in the incidence of the gastrointestinal tract (GIT) diseases in Russia (Fig. 46.1).

According to monitoring data by the Federal Information Fund, average adult incidence rates of eating disorders and metabolic disorders (classified as diseases of the digestive organs—gastric and duodenal ulcers) in Murmansk Region, Russia, are above the national averages. Child incidence rates have been 30–40% above the national averages over the course of many years (Ministry of Natural Resources and

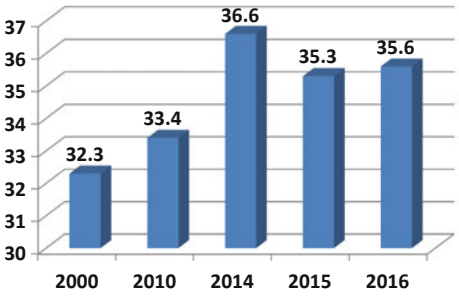


Fig. 46.1 Digestive system diseases in Russia (per 1000 residents), 2000–2016

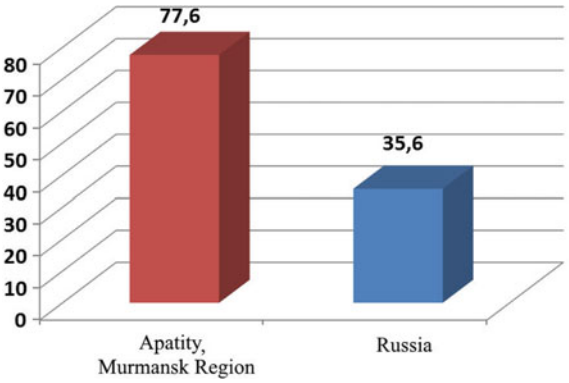


Fig. 46.2 Digestive system diseases in Apatity compared with the national averages (per 1000 residents), 2016

Ecology of the Murmansk region). In turn, metabolic disorders entail other disorders and diseases. The highest adult incidence rates exceeding the average national levels are observed in the Apatity and Kirovsk area and in the city of Apatity, where these indicators are more than twice the national averages (Fig. 46.2).

Of the factors that adversely affect the health of the residents of Murmansk Region with its developed mining and metals industry, pollution of drinking water sources is one of the primary. The toxic effects on the human body are due to the chemical nature of the elements, the number and composition of compounds, as well as the individual health condition (Moiseenko et al. 2010). Therefore, a vital task is to study the migration forms of elements in an aquatic environment, as these affect the penetration ability of pollutants and their toxicity to living organisms (Driscoll 1985; Linnik and Zhezherya 2013).

The most vital elements are cations: calcium (Ca^{2+}), sodium (Na^{+}), potassium (K^{+}), magnesium (Mg^{2+}), manganese (Mn^{2+}), zinc (Zn^{2+}), iron (Fe^{2+}), copper (Cu^{2+}), and cobalt (So^{2+}), as well as anions in the form of elements and complex anionic groups: chloride (Cl^{-}), iodide (I^{-}), phosphate ($PO_4{}^{3-}$), sulfate ($SO_4{}^{2-}$), molybdate ($MoO_4{}^{2-}$), and selenite ($SeO_3{}^{2-}$) (Skalny 2004).

The goal of this study is to examine the quantitative and qualitative composition of the solution—gastric juice system in the physiological environment of the human body using physicochemical modeling (software suite Selector). In this study, we chose to confined ourselves to the inorganic processes occurring in the human stomach. The study tasks included developing a model of gastric juice, studying the effect of HCl concentration on the stomach environment (Eh, pH), examining the mineral water—gastric juice system under the condition of high and low acidity.

46.2 Objects and Methods

The following published sources of data were used in this study: well 1—Marcial water (Borodulina and Mazukhina 2008), spring 1—sampling was carried out as part

of the research financed by the Russian Foundation for Fundamental Research grant 17-45-510640 p_a. (Mazukhina et al. 2018).

In the study of the elemental composition of the water, we applied the method of inductively coupled plasma mass spectrometry. A method has been developed for the simultaneous identification of trace elements in water by Institute of Chemistry and Technology of Rare Elements and Minerals, FRC KSC RAS. The measurements were carried out using an ICP-MS system fitted with a dynamic reaction cell (ELAN 9000 DRC-e, PerkinElmer SCIEX). The reference samples (CRM-TMDW-A, CWW-TM-A, CRM-SOIL-A) used in this study were collected from High-Purity Standards.

The main research method is the physicochemical (thermodynamic) modeling method implemented in the software suite Selector developed at the Vinogradov Institute of Geochemistry, Siberian Branch of the Russian Academy of Sciences, Irkutsk. The algorithm used (Chudnenko 2010) supports calculations of complex chemical equilibria in isobaric-isothermal, isochemical, and adiabatic conditions in multisystems with the simultaneous presence of an aqueous electrolyte solution, gas mixture, and solids. The software makes it possible to investigate both multicomponent heterogeneous systems and mega-systems composed of interacting interconnected systems connected with the environment by flows of matter and energy. In this study, the software suite is used to model the aqueous solution—inorganic substance system. A preliminary basic physicochemical model (PCM) was developed to study the formation processes of natural and anthropogenically modified waters and to characterize the migration forms of elements. This model included 34 independent variables and 996 interdependent variables, including 369 in the aqueous solution, 76 in the gaseous phase, 111 liquid hydrocarbons and solid phases, 440 organic and mineral substances. The solid phase set of the multisystem was chosen taking into account the mineral composition of the Baltic Shield rocks, since the groundwater in the study area originated from the shield and preserves the geological profile. The model used has shown its high performance in multiple earlier studies (Mazukhina 2012; Kalinnikov et al. 2013, 2014).

In thermodynamic modeling of natural systems, it is assumed that the processes under consideration have time to reach an equilibrium state faster than changes in the external state parameters and mass balance occur. For each modeling object, this condition has to be confirmed or the task has to be split into a series of subtasks with constant values of the external parameters and mass balance. In a real-world aqueous solution—solid precipitate system, the mass balance of the reacting components depends on the rate of chemical reactions occurring in the system. Four types of chemical reactions are typical of the modeled system:

(1) dissolution—precipitation of a solid in an aqueous solution,
(2) electrolytic dissociation—the association of the particles dissolved in the aqueous phase,
(3) oxidation—the reduction of the variable valence components of the aqueous solution,
(4) sorption—desorption (ion exchange) of the components between the solid (gas) and aqueous phases.

The electrolytic association—dissociation reaction rates in an aqueous solution in natural conditions can be assumed nearly instantaneous.

Redox reaction rates [without O_2 or H_2O and sorption—desorption (ion exchange)] are also quite high. Redox decomposition reactions of the organic matter or reactions in matched pairs involving O_2 or H_2O (e.g. $SO_4^{2-} \Leftrightarrow S^{2-}$), occur more slowly (the half-reaction period is from a day to years). In aqueous solution—solid precipitate systems, the dissolution reactions of most substances are slow (Ryzhenko et al. 2003).

In this study, Collector software was used for modeling the liquid phase—mineral solid phase system and the liquid phase—gas phase system. Prior to the study of the processes taking place in the stomach, information was collected from the existing literature on the chemical composition of the gastric juice, stomach volume and temperature. According to the literature, the main chemical components of the gastric juice are water (995 g/l), chlorides (5–6 g/l), sulfates (10 mg/l), phosphates (10–60 mg/l), sodium, potassium bicarbonates, calcium, magnesium (0–1,2 g/l), and ammonia (20–80 mg/l). The total concentration of sodium is 50 mEq/l, potassium 15 mEq/l, calcium 5 mg/l (Bochkov et al. 1999; Borodulin and Topolyansky 2007).

The stomach of an adult produces about 2 L of gastric juice daily. Baseline (i.e. during periods of rest, without stimulation by the intake of food, chemical stimulants, etc.) secretion in men is: gastric juice 80–100 ml/h; hydrochloric acid 2.5–5.0 mmol/h, pepsin 20–35 mg/h. In women, secretion is 25–30% less. Maximum hydrochloric acid production in men can reach 22–29 mmol/h, in women—16–21 mmol/h (Kolman and Rem 2000; Roitberg and Strutynsky 2007; Sapin and Bilich 2008; Feher 2012; Blanco and Blanco 2017a, b; Prives et al. 2017).

Based on an analysis of the available information, the following assumptions were formulated and adopted: the stomach contains, mg: 5.03 Ca, 1160 Na, 590 K, 3.18 P, 5000 HCl, 1200 H_2CO_3, 10 SO_4^{2-}, 80 NH_4OH. Water content 993 g, average organ temperature +38 °C, pressure 1 bar.

46.3 Results and Discussion

The presence of acid in the gastric juice had been disputed for centuries until in 1826, William Beaumont demonstrated this. The rate of gastric acid secretion is known to be variable. This is a regulated process controlled by the intake of food, emotional state, and other factors. Schmidt and Bojko (1999) demonstrated that the smell, appearance, and taste of food stimulate the secretion of acid in the stomach and found that the central nervous system (CNS) plays an important role in the initial stage of acid secretion.

The volume of an average empty stomach is approximately 500 ml. After the intake of food, it usually expands to 1 L, but can expand to up to 4 L. Carbohydrates, ethanol, water, and some salt solutions (copper, molybdenum, fluorides, iodides) are absorbed in the stomach. The human stomach produces up to 2 L of gastric juice daily. The contents of the stomach can reside in it from 20 min (fruit juices, vegetable

juices, and broths) to 6 h (pork) (Sapin and Bilich 2008; Blanco and Blanco 2017a, b).

No biological processes exist that do not involve water in one way or another. According to (Blanco and Blanco 2017a, b), water makes up a major share of the total human body weight—65% of the body weight of an adult. Water is found intracellularly and extracellularly. Daily human intake of water is approximately 2500 ml: 1400 ml as drinks, 800 ml from solid food, and 300 ml formed as a result of metabolic reactions. Daily excretion of water can reach 1500 ml with the urine, 150 ml with the feces, and 850 ml through the skin and lungs.

In assessing the physiological effects of the mineral composition of water, the role and importance of the ionic composition—anions (hydrocarbonates, chlorides, sulfates) and cations (sodium, calcium, magnesium and potassium)—should be stressed. Bicarbonates are known to inhibit acid formation in the stomach (the first phase of the medicinal action of a mineral water). Reacting with gastric juice, they form carbon dioxide (the second phase), slightly stimulating gastric secretion. Neutralization of the acidic secretory products of the stomach causes emptying of the stomach and a decrease in gastrin secretion; therefore, bicarbonate mineral water intake is recommended when an elevated level of acid production, spasms, or hyperacidity have been confirmed. Mineral water intake is also recommended to patients with diabetes mellitus, since the water improves carbohydrate metabolism and normalizes the acid-base balance in the body. The favorable effect of the water on nucleic acid metabolism supports the practice of prescribing it in uric acid diathesis. At ingestion, chlorine ion stimulates the secretory and motor function of the stomach, bile secretion and pancreatic secretion, and kidney function. Chloride water is recommended in chronic gastritis with secretory insufficiency, and in a number of other diseases of the digestive tract (colitis, enterocolitis, cholecystitis, hepatitis, etc.). Sulfates in mineral waters are found in the form of calcium, sodium, magnesium sulfates. Sulfate mineral water has a beneficial effect on the functional state of the liver, primarily by supporting the function of hepatocytes, improves gallbladder motility, improves cholesterol metabolism and protein metabolism. It enhances intestinal absorption, motility and secretion, resulting in a laxative action. Sodium plays an important role in the regulation of water metabolism and osmotic pressure in tissues, has a stimulating effect on the secretory function of the digestive glands, enhances intestinal motility and stimulates bile formation and bile secretion in the digestive system. Potassium ion activates a number of enzymes, improves stomach and intestines tonus and motor function, participates in glycogen synthesis in the liver. The beneficial effect of magnesium on the functional state of the hepatobiliary system is associated with its choleretic action and its ability to reduce cholesterol levels in the blood and bile. Solutions of magnesium salts catalyze the activity of a number of enzymes in the digestive tract (trypsin) and reduce the excitability of the central nervous system, resulting in a laxative action. In diseases of the digestive system, the intake of mineral water containing calcium is recommended, whose therapeutic effect is largely based on its antispasmodic properties. Calcium's calcium binding properties and its analgesic effect also play a certain role. Therefore, calcium-containing mineral water activates

enzymes, reduces the permeability of cell membranes, prevents the formation of exudates, and promotes diuresis.

Medicinal waters, in addition to the primary ions, contain trace elements, which largely determine the action of the given mineral water (Deinega et al. 2014). Table 46.1 presents the monitoring data and models of the water from spring 1 (Mazukhina et al. 2012, 2018), Marcial water from well 1 (Borodulina and Mazukhina 2008), and gastric juice (Bochkov et al. 1999; Borodulin and Topolyansky 2007).

A comparison of the monitoring and modeling data of the presented systems indicates differences in pH and Eh values and element concentrations. Attention should be paid to the content and chemical forms of iron in the spring 1 and in the Marcial well. The concentration of iron in the spring 1 is rather low and it is found in hydrated form with an oxidation state of +3 (since there is oxygen in the system).

Table 46.1 Water models of the spring 1 and Marcial well 1

Parameter	Spring 1		Marcial waters		Gastric juice	
	MD	MR	MD	MR	MD	MR
pH	8.22	8.50	6.44	6.44	–	1.23
Eh, V	–	0.748	–	−0.103	–	0.092
Ca (mg/l)	34.3	32.4	24.6	24.4	5.03	5.03
Na	6.01	6.00	2.31	2.29	1160	1160
K	4.19	4.19	2.40	2.39	590	590
Mg	4.98	4.76	12.8	11.5	–	–
Fe	0.076	7.64E–02	13.0	13.0	–	–
Fe^{2+}	–	9.05E–14	–	12.3	–	–
$Fe(OH)_3$	–	1.00E–02	–	1.23 E–04	–	–
$Fe(OH)_4^-$	–	6.36E–03	–	8.14 E–07	–	–
$FeSO_4$	–	1.76E–13	–	1.92	–	–
FeO_2^-	–	2.26E–03	–	2.86 E–07	–	–
$HFeO_2$	–	1.01E–01	–	1.25 E–03	–	–
FeO^+	–	4.03E–03	–	4.37 E–03	–	–
P	–	5.50E–03	0.14	0.14	3.18	3.18
Cl^-	0.52	0.52	0.86	0.86	5000	4950
HCO_3^-	104.4	1.34E+02	80.3	83.14	–	0.005
O_2	–	3.23	–	–	–	–
CO_2	–	1.03	70.3	67.9	–	353
H_2S	–	–	–		–	3.19
CH_4	–	–	–		–	13.9
SO_4^{2-}				67.15	–	

MD monitoring data; *MR* modeling results

In the Marcial waters, the iron content is 2 orders of magnitude higher and it mainly migrates in the 2-valent form, precisely in the form that is absorbed by the human body, as shown by earlier studies (Skalny 2004).

Table 46.2 shows the migration forms of aluminum in the Marcial waters (well 1) and in the spring 1 in Apatity. Data analysis indicates that in the Marcial water, the concentrations of the 5 chemical forms of aluminum are within the same order of magnitude, whereas in the spring 1, there is a large variation in concentrations for the different migration forms and $Al(OH)_4^-$. According to Linnik and Zhezherya (2013), aluminum forms $Al(OH)^{2+}$ and $Al(OH)_2^+$ are considered the most toxic to humans.

Table 46.3 presents the modeling results of the interaction of 100 ml of gastric juice with the Marcial water at a change in the volume of water from 10 to 1000 ml (T + 38 °C, P—1 bar).

Data in Table 46.3 shows that the concentration of Fe^{2+} in the system increases with the introduction of up to 180 ml of the Marcial water, after which the new phase FeS_2 forms and the fraction of Fe^{2+} in the solution decreases, which is accompanied by a change in the values of Eh and pH. Iron is a trace element necessary for the normal functioning of the human body, is a component of hemoglobin and respiratory enzymes (cytochromes), carries oxygen, and takes part in the oxidative processes. Iron deficiency results in anemia, damage to the skin and its derivatives (hair and nails) (Gasche 2013).

Attention should be paid to the change in the chemical forms of aluminum in the gastric juice—Marcial waters system dominated by the Al^{3+} ion and its proportion increases as the added water volume increases. Aluminum is known to stimulate the growth of bone tissue, as well as the development of epithelium and connective tissue. This metal is directly involved in the recovery and regeneration processes and promotes the activity of digestive glands and enzymes. Different cell types contain different amounts of the element; everything depends on the place of residence, but it is absolutely certain that the cells of the liver, brain, and bones accumulate it faster than other tissues (Tutelyan et al. 2001). Aluminum causes inhibition of gastric secretion as a negative side effect, reducing acidity. According to Vignal et al. (2016), aluminum accumulates in the intestinal mucosa, affects the regulation of intestinal permeability, microflora, and the immune function, which may cause constipation.

Table 46.2 Migration forms of aluminum

Marcial waters (T +5.8 °C; Eh 0.194; pH 6.44)								
Chemical form	AlO_2^-	$HAlO_2$	$Al(OH)^{2+}$	$Al(OH)_2^+$	$Al(OH)_3$	$Al(OH)_4^-$	$AlSO_4^+$	Al^{3+}
C, mg/l	9.19E–03	2.74E–02	1.13E–02	2.55E–02	1.99E–02	1.53E–02	8.30E–05	9.21E–04
Spring 1 Apatity (T +3 °C; Eh 0.748; pH 8.50)								
Chemical form	AlO_2^-	$HAlO_2$	$Al(OH)^{2+}$	$Al(OH)_2^+$	$Al(OH)_3$	$Al(OH)_4^-$	$AlSO_4^+$	Al^{3+}
C, mg/l	1.41E–02	4.39E–04	2.06E–08	1.15E–06	3.06E–04	2.42E–02	1.49E–13	1.76E–11

Table 46.3 Modeling results of interaction of 100 ml gastric juice with Marcial waters (from 10 to 1000 ml), (C, mg/l)

V_{H2O}, ml	Na^+	$Al(OH)^{2+}$	Al^{3+}	Fe^{2+}	$FeCl^+$	NH_4^+
10	1.03E+03	4.07E–07	1.27E–03	1.12	8.72E–02	7.31E+01
20	9.67E+02	9.16E–07	2.59E–03	1.88	1.39E–01	6.83E+01
30	8.66E+02	2.10E–06	5.12E–03	3	2.04E–01	6.11E+01
60	7.31E+02	4.80E–06	9.36E–03	4.52	2.70E–01	5.14E+01
100	5.72E+02	1.19E–05	1.68E–02	6.32	3.10E–01	4.01E+01
180	4.13E+02	2.73E–05	2.56E–02	6.98	2.58E–01	2.89E+01
320	2.77E+02	5.89E–05	3.28E–02	3.92	1.03E–01	1.92E+01
560	1.75E+02	1.28E–04	3.79E–02	1.54	2.71E–02	1.21E+01
1000	1.06E+02	3.04E–04	4.14E–02	0.246	2.77E–03	7.28E+00
V_{H2O}, ml	H_2S	CO_2	CH_4	Cl^-	Eh, V	pH
10	5.20E+00	3.45E+02	1.40E+01	4510	0.0893	1.28
20	6.56E+00	3.39E+02	1.42E+01	4210	0.0875	1.308
30	8.62E+00	3.29E+02	1.44E+01	3770	0.0845	1.354
60	1.15E+01	3.14E+02	1.47E+01	3180	0.0797	1.427
100	1.49E+01	2.93E+02	1.51E+01	2490	0.0727	1.535
180	1.70E+01	2.68E+02	1.56E+01	1790	0.063	1.685
320	1.44E+01	2.42E+02	1.61E+01	1200	0.0509	1.875
560	1.22E+01	2.15E+02	9.25E+00	754	0.0377	2.112
1000	1.11E+01	1.93E+02	8.56E–01	454	0.0264	2.418
	Composition of formed new phases, mole					
V_{H2O}, ml	FeS_2		SiO_2			
180	5.96E–06		–		–	–
320	4.39E–05		–		–	–
560	1.12E–04		5.87E–09		–	–
1000	2.28E–04		2.16E–09		–	–

The findings indicate that the intake of small amounts of mineral water provides the body with vital elements in the most available form.

Table 46.4 presents the modeling results of the interaction of 100 ml of gastric juice with the water from the spring 1 at a change in the volume of water from 10 to 1000 ml.

The data in Table 46.4 indicates that in the gastric juice—spring water system, iron is present mainly as Fe^{2+} and aluminum as Al^{3+}, the solid phase is absent, the concentration of H_2S is lower, and pH and Eh values are close to those when recorded when the gastric juice interacted with the Marcial water (Table 46.3).

We examined the change in the parameters of the water—gastric juice system at deficient and excessive HCl. Figure 46.3 shows changes in the pH and Eh values of the gastric juice depending on the concentration of Cl^-.

Table 46.4 Modeling results of the interaction of 100 ml of gastric juice and the water of the spring 1 at T +38 °C, (C, mg/l)

V_{H2O}, ml	Na^+	$Al(OH)^{2+}$	Al^{3+}	Fe^{2+}	$FeCl^+$	Sr^{2+}
10	1.03E+03	1.56E–07	4.95E–04	4.70E–03	3.65E–04	1.51E–02
20	9.67E+02	2.62E–07	7.52E–04	7.79E–03	5.79E–04	2.61E–02
30	8.67E+02	4.91E–07	1.22E–03	1.33E–02	9.09E–04	4.27E–02
60	7.32E+02	9.73E–07	1.92E–03	2.02E–02	1.22E–03	6.48E–02
100	5.74E+02	2.08E–06	3.02E–03	3.17E–02	1.56E–03	9.11E–02
180	4.16E+02	5.49E–06	5.20E–03	4.30E–02	1.63E–03	1.18E–01
320	2.80E+02	1.33E–05	7.40E–03	5.37E–02	1.47E–03	1.41E–01
560	1.78E+02	3.23E–05	9.66E–03	6.21E–02	1.13E–03	1.58E–01
1000	1.10E+02	8.11E–05	1.13E–02	6.77E–02	7.83E–04	1.70E–01
V_{H2O}, ml	H_2S	CO_2	CH_4	Cl^-	Eh, V	pH
10	2.99	2.45E+02	1.19E+01	4.50E+03	0.089	1.270
20	2.95	2.36E+02	1.13E+01	4.20E+03	0.087	1.297
30	2.88	2.21E+02	1.03E+01	3.76E+03	0.085	1.343
60	2.79	2.01E+02	8.93E+00	3.17E+03	0.081	1.414
100	2.69	1.76E+02	7.15E+00	2.48E+03	0.074	1.521
180	2.58	1.51E+02	5.21E+00	1.79E+03	0.066	1.666
320	2.49	1.28E+02	3.40E+00	1.20E+03	0.055	1.854
560	2.42	1.11E+02	1.96E+00	7.53E+02	0.042	2.091
1000	2.37	9.91E+01	9.54E–01	4.54E+02	0.025	2.391

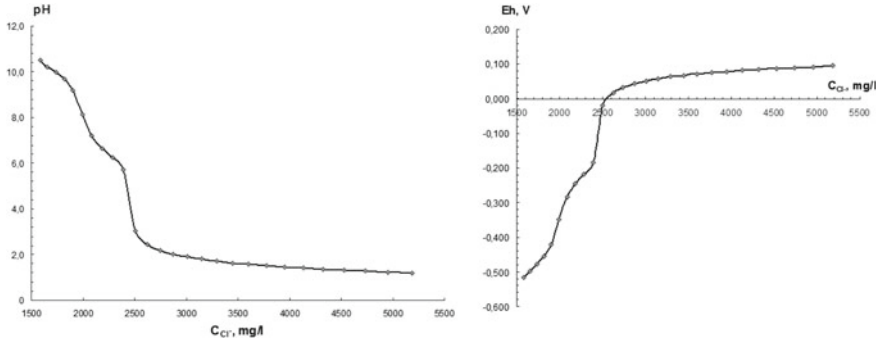


Fig. 46.3 Changes in the pH and Eh values of the gastric juice depending on the concentration of Cl^-, mg/l

Figure 46.4 shows changes in the stomach contents with an increase in the Marcial water content in the stomach from 10 to 1000 ml and initial pH 2.02 and Eh 0.0438 V, matching the normal acidity of the human stomach.

The findings indicate that the amount of water in the stomach affects the change in the Eh, pH of the solution, concentration, chemical forms of the elements, and the formation of solid phases. At a water content of 180 ml in the stomach, the values of Eh and pH change and the redox barrier is activated. The decrease in the iron content in the solution is explained by the potential formation of the solid phase FeS_2. There is a change in the chemical forms of aluminum Al^{3+}, $Al(OH)^{2+}$, $Al(OH)_2^+$ and concentrations thereof. At a water content of 560–1000 ml, montmorillonite (Mnt), amorphous silica (SiO_2), and apatite (Apt) may form. The main form of phosphorus migration in the form of H_3PO_4 is observed at a water content in the stomach of 10 to 30 ml and a concentration of 5–3.92 mg/l. With an increase in the volume of water in the system, the anion $H_2PO_4^-$ becomes the predominant form and its concentration decreases from 4 to 0.65 mg/l with an increase in the volume of water from 10 to 1000 ml. The concentration of monohydrogen phosphate HPO_4^{2-} varies from 4.81×10^{-5} to 3.51×10^{-2} mg/l. The maximum content of phosphate ion was recorded at 1.95×10^{-8} mg/l with 1000 ml of water only. At the same time, CO_2, H_2S, and CH_4 are observed in the system. Figure 46.4 shows the change in the concentration of the ion HCO_3^-.

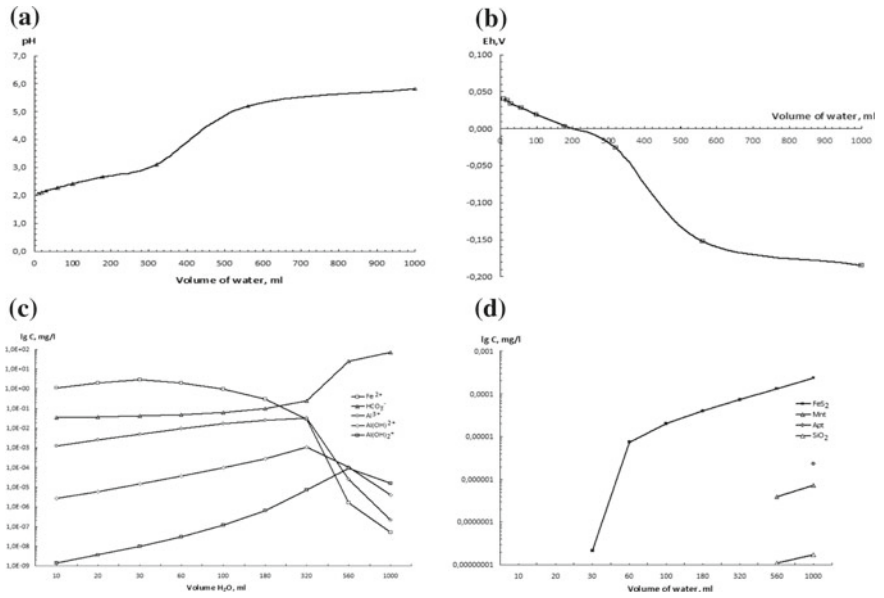


Fig. 46.4 Changes in the parameters of the system pH, Eh, and concentrations of chemical forms of iron and aluminum at a change in the Marcial water volume in the system, gastric juice volume 100 ml, T +38 °C, P 1 bar

Figure 46.5 shows changes in the stomach parameters with increasing spring water content in the stomach (from 10 to 1000 ml), with initial pH 6.24, Eh −0.218 V. As the results demonstrate, pH and Eh values change only slightly, but there is a decrease in the concentrations of aluminum forms $Al(OH)^{2+}$, AlO_2^-, $HAlO_2^+$, $Al(OH)_3$, $Al(OH)_4^-$ and new solid phases form containing aluminum—mixed-layer aluminosilicates (smectites, illites). The formation of FeS_2 leads to an extremely low Fe^{2+} content in the solution (1.0×10^{-7} mg/l), the formation of apatite reduces the concentration of other chemical forms of phosphorus, since the concentration of $H_2PO_4^-$ varies from 3.52 to 0.0256 mg/l when the volume of water changes from 10 to 1000 ml.

Solid phases may form outside the stomach and be transported from the stomach to other organs and tissues. For instance, the formation of apatite in a biological environment was observed earlier (Izatulina et al. 2018).

As shown, at excessive concentrations of aluminum in the system, the metabolism of phosphorus and calcium fails, osteoporosis and many other diseases of the musculoskeletal system develop. In some cases, aluminosis can arise, i.e. abnormalities in the lung tissue leading to persistent cough, pain (especially in the stomach), weight loss, constipation, poor digestion, and even changes in the blood count. Kidney function is also impaired, which leads to a risk of renal gravel development, and

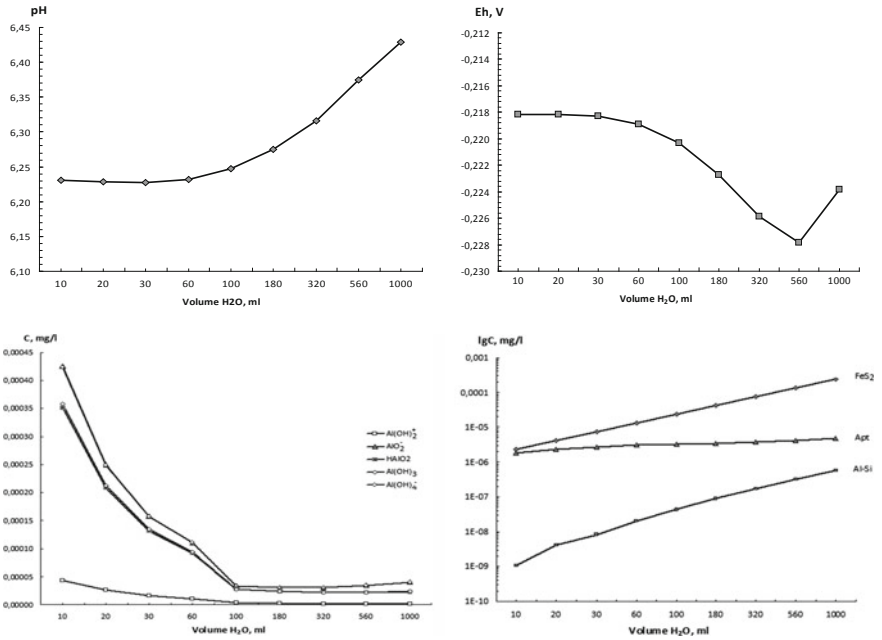


Fig. 46.5 Changes in system parameters pH, Eh, concentrations of aluminum forms in the solution, and the formation of solid phases (FrS_2, Apt—apatite, Al–Si—mixed-layer aluminosilicates, mol) when the volume of spring water in the system changes, gastric juice volume 100 ml, T +38 °C, P 1 bar

iron absorption suffers, resulting in a compromised immune system and metabolic deficiencies (Tutelyan et al. 2001). According to the recent research, aluminum may cause mutations and diseases such as Alzheimer disease, autism, bone diseases, skin cancer, and embryotoxicity (Yokel 2016).

46.4 Conclusions

The physicochemical modeling method allowed to:

- estimate the Eh and pH values of the gastric juice model,
- show the change in the Eh, pH values of the gastric juice model at deficient and excessive HCl,
- examine the migration forms of elements in the natural water—gastric juice system in a low and high acidity environment and the deposition conditions of the mineral phases that can be transported from the stomach to other organs and tissues,
- it was shown that, in stomach disorders, the transition of iron from the solution to the solid phase occurs, which may explain the anemic condition (a blood disease). To address this problem, the acid-base balance of the system needs to be restored,
- this study opens up prospects for examining the effect of concentrations of individual elements, water temperature and type on changes in the gastric juice,
- this study's findings may be relevant to and used in subsequent studies in the fields of geochemistry, hydrology, ecology, medicine.

Acknowledgements The study was carried out with the financial support of RFBR and the Ministry of Education and Science of Murmansk Region as part of the research project 17-45-510640 p_a "Geochemical examination of the groundwater in the Khibiny Mountains (dating, identification of the origin, chemical composition, migration forms of the elements)".

References

Agadzhanyan N et al (2006) Human ecology in a changing world. UB RAS, Ekaterinburg (in Russian)

Blanco A, Blanco G (2017a) Medical biochemistry. Academic Press

Blanco G, Blanco A (2017b) Medical biochemistry. chapter 12: digestion absorption. Academic Press

Bochkov N et al (1999) Directory of general practitioner. In: Paleev NR (ed) EKSMO-Press, in 2 tomes. tome 2 (in Russian)

Borodulin V, Topolyansky A (2007) Directory of practitioners. In: Vorobiev AI (ed) Book 2 (in Russian)

Borodulina GS, Mazukhina SI (2008) Physical-chemical modeling of chalybeate mineral waters composition. In: Ecological problems of the Northern Regions and ways to their solution: proceeding of the Russian scientific conference with international participation, Apatity. KSC RAS. Issue 1, pp 184–188 (in Russian)

Chudnenko K (2010) Thermodynamic modeling in geochemistry: theory, algorithms, software, applications. Akadem publishing house "Geo", Novosibirsk (in Russian)
Deinega B et al (2014) Physiotherapy and rehabilitation in the practice of a family doctor. Tutorial, Zaporizhzhia (in Ukrainian)
Driscoll CT (1985) Aluminum in acidic surface waters: chemistry, transport and effects. Environ Health Perspect 63:93–104
Feher J (2012) The stomach. Quantitative human physiology an introduction
Gasche C (2013) Iron physiology and pathophysiology in humans. Gastroenterology 144(2):464–465. https://doi.org/10.1053/j.gastro.2012.12.019
Izatulina AR et al (2018) Bacterial mechanisms of pathogenic crystallization in the human body. In: VI international symposium on biogenic—abiogenic interactions in natural and anthropogenic systems. VVM publishing Lld, Saint Petersburg, p 21
Kalinnikov V et al (2014) Physical-chemical factors of defect of chemical composition of the Khibiny massif natural waters. DAN 458(5):551–554 (in Russian)
Kalinnikov V et al (2013) Features of "oil-water" interaction in sea and fresh waters. DAN 449(5):535–538 (in Russian)
Kolman Ya, Rem K (2000) Visual biochemistry: trans from germ Mir (in Russian)
Kravchenko SM (1998) Calcium-phosphorus ratios in geochemical landscapes and its impact on human health. Geoecology (1):30–36 (in Russian)
Linnik PN, Zhezherya V (2013) Aluminum in the surface waters of Ukraine: content, migration forms, features of distribution among abiotic components. Water Resour 40(2):165–178 (in Russian)
Mazukhina S et al (2012) Monitoring and physical-chemical modeling of conditions of natural surface and underground waters forming in the Kola North. J Environ Sci Health, Part A: Toxic. Hazard Subst Environ Eng, Part A 47, 657–668 http://doi.org/10.1080/10934529.2012.660037
Mazukhina SI (2012) Formation of surface and underground waters of the Khibiny mountain massif. In: Masloboev VA (ed) Pupl. Kola Science Centre RAS, Apatity, p 173 (in Russian)
Mazukhina SI et al (2018) Results of the study of groundwater chemical composition in the Khibiny massif and its surroundings (Kola region of the Baltic shield). In: Proceedings of the third Russian scientific conference with international participation "Geological evolution of water-rock interaction". Chita, pp 122–126. https://doi.org/10.31554/978-5-7925-0536-0-2018-122-126 (in Russian)
Moiseenko T et al (2010) Impact of industrial waters on the population health of the industrial region of the North. Water Resour 37(2):199–208 (in Russian)
Prives M et al (2017) Human anatomy. 12th revised and enlarged. Hippocrates (in Russian)
Roitberg G, Strutynsky A (2007) Internal diseases. Digestive system. Study guide. MEDpress-inform, (in Russian)
Rosseeva E et al (2009) Formation of mineral phases in prototypes of human oral fluids. Vestnik of Saint-Petersburg University Series. 7. 2009. Issue 2, pp 12–20 (in Russian)
Rosseeva E et al (2006) Formation of analogues of kidney stones minerals from the prototype of biological fluid under experiment conditions. Mineral Technogenesis 212–233 (in Russian)
Russian statistical yearbook 2017: Rosstat, P76 M., 2017 (in Russian)
Ryzhenko BN et al (2003) Physical-chemical factors of formation of natural waters composition (verification of the model "rock-water"). Geochemistry (6):630–640 (in Russian)
Sapin M, Bilich G (2008) Human anatomy: textbook in 3 T. GEOTAR-Media. Tome 2 (in Russian)
Schmidt W, Bojko J (1999) Regulation of gastric acid secretion. In: Greeley GH (eds) Gastrointestinal endocrinology. Contemporary endocrinology, vol 8. Humana Press, Totowa, NJ. https://doi.org/10.1007/978-1-59259-695-9_15
Skalny A (2004) Chemical elements in human physiology and ecology. Mir. Moscow (in Russian)
Skalny A, Rudakov I (2004) Bioelements in medicine. Oniks 21 vek, Mir (in Russian)
Tereshchenko PS et al (2017) Ways of mineral metabolism in the human body and methods of its research. In: Proceedings of Fersman science sessions GI KSC RAS. Issue 14, pp 486–489 (in Russian)

Tutelyan V et al (2001) Vitamins and trace elements in clinical pharmacology. Paleya-M (in Russian)
Vignal C et al (2016) Gut: An underestimated target organ for Aluminum Le tube digestif: unorganecible sous-estimé pour l'aluminium. Morphologie 100(329):75–84. https://doi.org/10.1016/j.morpho.2016.01.003
Yokel RA (2016) Reference module in food science. Encyclopedia of food and health, pp 122–127

Internet Reference

Medical Encyclopedia https://dic.academic.ru/dic.nsf/enc_medicine/1919/%D0%90%D0%BB%D0%BA%D0%B0%D0%BB%D0%BE%D0%B7 (in Russian)
Ministry of Natural Resources and Ecology of the Murmansk region http://mpr.gov-murman.ru (in Russian)

Part VIII
Philosophical and Historical Aspects

Chapter 47
Time and Space of Biological Morphogenesis



Dmitry L. Sumin and Evgeniya L. Sumina

… modern interest to morphogenesis is not limited to biology
L. V. Beloussov

Abstract Time and space are regarded as phenomena arising from the flow of energy in the Universe and their own structure set by this process. Biological morphogenesis is regarded as a secondary to the common time-space system.

Keywords Morphogenesis · Time · Space · Accelerating the expansion of the universe · Energy

47.1 Introduction

Any processes can be accepted and studied only in the time and surface. These phenomena themselves do not have any concrete definitions and also their origin and interrelations between themselves and other phenomena remain unclear.

Authors suggest that, at the present moment, the study of more particular phenomena and their relations with each other is able to make it possible to clarify the general properties of time and space.

The purpose of this work is an attempt to identify their own properties of time and space, the structure of relations between them and their physical nature. As a way to

Dedication The work is dedicated to the memory of the outstanding Russian geologist Mikhail Aleksandrovich Semikhatov

D. L. Sumin
Network of Independent Scientists (NISEEB), Moscow, Russia

E. L. Sumina (✉)
Department of Paleontology, Geological Faculty, M.V. Lomonosov MSU, Moscow, Russia
e-mail: stromatolit@list.ru

© Springer Nature Switzerland AG 2020

O. V. Frank-Kamenetskaya et al. (eds.), *Processes and Phenomena on the Boundary Between Biogenic and Abiogenic Nature*, Lecture Notes in Earth System Sciences,
https://doi.org/10.1007/978-3-030-21614-6_47

solve this problem, it is proposed to identify the similarity of properties of phenomena having a different nature and occurring at different scales of length and duration. Such a similarity, due to the differences between the phenomena themselves, is most likely to be a manifestation of the properties of time and space as they are.

The main attention, in addition to general issues, is paid to the general properties of the structure of ontogenesis and phylogenesis of organisms of fundamentally different structures and their comparison with the general properties of the occurrence of abiogenic processes. Questions of space and time of biological morphogenesis historically occupy a central place in the study of this phenomenon (Beloussov 2015; Sekimura et al. 2003).

General Questions of Their Own Properties and the Relationship of Time and Space

Time and space are the most common features of the observed reality. On the one hand, in the sensations there is given the existence of common, or universal, time and space, on the other hand, every phenomenon or object has its own time and space, essentially independent of both common time and space, and of time and space of other phenomena or objects.. The complexity of studying issues of nature, structure and relations of time and space is about the fact, that, also, on the one hand, both the common time and space, and the time and space of large processes, include the observer as an element and therefore are not available for observation in the completed and limited, that is, full, form and in a variety of options. Oh the other hand, time and space of phenomena and objects, which were overcame by sizes and length of existence of the observer, thanks to what their complete research is possible, do not possess universality. A possible way to solve the problem authors consider as a joint study of the general properties of these two categories phenomena.

Among the most general properties as a reality itself, as its components, first of all, should be distinguished the property to exist. By the existence of objects we understand that the energy of the bounds between their elements is bigger than the energy of the bounds between their and environmental elements (Babaytsev 1998). Thus, by the appearance and development of the object we understand the accumulation of its connections energy. The most important consequence of the physical content of “existence” is that the environment is not able to be the energy source, that provides the existence and development, as far as the energy of its elements bounds is lower than the internal connections of objects energy.

For biological objects, this circumstance is quite obvious, since life in general does not reduce the environment organization, which could be connected with the extraction and assimilation of its components energy, but, on the contrary, constantly lower the entropy level of at least the outer Earth spheres, providing them the energy through waste products and «former living substance» (Ostroumov 2011; Sumina and Sumin 2016).

The time of biological morphogenesis in a phylogenetic and evolutionary sense in a generalized way is reflected in a form of a geochronological scale. Despite the name, geochronological scale does not reflect geological time as a sequence of geological events, but it does reflect only the biological time, that goes independently. However, there is no contradiction in the name—because of the methodological

reasons characteristics of one object may be established reliably only with comparing them with the similar characteristics of another, independent object. This, again, shows that the course of biological time is primary and does not depend on the external conditions, and the external conditions themselves, in particular, geological, are secondary and substantially depend on it.

Peculiar property of biological time, in addition to the independence of its flow from the sequence of geological events, is a positive acceleration of its flow in the direction of reducing the entropy (Mikhailova and Bondarenko 2006; Dolitsky 2000). It is expressed in the fact that the complexity of organisms constantly increases, which is also expressed in the discrete events of diversity changes, that allow to concrete the phases of this complication, and the intervals of the «absolute», is established by radiological methods, time between the comparable milestone events is reduced.

By the direction of flow, the time properties of living and non-living matter in general coincide. All visible objects of the Universe reduce (or reduced during the process of their formation) their own entropy, which is expressed in the formation of new connections between their elements, and the entropy of the surrounding space, releasing into it the excess energy in the form of particle flows, radiation, fields, etc. Precisely due to the latter circumstance, the objects of the universe are visible.

Regarding the acceleration of the flow of time, not of individual phenomena or objects, but of the Universe in general, various assumptions were expressed. The establishment of the expansion of the Universe with positive acceleration (Riess et al. 1998), allows us to conclude that the objective reality most closely corresponds to the assumption of a "heating" Universe, the space of which expands simultaneously with the complication of both individual objects and the Universe itself.

The observed positive acceleration of the expansion of the Universe simultaneously with the complication of its objects inevitably leads to the conclusion that there is a constant flow of energy, the expression of which are these interrelated processes. Thus, time, as perceived by us from the outside as a sequence of events, and given as an internal sensation, is the influx of energy into the volume of the Universe, assimilated by all its components. It also follows from this that energy is an independent material object, due to which the conservation law is valid.

The proper time of objects arises as a result of a different speed and possible amount of this energy assimilation. This also explains the connection between irreversibility, or "half-dimensionality", of time and the acceleration of its course—the concentration of energy in the volume of the Universe is constantly increasing. To accelerate the course of time in this case, it is sufficient that the volume of the Universe is simplified proportionally to the cube of its size, and the surface, through which energy is dissipated, is proportional only to their square. As a result, the relative surface and the possibility of dissipation of the incoming energy through it is reduced in proportion to the increase of the size of the Universe.

This leads to an increase in the proportion of energy outputted by objects not through its dissipation, but through the formation of new levels of internal connections.

Thus, time is a physical phenomenon, which leads to the objects complexity raise and destructive when it is impossible to remove excess energy from its structure,

and its irreversibility and acceleration are associated with a constant increase in energy concentration. In relation to the volume of the Universe, the source of energy can be either extended or local. The discreteness of the distribution of objects in space is the evidence of its locality. The space in this case is a region of energy dissipation and has its own structure with a fractional dimension, defined by time (the primacy of time in relation to space). Also, the space should be considered as an independent object, the structure of which dynamically affects the structure and location of other objects. The structure of the relationship of time and space is determined by the qualitative differences and the incompatibility of the processes of influx and dissipation of energy, since they cannot go in one direction. The only possible direction is a perpendicular one to the time axis with a shift in time forward, in other words, the energy dissipation goes along with its assimilation at some levels of the organization. Thus, the structure of the time-space corresponds to the polar-acute angle system with a sliding reference point (Fig. 47.1). In a view, available to be observed, such picture dissipates in it—for example, when a bullet moves in a gas or a ship moves on the liquid surface.

In order to judge about the presence or absence of the peculiar discreteness of the time-space structure, at this moment there is needed much more data, but the objects moving in it form discrete communities of three different types.

The first communities have the form of cones, diverging forward in time. The objects in them are connected by centrifugal evolutionary lines and are not similar to each other.

The second ones have the form of cones that converge in time and that are surfaces with an equal concentration of energy. The objects in them are not related by common origin, but have similarities due to the generality of conditions.

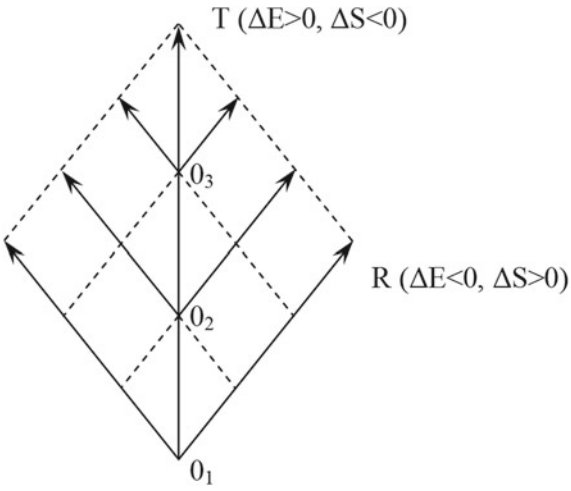


Fig. 47.1 Estimated time-space structure. T—time, R—space, E—energy, S—entropy, $0_{1,2,3}$—a sliding reference point. Solid lines indicate evolution lines, dashed lines indicate surfaces with equal concentration of energy (organization levels)

The third, a special evolutionary line of objects occupies an axial position, moving in time, but not shifting in space, in other words it does constantly exist in the region of maximum excess energy.

Expression of the Properties of Time and Space in the Structure of the Organisms Evolution

Time and space of biological evolution (here we speak mostly about a featural space) have a similar structure. Its central axis—the development of «common ancestor», which defines the time of evolution—in a moment allocated mostly theoretically, basing on the common structure of construction of organisms, that belong to groups of any evolutionary distance, and it can not be traced on a specific material. However, the system of phylogenetic lines crossing a sequence of levels of organization can be traced quite clearly, in particular, for tetrapods (Tatarinov 1974; Ivakhnenko 1987). Currently, there is no doubt that there are no such monophyletic groups as "fish", "worms" or "algae"—these are levels of organization crossed by many unrelated groups at this level. The history of prokaryotes and early eukaryotes is also most likely a similar picture (Gusev and Gohlerner 1980). In general these phenomena in evolution are well known as parallelisms and convergences.

In ontogenetic terms, biological morphogenesis is represented by autonomous reproducible finite space-time systems. Due to their limitations, multiple and external observation of their development is possible during the lifetime of the observer. The most important feature of ontogenesis is the unambiguous connection of its time and space. The time and space of this ontogeny always have a common beginning. Until an adult stage is reached, the length of time is uniquely associated with an increase in the length of space. During this period of ontogenesis, the organism captures objects of the external environment, lowers their entropy to its own level and incorporates into its own structure, increasing and complicating, due to this, its own space. For organisms with equifinal morphogenesis, the course of their own ontogeny time goes with a negative acceleration, thus, the duration of the time external to the organism between comparable ontogenetic events increases. When the adult stage is reached, the increase and change in the structure of its own ontogenetic space ceases, or rather, it slows down significantly. The metabolism, that is, the capture of objects of the environment and the message of excess energy to them, causing a decrease in their entropy, continues, but the organism does not embed them in its own structure, but in the structure of reproduction products. At this stage, the body's own time mainly causes an increase in phylogenetic space, and is also the engine of phylogenetic time, and is minimally related to its ontogenetic space. Due to the excess of the number of descendants of ancestors and the increase in their concentration in the volume of the medium, the phylogenetic time goes with a positive acceleration exceeding the acceleration of the general course of events.

Expression of the properties of time and space in the structure of the individual development

The limited time and space of ontogenesis has many options, among which there are two extreme states.

The time and space of ontogenesis of multicellular eukaryotes is limited by internal causes due to the equifinality of their ontogenesis. When sexual reproduction is widespread among them, it starts in the merge of gametes, and it ends with the death of the organism. This is due to the fact that in their morphogenesis the rate of decrease in entropy decreases and it comes to a final, irreversible state of the structure, the entropy of which cannot decrease any longer and consequently increases spasmodically, resulting in the passage of time of a given organism, and the energy of its space is irreversibly dissipated in the environment, already reducing its entropy (Ostroumov 2011). Simultaneously with the structure of this organism, its biomass and individual information are destroyed. The rapid morphological progress of multicellular eukaryotes is associated with the irreversibility of ontogenesis, since phylogenetic information is accumulated as irreversible and multivariate. The second option of ontogenesis is non-equifinal ontogenesis observed in filamentous cyanobacteria (Sumina and Sumin 2013). Their communities are the bodies that have a complex structure and are not inferior to other organisms according to the degree of morphofunctional differentiation and correlation. On the one hand, the options of the structure of their mineralized buildings are that stable and discrete that a binary biological nomenclature may be applied to them, on the other hand, they experience evolutionary development over time, which is also characteristic only of organisms. They differ fundamentally from organisms comparable in size, which are multicellular eukaryotes, only with the fact that all of their structures, including the discreteness of single individuals, are formed only for the duration of the corresponding functions and can later be transformed into any others due to the fact that differentiation does not affect the structure of the individual threads. Due to the lack of predetermined final states, there is no phase of death in their ontogenesis, in other words, periodic reduction of biomass and information. For this reason, the organizational nature of cyanobacterial communities remained a controversial issue for a long time. These organisms are in a state of continuous ontogenesis, some events of which can be considered as phylogenetic, as they occur on a geological time scale. Due to the reversibility of differentiation, neither time nor the space of their ontogenesis has internal limitations, and their specific expression depends only on external conditions. The duration of the continuous ontogenesis of cyanobacterial communities can be presumably estimated as exceeding the age of the oldest surviving sedimentary rocks (3.7–3.8 billion), and its space is limited only by habitable areas of the planet's surface, that is, it is global or at least subglobal. The evolution of cyanobacteria, which is basically the accumulation of energy in their structure, judging by the oldest remains (Sergeev et al. 2012), goes extremely slowly due to the fact that they have mostly membranous bodies with a huge relative surface that allows them to displace incomparably large amounts of excess energy than it is available, for example, for multicellular eukaryotes. During the geologically documented period of the Earth's development, this led to a fundamental decrease in the entropy of the outer shells of the planet—the emergence of an oxygenic atmosphere and hydrosphere, and the complex structure of the lithosphere. In general, with regard to the proper time of ontogeny of cyanobacterial communities, it can be stated that its slow flow is the cause of a faster time flow of the environment as a geological

time, during the formation of sedimentary rocks, as well as metamorphic and igneous rocks genetically associated with them.

Thus, no matter the way of its organization, biological morphogenesis in the ontogenetical way is the front of the decrease in entropy, spreading in the environment from the local center. Due to the greater concentration of energy in the internal connections of living organisms than in external ones, their time and space are not only independent of events in the external environment (Bernard 1878), but also to a significant extent they are the leading factors determining the course of time and the organization of the space environment (Sumina and Sumin 2016). In general, this leads to the conclusion that living objects differ from non-living objects by the independency of the external factors and the most complete assimilation of energy, the flow of which leads to accelerated expansion and complication of the Universe.

Due to the fact that the time and space of observation strongly exceed the time and space of specific ontogeny, it is possible to study them on a scale adequate to the properties of the phenomenon. Observability, reproducibility and multivariate ontogeny of individual organisms allows to suggest the existence of a common archetypal structure for the organization of their own time and space systems, as well as to test this assumption.

The polar-acute time-space structure assumed above with a sliding reference point is otherwise called "tree-like", thus it does most obviously manifest itself in the morphogenesis of higher plants. Their bodies are naturally divided into axial and lateral. The difference between them is that the axial organ has an unlimited vertical growth throughout ontogenesis, as far as lateral organs with limited growth branch off from it. This often concerns not only the above-ground, but also the underground part. As the most correct geometric example of such a structure, there can be given an ordinary pine—*Pinus sylvestris*. The morphogenesis of higher plants occurs on the boundary between air and underground environments, which determines the presence of conductive and other specific tissues in their structure. In addition, their aerial parts are subjected by gravity. It is possible to assume that these factors will be leading in determination of the structure of morphogenesis, however, the fundamental similarity of the structure of the aerial (air) part, subjected to mechanical influence of gravity and underground, on which gravitation does not have a mechanical effect, because it is suspended in the soil, at least as we speak on gravity, this assumption is not confirmed.

Similar construction is preserved in many multicellular algae, despite the fact that their body does not need the formation of conductive tissues, and gravity does not affect their construction because they are suspended in water.

The «tree-like» structure is also characteristic for the organization of many multicellular protists and also bacteria (Shapiro 1988).

Thus, the polar acute-angular, «tree-like» structure of morphogenesis is manifested regardless of the level of organization, systematic affiliation and the impact of environmental factors of organisms.

We may assume that such a structure of morphogenetic relations appears because of one or another general patterns of morphological relations organization.

Filamentous cyanobacteria differ significantly from both other prokaryotes and eukaryotes in the organization of morphogenesis. They differ from prokaryotes with the fact that they construct large differentiated bodies with a size rather closer to eukaryotes, and from eukaryotes the differ, partially, with the lack of constant differentiation of these bodies.

In the case of carbonate mineralization these bodies—stromatolites—are well saved as fossil and they are the oldest macroscopic minerals known since the age of 3.5 billion years. Usually, like in other organisms, their morphogenesis is carried out by a morphologically continuous body of their characteristic film form. However, among them are the unusual forms Jacutophyton (Krylov and Shapovalova 1970) with a very complex natural tree branching and clear morphological differences between the axial and lateral parts of the building. These morphological differences are that large and constant that within the framework of artificial classification they are housed (Fig. 47.2) to the different groups (formal genus) of the columnar stromatolites—axial to the genus Conophyton, branches—Baicalia. Despite the fact that the "tree-like" structure of the building is reproduced with no less definiteness than the structure of morphologically continuous organisms, *Jacutophyton* morphogenesis is carried out by film sections that have no morphological connection with each other (Fig. 47.2). Differentiation of their morphogenetic functions is carried out without

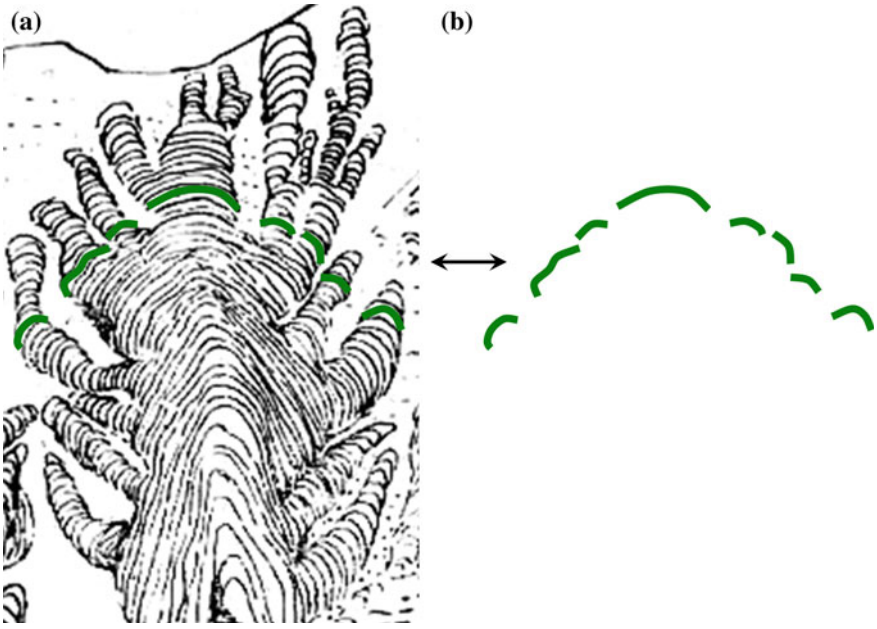


Fig. 47.2 The "tree-like" morphogenesis of Jacutophyton stromatolites. **a**—building in section. Green lines indicate simultaneously existing live cyanobacterial films. The image of the building by Krylov and Shapovalova 1970. **b**—separately shows the structure of simultaneously existing live cyanobacterial films

contact positioning and is not associated with the mutual influence of morphological structures. Thus, morphological connections are secondary with respect to the general structure of morphogenesis as a physical phenomenon of a decrease in the entropy of a substance of a medium to a substance of a living organism.

The minimal entropy of living objects points that as living objects we perceive ones that most fully assimilate this energy and further dissipate it both in a way of energy of its own connections, and in a way of energy of its movement. Thanks to that there appears the general structural similarity between fundamental bases of morphogenesis of various organisms—prokaryotes and eukaryotes, plants and animals, and, possibly, living objects and crystals. In addition, there is observed a structural similarity of ontogenesis and phylogenesis. It should be noted that the more intensive is the exchange of organisms, that is, the more additional energy they mobilize from the environment, than the more their structure is removed from the polar-acute (or "tree-like"). However, in various organisms, both ontogenesis and phylogenesis occur in the form of a diverging conical wave, leaving traces of its distribution in the form of evolutionary or morphological branches.

47.2 Conclusions

Comparison of the general properties of phenomena of a fundamentally different nature, length and duration, the flow of which is combined, as it seems to the authors, only by the time and space, and makes it possible to draw the following conclusions with regard to their physical nature, connection with each other and with other phenomena. Time and space are interconnected physical phenomena (expressions of one physical phenomenon). Time is the influx of energy into the universe. Space is an area of energy dissipation (the process of energy dissipation). Time sets the structure and fractional dimension of space (time is primary in relation to space). As a result, there arises its own "tree" structure of time-space, which corresponds to the polar-acute coordinate system with a sliding reference point. Biological morphogenesis creates significantly independent from the environment and more organized its own time and space due to the most complete assimilation of the energy entering the Universe and its subsequent dispersion in the form of its own connections energy and increasing the organization of the environment. Biological morphogenesis, both in evolution and in the development of individual organisms, is archetypically determined by the same "tree" structure as the own structure of time-space, but arising secondarily.

References

Babaytsev J (1998) System. In: The newest philosophical dictionary. Minsk (In Russian)
Beloussov L (2015) Morphomechanics of development. Springer, Cham, Heidelberg, New York, Dordrecht, London

Bernard K (1878) Course of general physiology. The phenomena of life, common to animals and plants. Saint-Petersburg (In Russian)
Dolitsky A (2000) Rotation of the mantle along the core: movement of geographical and geomagnetic poles, periodicity of geological and tectonic processes. Institute of physics of the Earth, Moscow (In Russian)
Gusev M, Gohlerner G (1980) Free oxygen and the evolution of cells. Moscow State University publishing, Moscow (In Russian)
Ivakhnenko M (1987) Perm parareptilia the Soviet Union. Nauka, Moscow (In Russian)
Krylov I, Shapovalova I (1970) Stromatolites of Jacutophyton group in the middle-Riphean deposits of the Urals and Siberia. In: Stratigraphy and paleontology of the Proterozoic and Cambrian of the East Siberian platform. Yakutsk (In Russian)
Mikhailova I, Bondarenko O (2006) Palaeontology. Publishing Moscow State University, Moscow (In Russian)
Ostroumov SA (2011) About the typology of the basic types of substance in biosphere. Ecol Chem 20(3):179–188 (In Russian)
Riess A, Filippenko A, Challis P (1998) Observational evidence from supernovae for an accelerating universe and a cosmological constant. Astron J 116:1009–1038
Sekimura T, Noji S, Ueno N, Maini PK (2003) Morphogenesis and pattern formation in biological systems. Springer, Cham, Heidelberg, New York, Dordrecht, London
Shapiro J (1988) Bacteria as multicellular organisms. Sci Am: 82–89
Sergeev V, Sharma M, Shukla Y (2012) Proterozoic fossil cyanobacteria. The Palaeobotanist 61(2):189–358
Sumina E, Sumin D (2013) Morphogenesis in a community of filamentous cyanobacteria. Russ J Dev Biol 44(3):158–172
Sumina E, Sumin D (2016) About the properties of relations between living and nonliving. In: Biogenic-abiogenic interactions in natural and anthropogenic systems. Springer, Cham, Heidelberg, New York, Dordrecht, London
Tatarinov L (1974) Theriodonts of the USSR. Tr PIN 143: 255 (In Russian)

Chapter 48
The Impact of Geodynamic Processes on the Emergence and Evolution of the Man



Evgeny M. Nesterov, Peter Mavopulos and Pavel I. Egorov

Abstract A systematic approach to the study of the geodynamic impact on human communities allows us to avoid the geodynamic determinism. Almost all discussed phenomena and structures related to geodynamics are open dissipative systems (Nesterov in Systems, systems thinking and geology. Geology at school and university. Herzen State Pedagogical University, St. Petersburg, pp. 24–28, 2001), and energy with matter exchange across their boundaries. It is essential for us that the paleoclimatic rhythm established for this time served as the background of the evolution of hominids, the emergence of humans and the history of the development of human cultures. The human society, its life support and development form complex systems, in which not only social, political, economic and technological but also natural processes that are represented by climate changes and geodynamic events. The impact of the systems of these natural processes of varying complexity influenced decisively on the formation of humans as a species, on establishing production economics, on the development of civilisation processes in the Alpine tectonogenesis from Greece and the Black Sea to India and Central Asia. The peculiarities of the mentality and thinking of the ancient Greeks was coherent with the features of the geographical environment of Hellas. For a long time, the environment in this area proved to be comparable with the man and determined the elements of his evolution.

Keywords Environment · Geodynamic events · Climate · Geochemistry of landscapes · Anthropogenesis · Civilizations · Systems approach

48.1 Introduction

The problem of the relationship between society and the environment has existed since the first civilisations appeared. Human influence on the environment is quantifi-

E. M. Nesterov · P. I. Egorov (✉)
Herzen State Pedagogical University of Russia, Saint Petersburg, Russia
e-mail: egorov.pavel26@gmail.com

P. Mavopulos
Aristotle University of Thessaloniki, Thessaloniki, Greece

© Springer Nature Switzerland AG 2020

O. V. Frank-Kamenetskaya et al. (eds.), *Processes and Phenomena on the Boundary Between Biogenic and Abiogenic Nature*, Lecture Notes in Earth System Sciences,
https://doi.org/10.1007/978-3-030-21614-6_48

able. Another thing is the influence of the geological and geographical environment on the formation of the culture and science of the civilisation. For example, in the conditions of the formation of ancient Greek civilisation, such influence was extremely significant at all stages of its development. Since the Late Cretaceous, the unique conditions of the environment of Greece have created favourable opportunities for the emergence and evolution of human and the ancient civilisations in different times of geological history.

The fundamental paleogeographic property of the Cenozoic era is the frequent and sharp fluctuations of the global climate against the background of the global cooling that began from the end of the Cretaceous (Duff and Duff 1993). In the Quaternary, the cooling showed in the alternation of glacial and interglacial ages, which alternated every 100–150 thousand years. There have been only four short-term intervals with a milder climate than the modern one, over the past 600,000 years (Fig. 48.1).

Global climate changes and other environmental parameters associated with them showed variously at different latitudes. Glacial phenomena characterise paleogeographic processes at high latitudes, while biological ones are more suitable for tropics and subtropics. Especially sharp changes began at the end of the Eocene (approximately 40 million years ago) and reached their maximum strength in the Quaternary period, which began 2.6 million years ago.

At the Quaternary, the level of the World Ocean fluctuated sharply every 100 thousand years, changing to 130–150 m (Astakhov 2008) in connection with the increase in thickness of continental ice, or with their rapid melting during the glacial cycles.

Human society's life support and development form complex systems in which not only social, political, economic and technological but also natural processes interact, represented by climate change and geodynamic events. The impact of the physical processes systems of different levels of complexity had the decisive influence on the formation of humans as a species, a producing economy, on the development of

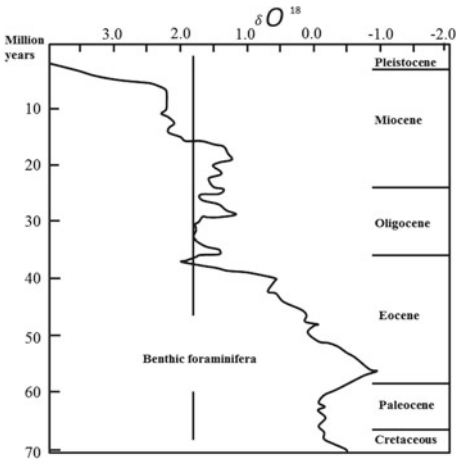


Fig. 48.1 Oxygen-isotope curve along the Atlantic bottom foraminifera (Duff and Duff 1993)

civilisation processes in the Alpine tectonogenesis from Greece and the Black Sea coast to India and Central Asia, and also European Russia.

Consideration of climatic changes in a series of geodynamic phenomena requires clarification. Geodynamic phenomena partly determine the cooling of the last millions of years. Thus, the high closeness of the continents, the abundance of land and mountains increases the heat transfer of the planet and enhances the contrast of climatic zonality. The episodes and periods of cooling associated with the increased release of ash into the atmosphere during subaerial explosive volcanic eruptions were established (Melekestsev 1980). However, the direct effects of geodynamics on climate were not decisive during the Holocene. But a correlation between these two groups of phenomena exists. It may be a consequence of the impact on both groups of changes in the parameters of the Earth's orbit and some astronomical factors.

One should consider not single natural processes but their interrelated groups and integral impact on humans and society. The range of tasks includes the study, analysis, and comparison of processes and phenomena, usually found in isolation by scientists of different specialities: geologists, geophysicists, geographers, geneticists, archaeologists, and historians. Each science has its limitations in the research methods and, accordingly, on the reliability and accuracy of the results. This fact also applies to assessments of the significance of certain phenomena and their dates. We come across with additional ideological and socio-psychological difficulties when analysing primary sources of historical materials or their interpretation. The reliability of the results decreases when such heterogeneous data are compared.

Any society arises, lives and develops in specific environmental conditions. The problem of the relationship between society and the environment has existed since the appearance of the first civilisations. Deep professional research is not sufficient in this area, although there is every reason for such studies.

The influence of geodynamic processes most clearly affected the early stages of social development and is still present now. The presence of overt and covert catastrophes and the importance of assessing the regularity of the recurrence of catastrophic phenomena make it necessary to consider environmental problems in a historical retrospect. It is impossible to understand the role of environmental factors in modern life and to make any reliable predictions in this area without such researches (Fig. 48.2).

48.2 Objects and Methods

The aim of the research was in revealing geological conditions of the Miocene-Holocene and defining their impact on directions and mechanisms of co-evolution of nature and society, including arising phenomena of culture and science. For this purpose it is necessary to reveal the directions and character of the Greek natural landscapes evolution; determine the factors, reasons and mechanisms that affect the emergence and evolution of the man and society; define the character of the human and social evolution, and geoecological condition of their life.

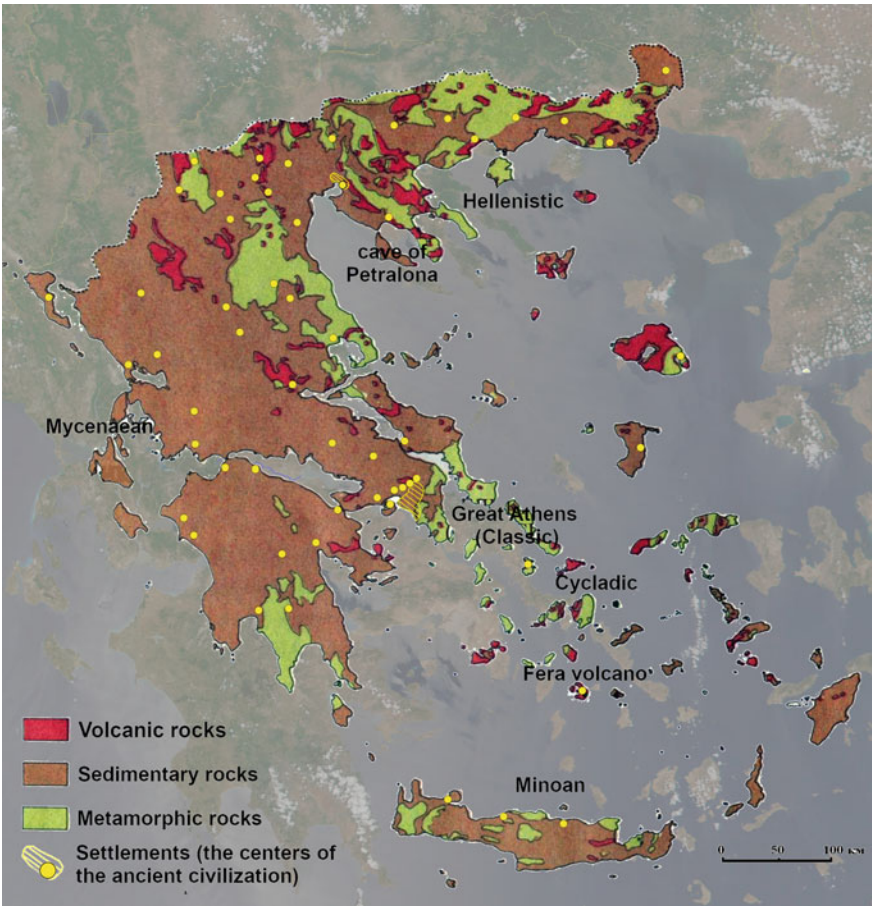


Fig. 48.2 The map of the distribution of the main groups of rocks that influenced the formation of human and civilizations

The object of the research is the territory of modern Greece and the adjacent areas having similar geodynamic histories. The subject of the research is the regional processes of environmental and human coevolution depending on geodynamic and natural factors. The chronological frames of the work encompass the period starting from the time of appearance of prehistoric men on the Balkan Peninsular up to the formation of developed civilizations on the territory of the Alpine tey zone from Greece and the Black Sea coast to India and Central Asia, and also European Russia.

The work uses scientific materials gathered within the period from 1998 to 2016 along with the analysis of numerous data received by Russian and foreign experts. The x-ray data on fossilized bones and the rocks bearing them were received in crystallographic laboratory of St. Petersburg State University. Geochemical research was carried out on the base of A. E. Fersman Geochemistry laboratory of the environ-

ment (St. Petersburg Herzen State Pedagogical University) by the method of x-ray fluorescent analysis on a vacuum spectrometer "Spektroscan Maks-GV". Paleoecological reconstructions were conducted by the methods of geochemical indication. This approach came into use in 1980-s and allows to reconstruct landscape-climate conditions of a recent past. The study of distribution of separate elements and their correlation by the section of bottom sediments gives us the key to understanding of sedimentation processes and influence on them on the part of paleographic and paleoecologic factors.

48.3 Results

Social and economic factors usually explain the processes of anthropogenesis. However, the most important for understanding the relationship between the biological and the social is the fact that the results of social and labour activities, according to the genetics, could not be recorded in the genes (Dubinin 1963). Therefore, we can conclude that the causes of anthropogenesis should be biological and depend on the natural features of the human ancestral home. The birthplace of mankind should be looked for in the environment which geographical conditions have contributed to genetic changes.

A number of significant events associated with the origin and evolution of humans, the source and development of society, the emergence of phenomena of science and culture is connected with the territory of the Balkan Peninsula. Geodynamic and paleoclimatic factors had a significant impact on the history of civilisations and most of all in the region of modern Greece. It is necessary to tie the ecological peculiarities and (or) historical and geographical studies. This is an inseparable part of geosystem research, which is insufficient for the given territory.

The Balkan Peninsula, including modern Greece, was free from ice cover, although its influence on the climate was always felt. It is important that paleoclimatic rhythm of this time served as the background (and for some causal relationships the driving force) of the evolution of hominids, the appearance of humans and the history of cultures.

Recent finds in Greece (Poulianos 2009; Mavopulo 2011) suggest that hominids appeared in the Miocene 17 million years ago. The Miocene is a time of rapid deterioration of the global climate, due to a sharp drop in temperature, which served as an evolutionary impetus for the emergence of Homo Erectus Trillensis and its further settlement.

One of the most important natural factors in the region is karst and the widespread development of caves associated with it. Karst determines the underground circulation of air and water masses. In winter it warms up the atmosphere in areas of karst caves or karst springs, and on the contrary cools it down in summer (Mavopoulos 2007). Olive tree (Olea europaea) is widespread in the natural and anthropogenic ecosystems of the karst regions of Greece and most part of the Mediterranean, which is uncharacteristic for non-karst areas. Therefore, if we take into account that the

spread of olive (apart from the tropics) is strongly associated with the particular environmental conditions noted in karst zones, we can say that karst indirectly gave a caveman the opportunity to survive and live permanently in one place (sedentary lifestyle) throughout the year and supplied him with food (olive tree). The development of prehistoric and historical cultures in Greece is not accidental, the karst as a physical factor provided the environmental prerequisites for their development. More than 70% of the territory of Greece are sedimentary rocks with predomination of carbonate rock, that form karst, primarily limestone and dolomite (Fig. 48.3). Carbonate rocks turn into marble after thermal processing. Marble due to its unique features: beauty, ease of handling, good preservation in the Mediterranean climate, sound resonance, providing exceptional acoustics and widespread prevalence in Greece is one of the natural factors involved the phenomenon of Greek civilization, directly contributed to the appearance of the theatre phenomenon, indirectly—the philosophy and Earth science.

The Petralona karst cave was discovered on the Katsika Hill in the first half of the 20th century in the north of Greece, in the province of Chalkidiki, south of Thessaloniki. For more than 50 years the cave and its environs have been studied by Aris Pulianos' anthropologist group, in whose work we have taken a direct part for the past 15 years. The research results were published in a number of articles (Mavopulo et al. 2011, Mavopulo and Nesterov 2002, 2012) and Mavopoulos (2007).



Fig. 48.3 Theater in Delphi

The authors studied the geochemistry of the section in details (38 layers were defined). It was formed for almost a million years during which men left and came back to the cave. The analysis of the calculated parameters, among which are the hydrolysis module, index of chemical weathering, Fe/Mg indicator, normative alkalinity, showed that such human behavior was connected either with opening or closing the entrance to the cave, which was fixed by the changes in geochemistry inside. One of the reasons for that is the change in the hydrodynamic regime in the cave. A detailed geochemical study of the Petralona cave and its surroundings was made for the first time. It allowed to reveal geoecological peculiarities of the environmental evolution and its qualitative parameters. The data received about the geochemistry of the hominids' bone remains allowed to form a notion of their diet and other conditions of the environment. Thus, geochemical research can let us reconstruct physical and geographical conditions of men's environment.

Not far from the Petralona Cave (Halkidiki) a discovery of incredible value was made—a part of the skeleton of a 14-year-old girl who lived 13 million years ago was found (Fig. 48.4). The specimen was named Homo Erectus Daphnae, in honour of Mrs. Daphne A. Pulianos. The measurement results showed that this individual spent more than 75% of the time in a vertical position. Therefore, it was much more upright than most modern African primates and it may be assumed that Helladopithecus (whose representative is Daphne) can claim the right to be called the close predecessor of a human being (Mavopulo et al. 2011). The oxygen-isotope curve for Atlantic benthic foraminifers reflects the cooling of the climate from the end of the Cretaceous period (Duff and Duff 1993) and the beginning of the sharp cooling in the middle of the Miocene, which can correspond to the lifetime of Daphne and the reasons for the evolution of its descendants forced to adapt to revolutionary environmental changes.

The strong earthquakes determined the most apparent consequences of a combination of both natural and social factors. Earthquake as a catastrophic event is a phenomenon more social than physical.

There are two main volcanic areas where Neogene-Holocene eruptions took place, and active volcanoes locate within the limits of the Eastern ecumene. One of these areas is the southern part of the Aegean Sea. In the Neogene and Holocene here,

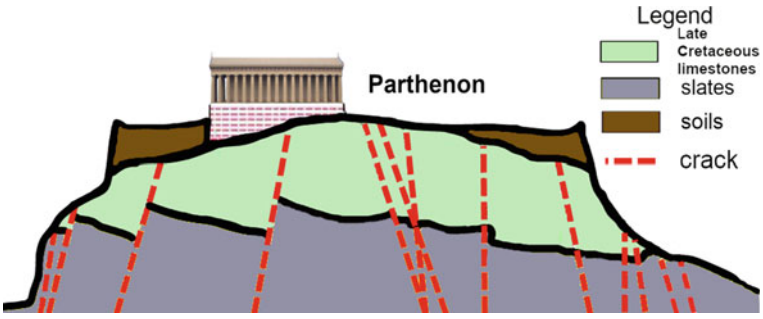


Fig. 48.4 Geological environment and Great Athens

in the rear of the Krito-Alinsky arc, were several volcanoes. The most significant consequences caused eruptions of volcano Santorini (Fera). Now Santorini has the form of a horseshoe, which is the remains of a caldera ring with a diameter of 13 km. The original caldera arose about 70 thousand years ago. Then it was filled with volcanic material and re-formed in outlines close to modern by the Minoan eruption about 21 thousand years ago. During the Minoan eruption the completion of the caldera formed. Traces of the Minoan eruption and the earthquake are found in some places in the Aegean region. The ashes found in the ruins of the Palace of Knossos in Crete possibly represent several eruptions. After the Minoan eruption, the Minoan civilisation did not revive, but left a noticeable mark in the culture of the conquerors and through them influenced the culture of classical ancient Greece.

The numerous results of radiocarbon dating give a wide variation in representing time immediately before the Great Minoan eruption or the earthquake preceding. In the course of field studies in 2009, we selected a series of samples of tamarisk which remained covered by ash from the eruption of the volcano Fera. Radiocarbon dating gave calibrated dates indicating the eruption time in the second half of the 16th century BC, which supports the idea of a so-called "low" period of the eruption.

The Minoan catastrophe was not the direct cause of the death of civilisation; it predetermined its collapse and therefore showed how significant the influence of geodynamic processes on the fate of human society could be.

The natural catastrophe undermined the power of the Minoan state, which, although could partly eliminate its consequences and continue its own policy, was in 50 years defeated and conquered by strengthened Acheans. Thus, under defining factors of nature one of the first mighty civilizations went into oblivion.

The human body can be a geo-indicator that integrates in itself the transformation of the natural environment. Vladimir I. Vernadsky concluded that, despite the negligible content of many chemical elements in the environment, they are present in plant and animal organisms constantly and not by chance. Vernadsky noted that the chemical composition of organisms is closely related to the chemical composition of the earth's crust. The history of a man's interaction with chemical elements constituting him as well changed over epochs, depended on geographical conditions and in many aspects determined his development and behaviour. Natural and anthropogenic changes in the geochemical background played the most crucial role.

The microelement composition of bone tissue from archaeological excavations carries much information. It reflects the microelement composition of the bone itself, as well as the blood at the time of the death of the organism. It is connected with the ability of the skeletal system biological function to release quickly its components into the blood contributing to maintain the homeostasis of the internal environment. The X-ray fluorescence analysis of bone remains allows to investigate unique objects (Table 48.1).

Geochemical analysis of bone remains gives information about a large number of microelements that were not previously considered or were considered only regarding the paleo diet. They were not studied as a possible source of information about the lifestyle of a particular person and an indicator of the steady excess incomes of a

Table 48.1 The results of x-ray fluorescence analysis of Daphne's bone

%	Bone				Host rock			
	1	2	3	Average	1	2	3	Average
TiO_2	0.0008	0.0002	0.0008	0.000604	0.3697	0.3702	0.3767	0.3722
Na	5.5720	4.8813	4.7415	5.06492	4.0856	3.5552	3.0984	3.5797
MnO	108.9378	107.2595	107.2824	107.8266	850.4756	849.7687	896.2537	865.4993
Fe_2O_3	0.6356	0.6389	0.6450	0.63956	4.6083	4.7093	4.6004	4.6393
CaO	56.6771	56.8100	56.7683	56.75179	31.7188	31.7534	31.9839	31.8187
Al_2O_3	2,3568	2,0423	1,8731	2,090729	10,8035	10,6646	10,0757	10,5146
SiO_2	15,4633	15,4644	15,4598	15,46251	42,3477	42,4338	42,1429	42,3081
P_2O_5	52,3443	52,3730	52,3311	52,34945	0,2337	0,2424	0,2231	0,2331
K_2O	–	–	–	–	0,7512	0,7432	0,7820	0,7588
MgO	1,8085	1,7798	1,8420	1,810094	3,4717	3.5308	3,4754	3,4926
Rb	24,2535	23,4745	22,7534	23,49371	9,9584	8,7241	11,8275	10,1700
Ba	202,4288	199,7373	200,5780	200,9147	200,9372	199,1208	191,6382	197,2321
Y	42,5686	41,8711	43,9878	42,80919	7,2908	6,6007	7,7269	70,2061
Zr	90,4012	91,0405	90,2623	90,56801	83,0504	83,2069	79,7122	81,9898
V	28,1199	29,3478	29,3700	28,94586	70,2857	70,5878	71,7059	70,8598
Cr	46,5063	46,5027	63,6012	52,20339	489,4304	497,3796	503,0831	496,6310
Co	14,1543	14,1801	13,8629	14,06574	15,2904	16,2894	16,0106	15,8634
Ni	25,2480	23,6128	24,3868	24,41589	334,5560	331,4557	340,5758	335,5292
Cu	41,0591	39,5178	40,4630	40,34664	290,1056	287,2409	295,6868	291,0111
Zn	55,7737	55,7913	53,5751	55,04671	35,9009	35,6132	36,8594	36,1245
Sr	954,5596	943,0335	956,4788	951,3573	75,1908	71,0281	72,9055	73,0415
Pb	19,9536	20,0887	2067,85	20,24028	5,3565	8,4794	12,3213	8,7191

specific element or its deficiency related to these causes. That could lead to a change in the bone tissue itself and also affect the general health and behaviour of the person.

Humans involve chemicals in the landscape cycle through food, water, and air, as well as a result of their activities. This activity developed with an increase in a human's ability to separate himself from the outside world, to purposefully manage objects and his behaviour. Archaeologically, this is represented by a change in technology and ways of life. At the same time, potential adaptive capabilities of a human were realised, including the chemical characteristics of various landscapes of the globe. It is found that the ancient foci of human culture did not appear in areas with the maximum primary productivity of the biosphere—tropical forests, but to the north of them, in areas with a more moderate climate (Fig. 48.5).

The state of the environment defined the system of settlement, economic and cultural types of using nature in regions. Scientific, engineering, technical and purely practical knowledge of the ecological services of the antiquity allowed the largest antique cities populated up to a million of people to exist for a long time, avoiding devastating infections.



Fig. 48.5 History and modernity. Monument to Alexander the Great on the restored embankment in Thessaloniki

48.4 Discussion

The human impact on the environment allows quantitative assessment. Another thing is the impact of the geological and geographical environment on the formation of the man, his civilisations, culture and science. The topicality of the problem causes an active discussion in the scientific world.

King, Geoff (2006), Poulianos (1989, 2003), Soulios (1991), Vavliakis E (1987), Pavlides and Kilias (1987), Pirazzoli (1996), Poulianos and Poulianos (2009), Trofimov and Kurilenko (2015), Egorov PI (2012), Mavopulo and Nesterov (2012), Poulianos A. N. (2011), Trifonov V. G, Karakhanyan A. S. (2008), Alexandrovskaya E., Alexandrovskiy A. (2018), Velichko A. A and Gvozdover M. D. (1969), Mavopoulo and Nesterov (2002), Morley, Mike, and Jamie Woodward (2007) and many others investigate the regional specifics of the man-environment relationship.

The nature on the territory of Balkan Peninsular for a long time was benevolent to the man, which determined the features of the man's evolution. In the course of the authors' research the synchronizm of geodynamic, climatic and historic periods was specified, and the mechanism of material cultures change under the influence of their changes in one of the most important world regions was substantiated; detailed geochemical reconstructions of the environmental quality were conducted, and the role of geoecological factors in its formation was defined.

The territory of the Balkan Peninsula, including modern Greece, was free from ice cover, although its constant influence was felt regularly. The paleoclimatic rhythm of this time served as the background (and for some causal relationships also as the

driving force) in the evolution of hominids, the emergence of man and the history of human cultures.

- natural-climatic and geodynamic restructuring of the environment naturally took place in the studied territory during the Miocene-Holocene, which determined the conditions for the emergence and the direction of human evolution;
- geographical and geodynamic determinants are distinctly revealed in the evolution, character, and change of cultures of ancient Greece;
- in the process of co-evolution of the natural environment and man in Ancient Greece, the conditions for the emergence of the phenomena of science and art were created. Features of the mentality and thinking of the ancient Greeks are coherent with the characteristics of the geographical environment of Hellas. For a long time, nature in this area turned out to be proportional to a man, which determined the features of his evolution. Evaluation of the historical retrospective of the interaction of the environment and a man is one of the urgent tasks of the modern science.

48.5 Conclusion

The problem of emergence of the phenomenon of science needs further research. It must answer the question: how and why it was in Greece, where the type of thinking that prevented the emergence of science was overcome? And why nowhere else not only in ancient times but even in the Middle Ages the science started to develop only two millenia after it had begun in Greece. At that, the preventing type of thinking is not necessary introverted. Romans were quite active, but they did not created the science on their own and did not developed the Greeks' achievements.

References

Astakhov VI (2008) The beginning of the quaternary geology. Publishing House of Saint Petersburg State University, St. Petersburg (in Russian)

Dubinin NP (1963) Molecular genetics and the effect of radiation on heredity. Gosatomizdat/State Publishing House of Literature on Atomic Science and Technology of the State Committee on the Use of Atomic Energy of the USSR, Saint-Petersburg (in Russian)

Duff P MD, Duff D (eds) (1993) Holmes' principles of physical geology. Taylor & Francis

Egorov PI (2012) Paleoecological reconstruction of the Mesozoic-Cenozoic in the sections of Gubbio (Italy) and Sumaia (Spain). Izvestia. Herzen Univ J Humanit Sci St. Petersburg. 144:92–99 (in Russian)

King G, Geoff B (2006) Tectonics and human evolution. Antiquity 80(308):265–286

Mavopulo PN, Nesterov DA, Pulianos AN (2011) Hominids and the environment. Bull MANEB. Sci Tech J Int Acad Ecol Hum Secur Nat 15(5):49–56 (in Russian)

Mavopulo PN, Nesterov DA (2012) The influence of paleoecological conditions on the evolution of prehistoric man. Izvestia: Herzen Univ J Humanit Sci St. Petersburg. 144:130–135 (in Russian)

Mavopulo PN, Nesterov EM (2002) The main features of the geological structure and topography of Greece. In: Historical geology and evolutionary geography: the collective. Epigraf, Saint-Petersburg (in Russian)
Mavopoulos PN (2007) Geographical environment and the formation of the ancient Greek civilisation. Izvestia: Herzen Univ J Humanit Sci St. Petersburg St. Petersburg 12(33):154–157 (in Russian)
Melekestsev IV (1980) Volcanism and relief formation. Science, Moscow (in Russian)
Nesterov EM (2001). Systems, systems thinking and geology. Geology at school and university. Herzen State Pedagogical University, St. Petersburg, pp 24–28 (in Russian)
Pavlides SB, Kilias AA (1987) Neotectonic and active faults along the Serbomacedinian zone (SE Chalkidiki, northern Greece). Ann Tectonicae 1(2):97–104
Pirazzoli PA (1996) Uplift of Ancient Greek coastal sites: Study, methods and results. Archaeoseismology. Athens: I. G. M. E. and British School at Athens. Fitch Lab Occas Paper 7:237–246
Poulianos A, Poulianos D (2009) The process of Hominization. Kunming 1:75–84
Poulianos NA (1989) Petralona cave within lower-middle Pleistocene sites. Palaeogeogr Palaeoclimatol Palaeoecol 73(3–4):287–294
Poulianos NA (2013) Significant «errors» of some thessalonica's geologists and archaeologists regarding Petralona cave. 16th Int Congr Speleol 1:88–92
Soulios G (1991) Contribution à l'étude des courbes de récession des sources karstiques: Exemples du pays Hellénique. J Hydrol 124(1–2):29–42
Trifonov VG, Karakhanyan AS (2008) Earth dynamics and social development. OGI, Moscow (in Russian)
Trofimov VT, Kurilenko VV (2015) Ecological functions of the abiotic spheres of the Earth: the content and significance for the formation of a new theoretical basis of geoecology. Mosc Univ Geol Bull 70(3):270–279 (in Russian)
Vavliakis E (1987) Prehistorische Besiedlung und Karsthydrographie ίπ Griechenland die Hohle
Velichko AA, Gvozdover MD (1969) The role of the environment in the development of primitive society. In: The nature and development of a primitive society in the territory of the European part of the USSR. Science, Moscow (in Russian)

Index

A

Accelerating the expansion of the Universe, 883
Algae, 216, 218, 458, 488, 490, 495–497, 536, 538, 544, 545, 551, 552, 561, 563, 565, 573–575, 578, 606, 732, 885, 887
Alkaline sand, 363, 364, 365, 367, 371, 372, 375
Amino acids, 5, 392, 550, 551, 696–698, 707, 716, 754, 765–768, 772, 775–777, 779–781
Antarctic, 146, 431, 457, 461–463, 475, 476, 481–485, 489, 492, 494, 496–498, 606, 608
Antarctica, 457, 458, 461, 475–477, 481, 482, 484–486, 494–498, 606, 608
Antarctic oases, 458, 482, 489, 498
Anthropogenesis, 895
Antigenicity, 3, 15
Antioxidants, 613
Apatite, 17, 60, 72, 79–83, 85, 88, 93–96, 99, 102–104, 107–110, 112, 113, 115, 116, 119, 123, 128, 130, 133, 138, 225, 230, 446, 447, 561, 562, 565, 571, 574, 581–590, 592, 597–601, 747, 748, 754, 803, 807, 819, 821, 822, 831, 835, 844, 873, 874
Apatite-nepheline ore, 562, 571, 574, 582, 583, 821, 835
Aqueous solutions, 39, 40, 42, 43, 45, 46, 63, 65, 103, 121, 701, 765, 767, 768, 778, 781, 834
Archaeological sites, 651
Arsenates, 261, 262, 264, 265, 269–272, 274
Artificial blood serum, 39, 43, 766
Aspergillus niger, 520, 542, 581, 582, 585, 601, 624, 625, 631, 632, 636, 683, 686, 687
Astrobiology, 607, 608
Australopithecus afarensis, 669–671, 674

B

Bacteria, 109, 196, 200, 209, 216, 260, 280, 284–286, 288, 289, 384, 395, 404, 405, 412–414, 436, 535, 536, 538–540, 544, 545, 555–557, 561, 563–568, 606, 621, 639, 640, 642, 649, 651–654, 657, 658, 661, 663, 664, 670, 671, 677–680, 682, 688–690, 732, 858, 887
Bacterial activity, 43, 260, 527, 658
Bedrock morphology, 315
Bioapatite, 60, 79–90, 93–96, 98–104, 104, 598, 748–751, 757, 760
Biocidal material, 639, 654
Biocrystallization, 582, 598
Biodegradation, 12, 138, 148, 182, 192, 195–198, 200, 201, 203, 204, 620, 649, 680
Biodeterioration, 137, 149, 554, 671
Biofilm formation, 503, 688
Biofilms, 109, 180, 181, 188, 191, 193, 501, 502, 510–513, 535, 536, 538–542, 544–554, 558, 621, 624, 641, 661, 670, 677, 680, 684, 686, 687, 690
Biofouling, 535–538, 541, 550–552, 558
Biogenic and abiogenic properties, 277, 293
Biogenic ultramicrostructures, 209, 210, 212, 213, 215–217

© Springer Nature Switzerland AG 2020

O. V. Frank-Kamenetskaya et al. (eds.), *Processes and Phenomena on the Boundary Between Biogenic and Abiogenic Nature*, Lecture Notes in Earth System Sciences,
https://doi.org/10.1007/978-3-030-21614-6

Biogenic weathering, 491, 493, 501, 503, 510–513
Bioglass, 10–12, 23, 34
Biological productivity, 315–317, 333, 335, 339, 340, 342
Biomat, 181, 188, 189, 192
Biomaterials, 3, 4, 8, 14, 15, 18, 108, 124, 730
Biomedical, 3, 4, 6, 8, 12, 13, 18, 23, 24, 35
Biomimetic apatites, 17
Biomineralization, 17, 108, 619, 633, 636
Biominerals, 80, 657
Bioresorbability, 10, 15, 126
Black shales, 729–736
Blood plasma, 59–69, 72, 75
Brushite, 63, 65, 66, 107–110, 112–116, 230
Butte relief, 329

C
Calcium oxalate hydrates, 688
Calcium phosphates, 10, 51, 52, 65, 107, 109, 111, 113–116, 120, 122
Caries, 221, 222, 226, 227
Cementing agents, 791
Ceramics, 131, 522, 532, 643, 653
Children's morbidity, 806, 808, 820, 830
Chiral molecules, 696, 700, 714
Chitosan, 15, 18, 23–35
Civilizations, 894, 898
Classification, 158, 210, 214, 216, 217, 230, 234, 235, 261, 263, 297, 304, 305, 397, 399, 401, 403, 425, 438, 464, 466, 470, 482, 509, 540, 677, 721–723, 727, 849, 888
Clay mineralogy, 786, 787
Clay minerals, 156, 158, 180, 482, 649, 729, 730, 786, 787, 798
Climate, 148, 196, 316, 318, 323, 324, 331, 332, 336, 368, 383, 397, 421, 422, 459, 461, 483, 484, 491, 502, 536, 606, 891–893, 895–897, 899
Collagen, 3–19, 60, 715, 748, 754, 756
Complexation, 373, 765–767, 776–778
Conodonts, 747, 748, 753, 757, 760
Contact angle, 179–182, 187, 192, 505, 627
Contaminated soils, 347, 351, 358
Corrosion, 524, 528, 642, 649, 657–659, 664, 666
Critical loads, 318, 334
Cryosols, 458, 466–474, 477, 490
Crystallization, 53, 55, 59–67, 70–75, 107–116, 119, 121, 128, 133, 230, 271, 528, 581, 582, 584, 585, 588, 590, 591, 593–602, 627, 633–636, 663, 699, 705, 729, 741, 743, 744, 766, 768
Cultural layer, 409, 640, 642–644, 646, 647, 649, 653
Cyanobacteria, 207, 208, 211, 213, 214, 217–219, 501, 504, 535, 538, 539, 546–549, 561, 563, 565, 573–578, 670, 677, 690, 760, 886, 888

D
$\delta^{13}C_{org}$, 749–752, 758–762
Degradation, 4, 6, 7, 9, 128, 133, 183, 196, 202, 209, 217, 218, 364, 365, 384, 465, 553, 760
Dentin, 222–225, 227, 230, 584, 587, 588, 595, 600
Detonation nanodiamond, 621–623, 633, 635
Dewatering, 237, 240, 245, 253
Dissolution kinetics, 119
DNA, 141, 397, 399, 400, 410, 605, 607, 609, 610, 612, 614, 675
Drug delivery, 3, 8, 24–31, 34, 35, 119, 133

E
EDX-analysis, 46, 47, 221–223, 266, 230
Eh–pH diagrams, 259, 261, 265–270, 272–274
Electron microscope, 47, 209–211, 214, 216, 218, 223, 225, 541, 585, 646, 676
Electron microscopy, 14, 47, 214, 217, 481, 504, 506, 512, 519, 521, 522, 535, 539, 540, 553, 585, 627, 636, 657, 676, 687, 731, 732
Elemental analysis, 803, 821
Enamel, 39, 221–227, 230, 530, 635
Energy, 46, 47, 62, 64, 70, 98, 111, 139–141, 180, 182, 186, 192, 195, 196, 198, 200, 209, 210, 218, 223, 233–240, 265, 274, 278, 330, 396, 510, 585, 586, 606, 641, 657–659, 716, 731, 741, 746, 831, 866, 881–887, 889, 891
Environment, 80–82, 87, 88, 90, 95, 96, 100, 102, 108, 141–143, 148, 150, 181, 185, 259, 268, 273, 278, 297, 298, 300, 305, 306, 308, 311, 312, 316, 346, 364, 365, 376, 406, 411, 420, 421, 436, 475, 493, 497, 519, 535, 536, 542–545, 549, 550, 552, 553,

555–558, 562, 574, 601, 613, 620, 624, 639, 642, 651, 652, 658, 671, 680, 682, 687, 689, 730, 743, 803, 804, 806, 815, 816, 818, 820, 821, 830, 831, 843, 848, 863–866, 874, 875, 882, 885–887, 889, 891–893, 895, 897–901
Environmental management, 237
Environmental mineralogy and geochemistry, 259, 261
Environmental pollution, 298, 346, 435, 818, 848
Enzyme activity, 285, 291
Epiphytic formations, 417, 421, 430
Epiphytic soils, 418
Epoxy-titanate coatings, 619, 630, 633–636
Extracellular fluid, 121, 133
Extreme cold environments, 501, 502, 511

F
Fitting, 32, 82, 88, 150, 185, 657–662, 664, 665
Food safety, 346, 786
Footprint, 669–677, 683–687, 689, 690
Forest ecosystems, 315, 316, 318, 334, 339–342, 431
Formation kinetics, 65, 69
Formation mechanism, 742
Fractal structure, 511, 628, 629, 636, 734
Fuel resources, 234

G
Gas hydrates, 196, 200
Geochemistry of landscapes, 155, 259, 261, 340, 670, 831, 843, 844, 866, 875, 894, 897
Geodynamic events, 891–895, 898, 900, 901
Geomorphology, 797, 799
Geophagic clays, 785, 787
Gibbs energy, 62, 66, 67, 265
GIS, 297, 299, 303, 305
Gorny Altai, 277, 279, 289, 291–294
Granite, 484, 519, 525–527, 531, 535–558
Gravitational anomalies, 315, 329
Green, 144, 346, 363, 365, 368, 376, 465, 490, 538, 544–546, 550, 551, 561, 574, 732, 888
Green beans, 363, 365, 368, 376
Groundwater, 260, 269, 278, 286, 326, 327, 330, 332, 333, 829–832, 842–844, 866, 875

H
Hair children environmental biomonitoring, 859
Hard tooth tissue, 221, 230, 231
Heavy metals, 156, 260, 297–301, 303, 311, 312, 315, 316, 318, 334, 335, 337–341, 345, 346, 348, 350, 354, 360, 361, 435, 804, 805, 819, 848, 852, 857–859
Humidity, 144–147, 236, 239, 240, 278, 359, 418, 424, 459, 484, 519, 527, 531, 548, 606, 624, 639, 644, 646, 647, 654, 671, 680, 682, 684, 689, 690
Hydrochemical regime, 318
Hydronic heating, 657, 658, 661, 664, 666
Hydrophilicity, 179, 188, 190, 246
Hydrophobicity, 179, 182, 188, 189, 191, 192
Hydroxyapatite, 10, 39–41, 53, 56, 63, 65–67, 69, 79, 80, 82, 107–109, 112, 113, 115, 116, 119–130, 132, 133, 149, 582, 584, 585, 587, 588, 590, 591, 597, 599, 600
Hydroxyapatite solubility, 40, 41, 599
Hydroxylapatite, 60, 126–129, 133, 225
Hyperacidity, 868
Hypoacidity, 864
Hysteresis of wettability, 188

I
Icosahedral Viruses, 722, 723, 727
ICP-MS, 41, 156, 348, 556, 729, 731, 803, 807, 831, 850, 851, 866
Industrial pollution, 345–347, 350, 355, 359–361
Insoluble compounds, 16, 29
Internal pores, 503
IR spectroscopy, 104, 119, 121, 125, 129, 524, 586–588, 605, 614, 792

K
Khibinites, 833–835, 837
Khibiny massif, 831–838, 842, 844
Kinetic thermodynamics, 765
Kola North, 568, 803, 804, 806, 807, 818, 819

L
Laetoli, 669, 670, 682, 690, 691
Lake Untersee, 457–462, 467, 469
Leccinum scabrum, 345, 347

Leptosols, 466–471, 473, 477
Limestone, 315, 322, 324, 327, 332, 421, 436, 519, 522, 527, 528, 581, 646, 649, 749, 789, 790, 896
Long-term immobilization, 318, 338, 340
Loparite ore, 803, 821, 822

M

Macro-, micro- and organic structures, 729, 738, 746, 744
Macromycetes, 345, 346, 348, 354, 357, 359, 360
Marble, 519, 527, 531, 581, 582, 601, 602, 625, 676, 896
Medical-ecological studies, 844
Metabolism, 24, 149, 196, 260, 395, 396, 415, 420, 549, 550, 558, 581, 633–635, 641, 715, 820, 821, 858, 868, 874, 885
Microbial biomass C, 388, 390, 392
Microbial metabolism, 149, 549
Microbiome, 395–397, 400, 401, 404–406, 410–415
Microbiota, 530, 563, 639–642, 646, 647, 652–654, 670, 689, 690, 858
Microfungi, 538, 561, 608, 669, 670, 674, 676, 680–682, 684–689
Micromorphological analysis, 494, 504
Micromorphological structure, 435, 436, 438, 442, 443, 452, 492
Microorganisms, 138, 149, 179–183, 191, 195–197, 200, 202–204, 209, 216, 218, 260, 273, 279, 285, 286, 289, 294, 384, 390, 391, 396, 411, 508, 511, 512, 520, 521, 536, 538–541, 548, 549, 553, 554, 556, 558, 563, 565–568, 577, 606–608, 611–613, 620, 640–642, 649, 651–654, 658, 661, 669–671, 673, 674, 677, 680, 682, 684, 687–691, 732, 798
Microscopic fungi, 538, 541, 563, 565–567, 569, 571, 572, 578, 581, 582, 605, 606, 608, 613, 614, 652, 653
Micro structures, 729, 746
Migration, 155, 156, 161, 277, 279, 280, 283, 284, 291, 293, 294, 298, 316, 318, 319, 329, 333, 339, 340, 419, 420, 435, 436, 453, 804, 830, 835, 844, 848, 873
Migration forms, 863, 865, 866, 870, 875
Mineral composition, 61, 67, 179, 182, 184–186, 222, 436, 438, 446, 447, 451, 519–522, 526, 531, 641, 785, 834, 850, 854, 857, 866, 868
Mineral metabolism, 808, 816
Mining activities, 848
Model experiments, 61
Modeling, 39, 41, 50, 60, 61, 66, 75, 109, 110, 115, 259, 263, 333, 436, 511, 831, 834, 835, 840, 864–867, 869–872, 875
Mold fungi, 619, 624, 633, 639, 646, 647, 649–651, 654
Morphogenesis, 740, 881, 882, 885–889
Morphology, 13, 15, 16, 28, 47, 111, 112, 122, 123, 126, 129, 208, 211, 213, 214, 217, 218, 221–223, 225, 231, 322, 330, 331, 341, 389, 402, 407, 420, 457, 458, 463, 468, 469, 504, 508, 519, 521, 531, 581, 585, 600, 620, 634, 657, 658, 661, 664, 676, 722, 732, 733, 738, 741, 744, 747, 748, 751, 754, 757, 760
Mycoremediation, 346
Mycorrhizal colonization, 383, 384, 389, 391

N

Nanocomposites, 23, 24, 26, 30, 31, 34, 629, 630, 636, 747, 748
Nanotubes, 23, 26, 33, 34
Nepheline-containing tailings, 563
Newly formed phases, 733, 841
New method, 175
Noble metals, 23, 35
Nomenclature, 261, 540, 564, 721, 722, 724, 726, 886
Non-carious lesions, 221, 222
Non-equimolar compounds, 695, 699, 703, 705, 712, 715, 716

O

Octacalcium phosphate, 10, 40, 52, 63, 65, 107, 108, 112–116
Odontoid, 227, 228, 230
Odontoma, 221–223, 227, 228–230, 231
OH radical, 612
Oil, 160, 161, 179, 182, 183, 185, 186, 188–192, 195–204, 364, 366, 461, 466, 486, 696
Optical microscopy, 72, 119, 122, 217, 221, 222, 231, 504, 519, 522, 785, 788
Optical petrology, 519

Organic acids, 24, 198, 291, 373, 430, 550–552, 563, 597, 601, 606, 687, 690, 696, 715, 766
Organic matter, 139, 156, 158, 159, 182, 200, 278, 281, 397, 401, 417–421, 423, 425, 427–431, 438, 444, 446, 452, 453, 457, 465, 470, 475, 476, 483, 485, 495, 550, 573, 659, 682, 684, 687, 690, 729, 730, 732, 733, 742, 743, 745, 747–751, 753–757, 759, 760, 843, 867
Ozone monitoring, 137

P

Pathogenic crystallization, 108
Peat deposit, 233, 234, 237, 242, 247, 252, 253, 277, 278, 281, 283–286, 290, 291, 293, 294
Peat processing, 240, 244
Phase composition, 112, 126, 128, 522, 619, 621, 623, 659, 661
Phase diagrams, 700, 702, 703, 705, 706
Phase equilibrium, 699
Photocatalytic activity, 149, 621, 623, 630, 636
Photocatalytic materials testing, 142
Physical-chemical model, 834
Physicochemical modeling, 259, 263, 865, 875
Phytotoxicity, 364
Pine derived biochar, 383
Polar regions, 605
Polymers, 8, 12, 14, 15, 18, 23, 26, 29, 30, 34, 35, 181, 574, 620
Polyphenols, 280, 283, 286, 293, 294, 335, 363, 364, 366, 376
Potentiometry, 122, 832
Precipitation method, 10, 107
Prokaryotic community structure, 401, 412

R

Racemates, 701–706, 714
Radiocarbon, 297–300, 308–312, 458, 461, 898
Recultivation, 437, 561, 562, 577
Renal stones, 115
Rock art, 519, 521, 522
Rock leaching, 524
Root growth, 383, 384, 387, 389, 390, 392
ROS, 607, 613

S

Salts, 41, 56, 59, 63, 64, 159, 475, 476, 489, 528, 539, 581, 730–732, 766, 798, 868
Scanning Electron Microscopy (SEM), 13, 14, 47, 111, 193, 207, 214, 221–224, 226, 231, 481, 506, 510, 511, 513, 522, 532, 535, 539–541, 553, 556, 583, 585, 588, 590–596, 598, 601, 602, 657, 658, 661–666, 676, 687, 688, 690, 731–733, 735–744
Siberia, 197, 200, 203, 277, 278, 280, 286, 291, 293, 294, 328, 436, 511, 519, 521, 522
Singlet oxygen, 137–148, 150, 623
Singlet oxygen gas analyzer, 137, 142, 623
Singlet oxygen monitoring, 143
Singlet oxygen sources, 138, 140, 141, 150
Smectite, 12, 158, 506, 508, 511, 730, 785, 791, 793, 795–799
Snow cover, 150, 297–306, 308–311, 318, 848
Soddy-eluvial-metamorphic soil (Stagnosol), 170
Soddy-podzol (Albic Podzol), 158
Soft biocides, 620
Soil chemistry, 389
Soil morphology, 466, 470, 496
Soils, 155–161, 169, 170, 173, 174, 176, 179–182, 184, 191, 260, 345–347, 349–353, 358–360, 364, 366, 372–375, 383–385, 395–398, 400, 401, 406, 408, 409, 411–415, 417–419, 421, 423, 425, 426, 428–431, 435–439, 442–444, 446–452, 457, 458, 464, 466, 467, 469, 470, 475–477, 481–483, 485–489, 491–498, 502, 549, 561, 563, 567, 568, 573, 577, 606, 608, 624, 639–641, 684, 847–849, 851, 852, 854, 856, 857, 859
Soil substrate, 346, 350, 354, 357–360
Sol-gel technology, 619–621
Solid solutions, 695, 699, 701, 705, 707–709, 712–715, 831
Solid-state ^{1}H NMR, 142, 425
Solutions, 4, 39, 41–47, 49–51, 53, 56, 60, 61, 63–65, 69, 75, 107, 109–111, 113–116, 120, 121, 131, 141, 157, 159, 160, 175, 201, 234, 235, 237, 239, 274, 339, 397, 436, 465, 466, 502, 522, 584, 640, 652, 676, 730,

746, 766, 767, 769, 772, 775, 779, 807, 832, 850, 867, 868
Space, 5, 6, 66, 98, 99, 122, 138, 161, 216, 262, 316, 461, 496, 504, 508–510, 513, 607, 608, 640–642, 646, 647, 649, 653, 654, 696, 708, 730, 731, 744, 766, 789, 791, 798, 834, 881–887, 889
Spherical aggregates, 657, 661, 662, 664, 665
Spring, 144, 146, 348, 355, 359, 360, 374, 463, 831, 832, 863, 865, 869–872, 874, 895
Sr/Ca ratio, 753, 759, 762
Stability of complexes, 777
Stabilization, 159, 417, 418, 421, 423, 425, 429–431, 483, 487, 640–642, 644, 731
Stomach model, 865
Stromatolite structures, 208, 209, 214, 216
Structural water, 80, 95, 100
Structure, 3–5, 8, 9, 13, 14, 17, 60, 79–83, 85–88, 90, 93–96, 98–104, 119, 120, 123–130, 133, 139, 142, 181, 196, 201, 209, 211, 213–218, 221, 222, 225, 230, 231, 233–235, 237, 239, 241, 242, 244–248, 252, 253, 262, 278, 283, 285, 288, 289, 291, 294, 316, 318, 319, 324, 335, 384, 395–397, 400, 401, 403–406, 408–415, 420, 423, 425, 435–439, 442, 443, 450, 452, 462, 477, 481–485, 488, 489, 491, 492, 495–498, 502, 505, 506, 519–523, 526, 527, 531, 535, 536, 538, 549, 558, 572, 600, 612, 621, 623, 627–630, 632, 634, 636, 640, 641, 659, 663–665, 677, 700–702, 704, 705, 708, 710, 712, 715, 722–724, 730, 735, 739, 740, 743, 744, 746, 749–751, 754, 767, 777, 791, 803, 830–832, 842, 849, 881–889
Struvite, 107–110, 112–116
Sub-micron fraction, 729, 731, 733, 734, 746
Supersaturation, 39, 53, 55, 59, 61–75, 109, 110, 599
Surface tension, 179, 180, 241, 244, 505
Suspended soils, 417–421, 423, 425, 428–431
Swamp, 237, 277–280, 282–294, 435, 437–439, 442–444, 446–452
Synthesis, 4, 25, 26, 29, 31, 81, 100, 102, 110, 111, 120, 121, 126, 131, 584, 585, 622, 658, 659, 663, 698, 699, 715, 716, 767, 868
Systems approach, 891

T
Tailings dump, 437–440, 442, 444–447, 449, 452
Tanzania, 669, 670, 691
Taxonomy, 425, 458, 466, 470, 482, 678, 681
Thermal effects, 93
Thermal treatment, 30, 93, 627, 631, 632, 796
Thermodynamic modeling, 41, 61, 62, 843, 863, 864, 866
Time, 17, 28, 39, 41, 43–47, 56, 63–65, 69–73, 96, 108, 109, 132, 138, 140, 145, 149, 150, 159, 179, 181, 182, 184–186, 189, 191, 192, 195, 200, 203, 204, 207–209, 211, 216, 222, 230, 231, 237, 240, 242, 243, 253, 262, 282, 283, 289, 291, 293, 317, 319, 324, 327, 330, 331, 333, 334, 339–342, 346, 390, 392, 409–411, 413, 414, 418, 429, 430, 435, 437, 450, 452, 457, 460–462, 464, 470, 495, 497, 520, 536, 537, 544, 545, 548, 552, 558, 563, 564, 566, 577, 585, 595, 599, 610, 613, 620, 621, 624, 629, 632–634, 636, 639, 640, 643, 644, 649, 666, 697, 698, 712, 729, 773–775, 798, 812, 831, 849, 864, 866, 873, 881–887, 889, 891, 894, 895, 897–901
TiO_2-coatings, 621, 632, 636
TiO_2 nanoparticles, 621, 630, 635, 636
Toxic element, 350, 354, 360, 820, 821
Transformation of Capsids, 724, 725
Tritium, 297–300, 304–310, 312
Trophic specialization, 749, 750, 759, 762
Tuff, 669–671, 673–678, 680–682, 684–690, 789–791
Tungsten deposits, 435

U
Ultraviolet irradiator, 652, 654
Umbric Albic Luvisols, 398, 400–404, 406–415
Urban soils, 351, 358, 395, 396, 415, 849

V
Verpa bohemica, 345, 347

VUV, 605–614

W
Wall cell, 607–612, 614, 664, 673
Water repellency, 181
Water-Soluble Fraction (WSF), 159–161, 163, 165, 166, 169, 171, 173, 175
Water spreading, 181
Weathering, 156, 161, 170, 259, 260, 451, 452, 457, 470, 476, 485, 489, 492, 494, 498, 501–504, 507, 511–513, 520, 521, 525, 526, 536, 538, 546, 548–550, 554, 832, 835, 897
Weddellite, 581, 582, 590–602
Wheat, 147, 148, 363–365, 368–376, 383, 384, 386, 389
Whewellite, 581, 582, 588, 590–601
Whitlockite, 83, 84, 93, 107, 108, 112, 113, 115, 116

X
X-ray computed microtomography, 221, 226, 227, 231
X-ray diffraction, 79, 93, 95, 104, 119, 121, 122, 182, 519, 521, 586, 601, 602, 630, 657, 660, 691, 701, 704, 708, 710, 711, 716, 799
XRD, 82, 83, 85, 121, 125, 128, 129, 133, 184, 506, 586, 592, 594, 595, 602, 627, 630, 658, 661, 754, 789, 791, 793–797, 799
Xylem transport, 335

Z
Zinc minerals, 661